The international journal of science / 13 August 2020

nature

GROUND CONTROL

Warming increases carbon release from tropical soils

States of mind
Tuning into the neural patterns that drive behaviour

Burning issue
Australia needs a national surveillance system to fight wildfires

Coronavirus
How effective are lockdowns and travel restrictions?

The international journal of science / 13 August 2020

nature

AIDS, malaria and tuberculosis are surging

Efforts to defeat the coronavirus have fuelled a rise in other infectious diseases. Urgent action is needed to avert a catastrophe.

AIDS, malaria and tuberculosis (TB), three of the deadliest infectious diseases, together kill 2.4 million people every year, with TB alone responsible for 1.5 million deaths. And deaths from these diseases could almost double over the next year, according to the Global Fund to Fight AIDS, Tuberculosis and Malaria, a consortium of donors that funds treatments. The reason: coronavirus. It's a horrifying prospect, and calls for an urgent action plan.

More than three months of lockdowns have prevented many people from accessing treatments for non-COVID infectious diseases; at the same time, new cases of these illnesses will have gone undetected. Although lockdowns are easing, it will take some time for health care to get back to normal, as authorities continue to prioritize COVID-19. Taken together, this is resulting in a surge of cases.

That's why there needs to be a step change in funding for AIDS, malaria and TB prevention, treatment and research, and greater public awareness of the rising threat posed by infectious diseases. And researchers – particularly epidemiologists – must continue to refine the models that are alerting the world to this approaching catastrophe.

One model, developed by researchers at the London School of Hygiene and Tropical Medicine, projects that there will be around 200,000 extra deaths from TB across China, India and South Africa between 2020 and 2024 (C. F. McQuaid *et al. Eur. Respir. J.* http://doi.org/d6ck; 2020). The data for AIDS and malaria are just as troubling. In 2018, nearly half a million people in sub-Saharan Africa died from AIDS-related illnesses. If access to antiretroviral therapies is disrupted for just six months, this number is projected to double in the coming year, according to modelling by the WHO and the Joint United Nations Programme on HIV/AIDS (UNAIDS) published in May, a high not seen in more than a decade.

A study by researchers at Nigeria's National Malaria Elimination Programme in Abuja and Imperial College London, published in *Nature Medicine,* predicts that 779,000 people are at risk of dying from malaria in sub-Saharan Africa in 2020 – more than double the number for 2019 (E. Sherrard-Smith *et al. Nature Med.* http://doi.org/d6cn; 2020). Researchers at the WHO reached a similar estimate. They modelled the impact of COVID-19 on malaria in 41 countries under 9 scenarios. The worst case – a continuing suspension of campaigns to distribute insecticide-treated bed nets, and a 75% drop in access to antimalarial drugs – would lead to 769,000 malaria deaths in sub-Saharan Africa this year, a mortality level not seen in 20 years.

> "COVID-19 has turned the clock back years, if not decades, in the fight against infectious diseases."

Right now, with the total number of COVID-19 infections approaching 20 million and deaths standing at more than 700,000, we can't say how bad the pandemic will get. But we can say that, without interventions, TB, AIDS and malaria are likely to take more lives.

Four proposals

Several things must now happen. First, hospitals and health authorities in affected cities and regions must recognize that AIDS, malaria and TB are surging again. In the case of TB, case detection – which has been affected by hospital testing facilities being diverted for COVID-19 – needs to be resumed quickly. It is possible for testing facilities to be shared for the two diseases. Some hospitals in the Asia–Pacific region are using the same equipment to run COVID-19 tests in the morning and TB tests in the afternoon – or vice versa. It is also possible to coordinate COVID-19 testing with rapid diagnostic testing for HIV and malaria.

Second, researchers must keep refining their models using more real-world data.

Third, there is a need for public-information campaigns. Public, private and non-governmental organizations must alert people to the risks of rising levels of infectious diseases. Such campaigns will also go some way towards reassuring existing patients, as well as those who become unwell, that they need to seek – or continue – treatment.

Fourth, these campaigns cannot on their own keep surgeries and wards open, or equipment functioning. The resurgence of infectious diseases has created a greater demand for tests, treatments and research. All of these need more funding. In a June report (go.nature.com/3aez6jd), the Global Fund calculated that an extra US$28.5 billion is needed to ensure that HIV, TB and malaria programmes can continue to function, and that researchers can continue to develop common diagnostic tools – especially for TB and COVID-19. And this is just for the next 12 months.

The Global Fund is confident it can access $6 billion of this sum, on top of its annual spending, but it cannot raise the rest alone. Some of the fund's largest international donors, such as the United Kingdom, are cutting back on science-aid funding.

If the usual channels for fundraising seem unlikely to deliver, alternative approaches should be tried, such as public events at which governments, companies and philanthropic organizations are invited to make funding pledges. The governments of richer countries do donate at such events, as seen in May, when a live COVID-19 donor conference organized by the European Union received €6.15 billion (US$7.2 billion) in pledges.

COVID-19 has turned the clock back years, if not decades, in the fight against infectious diseases. It is, of course, imperative that all measures possible are taken to protect people from coronavirus and to treat those who have become sick. But saving people from one infectious disease only to have them die of another is the last thing anyone wants.

A personal take on science and society

World view

NISREEN A. ALWAN

By Nisreen A. Alwan

A negative COVID-19 test does not mean recovery

Pandemic policy must include defining and measuring what we mean by mild infection.

Eight months into the global pandemic, we're still measuring its effects only in deaths. Non-hospitalized cases are loosely termed 'mild' and are not followed up. Recovery is implied by discharge from hospital or testing negative for the virus. Ill health in those classed as 'recovered' is going largely unmeasured. And, worldwide, millions of those still alive who got ill without being tested or hospitalized are simply not being counted.

Previously healthy people with persistent symptoms such as chest heaviness, breathlessness, muscle pains, palpitations and fatigue, which prevent them from resuming work or physical or caring activities, are still classed under the umbrella of 'mild COVID'. Data from a UK smartphone app for tracking symptoms suggests that at least one in ten of those reporting are ill for more than three weeks. Symptoms lasting several weeks and impairing a person's usual function should not be called mild.

Defining and measuring recovery from COVID-19 should be more sophisticated than checking for hospital discharge, or testing negative for active infection or positive for antibodies. Once recovery is defined, we can differentiate COVID that quickly goes away from the prolonged form.

I had COVID symptoms of fever, cough, gastrointestinal upset, chest and leg pains in late March. But at that time, non-hospitalized patients were not tested. Since then, I have had bad days with some symptoms, then OK days, then worse days of exhaustion, making me regret what I did on the OK days, such as taking a short walk.

This is a difficult time for me as a public-health academic engaged in pandemic action while struggling with this strange pattern of illness. I don't know what it means for my long-term health, which is concerning as a mother caring for young children.

One consolation is knowing that I am not alone. There are many others who have not regained their previous health, even months after their initial symptoms. Among them, fluctuating symptoms like mine are common.

Although clinicians and researchers have an idea of who is at increased risk of dying from COVID, we don't know who is more likely to experience prolonged ill health following symptomatic, or even asymptomatic, infection. The idea of accepting certain levels of infection to run through society, while protecting the vulnerable, becomes meaningless without considering health and productivity as outcomes alongside death.

Research that follows COVID patients after discharge from hospital is starting. But there is still a gap in quantifying and characterizing COVID-related illness in those not hospitalized. The consequences of failing to do so are significant. Some people, especially the young and healthy, might not see a need to follow preventive measures, because they expect only a few days of flu-like symptoms at the worst. Sick people might not get the support they need, and the true human and economic costs of the pandemic will not be correctly estimated.

As long as 'long COVID' is labelled as anecdotal, it will not be taken seriously, and public communication will neglect it. We need to quantify it properly and accurately. We must measure recovery in those not presenting with severe disease at the outset.

Let us start simple. With other common viral illnesses, such as flu, we would expect recovery to mean going back to pre-infection levels of functionality and quality of life. This means we must follow up all patients with confirmed (by test) or highly probable (by symptoms) COVID and find out whether they have returned to their previous normal within a specified time from the onset of their symptoms.

The 'recovery' definition must include duration, severity and fluctuation of symptoms, as well as functionality and quality of life. Everyone who is symptomatic would remain a 'case' until they fulfilled the recovery criteria or died. This is basic bread-and-butter epidemiology. We just need to apply it to this pandemic.

To do so, we must also define who had the infection in the first place. When testing is absent or inaccurate, physicians must be provided with universal and simple criteria for what constitutes clinical COVID. A good starting point are the studies characterizing typical symptoms on a population level.

Measuring recovery is not an easy ask with health and surveillance systems already struggling to cope. It makes sense to set up disease registers, akin to cancer registries, to track people over time and record their condition. This could be done through quick monthly, and subsequently annual, check-ups with health-care providers. If national registers are not quickly forthcoming, local ones could be started.

For surveillance, public-health agencies must prioritize agreement on criteria for a definition of recovery, and on the structures in which these criteria could be implemented. We must overlay research on surveillance with studies of the characteristics of those experiencing prolonged ill health. We must learn to identify and protect the most vulnerable.

The narrow narrative of death as the only bad outcome from COVID needs broadening to include people becoming less healthy, less capable, less productive and living with more pain. For that, we'll need better surveillance. The essential first step is getting clear and universal definitions for recovery and COVID severity.

> **"Once recovery is defined, we can differentiate COVID that quickly goes away from the prolonged form."**

Nisreen A. Alwan is an associate professor of public health at the University of Southampton, UK.
e-mail: n.a.alwan@soton.ac.uk

News in brief

Beirut blast among largest involving ammonium nitrate

An explosion in Beirut's port has killed at least 220 people, injured more than 5,000 and left an estimated 300,000 people homeless.

Lebanese authorities say that the explosion on 4 August was caused by 2,750 tonnes of ammonium nitrate, a chemical compound commonly used as an agricultural fertilizer, which had been stored for 6 years at a port warehouse. An investigation into what triggered the explosion is under way, and early reports suggest that it was probably a nearby fire.

The blast is one of the largest accidental ammonium nitrate explosions ever recorded (see 'Explosive chemical') – so powerful that it was heard more than 200 kilometres away in Cyprus.

Ammonium nitrate is cheap and usually safe to handle, but storing it can be a problem. Over time, it absorbs moisture and forms clumps. When a large quantity of compacted ammonium nitrate is exposed to intense heat, it can trigger an explosion.

The disaster comes as Lebanon is struggling to cope with the coronavirus pandemic and an economic crisis. Efforts to treat injured people have been hampered by damage to hospitals, and the explosion destroyed grain silos and much of Beirut's port.

EXPLOSIVE CHEMICAL

The Beirut blast, which killed at least 220 people and injured more than 5,000, is one of the largest industrial disasters ever linked to ammonium nitrate (NH_4NO_3).

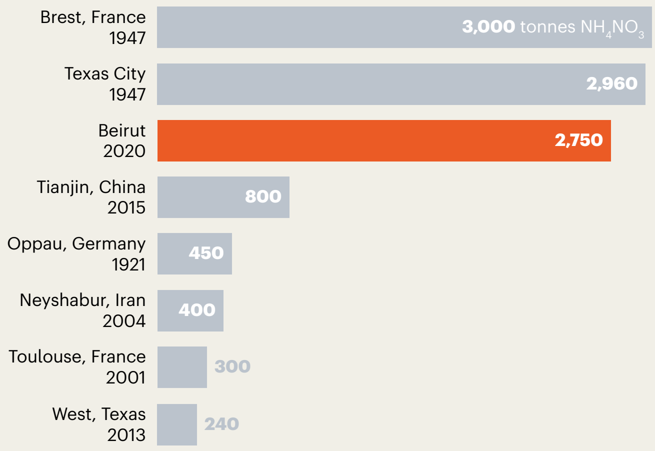

SOURCE: *NATURE* NEWS TEAM ANALYSIS; IMAGE: TOMOHIRO OHSUMI/GETTY

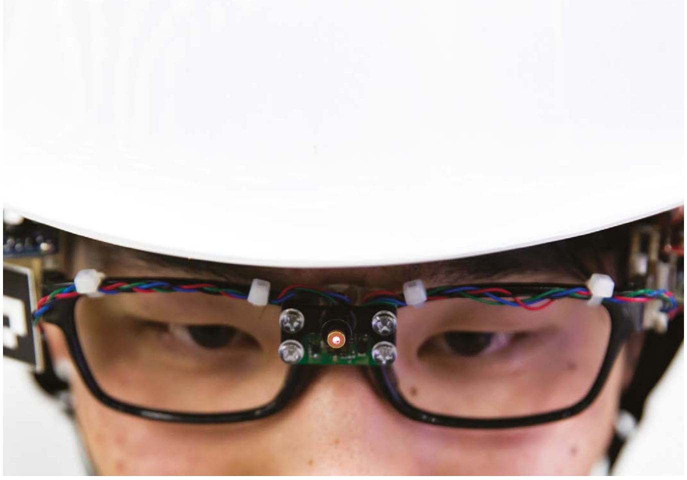

JAPAN CONSIDERS NEW RULES ON RESEARCH INTERFERENCE AMID US–CHINA TENSIONS

The Japanese government is considering tougher rules to address the risk of foreign interference in scientific research, such as more-thorough vetting of visa applications from international students and researchers, and requiring institutions to declare foreign sources of income.

Last month, Japan's cabinet approved an innovation strategy for 2020. This asks government agencies, research institutes and companies to strengthen codes of conduct around research integrity and conflicts of interest, and to prevent the outflow of sensitive research and technologies linked to national security, such as artificial intelligence and semiconductor manufacturing. It also proposes that government agencies consider withholding funding from institutions that fail to declare foreign income.

No countries are named by the strategy, but researchers say the government is concerned mainly with the activities of Chinese institutions, including those with ties to the military.

The government is now considering drawing up guidelines on these issues, says Takahiro Ueyama, an executive member of Japan's Council for Science, Technology and Innovation (CSTI), which is chaired by Prime Minister Shinzō Abe. "This is a very sensitive issue," Ueyama says.

The development follows crackdowns by US science agencies on researchers who do not disclose foreign ties, mainly with China. In the past two months, four ethnic Chinese researchers working in the United States have been charged with visa fraud for failing to declare links to China's military.

The Japanese government feels under pressure to strengthen its research-integrity guidelines and safeguard its scientific relationship with the United States, says Atsushi Sunami, a science-policy analyst at the National Graduate Institute for Policy Studies in Tokyo. "When the US and other Western countries started talking about these issues, it was natural that Japan would also address them more clearly."

The strategy's language mirrors that of a 2019 report by the science group JASON, which advises the US government. The report was commissioned by the US National Science Foundation over concerns about foreign governments acquiring US science and technology.

News in focus

PATRICK LANDMANN/SPL

Controlling deforestation (shown here, in a tropical rainforest in the Congo Basin) could decrease the risk of future pandemics, experts say.

WHY DEFORESTATION AND EXTINCTIONS MAKE PANDEMICS MORE LIKELY

Researchers are redoubling efforts to understand links between biodiversity and emerging diseases – and to use that information to predict and stop future outbreaks.

By Jeff Tollefson

As humans diminish biodiversity by cutting down forests and building more infrastructure, they're increasing the risk of pandemics of diseases such as COVID-19. Many ecologists have long suspected this, but a study now helps to reveal why. When some species are going extinct, those that tend to survive and thrive – rats and bats, for instance – are more likely to host potentially dangerous pathogens that can make the jump to humans.

The analysis of around 6,800 ecological communities on 6 continents adds to a growing body of evidence that connects trends in human development and biodiversity loss to disease outbreaks – but stops short of projecting where new disease outbreaks might occur.

"We've been warning about this for decades," says Kate Jones, an ecological modeller at University College London and an author of the study, published on 5 August in *Nature*[1]. "Nobody paid any attention."

Jones is one of a cadre of researchers that has long been delving into relationships between biodiversity, land use and emerging infectious diseases. Their work has mostly flown below the radar, but now, as the world reels from the COVID-19 pandemic, efforts to map risks in communities around the globe and to project where diseases are most likely to emerge are taking centre stage.

Last week, the Intergovernmental Science-Policy Platform on Biodiversity and Ecosystem Services (IPBES) hosted an online workshop on the nexus between biodiversity loss and emerging diseases. The organization's goal now is to produce an expert assessment of the science underlying that connection ahead of a United Nations summit that's planned for September in New York City, where governments are expected to make new commitments to preserve biodiversity.

Others are calling for a more wide-ranging course of action. On 24 July, an interdisciplinary group of scientists, including virologists, economists and ecologists, published an essay in *Science*[2] arguing that governments can help to reduce the risk of future pandemics by controlling deforestation and curbing the wildlife trade, which involves the sale and consumption of wild – and often rare – animals that can host dangerous pathogens.

Most efforts to prevent the spread of new diseases tend to focus on vaccine development, early diagnosis and containment, but that's like treating the symptoms without addressing the underlying cause, says Peter Daszak, a zoologist at the non-governmental organization EcoHealth Alliance in New York City, who chaired the IPBES workshop. He says COVID-19 has helped to clarify the need to investigate biodiversity's role in pathogen transmission.

The latest work by Jones's team bolsters the case for action, Daszak says. "We're looking for ways to shift behaviour that would directly benefit biodiversity and reduce health risks."

Concentrating risk

Previous research has shown that outbreaks of diseases such as severe acute respiratory syndrome (SARS) and bird influenza that cross over from animals to humans have increased in the past few decades[3,4]. This phenomenon is likely to be the direct result of increased contact between humans, wildlife and livestock, as people move into undeveloped areas. These interactions happen more frequently on the frontier of human expansion because of changes to the natural landscape and increased encounters with animals.

But a key question over the past decade has been whether the decline in biodiversity that inevitably accompanies human expansion on the rural frontier increases the pool of pathogens that can make the jump from animals to humans. Work by Jones and others[5] suggests that the answer in many cases is yes, because a loss of biodiversity usually results in a few species replacing many – and these species tend to be the ones hosting pathogens that can spread to humans.

For their latest analysis, Jones and her team compiled more than 3.2 million records from several hundred ecological studies at sites around the world, ranging from native forests to cropland to cities. They found that the populations of species known to host diseases transmissible to humans – including 143 mammals such as bats, rodents and various primates – increased as the landscape changed from natural to urban, and as biodiversity generally decreased.

"We've been warning about this for decades. Nobody paid any attention."

Some researchers urge caution when communicating that biodiversity hotspots are where outbreaks are likely to occur. "My worry, frankly, is that people are going to cut down the forests more if this is where they think the next pandemic is going to come from," says Dan Nepstad, a tropical ecologist and founder of the Earth Innovation Institute based in San Francisco, California, a non-profit organization that campaigns for sustainable development. Efforts to preserve biodiversity will work, he says, only if they address the economic and cultural factors that drive deforestation and the dependency of rural poor people on hunting and trading wild animals.

Ibrahima Socé Fall, an epidemiologist and head of emergency operations at the World Health Organization in Geneva, Switzerland, agrees that understanding the ecology – as well as the social and economic trends – of the rural frontier will be essential to projecting the risk of future disease outbreaks. "Sustainable development is crucial," he says. "If we continue to have this level of deforestation, disorganized mining and unplanned development, we are going to have more outbreaks."

Coordinating efforts

One message that the upcoming IPBES report is likely to deliver is that scientists and policymakers need to treat the rural frontier more holistically, addressing issues of public health, the environment and sustainable development in tandem. In the wake of the COVID-19 pandemic, many scientists and conservationists have emphasized curbing the wildlife trade – an industry worth an estimated US$20 billion annually in China, where the first coronavirus infections appeared. China has temporarily suspended its trade. But Daszak says the industry is just one piece of a larger puzzle that involves hunting, livestock, land use and ecology.

"Ecologists should be working with infectious-disease researchers, public-health workers and medics to track environmental change, assess the risk of pathogens crossing over and reduce risky human activities," he says.

Daszak was an author of last month's essay in *Science*, which argued that governments could substantially reduce the risk of future pandemics such as that of COVID-19 by investing in efforts to curb deforestation and the wildlife trade, as well as in efforts to monitor, prevent and control new virus outbreaks from wildlife and livestock. The team estimated that the cost of these actions would ring in at $22 billion to $33 billion annually. The total investment would be two orders of magnitude less than the $5.6-trillion price tag estimated for the COVID-19 pandemic, the team estimates.

Fall says the key is to align efforts by government and international agencies focused on public health, animal health, the environment and sustainable development.

With the right collaboration between human-health, animal-health and environmental authorities, Fall says, "you have some mechanisms for early warnings".

Wildlife markets such as this one in Bali, Indonesia, sustain the livelihoods of many people.

AMILIA ROSO/*THE SYDNEY MORNING HERALD* VIA GETTY

1. Gibb, R. *et al. Nature* https://doi.org/10.1038/s41586-020-2562-8 (2020).
2. Dobson, A. P. *et al. Science* **369**, 379–381 (2020).
3. Jones, K. E. *et al. Nature* **451**, 990–993 (2008).
4. Smith, K. F. *et al. J. R. Soc. Interface* **11**, 20140950 (2014).
5. Faust, C. L. *et al. Ecol. Lett.* **21**, 471–483 (2018).

YANG JIANZHENG/VCG VIA GETTY

Artificial intelligence is one of the areas that the US National Science Foundation will prioritize.

NSF'S COMMITMENT TO BASIC RESEARCH QUESTIONED

The US National Science Foundation shifts the focus of its graduate fellowships to computer science.

By Giuliana Viglione

The major US agency tasked with funding basic research, the National Science Foundation (NSF), raised alarm among scientists late last month when it updated the guidance for its prestigious graduate-student fellowships to emphasize research in three areas of applied computational science.

Critics fear that the new focus on artificial intelligence, computationally intensive research and quantum information science – despite the 70-year-old agency's historical mandate to promote and support all basic scientific research – will decrease money for fundamental science that can struggle to attract funding from other government or industry sources. They also fear that the changes could make it even harder for graduate students from under-represented groups – including white women and Black and Latinx scientists – to win these grants.

The change to the guidance for the Graduate Research Fellowship Program (GRFP) – which hands out hundreds of millions of dollars of research funding each year – comes amid concern in the United States about the growth of China as a research superpower.

It is just one of several recent efforts to steer the NSF towards applied-technology research that have concerned researchers. In late May, bills introduced to both houses of Congress with bipartisan support proposed to increase the NSF's budget by US$100 billion over 5 years. The bills, which have not yet been voted on, would rebrand the organization as the National Science and Technology Foundation, and would allocate the new money to technology development, rather than to basic science.

Fears for basic science

"The value of basic science is not always apparent to non-scientists," says Margaret Byron, a mechanical engineer at Pennsylvania State University in State College, who received the fellowship in 2012. "If there's pressure from those outside of science to push towards directions that have more immediate applications, then we need to push back."

The NSF said in both a public statement and an e-mail to *Nature* that the move is part of "a coordinated federal strategy to secure America's position as a global leader in research and innovation", but that the fellowship "will continue to encourage and accept applications in all eligible fields of science and engineering".

The agency awards around 2,000 graduate fellowships each year, and it requested just over $275 million for the programme in 2021. The fellowships, which fund master's or PhD students for 3 years, are typically awarded in 11 major fields of study, including engineering, life sciences and chemistry, but had previously not given preference to any particular subfields within these broad categories.

The new GRFP guidance says applications are "encouraged" in all disciplines supported by the NSF that incorporate the three new high-priority research areas.

The focus on three types of computer-based science is "kind of bonkers to me", says Michael Hoffman, who received the fellowship in 2003 and is now a computational biologist at the University of Toronto and the Princess Margaret Cancer Centre in Toronto, Canada. "These are focus areas that are already, right now, very well funded." The strength of the GRFP, he says, is that it trains scientists across a broad range of disciplines that are not typically funded by other agencies. That's important because "you can never predict which areas are going to have the really important discoveries", Hoffman says.

Twitter backlash

The changes prompted a backlash almost immediately, with scores of scientists expressing their discontent on Twitter. "These changes are incredibly restrictive and will almost certainly hurt bringing in bright and diverse students in the sciences broadly," wrote Alexandra Harmon-Threatt, a pollination ecologist at the University of Illinois at Urbana–Champaign. Amy Tarangelo, a cancer biologist at the University of Texas Southwestern Medical Center in Dallas, tweeted: "As a former fellow, I'm super disappointed in this decision from @NSFGRFP. GRFP should fund promising scientists in ALL fields without regard to the 'hot topic' of the moment. This will hurt students at unis without resources for high-level computing, etc."

Some welcome the move towards computer science, however. "I think the changes are important and reflect the country's need for more talents and advances in the fields," says Anh Nguyen, a machine-learning researcher at Auburn University in Alabama. These fields "have a strong potential to transform human lives" across a variety of disciplines, he says.

Still, the concentration of funding in certain fields without an expansion of the programme means that other areas – such as basic science – will be cut back, says Kelsey Lucas, a marine and aquatic comparative biomechanist at the University of Michigan in Ann Arbor, whose graduate work was supported by the GRFP. "By focusing on certain areas, that means other areas are going to be getting less funding."

In an e-mail to *Nature*, a spokesperson for the NSF wrote, "These changes are not intended to exclude any areas of science supported by NSF," and pointed to the advances in basic science that the NSF has funded over the past seven decades. "NSF is simply signifying that these are areas of national importance and we are encouraging students to apply." The spokesperson also said that the areas of emphasis would not change the review or selection process.

Diversity at risk

Nevertheless, scientists fear that the move could make it harder for certain people to win these prestigious grants – including Black and Latinx scientists.

"Frankly, I was disappointed," says Christian Cazares, a neuroscientist at the University of California, San Diego, and a current GRFP award recipient. He views the changes as "completely antithetical" to the NSF's stated commitment to promoting diversity in science. The lack of diversity in the three new priority fields – only 18.8% of US computer-science bachelor's degrees went to Black and Latinx students and 18.7% to women in 2016 – means that the move will perpetuate already-existing disparities, he says. (According to a 2014 review of the programme, between 1994 and 2004, about 80% of GRFP awards went to white applicants.)

Research has shown funding priorities to be one of the main drivers of inequity in grants awarded to Black scientists, says Alexandra Clark, a neuropsychologist at the University of California, San Diego. In 2019, a team at the US National Institutes of Health found that topic choice had the second-largest effect on the gap in award rates between white and Black researchers among proposals selected for discussion by reviewers (T. A. Hoppe *et al. Sci. Adv.* **5**, eaaw7238; 2019). "When we know there's an opportunity gap that's at play," Clark says, "we can't really just continue on like business as usual."

"Increasing diversity and inclusiveness is a top priority for the Director and NSF," wrote a spokesperson for the NSF in an e-mail to *Nature*, adding that the agency's director has established a task force to make recommendations for addressing barriers to inclusion.

Byron is hopeful that the changes will not significantly alter the GRFP selection process. But she does worry that students from under-represented backgrounds or lower-resourced schools will be dissuaded from applying because of the programme's new emphasis. "The last thing anybody wants to see is for a really stellar young scientist to look at this new solicitation and say, 'that's not me'."

There are growing concerns about ties between China's military and its universities.

AUSTRALIA'S PLAN TO END FOREIGN INTERFERENCE IN SCIENCE: DID IT WORK?

Pioneering guidelines aren't enough to prevent overseas militaries co-opting research, say experts.

By Dyani Lewis

Almost a year after Australia introduced a pioneering system for minimizing the risk of foreign interference in research – in particular, from overseas militaries – observers are divided about whether it is working.

The guidelines, which were introduced last November and are widely assumed to be a response to concerns about the Chinese military's ties to universities, encourage institutions to perform risk assessments on potential collaborators, communicate the risk of foreign interference to staff and bolster cybersecurity. They also urge universities to ensure that they comply with laws that restrict exports of certain technologies, such as those that have military uses.

Although other countries, including the United States, the United Kingdom and Japan, are grappling with similar concerns, Australia is the first to set such a specific set of guidelines for its universities.

But some specialists warn that Australia's guidelines and export laws aren't sufficient to help universities identify collaborations in which research could lead to military applications. Although the guidelines outline 'best practice' steps that universities could take to mitigate risks, the measures are optional, says Alex Joske, a China analyst at the Australian Strategic Policy Institute, a think tank in Canberra.

Others question whether universities are up to the task of scrutinizing international partners, particularly those in China. The guidelines are "basically saying, do due diligence on your partner in an opaque authoritarian political system", says Jeffrey Wilson, a political scientist at the think tank Perth USAsia Centre in Crawley, Australia. "You're asking people to do something no one can do, except maybe a spy agency," he says.

Others say the system is working well. James Laurenceson, director of the Australia–China Relations Institute at the University of Technology Sydney, says export controls on weapons and technologies that could have military uses, such as facial-recognition or cybersecurity software, reduce the risk of research being used by international armed

KEVIN FRAYER/GETTY

forces. He says this is the right approach — focusing on the research, rather than who the collaboration is with. "Fundamental questions about the science being conducted — I think they're more important ones for us to be asking," he says.

Research partners

On paper, China is Australia's biggest research partner. In 2019, Australian researchers co-authored close to 14,000 papers with authors who had affiliations in China, according to an analysis of papers indexed in the Scopus database (go.nature.com/3adyful). That's 16.2% of Australia's research output, more than for any other international partner nation (see 'Australia's top collaborators').

Fierce competition for limited government funds in Australia is driving collaborations, particularly with China, says Wilson, adding that this exacerbates the risk of interference. "One of the challenges for Australian universities is that they have been heavily incentivized to seek foreign research income," he says.

In most cases, research collaboration benefits all parties, says Yun Jiang, a geoeconomist at the Australian National University in Canberra. Problematic research is only a small part of research collaborations, she says.

But as China increases links between its civilian universities and the armed forces — a policy known as military–civil fusion — those links are becoming more difficult to identify, says Joske. Chinese universities, he says, "are more and more integrated with military assets, especially around research and development. They're working on classified projects and a lot of their graduates are going into the military or the defence industry."

Military ties

In 2019, Joske and his colleagues developed the China Defence Universities Tracker, which places Chinese institutions on a risk scale according to how closely they are associated with the military and whether they have been accused of or engaged in espionage and intellectual-property theft.

Ninety-two institutions — including 60 run by the People's Liberation Army or security and intelligence agencies, and 20 civilian universities — are rated as very high risk. A further 23 civilian universities are graded as high risk.

Joske is concerned about collaborations with universities in China that have military ties — and about how these should be policed. In his view, the Australian government should provide universities with information about which foreign institutions deserve more scrutiny, and should establish a national research-integrity office that can enforce existing national-security and export-control laws.

Some academics think that collaborations with military institutions should be ruled out entirely. "These universities are exceptionally important to the development of China's military technology," says Clive Hamilton, a public-policy researcher at Charles Sturt University in Canberra, who has investigated Chinese influence at Australian universities. "So why take the risk?"

The tracker also lists 12 state-owned defence-industry conglomerates, 4 of which have links to overseas universities.

One example of the kinds of relationship that are raising alarm is outlined by Joske in a 2019 report accompanying the tracker (see go.nature.com/3gjynsf). The report noted that one of those conglomerates, the Commercial Aircraft Corporation of China (COMAC), signed a memorandum of understanding with Monash University in Melbourne in May 2017 to design 3D-printed aircraft components. The collaboration will also fund a Aus$10-million (US$7-million) Aeronautical Research Centre that will be established at the university, a spokesperson from the university said.

> **"We want to be transparent. But how do you deal with that when your research partner is fundamentally not?"**

Joske says the collaboration is a cause for concern because, last year, the cybersecurity company CrowdStrike in Sunnyvale, California, accused COMAC of using technology stolen through cyberespionage from rival airlines to design its C919 commercial aircraft, which could be converted into a military surveillance aircraft.

AUSTRALIA'S TOP COLLABORATORS

Last year, researchers in Australia co-authored almost 14,000 papers with people at Chinese institutions — more than with any other country.

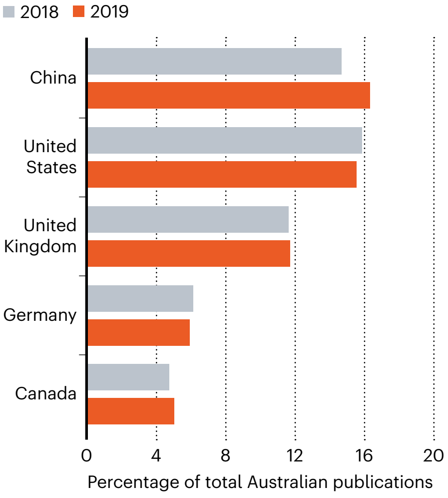

SOURCE: J. LAURENCESON & M. ZHOU *THE AUSTRALIA-CHINA SCIENCE BOOM* HTTPS://GO.NATURE.COM/3ADYFUL (2020)

COMAC did not respond to *Nature*'s questions about the allegations.

But the university defended the partnership, saying it followed the Australian Code for the Responsible Conduct of Research and the university's own policies and procedures. "The university regularly monitors advice provided by the government, intelligence agencies and the wider education sector, and acts in accordance with advice received," the spokesperson said.

Group of Eight

Several Australian institutions have made changes in response to the guidelines produced last year. *Nature* contacted the 'Group of Eight' leading research universities, and of the seven that responded, five said they had introduced new processes or were deciding whether to do so.

But some experts think that more needs to be done. The guidelines recommend that foreign affiliations and funding be recorded. Hamilton says universities should go a step further, and make these registers public. "Transparency must be priority number one," he says. "Australian universities are public institutions, and I can see no reason why the public should not be permitted to know the affiliations and financial links academics may have with other organizations, at home or abroad," he says.

And he says the universities should take a hard line with researchers who fail to disclose foreign ties, including firing them in some cases. The government should also be stricter with universities, says Hamilton: "Universities that fail to heed government rules and guidelines concerning research links that jeopardize national security should be excluded from receiving funding from the Australian Research Council."

Limits to transparency

In the United States, funding agencies have alerted institutions to grant recipients with potential undisclosed foreign ties. Investigations have led to dozens of researchers being sacked or forced to give back research funding.

But transparency has its limits, says Wilson. "We want to be transparent. But how do you deal with that when your research partner is fundamentally not?" he asks. Although information on connections to the military is openly available in some instances, he says, it could easily be hidden.

In June, the Australian government announced that it had created a new integrity unit to identify and analyse emerging threats to the quality of higher education, and to assist universities in addressing foreign-interference threats. Joske says it's a positive move, but it will take time to prove that it is working.

Q&A

THOMAS HENRIKSON

Pioneering research director: 'We're in a cataclysmic time of change'

Rita Colwell is the former director of the US National Science Foundation (NSF) — the first woman to hold that post — and a leader in cholera research. In her new book, *A Lab of One's Own: One Woman's Personal Journey Through Sexism in Science* (written with Sharon Bertsch McGrayne), she opens up on one topic she hasn't said much about publicly: her battle to improve the situation for women in science. Colwell, a microbiologist at the University of Maryland College Park, spoke to *Nature* about discrimination, and how her experiences as a researcher and agency leader during the 2001 anthrax bioterror attacks can inform the response to the coronavirus pandemic.

You've been a scientist since the 1950s. What's changed, and what hasn't, regarding sexism in science?
When I was an undergraduate, I went to the department chair to ask for a fellowship to allow me to pursue a master's degree. He told me, quite bluntly, that they didn't waste fellowships on women. I don't think any chair, dean or faculty member would say that today. It would probably be nuanced, to the effect of, "We don't have any available." That makes it less obvious, and I'm not so sure less hurtful — because it still deflects the career path.

What do you want early-career female scientists to take away from your book?
That you're not alone. Your experiences that you endure are shared. Like other women, I assumed the problems I have had were some sort of problem of mine. But in fact, it's really the system.

What should institutions do to improve the situation for women?
Agencies, particularly funding agencies, can have a tremendous effect. The NSF has really been a leader, tracing back to when Mary Clutter, who was an assistant director, forcibly mandated [in 1989] that committees and scientific meetings that received funding had to have female representatives on the committee and female speakers at the meeting.

Racism in science is also deeply entrenched. Why is it important to change that?
There's tremendous talent distributed throughout the population, and the country needs all of it. It's really important to draw from 100% of the population — and not 50% or less. The challenges we're facing right now are huge. We're in one of the cataclysmic times of change.

Protests have erupted in the United States over racism and COVID-19 shutdowns.

FREDERIC J. BROWN/AFP/GETTY

In 2001, you helped to hunt down the source of the US anthrax attacks. What lessons from that could help scientists investigating COVID-19?
The anthrax episode was a fantastic experience showing patriotic cooperation among agencies and among branches of Congress. Because I was director of the NSF, I was able to have a leadership role, and because I was a microbiologist, I was poised to recognize immediately that we had to sequence the bacterium that had been sent out as a bioweapon. The group met every week for an hour in a classified meeting. We had maybe 16 or 17 agencies represented.

The lesson was collaboration and cooperation. No single agency could solve the problem. There was shared trust and shared commitment, and no politics in any of our decisions. If we had been able to have an inter-agency, intergovernmental interaction straight away in January or February, I think we would not have 150,000 COVID-19 deaths — and climbing — in the United States.

How has your laboratory changed its emphasis in response to COVID-19?
I have been working on cholera for my entire career. It is an aquatic bacterium distributed in the environment. Twenty years ago, we developed the use of satellite sensing to monitor environmental parameters that allowed us to track and predict cholera outbreaks. We're modifying that model for COVID. It's very interdisciplinary. That's the power of understanding diversity — human, as well as environmental — and protecting both.

What role should international scientific collaboration have in fighting the pandemic?
Diseases don't carry passports, and they don't behave like tourists clearing the border. It's almost anti-human not to understand that we are a global society, and that the benefit of science — for example, vaccines — needs to be shared. And it needs to be shared empathetically in a way that makes it affordable for the poorest citizens of the world.

Interview by Alexandra Witze
This interview has been edited for length and clarity.

ILLUSTRATION BY KAROL BANACH

WHAT ANIMALS REALLY THINK

Neuroscientists are scrutinizing mountains of data to uncover how brains create emotions and other internal states, such as aggression or desire. **By Alison Abbott**

Two years ago, Jennifer Li and Drew Robson were trawling through terabytes of data from a zebrafish-brain experiment when they came across a handful of cells that seemed to be psychic.

The two neuroscientists had planned to map brain activity while zebrafish larvae were hunting for food, and to see how the neural chatter changed. It was their first major test of a technological platform they had built at Harvard University in Cambridge, Massachusetts. The platform allowed them to view every cell in the larvae's brains while the creatures — barely the size of an eyelash — swam freely in a 35-millimetre-diameter dish of water, snacking on their microscopic prey.

Out of the scientists' mountain of data emerged a handful of neurons that predicted when a larva was next going to catch and swallow a morsel. Some of these neurons even became activated many seconds before the larva fixed its eyes on the prey[1].

Something else was strange. Looking in more detail at the data, the researchers realized that the 'psychic' cells were active for an unusually long time — not seconds, as is typical for most neurons, but many minutes. In fact, more or less the duration of the larvae's hunting bouts.

"It was spooky," says Li. "None of it made sense."

Li and Robson turned to the literature and slowly realized that the cells must be setting an overall 'brain state' — a pattern of prolonged brain activity that primed the larvae to engage with the food in front of them. The pair learnt that, in the past few years, other scientists using various approaches and different species had also found internal brain states that alter how an animal behaves, even when nothing has changed in its external environment.

Some, such as Li and Robson, had come to the discovery serendipitously while trudging through their own brain-wide data. Others have hypothesized that neurons coding for internal brain states must exist, and have actively sought them in discrete and well-researched brain regions. For example, earlier this year[2], neurobiologist David Anderson at the California Institute of Technology (Caltech) in Pasadena and his colleagues identified an internal brain state — represented by a small network of neurons — that prepares fruit flies to engage in courtship or fighting behaviours.

Neuroscientists wanting to understand the brain's coding language have conventionally studied how its networks of cells respond to sensory information and how they generate behaviour, such as movement or speech. But they couldn't look in detail at the important bit in between — the vast quantities of neuronal activity that conceal patterns representing the animal's mood or desires, and which help it to calibrate its behaviour. Even just a few years ago, measuring the activities of specific networks that underlie internal brain states was impossible.

A slew of new techniques is starting to change that. These methods allow scientists to track electrical activity in the brain in unprecedented detail, to quantify an animal's natural behaviour on millisecond timescales, and to find patterns in the mountains of data these experiments generate. These patterns could be signatures of the innumerable internal states that a brain can adopt. Now the challenge is to find out what these states mean.

Some neuroscientists are daring to wield the technologies to probe one powerful group of internal brain states: emotions. Others are applying them to states such as motivation, or existential drives such as thirst. Researchers are even finding signatures of states in their data for which they have no vocabulary.

The current trickle of research papers on internal brain states is gaining momentum. The work might even have potential clinical applications. "Mental illness is essentially disruption of internal states," says Joshua Gordon, director of the US National Institute of Mental Health in Bethesda, Maryland. "They need to be understood."

Frames of mind

The brain of any animal is constantly bombarded with information about the creature's environment from sensory organs such as the eyes, ears, nose or skin. All of this information is initially processed in the brain's sensory cortex. Then come more mysterious processing steps, in which that information is filtered through multiple internal brain states representing the creature's constantly changing moods and needs. That finally leads the motor cortex to generate movements that are appropriate to the circumstances — to flap away a tickling fly, for example, or to move towards a tasty treat. Internal states can also be generated entirely in the brain, without sensory input and without a behavioural output: think of daydreaming, or replaying the events of the day in your mind.

Over the past few years, insights into the nature of internal states are changing how neuroscientists who study brain networks think about animal behaviour. “We used to think of animals as being kind of stimulus-response machines,” says neuroscientist Anne Churchland at Cold Spring Harbor Laboratory, New York. “Now we’re starting to realize that all kinds of really interesting stuff is being generated within their brains that changes the way that sensory inputs are processed — and so changes the animals’ behavioural output.”

Sketching out how to study this intriguing middle ground has long been a preoccupation for Anderson. Six years ago, he decided to create a theoretical framework for research into internal brain states that represent emotion. He was irked by the view of some psychologists, who think that because animals can’t express their feelings in words, those feelings can’t be studied at all. Together with his Caltech colleague Ralph Adolphs, Anderson developed and published a hypothesis[3] about the characteristics that neural circuits associated with internal brain states should have.

Most importantly, they thought, an internal brain state should outlast the original stimulus that triggered it. So a key feature of a neural circuit underpinning such a state would be its persistence, he says. “If you are hiking in mountains and see a snake, then you might jump in fear,” says Anderson. “Ten minutes later, your brain’s internal state of fear is still active, so when you see a stick on your path you might jump again.”

Other characteristics of internal states should include generalizability, meaning that different stimuli should be able to prompt the same state, and scalability, in which different stimuli can create states of different strength. The paper became influential. Li says that it “was inspirational” as she and Robson were trying to make sense of their psychic cells.

Anderson and Adolphs published their paper in 2014, just as a raft of neurotechnologies was starting to make the necessary experiments feasible. It was already possible to record from large numbers of individual neurons at the same time, and since then the technologies have improved and expanded remarkably, allowing scientists to analyse previously inaccessible activity.

Leading the pack is the Neuropixels probe, just 10 mm long, which can directly record activity in hundreds of neurons across different brain areas[4]. And special imaging techniques can indicate where as many as tens of thousands of individual neurons are active across the brain. In calcium imaging, for instance, animals are genetically engineered to express a molecule in their cells that detects calcium ions — when these pour into a neuron as it fires, the molecule fluoresces.

New automatic behaviour monitors take video recordings of freely behaving animals over many hours, and analyse every movement in millisecond elements. The elements can then be aligned with neural recordings, matching moment-to-moment brain activity with specific movements.

Neuroscientists have capitalized on a surge in machine learning, artificial intelligence and new mathematical tools to make sense of the gigabytes or terabytes of data that any experiment with these technologies can generate, and to coax out the neural activation patterns that could represent internal brain states.

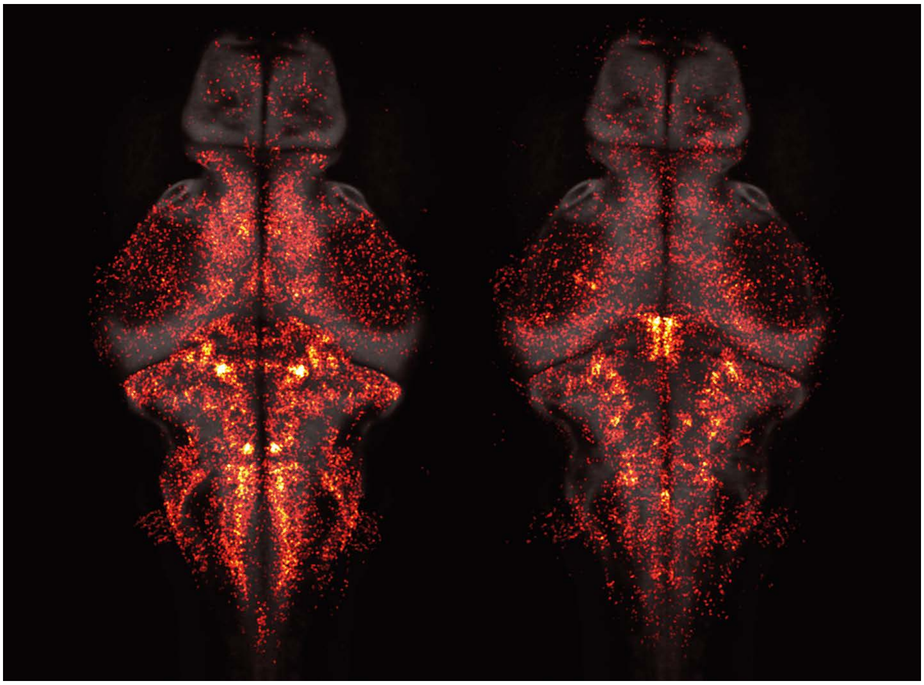

J. C. MARQUES *ET AL./NATURE* (REF. 1)

Distinct groups of neurons control whether zebrafish larvae explore (right) or stay put (left).

Ready to engage

For his first study of an internal state, Anderson decided to build on his laboratory’s previous interest in aggression in the fruit fly, which has a tiny brain containing about 100,000 neurons. In many animal species, males start to fight each other in the presence of females — a well-established behaviour that Anderson calls the ‘Helen of Troy effect’, after the Greek myth about a woman whose competing suitors started a war. Fruit flies are no exception: indirect evidence suggests that exposure to females causes males to engage in both courtship songs and aggressive behaviour towards other males for many minutes. “That’s a long time in the short life of a fruit fly,” he says.

He decided to search for neural activity that correlated with the persistent courtship and fighting behaviours that are initiated by neurons known as P1, found in a region that controls such social behaviours. These neurons fire so quickly that they alone couldn’t be responsible for maintaining an internal state. Using imaging techniques along with automated behavioural analysis, his group identified cells in other brain areas that become active as a consequence of P1 activation.

Most of these ‘follower cells’ switched quickly on and off, but a cluster called pCd neurons stayed active for many minutes. When the researchers inserted a light-sensitive protein into these cells and switched them off using a flash from a laser, the persistent effect of P1 activation on behaviour disappeared. When they activated them directly, bypassing P1, nothing happened: the pCd neurons needed P1 as a trigger and, once sparked into action, they stayed on for much longer than the initial prompt[2]. If Anderson had to give the state a name, he might call it the ‘ready-to-engage-in-these-social-behaviours’ state, he says.

His team has conducted a similar experiment in mice[5], which have more complex brains containing about 100 million neurons. The researchers found a particular group of neurons in the hypothalamus that, just like the pCd neurons, became persistently activated in association with an innate drive — this time, fear. When the scientists placed a rat close to experimental mice for just a few seconds, the mice responded defensively by hugging the wall for several minutes and the group of neurons remained active for all this time. When the team again used light to switch the neurons on and off, the wall-hugging behaviour came and went in tandem, even with no rat present.

Neuroscientists are now discovering other groups of neurons with persistent activity in different brain areas. Using calcium imaging in mice, Andreas Lüthi at the Friedrich Miescher Institute for Biomedical Research in Basel, Switzerland, and Jan Gründemann at the University of Basel searched in the amygdala, which is central to the regulation of a range of emotions and behaviours. The team found two different populations of neurons that displayed sustained but opposing activation when the mice switched between two distinct behaviours[6] – exploring the environment and performing defensive behaviours such as freezing.

Gründemann acknowledges that the amygdala cells are unlikely to be working in isolation, and that cells across the whole brain are involved in maintaining the explorative or defensive states. “I’m sure it is just one node in larger, brain-wide networks,” he says.

The whole picture

Whereas many researchers have searched particular brain areas for neurons that have enduring activity, Li and Robson, who moved to Germany last September to jointly run a lab at the Max Planck Institute for Biological Cybernetics in Tübingen, came across their persistently active neurons almost by chance.

Their zebrafish larvae are less complex than fruit flies, having only 80,000 or so brain cells. Because these baby fish are transparent, the activity of nearly all of their neurons can be monitored simultaneously using calcium imaging.

The pair has developed a method of concurrently following both the movements and the neural activity as fish larvae swim freely around a dish. They deploy a fluorescent-microscope tracking system that moves on its imaging platform to keep the fish in constant view, and captures every flash of each neuron as the larvae move. The system also films them – typically for 90 minutes, generating 4.5 terabytes of data – allowing the experimenters to align movement with neuronal activity second by second.

Fish larvae might not seem to have the rich internal life enjoyed by mice, or even flies, but they have at least one robust behavioural choice to make in their lives – whether to hunt locally, or to swim to unfamiliar waters to search for new food sources. When Li and Robson watched larvae making this choice, they found three groups of neurons: one that was persistently active during local hunting, another that stayed active during exploration and a third that flashed on briefly as the fish switched states[1]. Surprisingly, hunger didn’t seem to influence the states, which switched automatically every few minutes – “just like our own sleep–wake states switch automatically, but on a much shorter timescale”, Robson says.

Neuroscientists working with more complex organisms can’t monitor the whole brain at once, but they have been able to find hints of internal brain states with networks that are widely distributed in the brain. In technically challenging experiments in mice, they have recorded the activity of thousands of neurons throughout the brain using calcium imaging, and of hundreds of neurons using a single Neuropixels electrode, several of which can be inserted at once.

In a study published last year[7], neuroscientist Karl Deisseroth at Stanford University in California and his team used Neuropixels probes to record the activity of 24,000 neurons across 34 cortical and subcortical brain regions in thirsty mice that were licking water from a spout. The scientists were able to tease out signals related to the brain state of thirst from signals related to licking behaviour. They found that these state-signalling neurons were activated throughout the brain – not just in the hypothalamus, where dedicated thirst neurons are located.

Using these extensive recording techniques, neuroscientists are finding that there is a lot going on beneath the surface when an animal performs a task – and not all of it seems relevant at first glance. In landmark papers last year, groups led by Kenneth Harris at University College London and by Churchland showed that when a mouse is engaged in a task, neurons activate throughout the brain, but that a large proportion of the activation is not correlated with the task at all[8,9]. Some activity correlated instead with the animals’ fidgety movements. But around two-thirds of the off-task activation didn’t tally with any movement or action. “Part of this may be related to internal brain states,” says Harris.

> “MENTAL ILLNESS IS ESSENTIALLY DISRUPTION OF INTERNAL STATES. THEY NEED TO BE UNDERSTOOD.”

Busy brain

Many neuroscientists say that the sheer volume of data pouring out of whole-brain experiments is also the field’s biggest bottleneck. But they have been making progress in developing techniques to sift through the flood of measurements. One popular approach is to use a mathematical method called the hidden Markov model (HMM) to predict the probability that a system will switch between different states at a particular time.

Mala Murthy at Princeton University, New Jersey, and her colleagues used the HMM to discover rhythms in the brains of male fruit flies[10] that influenced their choice of song pattern when courting females. Whether male flies choose on a moment-to-moment basis to sing in staccato pulses or longer hums depends in large part – but not totally – on how the females respond to them. Murthy’s group found that three different internal brain states also affected the male’s song choice. They dubbed the fly dispositions Close, Chasing and Whatever.

No matter the complexity of the model organism that individual researchers have adopted – worm, fish, fly or mouse – the question of how the entire brain coordinates internal states “is what we are all starting to think about”, says Steve Flavell at the Massachusetts Institute of Technology in Cambridge. In 2013, Flavell and his colleagues discovered that even the brain of the *Caenorhabditis elegans* worm, which has only 302 neurons, displays properties of internal brain states that drive particular behaviours, including two sets of persistently active neurons controlling whether the animal lingers locally or moves with purpose[11]. His group has since identified the full circuitry involved in the two states and switching between them[12].

Aside from their questions about the basic biology, researchers have an eye on the clinical benefit of understanding how a particular state manifests in the brain. Those studying pain in rodent models, for instance, rely on standard tests such as observing when a rat lifts its paw from a hot plate. “That movement reflects protective aspects of pain, but not the actual perception of pain,” says neurologist Clifford Woolf at the Boston Children’s Hospital in Massachusetts. That makes it a poor model for pain, he argues, because it is one step removed from the actual sensation. He has launched a research programme to try to directly read brain signals that indicate the internal state of pain perception – potentially a more timely and specific readout than waiting for the animal’s response. “I’m extremely optimistic that we’re in one of those rare stages in science where this is going to be a transformation of the way we do things,” he says.

In this new field, even the basics are up for grabs, says Li. “At this stage, we are still trying to understand what the questions are.”

Alison Abbott is a writer based in Munich, Germany.

1. Marques, J. C., Li, M., Schaak, D., Robson, D. N. & Li, J. M. *Nature* **577**, 239–243 (2020).
2. Jung, Y. *et al. Neuron* **105**, 322–333 (2020).
3. Anderson, D. J. & Adolphs, R. *Cell* **157**, 187–200 (2014).
4. Jun, J. J. *et al. Nature* **551**, 232–236 (2017).
5. Kennedy, A., Kunwar, P. S., Li, L., Wagenaar, D. & Anderson, D. J. Preprint at bioRxiv https://doi.org/10.1101/805317 (2020).
6. Gründemann, J. *et al. Science* **364**, eaav8736 (2019).
7. Allen, W. E. *et al. Science* **364**, eaav3932 (2019).
8. Stringer, C. *et al. Science* **364**, eaav7893 (2019).
9. Musall, S., Kaufman, M. T., Juavinett, A. L., Gluf, S. & Churchland, A. K. *Nature Neurosci.* **22**, 1677–1686 (2019).
10. Calhoun, A. J., Pillow, J. W. & Murthy, M. *Nature Neurosci.* **22**, 2040–2049 (2019).
11. Flavell, S. W. *et al. Cell* **154**, 1023–1035 (2013).
12. Cermak, N. *et al. eLife* **9**, e57093 (2020).

Books & arts

Crunch, rip, freeze or decay — how will it all end?

Astrophysicist Katie Mack's book explores all the ways the Universe could destroy itself. **By Ramin Skibba**

Scientists know how the world will end. The Sun will run out of fuel and enter its red-giant phase. Its final burst of glory will expand and engulf the closest planets, leaving Earth a charred, lifeless rock. Our planet has around five billion years left.

With this grim image, theoretical astrophysicist Katie Mack begins her book on the end of the Universe — a much more uncertain prospect. Cosmologists generally look backwards, because all the evidence they can examine with telescopes is far away and concerns things that happened long ago. Using the motions of distant stars and galaxies to predict possible futures involves more speculation.

In Mack's hands, this speculation makes for a fascinating story. Humans are, she writes, "a species poised between an awareness of our ultimate insignificance and an ability to reach far beyond our mundane lives, into the void, to solve the most fundamental mysteries of the cosmos". She is a talented communicator of complex physics, and the passion and curiosity about astronomy that have made her a popular speaker and Twitter presence are evident here. (As are some nerdy jokes and a less compelling coda about new physics research tangential to the central theme.)

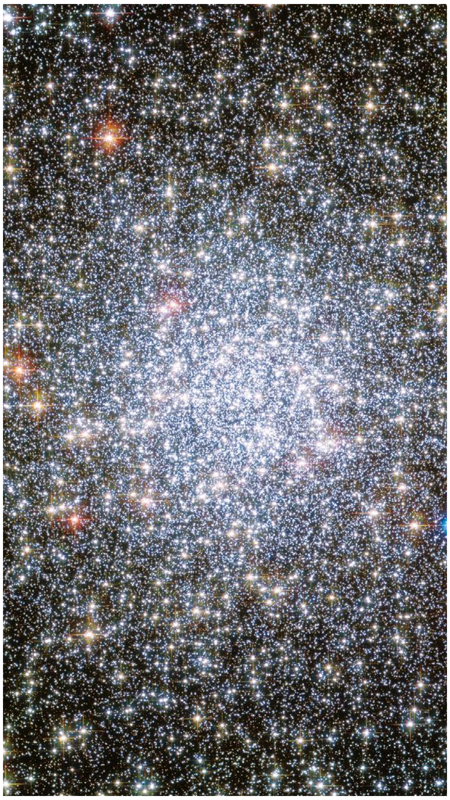

NASA/ESA

The Universe is expanding — for now.

Mack begins at the beginning, with the Big Bang. What followed was inflation — a period of rapid expansion. Then, structures of dark matter formed and the building blocks of stars, planets, life and galaxies assembled. Currently, dark energy, thought to pervade the Universe, somehow counteracts the forces of gravity to keep driving expansion.

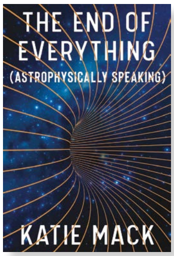

The End of Everything (Astrophysically Speaking)
Katie Mack
Scribner (2020)

The Universe's fate depends on whether that expansion will continue, accelerate or reverse.

Astrophysicists long considered the most likely denouement to be a reversal of the Big Bang — the Big Crunch. Outside our cosmic neighbourhood, every galaxy is zooming away from us; a clear sign of expansion. If the Universe holds enough matter, including dark matter, the combined gravitational attraction of everything will gradually halt this expansion and precipitate the ultimate collapse. Over time, galaxies, then individual stars, will smash into each other more frequently, killing off any life on nearby planets. In the final moments, as densities and temperatures soar in a contracting inferno, all that remains will extinguish in a single point.

But dark energy might mean that a different end awaits. The early years of the Universe's evolution were determined by the amount of matter it held; over the past few billion years, dark energy has begun to dominate, pushing the universe outwards. Current data from the European Space Agency's Planck telescope and other sources are consistent with this expansion continuing forever.

Called the Heat Death or Big Freeze, this apocalypse will be "slow and agonizing", Mack writes. In thermodynamic terms, she explains, the Universe will approach a state of minimum temperature and maximum entropy. As everything gets farther and farther apart, the material of dead stars will disperse so that new stars can't form, and the galaxies they're part of will gradually stop growing. It's like a suffocation of all astrophysical activity, as the fuel for growth and reproduction becomes so diffuse as to be unusable. It is an end "marked by increasing isolation, inexorable decay, and an eons-long fade into darkness".

The third demise that Mack discusses is the Big Rip. This is in store if dark energy accelerates expansion even more than is currently expected. As the Universe balloons, eventually, gravitational forces won't be able to keep galactic clusters together. Stars will be stripped away from each other, and solar systems such as ours won't have the strength to stay together. The remaining stars and planets will explode. Finally, the last atoms will be ripped apart.

The latest measurements point to a Heat Death, but a Big Crunch or Big Rip are within their uncertainties.

The final doomsday scenario that Mack describes is extremely unlikely: vacuum decay. A tiny bubble of 'true vacuum' could form, owing to instability in the field associated with the Higgs boson. That might happen if, say, a black hole evaporates in just the wrong way. Such a bubble would expand at the speed of light, destroying everything, until it cancels the universe. Vacuum decay might already have begun in some distant place. We won't see it coming.

Not to worry, though. As Mack counsels, whatever it looks like, the end probably won't be nigh for at least 200 billion years.

Ramin Skibba is an astrophysicist turned science writer based in San Diego, California.
e-mail: raminskibba@gmail.com

Readers respond

Correspondence

COVID-19: time to re-imagine academic publishing

High-profile retractions have highlighted how the conventional model of academic publishing has struggled to keep pace with the race to understand the new coronavirus, SARS-CoV-2. The system is ripe for innovation. To that end, an open-access overlay journal known as *Rapid Reviews: COVID-19* (*RR:C19*; see go.nature.com/3fufauw) uses the speed of technology to democratize the review process and strengthen the quality of research.

RR:C19 was launched this year by the MIT Press and the University of California, Berkeley, with support from the Patrick J. McGovern Foundation. Scientists, publishers and philanthropic foundations work together to swiftly deploy new models for digitally enabled publishing. The journal promotes rapid and transparent peer review of promising or controversial preprints, as well as dynamic curation of content (see B. M. Stern and E. K. O'Shea *PLoS Biol.* **17**, e3000116; 2019).

Philanthropic foundations have been leaders in funding risky scientific ventures. In our experience, extending that support to advance the publishing process will boost the quality of research and accelerate its dissemination.

Vilas Dhar* Patrick J. McGovern Foundation, Boston, Massachusetts, USA.

Amy Brand* The MIT Press, Cambridge, Massachusetts, USA.
amybrand@mit.edu

*V.D. and A.B declare competing interests; see go.nature.com/2xajnzt

COVID-19: indexed data speed up solutions

Since the COVID-19 pandemic began, cross-disciplinary data sets for the virus have been proliferating daily. However, these can be difficult for researchers to find, link to and reuse — for example, if they want to explore new hypotheses or to test existing ones. To this end, we have developed the COVID-19 Data Index (www.covid19dataindex.org).

Originally funded by the US National Institutes of Health as part of the Big Data to Knowledge project, the index hosts a metadata catalogue of COVID-19 data sets.

These range from, for example, clinical, sociodemographic, environmental, economic and mobility data to case statistics and genomic sequences. These data are collected from large repositories, research papers and individual online sources, among others. Users can filter search results by type ('-omics' data versus clinical data, for instance), repository or geographic location. The index then supplies links to the original data and the download page.

We update the COVID-19 Data Index daily. Finding data on COVID-19 is no longer an obstacle that could delay discoveries.

Lucila Ohno-Machado* University of California, San Diego, La Jolla, California, USA.
lohnomachado@health.ucsd.edu

Hua Xu The University of Texas Health Science Center at Houston, Texas, USA.

*L.O.-M. declares competing interests; see go.nature.com3gfcgv

Denmark recycling plan will cut waste by two-thirds

As one of the European Union's largest energy consumers and greenhouse-gas polluters (go.nature.com/33piuuv), Denmark will launch the EU's most-ambitious recycling plan in July next year. It aims to cut the country's annual amount of waste for incineration from 800 to 250 kilograms per capita, reducing carbon dioxide emissions to 0.7 million tonnes by 2030. Citizens will sort their waste into ten different types.

The move is in part a response to the COVID-19 pandemic and to a new EU directive for environmental sustainability that promotes a circular economy, lower emissions and a reduction in the use of raw materials and hazardous substances (J. B. Zimmerman *et al. Science* **367**, 397–400; 2020). It is hoped that the plan will limit ecosystem damage and the health effects of toxic industrial chemicals. It will also discourage Denmark's unacceptable export of waste to low-income countries.

If other countries were to adopt similar practices, the world would align faster with the United Nations Sustainable Development Goals on sustainability and planetary health.

Su Shiung Lam Universiti Malaysia Terengganu.

Aage K. O. Alstrup Aarhus University, Aarhus, Denmark.

Christian Sonne Aarhus University, Roskilde, Denmark.
cs@bios.au.dk

COVID-19: full peer review in hours

The impetus to rapidly disseminate scientific results during a crisis ahead of peer review could cause governments and international organizations to act prematurely — or to be reluctant to act at all. Having struggled with such challenges in our COVID-19 work, we recommend our tested review system, which has an ultrashort submission-to-acceptance time.

One of us (W.S.) runs a workshop every September to identify horizon-scanning issues in conservation, which we aim to report on in *Trends in Ecology and Evolution* the following January. The journal's editor (formerly K.A.L.) agrees a submission date and selects referees. Authors send in a working draft a week before formal submission so that referees have time to prepare their comments. In the first year (2009), the time from formal submission to return of detailed comments was 90 minutes.

The crucial features of this process are advance selection of referees and the provision of a draft manuscript. Agreeing a submission date makes planning easier for referees but is not essential.

Our model could be used for ultrafast peer review of COVID-19 papers (see M. A. Johansson and D. Saderi *Nature* **579**, 29; 2020). Setting up a pool of referees dedicated to rapid review of key papers would help relieve pressure on overstretched individuals.

William J. Sutherland University of Cambridge, UK.
w.sutherland@zoo.cam.ac.uk

Katrina A. Lythgoe University of Oxford, UK.

News & views

Chemical biology

Protein degraders extend their reach

Claire Whitworth & Alessio Ciulli

Molecules have previously been made that induce protein destruction inside cells. A new class of molecule now induces the degradation of membrane and extracellular proteins – opening up avenues for drug discovery. **See p.291**

Most drugs act by binding to a specific site in a target protein to block or modulate the protein's function. The activity of many proteins, however, cannot be altered in this way. An emerging class of drug instead brings proteins into proximity with other molecules, which then alter protein function in unconventional ways[1–3]. One such approach uses drug molecules called protein degraders, which promote the tagging of proteins with ubiquitin, another small protein. Tagged proteins are then broken down into small peptide molecules by the cell's proteasome machinery. But because the ubiquitin-mediated degradation pathway occurs inside the cell, protein degraders developed so far attack mainly intracellular targets. On page 291, Banik *et al.*[4] now report a different mechanism that opens up extracellular and membrane-bound proteins for targeted degradation.

The authors report protein degraders that they call lysosome-targeting chimaeras (LYTACs), which are bifunctional (they have two binding regions; Fig. 1). One end carries an oligoglycopeptide group that binds to a transmembrane receptor (the cation-independent mannose-6-phosphate receptor; CI-M6PR) at the cell surface. The other end carries either an antibody or a small molecule that binds to the protein targeted for destruction. These two regions are joined by a chemical linker.

The formation of a trimeric CI-M6PR–LYTAC–target complex at the plasma membrane directs the complex for destruction by protease enzymes in membrane-enclosed organelles called lysosomes. LYTACs are conceptually related, but complementary, to proteolysis-targeting chimaeras[5] (PROTACs) – another bifunctional class of protein degrader that mainly targets intracellular proteins by recruiting them to E3 ligases (the enzymes that tag proteins with ubiquitin).

Banik *et al.* began by making LYTACs of varying size and linker composition, and which used a small molecule called biotin as the protein-binding component – biotin binds with exceptionally high affinity to avidin proteins. The authors observed that these LYTACs rapidly shuttled an extracellular fluorescent avidin protein to intracellular lysosomes in a way that required engagement with CI-M6PR. When the authors replaced biotin with an antibody that recognizes apolipoprotein E4 (a protein implicated in neurodegenerative diseases), this protein was also internalized and degraded by lysosomes. LYTACs can, therefore, repurpose antibodies from their normal immune function to direct extracellular proteins for lysosomal degradation.

Next, Banik *et al.* investigated whether LYTACs could induce the degradation of membrane proteins that are targets for drug discovery. In several cancer cell lines, LYTACs did indeed induce the internalization and lysosomal degradation of the epidermal growth factor receptor (EGFR) – a membrane protein that drives cell proliferation by activating a signalling pathway. Depletion of EGFR levels by LYTACs in the cancer cell lines reduced signal activation downstream of EGFR, compared with the amount observed when EGFRs were blocked by antibodies alone. This result confirms a previously reported[5] advantage of using target degradation in therapeutic applications, rather than target blocking.

Similar outcomes were observed with LYTACs for other single-pass transmembrane proteins (proteins that span the cell membrane only once), including programmed

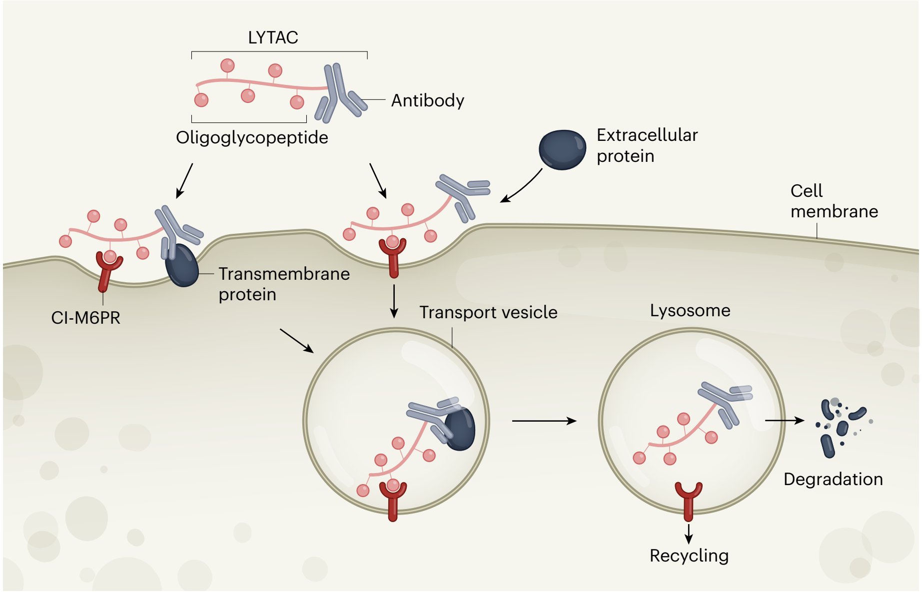

Figure 1 | Mechanism of action of lysosome-targeting chimaeras (LYTACs). Banik *et al.*[4] report LYTAC molecules, which consist of an oligoglycopeptide group (which binds to a cell-surface receptor, CI-M6PR) and an antibody that binds to a specific transmembrane or extracellular protein. The antibody can also be replaced by a small protein-binding molecule (not shown). On simultaneously binding to both CI-M6PR and the target protein, the resulting complex is engulfed by the cell membrane, which forms a transport vesicle. This carries the complex to a lysosome (an organelle that contains protein-degrading enzymes). The protein is degraded and the receptor is recycled; it remains to be seen whether the LYTAC is also degraded. LYTACs are potentially useful for therapeutic applications.

death ligand 1 (PD-L1), which helps cancer cells to evade the immune system. The next step will be to establish whether LYTACs can also induce the degradation of multi-pass proteins that span the membrane several times, such as the ubiquitous G-protein-coupled receptors and proteins that transport materials across membranes (ion channels and solute-carrier proteins, for example). If so, it will be interesting to compare the performance of LYTACs, which would bind to the extracellular domains of such proteins, with that of PROTACs, which can bind to the intracellular domains of these proteins (as was recently demonstrated[6] for solute-carrier proteins).

As with any new drug modality, there is scope for improvement. For example, Banik and colleagues' first PD-L1-targeting LYTACs produced only partial degradation of the protein, which the authors attributed to low expression of CI-M6PR in the cell lines used. When the authors made a second type of LYTAC that incorporated a more potent PD-L1 antibody, degradation increased, albeit in cells that expressed greater levels of CI-M6PR than did the original cell lines. This shows that low abundance of the lysosome-shuttling receptor hijacked by the LYTAC (in this case, CI-M6PR) can reduce the effectiveness of these degraders. Similarly, the loss of core components of E3 ligases is a common mechanism by which cells become resistant to PROTACs[7]. Lysosome-shuttling receptors other than CI-M6PR could be used by LYTACs as alternatives, should resistance emerge. Degraders that target cell-type-specific receptors might also have improved safety profiles compared with conventional small-molecule therapeutics, which are not always cell-type selective.

What sets PROTACs and LYTACs apart from conventional drugs is their mode of action. For example, after a PROTAC has brought about the destruction of a target protein, the PROTAC is released and can induce further cycles of ubiquitin tagging and degradation, thereby acting as a catalyst at low concentrations[1,5]. Mechanistic studies are now warranted to determine whether LYTACs also work catalytically.

Another aspect of the mode of action of both PROTACs and LYTACs is that they bring two proteins together, to form a trimeric complex. A general feature of such processes is the hook effect, whereby trimer formation, and thereby the associated biological activity, decreases at high drug concentrations. This is because dimeric complexes generally form preferentially at high drug concentrations – an undesirable effect that can be alleviated by ensuring that all three components interact in such a way that trimer formation is more favourable than is dimer formation[1].

Kinetics also matters for protein degraders. For example, stable and long-lived trimeric complexes that involve PROTACs accelerate target degradation, improving drug potency and selectivity[8]. It will be crucial to understand how the complexes formed by LYTACs can be optimized to improve degradation activity.

PROTACs and LYTACs are larger molecules than conventional drugs. As a result of their size, PROTACs often do not permeate well through biological membranes, which can make them less potent drugs than the biologically active groups they contain. Size should be less of a problem for LYTACs because they do not need to cross the cell membrane, although they would still need to pass through biological barriers to combat diseases of the central nervous system. The development of lysosomal degraders that are smaller and less polar than LYTACs – and therefore more able to pass through membranes – will be eagerly anticipated. Small 'glue' molecules that bind to E3 ligases can already do the same job as PROTACs[9].

Targeted protein degradation is a promising therapeutic strategy, and the first PROTACs are currently in clinical trials[10]. LYTACs will need to play catch-up, but they have earned their place as a tool poised to expand the range of proteins that can be degraded. Their development as therapies will require an understanding of their behaviour in the human body – their pharmacokinetics, toxicity, and how they are metabolized, distributed and excreted, for example. It can be challenging to optimize the biological behaviour of molecules that incorporate large groups, such as antibodies and oligoglycopeptides, during drug discovery, but this problem can be overcome by further engineering the structures of these groups[11]. Banik and colleagues' new approach to degradation therefore warrants an all-hands-on deck approach.

Scientists working in drug discovery will eagerly await the development of LYTACs and the emergence of other methods for the drug-induced degradation of proteins[12]. Is no protein beyond the reach of degraders?

Claire Whitworth and **Alessio Ciulli** are in the Division of Biological Chemistry and Drug Discovery, School of Life Sciences, James Black Centre, University of Dundee, Dundee DD1 5EH, UK.
e-mail: a.ciulli@dundee.ac.uk

1. Maniaci, C. & Ciulli, A. *Curr. Opin. Chem. Biol.* **52,** 145–156 (2019).
2. Deshaies, R. J. *Nature* **580**, 329–338 (2020).
3. Gerry, C. J. & Schreiber, S. L. *Nature Chem. Biol.* **16,** 369–378 (2020).
4. Banik, S. M. *et al. Nature* **584**, 291–297 (2020).
5. Burslem, G. M. & Crews, C. M. *Cell* **181**, 102–114 (2020).
6. Bensimon, A. *et al. Cell Chem. Biol.* **27**, 728–739 (2020).
7. Zhang, L., Riley-Gillis, B., Vijay, P. & Shen, Y. *Mol. Cancer Ther.* **18**, 1302–1311 (2019).
8. Roy, M. J. *et al. ACS Chem. Biol.* **14,** 361–368 (2019).
9. Hanan, E. J. *et al. J. Med. Chem.* https://doi.org/10.1021/acs.jmedchem.0c00093 (2020).
10. Mullard, A. *Nature Rev. Drug Discov.* **19**, 435 (2020).
11. Chiu, M. L. & Gilliland, G. L. *Curr. Opin. Struct. Biol.* **38,** 163–173 (2016).
12. Takahashi, D. *et al. Mol. Cell* **76**, 797–810 (2019).

Ecology

Rethinking extinctions that arise from habitat loss

Joaquín Hortal & Ana M. C. Santos

Does the loss of species through habitat decline follow the same pattern whether the area lost is part of a large or a small habitat? An analysis sheds light on this long-running debate, with its implications for conservation strategies. **See p.238**

Understanding how habitat size affects the abundance of all the species living in a community provides ecological insights and is valuable for developing strategies to boost biodiversity. On page 238, Chase *et al.*[1] report results that might help to settle a long-running debate about the relationship between the area of a habitat and the diversity of species it can host.

Land transformation by human activity is a major component of global change. The loss of natural habitats reduces the local diversity and abundance of species[2], and has been implicated in more than one-third of animal extinctions worldwide between 1600 and 1992 (ref. 3). A report from the Intergovernmental Science-Policy Platform on Biodiversity and Ecosystem Services estimates that currently more than half a million species – about 9% of all terrestrial species – might lack the amount of habitat needed for their long-term survival[4]. Moreover, their disappearance would compromise many key ecosystem services, such as pollination or the control of pests or disease-causing agents.

The effect of habitat loss on biodiversity has been conventionally estimated on the basis of the relationship between area and species richness, which was first described more than 150 years ago[5]. This seemingly universal relationship is simple: the larger a given habitat's area, the more species it holds, although the number of species increases with area in a nonlinear way[6]. There is a limit to the number of individuals of ecologically similar species that can persist in an area, owing to the limited resources that it harbours[7]. When a habitat loses part of its area, therefore, for many species, it also loses its capacity to support populations that are large enough to be viable. These species become extinct as habitat area diminishes with land-use intensification[8].

Chase and colleagues propose an elegant and simple approach to account for the dynamics of communities occupying habitat patches of different size. Rather than considering only the overall number of species in each habitat fragment, the authors focused on the number and relative abundance of different species in samples obtained from such fragments. This allows the structure of ecological communities to be compared directly[2], while avoiding problems that can arise when taking into account the differences in the effort needed to sample large and small areas[9]. The authors' approach also allows a comparison of variations in the relative abundance of individuals of all species, a measure of community structure that is associated with ecosystem dynamics[10].

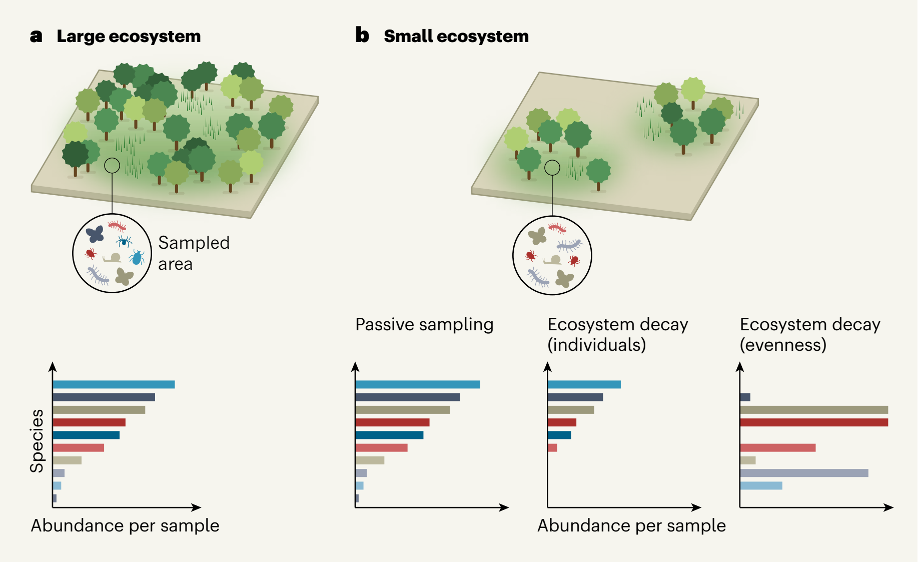

Figure 1 | Assessing how habitat size affects ecosystem dynamics. Understanding the relationship between a decline in habitat area and the effect on species is crucial for designing conservation strategies. **a**, **b**, Chase *et al.*[1] analysed studies that sampled species in particular habitats. The authors compared the diversity of organisms, such as insects, in samples obtained from large ecosystems (**a**) with samples taken from the same sampling area in a smaller fragments of the same type of habitat (**b**). These graphs show hypothetical results for species abundance per sample, and different species are shown in different colours. This method enabled the authors to distinguish between three possible outcomes as habitats become smaller. In the passive-sampling model, species are equally distributed in habitat fragments of any size, so the richness, abundance and relative species prevalence (evenness) per sample is constant, regardless of the total habitat size. In the ecosystem-decay (individuals) model, samples from smaller fragments have fewer individuals and species per sample than do samples from larger fragments, and all species abundances decline in a similar way as habitat is lost. In the ecosystem-decay (evenness) model, species vary in their response to habitat loss, and there is a change in their relative abundances. Chase *et al.* find that ecosystem decay, usually following the evenness model, is the best match for the observed data.

Thanks to this method, Chase *et al.* could distinguish between three patterns of change that might occur as an outcome of habitat loss (Fig. 1). In the pattern described by the 'passive sampling' model, the structure of the community remains the same in large and small fragments. Therefore, each sample provides similar species richness (the number of species), abundance (the number of individuals) and evenness (the allocation of individuals to the different species), regardless of the total habitat size. In this case, species decline will mirror the loss of habitat area under the classical species–area theory[5], and the total number of species in the entire fragment would depend solely on its size.

The other two patterns are described as types of ecosystem decay – a hypothesis proposing that a habitat that shrinks undergoes a disproportionately high loss of organisms compared with the loss of habitat area. One type of ecosystem decay is proposed to occur owing to excessive loss of individuals. Smaller habitat fragments will contain fewer individuals per sample than will larger ones, and all species are equally affected. This generates communities with fewer species in smaller fragments, but no changes in the relative abundance of species per sample between small and large fragments.

The other type of ecosystem decay occurs owing to uneven changes in relative species abundances coupled to species loss. In this scenario, the species present have different responses to habitat loss, and therefore species become relatively more or less abundant in smaller fragments than in larger fragments. Their relative abundance becomes more uneven in samples from smaller fragments as some species increase their numerical dominance, impoverishing the community and causing it to become species poor.

Using data from around 120 human-transformed landscapes worldwide, Chase *et al.* show that, in general, samples from small fragments of natural habitat have fewer individuals, fewer species and a more uneven abundance of species than samples taken from larger fragments do. This outcome is consistent with a generalized pattern of ecosystem decay, mainly as a result of a decline in evenness (see Fig. 1), and this result holds, regardless of the type of habitat or organism studied. This implies that the alteration of natural habitats causes major functional changes in ecosystem dynamics that go beyond simply losing populations and species. Therefore, current estimates of extinctions associated with habitat loss made on the basis of the passive-sampling model might be underestimating not only the number of species that are threatened or already gone, but also the consequences of their loss for ecological functioning and the provision of ecosystem services.

Changes in biodiversity after habitat loss alter many ecological processes[11], eventually causing catastrophic effects that accelerate the extinction process[12]. But local extinctions are often not immediate. Some species persist with reduced abundances and declining population dynamics – known as 'extinction debt' – that lasts until the final individuals perish[13]. This causes an uneven distribution of species abundance that is vividly demonstrated by Chase and colleagues' method. Their analysis reveals a few 'winning' species that dominate the community in small habitats, and a very large number of rare species, many of which are probably heading towards extinction.

Declining species can be replaced by others coming from the neighbouring human-altered landscape, particularly in habitat edges[14], producing what are described as 'edge effects' that are comparatively more important in smaller fragments. Indeed, in the early stages of land transformation, communities in small fragments are more different from pristine communities than are those in large fragments, with communities in small fragments becoming more similar to those in large fragments over time, as they recover from the effect of land transformation[2]. According to Chase and colleagues, the degree of decay in diversity and species abundance found between large and small fragments is smaller in the older or 'softly' transformed European landscapes than in the more recently and dramatically transformed North American ones. This indicates that, over time, species moving in from the edges of the human-altered habitats might compensate, at least in part, for the ecological functions carried out by native species in larger habitats, causing small fragments to reach a new – yet different – ecological balance.

Although this work underscores the key role of habitat area in maintaining ecosystem processes, there is little exploration of how these processes are altered by habitat loss. Species from higher trophic levels (the upper levels of the food chain), such as predators, require larger areas to maintain their populations compared with species from lower trophic levels, so the number of individuals supported by smaller habitat fragments might not suffice to maintain populations of top predators or consumers, and hence would produce shorter food chains and alter the ecosystem structure[15]. Differences in extinction rates between trophic levels can cause striking changes in ecosystem functioning at habitat edges[16], jeopardizing the functioning and ecosystem-service provision as natural habitats diminish in size[11].

Chase and colleagues' results call for a reconsideration of the debate over whether a single large area devoted to conservation would preserve more species than would several small ones that combine to make up the same total size[17]. Some current evidence suggests that one continuous habitat might host fewer species than do many small patches that total the same area[18]. However, the large ecological changes that these small fragments might undergo could end up resulting in massive reductions in ecosystem function and, ultimately, increased extinction rates of native species over the long term compared with the case for a single, large protected area.

Chase and colleagues' approach is good for providing a general overview of the extent of these effects, but to understand exactly how ecological processes are changing locally, a higher level of detail will be needed. This will require going beyond the studies of trophic chains[14,16] to assess more-complex food webs[15], and to gather information on changes in species' functional responses and trait diversity in increasingly smaller habitats. Ultimately, this information will reveal which ecological processes are decaying, and what the consequences of such ecosystem decay are for the maintenance of fully functional biodiversity.

Joaquín Hortal is in the Department of Biogeography and Global Change, Museo Nacional de Ciencias Naturales, Spanish National Research Council, Madrid 28006, Spain. **Ana M. C. Santos** is in the Department of Ecology, Autonomous University of Madrid, Madrid 28049, Spain, and at the Centro de Investigación en Biodiversidad y Cambio Global, Autonomous University of Madrid.
e-mails: jhortal@mncn.csic.es; ana.margarida.c.santos@gmail.com

1. Chase, J. M., Blowes, S. A., Knight, T. M., Gerstner, K. & May, F. *Nature* **584**, 238–243 (2020).
2. Newbold, T. *et al. Nature* **520**, 45–50 (2015).
3. World Conservation Monitoring Centre. *Global Biodiversity: Status of the Earth's Living Resources* 199 (Chapman & Hall, 1992).
4. Díaz, S. *et al.* (eds) *The Global Assessment Report on Biodiversity and Ecosystem Services: Summary for Policymakers* (IPBES, 2019).
5. Rosenzweig, M. L. *Species Diversity in Space and Time* (Cambridge Univ. Press, 1995).
6. Arrhenius, O. *J. Ecol.* **9**, 95–99 (1921).
7. Wright, D. H. *Oikos* **41**, 496–506 (1983).
8. Di Marco, M., Venter, O., Possingham, H. P. & Watson, J. E. M. *Nature Commun.* **9**, 4621 (2018).
9. Chase, J. M. *et al. Front. Biogeogr.* **11**, e40844 (2019).
10. Simons, N. K. *et al. Agric. Ecosyst. Environ.* **237**, 143–153 (2017).
11. Dobson, A. *et al. Ecology* **87**, 1915–1924 (2006).
12. Fischer, J. & Lindenmayer, D. B. *Global Ecol. Biogeogr.* **16**, 265–280 (2007).
13. Tilman, D., May, R. M., Lehman, C. L. & Nowak, M. A. *Nature* **371**, 65–66 (1994).
14. Didham, R. K., Lawton, J. H., Hammond, P. M. & Eggleton, P. *Phil. Trans. R. Soc. B* **353**, 437–451 (1998).
15. Holt, R. D. in *The Theory of Island Biogeography Revisited* (eds Losos, J. B. & Ricklefs, R. E.) 143–185 (Princeton Univ. Press, 2010).
16. Harrison, M. L. K. & Banks-Leite, C. *Conserv. Biol.* https://doi.org/10.1111/cobi.13438 (2019).
17. Simberloff, D. S. & Abele, L. G. *Science* **191**, 285–286 (1976).
18. Fahrig, L. *Glob. Ecol. Biogeogr.* **29**, 615–628 (2020).

Mechanobiology

Stretch exercises for stem cells expand the skin

Matthias Rübsam & Carien M. Niessen

Stretching the skin of mice reveals that mechanical strain is communicated by a subpopulation of stem cells that proliferate and promote mechanical resistance, and so generate extra skin. **See p.268**

The cells of our bodies are exposed to a range of mechanical forces – including compression, shear and stretching – that they must resist to maintain tissue integrity and function. For example, skin responds to stretching forces by expanding. Physicians have exploited this particular response for more than 60 years[1], implanting stretching devices in the skin to cause tissue expansion for plastic surgery or to repair birth defects[2]. But exactly how mechanical strain creates extra tissue in a living organism has not been known. On page 268, Aragona *et al.*[3] now provide compelling insights (at the molecular, single-cell and cell-population level) into how stem cells in the skin of mice sense and communicate stretch to make new tissue.

The surface of the skin – a multi-layered tissue called the epidermis – protects organisms against dehydration and environmental stresses, including mechanical challenges. To ensure lifelong protection, the epidermis is constantly renewed through the generation of new stem cells in its basal layer. This renewal is balanced with differentiation and the movement of stem cells to generate the upper, barrier-forming layers of the epidermis. Ultimately, the barrier-forming cells are shed from the surface, to be replaced by new cells.

Aragona *et al.* set out to examine how the epidermis responds to strain. The group positioned a device used in human surgeries – a self-inflating gel – under the skin of mice. They then examined indicators of force perception, including changes in cell shape, the structure of a mechanosensitive protein called α-catenin, and a network of keratin proteins that provides cells with mechanical resilience. This analysis revealed that epidermal stem cells do indeed sense and respond to strain. The authors observed a temporary increase in stem-cell division, followed by thickening of the epidermis. Thus, increased stem-cell renewal fuels stem-cell differentiation. The two effects combine to maintain a functional barrier at the same time as extra skin is generated.

The researchers next genetically engineered cells in the basal epidermal layer such that the stem cells and their descendants were fluorescently marked. Tracking of these cell lineages over time confirmed that stretching tips the renewal–differentiation balance in favour of making more stem cells. This explains why the epidermis expands in response to stretching.

https://doi.org/10.1038/d41586-020-02158-y

News & views

Mechanobiology

Stretch exercises for stem cells expand the skin

Matthias Rübsam & Carien M. Niessen

Stretching the skin of mice reveals that mechanical strain is communicated by a subpopulation of stem cells that proliferate and promote mechanical resistance, and so generate extra skin.

The cells of our bodies are exposed to a range of mechanical forces – including compression, shear and stretching – that they must resist to maintain tissue integrity and function. For example, skin responds to stretching forces by expanding. Physicians have exploited this particular response for more than 60 years[1], implanting stretching devices in the skin to cause tissue expansion for plastic surgery or to repair birth defects[2]. But exactly how mechanical strain creates extra tissue in a living organism has not been known. Writing in *Nature*, Aragona *et al.*[3] now provide compelling insights (at the molecular, single-cell and cell-population level) into how stem cells in the skin of mice sense and communicate stretch to make new tissue.

The surface of the skin – a multi-layered tissue called the epidermis – protects organisms against dehydration and environmental stresses, including mechanical challenges. To ensure lifelong protection, the epidermis is constantly renewed through the generation of new stem cells in its basal layer. This renewal is balanced with differentiation and the movement of stem cells to generate the upper, barrier-forming layers of the epidermis. Ultimately, the barrier-forming cells are shed from the surface, to be replaced by new cells.

Aragona *et al.* set out to examine how the epidermis responds to strain. The group positioned a device used in human surgeries – a self-inflating gel – under the skin of mice. They then examined indicators of force perception, including changes in cell shape, the structure of a mechanosensitive protein called α-catenin, and a network of keratin proteins that provides cells with mechanical resilience. This analysis revealed that epidermal stem cells do indeed sense and respond to strain. The authors observed a temporary increase in stem-cell division, followed by thickening of the epidermis. Thus, increased stem-cell renewal fuels stem-cell differentiation. The two effects combine to maintain a functional barrier at the same time as extra skin is generated.

The researchers next genetically engineered cells in the basal epidermal layer such that the stem cells and their descendants were fluorescently marked. Tracking of these cell lineages over time confirmed that stretching tips the renewal–differentiation balance in favour of making more stem cells. This explains why the epidermis expands in response to stretching.

Aragona *et al.* demonstrated that force changes stem cells at the molecular level in several ways. First, stretching increased the expression of genes involved in cell–cell adhesion, which have been shown to communicate force *in vitro*[4]. Second, expression of components of the actomyosin cytoskeleton – a network of protein filaments that generates contractile forces in cells[5] – was increased. Third, stretching promoted signalling through the EGF–Map kinase–ERK pathway (a cascade of proteins that promotes growth). The researchers also assessed changes in chromatin, the DNA–protein complex that parcels up the genome in cells; such changes can lead to altered gene expression. This analysis revealed that stretch induced the expression of a network of regulatory genes that links stem-cell proliferation to skin maintenance.

The authors then examined how strain alters gene-expression profiles of single epidermal stem cells, by sequencing the cells' RNA. This revealed that only a subpopulation of stem cells undergoes the molecular changes associated with a stretched state. Why might this be? Perhaps those that take on the stretched state experience greater force. Alternatively, maybe stem cells exist in varying biochemical states, and thus are more or less sensitive to

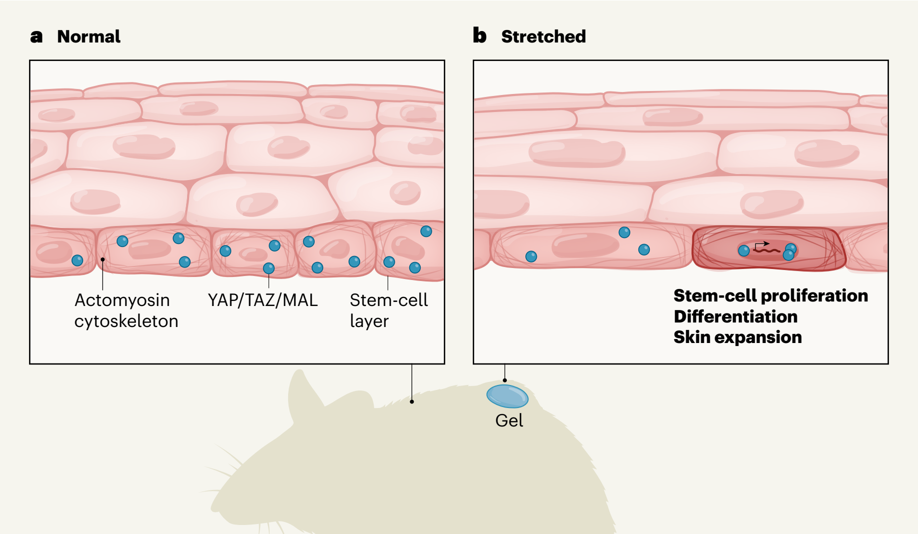

Figure 1 | How skin stem cells respond to stretching. a, The surface of skin is a multi-layered tissue called the epidermis, which has stem cells in its basal layer. Like all cells, the stem cells have a contractile network of protein filaments called the actomyosin cytoskeleton, and express the transcription factors YAP, TAZ and MAL. **b**, Aragona *et al.*[3] placed an expanding gel under the skin of mice. They report that, in a subset of epidermal stem cells, the actomyosin cytoskeleton is reorganized. This somehow triggers movement of YAP, TAZ and MAL to the nucleus. The proteins induce gene-expression changes that promote an increase in both stem-cell proliferation and differentiation into cells that move into the upper layers of the epidermis. This dual response leads to expansion of skin tissue without compromising the barrier function of the epidermis.

force. Or local differences in stem-cell shape and mechanics could determine how each cell responds to stretch. Answering this question will require measurements of cellular forces and stiffness *in vivo*, which is still a major challenge. In addition, it remains unclear whether the stretched stem cells alone are driven to proliferate — or whether these cells then induce expansion of surrounding stem cells.

Aragona *et al.* next genetically engineered mice to lack *Diaph3* and *Myh9*, genes involved in regulation of the actomyosin cytoskeleton. Without these genes, stem-cell responses to stretch were absent, leading to a barrier defect in the animals. The group observed similar effects in animals engineered to lack the genes encoding YAP and TAZ, and/or in which MAL was inhibited — these three transcription factors normally move to the nucleus to regulate gene expression in response to mechanical signals[6]. Next, the authors examined YAP, TAZ and MAL in mice lacking *Diaph3* and *Myh9*. The transcription factors did not move to the nucleus in response to stretch in these animals. Thus, in normal skin, stretch reorganizes the actomyosin cytoskeleton to promote entry of YAP, TAZ and MAL into the nucleus. These proteins then coordinate transcriptional programs that promote skin growth and barrier formation (Fig. 1).

Finally, the researchers inhibited MAL or the EGF-pathway component ERK in their animals. Inhibition of either protein blocked stem-cell proliferation, but only MAL inhibition led to loss of the 'stretched' molecular state in a subset of stem cells. Thus, MAL regulates variable cell response to strain, whereas both ERK and MAL are necessary to promote the self-renewal of stem cells. Whether ERK is downstream of YAP, TAZ and MAL, or directly activated by the cytoskeleton[7], and whether EGF–ERK signalling promotes adaptation to strain in the upper epidermal layers to maintain barrier function during skin expansion[8], remain open questions.

Overall, Aragona and colleagues' data support a model in which stretch is initially sensed by a subset of stem cells. These cells, through cytoskeletal reorganization and changes in gene expression, coordinate stem-cell renewal and differentiation with adaptation to the mechanical force being experienced. This response guarantees that the skin can maintain its protective function while expanding.

The research opens several avenues for future research. First, what is the contribution of other compartments of the skin (such as the upper, barrier-forming epidermal layers, or the thick dermal layer that underlies the epidermis) in sensing and communicating stretch? The authors' analysis of mice lacking YAP or MAL suggests that stretch also induces a cytoskeletal response in differentiated cells of the upper epidermal layers. Stem-cell differentiation and upward movement can trigger renewal of neighbouring stem cells[9], thus begging the question of whether the cells immediately above the basal layer are also required for stem-cell responses to strain.

Second, *in vitro* experiments have demonstrated[10] that chromatin regulation in the nucleus is key to maintaining stem-cell identity and genome integrity under mechanical stress. Aragona and co-workers' skin-expander model will now allow us to explore these mechanisms *in vivo*.

Third, current models of stem-cell renewal postulate that a single stem cell is equally capable of undergoing renewal or differentiation. However, Aragona and colleagues' lineage-tracing experiments revealed that the number of cells derived from one stem cell (called basal-cell clones) tended to be even. This bias towards clones that have even numbers of cells became much more pronounced on stretching. How the stretched state promotes even-numbered clones is unclear.

The authors propose that this bias can be explained by a model in which stem cells exist in two-progenitor units, in which one stem cell is committed to renewal and the other to differentiation. Communication within and between units would balance the loss of cells through differentiation with renewal. The group performed a mathematical comparison, which indicated that the even-numbered-cell bias and clone dynamics they observed were more consistent with a two-progenitor than with a single-progenitor model. However, the jury on this is still out, because a recent study has provided fresh evidence for the one-progenitor model[11].

The current work provides a major step forward in our understanding of how force is interpreted at the single-cell level in living organisms. Furthermore, it should encourage others to explore the use of mechanical signals to generate extra skin — not only for reconstructive surgery, but also for diseases associated with impaired regeneration.

Matthias Rübsam and **Carien M. Niessen** are in the Cologne Excellence Cluster on Stress Responses in Aging-associated Diseases (CECAD), University of Cologne, 50931 Cologne, Germany. **M.R.** is also at the Max Planck Institute for Biology of Aging, Cologne. **C.M.N.** is also in the Department Cell Biology of the Skin and the Center for Molecular Medicine Cologne, University of Cologne.
e-mails: ruebsam@age.mpg.de; carien.niessen@uni-koeln.de

1. Neumann, C. G. *Plast. Reconstruct. Surg.* **19**, 124–130 (1957).
2. Zöllner, A. M., Holland, M. A., Honda, K. S., Gosain, A. K. & Kuhl, E. *J. Mech. Behav. Biomed. Mater.* **28**, 495–509 (2013).
3. Aragona, M. *et al. Nature* https://doi.org/10.1038/s41586-020-2555-7 (2020).
4. Ladoux, B. & Mège, R.-M. *Nature Rev. Mol. Cell Biol.* **18**, 743–757 (2017).
5. Chug, P. & Paluch, E. K. *J. Cell Sci.* **131**, jcs186254 (2018).
6. Panciera, T., Azzolin, L., Cordenonsi, M. & Piccolo, S. *Nature Rev. Mol. Cell Biol.* **18**, 758–770 (2017).
7. Hirata, H. *et al. EMBO Rep.* **16**, 250–257 (2015).
8. Rübsam, M. *et al. Nature Commun.* **8**, 1250 (2017).
9. Mesa, K. R. *et al. Cell Stem Cell* **23**, 677–686 (2018).
10. Nava, M. M. *et al. Cell* **181**, 800–817 (2020).
11. Piedrafita, G. *et al. Nature Commun.* **11**, 1429 (2020).

organisms. Furthermore, it should encourage others to explore the use of mechanical signals to generate extra skin — not only for reconstructive surgery, but also for diseases associated with impaired regeneration.

Matthias Rübsam and **Carien M. Niessen** are in the Cologne Excellence Cluster on Stress Responses in Aging-associated Diseases (CECAD), University of Cologne, 50931 Cologne, Germany. **M.R.** is also at the Max Planck Institute for Biology of Aging, Cologne. **C.M.N.** is also in the Department Cell Biology of the Skin and the Center for Molecular Medicine Cologne, University of Cologne.

e-mails: ruebsam@age.mpg.de;
carien.niessen@uni-koeln.de

1. Neumann, C. G. *Plast. Reconstruct. Surg.* **19**, 124–130 (1957).
2. Zöllner, A. M., Holland, M. A., Honda, K. S., Gosain, A. K. & Kuhl, E. *J. Mech. Behav. Biomed. Mater.* **28**, 495–509 (2013).
3. Aragona, M. *et al. Nature* **584**, 268–273 (2020).
4. Ladoux, B. & Mège, R.-M. *Nature Rev. Mol. Cell Biol.* **18**, 743–757 (2017).
5. Chug, P. & Paluch, E. K. *J. Cell Sci.* **131**, jcs186254 (2018).
6. Panciera, T., Azzolin, L., Cordenonsi, M. & Piccolo, S. *Nature Rev. Mol. Cell Biol.* **18**, 758–770 (2017).
7. Hirata, H. *et al. EMBO Rep.* **16**, 250–257 (2015).
8. Rübsam, M. *et al. Nature Commun.* **8**, 1250 (2017).
9. Mesa, K. R. *et al. Cell Stem Cell* **23**, 677–686 (2018).
10. Nava, M. M. *et al. Cell* **181**, 800–817 (2020).
11. Piedrafita, G. *et al. Nature Commun.* **11**, 1429 (2020).

Biogeochemistry

Carbon loss from tropical soils increases on warming

Eric A. Davidson

Plots of tropical forest soils were warmed by 4 °C for two years to observe the effects on soil carbon emissions. The increase in efflux of carbon dioxide was larger than expected — a result with worrying implications for climate change. **See p.234**

The carbon stored in soil could have a big impact on climate change. The global flux of carbon in and out of soils is six to ten times greater than the emissions of carbon dioxide produced as a result of human activities[1,2]. The inputs of carbon to soils from plant detritus (dead wood, leaves and roots) roughly balance the losses to the atmosphere produced by the respiration of soil microorganisms that feed on that material. However, just a 1% imbalance of global soil-carbon effluxes over influxes would equal about 10% of global anthropogenic carbon emissions. Carbon in tropical soils was thought to be less vulnerable to loss under climate change than is soil carbon at higher latitudes, but experimental evidence for this was lacking. On page 234, Nottingham *et al.*[3] report that tropical-forest soils might be more vulnerable to warming than was thought.

Various soil management practices (such as changes of land use and of tillage methods) can influence the amount of soil carbon present[4], but climate affects the respiration rate of the microbes that feed on soil carbon, and hence the CO_2 efflux from soil[5]. If the net efflux of carbon from soils to the atmosphere increases in a warming world, a positive feedback will accelerate the warming.

Soils are amazingly diverse and differ in several respects that affect microbial respiration[6]. These include: the amount of minerals to which soil carbon can bind and thereby be protected from decomposition by microbial enzymes; water content, which affects the diffusion of carbon to microbial enzymes; the amount, timing and quality of the plant detritus going into the soil; and genetic variation in soil microbial communities. The intrinsic temperature sensitivity of microbial respiration reactions indicated by theory and demonstrated in the laboratory (where other factors are not limiting) therefore often varies from the apparent temperature sensitivity measured in real-world settings[5,6]. Several *in situ* soil-warming experiments have yielded insights into the effects of temperature on CO_2 efflux from soil in temperate and boreal regions[6,7], but such research is logistically more challenging to implement in tropical forests.

Nottingham and co-workers now present results of a soil-warming experiment (Fig. 1). The authors placed warming rods around the perimeter of undisturbed soil plots in a tropical forest on Barro Colorado Island, Panama, and increased the temperature of the whole soil profile (to a depth of 1.2 metres) by 4 °C for two years. They measured CO_2 efflux using chambers periodically placed over the soil, and observed an unexpectedly large increase (55%) in soil CO_2 emissions. By excluding roots from the soil under some of the chambers, the authors determined that most of the increased CO_2 efflux was due to a greater-than-expected increase in the respiration of soil microbes.

The dependence of reaction rates on temperature, including the rates of enzymatic reactions, is described by the Arrhenius equation[5]. According to this equation, the fractional increase in reaction rate is less for a temperature increase of one degree Celsius at higher temperatures than at lower temperatures. This suggests that the response of soil microbial respiration to temperature changes

GEETHA IYER

Figure 1 | Preparing to use a heating device in an experiment. Nottingham *et al.*[3] buried heating equipment in plots in a topical forest in Panama and monitored the affect of warming on carbon dioxide release from the soil.

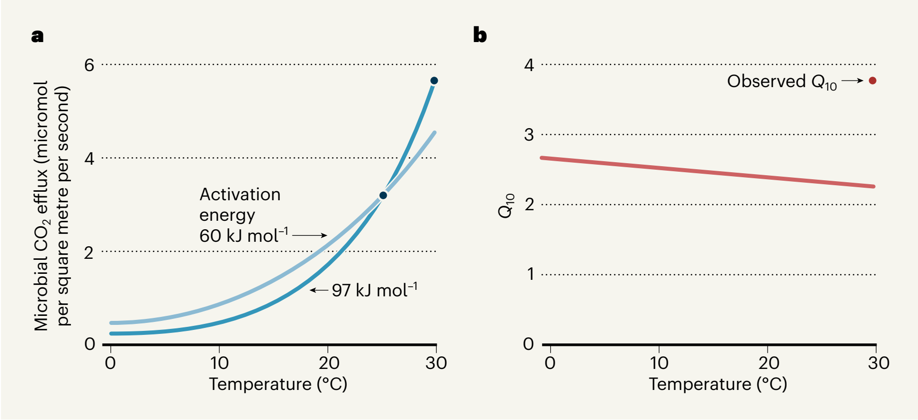

Figure 2 | Theoretical and observed temperature sensitivity of CO_2 efflux from tropical soils. **a**, Nottingham *et al.*[3] observed an increase in CO_2 efflux from tropical soils warmed *in situ* from an ambient temperature of 26 °C to 30 °C (dark blue circles). The pale blue line shows the theoretical dependence of CO_2 efflux associated with soil microbial respiration, calculated using an Arrhenius function[5] (which describes the kinetic response of enzymes to temperature) and assuming that the activation energy (E_a; simplistically, the minimum amount of energy needed for a reaction to occur) of the microbial respiratory reactions is 60 kilojoules per mol, which is typical for such reactions[8]. The observed increase in efflux on warming is larger than that predicted from this Arrhenius function. To fit the observations, E_a would have to be 97 kJ mol^{-1} (dark blue line), which is unlikely for respiratory enzymes. **b**, The Arrhenius function also predicts much lower Q_{10} values (red line; the multiplication factor of the increase in efflux observed when the temperature increases by 10 °C) than that observed by the authors at 30 °C (red circle). The authors' results suggest that unknown factors co-vary with temperature to increase CO_2 efflux, and that the kinetic responses of respiratory enzymes, alone, are insufficient to account for their observations.

should be less pronounced in tropical climates than it is in temperate or boreal climates. The Arrhenius relationship breaks down for enzymatic reactions at temperatures beyond those that are optimal for enzyme function, and therefore should not be extrapolated beyond temperatures that enzymes normally experience. But such extreme temperatures were not reached in Nottingham and colleagues' experiment.

Each enzyme-catalysed reaction has a characteristic activation energy (E_a, simplistically defined as the minimum energy needed for the reaction to occur), but the E_a values of the vast majority of respiratory enzymes fall within a fairly narrow range[8], averaging about 60 kilojoules per mol. If this common E_a value is used in an Arrhenius function to calculate how the average microbial CO_2 efflux from Nottingham and colleagues' plots varies with temperature (fitting the resulting curve to the efflux recorded in the non-warmed plots), the observed efflux from the warmed plots is found to be much higher than the calculated value (Fig. 2a). The E_a value would have to be an unlikely 97 kJ mol^{-1} to make the Arrhenius function fit with the efflux observed from the warmed plots.

A short-hand indicator of the temperature sensitivity of soil CO_2 efflux is Q_{10}, the multiplication factor of the increase observed when the temperature increases by 10 °C. The Q_{10} for microbial CO_2 efflux in Nottingham and co-workers' experiment was 3.6, which is well above expectations for most respiratory enzymatic processes on the basis of common E_a values and the Arrhenius equation (Fig. 2b). Temperature sensitivities as high as this indicate that the increased efflux in the warmed plots probably cannot be attributed only to the kinetic response of enzymes to warming – other confounding factors must also co-vary with temperature[9]. Indeed, in *in vitro* assays, Nottingham *et al.* report Q_{10} values of 2 or less for specific respiratory enzymes in soil samples from the studied plots. The authors rule out the possibility that significant confounding effects arose during their warming experiment as a result of the modest changes in soil-water content and microbial carbon-use efficiency. The cause of the unexpectedly high observed apparent temperature sensitivity therefore remains a mystery.

These results suggest that caution is needed when using only an Arrhenius or Q_{10} function to describe the temperature responses of soil microbial respiration – which most numerical models of Earth's systems and their carbon cycling responses to climate change unfortunately do[10]. The Arrhenius function (where E_a is about 60 kJ mol^{-1}) predicts a modest decrease in Q_{10} from about 2.6 at temperatures typical of high-latitude ecosystems to 2.2 at temperatures typical of tropical forests (Fig. 2b), whereas the current study and others[2,5,6] report a broader range of observed Q_{10} values.

Nottingham and colleagues' results suggest that other factors affecting soil CO_2 efflux merit further study. Efflux responses to experimental warming often decline after a few years, perhaps because the readily decomposable components of soil carbon that act as substrates for respiration reactions become depleted, or because of shifts in microbial community structures[6,7]. The Panamanian forest soil studied in the present work is relatively fertile as a result of the historical deposition of volcanic ash; this soil fertility might have enabled high rates of inputs of plant detritus to the soil, preventing soil microbial respiration from being limited by the availability of substrates. Indeed, the authors report an increase in soil microbial biomass in the warmed plots compared with control plots, indicating that warming might have increased the total microbial enzymatic capacity – thereby increasing CO_2 efflux beyond the expected kinetic response of the pre-existing enzymatic capacity.

> **"Tropical forests are unlikely to continue indefinitely to be carbon sinks as the world warms."**

Besides the clear take-home message that the responses of soil respiration processes under climate change should not be represented in Earth-system models only by simple Q_{10} or Arrhenius functions, Nottingham and co-workers' study adds to recently accumulating evidence that tropical forests are unlikely to continue indefinitely to be carbon sinks as the world warms[11]. Tropical soil carbon does not receive as much attention as do the large and vulnerable soil-carbon stocks at high latitudes, which pose major concerns as a potential source of positive feedback to climate change[12]. But tropical-forest soils also contain substantial carbon stores that might be more vulnerable to loss in a warming world than was previously recognized.

Eric A. Davidson is in the Appalachian Laboratory, University of Maryland Center for Environmental Science, Frostburg, Maryland 21532, USA.
e-mail: edavidson@umces.edu

1. Friedlingstein, P. *et al. Earth Syst. Sci. Data* **11**, 1783–1838 (2019).
2. Bond-Lamberty, B. & Thomson, A. *Biogeosciences* **7**, 1915–1926 (2010).
3. Nottingham, A. T., Meir, P., Velasquez, E. & Turner, B. L. *Nature* **584**, 234–237 (2020).
4. Lal, R. *Carbon Mgmt* **4**, 439–462 (2014).
5. Davidson, E. A. & Janssens, I. A. *Nature* **440**, 165–173 (2006).
6. Conant, R. T. *et al. Glob. Change Biol.* **17**, 3392–3404 (2011).
7. Carey, J. C. *et al. Proc. Natl Acad. Sci. USA* **113**, 13797–13802 (2016).
8. Gillooly, J. F., Brown, J. H., West, G. B., Savage, V. M. & Charnov, E. L. *Science* **293**, 2248–2251 (2001).
9. Davidson, E. A., Janssens, I. A. & Luo, Y. *Glob. Change Biol.* **12**, 154–164 (2006).
10. Wieder, W. R. *et al. Glob. Biogeochem. Cycles* **29**, 1782–1800 (2015).
11. Sullivan, M. J. P. *et al. Science* **368**, 869–874 (2020).
12. Turetsky, M. R. *et al. Nature* **569**, 32–34 (2019).

A dynamically cold disk galaxy in the early Universe

https://doi.org/10.1038/s41586-020-2572-6

Received: 26 September 2019

Accepted: 4 June 2020

F. Rizzo[1]✉, S. Vegetti[1], D. Powell[1], F. Fraternali[2], J. P. McKean[2,3], H. R. Stacey[1,2,3] & S. D. M. White[1]

The extreme astrophysical processes and conditions that characterize the early Universe are expected to result in young galaxies that are dynamically different from those observed today[1–5]. This is because the strong effects associated with galaxy mergers and supernova explosions would lead to most young star-forming galaxies being dynamically hot, chaotic and strongly unstable[1,2]. Here we report the presence of a dynamically cold, but highly star-forming, rotating disk in a galaxy at redshift[6] $z = 4.2$, when the Universe was just 1.4 billion years old. Galaxy SPT–S J041839–4751.9 is strongly gravitationally lensed by a foreground galaxy at $z = 0.263$, and it is a typical dusty starburst, with global star-forming[7] and dust properties[8] that are in agreement with current numerical simulations[9] and observations[10]. Interferometric imaging at a spatial resolution of about 60 parsecs reveals a ratio of rotational to random motions of 9.7 ± 0.4, which is at least four times larger than that expected from any galaxy evolution model at this epoch[1–5] but similar to the ratios of spiral galaxies in the local Universe[11]. We derive a rotation curve with the typical shape of nearby massive spiral galaxies, which demonstrates that at least some young galaxies are dynamically akin to those observed in the local Universe, and only weakly affected by extreme physical processes.

SPT–S J041839–4751.9 (hereafter SPT0418–47) was observed with the Atacama Large Millimeter/submillimetre Array (ALMA) to image the thermal continuum emission from the galaxy's dust and the emission from the 158-μm fine-structure line of ionized carbon [C II] (Fig. 1a). The [C II] line is typically the brightest fine-structure line emitted in star-forming galaxies, and it is the main gas coolant, coming from multiple phases of the inter-stellar medium, including the warm ionized, the warm and cold neutral atomic, and the dense molecular medium[12]. We applied a three-dimensional (3D) lens–kinematic modelling technique[13] to the interferometric data cube containing the [C II] line to determine the gas surface brightness distribution in each spectral channel (Figs. 1, 2, Extended Data Figs. 1, 2, Extended Data Table 1; see Methods for full discussion), from which we derived the gas kinematics, and performed a robust dynamical analysis of the galaxy. In addition, we reconstructed the far-infrared surface brightness distribution of the heated dust emission from the interferometric continuum dataset.

We find that the rotation curve of SPT0418–47 has the typical shape of a bulge-dominated spiral galaxy in the local Universe[11]; it has a bump at 0.2 kpc from the galaxy centre and then declines before flattening at radii greater than 1.5 kpc (Fig. 2a, c). The [C II] velocity dispersion σ is well described by an exponential profile, with average velocities of ~45 km s^{-1} in the inner regions (≲1 kpc) and ~18 km s^{-1} in the outer disk (≳1 kpc) (Fig. 2b, d, Extended Data Table 1). From a decomposition of the rotation curve, we derive the relative contribution of the different mass components—the stellar component, the gaseous disk and the dark-matter halo—to the total galactic gravitational potential (Extended Data Table 5, Fig. 2c; see Methods).

SPT0418–47 has global physical properties (total stellar mass $M_{\rm star} = 1.2^{+0.2}_{-0.1} \times 10^{10} M_\odot$, dark-matter mass $M_{\rm DM} = 1.7^{+0.3}_{-0.3} \times 10^{12} M_\odot$, gas / fraction $f_{\rm gas} = 0.53^{+0.06}_{-0.08}$ and stellar effective radius $R_{\rm e} = 0.22^{+0.04}_{-0.02}$kpc; uncertainties are the 16th and 84th percentile ranges of the probability distribution function of each parameter; $M_\odot$ is the mass of the Sun; see Extended Data Table 5 for further parameters) that are in agreement with the predictions from the most recent theoretical models[9], as well as observations of the population of starburst galaxies at this redshift[10]. From the delensed dust emission, we derive an intrinsic infrared luminosity of $(2.4 \pm 0.4) \times 10^{12} L_\odot$ ($L_\odot$, luminosity of the Sun) a star formation rate (SFR) of $(352 \pm 65) M_\odot$ yr^{-1} and a gas-depletion timescale of 38 ± 9 Myr, which are all typical of millimetre-selected starburst galaxies at this redshift[10] (see Methods).

Our high-resolution 3D kinematic analysis shows that SPT0418–47 has a ratio of rotational velocity (V) to velocity dispersion σ of $V/\sigma = 9.7 \pm 0.4$ (Extended Data Table 2), which is similar to that of spiral galaxies in the local Universe[11], but considerably larger than what is predicted by most numerical[1,3] and analytical[2,4,5] models. For example, for the majority of star-forming galaxies at $z \approx 4$ with stellar masses in the range $10^9 M_\odot$ – $10^{10.5} M_\odot$, the most recent cosmological magneto-hydrodynamical simulation TNG50[1] gives $V/\sigma \lesssim 3$ (light-blue band in Fig. 3); even though such galaxies have rotationally supported gas-rich disks, they are dynamically hotter than their low-redshift counterparts. Complex astrophysical processes—such as stellar feedback by supernovae or radiation pressure, or active galactic nucleus (AGN) feedback from the central supermassive black-hole, galaxy mergers, and gas inflows and outflows—are expected to have a substantial effect on the

---

[1]Max-Planck Institute for Astrophysics, Garching, Germany. [2]Kapteyn Astronomical Institute, University of Groningen, Groningen, The Netherlands. [3]ASTRON, Netherlands Institute for Radio Astronomy, Dwingeloo, The Netherlands. ✉e-mail: frizzo@mpa-garching.mpg.de

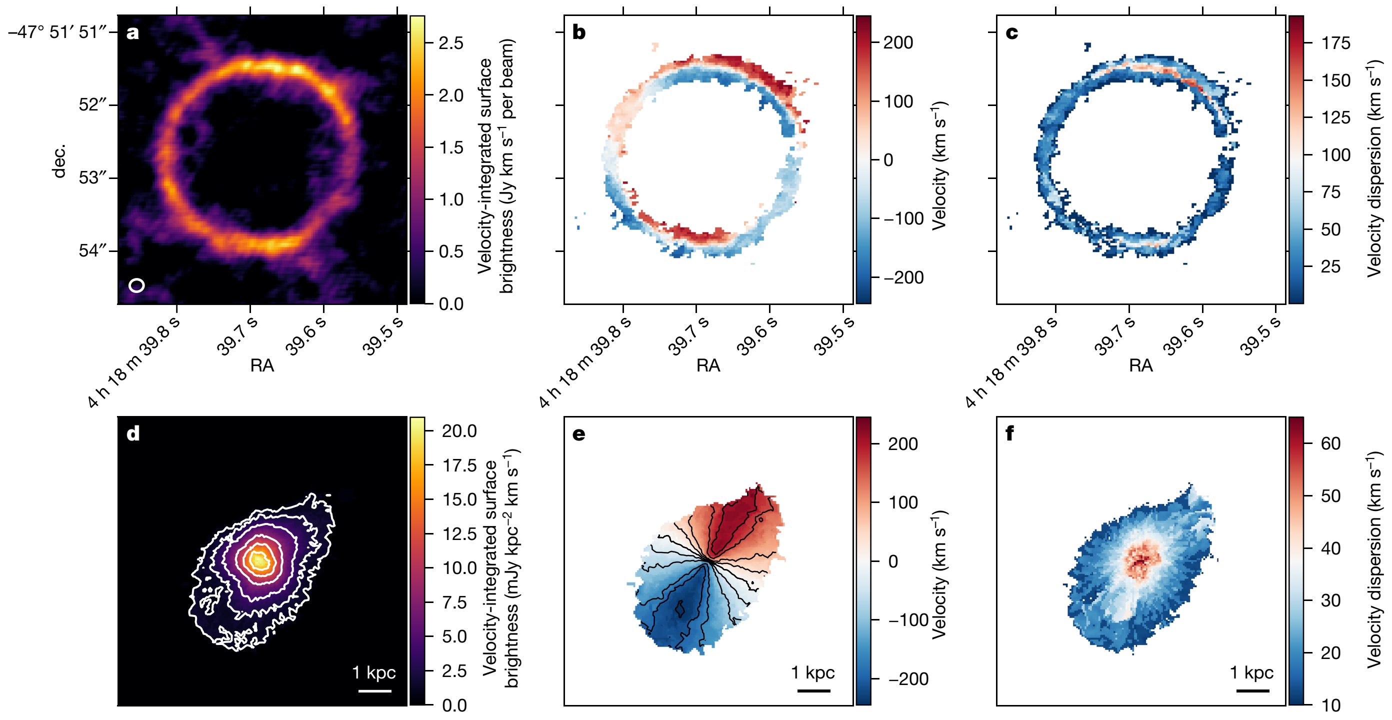

Fig. 1 | [C II] emission from the lensed galaxy SPT0418-47 and source plane reconstruction. a, Emission of the 158-μm fine-structure line of ionized carbon [C II] integrated across a velocity range of 721 km s^{-1} (zeroth-moment map). The beam size, shown as a white ellipse on the lower left corner, is 0.19″ × 0.17″ at a position angle of −85.22°. **b**, **c**, As in **a**, but the emission is colour-coded by the flux-weighted velocity (**b**) and velocity dispersion (**c**) (first- and second-moment maps). **d**–**f**, Zeroth-, first- and second moment-maps of the reconstructed source. In **d** the white contours are set at $n = 0.05, 0.1, 0.2, 0.4, 0.6, 0.8$ times the value of the maximum flux of the zeroth-moment map. In **e** the black solid contours are at $V_{\mathrm{sys}} \pm \Delta V$, where V_{sys} is the systemic velocity $V_{\mathrm{sys}} = 0$ km s^{-1} and $\Delta V = 40$ km s^{-1}. We note that the scales of the second-moment maps (**c** and **f**) are different because **c** shows the observed values, whereas **f** shows the intrinsic ones (beam-smearing corrected). These six maps are intended only for visualization; the source reconstruction and its kinematic modelling are performed using the full 3D information of the data cube containing the [C II] emission line (seeMethods and Extended Data Fig. 1 for further details). dec., declination; RA, right ascension.

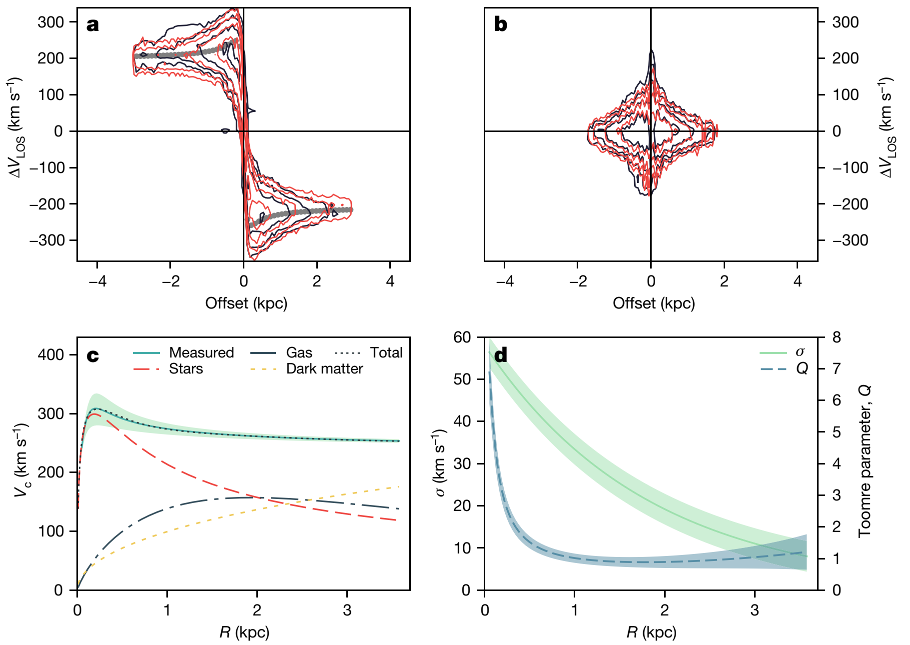

Fig. 2 | Kinematic and dynamical properties of SPT0418-47. a, **b**, [C II] emission in the position–velocity diagrams along the major (**a**) and minor (**b**) axis. These diagrams show slices—the equivalent of putting long slits along the two axes. The *x* axis shows the offset from the galaxy centre along the major and minor axis, and the *y* axis represents the line-of-sight velocity (ΔV_{LOS}) centred at the systemic velocity of the galaxy. The dark-blue contours show the reconstructed source, and the red contours show the best kinematic model (see Methods). The contour levels are set at $n = 0.1, 0.2, 0.4, 0.8$ times the value of the maximum flux in the major-axis position–velocity diagram. The grey circles show the rotation velocities derived using our 3D lens-kinematic methodology. **c**, Rotation curve decomposition. The green solid line shows the circular velocity (V_c) profile. The black dotted line is the best dynamical model, obtained by fitting the different mass components contributing to the total gravitational potential, as shown in the key. **d**, Velocity dispersion profile (solid green line) and Toomre parameter profile (dotted blue line). The coloured bands in **c** and **d** represent uncertainties obtained by error propagation from the 1 s.d. uncertainties of the parameters that define the respective profiles (see Methods and Extended Data Table 1).

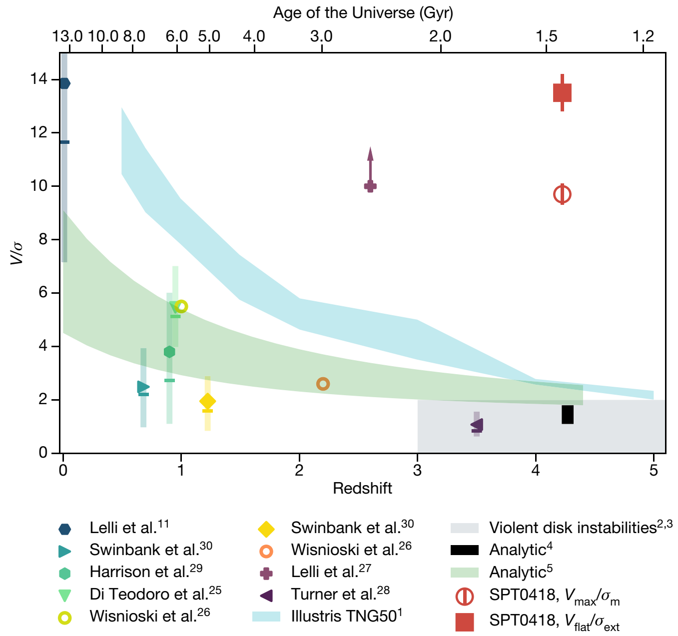

Fig. 3 | Comparison between SPT0418-47 and samples of observed and simulated galaxies. Mean ratios of the rotational to random motion (*V*/*σ*) of the gas versus redshift for the comparison samples[11,25–30] of observed star-forming galaxies indicated in the key and for SPT0418-47 (red square and empty red circle). The gas tracers are: H I (ref. [11]), Hα (refs. [25,26,29,30]), [O II] (ref. [30]), [O III] (ref. [28]) and [C I] (ref. [27]). For SPT0418, *V*/*σ* was obtained from the [C II] emission line. For the comparison samples, the shaded regions show the area between the 16th and 84th percentiles of the distributions, and the horizontal bars show the median values (where available). In Extended Data Table 3 we show the different extraction methods used to compute *V*/*σ*. For the empty markers, the *V*/*σ* values were calculated using for each galaxy a proxy for the maximum rotation velocity, $V_{\max}$. The *V*/*σ* values shown by the full markers were calculated using the flat or the outer part of the rotation curve, $V_{\rm flat}$. The violet cross is a lower limit for a single galaxy[27]. The light-blue band shows *V*/*σ* for simulated galaxies from Illustris TNG50[1] in the mass range $10^9 M_\odot$–$10^{11} M_\odot$. For these simulated galaxies, *V*/*σ* is calculated as the ratio between the maximum rotation velocity, $V_{\max}$, and the mean velocity dispersion, σ_m. The grey area shows the expected *V*/*σ* for galaxies dominated by violent disk instabilities[2,3]. The black and green areas show a prediction and an assumption, respectively, from two different analytical models (Analytic 1[4] and Analytic 2[5]). The red square is the $V_{\max}/\sigma_m$ for SPT0418-47, and the empty red circle shows the position of the *V*/*σ* value for SPT0418-47, calculated as the ratio between $V_{\rm flat}$ and the velocity dispersion at outer radii, $\sigma_{\rm ext}$ (see Extended Data Table 2). The error bars for the red square and empty red circle show the 1 s.d. uncertainties.

gas kinematics within galaxies at this early epoch, and are predicted to be responsible for a progressive increase of chaotic, random motions with redshift[1,4,5]. Our finding firmly rules out models in which a high star-formation feedback and a high gas fraction necessarily produce large turbulent motions[1,4] (light-blue, green and black bands in Fig. 3) and violent disk instabilities[2,3], resulting in dispersion dominated systems with $V/\sigma \lesssim 2$ at these redshifts (grey band in Fig. 3; see Methods for further discussion about these comparisons). Our result requires galaxy evolution models to produce dynamically cold galaxies that are not characterized by large turbulent motions[1,4] and violent instabilities[2,3], even at early times.

Our kinematic analysis also allows the level of axisymmetric disk instabilities to be measured within SPT0418−47 via the Toomre parameter[14] *Q*: a value of $Q > 1$ ensures that no instabilities will develop because large-scale collapse is prevented by differential rotation, whereas $Q \lesssim 1$ indicates that instabilities will be able to grow and lead to the creation of gas and star-formation clumps within the disk. For SPT0418−47, we find an average value of $Q = 0.97 \pm 0.06$ at a distance of $R > 1$ kpc (Fig. 2d), where the gas component is dominant (Fig. 2c), indicating a potentially unstable disk, prone to form clumpy star-forming regions. This result supports the hypothesis[15] that the irregular morphologies found for dusty starburst galaxies in the optical/ultraviolet rest-frame wavelengths[16] are poorly resolved clumpy star-forming regions, and not objects that are undergoing or have recently experienced a merging event.

Using our rotation-curve decomposition (see Methods), we find that the stellar component of SPT0418−47 is well described by a Sérsic profile with a Sérsic index of $2.2^{+0.3}_{-0.2}$ and a stellar mass of $1.2^{+0.2}_{-0.1} \times 10^{10} M_\odot$. Several observational studies of the structural properties[17] of galaxies have confirmed that the Hubble sequence is already in place at $z \approx 2.5$, with galaxies showing a large variety of morphologies. However, at $z \gtrsim 3$, the lack of spatially resolved data in the rest-frame optical emission for these galaxies has prevented the study of their structures and morphologies. The unprecedented spatial resolution of 60 pc of the dataset for SPT0418−47 allows one to study the morphological properties of a $z \approx 4$ galaxy. The bump in the inner region of the rotation curve clearly indicates that a bulge is already in place at $z \approx 4$, whereas the Sérsic index of ~2 is a signature of either a disky bulge[18] or an embedded disk-like component.

Dusty starburst galaxies are believed to be the progenitors of early-type galaxies (ETGs), which are the most massive galaxies observed today, dominated by old stellar populations. The most popular evolutionary track for this transformation[2,3,19] predicts that the dusty starburst phase is followed by a quenching phase, during which AGN feedback leads to gas consumption and heating, with the consequent formation of a population of compact quiescent galaxies[20] at $z \approx 2$. In the final phase, minor dry mergers are expected to be responsible for a growth in galaxy size and the transformation into present-day ETGs. In Fig. 4a–d we compare the main physical quantities of SPT0418–47, as inferred from our dynamical model, with the corresponding quantities for the sample of local ETGs from the ATLAS^{3D} survey[21]. We consider only those local ETGs with estimated stellar ages of ≥12 Gyr (ref. [22]), which is the look-back time corresponding to $z \approx 4$. The orange thin diamond in each panel shows the values derived for SPT0418−47 as observed today, and the red diamond shows the corresponding baryonic values (gas plus stars), under the assumption that all the gas that we observe today will be converted into stars, preserving the disk configuration. Given the SFR estimated for SPT0418−47, this conversion will happen in ~38 Myr (see Methods). The comparison between the ETGs and the stellar/baryonic quantities for SPT0418−47 in the size–mass plane (Fig. 4a) indicates that this starburst galaxy should increase its stellar mass by a factor of 6 (3 for the red diamond) and its effective radius by a factor of 11 (3 for the red diamond), in order to evolve into an average ETG (yellow cross). This is in agreement with a simple toy model[23] for mergers, in which a single major dry merger event would be responsible for an increase in both the size and the stellar mass of SPT0418−47 by a factor of 3. In Fig. 4a, the grey stars show the populations of compact galaxies[20] at $2 < z < 3$. Notably, the median size for this population is comparable to the size of SPT0418−47 (red diamond), but its median stellar mass is larger by a factor of 3. In addition, the position of SPT0418−47 on the mass–size plane is compatible with the low-mass end of both ETGs and compact $z \approx 2$ galaxies. This implies that either this galaxy will evolve smoothly into a low-mass ETG after the consumption and/or heating of the cold gas reservoir or, as predicted by the merger scenario, it will reach the bulk of the ETG population in the size–mass plane. Figure 4c shows that a potential progenitor of an ETG has already at $z \approx 4$ a disky stellar component, a feature that is very common especially amongst local fast-rotator ETGs[18]. Finally, we derived the fraction of dark-matter mass within the effective radius and found that, with a value of $f_{\rm DM}(R < R_e) = 0.095^{+0.004}_{-0.004}$ (red diamond), the central regions of SPT0418−47 are dominated by baryons. As shown in Fig. 4c, such a low fraction of dark matter is compatible with observations of local ETGs[24], implying that the physical

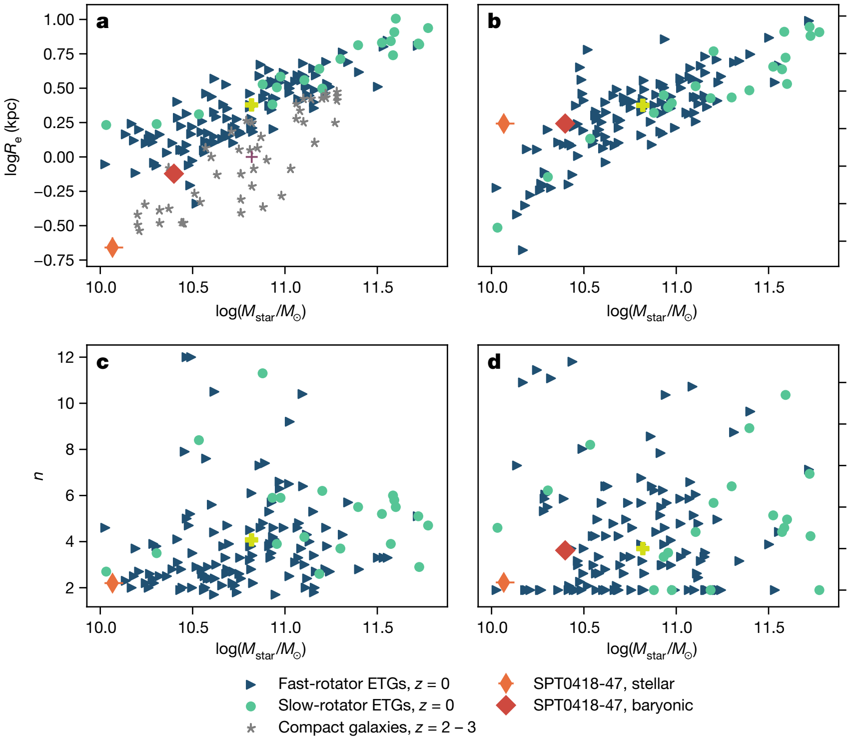

Fig. 4 | Comparison between SPT0418-47 and samples of its plausible descendants. In all panels, the orange thin diamond shows the position of SPT0418-47, and the red diamond shows the baryonic quantities (gas plus stars), under the assumption that all the gas that we observe today will be converted into stars, preserving the disk configuration. The error bars show the 1 s.d. uncertainties. The $z \approx 0$ ETGs (from the ATLAS^{3D} survey[18,21,22,24]), the plausible descendants of SPT0418-47, are shown according to their kinematic classification: blue triangles show fast rotators, green circles show slow rotators and yellow crosses show the median values. **a**, Size–stellar mass (M_{star}) plane. The grey stars show the compact galaxies[20] at $z \approx 2$–3 and the violet cross shows the median values for this sample. **b**, Circular velocity versus stellar mass. **c**, Sérsic index n versus stellar mass. **d**, Fraction of dark matter within the effective radius versus stellar mass.

mechanisms responsible for the mass and size growth of this galaxy with cosmic time should preserve the dark-matter contribution within the innermost ~1 kpc.

Online content

Any methods, additional references, Nature Research reporting summaries, source data, extended data, supplementary information, acknowledgements, peer review information; details of author contributions and competing interests; and statements of data and code availability are available at https://doi.org/10.1038/s41586-020-2572-6.

1. Pillepich, A. et al. First results from the TNG50 simulation: the evolution of stellar and gaseous discs across cosmic time. *Mon. Not. R. Astron. Soc.* **490**, 3196–3233 (2019).
2. Dekel, A. & Burkert, A. Wet disc contraction to galactic blue nuggets and quenching to red nuggets. *Mon. Not. R. Astron. Soc.* **438**, 1870–1879 (2014).
3. Zolotov, A. et al. Compaction and quenching of high-z galaxies in cosmological simulations: blue and red nuggets. *Mon. Not. R. Astron. Soc.* **450**, 2327–2353 (2015).
4. Krumholz, M. R., Burkhart, B., Forbes, J. C. & Crocker, R. M. A unified model for galactic discs: star formation, turbulence driving, and mass transport. *Mon. Not. R. Astron. Soc.* **477**, 2716–2740 (2018).
5. Hayward, C. C. & Hopkins, P. F. How stellar feedback simultaneously regulates star formation and drives outflows. *Mon. Not. R. Astron. Soc.* **465**, 1682–1698 (2017).
6. Weiß, A. et al. ALMA redshifts of millimeter-selected galaxies from the SPT survey: the redshift distribution of dusty star-forming galaxies. *Astrophys. J.* **767**, 88 (2013).
7. De Breuck, C. et al. A dense, solar metallicity ISM in the z= 4.2 dusty star-forming galaxy SPT 0418–47. *Astron. Astrophys.* **631**, A167 (2019).
8. Gullberg, B. et al. The nature of the [C II] emission in dusty star-forming galaxies from the SPT survey. *Mon. Not. R. Astron. Soc.* **449**, 2883–2900 (2015).
9. McAlpine, S. et al. The nature of sub-millimeter and highly star-forming galaxies in the EAGLE simulation. *Mon. Not. R. Astron. Soc.* **488**, 2440–2454 (2019).
10. Hodge, J. A. et al. The kiloparsec-scale star formation law at redshift 4: widespread, highly efficient star formation in the dust-obscured starburst galaxy GN20. *Astrophys. J. Lett.* **798**, 18 (2015).
11. Lelli, F., McGaugh, S. S. & Schombert, J. M. SPARC: mass models for 175 disk galaxies with spitzer photometry and accurate rotation curves. *Astron. J.* **152**, 157 (2016).
12. Stacey, G. J. et al. A 158 μm [C II] line survey of galaxies at z~ 1–2: an indicator of star formation in the early Universe. *Astrophys. J.* **724**, 957–974 (2010).
13. Rizzo, F., Vegetti, S., Fraternali, F. & Di Teodoro, E. A novel 3D technique to study the kinematics of lensed galaxies. *Mon. Not. R. Astron. Soc.* **481**, 5606–5629 (2018).
14. Toomre, A. On the gravitational stability of a disk of stars. *Astrophys. J.* **139**, 1217–1238 (1964).
15. Carilli, C. L. & Walter, F. Cool gas in high-redshift galaxies. *Annu. Rev. Astron. Astrophys.* **51**, 105–161 (2013).
16. Chen, C.-C. et al. An ALMA survey of submillimeter galaxies in the Extended Chandra Deep Field South: near-infrared morphologies and stellar sizes. *Astrophys. J.* **799**, 194 (2015).
17. Lang, P. et al. Bulge growth and quenching since z = 2.5 in CANDELS/3D-HST. *Astrophys. J.* **788**, 11 (2014).
18. Krajnović, D. et al. The ATLAS^{3D} project – XVII. Linking photometric and kinematic signatures of stellar discs in early-type galaxies. *Mon. Not. R. Astron. Soc.* **432**, 1768–1795 (2013).
19. Toft, S. et al. Submillimeter galaxies as progenitors of compact quiescent galaxies. *Astrophys. J.* **782**, 68 (2014).
20. Barro, G. et al. CANDELS+3D-HST: compact SFGs at z ~ 2–3, the progenitors of the first quiescent galaxies. *Astrophys. J.* **791**, 52 (2014).
21. Cappellari, M. et al. The ATLAS^{3D} project – I. A volume-limited sample of 260 nearby early-type galaxies: science goals and selection criteria. *Mon. Not. R. Astron. Soc.* **413**, 813–836 (2011).
22. McDermid, R. M. et al. The ATLAS^{3D} Project – XXX. Star formation histories and stellar population scaling relations of early-type galaxies. *Mon. Not. R. Astron. Soc.* **448**, 3484–3513 (2015).
23. Naab, T., Johansson, P. H. & Ostriker, J. P. Minor mergers and the size evolution of elliptical galaxies. *Astrophys. J. Lett.* **699**, 178–182 (2009).
24. Cappellari, M. et al. The ATLAS^{3D} project – XX. Mass-size and mass-σ distributions of early-type galaxies: bulge fraction drives kinematics, mass-to-light ratio, molecular gas fraction and stellar initial mass function. *Mon. Not. R. Astron. Soc.* **432**, 1862–1893 (2013).
25. Di Teodoro, E. M., Fraternali, F. & Miller, S. H. Flat rotation curves and low velocity dispersions in KMOS star-forming galaxies at z ~ 1. *Astron. Astrophys.* **594**, A77 (2016).
26. Wisnioski, E. et al. The KMOS^{3D} survey: design, first results, and the evolution of galaxy kinematics from $0.7 \le z \le 2.7$. *Astrophys. J.* **799**, 209 (2015).
27. Lelli, F. et al. Neutral versus ionized gas kinematics at $z \simeq 2.6$: the AGN-host starburst galaxy PKS 0529–549. *Mon. Not. R. Astron. Soc.* **479**, 5440–5447 (2018).
28. Turner, O. J. et al. The KMOS Deep Survey (KDS) - I. Dynamical measurements of typical star-forming galaxies at $z \simeq 3.5$. *Mon. Not. R. Astron. Soc.* **471**, 1280–1320 (2017).
29. Harrison, C. M. et al. The KMOS Redshift One Spectroscopic Survey (KROSS): rotational velocities and angular momentum of $z \approx 0.9$ galaxies. *Mon. Not. R. Astron. Soc.* **467**, 1965–1983 (2017).
30. Swinbank, A. M. et al. Angular momentum evolution of galaxies over the past 10 Gyr: a MUSE and KMOS dynamical survey of 400 star-forming galaxies from z = 0.3 to 1.7. *Mon. Not. R. Astron. Soc.* **467**, 3140–3159 (2017).

Methods

Observations

SPT0418−47 was identified during the South Pole Telescope Survey[31] as a far-infrared luminous source with dust-like spectral indices at 1.4 mm and 2.0 mm (ref. [32]). Follow-up observations[32] with ALMA confirmed SPT0418−47 to be a dusty starburst galaxy at redshift $z = 4.2248$ (ref. [6]) that is strongly gravitationally lensed by a foreground galaxy at $z = 0.263$.

The data used for the analysis described here were taken from the ALMA Archive. SPT0418−47 was observed with ALMA on 5 July 2017 under project code 2016.1.01499.S (Principal investigator, K. Litke). Observations were taken at a central frequency of 358 GHz with an antenna configuration with a maximum baseline of 1,400 m. The data were correlated with both linear polarizations (*XX* and *YY*), with a visibility integration time of 6 s, in four spectral windows, each with 240 channels and 1.875 GHz bandwidth. The spectral windows were centred on 350.8, 352.7, 362.8 and 364.6 GHz, and the last spectral window covers the redshifted rest frequency of the [C II] line ($\nu_{\mathrm{rest}} = 1{,}900.5369$ GHz). J0519-4546 was observed to calibrate the flux density scale and J0522-3627 was used to correct the spectral bandpass. J0428-5005 was observed as a secondary check source. Phase switching to J0439-4522 was carried out at 7-min intervals to calibrate the complex gains resulting from atmosphere-induced phase and amplitude fluctuations. The total on-source integration time was 21 min.

We calibrated the raw visibility data using the ALMA pipeline in the Common Astronomy Software Applications (CASA) package[33]. The data were then inspected to confirm the quality of the pipeline calibration and that no further flagging was required. Phase-only self-calibration was performed on the continuum with a solution interval of 100 s to correct for residual phase errors. The complex gain corrections from the continuum were applied to the line spectral window. The line data were prepared by fitting a model to the line-free spectral windows and subtracting it from the visibilities, to produce a dataset with only the spectral line emission. To improve the signal-to-noise ratio, we averaged the data into groups of four velocity channels resulting in 28 independent channels, each with a width of 25.7 km s^{-1}.

SPT0418-47 was imaged on a pixel scale of 0.03 arcsec per pixel with natural weighting of the visibilities, and deconvolved using CLEAN[34]. The zeroth-, first- and second-moment maps of the [C II] emission are shown in Fig. 1a–c; we note that these images are intended only for visualization, as all the modelling and analysis were performed on the visibility data directly. Throughout the manuscript, we assume a ΛCDM cosmology, with Hubble constant $H_0 = 67.8$ (km s^{-1})/Mpc, matter density $\Omega_{\mathrm{m}} = 0.308$, and vacuum energy density $\Omega_\Lambda = 0.691$[70].

Lens and kinematic model

We model the data cube containing the [C II] emission line using a 3D Bayesian lens–kinematic modelling technique that fits the data directly in visibility space (Extended Data Fig. 1). See Rizzo et al.[13] and Powell et al.[35] for a more detailed description of the modelling approach, which is briefly summarized below.

The method used for source reconstruction is grid-based: the background source surface brightness distribution is reconstructed on a triangular adaptive grid[36] defined by a Delaunay tessellation. The source grid automatically adapts with the lensing magnification, so that there is a high pixel density in the high-magnification regions, resulting in a spatial resolution of ~40 pc in the inner regions and ~90 pc in the outer regions for this system. The kinematics of the background galaxy are obtained by fitting the lensed data directly in a hierarchical Bayesian fashion, where a 3D kinematic model, $\mathbf{s}_{\mathrm{kin}}$, that describes a rotating disk is used as a regularizing prior for a pixellated source reconstruction.

Taking advantage of the fact that gravitational lensing conserves surface brightness, and considering the observational noise $\mathbf{n}$, the data in the visibility space $\mathbf{d}$ and the source surface brightness distribution $\mathbf{s}$ can be related to each other via the following set of linear equations:

$$DL(\eta_{\mathrm{lens}})\mathbf{s} + \mathbf{n} = \mathbf{d}, \tag{1}$$

where L is the lensing operator, which is a function of the lensing parameters η_{lens}, and D is the non-uniform discrete Fourier transform operator. Because both η_{lens} and $\mathbf{s}$ are unknown, equations (1) can not be simply inverted. We therefore fit the data within the framework of Bayesian statistics by using two levels of inference.

At the first level of inference, it can be shown that given the data, a lens–mass model and a source kinematic model, the most probable a posteriori source $\mathbf{s}_{\mathrm{MP}}$ is obtained by solving the following set of linear equations:

$$[(DL)^{\mathrm{T}}C^{-1}DL + \lambda R^{\mathrm{T}}R]\mathbf{s} = (DL)^{\mathrm{T}}C^{-1}\mathbf{d} + \lambda R^{\mathrm{T}}R\mathbf{s}_{\mathrm{kin}}, \tag{2}$$

where C^{-1} is the noise covariance and R is the source regularization form with regularization strength λ.

At the second level of inference, the lens parameters η_{lens}, the regularization strength λ and the kinematic parameters η_{kin} defining $\mathbf{s}_{\mathrm{kin}}$ are obtained by maximizing the posterior probability distribution $P(\mathbf{d} \mid \eta_{\mathrm{lens}}, \eta_{\mathrm{lens}}, \lambda)$ defined as:

$$\begin{aligned} &2\log P(\mathbf{d}|\eta_{\mathrm{lens}}, \eta_{\mathrm{kin}}, \lambda) = \\ &-\chi^2 - \lambda(\mathbf{s}_{\mathrm{MP}} - \mathbf{s}_{\mathrm{kin}})^{\mathrm{T}}R^{\mathrm{T}}R\,(\mathbf{s}_{\mathrm{MP}} - \mathbf{s}_{\mathrm{kin}}) - \log(\det A) \\ &+ \log[\det(\lambda R^{\mathrm{T}}R)] + \log[\det(2\pi C^{-1})]\,. \end{aligned} \tag{3}$$

In equation (3), $\chi^2 = (DL\mathbf{s} - \mathbf{d})^{\mathrm{T}}C^{-1}(DL\mathbf{s} - \mathbf{d})$ and the matrix A is defined as $A = [(DL)^{\mathrm{T}}C^{-1}DL + \lambda R^{\mathrm{T}}R]$.

Because of the large number of visibilities per channel ($n_{\mathrm{vis},i} = 163{,}190$), we replace the non-uniform discrete Fourier transform operator D with a non-uniform fast Fourier transform (FFT) operator[37,38], which first uses a gridding kernel to interpolate the visibilities onto a regular gridded u–v plane, then applies an FFT, and finally uses an apodization correction to remap the model and the data onto the original u–v sampling. Because the non-uniform FFT does not have an explicit matrix representation, the source inversion (equation (2)) is solved using a preconditioned conjugate gradient solver. We note that for the conjugate gradient method we use a tolerance of 10^{-12}, which results in typical accuracies of 10^{-6} for the source inversions.

As usually done when modelling galaxy–galaxy strong lensing observations, the lens is described by a projected mass density profile with a cored elliptical power-law distribution plus the contribution of an external shear component of strength Γ_{sh} and position angle θ_{sh} (see Extended Data Table 1). This assumption has been shown to provide a good fit to large samples of known lenses, as discussed, for example, by Koopmans et al.[39] and Barnabè et al.[40]. The dimensionless projected mass density profile is defined as

$$\kappa(x, y) = \frac{\kappa_0\left(2 - \frac{\gamma}{2}\right)q^{\gamma - \frac{3}{2}}}{2[q^2(x^2 + r_{\mathrm{c}}^2) + y^2]^{\frac{\gamma-1}{2}}}, \tag{4}$$

where κ_0 is the normalization factor, q is the projected flattening, γ is the density slope (a value of $\gamma = 2$ corresponds to an isothermal profile), x_0 and y_0 define the centre of the mass distribution, r_{c} is the core radius and θ is the position angle of the major axis. The lens mass model parameters are in agreement within 2 s.d. with those derived from modelling the dust continuum[41].

The kinematic model $\mathbf{s}_{\mathrm{kin}}$ is defined by the parameters describing the rotation velocity, the velocity dispersion profile and the geometry of the galaxy. We choose the multi-parameter function

$$V_{\mathrm{rot}}(R) = V_{\mathrm{t}} \frac{\left(1+\frac{R_{\mathrm{t}}}{R}\right)^{\beta}}{\left[1+\left(\frac{R_{\mathrm{t}}}{R}\right)^{\xi}\right]^{1/\xi}} \tag{5}$$

as the functional form for the rotation velocity (see Extended Data Table 1). In equation (5), V_{t} is the velocity scale, R_{t} is the turnover radius between the inner rising and outer part of the curve, β specifies the power-law behaviour of the curve at large radii and ξ defines the sharpness of the turnover. We choose the above multi-parameter function because it is flexible enough to reproduce the large variety of observed rotation curves, and therefore allows much more freedom than other typically used functions, for example, the arctangent.

The velocity dispersion profile, $\sigma(R)$ is described by an exponential function, which is more flexible than the more commonplace choice of a constant value[26,28]. We also tested a linear function but found it to be significantly less favoured by the data, by a Bayes factor of 1.8 relative to the exponential model.

For the geometry of the kinematic model, defined by the inclination (i) and position angle (PA), we assume that there is no radial variation (Extended Data Table 1). The surface density of the gas is not a free parameter; instead, we impose a pixel-by-pixel normalization, which is given by the surface brightness distribution obtained from the lens modelling of the zeroth-moment map. The advantage of using this normalization is that it allows us to account for possible asymmetries in the gas distribution. The derivation of the lens mass model and the source kinematics is done using a four-step optimization scheme, and the uncertainties on the parameters are obtained from the posterior distributions calculated with MULTINEST[42] (Extended Data Fig. 2), by adopting the user-defined tolerance, sampling efficiency and live points of 0.5, 0.8 and 200. We then verified that the evidence estimated by MULTINEST flatten as a function of the prior volume. As described in our method paper[13], for each parameter, we adopt priors that are flat in the intervals $[\tilde{\eta}_{\mathrm{lens/kin}} - 0.2\tilde{\eta}_{\mathrm{lens/kin}}, \tilde{\eta}_{\mathrm{lens/kin}} + 0.2\tilde{\eta}_{\mathrm{lens/kin}}]$, where $\tilde{\eta}_{\mathrm{lens/kin}}$ are the best-/fitting parameters, inferred from the nonlinear optimization. To be conservative, we report as errors in the parameters the sum in quadrature of the following two contributions: the 1 s.d. uncertainty on the posterior distributions derived by MULTINEST and the difference between the maximum a posteriori parameter values obtained by MULTINEST and by the nonlinear optimizer. These values of the uncertainties are in line with what is expected from the tests presented in Rizzo et al.[13], where we applied our methodology to data characterized by spatial and spectral resolutions of at least a factor of three worse than those analysed in this manuscript.

Direct forward modelling

For a consistency check, we also derived the lens (η_{lens}) and kinematic (η_{kin}) parameters by using a direct forward modelling methodology. The main difference to the methodology described in Rizzo et al.[13] and summarized above is that a parametric, rather than pixelated, source is used to fit the data. The parametric source is defined by the same 3D kinematic model, $\mathbf{s}_{\mathrm{kin}}$, used as a regularizing prior for the source in our fiducial method. In this implementation, to marginalize over η_{lens} and η_{kin}, we maximize the posterior probability distribution (see equation (3) for comparison), defined as $2\log P(\mathbf{d}|\eta_{\mathrm{lens}}, \eta_{\mathrm{kin}}) = -(DL\mathbf{s}_{\mathrm{kin}} - \mathbf{d})^{\mathrm{T}} C^{-1}(DL\mathbf{s}_{\mathrm{kin}} - \mathbf{d})$.

The parameters obtained with the forward modelling method are within the 1 s.d. uncertainties with respect to those obtained with our fiducial model (see Extended Data Fig. 2).

In the direct forward modelling method, the source is forced to have a regular configuration, chosen a priori using the assumptions on the kinematic parametrizations. As explained in detail in Rizzo et al.[13], by assuming our fiducial methodology, we instead use the kinematic model as a prior for the source reconstruction. The main advantage of the fiducial approach is that it does not directly impose a parametric model that may not be a good fit to the data.

Beam-smearing correction

In recent years, observational studies have used the V/σ ratio to study the kinematic evolution of galaxy populations and distinguish between rotation- and dispersion-dominated systems. However, the measurement of the V/σ ratio is a challenge for high-redshift, marginally resolved studies because of the so-called beam-smearing effect[43]. This effect can cause a strong overestimation of the velocity dispersion and underestimation of the rotation velocity. For galaxies in the redshift range of 1–3, there is no consensus on whether there is an increase of the V/σ ratio with time[25–30]. For galaxies at $z \gtrsim 4$, there have been very few attempts to go beyond the fitting of the integrated line profile[44,45]. However, marginally resolved observations and a low signal-to-noise ratio have prevented a measurement of a beam-smearing-corrected V/σ ratio. The combination of the high signal-to-noise ratio and the spatial resolution that is achievable thanks to gravitational lensing and to an intrinsically beam-smearing corrected kinematic analysis has allowed us to probe the intrinsic V/σ ratio at this high redshift. Different definitions of the V/σ ratio can be found in the literature[25–30]. Here we use the two most popular ones (see Extended Data Table 2). We obtain $V/\sigma = 9.7 \pm 0.4$ when we calculate V/σ as the ratio between the maximum rotation velocity V_{max} and the mean velocity dispersion σ_{m}, whereas we get $V/\sigma = 13.7 \pm 0.7$ when we calculate it as the ratio between the flat part of the rotation velocity V_{flat} and the velocity dispersion σ_{ext} at outer radii ($R > 1$ kpc). The values of V/σ for SPT0418−47 seem to indicate that there is no decrease of V/σ with time. However, larger samples will be needed to confirm this trend.

V/σ for the comparison samples

To determine the evolution of the dynamical properties of galaxies across cosmic time, different studies have used different gas tracers (see column 2 of Extended Data Table 3) and different extraction methods to obtain their physical parameters. The comparison of V/σ for SPT0418−47 with values derived from different gas tracers is based on the assumption that the ionized gas kinematics reflects the cold-gas motions of galaxies, as observed for a few galaxies[46,47]. However, by comparing the results obtained from different tracers and with different techniques, a recent study[48] found that velocity dispersions measured from ionized tracers tend to be ~10–15 km s^{-1} higher than those measured from molecular tracers. If we add this 15 km s^{-1} to our inferred [C II] velocity dispersions, we find $V_{\mathrm{max}}/\sigma_{\mathrm{m}} = 6.6$ and $V_{\mathrm{Flat}}/\sigma_{\mathrm{ext}} = 7.8$, which are still much higher than those observed and those predicted by galaxy evolution models. We also stress that whereas the above analysis mostly compared the molecular with the ionized gas tracers, in this study we focus on the [C II] emission, which traces both cold and warm gas. In Extended Data Table 3, we show the main assumptions made to extract the velocities and velocity dispersions that enter the calculation of the V/σ ratio for the samples shown in Fig. 3.

V/σ in galaxy evolution models

There is a general consensus[49–52] that galaxy disks at high redshift are much more turbulent than their local counterparts in all components (stars, warm and cold gas). In Fig. 3 we show the V/σ predicted (or assumed) by current galaxy evolution models.

The light-blue area shows the predicted evolution of V/σ in the TNG50 simulation[1], where the gas kinematics is derived from Hα-emitting gas. However, because, by construction, the ionized and molecular gas of TNG50 galaxies have the same dynamics, we can compare these estimations with our measurement from the [C II] emission line. TNG50 galaxies at $z \approx 4$ have median $V_{\mathrm{max}}/\sigma_{\mathrm{m}} \approx 3$ with a standard deviation of 1.5, which means that SPT0418−47 is 4.5 standard deviations away from the median value.

By using an analytical approach and a cosmological mesh-refinement simulation, two recent studies[2,3] found that galaxies at $z \gtrsim 3$ are dominated by violent disk instabilities, which lead to V/σ values of $\lesssim 2$ in all components (grey area in Fig. 3).

By using an analytical model that combines stellar feedback and gravitational instabilities, Krumholz et al.[4] derived a prediction for the correlation between cold-gas velocity dispersion and SFR as SFR = $0.42 f_{\mathrm{eff,gas}} V^2 \sigma / (\pi G Q_{\mathrm{min}})$ (equation (60) in ref. [4]), where we have used the constants that are appropriate for high-redshift galaxies[4,48]. By using $f_{\mathrm{eff,gas}} = f_{\mathrm{gas}} \times 1.5 = 0.53 \times 1.5$, SFR = $352 M_\odot$ yr^{-1}, $V = 259$ km s^{-1}, $Q_{\mathrm{min}} = 0.88$, we derived a value of $\sigma = 183^{+53}_{-42}$ km s^{-1}, which is a factor of ~6 higher than our measured value of 32 km s^{-1} and implies $V/\sigma = 1.4^{+0.4}_{-0.3}$ (black band in Fig. 3).

Hayward and Hopkins[5] used an analytical model to study the effects of stellar feedback in regulating star formation and driving outflow. In this case, the gas velocity dispersion is not a predicted quantity, but it is derived by assuming the following relation between σ and the circular velocity: $\sigma \approx f_{\mathrm{gas}} V_{\mathrm{c}} / \sqrt{2}$. For the values of the gas fraction and V_{c} measured for SPT0418–47 by our analysis, this analytical model implies $\sigma = 120$ km s^{-1}, which is a factor of ~4 higher than the measured value, resulting in $V/\sigma = 2.6$. In Fig. 3 (green band), we show the predictions of V/σ for this model, obtained by using the relations of ref. [5] for velocity versus stellar mass and the redshift evolution of the velocity dispersion with respect to the gas fraction.

Dynamical model and Toomre parameter

Under the assumption that the total galactic gravitational potential Φ is axisymmetric, the rotation velocity $V_{\mathrm{rot}}(R)$ of the gas, in cylindric coordinates (R, ϕ, z), is related to Φ by the equation $R(\partial\Phi/\partial R)_{z=0} = V_{\mathrm{c}}^2 = V_{\mathrm{rot}}^2 + V_{\mathrm{A}}^2$, where V_{c} is the circular velocity and V_{A} is the asymmetric-drift correction that accounts for the pressure support due to the random motions. Under the assumptions that the gas of the rotating disk has a thickness that is independent of the radius[53], it is thin and it has a spatial distribution described by an exponential profile, $\Sigma_{\mathrm{gas}} = \Sigma_0 \exp(-R/R_{\mathrm{gas}})$, the expression for V_{A} is given by

$$V_{\mathrm{A}}^2 = -R\sigma^2 \partial \ln(\sigma^2 \Sigma_{\mathrm{gas}})/\partial R = -R\sigma^2 \partial \ln[\sigma^2 \exp(-R/R_{\mathrm{gas}})]/\partial R. \quad (6)$$

To measure the scale radius R_{gas}, we divide the zeroth-moment map of the reconstructed source (Fig. 1d) into rings (with centres, position angles and inclinations defined by the values of the kinematic model; see Extended Data Table 1) and we calculate the surface densities at a certain radius as azimuthal averages inside that ring. The surface density profile obtained in this way is then fitted using the exponential profile, resulting in a value of $R_{\mathrm{gas}} = 0.9$ kpc. The resulting asymmetric-drift correction, equation (6), gives a small contribution (≲1%) with respect to $V_{\mathrm{rot}}(R)$.

To derive the contribution of the gas, stellar and dark-matter components to the total gravitational potential, we model the circular velocity as $V_{\mathrm{c}} = \sqrt{V_{\mathrm{star}}^2 + V_{\mathrm{gas}}^2 + V_{\mathrm{DM}}^2}$. Here V_{star} is the stellar contribution to the circular velocity, under the assumption that this component is described by a Sérsic profile[54,55], defined by the total stellar mass M_{star}, the effective radius radius R_{eff} and the Sérsic index n. V_{gas} is the gas contribution, under the assumption that the gas in this galaxy has a distribution described by an exponential profile, as traced by the [C II] emission line. The scale length that enters V_{gas} is fixed at the value R_{gas} found as described in the previous section, and the only free parameter of the fit for V_{gas} is the conversion factor ($\alpha_{[\mathrm{CII}]}$) between the total [C II] luminosity and the total gas mass. A number of recent studies have found that [C II] is a good tracer of the total gas mass[56,57]. For SPT0418–47, the [C II] luminosity is $1.8 \times 10^9 L_\odot$, obtained by computing the zeroth-moment map of the [C II] emission as the signal integrated along the spectral axis at each pixel of the reconstructed source. The dark-matter contribution V_{DM} is modelled as a Navarro–Frenk–White[58] (NFW) spherical halo, with a concentration parameter of $c = 3.06$. The latter is obtained by averaging the values of c at $z = 4.22$ for dark-matter haloes with masses between $10^{10} M_\odot$ and $10^{13} M_\odot$, assuming the mass–concentration relation estimated by N-body cosmological simulations[59]. We note that at this redshift, c is almost independent of the dark-matter halo mass, varying by just 6% for a variation of 3 orders of magnitude in the halo mass. To test the effect of our assumption of a constant concentration, we repeated the analysis with a c that is free to vary according to either a uniform prior or a Gaussian prior centred on the predicted mass–concentration relation, and found that all inferred dynamical parameters do not change considerably with c.

We summarize our assumptions for the dynamical model in the second column of Extended Data Table 4, and the corresponding free parameters are shown in the third column of the same table. We compute the Bayesian posterior distribution of these parameters using DYNESTY, a python implementation of the Dynamic Nested Sampling algorithm[60] (see Extended Data Fig. 3 and Extended Data Table 5). We use log-uniform priors for the mass parameters and uniform priors for the scale radii (fourth column of Extended Data Table 4). The inferred $M_{\mathrm{star}} = 1.2^{+0.2}_{-0.1} \times 10^{10} M_\odot$ is in excellent agreement with the value of $9.5 \pm 3.0 \times 10^9 M_\odot$ found in a recent independent study[7] by fitting the spectral energy distribution of this galaxy. For $\alpha_{[\mathrm{CII}]}$ we employ a uniform prior in the range corresponding to ±3 standard deviations around the mean value of $30 M_\odot/L_\odot$, derived from a large sample of low- and high-redshift galaxies[56]. We infer a value of $\alpha_{[\mathrm{CII}]} = 7.3^{+1.0}_{-1.2} M_\odot/L_\odot$, in agreement with other studies of $z \approx 4$ dusty starburst galaxies[57].

In Extended Data Table 5 we show some relevant physical quantities (see also Fig. 4d) derived from our dynamical analysis. In particular, for each of these we quote the 16th, 50th and 84th percentile, which were obtained from the full posterior sample points returned by DYNESTY.

We also calculate the Toomre parameter[14] (Fig. 2d) using the general definition $Q(R) = \sigma\kappa/(\pi G \Sigma_{\mathrm{gas}})$. Here, κ is the epicycle frequency defined as $\kappa = \sqrt{R \mathrm{d}\Omega^2/\mathrm{d}R + 4\Omega^2}$, where $\Omega = V_{\mathrm{rot}}/R$ is the angular frequency.

Comparison with local ETGs

In Fig. 4 we show some physical quantities for local ETGs taken from several studies of the ATLAS^3 survey[18,21,22,24,61,62]. For comparison with SPT0418–47, we show for each quantity an upper limit, calculated under the assumption that all gas is converted into stars, and the observed quantities (orange diamonds), which can also be interpreted as a lower limit if all the gas that we observe is ejected by feedback processes. However, we caution that this upper limit does not take into account the accretion of gas if no baryons are expelled by outflows. In this case, the red diamond could move farther towards the upper right corner in the size–mass plane (panel a, Fig. 4).

Dust continuum and SFR

Using the parameters of the lens mass model shown in Extended Data Table 1, we perform a pixelated source reconstruction of the dust continuum at 160 μm (rest frame), which allows us to calculate a total magnification factor of $\mu = 32.3 \pm 2.5$. SPT0418–47 has an observed (unlensed) infrared luminosity of $L_{\mathrm{IR,obs}} = (7.7 \pm 1.3) \times 10^{13} L_\odot$ (ref. [63]). This value was obtained from a spectral energy distribution fitting of seven photometric data points in the wavelength rest frame range 48–574 μm. Under the assumption that the morphology of the source is the same for all photometric points in the infrared band, we can use the magnification factor estimated from the emission at 160 μm to estimate an intrinsic luminosity of $L_{\mathrm{IR}} = L_{\mathrm{IR,obs}}/\mu = (2.4 \pm 0.4) \times 10^{12} L_\odot$. By assuming that the infrared emission comes from the thermal emission of dust, heated by the radiation field coming from young stars, we compute SFR = $(352 \pm 65) M_\odot$ yr^{-1}. This value is derived from L_{IR} by applying a conversion factor of $1.48 \times 10^{-10} M_\odot L_\odot^{-1}$ yr^{-1}, which is valid for a Kroupa initial mass function[64]. The gas-depletion timescale is M_{gas}/SFR = 38 ± 9 Myr.

Velocity dispersion in starburst galaxies

By comparing the gas kinetic energy and the energy injected by stellar feedback, we determine whether the turbulence driven by supernova explosions can explain the velocity dispersion measured for SPT0418–47. The gas kinetic energy is given by[65,66] $E_{\mathrm{kin}} = 3/2\, M_{\mathrm{gas}}\, \sigma_{\mathrm{m}}^2 \approx 5 \times 10^{56}$

(see Extended Data Table 5). We estimate the energy injected by supernova explosions as[65,66] $E_{\rm SNe} = \eta_{\rm SN}{\rm SFR}\varepsilon_{\rm SN}E_{\rm SN}t_{\rm D}$. Here, $\eta_{\rm SN}$ is the supernova rate, $\varepsilon_{\rm SN}$ is the SFR efficiency (that is, the fraction of the SN energy, $E_{\rm SN} = 10^{51}$ erg, converted into turbulence) and $t_{\rm D}$ is the dissipation rate of the turbulence. We assume $\eta_{\rm SN} = 0.01\ M_{\odot}^{-1}$ (ref. [65]). For the highly uncertain parameter $\varepsilon_{\rm SN}$ we assume an upper limit of 0.1, based on high-redshift observations[67]. $t_{\rm D}$ is calculated as $t_{\rm D} = h/\sigma_{\rm m}$ where h is the scale height of the gas, assumed to be ~500 pc. Under this assumption, we estimate $E_{\rm SNe} \approx 5 \times 10^{56}$ erg, in agreement with $E_{\rm kin}$, suggesting that the velocity dispersion measured for SPT0418−47 can be explained as being produced by turbulence driven by stellar feedback. Furthermore, we note that starburst galaxies both at low[68,69] and high[27] redshifts have values of velocity dispersions, measured from molecular or neutral gas, that are comparable with those found for SPT0418−47.

Data availability

This study used the ALMA data 2016.1.01499.S, available at http://almascience.eso.org/aq/.

Code availability

The methodology used for the source reconstruction and its kinematic modelling is fully explained in ref. [13]. The code is available from the corresponding author upon reasonable request.

31. Carlstrom, J. E. et al. The 10 meter South Pole Telescope. *Publ. Astron. Soc. Pacif.* **123**, 568–581 (2011).
32. Vieira, J. D. et al. Dusty starburst galaxies in the early Universe as revealed by gravitational lensing. *Nature* **495**, 344–347 (2013).
33. McMullin, J. P., Waters, B., Schiebel, D., Young, W. & Golap, K. CASA architecture and applications. *ASP Conf. Ser*. **376**, 127–130 (2007).
34. Högbom, J. A. Aperture synthesis with a non-regular distribution of interferometer baselines. *Astron. Astrophys. Suppl. Ser*. **15**, 417–426 (1974).
35. Powell, D., Vegetti, S., McKean, J. P. & Spingola, C. A novel approach to visibility-space modelling of interferometric gravitational lens observations at high angular resolution. Preprint at https://arxiv.org/abs/2005.03609 (2020).
36. Vegetti, S. & Koopmans, L. V. E. Bayesian strong gravitational-lens modelling on adaptive grids: objective detection of mass substructure in Galaxies. *Mon. Not. R. Astron. Soc*. **392**, 945–963 (2009).
37. Greengard, L. & Lee, J.-Y. Accelerating the nonuniform fast Fourier transform. *SIAM Rev*. **46**, 443–454 (2004).
38. Beatty, P. J., Nishimura, D. G. & Pauly, J. M. Rapid gridding reconstruction with a minimal oversampling ratio. *IEEE Trans. Med. Imaging* **24**, 799–808 (2005).
39. Koopmans, L. V. E., Treu, T., Bolton, A. S., Burles, S. & Moustakas, L. A. The Sloan Lens ACS Survey. III. The structure and formation of early-type galaxies and their evolution since z~1. *Astrophys. J*. **649**, 599–615 (2006).
40. Barnabè, M. et al. Two-dimensional kinematics of SLACS lenses – II. Combined lensing and dynamics analysis of early-type galaxies at z=0.08–0.33. *Mon. Not. R. Astron. Soc*. **399**, 21–36 (2009).
41. Spilker, J. S. et al. ALMA imaging and gravitational lens models of south pole telescope—selected dusty, star-forming galaxies at high redshifts. *Astrophys. J*. **826**, 112 (2016).
42. Feroz, F., Hobson, M. P., Cameron, E. & Pettitt, A. N. Importance nested sampling and the MultiNest algorithm. *Open J. Astr*. **2**, 10 (2019).
43. Di Teodoro, E. M. & Fraternali, F. $^{\rm 3D}$BAROLO: a new 3D algorithm to derive rotation curves of galaxies. *Mon. Not. R. Astron. Soc*. **451**, 3021–3033 (2015).
44. Jones, G. C. et al. Dynamical characterization of galaxies at z~ 4–6 via tilted ring fitting to ALMA [C ii] observations. *Astrophys. J*. **850**, 180 (2017).
45. Smit, R. et al. Rotation in [C ii]-emitting gas in two galaxies at a redshift of 6.8. *Nature* **553**, 178–181 (2018).
46. Übler, H. et al. Ionized and molecular gas kinematics in a z=1.4 star-forming galaxy. *Astrophys. J*. **854**, L24 (2018).
47. Girard, M. et al. Towards sub-kpc scale kinematics of molecular and ionized gas of star-forming galaxies at z~1. *Astron. Astrophys*. **631**, A91 (2019).
48. Übler, H. et al. The evolution and origin of ionized gas velocity dispersion from z~2.6 to z~0.6 with KMOS$^{\rm 3D}$. *Astrophys. J*. **880**, 48 (2019).
49. Hung, C.-L. et al. What drives the evolution of gas kinematics in star-forming galaxies? *Mon. Not. R. Astron. Soc*. **482**, 5125–5137 (2019).
50. Teklu, A. F. et al. Declining rotation curves at z=2 in ΛCDM galaxy formation simulations. *Astrophys. J*. **854**, L28 (2018).
51. Bird, J. C. et al. Inside out and upside down: tracing the assembly of a simulated disk galaxy using mono-age stellar populations. *Astrophys. J*. **773**, 43 (2013).
52. Martizzi, D. Global simulations of galactic discs: violent feedback from clustered supernovae during bursts of star formation. *Mon. Not. R. Astron. Soc*. **492**, 79–95 (2020).
53. Iorio, G. et al. LITTLE THINGS in 3D: robust determination of the circular velocity of dwarf irregular galaxies. *Mon. Not. R. Astron. Soc*. **466**, 4159–4192 (2017).
54. Lima Neto, G. B., Gerbal, D. & Márquez, I. The specific entropy of elliptical galaxies: an explanation for profile-shape distance indicators? *Mon. Not. R. Astron. Soc*. **309**, 481–495 (1999).
55. Terzić, B. & Graham, A. W. Density-potential pairs for spherical stellar systems with Sérsic light profiles and (optional) power-law cores. *Mon. Not. R. Astron. Soc*. **362**, 197–212 (2005).
56. Zanella, A. et al. The [C ii] emission as a molecular gas mass tracer in galaxies at low and high redshifts. *Mon. Not. R. Astron. Soc*. **481**, 1976–1999 (2018).
57. Gullberg, B. et al. The dust and [C ii] morphologies of redshift ~4.5 sub-millimeter galaxies at ~200 pc resolution: the absence of large clumps in the interstellar medium at high-redshift. *Astrophys. J*. **859**, 12 (2018).
58. Navarro, J. F., Frenk, C. S. & White, S. D. M. The structure of cold dark matter halos. *Astrophys. J*. **462**, 563 (1996).
59. Dutton, A. A. & Macciò, A. V. Cold dark matter haloes in the Planck era: evolution of structural parameters for Einasto and NFW profiles. *Mon. Not. R. Astron. Soc*. **441**, 3359–3374 (2014).
60. Speagle, J. S. dynesty: a dynamic nested sampling package for estimating Bayesian posteriors and evidences. Preprint at https://arxiv.org/abs/1904.02180 (2019).
61. Cappellari, M. et al. The ATLAS$^{\rm 3D}$ project – XV. Benchmark for early-type galaxies scaling relations from 260 dynamical models: mass-to-light ratio, dark matter, Fundamental Plane and Mass Plane. *Mon. Not. R. Astron. Soc*. **432**, 1709–1741 (2013).
62. Emsellem, E. et al. The ATLAS$^{\rm 3D}$ project – III. A census of the stellar angular momentum within the effective radius of early-type galaxies: unveiling the distribution of fast and slow rotators. *Mon. Not. R. Astron. Soc*. **414**, 888–912 (2011).
63. Aravena, M. et al. A survey of the cold molecular gas in gravitationally lensed star-forming galaxies at z>2. *Mon. Not. R. Astron. Soc*. **457**, 4406–4420 (2016).
64. Kennicutt, R. C. & Evans, N. J. Star formation in the Milky Way and nearby galaxies. *Annu. Rev. Astron. Astrophys*. **50**, 531–608 (2012).
65. Tamburro, D. et al. What is driving the H i velocity dispersion? *Astrophys. J*. **137**, 4424–4435 (2009).
66. Utomo, D., Blitz, L. & Falgarone, E. The origin of interstellar turbulence in M33. *Astrophys. J*. **871**, 17 (2019).
67. Rafelski, M. et al. The star formation rate efficiency of neutral atomic-dominated hydrogen gas in the outskirts of star-forming galaxies from z~1 to z~3. *Astrophys. J*. **825**, 87 (2016).
68. Leroy, A. K. et al. The multi-phase cold fountain in M82 revealed by a wide, sensitive map of the molecular interstellar medium. *Astrophys. J*. **814**, 83 (2015).
69. Lelli, F., Verheijen, M. & Fraternali, F. Dynamics of starbursting dwarf galaxies. III. A H I study of 18 nearby objects. *Astron. Astrophys*. **566**, A71 (2014).
70. Planck Collaboration. Planck 2015 results XIII. Cosmological parameters. *Astron. Astrophys*. **594**, A13 (2016).

Acknowledgements This study used ALMA data 2016.1.01499.S. ALMA is a partnership of ESO (representing its member states), NSF (USA) and NINS (Japan) with NRC (Canada), NSC and ASIAA (Taiwan) and KASI (Republic of Korea), in cooperation with the Republic of Chile. The Joint ALMA Observatory is operated by ESO, AUI/NRAO and NAOJ. S.V. received funding from the European Research Council (ERC) under the European Union's Horizon 2020 research and innovation programme (grant agreement number 758853). F.R. thanks T. Naab and T. Costa for useful comments and discussions.

Author contributions F.R., F.F. and S.V. analysed the data. D.P., F.R. and S.V. developed the software used for the lens–kinematic modelling. F.R. developed the software for the dynamical analysis. H.R.S. and F.R. reduced the data. F.R., J.P.M., S.V. and H.R.S. contributed to the writing of the manuscript. F.F. and S.D.M.W. helped with the interpretation of the scientific results. All authors discussed the results and provided comments on the paper.

Competing interests The authors declare no competing interests.

Additional information
Correspondence and requests for materials should be addressed to F.R.
Reprints and permissions information is available at http://www.nature.com/reprints.

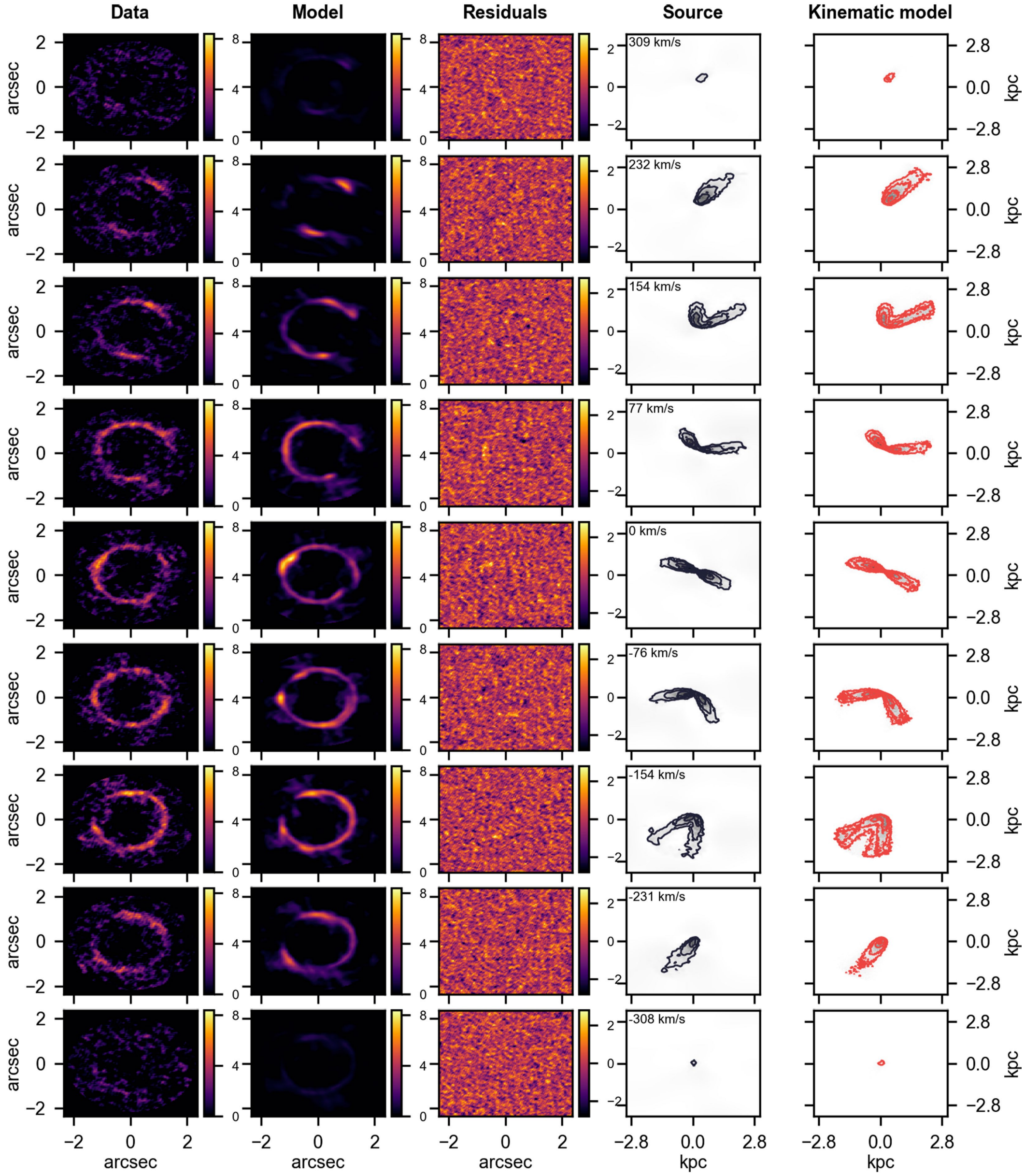

Extended Data Fig. 1 | Reconstruction of the [C II] emission and kinematic model. The rows show representative channel maps at the velocity shown on the upper left corner of column 4. Columns 1 and 2 show the 'dirty' image of the data and the model, respectively, colour-coded by the flux in units of mJy per beam. Column 3 shows the residuals (data minus model) normalized to the noise. Columns 5 and 6 show the contours of the reconstructed source and of the kinematic model used to constrain the source reconstruction. The contour levels in the last columns are set at $n = 0.1, 0.2, 0.4, 0.6, 0.8$ times the value of the maximum flux of the kinematic model.

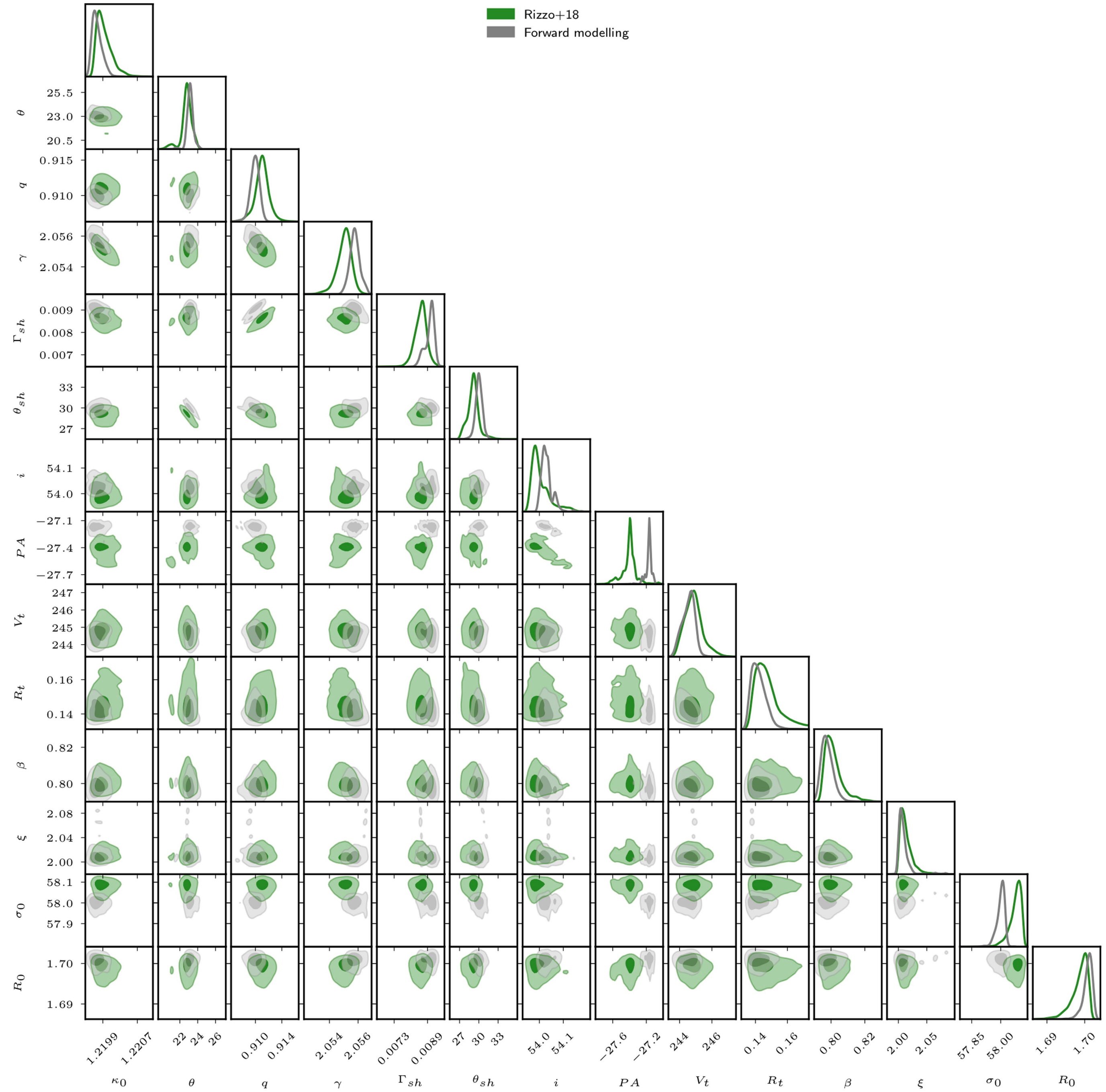

Extended Data Fig. 2 | Corner plot showing the posterior distributions of the lens and kinematic parameters. The dark and light areas in the two-dimensional distributions show the 39% and 86% confidence levels, corresponding to 1 s.d. and 2 s.d., respectively, obtained with the fiducial methodology described in Rizzo et al.[13] (green) and with the direct forward modelling method (grey). From left to right, the first six panels show the lens parameters, and the other panels show the source kinematic parameters (see also Extended Data Table 1).

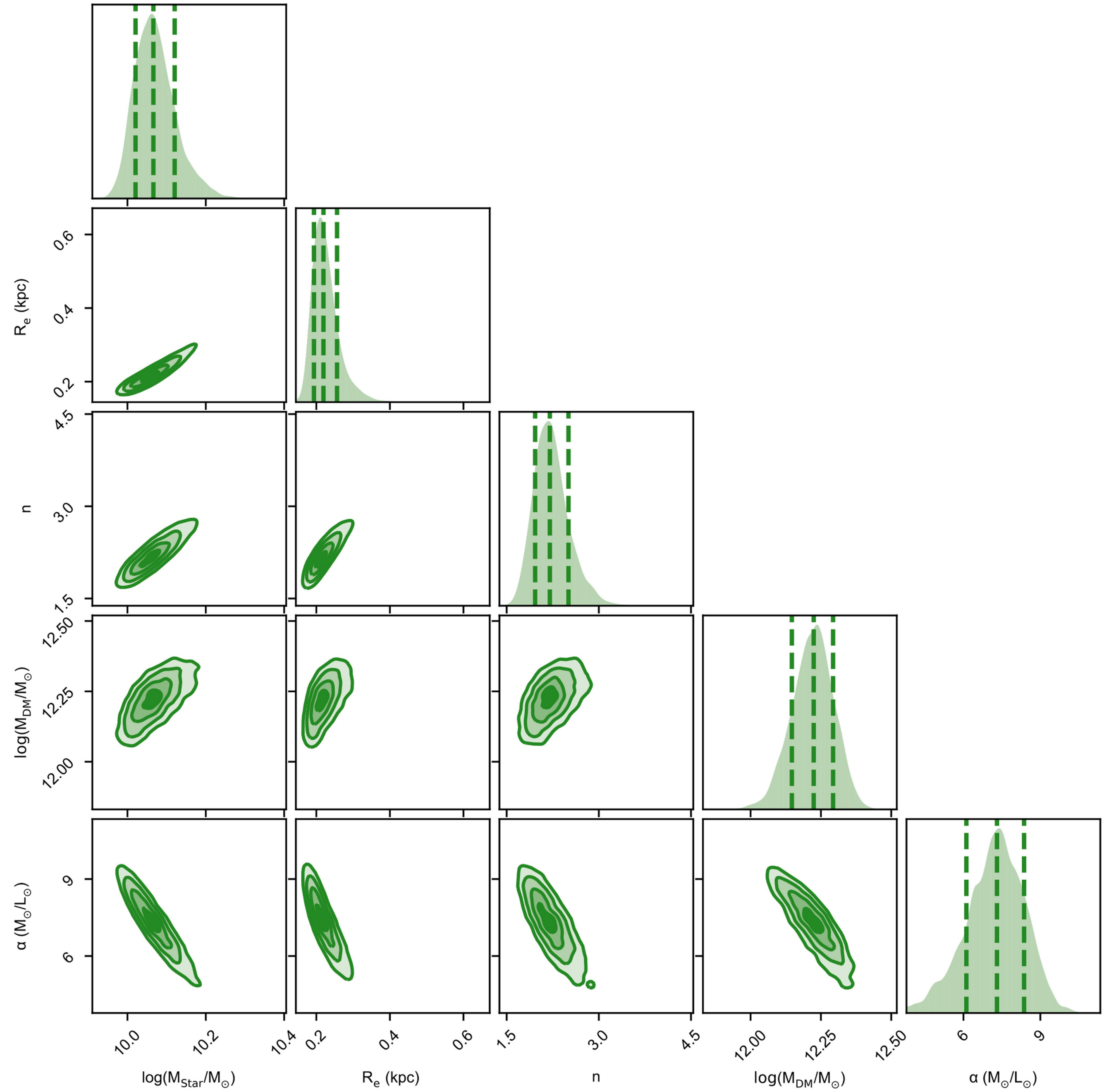

Extended Data Fig. 3 | Corner plot showing the posterior distributions of the dynamical parameters. The posterior distributions are the results of the decomposition of the circular velocity (Fig. 2c) into the physical components contributing to the total gravitational potential: the stars, the gas disks and the dark-matter halo. The fitted parameters are the stellar mass M_{star}, the effective radius, R_{e}, the Sérsic index, n (Sérsic profile), the mass of an NFW dark-matter halo, M_{DM} and the conversion factor between the [C II] luminosity and the gas mass, $\alpha_{\mathrm{[CII]}}$. The dashed lines in the one-dimensional histograms show the 16th, 50th and 84th percentiles (see Extended Data Table 5).

Extended Data Table 1 | Lens and source kinematic parameters

Lens parameters		Kinematic parameters	
κ_0 (arcsec)	1.22 ± 0.04	i (°)	54 ± 2
θ (°)	22.6 ± 1.6	PA (°)	-27 ± 3
q	0.91 ± 0.02	V_t (km s^{-1})	245.1 ± 0.8
γ	2.05 ± 0.09	R_t (kpc)	0.14 ± 0.03
Γ_{sh}	0.0082 ± 0.0003	β	0.80 ± 0.02
θ_{sh} (°)	29.9 ± 3.0	ξ	2.0 ± 0.4
		σ_0 (km s^{-1})	58.1 ± 1.8
		R_0 (kpc)	1.7 ± 0.1

The lens parameters describe a projected mass density profile with a cored elliptical power-law distribution (equation (1)) plus the contribution of an external shear component (Γ_{sh}, θ_{sh}). The kinematic parameters describe a rotating disk with a rotation curve defined by a multi-parameter function (equation (2)), a velocity dispersion profile defined by an exponential function (σ_0, R_0) and a geometry defined by the inclination (i) and the position angles (PA).

Extended Data Table 2 | Kinematic properties for SPT0418-47 derived under different assumptions

Global kinematic properties			
[a] V_{Max} (km s^{-1})	308±4	[d] V_{Flat} (km s^{-1})	259±1
[b] σ_{m} (km s^{-1})	32±1	[e] σ_{ext} (km s^{-1})	18±1
[c] $V_{\mathrm{Max}}/\sigma_{\mathrm{m}}$	9.7±0.4	[f] $V_{\mathrm{Flat}}/\sigma_{\mathrm{ext}}$	13.5±0.7

Parameters representing the rotation velocities and velocity dispersion profile, as well as the rotation support for this galaxy, calculated under different definitions.

[a] Maximum rotation velocity.

[b] Mean velocity dispersion.

[c] Rotation-to-random-motion ratio, calculated from V_{max} and σ_{m}.

[d] Flat rotation velocity, calculated using the flat part of the rotation curve ($R > 2$ kpc; see Fig. 2c).

[e] Velocity dispersion at outer radii ($R > 1$ kpc).

[f] Rotation-to-random-motion ratio, calculated from V_{flat} and σ_{ext}.

Extended Data Table 3 | Kinematic measurements for the comparison samples

Study	Tracer	V	σ
Lelli et al.[11]	HI	Flat part of the rotation curve ($V_{\rm Flat}$)	[a] 10 km/s
Swinbank et al.[30]	Hα, [OII]	Extracted at $3R_{\rm Disk}$	Average ($\sigma_{\rm m}$)
Harrison et al.[29]	Hα	Extracted at $3.4R_{\rm Disk}$	Median value at $R > 3.4\,R_{\rm Disk}$
Di Teodoro et al.[25]	Hα	Flat part of the rotation curve ($V_{\rm Flat}$)	Average ($\sigma_{\rm m}$)
Wisnioski et al.[26]	Hα	$(V_{\rm PV,\,max} - V_{\rm PV,\,min})/2$[b]	Average from outer regions ($\sigma_{\rm ext}$)
Lelli et al.[27]	[CI]	Flat part of the rotation curve ($V_{\rm Flat}$)	Average ($\sigma_{\rm m}$)
Turner et al.[28]	[OIII]	Extracted at $3.4R_{\rm Disk}$	Median

See refs. [11,25–30].

[a] We assume a value of $\sigma = 10$ km s^{-1}, typical of H I in local spiral galaxies[11].

[b] $V_{\rm PV,max}$ and $V_{\rm PV,min}$ are the maximum and minimum velocities, respectively, along the position–velocity diagram.

Extended Data Table 4 | Assumptions for the dynamical fit

Component	Density profile	Free parameters	Priors
Stars	Sérsic	M_{Star}	$[10^{7}, 10^{11}]\ M_{\odot}$
		R_{e}	$[0.04, 2.0]$ kpc
		n	$[0.5, 10]$
Gas	Exponential	$\alpha_{\mathrm{[CII]}}$	$[3.8, 238.0]\ M_{\odot}/L_{\odot}$
Dark matter	NFW	M_{DM}	$[10^{10}, 10^{13}]\ M_{\odot}$

Extended Data Table 5 | Physical quantities for SPT0418-47 derived from the kinematic and dynamical modelling

Parameters of the dynamical model		Derived parameters	
$M_{\rm Star}$ ($10^{10} M_\odot$)	$1.2^{+0.2}_{-0.1}$	[a] $M_{\rm Gas}$ ($10^{10} M_\odot$)	$1.3^{+0.2}_{-0.2}$
$R_{\rm e}$ (kpc)	$0.22^{+0.04}_{-0.02}$	[b] $M_{\rm Bar}$ ($10^{10} M_\odot$)	$2.5^{+0.2}_{-0.1}$
n	$2.2^{+0.3}_{-0.2}$	[c] $R_{\rm e,\,bar}$ (kpc)	$[0.75^{+0.06}_{-0.06}]$
$M_{\rm DM}$ ($10^{12} M_\odot$)	$1.7^{+0.3}_{-0.3}$	[d] $f_{\rm DM}(< R_{\rm e})$	$0.018^{+0.005}_{-0.003}$ $[0.095^{+0.008}_{-0.007}]$
$\alpha_{\rm [CII]}$ ($M_\odot/L_\odot$)	$7.3^{+1.0}_{-1.2}$	[e] $f_\star$ (10^{-3})	$7.1^{+1.0}_{-0.8}$ $[14.9^{+3.7}_{-2.6}]$
		[f] $f_{\rm Gas}$	$0.53^{+0.06}_{-0.08}$
		[g] V_{200} (km s^{-1})	320^{+17}_{-18}
		[h] R_{200} (kpc)	70^{+4}_{-4}
		[i] $V_{\rm max}$ (km s^{-1})	323^{+18}_{-19}

Left: parameters inferred from a dynamical fit to the circular velocity. The stellar component is described by a Sérsic profile, the gas disk by an exponential profile and the dark matter by an NFW profile. Right: the quantities in square brackets are calculated considering the gas component, under the assumption that all the gas that we observe today will be converted into stars, preserving the disk configuration.

[a] Total gas mass, computed as $M_{\rm gas} = \alpha_{\rm [CII]} L_{\rm [CII]}$.

[b] Total baryonic mass, computed as $M_{\rm bar} = M_{\rm star} + M_{\rm gas}$.

[c] Baryonic half-mass radius.

[d] Dark-matter fraction within the half-mass radius.

[e] Stellar-to-halo-mass ratio, $M_{\rm star}/M_{\rm DM} = (M_{\rm star} + M_{\rm gas})/M_{\rm DM}$.

[f] Gas fraction, $M_{\rm gas}/(M_{\rm star} + M_{\rm gas})$.

[g] Virial velocity of the dark-matter halo.

[h] Virial radius of the dark-matter halo.

[i] Maximum velocity for an NFW halo, computed as $V_{200}\sqrt{0.216\, c/[\ln(1+c) - c/(1+c)]}$.

Stabilization and operation of a Kerr-cat qubit

https://doi.org/10.1038/s41586-020-2587-z

Received: 28 July 2019

Accepted: 20 May 2020

A. Grimm[1,4,6] ✉, N. E. Frattini[1,6], S. Puri[2], S. O. Mundhada[1], S. Touzard[1], M. Mirrahimi[3], S. M. Girvin[2], S. Shankar[1,5] & M. H. Devoret[1] ✉

Quantum superpositions of macroscopically distinct classical states—so-called Schrödinger cat states—are a resource for quantum metrology, quantum communication and quantum computation. In particular, the superpositions of two opposite-phase coherent states in an oscillator encode a qubit protected against phase-flip errors[1,2]. However, several challenges have to be overcome for this concept to become a practical way to encode and manipulate error-protected quantum information. The protection must be maintained by stabilizing these highly excited states and, at the same time, the system has to be compatible with fast gates on the encoded qubit and a quantum non-demolition readout of the encoded information. Here we experimentally demonstrate a method for the generation and stabilization of Schrödinger cat states based on the interplay between Kerr nonlinearity and single-mode squeezing[1,3] in a superconducting microwave resonator[4]. We show an increase in the transverse relaxation time of the stabilized, error-protected qubit of more than one order of magnitude compared with the single-photon Fock-state encoding. We perform all single-qubit gate operations on timescales more than sixty times faster than the shortest coherence time and demonstrate single-shot readout of the protected qubit under stabilization. Our results showcase the combination of fast quantum control and robustness against errors, which is intrinsic to stabilized macroscopic states, as well as the potential of of these states as resources in quantum information processing[5–8].

A quantum system that can be manipulated and measured tends to interact with uncontrolled degrees of freedom in its environment, leading to decoherence. This presents a challenge to the experimental investigation of quantum effects and in particular to the field of quantum computing, where quantum bits (qubits) must remain coherent while operations are performed. Most noisy environments are only locally correlated and thus cannot decohere quantum information encoded in a non-local manner. Therefore, quantum information can be protected through the use of spatial distance[9–11] or entangled qubit states[12,13]. Crucially, this concept can be extended to non-local states in the phase space of a single oscillator[2,14], with the additional benefit of involving fewer physical components, a property termed hardware efficiency. The latter is desirable because fully protecting a quantum system against all forms of decoherence is likely to involve several layers of encodings, and it is crucial to introduce efficient error protection into the physical layer while maintaining simplicity[6,7,15].

A natural choice for non-locally encoding a qubit into the phase space of an oscillator is superpositions of macroscopically distinct coherent states—the so-called Schrödinger cat states. Here we choose the states $|\mathcal{C}_\alpha^\pm\rangle = (|+\alpha\rangle \pm |-\alpha\rangle)/\sqrt{2}$ with average photon number $\bar{n} = |\alpha|^2$ and, respectively, even and odd photon number parity as the Z eigenstates of the encoded qubit (Fig. 1a). The coherent states $|+\alpha\rangle$ and $|-\alpha\rangle$ are the approximate X eigenstates (Supplementary Information section I), and their distance in phase space ensures protection against any noise process that causes local displacements in this space. Crucially, this leads to a suppression of phase flips that is exponential in the average photon number $\bar{n}$ (refs. [1,2]). In particular, photon loss, the usual noise process in an oscillator, cannot induce transitions between $|+\alpha\rangle$ and $|-\alpha\rangle$ because they are eigenstates of the annihilation operator $\hat{a}$. This is not the case for their superpositions, so a stochastic photon-loss event corresponds to a bit-flip error on the encoded qubit: $\hat{a}|\mathcal{C}_\alpha^\pm\rangle = \alpha|\mathcal{C}_\alpha^\mp\rangle$, which also affects the parity-less Y eigenstates $|\mathcal{C}_\alpha^{\mp i}\rangle = (|+\alpha\rangle \mp i|-\alpha\rangle)/\sqrt{2}$, where $i = \sqrt{-1}$. However, for a given single-photon-loss rate κ_a, the bit-flip rate of approximately $2\bar{n}\kappa_a$ (ref. [16], Supplementary Information section XI) increases only linearly with the photon number. A qubit with such 'biased noise' is an important resource in fault-tolerant quantum computation[17,18]. Additional layers of error correction can then focus strongly on the remaining bit-flip error[6,7,18]. This substantially reduces the hardware complexity compared with conventional approaches that use qubits without such error protection.

Here we show that such a protected qubit can be stabilized autonomously in a simple and versatile implementation similar to a superconducting transmon under parametric driving. Unlike in other hardware-efficient encodings[19–21], the most nonlinear mode of our

---

[1]Department of Applied Physics, Yale University, New Haven, CT, USA. [2]Department of Physics, Yale University, New Haven, CT, USA. [3]QUANTIC team, Inria Paris, Paris, France. [4]Present address: Photon Science Division, Paul Scherrer Institut, Villigen, Switzerland. [5]Present address: Electrical and Computer Engineering, University of Texas, Austin, TX, USA. [6]These authors contributed equally: A. Grimm, N. E. Frattini. ✉e-mail: alexander.grimm@psi.ch; michel.devoret@yale.edu

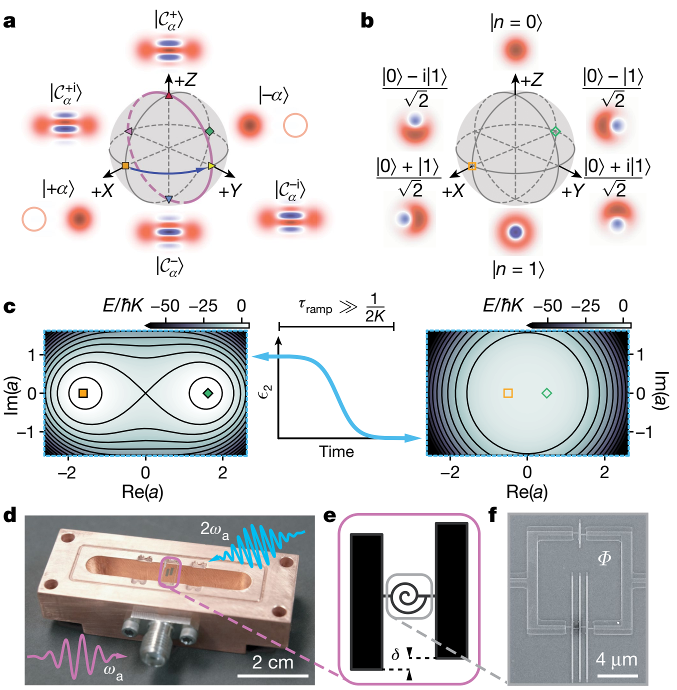

Fig. 1 | Qubit encoding, stabilization and implementation. **a**, Bloch sphere of the protected Kerr-cat qubit (KCQ) in the large-α limit (Supplementary Information section I). The states on all six cardinal points are labelled, indicated by coloured markers, and their Wigner function[16] phase-space representations are sketched. Here, $|\pm Z\rangle = |\mathcal{C}_\alpha^\pm\rangle = (|+\alpha\rangle \pm |-\alpha\rangle)/\sqrt{2}$ and $|\pm Y\rangle = |\mathcal{C}_\alpha^{\mp i}\rangle = (|+\alpha\rangle \mp i|-\alpha\rangle)/\sqrt{2}$. The continuous $X(\theta)$ gate with the arbitrary rotation angle θ and the discrete $Z(\pi/2)$ gate are shown by a purple circle and a blue arrow, respectively. **b**, Bloch sphere of the single-photon Fock qubit (FQ). **c**, Energy (E) dependence of equation (1) on classical phase-space coordinates Re(a) and Im(a) for squeezing drive amplitudes $\epsilon_2/2\pi = 17.75$ MHz (left) and $\epsilon_2 = 0$ (right) with a sketch showing the adiabatic ramp of the drive over a time $\tau_{\rm ramp} \gg 1/2K$. Black lines are constant energy contours. The quadrature expectation values of the $|\pm X\rangle$ states from **a**, **b** are indicated by their respective markers. **d**, Photograph of the nonlinear resonator (purple frame) inside the copper section of the readout cavity (Methods). Also represented are the $X(\theta)$-rotation drive (ω_a) and the squeezing-generation drive ($2\omega_a$). **e**, Schematic of the nonlinear resonator with pad offset δ to set the dispersive coupling to the readout cavity (Methods) and spiral symbol representing the nonlinear inductor (SNAIL element). **f**, Scanning electron micrograph of the SNAIL element consisting of four Josephson junctions in a loop threaded by an external magnetic flux Φ.

system encodes and stabilizes the qubit without requiring auxiliary nonlinear modes that could introduce additional uncorrectable errors.

For this protected qubit to be practical, it is essential that operations can be performed faster than the shortest decoherence timescale, here the bit-flip time. We experimentally demonstrate such fast gate operations and quantum non-demolition single-shot readout in a system that maintains phase-flip protection via the simultaneous stabilization of two opposite-phase coherent states.

Our approach is based on the application of a resonant single-mode squeezing drive to a Kerr-nonlinear resonator[4]. In the frame rotating at the resonator frequency ω_a, the system is described by the Hamiltonian

$$\hat{H}_{\rm cat}/\hbar = -K\hat{a}^{\dagger 2}\hat{a}^2 + \epsilon_2(\hat{a}^{\dagger 2} + \hat{a}^2), \qquad (1)$$

where K is the Kerr nonlinearity, ϵ_2 is the amplitude of the squeezing drive and $\hbar$ is the reduced Planck's constant. Some intuition on this system can be gained from computing $\langle \hat{H}_{\rm cat}\rangle$ as a function of classically treated phase-space coordinates. There are two stable extrema at $\pm\alpha = \pm\sqrt{\epsilon_2/K}$, as indicated by the markers in Fig. 1c. They correspond to the lowest degenerate eigenstates of the quantum Hamiltonian[4] (Supplementary Information) and thus do not decay to vacuum. These eigenstates are separated from the rest of the spectrum by an energy gap $E_{\rm gap}/\hbar \approx 4K\bar{n}$ (Supplementary Information section III, Supplementary Fig. 1), which sets the speed limit for operations and readout. The energy barrier between these eigenstates prevents jumps along the X-axis of this 'Kerr-cat qubit' (KCQ). If no squeezing drive is applied, $\hat{H}_{\rm cat}$ reduces to the Hamiltonian of an anharmonic oscillator. This resembles a superconducting transmon with anharmonicity $2K$, commonly used to encode a 'Fock qubit' (FQ) into the first two photon number states $|0\rangle$ and $|1\rangle$ (Fig. 1b). Its classical energy displays one single extremum in phase space harbouring the quadrature expectation values of both X eigenstates without the protection of an energy barrier (Fig. 1c, right panel). By toggling the squeezing drive, a Kerr-nonlinear resonator can be tuned to implement either type of qubit.

Our experimental implementation consists of a superconducting nonlinear resonator placed inside a three-dimensional (3D) microwave cavity (Fig. 1d). This is a standard setup in 3D transmon qubits with a few key modifications (Methods). The foremost modification, employing a superconducting nonlinear asymmetric inductive element (SNAIL)[22] as a nonlinear inductor (Fig. 1f), allows us to create single-mode squeezing by applying a coherent microwave drive ω_s at twice the resonator frequency ω_a and makes the resonator flux tunable. Here we tune our device to a frequency $\omega_a/2\pi = 6$ GHz and Kerr nonlinearity $K/2\pi = 6.7$ MHz. At this frequency, the FQ has an amplitude damping time $T_1 = 15.5$ μs and a transverse relaxation time $T_2 = 3.4$ μs.

The FQ is employed for initialization and measurement of the KCQ during most experiments described in this work. This is possible because the states $|0\rangle$, $|\mathcal{C}_\alpha^+\rangle$ ($|1\rangle$, $|\mathcal{C}_\alpha^-\rangle$) spanning the two Bloch spheres have the same even (odd) photon number parity, which is conserved by the system Hamiltonian (equation (1)). Consequently, ramping the squeezing drive on and off slowly with respect to $1/2K$, as sketched in Fig. 1c, adiabatically maps between the FQ and KCQ (Methods).

We now show that we indeed implement the Hamiltonian (1), and thus initialize and stabilize a KCQ, by demonstrating the unique features of Rabi oscillations around the X axis of its Bloch sphere. To this end, we apply an additional coherent drive $\epsilon_x\hat{a}^\dagger + \epsilon_x^*\hat{a}$ with amplitude ϵ_x and frequency $\omega_a = \omega_s/2$ to the system. This lifts the degeneracy between the states $|+\alpha\rangle$ and $|-\alpha\rangle$, and therefore leads to oscillations with a Rabi frequency

$$\Omega_x = {\rm Re}(4\epsilon_x\alpha) \qquad (2)$$

between their superposition states along the purple circle in Fig. 1a. This picture is valid for large enough α and for $\epsilon_x \ll E_{\rm gap}/\hbar$ (ref. [4]; see also Supplementary Information section IV). Note that equation (2) is different from the Rabi frequency of a FQ in two ways. First, it depends on the amplitude of the squeezing drive through $\alpha \propto \sqrt{\epsilon_2}$. Second, it varies with the phase of the applied Rabi drive arg(ϵ_x) (for simplicity we chose $\epsilon_2, \alpha \in \mathbb{R}$).

We first focus on the effect of the squeezing drive on the Rabi frequency. We initialize in $|\mathcal{C}_\alpha^+\rangle$ and apply a Rabi drive with constant $|\epsilon_x|$ and arg(ϵ_x) = 0 for a variable time Δt and a variable amplitude ϵ_2 (Fig. 2a). Figure 2b shows the Rabi frequencies for each ϵ_2, extracted from the oscillations in the measured FQ $|0\rangle$-state population fraction at the end of the experiment. For $\epsilon_2 = 0$, we are simply driving FQ Rabi oscillations giving a direct calibration of $|\epsilon_x|/2\pi = 740$ kHz. For large values of ϵ_2, the Rabi frequency becomes a linear function of $\sqrt{\epsilon_2}$, confirming the theoretical prediction of equation (2). The solid black line shows a one-parameter fit to a numerical simulation of our experiment (Methods).

We now turn to another unique feature of these Rabi oscillations by setting $\epsilon_2/2\pi = 15.5$ MHz and varying Δt and arg(ϵ_x). As expected, the measured oscillations shown in Fig. 2c are π-periodic in arg(ϵ_x). Three cuts through this data (dashed lines) are shown in Fig. 2d. The top panel

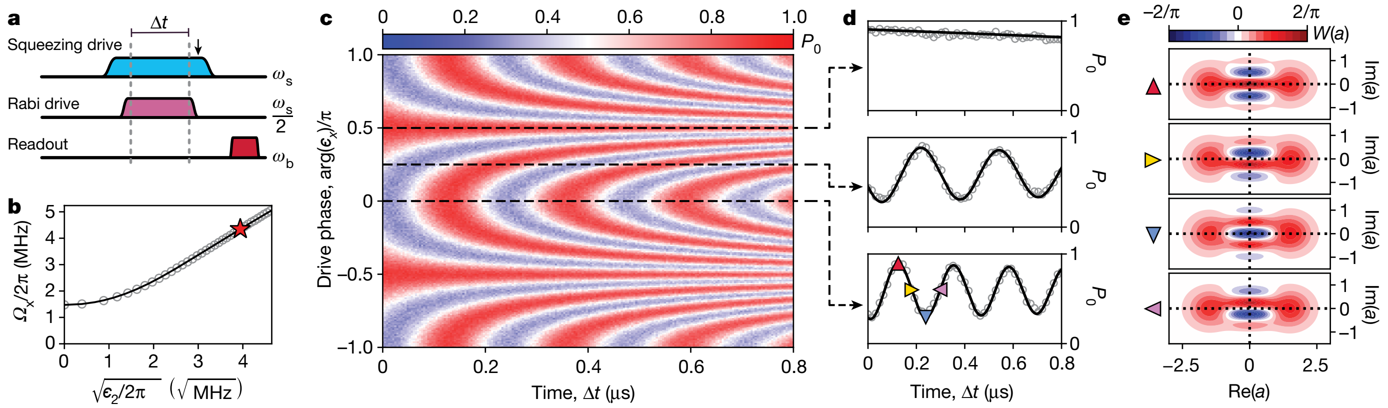

Fig. 2 | Rabi oscillations of the protected KCQ. a, Pulse sequence to perform the following functions: (1) initialize the KCQ ($|0\rangle \to |\mathcal{C}_\alpha^+\rangle$), (2) drive Rabi oscillations for a varying time Δ*t*, and (3) map onto the FQ and perform dispersive readout. ω_s, $\omega_s/2$ and ω_b are the frequencies of the respective drives. A black arrow indicates the endpoint of the numerical simulations performed for **b**, **d**, **e** (Methods). **b**, Dependence of the Rabi frequency Ω_x on $\sqrt{\epsilon_2}$. Experimental data are open grey circles. The solid black line is a one-parameter fit to the data used to calibrate ϵ_2 (Methods). The red star indicates the condition $\epsilon_2/2\pi = 15.5$ MHz used for **c**, **d**, **e**. **c**, Dependence of the experimentally measured Rabi oscillations on time Δ*t* and on the phase of the Rabi drive $\arg(\epsilon_x)$. The colour scale gives the ground state population of the FQ (P_0) at the end of the experiment. **d**, Cuts of **c** for the three Rabi-drive phases indicated by dashed lines. Open grey circles are the experimental data and black lines are the simulation. Symbols in the bottom panel indicate the times for which the simulated oscillator state is shown in **e**. **e**, Simulated phase-space representation of the oscillator density matrix corresponding to the $|+Z\rangle$, $|+Y\rangle$, $|-Z\rangle$ and $|-Y\rangle$ states of the KCQ (from top to bottom). The colour scale gives the value of the Wigner function $W(a)$ as a function of the real and imaginary part of the phase-space coordinate *a*.

corresponds to a phase difference of π/2 between the coherent state amplitude and the Rabi drive, meaning that oscillations are suppressed. The middle and bottom panels at respective phase differences of π/4 and 0 display increasing Rabi frequencies, with the latter corresponding to the red star marker in Fig. 2b. In the bottom panel, the black line is the result of a numerical simulation scaled to match the contrast of the data. The black lines in the top and middle panels use the same scaling factor and are thus parameter-free predictions in good agreement with the measured data. Having benchmarked our simulation in this way, we use it to compute the full density matrix of the resonator, which we represent with Wigner functions (Fig. 2e). Apart from slight asymmetries due to the finite ramp time of the initial mapping pulse, they agree well with the expected $|+Z\rangle$, $|+Y\rangle$, $|-Z\rangle$ and $|-Y\rangle$ states of the KCQ.

Next, we characterize the mapping operation and a set of single-qubit gates on the KCQ by performing process tomography (Methods). In all subsequent experiments, the average photon number of the cat states is set to $\bar{n} \approx 2.6$ and frequency shifts induced by the squeezing drive are taken into account by setting $\omega_s/2 = \tilde{\omega}_a$, where $\tilde{\omega}_a$ is the Stark-shifted resonator frequency (Supplementary Information section II). The pulse sequence for tomography of the mapping between the FQ and the KCQ is shown in Fig. 3a and the measured state vectors are plotted on a Bloch sphere in Fig. 3b. An estimate of the fidelity $\mathcal{F}_{\mathrm{map}} \approx 0.855 \pm 0.002$ (± one standard deviation here and for all subsequent values) is obtained by using the Pauli transfer matrix approach[23] (Supplementary Information). This number reflects the fidelity of the tomography FQ pulses as well as of the mapping itself, because, apart from a normalization by the FQ Rabi contrast, the presented fidelities include state-preparation-and-measurement (SPAM) errors (Supplementary Information section V). We expect these errors to be dominated by decoherence during the comparatively slow adiabatic ramps. This could be remedied in future experiments by using optimal pulse shapes, which can reduce the duration of the mapping operation by a factor of more than 40 with respect to its present value[4].

We now turn to the pulse sequence shown in Fig. 3c, which additionally performs an $X(\pi/2)$ gate on the KCQ. The process tomography data (Fig. 3d) shows the desired rotation around the *X*-axis with a fidelity of $\mathcal{F}_{X(\pi/2)} \approx 0.857 \pm 0.001$. Comparing this value to $\mathcal{F}_{\mathrm{map}}$ indicates that $\mathcal{F}_{X(\pi/2)}$ is mostly limited by SPAM errors. From a complementary

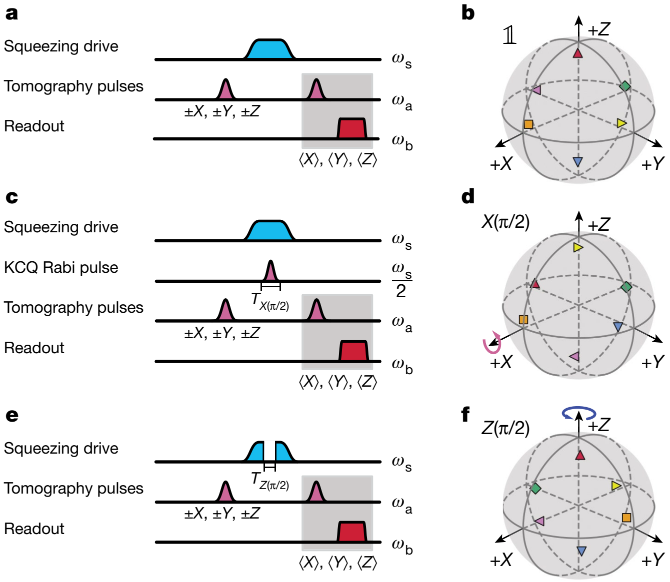

Fig. 3 | KCQ gate process tomography. a, **c**, **e**, Pulse sequences for process tomography of mapping between FQ and KCQ, which is ideally the identity operation 𝟙 (**a**), mapping and the $X(\pi/2)$ gate (**c**), as well as mapping and the $Z(\pi/2)$ gate (**e**). In each sequence, the FQ is initialized on the ±*X*, ±*Y* and ±*Z* cardinal points of the Bloch sphere, the respective operation is performed, and the expectation values ⟨*X*⟩, ⟨*Y*⟩ and ⟨*Z*⟩ are measured by a combination of FQ pulses and dispersive readout (grey box). In **c**, $T_{X(\pi/2)} = 24$ ns is the total duration of the Gaussian Rabi pulse applied to the KCQ. In **e**, $T_{Z(\pi/2)} = 38$ ns is the duration for which the squeezing drive is switched off to perform the gate. **b**, **d**, **f**, Process tomography results presented on a Bloch sphere for the operations 𝟙 (**b**), $X(\pi/2)$ (**d**) and $Z(\pi/2)$ (**f**). The expectation-value vector after the operation for an initialization on the (+*X*, −*X*, +*Y*, −*Y*, +*Z*, −*Z*) cardinal point is represented by an (orange square, green diamond, gold right-facing triangle, purple left-facing triangle, red upward-facing triangle, blue downward-facing triangle). Error bars are smaller than the size of the markers. The fidelities are 0.855 ± 0.002, 0.857 ± 0.001 and 0.811 ± 0.001, respectively.

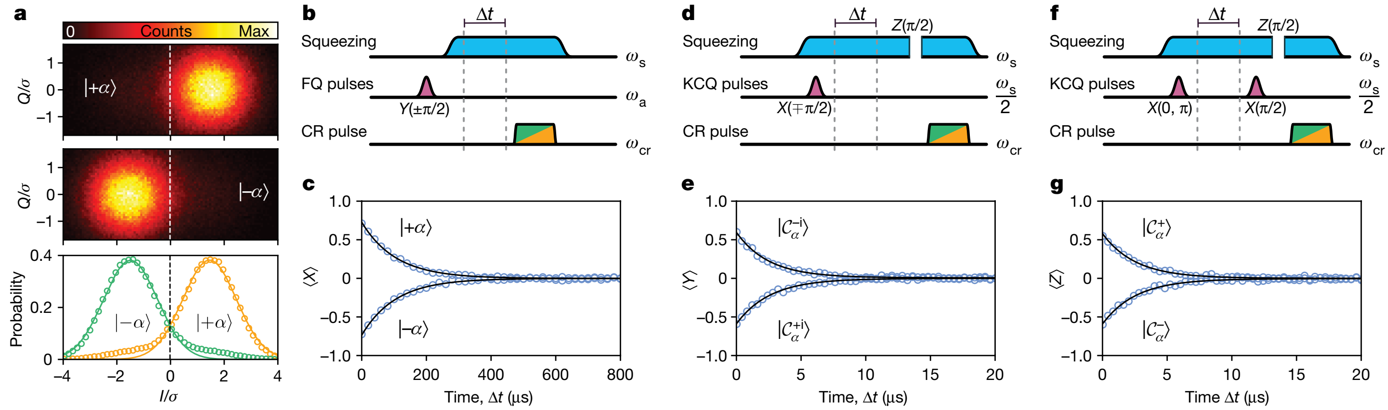

Fig. 4 | Cat-quadrature readout (CR) and coherence times. a, Top and middle: histogram of the cavity output field when performing CR (see **b**) after preparation of either $|+\alpha\rangle$ (top) or $|-\alpha\rangle$ (middle). Bottom: corresponding probability distribution along the I quadrature. Open orange (green) circles show measured data for $|+\alpha\rangle$ ($|-\alpha\rangle$) and solid lines are Gaussian fits of width σ used to scale the quadrature axes, I and Q. Setting a threshold at $I/\sigma = 0$ (dashed line) implements a direct single-shot readout of the KCQ along its X-axis. **b**, CR pulse sequence for the measurements presented in **a**, **c**. After state initialization in $|\pm\alpha\rangle$ ($Y(\pm\pi/2)$ gate on the FQ and mapping), a pulse at frequency $\omega_{cr} = \omega_b - \omega_s/2$ is applied for a time $T_{cr} = 3.6$ μs converting the quadrature amplitude of the KCQ to a drive on the readout cavity at ω_b. The wait time Δt is set to zero to obtain the results shown in **a** and varied in **c**. **c**, KCQ $\langle X\rangle$-component coherence. Open blue circles are data and solid black lines are single-exponential fits with decay times $\tau_{+X} = 105$ μs ± 1 μs and $\tau_{-X} = 106$ μs ± 1 μs. **d**, Pulse sequence for **e**. After initialization in $|\mathcal{C}_\alpha^{\mp i}\rangle$ (mapping $|0\rangle \to |\mathcal{C}_\alpha^{+}\rangle$ and $X(\mp\pi/2)$ gate) and variable wait time Δt, a $Z(\pi/2)$ gate is performed followed by CR. **e**, KCQ $\langle Y\rangle$-component coherence. Open blue circles are data and solid black lines are single-exponential fits with decay times $\tau_{+Y} = 2.51$ μs ± 0.06 μs and $\tau_{-Y} = 2.60$ μs ± 0.05 μs. **f**, Pulse sequence for **g**. After initialization in $|\mathcal{C}_\alpha^{\pm}\rangle$ (mapping $|0\rangle \to |\mathcal{C}_\alpha^{+}\rangle$ and either $X(0)$ or $X(\pi)$ gate) and variable wait time Δt, a $X(\pi/2)$ gate and a $Z(\pi/2)$ gate are performed followed by CR. **g**, KCQ $\langle Z\rangle$-component coherence. Open blue circles are data and solid black lines are single-exponential fits with decay times $\tau_{+Z} = 2.60$ μs ± 0.07 μs and $\tau_{-Z} = 2.56$ μs ± 0.07 μs.

measurement (Supplementary Fig. 3), we estimate the infidelity due to over-rotation and decoherence during the gate operation to about 0.01.

As this operation is compatible with an arbitrary angle of rotation, only a π/2 rotation around the Z-axis is needed to reach any point on the KCQ Bloch sphere. Nominally, such a gate is incompatible with the stabilization as it could be used to go between the states $|+\alpha\rangle$ and $|-\alpha\rangle$. However, for $\epsilon_2 = 0$, the free evolution of the Kerr Hamiltonian for a time $\pi/2K \approx 37.3$ ns achieves the required operation[4,24,25] (Methods and Fig. 3e). The tomography data shown in Fig. 3f gives a fidelity $\mathcal{F}_{Z(\pi/2)} \approx 0.811 \pm 0.001$. We attribute the reduction of fidelity with respect to $\mathcal{F}_{\text{map}}$ to the difference between the actual gate time $T_{Z(\pi/2)} = 38$ ns and $\pi/2K$, and to the finite rise time of the step function in ϵ_2 of about 4 ns; both of which are not limitations of our device but of our room-temperature electronics (Supplementary Information section VI).

So far, we have characterized the basic properties and gate operations of the KCQ by mapping back onto the FQ and using the well-understood dispersive readout method. This readout, however, destroys the state of the KCQ. We now demonstrate an entirely new way to perform a quantum non-demolition measurement on the X component of the stabilized KCQ, which we call the 'cat-quadrature readout' (CR). We apply an additional drive at frequency $\omega_{cr} = \omega_b - \omega_s/2$, where ω_b is the frequency of the readout cavity. Through the three-wave mixing capability of our system, this generates a frequency-converting interaction between the nonlinear resonator and the readout cavity. In the frame rotating at both $\omega_s/2 = \tilde{\omega}_a$ and ω_b, this adds the following term to equation (1):

$$\hat{H}_{cr}/\hbar = \mathrm{i}g_{cr}(\hat{a}\hat{b}^\dagger - \hat{a}^\dagger\hat{b}). \quad (3)$$

Here, $\hat{b}$ is the annihilation operator of the cavity field and $g_{cr}/2\pi = 1.7$ MHz is the independently measured coupling strength (Supplementary Fig. 6). For a quadrature expectation value $\langle\hat{a} + \hat{a}^\dagger\rangle/2 = \pm\alpha$ in the nonlinear resonator, this causes an effective coherent drive on the cavity and projects the KCQ onto the corresponding state $|\pm\alpha\rangle$ along its X-axis. We gain information about the result of this projection by measuring the emitted cavity field.

We characterize the fidelity of this readout by first initializing the KCQ along its X-axis and then applying a CR pulse for a time $T_{cr} = 3.6$ μs as shown in Fig. 4b. Two histograms of the measured cavity field are shown in Fig. 4a for initialization in $|+\alpha\rangle$ and $|-\alpha\rangle$, respectively. Their separation is large enough to implement a single-shot readout by setting a threshold at $I/\sigma = 0$ with total fidelity $\mathcal{F} = 0.74$ (Methods), where I/σ is a dimensionless quantity corresponding to the I-quadrature signal divided by the the standard deviation σ of the histograms. This fidelity is a lower bound including errors in state preparation caused by the thermal population of the FQ $|1\rangle$ state (contributing an infidelity of about 2 × 4% = 8%) and imperfections during the initial FQ pulse and mapping. Finally, we characterize the quantum-non-demolition aspect of the CR as $\mathcal{Q} = 0.85$ from two successive measurements (Methods).

We now use this CR to investigate the phase-flip time of the KCQ. The decay of the $\langle X\rangle$ component for either initial state along this axis is measured using the pulse sequence shown in Fig. 4b. We fit the data to a single-exponential decay with characteristic times $\tau_{+X} = 105$ μs ± 1 μs and $\tau_{-X} = 106$ μs ± 1 μs. Additional measurements with dispersive readout confirm this result (Supplementary Fig. 7).

Similarly, the coherence times of both the $\langle Y\rangle$ and $\langle Z\rangle$ components are measured using CR, but employing only operations on the KCQ after the initial $|0\rangle \to |\mathcal{C}_\alpha^{+}\rangle$ mapping operation (Fig. 4d, f). The resulting decay curves are displayed in Fig. 4e, g. Single-exponential fits of the data yield the decay times $\tau_{+Y} = 2.51$ μs ± 0.06 μs, $\tau_{-Y} = 2.60$ μs ± 0.05 μs, $\tau_{+Z} = 2.60$ μs ± 0.07 μs and $\tau_{-Z} = 2.56$ μs ± 0.07 μs. These values are slightly smaller than the predicted bit-flip time due to photon loss $\tau_{\text{loss}} = T_1/2\bar{n} = 2.98$ μs. We expect that photon-gain processes play a role in this reduction (Supplementary Information section XI, Supplementary Fig. 8).

Our results demonstrate a 30-fold increase in the phase-flip time of the protected KCQ with respect to the FQ. Crucially, we perform a full set of single-qubit gates on the protected qubit on timescales that are much shorter than its bit-flip time. Although the measured gate fidelities are limited by SPAM errors, an upper bound of the error rate due to decoherence during the gate operations is given by: $T_{X(\pi/2)}/\tau_{+Y} \approx T_{Z(\pi/2)}/\tau_{+Y} < 2 \times 10^{-2}$. The combination of error protection, fast gates and single-shot readout opens the door to using stabilized Schrödinger cat states as physical qubits in a future quantum computer.

The simplicity of our implementation provides a straightforward path to coupling several KCQs and demonstrating operations between them. In particular, our qubit permits a noise-bias-preserving controlled-NOT gate[6], which would be impossible with standard two-level qubits[7]. Moreover, KCQs could be applied as auxiliary systems for fault-tolerant error detection on other logical qubits[5]. This will require further improvements in device performance such as the bit-flip time, currently limited by losses due to the copper cavity.

The limitation of the phase-flip time also requires further investigation. Measurements performed at other flux points with different strengths of the third- and fourth-order nonlinearities indicate that coherence decreases when stronger drives have to be applied to the system to reach similar photon numbers. Similarly, an increase in photon number beyond the $\bar{n} \approx 2.6$ operating point chosen in this work decreases coherence. This is probably related to heating effects associated with the strong driving of Josephson junction devices[26,27] causing leakage to higher excited states outside of the KCQ encoding. Such leakage can be counteracted through controlled two-photon dissipation back towards the states of the KCQ[5]. This dissipation-based approach to stabilization has been effective in achieving strongly biased noise[28], but quantum operations that are much faster than all coherence timescales of the encoded qubit remain difficult to achieve[29]. The optimal solution should be to rely on a combination of two-photon dissipation, squeezing drive and Kerr nonlinearity for phase-flip suppression and on the Kerr nonlinearity for high gate speeds.

In addition to its applications in fault-tolerant quantum computation[4–6,8], our system extends the understanding of bistability in parametrically driven Kerr nonlinear oscillators from the classical regime[30–33] to the quantum regime where nonlinearity dominates over losses[24,25,34,35]. Our results demonstrate long-lived quantum superpositions of degenerate, macroscopically distinct semi-classical states arising from Hamiltonian bistability. Such states could shed light on the quantum-classical transition[36] and can be useful in weak force measurements[37]. Networks of coupled bistable oscillators can be mapped onto Ising spins and used to investigate non-equilibrium quantum phase transitions[38] or to solve combinatorial optimization problems[39–41]. These examples suggest that our Kerr-cat system is likely to be applied both to quantum computation and for the investigation of fundamental quantum effects.

Online content

Any methods, additional references, Nature Research reporting summaries, source data, extended data, supplementary information, acknowledgements, peer review information; details of author contributions and competing interests; and statements of data and code availability are available at https://doi.org/10.1038/s41586-020-2587-z.

1. Cochrane, P. T., Milburn, G. J. & Munro, W. J. Macroscopically distinct quantum-superposition states as a bosonic code for amplitude damping. *Phys. Rev. A* **59**, 2631–2634 (1999).
2. Mirrahimi, M. et al. Dynamically protected cat-qubits: a new paradigm for universal quantum computation. *New J. Phys*. **16**, 045014 (2014).
3. Milburn, G. J. & Holmes, C. A. Quantum coherence and classical chaos in a pulsed parametric oscillator with a Kerr nonlinearity. *Phys. Rev. A* **44**, 4704–4711 (1991).
4. Puri, S., Boutin, S. & Blais, A. Engineering the quantum states of light in a Kerr-nonlinear resonator by two-photon driving. *npj Quantum Inf*. **3**, 18 (2017).
5. Puri, S. et al. Stabilized cat in a driven nonlinear cavity: a fault-tolerant error syndrome detector. *Phys. Rev. X* **9**, 041009 (2019).
6. Puri, S. et al. Bias-preserving gates with stabilized cat qubits. *Sci. Adv*. (in the press); preprint at https://arxiv.org/abs/1905.00450 (2019).
7. Guillaud, J. & Mirrahimi, M. Repetition cat qubits for fault-tolerant quantum computation. *Phys. Rev. X* **9**, 041053 (2019).
8. Goto, H. Universal quantum computation with a nonlinear oscillator network. *Phys. Rev. A* **93**, 050301 (2016).
9. Kitaev, A. Y. Fault-tolerant quantum computation by anyons. *Ann. Phys*. **303**, 2–30 (2003).
10. Oreg, Y., Refael, G. & von Oppen, F. Helical liquids and Majorana bound states in quantum wires. *Phys. Rev. Lett*. **105**, 177002 (2010).
11. Lutchyn, R. M., Sau, J. D. & Das Sarma, S. Majorana fermions and a topological phase transition in semiconductor–superconductor heterostructures. *Phys. Rev. Lett*. **105**, 077001 (2010).
12. Shor, P. W. Scheme for reducing decoherence in quantum computer memory. *Phys. Rev. A* **52**, R2493–R2496 (1995).
13. Fowler, A. G., Mariantoni, M., Martinis, J. M. & Cleland, A. N. Surface codes: towards practical large-scale quantum computation. *Phys. Rev. A* **86**, 032324 (2012).
14. Gottesman, D., Kitaev, A. & Preskill, J. Encoding a qubit in an oscillator. *Phys. Rev. A* **64**, 012310 (2001).
15. Vuillot, C., Asasi, H., Wang, Y., Pryadko, L. P. & Terhal, B. M. Quantum error correction with the toric Gottesman–Kitaev–Preskill code. *Phys. Rev. A* **99**, 032344 (2019).
16. Haroche, S. & Raimond, J.-M. *Exploring the Quantum: Atoms, Cavities and Photons* (Oxford Univ. Press, 2006).
17. Aliferis, P. & Preskill, J. Fault-tolerant quantum computation against biased noise. *Phys. Rev. A* **78**, 052331 (2008).
18. Tuckett, D. K., Bartlett, S. D. & Flammia, S. T. Ultrahigh error threshold for surface codes with biased noise. *Phys. Rev. Lett*. **120**, 050505 (2018).
19. Ofek, N. et al. Extending the lifetime of a quantum bit with error correction in superconducting circuits. *Nature* **536**, 441–445 (2016).
20. Hu, L. et al. Quantum error correction and universal gate set operation on a binomial bosonic logical qubit. *Nat. Phys*. **15**, 503–508 (2019).
21. Campagne-Ibarcq, P. et al. Quantum error correction of a qubit encoded in grid states of an oscillator. *Nature* http://doi.org/10.1038/s41586-020-2603-3 (2020).
22. Frattini, N. E. et al. 3-wave mixing Josephson dipole element. *Appl. Phys. Lett*. **110**, 222603 (2017).
23. Chow, J. M. et al. Universal quantum gate set approaching fault-tolerant thresholds with superconducting qubits. *Phys. Rev. Lett*. **109**, 060501 (2012).
24. Yurke, B. & Stoler, D. The dynamic generation of Schrödinger cats and their detection. *Physica B+C* **151**, 298–301 (1988).
25. Kirchmair, G. et al. Observation of quantum state collapse and revival due to the single-photon Kerr effect. *Nature* **495**, 205–209 (2013).
26. Sank, D. et al. Measurement-induced state transitions in a superconducting qubit: beyond the rotating wave approximation. *Phys. Rev. Lett*. **117**, 190503 (2016).
27. Lescanne, R. et al. Escape of a driven quantum Josephson circuit into unconfined states. *Phys. Rev. Appl*. **11**, 014030 (2019).
28. Lescanne, R. et al. Exponential suppression of bit-flips in a qubit encoded in an oscillator. *Nat. Phys*. **16**, 509–513 (2020).
29. Touzard, S. et al. Coherent oscillations inside a quantum manifold stabilized by dissipation. *Phys. Rev. X* **8**, 021005 (2018).
30. Dykman, M. I., Maloney, C. M., Smelyanskiy, V. N. & Silverstein, M. Fluctuational phase-flip transitions in parametrically driven oscillators. *Phys. Rev. E* **57**, 5202–5212 (1998).
31. Wustmann, W. & Shumeiko, V. Parametric resonance in tunable superconducting cavities. *Phys. Rev. B* **87**, 184501 (2013).
32. Siddiqi, I. et al. Direct observation of dynamical bifurcation between two driven oscillation states of a Josephson junction. *Phys. Rev. Lett*. **94**, 027005 (2005).
33. Wilson, C. M. et al. Photon generation in an electromagnetic cavity with a time-dependent boundary. *Phys. Rev. Lett*. **105**, 233907 (2010).
34. Zhang, Y. & Dykman, M. I. Preparing quasienergy states on demand: a parametric oscillator. *Phys. Rev. A* **95**, 053841 (2017).
35. Wang, Z. et al. Quantum dynamics of a few-photon parametric oscillator. *Phys. Rev. X* **9**, 021049 (2019).
36. Zurek, W. H. Decoherence, einselection, and the quantum origins of the classical. *Rev. Mod. Phys*. **75**, 715–775 (2003).
37. Munro, W. J., Nemoto, K., Milburn, G. J. & Braunstein, S. L. Weak-force detection with superposed coherent states. *Phys. Rev. A* **66**, 023819 (2002).
38. Dykman, M. I., Bruder, C., Lörch, N. & Zhang, Y. Interaction-induced time-symmetry breaking in driven quantum oscillators. *Phys. Rev. B* **98**, 195444 (2018).
39. Puri, S., Andersen, C. K., Grimsmo, A. L. & Blais, A. Quantum annealing with all-to-all connected nonlinear oscillators. *Nat. Commun*. **8**, 15785 (2017).
40. Goto, H. Bifurcation-based adiabatic quantum computation with a nonlinear oscillator network. *Sci. Rep*. **6**, 21686 (2016).
41. Marandi, A., Wang, Z., Takata, K., Byer, R. L. & Yamamoto, Y. Network of time-multiplexed optical parametric oscillators as a coherent Ising machine. *Nat. Photon*. **8**, 937–942 (2014).

Publisher's note Springer Nature remains neutral with regard to jurisdictional claims in published maps and institutional affiliations.

Methods

Experimental implementation

As described in the main text, our experimental implementation consists of a superconducting nonlinear resonator placed inside a 3D microwave cavity (Fig. 1d, Supplementary Information section VI). The main differences with respect to a 3D transmon qubit are as follows. Large capacitor pads help reduce the Kerr nonlinearity of the resonator relative to a transmon and thus limit the drive strength ϵ_2 necessary to reach appreciable coherent-state amplitudes. We orient the resonator such that its dipole moment is perpendicular to the electric field direction of the lowest-frequency cavity mode ($\omega_b/2\pi = 8.9$ GHz) to avoid strong hybridization despite the large pads, and reintroduce a small precisely tuned coupling necessary for dispersive readout by slightly offsetting the pads (note δ in Fig. 1e). Furthermore, instead of a single Josephson junction, we employ a SNAIL[22] (Fig. 1f). This makes the resonator flux tunable and endows it with both third- and fourth-order nonlinearities. We use the former to generate single-mode squeezing by applying a coherent microwave drive ω_s at twice the resonator frequency, thus converting one drive photon into two resonator photons through three-wave mixing; the latter yields the required Kerr nonlinearity. An in-depth description of the device design and a full list of system parameters are given in Supplementary Information sections VI, VII, Supplementary Table 2.

Adiabatic mapping between the FQ and KCQ Bloch spheres

Without the large-α approximation from the main text, the expressions for the even and odd cat states are given by $|\mathcal{C}_\alpha^\pm\rangle = \mathcal{N}_\alpha^\pm(|+\alpha\rangle \pm |-\alpha\rangle)$, where $\alpha = \sqrt{\epsilon_2/K}$ is the amplitude of the coherent states in the superposition and $\mathcal{N}_\alpha^\pm = 1/\sqrt{2(1 \pm e^{-2\bar{n}})}$ is a normalization coefficient accounting for $|\langle +\alpha|-\alpha\rangle| = e^{-2\bar{n}} \neq 0$ (ref. [4], Supplementary Information). These expressions are valid for all ϵ_2/K and, in the limit $\epsilon_2/K \to 0$, they become $|\mathcal{C}_\alpha^+\rangle \to |n=0\rangle$ and $|\mathcal{C}_\alpha^-\rangle \to |n=1\rangle$. This validates the mapping between the FQ and KCQ Bloch spheres, which share a common definition $|\pm Z\rangle = |\mathcal{C}_\alpha^\pm\rangle$ for their respective values of α. We perform the mapping by ramping the squeezing drive on and off with a hyperbolic-tangent profile over 320 ns. To avoid leakage to higher excited states, this time is chosen to be much longer than $1/2K$, where $2K$ corresponds to the anharmonicity of the FQ.

Numerical simulation

Here we describe the numerical simulation performed to obtain the results shown in Fig. 2. For the data presented in Figs. 3, 4 we compensate for all drive-related detunings by calibrating the drive frequencies (Supplementary Information section VIII, Supplementary Fig. 5). However, when measuring the data shown in Fig. 2, it would be impractical to perform this calibration for each drive strength ϵ_2. Instead we apply the tone generating the squeezing drive at twice the unshifted mode frequency $\omega_s = 2\omega_a$ and the X-rotation drive a frequency $\omega_s/2$. The resulting system Hamiltonian is

$$\hat{H}_s/\hbar = -K\hat{a}^{\dagger 2}\hat{a}^2 + 3g_3\xi(\hat{a}^{\dagger 2} + \hat{a}^2) - 4K|\xi|^2\hat{a}^\dagger\hat{a} + \epsilon_x\hat{a}^\dagger + \epsilon_x^*\hat{a},$$

where we have expressed ϵ_2 in terms of the independently calibrated third-order nonlinearity $g_3 \approx 20$ MHz and the dimensionless drive strength ξ (Supplementary Information section II). The third term corresponds to a drive-dependent frequency detuning due to the a.c. Stark shift.

We perform a numerical simulation of our system, which is described by the master equation

$$\dot{\hat{\rho}} = -\frac{i}{\hbar}[\hat{H}_s, \hat{\rho}] + \kappa_a(1 + n_{th})\mathcal{D}[\hat{a}]\hat{\rho} + \kappa_a n_{th}\mathcal{D}[\hat{a}^\dagger]\hat{\rho},$$

here $\mathcal{D}[\hat{\mathcal{O}}]\hat{\rho} = \hat{\mathcal{O}}\hat{\rho}\hat{\mathcal{O}}^\dagger - \frac{1}{2}\hat{\mathcal{O}}^\dagger\hat{\mathcal{O}}\hat{\rho} - \frac{1}{2}\hat{\rho}\hat{\mathcal{O}}^\dagger\hat{\mathcal{O}}$, $\hat{\rho}$ is the simulated density matrix of the nonlinear resonator, the dot indicates the time derivative, $\kappa_a = 1/T_1$ is the single-photon-loss rate of the nonlinear resonator and $n_{th} = 0.04$ its equilibrium thermal $|1\rangle$-state occupation number. Our simulation mimics the experiment using the same rise times for the tanh ramps of the squeezing drive (320 ns) and the X-rotation drive (80 ns) up to the point just before mapping back onto the FQ marked by a black arrow in Fig. 2a. At this point, we compute $\langle\mathcal{C}_\alpha^+|\hat{\rho}|\mathcal{C}_\alpha^+\rangle$.

We calibrate the abscissa of Fig. 2b by fitting this simulation to the Rabi frequency obtained at the maximum strength of the squeezing drive using the corresponding value of ξ (or equivalently ϵ_2) as the only free parameter. We then perform the simulation for all other values of ϵ_2 to obtain the solid black line shown in the figure. The black line in the bottom panel of Fig. 2d corresponds to the result of one of these simulations (marked by a red star in Fig. 2b) scaled to match the contrast of the data. This accounts for the fact that in the experiment the state $|\mathcal{C}_\alpha^+\rangle$ is mapped onto the $|0\rangle$ state of the FQ, which is then measured. This process as well as the finite mapping and measurement fidelities are not part of the simulation. The black lines in the other two panels of this figure are obtained by changing $\arg(\epsilon_x)$ but using same scaling factor.

Experimental details of the gate process tomography

Here we describe pulse sequences used to obtain the data presented in Fig. 3a, c, e. At the beginning of each sequence, the FQ is initialized in one of the six states $|\pm X\rangle$, $|\pm Y\rangle$ and $|\pm Z\rangle$. These are then adiabatically mapped onto the KCQ. Each sequence ends with the reverse mapping and measurement of the resulting $\langle X\rangle$, $\langle Y\rangle$ and $\langle Z\rangle$ component of the FQ state using appropriate FQ pulses (grey box in the figures).

To perform the $X(\pi/2)$ gate, we apply a Gaussian pulse with a duration of 24 ns and a maximum amplitude of $\epsilon_{X,\frac{\pi}{2}} = 6.5$ MHz.

To implement a $Z(\pi/2)$ gate, we abruptly set the squeezing drive amplitude to zero for a duration $T_{Z(\pi/2)} = 38$ ns and then switch it on again, as shown in Fig. 3e. Our room-temperature electronics limit the rise and fall times of ϵ_2 to about 4 ns with a maximum time resolution of 2 ns.

Experimental details of the CR

During the CR, we perform heterodyne detection of the emitted cavity field. The data in Fig. 4a are a histogram of 3×10^5 measurements of this demodulated and integrated field.

We conservatively define the total readout fidelity as $\mathcal{F} = 1 - p(-\alpha|+\alpha) - p(+\alpha|-\alpha) = 0.74$, where $p(-\alpha|+\alpha) = 0.13$ ($p(+\alpha|-\alpha) = 0.13$) is the probability of measuring the qubit in $|-\alpha\rangle$ ($|+\alpha\rangle$) after initialization in $|+\alpha\rangle$ ($|-\alpha\rangle$).

We characterize the quantum-non-demolition aspect by evaluating $\mathcal{Q} = (P(+\alpha|+\alpha) + P(-\alpha|-\alpha))/2 = 0.85$, where $P(i\,|\,i)$ is the probability of obtaining the measurement outcome i in two successive measurements (Supplementary Information section IX, Supplementary Fig. 6).

Supplementary information content

The accompanying Supplementary Information contains further details on: the general encoding (section I), the full system Hamiltonian (section II), direct spectroscopy of the energy gap (section III, Supplementary Fig. 1), the continuous X rotation (section IV), the characterization of the gate operations (section V, Supplementary Figs. 2, 3, Supplementary Table 1), the experimental setup (section VI, including a detailed wiring diagram in Supplementary Fig. 4), the system parameters (section VII, including a summary Supplementary Table 2), the experimental tune-up sequence (section VIII, Supplementary Fig. 5), the CR (section IX, Supplementary Fig. 6), the measurement of the KCQ coherence times obtained by mapping back onto the FQ and performing dispersive readout (section X, Supplementary Fig. 7) and a discussion of the impact of different decoherence processes on the KCQ (section XI, Supplementary Fig. 7).

Data availability

The data that support the findings of this study are available from the corresponding authors upon reasonable request.

Code availability

Numerical simulations were performed using a Python-based open source software (QuTiP). Custom Python code was used to obtain and analyse the experimental data following standard practices as outlined in Methods and the Supplementary Information. The code used in this study is available from the corresponding authors upon reasonable request.

Acknowledgements We acknowledge the contributions of L. Burkhart, P. Campagne-Ibarcq, A. Eickbusch, L. Frunzio, P. Reinhold, K. Serniak and Y. Zhang. Facilities use was supported by YINQE and the Yale SEAS cleanroom. This work was supported by ARO under grant number W911NF-18-1-0212 and grant number W911NF-16-1-0349, and NSF under grant number DMR-1609326. We also acknowledge support of the Yale Quantum Institute.

Author contributions A.G. designed and carried out initial experiments with help from S.T. and S.O.M., and designed the final experiment with input from N.E.F., M.H.D. and S.P. A.G. and N.E.F. fabricated the sample, performed measurements and analysed the data used in the manuscript. A.G., N.E.F. and M.H.D. wrote the manuscript with input from all authors.

Competing interests M.H.D. is a co-founder of Quantum Circuits, Incorporated. A.G., S.P., S.M.G. and M.H.D. are inventors on US Provisional Patent Application Number 62/692,243 submitted by Yale University, which covers quantum information processing with an asymmetric error channel.

Additional information

Supplementary information is available for this paper at https://doi.org/10.1038/s41586-020-2587-z.

Correspondence and requests for materials should be addressed to A.G. or M.H.D.

Electronic phase separation in multilayer rhombohedral graphite

https://doi.org/10.1038/s41586-020-2568-2

Received: 11 November 2019

Accepted: 5 May 2020

Yanmeng Shi[1,10], Shuigang Xu[2,10], Yaping Yang[1,2,10], Sergey Slizovskiy[1,2], Sergey V. Morozov[3], Seok-Kyun Son[1,2,9], Servet Ozdemir[1], Ciaran Mullan[1], Julien Barrier[1,2], Jun Yin[1,2], Alexey I. Berdyugin[1], Benjamin A. Piot[4], Takashi Taniguchi[5], Kenji Watanabe[5], Vladimir I. Fal'ko[1,2,6], Kostya S. Novoselov[1,2,7,8], A. K. Geim[1,2] & Artem Mishchenko[1,2]✉

Of the two stable forms of graphite, hexagonal and rhombohedral, the former is more common and has been studied extensively. The latter is less stable, which has so far precluded its detailed investigation, despite many theoretical predictions about the abundance of exotic interaction-induced physics[1–6]. Advances in van der Waals heterostructure technology[7] have now allowed us to make high-quality rhombohedral graphite films up to 50 graphene layers thick and study their transport properties. Here we show that the bulk electronic states in such rhombohedral graphite are gapped[8] and, at low temperatures, electron transport is dominated by surface states. Because of their proposed topological nature, the surface states are of sufficiently high quality to observe the quantum Hall effect, whereby rhombohedral graphite exhibits phase transitions between a gapless semimetallic phase and a gapped quantum spin Hall phase with giant Berry curvature. We find that an energy gap can also be opened in the surface states by breaking their inversion symmetry by applying a perpendicular electric field. Moreover, in rhombohedral graphite thinner than four nanometres, a gap is present even without an external electric field. This spontaneous gap opening shows pronounced hysteresis and other signatures characteristic of electronic phase separation, which we attribute to emergence of strongly correlated electronic surface states.

Films of rhombohedral graphite (RG; also described as chirally stacked ABC graphene multilayers) are predicted to possess nearly flat bands localized at the surfaces; these bands are particularly suitable for exploring electron–electron interactions[3]. In RG, interlayer hopping (parameterized by γ_1; see Fig. 1a) dimerizes the electronic states of the opposite sublattices of all contiguous graphene layers in the bulk, shifting their energies away from the Fermi level[9,10]. Electrons of only two sublattices, one in the top layer, and the other in the bottom layer, remain at low energies. These surface states are considered to be equivalent to topological edge states in the 'polyacetylene' Su–Schrieffer–Heeger model[11]. The surface states residing on the inequivalent sublattices of the opposite surfaces of N-layer-thick samples are expected to form nearly flat bands with approximate energy dispersion relations of the form $E \propto \pm p^N$ (refs. [3,9,12]), where p is the in-plane momentum. These surface states are further theorized to have strong electron–electron interactions, hypothetically leading to spontaneous quantum Hall states, ferromagnetism and superconductivity[1–6,13]. When considering other hopping parameters (γ_0–γ_4 are shown in Fig. 1a; Methods), the surface flat bands acquire a finite bandwidth of the order of $2\gamma_4\gamma_1/\gamma_0$ as well as electron–hole asymmetry, and trigonal warping due to γ_2 and γ_3 (Fig. 1b), which could affect electron–electron interactions, spontaneous symmetry breaking and the opening of a bandgap (Fig. 1c). Owing to the metastable nature of RG, the reported transport experiments have been limited to ABC trilayer and ABCA tetralayer graphene, either in suspended two-terminal devices, or with the spectrum modified by moiré superlattices[14–17]; longer ABC sequences have been studied using magneto-Raman[18] and ARPES[19]. Here we report electronic transport in high-quality RG of up to $N \approx 50$ graphene layers thick, where we observe strong electronic correlations and phase separation, phenomena typically reserved for unconventional superconductors and heavy fermion materials. Eight RG devices were studied in detail in this work, with thicknesses ranging from about 2.3 nm ($N = 7$) to about 16.5 nm ($N \approx 50$).

We identified the stacking order of graphite films using Raman spectroscopy and, to retain their high electronic quality, we encapsulated the exfoliated films with hexagonal boron nitride (hBN) crystals using the directional dry transfer technique[7] (Methods). Figure 1d compares low-temperature ($T = 20$ mK) resistivity ρ_{xx} of RG and hexagonal graphite (HG) devices of the same thickness (device 1, about 3 nm thick, 9 graphene layers) as a function of total carrier density $n = \frac{C_\mathrm{t}V_\mathrm{t} + C_\mathrm{b}V_\mathrm{b}}{e}$. (Here V_t and V_b are the gate voltages, and C_t and C_b are the unit-area capacitances, of the top and bottom gates, respectively, and e is the

---

[1]Department of Physics and Astronomy, University of Manchester, Manchester, UK. [2]National Graphene Institute, University of Manchester, Manchester, UK. [3]Institute of Microelectronics Technology and High Purity Materials, Russian Academy of Sciences, Chernogolovka, Russia. [4]Université Grenoble Alpes, Laboratoire National des Champs Magnétiques Intenses, UPS-INSA-EMFL-CNRS-LNCMI, Grenoble, France. [5]National Institute for Materials Science, Tsukuba, Japan. [6]Henry Royce Institute for Advanced Materials, Manchester, UK. [7]Centre for Advanced 2D Materials, National University of Singapore, Singapore, Singapore. [8]Chongqing 2D Materials Institute, Chongqing, China. [9]Present address: Department of Physics, Mokpo National University, Muan, South Korea. [10]These authors contributed equally: Yanmeng Shi, Shuigang Xu, Yaping Yang. ✉e-mail: artem.mishchenko@gmail.com

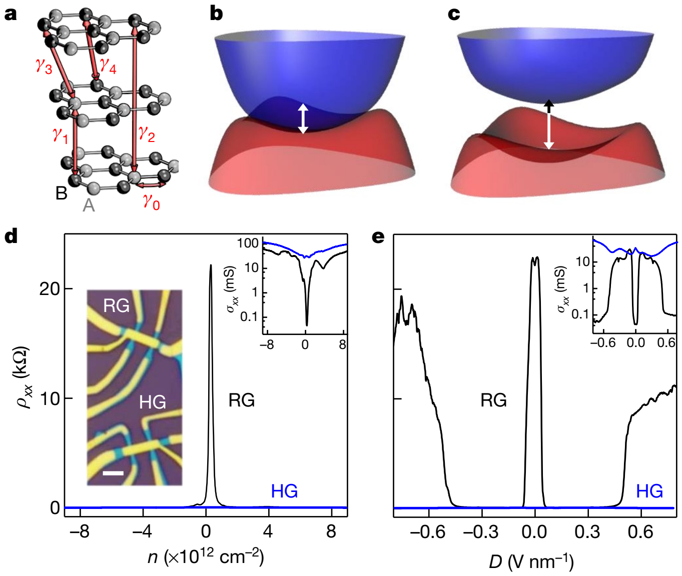

Fig. 1 | Transport characteristics of thin RG films. a, Schematic of RG hopping parameters, γ_i. Light- and dark-grey spheres represent carbon atoms of sublattices A and B, respectively. **b**, Dispersion of the surface states including all the hopping parameters in **a**. The vertical axis is energy, E, and horizontal axes are in-plane momenta, p. Skew hopping γ_4 adds an appreciable bandwidth $2\gamma_4\gamma_1/\gamma_0$ to the otherwise flat surface state bands, and introduces electron–hole asymmetry. The presence of γ_2 and γ_3 leads to trigonal warping. Blue and red colours indicate conduction and valence bands, respectively, and the double-headed arrow shows the finite band overlap between conduction and valence bands. **c**, Scenario when a bandgap $\Delta > 2\gamma_4\gamma_1/\gamma_0$ spontaneously opens in the RG spectrum. The double-headed arrow indicates the size of the bandgap. **d**, ρ_{xx} as a function of total carrier density $n = n_t + n_b$ measured at $D = 0$ for device 1 with rhombohedral (black curve) and hexagonal (blue curve) crystal structures (both are nine graphene layers thick). n_t (n_b) is the charge density induced by top (back) gate voltage. Left inset, optical micrograph of device 1; scale bar, 2 μm. **e**, ρ_{xx} as a function of the displacement field D; $n = 0$, $T = 20$ mK. Inset graphs in **d** and **e** show the corresponding σ_{xx} curves on a logarithmic scale.

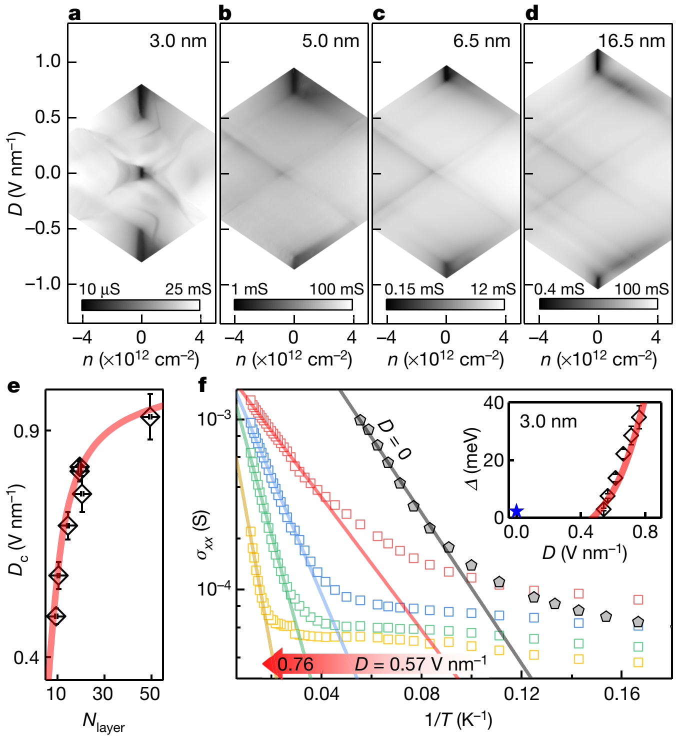

Fig. 2 | Thickness dependence of the transport characteristics of multilayer RG. a–d, Conductivity maps $\sigma_{xx}(n, D)$ for RG devices 1 to 4, respectively, of different thicknesses as specified in the panels. **e**, Thickness dependence of the critical field D_c, above which the transport gap is opened (black diamonds); thickness is expressed as number of layers, N_{layer}. D_c values were extracted from linear fits of $\sigma_{xx}(D)$ at $n = 0$ near the insulating states in the maps shown in **a**–**d**. Error bars represent uncertainties of the fitting procedure. The red curve is the self-consistent model (Methods). **f**, Arrhenius plot of σ_{xx} for RG device 1 at $D = 0.57$ V nm^{-1} (red squares), 0.62 V nm^{-1} (blue squares), 0.66 V nm^{-1} (green squares) and 0.76 V nm^{-1} (yellow squares). The grey pentagons are the data for $D = 0$. Linear fits of high-T regions (solid lines) give the bandgap Δ presented in the inset. The red curve in the inset is the bandgap estimation using the self-consistent screening model (Methods). For comparison, the thermal activation energy of the high-resistance state at $D = 0$ V nm^{-1} is also plotted in the inset (blue star).

elementary charge.) The RG device shows much stronger modulation of $\rho_{xx}(n)$ as compared to the reference HG device, such that ρ_{xx} of the former spans 10 Ω to 23 kΩ and exhibits a profound high-resistivity region near $n = 0$. At the same time, the HG device displays metallic behaviour over the entire range of carrier densities (ρ_{xx} varies only from 8 Ω to 63 Ω), similarly to the reported dual-gated devices of tetralayer and hexalayer Bernal-stacked graphene[20,21].

Figure 1e shows three distinct high-resistance regions for RG device 1 (which are absent in the HG device) as a function of displacement field $D = \frac{C_t V_t - C_b V_b}{2\varepsilon_0}$ measured at $n = 0$ (ε_0 is the vacuum permittivity). The appearance of the high-resistivity region at the neutrality point ($n = 0$, $D = 0$) suggests that an energy gap opens in the surface states spectrum, whereas the ρ_{xx} value close to the resistance quantum h/e^2 hints at edge-state transport caused possibly by topological character of the insulating state. The resistivity peak at the neutrality point was observed only in sufficiently thin (<4 nm) RG devices and cannot be explained within a free-particle model (Methods). Before discussing this high-resistivity feature, we consider states induced by a large displacement field. These regions of high resistivity, observed in all RG devices, emerging above a critical displacement field, $|D| > D_c$ (see Fig. 2a–d), are in agreement with the theoretical prediction that a high enough D opens an energy gap in the surface state spectrum of RG[22]. The effect is similar to that observed in bilayer graphene under displacement but has much stronger nonlinear screening of charges at the two RG surfaces (Methods). Note that the observation of these displacement-induced gaps requires a gapped bulk of multilayer RG (Methods). The resistivity of our fully gapped RG film (both surface and bulk states are gapped) is of the order of 20 kΩ for the thin RG sample at 20 mK (device 1), and 2–3 kΩ for the 16.5-nm-thick sample (device 4) at 1.5 K.

The effect of RG thickness on the displacement-field-induced bandgap is shown in Fig. 2a–d, which shows $\sigma_{xx}(n, D)$ maps for four RG devices with thicknesses ranging from 3 nm to 16.5 nm (devices 1 to 4). Figure 2e summarizes how the critical displacement field D_c increases with sample thickness. The solid line is the self-consistent theory (see Methods). From the T dependence of σ_{xx} of 3-nm-thick RG device 1, we extracted the sizes of thermally activated gaps Δ at different D (Fig. 2f), which are plotted in Fig. 2f inset. The bandgap observed in RG at $|D| > D_c$ is in stark contrast to the HG response to the displacement field where D causes the resistivity to decrease (Fig. 1e) due to the growing size of the Fermi surfaces of the top and bottom surface states[22,23]. The behaviour of $\sigma_{xx}(D)$ presented in Fig. 2a–d is characteristic of the uniform ABCABC… stacking in our RG samples. We note that, if mixed ABC/ABA stacking were present in our devices, this should have prevented gap opening by the displacement field (Methods), which provides complementary evidence for complete ABC stacking in our RG devices (Extended Data Figs. 1 and 2).

Next we explore electron transport in multilayer RG using magnetic field B applied perpendicular to the plane. Longitudinal (ρ_{xx})

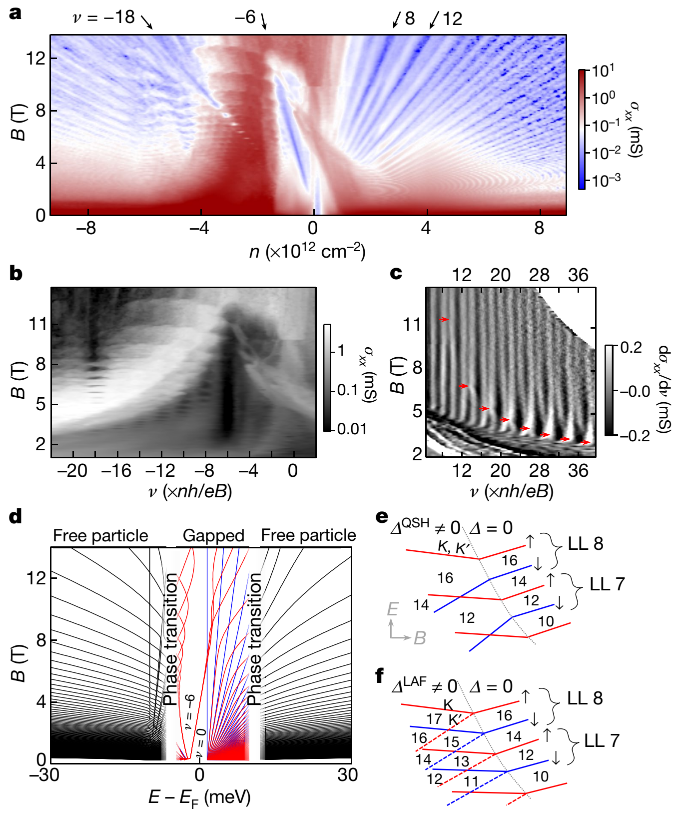

Fig. 3 | Quantum Hall effect in RG. a, Map of longitudinal conductivity $\sigma_{xx}(n, B)$ for device 1; $D = 0$; $T = 20$ mK. Arrows and numbers indicate the filling factors of quantum Hall states. **b**, $\sigma_{xx}(\nu, B)$ for the hole side (same data as in **a**). **c**, Differential $\mathrm{d}\sigma_{xx}/\mathrm{d}\nu(\nu, B)$ map for the electron side (data from **a**). Red arrows mark the positions of LL crossings. **d**, Calculated spectra of LLs in multilayer RG, using gapped and gapless band structures at low (coloured curves) and high (black) energies, respectively. The free-particle and gapped regions are separated by phase transitions. Red and blue lines, depending on the order parameter, correspond to electronic states with opposite spins (quantum spin Hall) or of opposite valleys (layer antiferromagnetism). E_F, Fermi energy. **e**, Effect of quantum spin Hall order parameter on the Landau spectrum. Numbers indicate the filling factors. LL 7 and LL 8 refer to the orbital indices of the zeroth LL. ↑ (red lines) and ↓ (blue lines) label spin-split LLs. Δ_{QSH} is the QSH order parameter, and K and K′ are the opposite valleys. The dotted line demarcates the transition between gapped and free-particle regimes. **f**, Same as in **e** but for layer antiferromagnetism. Solid (dashed) coloured lines refer to K (K′) valleys.

and transverse (ρ_{xy}) resistivities of device 1 are shown in Extended Data Fig. 3a as a function of B at $n = 2.3 \times 10^{12}$ cm^{-2} and $D = 0$. Shubnikov–de Haas oscillations emerge at $B \approx 1$ T, and well-quantized ρ_{xy} plateaux develop for $B > 3$ T manifesting the onset of the quantum Hall effect (QHE), such that under a strong magnetic field the electronic spectrum of 2D surface states collapses into a series of discrete Landau levels (LLs), leading to quantized ρ_{xy}. In high B (see, for example, Extended Data Fig. 3b for $B = 10$ T), $\rho_{xy}(n)$ plateaux appear at even fractions of h/e^2, indicating a two-fold (valley) degeneracy of the LLs. To examine the quantization, Fig. 3a shows the Landau fan diagram $\sigma_{xx}(n, B)$ for device 1 at $D = 0$. We note strong electron–hole asymmetry in the diagram: the electron side exhibits straight LLs (blue lines follow the slopes $B/n = h/e\nu$, where ν is the filling factor) fanning out from the neutrality point, while the hole side shows a criss-cross pattern. We observed similar behaviour in RG devices of different thicknesses, which is consistent with the surface origin of the LLs (Extended Data Fig. 4). The QHE has also been reported in thin films of Bernal-stacked graphite[23]. In the latter case, the quantization was due to the formation of standing waves in the bulk. In contrast, our multilayer RG has a gapped bulk but conducting surfaces, which should exhibit the QHE if their electronic quality is sufficiently high.

In N-layer RG, a Berry phase $\pm N\pi$ around the opposite K points leads to N-degenerate zero-energy LLs for each spin and valley, which are localized on the opposite surfaces for opposite valleys[24,25]. A free-particle spectrum of LLs in RG calculated using the same method as in ref. [26] is plotted in Extended Data Fig. 4a. Typically for semimetals, conduction- and valence-band LLs make numerous crossings at moderate B, which for multilayer RG happens on the hole side of the spectrum. In the absence of a displacement field, all LLs are valley degenerate. In addition, low-index valence-band LLs are triply degenerate, reflecting the triply degenerate maxima of the valence band (Fig. 1b). They are split at higher B where the three Fermi surfaces of the valence band merge into one. For device 1 (9 layers) in Fig. 3a, the total number of the zeroth LLs is 36 (2 spins, 2 valleys and 9 orbitals), and the lines corresponding to filling factors up to ±18 come from these zeroth LLs. Lines on the electron side, which trace $\nu = 8, 12, 16, \ldots$ are well pronounced. These filling factors in multiples of 4 can be explained by relatively large Zeeman gaps between two-fold degenerate orbital levels of zeroth LLs. A pronounced gap at $\nu = -18$ followed by a series of crossings below 8 T could be traced back to the crossings between the 2N-fold degenerate zeroth LL and the valence-band LLs. The robust $\nu = -18$ state emerges when these crossings stop (Extended Data Fig. 4a). When only a single gate is used (Extended Data Fig. 5), the valley degeneracy becomes lifted, and a robust gap appears at $\nu = -7$ (for 7-layer-thick device 7), $\nu = -9$ (for 9-layer device 1) and at $\nu = -11$ (for 11-layer device 6). This provides additional support for our assignment of the observed spectrum to the N-degenerate zeroth LL, which is in turn a manifestation of an $N\pi$ Berry phase in N-layer RG.

Although the free-particle theory adequately describes the experimental results at high doping (Fig. 3a, d above $|n| > 2.5 \times 10^{12}$ cm^{-2}), it fails to explain the pronounced gaps observed at $\nu = 0$ and $\nu = -6$ (Fig. 3a). Apart from the crisscross pattern on the hole side (Fig. 3b), which agrees with the free-particle theory, there is a series of crossing points on the electron side at the symmetry broken states $\nu = 10, 14, 18, 22\ldots$ The crossings are better seen if we replot the Landau fan as a function of ν (Fig. 3c; the crossing points are marked with red arrows). These crossings also cannot be explained using the free-particle picture. To account for the latter features, we suggest a spontaneous appearance of an interaction-induced spin and/or valley symmetry-breaking order parameter. It leads to a bandgap when the resulting band splitting exceeds the single-particle overlap between the conduction and valence bands, thus allowing the observation of quantum Hall states at $\nu = 0$ and -6 (Fig. 3a, d). With increasing B, the gap switches from $\nu = 0$ to $\nu = -6$. This can be explained by large orbital magnetic moments that have opposite signs for opposite spins (or valleys) and lead to closure of the $\nu = 0$ gap, as shown in Fig. 3d. The bandgap disappears with increasing doping, but the observed crossings on the electron side (Fig. 3c, and also Extended Data Fig. 4c, d for 3.3-nm-thick device 5) suggest that a small interaction-induced order parameter remains present up to $n \approx 2.5 \times 10^{12}$ cm^{-2}.

The interplay between the orbital, valley and spin degrees of freedom leads to several possible states with spontaneously broken symmetry in multilayer RG. They include quantum valley Hall, quantum anomalous Hall, layer antiferromagnetic insulator and quantum spin Hall states[3] (see Methods). The crossing points on the electron side (Fig. 3c, and Extended Data Fig. 4d for similar results in device 5) can be explained by the phase transition from spin-polarized states due to Zeeman splitting at higher electron concentration to quantum spin Hall states at electron concentration $n < 2.5 \times 10^{12}$ cm^{-2} (Fig. 3e). The quantum spin Hall phase is accompanied by a giant Berry curvature and a related giant orbital magnetic moment (the same in both valleys but opposite for the two spin directions)[3]. The observed crossings cannot be explained by any other of the conjectured phases listed above. For instance, the

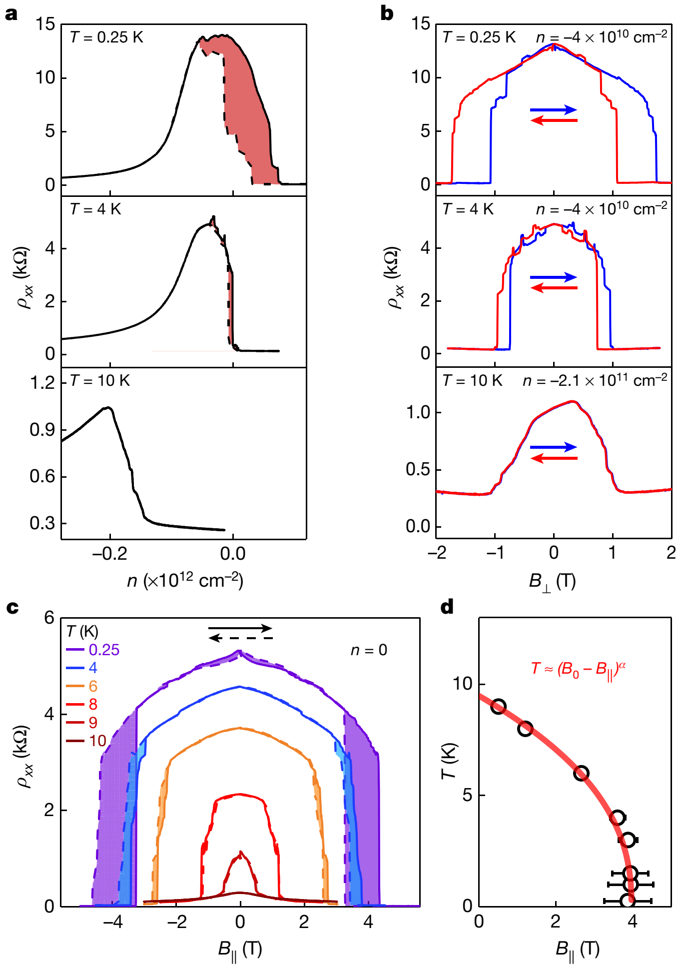

Fig. 4 | Hysteretic behaviour of the insulating state in multilayer RG. **a**, $\rho_{xx}(n)$ of dual-gated device 5 (RG about 3.3 nm thick) at $D = 0$; data were taken at three different temperatures (top, 0.25 K; middle, 4 K; bottom, 10 K). The solid (dashed) curves indicate positive (negative) sweep directions; the coloured areas highlight the hysteresis. **b**, Hysteresis in $B_\perp$ of the same device used in **a**. Panels show $\rho_{xx}(B_\perp)$; the data were taken at the same three temperatures as in **a**, with n values shown at the top right of each panel. Coloured arrows show sweep directions. **c**, Hysteresis in $B_\parallel$ for device 6 (single-gated RG about 3.6 nm thick). $\rho_{xx}(B_\parallel)$ is shown for six different temperatures; the coloured areas highlight the hysteresis. **d**, Phase diagram of the critical behaviour in **c**: the temperature at which the insulating state appears depends on $B_\parallel$ (error bars are due to hysteresis). The red curve is the fit $T \approx (B_0 - B_\parallel)^\alpha$, where $B_0 \approx 4$ T is the critical field at $T = 0$ K, and $\alpha \approx 0.4$ is the critical exponent.

layer antiferromagnetic phase leads to lifted valley degeneracy and the presence of gaps and crossings at both even and odd filling factors (Fig. 3f), which contradicts the experiment. Note that there is no evidence that the observed quantum spin Hall phase becomes stronger towards zero doping, because the development of another competing order cannot be excluded.

In the absence of a magnetic field, thin (<4 nm) RG devices reveal an intrinsic insulating state at the neutrality point (Fig. 1d, e). Extended Data Fig. 6a shows the temperature dependence of $\rho_{xx}(n)$ around the insulating state at $D = 0$ in another RG device about 3.3 nm thick. At T below 10 K, the resistance shoots up by orders of magnitude, showing thermal activation behaviour consistent with a gap of 2–3 meV (Extended Data Fig. 6a). We note that this value represents an effective transport gap, after accounting for the lifted overlap of about $2\gamma_4\gamma_1/\gamma_0$ (Extended Data Fig. 9).

Surprisingly, pronounced hysteretic behaviour is observed in the resistivity of multilayer RG around the neutrality point as a function of doping (see Fig. 4a and Extended Data Fig. 6a, b). The hysteresis rapidly decreases with increasing T and disappears if the RG enters a metallic state. Note that the hysteresis strongly favours electron doping, reflecting the electron–hole asymmetry of the RG band structure. In addition to the hysteresis as a function of n, we also observed pronounced hysteresis in response to both perpendicular ($B_\perp$) and parallel ($B_\parallel$) magnetic fields. $B_\perp$ suppresses the insulating state (Fig. 4b) but the accompanying Landau quantization unfortunately complicates analysis of the observed T dependence. In contrast, measurements in $B_\parallel$ (Fig. 4c), where the orbital degree of freedom remains unaffected, provide a clearer picture. With increasing T, both the hysteresis and the transition field rapidly decrease, and the $B_\parallel$–T phase diagram follows the power-law $T \approx (B_0 - B_\parallel)^\alpha$ where $\alpha \approx 0.4$ is the critical exponent (Fig. 4d). Our fit is comparable to those reported for the 'hidden order' phase in strongly correlated heavy fermion systems like[27] URu_2Si_2. The pronounced hysteretic behaviour with abrupt switching hints at spontaneous formation of insulating electronic phases that are separated into domains, similar to those observed in other correlated systems such as manganites, cuprates, and transition metal oxides[28]. The hysteresis as a function of both electric and magnetic fields is characteristic of multiferroic materials, and advanced scanning probe techniques could be helpful in identifying the nature of those electronic domains in future.

The present work offers a novel experimental system in which to explore strongly correlated phenomena that does not rely on spin–orbit or exchange interactions in transition metal oxides[28] or on precise structuring of graphene superlattices[29–32]. Electronic coupling between top and bottom surfaces in thin RG films is similar to that observed in thin films of topological insulators[33,34] and could be responsible for the spontaneous gap opening in our case. However, this coupling cannot explain the observed hysteretic behaviour. We believe that multilayer RG provides an interesting system in which to explore strong correlations, quantum criticality and other many-body phenomena, usually reserved to *f*-element-based heavy fermions or *d*-element-based transition metal oxides.

Online content

Any methods, additional references, Nature Research reporting summaries, source data, extended data, supplementary information, acknowledgements, peer review information; details of author contributions and competing interests; and statements of data and code availability are available at https://doi.org/10.1038/s41586-020-2568-2.

1. Kopnin, N. B., Ijäs, M., Harju, A. & Heikkilä, T. T. High-temperature surface superconductivity in rhombohedral graphite. *Phys. Rev. B* **87**, 140503(R) (2013).
2. Otani, M., Koshino, M., Takagi, Y. & Okada, S. Intrinsic magnetic moment on (0001) surfaces of rhombohedral graphite. *Phys. Rev. B* **81**, 161403(R) (2010).
3. Zhang, F., Jung, J., Fiete, G. A., Niu, Q. & MacDonald, A. H. Spontaneous quantum Hall states in chirally stacked few-layer graphene systems. *Phys. Rev. Lett.* **106**, 156801 (2011).
4. Pamuk, B., Baima, J., Mauri, F. & Calandra, M. Magnetic gap opening in rhombohedral-stacked multilayer graphene from first principles. *Phys. Rev. B* **95**, 075422 (2017).
5. Muñoz, W. A., Covaci, L. & Peeters, F. M. Tight-binding description of intrinsic superconducting correlations in multilayer graphene. *Phys. Rev. B* **87**, 134509 (2013).
6. Xu, D. H. et al. Stacking order, interaction, and weak surface magnetism in layered graphene sheets. *Phys. Rev. B* **86**, 201404(R) (2012).
7. Yang, Y. et al. Stacking order in graphite films controlled by van der Waals technology. *Nano Lett.* **19**, 8526–8532 (2019).
8. Ho, C. H., Chang, C. P. & Lin, M. F. Evolution and dimensional crossover from the bulk subbands in ABC-stacked graphene to a three-dimensional Dirac cone structure in rhombohedral graphite. *Phys. Rev. B* **93**, 075437 (2016).
9. Haering, R. R. Band structure of rhombohedral graphite. *Can. J. Phys.* **36**, 352–362 (1958).
10. Mcclure, J. W. Electron energy band structure and electronic properties of rhombohedral graphite. *Carbon* **7**, 425–432 (1969).
11. Xiao, R. J. et al. Density functional investigation of rhombohedral stacks of graphene: topological surface states, nonlinear dielectric response, and bulk limit. *Phys. Rev. B* **84**, 165404 (2011).
12. Xiao, D., Chang, M. C. & Niu, Q. Berry phase effects on electronic properties. *Rev. Mod. Phys.* **82**, 1959–2007 (2010).
13. Velasco, J. et al. Transport spectroscopy of symmetry-broken insulating states in bilayer graphene. *Nat. Nanotechnol.* **7**, 156–160 (2012).

14. Lee, Y. et al. Competition between spontaneous symmetry breaking and single-particle gaps in trilayer graphene. *Nat. Commun*. **5**, 5656 (2014).
15. Myhro, K. et al. Large tunable intrinsic gap in rhombohedral-stacked tetralayer graphene at half filling. *2D Mater*. **5**, 045013 (2018).
16. Chen, G. et al. Evidence of a gate-tunable Mott insulator in a trilayer graphene moiré superlattice. *Nat. Phys*. **15**, 237–241 (2019).
17. Lee, Y. et al. Gate tunable magnetism and giant magnetoresistance in ABC-stacked few-layer graphene. Preprint at http://arXiv.org/abs/1911.04450 (2019).
18. Henni, Y. et al. Rhombohedral multilayer graphene: a magneto-Raman scattering study. *Nano Lett*. **16**, 3710–3716 (2016).
19. Henck, H. et al. Flat electronic bands in long sequences of rhombohedral-stacked graphene. *Phys. Rev. B* **97**, 245421 (2018).
20. Shi, Y. et al. Tunable Lifshitz transitions and multiband transport in tetralayer graphene. *Phys. Rev. Lett*. **120**, 096802 (2018).
21. Nakasuga, T. et al. Low-energy band structure in Bernal stacked six-layer graphene: Landau fan diagram and resistance ridge. *Phys. Rev. B* **99**, 085404 (2019).
22. Koshino, M. Interlayer screening effect in graphene multilayers with ABA and ABC stacking. *Phys. Rev. B* **81**, 125304 (2010).
23. Yin, J. *et al*. Dimensional reduction, quantum Hall effect and layer parity in graphite films. *Nature Phys*. **15**, 437–442 (2019).
24. Koshino, M. & McCann, E. Trigonal warping and Berry's phase Nπ in ABC-stacked multilayer graphene. *Phys. Rev. B* **80**, 165409 (2009).
25. Min, H. K. & MacDonald, A. H. Chiral decomposition in the electronic structure of graphene multilayers. *Phys. Rev. B* **77**, 155416 (2008).
26. Slizovskiy, S., McCann, E., Koshino, M. & Fal'ko, V. I. Films of rhombohedral graphite as two-dimensional topological semimetals. *Commun. Phys*. **2**, 164 (2019).
27. Ran, S. et al. Phase diagram of $URu_{2-x}Fe_xSi_2$ in high magnetic fields. *Proc. Natl Acad. Sci. USA* **114**, 9826–9831 (2017).
28. Dagotto, E. Complexity in strongly correlated electronic systems. *Science* **309**, 257–262 (2005).
29. Cao, Y. et al. Correlated insulator behaviour at half-filling in magic-angle graphene superlattices. *Nature* **556**, 80–84 (2018).
30. Cao, Y. et al. Unconventional superconductivity in magic-angle graphene superlattices. *Nature* **556**, 43–50 (2018).
31. Sharpe, A. L. et al. Emergent ferromagnetism near three-quarters filling in twisted bilayer graphene. *Science* **365**, 605–608 (2019).
32. Serlin, M. et al. Intrinsic quantized anomalous Hall effect in a moiré heterostructure. *Science* **367**, 900–903 (2020).
33. Zhang, Y. et al. Crossover of the three-dimensional topological insulator Bi_2Se_3 to the two-dimensional limit. *Nat. Phys*. **6**, 584–588 (2010); erratum **6**, 712 (2010).
34. Neupane, M. et al. Observation of quantum-tunnelling-modulated spin texture in ultrathin topological insulator Bi_2Se_3 films. *Nat. Commun*. **5**, 3841 (2014).

Methods

Device fabrication

The RG films were obtained by mechanical exfoliation of natural graphite flakes (Graphenium Flakes 25–30 mm, NGS Naturgraphit) onto a SiO_2 (290 nm)/Si wafer. Exfoliated graphite films often show domains of various stacking orders, which can be identified by Raman spectroscopy. By mapping the ratio of the integrated area of the low-frequency component (ranging around 2,670–2,700 cm^{-1}) and the high-frequency component (ranging around 2,700–2,730 cm^{-1}) of the Raman 2D band, we can visualize the distribution of rhombohedral stacking in the films[7]. Raman spatial maps were taken with a step size of 0.5 µm.

RG films often revert back into Bernal stacking during the flake transfer process, and only a small region of the flake remains in the original stacking order. The transition between rhombohedral stacking and Bernal stacking occurs during the shift of graphene layers along armchair directions, whereas it does not happen along zig-zag directions. To retain the high electronic quality of RG, we used a directional van der Waals assembly technique[7] as follows. First, we identified the crystal orientation of graphite from the edge chirality of graphite films using Raman spectroscopy. Next, we used a polymer (a polymethylmethacrylate (PMMA)/polydimethylsiloxane (PDMS) stack mounted on a glass slide)-mediated dry transfer method to encapsulate RG films in hexagonal boron nitride (hBN). During the encapsulation process, the pressing-down direction of the PDMS/PMMA layers was controlled along the zig-zag direction of the graphite films, so that the stacking transformation could be avoided. Then, we used the above-mentioned Raman-ratio map again to confirm that rhombohedral stacking was retained in the hBN-encapsulated graphite. Finally, multiterminal Hall bar devices were made from the hBN/RG films/hBN heterostructures using standard electron-beam lithography. Examples of our Raman analysis during device fabrication are presented in Extended Data Fig. 7 for device 6 (3.6-nm-thick RG).

Surface and bulk contributions

Extended Data Figure 8 shows the temperature dependence of resistivity, $\rho_{xx}(T)$, at $n = 0$ for 16.5-and 3.3-nm-thick RG (devices 4 and 5, respectively). In contrast to the metallic behaviour of Bernal-stacked graphite[23], we observed a semiconductor-to-metal-transition with decreasing temperature. We attribute this transition to the interplay between three parallel conduction channels: the bulk and the two surfaces. Infinitely thick RG has 3D Dirac cones in its bulk energy spectrum[8], but in films of a finite thickness (with N layers), these Dirac cones are gapped by $\Delta \approx 2.1$ eV per N (see below). At high temperatures, the RG bulk conducts as a result of thermal activation across this gap, and this conductivity dominates over the 2D surface states. With decreasing T, the bulk contribution decreases and, finally, below some critical temperature T_c (about 20 K and 40 K for 16.5-nm and 3.3-nm RG, respectively), the contribution from the surfaces dominates, and $\rho_{xx}(T)$ shows metallic behaviour. This temperature behaviour of resistivity is similar to that observed in 3D topological insulators, which is also ascribed to competing conductances of bulk and surface states[35]. The observed T_c is smaller for thicker samples, in agreement with the expected $1/N$ dependence of the bulk gap. The observed T dependence indicates that at low temperatures ($T < T_c$), the conductivity through 3D bulk bands is suppressed and mostly 2D surface states contribute to electron transport. Thermal activation within the RG bulk limits the interval of exponential T dependence, preventing us from evaluating the bulk gaps at high D.

Tight-binding model

To describe multilayer RG, we employ the Slonczewski–Weiss–McClure (SWMC) parameterization of graphite[10,24,26,36], with interlayer hopping parameters that take into account the lattice arrangement of rhombohedral graphite, as shown in Fig. 1a. Multilayer RG has bulk subbands shifted away from zero energy, leading to a bulk gap of about $3\pi\gamma_1/N$ for N layers, making only the surface bands relevant for electronic transport at low T. The surface states have shallow dispersion for quasi-momenta $p < p_c = \gamma_1/\upsilon$, where υ is the Dirac velocity determined by intralayer nearest-neighbour hopping γ_0. There is also a quadratic term in the dispersion of surface states[26], $p^2/(2\,m_*)$ with $m_*^{-1} = 2\,\upsilon^2/\gamma_1(2\,\gamma_4/\gamma_0 + \delta/\gamma_1) \approx (0.4\,m_e)^{-1}$, which breaks the electron–hole symmetry, and trigonal warping terms controlled by γ_2 and γ_3. Here m_e is the free electron mass. Since the SWMC parameters are poorly known for RG, we use the conventional HG values[23,36] for the larger hopping amplitudes ($\gamma_0 = 3.16$ eV, $\gamma_1 = 0.39$ eV, $\gamma_3 = 0.25$ eV) while tuning the unknown γ_2 to −0.01 eV and m_* to $0.4m_e$ to better describe the experiment. We also set the energy difference of dimerized (that carry bulk states) and non-dimerized (that carry surface states) sublattices to zero, $\delta = 0$, and tuned γ_4 to about 0.13 eV. These parameter values have been chosen by comparing Fig. 3a with Extended Data Fig. 4a and matching the electron density of the first crossing of valence and conduction bands ($n = -6.3 \times 10^{12}$ cm^{-2}), which corresponds to the valence-band population where the chemical potential is at the bottom of the conduction band. Other crossings lead to extra constraints that can be satisfied reasonably well at positive filling factors ($4 < \nu < 40$, where crossings are in the range $5\ T > B > 2\ T$), while the matching becomes worse near zero filling and at larger magnetic fields, suggesting an increased role of interaction effects.

Bandgap induced by displacement field

Introducing a vertical electric displacement field D via asymmetric gating leads to a potential difference $\tilde{\Delta}$ between the top and the bottom layers, resulting in a density redistribution that strongly screens the external electric field. The dispersion of surface states with non-zero $\tilde{\Delta}$ is shown in Extended Data Fig. 9. Note that the difference between the energies of valence- and conduction-band states at the K point equals $\tilde{\Delta}$ (only γ_1 vertical hopping and the $\tilde{\Delta}$ potential contribute to the Hamiltonian at K points, leading to states localized at A_1 and B_N sublattices with energies $\pm\tilde{\Delta}/2$, while all the other states belong to dimers, connected by γ_1 vertical hopping and having energies $\pm\gamma_1$). After calculating the energy dispersion, the screening electron density accumulated at layer i is calculated as

$$n_i = 2\int_{\mathrm{BZ}} \frac{\mathrm{d}^2k}{(2\pi)^2} \sum_{l=1}^{2N} [(|\Psi^l_{\mathrm{A}_i}(k)|^2 + |\Psi^l_{\mathrm{B}_i}(k)|^2) f(\varepsilon_l - E_{\mathrm{F}}) - 1]$$

where i is the layer number in N-layer RG, the integration is over the Brillouin zone (BZ), l stands for band index, $\Psi^l_{\mathrm{A}_i}(k)$ and $\Psi^l_{\mathrm{B}_i}(k)$ are normalized wavefunctions of two sublattices in layer i, f is the Fermi function, E_F is the Fermi level, ε_l is the energy of band l, and −1 subtracts a homogeneous charge jelly that neutralizes the Fermi sea electron density. Denoting the total screening charge accumulated near the top and bottom surfaces by $n_{\mathrm{t}}^{\mathrm{scr}}(\tilde{\Delta})$ and $n_{\mathrm{b}}^{\mathrm{scr}}(\tilde{\Delta})$ respectively, we relate the displacement field to the charge density and the potential asymmetry as

$$\frac{-e[n_{\mathrm{t}} - n_{\mathrm{b}}]}{2\,\varepsilon_0} \equiv D = \frac{e[n_t^{\mathrm{scr}}(\tilde{\Delta}) - n_{\mathrm{b}}^{\mathrm{scr}}(\tilde{\Delta})]}{2\,\varepsilon_0} + \frac{\varepsilon\tilde{\Delta}}{d}$$

where e is the electron charge, d is the thickness of the graphite film, and ε_0 is the vacuum permittivity. We employed the Hartree approximation and used the fact that the dominant screening charge is localized at the surface layers. By varying the potential difference of the surface layers, tuning the chemical potential to maintain overall charge neutrality, and finding the electron density distribution, we determined the relation between the bandgap and applied external displacement field, as shown in Fig. 2f inset. The bandgap Δ, defined as the difference between the conduction-band minimum and the valence-band maximum, is shown in Extended Data Fig. 9.

In the absence of displacement field D, the conduction and valence bands of RG overlap. Therefore, one has to apply a field D larger than some critical D_{crit} so that the potential asymmetry exceeds the bandwidth of overlapping, and drives the system from a semimetallic to a semiconducting phase, Extended Data Fig. 9. Calculated values of D_{crit} are shown in Fig. 2e and compared to experimental results. When the total electron concentration is zero, $n_{\mathrm{t}} - n_{\mathrm{b}} = 0$, the Fermi level is in the gap, resulting in the experimentally observed transport gap presented in the main text.

Possibility of stacking faults

It is important to have a reliable method to check for possible stacking faults in the sample. Apart from Raman[7] (Extended Data Fig. 1a–d) and electronic Raman scattering signatures[37], measurements of an in-plane transport gap opened by the vertical displacement field (asymmetric gating) provides another diagnostic tool (Extended Data Fig. 1e–g). Our calculations reveal that it is impossible to open a transport gap if stacking faults or thicker inclusions of ABA stacking are present. We considered the most elementary A**BCB**A stacking fault that joins ABC stacking with its mirror-image CBA stacking (Extended Data Fig. 2a); a Bernal stacking fault that joins two ABC multilayers, as shown in Extended Data Fig. 2d for the A**BCBC**A multilayer; and surface stacking fault AB**CAC** (Extended Data Fig. 2g). The bold characters indicate the type and position of stacking faults.

At the K points of the Brillouin zone of RG, the in-plane hoppings γ_0 destructively interfere, leaving only γ_1 as a high-energy scale. For the twin-boundary stacking, the low-energy states are localized on sublattices A_1, A_5 and B_3, and on a zero-energy eigenstate $(\Psi_{B_2}, \Psi_{B_4}) = \left(\frac{1}{\sqrt{2}}, -\frac{1}{\sqrt{2}}\right)$ of a $B_2A_3B_4$ trimer, which we denote as $B_2 - B_4$, Extended Data Fig. 2a. Away from the K point, chiral decomposition[25] leads to the appearance of effective 2- and 3-layer ABC chiral subsystems with obvious generalization to films thicker than 5 graphene layers. So, there are four low-energy sub-bands: two with energies growing away from the K point (conduction-band type) and two with energies decreasing away from the K point (valence-band-type). Similarly to RG discussed before, the hopping γ_4 leads to an overlap of valence and conduction sub-bands of the order of 20 meV. Application of the vertical electric field (creating layer potentials $U_1 < U_2 < \ldots < U_5$) splits the four almost degenerate sub-bands into two outer valence and conduction bands, localized on A_1 and A_5 (with energies U_1 and U_5 at the K point), and two inner valence and conduction bands, localized on B_3 and $B_2 - B_4$ (with energies U_3 and $(U_2 + U_4)/2$ at the K point). The energy splitting of the two inner bands is $U_3 - (U_2 + U_4)/2 = \frac{e^2 d_1 n_{B_3}}{2\varepsilon_0}$, where $d_1 = 0.335$ nm is the distance between layers, and it only depends on the charge density of the third layer, n_{B_3}.

For the A**BCBC**A stacking fault in Extended Data Fig. 2d, the low-energy states at the K point are localized on sublattices A_1, B_3, A_4 and B_6, with the splitting of the inner band determined by the electric field between layers 3 and 4. In both A**BCB**A and A**BCBC**A stacking fault cases, to open a gap one requires a displacement field sufficient to overcome the doubled screening of four low-energy bands and, additionally, to create a potential difference of about 20 meV between the two consecutive layers forming a stacking fault. Such displacement fields would strongly exceed the values plotted in Fig. 2e, and are beyond our experimental reach. Large but experimentally attainable displacement fields would split the inner B_3 and A_4 bands at the K point, as shown in Extended Data Fig. 2e, f, but such high fields would also substantially increase the dispersion of these bands, resulting in band overlap near $p = p_{\mathrm{c}}$, thus closing the gap. As for the ABA surface stacking fault in Extended Data Fig. 2g–i, the ABA surface bands overlap with a Dirac cone having velocity $v/\sqrt{2}$, which shunts the gapped state.

Thus we conclude that any stacking faults make opening of a transport gap impossible. We also note that stacking faults would, generically, lead to asymmetric behaviour with respect to reversal of the direction of D. Calculated dispersions with non-zero displacement field are shown for the twin-boundary defect in Extended Data Fig. 2b, c; for the stacking fault buried inside the ABC bulk in Extended Data Fig. 2e, f; and for the surface stacking fault in Extended Data Fig. 2h, i. Examples of transport data for multilayer graphite devices with stacking faults are shown in Extended Data Fig. 1. The presence of faults is established by measuring Raman spectra.

Landau levels in multilayer RG

We have calculated the LL spectrum by employing the same method as in ref. [26]. Numerical diagonalization is performed in a regularized finite basis consisting of oscillator states for each sublattice component, namely $(\phi_0, \phi_1, \ldots, \phi_{N_0+n-1})$ for sublattice A_n and $(\phi_0, \phi_1, \ldots, \phi_{N_0+n})$ for B_n where $N_0 = 250$ is a cut-off LL index, sufficient for convergence at $B > 0.5$ T.

To qualitatively understand the LL spectrum, let us start with the minimal model[24] with only the nearest-neighbour in-plane (γ_0) and interlayer (γ_1) hoppings. In the absence of a displacement field ($D = 0$), the low-energy LL spectrum consists of $4N$-degenerate levels at zero energy, which we refer to as zeroth LLs (where 4 is due to double-spin and double-valley degeneracy, and N comes from N-fold orbital degeneracy), plus four-fold degenerate levels arising from the conduction and valence bands that disperse as $E^{\pm} \approx \pm B^{N/2}$. Within the two-band model, the vector wavefunctions of zeroth LLs of one valley reside on one (for example, the top) surface, $\Psi_{K^+,i} = \begin{pmatrix} \varphi_i \\ 0 \end{pmatrix}$, $i = 0, \ldots, N-1$, while for the other valley the wavefunctions sit on the opposite (for example, the bottom) surface, $\Psi_{K^-,i} = \begin{pmatrix} 0 \\ \varphi_i \end{pmatrix}$. Therefore, for zeroth LLs the valley degeneracy is equivalent to the top/bottom surface degeneracy.

The minimal model is insufficient to describe the experimental results, making it necessary to consider further electron hopping amplitudes. The presence of inter-layer same-sublattice hopping γ_4 leads to strong electron–hole asymmetry and breaks the orbital degeneracy of zeroth LLs, leading to dispersion $E_n^0 = n\hbar\omega_{\mathrm{c}}$, $n = 0, \ldots, N-1$, with $\omega_{\mathrm{c}} = e\,B/m_*$, $m_* \approx 0.4\,m_e$. The conduction-band LLs continue the sequence of four-fold degenerate LLs as $E_n^+ = n\hbar\omega_{\mathrm{c}}$, $n = N, N+1, \ldots$. The valence-band dispersion is non-monotonic and produces a series of four-fold degenerate LLs $E_n^- = n\hbar\omega_{\mathrm{c}}$, $n = 1, 2, \ldots$ near zero energy, as well as a sequence of 12-fold degenerate levels at higher energies, originating from the three equivalent valence-band maxima caused by trigonal warping (hoppings γ_3, γ_2).

At moderate B, valence-band LLs bend down, forming numerous crossings with zeroth LLs and conduction-band LLs[24]. This explains the multiple crossings of the LLs on the hole side in Fig. 3a, b. The two-fold degeneracy of the filling factors (for example, $\nu = 6, 8, 10\ldots$) at $D = 0$ can be attributed to the preserved valley degeneracy, while the gaps are given by combination of the orbital splitting ($\nu = 6, 10, 14\ldots$ for odd N and $\nu = 4, 8, 12, 16\ldots$ for even N) and spin splitting ($\nu = 4, 8, 12, 16\ldots$ for odd N and $\nu = 6, 10, 14\ldots$ for even N). Although the theory qualitatively agrees with the experiment, it predicts a twice higher value of B at which the last crossings occur. This discrepancy can be attributed to exchange interactions.

The filling factor at a specified chemical potential is determined as the number of filled LLs in the regularized basis, with half the total number of levels subtracted to account for the background charge neutralizing the Fermi sea. Normally, this would place the zero electron density between LLs originating from valence and conduction bands that form the pairs related by approximate electron–hole symmetry $(\Psi_A, \Psi_B) \to (\Psi_A, -\Psi_B)$. However, there are N additional (spin and valley degenerate) zero LLs (numbered as $0, \ldots, N-1$) with wavefunctions localized only on one of the sublattices. At low B, zero LLs overlap with valence-band LLs, leading to complicated counting of the filling factors but, for $B \gtrsim 10$ T, conventional valence-band LLs are below the zero energy, leading to zero electron density ($\nu = 0$) located in the middle point of zeroth LLs. This middle point is located either in between the

Zeeman-split zeroth LLs with index $(N-1)/2$ for odd N, or between the orbital-split zeroth LLs with indices $N/2-1$ and $N/2$ for even N.

Spin- and valley-polarized states

Coulomb and phonon-mediated interactions between electrons can lead to a multitude of patterns for spontaneous symmetry breaking. These include breaking a 'top–bottom' symmetry of the two surfaces, a spin/valley symmetry, a six-fold rotation symmetry (nematic phase), a lattice translational symmetry (charge density wave), or a U(1) gauge symmetry (superconductivity)[38–40]. The presented experiments provide evidence that symmetry breaking occurs for a limited range of sample thicknesses (<10 layers), hinting at the importance of interaction between the surfaces, which suggests a 'top–bottom' type of symmetry breaking order. The candidates are thus the quantum valley Hall (VH; ferroelectric) phase with order parameter $\Delta^{\mathrm{VH}} = \lambda\, \sigma_z^{\mathrm{layer}}$, quantum layer antiferromagnetism (LAF) $\Delta^{\mathrm{LAF}} = \lambda\, \sigma_z^{\mathrm{layer}} \otimes \sigma_z^{\mathrm{spin}}$, the quantum spin Hall (QSH) phase (also called the 'spin flux' phase) $\Delta^{\mathrm{QSH}} = \lambda\, \sigma_z^{\mathrm{layer}} \otimes \sigma_z^{\mathrm{spin}} \otimes \sigma_z^{\mathrm{valley}}$, or the quantum anomalous Hall (AH) phase $\Delta^{\mathrm{AH}} = \lambda\, \sigma_z^{\mathrm{layer}} \otimes \sigma_z^{\mathrm{valley}}$. Here, σ_z is a Pauli matrix. In the absence of a B field, only the relative orientation of spins matters, while the presence of a B field lifts this degeneracy to fix an optimal 'canted' orientation of spins[41]. The AH phase breaks the time-reversal symmetry and implies a Hall signal at $B=0$, which has not been observed. The VH phase is the one induced by displacement field and discussed above, but it is not continuously connected to the observed spontaneous insulating phase, and, instead, competes with it. So we are left with two candidates: LAF and the QSH effect. Both phases lead to giant Berry curvatures and, consequently, to large orbital magnetic moments, which peak near the three degenerate maxima of the valence band[17]. The orbital magnetic moment has opposite signs in the two valleys for Δ^{LAF} or for the gate-induced displacement field. In the case of Δ^{QSH}, the orbital moment becomes the same in both valleys but opposite for the two spin directions. The orbital moment leads to pronounced lifting of the 12-fold degeneracy of LLs originating from valence-band maxima, which results in two groups of six-fold LLs. This explains the observed robust gap at $\nu = -6$ (Fig. 3a, b, d). The six unoccupied valence-band LLs lead to the layer-antiferromagnet (three K↑ and three K′↓ levels) in the case of the quantum LAF order parameter and to a ferromagnet (three K↑ and three K′↑) in the case of QSH ordering. Canting effects can be neglected since the magnitude of the order parameter is much larger than the Zeeman splitting.

The effect of order parameters on the spectrum of zeroth LLs amounts to valley-/spin-dependent shifts for LAF/QSH phases, which follows from localization of zeroth LLs on the top/bottom surfaces in the K/K′ valleys. Hence, Δ^{LAF} breaks the valley degeneracy, leading to the appearance of gaps at odd filling factors (Fig. 3f) whereas the valley degeneracy remains intact for Δ^{QSH} (Fig. 3e). The experimental data in Fig. 3c are consistent with the QSH order for electron doping below $2.5 \times 10^{12}\ \mathrm{cm}^{-2}$, where the orbital and spin magnetic moments align. Note that a QSH order parameter fits finite magnetic field data at substantial electron doping, and does not necessarily connect to the observed spontaneous gap near charge neutrality.

Data availability

The data that support the findings of this study are available from the corresponding author upon reasonable request.

35. Cai, S. et al. Independence of topological surface state and bulk conductance in three-dimensional topological insulators. *npj Quantum Mater*. **3**, 62 (2018).
36. Dresselhaus, M. S. & Dresselhaus, G. Intercalation compounds of graphite. *Adv. Phys*. **51**, 1–186 (2002).
37. García-Ruiz, A., Slizovskiy, S., Mucha-Kruczynski, M. & Fal'ko, V. I. Spectroscopic signatures of electronic excitations in Raman scattering in thin films of rhombohedral graphite. *Nano Lett*. **19**, 6152–6156 (2019).
38. Zhang, F. & MacDonald, A. H. Distinguishing spontaneous quantum Hall states in bilayer graphene. *Phys. Rev. Lett*. **108**, 186804 (2012).
39. Lemonik, Y., Aleiner, I. & Fal'ko, V. I. Competing nematic, antiferromagnetic, and spin-flux orders in the ground state of bilayer graphene. *Phys. Rev. B* **85**, 245451 (2012).
40. Kharitonov, M. Canted antiferromagnetic phase of the $\nu = 0$ quantum Hall state in bilayer graphene. *Phys. Rev. Lett*. **109**, 046803 (2012).
41. Kharitonov, M. Antiferromagnetic state in bilayer graphene. *Phys. Rev. B* **86**, 195435 (2012).

Acknowledgements This work was supported by the EU Graphene Flagship Program, the European Research Council, the Royal Society, and the Engineering and Physical Sciences Research Council (EPSRC). A.M. acknowledges the support of an EPSRC Early Career Fellowship (EP/N007131/1). S.V.M. was supported by the RFBR (20-02-00601). This work was partially supported by the French National Research Agency (ANR) in the framework of a RhomboG grant (ANR-17-CE24-0030).

Author contributions A.M. conceived the presented idea and directed the project. Y.S., S.V.M., S.O., C.M., J.B., J.Y., A.I.B. and B.A.P. performed transport measurements. S.X., Y.Y. and S.-K.S. fabricated devices. Y.S., S.O., C.M. and J.Y. performed data analysis. S.S. and V.I.F. developed the theory and performed theoretical calculations. Y.S., S.O., A.K.G., V.I.F. and A.M. contributed to the interpretation of data. K.W. and T.T. grew hBN single crystals. A.M., Y.S., A.K.G., S.S., V.I.F. and K.S.N. contributed to the writing of the manuscript. All authors discussed the results and commented on the manuscript.

Competing interests The authors declare no competing interests.

Additional information

Correspondence and requests for materials should be addressed to A.M.

Peer review information *Nature* thanks Dmitri Efetov and the other, anonymous, reviewer(s) for their contribution to the peer review of this work.

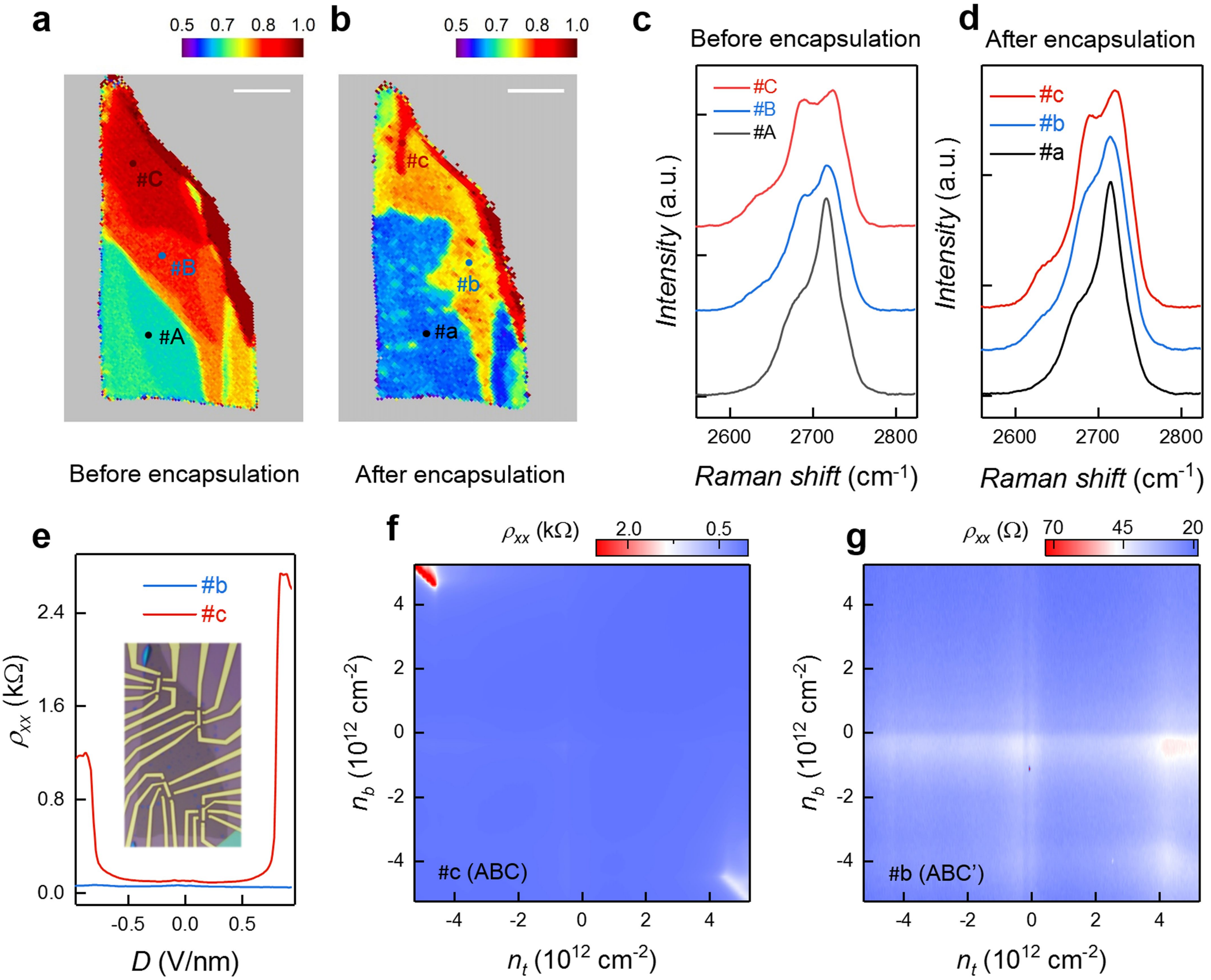

Extended Data Fig. 1 | Effect of stacking sequence on the displacement-field-induced bandgap. a, **b**, Raman maps of device 3, a 6.5-nm graphite flake with domains of differing local stacking sequence, shown before (**a**) and after (**b**) encapsulation. The colour coding indicates the ratio of the integrated area of the low-frequency component of the graphite Raman 2D band (ranging around 2,670–2,700 cm^{-1}) to that of the high-frequency component (ranging around 2,700–2,730 cm^{-1}). Coloured dots in **a** and **b** mark the positions where the Raman spectra shown in **c** and **d** respectively were taken. Scale bars, 10 µm. **c**, **d**, Typical 2D Raman peaks of HG (black curves A and a), RG (red curves C and c) and graphite of mixed ABA and ABC stacking (blue curves B and b), before (**c**) and after (**d**) encapsulation. Laser wavelength, 532 nm. **e**, ρ_{xx} as a function of D for Hall bar devices made using domains at point b (light blue) and point c (red), respectively, $T = 1.6$ K. Inset, optical micrograph of the devices before shaping them into the Hall bar geometry. **f**, **g**, Resistivity maps $\rho_{xx}(n_t, n_b)$ of graphite with ABC stacking (**f**) and mixed stacking (**g**); $T = 1.6$ K, $B = 0$ T.

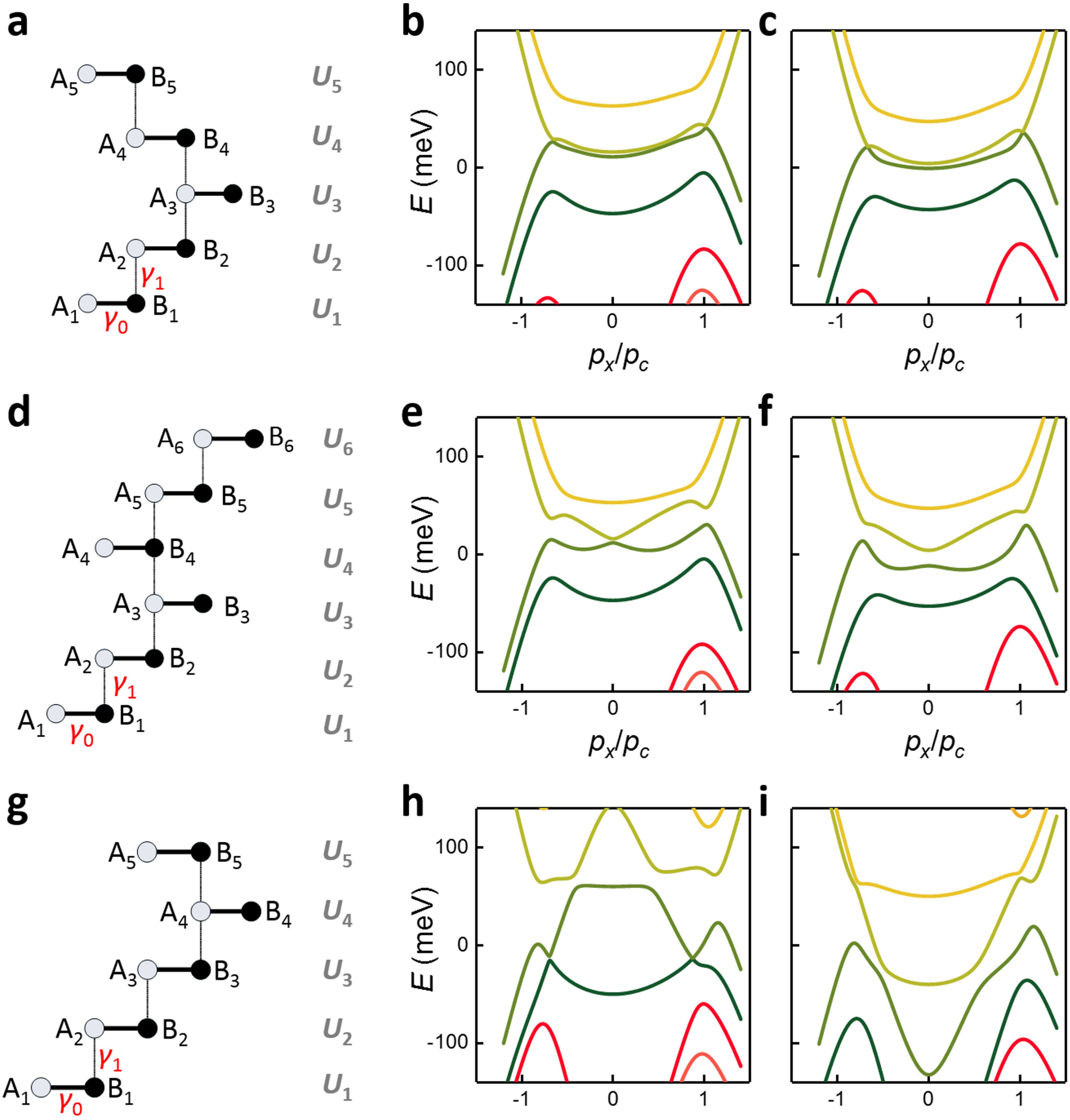

Extended Data Fig. 2 | Band structures of multilayer RG with stacking faults. **a**, Schematic of twin-boundary defect. **b**, **c**, Calculated spectra for the ABCABC**ABA**CBACBACBA sequence at positive (**b**) and negative (**c**) *D*. **d**, Schematic of a buried Bernal stacking fault A**BCBC**A. **e**, **f**, Calculated band structure for such a defect: ABCABC**ABAB**CABCABCA sequence at positive (**e**) and negative (**f**) *D*. **g**, Schematic of surface stacking fault ABCAC. **h**, **i**, Spectra for the ABCABCABCABCABC**ABA** sequence at positive (**h**) and negative (**i**) *D*. In all the calculations we used $D = \pm 1$ V nm^{-1}. See Methods section 'Possibility of stacking faults' for details of nomenclature used in **a**, **d**, **g**. *E* is the band energy, p_x is the in-plane momentum, and $p_c = \gamma_1/v$, where v is the Dirac velocity.

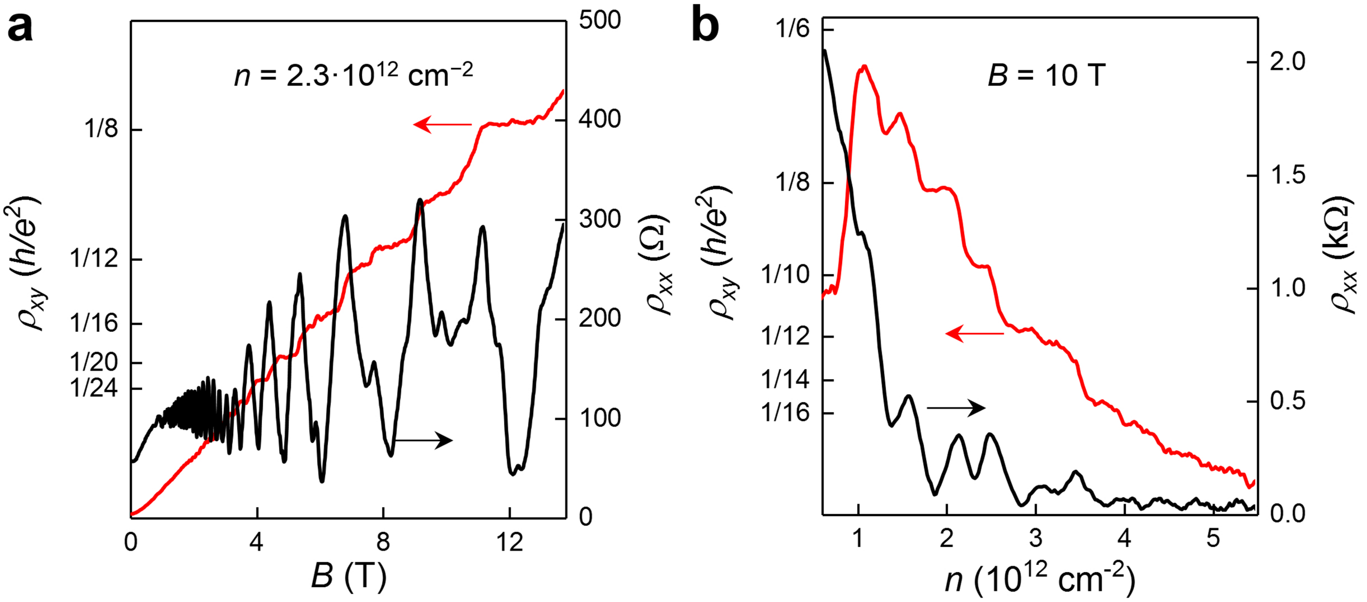

Extended Data Fig. 3 | The quantum Hall effect in thin RG. a, Hall resistivity ρ_{xy} (red curve) and longitudinal resistivity ρ_{xx} (black curve) as a function of magnetic field B measured at 20 mK for the same device as in main text Fig. 3 (device 1); $n = 2.3 \times 10^{12}$ cm^{-2}, $D = 0$ V nm^{-1}. **b**, ρ_{xy} and ρ_{xx} as a function of n for the same device as in **a**; $D = 0$, $B = 10$ T, $T = 20$ mK.

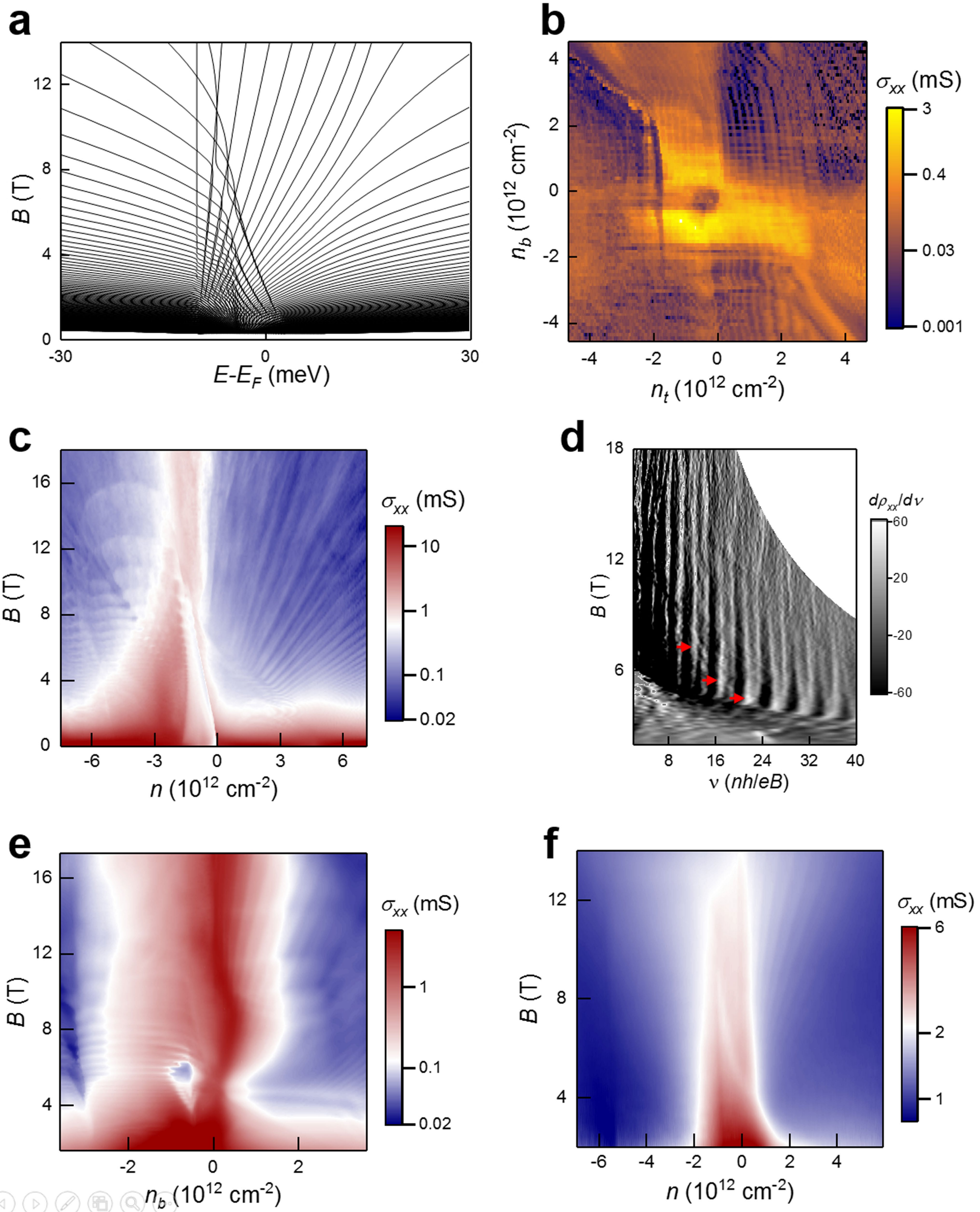

Extended Data Fig. 4 | Landau levels from surface states of multilayer RG. **a**, Calculated free-particle spectrum. **b**, Conductivity map $\sigma_{xx}(n_t, n_b)$ for 3-nm-thick RG (device 1) measured at $B = 9$ T and $T = 20$ mK. Note that, for two independent surfaces, LLs should form sets of horizontal and vertical lines. The observed behaviour suggests that top and bottom surfaces of our RG devices are nearly independent 2D systems. **c**, Landau fan $\sigma_{xx}(n, B)$ for device 5 (3.3-nm-thick RG); $D = 0$, $T = 0.25$ K. **d**, Differential $\mathrm{d}\rho_{xx}/\mathrm{d}\nu(\nu, B)$ map on the electron side (same device as in **c**). The red arrows indicate LL crossings. **e**, $\sigma_{xx}(n_b, B)$ for device 8 (7.2-nm-thick RG) measured at $T = 1.7$ K. **f**, $\sigma_{xx}(n, B)$ for device 4 (16.5-nm-thick RG) at $D = 0$ and $T = 0.25$ K.

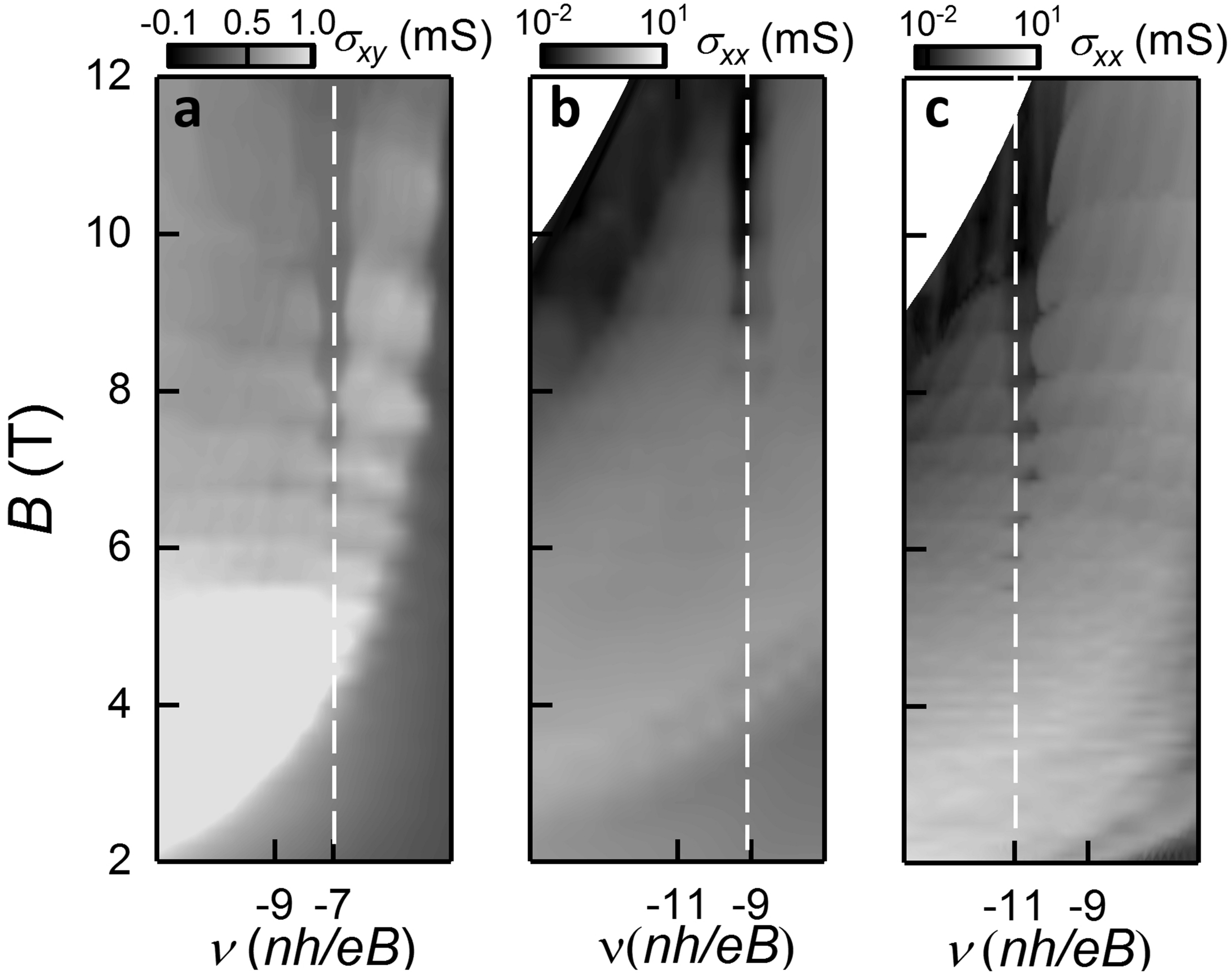

Extended Data Fig. 5 | Single-gate ($D \neq 0$) Landau fan diagrams highlighting the robust $\nu = -N$ quantum Hall state in N-layer-thick RG. a, Conductivity map $\sigma_{xy}(\nu, B)$ for 7-layer-thick RG (device 7). **b**, Conductivity map $\sigma_{xx}(\nu, B)$ for 9-layer-thick RG (device 1). **c**, $\sigma_{xx}(\nu, B)$ for 11-layer-thick RG (device 6).

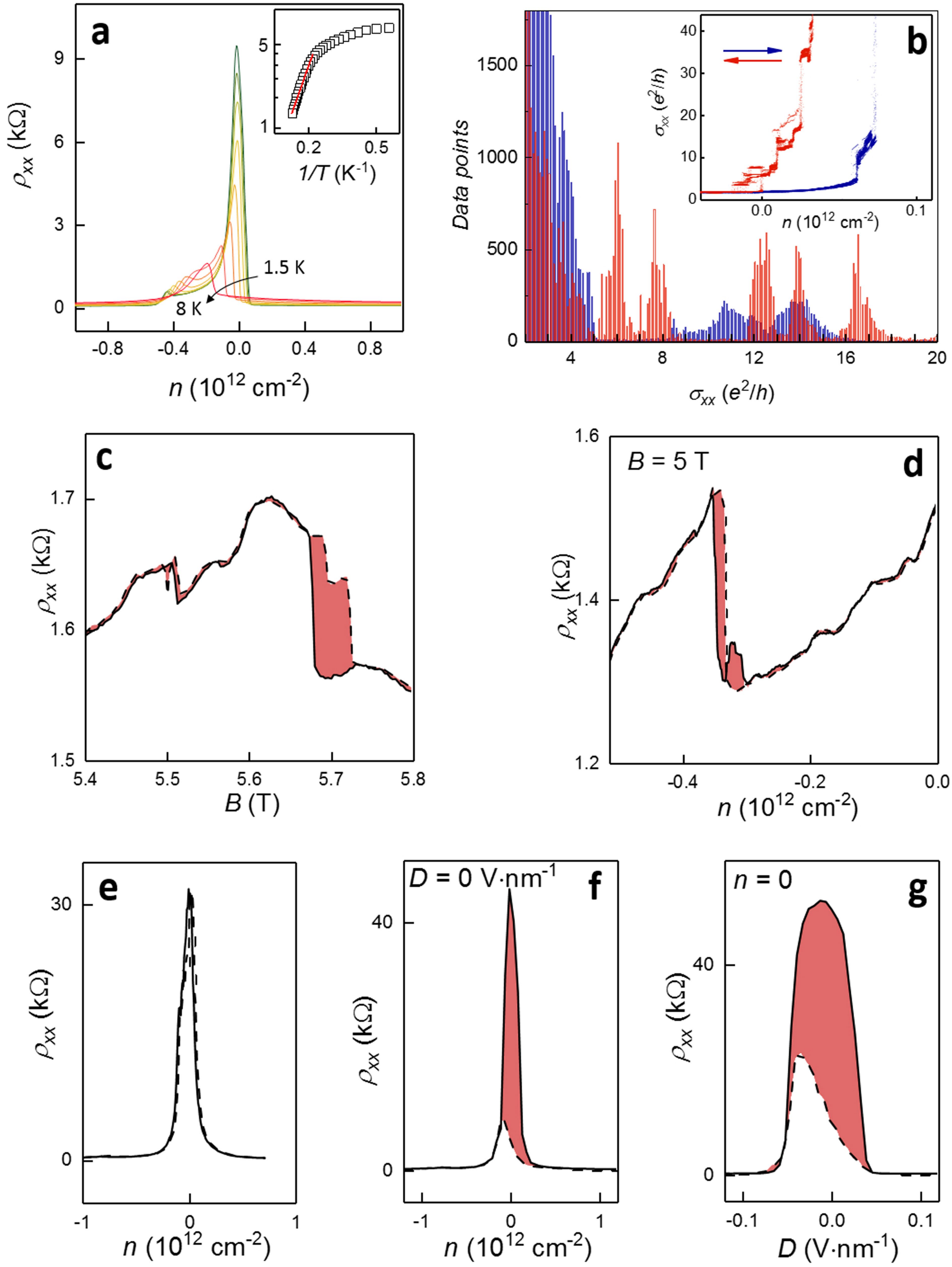

Extended Data Fig. 6 | See next page for caption.

Extended Data Fig. 6 | Insulating states and hysteretic behaviour in multilayer RG. a, **b**, Additional data for 3.3-nm-thick RG (device 5, same as in main text Fig. 4a, b). **a**, Main panel, temperature dependence of $\rho_{xx}(n)$ around the insulating state, $B = 0$ T. Inset, Arrhenius plot for the peak resistivity, indicating the presence of a bandgap of about 2–3 meV. The y axis shows peak resistivity, and red line indicates the fit. **b**, Main panel, histogram of the conductivity values found on the hysteretic curves $\sigma_{xx}(n)$, such as those shown in the inset. Eighty-three such curves were used to make the histogram, where data from forward and backward sweeps are plotted in blue and red, respectively. $D = 0$, $T = 250$ mK, $B = 0$. **c**, Hysteresis (shaded red) in $\rho_{xx}(B)$ observed in device 7 (2.3-nm-thick RG) at the charge neutrality point; **d**, hysteresis (shaded red) in $\rho_{xx}(n)$ at $B = 5$ T. For **c** and **d**, $T = 250$ mK. **e**–**g**, Hysteretic behaviour of device 1 for different cooling cycles. No noticeable hysteresis was found for the first cooling event (**e**). Hysteresis in $\rho_{xx}(n)$ (**f**) and $\rho_{xx}(D)$ (**g**) is clearly seen after another cooling. Solid (dashed) lines indicate positive (negative) sweep directions and the coloured areas highlight the difference between the sweep directions. $T = 20$ mK; $B = 0$ T.

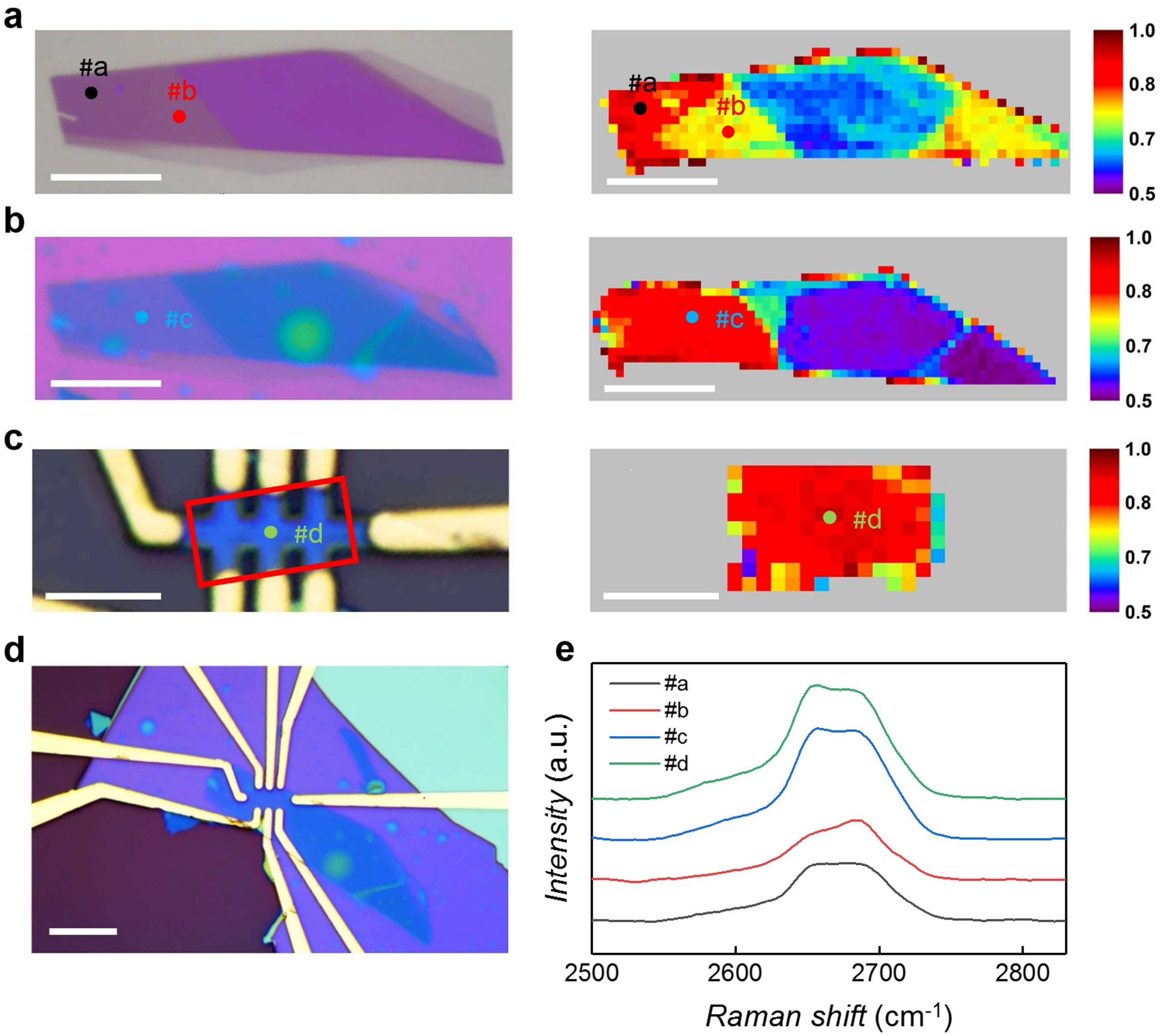

Extended Data Fig. 7 | Stacking order of device 6 at different fabrication stages. a, Optical image of the graphite flake (left) and the corresponding Raman map with a step size of 0.8 µm × 0.8 µm (right). Scale bar, 10 µm. **b**, Optical image of the graphite flake encapsulated by hBN (left) and the corresponding Raman map with a step size of 0.7 µm × 0.7 µm (right). Scale bar, 10 µm. **c**, Optical image of the finished Hall bar (left) and the corresponding Raman map with a step size of 0.5 µm × 0.5 µm (right). Scale bar, 4 µm. The colour coding of the Raman maps in **a**–**c** indicates the ratio of the integrated area of the low-frequency component (ranging around 2,635–2,665 $\mathrm{cm^{-1}}$) to that of the high-frequency component (ranging around 2,665–2,695 $\mathrm{cm^{-1}}$) of the graphite Raman 2D band. The coloured dots in **a**–**c** mark the positions where the Raman spectra shown in **e** were taken. **d**, Optical image showing that the Hall bar device is made from the ABC stacked region. Scale bar, 10 µm. **e**, Typical 2D Raman peaks of RG (dots a, c and d) and of graphite of mixed ABA and ABC stacking (dot b). Laser excitation wavelength, 633 nm.

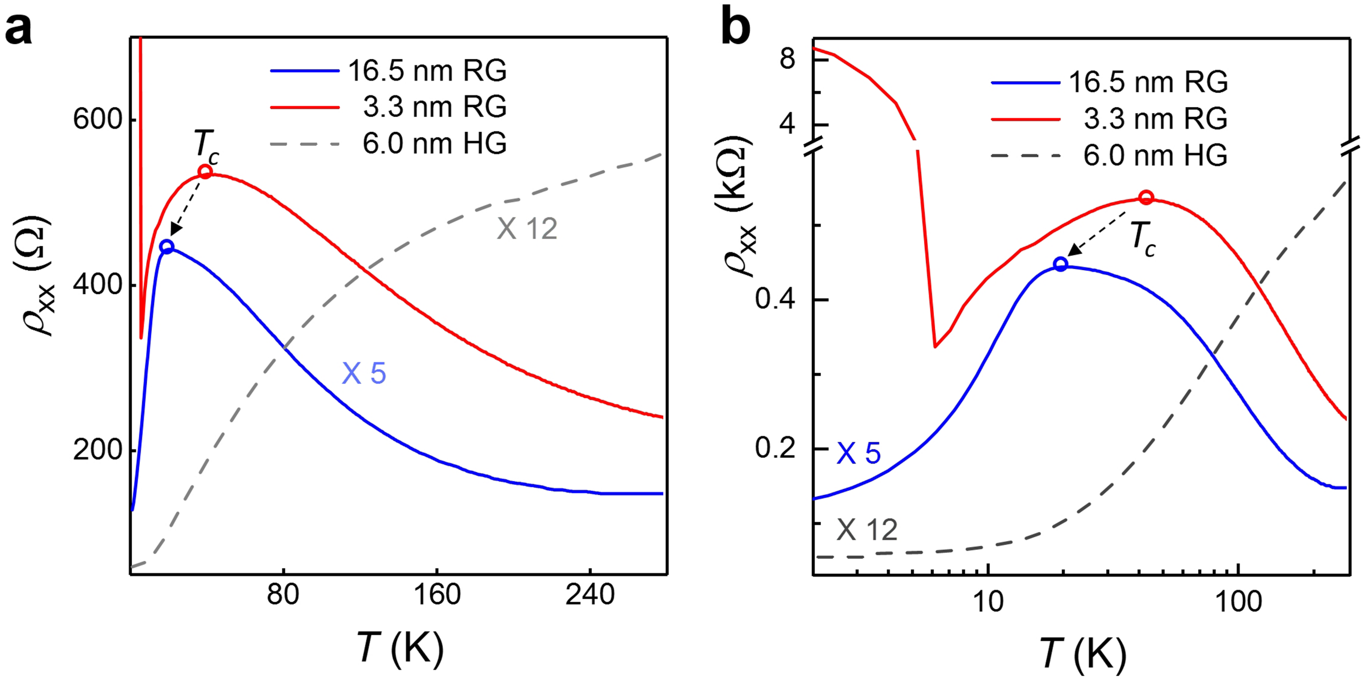

Extended Data Fig. 8 | Temperature dependence of resistivity. a, ρ_{xx} as a function of T at zero gate doping for RG device 4 with a thickness of 16.5 nm (blue solid curve), for RG device 5 with a thickness of 3.3 nm (red solid curve), and for 6-nm HG (grey dashed line). **b**, Same data as **a** but plotted on a log scale. While cooling down, ρ_{xx} of RG first increases for $T > T_c$, and then decreases, in sharp contrast to the monotonic decrease of ρ_{xx} for HG. The critical temperature T_c decreases with increasing thickness of RG. Besides the presence of T_c, ρ_{xx} of the 3.3-nm RG device 5 shows a sharp increase for $T < 6$ K owing to the phase transition to the insulating state.

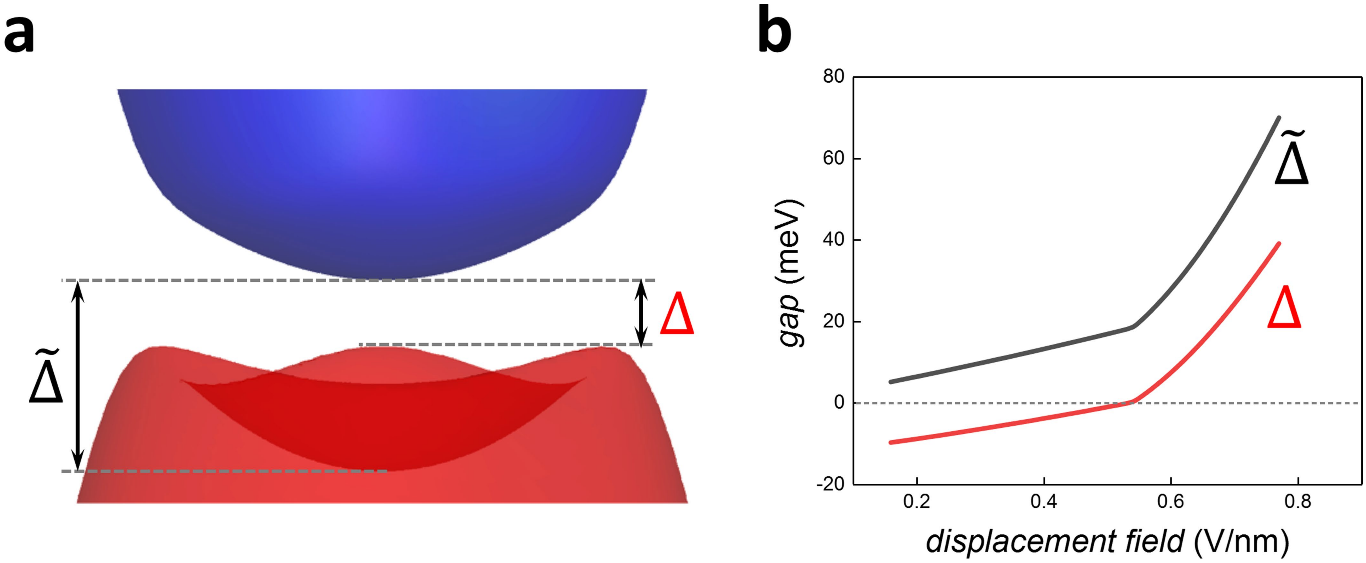

Extended Data Fig. 9 | Bandgap opening by displacement field. **a**, Band dispersion of RG under an applied displacement field; bandgap $\tilde{\Delta}$ is masked by a bandwidth of $2\gamma_4\gamma_1/\gamma_0$ such that only the effective gap $\Delta = \tilde{\Delta} - 2\gamma_4\gamma_1/\gamma_0$ is visible in transport measurements. **b**, Calculated dependence of $\tilde{\Delta}$ and Δ on displacement field for $N = 9$ layers.

Evidence of flat bands and correlated states in buckled graphene superlattices

https://doi.org/10.1038/s41586-020-2567-3

Received: 29 January 2020

Accepted: 16 June 2020

Jinhai Mao[1,2], Slaviša P. Milovanović[3], Miša Anđelković[3], Xinyuan Lai[1], Yang Cao[4], Kenji Watanabe[5], Takashi Taniguchi[5], Lucian Covaci[3], Francois M. Peeters[3], Andre K. Geim[4], Yuhang Jiang[1,6] ✉ & Eva Y. Andrei[1] ✉

Two-dimensional atomic crystals can radically change their properties in response to external influences, such as substrate orientation or strain, forming materials with novel electronic structure[1–5]. An example is the creation of weakly dispersive, ‘flat’ bands in bilayer graphene for certain ‘magic’ angles of twist between the orientations of the two layers[6]. The quenched kinetic energy in these flat bands promotes electron–electron interactions and facilitates the emergence of strongly correlated phases, such as superconductivity and correlated insulators. However, the very accurate fine-tuning required to obtain the magic angle in twisted-bilayer graphene poses challenges to fabrication and scalability. Here we present an alternative route to creating flat bands that does not involve fine-tuning. Using scanning tunnelling microscopy and spectroscopy, together with numerical simulations, we demonstrate that graphene monolayers placed on an atomically flat substrate can be forced to undergo a buckling transition[7–9], resulting in a periodically modulated pseudo-magnetic field[10–14], which in turn creates a ‘post-graphene’ material with flat electronic bands. When we introduce the Fermi level into these flat bands using electrostatic doping, we observe a pseudogap-like depletion in the density of states, which signals the emergence of a correlated state[15–17]. This buckling of two-dimensional crystals offers a strategy for creating other superlattice systems and, in particular, for exploring interaction phenomena characteristic of flat bands.

Flat bands facilitate the emergence of strongly correlated electronic phases[18–20]. A celebrated example is the Landau-level (LL) sequence of magnetically induced flat bands that can host correlated phases, such as fractional quantum-Hall states[21,22] or magnetically induced Wigner crystals[23]. Magnetically induced flat bands, however, have limited applicability because the broken time-reversal symmetry precludes the emergence of certain correlated states, such as superconductivity. More recently, twisted bilayer graphene that is finely tuned to a magic angle where a flat band emerges has introduced a new platform for the creation of correlated phases[4,5].

Here we explore an alternative path to flat bands that does not require fine-tuning or breaking time-reversal symmetry. The strategy involves creating flat bands by using the band-structure reconstruction that occurs when a two-dimensional (2D) membrane undergoes a buckling transition[14,19,20]. Buckling transitions in stiff membranes are typically triggered by in-plane compressive strain[7–9] that can be generated during thermal cycling, by solvent-induced capillary forces, or by substrate-induced stress. On exceeding a critical strain value, buckling of the membrane reduces its elastic energy through out-of-plane distortions, resulting in intriguing periodic strain patterns (Fig. 1b, c) whose structures are dictated by boundary conditions and strain distribution[9]. We find that in graphene, buckling-induced strain arrays give rise to a periodic pseudo-magnetic field (PMF)[10–13], which reconstructs the low-energy band structure into a series of essentially flat bands. Unlike earlier realizations of PMF that were mostly local in nature[24], the buckling transitions studied here produce a global change in the electronic structure, which comprises a sequence of flat bands that percolate throughout the material.

We employed the thermally induced buckling transition in graphene deposited on $NbSe_2$ or hexagonal boron nitride (hBN) substrates to create a periodic PMF. The buckling structures studied here are typically nested between ridges (Extended Data Fig. 1) that often form in graphene during fabrication. Topographical analysis suggests that the buckling is triggered by compressive strain generated by the collapse of ridges during thermal cycling (see Methods section ‘Sample preparation’). This produces various buckling patterns, from 1D to 2D, with similar nanometre-scale periods (Fig. 1b, c), suggesting a universal buckling mechanism that is insensitive to the lattice mismatch between graphene and its substrate.

In Fig. 1a we show a schematic of the sample and scanning tunnelling microscopy (STM) measurement set-up. The topography of a buckling-induced triangular superstructure in graphene deposited on $NbSe_2$ is shown in Fig. 1b, right panel. This superlattice consists of alternating crests and troughs (bright and dark, respectively; Fig. 2a) with

---

[1]Department of Physics and Astronomy, Rutgers University, Piscataway, NJ, USA. [2]School of Physical Sciences and CAS Center for Excellence in Topological Quantum Computation, University of Chinese Academy of Sciences, Beijing, China. [3]Departement Fysica, Universiteit Antwerpen, Antwerp, Belgium. [4]School of Physics and Astronomy, University of Manchester, Manchester, UK. [5]Advanced Materials Laboratory, National Institute for Materials Science, Tsukuba, Japan. [6]Center of Materials Science and Optoelectronics Engineering, College of Materials Science and Optoelectronic Technology, University of Chinese Academy of Sciences, Beijing, China. ✉e-mail: yuhangjiang@ucas.edu.cn; eandrei@physics.rutgers.edu

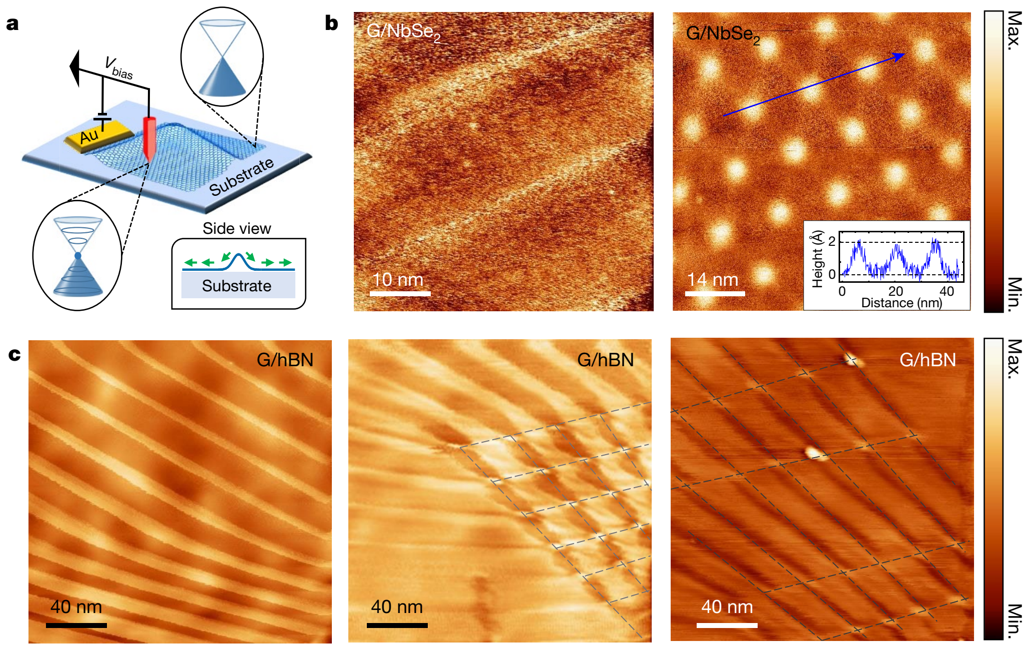

Fig. 1 | Buckled structures in graphene membranes. a, Schematic of sample geometry and measurement set-up. Top inset, Dirac cone representing the low-energy band structure of unstrained graphene outside the ridges. Bottom inset, pseudo-Landau levels (PLLs) renormalize the band structure in the strained superlattice. **b**, Left, buckling modes observed by STM topography in a G/NbSe$_2$ sample. Right, topography in a different area of the same sample shows a triangular buckling pattern ($V_b = 0.5$ V, $I = 40$ pA). Inset, height profile along the arrow shows the approximately 0.17-nm height modulation of the buckling pattern with lateral period 14.4 ± 0.5 nm. **c**, 1D and 2D buckling modes observed by STM topography in different areas of the same G/hBN sample ($V_b = -300$ mV, $I = 20$ pA). Grey dashed lines are guides to the eye, marking the periodic structure.

0.17-nm height modulation and period $a_b = 14.4 \pm 0.5$ nm. The large lattice mismatch between graphene (0.246 nm) and NbSe$_2$ (0.36 nm) rules out a moiré pattern[2] interpretation (Methods). We first focus on the electronic structure obtained from the dI/dV spectra (I is the current, V is the bias) in the crest regions (Fig. 2b). The spectra comprise a sequence of peaks identified as PMF-induced pseudo-Landau levels (PLLs)[14,24,25]. The energy of the most pronounced peak (labelled $N = 0$) is aligned with the charge neutrality point (CNP) as determined from the spectra taken in the non-buckled area (Extended Data Fig. 2a). The CNP energy, E_D, is shifted to about 0.5 eV above the Fermi level, owing to the hole doping induced by the NbSe$_2$ substrate[26]. Starting from the $N = 0$ PLL, which coincides with E_D, we label the remaining PLLs in order of increasing (decreasing for the hole sector, $N < 0$) energies as $N = \pm1$, ±2, and we find that they follow the sequence expected of LLs in flat monolayer graphene[27], $E_N = E_D + \mathrm{sgn}(N)\upsilon_F\sqrt{2e\hbar|N|B_{\mathrm{PMF}}}$ (here e is the electron charge and $\hbar = h/(2\pi)$ is the reduced Planck constant). This PLL sequence confirms the existence of a PMF in the buckled graphene membrane. Using the Fermi-velocity value of unbuckled graphene, $\upsilon_F = 1.0 \times 10^6$ m s^{-1}, we estimate the value of the PMF in the centre of the crest region as $B_{\mathrm{PMF}} = 108 \pm 8$ T (Fig. 2b, right inset). Outside the buckled region, where the STM topography is flat, the spectrum exhibits a featureless 'V'-shape, as expected of unstrained graphene on NbSe$_2$, with the minimum at $E_D \approx 0.5$ eV (Extended Data Fig. 2).

Another hallmark of a PMF is the sublattice polarization of the electronic wavefunction in the $N = 0$ level. This means that for a given PMF sign, the $N = 0$ electronic wavefunction is localized on one sublattice, while for the opposite sign PMF it resides on the other sublattice[12,28,29]. The PMF-induced sublattice polarization, which is the counterpart of the magnetically induced valley polarization of the $N = 0$ level, follows directly from the opposite signs of the PMF in the K and K′ valleys. The observation of sublattice polarization in the atomic-resolution STM images shown in Fig. 2d–f (see below) thus provides a direct experimental signature of the extant PMF in buckled graphene superstructures[28–32].

In both crests (Fig. 2e) and troughs (Fig. 2f), sublattice polarization is clearly revealed by the triangular structure, which reflects the fact that only atoms in one sublattice, say A, are visible in the crests while only atoms in the B sublattice are visible in the troughs. This in turn confirms that the sign of the PMF in the crests is opposite to that in the troughs. In the transition regions between crests and the troughs (Fig. 2d), we observe a honeycomb pattern where both A and B sublattices are visible, indicating a zero-crossing of the PMF. This PMF sublattice polarization is closely reproduced in the numerical simulations (Fig. 3) discussed below.

Turning to the dI/dV spectra in the trough regions (Fig. 2c), we note that they also exhibit a sequence of peaks. Plotting the energy of these peaks versus the level index we find that the sequence is essentially linear in N, with a roughly equidistant energy spacing of about 89 ± 2 meV.

To better understand these results, we performed tight-binding calculations in the presence of a periodic PMF with a triangular structure similar to that in the experiment (Fig. 3d):

$$B_{\mathrm{PMF}}(x, y) = B[\cos(\mathbf{b}_1 \cdot \mathbf{r}) + \cos(\mathbf{b}_2 \cdot \mathbf{r}) + \cos(\mathbf{b}_3 \cdot \mathbf{r})] \quad (1)$$

Here B is the PMF amplitude, $\mathbf{b}_1 = \frac{2\pi}{a_b}\left(1, -\frac{1}{\sqrt{3}}\right)$, $\mathbf{b}_2 = \frac{2\pi}{a_b}\left(0, \frac{2}{\sqrt{3}}\right)$, $\mathbf{b}_3 = \mathbf{b}_1 + \mathbf{b}_2$, and a_b is the superlattice period. This choice of coordinates reflects the $C6$ symmetry of the PMF superlattice and the fact that the total PMF flux has to vanish, because time-reversal symmetry is not broken. Note that because B_{PMF} is defined as a sum of three cosines of amplitude B, its maximum value, attained on the crests, equals $3B$. Its minimum value, attained in the percolating network of troughs surrounding the crests, is $-1.5B$. The zeros of this PMF configuration form circles surrounding each crest. Because of the spatial PMF variation, the measured spectra correspond to an effective PMF value, B_{eff}, which approximately averages the field over the pseudo-cyclotron orbit. This averaging effect becomes more pronounced as the ratio between the magnetic length and the lattice period decreases (Extended Data Fig. 6). We found that the PLL

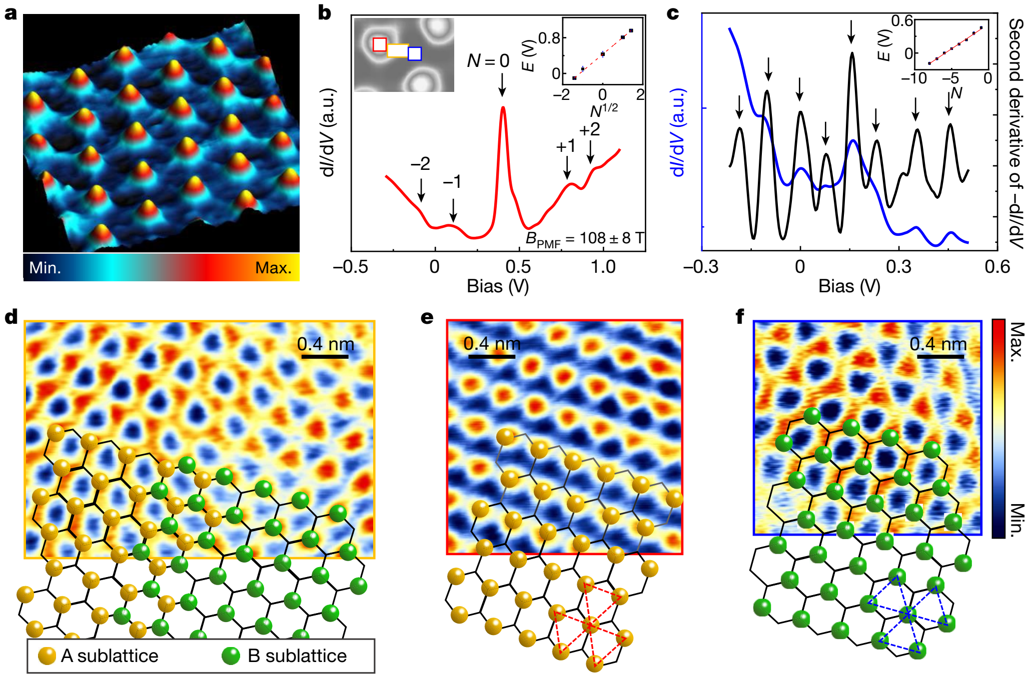

Fig. 2 | Pseudo-Landau level quantization and sublattice polarization in buckled graphene. a, STM topography (70 nm × 70 nm) of a buckled graphene membrane supported on NbSe$_2$ reveals a 2D triangular lattice (V_b = 0.6 V, I = 20 pA). **b**, dI/dV spectrum taken in the crest region labelled by the red square in the left inset. The black down-arrows label the LL index, N = 0, ±1, ±2... Right inset, pseudo-Landau level (PLL) energy E plotted against the square root of the LL index, N = 0, ±1, ±2,... **c**, Same as **b** taken in a trough region (blue square in the left inset of **b**). The negative second derivative of the dI/dV signal (black curve) is superposed to better reveal the peak energies (black arrows). Inset, linear dependence of the peak energy on the level index, N. **d**–**f**, Atomic-resolution STM topography in the transition, crest and trough regions (shown respectively in the left inset of **b** as orange rectangle, red square and blue square). The colour scale for **d** and **e** is shown in **f**. A schematic honeycomb lattice, with the yellow and green balls representing the two sublattices, A and B, is superposed to highlight the sublattice polarization in the different regions. The dashed-line triangles indicate opposite orientations of the lattice polarization in each region. a.u., arbitrary units.

sequence obtained for B_{eff} = 112 T (B = 120 T) matches the experimentally measured sequence shown in Fig. 2b.

Figure 3a–c plots the evolution of the calculated local density of states (LDOS) with PMF amplitude, for each sublattice in the crest, transition and trough regions. In the crest and trough regions, we observe a strong imbalance in low-energy LDOS intensity between the A and B sublattices (Fig. 3a, c), which is absent in the intermediate transition region (Fig. 3b). This is consistent with the experimentally observed sublattice polarization in the crest (Fig. 2e) and trough regions (Fig. 2f), and with its absence in the transition region (Fig. 2d). In Fig. 3e we show the simulated LDOS spectrum in the crest region for B_{eff} = 112 T, together with a fit to the square-root dependence on N, which is consistent with the experimentally measured spectra shown in Fig. 2b as discussed in Extended Data Fig. 6. The simulated LDOS spectrum in the trough region (Fig. 3f) is approximately linear in N with a level spacing of about 90 meV, consistent with the experimental results in Fig. 2c. To elucidate the origin of this linear peak sequence, we show in Fig. 3g the evolution of the LDOS calculated along a path connecting two crests (arrow in Fig. 3d, lower panel). The experimental peak positions in the crest (trough) regions are shown by right-pointing (left-pointing) arrows, respectively. In the centre of the trough the equidistant level sequence is clearly seen. We note that these levels are not solely determined by the local value of the PMF and they do not exhibit spatial dispersion. Furthermore, although these states spread into the crest regions, they disappear on approaching the PLLs in the crest centre. The discrete nature of these equidistant levels indicates that they originate from strain-induced confinement within the quantum well defined by the PMF, closely resembling magnetic confinement in quantum dots in 2D semiconductors[33,34]. As in the case of quantum dots, here the electrons are trapped in a PMF-induced potential well, which produces a set of levels spaced by a characteristic (geometry-dependent) energy scale $\Delta E \approx \hbar v_F \pi / W$, where W is the dot size. Using the energy scale of the levels in the troughs, approximately 90 meV, we estimate $W \approx$ 21 nm, which is approximately the size of the well indicated by the grey dashed lines in Fig. 3g, lower panel. In the troughs, the energy of each level decreases with increasing PMF (Fig. 3c) until all levels merge into one degenerate level that approaches the CNP when the magnetic length becomes considerably smaller than the dot size.

We next discuss the emergence of flat bands in this system. The periodic potential imposed by the PMF superlattice breaks up the low-energy conical band of graphene into a series of mini-bands whose width is controlled by the strength of the PMF amplitude, B. At low values of B, the minibands restructure the LDOS into a series of semi-discrete levels, as illustrated in Extended Data Fig. 7. As B increases, these levels evolve into increasingly narrower bands that become flat in the limit of large B. In Fig. 4a, we plot the first few minibands in the buckled graphene G/NbSe$_2$ sample for B_{eff} = 112 T. They all show flat-band segments along the K′–M′ line in the mini-Brillouin zone. The corresponding simulated LDOS contours in the three minibands with energies $E_0 - E_D$ = −0.03 eV, $E_1 - E_D$ = −0.17 eV and $E_2 - E_D$ = −0.28 eV, shown in Fig. 4b, show good agreement with the measured dI/dV maps in Fig. 4c, indicating that the model captures the salient features of the data. This sequence of buckling-induced flat bands that are well separated from each other would be ideally suited for hosting correlated electronic states, if it were possible to align the Fermi energy within one of the flat bands. However, this was not possible in the buckled G/NbSe$_2$ sample, because of the finite conductance of the NbSe$_2$ substrate. Nevertheless, our observations indicate that this could be achieved by creating

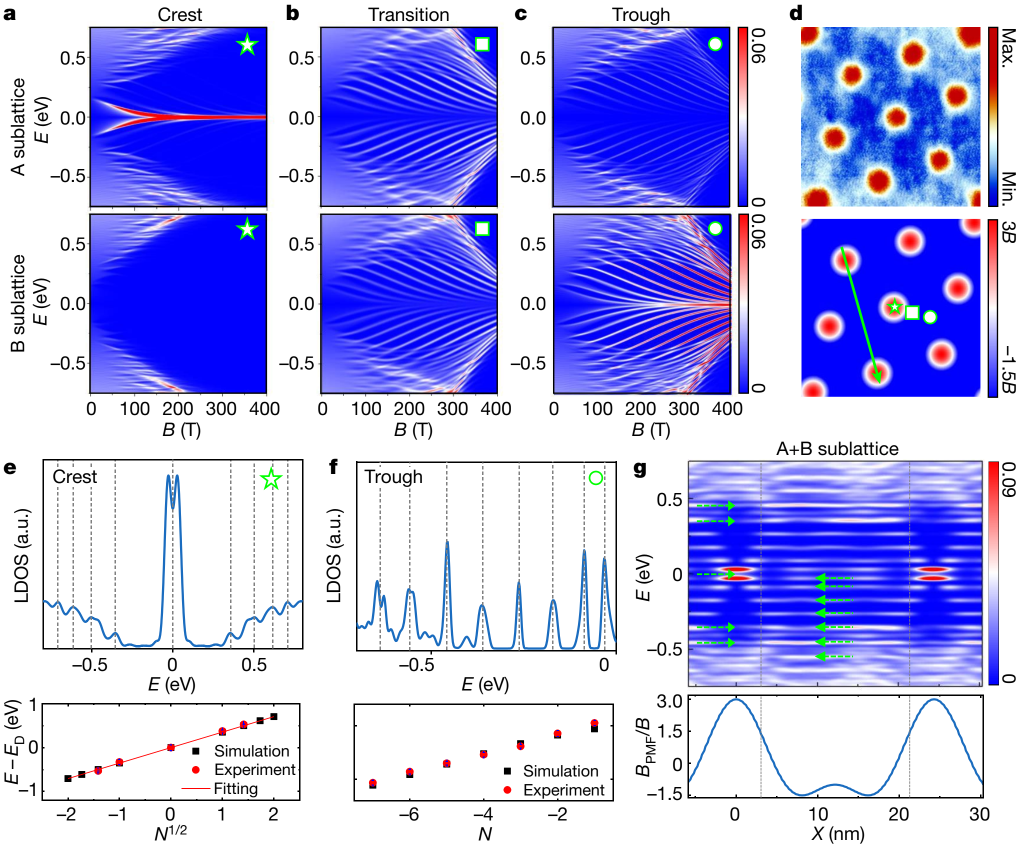

Fig. 3 | Simulated LDOS in buckled graphene. **a**–**c**, Simulated evolution of the LDOS with energy (E) and PMF amplitude (B as defined in equation (1)) in the crest (**a**), transition (**b**) and trough (**c**) regions. Upper (lower) panels represent the A (B) sublattice. The colour scale represents the LDOS intensity. **d**, Upper panel, STM topography ($V_b = 500$ mV, $I = 20$ pA) showing the triangular superlattice with alternating crest (red) and trough (blue) regions. Lower panel, PMF configuration used in the simulation. The colour scale represents the PMF amplitude B (see equation (1)). The symbols indicate the positions of the calculated LDOS in **a**–**c**, and the green line indicates the calculated path for **g**. **e**, **f**, Upper panels, calculated LDOS as a function of energy E in the crest and trough regions for $B_{\mathrm{eff}} = 112$ T ($B = 120$ T). Lower panels, level-index dependence of the simulated (black squares) and experimental (red dots) peak energy levels, measured relative to the charge neutrality point, $E - E_D$. The red line represents a fit to the experimental data. $E_D = 0.43$ eV is taken from the experimental data on an unbuckled region of the sample. **g**, Upper panel, contour plot of the LDOS spectra (sublattice averaged) as a function of energy (E) and position (x) connecting two crests along the green line in **d**. Green arrows indicate the positions of the peaks in the measured spectra shown in Fig. 2b (right-pointing arrows) and Fig. 2c (left-pointing arrows). The colour scale represents the LDOS intensity. Lower panel, evolution of the simulated value of B_{PMF}/B along the green path in **d**.

a buckling pattern in graphene deposited on an insulating substrate, as shown below.

In order to study correlation effects in buckling-induced flat bands, we turn to the G/hBN sample. In this case, applying a gate voltage across the insulating hBN layer allows us to bring the Fermi level within the flat band. Using the same sample preparation process as for the G/NbSe$_2$ sample, we again obtain buckling superlattices as illustrated in Fig. 5a, b.

The gate-voltage dependence of the dI/dV spectra of the G/hBN sample in the transition region where the strain is minimal (Fig. 5c) shows that for $V_g = 0$ the spectrum is 'V'-shaped and that its minimum, which marks the CNP, is aligned with the Fermi level. This indicates that, unlike the case of G/NbSe$_2$, the G/hBN sample is not doped by the hBN substrate. Tuning the gate voltage from −62 V to +38 V gradually moves the CNP from the hole-doped (about −100 mV) to the electron-doped sector (about +200 mV) in Fig. 5c. In Fig. 5d we compare the dI/dV spectra in the crest and transition regions for the heavily hole-doped ($V_g = -62$ V) case. Here, the crest spectrum features a prominent peak at the CNP that is flanked by a sequence of weaker peaks (blue arrows), closely resembling the crest spectrum in the G/NbSe$_2$ sample (Fig. 2b). As before, we identify the prominent peak with the strain-induced $N = 0$ PLL, and fitting the peak sequence with a square-root level-index dependence, we obtain the PMF value $B_{\mathrm{eff}} \approx 104$ T (Fig. 5d inset) consistent with the simulations described in Extended Data Fig. 9. Changing the backgate voltage from the hole-doped ($V_g = -62$ V) to the electron-doped ($V_g = +38$ V) sector (Fig. 5e) we note that the $N = 0$ PLL tracks the CNP. As before the $N = 0$ PLL corresponds to a buckling-induced weakly dispersive flat band. When doping the sample to partially fill this band, a pseudo-gap feature at the Fermi level splits the peak in two, indicating the appearance of a correlation-induced state. Labelling the peaks above and below the Fermi level as upper band and lower band, respectively, we find that when the Fermi level is aligned with the CNP, the upper- and lower-band peaks have equal intensities. Doping away from charge neutrality, we observe a pronounced spectral weight redistribution between the two peaks, so that in the electron-doped regime ($V_g > 0$) the intensity of the lower band dominates that of the upper band, whereas in the hole-doped regime ($V_g < 0$) the upper-band intensity becomes dominant. The appearance of the pseudo-gap feature and the spectral weight redistribution in the partially filled flat band in the crest regions of buckled G/hBN is strikingly similar to that observed in the partially filled flat band of magic-angle twisted bilayer graphene[15–17], where correlation-induced insulating and superconducting states have been observed.

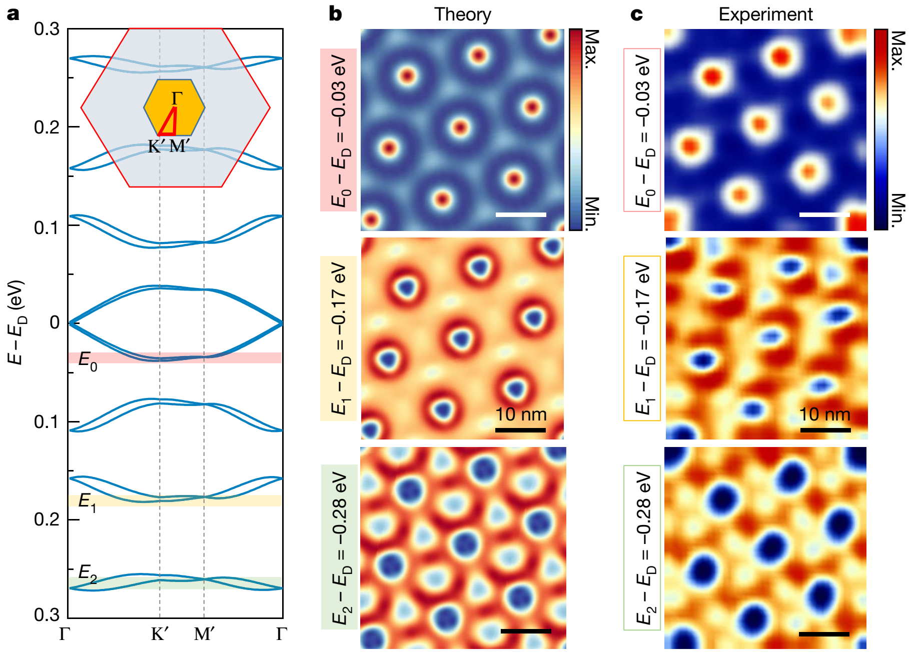

Fig. 4 | Flat bands and LDOS maps. a, Calculated band structure for a buckled graphene superlattice with period $a_b = 14$ nm and PMF amplitude $B_{\mathrm{eff}} = 112$ T ($B = 120$ T). Inset, superlattice mini-Brillouin zone, nested within the original Brillouin zone of flat graphene, together with the trajectory along which the band structure is calculated. **b**, **c**, Calculated LDOS contours ('Theory', **b**) and measured d*I*/d*V* maps ('Experiment', **c**) at $B_{\mathrm{eff}} = 112$ T for the three energies ($E_0 - E_D$, $E_1 - E_D$, $E_2 - E_D$) that correspond to the flat-band regions in **a**, as indicated by the colour-coded boxes.

These findings demonstrate that buckling-induced periodic strain patterns offer a new experimental strategy for the creation of flat bands and for inducing correlated states with exceptional flexibility. The shape, period and symmetry of the buckled structures can be controlled by experimentally adjustable parameters, such as boundary geometry and strain distribution, enabling the realization of flat bands with prescribed geometry[35]. We believe that the described way of buckling 2D crystals will be used widely to create other superlattice systems with controllable electronic band structure, thereby enabling the exploration of strong interaction effects and the emergence of correlated phases.

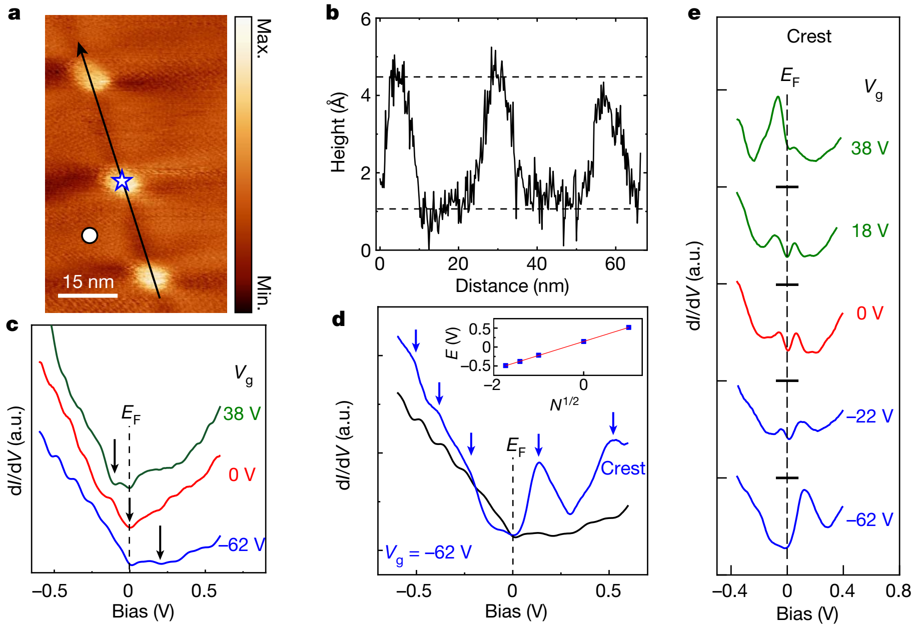

Fig. 5 | Flat bands in buckled G/hBN. a, STM topography of the buckled G/hBN sample ($V_b = -300$ mV, $I = 20$ pA). **b**, Height profile along the black line in **a** shows the approximately 3.5-Å height modulation of the buckling pattern. The horizontal dashed lines demarcate the extent of the height modulation. **c**, Gate-voltage dependence of the spectra in the transition region shows the shift of the CNP (arrows) with doping ($V_b = -400$ mV, $I = 20$ pA). The black dashed line labels the Fermi level (E_F). **d**, d*I*/d*V* spectra from the crest (blue trace) and transition (black trace) regions labelled respectively by the star and the circle in **a** ($V_b = -400$ mV, $I = 20$ pA). Inset, PLL energy in the crest area plotted against the square root of the LL index, $N = 0, \pm1, \pm2, \ldots$ **e**, Gate-voltage (V_g) dependence of the spectra in the crest region shows the pseudo-gap feature and spectral weight redistribution in the partially filled flat band ($V_b = -400$ mV, $I = 20$ pA).

Online content

Any methods, additional references, Nature Research reporting summaries, source data, extended data, supplementary information, acknowledgements, peer review information; details of author contributions and competing interests; and statements of data and code availability are available at https://doi.org/10.1038/s41586-020-2567-3.

1. Novoselov, K. S., Mishchenko, A., Carvalho, A. & Castro Neto, A. H. 2D materials and van der Waals heterostructures. *Science* **353**, aac9439 (2016).
2. Li, G. et al. Observation of Van Hove singularities in twisted graphene layers. *Nat. Phys*. **6**, 109–113 (2010).
3. Luican, A. et al. Single-layer behavior and its breakdown in twisted graphene layers. *Phys. Rev. Lett*. **106**, 126802 (2011).
4. Cao, Y. et al. Correlated insulator behaviour at half-filling in magic-angle graphene superlattices. *Nature* **556**, 80–84 (2018).
5. Cao, Y. et al. Unconventional superconductivity in magic-angle graphene superlattices. *Nature* **556**, 43–50 (2018).
6. Bistritzer, R. & MacDonald, A. H. Moiré bands in twisted double-layer graphene. *Proc. Natl Acad. Sci. USA* **108**, 12233–12237 (2011).
7. Bao, W. et al. Controlled ripple texturing of suspended graphene and ultrathin graphite membranes. *Nat. Nanotechnol*. **4**, 562–566 (2009).
8. Cai, S., Breid, D., Crosby, A. J., Suo, Z. & Hutchinson, J. W. Periodic patterns and energy states of buckled films on compliant substrates. *J. Mech. Phys. Solids* **59**, 1094–1114 (2011).
9. Cerda, E. & Mahadevan, L. Geometry and physics of wrinkling. *Phys. Rev. Lett*. **90**, 074302 (2003).
10. Guinea, F., Katsnelson, M. I. & Geim, A. K. Energy gaps and a zero-field quantum Hall effect in graphene by strain engineering. *Nat. Phys*. **6**, 30–33 (2010).
11. Ramezani Masir, M., Moldovan, D. & Peeters, F. M. Pseudo magnetic field in strained graphene: Revisited. *Solid State Commun*. **175–176**, 76–82 (2013).
12. Schneider, M., Faria, D., Kusminskiy, S. V. & Sandler, N. Local sublattice symmetry breaking for graphene with a centrosymmetric deformation. *Phys. Rev. B*. **91**, 161407 (2015).
13. Amorim, B. et al. Novel effects of strains in graphene and other two dimensional materials. *Phys. Rep*. **617**, 1–54 (2016).
14. Jiang, Y. et al. Visualizing strain-induced pseudomagnetic fields in graphene through an hBN magnifying glass. *Nano Lett*. **17**, 2839–2843 (2017).
15. Kerelsky, A. et al. Maximized electron interactions at the magic angle in twisted bilayer graphene. *Nature* **572**, 95–100 (2019).
16. Jiang, Y. et al. Charge order and broken rotational symmetry in magic-angle twisted bilayer graphene. *Nature* **573**, 91–95 (2019).
17. Xie, Y. et al. Spectroscopic signatures of many-body correlations in magic-angle twisted bilayer graphene. *Nature* **572**, 101–105 (2019).
18. Kopnin, N. B., Heikkilä, T. T. & Volovik, G. E. High-temperature surface superconductivity in topological flat-band systems. *Phys. Rev. B* **83**, 220503 (2011).
19. Kauppila, V. J., Aikebaier, F. & Heikkilä, T. T. Flat-band superconductivity in strained Dirac materials. *Phys. Rev. B* **93**, 214505 (2016).
20. Tang, E. & Fu, L. Strain-induced partially flat band, helical snake states and interface superconductivity in topological crystalline insulators. *Nat. Phys*. **10**, 964–969 (2014).
21. Du, X., Skachko, I., Duerr, F., Luican, A. & Andrei, E. Y. Fractional quantum Hall effect and insulating phase of Dirac electrons in graphene. *Nature* **462**, 192–195 (2009).
22. Bolotin, K. I., Ghahari, F., Shulman, M. D., Stormer, H. L. & Kim, P. Observation of the fractional quantum Hall effect in graphene. *Nature* **462**, 196–199 (2009); erratum **475**, 122 (2011).
23. Andrei, E. Y. et al. Observation of the magnetically induced Wigner solid. *Phys. Rev. Lett*. **60**, 2765 (1988).
24. Levy, N. et al. Strain-induced pseudo-magnetic fields greater than 300 tesla in graphene nanobubbles. *Science* **329**, 544–547 (2010).
25. Carrillo-Bastos, R. et al. Strained fold-assisted transport in graphene systems. *Phys. Rev. B* **94**, 125422 (2016).
26. Giovannetti, G. et al. Doping graphene with metal contacts. *Phys. Rev. Lett*. **101**, 026803 (2008).
27. Luican, A., Li, G. & Andrei, E. Y. Scanning tunneling microscopy and spectroscopy of graphene layers on graphite. *Solid State Commun*. **149**, 1151–1156 (2009).
28. Moldovan, D., Masir, M. R. & Peeters, F. M. Electronic states in a graphene flake strained by a Gaussian bump. *Phys. Rev. B* **88**, 035446 (2013).
29. Neek-Amal, M., Covaci, L., Shakouri, K. & Peeters, F. M. Electronic structure of a hexagonal graphene flake subjected to triaxial stress. *Phys. Rev. B* **88**, 115428 (2013).
30. Gomes, K. K., Mar, W., Ko, W., Guinea, F. & Manoharan, H. C. Designer Dirac fermions and topological phases in molecular graphene. *Nature* **483**, 306–310 (2012).
31. Settnes, M., Power, S. R. & Jauho, A. P. Pseudomagnetic fields and triaxial strain in graphene. *Phys. Rev. B* **93**, 035456 (2016).
32. Georgi, A. et al. Tuning the pseudospin polarization of graphene by a pseudomagnetic field. *Nano Lett*. **17**, 2240–2245 (2017).
33. Zhang, Z. Z., Chang, K. & Peeters, F. M. Tuning of energy levels and optical properties of graphene quantum dots. *Phys. Rev. B* **77**, 235411 (2008).
34. Palacios-Berraquero, C. et al. Large-scale quantum-emitter arrays in atomically thin semiconductors. *Nat. Commun*. **8**, 15093 (2017).
35. Milovanović, S. P., Anđelković, M., Covaci, L. & Peeters, F. M. Periodically strained graphene lattice: flat bands. Preprint at http://arXiv.org/abs/1910.11752 (2019).

Methods

Sample preparation

To avoid oxygen and moisture contamination, the heterostructures are fabricated in a dry Ar atmosphere in a glovebox. Graphene is first exfoliated on a PMMA—poly (methyl methacrylate)—film and then transferred onto a thin $NbSe_2$ flake deposited on a SiO_2/Si substrate. Instead of dissolving the PMMA in acetone, we mechanically peeled it off. The Au electrodes were deposited by standard SEM lithography. Before loading the sample into the STM chamber, the sample is annealed at 230 °C in forming gas (10% H_2 and 90% Ar) overnight to remove the PMMA residue. The STM experiments are performed in a home-built STM[27] at 4.6 K with a cut $Pt_{0.8}Ir_{0.2}$ tip, and the sample is located using a capacitive-based self-navigation technique[36]. The tip used here is calibrated on the Au electrode, and the dI/dV curves are measured using a standard lock-in technique with a small a.c. voltage modulation (2 mV at 473.1 Hz) added to the d.c. junction bias[27].

Buckling pattern formation

Periodic pattern formation following a buckling transition is largely determined by the boundary conditions and stress distribution[8,9]. In order to understand the buckling pattern in the G/$NbSe_2$ sample, we carried out large-area topography measurements that include the boundaries of the pattern (Extended Data Fig. 1). In Extended Data Fig. 1a, the triangular pattern is delimited by two intersecting ridges (labelled as ridge 1 and ridge 2, ~0.5 μm long and 4 nm tall) that form a 60° fan. Zooming into the fan area (Extended Data Fig. 1c), we discern the buckling pattern. In Extended Data Fig. 1c, d, we show that the period of the pattern increases monotonically with the distance from the apex where the two ridges meet.

When graphene is deposited on a substrate, folds, ridges and bubbles due to trapped gas or solvents are produced. Many of these defects disappear on annealing (see Methods section 'Sample preparation'), but not all, presumably because their geometry is such that it does not allow the trapped species to escape or because the defect is pinned to the substrate. We observe that the ridges that survive the annealing step (Extended Data Fig. 1a) do not show the usual concave profile seen before annealing, but rather show evidence of collapse, probably due to freezing of the trapped gas that supported the ridge. Following the collapse, the ridge profile becomes convex and is flanked by two tall lips on the boundaries of the original fold (Extended Data Fig. 1e). The lip pointing inwards towards the fan area is consistently shorter than the outside lip, suggesting that some of the graphene membrane comprising the original fold was pushed inwards. This increases the area of the membrane trapped between the two ridges (ridges 1 and 2 in Extended Data Fig. 1a), resulting in biaxial compressive strain which can trigger the buckling transition. To test this scenario, we conjecture that the concave region of the ridge was originally part of the convex top. This suggests that one can reconstruct the original shape by a mirror transformation of the concave part relative to the green dashed line in Extended Data Fig. 1e (the line intersects the tallest point of the convex part and is parallel to the substrate). This produces the reconstructed dome shown by the red symbols in Extended Data Fig. 1e. Using this procedure immediately reveals a missing part of the original dome of length ΔL as indicated in the figure. The strain produced by this increased length is estimated from the ratio between ΔL and the bisector of the 60° triangle: $\varepsilon = (\Delta L/L)\sin 30^\circ = 2\Delta L/L$, where L is the distance from the apex formed by the intersection of the two ridges (Extended Data Fig. 1f).

Theoretical models and simulations of wrinkling based on minimizing the energy of a stretched or compressed membrane by allowing out of plane distortions[8,9] have shown that there are simple scaling laws relating the period of the buckled membrane λ to the strain ε,

$$\frac{\lambda^4}{(tL)^2} = \frac{4\pi^2 \nu}{3(1-\nu^2)\varepsilon}.$$

Using $t = 0.3$ nm for the graphene thickness, $\nu \approx 0.15$ for its Poisson ratio and the expression for the strain as a function of distance L, we find

$$\lambda = \left[\frac{4\pi^2 \nu t^2}{3(1-\nu^2)440}\right]^{1/4} L^{3/4} = 0.14 L^{3/4}.$$

Fitting the data for the distance dependence of the strain, shown in Extended Data Fig. 1d, to the expression $\lambda = \lambda_0 + cL^{3/4}$, we obtain the constant $c = 0.154 \pm 0.005$, consistent with the above estimate. The value of the offset $\lambda_0 = (6 \pm 0.3)$ nm suggests that this formula breaks down at short distances.

To understand why the 1D scaling of the buckling period is consistent with our results, we consider the sketch shown in Extended Data Fig. 1b. We note that it is unlikely that both ridges collapse at the same instant. Now if we suppose that the ridge marked by the green line in the sketch collapses first, it will produce a set of roughly parallel wrinkles whose spacing increases with distance as the strain decreases according to the scaling formula above. When subsequently the yellow ridge collapses, it produces a similar set of wrinkles roughly parallel to itself. The points of intersection of the two wrinkle sets will thus produce a triangular pattern of crests (black dots) while the areas in between will be troughs.

Buckling transitions in thin stiff membranes have been studied extensively both experimentally and theoretically in the context of mechanical engineering. The details of the patterns that emerge after the buckling transition has taken place are controlled by boundary geometry and the strain distribution[8,9]. Depending on the value of these parameters, a variety of buckling patterns are observed, including square, hexagonal, herringbone and stripes[7–9].

Flat areas in G/$NbSe_2$ and G/hBN samples

Superposing two 2D crystal structures produces a moiré pattern whose period is controlled by the two atomic lattice constants, a and b, and by the angle between their crystal orientations. The largest moiré period, which is obtained when the two crystals are aligned, is given by $\lambda_{max} = (1+1/\delta)a$, where $\delta = (b-a)/a$ is the lattice mismatch[37]. The lattice constants for graphene and $NbSe_2$ are $a = 0.246$ nm and $b = 0.36$ nm, respectively, leading to $\lambda_{max} = 0.77$ nm. This is more than an order of magnitude smaller than the superlattice periods observed in our work, immediately ruling out an interpretation in terms of a moiré pattern.

To further confirm that the observed pattern is not due to a moiré structure, we show in Extended Data Fig. 2 the atomically resolved topography of a region far from the two ridges, which shows the honeycomb structure characteristic of flat graphene (Extended Data Fig. 2b). In this region, the featureless STM topography (Extended Data Fig. 2a) together with the 'V'-shaped dI/dV spectrum confirm that the graphene is well decoupled from the bottom $NbSe_2$. This procedure of taking spectra in an unbuckled region of the sample also served for tip selection in all our measurements. When the spectra outside the buckled region showed an anomalous feature such as a gap or large dip at the Fermi energy[38], the tip was reconditioned or replaced. Tip integrity is particularly important for distinguishing between correlation-induced gap features and artefacts introduced by the tip.

Buckling patterns and dI/dV maps

The two panels of Extended Data Fig. 3a show the STM topography of the buckled graphene in the G/$NbSe_2$ sample taken with two different bias voltages. The blue lines are guides to the eye, connecting the crests. The crests remain bright for different bias voltages, consistent with their higher topography.

In Extended Data Fig. 3b, we show the dI/dV map at an energy corresponding to the $N = 0$ PLL in the crest area of the G/$NbSe_2$ sample.

The uniform LDOS represented by this map differs from the petal structure expected for a Gaussian bump[12,25] and reflects the unique geometry of the PMF induced by the buckled structure, which further confirms the theoretical model.

Transition area in the G/NbSe$_2$ sample

Extended Data Fig. 4a shows the theoretical contour plot of the LDOS spectra connecting two crest areas (see also the upper panel of Fig. 3g). In the transition area labelled by the yellow dashed line, we note that features from the crest (green arrows) and trough (red arrows) coexist. This coexistence is also observed in the experimental dI/dV spectrum (Extended Data Fig. 4b), which exhibits peaks that can be traced back to both the crest (green arrows) and the trough (red arrows) regions.

PMF dependence on superlattice period

Extended Data Fig. 5 shows the simulated LDOS in the crest region as a function of PMF amplitude for several values of the superlattice period, a_b, as marked. The dashed lines represent the field dependence of the LL energy in uniform fields. We note that as the lattice spacing increases, the spectra start approaching the unstrained LL sequence at lower values of the PMF. This is consistent with the fact that LLs, which correspond to cyclotron motion, can only form if the magnetic field B is fairly constant over length scales that are several times the magnetic length, $l_B = \sqrt{\frac{\hbar}{eB}} \approx \frac{25.7\,\mathrm{nm}}{\sqrt{B}}$.

Effective PMF (B_{eff}) in the crest area

Extended Data Fig. 6a shows LDOS cuts in the crest region from Fig. 3a (A sublattice) for several values of B, as marked. For each spectrum we calculated the value of the effective magnetic field, B_{eff}, from the energy of the first peak, $E_1 = v_F\sqrt{2e\hbar B_{\mathrm{eff}}}$. In order to check if the peaks can be interpreted as LLs, we mark by arrows the calculated peak sequence for the corresponding B_{eff}, $E_N = \pm v_F\sqrt{2e\hbar B_{\mathrm{eff}}N}$. We note that the arrows coincide with the spectral peaks for sufficiently large PMF amplitudes, suggesting that the LL language is appropriate for these spectra, as long as the B_{eff} is used. However, the extracted effective field is much smaller than the maximum PMF value, that is, $B_{\mathrm{PMF}}^{\mathrm{max}} = 3B$, reflecting the fact that the cyclotron orbit averages the field over an area of size $\sqrt{2N+1}\,l_B$. For example, for a 14-nm lattice period and amplitude $B = 120$ T, the peak sequence gives $B_{\mathrm{eff}} = 112$ T, which is consistent with the experimental result in Fig. 2b.

As shown in Fig. 3a and Extended Data Fig. 5, the $N = 0$ PLL undergoes a transition from a double peak at low PMF to a single one at a higher PMF: this transition occurs at a critical PMF value that is highly sensitive to the lattice spacing. This is clearly illustrated in Extended Data Fig. 6b, where we show that the simulated $N = 0$ double peak for $B_{\mathrm{eff}} = 112$ T and $a_b = 14$ nm merges into a single peak for $a_b = 14.8$ nm. The data in Fig. 2—where $a_b = 14.4 \pm 0.5$ nm, $B_{\mathrm{eff}} = 112$ T and the $N = 0$ PLL peak is unsplit—is consistent with the simulated spectrum (Extended Data Fig. 6b, red curve) in the regime above the critical PMF.

Flat-band structure in buckled G/NbSe$_2$

In Extended Data Fig. 7 we plot the band structure and LDOS in the trough region for $B = 140$ T (Extended Data Fig. 7a, b) and $B = 180$ T (Extended Data Fig. 7c, d). The figure shows the flattening of the bands with increasing field amplitude.

Tight-binding model for the strained triangular lattice

The effect of strain is included in the tight-binding Hamiltonian through the modulation of the hopping energy. This is given by

$$t_{ij} = t_0 \mathrm{e}^{-\beta(d_{ij}/a_{\mathrm{cc}}-1)}, \tag{2}$$

where β is the decay coefficient, a_{cc} is the unstrained carbon–carbon bond, and d_{ij} is the strained bond length defined by the strain tensor $\bar{\varepsilon}$ as

$$d_{ij} = (I + \bar{\varepsilon})\boldsymbol{\delta}_{ij}, \tag{3}$$

where $\boldsymbol{\delta}_{ij}$ is the vector in the direction of the bond between atoms i and j, and I is the unitary matrix. Changes in the hopping energies generate a strain-induced vector potential in the system, which in the case of hexagonal lattices is given by

$$A_x - \mathrm{i}A_y = -\frac{1}{ev_F}\sum_j \delta t_{ij} e^{\mathrm{i}\mathbf{K}\cdot\mathbf{r}_{ij}}. \tag{4}$$

The corresponding PMF is calculated using

$$\mathbf{B} = \nabla \times \mathbf{A} = \left[\partial_x \mathrm{A}_y - \partial_y \mathrm{A}_x\right] e_z. \tag{5}$$

Owing to gauge invariance, we may choose $A_y = 0$. Hence, our vector potential is then given by $A_x = \int B(x,y)\mathrm{d}y$, where $B(x, y)$, shown in Extended Data Fig. 8a, is given by equation (1). This leads to

$$A_x = B\frac{a_b}{2\pi}\left[\frac{1}{b_{1y}}\sin(\mathbf{b}_1\cdot\mathbf{r}) + \frac{1}{b_{2y}}\sin(\mathbf{b}_2\cdot\mathbf{r}) + \frac{1}{b_{3y}}\sin(\mathbf{b}_3\mathbf{r})\right]. \tag{6}$$

Substituting $t_{ij} = t_0(1+\delta t_{ij})$ and expanding equation (4) up to first order, we obtain the following expression for the vector potential[6]

$$(A_x, A_y) = -\frac{1}{2ev_F}\left[2\delta t_1 - \delta t_2 - \delta t_3, \frac{1}{\sqrt{3}}(\delta t_2 - \delta t_3)\right], \tag{7}$$

where δt_1, δt_2 and δt_3 are the strain modulations of hopping energies along the directions of graphene's nearest neighbours δ_1, δ_2 and δ_3, as shown in Extended Data Fig. 8b, and $v_F = 3t_0a_{cc}/(2\hbar)$ is the Fermi velocity. The choice of the gauge ($A_y = 0$) results in $\delta t_2 = \delta t_3 = \delta t$. We choose $\delta t_1 = -\delta t$ and, finally, the strain modified hopping energies are given by

$$t_1 = t_0\left(1 - \frac{3A_x\pi a_{cc}}{2\phi_0}\right),$$

$$t_2 = t_3 = t_0\left(1 + \frac{3A_x\pi a_{cc}}{2\phi_0}\right), \tag{8}$$

where $\phi_0 = h/e$ is the magnetic flux quantum.

Theoretical results for the G/hBN sample

To simulate the buckling pattern in graphene on hBN, we use a similar expression as in the case of graphene on NbSe$_2$, given by equation (2), but without the last cosine term:

$$B_{\mathrm{PMF}}(x,y) = B[\cos(\mathbf{b}_1\cdot\mathbf{r}) + \cos(\mathbf{b}_2\cdot\mathbf{r})] \tag{9}$$

with $\mathbf{b}_1 = (2\pi/a_b^x)(0,1)$ and $\mathbf{b}_2 = (2\pi/a_b^y)(1,0)$. This changes the symmetry of the unit cell from triangular to rectangular. The profile of the field is shown in Extended Data Fig. 9a with the unit cell marked by the dashed rectangle. The size of the unit cell is chosen so as to match the buckling periods shown in Fig. 5a. The LDOS in the crest region is given in Extended Data Fig. 9b, where clear LLs can be observed in the spectra. A cut of the LDOS map at a constant value of $B = 62$ T (white dashed line in Extended Data Fig. 9b) shows LLs that scale with the square root of the LL index (see Extended Data Fig. 9e, g) and result in an effective field of $B_{\mathrm{eff}} = 100$ T. Moving towards the transition region (magenta square in Extended Data Fig. 9a) where $B = 0$ T, the LDOS spectrum changes substantially, as shown by Extended Data Fig. 9c. Here, the spectrum does not show LLs, which is expected since there is no PMF. However, the LDOS reveals new sets of peaks that depend weakly on the amplitude of the field. This is further confirmed in Extended Data Fig. 9d, which shows that the dispersion of these peaks with unit cell size a_b is consistent with that expected of confinement states. Taking a cut of the LDOS map from Extended Data Fig. 9c, at $B = 62$ T results in equidistant peaks separated by about 83 meV as shown in Extended Data Fig. 9f, h.

Robustness of the PLLs against disorder

As seen in Fig. 1c, the rectangular buckling array in the G/hBN sample is not perfectly periodic as implied by the double cosine potential used in the simulation. It is then natural to ask how robust are the simulated DOS and the corresponding d*I*/d*V* spectrum against lattice distortions. To address this question, we carried out numerical simulations where the periodicity condition was relaxed. As detailed below, we find that the PMF spectrum of the rectangular buckling structure is quite robust, and can survive substantial deviations from the perfectly periodic lattice structure.

To study the effect of relaxing the condition of perfect periodicity, we introduced a random variation in the unit cell of the PMF within a predefined range. The procedure is as follows. Since the original unit cell is too large, we reduced the larger unit vector to the size of the smaller one, that is, $a_x = a_y = 20$ nm. The PMF profile for this case is shown in Extended Data Fig. 10a. Changing the size of the unit cell should not change the physics of the problem, but numerically this substantially speeds up our calculations. The system is a circle of radius of 200 nm with absorbing boundary conditions applied at the edges (the method is described in detail in ref. [39]). A vector potential is added to the Hamiltonian as described above, with the unit cell period given by $[(1+\Delta R_x)a_x, (1+\Delta R_y)a_y]$, where R_x and R_y are random numbers from a uniform distribution in the range $[-1, 1]$ and Δ is the weight parameter. As an example, in Extended Data Fig. 10b–d we plot a few PMF profiles using $\Delta = 0.15, 0.25, 0.33$, respectively. The calculated DOS is shown in Extended Data Fig. 10e (the DOS is calculated using the kernel polynomial method, as explained in ref. [40]). The blue curve in this plot shows the DOS of the perfectly periodic system. The peaks observed here are the flat bands, and the separation between the peaks is around 60 meV. As Δ is increased, the peaks are averaged out and eventually disappear for large Δ, which is the expected result. However, up to $\Delta = 0.25$, the peaks are still present in spite of the substantial disorder introduced in the system.

In addition to the robustness of the PLL spectrum against lattice disorder, the resemblance between the spectral features of the G/hBN and G/NbSe$_2$ samples in the crest regions further indicates their common origin, as detailed below.

(1) In both systems, the features are observed only in the buckled regions of the graphene membrane and are absent in the unbuckled parts of the sample.

(2) In both systems, the buckling gives rise to a strain-induced PMF resulting in the PLL observed in the d*I*/d*V* spectra. The PLL sequence, which is characterized by a peak at the Dirac point and a square-root dependence on level index, is observed on the crests, consistent with the numerical simulation results.

(3) In both systems, the spectra in the regions between maxima of the PMF show confinement character, rather than PLLs. Specifically, they do not feature the peak at the Dirac point corresponding to the $N = 0$ PLL and the peak sequence does not follow a square-root level index dependence. Instead the spectrum in this regime is consistent with magnetic confinement states.

Transition region in the G/hBN sample

In the case of the G/NbSe$_2$ sample, the crest and trough regions of the triangular buckling pattern observed in topography coincide with the maximum and minimum PMF, respectively. This designation is not as straightforward in the rectangular buckling pattern observed in the G/hBN sample. While in this sample the crest regions where the PMF has its maximum magnitude are readily identified in the topography as the intersection point between two of the quasi-1D wrinkles that form the rectangular buckling pattern (Fig. 1c), it is less easy to identify the transition regions where the PMF is vanishingly small. We instead used the fact that in the transition region the PMF vanishes, resulting in the disappearance of the PLLs and the characteristic peak at the CNP. By using this criterion, we identified the transition region marked by the circle in Fig. 5a.

Data availability

The data that support the findings of this study are available from the corresponding authors on reasonable request.

36. Li, G., Luican, A. & Andrei, E. Y. Self-navigation of a scanning tunneling microscope tip toward a micron-sized graphene sample. *Rev. Sci. Instrum*. **82**, 073701 (2011).
37. Yankowitz, M. et al. Emergence of superlattice Dirac points in graphene on hexagonal boron nitride. *Nat. Phys*. **8**, 382–386 (2012).
38. Andrei, E. Y., Li, G. H. & Du, X. Electronic properties of graphene: a perspective from scanning tunneling microscopy and magnetotransport. *Rep. Prog. Phys*. **75**, 056501 (2012).
39. Anđelković, M., Covaci, L. & Peeters, F. M. DC conductivity of twisted bilayer graphene: angle-dependent transport properties and effects of disorder. *Phys. Rev. Mater*. **2**, 034004 (2018).
40. Weiße, A., Wellein, G., Alvermann, A. & Fehske, H. The kernel polynomial method. *Rev. Mod. Phys*. **78**, 275–306 (2006).

Acknowledgements We acknowledge support from the DOE (DOE-FG02-99ER45742; E.Y.A., Y.J.), the Gordon and Betty Moore Foundation (GBMF9453; E.Y.A.), the National Key R&D Program of China (2019YFA0307800, 2018YFA0305800; J.M.), the Beijing Natural Science Foundation (Z190011; J.M.), the Flemish Science Foundation (FWO-Vl; S.P.M. and F.M.P.), and the TRANS2DTMD Flag-Era project (M.A., L.C. and F.M.P.). We thank F. Guinea, B. Davidovitch and D. Vella for stimulating discussions during the Aspen winter workshop on low-dimensional solids in hard and soft condensed matter.

Author contributions J.M. and Y.J. performed STM/STS measurements. Y.J., J.M. and E.Y.A. designed the research strategy, performed data analysis and wrote the manuscript with input from all authors. S.P.M., M.A., L.C. and F.M.P. performed theoretical calculations. Y.C., A.K.G. and X.L. fabricated the devices. K.W. and T.T. provided hBN. E.Y.A. supervised the project.

Competing interests The authors declare no competing interests.

Additional information

Correspondence and requests for materials should be addressed to Y.J. or E.Y.A.

Peer review information *Nature* thanks Dante Kennes and the other, anonymous, reviewer(s) for their contribution to the peer review of this work.

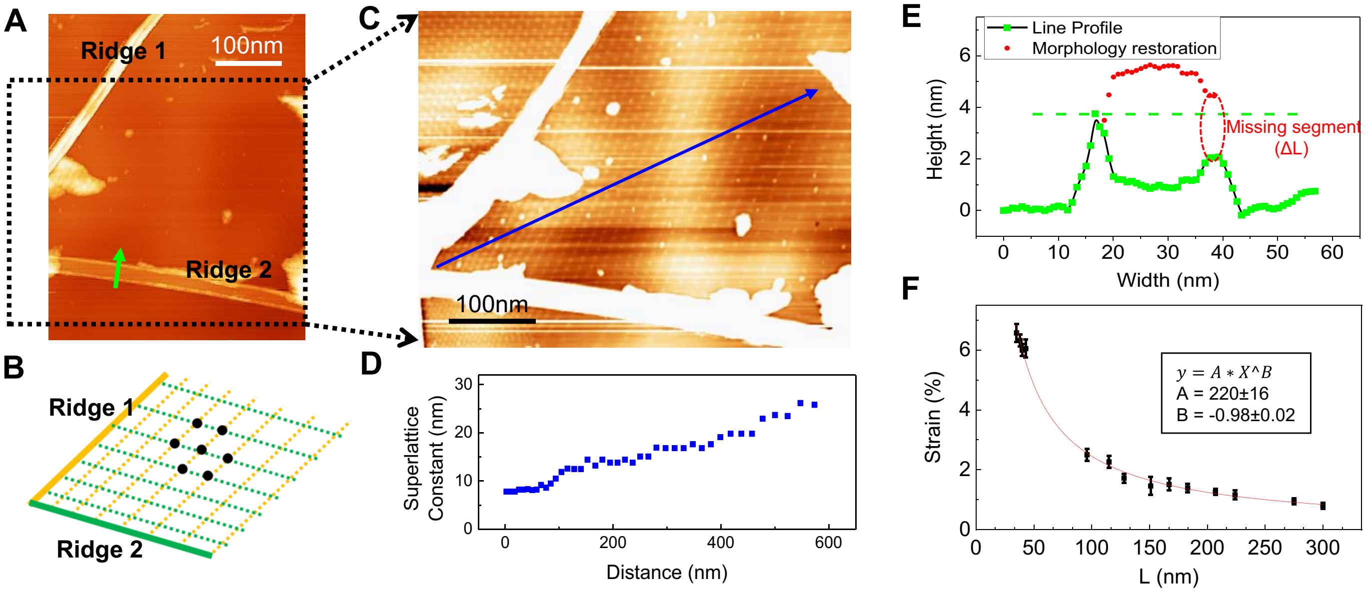

Extended Data Fig. 1 | Buckling pattern of graphene. a, Large-area STM topography of G/NbSe$_2$ shows two ridges that delimit the buckling pattern (V_b = −0.3 V, I = 20 pA). **b**, Schematic of wrinkles arising from the compressive strain at each boundary ridge. Crests form at the wrinkle intersections, marked by black dots. **c**, Zoomed-in topography image of the triangular buckling pattern (V_b = 0.5 V, I = 20 pA) in **a**. **d**, The superlattice constant, measured along the line marked by the blue arrow in **c**, increases monotonically with distance from the apex where the two ridges meet. **e**, Height profile along the green arrow in **a**. **f**, Strain produced by the collapse of the ridges calculated from **e**, as described in Methods section 'Buckling pattern formation'.

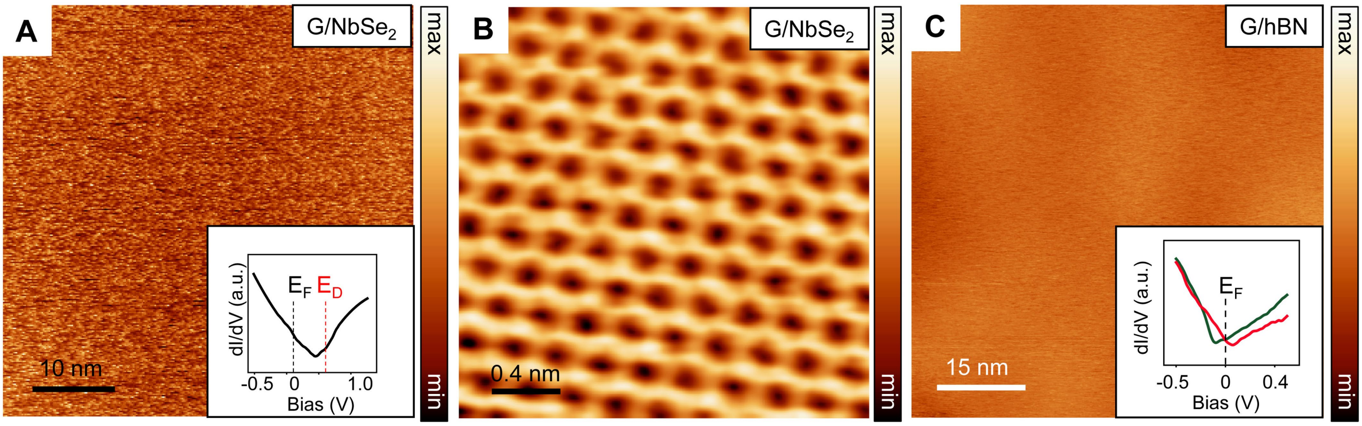

Extended Data Fig. 2 | Topography of unbuckled regions in the G/NbSe$_2$ sample. a, Main panel, STM topography of a flat (unbuckled) region of the G/NbSe$_2$ surface far from the ridges. Inset, d*I*/d*V* spectrum from the region shown in the main panel ($V_b = 0.5$ V, $I = 30$ pA). **b**, Atomic-resolution view of G/NbSe$_2$ in **a** ($V_b = -0.3$ V, $I = 30$ pA). **c**, Same as **a** but from a flat region of the G/hBN sample. Inset, d*I*/d*V* spectra of flat G/hBN for conditions of electron-doping (green trace) and hole-doping (red trace); $V_b = -0.3$ V, $I = 20$ pA.

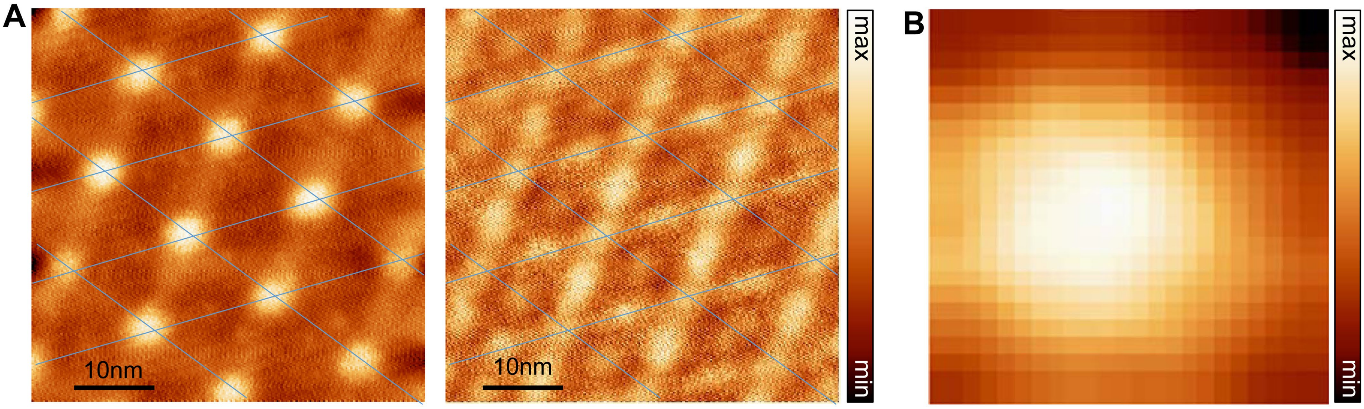

Extended Data Fig. 3 | Topography of buckled regions in the G/NbSe$_2$ sample. **a**, STM topography of a region in the buckled graphene membrane measured with different bias voltages: 500 mV (left) and 50 mV (right). **b**, d*I*/d*V* map over an area of size 6 nm × 6 nm in the crest region at the energy of the *N* = 0 PLL.

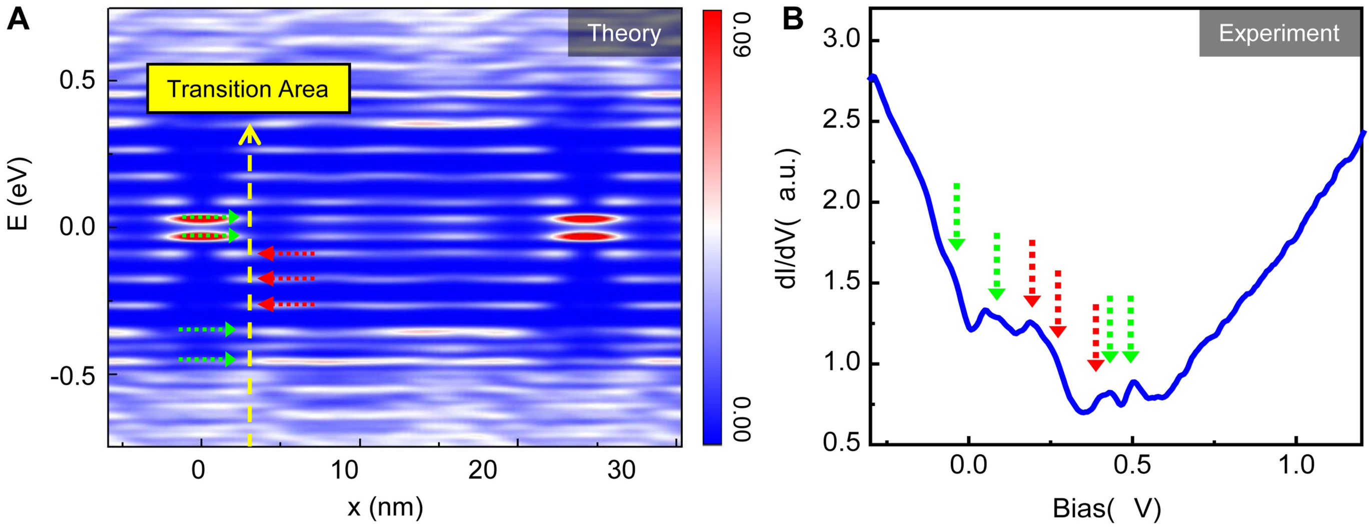

Extended Data Fig. 4 | Transition area in the triangular buckling pattern of the G/NbSe$_2$ sample. a, Theoretical contour plot of the LDOS spectra connecting two crest areas (at $x = 0$ nm and $x = 25$ nm; see Fig. 3g, upper panel) versus energy, E, and position, x. The colour scale bar represents the LDOS intensity. The yellow dashed line labels the LDOS spectrum in the transition region plotted in **b**. **b**, Experimental dI/dV spectrum in the transition region between crests and troughs. Green and red arrows indicate the corresponding peaks in **a**.

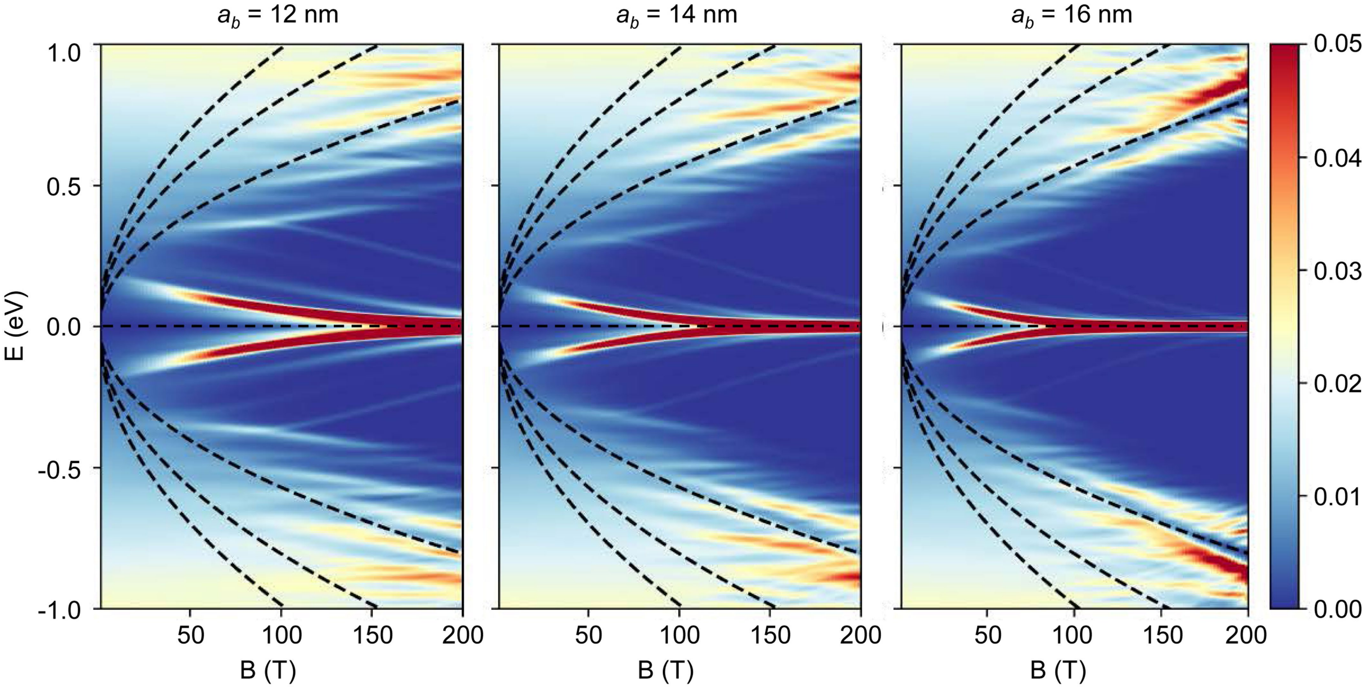

Extended Data Fig. 5 | Evolution of the calculated LDOS with PMF amplitude for several superlattice periods. Shown are contour plots of the LDOS for several values of a_b (left to right: 12 nm, 14 nm, 16 nm) in the crest region versus the amplitude of the magnetic field, *B*, and energy, *E*. Dashed lines represent the field dependence of the PLL energy in a uniform magnetic field given by the *x*-axis values.

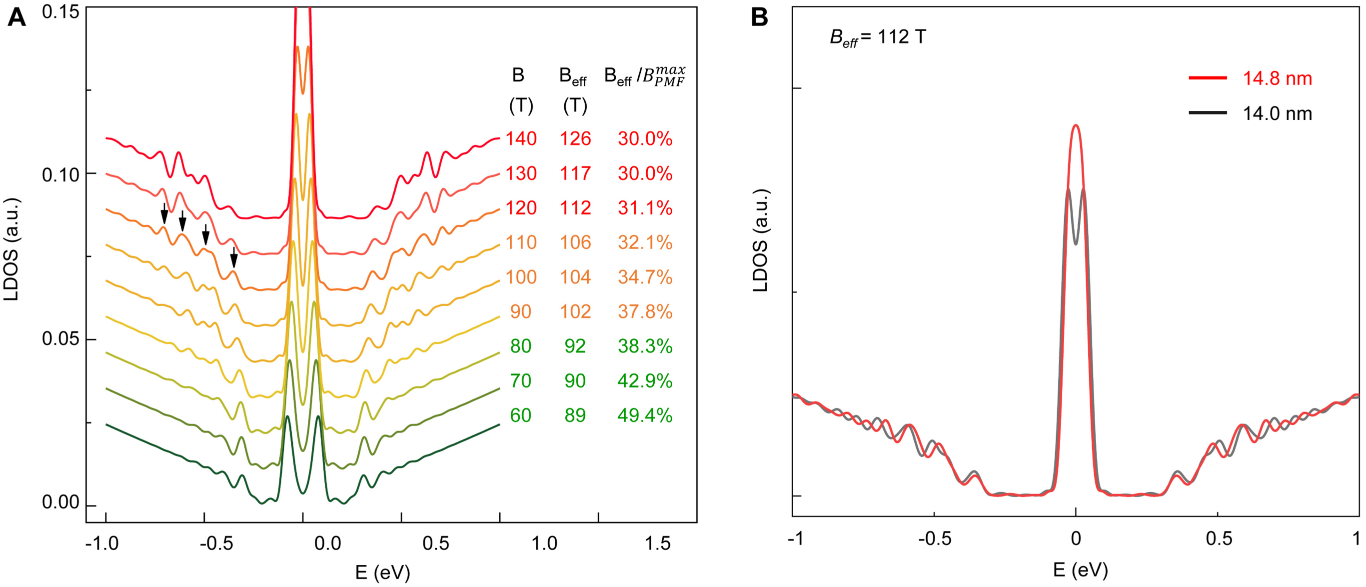

Extended Data Fig. 6 | Calculated PMF in the crest areas of the buckled G/NbSe$_2$ sample. a, LDOS cuts in the crest region from Fig. 3a, upper panel (A sublattice), for several values of *B* and corresponding B_{eff} (first and second columns in the key). The ratio of the effective PMF obtained from the PLL spectrum on the crests to the maximum PMF value ($B_{\mathrm{eff}}/B_{\mathrm{PMF}}^{\mathrm{max}}$) is shown in the rightmost column of the key. **b**, Comparison of crest LDOS at $B_{\mathrm{eff}} = 112$ T for two lattice constants (14.0 nm and 14.8 nm) in the regime where the $N = 0$ peaks merge into one.

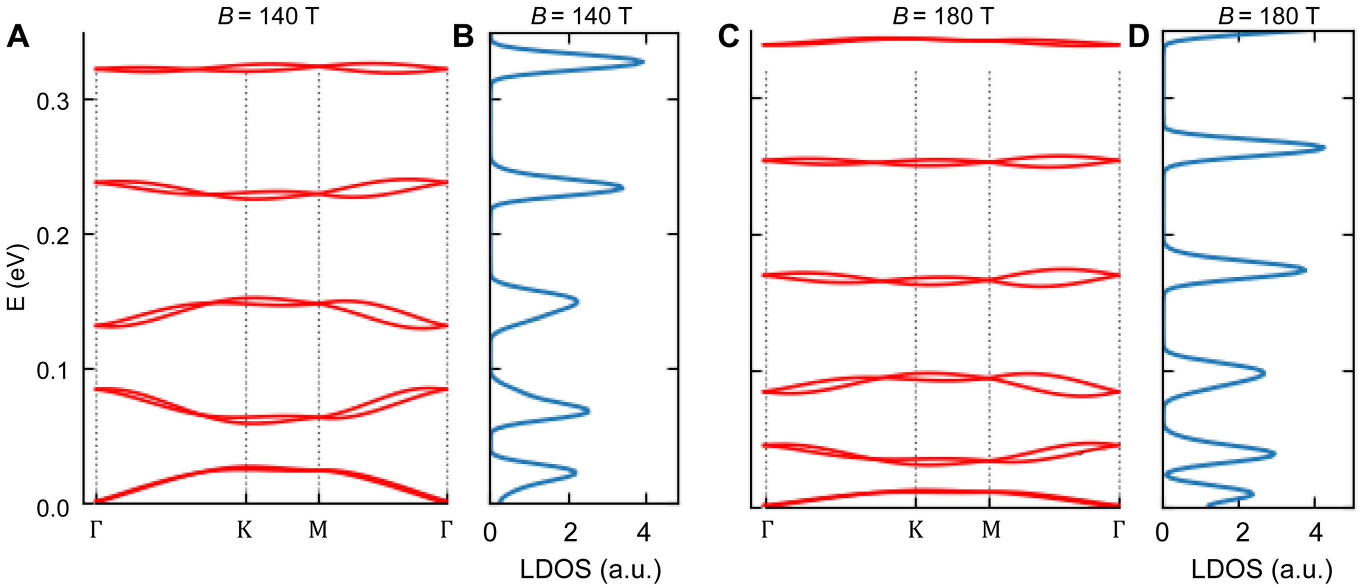

Extended Data Fig. 7 | Calculated low-energy band structure and LDOS in the trough regions of the buckled G/NbSe$_2$ sample. a, **b**, Band structure (**a**) and LDOS (**b**) for a PMF of 140 T. **c**, **d**, As **a** but for a PMF of 180 T. Calculations are for a superlattice period of 14 nm.

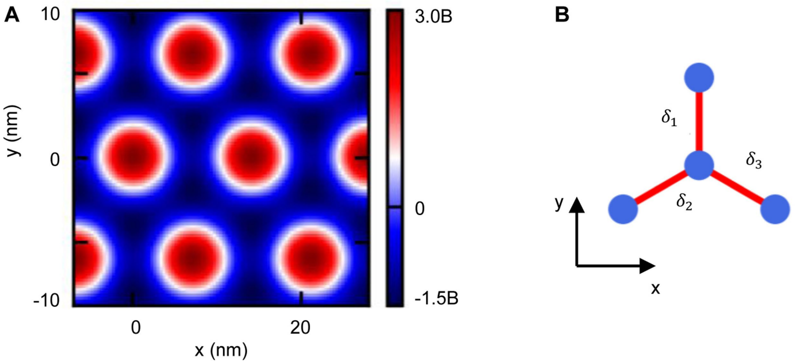

Extended Data Fig. 8 | Tight-binding model for a strained lattice. a, Calculated profile of the PMF given by equation (1) for lattice spacing $a_b = 14$ nm. **b**, Schematic of nearest neighbour vectors, $\boldsymbol{\delta}_1$, $\boldsymbol{\delta}_2$ and $\boldsymbol{\delta}_3$, in a graphene lattice.

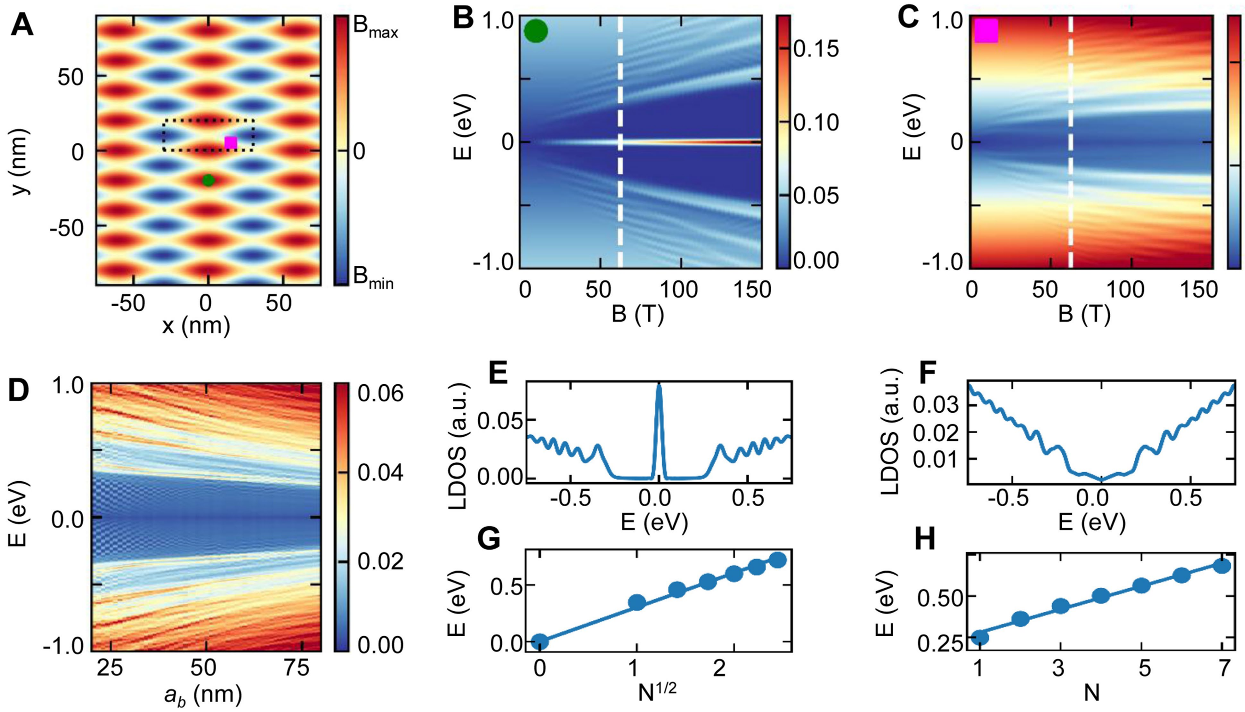

Extended Data Fig. 9 | PMF for a rectangular buckling pattern in graphene. **a**, Profile of the PMF in a rectangular buckling pattern. Dashed rectangle shows the magnetic unit cell. **b**, LDOS (sublattice averaged) versus the PMF amplitude *B* and energy *E* at a crest position in **a** (centre of red region marked by a green dot). The colour scale bar represents the LDOS intensity in arbitrary units. Note that the same result is obtained in the centre of troughs (blue regions) where the PMF sign is reversed. **c**, As **b** but for a point with zero field, marked in **a** by the magenta square. **d**, Contour plot of the LDOS versus energy and superlattice spacing shows the evolution of the confinement levels with unit cell size. The colour scale bar represents the LDOS intensity. **e**, Cut of the LDOS from **b** for a constant value of the field, *B* = 62 T, shown by the dashed white line. **f**, Cut of the LDOS from **c** for a constant value of the field, *B* = 62 T, shown by the dashed white line. **g**, Fitting the peak sequence to a square-root dependence on the PLL index gives an effective PMF of 100 T. **h**, The peak sequence in **f** gives a linear dependence on the peak index with an energy spacing of about 83 meV.

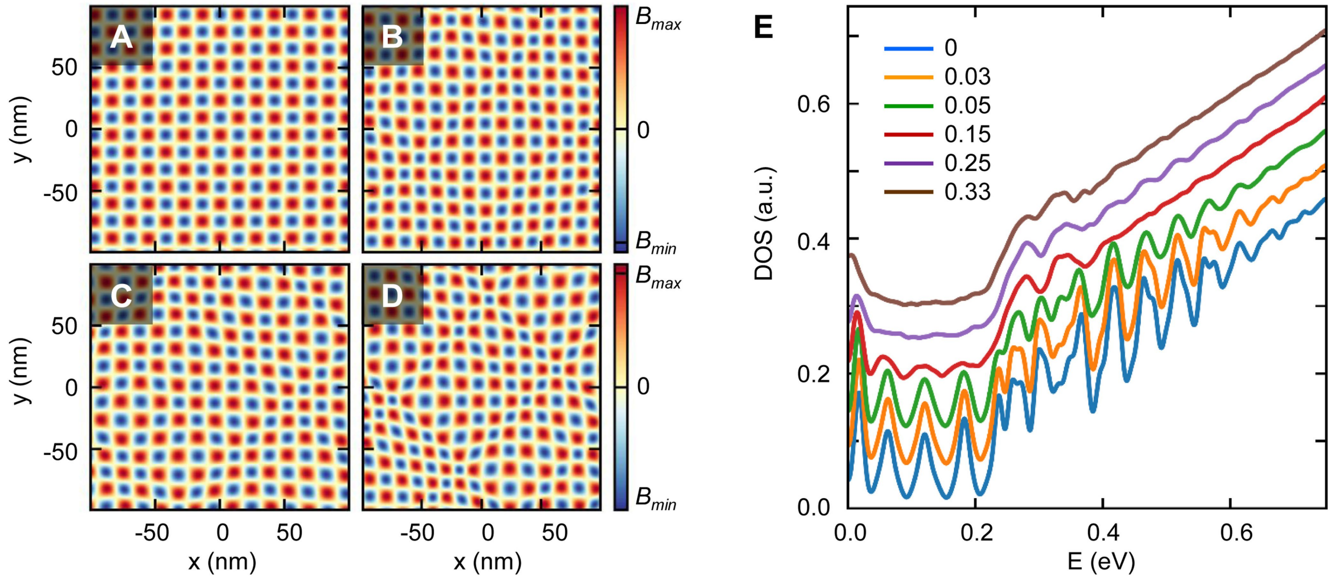

Extended Data Fig. 10 | DOS versus unit cell size in the presence of lattice disorder. a–**d**, The PMF profile used for calculating the DOS shown in **e**. The unit cell period variation range is given by $(1 \pm \Delta)_0$ with $a_0 = 20$ nm and $\Delta = 0$ (**a**), 0.15 (**b**), 0.25 (**c**) and 0.33 (**d**). **e**, DOS obtained for different values of Δ given in the key for $B = 62$ T (as in Extended Data Fig. 9).

Coupling dinitrogen and hydrocarbons through aryl migration

https://doi.org/10.1038/s41586-020-2565-5

Received: 18 December 2019

Accepted: 19 May 2020

Sean F. McWilliams[1,4], Daniël L. J. Broere[1,3,4], Connor J. V. Halliday[2], Samuel M. Bhutto[1], Brandon Q. Mercado[1] & Patrick L. Holland[1]✉

The activation of abundant molecules such as hydrocarbons and atmospheric nitrogen (N_2) remains a challenge because these molecules are often inert. The formation of carbon–nitrogen bonds from N_2 typically has required reactive organic precursors that are incompatible with the reducing conditions that promote N_2 reactivity[1], which has prevented catalysis. Here we report a diketiminate-supported iron system that sequentially activates benzene and N_2 to form aniline derivatives. The key to this coupling reaction is the partial silylation of a reduced iron–dinitrogen complex, followed by migration of a benzene-derived aryl group to the nitrogen. Further reduction releases N_2-derived aniline, and the resulting iron species can re-enter the cyclic pathway. Specifically, we show that an easily prepared diketiminate iron bromide complex[2] mediates the one-pot conversion of several petroleum-derived arenes into the corresponding silylated aniline derivatives, by using a mixture of sodium powder, crown ether, trimethylsilyl bromide and N_2 as the nitrogen source. Numerous compounds along the cyclic pathway are isolated and crystallographically characterized, and their reactivity supports a mechanism for sequential hydrocarbon activation and N_2 functionalization. This strategy couples nitrogen atoms from N_2 with abundant hydrocarbons, and maps a route towards future catalytic systems.

Reduction or 'fixation' of N_2 is accomplished by a few catalytic systems[3–8] that fully reduce N_2 to ammonia (NH_3)[9]. It is difficult to adapt these processes to form C–N bonds from N_2, even though several functionalizations of N_2 are thermodynamically feasible[10]. Efforts to form C–N bonds from N_2 generally require reduction of N_2 to make it nucleophilic enough to react with carbon electrophiles[11,12]. Notable examples include synthetic cycles for C–N bond formation[13–17]. A frequent difficulty is the direct reaction of the reducing agents with the carbon electrophiles.

There would be a substantial advantage if N_2 could be induced to form a C–N bond with a simple hydrocarbon, without prior functionalization of the hydrocarbon to convert it into an electrophile. Such a strategy would require C–H activation of the hydrocarbon, making use of decades of work on oxidative addition of C–H bonds by low-valent transition metal complexes[18]. Although C–H functionalization to form cross-coupling products is well known[19], we know of no previous examples of cross-coupling of C–H bonds with the relatively unreactive N_2 molecule.

Here, we report an iron complex that couples N_2 and unactivated arenes at low temperature, taking advantage of silyl activation of the N_2 to produce silylated anilines in a one-pot procedure. The overall strategy (Fig. 1) begins with C–H bond activation of benzene to form a phenyl fragment, which could migrate to N_2 upon silylation to form the key C–N bond. To explore the feasibility of this pathway, we converted the iron(II) bromide complex $[LFe(\mu\text{-}Br)]_2$ (**1**) into the iron(I)

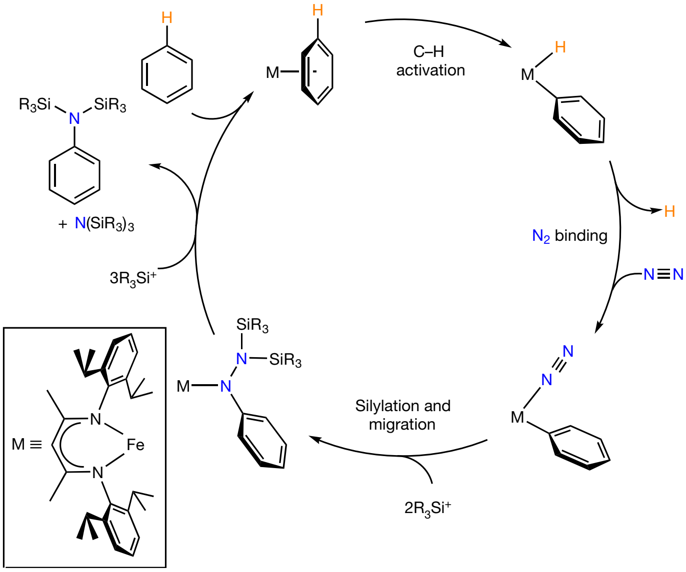

Fig. 1 | Strategy for converting benzene and N_2 into silylated aniline without the use of carbon electrophiles. The reduction steps are not shown here for simplicity, but are elaborated in Fig. 4. Inset, the iron β-diketiminate fragment used in this implementation of the strategy.

---

[1]Department of Chemistry, Yale University, New Haven, CT, USA. [2]EaStCHEM School of Chemistry, University of Edinburgh, Edinburgh, UK. [3]Present address: Debye Institute for Nanomaterials Science, Utrecht University, Utrecht, The Netherlands. [4]These authors contributed equally: Sean F. McWilliams, Daniël L. J. Broere. ✉e-mail: patrick.holland@yale.edu

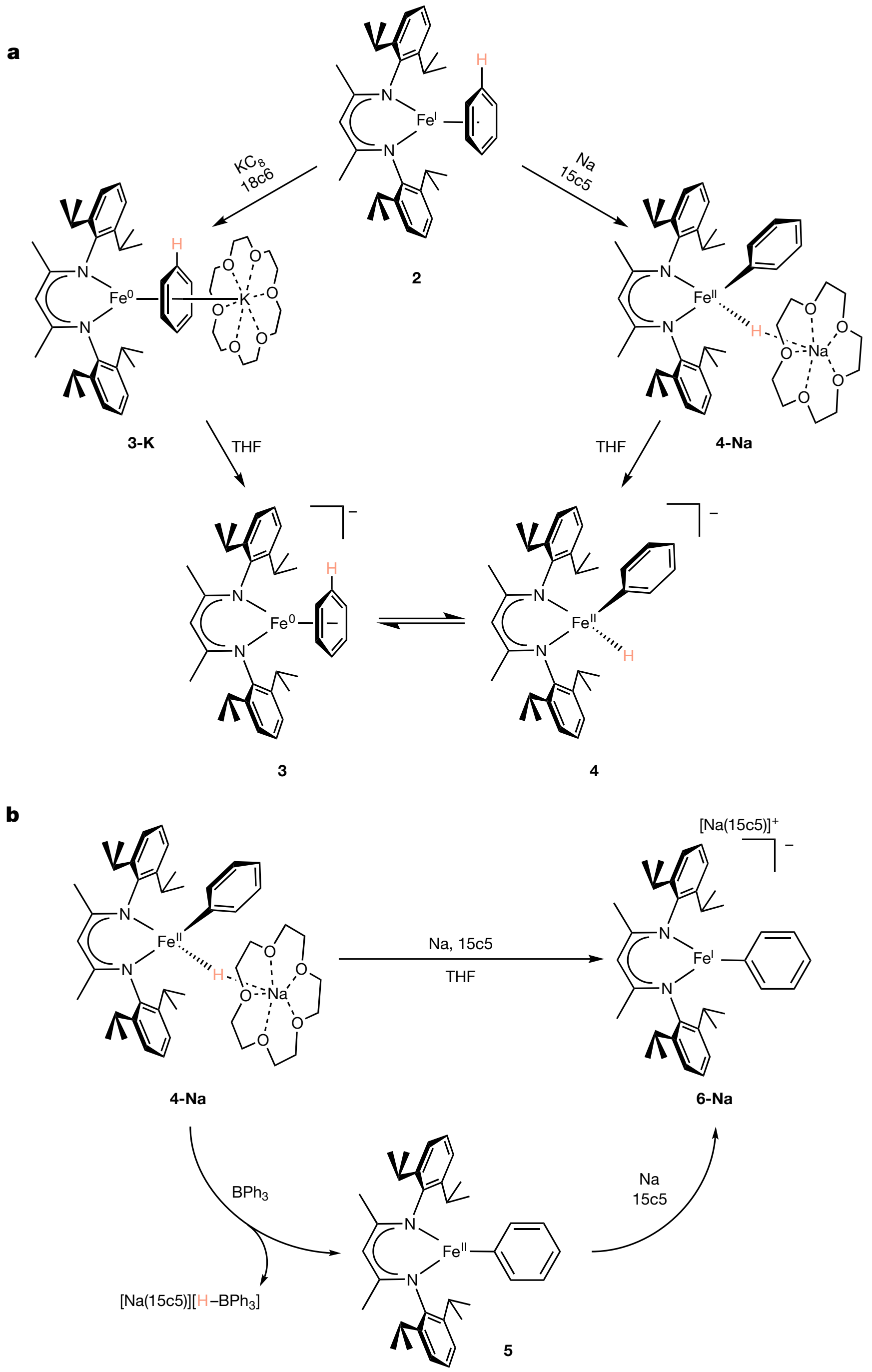

Fig. 2 | Activation of benzene. a, Reduction of **2** with KC$_8$/18c6 formed **3-K** (left) and reduction with Na/15c5 formed **4-Na** (right). In THF solvent the cations dissociate, and isomeric anions **3** and **4** are in equilibrium. **b**, Conversion of **4-Na** to **6-Na** occurred spontaneously in 18% yield (top pathway) but gave a higher yield of 75% with the hydride acceptor BPh$_3$ (bottom pathway), suggesting that hydride loss is probably the main reaction pathway.

benzene complex LFe(η^6-C$_6$H$_6$) (**2**)[20]. Figure 2 shows the structure of **2** and illustrates the β-diketiminate ligand L, which controls the coordination environment of iron[21]. Reduction of **2** with KC$_8$ in the presence of 18-crown-6 (18c6) at room temperature led to the isolable, purple iron(0) complex LFe(η^4-C$_6$H$_6$)K(18c6) (**3-K**)[2]. When **2** was reduced with Na and 15-crown-5 (15c5) in benzene, the product was the red iron(II) complex LFe(H)(Ph)Na(15c5) (**4-Na**), in which a C–H bond of benzene is broken to give an iron(II) complex with phenyl and hydride groups on the iron (Supplementary Fig. 50). Thus, **3-K** and **4-Na** have isomeric anions (bottom of Fig. 2a). Mössbauer spectra of solid **3-K** and **4-Na** (Supplementary Figs. 23–25) support this difference, and density functional theory (DFT) studies indicate that the molecules have high-spin electronic configurations (spin states are $S = 1$ for **3-K** and $S = 2$ for **4-Na**). This is a rare case of room-temperature C–H activation using a high-spin iron complex[22,23]. Reduction of **2** with Na and 15c5 in toluene similarly gave LFe(H)(Tol)Na(15c5), from activation of the aryl C–H bonds of the solvent. The X-ray crystal structure refined best to a 61:39 mixture of *meta* and *para* isomers (Supplementary Fig. 54).

The solution ^{1}H nuclear magnetic resonance (NMR) spectra of **3-K** and **4-Na** in C$_6$D$_6$ showed a few peaks that disappeared over several hours, suggesting that these benzene or phenyl groups exchange with C$_6$D$_6$. Additionally, a minor component was observed in the ^{1}H NMR spectrum of the C$_6$D$_6$ solutions of **3-K** that resembled those of **4-Na**, and vice versa. These observations suggested that the arene-bound iron(0) complex **3** and the C–H activated iron(II) complex **4** are in equilibrium with one another, and the iron(0) arene isomer (**3**) predominates with $K(18c6)^+$, whereas the oxidatively added iron(II) phenyl hydride isomer (**4**) predominates with $Na(15c5)^+$ (see Supplementary Tables 7, 8). This hypothesis was supported by solution studies in tetrahydrofuran (THF), a solvent that can disrupt the interactions with the alkali metal. Dissolving either purified **3-K** or purified **4-Na** in THF gave mixtures with characteristic peaks of both isomers **3** and **4** in ^{1}H NMR and Mössbauer spectra (Supplementary Figs. 9, 26). The ability of each isomer to produce the other one demonstrates that there is reversible oxidative addition of the aryl C–H bond of **3** to form **4**.

Purple THF solutions of LFe(H)(Ph)Na(15c5) (**4-Na**) turned green after standing at room temperature for several hours, and ^{1}H NMR spectra showed formation of the iron(I) phenyl complex [LFePh][Na(15c5)] (**6-Na**) (Fig. 2b). Although the formation of **6-Na** from **4-Na** corresponds to formal loss of H•, the spectroscopic yield of **6-Na** from **4-Na** in THF was only 18% (Supplementary Fig. 17), and the best yield of **6-Na** (44%) came from addition of excess 15c5 and Na to **2** in diethyl ether (Supplementary Fig. 18). These results suggest that the reaction could proceed through a disproportionation pathway. In a mechanistically revealing experiment, **4-Na** transferred the hydride to triphenylborane (BPh_3) to give the previously characterized[24] **5** and [Na(15c5)][$HBPh_3$] (Supplementary Figs. 19, 20) in a higher yield of 75%. Therefore, it is possible that in the presence of excess reducing agent, **4-Na** can similarly lose hydride to give **5**, which is subsequently reduced by **3** or by Na to give the observed **6-Na**.

Next, we explored N_2 binding. Cooling a solution of **6-Na** in THF under an atmosphere of N_2 led to changes in the electronic absorption (ultraviolet–visible; UV-vis) spectrum (Fig. 3a) and the Mössbauer spectrum (Fig. 3b) that did not occur in control experiments under argon. Van't Hoff analysis of the UV-vis data for **6-Na** gave $\Delta H = -17 \pm 2$ kJ mol^{-1} and $\Delta S = -55 \pm 10$ J K^{-1} mol^{-1} (Supplementary Fig. 40; ΔH is the enthalpy change, ΔS is the entropy change; uncertainties represent standard deviations), which are consistent with the binding of N_2. To obtain crystallographic verification of N_2 binding, we cooled a concentrated sample of the potassium analogue **6-K** at −78 °C for 3 h, which led to crystals of the N_2 complex **7-K**. The X-ray crystal structure of this potassium salt of **7** (Fig. 4, bottom) demonstrates end-on binding of the N_2 unit and a pseudotetrahedral geometry at the iron(I) site, and the spectroscopic similarity to the Na system (Supplementary Figs. 36–39) indicates that **7-Na** has a similar structure.

Next, we silylated the N_2 ligand that had been activated through Fe coordination. Treating a cold solution of **7-K** with 2 equivalents (equiv.) of Me_3SiX (X = Br, I) formed the hydrazido complex LFe(N(Ph)N($SiMe_3$)$_2$) (**8**). To our knowledge, the transformation of **7** to **8** is the first crystallographically verified example of the migration of a hydrocarbyl group from a metal to the α position of N_2 (refs. [25,26]). This is the key C–N bond-forming step during the formation of silylated anilines (Fig. 1), which differs from the previously used attacks on bound N_2 by carbon electrophiles.

Although we did not detect any intermediates during the conversion of **7** to **8**, the treatment of a cold solution of **7-K** with 0.5 molar equivalents of the bulkier triisopropylsilyl triflate (TIPSOTf; OTf = SO_3CF_3) gave the formally iron(II) diazenido complex **9**, in which the N_2 is singly silylated while the phenyl group remains bound to the iron (Supplementary Fig. 55). The conversion of **7** to **9** is accompanied by a similar yield of the iron(II) complex **5**, which results from half of **7** acting as a reducing agent. Considering this stoichiometry, the formation of **9** occurs in 67% yield. The isolation of **9**, in which the phenyl has not migrated, suggests that the initial silylation of the β position of the coordinated N_2 in **7** takes place before the migration of the aryl group. It is likely that the second silylation induces the aryl migration, because a recent study[27] reported the migration of H from an iron centre to the α position of a doubly silylated N_2 group to form an iron disilylhydrazido complex. Accordingly, addition of excess trimethylsilyl triflate (Me_3SiOTf) and excess Na to **9** gave a 14% yield of PhN($SiMe_3$)$_2$, showing that addition of a second silyl group can initiate C–N bond formation. This could be because the second silylation leads to a formally iron(IV) complex with an Fe=N double bond, a migration that is reminiscent of alkyl migration to N in an imidoiron(IV) complex[28].

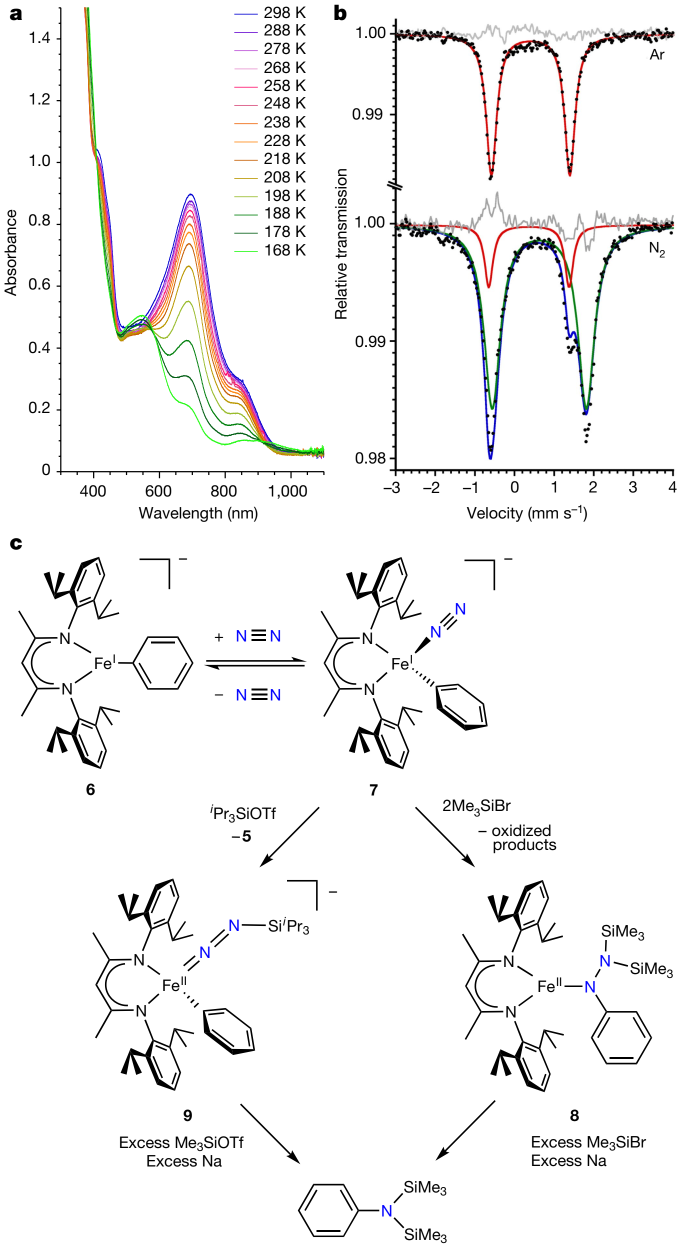

Fig. 3 | Binding and functionalization of N_2. **a**, Electronic absorption spectra of **6-Na** in THF solution at various temperatures under 1 atm N_2, demonstrating the formation of **7-Na** at lower temperatures. The data for **6-K** are similar (Supplementary Fig. 37). **b**, ^{57}Fe Mössbauer spectra at 80 K. The black circles are the data from samples of **6-K** in THF solution frozen under 1 atm Ar (top) and 1 atm N_2 (bottom), demonstrating the formation of a new doublet attributed to the N_2 complex **7-K** (green subspectrum) in addition to some remaining **6-K** (red subspectrum). The blue line is the sum of the green and red fits, and the grey lines are the residuals between the fits and the data. **c**, Illustration of the equilibrium of **6** and N_2 to form **7**. In a key transformation, silylation of the bound N_2 in **7** induces migration of the phenyl group to the N_2 fragment, giving **8**. When a bulkier silyl group is used, it is possible to isolate the singly silylated species **9**, which can subsequently form C–N bonds. Each of the iron species is characterized through X-ray crystallography (Fig. 4, Supplementary Figs. 50–55).

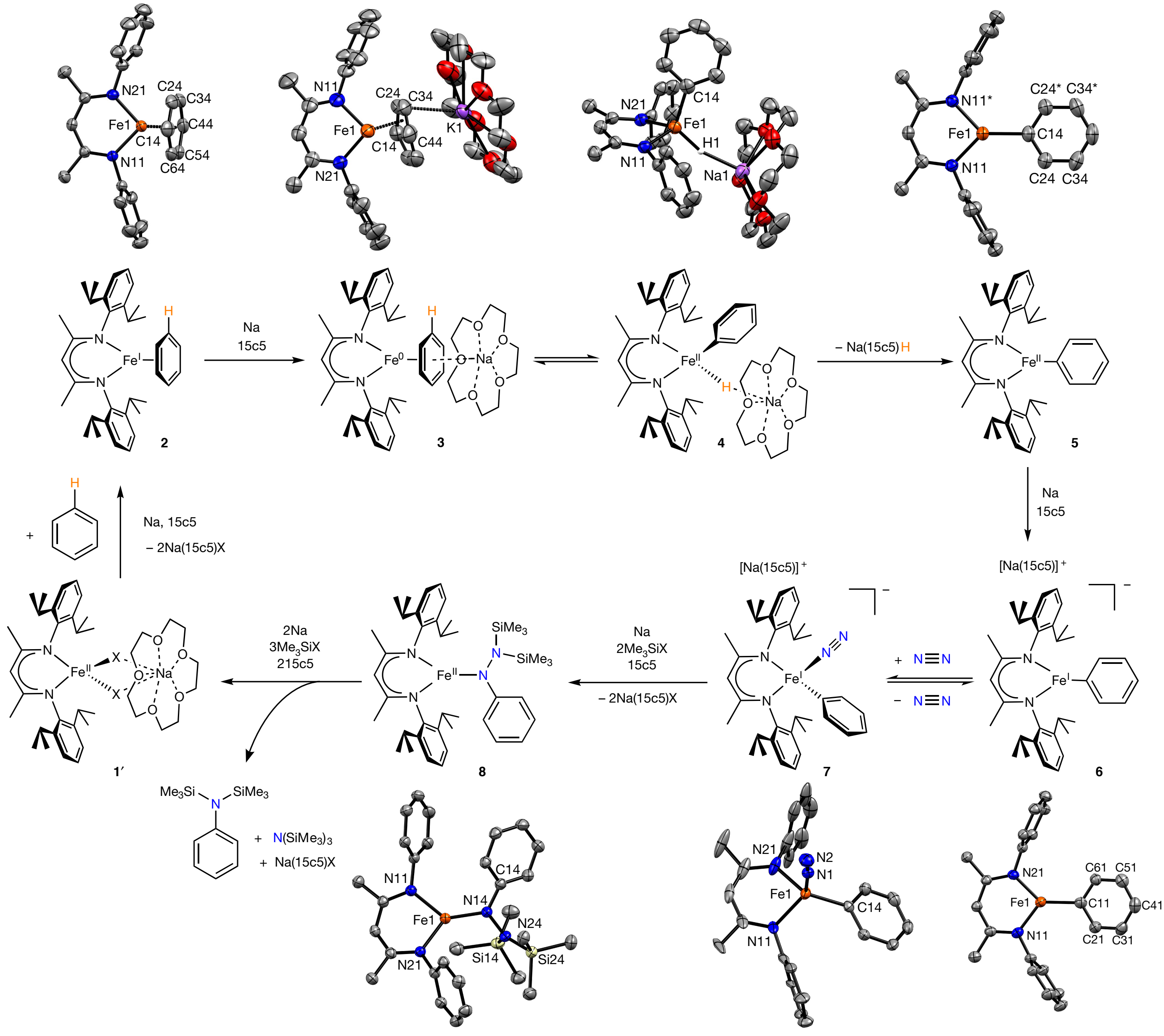

Fig. 4 | Proposed cyclic reaction mechanism for the conversion of N$_2$ and benzene to aniline, mediated by iron β-diketiminate complexes. Thermal ellipsoid plots of the isolated intermediates (and the K analogue of **3**) are shown at the top and bottom (for ionic compounds, only the anion is shown). Most hydrogen atoms and isopropyl groups are omitted from the thermal ellipsoid plots for clarity.

The conversion of **8** to the silylated aniline and amine occurred upon the addition of 1 equiv. KC$_8$ and 2 equiv. Me$_3$SiX (X = Br, I) to solutions of **8**; this treatment led to mixtures containing PhN(SiMe$_3$)$_2$, PhN(SiMe$_3$)N(SiMe$_3$)$_2$ and N(SiMe$_3$)$_3$ within 30 min, either at room temperature or at −100 °C. By contrast, **8** did not react with 2 equiv. Me$_3$SiBr alone within 3 days at room temperature. This result suggests that reduction precedes the electrophilic attack of silyl groups on **8**; alternatively, this final step could involve the formation of Me$_3$Si• radicals[28–30]. Other studies have also reported on the reductive silylation of disilylhydrazido complexes[30,31].

After release of the silylated nitrogen products from **8**, the large excess of bromide is expected to give iron(II) bromide species that are poised to be reduced with further arene binding. This suggests the feasibility of a cyclic process (Fig. 4) in a single pot, which forms silylated anilines from arenes and N$_2$. However, the C–H activation and hydride loss to reform complex **6** requires room-temperature treatment with Na, and at this temperature Na degrades Me$_3$SiBr. Further, N$_2$ binds to **6** at low temperatures. Thus, we treated **8** with Na (25 equiv.), benzene (20 equiv.), Me$_3$SiBr (6 equiv.) and 15c5 (5 equiv.) at −100 °C in diethyl ether, then warmed it to room temperature for 1 h, then cooled it again and treated it with additional Me$_3$SiBr (6 equiv.). This led to a 92% yield of PhN(SiMe$_3$)$_2$ and a 135% yield of N(SiMe$_3$)$_3$ (yields versus Fe). To verify that the overall process is indeed cyclic, **8** was treated under the same conditions with added toluene in place of benzene. Analysis of the organic reaction products after two cycles of Me$_3$SiBr addition showed a 163% yield of N(SiMe$_3$)$_3$, a 62% yield of PhN(SiMe$_3$)$_2$ and a 16% yield of (tolyl)N(SiMe$_3$)$_2$ (both *meta* and *para* isomers). The ability of the phenylhydrazido complex to give products from toluene amination demonstrates that the iron-containing products of the hydrazido reduction can activate toluene and continue to another reaction cycle, although the yields are low.

To test the overall cycle, we reacted the easily prepared iron(II) complex **1** with 30 molar equivalents (equivalents relative to [Fe]) of Na, 20 equiv. C$_6$H$_6$ and 5 equiv. 15c5 at ambient temperature in diethyl ether,

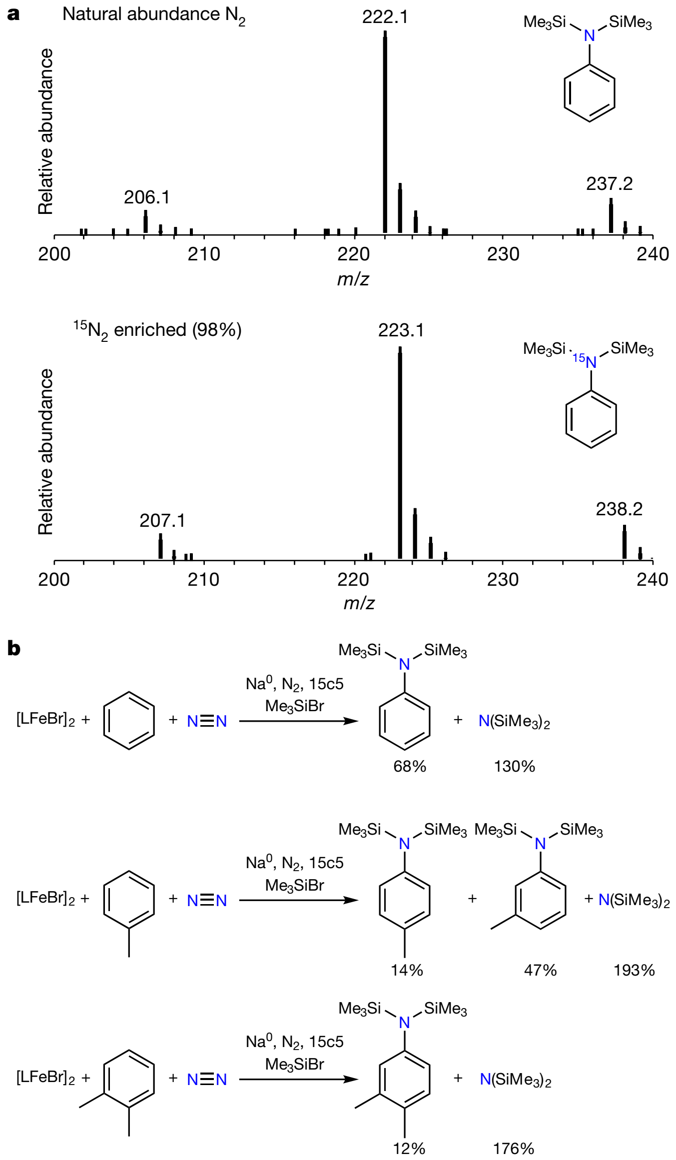

Fig. 5 | Aniline products from amination of arenes with N_2. **a**, Mass spectra of $PhN(SiMe_3)_2$ products from the reaction under 1 atm of natural-abundance N_2 (top) and under 1 atm of $^{15}N_2$ (bottom), showing that the nitrogen atom in the product derives from N_2. **b**, Yields (relative to Fe) of N-containing products obtained during N_2-based amination of different arenes, using five cycles of Me_3SiBr addition (2 equiv. per cycle).

followed by addition of 6 equiv. trimethylsilyl bromide (Me_3SiBr) at −108 °C, which afforded $PhN(SiMe_3)_2$ in a yield of 24% per iron atom, as determined by gas chromatography. The yield of the reaction could be increased by adding Me_3SiBr in one portion per temperature cycle. First, a mixture of **1**, 35 equiv. Na, 20 equiv. benzene and 5 equiv. 15c5 in diethyl ether was stirred vigorously for 1.5 h at room temperature until it became green, corresponding to the colour of **6**. Cooling the mixture to −108 °C under 1 atm N_2 resulted in a colour change to dark red, corresponding to **7**. Then, addition of 2 equiv. Me_3SiBr (per iron atom) to this cold solution and warming to room temperature for 1 h resulted in another green reaction mixture, suggesting that **6** was regenerated. Cooling again caused the same colour change to red (**7**), and more Me_3SiBr was then added in a second cycle. Repeating 10 cooling–silylation–warming cycles with 2 equiv. Me_3SiBr per cycle gave a cumulative yield of (85 ± 14)% $PhN(SiMe_3)_2$ (versus Fe; average and standard deviation of six trials; Supplementary Table 1). The ability to produce more product with repeated Me_3SiBr additions suggests a cyclic process, albeit one in which a substantial amount of the active species decomposes in each cycle. Although aniline formation was attenuated with repeated cycles, the yield of $N(SiMe_3)_3$ continued to increase with the number of additions of Me_3SiBr, reaching (380 ± 41)% (versus Fe) (Supplementary Figs. 1, 2). Under the same conditions but in the absence of benzene, no $PhN(SiMe_3)_2$ was produced, but a similar catalytic yield of $N(SiMe_3)_3$ was observed. Neither product was detected in the absence of **1**. These results suggest that the iron decomposition products lose the ability to aminate benzene but remain able to silylate N_2 to $N(SiMe_3)_3$—a more frequent reaction that has been reported with other homogeneous catalysts and decomposition products[32–40].

Isotope labelling experiments were used to verify that the aniline product arises from benzene and N_2. When performing the reaction under an atmosphere of $^{15}N_2$, gas chromatography coupled with mass spectrometry indicated the formation of $Ph^{15}N(SiMe_3)_2$ and $^{15}N(SiMe_3)_3$ (Fig. 5a), demonstrating that N_2 is the source of the N atoms. Performing the reaction with C_6D_6 as the arene substrate gave $(C_6D_5)N(SiMe_3)_2$, showing that benzene is the source of the phenyl group. The reaction with an equimolar mixture of C_6H_6 and C_6D_6 gave a 1:1 mixture of $(C_6H_5)N(SiMe_3)_2$ and $(C_6D_5)N(SiMe_3)_2$ (Fig. 5b), but partially deuterated 1,3,5-d_3-benzene gave $(C_6H_2D_3)N(SiMe_3)_2$ and $(C_6H_3D_2)N(SiMe_3)_2$ in a ratio of 2.01 ± 0.05, indicating a normal primary kinetic isotope effect for the C–H cleavage step. The difference between the intramolecular and the intermolecular isotope effects[41] indicates that arene binding/exchange is not much more rapid than the irreversible step after C–H cleavage, which is qualitatively consistent with the timescales of the experiments described above with the **3**/**4** equilibrium (which is established over 1–2 h in diethyl ether) and the formation of **6** (which takes a few hours).

Other arene substrates were also tested using 5 cycles of Me_3SiBr addition (Fig. 5c), with a yield of benzene to $PhN(SiMe_3)_2$ of (68 ± 4)% per iron. Toluene gave a mixture of (*m*-tolyl)$N(SiMe_3)_2$ and (*p*-tolyl)$N(SiMe_3)_2$ in a 3:1 ratio with a total yield of (61 ± 7)% per iron. The overall yield is similar to that for benzene, and the ratio of isomers is comparable to that observed in the crystal of LFe(H)(Tol)Na(15c5) (Supplementary Fig. 54). When *o*-xylene was used, a (12 ± 2)% yield of *N*,*N*-bis(trimethylsilyl-3,4-xylidine) was observed. These silylated aniline products could be hydrolysed to the deprotected anilines with weak aqueous acid when desired. Arenes with easily reducible functionalities—such as aryl halides, aryl ethers and polycyclic aromatics—did not give aminated products. Formation of the silylated aniline and $N(SiMe_3)_3$ also occurred with other Me_3SiX reagents (X = Cl, I, OTf), although the reaction gave the highest yields with Me_3SiBr.

The strategy outlined here differs fundamentally from previously described strategies for the formation of C–N bonds from N_2. Typically, carbon electrophiles have been used to create C–N bonds, either from N_2 (refs. [11,13,42–45]) or nitrides that result from cleavage of N_2 (refs. [15–17,46]). In the proposed reaction, silylation plays a key part by making the coordinated N_2 sufficiently reactive to accept the migrating aryl group from the metal centre. The silylated amines that are formed can be used in further synthetic steps or can be deprotected to the parent anilines using mild aqueous acid. In this method, the C–N bond comes from the migration of a hydrocarbyl from a metal to a N_2-derived group, a strategy that has been used in few stoichiometric C–N bond formation reactions[18,47]. The ability of these iron complexes to generate a hydrocarbyl group on the iron through C–H activation, and then transfer it to an activated N_2, provides a new tactic for coupling hydrocarbons to N atoms from atmospheric N_2, combining the powers of these bond-cleaving reactions.

Online content

Any methods, additional references, Nature Research reporting summaries, source data, extended data, supplementary information, acknowledgements, peer review information; details of author contributions and competing interests; and statements of data and code availability are available at https://doi.org/10.1038/s41586-020-2565-5.

1. Kim, S., Loose, F. & Chirik, P. J. Beyond ammonia: nitrogen-element bond forming reactions with coordinated dinitrogen. *Chem. Rev*. **120**, 5637–5681 (2020).
2. McWilliams, S. F. et al. Effects of N_2 binding mode on iron-based functionalization of dinitrogen to form an iron(III) hydrazido complex. *J. Am. Chem. Soc*. **140**, 8586–8598 (2018).
3. Schlögl, R. in *Handbook of Heterogeneous Catalysis* Vol. 5 2501–2575 (Wiley, 2008).
4. Burgess, B. K. & Lowe, D. J. Mechanism of molybdenum nitrogenase. *Chem. Rev*. **96**, 2983–3012 (1996).
5. Hoffman, B. M., Lukoyanov, D., Yang, Z. Y., Dean, D. R. & Seefeldt, L. C. Mechanism of nitrogen fixation by nitrogenase: the next stage. *Chem. Rev*. **114**, 4041–4062 (2014).
6. Schrock, R. R. Catalytic reduction of dinitrogen to ammonia at a single molybdenum center. *Acc. Chem. Res*. **38**, 955–962 (2005).
7. Chalkley, M. J., Del Castillo, T. J., Matson, B. D., Roddy, J. P. & Peters, J. C. Catalytic N_2-to-NH_3 conversion by Fe at lower driving force: a proposed role for metallocene-mediated PCET. *ACS Cent. Sci*. **3**, 217–223 (2017).
8. Nishibayashi, Y. Development of catalytic nitrogen fixation using transition metal-dinitrogen complexes under mild reaction conditions. *Dalton Trans*. **47**, 11290–11297 (2018).
9. Chen, J. G. et al. Beyond fossil fuel–driven nitrogen transformations. *Science* **360**, eaar6611 (2018).
10. Andino, J. G., Mazumder, S., Pal, K. & Caulton, K. G. New approaches to functionalizing metal-coordinated N_2. *Angew. Chem. Int. Ed*. **52**, 4726–4732 (2013).
11. Hidai, M. & Mizobe, Y. Recent advances in the chemistry of dinitrogen complexes. *Chem. Rev*. **95**, 1115–1133 (1995).
12. MacKay, B. A. & Fryzuk, M. D. Dinitrogen coordination chemistry: on the biomimetic borderlands. *Chem. Rev*. **104**, 385–402 (2004).
13. Mori, M. Activation of nitrogen for organic synthesis. *J. Organomet. Chem*. **689**, 4210–4227 (2004).
14. Keane, A. J., Farrell, W. S., Yonke, B. L., Zavalij, P. Y. & Sita, L. R. Metal-mediated production of isocyanates, R_3ENCO from dinitrogen, carbon dioxide, and R_3ECl. *Angew. Chem. Int. Ed*. **54**, 10220–10224 (2015).
15. Figueroa, J. S., Piro, N. A., Clough, C. R. & Cummins, C. C. A nitridoniobium(V) reagent that effects acid chloride to organic nitrile conversion: synthesis via heterodinuclear (Nb/Mo) dinitrogen cleavage, mechanistic insights, and recycling. *J. Am. Chem. Soc*. **128**, 940–950 (2006).
16. Curley, J. J., Cozzolino, A. F. & Cummins, C. C. Nitrogen fixation to cyanide at a molybdenum center. *Dalton Trans*. **40**, 2429–2432 (2011).
17. Klopsch, I., Kinauer, M., Finger, M., Würtele, C. & Schneider, S. Conversion of dinitrogen into acetonitrile under ambient conditions. *Angew. Chem. Int. Ed*. **55**, 4786–4789 (2016).
18. Kakiuchi, F. & Chatani, N. Catalytic methods for C-H bond functionalization: application in organic synthesis. *Adv. Synth. Catal*. **345**, 1077–1101 (2003).
19. Davies, H. M. L., Du Bois, J. & Yu, J.-Q. C–H functionalization in organic synthesis. *Chem. Soc. Rev*. **40**, 1855–1856 (2011).
20. Smith, J. M. et al. Studies of low-coordinate iron dinitrogen complexes. *J. Am. Chem. Soc*. **128**, 756–769 (2006).
21. Holland, P. L. Electronic structure and reactivity of three-coordinate iron complexes. *Acc. Chem. Res*. **41**, 905–914 (2008).
22. Kalman, S. E. et al. Facile and regioselective C–H bond activation of aromatic substrates by an Fe(II) complex involving a spin-forbidden pathway. *Organometallics* **32**, 1797–1806 (2013).
23. Hickey, A. K., Lutz, S. A., Chen, C.-H. & Smith, J. M. Two-state reactivity in C–H activation by a four-coordinate iron(0) complex. *Chem. Commun*. **53**, 1245–1248 (2017).
24. Yu, Y., Brennessel, W. W. & Holland, P. L. Borane B–C bond cleavage by a low-coordinate iron hydride complex and N–N bond cleavage by the hydridoborate product. *Organometallics* **26**, 3217–3226 (2007).
25. Sellmann, D. & Weiss, W. First reaction of dinitrogen ligands with bases: reduction of coordinated dinitrogen by nucleophilic attack. *Angew. Chem*. **89**, 918–919 (1977).
26. Sellmann, D. & Weiss, W. Consecutive nucleophilic and electrophilic attack on nitrogen ligands: synthesis of azomethane from molecular nitrogen. *Angew. Chem*. **90**, 295–296 (1978).
27. Deegan, M. M. & Peters, J. C. Electrophile-promoted Fe-to-N_2 hydride migration in highly reduced $Fe(N_2)(H)$ complexes. *Chem. Sci*. **9**, 6264–6270 (2018).
28. Jacobs, B. P., Wolczanski, P. T., Jiang, Q., Cundari, T. R. & MacMillan, S. N. Rare examples of Fe(IV) alkyl-imide migratory insertions: impact of Fe–C covalency in $(Me_2IPr)Fe(=NAd)R_2$. *J. Am. Chem. Soc*. **139**, 12145–12148 (2017).
29. Nishibayashi, Y. Recent progress in transition-metal-catalyzed reduction of molecular dinitrogen under ambient reaction conditions. *Inorg. Chem*. **54**, 9234–9247 (2015).
30. Siedschlag, R. B. et al. Catalytic silylation of dinitrogen with a dicobalt complex. *J. Am. Chem. Soc*. **137**, 4638–4641 (2015).
31. Piascik, A. D., Li, R., Wilkinson, H. J., Green, J. C. & Ashley, A. E. Fe-catalyzed conversion of N_2 to $N(SiMe_3)_3$ via an Fe-hydrazido resting state. *J. Am. Chem. Soc*. **140**, 10691–10694 (2018).
32. Tanabe, Y. & Nishibayashi, Y. Recent advances in catalytic silylation of dinitrogen using transition metal complexes. *Coord. Chem. Rev*. **389**, 73–93 (2019).
33. Lee, Y., Mankad, N. P. & Peters, J. C. Triggering N_2 uptake via redox-induced expulsion of coordinated NH_3 and N_2 silylation at trigonal bipyramidal iron. *Nat. Chem*. **2**, 558–565 (2010).
34. Tanaka, H. et al. Molybdenum-catalyzed transformation of molecular dinitrogen into silylamine: experimental and DFT study on the remarkable role of ferrocenyldiphosphine ligands. *J. Am. Chem. Soc*. **133**, 3498–3506 (2011).
35. Yuki, M. et al. Iron-catalysed transformation of molecular dinitrogen into silylamine under ambient conditions. *Nat. Commun*. **3**, 1254 (2012).
36. Liao, Q., Saffon-Merceron, N. & Mézailles, N. N_2 reduction into silylamine at tridentate phosphine/Mo center: catalysis and mechanistic study. *ACS Catal*. **5**, 6902–6906 (2015).
37. Liao, Q., Cavaillé, A., Saffon-Merceron, N. & Mézailles, N. Direct synthesis of silylamine from N_2 and a silane mediated by a tridentate phosphine molybdenum fragment. *Angew. Chem. Int. Ed*. **55**, 11212–11216 (2016).
38. Prokopchuk, D. E. et al. Catalytic N_2 reduction to silylamines and thermodynamics of N_2 binding at square planar Fe. *J. Am. Chem. Soc*. **139**, 9291–9301 (2017).
39. Suzuki, T. et al. Efficient catalytic conversion of dinitrogen to $N(SiMe_3)_3$ using a homogeneous mononuclear cobalt complex. *ACS Catal*. **8**, 3011–3015 (2018).
40. Ferreira, R. B. et al. Catalytic silylation of dinitrogen by a family of triiron complexes. *ACS Catal*. **8**, 7208–7212 (2018).
41. Gómez-Gallego, M. & Sierra, M. A. Kinetic isotope effects in the study of organometallic reaction mechanisms. *Chem. Rev*. **111**, 4857–4963 (2011).
42. Betley, T. A. & Peters, J. C. Dinitrogen chemistry from trigonally coordinated iron and cobalt platforms. *J. Am. Chem. Soc*. **125**, 10782–10783 (2003).
43. Bernskoetter, W. H., Olmos, A. V., Pool, J. A., Lobkovsky, E. & Chirik, P. J. N–C bond formation promoted by a hafnocene dinitrogen complex: comparison of zirconium and hafnium congeners. *J. Am. Chem. Soc*. **128**, 10696–10697 (2006).
44. Knobloch, D. J., Lobkovsky, E. & Chirik, P. J. Dinitrogen cleavage and functionalization by carbon monoxide promoted by a hafnium complex. *Nat. Chem*. **2**, 30–35 (2010).
45. Moret, M.-E. & Peters, J. C. N_2 functionalization at iron metallaboratranes. *J. Am. Chem. Soc*. **133**, 18118–18121 (2011).
46. MacLeod, K. C. et al. Alkali-controlled C–H cleavage or N–C bond formation by N_2-derived iron nitrides and imides. *J. Am. Chem. Soc*. **138**, 11185–11191 (2016).
47. Morello, L., Love, J. B., Patrick, B. O. & Fryzuk, M. D. Carbon-nitrogen bond formation via the reaction of terminal alkynes with a dinuclear side-on dinitrogen complex. *J. Am. Chem. Soc*. **126**, 9480–9481 (2004).

Data availability

Materials and methods, experimental procedures, useful information, spectra and mass spectrometry data are available in Supplementary Information. Raw data are available from the corresponding author on reasonable request. The crystallographic datasets generated during the current study are publicly available from the Cambridge Crystallographic Data Centre (CCDC) repository at https://www.ccdc.cam.ac.uk/structures/ with CCDC numbers 1937999, 1978000, 1938001, 1938002, 1939265, 1939266 and 1966313.

Acknowledgements This research was supported by the US Department of Energy, Office of Science, Office of Basic Energy Sciences, Catalysis Program under award DE-SC0020315 (final phases of the work), and by the National Institutes of Health under award R01 GM-065313 (initial phases of the work). Additional fellowship support came from the National Institutes of Health (F31 GM-116463 to S.F.M.), the Netherlands Organization for Scientific Research (Rubicon Postdoctoral Fellowship 680-50-1517 to D.L.J.B.) and the EPSRC Centre for Doctoral Training in Critical Resource Catalysis (internship for C.J.V.H.). This work was supported in part by the facilities and staff of the Yale University Faculty of Arts and Sciences High Performance Computing Center, which was partially funded by the National Science Foundation under award CNS-08-21132. We thank N. Hazari, J. Mayer, J. Ellman and K. Skubi for critical feedback on the manuscript.

Author contributions S.F.M., D.L.J.B. and P.L.H. conceived the ideas and designed the experiments. S.F.M., D.L.J.B., C.J.V.H. and S.M.B. performed the experiments. B.Q.M. performed crystallographic measurements and interpretation. S.F.M., D.L.J.B. and P.L.H. wrote the manuscript.

Competing interests The authors declare no competing interests.

Additional information

Supplementary information is available for this paper at https://doi.org/10.1038/s41586-020-2565-5.

Correspondence and requests for materials should be addressed to P.L.H.

Heat and carbon coupling reveals ocean warming due to circulation changes

https://doi.org/10.1038/s41586-020-2573-5

Received: 24 January 2020

Accepted: 2 June 2020

Ben Bronselaer[1,2,3,4] ✉ & Laure Zanna[1,5]

Anthropogenic global surface warming is proportional to cumulative carbon emissions[1–3]; this relationship is partly determined by the uptake and storage of heat and carbon by the ocean[4]. The rates and patterns of ocean heat and carbon storage are influenced by ocean transport, such as mixing and large-scale circulation[5–10]. However, existing climate models do not accurately capture the observed patterns of ocean warming, with a large spread in their projections of ocean circulation and ocean heat uptake[8,11]. Additionally, assessing the influence of ocean circulation changes (specifically, the redistribution of heat by resolved advection) on patterns of observed and simulated ocean warming remains a challenge. Here we establish a linear relationship between the heat and carbon uptake of the ocean in response to anthropogenic emissions. This relationship is determined mainly by intrinsic parameters of the Earth system—namely, the ocean carbon buffer capacity, the radiative forcing of carbon dioxide and the carbon inventory of the ocean. We use this relationship to reveal the effect of changes in ocean circulation from carbon dioxide forcing on patterns of ocean warming in both observations and global Earth system models from the Fifth Coupled Model Intercomparison Project (CMIP5). We show that historical patterns of ocean warming are shaped by ocean heat redistribution, which CMIP5 models simulate poorly. However, we find that projected patterns of heat storage are primarily dictated by the pre-industrial ocean circulation (and small changes in unresolved ocean processes)—that is, by the patterns of added heat owing to ocean uptake of excess atmospheric heat rather than ocean warming by circulation changes. Climate models show more skill in simulating ocean heat storage by the pre-industrial circulation compared to heat redistribution, indicating that warming patterns of the ocean may become more predictable as the climate warms.

The increase in emissions of anthropogenic greenhouse gases such as CO_2 has led to rising atmospheric temperatures since pre-industrial times. The ocean absorbs most of the excess heat and some of the excess carbon, mitigating atmospheric warming[12]. However, the storage of heat and carbon by the ocean leads to adverse regional effects such as sea-level rise, coral bleaching and ocean acidification[8,10,13–16]. Ocean transport affects both global and regional ocean temperature and also carbon changes[9,17]. In particular, changes in ocean transport can shape ocean warming patterns[5,7,8,10]. Yet, directly assessing the effects of changing ocean currents on ocean warming both in observations and also in climate models[8] remains challenging. In addition, there is a lack of agreement between modelled and observed heat storage and also a large spread among different models in the simulated patterns of ocean heat storage—the causes for these discrepancies are difficult to attribute[11]. To diagnose the effect of changes in large-scale ocean circulation (namely, resolved advection) on ocean warming patterns across observations and model ensembles, we here exploit the intrinsic similarities between the ocean's storage of heat and carbon.

Previous studies have shown that changes in global atmospheric surface temperatures are proportional to cumulative CO_2 emissions[1–3]. This emergent linear relationship is driven by the ocean, and the linearity arises in part from the ocean processes that are responsible for the uptake of heat and carbon[4,18] ('uptake' is the absorption of atmospheric anomalies by the ocean, and 'storage' is how these anomalies are stored spatially in the ocean). The result highlights a salient connection between the uptake and storage of heat and carbon in the ocean, setting the transient climate response to CO_2 emissions. Our study aims to quantify how changes in ocean processes and ocean circulation affect the ocean storage of heat and carbon at global and regional scales and we use our findings to establish the origin of ocean warming patterns.

On the global scale, we find that the ratio of heat to carbon uptake by the ocean spans a narrow range across observations, models and scenarios. On the regional scale, patterns of ocean heat and carbon storage are identical if ocean circulation—where 'circulation' herein refers to resolved advection (see below)—is unaltered by anthropogenic climate change, in both a coupled[7] and an ocean-only model. We use

---

[1]Atmospheric, Oceanic and Planetary Physics, University of Oxford, Oxford, UK. [2]Geophysical Fluid Dynamics Laboratory, Princeton, NJ, USA. [3]Department of Geosciences, University of Arizona, Tucson, AZ, USA. [4]Program in Atmospheric and Oceanic Sciences, Princeton University, Princeton, NJ, USA. [5]Courant Institute of Mathematical Sciences, New York University, New York, NY, USA. ✉e-mail: benjamin.bronselaer@cantab.net

these two findings to attribute changes in the patterns of ocean heat storage to ocean circulation changes in an ensemble of coupled climate models and also in observations. We find that circulation changes have a dominant effect on observed heat storage patterns. However, the effect of circulation changes on the patterns of ocean heat storage diminishes as the climate warms over the twenty-first century.

To obtain our results, we initially use two 100-yr-long simulations of the Geophysical Fluid Dynamics Laboratory Earth System Model 2 (GFDL ESM2M) forced with a transient increase of 1% atmospheric CO_2 per year[7] (the 1%CO_2 experiment; see Methods). We analyse the results at the time of doubling of atmospheric CO_2, averaged over years 61–80 of the simulation. One simulation allows ocean currents to evolve freely (the free-circulation experiment) and the other prescribes monthly mean horizontal Eulerian velocities (ocean currents) from a pre-industrial control simulation (the fixed-circulation experiment), removing changes in ocean circulation induced by CO_2 forcing. Throughout this text, we define circulation as the advection by Eulerian velocities only—we therefore do not include parametrizations such as eddy velocities and mixing, which are allowed to vary in the fixed-circulation experiment. However, the changes in the eddy transport and convection in the fixed-circulation experiment are small, except in ice-covered regions (see Extended Data Fig. 1).

As a result of increased CO_2 forcing, excess energy in the climate system is mainly stored in the ocean. In our numerical experiments, the ocean heat storage in the fixed-circulation experiment—the added heat, H_{ad}—represents the storage of excess atmospheric heat as a result of pre-industrial ocean circulation and the changes in sub-grid processes (mixing and mesoscale eddies) owing to increased CO_2 forcing. The ocean heat storage in the free-circulation experiment, H, additionally includes the effect of circulation changes. The difference between the total heat storage H and the added heat $H_{ad,}$ (both owing to anthropogenic climate change), here defined as the redistributed heat, H_r, is thus the redistribution of both the added and pre-industrial (background) heat throughout the ocean by the changing ocean circulation:

$$H = H_{ad} + H_r \qquad (1)$$

Heat redistribution from circulation changes can strongly alter regional patterns of heat storage[5,8,10], and local climate feedback such as from clouds and albedo[7]; however, heat redistribution has little effect on global anthropogenic ocean heat uptake: the difference in global ocean heat uptake between the fixed-circulation and free-circulation experiments is only 4% in ESM2M[7] (this could vary slightly from model to model). A decomposition similar to equation (1) can be applied to any tracer anomaly in the ocean, including the anthropogenic ocean carbon storage, C_{ant}. We here refer to 'anthropogenic' heat and carbon as the anomalies from the pre-industrial state induced by increased atmospheric CO_2 concentration. All anomalies are calculated using 20-yr temporal averages to minimize the effects of natural variability. Given that heat and carbon anomalies are concentrated in the upper ocean[6,7,10], and for comparison with observations, we focus on the top 2,000 m vertically integrated fields. To verify our results from ESM2M, we also conduct similar simulations in an ocean-only model, here the Massachusetts Institute of Technology General Circulation Model (MITgcm), with free-circulation and fixed-circulation experiments, discussed in Methods.

Heat and carbon storage in GFDL ESM2M

In our ESM2M 1%CO_2 simulations, C_{ant} is concentrated in the mid and high latitudes, and is similar in both the free-circulation and fixed-circulation experiments, with a spatial correlation coefficient (CR) of 0.98 (Fig. 1a, b). The ocean redistribution of C_{ant} is negligible compared to the total C_{ant} (ref. [7]). The added heat in the fixed-circulation experiment is also predominantly stored in the mid and high latitudes (Fig. 1e). In the fixed-circulation experiment, added heat is absorbed by the ocean as a result of air–sea exchange and is transported in the interior by background circulation and sub-grid processes. This heat storage H_{ad} is dominated by physical processes such as Ekman pumping and vertical mixing, and is heavily influenced by the pre-industrial stratification[19,20]. However, in the free-circulation experiment, there is noticeably more heat stored in the low latitudes of the Atlantic Ocean compared to in the fixed-circulation experiment, owing to the changing circulation (Fig. 1d)—either a change in gyre transport or overturning circulation[10,17]. Redistribution of heat (H_r) from the changing circulation is evident in all ocean basins, not just in the Atlantic Ocean. The patterns of C_{ant}, in the free-circulation and the fixed-circulation experiments, closely match H_{ad}, with CRs of 0.92 and 0.93, respectively. Additionally, this similarity is evident in ocean-only MITgcm simulations, and also evident when comparing reconstructions of ocean heat and carbon storage using a constant ocean circulation[10,21].

The similarity of C_{ant} and H_{ad} is due to the effect of chemistry on ocean carbon uptake, through the Revelle buffer factor[22]. The spatial pattern of the buffer factor is largely determined by the pattern of the background ocean temperature (see Methods). By contrast, ocean uptake of other tracers such as chlorofluorocarbon (CFC) lacks chemical buffering, such that the ocean CFC storage does not have the same relationship with H_{ad} as C_{ant} does; H_{ad} and C_{ant} therefore have a unique similarity (see Methods for a detailed analysis).

Global heat–carbon coupling

Owing to the unique similarity between the spatial patterns of storage of C_{ant} and H_{ad} in the simulations, the spatial pattern of H_{ad} can be reconstructed using C_{ant} in the free-circulation experiment, without the need for a fixed-circulation experiment. To reconstruct H_{ad}, we require an appropriate time-varying scaling parameter, $\alpha(t)$, such that $H_{ad} = \alpha(t)C_{ant}$. Here, the coefficient α is called the heat–carbon coupling parameter. α can be estimated locally using a regression of C_{ant} onto H_{ad}, although this still requires a fixed-circulation experiment. Although the patterns of ocean heat storage differ between the free-circulation and fixed-circulation experiments, the global integrals of anthropogenic heat and carbon content are nearly unchanged (Fig. 2a)[7]. Therefore, we opt to estimate α globally such that

$$\alpha(t) = \frac{\int H(x, y, t)\mathrm{d}A}{\int C_{ant}(x, y, t)\mathrm{d}A} = \frac{\hat{H}(t)}{\hat{C}_{ant}(t)}, \qquad (2)$$

where $\hat{H}$ and $\hat{C}_{ant}$ are the global spatial integrals of H and C_{ant}, respectively, and A is the surface area of the Earth. The value of α is generally in the range 2×10^7–6×10^7 J mol^{-1} when calculated for different model simulations, scenarios and observations (Fig. 2a). This relatively narrow range of values for α represents a tight coupling between the global ocean anthropogenic uptake of heat and carbon in the climate system.

To understand the leading terms that set the magnitude of α, denoted as $\tilde{\alpha}$, we consider how atmospheric CO_2 changes drive the anthropogenic ocean uptake of heat and carbon. Using the analytic expressions for the dependence of $\hat{H}$ and $\hat{C}_{ant}$ on atmospheric CO_2 (derived in Methods), we can express $\tilde{\alpha}$ as a function of simple parameters of the Earth system. We assume that ocean warming $\hat{H}$ is driven by the radiative forcing imbalance that stems from the strength of CO_2 as a greenhouse gas, F_0 (in W m^{-2}). In addition, we assume that changes in ocean carbon uptake are directly driven by excess atmospheric CO_2 concentration and that C_{ant}, the amount of anthropogenic carbon absorbed by the ocean, is set by the capacity of the ocean to buffer CO_2 anomalies, expressed by the Revelle buffer factor[4,22], R_{DIC} (DIC, dissolved inorganic carbon). A lower value of R_{DIC} and a higher total ocean carbon inventory I_0 can both contribute to a lower capacity for the ocean to absorb additional CO_2. We combine the relationships for the uptake of ocean heat

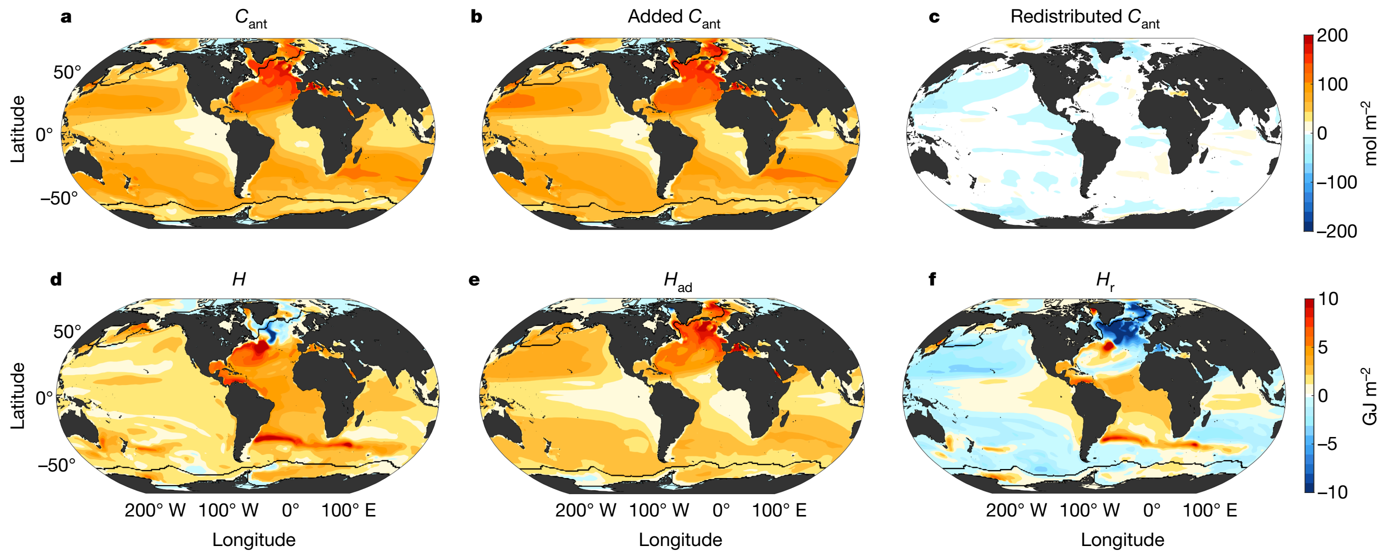

Fig. 1 | Simulated anthropogenic changes in C_{ant} and H. **a–f**, Upper 2,000 m vertically integrated anomalies in years 61–80 of the 1%CO$_2$ ESM2M simulation for tracers C_{ant} (**a**–**c**) and H (**d**–**f**). **a**, **d**, C_{ant} and H relative to the tandem control simulation for the free-circulation experiment. **b**, **e**, Added C_{ant} and added H (H_{ad}) relative to the tandem control simulation fixed-circulation experiments. **c**, **f**, The difference in C_{ant} and H between the free-circulation and fixed-circulation experiments, which is attributed to the changing ocean currents—that is, the redistributed values of C_{ant} and H (that is, H_r). The black line shows the annual-mean maximum sea-ice extent.

and carbon and, by neglecting climate feedback, we obtain an expression for $\tilde{\alpha}$ given by (see Methods):

$$\tilde{\alpha}(t) \approx A\frac{R_{\mathrm{DIC}}F_0}{I_o}\Delta t, \qquad (3)$$

where Δt is the time interval elapsed (see Methods for further details). In ESM2M, the estimated α ($\tilde{\alpha}$) determined by equation (3) is of similar magnitude to the directly obtained α (equation (2)), particularly after the first 20 yr of simulations (during which time natural variability dominates over the anthropogenic response; see Extended Data Fig. 2 and Methods). However, after a few decades, observations and models show little temporal dependence on α (Fig. 2b and Extended Data Fig. 2), probably owing to the importance of the feedback processes that are neglected in equation (3). The observed and modelled constant slope of $\hat{H}$ versus $\hat{C}_{ant}$—that is, α (Fig. 2b)—therefore highlights that the ocean takes up heat at the same rate as it takes up carbon. This relationship is similar to the linear relationship between atmospheric warming and cumulative carbon emissions. Thus we determine that, to first order, the linear relationship between the global uptake of heat and carbon is determined by the capacity of the ocean to take up carbon and the strength of the radiative forcing of CO$_2$.

Past and future heat redistribution

By exploiting this relationship between global heat and carbon uptake, H_{ad} can be locally reconstructed from C_{ant} using $H_{ad}(x,y,t) = \alpha(t)C_{ant}(x,y,t)$, where $\alpha(t)$ (equation (2)) is obtained for each individual simulation or observational product. The global-mean error in ice-free regions for the estimated H_{ad} over the upper 2,000 m of the ocean, compared to the simulated H_{ad} in ESM2M, is 11%. We obtain similar errors using different depth integrals (shown in Fig. 3) or using an ocean-only model (see Methods). We can then infer vertically integrated patterns of redistribution, $H_r(x,y,t)$, as residuals using equation (1). The reconstruction of depth-dependent profiles of zonal-mean heat redistribution is just as accurate below 300 m (Extended Data Fig. 3).

We apply our method to observational products using spatially and temporally varying ocean heat storage (from ref. [23]) and anthropogenic carbon (from ref. [24]), from 1951 to 2011 in the top 2,000 m of the ocean. The storage of anthropogenic heat and carbon is calculated by fitting linear trends locally over the period, multiplied by the time period considered (Fig. 4). We apply the same procedure to 11 Earth system models from the CMIP5 archive with a full carbon cycle. Although there is a large inter-model spread in historical ocean heat storage among CMIP5 simulations (±71%), the CMIP5 ensemble mean agrees well with observations of net global ocean heat storage over the past 40 yr[11]. We use historical and climate change simulations (following the Recommended Concentration Pathway 8.5, RCP8.5) for 1951–2011 and 2011–2060, respectively. We also reconstruct projections of redistributed heat using the 2011–2060 trends from CMIP5 in the RCP8.5 simulations (Fig. 4).

Overall, the CMIP5 models reproduce the observed 1951–2011 added heat storage better than they do the redistributed heat storage; the CR for the observed and simulated mean H_{ad} is 0.83, whereas the CR for observed and simulated H_r is 0.31. However, some features in the spatial patterns of H_r over 1951–2011 are consistent between observations and the CMIP5 simulations, as well as in our ESM2M 1%CO$_2$ simulation; for example, cooling in the Pacific sub-tropical gyres and the Indian Ocean, and warming in the tropics. However, the ensemble mean of the CMIP5 simulations underestimates the strength of tropical redistributed warming compared to the observations, especially in the Atlantic Ocean. This is partly due to inter-model variability. In the Southern Ocean, the observed patterns of warming show substantial contributions from added heat in all three sectors of the Southern Ocean: large redistributed warming in the Atlantic and Indian sectors, and weak cooling in the Pacific sector. The zonally integrated heat storage in the Southern Ocean is dominated by the added heat[25], owing in part to the integration both over the redistributed warming anomalies (in the Atlantic and Indian sectors of the Southern Ocean) and also over the cooling anomalies (in the Pacific sector). The CMIP5 models simulate more redistributed cooling in the Pacific sector of the Southern Ocean compared to observations over the same period, but simulate a weaker redistributed warming feature in the Atlantic and Indian sectors, seen also in the Atlantic zonal mean (see Extended Data Fig. 4).

A key feature of H_r inferred from the observations is the cooling effect of the redistributed heat in the North Atlantic subpolar gyre, consistent

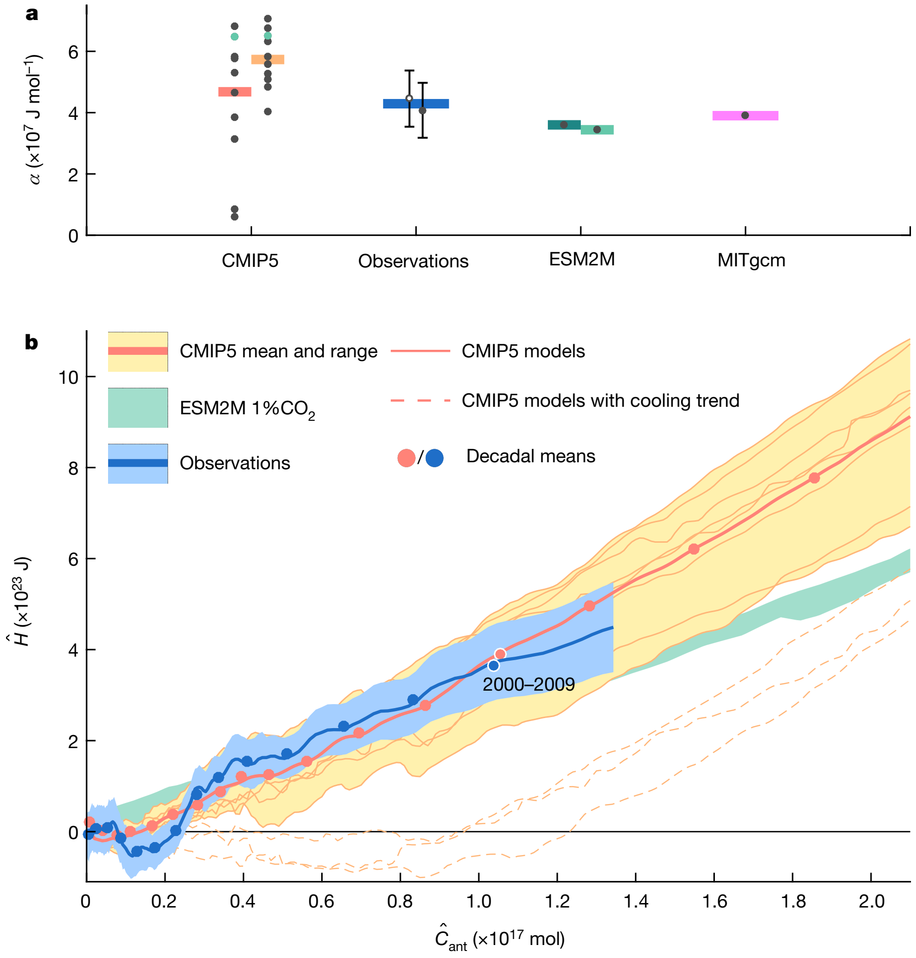

Fig. 2 | Heat–carbon coupling. a, α calculated from (left to right): the 1951–2011 trend in the CMIP5 ensemble historical simulations (ensemble mean in red); the 1951–2060 trend in the CMIP5 ensemble RCP8.5 simulation (ensemble mean in orange); the 1951–2011 trend in observations of ocean heat content (white circle from ref. [10], filled circle from ref. [23]), and in observations of ocean carbon content[24] (mean, blue); our ESM2M 1%CO$_2$ model after 70 yr of the fixed-circulation (dark green) and free-circulation (light green) experiments; and from the perturbed MITgcm simulation after 70 yr (magenta). The grey dots show individual estimates; the green circles show ESM2M within the CMIP5 ensemble. The error bars show the 66% confidence interval stemming from the combined observational uncertainty in H and C_{ant}. **b**, $\hat{H}$ as a function of $\hat{C}_{\mathrm{ant}}$ relative to the years 1870–1890, where the slope is equal to α. The CMIP5 historical-RCP8.5 ensemble members are given up to the year 2060, where the ensemble mean is the thick solid pink line, the range is shaded in pale yellow and the thin solid pink lines show individual models. The dashed lines show the CMIP5 models that simulate a decrease in the ocean heat content in the twentieth century, which are excluded from the mean and range. The blue line shows observations (ocean heat storage from ref. [10]), and the green shading shows the range of the fixed-circulation and free-circulation 1%CO$_2$ ESM2M simulations that we conduct here. The solid circles show the decadal means, and the white rings highlight the 2000–2009 mean. The blue shading shows the 66% confidence interval from observations.

with a reduction in the meridional ocean heat transport that is probably due to a reduction in the meridional overturning circulation or gyre transport[10,17], which counteracts the warming from the added heat. This North Atlantic redistribution is not captured in the CMIP5 ensemble mean but is present in a few of the ensemble members (Extended Data Fig. 5). This could indicate either that the sub-polar cooling is due to natural variability (an anthropogenic signal in meridional heat transport only emerged in 2000)[26] and therefore eliminated owing to the averaging over multiple historical simulations, or that most CMIP5 ESM models fail to capture the emergence of a forced trend in that region because they contain structural biases[27].

In our projections from 2011 to 2060, in all CMIP5 models—including in the three CMIP5 models that best match the observed patterns of H_{r} from 1951 to 2011—H_{r} exhibits a cooling signal in the Atlantic sub-polar gyre and warming in the Gulf Stream and in low-latitude regions (Extended Data Fig. 5). This agreement could indicate that the observed pattern of ocean redistribution from anthropogenic climate change might persist over the coming decades, despite the past influence of natural variability. However, it is important to note that model agreement does not necessarily mean that the models are correct.

Heat redistribution explains most of the warming pattern over the historical period—H_{r} has a CR of 0.92 with H in observations (CR = 0.87 in CMIP5). However, the projected added heat becomes relatively more important between 2011 and 2060, with a CR of 0.52 for H_{ad} with H, as opposed to CR = 0.27 in observations and CR = 0.26 in CMIP5 over the historical period. As the climate warms, added heat storage will therefore probably begin to shape ocean warming patterns.

Discussion

We identify an emergent coupling between the global ocean uptake of heat and carbon. The order of magnitude of the heat–carbon coupling parameter is consistent across models, scenarios and observations and is mostly constant over time. The magnitude of the heat–carbon coupling parameter is, to first order, set by the ocean buffer factor,

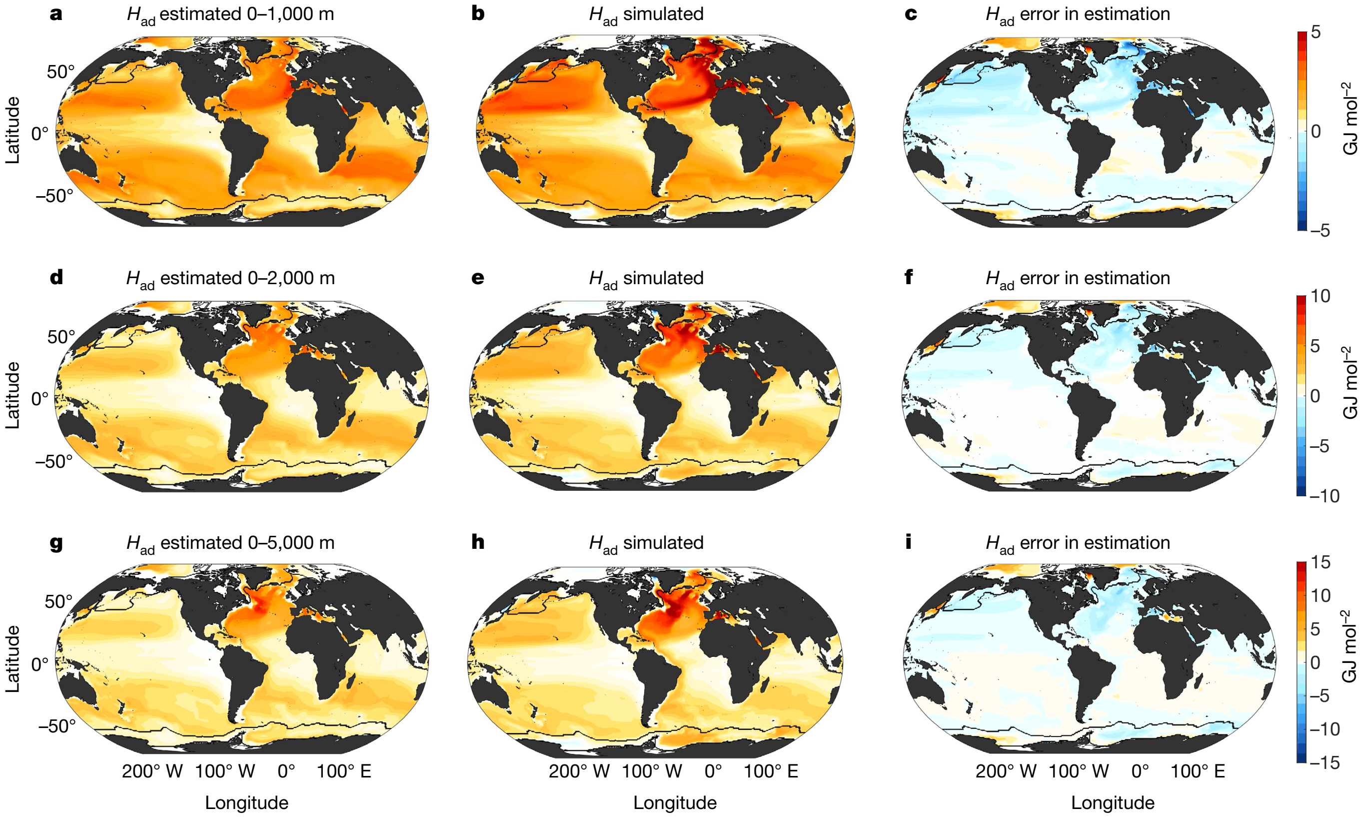

Fig. 3 | Error in the redistributed ocean heat storage from ESM2M. **a**–**i**, Ocean heat storage from the fixed-circulation experiment in terms of the added H (H_{ad}), depth-integrated over 0–1,000 m (**a**–**c**), 0–2,000 m (**d**–**f**), and 0–5,000 m (**g**–**i**), averaged over years 61–80 of the ESM2M 1%CO$_2$ simulation. **a**, **d** and **g** show H_{ad} estimated using only the free-circulation experiment quantity αC_{ant}, and **b**, **e** and **h** show H_{ad} simulated by the fixed-circulation experiment. **c**, **f** and **i** show the difference between H_{ad} as determined by the two experiments. The average percentage errors in the estimation of H_{ad} using C_{ant} are 3%, 11% and 12% for the models over 0–1,000 m, 0–2,000 m and 0–5,000 m, respectively.

the pre-industrial ocean carbon inventory and the radiative forcing strength of CO$_2$. This similarity is unique in that it is not shared with other passive tracers such as ocean CFC storage. We use the global and regional coupling of heat and carbon to calculate patterns of the ocean heat redistribution that arises from circulation changes in observational-based products and in CMIP5 models from 1951 to 2060.

The method allows us to attribute observed ocean warming and cooling to circulation changes on a global scale using only observational products, thereby avoiding the biases in climate models that are associated with their simulated heat-storage patterns. In some ocean basins, the effect of warming from redistribution is more than three times larger than the effect of added heat storage in the fixed-circulation experiment, leading to an increased rise in regional sea levels. We find that warming from redistribution has had an important role in the observed warming of the Atlantic Ocean between 40° S and 40° N and in the eastern tropical Pacific Ocean, up to 6.4 GJ m^{-2} along the Gulf Stream. In contrast to warming from redistribution, changes in ocean circulation have probably cooled the sub-tropical gyres in both the Indian and Pacific Oceans by up to 2.4 GJ m^{-2}, leading to mitigation of local sea-level rise. In the Southern Ocean, there is redistributed warming in the South Atlantic and Indian sectors, up to 4.0 GJ m^{-2}, but cooling in the Pacific sector, up to 1.7 GJ m^{-2}, such that the zonally integrated Southern Ocean warming is set by the added heat[25]. Over the historical period, some of these observed features are probably due to natural variability. However, both the Pacific and Indian sub-tropical redistributed cooling and Southern Ocean pattern are projected to continue into the future across all models[8], suggesting that the historical pattern of redistribution may persist over the next several decades.

Simulations of the storage of ocean anthropogenic carbon—and by extension the added heat storage—within the CMIP5 ensemble agree well with each other[28]. Therefore, the differences in heat-storage patterns simulated in the CMIP5 models are not due to the background state, which governs the added heat storage, but are predominantly due to the response of the ocean circulation to forcing in these models (natural or anthropogenic). In future projections, however, the influence of ocean heat redistribution on patterns of heat storage is reduced as the added heat becomes more dominant, despite changes in ocean circulation becoming more severe[29]. In addition, the patterns of added heat storage in CMIP5 models agree well with observations. As added heat storage becomes more dominant, future CMIP simulations of ocean heat storage will therefore probably agree better with real patterns of warming than in the past. As a result, long-term ocean warming and patterns of sea-level rise may become more predictable as the climate warms. However, we cannot exclude that at even higher atmospheric CO$_2$ levels than tested here, extreme and abrupt changes in circulation may have an important role.

A main caveat of our work is the use of a single coupled climate model (ESM2M) to test our method. However, all key results found using ESM2M are also found in ocean-only simulations with MITgcm. In the MITgcm simulations, we also find a 4% difference in global heat uptake between the fixed-circulation and free-circulation experiments after 100 yr of simulation, that the redistribution of C_{ant} is negligible, that patterns of carbon and heat storage in the fixed experiment are highly correlated, that α lies in the range of other coupled models, and that all of these results can be used to skilfully reconstruct fixed heat storage (see Methods). In addition, both the spatial similarity of C_{ant}

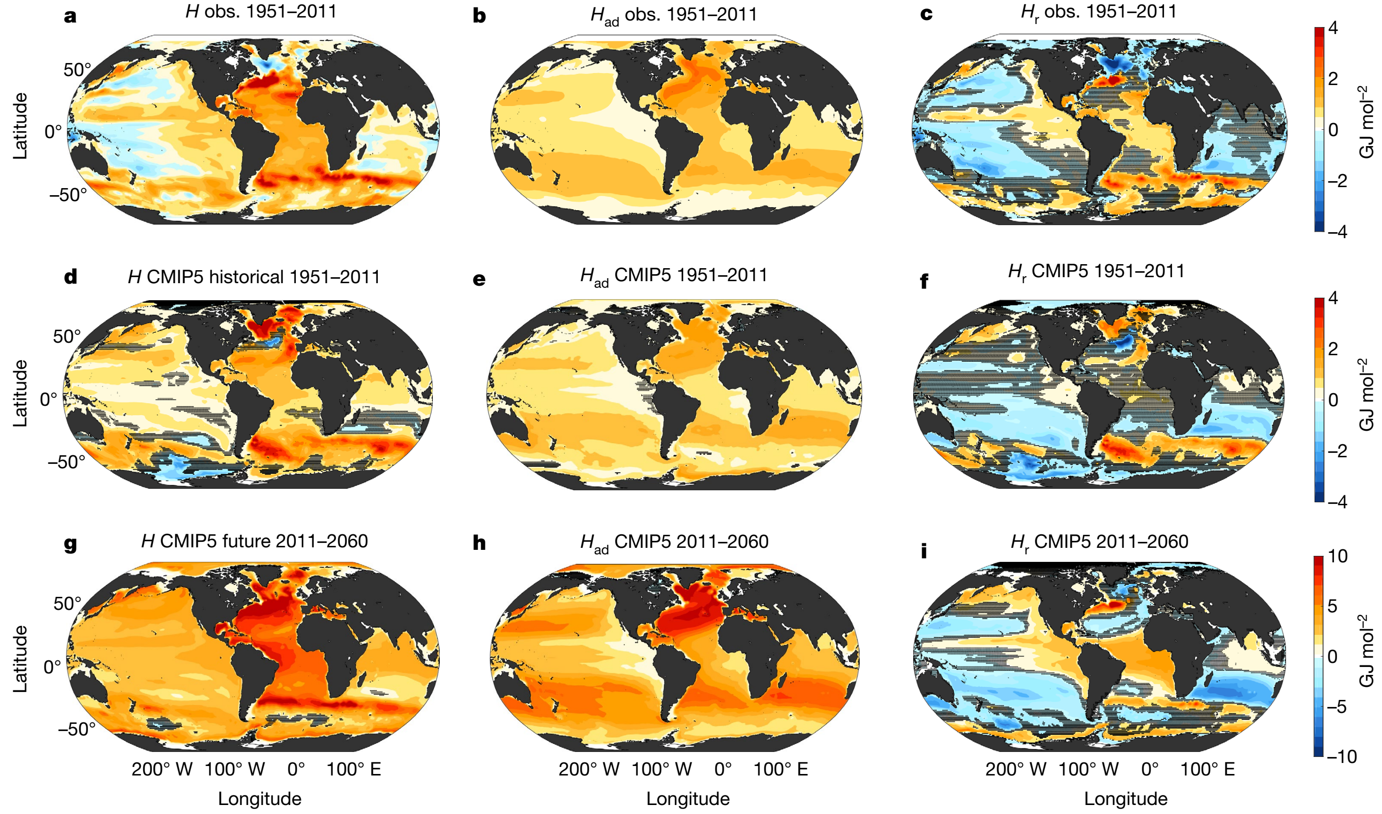

Fig. 4 | Redistribution of ocean heat storage in the upper 2,000 m. **a**, **d**, **g**, The change in heat storage H. **b**, **e**, **h**, The change in the added heat storage H_{ad}, calculated as αC_{ant}. **c**, **f**, **i**, The ocean redistributed heat $H_{\mathrm{r}} = H - \alpha C_{\mathrm{ant}}$. The changes are shown as the linear trends over the indicated periods multiplied by the length of the period. The results from observational estimates (obs.) for the period 1951–2011 are given in **a**–**c**; the results from 1951–2011 changes in the CMIP5 historical-RCP8.5 ensemble are given in **d**–**f**; and **g**–**i** show the 2011–2060 changes in the CMIP5 RCP8.5 ensemble. The hatching indicates where the changes are not significant at the 66% uncertainty level. For the observations, the uncertainty is from the estimates of H and C_{ant}, whereas for the CMIP5 models, the uncertainty is from the mean of the ensemble that emerges from the inter-model spread.

under free-circulation and fixed-circulation conditions[6,21], and also the small effect of biological changes[6,21,30–32] on C_{ant} are consistent with previous modelling work. In the fixed-circulation experiment, parameterizations are still allowed to vary. However, the effect of changes in these parameterizations on the passive heat and carbon storage is found to be less than 10% (see Methods). Finally, the similarity between H_{ad} and C_{ant} is also present when comparing passive reconstructions of the storage of ocean heat and carbon[10,21]. Another caveat of our work is that many models tend to underestimate variability, including air–sea carbon fluxes[33,34]. However, because we consider the multi-decadal time-integrated carbon storage, the effects of variability in the flux are mostly mitigated.

In summary, we present a method to calculate the redistribution of ocean heat without the need for any additional measurements or simulations, and we infer changes in heat transport owing to anthropogenic climate change. The method provides a way to assess the quality of climate models, by comparing the physical response to forcing with our observational estimate of ocean heat redistribution. We show that ocean heat redistribution, although dominant in the past, becomes less important in the future, leading to potentially more predictable warming patterns in coarse-resolution climate models. Further work is necessary to assess our results in eddy-rich ocean climate models, and to constrain the mechanisms and sensitivity of ocean heat to carbon uptake and their potentially strong link to the transient climate response to CO_2 emissions[1]. However, our method can be used to understand the mechanisms which regionally redistribute ocean heat, impacting sea-ice formation[35], marine heat waves[36], ocean oxygen[37] and sea-level rise[10,38].

Online content

Any methods, additional references, Nature Research reporting summaries, source data, extended data, supplementary information, acknowledgements, peer review information; details of author contributions and competing interests; and statements of data and code availability are available at https://doi.org/10.1038/s41586-020-2573-5.

1. Allen, M. R. et al. Warming caused by cumulative carbon emissions towards the trillionth tonne. *Nature* **458**, 1163–1166 (2009).
2. Matthews, H. D., Gillett, N. P., Stott, P. A. & Zickfeld, K. The proportionality of global warming to cumulative carbon emissions. *Nature* **459**, 829–832 (2009).
3. Solomon, S., Plattner, G., Knutti, R. & Friedlingstein, P. Irreversible climate change due to carbon dioxide emissions. *Proc. Natl Acad. Sci. USA* **106**, 1704–1709 (2009).
4. Goodwin, P., Williams, R. G. & Ridgwell, A. Sensitivity of climate to cumulative carbon emissions due to compensation of ocean heat and carbon uptake. *Nat. Geosci.* **8**, 29–34 (2015).
5. Xie, P. & Vallis, G. K. The passive and active nature of ocean heat uptake in idealized climate change experiments. *Clim. Dyn.* **38**, 667–684 (2012).
6. Khatiwala, S. et al. Global ocean storage of anthropogenic carbon. *Biogeosciences* **10**, 2169–2191 (2013).
7. Winton, M., Griffies, S. M., Samuels, B. L., Sarmiento, J. L. & Frölicher, T. L. Connecting changing ocean circulation with changing climate. *J. Clim.* **26**, 2268–2278 (2013).
8. Gregory, J. M. et al. The Flux-Anomaly-Forced Model Intercomparison Project (FAFMIP) contribution to CMIP6: investigation of sea-level and ocean climate change in response to CO_2 forcing. *Geosci. Model Dev.* **9**, 3993–4017 (2016).
9. DeVries, T., Holzer, M. & Primeau, F. Recent increase in oceanic carbon uptake driven by weaker upper-ocean overturning. *Nature* **542**, 215–218 (2017).
10. Zanna, L., Khatiwala, S., Gregory, J. M., Ison, J. & Heimbach, P. Global reconstruction of historical ocean heat storage and transport. *Proc. Natl Acad. Sci. USA* **116**, 1126–1131 (2019).
11. Frölicher, T. L. et al. Dominance of the Southern Ocean in anthropogenic carbon and heat uptake in CMIP5 models. *J. Clim.* **28**, 862–886 (2015).

12. Stocker, T.F. et al. (eds) *Climate Change 2013: The Physical Science Basis: Contribution of Working Group I to the Fifth Assessment Report of the Intergovernmental Panel on Climate Change* (Cambridge Univ. Press, 2013).
13. Drijfhout, S., van Oldenborgh, G. J. & Cimatoribus, A. Is a decline of AMOC causing the warming hole above the North Atlantic in observed and modeled warming patterns? *J. Clim*. **25**, 8373–8379 (2012).
14. Wilson, L. J. et al. Climate-driven changes to ocean circulation and their inferred impacts on marine dispersal patterns. *Glob. Ecol. Biogeogr*. **25**, 923–939 (2016).
15. Smeed, D. A. et al. The North Atlantic Ocean is in a state of reduced overturning. *Geophys. Res. Lett*. **45**, 1527–1533 (2018).
16. Matear, R. J., Hirst, A. C. & McNeil, B. I. Changes in dissolved oxygen in the Southern Ocean with climate change. *Geochem. Geophys. Geosyst*. **1**, 1050 (2000).
17. Caesar, L., Rahmstorf, S., Robinson, A., Feulner, G. & Saba, V. Observed fingerprint of a weakening Atlantic Ocean overturning circulation. *Nature* **556**, 191–196 (2018).
18. Zickfeld, K., Eby, M., Matthews, H. D. & Weaver, A. J. Setting cumulative emissions targets to reduce the risk of dangerous climate change. *Proc. Natl Acad. Sci. USA* **106**, 16129–16134 (2009).
19. Marshall, D. P. & Zanna, L. A conceptual model of ocean heat uptake under climate change. *J. Clim*. **27**, 8444–8465 (2014).
20. Saenko, O. A., Yang, D. & Gregory, J. M. Impact of mesoscale eddy transfer on heat uptake in an eddy-parameterizing ocean model. *J. Clim*. **31**, 8589–8606 (2018).
21. Khatiwala, S., Primeau, F. & Hall, T. Reconstruction of the history of anthropogenic CO_2 concentrations in the ocean. *Nature* **462**, 346–349 (2009).
22. Revelle, R. & Suess, H. S. Carbon dioxide exchange between atmosphere and ocean and the questions of an increase of atmospheric CO_2 during the past decades. *Tellus* **9**, 18–27 (1957).
23. Cheng, L. et al. Improved estimates of ocean heat content from 1960 to 2015. *Sci. Adv*. **3**, e1601545 (2017).
24. DeVries, T. The oceanic anthropogenic CO_2 sink: storage, air–sea fluxes, and transports over the industrial era. *Glob. Biogeochem. Cycles* **28**, 631–647 (2014).
25. Armour, K. C., Marshall, J., Scott, J. R., Donohoe, A. & Newsom, E. R. Southern Ocean warming delayed by circumpolar upwelling and equatorward transport. *Nat. Geosci*. **9**, 549–554 (2016).
26. Chemke, R., Zanna, L. & Polvani, L. M. Identifying a human signal in the North Atlantic warming hole. *Nat. Commun*. **11**, 1540 (2020).
27. Huber, M. B. & Zanna, L. Drivers of uncertainty in simulated ocean circulation and heat uptake. *Geophys. Res. Lett*. **44**, 1402–1413 (2017).
28. Bronselaer, B., Winton, M., Russell, J., Sabine, C. L. & Khatiwala, S. Agreement of CMIP5 simulated and observed ocean anthropogenic CO_2 uptake. *Geophys. Res. Lett*. **44**, 12298–12305 (2017).
29. Cheng, W., Chiang, J. C. H. & Zhang, D. Atlantic Meridional Overturning Circulation (AMOC) in CMIP5 models: RCP and historical simulations. *J. Clim*. **26**, 7187–7197 (2013).
30. Friedlingstein, P. et al. Climate–carbon cycle feedback analysis: results from the C4MIP model intercomparison. *J. Clim*. **19**, 3337–3353 (2006).
31. Arora, V. K. et al. Carbon–concentration and carbon–climate feedbacks in CMIP5 Earth system models. *J. Clim*. **26**, 5289–5314 (2013).
32. Friedlingstein, P. et al. Uncertainties in CMIP5 climate projections due to carbon cycle feedbacks. *J. Clim*. **27**, 511–526 (2014).
33. Landschützer, P., Gruber, N. & Bakker, D. C. E. Decadal variations and trends of the global ocean carbon sink. *Glob. Biogeochem. Cycles* **30**, 1396–1417 (2016).
34. DeVries, T. et al. Decadal trends in the ocean carbon sink. *Proc. Natl Acad. Sci. USA* **116**, 11646–11651 (2019).
35. Winton, M. On the climatic impact of ocean circulation. *J. Clim*. **16**, 2875–2889 (2003).
36. Frölicher, T. L., Fischer, E. M. & Gruber, N. Marine heatwaves under global warming. *Nature* **560**, 360–364 (2018).
37. Palter, J. B. & Trossman, D. S. The sensitivity of future ocean oxygen to changes in ocean circulation. *Glob. Biogeochem. Cycles* **32**, 738–751 (2018).
38. Banks, H. & Gregory, J. Mechanisms of ocean heat uptake in a coupled climate model and the implications for tracer-based predictions of ocean heat uptake. *Geophys. Res. Lett*. **33**, L07608 (2006).

Methods

Experimental design

The main coupled climate model used in this study is the GFDL ESM2M, which includes a fully coupled carbon cycle[39,40] forced with a transient increase of 1% atmospheric CO_2 per year[7]. To investigate the effect of changing currents, in addition to a free-running forced experiment, we use the fixed-circulation experiments from ref. [7]. In these experiments, the ocean currents (namely, the horizontal velocities) are prescribed to follow a fixed seasonal cycle. The prescribed (fixed) currents are taken from the first 100 yr of the 1860 control simulation. To maintain the mass balance and avoid unrealistic local sea levels, the ocean surface freshwater flux in the 1%CO_2 fixed-circulation experiment is also prescribed from the pre-industrial fixed-circulation control. Although the resolved currents are prescribed, the parameterizations for subgrid-scale mesoscale eddy mixing and convection are allowed to operate as normal and respond to the imposed CO_2 forcing.

The experiments are run for 100 yr but herein we show the spatial maps of anomalies over the years 61–80, which coincide with the time at which the atmospheric CO_2 concentration is twice the pre-industrial value. In the ESM2M simulations, the difference in the net ocean heat uptake for the average of the years 61–80 between the fixed-circulation and free-circulation simulations is 4%.

In the fixed-circulation experiment, there are some changes in the circulation owing to the eddy parameterization schemes (Gent–McWilliams and vertical mixing), shown in Extended Data Fig. 1. However, these changes are negligible. Extended Data Fig. 1 also shows the mixed layer depth in the control simulation and calculated changes in the mixed layer depth in the free-circulation and fixed-circulation experiments. Changes in the mixed layer depths reflect changes in convection. Although there are large changes in mixed layer depths in the free-circulation experiment in the North Atlantic (particularly in the Labrador Sea), there are only small changes in the ice-free regions of the fixed-circulation experiment, where convection is maintained. In the fixed-circulation experiment, in the North Atlantic north of 30° N, there is an average reduction in the mixed layer depth of 13%, where mixed layer depths were deeper than 200 m in the control case. These results show that, outside ice-covered regions, the changes in the eddy and convection parameterizations in the fixed-circulation experiment are small.

Similarity between C_{ant} and H_{ad}

To demonstrate the similarity between C_{ant} and H_{ad}, we investigate the relationship between heat and CFC storage from an RCP8.5 simulation, also at the time of the doubling of the atmospheric partial pressure of CO_2, p_{CO_2} (Extended Data Fig. 6). Ocean uptake of atmospheric CO_2 is driven by the air–sea imbalance of the partial pressure of CO_2. At the ocean surface, changes in p_{CO_2} are largely latitudinally uniform[41,42] (Extended Data Fig. 6), which is a result of surface waters being mostly equilibrated with respect to well-mixed atmospheric CO_2[43,44]. Changes in ocean p_{CO_2}, Δp_{CO_2}, therefore follow the nearly latitudinally uniform atmospheric CO_2 changes, imposing a strong constraint on the pattern of surface p_{CO_2}.

p_{CO_2} can be decomposed as the change in p_{CO_2} from temperature changes ΔT, and changes owing to chemistry, using linearity and the chain rule. In this case, we can express the contribution of chemistry through the changes in concentrations of DIC, ΔDIC, and of alkalinity (ALK), ΔALK:

$$\Delta p_{CO_2}(T,\mathrm{DIC},\mathrm{ALK},S) \approx \frac{\partial p_{CO_2}}{\partial T}\Delta T + \frac{\partial p_{CO_2}}{\partial \mathrm{DIC}}\Delta\mathrm{DIC} + \frac{\partial p_{CO_2}}{\partial \mathrm{ALK}}\Delta\mathrm{ALK}, \quad (4)$$

where the contribution from changes in salinity is negligible compared to the other factors[45] in equation (4). The ΔDIC term dominates Δp_{CO_2} (Extended Data Fig. 6). Using the following expressions for the buffer factors for DIC and alkalinity (ALK), R_{DIC} and R_{ALK}, respectively[45,46]:

$$R_{\mathrm{DIC}} \approx \frac{3\times\mathrm{ALK}\times\mathrm{DIC} - 2\times\mathrm{DIC}^2}{(2\times\mathrm{DIC}-\mathrm{ALK})(\mathrm{ALK}-\mathrm{DIC})}, \quad (5)$$

$$R_{\mathrm{ALK}} \approx \frac{\mathrm{ALK}^2}{(2\times\mathrm{DIC}-\mathrm{ALK})(\mathrm{ALK}-\mathrm{DIC})}, \quad (6)$$

and an empirically derived relationship[47] for $\partial p_{CO_2}/\partial T$, we can rewrite equation (4) as follows:

$$p_{CO_2}(T,\mathrm{DIC},\mathrm{ALK}) = 0.0423 p_{CO_2}\Delta T + \frac{R_{\mathrm{DIC}} p_{CO_2}}{\mathrm{DIC}}\Delta\mathrm{DIC} + \frac{R_{\mathrm{ALK}} p_{CO_2}}{\mathrm{DIC}}\mathrm{DIC} + \frac{R_{\mathrm{ALK}} p_{CO_2}}{\mathrm{ALK}}\mathrm{ALK}. \quad (7)$$

The sensitivity $\partial p_{CO_2}/\partial\mathrm{DIC}$ is set by the background ocean chemistry[22], the spatial pattern of which is partly determined by the background ocean temperature, as shown in Extended Data Fig. 6. To determine the role of temperature on $\partial p_{CO_2}/\partial\mathrm{DIC}$, we remove latitudinal variations in temperature: we first calculate the pre-formed DIC (that is, C_{SAT}, the component of DIC that is in equilibrium with atmosphere, and the solubility of which is determined by temperature and salinity)[48] in the case of DIC. The pre-formed DIC was calculated twice, first using the simulated spatially varying background temperature field, and then using a uniform temperature field. The difference between the two is then removed from the actual simulated DIC to remove the effects of the spatially varying temperature. p_{CO_2} is also calculated with the same simulated and uniform temperature field, and the difference is used to remove the effects of the spatially varying temperature field.

To satisfy the latitudinally uniform surface Δp_{CO_2} constraint, ΔDIC must be anti-correlated to $\partial p_{CO_2}/\partial\mathrm{DIC}$; in the ESM2M, CR = −0.84, with similar correlations in other models and observations (Extended Data Fig. 7). The patterns of ΔDIC, which are dictated by $\partial p_{CO_2}/\partial\mathrm{DIC}$ and therefore by the background state, are similar in both the fixed-circulation and free-circulation experiments (CR = 0.98), as expected.

The patterns of ΔDIC are also found to correlate with the temperature change in the fixed-circulation experiment (that is, the added temperature ΔT_{ad}; CR = 0.64), and with the background temperature (CR = 0.8). However, concentration changes of CFCs are not strongly correlated with ΔT_{ad}. Similar to CO_2, the ocean uptake of CFCs is set by the air–sea imbalance in partial pressure of CFC, p_{CFC}, but unlike CO_2, CFCs lack chemical buffering and the surface p_{CFC} is only related to the CFC concentration by the inverse of solubility[49], and the lack of chemical buffering of CFCs breaks the correlation between CFC changes and ΔT_{ad}.

Once carbon and heat anomalies are absorbed by the ocean at the surface, the interior C_{ant} and H_{ad} patterns are set only by the background physical processes, with little impact from changes in sub-grid processes, as illustrated using a 'fixed-climate simulation'[30] in which atmospheric CO_2 has no radiative forcing effect. In this simulation, the ocean only sees a pre-industrial climate, without physically driven changes in temperature and ocean circulation. Between the fixed-climate ESM2M simulation and the fixed-circulation and free-circulation simulations, C_{ant} is almost identical (Extended Data Fig. 8), confirming that temperature and circulation changes have negligible effects on C_{ant}[28]. The fixed-climate simulation also shows that changes in biology have little effect, because modelled biological changes are primarily driven by physical changes in stratification that do not occur in the fixed-climate simulation[50–52]. Lastly, parameterizations such as convection, mixing and eddy transports are unperturbed in the fixed-climate simulation. The difference in C_{ant} between the fixed-climate and fixed-circulation experiments is less than 10% locally. These simulations therefore also show that the parameterizations have only a small effect on passive tracer storage and are consistent with results from previous studies with other CMIP5 models[21,53,54].

The correlation between ΔDIC and fixed-circulation ΔT_{ad} at the surface owing to chemical buffering, as well as the dominance of background physical processes in setting H_{ad} and C_{ant} explain their strong correlation. By contrast, the lack of correlation between changes in surface CFC and ΔT_{ad} leads to a mismatch in storage patterns (Extended Data Fig. 6). CFCs therefore cannot be used to reconstruct H_{ad}, whereas C_{ant} uniquely can.

Relationship between global ocean anthropogenic heat and carbon

This section outlines a more detailed derivation of equation (3). We express the top-of-the-atmosphere radiative imbalance[55], $N(t)$, as the imbalance between the radiative forcing from CO_2, $F(t)$, and the climate feedback, $\lambda(t)T_{\mathrm{a}}(t)$, such that:

$$N(t) = F(t) - \lambda(t)T_{\mathrm{a}}(t) = \frac{\hat{H}(t)}{A\Delta t}, \tag{8}$$

where $\hat{H}(t)$ is the global heat uptake $\hat{H}$ since $t = 0$, Δt is the time interval elapsed, A is the surface area of the Earth, $T_{\mathrm{a}}(t)$ is the mean atmospheric warming and $\lambda(t)$ is the climate sensitivity parameter. Note that in effect, $\Delta t = t$, but we use this notation to make it clear when a quantity is evaluated at a time t, and when the time elapsed appears as a separate quantity Δt. Most of the excess heat is absorbed by the ocean such that $A \times N(t) \approx \hat{H}(t)/\Delta t$. The radiative forcing owing to CO_2 can be calculated as $F(t) = F_0 \ln[p_{CO_2}(t)/p_{CO_2}(0)]$, where $F_0 = 5.35\ \mathrm{W\,m^{-2}}$ is the radiative forcing coefficient for CO_2. We can therefore write:

$$F(t) = \lambda(t)T_{\mathrm{a}}(t) + N(t) = F_0 \ln[p_{CO_2}(t)/p_{CO_2}(0)]. \tag{9}$$

We assume linearity of the response in equation (9), as is commonly done, because we are only interested in an order-of-magnitude calculation, and nonlinear responses are second order. Combining equations (8) and (9), we obtain the heat content change over Δt as:

$$\hat{H}(t) \ = \ AF_0 \ln[p_{CO_2}(t)/p_{CO_2}(0)]\Delta t - A\lambda(t)T_{\mathrm{a}}(t)\Delta t. \tag{10}$$

Neglecting the anthropogenic carbon uptake by the land, and assuming that p_{CO_2} of the surface of the ocean is in equilibrium with the atmosphere[41] (which follows the argument that the pattern of surface ocean p_{CO_2} does not change under climate change, as outlined above), we can use the definition of the Revelle buffer factor R_{DIC}:

$$R_{\mathrm{DIC}} = \frac{\Delta\overline{p_{CO_2}}}{\Delta\overline{\mathrm{DIC}}}\frac{\overline{\mathrm{DIC}}}{\overline{p_{CO_2}}} \approx \frac{\Delta I_{\mathrm{a}}}{\Delta I_{\mathrm{o}}}\frac{I_{\mathrm{o}}}{I_{\mathrm{a}}}. \tag{11}$$

Here, I_{o} is the pre-industrial global ocean inventory of carbon, $I_{\mathrm{o}} = V\overline{\mathrm{DIC}}$ (where V is the volume of the ocean), and I_{a} is the atmospheric inventory of carbon. In the formal definition of R_{DIC}, $\overline{\mathrm{DIC}}$ is the mean surface ocean DIC concentration. However, the ratio $\overline{\mathrm{DIC}}/\Delta\overline{\mathrm{DIC}}$ only differs by 1% in ESM2M if we consider the mean of DIC across the upper 2,000 m instead of the surface of the ocean (and similarly in the estimate of total and anthropogenic ocean DIC from ref. [24]). The overline indicates an average over the ocean area (for p_{CO_2}) and over the volume—of the upper 2,000 m, in our case—for DIC. We can therefore write:

$$\ln\left(\frac{p_{CO_2}(t)}{p_{CO_2}(0)}\right) = \ln\left(1 + \frac{\Delta p_{CO_2}(t)}{p_{CO_2}(0)}\right) \approx \frac{\Delta p_{CO_2}(t)}{p_{CO_2}(0)} = \frac{R_{\mathrm{DIC}}\hat{C}_{\mathrm{ant}}(t)}{I_{\mathrm{o}}(0)} \tag{12}$$

where $\hat{C}_{\mathrm{ant}}(t) = \Delta I_{\mathrm{o}}$ is total ocean anthropogenic carbon. In our approximation, $I_{\mathrm{o}}(0) = I_{\mathrm{o}}$, so we can re-write equation (10) as follows:

$$\hat{H}(t) = \frac{R_{\mathrm{DIC}}AF_0}{I_{\mathrm{o}}}\hat{C}_{\mathrm{ant}}(t)\Delta t - A\lambda(t)T_{\mathrm{a}}(t)\Delta t, \tag{13}$$

leading to the final equation for the linearly approximated heat–carbon coupling parameter $\tilde{\alpha}$ in a one-dimensional model:

$$\tilde{\alpha} = \frac{\hat{H}(t)}{\hat{C}_{\mathrm{ant}}(t)} = \frac{R_{\mathrm{DIC}}AF_0}{I_{\mathrm{o}}}\Delta t - A\lambda(t)\frac{T_{\mathrm{a}}(t)}{\hat{C}_{\mathrm{ant}}(t)}\Delta t. \tag{14}$$

The left- and right-hand sides of equation (14) are shown in Extended Data Fig. 2, for the ESM2M 1%CO_2 simulation. The first term of the right-hand side of equation (14)—which depends on carbon buffering effects—captures the magnitude of α, but has too steep a slope. The second term of the right-hand side of equation (14) acts to flatten out the behaviour of the coupling parameter with time. To first order, α therefore does not depend on $\hat{H}(t)$ or $\hat{C}_{\mathrm{ant}}(t)$ explicitly, but instead is set by F_0, R_{DIC} and I_{o}, which we have approximated as constants in this simple formulation. The results imply that the strength of CO_2 as a greenhouse gas, the buffer factor and the pre-industrial ocean carbon content (which is linked to the pre-industrial ocean stratification)—all of which are intrinsic quantities of the pre-industrial climate system—lead to a tight coupling between $\hat{H}$ and $\hat{C}_{\mathrm{ant}}$, and as a result a tight coupling between H_{ad} and C_{ant}. The parameters R_{DIC} and I_{o} only vary up to 15% across different models, scenarios and observations, and so the spread in α across models and observations is due to the T_{a} term in equation (14), reflecting differences in non-CO_2 forcing agents and variations in various climate feedback processes. Over the historical period, natural variability in atmospheric warming trends probably also explains part of the large spread in α.

The error in $\tilde{\alpha}(t)$ as estimated using equation (14), compared to the diagnosed $\alpha(t)$ is due to the assumption of linearity, and that the land does not absorb any carbon. In realistic scenarios, the land is both a sink and a source of carbon, owing to differing land use. In 2009, the cumulative land sink and sources could balance, although the uncertainty on this number is large[21]. The error arising from land-use uncertainty is therefore a large component in the idealized 1%CO_2 simulation, but may have less importance in the real world. Similarly, the 1%CO_2 simulation also does not include radiative forcing from other greenhouse gases or aerosols. These effects are thought to be largely similar in magnitude but opposite in sign, and therefore to a large extent cancel out[56]. Nonetheless, equation (14) shows that, owing to intrinsic variables of the climate system, the relationship between H and C_{ant} is linear to first order, explaining why the values of α are similar across the ESM2M, MITgcm and CMIP5 models and observations.

MITgcm

We compare the results from our ESM2M simulations to ocean-only simulations using the MITgcm, in which the atmospheric forcing remains constant. We do this, first, to demonstrate that our method holds for various modelling set-up and conditions. Second, the goal of using anthropogenic carbon to estimate the fixed-circulation anthropogenic heat content is to be able to apply this method to CMIP5 models and observations. In the ESM2M simulations, the atmospheric circulation and temperatures are different in the fixed-circulation and free-circulation experiments[7]. Using an ocean-only model with fixed boundary conditions, we can show that the coupling of the ocean's heat and carbon storage is independent of ocean–atmosphere coupling.

Our global MITgcm[57] set-up uses a 1° × 1° horizontal resolution and 42 vertical levels with a realistic bathymetry. The model has a biological module[58] that resolves five tracers: DIC, ALK, PO_4, dissolved organic phosphorus (DOP) and O_2. The model is forced at the surface with NCEP reanalysis wind stress and freshwater flux[59], and the surface temperature and salinity are restored towards Levitus' monthly temperature and salinity climatology[60] to avoid model drift. We use this ocean-only model to perform free-circulation and fixed-circulation climate change experiments that resemble those performed with the ocean–atmosphere coupled GFDL ESM2M described in the text.

In testing the fixed-circulation experiments, the seasonality of the surface forcing alongside a prescribed yearly mean circulation field produces strong atmosphere–ocean flux anomalies, leading to unphysical feedback. We therefore spin up the model both for the free-circulation and fixed-circulation experiments using October conditions without a seasonal cycle. October is chosen because it produces a mean-state circulation and air–sea carbon and heat fluxes most similar to the yearly climatology of the model that is forced with the full monthly varying forcing fields. The mean overturning and barotropic streamfunctions, Ψ_{MOC} and Ψ_{BARO}, respectively, are shown in Extended Data Fig. 9.

To simulate anthropogenic warming due to CO_2 emissions, we perturb the prescribed zonally uniform climatological temperature restoring profile with a latitudinally varying temperature perturbation. The idealized perturbation curve prescribes a smooth transition from a warming of 0 °C at 90° S, to 1.5 °C at the equator, to 0.5 °C at 90° N. We introduce anthropogenic carbon by raising the value of atmospheric $p_{\mathrm{CO_2}}$ from 280 ppm in the pre-industrial state to 560 ppm in the first time step of the climate change experiment, after which time the carbon cycle model evolves freely (therefore adding a pulse injection of carbon). We perform this experiment with both fixed and free ocean circulation.

In the free experiment, the circulation is changing owing to the changes in surface temperature, whereas in the fixed experiment the circulation (the 3D Eulerian and bolus velocity fields) is fixed and set to its pre-industrial value. However, parameterizations such as convective and eddy mixing are allowed to act freely for the both the free-circulation and fixed-circulation experiments, as in ESM2M. To remove the effects of the drift in the fixed-circulation warming experiment, we run a tandem fixed-circulation pre-industrial control simulation. All anomalies are calculated as the difference between the perturbation experiment and the tandem control simulation. After 50 yr (100 yr), there is a 3% (4%) difference in total ocean anthropogenic carbon uptake between the fixed-circulation and free-circulation experiments, and a 4% (6%) difference in total heat storage, which agrees well with previous coupled climate simulations[7]. The total ocean heat and carbon uptake are therefore similar between the free-circulation and fixed-circulation experiments, although their spatial distributions are different.

The perturbed overturning and barotropic streamfunctions, Ψ_{MOC} and Ψ_{BARO}, respectively, are shown in Extended Data Fig. 9. The experiments have been designed to optimally and rigorously test the presented method. Therefore, our scenarios are idealized, inducing large warming-induced circulation changes, instead of inducing realistic climate change scenarios from historical forcing or projections. However, our model simulations show very similar quantitative and qualitative results to coupled climate models under climate change scenarios as well as observational patterns of ocean warming and anthropogenic carbon storage[7,24,61–63].

The results for fixed-circulation and free-circulation 0–2,000 m column-integrated anthropogenic heat and carbon storage, as well as for the carbon and heat redistribution, are shown in Extended Data Fig. 10. Extended Data Fig. 10 also shows the fixed circulation and redistributed heat content, as calculated using only free-circulation quantities and equations (1) and (2). Similarly to fully coupled climate model experiments[7], discrepancies in the patterns of anthropogenic heat content between the free-circulation and fixed-circulation simulations are apparent, whereas patterns of anthropogenic carbon storage remain largely unaffected by changes in ocean currents that arise from warming. After 70 yr, the anthropogenic heat storage in the fixed experiment, H_{ad}, has increased in all regions, whereas in the free experiment, the ocean heat storage H has decreased in the North Atlantic and more heat is stored in the low latitudes in the South Atlantic. The pattern of anthropogenic heat storage in the Atlantic is due to the redistribution of heat by the modified circulation as the weakening of the Atlantic meridional overturning circulation can lead to a reduction of heat transport from the South Atlantic to the North Atlantic[11,13,61,62]. The redistribution of anthropogenic carbon however, is much smaller.

The fixed heat that is calculated using equations (1) and (3) (Extended Data Fig. 10) agrees very well with the explicitly simulated fixed heat. The corresponding redistributed heat patterns are also similar to those calculated using the fixed-circulation experiment, demonstrating the usefulness of our method for models with different structure and forcing.

Significance testing

To test the statistical significance of the redistributed heat in the CMIP5 ensemble, we test at the 66% confidence level. The redistributed heat is not significant where the mean signal is less than $\sigma/\sqrt{N}$, where σ is the standard deviation of the signal and N is the number of CMIP5 models, $N = 11$. The mean state has a zero mean and zero standard deviation of redistributed heat.

To test the significance of the redistributed heat in the observations, we test at the 66% confidence level by calculating whether the signal is larger than the 1σ confidence interval. The 1σ confidence interval is determined by quadratically combining the 1σ uncertainty in the observational estimates of heat and carbon storage.

CMIP5

The 11 CMIP5 models used in this study are the following: CMCC-CESM, CNRM, IPSL-CM5A LR, IPSL-CM5A MR, IPSL-CM5B LR, HadGEM2-ES, HadGEM2-CC, MPI ESM MR, NorESM, GFDL ESM2M and GFDL ESM2G. All of these models are Earth system models with fully coupled carbon cycles. Heat and carbon anomalies are calculated with respect to a tandem 1850 pre-industrial control simulation.

Data availability

The code of the GFDL ESM2M model is available from https://github.com/mom-ocean and the results from the free-circulation and fixed-circulation 1%CO_2 simulations are available from https://doi.org/10.1594/PANGAEA.914424. CMIP5 model data are available from the Earth System Grid Federation data portal at https://esgf-node.llnl.gov/projects/cmip5/. The historical ocean temperature reanalysis[23] from is available at http://159.226.119.60/cheng/. The estimate of historical ocean anthropogenic carbon[24] is available at https://tdevries.eri.ucsb.edu/models-and-data-products/. The observed ocean heat uptake[10] is available at https://laurezanna.github.io/publication/zanna-et-al-2017b/. The MITgcm code is available at http://mitgcm.org/. The GLODAPv2 synthesis product is available at https://www.nodc.noaa.gov/ocads/oceans/GLODAPv2/. The topographical data used in Figs. 1, 3, 4 and Extended Data Figs. 1, 5, 8–10 are available in MATLAB and provided by NOAA[64]. The CMIP5 and observational estimates of total, added and redistributed heat are available at https://laurezanna.github.io/publication/bronselaer-zanna-2020/.

39. Dunne, J. P. et al. GFDL's ESM2 global coupled climate–carbon Earth system models. Part I: Physical formulation and baseline simulation characteristics. *J. Clim.* **25**, 6646–6665 (2012).
40. Dunne, J. P. et al. GFDL's ESM2 global coupled climate–carbon Earth system models. Part II: Carbon system formulation and baseline simulation characteristics. *J. Clim.* **26**, 2247–2267 (2013).
41. Fay, A. R. & McKinley, G. A. Global trends in surface ocean $p_{\mathrm{co_2}}$ from in situ data. *Glob. Biogeochem. Cycles* **27**, 541–557 (2013).
42. Tjiputra, J. F. et al. Long-term surface $p_{\mathrm{co_2}}$ trends from observations and models. *Tellus B* **66**, 23083 (2014).
43. Fine, R. A., Peacock, S., Maltrud, M. E. & Bryan, F. O. A new look at ocean ventilation time scales and their uncertainties. *J. Geophys. Res. Oceans* **122**, 3771–3798 (2017).

44. Jones, D. C., Ito, T., Takano, Y. & Hsu, W.-C. Spatial and seasonal variability of the air–sea equilibration timescale of carbon dioxide. *Glob. Biogeochem. Cycles* **28**, 1163–1178 (2014).
45. Lovenduski, N. S., Gruber, N., Doney, S. C. & Lima, I. D. Enhanced CO_2 outgassing in the Southern Ocean from a positive phase of the Southern Annular Mode. *Glob. Biogeochem. Cycles* **21**, GB2026 (2007).
46. Sarmiento, J. & Gruber, N. *Ocean Biogeochemical Dynamics* (Princeton Univ. Press, 2006).
47. Takahashi, T., Olafsson, J., Goddard, J., Chipman, D. & Sutherland, S. Seasonal variation of CO_2 and nutrients in the high-latitude surface oceans: a comparative study. *Glob. Biogeochem. Cycles* **7**, 843–878 (1993).
48. Williams, R. G. et al. Nutrient streams in the north Atlantic: advective pathways of inorganic and dissolved organic nutrients. *Glob. Biogeochem. Cycles* **25**, GB4008 (2011).
49. Fine, R. A. Observations of CFCs and SF6 as ocean tracers. *Annu. Rev. Mar. Sci*. **3**, 173–195 (2011).
50. Steinacher, M. et al. Projected 21st century decrease in marine productivity: a multi-model analysis. *Biogeosciences* **7**, 979–1005 (2010).
51. Schwinger, J. et al. Nonlinearity of ocean carbon cycle feedbacks in CMIP5 Earth system models. *J. Clim*. **27**, 3869–3888 (2014).
52. Fu, W., Randerson, J. T. & Moore, J. K. Climate change impacts on net primary production (NPP) and export production (EP) regulated by increasing stratification and phytoplankton community structure in the CMIP5 models. *Biogeosciences* **13**, 5151–5170 (2016).
53. Arora, V. K. et al. Carbon–concentration and carbon–climate feedbacks in CMIP5 Earth system models. *J. Clim*. **26**, 5289–5314 (2013).
54. Randerson, J. T. et al. Multi-century changes in ocean and land contributions to climate-carbon feedbacks. *Glob. Biogeochem. Cycles* **29**, 744–759 (2015).
55. Myhre, G., Highwood, E., Shine, K. & Stordal, F. New estimates of radiative forcing due to well mixed greenhouse gases. *Geophys. Res. Lett*. **25**, 2715–2718 (1998).
56. Solomon, S. et al. (eds) *Climate Change 2007: The Physical Science Basis. Working Group I Contribution to the Fourth Assessment Report of the Intergovernmental Panel on Climate Change* (Cambridge Univ. Press, 2007).
57. Marshall, J., Adcroft, A., Hill, C., Perelman, L. & Heisey, C. A finite-volume, incompressible Navier–Stokes model for studies of the ocean on parallel computers. *J. Geophys. Res. Oceans* **102**, 5753–5766 (1997).
58. Dutkiewicz, S., Follows, M. & Parekh, P. Interactions of the iron and phosphorus cycles: a three-dimensional model study. *Glob. Biogeochem. Cycles* **19**, GB1021 (2008).
59. Kalnay, E. et al. The NCEP/NCAR 40-year reanalysis project. *Bull. Am. Meteorol. Soc*. **77**, 437–471 (1996).
60. Levitus, S. E. *Climatological Atlas of the World Ocean* NOAA Professional Paper 13 (US Department of Commerce, NOAA, 1982).
61. Stouffer, R. et al. Investigating the causes of the response of the thermohaline circulation to past and future climate changes. *J. Clim*. **19**, 1365–1387 (2006).
62. Rahmstorf, S. et al. Exceptional twentieth-century slowdown in Atlantic Ocean overturning circulation. *Nat. Clim. Chang*. **5**, 475–480 (2015); correction **5**, 956 (2015).
63. Sgubin, G., Swingedouw, D., Drijfhout, S., Mary, Y. & Bennabi, A. Abrupt cooling over the North Atlantic in modern climate models. *Nat. Commun*. **8**, 14375 (2017).
64. National Geophysical Data Center. *ETOPO5: Data Announcement 88-MGG-02, Digital Relief of the Surface of the Earth* (NOAA, 1988); https://doi.org/10.7289/V5C8276M
65. Olsen, A. et al. The Global Ocean Data Analysis Project version 2 (GLODAPv2) – an internally consistent data product for the world ocean. *Earth Syst. Sci. Data* **8**, 297–323 (2016).
66. Key, R. M.et al. *Global Ocean Data Analysis Project, Version 2 (GLODAPv2)* Report no. ORNL/CDIAC-162, ND-P093 (Carbon Dioxide Information Analysis Center, Oak Ridge National Laboratory, US Department of Energy, 2015).
67. Lauvset, S. K. et al. A new global interior ocean mapped climatology: the 1° × 1° GLODAP version 2. *Earth Syst. Sci. Data* **8**, 325–340 (2016).
68. van Heuven, S., Pierrot, D., Rae, J. W. B., Lewis, E. & Wallace, D. W. R. *MATLAB Program Developed for CO2 System Calculations* https://cdiac.ess-dive.lbl.gov/ftp/co2sys/CO2SYS_calc_MATLAB_v1.1/ (Carbon Dioxide Information Analysis Center, US Department of Energy, 2011).

Acknowledgements We thank M. Winton for providing the ESM2M simulations. We acknowledge the MITgcm team for making their code publicly available, the World Climate Research Programme's Working Group on Coupled Modelling, which is responsible for CMIP5, and the climate modelling groups for producing and making available the output of their models. We thank R. Keeling for comments. B.B. was supported by a NERC CASE studentship with the Met Office. L.Z. thanks NERC NE/P019218/1, NE/R000727/1, and Princeton University, AOS and GFDL for additional support during part of this work. This work made use of the facilities of HECToR and Archer.

Author contributions B.B. and L.Z. conceptualized the study, analysed the data and wrote the manuscript. B.B. performed the MITgcm simulations.

Competing interests The authors declare no competing interests.

Additional information
Correspondence and requests for materials should be addressed to B.B.
Reprints and permissions information is available at http://www.nature.com/reprints.

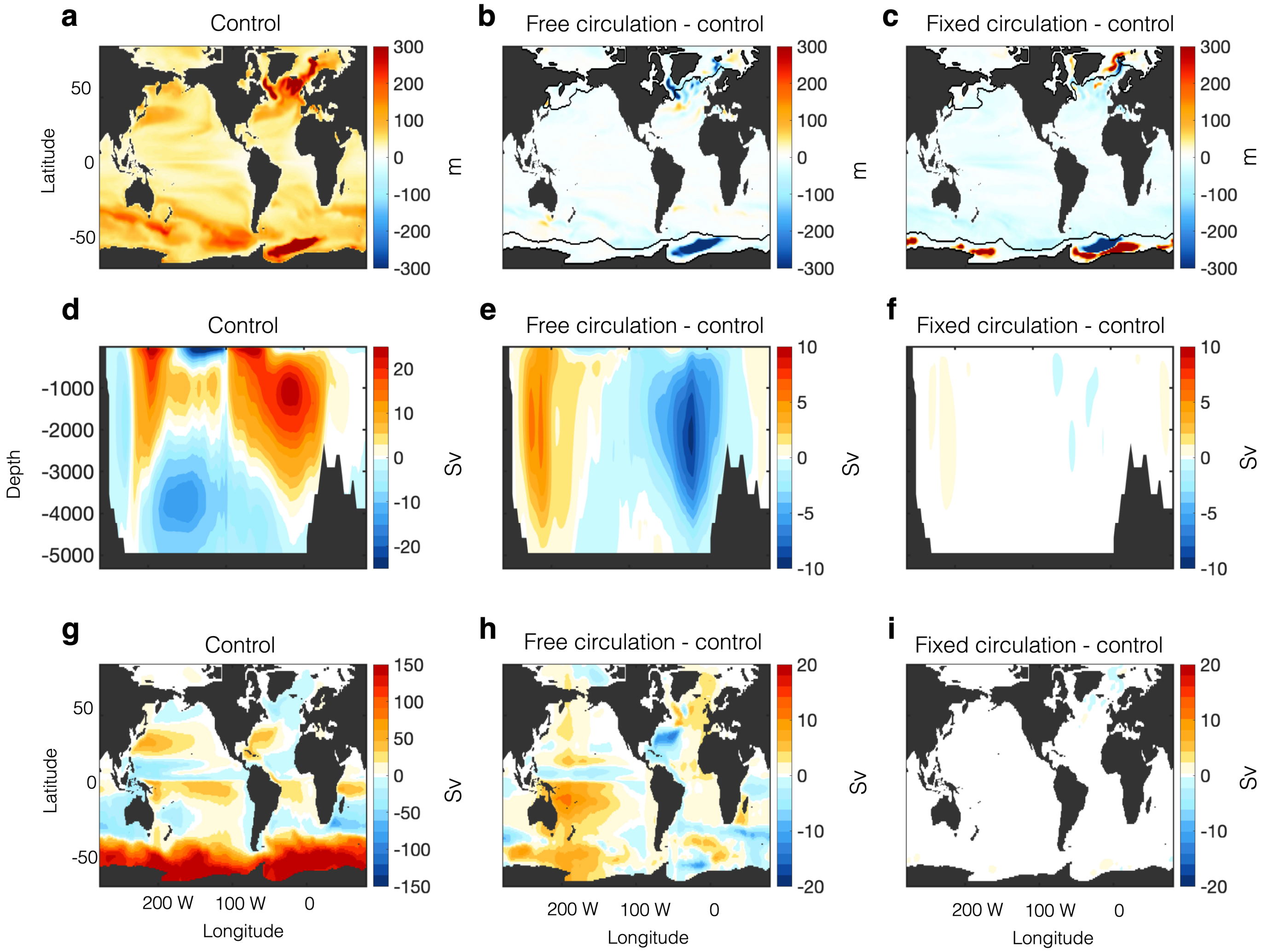

Extended Data Fig. 1 | Physical changes in ESM2M experiments. a, **b**, Using the free-circulation model, the fixed-layer depth of the pre- industrial control mean (**a**) and the change in mixed-layer depth (relative to the control) (**b**), for years 61–80 of the 1%CO_2 free circulation. **c**, Years 61–80 of the 1%CO_2 fixed-circulation simulation. In the fixed-circulation experiment, north of 30° N in the North Atlantic Ocean, there is an average reduction in mixed-layer depth of 15%, where mixed layer depths were deeper than 200 m in the control mean. **d**–**f**, As in **a**–**c**, but for the meridional overturning streamfunction, where 1 Sv = 10^6 m^3 s^{-1}. **g**–**i**, As in **a**–**c**, but for the barotropic streamfunction.

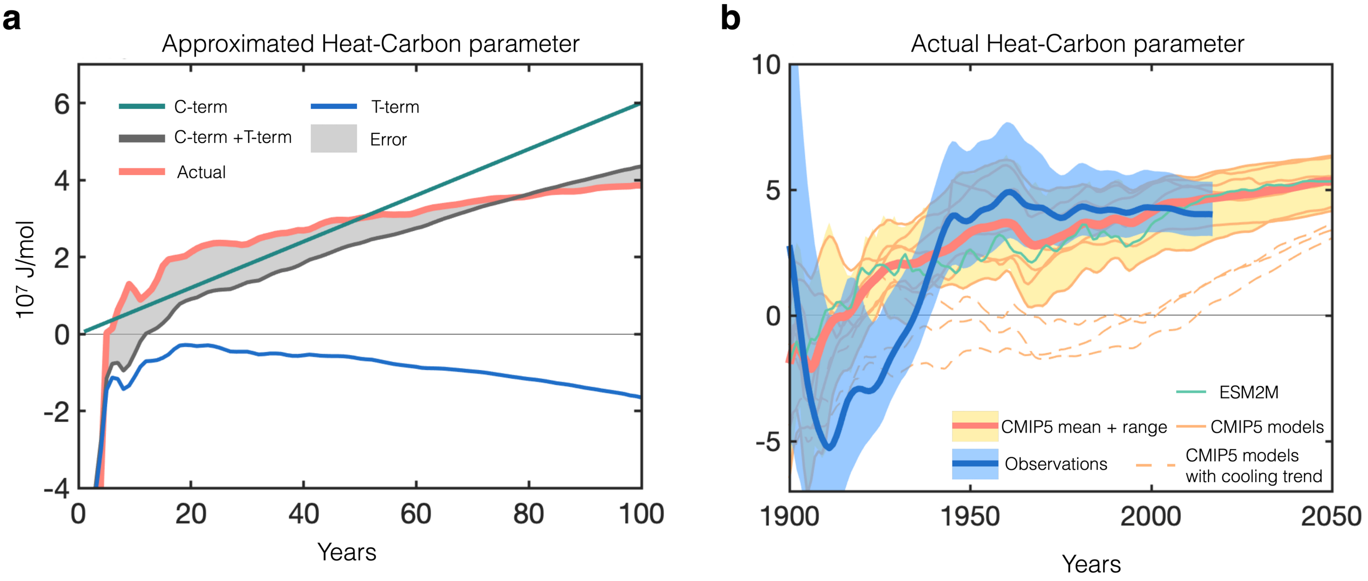

Extended Data Fig. 2 | The heat–carbon coupling parameter, *α*. **a**, α, obtained in ESM2M using $\alpha(t) = \hat{H}(t)/\hat{C}_{\text{ant}}(t)$ (pink), and as estimated using equation (14) for $\tilde{\alpha}$ (grey line). The green line shows the magnitude of the first term of the right-hand side of equation (14), and the blue line shows the second term of the right-hand side of equation (14), which is related to the temperature-feedback term. The grey shading shows the error in the estimate that is due to the assumption of linearity and to various other processes and feedback mechanisms ignored, such as land carbon uptake. The negative values of α and $\tilde{\alpha}$ at the start of the experiment are due to natural variability when the external forcing is small (giving a low signal-to-noise ratio). **b**, $\alpha(t) = \hat{H}(t)/\hat{C}_{\text{ant}}(t)$, relative to the years 1870–1890 in CMIP5 historical/RCP8.5 simulations, with the mean given by the thick pink line and the range given by the pale yellow area. Thin lines show individual models (ESM2M is shown in green for reference) and dashed lines show the models that simulate ocean heat loss in the mid-twentieth century that are excluded from the mean and range. The blue solid line shows the observations (using ref.[10] for heat) and its blue shading shows the 66% confidence interval from observations.

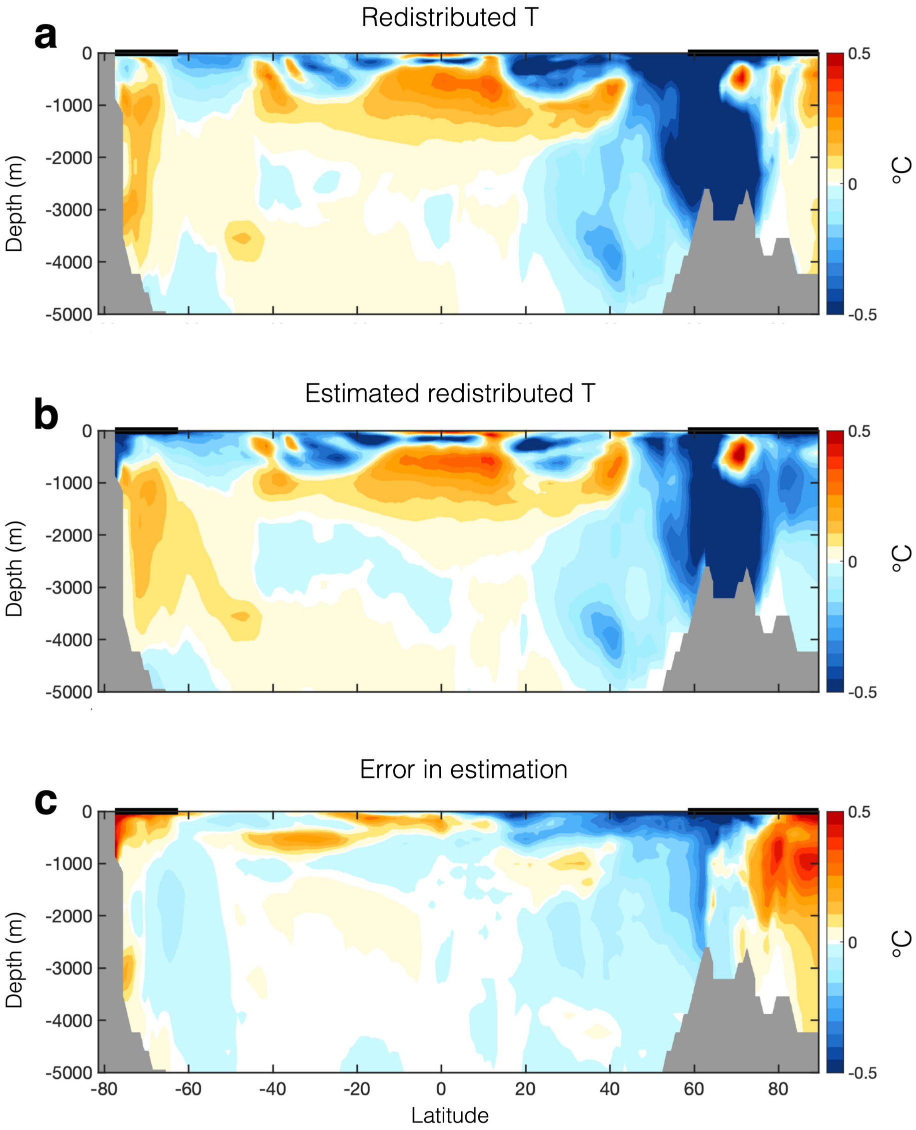

Extended Data Fig. 3 | ESM2M zonal-mean ocean redistributed warming. **a**, **b**, The year 61–80 zonal-mean ocean redistributed heat, here expressed as the zonal-mean temperature change, and calculated using the diagnosed fields from the ESM2M fixed-circulation experiment (**a**), and using the expression $H_{\mathrm{ad}}(y,z,t) = \alpha(t)C_{\mathrm{ant}}(y,z,t)$ (**b**). The parameters (y,z,t) indicate the zonal-mean quantities instead of vertical integrals, and $\alpha(t)$ is calculated globally as before, except here divided by volume, density and specific heat capacity so that values are given in terms of temperature instead of heat capacity. **c**, The difference between **a** and **b**; the black lines on the $z = 0$ axis show the mean sea-ice extent.

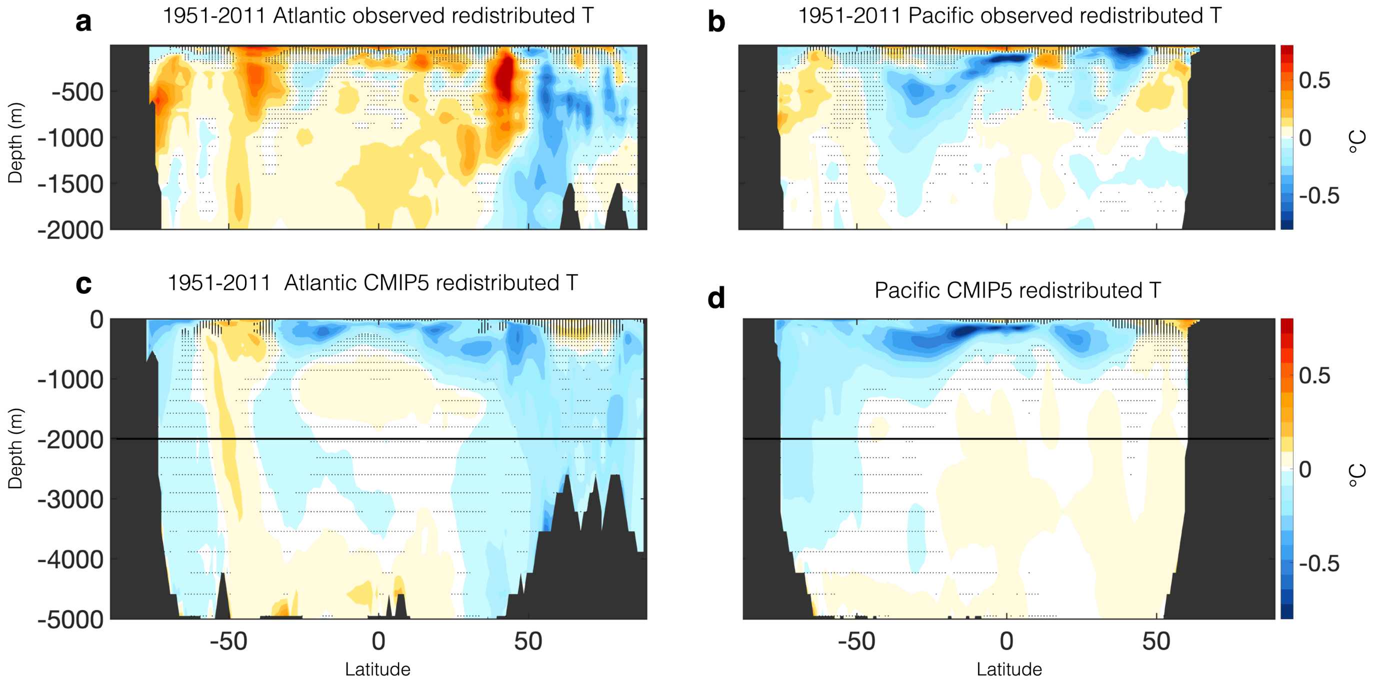

Extended Data Fig. 4 | 1951–2011 zonal-mean ocean redistributed warming. Ocean redistributed heat $H_{ad}(y,z,t) = \alpha(t)C_{ant}(y,z,t)$ in terms of temperature instead of than heat. Changes are shown as the linear trends over the indicated periods multiplied by the length of the period. **a**, **b**, The results from observational estimates for the Atlantic basin (**a**) and the Pacific basin (**b**). **c**, **d**, Changes in the CMIP5 historical RCP8.5 ensemble. The black horizontal line indicates the 2,000 m depth level above which we show the observations. The hatching indicates where the changes are not significant at the 66% uncertainty level. For the observations, the uncertainty is from the estimates of H and C_{ant}, whereas for the CMIP5 models the uncertainty is from the mean of the ensemble due to inter-model spread.

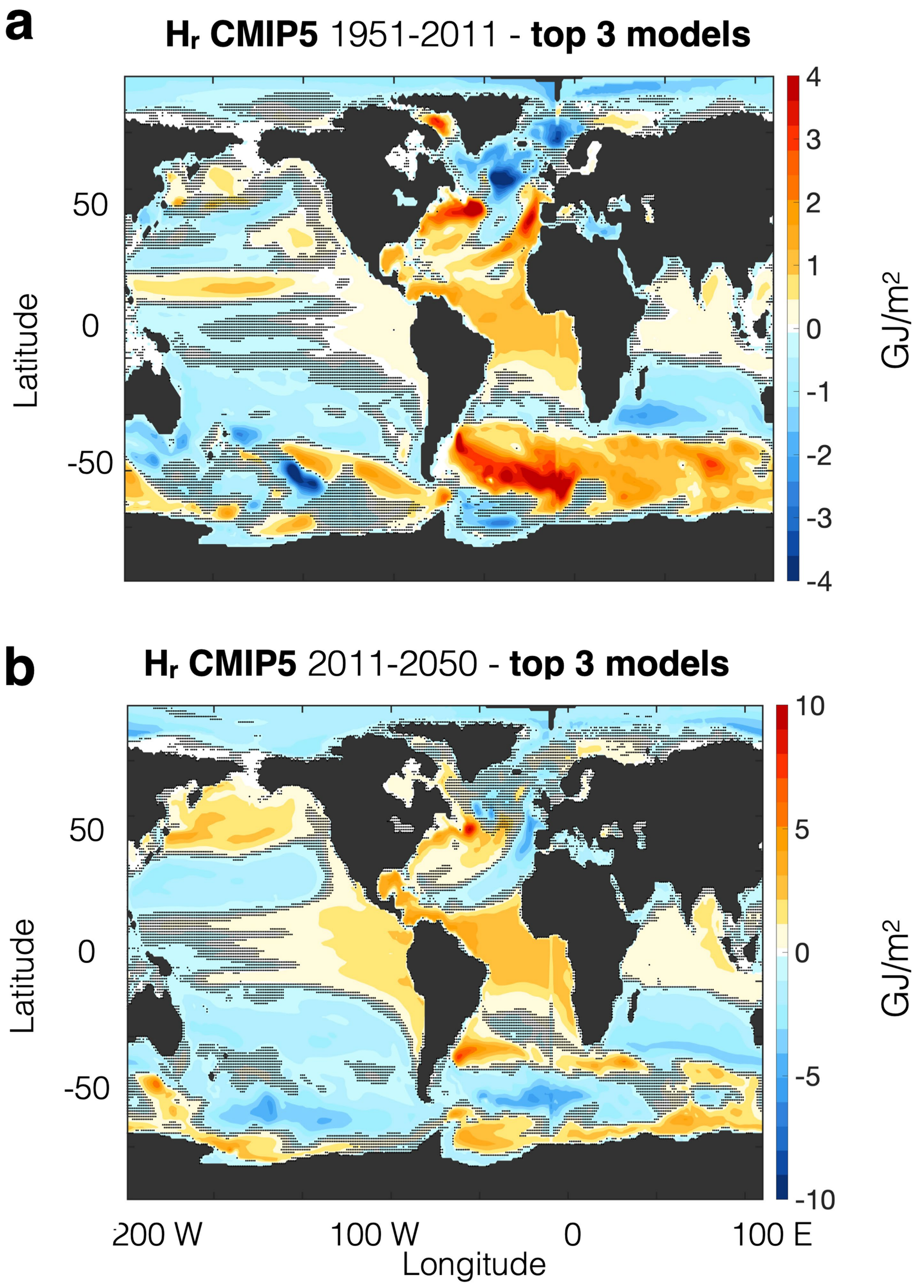

Extended Data Fig. 5 | CMIP5 ocean redistributed heat. **a**, Average 1951–2011 H_r for the three CMIP5 models (CNRM-CM5, GFDL ESM2M and GFDL ES2MG) with a value of H_r that best match the observational reconstruction. **b**, Average 2011–2060 H_r for the same models as in **a**. The hatching indicates where the changes are not significant at the 66% uncertainty level; the uncertainty is from the mean of the ensemble due to inter-model spread.

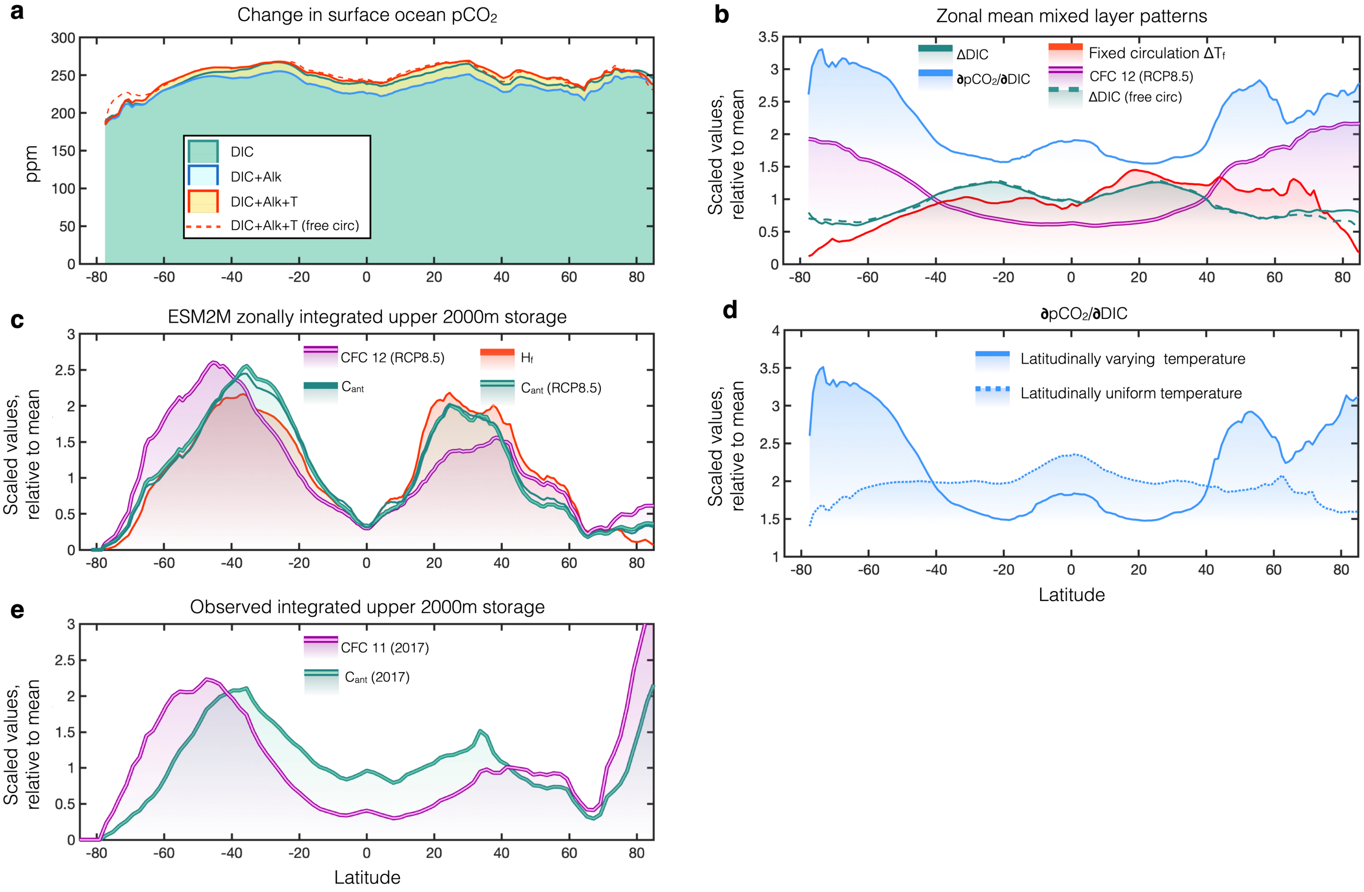

Extended Data Fig. 6 | Latitudinal profiles of ocean carbon and CFCs. **a**, ESM2M zonal-mean contribution of DIC (green), DIC+ALK (blue) and DIC+ALK+T (red) towards the change in ocean surface p_{CO_2}. Changes in p_{CO_2} (Δp_{CO_2}), are roughly equal to ($\partial p_{CO_2}/\partial$DIC)$\Delta$DIC. **b**, ESM2M zonal-mean mixed layer change, relative to the pre-industrial control, in ΔDIC (green), fixed-circulation added temperature ΔT_{ad} (red), and ΔCFC 12 (purple). The blue line shows the sensitivity term $\partial p_{CO_2}/\partial$DIC. **c**, ESM2M zonally integrated C_{ant} (green), CFC 12 (purple) and H_{ad} (red) storage in the upper 2,000 m relative to the pre-industrial control. Solid single lines show year 70 from the fixed-circulation 1%CO_2 and double lines show year 2060 of the ESM2M RCP8.5 simulation. **d**, ESM2M $\partial p_{CO_2}/\partial$DIC with a latitudinally varying temperature (solid) and a latitudinally constant temperature (dotted). **e**, Observed zonally integrated C_{ant} (green) and CFC 11 (purple) storage in the upper 2,000 m in year 2017, from ref. [24]. The quantities in **b**–**d** have been scaled by the global mean value for each tracer, and the blue line in **b** has been offset upwards by a scaled value of 1 for clarity.

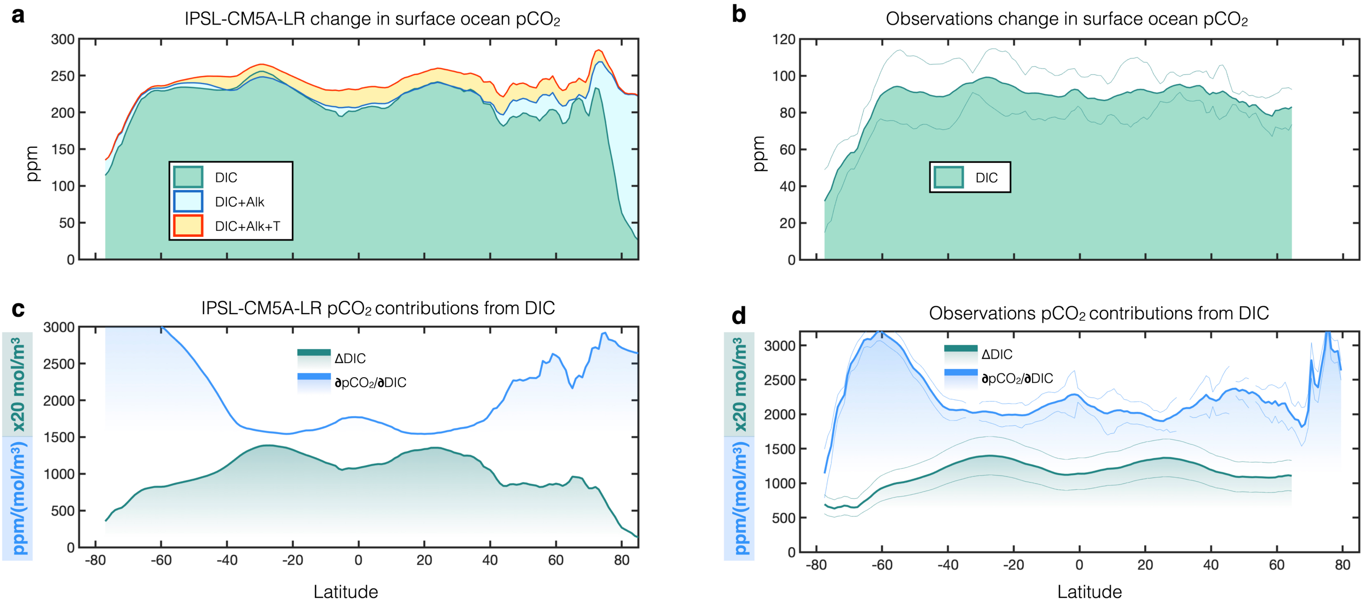

Extended Data Fig. 7 | Latitudinal p_{CO_2} changes. a, **b**, Zonal-mean contribution of DIC (green), DIC + ALK (blue) and DIC + ALK + T (total; red), towards the change in ocean surface p_{CO_2} at year 70 of the 1%CO$_2$ simulation with IPSL-CM5A-LR, relative to the pre-industrial control (**a**), and at year 2011 best-estimate from observations, relative to year 1765, using GLODAPv2[65–67] for mean-state fields and ΔDIC (C_{ant}) from ref. [24]. **c**, **d**, Zonal-mean contribution of ΔDIC (green) and $\partial p_{CO_2}/\partial$DIC (blue) towards ocean surface p_{CO_2} changes at year 70 of the 1%CO$_2$ simulation with IPSL-CM5A-LR (**c**), and year 2011 from observations (using GLODAPv2 for mean states fields[37] and ΔDIC from ref. [24]; **d**). The thin lines in **b** and **d** show the 66% confidence interval. p_{CO_2} values from observations are calculated using CO2SYS[68]. The correlation coefficients between ΔDIC and $\partial p_{CO_2}/\partial$DIC are −0.88 and −0.82 for IPSL-CM5A-LR and observations, respectively.

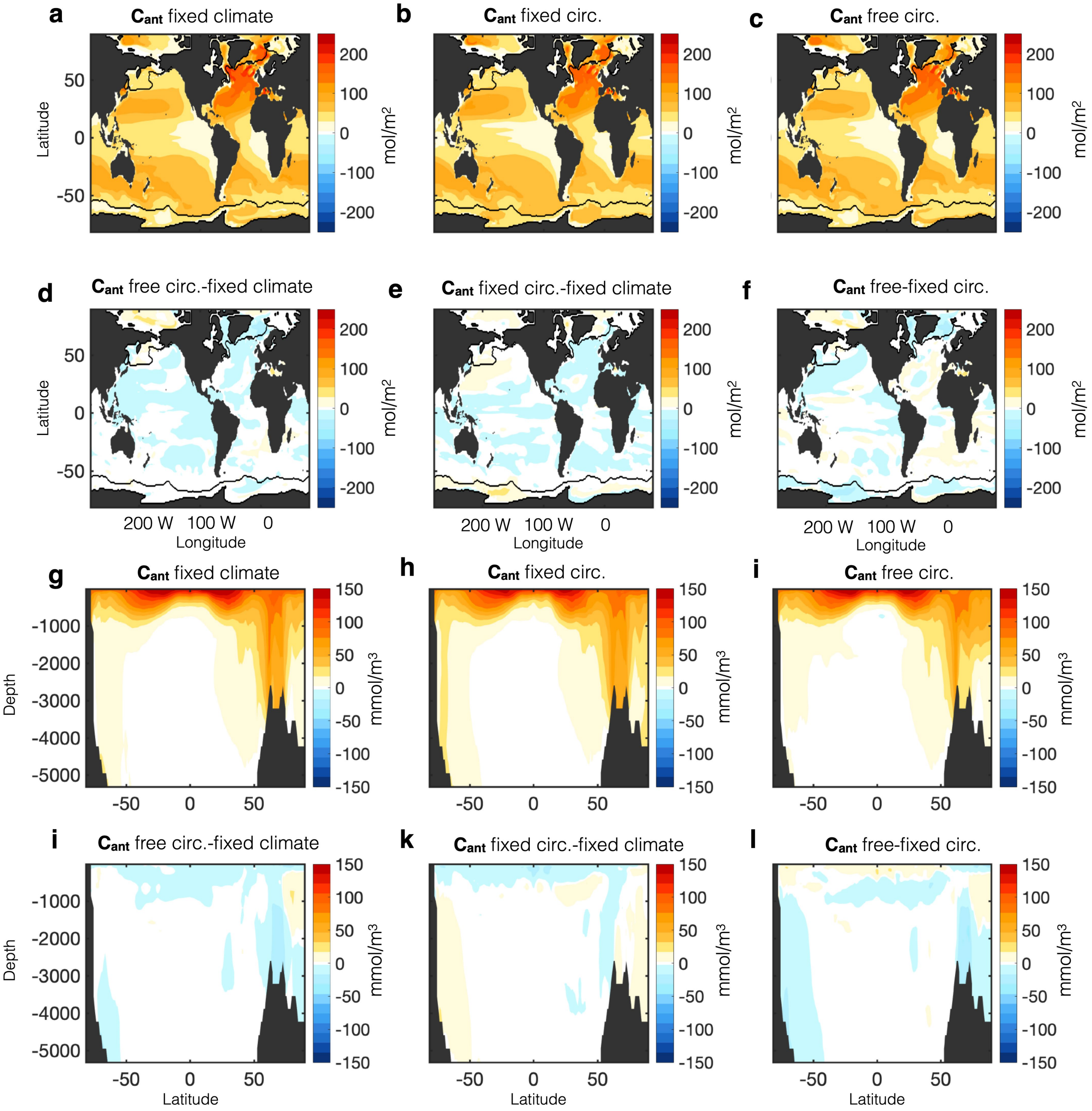

Extended Data Fig. 8 | Fixed-climate C_{ant}. a–**c**, Year 61–80 mean upper 2,000 m C_{ant} in the fixed-climate (**a**), fixed-circulation (**b**) and free-circulation (**c**) 1%CO_2 ESM2M simulations. In the fixed-climate simulation, atmospheric CO_2 is treated as a non-radiative gas[29]. The correlation coefficients of the fixed-circulation and fixed-climate C_{ant}, with free-circulation C_{ant} as shown, are 0.98 and 0.98, respectively. **d**, The difference between the free-circulation and fixed-climate experiments. **e**, The difference between the fixed-circulation and fixed-climate experiment. **f**, The difference between the free-circulation and fixed-circulation experiments. **g**–**l**, As in **a**–**f**, but for zonal-mean C_{ant}.

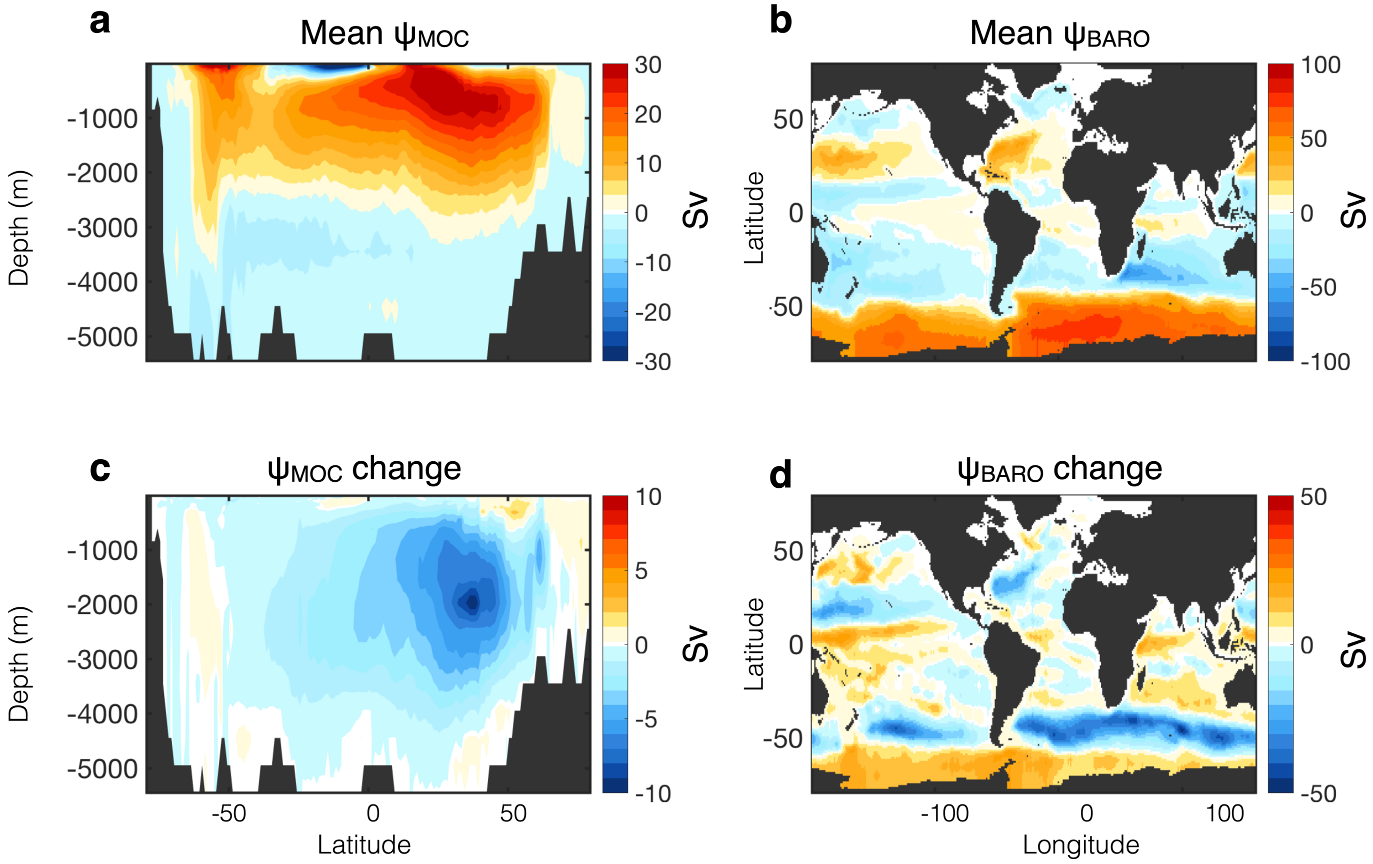

Extended Data Fig. 9 | MITgcm ocean circulation. a, **b**, The mean-state (**a**) and overturning (**b**) barotropic streamfunctions in the MITgcm control simulation, where 1 Sv = 10^6 $m^3 s^{-1}$. **c**, **d**, The perturbed (**c**) and overturning (**d**) barotropic streamfunctions in the MITgcm climate change simulation after 70 yr of warming (taken as the mean of years 61–80).

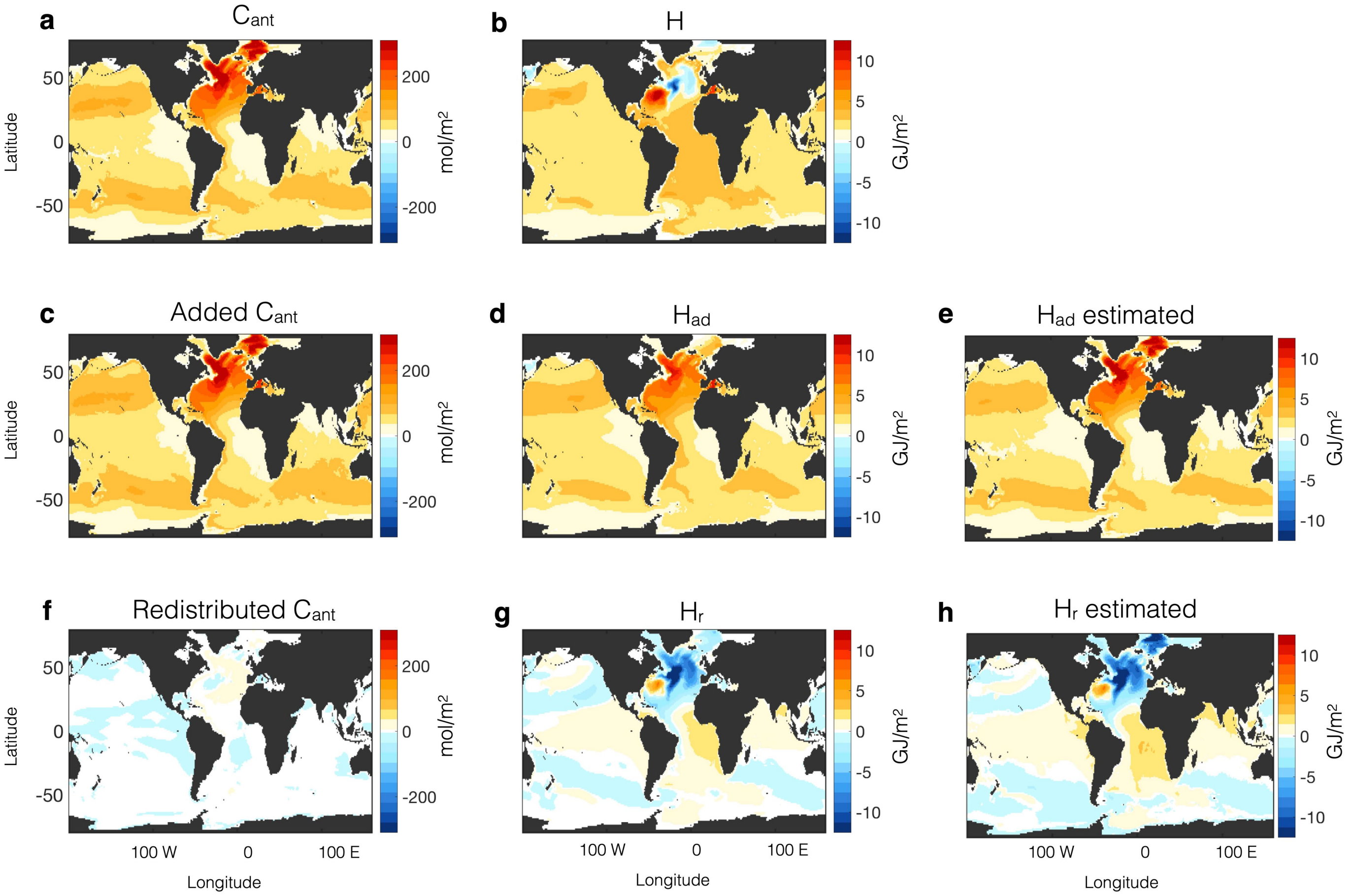

Extended Data Fig. 10 | MITgcm simulated anthropogenic tracer changes. **a**–**d**, Upper 2,000 m column-integrated anomalies in the MITgcm climate change experiments, for free-circulation carbon (**a**), free-circulation heat (**b**), fixed-circulation carbon (**c**), and fixed-circulation heat (**d**). **e**, **f**, The re-distributions of carbon (**e**) and heat (**f**) are taken as the difference between the free-circulation and fixed-circulation anomalies. Anomalies are taken as the difference between years 61–80 of the perturbed run and a tandem control. **g**, **h**, The fixed-circulation heat estimated using only the free-circulation experiment quantities (**g**), and the corresponding estimated redistributed heat (**h**).

Soil carbon loss by experimental warming in a tropical forest

https://doi.org/10.1038/s41586-020-2566-4

Received: 7 June 2019

Accepted: 18 June 2020

Andrew T. Nottingham[1,2]✉, Patrick Meir[1,3], Esther Velasquez[2] & Benjamin L. Turner[2]

Tropical soils contain one-third of the carbon stored in soils globally[1], so destabilization of soil organic matter caused by the warming predicted for tropical regions this century[2] could accelerate climate change by releasing additional carbon dioxide (CO_2) to the atmosphere[3–6]. Theory predicts that warming should cause only modest carbon loss from tropical soils relative to those at higher latitudes[5,7], but there have been no warming experiments in tropical forests to test this[8]. Here we show that in situ experimental warming of a lowland tropical forest soil on Barro Colorado Island, Panama, caused an unexpectedly large increase in soil CO_2 emissions. Two years of warming of the whole soil profile by four degrees Celsius increased CO_2 emissions by 55 per cent compared to soils at ambient temperature. The additional CO_2 originated from heterotrophic rather than autotrophic sources, and equated to a loss of 8.2 ± 4.2 (one standard error) tonnes of carbon per hectare per year from the breakdown of soil organic matter. During this time, we detected no acclimation of respiration rates, no thermal compensation or change in the temperature sensitivity of enzyme activities, and no change in microbial carbon-use efficiency. These results demonstrate that soil carbon in tropical forests is highly sensitive to warming, creating a potentially substantial positive feedback to climate change.

Tropical forests have a large role in the global carbon cycle because they exchange more CO_2 with the atmosphere than any other ecosystem, contain roughly two-thirds of terrestrial plant biomass[9] and harbour a substantial fraction of global soil carbon[1]. Between 30% and 50% of the carbon respired from tropical forests originates from soil, most of which is derived from the decomposition of organic matter[10–12]. Thus, even a small increase in respiration from tropical forest soils could have a large effect on atmospheric CO_2 concentrations, with consequences for global climate.

There is considerable concern that increased global temperatures will destabilize soil carbon and increase the flux of CO_2 from soil to the atmosphere[3–6]. Experiments in temperate and arctic regions have consistently found that short-term warming causes a considerable increase in soil CO_2 efflux compared to soil at ambient temperature[3,6,13] (for example, a 37% increase over 2 years in temperate forest)[6]. For the tropics, the response of soil carbon to warming is expected to be smaller than at higher latitudes because kinetic theory predicts that the intrinsic temperature sensitivity of reaction rates is reduced at higher temperatures[5,14]. Consistent with this, a meta-analysis of warming experiments has shown that the temperature sensitivity of soil CO_2 efflux increases with latitude[7]. However, the extent to which intrinsic temperature sensitivity translates into actual ('apparent') temperature sensitivity depends on covariation of other environmental factors that influence respiration, such as soil moisture and substrate availability[5,15]. As there have been no in situ warming experiments conducted in tropical forests, the apparent temperature sensitivity of soil organic matter in this biome remains unknown. As a result, earth system models continue to use kinetic theory to define the temperature sensitivity of soil carbon in the tropics[16], limiting how well they predict the response of tropical forests to global environmental change[17,18].

Several factors could influence the apparent temperature sensitivity of soil organic matter. For example, soil warming is typically accompanied by soil drying, which can either reduce respiration in aerobic soils by reducing water availability, or increase respiration in waterlogged soils by increasing oxygen availability[5,8,15]. Warming can also affect respiration rates by inducing changes in biotic processes, such as the physiology or community composition of microbes, or changes in substrate availability to decomposers[14]. In experiments performed at higher latitudes, temperature-adaptive or compensatory responses of microbial communities and enzyme activities have been shown to modulate the effect of warming on the soil carbon cycle[3,14]. In the tropics, future new temperature maxima could exceed critical biochemical thresholds[8,19,20], with added complexity emerging from altered interactions among species-rich plant and microbial communities[21] and covarying changes in hydrological or nutrient cycles[8].

Here we present results from the first warming experiment in a tropical forest (SWELTR: Soil Warming Experiment in Lowland Tropical Rainforest). The experiment tests the response of the whole soil profile to the 4 °C warming predicted for tropical latitudes by the end of this century[17] (Fig. 1a, Extended Data Figs. 1, 2). SWELTR consists of five pairs of circular control and warmed plots distributed evenly within approximately 1 ha of semideciduous moist lowland tropical forest on Barro Colorado Island, Panama. The soils are moderately weathered Dystric Eutrudepts (Inceptisols) that

---

[1]School of Geosciences, University of Edinburgh, Edinburgh, UK. [2]Smithsonian Tropical Research Institute, Panama City, Panama. [3]Research School of Biology, Australian National University, Canberra, Australian Capital Territory, Australia. ✉e-mail: Andrew.Nottingham@ed.ac.uk

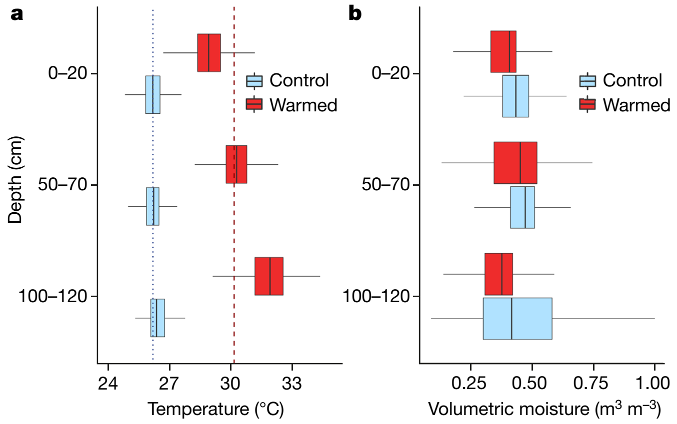

Fig. 1 | Soil temperature and moisture content in control and warmed plots by depth. a, Soil temperature. **b**, Volumetric soil moisture content. Data are measurements from integrated soil temperature and moisture probes for the two-year period after the warming treatment began (December 2016 to December 2018). The vertical lines in **a** (dotted blue and dashed red) show the mean soil temperature across the soil profile, which is 26.18 °C for control plots and 30.14 °C for warmed plots (3.96 °C difference). The treatment effect was $P < 0.001$ for all comparisons, based on the temporal variation across $n = 5$ plots. Box plots are standard Tukey plots, where the centre line represents the median, the lower and upper hinges represent the first and third quartiles, and whiskers represent + 1.5 the interquartile range. The treatments are offset on the *y* axis (depth) for easier viewing.

have developed on the volcanic facies of the Bohio formation (Extended Data Table 1, Methods). Each warmed plot has a ground surface area of around 20 m^2 heated to 1.2 m depth, resulting in a total volume of 120 m^3 of warmed soil across the experiment.

Two years of experimental warming increased soil CO_2 emissions by 55%, from 18.8 ± 1.9 megagrams of carbon per hectare per year ($Mg\,C\,ha^{-1}\,yr^{-1}$) in control plots to 29.2 ± 5.0 $Mg\,C\,ha^{-1}\,yr^{-1}$ in warmed plots (treatment effect, $P < 0.05$; Fig. 2, Extended Data Table 2, Extended Data Fig. 3). The soil CO_2 emission rate from unheated (control) plots is representative of tropical forests worldwide (8–40 $Mg\,C\,ha^{-1}\,yr^{-1}$), including in the Amazon basin (12–24 $Mg\,C\,ha^{-1}\,yr^{-1}$)[22]. Using exclusion and ingrowth cores to partition respiration from heterotrophic (soil-derived) and autotrophic (root-derived) sources, we find that the increase in CO_2 efflux was derived predominantly from heterotrophic sources, whether from the decomposition of leaf-litter inputs or from pre-existing soil organic matter (Figs. 2, 3, Extended Data Fig. 4). Soil-derived respiration increased from 12.0 ± 2.1 $Mg\,C\,ha^{-1}\,yr^{-1}$ in control plots to 20.1 ± 4.2 $Mg\,C\,ha^{-1}\,yr^{-1}$ in warmed plots (a 68% increase of 8.2 $Mg\,C\,ha^{-1}\,yr^{-1}$; treatment effect, $P < 0.05$), whereas root-derived respiration was not altered significantly ($P = 0.21$; 6.8 ± 1.2 $Mg\,C\,ha^{-1}\,yr^{-1}$ and 9.0 ± 3.4 $Mg\,C\,ha^{-1}\,yr^{-1}$ in control and warmed plots, respectively; Fig. 3, Extended Data Table 3).

It is possible that the large warming-induced increase in soil CO_2 efflux was due in part to soil drying because the warmed plots were slightly drier than the controls, particularly in the early wet season (Extended Data Fig. 2). In very wet soils, soil drying can increase respiration by increasing the supply of oxygen to microbes. By contrast, soil drying under aerobic conditions can reduce heterotrophic respiration by promoting water limitation of microbial metabolism[20]. Here, we find a marginally non-significant effect of soil moisture on CO_2 efflux across seasons (Extended Data Table 2; annual, $P = 0.69$; wet-season, $P = 0.07$; dry-season, $P = 0.06$), consistent with the parabolic relationship of CO_2 efflux with soil moisture for this site[22]. However, there was no direct effect of warming on soil moisture (surface soils, $P = 0.19$; whole-profile, $P = 0.24$; Extended Data Table 4) and the interaction between soil moisture and warming in the CO_2 efflux model was not significant (annually and for individual seasons; $P > 0.2$; Extended Data Table 2), indicating that the warming effect on CO_2 efflux was not influenced by soil moisture. Furthermore, soil moisture was not correlated with soil CO_2 efflux in the warmed plots (Extended Data Fig. 3), and drying during the early wet season in warmed soil (Extended Data Fig. 2) should decrease rather than increase CO_2 efflux because the soil was aerobic during this period and below the moisture content of 0.45 $m^3\,m^{-3}$ at which soil CO_2 efflux peaks in this forest[22]. Our data thus show that although soil moisture influenced soil CO_2 efflux and that warmed plots were slightly drier than control plots, particularly during the early wet season, this did not contribute significantly to the increased CO_2 efflux from the warmed soil.

There was no moderation of the warming-induced increase in soil CO_2 efflux over the two years of the experiment. Such a moderation might be expected in the long-term, through substrate limitation, adaptation of microbial communities (through changes in microbial carbon-use efficiency; CUE) or thermal compensation of enzyme activities (reduced maximum potential activity (V_{max}) at higher temperatures)[3,14,23]. We found no reduction in extractable or mineralized nitrogen or phosphorus with warming, as would be expected under nutrient limitation (Extended Data Fig. 5). Almost all hydrolytic enzymes were unaffected by warming (Extended Data Fig. 5), except for β-xylanase (an enzyme involved in hemicellulose degradation), for which activity increased with warming during the wet season—an opposite response to that predicted by thermal compensation[19]. The temperature sensitivity of enzyme activity (Q_{10} of V_{max}) was unaffected by warming (Extended Data Fig. 5a), indicating no dampening effect on soil carbon breakdown via thermal adaptation of enzyme production as expected at warmer temperatures[24]. Microbial CUE, which broadly represents carbon stabilized in biomass relative to carbon lost in respiration and can influence long-term (decadal) soil carbon loss[3,23], was unaffected by warming (treatment effect, $P = 0.37$; Extended Data Fig. 5). Microbial biomass carbon, however, increased with warming at the annual scale (treatment effect, annual scale, $P = 0.02$), with a marginally non-significant increase at the seasonal scale ($P < 0.1$; Extended Data Fig. 5). Together, these results suggest slightly increased growth in response to greater organic-matter turnover in the absence of nutrient constraints to carbon degradation, which did not translate into changes in CUE.

Our finding that tropical forest soil carbon has a high apparent temperature sensitivity challenges the prevailing expectation that the temperature sensitivity of soil carbon is lower in the tropics compared to cooler ecosystems at higher latitudes[5,7]. The 55% increase in total soil CO_2 emissions we report here (from 18.8 to 29.2 $Mg\,C\,ha^{-1}\,yr^{-1}$) following two years of 4 °C whole-soil-profile warming is larger than that found in a temperate forest using a similar whole-profile experimental design (34%–37% increase over two years of 4 °C whole-profile warming, from 13.0 to 17.5 $Mg\,C\,ha^{-1}\,yr^{-1}$)[6]. Furthermore, the rate of additional soil carbon loss (8.2 $Mg\,C\,ha^{-1}\,yr^{-1}$) is greater than for all the studies in a recent meta-analysis of surface-only soil warming experiments at higher-latitude sites (all loss rates less than 5 $Mg\,C\,ha^{-1}\,yr^{-1}$)[4]. The expectation that the temperature sensitivity of soil carbon breakdown is lower in the tropics compared to higher latitudes, based in part on kinetic theory and commonly used to describe soil carbon responses in earth system models[16], is therefore not consistent with the ('apparent')[5,15] temperature sensitivity of the breakdown of tropical forest soil carbon reported here. However, our results are consistent with recent atmospheric and satellite measurements, which have shown a high sensitivity of ecosystem-scale carbon cycling in tropical regions in response to interannual temperature variation[25,26]. Our findings suggest that tropical soils contribute substantially to these ecosystem-scale responses to warming.

This high apparent temperature sensitivity of tropical forest soil carbon under in situ experimental warming must arise through the temperature response of covarying ecosystem properties rather than as

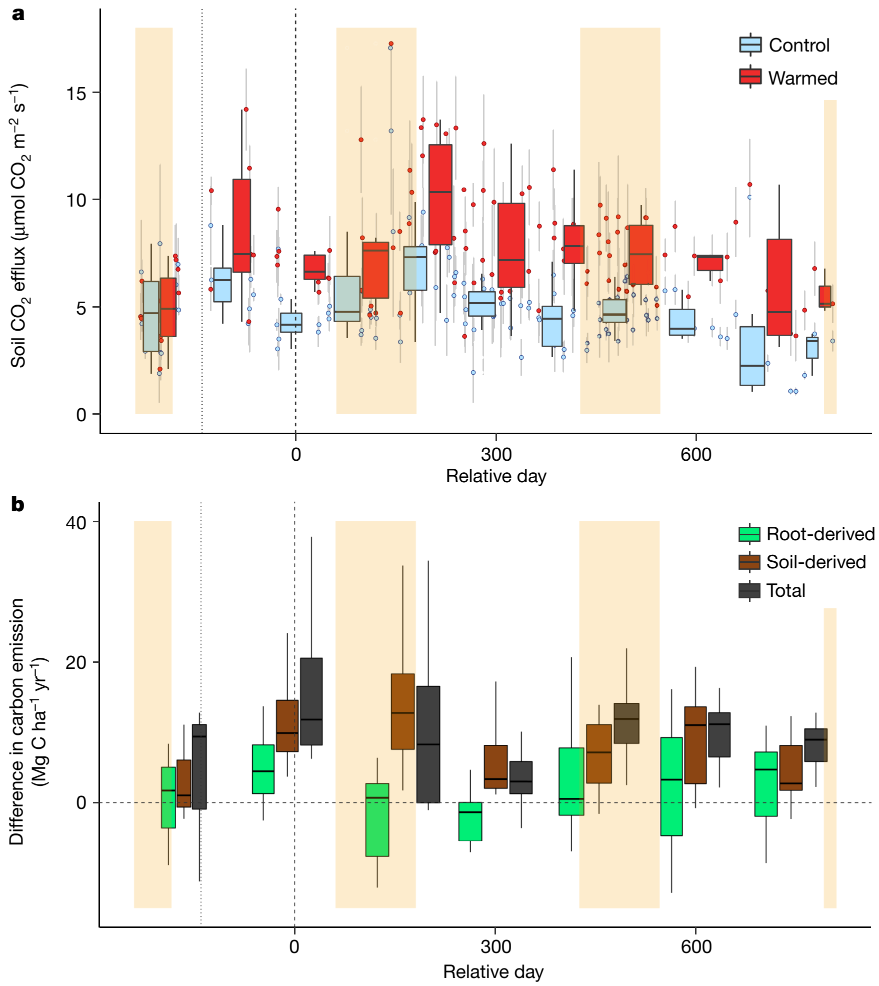

Fig. 2 | Soil CO$_2$ efflux from control and warmed soils over two years. a, Total soil CO$_2$ flux during the study period (2017–2019), relative to the beginning of the warming treatment (relative day 0). **b**, Difference in carbon emission (warmed minus control) partitioned into soil-derived and root-derived components. Measurements were made every two weeks. Points in **a** represent the mean value of five plots, with error bars representing one standard error of the spatial variation ($n = 5$ plots). The box plots represent the temporal variation over sequential 100-day periods to show seasonal dynamics. Box plots are standard Tukey plots, where the centre line represents the median, the lower and upper hinges represent the first and third quartiles, and whiskers represent +1.5 the interquartile range. The dotted vertical line shows when installation and testing of warming plots began (during this period each plot was warmed by 4 °C relative to controls for a period of 1–2 weeks); the dashed vertical line (relative day 0; 1 November 2017) shows when all five warming plots were switched on permanently. The yellow shaded areas represent dry seasons (1 January to 1 April). Soil CO$_2$ efflux was significantly higher in warmed plots for annual data and for dry or wet seasons individually (Extended Data Table 2).

the sole consequence of intrinsic kinetic processes. Although our data do not provide conclusive evidence for the mechanism(s) underlying this marked increase in soil carbon loss from warmed soil, several findings point to a possible explanation: (i) the general absence of thermal compensation in enzyme activities (no decrease in V_{max}); (ii) the lack of change in the temperature sensitivity of enzymes under warming (no decrease in Q_{10} of V_{max}); and (iii) the lack of a moderating thermal response of microbial CUE (Extended Data Fig. 5)[23,27,28]. Together, our results indicate that organic-matter degradation increased under warming with no moderating responses or acclimation among microbial communities or the enzymes they synthesize.

This surprisingly large loss of soil carbon from warmed soil represents a substantial positive climate feedback over the period of this study. The additional carbon loss from warming observed here

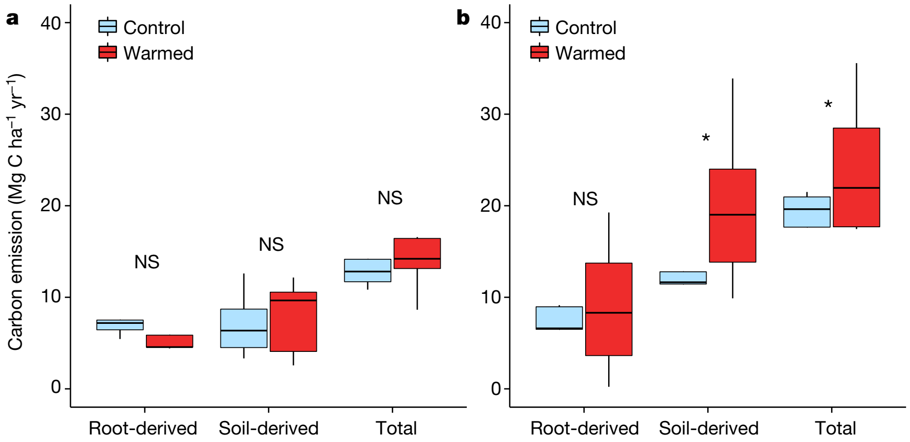

Fig. 3 | The annual carbon emission partitioned into soil-derived and root-derived components. a, The pre-treatment period (January–May 2016; predominantly dry season). **b**, The two years with warming. The figures show total CO$_2$ and the root-derived and soil-derived components calculated using CO$_2$ efflux from partition cores (equations (1) and (2) in Methods). Differences between control and warmed plots are shown by asterisks where $P \leq 0.05$ or as non-significant (NS); determined using mixed effect models (Extended Data Tables 2, 3). Box plots are standard Tukey plots, where the centre line represents the median, the lower and upper hinges represent the first and third quartiles, and whiskers represent +1.5 the interquartile range (for $n = 5$ plots).

is of similar magnitude to annual carbon input from litterfall at this site (5–7 Mg C ha^{-1} yr^{-1})[29] and is equivalent to approximately 13% of the total soil carbon stock, or 30% of gross primary productivity (27.5 Mg C ha^{-1} yr^{-1})[30]. Extrapolation of the first two years of carbon loss in our experiment across the entire tropical forest soil carbon stock (502 Pg C)[1] indicates a global loss of more than 65 Pg C with 4 °C warming this century, which is in broad agreement with estimated carbon loss based on a five-year soil translocation experiment in tropical forests elsewhere[31]. In light of these findings, earlier estimates of global soil carbon loss under 4 °C warming (110–190 Pg C)[3,32], which were based on experiments performed at higher latitudes, underestimate the magnitude of this global earth–atmosphere feedback.

We expect that the rate of soil carbon loss will eventually decline in warmed soils as substrate limitation increases, but we do not know how long this will take, nor whether the long-term soil carbon balance will be affected by plant–soil interactions or changes in soil microbial communities as they adapt to warmer temperatures[3,13,14,23]. The nature of these longer-term responses will determine the strength of this positive earth–atmosphere feedback, which is already substantial in the short-term, in contributing to further climate warming.

Online content

Any methods, additional references, Nature Research reporting summaries, source data, extended data, supplementary information, acknowledgements, peer review information; details of author contributions and competing interests; and statements of data and code availability are available at https://doi.org/10.1038/s41586-020-2566-4.

1. Jackson, R. B. et al. The ecology of soil carbon: pools, vulnerabilities, and biotic and abiotic controls. *Annu. Rev. Ecol. Evol. Syst*. **48**, 419–445 (2017).
2. Ciais, P. et al. in *Climate Change 2013: The Physical Science Basis. Contribution of Working Group I to the Fifth Assessment Report of the Intergovernmental Panel on Climate Change* (eds Stocker, T. F. et al.) Ch. 6 (Cambridge Univ. Press, 2013).
3. Melillo, J. M. et al. Long-term pattern and magnitude of soil carbon feedback to the climate system in a warming world. *Science* **358**, 101–105 (2017).
4. van Gestel, N. et al. Predicting soil carbon loss with warming. *Nature* **554**, E4–E5 (2018).
5. Davidson, E. A. & Janssens, I. A. Temperature sensitivity of soil carbon decomposition and feedbacks to climate change. *Nature* **440**, 165–173 (2006).
6. Hicks Pries, C. E., Castanha, C., Porras, R. C. & Torn, M. S. The whole-soil carbon flux in response to warming. *Science* **355**, 1420–1423 (2017).
7. Carey, J. C. et al. Temperature response of soil respiration largely unaltered with experimental warming. *Proc. Natl Acad. Sci. USA* **113**, 13797–13802 (2016).
8. Wood, T. E. et al. in *Ecosystem Consequences of Soil Warming: Microbes, Vegetation, Fauna and Soil Biogeochemistry* (ed. Mohan, J. E.) Ch. 14, 385–439 (Academic Press, 2019).
9. Pan, Y. et al. A large and persistent carbon sink in the world's forests. *Science* **333**, 988–993 (2011).
10. Anderson-Teixeira, K. J., Wang, M. M. H., McGarvey, J. C. & LeBauer, D. S. Carbon dynamics of mature and regrowth tropical forests derived from a pantropical database (TropForC-db). *Glob. Change Biol*. **22**, 1690–1709 (2016).
11. Malhi, Y. The productivity, metabolism and carbon cycle of tropical forest vegetation. *J. Ecol*. **100**, 65–75 (2012).
12. Chambers, J. Q. et al. Respiration from a tropical forest ecosystem: partitioning of sources and low carbon use efficiency. *Ecol. Appl*. **14**, 72–88 (2004).
13. Romero-Olivares, A. L., Allison, S. D. & Treseder, K. K. Soil microbes and their response to experimental warming over time: a meta-analysis of field studies. *Soil Biol. Biochem*. **107**, 32–40 (2017).
14. Tang, J. et al. in *Ecosystem Consequences of Soil Warming: Microbes, Vegetation, Fauna and Soil Biogeochemistry* (ed. Mohan, J. E.) Ch. 8, 175–201 (Academic Press, 2019).
15. Nottingham, A. T. et al. Climate warming and soil carbon in tropical forests: insights from an elevation gradient in the Peruvian Andes. *Bioscience* **65**, 906–921 (2015).
16. Todd-Brown, K. E. O. et al. Causes of variation in soil carbon predictions from CMIP5 Earth system models and comparison with observations. *Biogeosciences* **10**, 1717–1736 (2013).
17. Intergovernmental Panel on Climate Change (IPCC). *Global Warming of 1.5 °C: An IPCC Special Report on the Impacts of Global Warming of 1.5 °C Above Pre-Industrial Levels and Related Global Greenhouse Gas Emission Pathways, in the Context of Strengthening the Global Response to the Threat of Climate Change, Sustainable Development, and Efforts to Eradicate Poverty* (eds Masson-Delmotte, V. et at.) Ch. 3 (World Meteorological Organization, 2018).
18. Cox, P. M. et al. Sensitivity of tropical carbon to climate change constrained by carbon dioxide variability. *Nature* **494**, 341–344 (2013).
19. Mora, C. et al. The projected timing of climate departure from recent variability. *Nature* **502**, 183–187 (2013).
20. Beaumont, L. J. et al. Impacts of climate change on the world's most exceptional ecoregions. *Proc. Natl Acad. Sci. USA* **108**, 2306–2311 (2011).
21. Steidinger, B. S. et al. Climatic controls of decomposition drive the global biogeography of forest-tree symbioses. *Nature* **569**, 404–408 (2019).
22. Rubio, V. E. & Detto, M. Spatiotemporal variability of soil respiration in a seasonal tropical forest. *Ecol. Evol*. **7**, 7104–7116 (2017).
23. Frey, S. D., Lee, J., Melillo, J. M. & Six, J. The temperature response of soil microbial efficiency and its feedback to climate. *Nat. Clim. Chang*. **3**, 395–398 (2013).
24. Bradford, M. A. Thermal adaptation of decomposer communities in warming soils. *Front. Microbiol*. **4**, https://doi.org/10.3389/fmicb.2013.00333 (2013).
25. Wang, X. H. et al. A two-fold increase of carbon cycle sensitivity to tropical temperature variations. *Nature* **506**, 212–215 (2014).
26. Liu, J. J. et al. Contrasting carbon cycle responses of the tropical continents to the 2015–2016 El Nino. *Science* **358**, eaam5690 (2017).
27. Karhu, K. et al. Temperature sensitivity of soil respiration rates enhanced by microbial community response. *Nature* **513**, 81–84 (2014).
28. Bradford, M. A. et al. Cross-biome patterns in soil microbial respiration predictable from evolutionary theory on thermal adaptation. *Nat. Ecol. Evol*. **3**, 223–231 (2019).
29. Wieder, R. K. & Wright, S. J. Tropical forest litter dynamics and dry season irrigation on Barro Colorado Island, Panama. *Ecology* **76**, 1971–1979 (1995).
30. Chave, J. et al. Spatial and temporal variation of biomass in a tropical forest: results from a large census plot in Panama. *J. Ecol*. **91**, 240–252 (2003).
31. Nottingham, A. T. et al. Microbial responses to warming enhance soil carbon loss following translocation across a tropical forest elevation gradient. *Ecol. Lett*. **22**, 1889–1899 (2019).
32. Crowther, T. W. et al. Quantifying global soil carbon losses in response to warming. *Nature* **540**, 104–108 (2016).

Methods

Site and experiment

The experiment is situated in approximately 1 ha of seasonally moist lowland tropical forest on Barro Colorado Island, Panama[33]. Within the plot area, the dominant tree species include *Anarcardium excelsum* and *Poulsenia armata*. The soils are Inceptisols (fine, isohyperthermic, Dystric Eutrudepts) that are rich in clay (about 54% profile-weighted clay concentration) and secondary metal oxides. They are developed on the volcanic facies of the Bohio formation, a basaltic conglomerate of Oligocene age[34]. Although these moderately weathered Inceptisols are less infertile than soils under larger areas of lowland tropical forests, Inceptisols still account for 14% of total land area in the tropics (Ultisols and Oxisols account for 20% and 23%, respectively)[35], and soil respiration in the control plots in our experiment is comparable to that in lowland tropical forests in general, including those on Ultisols and Oxisols[22].

The SWELTR experiment consists of ten circular plots (five paired 'warm' and 'control' plots). Each plot measures 5 m diameter, with approximately 10 m between each pair of control and warmed plots and a minimum of 20 m between different plot pairs. The warmed plots contain two heating structures, each consisting of eight 1-m-long stainless-steel rods, connected by approximately 50 cm of flexible stainless-steel conduit. We used stainless-steel T-junctions at the top of each rod (adjoining the flexible conduit) and conical caps at the bottom of each rod. The final structure was 1.2 m tall. Inside each of the structures, we threaded 25 m of heating cable (SLMCAB10120BF, Briskheat) and filled the remaining space in the rods and conduit with quartz sand, selected for its high thermal conductivity. The complete structure was welded to seal the heating cable and sand inside. Two of these structures were buried around a 3.5-m-diameter circumference, with the top of the flexible conduit 5 cm belowground. Thus, each plot contained 50 m of heating cable inserted to 1.2 m depth, encircling a 3.5-m-diameter area, with an effective heated plot area of 5 m diameter. The experiment heats approximately 120 m^3 of soil in total (five plots, 5 m diameter, 1.2 m depth). The plot design and heating methodology follows previous studies[6,36].

Experiment power supply

The experiment was powered using a 120-V supply, delivered from a mains outlet situated approximately 300 m from the experimental site. The power cables from the mains outlet to each of the five experiment control units were placed inside 19-mm-diameter liquid-tight flexible steel conduit and buried in roughly 20-cm-deep trenches. For each of the five control units (situated next to each warm–control plot pair), we installed a 20-A circuit breaker and a 12-V outlet, supplied by a battery connected to a 12-V battery maintainer. The 120-V outlets provided power to the heating cables, gas analyser system and battery maintainers; the 12-V outlet provided power to the dataloggers, relays and sensors. Maximum power consumption is 2,500 W (500 W per plot), although average consumption is roughly 500–1,000 W.

Temperature control

Each warming and control plot was connected to a thermostat system, which maintained soil temperature in the warmed plots at 4 °C above ambient temperature. The thermostat system consisted of three integrated temperature and moisture sensors per plot (CS655 Reflectometer, Campbell Scientific; 20 cm in length), inserted to depths of 0–20 cm, 50–70 cm and 100–120 cm at the mid-radius point in each plot, which were connected to a control unit (one control unit for each plot pair; five in total). The CS655 sensors continuously measured soil temperature to control the thermostat and logged the soil temperature and volumetric soil moisture every hour. These whole-profile measurements were complemented by independent measurements of surface (0–20 cm) soil temperature and moisture (see below). The control units consisted of waterproof (IP68) enclosures containing a solid-state power controller (DA10-24C0-0000, Watlow), relay (12-V single channel), datalogger (CR1000, Campbell Scientific), and 12-V and 120-V power supply. Temperature in each warmed plot was therefore maintained at 4 °C above the temperature in each corresponding paired control plot, based on the average temperature from 0 cm to 120 cm depth at the mid-radius point in each plot. The average temperature difference over two years was 3.96 °C, which corresponds to the average of 2.7 °C at 0–20 cm depth, 4.0 °C at 50–70 cm depth and 5.2 °C at 100–120 cm depth.

This experimental design has been shown to warm the soil approximately uniformly across the soil volume, with minor anomalies of warmer soil very close to the heating rods (within 10 cm) and slightly cooler surface soils as a result of heat-transfer to the air[6,36]. Therefore, surface soils were slightly cooler compared to subsoils, although the response of surface soils (rather than subsoils) will probably dominate the warming response across the soil profile because they contain greater organic matter (two-thirds of the carbon stock occurs in the upper 50 cm of the soil profile; Extended Data Table 1). The heating structures were installed during May–July 2016, and plots were tested during June–October 2016. The testing phase consisted of heating each plot by 4 °C for approximately 2-week periods. The experiment was switched on in full on 1 November 2016.

Soil gas-exchange and partitioning

Soil CO_2 efflux was measured every two weeks from 2016 until 2019 at four systematically distributed locations within each plot using an infrared gas analyser (IRGA Li-8100; LI-COR Biosciences). The measurement period was increased to every week during seasonal transitions. The soil collars for CO_2 efflux measurements were assigned to zones within each plot ('centre 1', 'centre 2', 'side 1' and 'side 2') and were relocated randomly within each zone every three months, for long-term within-plot spatial independence. Soil CO_2 efflux was also measured every two weeks for four root-partition cores per plot (two root-exclusion and two root-ingrowth) to determine soil- and root-derived components of the CO_2 efflux. At the same time as soil CO_2 efflux measurements, we measured soil temperature (using a HI98509 thermometer probe; Hanna Instruments) and soil moisture (using a Thetaprobe; Delta-T) at 0–20 cm soil depth for a random location within a 1 m radius of each soil collar, or within the root-partition cores.

Root-exclusion cores were made from PVC tubing (30 cm height, 10 cm diameter) with a 1-μm nylon mesh base for drainage. Root-ingrowth cores (disturbance controls) had additional windows (around 340 cm^2) covered with 2-mm mesh around the sides[35]. In each plot, two root-exclusion cores and two root-ingrowth cores were buried within each plot, approximately 30 cm from the heating cable (where the soil profile is warmed on average by 4 °C).

The percentage contributions of fine roots and rhizo-microorganisms (root-derived) and free-living heterotrophic microorganisms (soil-derived) to the total soil CO_2 efflux were calculated as follows:

$$\begin{aligned}&\text{soil-derived } CO_2 \text{ efflux (\%)}\\&\quad= (\text{root-exclusion core } CO_2 \text{ efflux})\\&\qquad/(\text{root-ingrowth core } CO_2 \text{ efflux}) \times 100,\end{aligned} \tag{1}$$

$$\begin{aligned}&\text{root-derived } CO_2 \text{ efflux (\%)}\\&\quad= 100 - \text{soil-derived } CO_2 \text{ efflux (\%)}.\end{aligned} \tag{2}$$

Total soil CO_2 efflux measured for soil collars was multiplied by the results from equations (1) and (2) to estimate the absolute contributions of root-derived (roots, rhizo-microbial and mycorrhizal) and soil-derived (free-living microbial through the decomposition of litter and soil organic matter) components[37]. The partition cores were buried to 0–25 cm depth, where 95% fine roots occur[38]. Therefore, the soil component consists of soil-derived CO_2 from the entire soil profile (with a minor contribution from fine roots at greater than 20 cm depth).

Soil properties

Soil was sampled before the experimental treatments began (to 100 cm depth; Extended Data Table 1) and then every three months after the beginning of the experiment (0–10 cm; average responses in Extended Data Fig. 5), at a point within the plots where the surface soil is heated evenly (at approximately 30 cm from the heating structure). These samples were then analysed using standard procedures to determine the soil properties: total elements, available nutrients, microbial carbon, nitrogen and phosphorus, and enzyme activities (see below). We calculated microbial CUE using microbial carbon, nitrogen and phosphorus and enzyme activity data using a stoichiometric method[39]. Here we describe the responses following two years of warming, by using the average change in soil properties over two years (average of eight temporal measurements per plot, with $n = 5$ per plot).

Total carbon and nitrogen were determined simultaneously by automated combustion and gas chromatography using a Thermo Flash 1112 elemental analyser (CE Elantech). Total phosphorus was determined by ignition (550 °C, 1 h) and extraction in 1 M H_2SO_4 (16 h; 1:50 soil to solution ratio) with phosphate detection by automated molybdate colorimetry. Exchangeable cations were determined by extraction in 0.1 M $BaCl_2$ and detection by inductively coupled plasma-optical emission spectrometry with an Optima 7300 DV (Perkin-Elmer)[40]. Effective cation exchange capacity (ECEC) was calculated as the sum of the charge equivalents of Al, Ca, Fe, K, Mg, Mn and Na. Soil pH was determined in deionized water in a 1:2 soil to solution ratio.

Extractable carbon and nitrogen were determined by fresh soil extraction in 0.5 M K_2SO_4. Soil microbial biomass carbon and nitrogen were measured by fumigation–extraction[41,42], using ethanol-free chloroform as the fumigant followed by extraction with K_2SO_4. Extracts of fumigated and unfumigated soil were analysed for extractable organic carbon and nitrogen using a TOC-VCHN analyser (Shimadzu). Microbial carbon and nitrogen were calculated as the difference in the respective nutrient between fumigated and unfumigated extracts and corrected for unrecovered biomass using a k factor[43] of 0.45. Microbial biomass phosphorus was determined by hexanol fumigation and extraction with anion-exchange membranes[44]. Phosphate was recovered from anion-exchange membranes by shaking for 1 h in 50 ml of 0.25 M H_2SO_4, with detection in the acid solution by automated molybdate colorimetry using a Lachat Quikchem 8500 (Hach). Extractable phosphorus was determined on unfumigated samples and microbial phosphorus was calculated as the difference between the fumigated and unfumigated samples, with correction for unrecovered biomass using a k_p factor[44] of 0.4.

Soil enzyme activity (V_{max}) was determined for seven enzymes involved in carbon and nutrient cycling. We used microplate fluorimetric assays with 100 μM methylumbelliferone (MU)-linked substrates to measure the activity of β-glucosidase (degradation of β bonds in glucose), cellobiohydrolase (degradation of cellulose), *N*-acetyl β-glucosaminidase (degradation of *N*-glycosidic bonds), phosphomonoesterase (degradation of monoester-linked simple organic phosphates), sulfatase (degradation of sulfate esters) and β-xylanase (degradation of hemicellulose). For each soil sample, five replicate microplates were prepared and incubated at 2 °C, 10 °C, 22 °C, 30 °C or 40 °C to calculate the temperature sensitivity (Q_{10}) of V_{max} and determine V_{max} at control (26 °C) and warmed (30 °C) soil temperatures. Further information on protocols for enzyme analyses is provided elsewhere[45,46]. All analyses apart from total elements (carbon, nitrogen, phosphorus), cations and pH were determined on fresh soils within 24 h of sampling, and K_2SO_4 extracts within 6 h, to avoid the rapid changes that can occur during storage or pretreatment[47]. All soil chemical properties are expressed on the basis of oven-dry equivalent soil (determined by drying at 105 °C for 24 h).

Determination of carbon and nutrient use efficiencies

We estimated carbon, nitrogen and phosphorus use efficiencies (CUE, NUE and PUE) from ecological stoichiometry, whereby the CUE, NUE or PUE of an organism is a function of the difference between its elemental requirements for growth (carbon, nitrogen or phosphorus in biomass and enzymatic investment for acquisition) and the abundance of environmental substrate (carbon, nitrogen or phosphorus in soil organic matter). This approach assumes that enzyme activities scale with microbial production and organic-matter concentration, and that microbial communities exhibit optimum resource allocation with respect to enzyme expression and environmental resources. These assumptions are empirically supported by Michaelis–Menten kinetics and metabolic control analysis[39]. On the basis of this underlying assumption, CUE is calculated as

$$\mathrm{CUE}_{\mathrm{C:X}} = \mathrm{CUE}_{\mathrm{MAX}}[S_{\mathrm{C:X}}/(S_{\mathrm{C:X}} + K_{\mathrm{X}})],$$

$$S_{\mathrm{C:X}} = (B_{\mathrm{C:X}}/L_{\mathrm{C:X}})/\mathrm{EEA}_{\mathrm{C:X}}.$$

Here $S_{C:X}$ represents the extent to which the allocation of enzyme activities offsets the disparity between the elemental composition of available resources and the composition of microbial biomass. $K_X = 0.5$ and $\mathrm{CUE}_{MAX} = 0.6$ are the half-saturation constant and the upper limit for microbial growth efficiency based on thermodynamic constraints, respectively. $\mathrm{EEA}_{C:X}$ is the extracellular enzyme activity (nmol g^{-1} h^{-1}): $\mathrm{EEA}_{C:N}$ was calculated as BG/NAG, where BG = β-glucosidase and NAG = *N*-acetyl β-glucosaminidase, and $\mathrm{EEA}_{C:P}$ was calculated as BG/P, where P = phosphomonoesterase. Molar ratios of soil organic carbon to total nitrogen to total phosphorus were used as estimates of $L_{C:X}$. Microbial biomass ratios $B_{C:X}$ were also calculated as molar ratios.

Statistical analyses

Treatment (warming) effects on time-averaged total and partitioned CO_2 emissions and other soil properties (nutrients and microbial properties) were tested using ANOVA. Treatment effects on soil CO_2 emissions were primarily tested for using mixed-effects models with CO_2 efflux as the response variable, warming treatment, soil moisture, season, warming × soil moisture and season × soil moisture as fixed effects, and plot number as a random effect[48]. As the within-plot location of the four soil CO_2 efflux sampling points (soil collar) was changed every three months, we did not include time as a random effect (repeated measures) in the primary model. The soil collars within each plot were moved every three months, but always systematically assigned to zones within the plot: centre 1, centre 2, side 1 and side 2. The soil collars were moved to avoid long-term disturbance of the soil due to the presence of the soil collar, and to ensure that the within-plot soil CO_2 efflux measurements were spatially independent in the long-term. To test whether this pattern of measurement frequency and soil-collar movement influenced our results, we also ran models using a repeated-measures approach, with both space (soil-collar zonal location, nested in plot) and time as random effects. This repeated-measures analysis reinforced the findings from the primary model analysis (Extended Data Table 2). To test the response of partitioned soil- and root-derived CO_2 emissions to warming, we used repeated-measures analyses because the partition cores were fixed, with plot number and time as random effects. Treatment effects on partitioned root- and soil-derived CO_2 efflux components were tested using repeated-measures mixed models with time and plot number as random effects.

Treatment effects on soil-surface moisture content (0–20 cm depth) were tested using mixed-effects models with volumetric soil moisture as the response variable, warming treatment, season and warming × season as fixed effects, and plot number as a random effect. In this case, we did not use a repeated-measures analysis because each within-plot soil-moisture sampling point was wholly independent.

Treatment effects on whole-soil-profile moisture, which were repeated measures, were tested using a repeated-measures analysis with space (depth nested in plot) and time as random effects. All statistical analyses were performed in R (version 3.5.2).

Data availability

The source data for this study (soil gas exchange, soil and microbial properties) are available at https://doi.org/10.6084/m9.figshare.12144768. Source data are provided with this paper.

33. Leigh, E. G. J. *Tropical Forest Ecology: A View from Barro Colorado Island* (Oxford Univ. Press, 1999).
34. Woodring, W. P. Geology of Barro Colorado Island. *Smithson. Misc. Collect*. **135**, 1–39 (1958).
35. Sanchez, P. A. & Logan, T. J. Myths and science about the chemistry and fertility of soils in the tropics. *SSSA Spec. Publ*. **29**, 35–46 (1992).
36. Hanson, P. J. et al. A method for experimental heating of intact soil profiles for application to climate change experiments. *Glob. Change Biol*. **17**, 1083–1096 (2011).
37. Nottingham, A. T., Turner, B. L., Winter, K., van der Heijden, M. G. A. & Tanner, E. V. J. Arbuscular mycorrhizal mycelial respiration in a moist tropical forest. *New Phytol*. **186**, 957–967 (2010).
38. Cavelier, J. Fine-root biomass and soil properties in a semideciduous and a lower montane rain-forest in Panama. *Plant Soil* **142**, 187–201 (1992).
39. Sinsabaugh, R. L. et al. Stoichiometry of microbial carbon use efficiency in soils. *Ecol. Monogr*. **86**, 172–189 (2016).
40. Hendershot, W. H. & Duquette, M. A simple barium-chloride method for determining cation-exchange capacity and exchangeable cations. *Soil Sci. Soc. Am. J*. **50**, 605–608 (1986).
41. Brookes, P. C., Landman, A., Pruden, G. & Jenkinson, D. S. Chloroform fumigation and the release of soil-nitrogen – a rapid direct extraction method to measure microbial biomass nitrogen in soil. *Soil Biol. Biochem*. **17**, 837–842 (1985).
42. Vance, E. D., Brookes, P. C. & Jenkinson, D. S. An extraction method for measuring soil microbial biomass-C. *Soil Biol. Biochem*. **19**, 703–707 (1987).
43. Jenkinson, D. S., Brookes, P. C. & Powlson, D. S. Measuring soil microbial biomass. *Soil Biol. Biochem*. **36**, 5–7 (2004).
44. Kouno, K., Tuchiya, Y. & Ando, T. Measurement of soil microbial biomass phosphorus by an anion-exchange membrane method. *Soil Biol. Biochem*. **27**, 1353–1357 (1995).
45. Nottingham, A. T. et al. Soil microbial nutrient constraints along a tropical forest elevation gradient: a belowground test of a biogeochemical paradigm. *Biogeosciences* **12**, 6489–6523 (2015).
46. Nottingham, A. T. et al. Temperature sensitivity of soil enzymes along an elevation gradient in the Peruvian Andes. *Biogeochemistry* **127**, 217–230 (2016).
47. Turner, B. L. & Romero, T. E. Short-term changes in extractable inorganic nutrients during storage of tropical rain forest soils. *Soil Sci. Soc. Am. J*. **73**, 1972–1979 (2009).
48. Zuur, A. F., Ieno, E. N., Walker, N. J., Saveliev, A. A. & Smith, G. M. *Mixed Effects Models and Extensions in Ecology with R* (Springer, 2007).

Acknowledgements This study was supported by two fellowships to A.T.N., a European Union Marie-Curie Fellowship FP7-2012-329360 (University of Edinburgh) and a Tupper Fellowship (Smithsonian Tropical Research Institute); a Smithsonian Institution Scholarly Studies Grant to B.L.T. and K. Winter; a UK NERC grant NE/K01627X/1 and an ANU Biology Innovation grant to P.M. We thank O. Acevado, D. Agudo, A. Bielnicka, M. Cano, D. Dominguez, M. Garcia, M. Larsen, B. Martin, M. Montero, S. O'Connor, J. Rodriguez, H. Szczygiel, I. Torres, W. Wcislo, K. Winter and S. J. Wright for their contributions to SWELTR.

Author contributions A.T.N. conceived the study with B.L.T. and P.M.; A.T.N., E.V. and B.L.T. performed the study. A.T.N. analysed the data and wrote the paper with B.L.T. and P.M.

Competing interests The authors declare no competing interests.

Additional information

Correspondence and requests for materials should be addressed to A.T.N.

Peer review information *Nature* thanks Eric Davidson and the other, anonymous, reviewer(s) for their contribution to the peer review of this work.

Reprints and permissions information is available at http://www.nature.com/reprints.

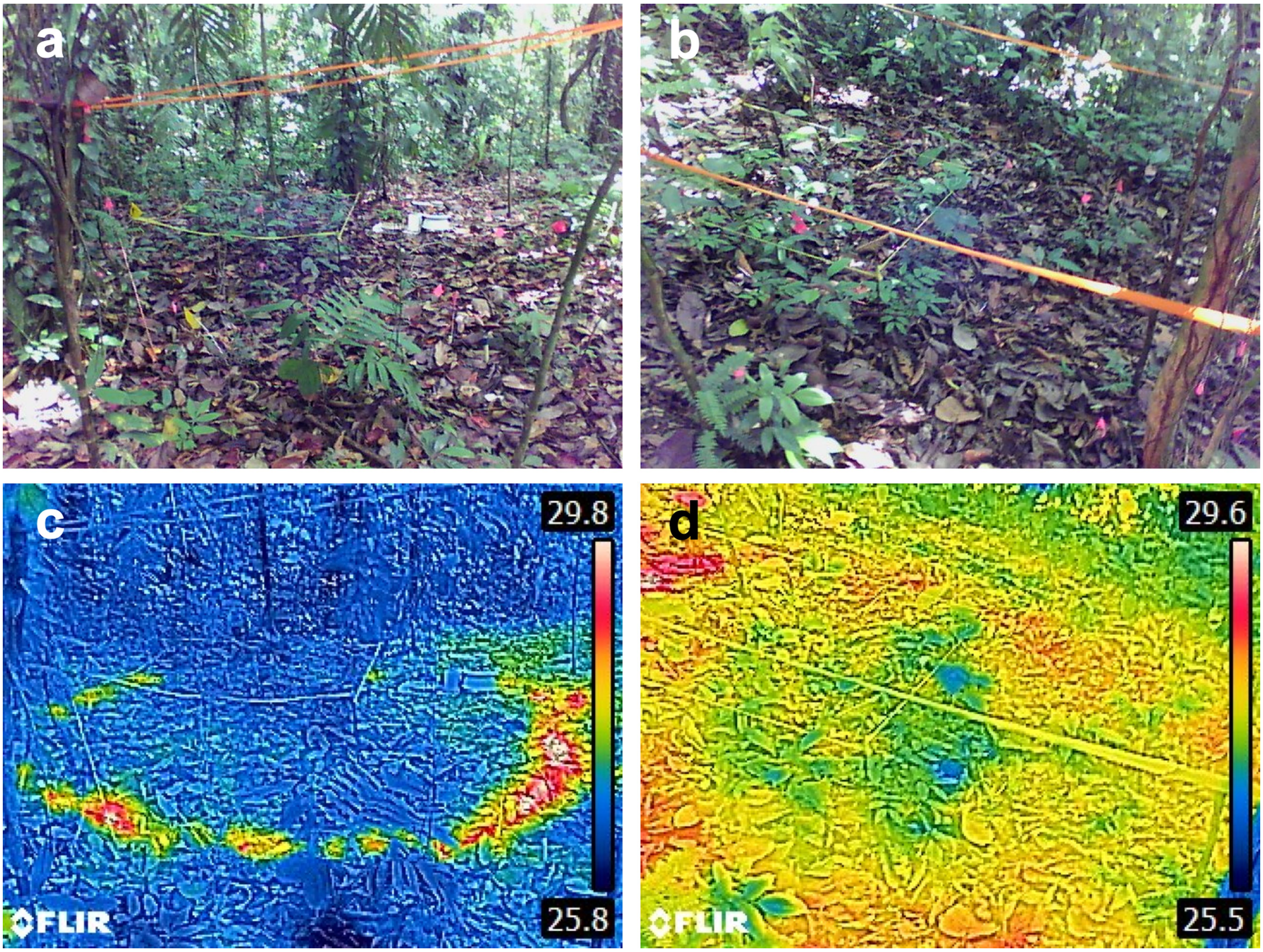

Extended Data Fig. 1 | Thermal images of a warmed plot. a–d, Pictures (**a**, **b**) and thermal images (**c**, **d**) of a warmed plot. The thermal images show the soil-surface temperature 1 h after the warming structure was switched on (**c**) and after a period of thermal equilibration of soil (**d**). The circular heating structure was 3.5 m in diameter and extended to 1.2 m depth, which resulted in an effective heated plot of approximately 5 m diameter and 1.2 m depth. The experiment consisted of five warmed and control plot pairs in total. Image credit: J. Bujan and E.V.

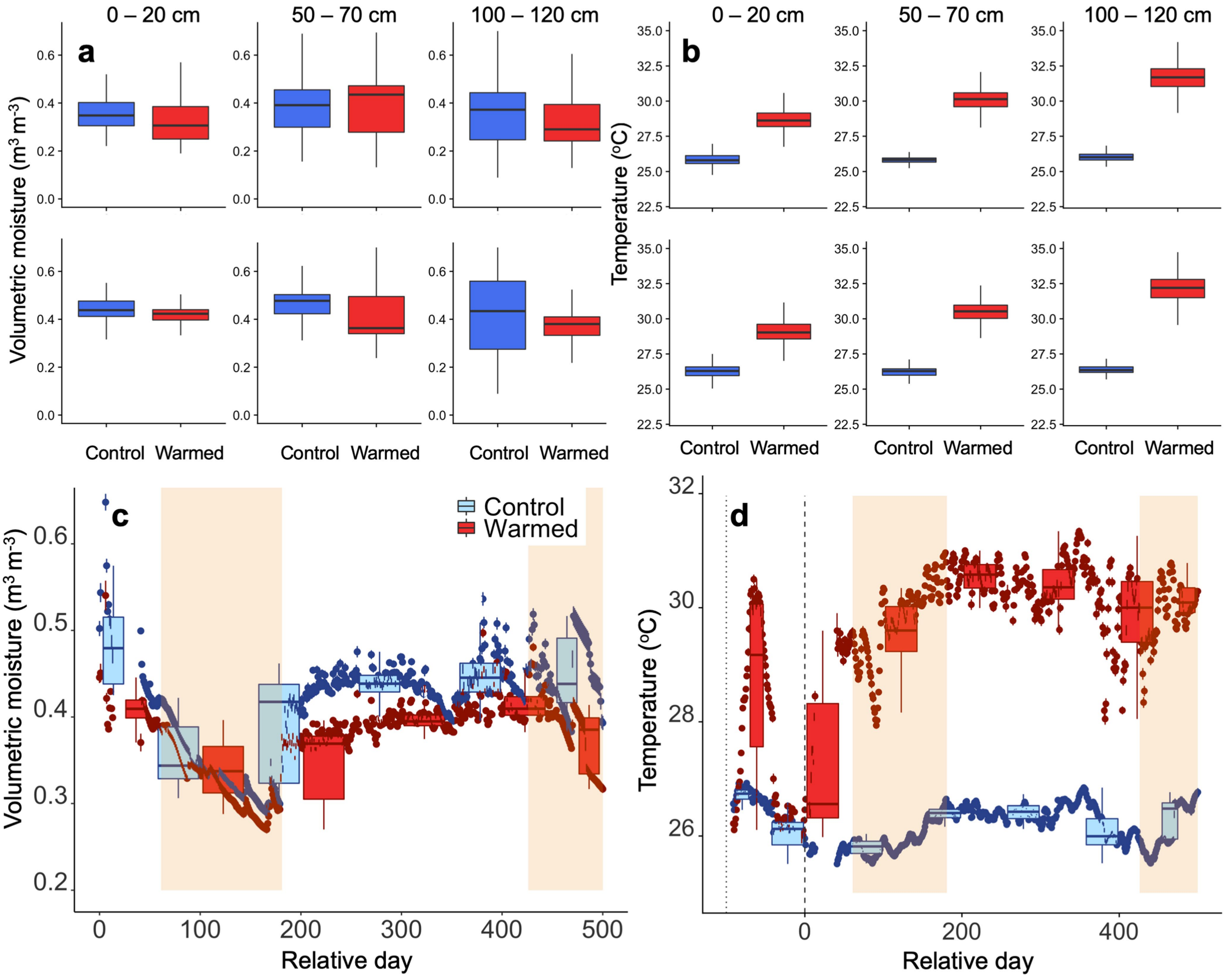

Extended Data Fig. 2 | Soil moisture content and temperature in control and warmed plots. a, **b**, Soil volumetric moisture content (**a**) and soil temperature (**b**), for the period after the warming treatment began (December 2016 to December 2018), partitioned by soil depth (columns) and season (rows). Box plots are standard (Tukey) plots, where the centre line represents the median across the five plots over the study period, the lower and upper hinges represent the first and third quartiles, and whiskers represent +1.5 the interquartile range. **c**, **d**, Temporal patterns in soil volumetric moisture content (**c**) and soil temperature (**d**), relative to when the warming treatment began (relative day 0; temperature temporarily increased in warmed plots before this during the testing phase). The points are daily means of soil profile and the error bars represent one standard error of the variation by plot ($n = 5$). The box (Tukey) plots show the median temporal value over sequential 100-day periods. The shaded areas represent dry seasons (1 January to 1 April). Treatment effects on annual or seasonal soil-profile moisture content were not significant; treatment effects on soil temperature were significant (repeated-measures ANOVA, $P < 0.001$; Extended Data Table 4).

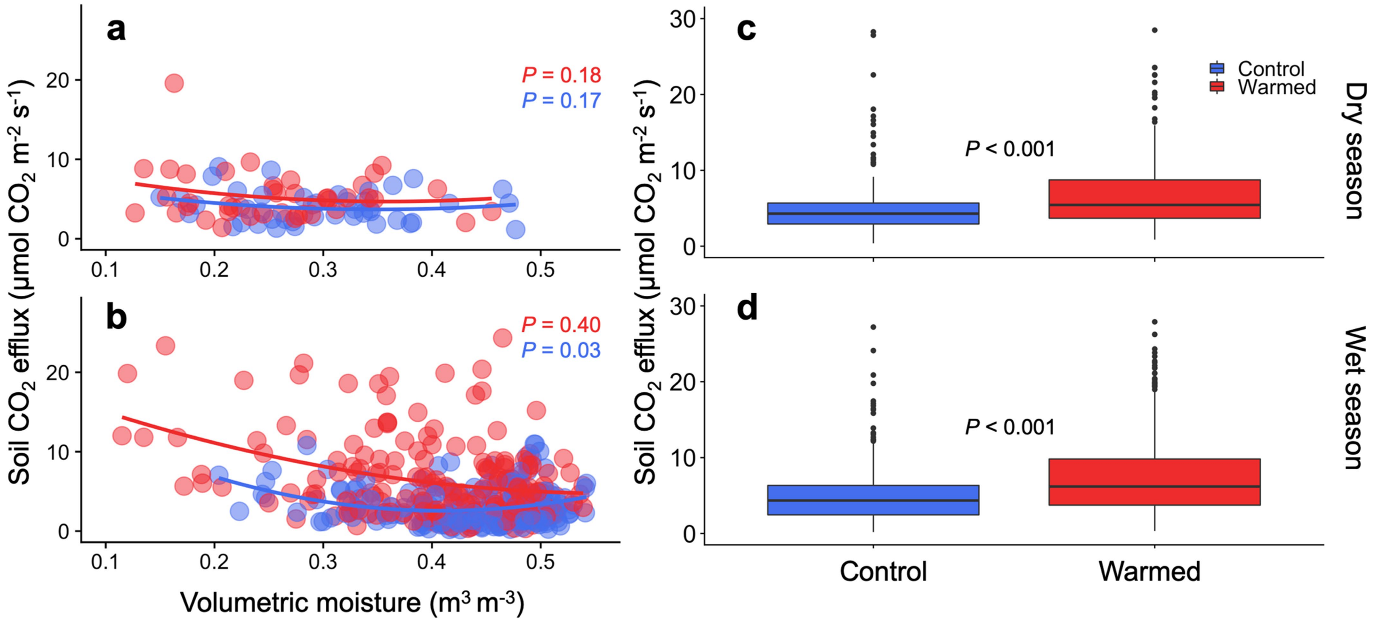

Extended Data Fig. 3 | Relationship between soil CO_2 efflux, soil moisture and season, in control and warmed plots. **a**, **b**, Relationship between soil CO_2 efflux and soil moisture in warmed (red) and control (blue) plots during the dry (**a**) and wet (**b**) seasons. Data were fitted (solid lines) using a quadratic function. **c**, **d**, Soil CO_2 efflux differences between warmed (red) and control (blue) plots during the dry (**c**) and wet (**d**) seasons. Soil CO_2 efflux in warmed plots was significantly higher than controls for both dry and wet season, although the difference was greater for the wet season (average difference of 2.8 μmol CO_2 m^{-2} s^{-1} for the wet season compared to 2.1 μmol CO_2 m^{-2} s^{-1} for the dry season).

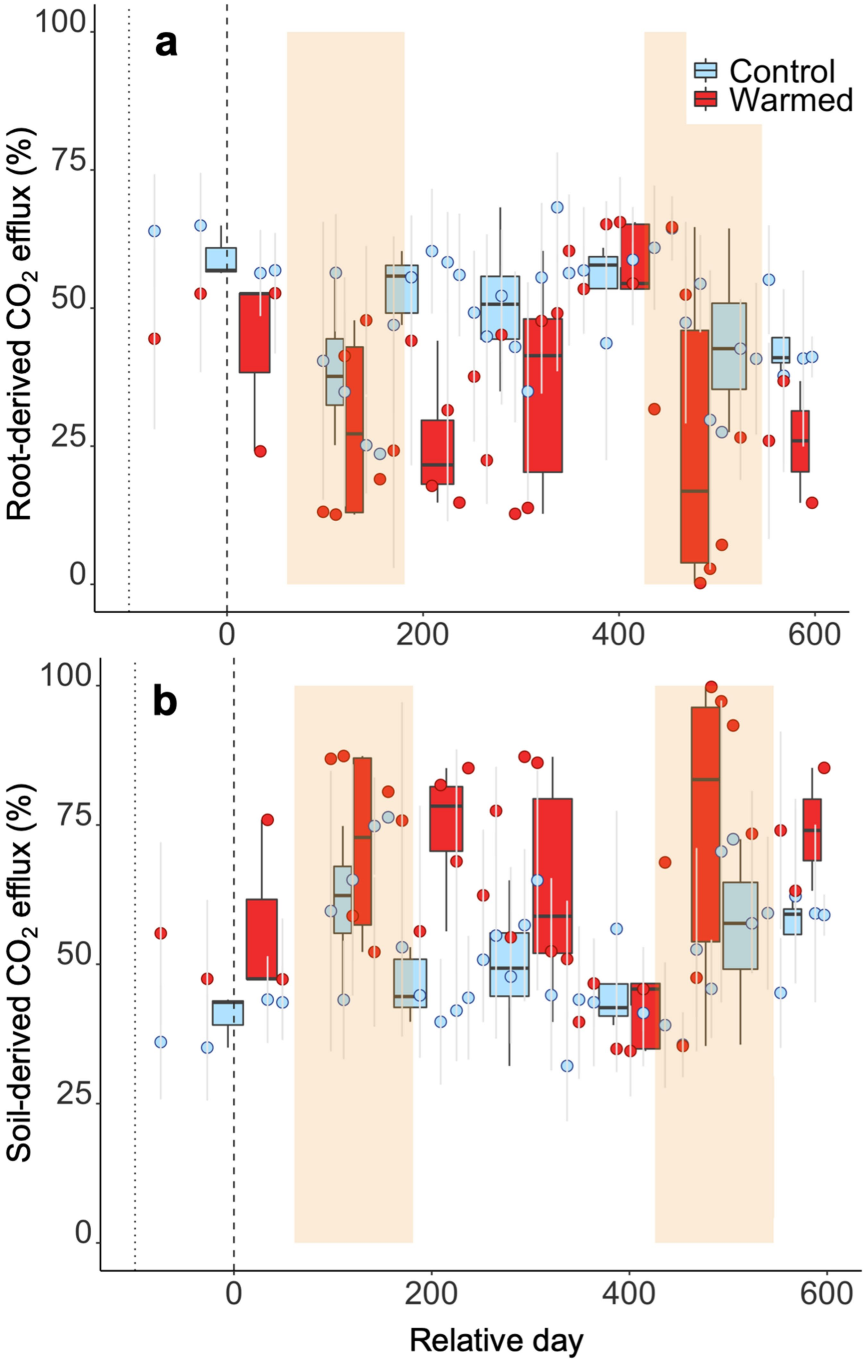

Extended Data Fig. 4 | Contribution of root-derived and soil-derived sources to total CO_2 efflux. a, **b**, Data for root-derived (**a**) and soil-derived (**b**) sources are for the study period. The error bars for points represent one standard error of the variation across the five plots. The box (Tukey) plots show the median temporal value over 100-day periods. The dotted vertical line is when installation and testing of warming plots began; the dashed vertical line shows when all five warming plots were switched on permanently. The shaded areas represent dry seasons (1 January to 1 April).

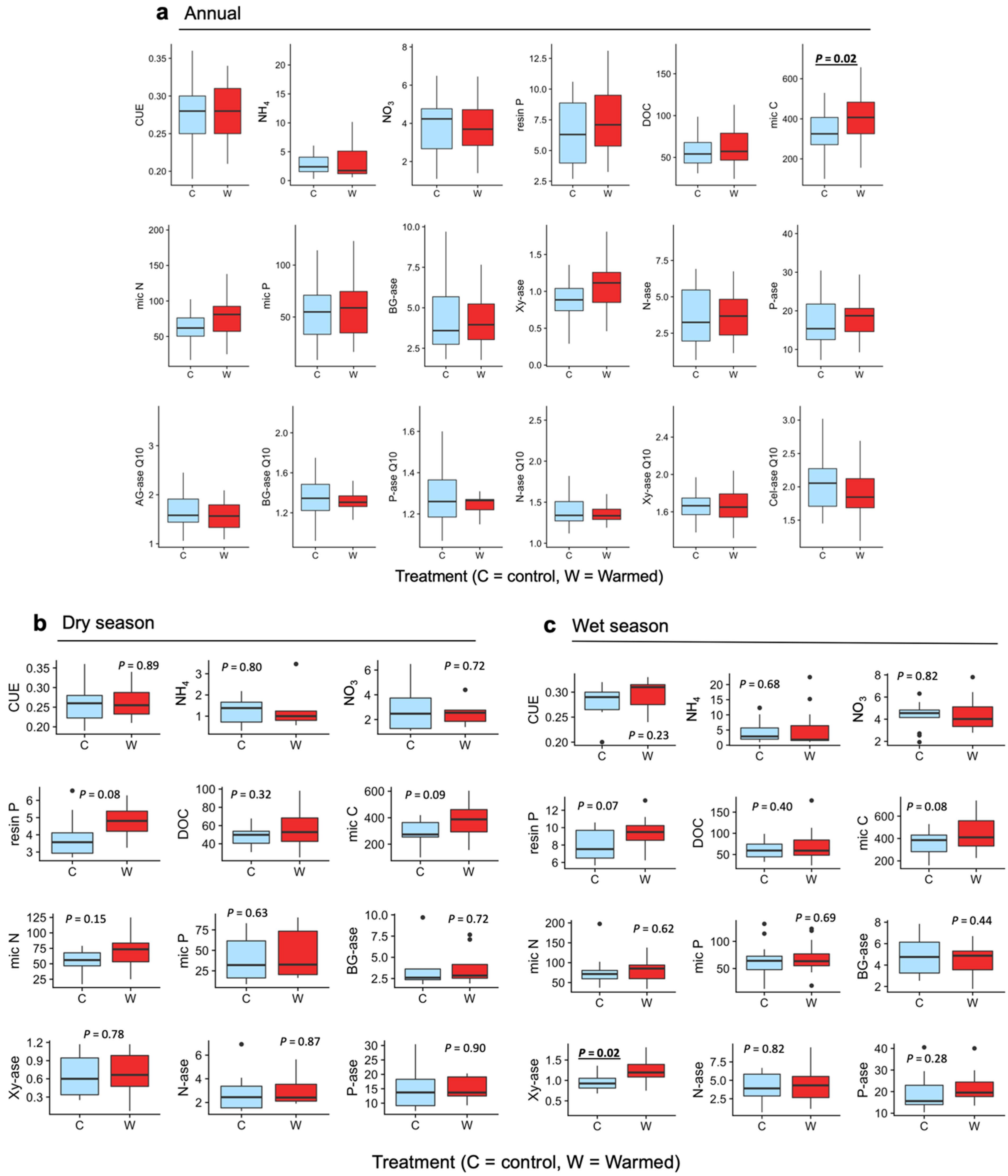

Extended Data Fig. 5 | Average response of soil properties to warming. **a**–**c**, Data are for the study period December 2016 to December 2018. Data are partitioned into annual (**a**), dry-season (**b**) and wet-season (**c**) responses. Soil properties are microbial CUE (ratio, no units), soil-extractable nutrients (NH_4, NO_3, resin P; mg kg^{-1}), dissolved organic carbon (DOC; mg kg^{-1}), microbial elements (mic C, mic N, mic P; mg kg^{-1}) and activities (V_{max}) of extracellular enzymes β-glucosidase (BG-ase), phosphomonoesterase (P-ase), *N*-acetyl β-glucosaminidase (N-ase) and β-xylanase (Xy-ase) (nmol MU g^{-1} min^{-1}). The temperature sensitivity of activities of extracellular enzymes (Q_{10} of V_{max}) was determined for α-glucosidase (AG-ase), BG-ase, P-ase, N-ase, Xy-ase and cellobiohydrolase (Cel-ase) (nmol MU g^{-1} min^{-1}). Significant responses ($P < 0.05$) are highlighted in bold and underlined. The only significant annual response (**a**) is for microbial carbon ($P = 0.02$), although there is also a marginal non-significant response for β-xylanase activity ($P = 0.07$). The centre line of each box plot represents the median across the five plots over the study period, the lower and upper hinges represent the first and third quartiles, and whiskers represent +1.5 the interquartile range.

Extended Data Table 1 | Soil properties

Depth	0-10 cm		10-30 cm		30-50 cm		50-100 cm	
C stocks (Mg C ha^{-1})	36.3	(3.3)	29.5	(1.5)	18.5	(1.0)	42.3	(3.3)
Total C (%)	3.63	(0.33)	1.34	(0.07)	0.77	(0.04)	0.65	(0.05)
Total N (%)	0.30	(0.02)	0.11	(0.01)	0.06	(0.00)	0.05	(0.00)
Total P (%)	0.34	(0.01)	0.20	(0.01)	0.14	(0.01)	0.11	(0.01)
K_2SO_4 extractable - NH_4 (mg N kg^{-1})	1.87	(0.27)	1.58	(0.10)	1.17	(0.24)	1.00	(0.17)
K_2SO_4 extractable - NO_3 (mg N kg^{-1})	1.38	(0.27)	0.35	(0.05)	0.15	(0.02)	0.12	(0.04)
Resin P (mg P kg^{-1})	1.40	(0.18)	0.90	(0.13)	0.40	(0.09)	0.61	(0.16)
ECEC (cmol$_c$ kg^{-1})	48.8	(2.33)	49.1	(5.33)	42.90	(3.06)	42.4	(3.46)
Soil pH (H_2O)	6.02	(0.06)	6.04	(0.05)	6.00	(0.05)	6.02	(0.07)

Average values across soil depths for the study site (mean and standard error, *n* = 10). Resin P is phosphate extracted by anion-exchange membrane. ECEC, effective cation exchange capacity. Values are pre-treatment and were determined in 2015 before the warming experiment was installed.

Extended Data Table 2 | The determinants of soil CO_2 efflux variation

1. No repeated measures				
a) Annual soil CO_2 efflux	*Parameter*	*SE*	*DF*	*P-value*
Fixed effects				
Warming	3.23	1.50	13	**< 0.05 ***
Season	-0.55	0.76	521	0.48
Soil moisture	-0.66	1.62	521	0.69
Warming * soil moisture	-1.24	1.52	521	0.42
Season * soil moisture	2.41	1.69	521	0.15
Random effect				
Space (plot number)	3.28	1.18	19	**< 0.05 ***
AIC value				2823
b) Wet season soil CO_2 efflux	*Parameter*	*SE*	*DF*	*P-value*
Fixed effects				
Warming	3.98	1.78	14	**< 0.05 ***
Soil moisture	2.43	1.34	2	0.07
Warming * soil moisture	-2.06	1.90	424	0.28
Random effect				
Space (plot number)	2.23	1.27	15	0.10
AIC value				2324
c) Dry season soil CO_2 efflux	*Parameter*	*SE*	*DF*	*P-value*
Fixed effects				
Warming	1.23	0.50	99	**< 0.05 ***
Soil moisture	-2.05	1.06	99	0.055
Random effect				
Space (plot number)	4.67	0.05	99	**< 0.01 ****
AIC value				469

2. With repeated measures				
a) Annual soil CO_2 efflux	*Parameter*	*SE*	*DF*	*P-value*
Fixed effects				
Warming	2.66	0.97	89	**< 0.01 ****
Season	1.34	1.48	52	0.37
Soil moisture	0.48	1.87	196	0.80
Warming * soil moisture	-0.46	1.23	494	0.71
Season * soil moisture	-0.08	2.10	169	0.97
Random effect				
Intercept (Space + Time)	2.71	1.40	69	0.06
AIC value				2644
b) Wet season soil CO_2 efflux	*Parameter*	*SE*	*DF*	*P-value*
Warming	3.09	1.12	104	**< 0.01 ****
Soil moisture	1.19	1.53	157	0.44
Warming * soil moisture	-0.80	1.55	402	0.61
Random effect				
Intercept (Space + Time)	3.49	1.14	99	**< 0.01 ****
AIC value				2181
c) Dry season soil CO_2 efflux	*Parameter*	*SE*	*DF*	*P-value*
Warming	1.52	0.93	81	0.11
Soil moisture	-2.72	1.53	44	0.08
Warming * soil moisture	-0.78	1.96	74	0.69
Random effect				
Intercept (Space + Time)	5.02	0.86	6	**< 0.001 *****
AIC value				465

The mixed-effect model analyses were performed with: (1) random effect of space (plot), that is, no repeated-measures effect; and (2) random effects of space (soil-collar location nested within plot) and time, that is, including the repeated-measures effect. We performed the analyses first including all annual data (a) and then partitioned by wet season (b) and dry season (c). We tested with and without a repeated-measures effect because within-plot soil CO_2 efflux measurements were partially spatially independent (within-plot locations of soil collars were changed every three months, but not on every two-week measurement occasion within each three-month period; when moved, soil collars were relocated to randomly specified locations, but always systematically assigned to zones. Mixed-effects models were fitted using maximum likelihood, by beginning with the full model (six variables: warming effect, soil moisture determined at 0–20 cm depth, season, interactions between soil moisture and warming and season, and random effects of space and time), followed by stepwise parameter removal. The final model was determined by lowest Akaike information criterion (AIC) value. For each parameter, the standard error (SE) and degrees of freedom (DF) are shown; significant values are in bold and highlighted by asterisks for $P < 0.05$ (*), $P < 0.01$ (**) and $P < 0.001$ (***).

Extended Data Table 3 | Treatment effects on root and soil components of CO_2 efflux

Pre-treatment				
Root-derived CO_2	*Parameter*	*SE*	*DF*	*P-value*
Fixed effects				
Warming	1.01	4.34	8.0	0.82
Random effect				
Space (plot) + Time	13.13	3.65	9.0	**< 0.001** ***
Soil-derived CO_2	*Parameter*	*SE*	*DF*	*P-value*
Fixed effects				
Warming	0.93	1.24	8.0	0.47
Random effect				
Space (plot) + Time	5.78	1.25	4.6	**< 0.05** *
Post-treatment				
Root-derived CO_2	*Parameter*	*SE*	*DF*	*P-value*
Fixed effects				
Warming	2.4	1.82	8.0	0.21
Random effect				
Space (plot) + Time	3.6	1.34	9.4	**< 0.05** *
Soil-derived CO_2	*Parameter*	*SE*	*DF*	*P-value*
Fixed effects				
Warming	2.90	0.98	8.0	**< 0.05** *
Random effect				
Space (plot) + Time	3.47	0.79	12.8	**< 0.001** ***

The flux components were derived from soil CO_2 efflux from root-ingrowth and root-exclusion cores. The mixed-effect model analyses were performed with random effects of space (plot) and time; a repeated-measures design was used because the partition cores were fixed. The analyses were performed including pre-treatment (January to June 2016) and post-treatment data following two years of warming (November 2016 to December 2018). For each parameter, the standard error (SE) and degrees of freedom (DF) are shown; significant values are in bold and highlighted by asterisks for $P < 0.05$ (*), $P < 0.01$ (**) and $P < 0.001$ (***).

Extended Data Table 4 | Determinants of soil moisture variation

1) Surface				
a) Annual soil moisture	*Parameter*	*SE*	*DF*	*P-value*
Fixed effects				
Warming	-0.05	0.04	84	0.19
Season	0.09	0.03	524	**< 0.01** **
Warming * Season	0.02	0.04	524	0.64
Random effect				
Space (plot number)	0.39	0.02	84	**< 0.001** ***
AIC value				-246
b) Wet season soil moisture	*Parameter*	*SE*	*DF*	*P-value*
Fixed effects				
Warming	-0.03	0.02	8	0.17
Random effect				
Space (plot number)	0.48	0.02	8	**< 0.001** ***
AIC value				-268
c) Dry season soil moisture	*Parameter*	*SE*	*DF*	*P-value*
Fixed effects				
Warming	-0.06	0.05	98	0.25
Random effect				
Space (plot number)	0.39	0.03	98	**< 0.001** ***
AIC value				469
2) Whole-profile				
a) Annual soil moisture	*Parameter*	*SE*	*DF*	*P-value*
Fixed effects				
Warming	$-7.0 \text{ x } 10^{-2}$	$5.8 \text{ x } 10^{-2}$	28	0.24
Season	0.15	$6.8 \text{ x } 10^{-3}$	681	**< 0.001** ***
Warming * Season	$9.0 \text{ x } 10^{3}$	$5.3 \text{ x } 10^{4}$	$7.2 \text{ x } 10^{5}$	**< 0.001** ***
Random effect				
Space (depth / plot) + Time (day)	0.42	$4.2 \text{ x } 10^{-2}$	29	**< 0.001** ***
AIC value				$-11 \text{ x } 10^{5}$
b) Wet season soil moisture	*Parameter*	*SE*	*DF*	*P-value*
Fixed effects				
Warming	-0.05	0.07	28	0.44
Random effect				
Space (depth / plot) + Time (day)	0.57	0.05	28	**< 0.001** ***
AIC value				$-7 \text{ x } 10^{5}$
c) Dry season soil moisture	*Parameter*	*SE*	*DF*	*P-value*
Fixed effects				
Warming	-0.07	0.05	28	0.13
Random effect				
Space (depth / plot) + Time (day)	0.42	0.03	29	**< 0.001** ***
AIC value				$-6 \text{ x } 10^{5}$

Data are for (1) surface soils, 0–20 cm soil, measured by soil moisture probe; and (2) whole profile, 0–20 cm, 50–70 cm and 100–120 cm, measured by fixed moisture sensors. For surface soils (1), the analyses were performed including all data (1a) and then partitioned by wet season (1b) and dry season (1c). Mixed-effects models were fitted using maximum likelihood, by beginning with the full model (four variables in 1a: warming effect, season, and interactions between soil moisture and warming and season, and a random plot effect; two variables in 1b and 1c: as above but without seasonal effects) and then using step-wise parameter removal. All measurements of within-plot soil moisture were spatially independent. For whole-profile data (2), the analyses were performed including all data (2a) and then partitioned by wet season (2b) and dry season (2c). Mixed-effects m©odels were fitted using maximum likelihood, by beginning with the full model (five variables in 2a: warming effect, season, and interactions between soil moisture and warming and season, and random effects of depth nested in plot and time; two variables in 2b and 2c: as above but without season effects) and then using step-wise parameter removal. Repeated-measures analyses were used because the soil-profile moisture data are from fixed sensors. The final model was determined by lowest Akaike information criterion (AIC) value. For each parameter, the standard error (SE) and degrees of freedom (DF) are shown; significant values are in bold and highlighted by asterisks for $P < 0.05$ (*), $P < 0.01$ (**) and $P < 0.001$ (***).

Ecosystem decay exacerbates biodiversity loss with habitat loss

https://doi.org/10.1038/s41586-020-2531-2

Received: 23 August 2019

Accepted: 18 June 2020

Jonathan M. Chase[1,2]✉, **Shane A. Blowes**[1,2], **Tiffany M. Knight**[1,3,4], **Katharina Gerstner**[1] & **Felix May**[1,5,6]

Although habitat loss is the predominant factor leading to biodiversity loss in the Anthropocene[1,2], exactly how this loss manifests—and at which scales—remains a central debate[3–6]. The 'passive sampling' hypothesis suggests that species are lost in proportion to their abundance and distribution in the natural habitat[7,8], whereas the 'ecosystem decay' hypothesis suggests that ecological processes change in smaller and more-isolated habitats such that more species are lost than would have been expected simply through loss of habitat alone[9,10]. Generalizable tests of these hypotheses have been limited by heterogeneous sampling designs and a narrow focus on estimates of species richness that are strongly dependent on scale. Here we analyse 123 studies of assemblage-level abundances of focal taxa taken from multiple habitat fragments of varying size to evaluate the influence of passive sampling and ecosystem decay on biodiversity loss. We found overall support for the ecosystem decay hypothesis. Across all studies, ecosystems and taxa, biodiversity estimates from smaller habitat fragments—when controlled for sampling effort—contain fewer individuals, fewer species and less-even communities than expected from a sample of larger fragments. However, the diversity loss due to ecosystem decay in some studies (for example, those in which habitat loss took place more than 100 years ago) was less than expected from the overall pattern, as a result of compositional turnover by species that were not originally present in the intact habitats. We conclude that the incorporation of non-passive effects of habitat loss on biodiversity change will improve biodiversity scenarios under future land use, and planning for habitat protection and restoration.

When habitat is lost, two different processes can lead to biodiversity decline. First, species are lost as habitat area is lost via the ubiquitous species–area relationship[11,12]; fewer species can persist in smaller habitats, and species that are rarer in the landscape will go extinct owing to passive sampling. Second, the demography of species within the remaining habitat can be altered, increasing extinction risk (or decreasing recolonization) subsequent to immediate species losses[9,10]. This process—which is referred to as ecosystem decay[9]—supposes that biological processes within intact habitats embedded within smaller habitat areas differ from those in larger patches (for example, owing to edge effects, lowered dispersal or demographic stochasticity). For a given sampling effort, we might expect fewer species, changes in total and relative abundances, and often altered ecosystem functions, in smaller relative to larger habitats as a result of ecosystem decay (see empirical examples in refs. [3,13–15]). Both of these processes—biodiversity loss owing to passive sampling or to altered demography that leads to ecosystem decay—are well-known, but often confounded in empirical tests for which sampling efforts are variable. Additionally, most models that forecast biodiversity loss as a result of habitat loss implicitly assume passive sampling from larger to smaller habitats when developing scenario projections (for example, refs. [11,12,16,17]), ignoring demographic effects. At present we are unable to synthesize the relative importance of the two main processes of biodiversity loss with habitat loss. Without this synthesis, we cannot address the necessity of incorporating loss owing to both passive sampling and ecosystem decay into forecasts of future biodiversity scenarios.

Passive sampling versus ecosystem decay

In Fig. 1, we visualize the primary processes by which biodiversity and its empirical estimates can respond to habitat loss when explicitly controlling for sampling effort to establish explicit testable hypotheses[18–20]. Although it is often impractical or impossible to count all of the individuals or species in a given habitat patch, we can readily establish a scheme to estimate the numbers of individuals, the numbers of species or other estimates of biodiversity (for example, relative abundances) within samples of the habitat (as illustrated by the square plots in Fig. 1). By standardizing this sampling effort, we can compare

---

[1]German Centre for Integrative Biodiversity Research (iDiv) Halle-Jena-Leipzig, Leipzig, Germany. [2]Institute of Computer Science, Martin Luther University Halle-Wittenberg, Halle (Saale), Germany. [3]Institute of Biology, Martin Luther University Halle-Wittenberg, Halle (Saale), Germany. [4]Department of Community Ecology, Helmholtz Centre for Environmental Research – UFZ, Halle (Saale), Germany. [5]Leuphana University, Lüneburg, Germany. [6]Theoretical Ecology, Institute of Biology, Freie Universität Berlin, Berlin, Germany. ✉e-mail: jonathan.chase@idiv.de

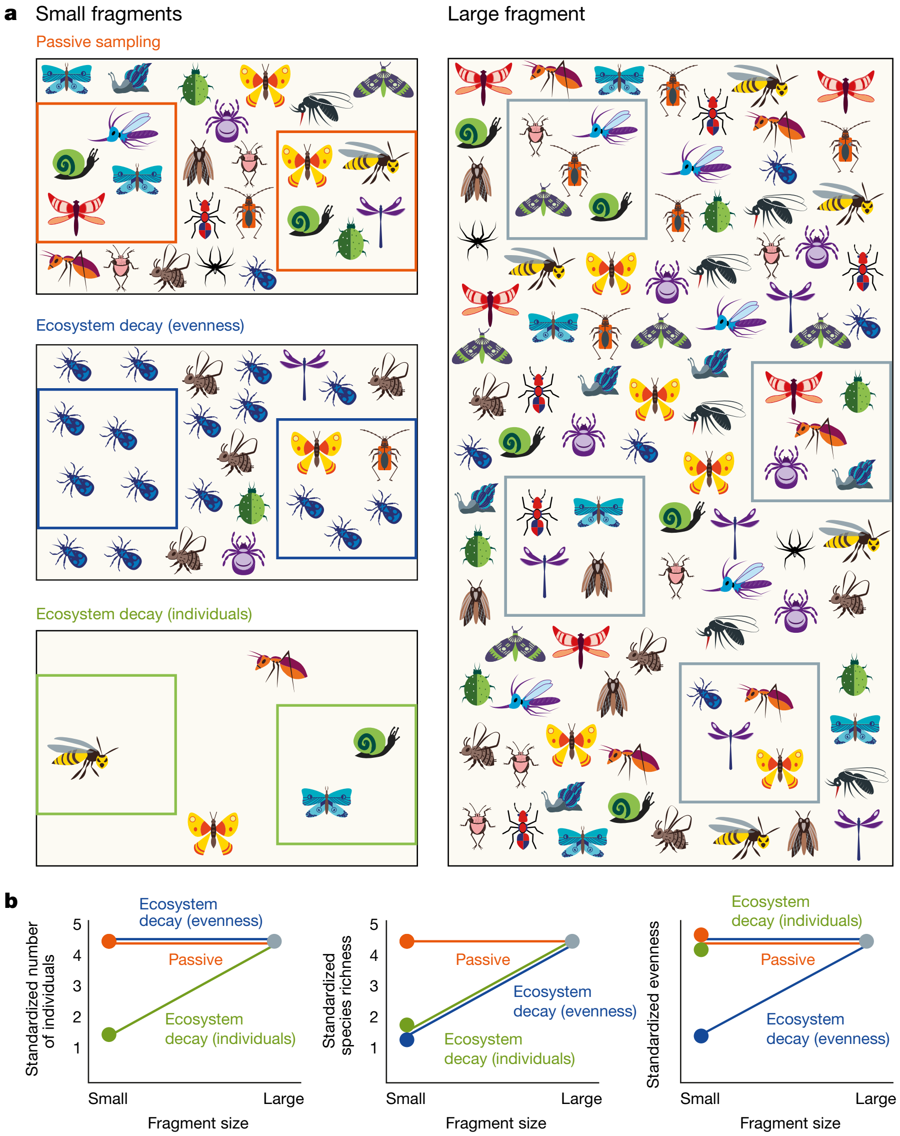

Fig. 1 | Conceptual illustration of the hypotheses and data structure. **a**, Small fragments (left) showing three hypotheses for comparisons made with the large fragment (right): (1) passive sampling, in which the densities of individuals and the relative abundances of species are similar to that of the large fragment; (2) ecosystem decay (evenness), in which the relative abundances of species are more uneven in the small fragment compared to the large fragment; and (3) ecosystem decay (individuals), in which the density of individuals is lower in the small fragment compared to the large fragment. Sampling is illustrated with boxes inside each fragment. In this example, the sampling effort increases from small (two samples) to large (four samples) fragments, but sampling effort can be standardized post hoc because sample-level data are available; other sampling methods are slightly different but can also be standardized (Methods). **b**, We compare the standardized number of individuals (average individuals per sample) (left), standardized species richness (average richness per sample) (centre) and standardized species evenness (average evenness per sample) (right) between a small fragment and a large fragment to illustrate how this information can be used to disentangle the passive sampling versus the ecosystem decay hypotheses. For the purposes of simple illustration, the large fragment has a completely even species abundance distribution, even though this is unrealistic. This figure was created for this paper by F. Arndt (www.Formenorm.de).

effort-standardized estimates from larger, more-continuous habitat patches to those from smaller habitat patches. With this, we can then explicitly test the importance of within-patch demographic changes that lead to the ecosystem decay of biodiversity measures amidst losses due to passive sampling[20]. Additionally, even if sampling effort among patches was not standardized in the original study, but is known, we can use post hoc methods for standardization (for example, various forms of rarefaction; Methods).

Several outcomes are possible when comparing sample-effort-controlled biodiversity patterns from larger habitat fragments to those from smaller habitat fragments[20]: three illustrative cases of these outcomes are shown in Fig. 1. The first is passive sampling: here, while there may be fewer total species in smaller relative to larger fragments, the numbers of individuals, species and relative abundances of species with a given standardized sampling effort is the same. That is, we expect there to be no relationship between any of these standardized estimates of biodiversity and habitat fragment size. In Extended Data Fig. 1, we use simulations to explore the robustness of this expectation and show that it is not sensitive to extreme non-randomness (that is, aggregation) in species distributions. Second, we consider ecosystem decay as a result of changes in the relative abundance of species. In this outcome, differential demographic responses of species in the assemblage lead to some species becoming relatively more abundant and others relatively less abundant (that is, relative abundances become more uneven)

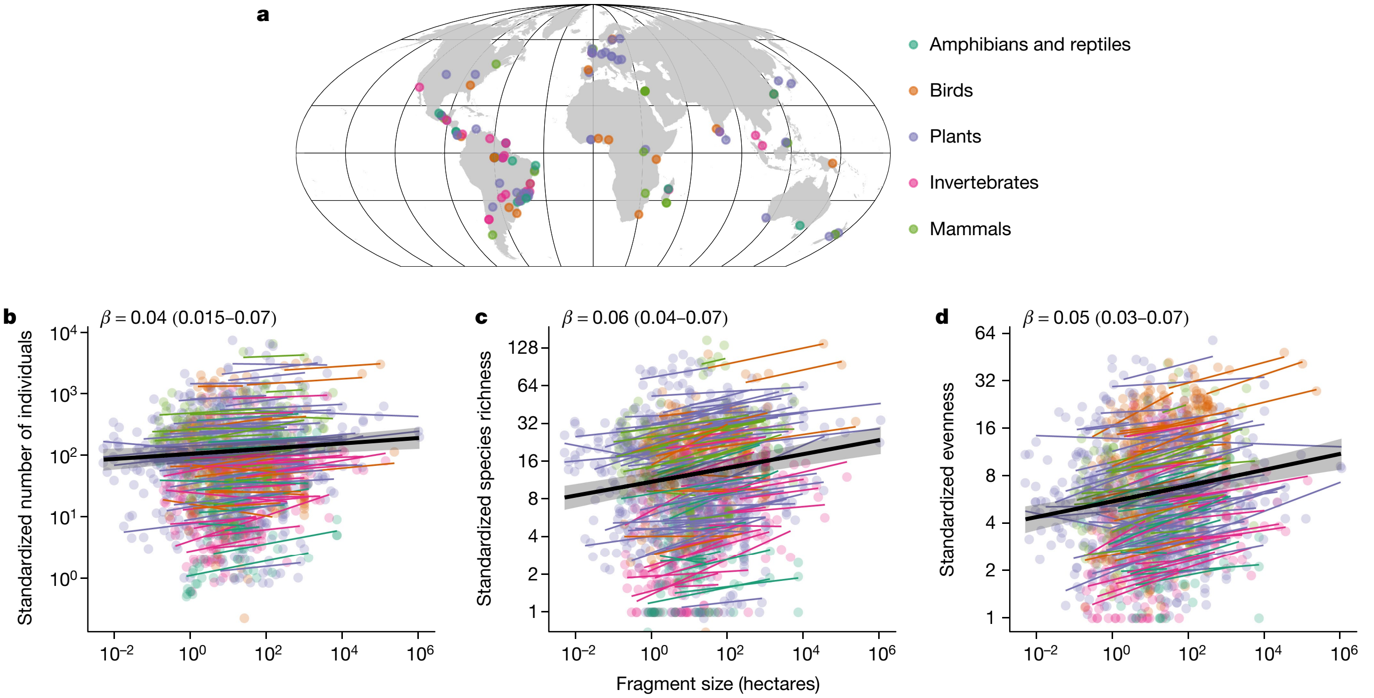

Fig. 2 | Ecosystem decay drives patterns of biodiversity loss in habitat fragments. **a**, Global map, indicating the taxon group and location of studies ($n = 123$) included in our analyses. **b**–**d**, Standardized samples show that number of individuals (**b**), species richness (**c**) and evenness (**d**) all increase as a function of fragment size. Solid black lines and shading show overall relationships and 95% credible intervals for each metric; the slope (β) coefficient for each metric and its 95% credible interval are shown at the top. Coloured lines show study-level relationships for different taxon groups (as shown in the map legend).

in smaller compared to larger fragments. As a result, the numbers of species for a given sampling effort declines, as do other measures of diversity based on relative abundances, with fragment size. The third example is ecosystem decay that results from reductions in the numbers of individuals. Here, there are fewer total species and also fewer species per standardized sampling effort in smaller relative to larger fragments, resulting from lower demographic rates of species in the small compared to the large fragments. In this scenario, while there are fewer individuals in samples from smaller fragments, all species have the same demographic response such that the relative abundances of species have not changed. As a result, the rarefied richness (standardized for the numbers of individuals) is similar in smaller and larger fragments. Although this is not shown in Fig. 1, it is also likely that ecosystem decay can result from changes both to the total numbers of individuals and to species relative abundances, from larger to smaller fragments. These are not the only possible outcomes, but other patterns—such as increases in abundance or evenness with decreasing habitat size—are less likely. Such increases in abundance or evenness would in turn lead to higher measures of diversity in standardized samples within smaller patches[4,6]. Some of these other outcomes are plausible, but we do not discuss them further as the bulk of our evidence indicates they are far less common than the three shown in Fig. 1.

Testing the hypotheses

Although the hypotheses illustrated in Fig. 1 are straightforward, appropriate syntheses have not heretofore been possible because of highly heterogeneous data that come from different sampling designs, as well as often-confounded analyses that do not control for sampling effort and grain[21]. However, if ecosystem decay in the form of changes to the numbers of species, individuals and/or relative species abundances in standardized samples is pervasive, this would mean that the majority of biodiversity loss scenarios—which assume passive sampling and ignore ecosystem decay—probably underestimate the effects of habitat loss on species loss. Here, we have developed an explicit and comprehensive evaluation of the passive sampling versus ecosystem decay hypotheses using 123 datasets in which species abundances were sampled from multiple habitat fragments of different sizes within once continuous landscapes[22] (Fig. 2a). Our dataset was explicitly compiled for this effort, and we developed an analytical pipeline that controls for sampling effort to test the hypotheses of biodiversity loss stemming from habitat loss. Datasets had from 2 to 53 habitat fragments of varying size within a given ecosystem, ranging from less than 1 ha to more than 10,000 ha of continuous habitat cover, and included studies on plant, invertebrate and vertebrate assemblages. Approximately 85% of our studies came from forested landscapes embedded within anthropogenic matrices (for example, agriculture), and the other studies came from shrublands, grasslands and wetlands. Although our search for datasets was global, there are clear geographical patterns in terms of where studies were collected; the majority come from tropical areas, especially Central and South America (Fig. 2a) (further details are provided in the Methods and ref. [22]).

Overall, we found strong support for the ecosystem decay hypothesis across all studies (Fig. 2, Extended Data Fig. 2). After controlling for sampling effort (Methods), we found that each of the biodiversity variables increased as the size of the habitat fragments increased. This included increases in the standardized number of individuals with fragment size (Fig. 2a), increases in standardized species richness with fragment size (Fig. 2b), increases in the evenness (relative abundance) of species in the community with fragment size (estimated via the effective number of species conversion of the probability of interspecific encounter (S_{PIE}), a measure of evenness that is relatively insensitive to sample size (Methods)) (Fig. 2c) and increases in several other sample-effort-controlled biodiversity measures with fragment size (Extended Data Fig. 2).

We developed a second analysis to explicitly account for the uncertainty surrounding the expected biodiversity estimates from the passive

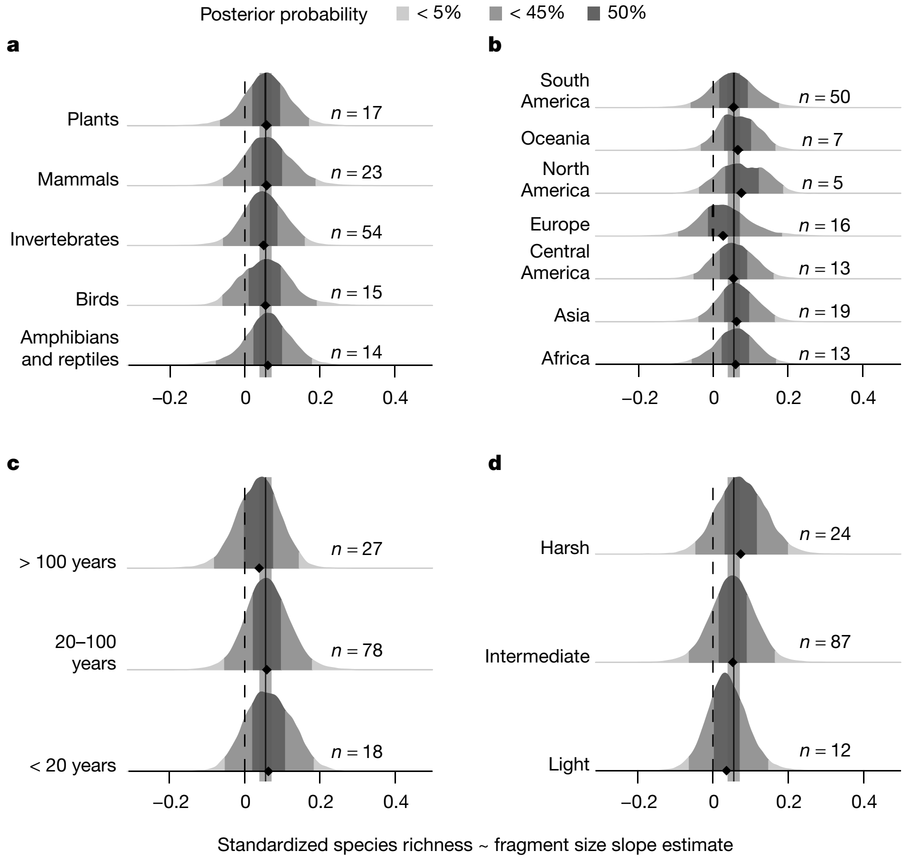

Fig. 3 | Study-level variation in the response of species richness to habitat loss. a–**d**, Density plots of posterior distributions for study-level slope estimates of standardized species richness grouped by taxon group (**a**), continent (**b**), time since fragmentation (**c**) and matrix filter (**d**). The dashed vertical line shows the zero slope expected from passive sampling. Each density plot is based on 1,000 samples from the posterior distribution of each study-level slope estimate. Densities are shaded by quantiles and the black diamond shows the median for each group. Solid line and surrounding shading show the overall slope and 95% credible interval. *n* values next to each plot refer to the number of studies included in each category.

sampling hypothesis. Simulations of the passive sampling hypothesis show that there can be variation in the expected slopes of biodiversity responses to the size of habitat fragments (Extended Data Fig. 1), although our observed responses (Fig. 2, Extended Data Fig. 2) were considerably greater than any departures in our simulations. Nevertheless, to account for this variation, we calculated variation in the 'expected' value for a given smaller fragment by resampling from the largest fragment. We then included uncertainty in the expected value under passive sampling when making comparisons to the 'observed' value in each smaller fragment. The resulting z-score (Methods) allows us to discern whether and by how much biodiversity in smaller fragments deviates from that expected under passive sampling. With this analysis, we found that for each sample-standardized diversity response, the observed values deviated more from expected values (lower z-scores) for smaller patch sizes, which indicates strong support for ecosystem decay having a role in the response of taxa to habitat loss (Extended Data Fig. 3). Moreover, to make all 123 datasets comparable, we made decisions regarding response variables (for example, how to rarefy from different types of data), as well as the driver variables (for example, how to estimate the size of habitats classified as 'continuous'). We present several analyses (Methods) that examine the sensitivity of our results, and show that our overall results are highly robust (Extended Data Fig. 4).

Variation in the effects

We were also interested in understanding how the response of biodiversity to fragment size varied across studies owing the taxa considered, the continent on which the studies were located, the time since fragmentation in the study, the quality of the matrix habitat surrounding the fragments in the study, and the latitude of the study. We focused on differences in the slopes of the response (with a slope of approximately zero expected from passive sampling) because differences in intercepts are influenced by the species pool and sampling methodology, and thus not meaningful in this context. We illustrate variation around the overall trend for sample-effort-standardized species richness in Fig. 3, and for sample-effort-standardized number of individuals and evenness in Extended Data Fig. 5.

With a few exceptions, all results are qualitatively similar to those for species richness, which showed—first—that there are no clear differences across taxa (Fig. 3a). This is somewhat surprising, as it has often been suggested that larger taxa or those that disperse poorly might respond to habitat loss more markedly than taxa with the opposite traits (for example, refs. [19,23]). However, the broad taxonomic groupings that were necessary for this global analysis do not allow for comparisons of species traits that vary within a group (for example, wind- versus animal-dispersed plants).

Second, we found little signal of continent, other than for temperate North America (which showed higher than average slopes) and Europe (which showed lower than average slopes) (Fig. 3b). One possibility is that these deviations reflect differences in other covariates. Specifically, habitats in 10 of the 16 studies from Europe were fragmented more than 100 years before the data were collected, whereas fragmentation occurred much more recently elsewhere. Likewise, studies from North America all had intermediate-to-harsh environmental filters. We explore time since fragmentation and matrix quality in more detail in the following two paragraphs.

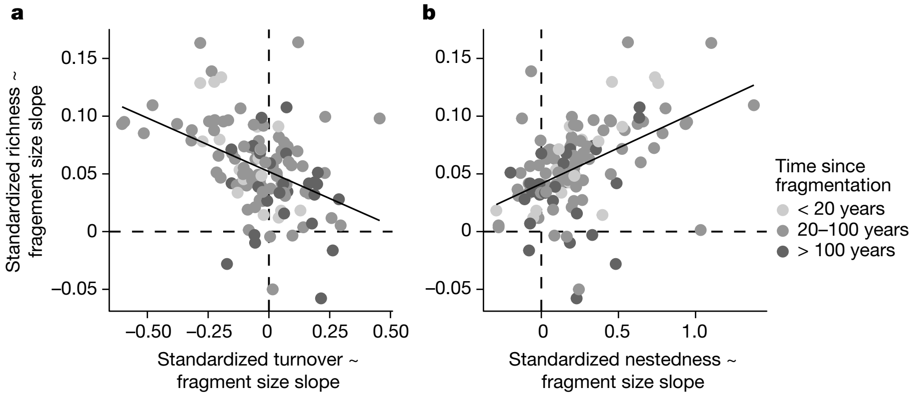

Fig. 4 | Relationship between the species-richness response and the species compositional turnover and nestedness. Studies with strong richness responses have higher turnover between small fragments (that is, a negative slope between turnover and fragment size) and the highest nestedness. **a**, Study-level slope estimates of the relationship with fragment size for species richness and the turnover component of Jaccard's dissimilarity (Pearson's correlation coefficient ρ = −0.42 (−0.56, −0.27; 95% confidence interval)). **b**, Study-level slope estimates of the relationship with fragment size for species richness and the turnover component of Jaccard's dissimilarity (Pearson's correlation coefficient ρ = 0.48 (0.34, 0.61; 95% confidence intervals)). Solid lines show linear models fit with ordinary least squares to aid visualization of relationships.

Third, studies with the longest time since habitat loss had the shallowest slopes (Fig. 3c). This result might seem counterintuitive given the 'extinction debt' concept, which refers to the fact that species may persist in fragments after habitat loss, but eventually go extinct as populations are no longer viable[24]. However, alternative explanations for shallower slopes in older habitat fragments could be that populations eventually compensate for early losses (for example, via dispersal into the fragment or recovery of the landscape matrix), or that species turnover via immigration of more-tolerant species compensate for losses of more-specialized species[25]. We address the latter in the 'Effects on species composition' section below.

Fourth, studies in which fragments had habitat matrices that were categorized as harsh (for example, intense agriculture or urban areas) had steeper slopes (Fig. 3d). Fragments within matrices that were categorized as light (for example, secondary forests or shade-grown low-intensity agriculture) had shallower slopes (Fig. 3d). Such a result is consistent with expectations that the effects of ecosystem decay should be more pronounced when matrices are distinct from the habitat of interest[14], and support the idea that less-intensive habitat use (and restoration) can reduce the effect of habitat loss on biodiversity loss within intact habitats.

Finally, we compared our results with those from a recent study that used very different methodology and scales to show greater responses to fragmentation in tropical compared to temperate areas[26]. We found a weak decline in the slope estimate with increasing (absolute) latitude (−0.0005; 95% credible interval of −0.001−−0.0001) (Extended Data Fig. 6), and there was no indication of variation among taxa in this result. Even though our study explicitly focused on local-scale variation in biodiversity within remnant fragments of different sizes (whereas ref. [26] examined landscape-level variation in biodiversity across fragmented habitats), these very different approaches both show stronger fragmentation effects in tropical areas.

A general feature of natural landscapes is that species are typically distributed non-randomly, and habitats are often destroyed non-randomly. As a result, it is possible that habitat fragments left remaining in the landscape are qualitatively different from those that were destroyed, and that diversity responses to habitat destruction can emerge from geometric, as well as demographic, effects[27]. For example, if a habitat fragment that remains after habitat destruction is of low quality, it may have less diversity even if there were no shifts in species demography following habitat destruction. If this were true, the patterns we observed would still be consistent with the ecosystem decay hypothesis, but the mechanism would be slightly different: they would be due to spatial rather than temporal variation in local demography after habitat loss. With the data that we have available, we have no indication of the quality of habitat patches before or after the surrounding habitats were destroyed, and thus we cannot differentiate whether spatial or temporal demographic variation (or both) underpin the observed ecosystem decay. Nevertheless, we argue that scenarios in which lower-quality patches are left behind (for example, if habitat destruction favours the removal of habitats with better resources to extract) are equally as likely as those in which higher-quality patches remain (for example, if regulations and habitat protection favour leaving particular higher-quality habitats). If true, then our null expectation that sample-controlled diversity estimates should be equal on average in larger versus smaller fragments should remain, and that any changes to this would be a result of shifts in demographic responses of species after habitat loss.

Effects on species composition

Our focus thus far has been on biodiversity change measured as numbers and relative abundances of species, but habitat fragmentation can also alter the composition of species. For example, habitat fragmentation often disadvantages habitat specialists but can benefit (or have a lower effect on) habitat generalists[28]. We examined compositional change and how it related to habitat loss by partitioning total community dissimilarity between large and small fragment pairs into: (i) the turnover component, which indicates the degree to which compositional dissimilarity results from different species; and (ii) the nestedness component, which indicates how much of the dissimilarity between fragments results from species in smaller habitats being subsets of more speciose fragments. On the whole, turnover among fragments was higher than nestedness components (Extended Data Fig. 7), consistent with the idea that there was an overall shift from more-specialist to more-tolerant species in smaller habitat fragments. However, there were enough cases of high nestedness between small and large fragments that there was no overall trend in the contribution of turnover to compositional change between large and small fragments (Extended Data Fig. 7a, b). On the other hand, nestedness components between fragments increased as the difference in size of habitat fragments increased, which indicates that biodiversity loss from larger to smaller fragments contributes to nested compositional differences among those fragments (Extended Data Fig. 7c, d).

Differences across studies in the species compositional turnover may also help to explain some of the variation in biodiversity responses to the size of habitat fragments. Studies with shallower slopes (for example, those with a long time since fragmentation or with less-harsh matrices) had greater contributions of species turnover to dissimilarity (Fig. 4a), potentially buffering the richness response (for example, if more-tolerant species replaced those species that were lost). On the other hand, studies with steeper slopes (for example, with less time since fragmentation or harsher matrices) had greater contributions of nestedness (Fig. 4b), indicating that species losses contributed more to the dissimilarity.

Discussion

Our results strongly support the notion of ecosystem decay; that is, the biodiversity loss that results from habitat loss is greater than that expected if species losses result from passive sampling with no changes in local demography. However, we also found that species turnover slightly buffers this effect, at least in some cases. Because our results include many taxa in many systems, we cannot discern among the many different mechanisms (for example, edge effects, demographic stochasticity or reduction of dispersal), or combinations thereof, by which ecosystem decay occurs. It is also important to emphasize that our analysis is conducted strictly within habitat patches. Thus, we cannot fully resolve the current debate as to whether and how habitat fragmentation per se (that is, the spatial configuration of habitat fragments when controlling for total habitat amount) influences biodiversity at the scale of the landscape[3–6]: the landscape-level data required to address this question are exceedingly rare. Even though our analyses point to a consistent decline in biodiversity in the habitats that remain after habitat loss and fragmentation, it is certainly possible that—at some scales—biodiversity might be unaffected or even increase at the landscape scale after fragmentation, depending on the balance between species that favour intact habitats and those that favour matrix habitats[6]. Nevertheless, assuming a given habitat type continues to be lost disproportionately, and that a number of species tend to specialize on the declining habitat type, then our results predict that the loss of biodiversity under an ecosystem decay scenario will extend beyond that expected from passive sampling.

Our results point to a critical limitation when forecasting the biodiversity loss expected due to habitat loss using the logic of the species–area relationship or the related relationship between endemic species and area (the endemics–area relationship)[11,12,18]. Any such modelling implicitly assumes that the underlying shape of the species–area or endemics–area relationships depends only on habitat geometry and the distribution of species before the habitats are destroyed, and thus implicitly assumes that species loss follows the passive sampling hypothesis (even if species distributions and habitat losses are not random per se). Improvements to these forecasts allow that species may persist in the matrix after habitat loss[29], but still assume that the distribution and demography of species in the remaining habitats is the same regardless of the amount of surrounding habitat. Because we find support for the ecosystem decay hypothesis (showing that biodiversity loss from habitat loss exceeds that which would have been expected simply from passive sampling of lost habitats), forecasts that use tools based on the species–area or endemics–area relationships will underestimate longer-term patterns of biodiversity loss. We can apply the results of our global synthesis to quantify proportional species loss with habitat loss under the endemics–area relationship (passive sampling) and ecosystem decay models, which has been attempted previously with limited data and much speculation[30]. In Extended Data Fig. 8, we show how one could begin to predict species loss with habitat loss using a version of the endemics–area relationship parameterized with data from our synthesis, and compare the expectations of biodiversity loss to those that would emerge if these demographic changes were not incorporated. This provides an important step towards making more realistic forecasts of biodiversity loss, which will pave the way for the development of more accurate tools for conservation-based management. At the same time, our results suggest that restoration in habitat matrices may moderate the pervasive ecosystem decay that we observed in our synthetic analysis.

Online content

Any methods, additional references, Nature Research reporting summaries, source data, extended data, supplementary information, acknowledgements, peer review information; details of author contributions and competing interests; and statements of data and code availability are available at https://doi.org/10.1038/s41586-020-2531-2.

1. Pimm, S. L. et al. The biodiversity of species and their rates of extinction, distribution, and protection. *Science* **344**, 1246752 (2014).
2. Díaz, S. et al. Pervasive human-driven decline of life on Earth points to the need for transformative change. *Science* **366**, eaax3100 (2019).
3. Haddad, N. M. et al. Habitat fragmentation and its lasting impact on Earth's ecosystems. *Sci. Adv*. **1**, e1500052 (2015).
4. Fahrig, L. Ecological responses to habitat fragmentation per se. *Annu. Rev. Ecol. Evol. Syst*. **48**, 1–23 (2017).
5. Fletcher, R. J. Jr et al. Is habitat fragmentation good for biodiversity? *Biol. Conserv*. **226**, 9–15 (2018).
6. Fahrig, L. et al. Is habitat fragmentation bad for biodiversity? *Biol. Conserv*. **230**, 179–186 (2019).
7. Connor, E. F. & McCoy, E. D. The statistics and biology of the species–area relationship. *Am. Nat*. **113**, 791–833 (1979).
8. Yaacobi, G., Ziv, Y. & Rosenzweig, M. L. Habitat fragmentation may not matter to species diversity. *Proc. R. Soc. Lond. B* **274**, 2409–2412 (2007).
9. Lovejoy, T. E. et al. in *Extinctions* (ed. Nitecki, M. H.) 295–325 (Univ. of Chicago Press, 1984).
10. Hanski, I., Zurita, G. A., Bellocq, M. I. & Rybicki, J. Species-fragmented area relationship. *Proc. Natl Acad. Sci. USA* **110**, 12715–12720 (2013).
11. Pimm, S. L. & Askins, R. A. Forest losses predict bird extinctions in eastern North America. *Proc. Natl Acad. Sci. USA* **92**, 9343–9347 (1995).
12. He, F. & Hubbell, S. P. Species–area relationships always overestimate extinction rates from habitat loss. *Nature* **473**, 368–371 (2011).
13. Terborgh, J. et al. Ecological meltdown in predator-free forest fragments. *Science* **294**, 1923–1926 (2001).
14. Laurance, W. F. et al. The fate of Amazonian forest fragments: a 32-year investigation. *Biol. Conserv*. **144**, 56–67 (2011).
15. Gibson, L. et al. Near-complete extinction of native small mammal fauna 25 years after forest fragmentation. *Science* **341**, 1508–1510 (2013).
16. Thomas, C. D. et al. Extinction risk from climate change. *Nature* **427**, 145–148 (2004).
17. Tilman, D. et al. Future threats to biodiversity and pathways to their prevention. *Nature* **546**, 73–81 (2017).
18. Halley, J. M., Sgardeli, V. & Monokrousos, N. Species–area relationships and extinction forecasts. *Ann. NY Acad. Sci*. **1286**, 50–61 (2013).
19. Bueno, A. S. & Peres, C. A. Patch-scale biodiversity retention in fragmented landscapes: reconciling the habitat amount hypothesis with the island biogeography theory. *J. Biogeogr*. **46**, 621–632 (2019).
20. Chase, J. M. et al. A framework for disentangling ecological mechanisms underlying the island species–area relationship. *Front. Biogeogr*. **11**, e40844 (2019).
21. Chase, J. M. et al. Embracing scale-dependence to achieve a deeper understanding of biodiversity and its change across communities. *Ecol. Lett*. **21**, 1737–1751 (2018).
22. Chase, J. M. et al. FragSAD: a database of diversity and species abundance distributions from habitat fragments. *Ecology* **100**, e02861 (2019).
23. Ewers, R. M. & Didham, R. K. Confounding factors in the detection of species responses to habitat fragmentation. *Biol. Rev. Camb. Philos. Soc*. **81**, 117–142 (2006).
24. Tilman, D., May, R. M., Lehman, C. L. & Nowak, M. A. Habitat destruction and the extinction debt. *Nature* **371**, 65–66 (1994).
25. Jackson, S. T. & Sax, D. F. Balancing biodiversity in a changing environment: extinction debt, immigration credit and species turnover. *Trends Ecol. Evol*. **25**, 153–160 (2010).
26. Betts, M. G. et al. Extinction filters mediate the global effects of habitat fragmentation on animals. *Science* **366**, 1236–1239 (2019).
27. Chisholm, R. A. et al. Species–area relationships and biodiversity loss in fragmented landscapes. *Ecol. Lett*. **21**, 804–813 (2018).
28. Matthews, T. J., Cottee-Jones, H. E. & Whittaker, R. J. Habitat fragmentation and the species–area relationship: a focus on total species richness obscures the impact of habitat loss on habitat specialists. *Divers. Distrib*. **20**, 1136–1146 (2014).
29. Koh, L. P., Lee, T. M., Sodhi, N. S. & Ghazoul, J. An overhaul of the species–area approach for predicting biodiversity loss: incorporating matrix and edge effects. *J. Appl. Ecol*. **47**, 1063–1070 (2010).
30. Halley, J. M., Monokrousos, N., Mazaris, A. D., Newmark, W. D. & Vokou, D. Dynamics of extinction debt across five taxonomic groups. *Nat. Commun*. **7**, 12283 (2016).

Methods

No statistical methods were used to predetermine sample size. The experiments were not randomized and investigators were not blinded to allocation during experiments and outcome assessment.

Literature search and data inclusion

Full details for the search criteria and process for developing the dataset analysed have previously been published[22]. In brief, the data needed for our analyses require data on the numbers of individuals of each species from each fragment of different sizes, as well as information on sampling design, numbers of samples (that is, plots, transects, traps, mist nets and so on) and sampling effort (that is, plot areas, transect length, trapping time, net lengths and so on) in each fragment. Because such data are exceedingly difficult to find, we did not restrict ourselves to formally standardized literature searches, but rather attempted to find as many datasets as possible. We also consulted important review papers (for example, refs. [4,23,29,31–35]) for possible data sources, including forward citation searches. By extracting data from publications, appendices, and online repositories from a number of studies, and contacting authors directly for many more, we collated data from 117 studies for our purpose[15,36–142]. In addition, we used data from six studies in the PREDICTS database[143] that met our inclusion criteria[144–148], giving us a total of 123 studies. Here, 'study' refers to sampling at a given time and place on a specific taxonomic group. If two or more taxonomic groups sampled in different ways were presented in the same paper, they were treated as two separate studies (hence the discrepancy between the number of studies and references).

Explanatory variables used for analysis

We also recorded metadata for each dataset, several of which we examined as covariates in the analysis. Specifically, we used absolute latitude and the following categories as covariates.

Taxon groupings. This included plants, invertebrates (mostly insects), birds, mammals and a category that included reptiles and amphibians (because they were often sampled together, and there were not enough studies of each for separate analyses).

Continent (or other geographical grouping). We classified studies as occurring in Africa, Asia, Central America (we included Mexico here for biogeographical, rather than political, reasons), Europe, North America, Oceania or South America.

Time size fragmentation. We classified studies as 'recent' (fragmentation occurred less than 20 years previous to the study), 'intermediate' (fragmentation occurred 20–100 years previous to the study) and 'long' (fragmentation occurred more than 100 years previous to the study).

Matrix quality. We categorized studies on the basis of three qualitative categories of matrix quality: 'light', in which remnant habitat fragments were surrounded by relatively hospitable habitats (for example, secondary forest or shade-grown coffee); 'intermediate', in which remnant habitats occurred within a matrix of lightly used habitats (for example, forests surrounded by early successional habitat or livestock grazing); and 'harsh', in which remnant habitats occurred within a matrix of largely inhospitable matrix (for example, intense agriculture or water when reservoirs were built to create islands).

Vegetation type. We categorized the vegetation type within the habitat fragments as forest ($n = 105$), shrubland ($n = 14$), grassland ($n = 3$) and wetland ($n = 1$). As the majority of studies were from forested areas, we do not present the study-level variation in slope estimates for this categorization (which did not show any meaningful variation).

Standardization and estimation of biodiversity parameters

We made no attempt to standardize sampling across studies because of the inherent limitations of doing so when sampling methodology varies. Instead, we calculated a series of biodiversity indices that allow standardized comparisons of biodiversity differences among fragments within studies, which was crucial for evaluating the hypotheses overviewed in Fig. 1.

Sampling designs fell into one of three broad categories: (i) standardized sampling with equal numbers of samples (often one, but sometimes several) and thus equal sampling effort among habitat fragments ($n = 50$ studies with this kind of data structure); (ii) unequal number of standardized samples (typically more samples in larger fragments), but where data were available for each sample such that average per sample metrics could be calculated for each habitat fragment ($n = 26$ studies with this kind of data structure); (iii) unequal sampling effort among fragments, because the number of standardized samples varied among fragments, and the data were not available on a per sample basis (that is, they were pooled across all samples in a fragment), or because the effort per sample varied among the fragments (for example, different length of transects in different fragments) ($n = 47$ studies with this kind of data structure).

For each habitat fragment, we calculated several biodiversity indices that reflect different aspects of the total and relative species abundances, as well as aspects of sample completeness[20,21]. When there were several samples in a given fragment, we took the average of the calculated indices to get a fragment-level per-sample estimate.

The standardized number of individuals (N_{std}) for each habitat fragment is typically the average number of individuals for a constant sampling effort. For studies in sample design (i), N_{std} was the number of individuals per sample in each fragment, or the average number of individuals when there were multiple samples per fragment. For studies in sample design (ii), N_{std} was the average number of individuals per sample in each fragment. For studies in sample design (iii), we calculated N_{std} by first calculating the relative sampling effort ($\mathrm{SE}_{\mathrm{rel}}$) for each fragment by dividing the total sampling effort in that fragment by the minimum sampling effort per fragment across all fragments in the study, and then second by dividing the observed number of individuals across all samples in that fragment (N_{obs}) by the relative sampling effort of that fragment (that is, $N_{\mathrm{std}} = N_{\mathrm{obs}}/\mathrm{SE}_{\mathrm{rel}}$, rounded to the nearest integer).

For each fragment, we calculated the number of species expected for a given constant sampling effort, which we call standardized species richness (S_{std}). For studies in sample design (i) or (ii), S_{std} was the average of the observed richness per sample in each fragment. For studies in sample design (iii), an individual-based rarefaction curve was created for each fragment (based on, for example, refs. [149,150]), and S_{std} was calculated as the expected species richness for the standardized number of individuals (N_{std}) in each fragment.

To measure standardized evenness, we quantified the effective number of species using the conversion of Hurlbert's[151] probability of interspecific encounter (S_{PIE}) (PIE = 1 − Simpson's diversity)[152]. Here, we calculate S_{PIE} per sample for each fragment (sample design (i) and (ii)). For studies in sample design (iii), we calculated S_{PIE} using the full data of each fragment. Although PIE (and S_{PIE}) can be influenced by sample size at very low sampling effort, it quickly stabilizes to provide a relatively unbiased estimate of relative species abundances in a community[153]. We hereafter refer to S_{PIE} as 'standardized evenness' for simplicity to indicate that it is influenced by the relative abundances of species[151–153], although we recognize that the term evenness is variously used in the literature. Furthermore, we compare results when only including studies with sample designs (i) and (ii) ($n = 76$ studies) to those that also include sample design (iii) ($n = 47$ studies) (see 'Sensitivity analysis').

Rarefied richness (S_n), the number of species for a standardized number of individuals[149], was calculated according to a previously published protocol[150]. The reference number of individuals for S_n was the minimum of two times the smallest number of individuals per sample and the maximum number of individuals per sample among all fragments in the study.

Coverage standardized richness (S_{cov}); this measure standardizes comparisons of species richness with respect to sample completeness[154]. We derived the reference coverage for comparisons among fragments following previously published suggestions[150]. Accordingly, the reference coverage for S_{cov} was the minimum of the maximum coverage per sample and the minimum of the sample-scale coverage with two times the observed numbers of individuals per sample.

Asymptotic richness for each fragment was calculated using the Chao 1 estimator (S_{chao})[155].

S_{PIE}, S_n and S_{chao} were calculated using the R package mobr[156], and S_{cov} was calculated from the R package iNEXT[157].

To account for uncertainty in our biodiversity indices that results from sampling of fragments, we resampled 200 abundance distributions by resampling the observed number of individuals with replacement from the observed species abundance distributions and calculated all 5 biodiversity indices from the 200 resamples. For each analysis, we used the mean of each biodiversity index across the 200 resamples for each fragment in each study.

Dissimilarity partitioning

We calculated the pairwise dissimilarity in community composition between pairs of fragments within a study[158] by partitioning the incidence-based dissimilarity metric (Jaccard) into turnover and nestedness components[159]. For each fragment pair, we also partitioned the abundance-based (Ruzicka) dissimilarity metric into balanced variation in species abundances (the abundances of some species decline and other species increase from one fragment to the other) and abundance gradient (the abundances of all species decline or increase equally from one fragment to the other) components[160]. Fragment pair calculations of the dissimilarity partitions were calculated for standardized sampling effort. For studies with the same number of samples in each fragment (study design (i)), we directly calculated the dissimilarity and its partitioning for all fragment pairs. When there were different numbers of samples in fragments and sample-level data (study design (ii)), we implemented a resampling approach for fragment pairs that differed in their number of samples. We randomly selected one sample from each fragment and calculated dissimilarity and its partitioning, and repeated this procedure 200 times to calculate the average values for the dissimilarity partitions across the resamples for each fragment pair. For fragment pairs in study design (iii), we used our calculations of the relative sampling effort (SE_{rel}) as well as the standardized number of individuals (N_{std}) for each habitat fragment. According to the calculation of standardized species richness (see 'Standardization and estimation of biodiversity parameters'), we resampled N_{std} individuals from the abundance distributions of each fragment in the pair and calculated the dissimilarity partitions from the resampled data. This procedure was repeated 200 times to calculate the average values for the dissimilarity partitions across the resamples for each fragment pair. We used the function beta.div.comp() function from the R package adespatial for dissimilarity partitioning calculations[161].

Establishment of the null expectation

Although Fig. 1 illustrates the expectation for passive sampling and the alternative hypotheses when habitat size varies, the uneven distribution of species across the landscape can influence habitat fragmentation effects[27]. This might lead some to wonder whether the same types of spatial structuring might also influence patterns expected at the within-patch level where sampling effort was held constant. We used a spatial simulation model to show that our null expectation under passive sampling (that is, a zero slope) was robust across different types of spatial aggregation pattern (Extended Data Fig. 1). The regional species pool was set to have 40,000 individuals, 2,000 species and a log-normal species abundance distribution with a coefficient of variation equal to 1. We examined three different levels of within species aggregation via a Thomas cluster process; each species had a single cluster, and the degree of intraspecific aggregation was controlled by setting the displacement of individuals of each species from the single cluster (or mother point) to values that resulted in either an approximately random distribution (sigma = 1), or increasingly aggregated spatial distributions (sigma = 0.1, 0.02). To avoid edge effects, fragments were randomly placed (without overlap) within the central square unit of the landscape (fragment area = {0.0005, 0.005, 0.05, 0.5}), and samples were taken from a single quadrat (area = 0.0001) randomly placed within each fragment. We quantified total numbers of individuals, species richness and evenness (S_{PIE}) for each sample, and fit ordinary least-squares linear models to log-transformed diversity (or total numbers of individuals) as a function of log-transformed fragment size. This process was repeated 2,000 times, and we plotted the slope coefficients from the linear models to illustrate the expectation of the passive sampling hypothesis (Extended Data Fig. 1). All simulations were run using the R package mobsim[162].

Statistical analyses

Although many ecological syntheses use meta-analytic tools to compare published estimates[163], our approach using underlying assemblage-level data enabled us to directly analyse data across studies[164]. To examine the relationship between biodiversity indices and fragment size, we fit two sets of hierarchical generalized linear models to the data: one to model each of the biodiversity indices described in 'Standardization and estimation of biodiversity parameters' as a function of fragment size; the second to explicitly account for uncertainty in the expected levels of biodiversity under the passive sampling hypothesis (see 'Estimating and analysing uncertainty'). As the results were qualitatively consistent between the two sets of models, we present the relationships between biodiversity indices and fragment size in the main text, and show the robustness of our results to the inclusion of uncertainty surrounding the passive sampling hypothesis in Extended Data Fig. 3.

In several studies, large habitat fragments were labelled as continuous, without provision of the actual size of these areas. For these cases, we imputed the size of the continuous habitat to be ten times as large as the next largest habitat fragment size reported in the respective study. However, we also used different multiplicative factors to assess the robustness of our results to this assumption (see 'Sensitivity analysis').

Fragment size was log-transformed and centred by subtracting the mean (log) fragment size of each study from the size of each fragment before fitting models, and back-transformed for presentation in the figures. For each biodiversity measure, we estimated the overall relationship with fragment size, and also allowed the slope and intercept of the relationship to vary for each study in the dataset (that is, the slope and intercept were estimated as fixed effects, as well as random effects for each study). Following standardization, none of our response variables remained with exclusively integer values, which precluded the use of Poisson or the negative binomial error distributions. Because all responses were constrained to be positive, we used the log-normal error distribution and an identity link function in the analysis of biodiversity indices.

We visualized variation in effects of fragment area on biodiversity associated with taxon group, geographical region, time since fragmentation and matrix quality using the posterior distributions of study-level slope estimates. Alternatively, we could have fit models with interactions between the covariates and fragment area, but—owing to data limitations—these would have been restricted to two-way interactions. However, it is likely that multiple covariates combine and contribute to variation in the effects of fragmentation on biodiversity. Because each study represents a combination of all these covariates in our analyses, examining study-level variation allows us to efficiently simultaneously adjust for and characterize relationships among multiple covariates and fragmentation effects on biodiversity. However, to assess the robustness of patterns found in the study-level variation for the different groups, we fit models with two-way interactions between fragment size and taxon group, geographic region, time since fragmentation and matrix quality, respectively (Extended Data Tables 1–3).

Estimating and analysing uncertainty

The passive sampling hypothesis posits that biodiversity in an effort-standardized sample in a small fragment is the same as the biodiversity in a corresponding effort-standardized sample in a large fragment (Fig. 1). That is, the expected value of the standardized biodiversity metrics under the passive sampling hypothesis in smaller fragments is equal to that in the largest fragment for each study (Fig. 1). To account for uncertainty associated with the passive sampling hypothesis, we calculated *z*-scores ((observed − expected)/s.d.(expected)) for each biodiversity index and for each fragment smaller than the largest in each study. To derive the *z*-score, we calculated the expected value and its s.d. for each biodiversity index from the resampling process for the largest fragment in each study. We used the observed value for each of the biodiversity indices for each smaller fragment to calculate the *z*-scores. As the standardized number of individuals was defined as $N_{\mathrm{std}} = N_{\mathrm{obs}}/\mathrm{SE}_{\mathrm{rel}}$, there was no estimate of uncertainty, and *z*-scores were calculated only for the five biodiversity indices.

We modelled the *z*-scores as a function of fragment size using models similar to those described in 'Statistical analyses'. Fragment size was log-transformed and centred by subtracting the mean (log) fragment size from each observation before fitting models. For the *z*-score of each measure, we estimated the overall relationship with fragment size, and also allowed the slope and intercept of the relationship to vary for each study in the dataset (that is, the slope and intercept were estimated as fixed effects, as well as random effects for each study). *z*-scores were distributed around zero for all metrics, and comparisons of models fit with Gaussian, asymmetric Laplacian (back-to-back exponential) or Student's error distribution showed strong support for assuming error to follow a Student distribution, and it was used for all analyses. Similar to the models of biodiversity indices, we found positive slopes (95% credible intervals did not overlap zero) for the relationship between *z*-scores of all metrics and fragment size (Extended Data Fig. 3). This suggests that our inference of pervasive ecosystem decay from Fig. 2 is robust to the inclusion of uncertainty in the passive sampling hypothesis.

Latitudinal variation

To examine whether there was a latitudinal gradient in the slope of the relationship between fragment size and biodiversity indices, we modelled the study-level slope estimates as a function of absolute latitude. We used a random-effects meta-analytic model that incorporated uncertainty associated with the study-level slope estimates (that is, the standard error of the posterior distributions) into our analysis; study was included as a random effect, and the model assumed a Gaussian error distribution and an identity link function. To examine whether the latitudinal gradients differed between taxa, we fit a second model that included an interaction between absolute latitude and taxon group.

Compositional dissimilarity

To examine the relationship between dissimilarity components among fragments and differences in fragment size, we modelled the turnover and nestedness components of Jaccard dissimilarity[159], and the balanced abundance and abundance gradient components of Ruzicka dissimilarity[160], as a function of the log-transformed ratio of the sizes for each fragment pair (that was centred before model fitting). We fit models that estimated the overall relationship, and also allowed both the slope and intercept to vary for each study. Models assumed zero–one inflated beta distributions and logit-link functions for the turnover components, and zero inflated beta distributions (and logit-link functions) for the nestedness components.

Model fitting

For Bayesian inference and estimates of uncertainty, all models were fit using the Hamiltonian Monte Carlo (HMC) sampler Stan[165] and coded using the brms package[166]. All models were fit with 4 chains and 2,000 iterations, with 1,000 used as a warm-up. We used weakly regularizing priors and visual inspection of the HMC chains showed excellent convergence.

Sensitivity analysis

Forty-seven studies had unequal numbers of samples across fragments and data were pooled (that is, sample design (iii)). This pooling of samples means that data from larger fragments, which encompass a larger sampling extent, will also encompass more heterogeneity. This can, in turn, influence diversity estimates. To examine whether our inferences of ecosystem decay were sensitive to the inclusion of studies with sample design (iii), we removed those studies and refit the models to the remaining data ($n = 79$ studies for which sampling extents were comparable).

For all analyses, we needed to assign a fragment size to fragments labelled as continuous without a specified size. In the main results, we calculated their size as ten times larger than the next largest fragment in a given study, which was an arbitrary—but reasonable—assumption (that is, no habitat is ever continuous). However, to assess the sensitivity of our results, we varied this multiplier so that continuous fragments were either 2 or 100 times larger than the next largest fragment.

The calculations of the biodiversity parameters used here typically require counts of individuals of each species (that is, integer abundance values). However, a few of the studies in our dataset report non-integer abundance values for samples (for example, based on averages for subsamples within each sample, where the subsample data were not available). In the results discussed in the main text, we calculated the biodiversity parameters directly from these non-integer abundances. To assess the potential sensitivity of our findings to the use of non-integer abundances, we implemented two additional methods. In one, we rounded all abundances to the next largest integer. In this way, we favoured rare species with respect to their relative abundance. The second method divided all abundances by the minimum abundance in the respective study. This resulted in the lowest abundance equalling 1 after scaling, but all relative abundances were maintained.

Adding ecosystem decay to extinction forecasts

Many published models of biodiversity loss implicitly or explicitly assume that scaling relationships of biodiversity are constant even when habitat is lost (that is, assume passive sampling). For example, forecasts based on the species–area relationship or the endemics–area relationship implicitly assume that passive sampling is the primary process by which habitat size influences species diversity (or, rather, only consider immediate extinctions, and not extinction debt). Here we illustrate how estimates such as ours—which quantify the degree to which ecosystem decay leads to extinctions beyond passive sampling—could improve forecasts of biodiversity loss due to habitat loss.

If smaller fragments are simply passive samples from the assemblages found in larger areas, then the expected number of species lost with a loss of area *a* (from a total area, *A*) can be calculated using the endemics–area relationship[12]:

$$S_a^N = \sum_{i=1}^{S} \left(\frac{a}{A}\right)^{N_i}$$

with species lost,

$$S_{\text{passive}} = S - S^{1}_{A-a} = \sum_{i=1}^{S} \left(\frac{a}{A}\right)^{N_i} = S_a^N$$

N_i is the total abundance of species i, and S is the total number of species in the region A.

We calculate the additional species lost under ecosystem decay using the slope estimated from our model fit to standardized species richness ($\beta = 0.06$). We assume that species lost owing to passive sampling equals S_{passive}, and that additional species lost owing to ecosystem decay are proportional to the area lost a, to calculate $S_{\text{decay}} = S_{\text{passive}} + \beta a$.

To illustrate the difference between species loss owing to random expectations and the empirically derived loss including ecosystem decay, we simulated a regional assemblage using the mobsim R package[162]. We calculated S_{passive} and S_{decay} using the equations described above. We set $A = 10{,}000$, $S = 1{,}000$ and simulated species in A using a log-normal species abundance distribution (total community $N = 10{,}000$, coefficient of variation = 1) randomly distributed in space. We examined area lost, a, that ranged from 1 to A, and show the number of extinctions as a function of the area (a) lost (Extended Data Fig. 8).

Reporting summary

Further information on research design is available in the Nature Research Reporting Summary linked to this paper.

Data availability

All of the data used in this analysis are open access and available in ref. [22] (117 of the datasets) and ref. [143] (5 of the datasets). Raw data (before standardization) are available from GitHub (https://github.com/FelixMay/FragFrame_1), and are mirrored on Zenodo (https://doi.org/10.5281/zenodo.3862409).

Code availability

The R code used for standardizing the data and doing the analyses presented here are available from GitHub (https://github.com/FelixMay/FragFrame_1), and are mirrored on Zenodo (https://doi.org/10.5281/zenodo.3862409).

31. Saunders, D. A., Hobbs, R. J. & Margules, C. R. Biological consequences of ecosystem fragmentation: a review. *Conserv. Biol*. **5**, 18–32 (1991).
32. Andrén, H. Effects of habitat fragmentation on birds and mammals in landscapes with different proportions of suitable habitat: a review. *Oikos* **71**, 355–366 (1994).
33. Debinski, D. M. & Holt, R. D. A survey and overview of habitat fragmentation experiments. *Conserv. Biol*. **14**, 342–355 (2000).
34. Fahrig, L. Effects of habitat fragmentation on biodiversity. *Annu. Rev. Ecol. Evol. Syst*. **34**, 487–515 (2003).
35. Jones, I. L., Bunnefeld, N., Jump, A. S., Peres, C. A. & Dent, D. H. Extinction debt on reservoir land-bridge islands. *Biol. Conserv*. **199**, 75–83 (2016).
36. Aguiar, W. M. D. & Gaglianone, M. C. Euglossine bee communities in small forest fragments of the Atlantic Forest, Rio de Janeiro state, southeastern Brazil (Hymenoptera, Apidae). *Rev. Bras. Entomol*. **56**, 210–219 (2012).
37. Aizen, M. A. & Feinsinger, P. Habitat fragmentation, native insect pollinators, and feral honey bees in Argentine "Chaco Serrano". *Ecol. Appl*. **4**, 378–392 (1994).
38. Almeida-Gomes, M. & Rocha, C. F. D. Diversity and distribution of lizards in fragmented Atlantic Forest landscape in southeastern Brazil. *J. Herpetol*. **48**, 423–429 (2014).
39. Andresen, E. Effect of forest fragmentation on dung beetle communities and functional consequences for plant regeneration. *Ecography* **26**, 87–97 (2003).
40. Báldi, A. & Kisbenedek, T. Orthopterans in small steppe patches: an investigation for the best-fit model of the species–area curve and evidences for their non-random distribution in the patches. *Acta Oecol*. **20**, 125–132 (1999).
41. Baz, A. & Garcia-Boyero, A. The SLOSS dilemma: a butterfly case study. *Biodivers. Conserv*. **5**, 493–502 (1996).
42. Bell, K. E. & Donnelly, M. A. Influence of forest fragmentation on community structure of frogs and lizards in northeastern Costa Rica. *Conserv. Biol*. **20**, 1750–1760 (2006).
43. Benedick, S. et al. Impacts of rain forest fragmentation on butterflies in northern Borneo: species richness, turnover and the value of small fragments. *J. Appl. Ecol*. **43**, 967–977 (2006).
44. Benítez-Malvido, J. et al. The multiple impacts of tropical forest fragmentation on arthropod biodiversity and on their patterns of interactions with host plants. *PLoS ONE* **11**, e0146461 (2016).
45. Berg, Å. Diversity and abundance of birds in relation to forest fragmentation, habitat quality and heterogeneity. *Bird Study* **44**, 355–366 (1997).
46. Bernard, E. & Fenton, M. B. Bats in a fragmented landscape: species composition, diversity and habitat interactions in savannas of Santarém, Central Amazonia, Brazil. *Biol. Conserv*. **134**, 332–343 (2007).
47. Bolger, D. T. et al. Response of rodents to habitat fragmentation in coastal southern California. *Ecol. Appl*. **7**, 552–563 (1997).
48. Bossart, J. L. et al. Richness, abundance, and complementarity of fruit-feeding butterfly species in relict sacred forests and forest reserves of Ghana. *Biodivers. Conserv*. **15**, 333–359 (2006).
49. Bossart, J. L. & Antwi, J. B. Limited erosion of genetic and species diversity from small forest patches: sacred forest groves in an Afrotropical biodiversity hotspot have high conservation value for butterflies. *Biol. Conserv*. **198**, 122–134 (2016).
50. Bragagnolo, C. et al. Harvestmen in an Atlantic forest fragmented landscape: evaluating assemblage response to habitat quality and quantity. *Biol. Conserv*. **139**, 389–400 (2007).
51. Brosi, B. J., Daily, G. C., Shih, T. M., Oviedo, F. & Durán, G. The effects of forest fragmentation on bee communities in tropical countryside. *J. Appl. Ecol*. **45**, 773–783 (2008).
52. Brosi, B. J. The effects of forest fragmentation on euglossine bee communities (Hymenoptera: Apidae: Euglossini). *Biol. Conserv*. **142**, 414–423 (2009).
53. Cabrera-Guzmán, E. & Reynoso, V. H. Amphibian and reptile communities of rainforest fragments: minimum patch size to support high richness and abundance. *Biodivers. Conserv*. **21**, 3243–3265 (2012).
54. Cadotte, M. W., Franck, R., Reza, L. & Lovett-Doust, J. Tree and shrub diversity and abundance in fragmented littoral forest of southeastern Madagascar. *Biodivers. Conserv*. **11**, 1417–1436 (2002).
55. Carneiro, M. S., Campos, C. C., Ramos, F. N. & Dos Santos, F. A. Spatial species turnover maintains high diversities in a tree assemblage of a fragmented tropical landscape. *Ecography* **7**, e01500 (2016).
56. Cayuela, L., Golicher, D. J., Benayas, J. M. R., González-Espinosa, M. & Ramírez-Marcial, N. Fragmentation, disturbance and tree diversity conservation in tropical montane forests. *J. Appl. Ecol*. **43**, 1172–1181 (2006).
57. Chiarello, A. G. Effects of fragmentation of the Atlantic forest on mammal communities in south-eastern Brazil. *Biol. Conserv*. **89**, 71–82 (1999).
58. Cosson, J. F. et al. Ecological changes in recent land-bridge islands in French Guiana, with emphasis on vertebrate communities. *Biol. Conserv*. **91**, 213–222 (1999).
59. Dami, F. D., Mwansat, G. S. & Manu, S. A. The effects of forest fragmentation on species richness on the Obudu Plateau, south-eastern Nigeria. *Afr. J. Ecol*. **51**, 32–36 (2013).
60. Dauber, J., Bengtsson, J. & Lenoir, L. Evaluating effects of habitat loss and land-use continuity on ant species richness in seminatural grassland remnants. *Conserv. Biol*. **20**, 1150–1160 (2006).
61. Davies, R. G. et al. Environmental and spatial influences upon species composition of a termite assemblage across neotropical forest islands. *J. Trop. Ecol*. **19**, 509–524 (2003).
62. de La Sancha, N. U. Patterns of small mammal diversity in fragments of subtropical interior Atlantic forest in eastern Paraguay. *Mammalia* **78**, 437–449 (2014).
63. de Souza, O. F. F. & Brown, V. K. Effects of habitat fragmentation on Amazonian termite communities. *J. Trop. Ecol*. **10**, 197 (1994).
64. Dickman, C. R. Habitat fragmentation and vertebrate species richness in an urban environment. *J. Appl. Ecol*. **24**, 337–351 (1987).
65. Didham, R. K., Hammond, P. M., Lawton, J. H., Eggleton, P. & Stork, N. E. Beetle species responses to tropical forest fragmentation. *Ecol. Monogr*. **68**, 295–323 (1998).
66. Ding, Z., Feeley, K. J., Wang, Y., Pakeman, R. J. & Ding, P. Patterns of bird functional diversity on land-bridge island fragments. *J. Anim. Ecol*. **82**, 781–790 (2013).
67. Dixo, M. & Metzger, J. P. Are corridors, fragment size and forest structure important for the conservation of leaf-litter lizards in a fragmented landscape? *Oryx* **43**, 435 (2009).
68. Dominguez-Haydar, Y. & Armbrecht, I. Response of ants and their seed removal in rehabilitation areas and forests at El Cerrejón coal mine in Colombia. *Restor. Ecol*. **19**, 178–184 (2011).
69. Echeverría, C. et al. Impacts of forest fragmentation on species composition and forest structure in the temperate landscape of southern Chile. *Glob. Ecol. Biogeogr*. **16**, 426–439 (2007).
70. Edwards, D. P. et al. Wildlife-friendly oil palm plantations fail to protect biodiversity effectively. *Conserv. Lett*. **3**, 236–242 (2010).
71. Estrada, A. & Coates-Estrada, R. Bats in continuous forest, forest fragments and in an agricultural mosaic habitat-island at Los Tuxtlas, Mexico. *Biol. Conserv*. **103**, 237–245 (2002).
72. Estrada, A. & Coates-Estrada, R. Dung beetles in continuous forest, forest fragments and in an agricultural mosaic habitat island at Los Tuxtlas, Mexico. *Biodivers. Conserv*. **11**, 1903–1918 (2002).
73. Filgueiras, B. K. C., Iannuzzi, L. & Leal, I. R. Habitat fragmentation alters the structure of dung beetle communities in the Atlantic forest. *Biol. Conserv*. **144**, 362–369 (2011).
74. da Fonseca, G. A. B. & Robinson, J. G. Forest size and structure: competitive and predatory effects on small mammal communities. *Biol. Conserv*. **53**, 265–294 (1990).
75. Fujita, A. et al. Effects of forest fragmentation on species richness and composition of ground beetles (Coleoptera: Carabidae and Brachinidae) in urban landscapes. *Entomol. Sci*. **11**, 39–48 (2008).
76. Gavish, Y., Ziv, Y. & Rosenzweig, M. L. Decoupling fragmentation from habitat loss for spiders in patchy agricultural landscapes. *Conserv. Biol*. **26**, 150–159 (2012).
77. Giladi, I. et al. Scale-dependent determinants of plant species richness in a semi-arid fragmented agro-ecosystem. *J. Veg. Sci*. **22**, 983–996 (2011).
78. Giraudo, A. R. et al. Comparing bird assemblages in large and small fragments of the Atlantic forest hotspots. *Biodivers. Conserv*. **17**, 1251–1265 (2008).
79. Gonçalves-Souza, T., Matallana, G. & Brescovit, A. D. Effects of habitat fragmentation on the spider community (Arachnida, Araneae) in three Atlantic forest remnants in southeastern Brazil. *Rev. Iber. Aracnol*. **16**, 35–42 (2008).
80. Goodman, S. M. & Rakotondravony, D. The effects of forest fragmentation and isolation on insectivorous small mammals (Lipotyphla) on the Central High Plateau of Madagascar. *J. Zool*. **250**, 193–200 (2000).

81. Guadagnin, D. L., Peter, Â. S., Perello, L. F. C. & Maltchik, L. Spatial and temporal patterns of waterbird assemblages in fragmented wetlands of southern Brazil. *Waterbirds* **28**, 261–272 (2005).
82. Halme, E., Niemela, J. & Haime, E. Carabid beetles in fragments of coniferous forest. *Ann. Zool. Fenn*. **30**, 17–30 (1993).
83. Henry, M., Pons, J.-M. & Cosson, J.-F. Foraging behaviour of a frugivorous bat helps bridge landscape connectivity and ecological processes in a fragmented rainforest. *J. Anim. Ecol*. **76**, 801–813 (2007).
84. Horváth, R. et al. Spiders are not less diverse in small and isolated grasslands, but less diverse in overgrazed grasslands: a field study (East Hungary, Nyirseg). *Agric. Ecosyst. Environ*. **130**, 16–22 (2009).
85. Jauker, F., Jauker, B., Grass, I., Steffan-Dewenter, I. & Wolters, V. Partitioning wild bee and hoverfly contributions to plant–pollinator network structure in fragmented habitats. *Ecology* **100**, e02569 (2019).
86. Jung, J. K. et al. A comparison of diversity and species composition of ground beetles (Coleoptera: Carabidae) between conifer plantations and regenerating forests in Korea. *Ecol. Res*. **29**, 877–887 (2014).
87. Jyothi, K. M. & Nameer, P. O. Birds of sacred groves of northern Kerala, India. *J. Threat. Taxa* **7**, 8226–8236 (2015).
88. Kapoor, V. Effects of rainforest fragmentation and shade-coffee plantations on spider communities in the Western Ghats, India. *J. Insect Conserv*. **12**, 53–68 (2008).
89. Kappes, H. et al. Response of snails and slugs to fragmentation of lowland forests in NW Germany. *Landsc. Ecol*. **24**, 685–697 (2009).
90. Klein, B. C. Effects of forest fragmentation on dung and carrion beetle communities in central Amazonia. *Ecology* **70**, 1715–1725 (1989).
91. Knapp, M. & Řezáč, M. Even the smallest non-crop habitat islands could be beneficial: distribution of carabid beetles and spiders in agricultural landscape. *PLoS ONE* **10**, e0123052 (2015).
92. Lambert, T. D. et al. Rodents on tropical land-bridge islands. *J. Zool*. **260**, 179–187 (2003).
93. Lasky, J. R. & Keitt, T. H. Abundance of Panamanian dry-forest birds along gradients of forest cover at multiple scales. *J. Trop. Ecol*. **26**, 67–78 (2010).
94. de Lima, M. G. & Gascon, C. The conservation of linear forest remnants in central Amazonia. *Biol. Conserv*. **91**, 241–247 (1999).
95. Lima, J. et al. Amphibians on Amazonian land-bridge islands are affected more by area than isolation. *Biotropica* **47**, 369–376 (2015).
96. Lion, M. B., Garda, A. A. & Fonseca, C. R. Split distance: a key landscape metric shaping amphibian populations and communities in forest fragments. *Divers. Distrib*. **20**, 1245–1257 (2014).
97. Lion, M. B., Garda, A. A., Santana, D. J. & Fonseca, C. R. The conservation value of small fragments for Atlantic forest reptiles. *Biotropica* **48**, 265–275 (2016).
98. Lövei, G. L. & Cartellieri, M. Ground beetles (Coleoptera, Carabidae) in forest fragments of the Manuwatu, New Zealand: collapsed assemblages? *J. Insect Conserv*. **4**, 239–244 (2000).
99. Mac Nally, R. & Brown, G. W. Reptiles and habitat fragmentation in the box-ironbark forests of central Victoria, Australia: predictions, compositional change and faunal nestedness. *Oecologia* **128**, 116–125 (2001).
100. Manu, S., Peach, W. & Cresswell, W. The effects of edge, fragment size and degree of isolation on avian species richness in highly fragmented forest in West Africa. *Ibis* **149**, 287–297 (2007).
101. Martensen, A. C., Ribeiro, M. C., Banks-Leite, C., Prado, P. I. & Metzger, J. P. Associations of forest cover, fragment area, and connectivity with Neotropical understory bird species richness and abundance. *Conserv. Biol*. **26**, 1100–1111 (2012).
102. McCollin, D. Avian distribution patterns in a fragmented wooded landscape (North Humberside, U.K.): the role of between-patch and within-patch structure. *Glob. Ecol. Biogeogr. Lett*. **3**, 48–62 (1993).
103. McIntyre, N. E. Effects of forest patch size on avian diversity. *Landsc. Ecol*. **10**, 85–99 (1995).
104. Meyer, C. F. J. & Kalko, E. K. V. Assemblage-level responses of phyllostomid bats to tropical forest fragmentation: land-bridge islands as a model system. *J. Biogeogr*. **35**, 1711–1726 (2008).
105. Nemésio, A. & Silveira, F. A. Orchid bee fauna (Hymenoptera: Apidae: Euglossina) of Atlantic Forest fragments inside an urban area in southeastern Brazil. *Neotrop. Entomol*. **36**, 186–191 (2007).
106. Nemésio, A. & Silveira, F. A. Forest fragments with larger core areas better sustain diverse orchid bee faunas (Hymenoptera: Apidae: Euglossina). *Neotrop. Entomol*. **39**, 555–561 (2010).
107. Neuschulz, E. L., Botzat, A. & Farwig, N. Effects of forest modification on bird community composition and seed removal in a heterogeneous landscape in South Africa. *Oikos* **120**, 1371–1379 (2011).
108. Nogueira, A. & Pinto-da-Rocha, R. The effects of habitat size and quality on the orb-weaving spider guild (Arachnida: Araneae) in an Atlantic forest fragmented landscape. *J. Arachnol*. **44**, 36–45 (2016).
109. Nufio, R. C., McClenahan, L. J. & Thurston, G. E. Determining the effects of habitat fragment area on grasshopper species density and richness: a comparison of proportional and uniform sampling methods. *Insect Conserv. Divers*. **2**, 295–304 (2009).
110. Nyeko, P. Dung beetle assemblages and seasonality in primary forest and forest fragments on agricultural landscapes in Budongo, Uganda. *Biotropica* **41**, 476–484 (2009).
111. Nyelele, C. et al. Woodland fragmentation explains tree species diversity in an agricultural landscape of Southern Africa. *Trop. Ecol*. **55**, 365–374 (2014).
112. Owen, C. L. *Mapping Biodiversity in a Modified Landscape*. MSc thesis, Imperial College London (2008).
113. Paciencia, M. L. B. & Prado, J. Effects of forest fragmentation on pteridophyte diversity in a tropical rain forest in Brazil. *Plant Ecol*. **180**, 87–104 (2005).
114. Pardini, R. Effects of forest fragmentation on small mammals in an Atlantic forest landscape. *Biodivers. Conserv*. **13**, 2567–2586 (2004).
115. Pineda, E. & Halffter, G. Species diversity and habitat fragmentation: frogs in a tropical montane landscape in Mexico. *Biol. Conserv*. **117**, 499–508 (2004).
116. Raheem, D. C. et al. Fragmentation and pre-existing species turnover determine land-snail assemblages of tropical rain forest. *J. Biogeogr*. **36**, 1923–1938 (2009).
117. Rocha, R. et al. Consequences of a large-scale fragmentation experiment for Neotropical bats: disentangling the relative importance of local and landscape-scale effects. *Landsc. Ecol*. **32**, 31–45 (2017).
118. Sam, K., Koane, B., Jeppy, S. & Novotny, V. Effect of forest fragmentation on bird species richness in Papua New Guinea. *J. Field Ornithol*. **85**, 152–167 (2014).
119. Savilaakso, S., Koivisto, J., Veteli, T. O. & Roininen, H. Microclimate and tree community linked to differences in lepidopteran larval communities between forest fragments and continuous forest. *Divers. Distrib*. **15**, 356–365 (2009).
120. Schnitzler, F. R. *Hymenopteran Parasitoid Diversity and Tri-Trophic Interactions: The Effects of Habitat Fragmentation in Wellington, New Zealand*. PhD thesis, Victoria Univ. of Wellington (2008).
121. Senior, M. J. M. *Assessing Biodiversity and Ecosystem Functioning in Fragmented Tropical Landscapes*. PhD Thesis, Univ. of York (2014).
122. Silva, M. P. P. & Porto, K. C. Effect of fragmentation on the community structure of epixylic bryophytes in Atlantic forest remnants in the northeast of Brazil. *Biodivers. Conserv*. **18**, 317–337 (2009).
123. Silva, R. J., Storck-Tonon, D. & Vaz-de-Mello, F. Z. Dung beetle (Coleoptera: Scarabaeinae) persistence in Amazonian forest fragments and adjacent pastures: biogeographic implications for alpha and beta diversity. *J. Insect Conserv*. **20**, 549–564 (2016).
124. Silveira, G. C. et al. The orchid bee fauna in the Brazilian savanna: do forest formations contribute to higher species diversity? *Apidologie* **46**, 197–208 (2015).
125. Slade, E. M. et al. Life-history traits and landscape characteristics predict macro-moth responses to forest fragmentation. *Ecology* **94**, 1519–1530 (2013).
126. Sridhar, H., Raman, T. S. & Mudappa, D. Mammal persistence and abundance in tropical rainforest remnants in the southern Western Ghats, India. *Curr. Sci*. **94**, 748–757 (2008).
127. Stireman, J. O. III, Devlin, H. & Doyle, A. L. Habitat fragmentation, tree diversity, and plant invasion interact to structure forest caterpillar communities. *Oecologia* **176**, 207–224 (2014).
128. Storck-Tonon, D. & Peres, C. A. Forest patch isolation drives local extinctions of Amazonian orchid bees in a 26 years old archipelago. *Biol. Conserv*. **214**, 270–277 (2017).
129. Struebig, M. J. et al. Conservation importance of limestone karst outcrops for Palaeotropical bats in a fragmented landscape. *Biol. Conserv*. **142**, 2089–2096 (2009).
130. Tellería, J. L. & Santos, T. Effects of forest fragmentation on a guild of wintering passerines: the role of habitat selection. *Biol. Conserv*. **71**, 61–67 (1995).
131. Tonhasca, A., Blackmer, J. L. & Albuquerque, G. S. Abundance and diversity of euglossine bees in the fragmented landscape of the Brazilian Atlantic forest. *Biotropica* **34**, 416–422 (2002).
132. Uehara-Prado, M., Brown, K. S. & Freitas, A. V. L. Species richness, composition and abundance of fruit-feeding butterflies in the Brazilian Atlantic forest: comparison between a fragmented and a continuous landscape. *Glob. Ecol. Biogeogr*. **16**, 43–54 (2007).
133. Ulrich, W., Lens, L., Tobias, J. A. & Habel, J. C. Contrasting patterns of species richness and functional diversity in bird communities of east African cloud forest fragments. *PLoS ONE* **11**, e0163338 (2016).
134. Usher, M. B. & Keiller, S. W. J. The Macrolepidoptera of farm woodlands: determinants of diversity and community structure. *Biodivers. Conserv*. **7**, 725–748 (1998).
135. Vallan, D. Influence of forest fragmentation on amphibian diversity in the nature reserve of Ambohitantely, highland Madagascar. *Biol. Conserv*. **96**, 31–43 (2000).
136. Vasconcelos, H. L., Vilhena, J. M., Magnusson, W. E. & Albernaz, A. L. M. Long-term effects of forest fragmentation on Amazonian ant communities. *J. Biogeogr*. **33**, 1348–1356 (2006).
137. Vieira, M. V. et al. Land use vs. fragment size and isolation as determinants of small mammal composition and richness in Atlantic forest remnants. *Biol. Conserv*. **142**, 1191–1200 (2009).
138. Vulinec, K. et al. Dung beetles and long-term habitat fragmentation in Alter do Chão, Amazônia, Brazil. *Trop. Conserv. Sci*. **1**, 111–121 (2008).
139. Wang, Y., Wang, X. & Ding, P. Nestedness of snake assemblages on islands of an inundated lake. *Curr. Zool*. **58**, 828–836 (2012).
140. Williams, M. R. Habitat resources, remnant vegetation condition and area determine distribution patterns and abundance of butterflies and day-flying moths in a fragmented urban landscape, south-west Western Australia. *J. Insect Conserv*. **15**, 37–54 (2011).
141. Zartman, C. E. Habitat fragmentation impacts on epiphyllous bryophyte communities in Central Amazonia. *Ecology* **84**, 948–954 (2003).
142. Ziter, C., Bennett, E. M. & Gonzalez, A. Functional diversity and management mediate aboveground carbon stocks in small forest fragments. *Ecosphere* **4**, 85 (2013).
143. Hudson, L. N. et al. The database of the PREDICTS (Projecting Responses of Ecological Diversity In Changing Terrestrial Systems) project. *Ecol. Evol*. **7**, 145–188 (2017).
144. Cáceres, N. C., Nápoli, R. P., Casella, J. & Hannibal, W. Mammals in a fragmented savannah landscape in south-western Brazil. *J. Nat. Hist*. **44**, 491–512 (2010).
145. Ewers, R. M., Thorpe, S. & Didham, R. K. Synergistic interactions between edge and area effects in a heavily fragmented landscape. *Ecology* **88**, 96–106 (2007).
146. Fernández, I. C. & Simonetti, J. A. Small mammal assemblages in fragmented shrublands of urban areas of Central Chile. *Urban Ecosyst*. **16**, 377–387 (2013).
147. Garmendia, A., Arroyo-Rodríguez, V., Estrada, A., Naranjo, E. J. & Stoner, K. E. Landscape and patch attributes impacting medium- and large-sized terrestrial mammals in a fragmented rain forest. *J. Trop. Ecol*. **29**, 331–344 (2013).
148. Stouffer, P. C., Johnson, E. I., Bierregaard, R. O. Jr & Lovejoy, T. E. Understory bird communities in Amazonian rainforest fragments: species turnover through 25 years post-isolation in recovering landscapes. *PLoS ONE* **6**, e20543 (2011).
149. Gotelli, N. J. & Colwell, R. K. Quantifying biodiversity: procedures and pitfalls in the measurement and comparison of species richness. *Ecol. Lett*. **4**, 379–391 (2001).
150. Chao, A. et al. Rarefaction and extrapolation with Hill numbers: a framework for sampling and estimation in species diversity studies. *Ecol. Monogr*. **84**, 45–67 (2014).

151. Hurlbert, S. H. The nonconcept of species diversity: a critique and alternative parameters. *Ecology* **52**, 577–586 (1971).
152. Jost, L. Entropy and diversity. *Oikos* **113**, 363–375 (2006).
153. Olszewski, T. D. A unified mathematical framework for the measurement of richness and evenness within and among multiple communities. *Oikos* **104**, 377–387 (2004).
154. Chao, A. & Jost, L. Coverage-based rarefaction and extrapolation: standardizing samples by completeness rather than size. *Ecology* **93**, 2533–2547 (2012).
155. Chao, A. Nonparametric estimation of the number of classes in a population. *Scand. J. Stat*. **11**, 265–270 (1984).
156. McGlinn, D. J. et al. Measurement of Biodiversity (MoB): a method to separate the scale-dependent effects of species abundance distribution, density, and aggregation on diversity change. *Methods Ecol. Evol*. **10**, 258–269 (2019).
157. Hsieh, T. C., Ma, K. H. & Chao, A. iNEXT: an R package for rarefaction and extrapolation of species diversity (Hill numbers). *Methods Ecol. Evol*. **7**, 1451–1456 (2016).
158. Marion, Z. H., Fordyce, J. A. & Fitzpatrick, B. M. Pairwise beta diversity resolves an underappreciated source of confusion in calculating species turnover. *Ecology* **98**, 933–939 (2017).
159. Baselga, A. Partitioning the turnover and nestedness components of beta diversity. *Glob. Ecol. Biogeogr*. **19**, 134–143 (2010).
160. Baselga, A. Separating the two components of abundance-based dissimilarity: balanced changes in abundance vs. abundance gradients. *Methods Ecol. Evol*. **4**, 552–557 (2013).
161. Dray, S. et al. adespatial: multivariate multiscale spatial analysis. R package version 0.3-4 https://CRAN.R-project.org/package=adespatial (2019).
162. May, F., Gerstner, K., McGlinn, D. J., Xiao, X. & Chase, J. M. mobsim: an R package for the simulation and measurement of biodiversity across spatial scales. *Methods Ecol. Evol*. **9**, 1401–1408 (2018).
163. Gurevitch, J., Koricheva, J., Nakagawa, S. & Stewart, G. Meta-analysis and the science of research synthesis. *Nature* **555**, 175–182 (2018).
164. Purvis, A. et al. Modelling and projecting the response of local terrestrial biodiversity worldwide to land use and related pressures: the PREDICTS project. *Adv. Ecol. Res*. **58**, 201–241 (2018).
165. Carpenter, B. et al. Stan: a probabilistic programming language. *J. Stat. Softw*. **76**, 1–32 (2017).
166. Bürkner, P. C. brms: an R package for Bayesian multilevel models using Stan. *J. Stat. Softw*. **80**, 1–28 (2017).

Acknowledgements All authors were supported by the German Centre of Integrative Biodiversity Research (iDiv) Halle-Jena-Leipzig (funded by the German Research Foundation; FZT 118). The contribution of T.M.K. was also supported by the Helmholtz Association and by the Alexander von Humboldt Foundation. We thank the many authors who supplied the data that went into the core analyses of this paper, and A. Sagouis and M. Liebergesell for help with data acquisition, collation and harmonization. A. Sagouis helped with the preparation of the simulations in Extended Data Fig. 1, and Fig. 1 was created by F. Arndt (Formenorm.de) for the express use in this paper. Finally, we thank R. Colwell and J. Hortal for important comments and criticisms that helped us to improve the manuscript.

Author contributions J.M.C. and T.M.K. conceived the project; J.M.C., K.G. and F.M. developed the initial protocol for data collation and hypothesis tests; J.M.C., F.M. and S.A.B. organized and cleaned the data; F.M. and S.A.B. performed the analyses; J.M.C. wrote the first draft, and all authors contributed to revisions.

Competing interests The authors declare no competing interests.

Additional information

Supplementary information is available for this paper at https://doi.org/10.1038/s41586-020-2531-2.

Correspondence and requests for materials should be addressed to J.M.C.

Peer review information *Nature* thanks Robert Colwell, Joaquin Hortal, James O'Dwyer and the other, anonymous, reviewer(s) for their contribution to the peer review of this work.

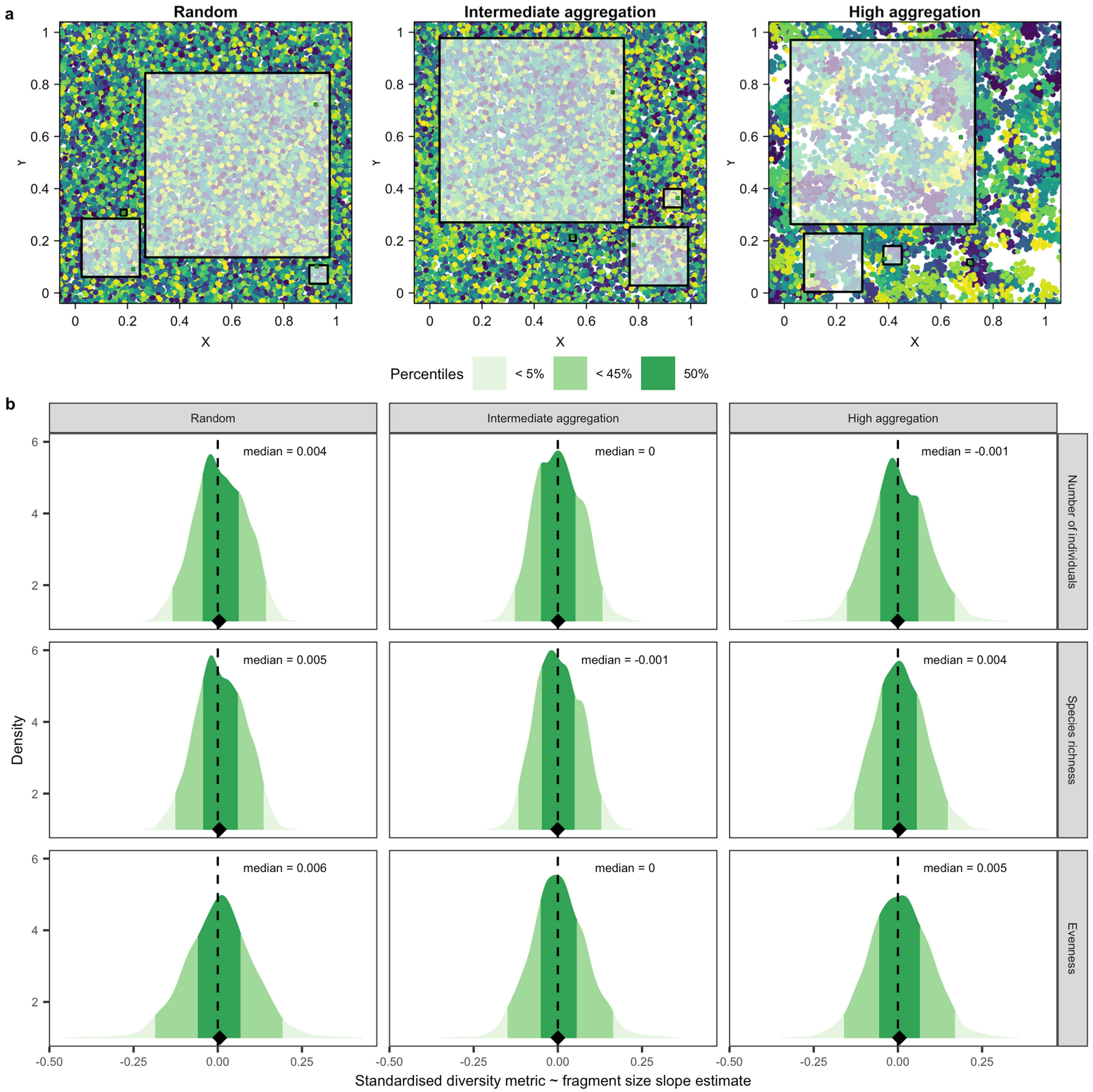

Extended Data Fig. 1 | Simulations of the null expectation under the random sampling hypothesis for varying degrees of within-species aggregation. To evaluate the robustness of the null expectation of a zero slope of biodiversity patterns in standardized samples with fragment size, we took different-sized samples from a simulated landscape and estimated biodiversity patterns. **a**, Examples of landscapes with different levels of intraspecific aggregation (left to right is from completely random to most-aggregated). From within each of these landscapes, we illustrate four different fragment sizes (shaded squares), and then take standardized (constant-sized) samples from each fragment. **b**, Density plots showing slope estimates of linear models fit to numbers of individuals (top), species richness (centre) and evenness (bottom) as a function of fragment areas for 2,000 simulated landscapes of each level of aggregation. Both the response and fragment area were log-transformed before model fitting. Densities are shaded by quantiles and the black diamond shows the median for each combination of aggregation and metric; vertical dashed line shows the zero expectation and the median result is given. In some cases, the median result lies very slightly above or below zero (though this does not seem to be associated with levels of aggregation). This is an outcome of the stochastic simulation we performed, and is sensitive to parameters and numbers of iterations, and thus we do not perform statistical tests.

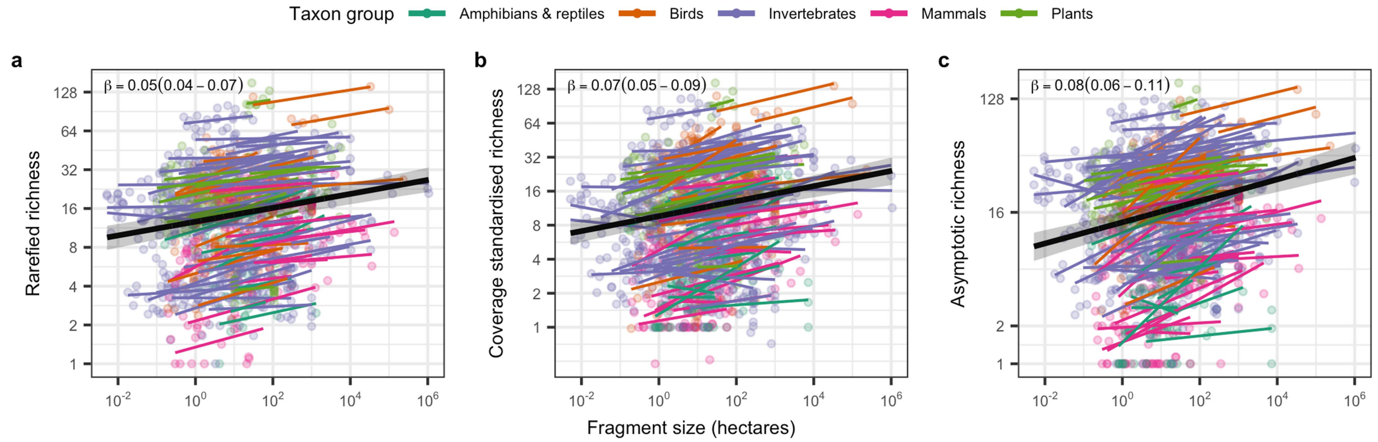

Extended Data Fig. 2 | Different measures of species richness related to the size of habitat fragments. For each case, richness metrics were positively associated with the size of habitat fragments, supporting ecosystem decay as the predominant driver. **a**, Richness standardized to a common number of individuals. **b**, Richness standardized to a common sample completeness. **c**, Asymptotic richness. Solid black lines and shading show overall relationships and 95% credible intervals for each metric. The slope (β) coefficient and its 95% credible interval are shown at the top. Coloured lines show study-level relationships for taxon groups.

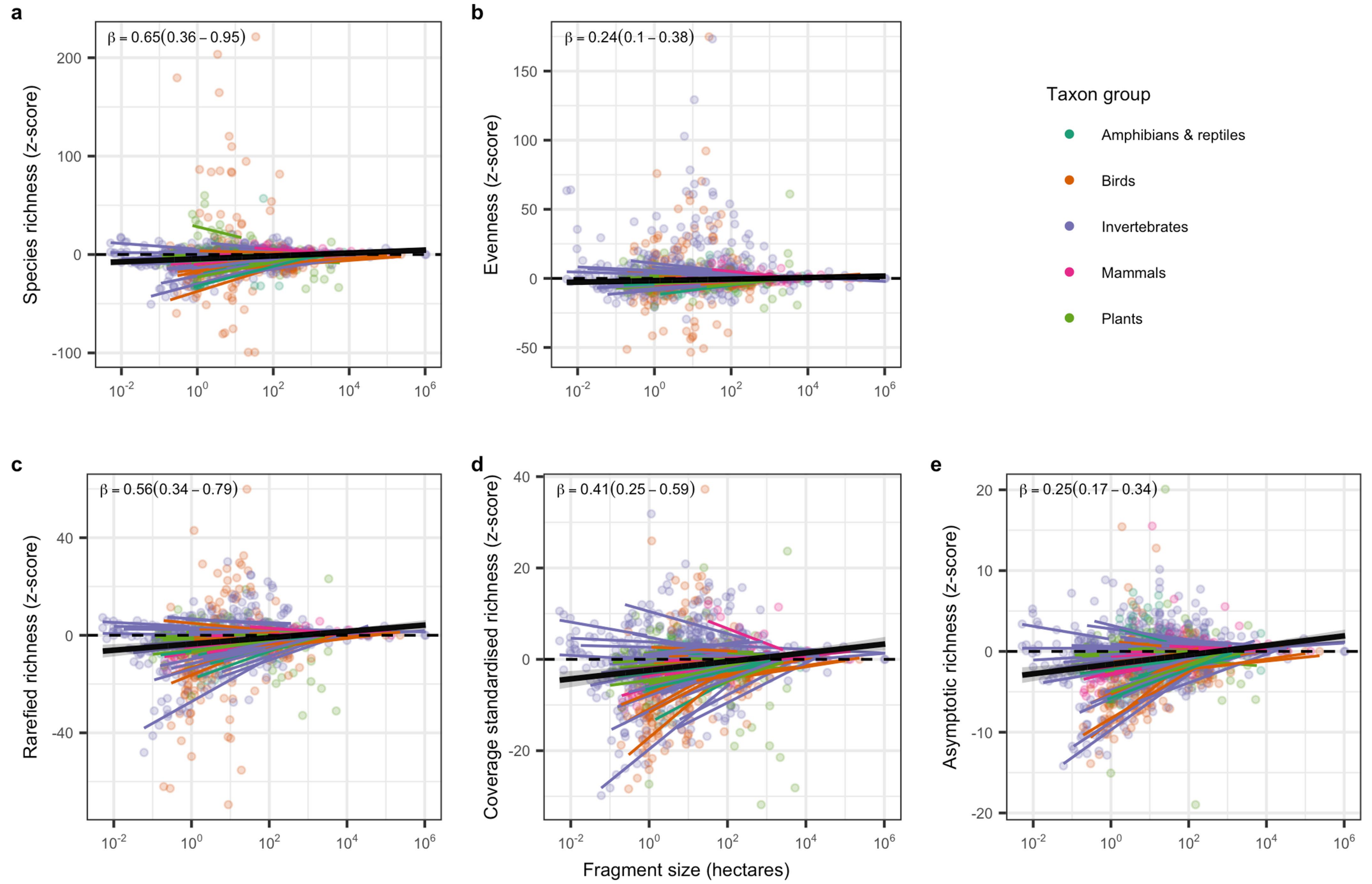

Extended Data Fig. 3 | Incorporation of uncertainty by calculating *z*-scores of observed versus null-expected outcomes. Because there is always uncertainty surrounding the expected outcomes based on passive sampling, we repeated analyses of all metrics recalculated as *z*-scores. After standardization, *z*-scores ((observed − expected)/s.d.(expected)) were calculated for the following. **a**, Standardized species richness. **b**, Standardized evenness (S_{PIE}). **c**, Richness standardized to a common number of individuals. **d**, Richness standardized to a common sample completeness. **e**, Asymptotic richness. As with the direct measurements, analyses of *z*-scores show—in total—greater biodiversity loss than expected from passive sampling in smaller habitat fragments, and thus support the ecosystem decay hypothesis. Solid black lines and shading show overall relationships and 95% credible intervals for each metric. Inset shows β-slope coefficient and its 95% credible interval. Coloured lines show study-level relationships for taxon groups. The *β*-coefficients are not directly comparable to the results from Fig. 2 and Extended Data Fig. 2, owing to differences in the response scale of the *z*-scores.

a

Metric	Fragment size slope estimated without studies with pooled samples	Q2.5	Q97.5
Standardised species richness (S_{std})	0.044	0.024	0.066
Standardised number of individuals (N_{std})	0.034	0.003	0.065
Standardised evenness (S_{PIE})	0.036	0.012	0.061
Richness standardised to a common number of individuals (S_n)	0.049	0.029	0.069
Coverage standardised richness (Scov)	0.043	0.018	0.067
Asymptotic richness (Schao)	0.043	0.021	0.065

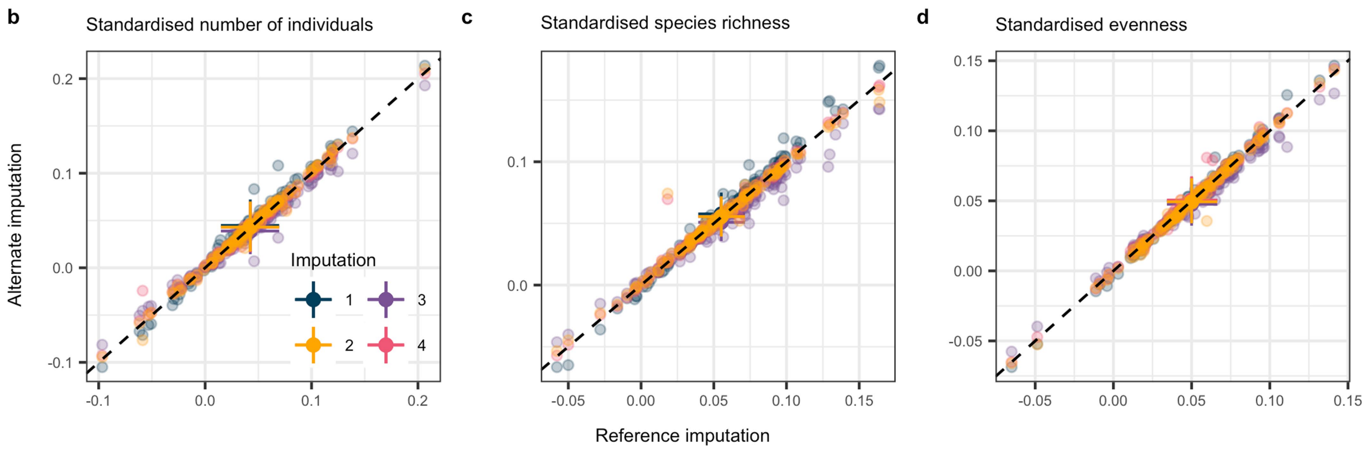

Extended Data Fig. 4 | Testing of robustness of results to alternative methods. a, Testing the sensitivity of our results to the exclusion of 47 studies in which data were pooled, and thus sample extent could not be controlled (Methods). Analyses on this subset of data ($n = 79$) were consistent with those from the full dataset (that is, the 95% credible intervals did not overlap zero). **b**–**d**, Testing the sensitivity of the results to decisions we made when imputing missing sizes of habitats labelled as continuous and the treatment of non-integer species abundances (Methods). In each case, the reference scenario imputed the size of continuous habitats to have 10× the area of the next largest fragment and calculated the biodiversity metrics using the non-integer abundance values. Alternate combinations were: (1) imputed area for continuous habitats assumed to be 2× that of next biggest fragment, and non-integer values unchanged; (2) imputed area for continuous habitats assumed to be 100× that of the next biggest fragment, and non-integer values unchanged; (3) imputed area for continuous habitats assumed to be 10× that of the next biggest fragment, and non-integer values rounded up; (4) imputed area for continuous habitats assumed to be 10× that of the next biggest fragment and all abundance values divided by the lowest value within each study, resulting in the lowest abundance equalling one, but retaining the same relative abundances. **b**, Slope estimates for the relationship between standardized numbers of individuals and fragment size. **c**, Slope estimates for the relationship between standardized species richness and fragment size. **d**, Slope estimates for the relationship between standardized evenness and fragment size. Colours depict different auxiliary decisions and imputation required in the analysis (Methods). Small points represent study-level estimates, and large points and error bars are the overall estimates and their 95% credible intervals.

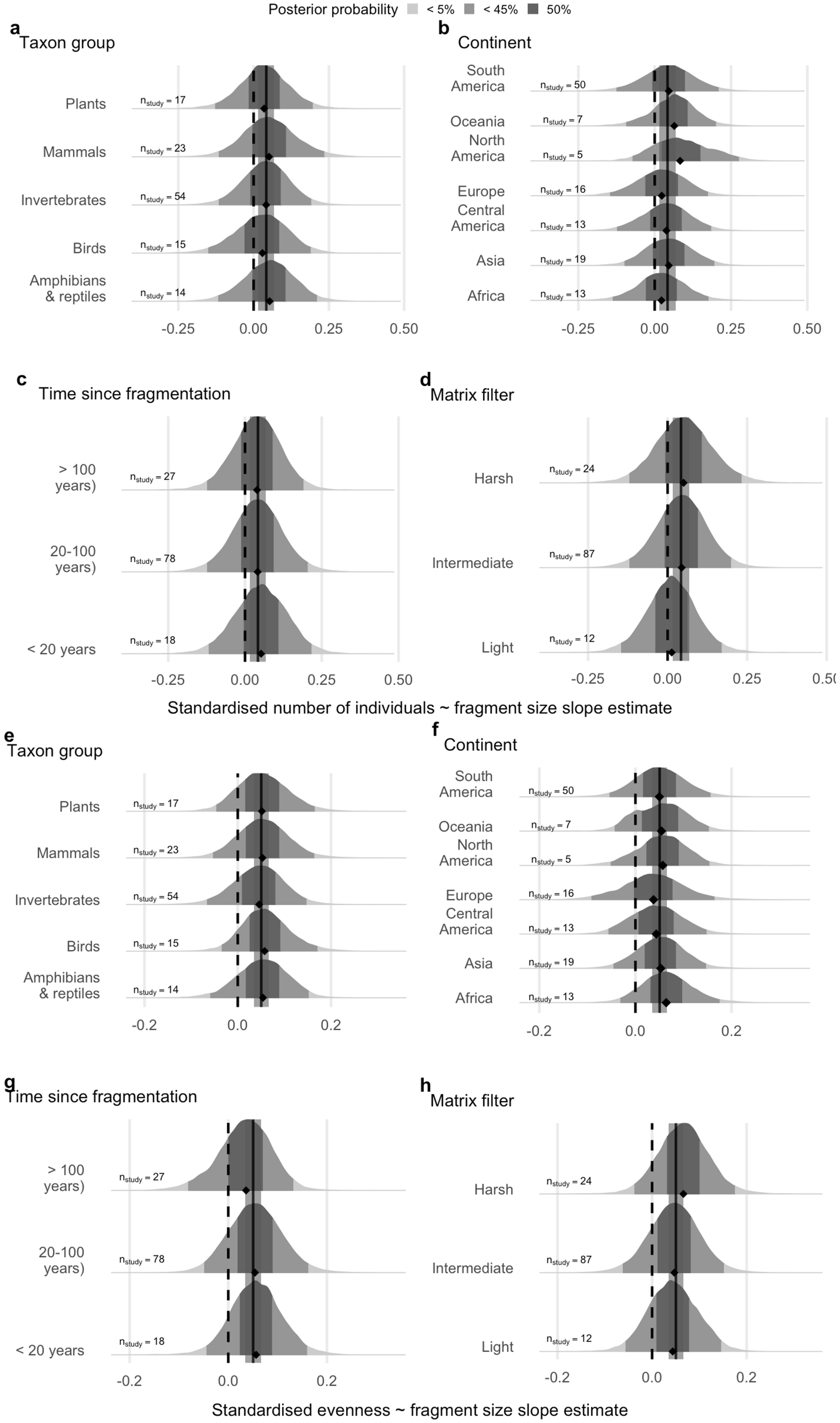

Extended Data Fig. 5 | Study-level variation in the number of individuals and evenness. a–h, Density plots of posterior distributions of study-level slope estimates for total abundance (**a**–**d**) and for evenness (S_{PIE}) (**e**–**h**). Groupings are by taxon group (**a**, **e**), continent (**b**, **f**), time since fragmentation (**c**, **g**) and matrix filter (**d**, **h**). Each density plot is based on 1,000 samples from the posterior distribution of each study-level slope estimate, and is accompanied by the number of studies for each group. Densities are shaded by quantiles and the black diamond shows the median for each group. Solid black line and surrounding shading show the overall slope estimate and its 95% credible interval.

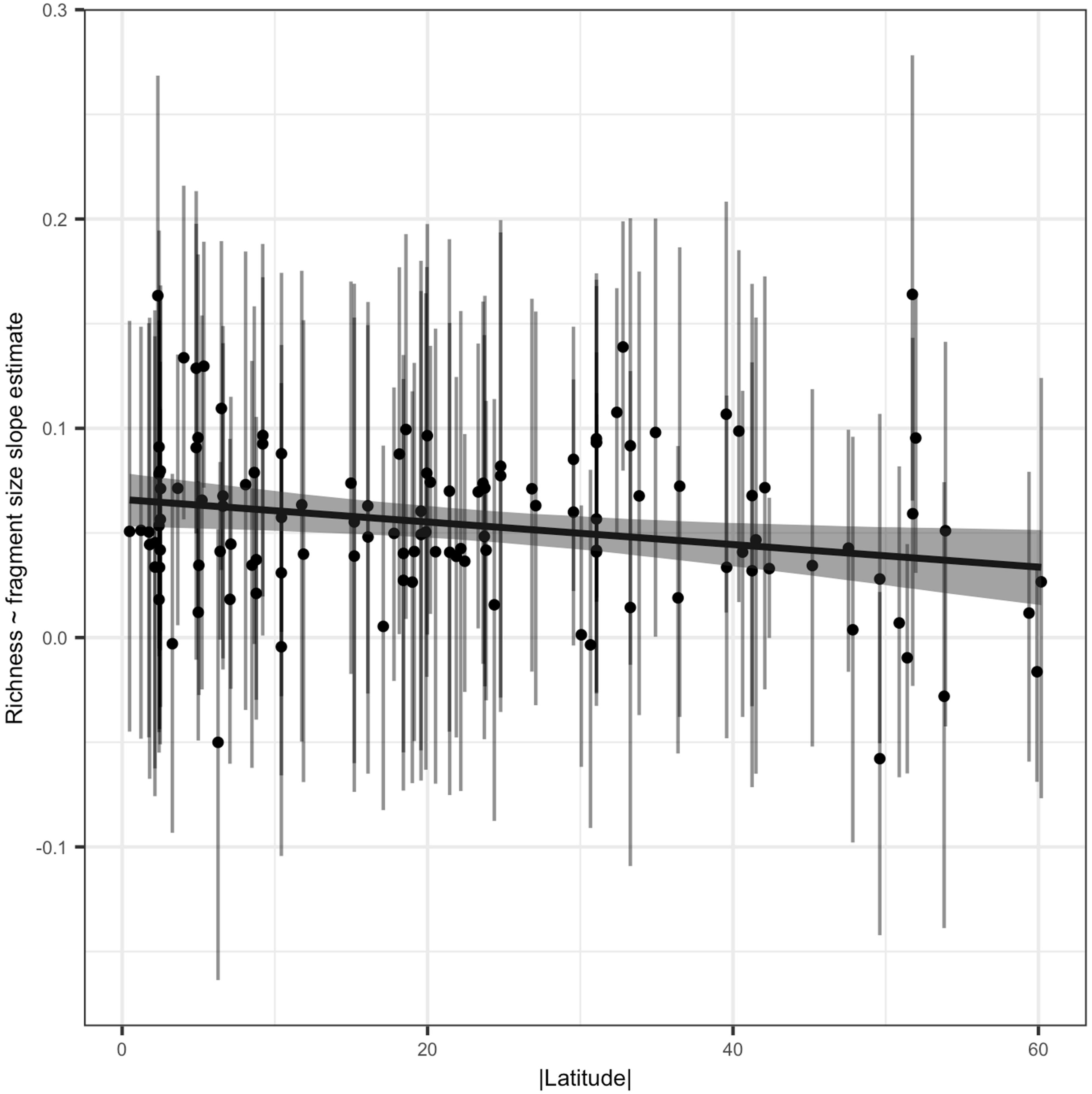

Extended Data Fig. 6 | Study-level slope estimates with latitude. We found that there was a weak negative signal between study-level slope and the absolute value of latitude, which suggests that the influence of ecosystem decay becomes stronger towards the tropics. Each point shows the study-level slope estimate from the standardized species richness as a function of fragment size. Vertical bars are the 95% credible interval associated with each study-level slope estimate. Solid black line and shading shows the relationship and 95% credible interval between the slope estimates and absolute latitude.

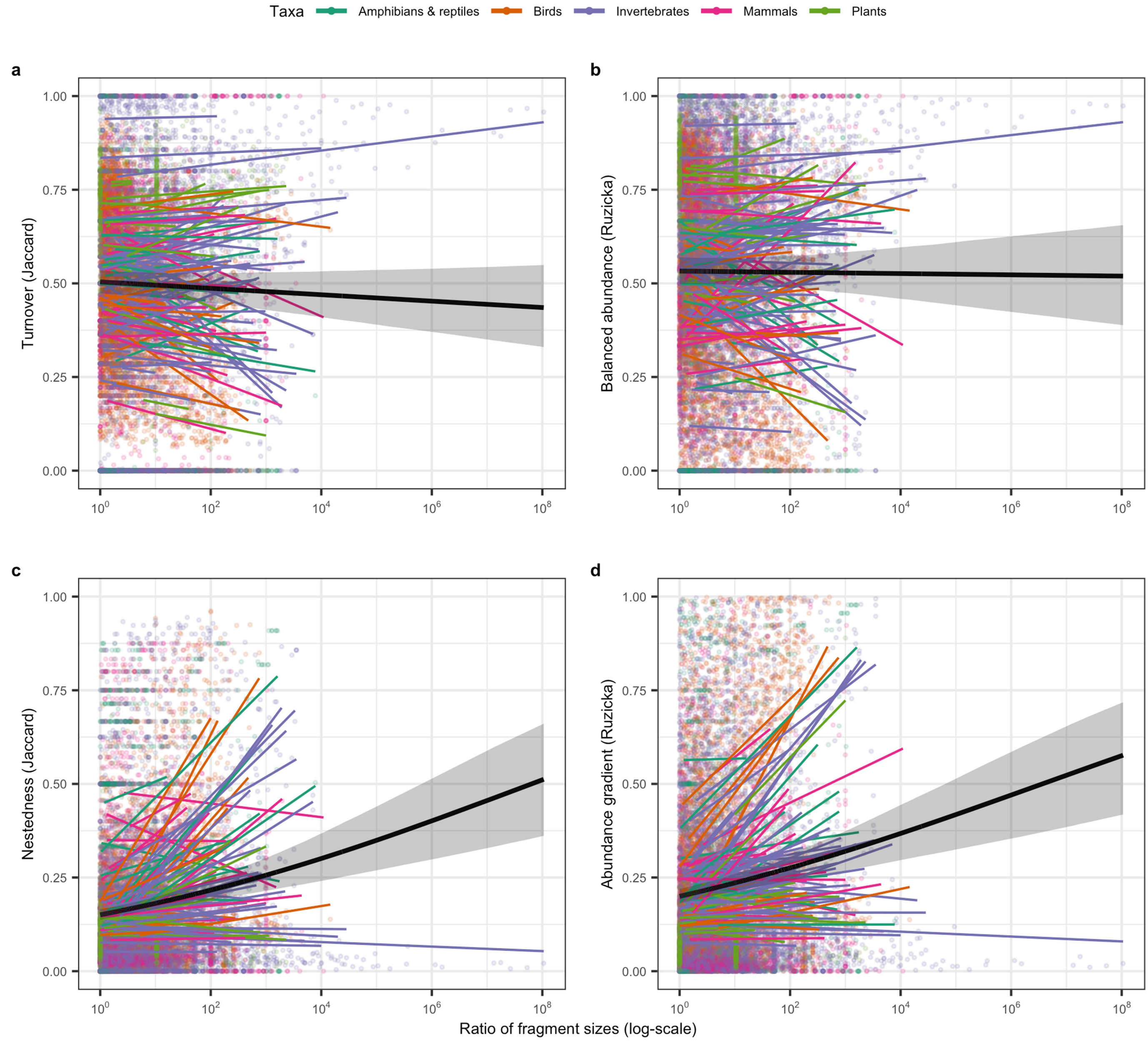

Extended Data Fig. 7 | Relationship between size of habitat fragment and species composition. Overall, we found that turnover contributes more than nestedness to pairwise dissimilarity between fragments within a study, but shows contrasting patterns with increasing fragment size differences. **a**, Turnover component of Jaccard dissimilarity. **b**, Turnover or balanced abundance component of Ruzicka dissimilarity. **c**, Nestedness component of Jaccard dissimilarity. **d**, Nestedness or abundance gradient component of Ruzicka dissimilarity. Solid black lines and shading show overall relationship and 95% credible interval between each dissimilarity component and the ratio of fragment sizes. Coloured lines show study-level relationships for taxon groups.

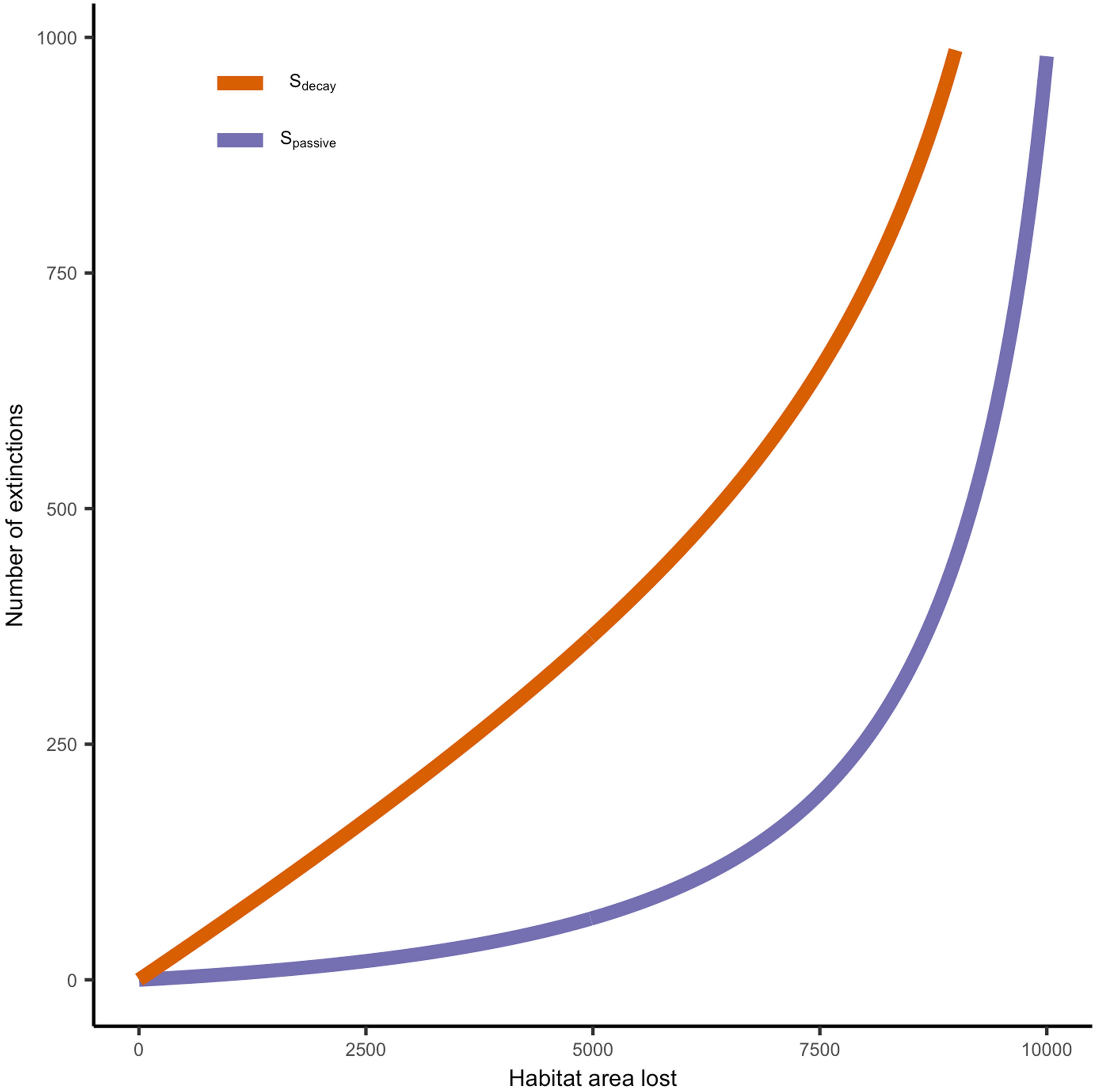

Extended Data Fig. 8 | Endemics–area relationships. Here, we illustrate the number of species expected to be lost as a function of area of habitat lost under the typically assumed passive sampling hypothesis (purple), and the number of species expected to be lost with habitat lost by inputting our observed parameters from the effect of ecosystem decay (orange).

Extended Data Table 1 | Models of standardized species richness (S_{std})

a. Model: taxon x fragment size interaction

Parameter	Estimate	Est.Error	Q2.5	Q97.5
Intercept	1.546	0.231	1.091	1.993
Fragment size (log scale)	0.070	0.025	0.022	0.118
Taxa (birds)	1.374	0.319	0.726	1.983
Taxa (invertebrates)	1.159	0.263	0.648	1.666
Taxa (mammals)	0.152	0.298	-0.428	0.721
Taxa (plants)	1.504	0.320	0.874	2.112
Fragment size:taxa (birds)	-0.015	0.033	-0.077	0.052
Fragment size:taxa (invertebrates)	-0.023	0.027	-0.076	0.029
Fragment size:taxa (mammals)	0.008	0.031	-0.055	0.070
Fragment size:taxa (plants)	-0.014	0.035	-0.081	0.057

b. Model: region x fragment size interaction

Parameter	Estimate	Est.Error	Q2.5	Q97.5
Intercept	2.753	0.283	2.201	3.308
Fragment size (log scale)	0.063	0.026	0.014	0.114
Region (Asia)	-0.182	0.367	-0.933	0.513
Region (Central America)	-0.075	0.405	-0.861	0.732
Region (Europe)	-0.205	0.386	-0.947	0.552
Region (North America)	-1.151	0.523	-2.183	-0.099
Region (Oceania)	-0.202	0.471	-1.139	0.696
Region (South America)	-0.427	0.320	-1.057	0.196
Fragment size:Region (Asia)	0.006	0.031	-0.055	0.069
Fragment size:Region (Central America)	-0.009	0.036	-0.079	0.060
Fragment size:Region (Europe)	-0.056	0.032	-0.118	0.007
Fragment size:Region (North America)	0.042	0.046	-0.048	0.133
Fragment size:Region (Oceania)	0.020	0.041	-0.062	0.098
Fragment size:Region (South America)	-0.007	0.029	-0.064	0.049

c. Model: time since fragmentation x fragment size interaction

Parameter	Estimate	Est.Error	Q2.5	Q97.5
Intercept	2.352	0.244	1.878	2.840
Fragment size (log scale)	0.081	0.023	0.036	0.125
Time since fragmentation (20-100 years)	0.176	0.269	-0.355	0.706
Time since fragmentation (> 100 years)	-0.018	0.311	-0.625	0.618
Fragment size:time since fragmentation (20-100 years)	-0.015	0.025	-0.064	0.034
Fragment size:time since fragmentation (> 100 years)	-0.065	0.028	-0.121	-0.012

d. Model: matrix quality x fragment size interaction

Parameter	Estimate	Est.Error	Q2.5	Q97.5
Intercept	2.731	0.295	2.159	3.304
Fragment size (log scale)	0.000	0.028	-0.055	0.055
Matrix (intermediate)	-0.201	0.316	-0.822	0.422
Matrix (harsh)	-0.622	0.359	-1.300	0.106
Fragment size:Matrix (intermediate)	0.048	0.030	-0.010	0.107
Fragment size:Matrix (harsh)	0.101	0.033	0.038	0.166

a–**d**, Each model includes two-way interactions between fragment size and taxon group (**a**), region (**b**), time since fragmentation (**c**) and matrix quality (**d**). Estimate is the mean of the posterior distribution; est.error is the s.d. of the posterior distribution; and Q2.5 and Q97.5 are the 2.5% and 97.5% (percentiles), respectively, of the posterior distribution.

Extended Data Table 2 | Models of the standardized number of individuals (N_{std})

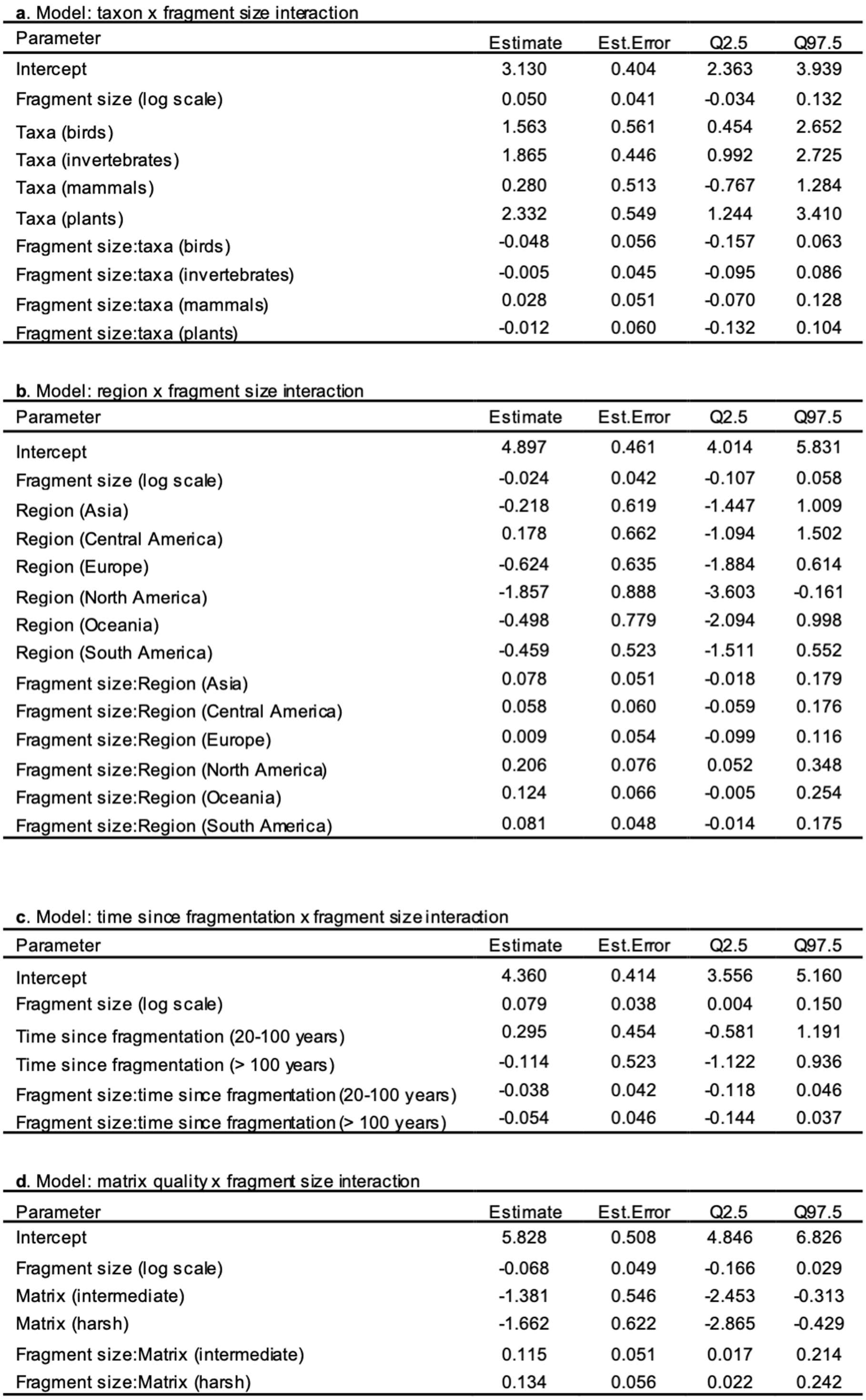

a. Model: taxon x fragment size interaction

Parameter	Estimate	Est.Error	Q2.5	Q97.5
Intercept	3.130	0.404	2.363	3.939
Fragment size (log scale)	0.050	0.041	-0.034	0.132
Taxa (birds)	1.563	0.561	0.454	2.652
Taxa (invertebrates)	1.865	0.446	0.992	2.725
Taxa (mammals)	0.280	0.513	-0.767	1.284
Taxa (plants)	2.332	0.549	1.244	3.410
Fragment size:taxa (birds)	-0.048	0.056	-0.157	0.063
Fragment size:taxa (invertebrates)	-0.005	0.045	-0.095	0.086
Fragment size:taxa (mammals)	0.028	0.051	-0.070	0.128
Fragment size:taxa (plants)	-0.012	0.060	-0.132	0.104

b. Model: region x fragment size interaction

Parameter	Estimate	Est.Error	Q2.5	Q97.5
Intercept	4.897	0.461	4.014	5.831
Fragment size (log scale)	-0.024	0.042	-0.107	0.058
Region (Asia)	-0.218	0.619	-1.447	1.009
Region (Central America)	0.178	0.662	-1.094	1.502
Region (Europe)	-0.624	0.635	-1.884	0.614
Region (North America)	-1.857	0.888	-3.603	-0.161
Region (Oceania)	-0.498	0.779	-2.094	0.998
Region (South America)	-0.459	0.523	-1.511	0.552
Fragment size:Region (Asia)	0.078	0.051	-0.018	0.179
Fragment size:Region (Central America)	0.058	0.060	-0.059	0.176
Fragment size:Region (Europe)	0.009	0.054	-0.099	0.116
Fragment size:Region (North America)	0.206	0.076	0.052	0.348
Fragment size:Region (Oceania)	0.124	0.066	-0.005	0.254
Fragment size:Region (South America)	0.081	0.048	-0.014	0.175

c. Model: time since fragmentation x fragment size interaction

Parameter	Estimate	Est.Error	Q2.5	Q97.5
Intercept	4.360	0.414	3.556	5.160
Fragment size (log scale)	0.079	0.038	0.004	0.150
Time since fragmentation (20-100 years)	0.295	0.454	-0.581	1.191
Time since fragmentation (> 100 years)	-0.114	0.523	-1.122	0.936
Fragment size:time since fragmentation (20-100 years)	-0.038	0.042	-0.118	0.046
Fragment size:time since fragmentation (> 100 years)	-0.054	0.046	-0.144	0.037

d. Model: matrix quality x fragment size interaction

Parameter	Estimate	Est.Error	Q2.5	Q97.5
Intercept	5.828	0.508	4.846	6.826
Fragment size (log scale)	-0.068	0.049	-0.166	0.029
Matrix (intermediate)	-1.381	0.546	-2.453	-0.313
Matrix (harsh)	-1.662	0.622	-2.865	-0.429
Fragment size:Matrix (intermediate)	0.115	0.051	0.017	0.214
Fragment size:Matrix (harsh)	0.134	0.056	0.022	0.242

a–**d**, Each model includes two-way interactions between fragment size and taxon group (**a**), region (**b**), time since fragmentation (**c**) and matrix quality (**d**). Estimate is the mean of the posterior distribution; est.error is the s.d. of the posterior distribution; and Q2.5 and Q97.5 are the 2.5% and 97.5% (percentiles), respectively, of the posterior distribution.

Extended Data Table 3 | Models of standardized evenness (S_{PIE})

a. Model: taxon x fragment size interaction

Parameter	Estimate	Est.Error	Q2.5	Q97.5
Intercept	1.226	0.179	0.874	1.577
Fragment size (log scale)	0.063	0.025	0.013	0.112
Taxa (birds)	1.177	0.250	0.695	1.680
Taxa (invertebrates)	0.607	0.200	0.208	0.997
Taxa (mammals)	0.044	0.227	-0.404	0.484
Taxa (plants)	0.799	0.249	0.317	1.293
Fragment size:taxa (birds)	0.008	0.033	-0.055	0.073
Fragment size:taxa (invertebrates)	-0.030	0.028	-0.084	0.025
Fragment size:taxa (mammals)	0.007	0.032	-0.057	0.071
Fragment size:taxa (plants)	-0.005	0.036	-0.075	0.067

b. Model: region x fragment size interaction

Parameter	Estimate	Est.Error	Q2.5	Q97.5
Intercept	2.056	0.218	1.629	2.487
Fragment size (log scale)	0.090	0.025	0.041	0.140
Region (Asia)	-0.389	0.271	-0.915	0.147
Region (Central America)	-0.252	0.312	-0.881	0.342
Region (Europe)	-0.208	0.290	-0.782	0.373
Region (North America)	-0.501	0.406	-1.297	0.286
Region (Oceania)	-0.075	0.362	-0.786	0.627
Region (South America)	-0.411	0.247	-0.916	0.068
Fragment size:Region (Asia)	-0.035	0.030	-0.094	0.026
Fragment size:Region (Central America)	-0.065	0.037	-0.135	0.009
Fragment size:Region (Europe)	-0.071	0.032	-0.135	-0.009
Fragment size:Region (North America)	-0.025	0.047	-0.119	0.069
Fragment size:Region (Oceania)	-0.036	0.041	-0.112	0.045
Fragment size:Region (South America)	-0.037	0.029	-0.092	0.021

c. Model: time since fragmentation x fragment size interaction

Parameter	Estimate	Est.Error	Q2.5	Q97.5
Intercept	1.736	0.187	1.372	2.105
Fragment size (log scale)	0.073	0.023	0.027	0.118
Time since fragmentation (20-100 years)	0.032	0.207	-0.385	0.430
Time since fragmentation (> 100 years)	-0.042	0.234	-0.483	0.410
Fragment size:time since fragmentation (20-100 years)	-0.010	0.025	-0.059	0.040
Fragment size:time since fragmentation (> 100 years)	-0.065	0.028	-0.121	-0.009

d. Model: matrix quality x fragment size interaction

Parameter	Estimate	Est.Error	Q2.5	Q97.5
Intercept	1.687	0.223	1.260	2.123
Fragment size (log scale)	0.034	0.030	-0.025	0.094
Matrix (intermediate)	0.169	0.235	-0.278	0.619
Matrix (harsh)	-0.228	0.273	-0.772	0.306
Fragment size:Matrix (intermediate)	0.004	0.032	-0.060	0.067
Fragment size:Matrix (harsh)	0.063	0.036	-0.008	0.132

a–**d**, Each model includes two-way interactions between fragment size and taxon group (**a**), region (**b**), time since fragmentation (**c**) and matrix quality (**d**). Estimate is the mean of the posterior distribution; est.error is the s.d. of the posterior distribution; and Q2.5 and Q97.5 are the 2.5% and 97.5% (percentiles), respectively, of the posterior distribution.

nature research

Corresponding author(s): *Double-blind peer review submissions: write DBPR and your manuscript number here instead of author names.*

Last updated by author(s): *YYYY-MM-DD*

Reporting Summary

Nature Research wishes to improve the reproducibility of the work that we publish. This form provides structure for consistency and transparency in reporting. For further information on Nature Research policies, see our Editorial Policies and the Editorial Policy Checklist.

Statistics

For all statistical analyses, confirm that the following items are present in the figure legend, table legend, main text, or Methods section.

n/a	Confirmed	
☐	☒	The exact sample size (*n*) for each experimental group/condition, given as a discrete number and unit of measurement
☐	☒	A statement on whether measurements were taken from distinct samples or whether the same sample was measured repeatedly
☐	☒	The statistical test(s) used AND whether they are one- or two-sided *Only common tests should be described solely by name; describe more complex techniques in the Methods section.*
☐	☒	A description of all covariates tested
☐	☒	A description of any assumptions or corrections, such as tests of normality and adjustment for multiple comparisons
☐	☒	A full description of the statistical parameters including central tendency (e.g. means) or other basic estimates (e.g. regression coefficient) AND variation (e.g. standard deviation) or associated estimates of uncertainty (e.g. confidence intervals)
☐	☒	For null hypothesis testing, the test statistic (e.g. *F*, *t*, *r*) with confidence intervals, effect sizes, degrees of freedom and *P* value noted *Give P values as exact values whenever suitable.*
☐	☒	For Bayesian analysis, information on the choice of priors and Markov chain Monte Carlo settings
☐	☒	For hierarchical and complex designs, identification of the appropriate level for tests and full reporting of outcomes
☐	☒	Estimates of effect sizes (e.g. Cohen's *d*, Pearson's *r*), indicating how they were calculated

Our web collection on statistics for biologists contains articles on many of the points above.

Software and code

Policy information about availability of computer code

Data collection	Data were collected from a literature search presented in Chase et al. 2019 (https://doi.org/10.1002/ecy.2861). For that data publication, we used a number of computational resources in R to scrap, clean and organize data. All code is presented in Chase et al. 2019 as well as in the code deposited for this study at: https://github.com/FelixMay/FragFrame_1 and mirrored at Zenodo https://doi.org/10.5281/zenodo.3862409
Data analysis	All code for analyses are deposited at: https://github.com/FelixMay/FragFrame_1 and mirrored at Zenodo https://doi.org/10.5281/zenodo.3862409

For manuscripts utilizing custom algorithms or software that are central to the research but not yet described in published literature, software must be made available to editors and reviewers. We strongly encourage code deposition in a community repository (e.g. GitHub). See the Nature Research guidelines for submitting code & software for further information.

Data

Policy information about availability of data

All manuscripts must include a data availability statement. This statement should provide the following information, where applicable:

- Accession codes, unique identifiers, or web links for publicly available datasets
- A list of figures that have associated raw data
- A description of any restrictions on data availability

All data were collected from a literature search and are available in Chase et al. 2019 (https://doi.org/10.1002/ecy.2861).

Field-specific reporting

Please select the one below that is the best fit for your research. If you are not sure, read the appropriate sections before making your selection.

☐ Life sciences ☐ Behavioural & social sciences ☒ Ecological, evolutionary & environmental sciences

For a reference copy of the document with all sections, see nature.com/documents/nr-reporting-summary-flat.pdf

Ecological, evolutionary & environmental sciences study design

All studies must disclose on these points even when the disclosure is negative.

Study description	This study compiled data from 123 studies examining habitat fragmentation and its influence on effort-controlled patterns of multivariate biodiversity metrics. It tested the primary hypothesis of passive sampling versus ecosystem decay in driving biodiversity patterns.
Research sample	Each study contained a site x species matrix, together with sampling and site meta-data. That is, for each habitat fragment in each study, we compiled the abundance of each species encountered in a given sample. For many samples, a considerable amount of effort was placed on standardizing effort so that fair comparisons could be made.
Sampling strategy	As this was a meta-analysis, studies differed widely in their sampling methodology. This included counts of trees, sampling quadrats and transects, traps (for flying and crawling organisms, etc). They also differed considerably in the methodology for standardizing (or not standardizing) effort within each study. The key for each study was that we could quantify effort within each fragment and use that to compare sample-effort standardized patterns of diversity across sites.
Data collection	Again, as this was a meta-analysis of more than 100 studies of multiple groups of organisms, many hundreds of people were involved in the data collection. The data compilation, however, was lead by Chase, along with help from co-authors and two technicians in Chase's lab group (Alban Saquois and Mario Liebergesell). All of this is recorded in the data paper developed expressly for this purpose.
Timing and spatial scale	As a meta-analysis, the time period ranged from datasets collected from the 1970s until 2019; most, however, took place between 1990-2019. The spatial scale and sampling effort varied considerably between studies, but in all cases, sampling effort was carefully controlled so that standardization could take place.
Data exclusions	No Data were excluded from the analyses.
Reproducibility	This was a compilation of mostly observation studies. Reproducibility was sometimes done for data collection over multiple years and seasons, but was highly variable among studies. We have provided the raw data and explicit code for how we dealt with data.
Randomization	As these were primarily observation data from natural forest fragments, randomization at the treatment level was not possible. However, for most studies, sampling within fragments was randomized with respect to location.
Blinding	Again, data come from hundreds of studies. In some, blinding was possible, not in most, as the observers would clearly know which treatment they were in when data were collected.

Did the study involve field work? ☐ Yes ☒ No

Reporting for specific materials, systems and methods

We require information from authors about some types of materials, experimental systems and methods used in many studies. Here, indicate whether each material, system or method listed is relevant to your study. If you are not sure if a list item applies to your research, read the appropriate section before selecting a response.

Materials & experimental systems

n/a	Involved in the study
☒	☐ Antibodies
☒	☐ Eukaryotic cell lines
☒	☐ Palaeontology and archaeology
☒	☐ Animals and other organisms
☒	☐ Human research participants
☒	☐ Clinical data
☒	☐ Dual use research of concern

Methods

n/a	Involved in the study
☒	☐ ChIP-seq
☒	☐ Flow cytometry
☒	☐ MRI-based neuroimaging

Index and biological spectrum of human DNase I hypersensitive sites

https://doi.org/10.1038/s41586-020-2559-3

Received: 15 November 2019

Accepted: 1 July 2020

Wouter Meuleman[1]✉, Alexander Muratov[1], Eric Rynes[1], Jessica Halow[1], Kristen Lee[1], Daniel Bates[1], Morgan Diegel[1], Douglas Dunn[1], Fidencio Neri[1], Athanasios Teodosiadis[1], Alex Reynolds[1], Eric Haugen[1], Jemma Nelson[1], Audra Johnson[1], Mark Frerker[1], Michael Buckley[1], Richard Sandstrom[1], Jeff Vierstra[1], Rajinder Kaul[1] & John Stamatoyannopoulos[1,2,3]✉

DNase I hypersensitive sites (DHSs) are generic markers of regulatory DNA[1–5] and contain genetic variations associated with diseases and phenotypic traits[6–8]. We created high-resolution maps of DHSs from 733 human biosamples encompassing 438 cell and tissue types and states, and integrated these to delineate and numerically index approximately 3.6 million DHSs within the human genome sequence, providing a common coordinate system for regulatory DNA. Here we show that these maps highly resolve the *cis*-regulatory compartment of the human genome, which encodes unexpectedly diverse cell- and tissue-selective regulatory programs at very high density. These programs can be captured comprehensively by a simple vocabulary that enables the assignment to each DHS of a regulatory barcode that encapsulates its tissue manifestations, and global annotation of protein-coding and non-coding RNA genes in a manner orthogonal to gene expression. Finally, we show that sharply resolved DHSs markedly enhance the genetic association and heritability signals of diseases and traits. Rather than being confined to a small number of distal elements or promoters, we find that genetic signals converge on congruently regulated sets of DHSs that decorate entire gene bodies. Together, our results create a universal, extensible coordinate system and vocabulary for human regulatory DNA marked by DHSs, and provide a new global perspective on the architecture of human gene regulation.

A fundamental challenge in modern biology is to delineate with the highest possible precision the repertoire of regulatory DNA elements encoded within the human genome sequence. A universal feature of active *cis*-regulatory elements—promoters, enhancers, silencers, chromatin insulators or enhancer blockers, and locus control regions—is focal alteration in chromatin structure triggered by binding of transcription factors (TFs), which supplants a canonical nucleosome and renders the underlying DNA accessible to nucleases and other protein factors[1,9]. For more than 40 years[2,10,11], DHSs have provided reliable signposts for high-precision delineation of regulatory DNA in complex genomes[1–5]. DHSs typically mark compact (less than 250 base pair (bp)) elements, and their appearance over a *cis*-regulatory region signifies its actuation (readying for activation), which may occur before, or coincident with, its functional activation. DHS mapping thus provides a generic tool for illuminating both active and potential regulatory landscapes.

The advent of genome-scale mapping of DHSs[12–15] and its application to diverse human and mouse cell and tissue types[16,17] has yielded many insights into the organization[16], evolution[17–19], activity[15,16,20], and function[16,21,22] of human regulatory DNA in both normal and malignant states[23]. A cardinal property of regulatory DNA is that its accessibility is cell type- and state-selective, with only a small fraction of all genome-encoded elements becoming actuated in a given cellular context[16,23].

The overwhelming majority of disease- and trait-associated variants identified by genome-wide association studies (GWASs) lie in non-coding regions of the genome, and these variants are most strongly enriched in DHSs mapped in disease-relevant cell contexts[6,7]. DHSs also collectively contain the GWAS variants that account for the majority of trait heritability explained by genotyped single-nucleotide polymorphisms (SNPs)[8]. Deeper insights into the connection between GWAS variants and gene regulation have been limited by the lack of comprehensive annotations that capture the biological behaviour of regulatory DNA.

As genome-scale data from diverse cellular contexts have accumulated, systematic annotation of cell type- and state-selective DHSs has grown increasingly challenging, and it has also become evident that large sets of DHSs distributed widely across the genome may share common regulatory programs[16]. However, the annotation and analysis of state-selective behaviours has been hampered by the lack of a common coordinate system for DHSs.

Here we sought to expand the breadth of high-quality DHS maps, and to unify them into a common reference framework that achieves precise genomic annotation by integrating observed biological variability

---

[1]Altius Institute for Biomedical Sciences, Seattle, WA, USA. [2]Department of Genome Sciences, University of Washington, Seattle, WA, USA. [3]Division of Oncology, Department of Medicine, University of Washington, Seattle, WA, USA. ✉e-mail: wouter@meuleman.org; jstam@altius.org

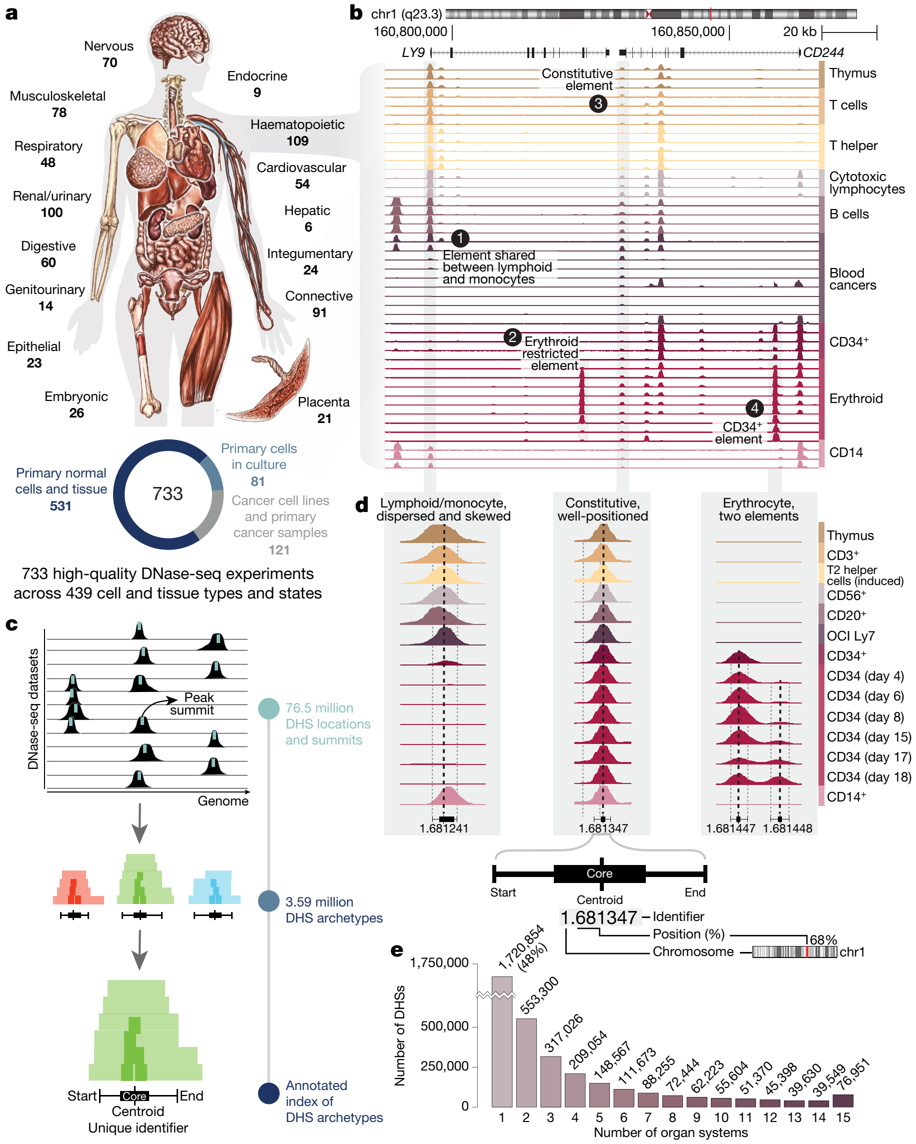

Fig. 1 | Index of DHSs in the human genome. a, DNA accessibility assayed across multiple biosamples (indicated) from the main human organ systems. Of 733 biosamples, 531 were derived from primary cells and tissues. **b**, Example locus on chromosome 1, showing DNase I cleavage density in haematopoietic biosamples (right) with cell type-selective differences. **c**, Outline of DHS index procedure; 76.5 million DHSs aggregated across individual datasets jointly delineate and annotate 3.59 million consensus DHSs. **d**, Examples of consensus DHSs with varying cell-type selectivity and genome positional stability. Annotations include consensus DHS coordinates (start/end), single-base 'centroid', 'core' region aggregating centroids across biosamples, and a unique numerical identifier. **e**, Number of organ systems across which DHSs are shared.

in the manifestation of accessibility at individual elements, and that captures complex cell-selective behaviours in a quantitative fashion. We report a coherent framework and demonstrate its utility for the annotation of human regulatory DNA and gene landscapes; for defining how regulatory programs are encoded within the genome; and for clarifying links between genetic signals and gene regulation to enable new insights into the organization and interpretation of non-coding variation associated with diseases and traits.

Index of consensus human DHSs

To create deeply sampled reference maps of human regulatory DNA marked by DHSs, we performed DNase I hypersensitive site sequencing (DNase-seq)[15] on a wide range of human cell and tissue biosamples that span all major human organ systems (Fig. 1a). Reference-grade data were created by rigorous quality screening for complex libraries yielding high signal-to-noise ratio data (Methods), and were aggregated with prior high-quality data from the ENCODE[16] and Roadmap Epigenomics[24] projects. We conservatively selected 733 biosamples that represent 438 cell or tissue types and states (Fig. 1a, Supplementary Table 1, Methods), the majority of which were derived from primary ex vivo cells and tissues (72% of samples) or from primary cells in culture (11%), with the remainder (17%) from immortalized cell lines. Collectively these samples represent an approximately 5.5-fold expansion of sampled cell and tissue types and states relative to the previous phase of ENCODE[16] (Extended Data Fig. 1a), and the resulting data reveal rich and varied patterns of DNase I hypersensitivity (Fig. 1b).

Common coordinates for regulatory DNA

We sought to create a precise and durable common reference framework for genomic elements that encode DHSs by (i) comprehensively and stringently (0.1% false discovery rate (FDR)) delineating DHSs within each biosample; (ii) integrating individual biosample DHS maps to define archetypal DHS-encoding sequence elements within the human genome sequence; and (iii) assigning to each archetypal element a unique numerical identifier (Fig. 1c).

We identified an average of 104,433 DHSs per biosample, and a total of 76,549,656 DHSs across all 733 biosamples. To delineate archetypal DHS-encoding genomic elements, we developed the consensus approach outlined in Fig. 1c and Extended Data Fig. 1b, c. First, we computed the summit coordinate (1 bp) of each DHS peak and aligned these across all biosamples to define a consensus centroid for each archetypal DHS. To resolve DHS boundaries, we collated the local linear extent of DNase I hypersensitivity into a consensus range (Methods). We then combined centroids and boundaries into a single index of 3,591,898 spatially distinct DHS-encoding sequence elements, greatly eclipsing both the number (approximately 2.5-fold) and precision of DHSs delineated during earlier phases of ENCODE (Extended Data Fig. 1d). In addition to a consensus summit (centroid) and start and end coordinates, each archetypal DHS additionally comprises a 'core' region that represents empirical confidence bounds on the centroid (Fig. 1d, Extended Data Fig. 1e). Each archetypal DHS derives from an average of 21 biosamples, and because each DHS from a given biosample contributes to a single archetypal DHS, the provenance of each DHS in the index can be directly traced back to its contributing biosample(s).

Finally, we assigned a unique identifier to each archetypal index DHS using a numerical schema (Fig. 1d) that (i) conveys the genomic localization of each DHS; (ii) enables unlimited extension to newly discovered elements; (iii) ensures compatibility with future reference genome builds and portability to personal genomes; and (iv) enables direct integration with DNase I footprints[25] or other experimental annotations (Methods). We also assigned confidence scores to all index DHSs that combine signal strength with propensity for repeated observation in independent biosamples (Extended Data Fig. 1f, g).

Index DHSs are broadly distributed across annotated genic and repetitive elements (Extended Data Fig. 2a–e). Fifty-three per cent of DHSs lie within introns, about 3% within non-coding exons and untranslated regions (UTRs), and about 2% are dually encoded within protein-coding exons (Extended Data Fig. 2c). Although DHSs are pronounced at annotated transcription start sites (TSSs), most localize to regions away from TSSs (Extended Data Fig. 2d, e). Fifty-four per cent of index DHSs overlap repetitive elements of all classes and subfamilies (Extended Data Fig. 2b), consistent with previous observations[26], although overlap with DHS cores (41%) and centroids (37%) suggests that a more focused subset of DHSs derives regulatory machinery from repeats.

Proportion of the genome that encodes DHSs

The full extent ot the DHS landscape should define—or at least closely approximate—the canonical *cis*-regulatory compartment of the genome, the size of which has been the subject of considerable debate[27]. The roughly 3.6 million consensus DHSs have an average width of 204 bp (median 196 bp, interquartile range (IQR) 151–240 bp) and collectively span 665.57 Mb (21.55%) of the reference human genome sequence. DHS cores have an average width of 55 bp (median 38 bp) (Extended Data Fig. 2f) and span 197.74 Mb (6.4%) of the genome. DHS centroids also precisely mark the peak in evolutionarily conserved nucleotides within DHSs, and the corresponding trough in the average density of human genetic variants (Extended Data Fig. 2g), which are discontinuously distributed between TF-occupied and unoccupied subsegments of DHSs[25]. Iterative subsampling of the 733 biosamples showed that the addition of any given new biosample would be expected to contribute about 1,676 new DHSs to the index (median 283, range 4–64,054, 95% confidence interval 1,344–2,009) (Extended Data Fig. 2h and Methods). Extrapolating from this, the addition of an additional biosample collection of equivalent size ($n = 733$) would be expected to increase annotated DHS elements by about 27% (Extended Data Fig. 2h). Notably, increasing biosamples should increase the precision of annotation and thus the resolution of some broader elements (such as Extended Data Fig. 1c, second DHS from the right) to two or more distinct archetypal DHSs; however, such elements are in the minority.

Cellular patterning of DNA accessibility

DHSs are extensively shared across both individual biosamples and groups of biosamples from different organ systems (Fig. 1e, Extended Data Fig. 2i). It was previously reported that groups of widely distributed DHSs with closely shared cross-cell-type actuation patterns also shared biological functions such as enhancer activity[16]. Patterns of index DHS actuation across the 733 biosamples (Fig. 2a) were complex, with both highly modular and less coherent structures (Fig. 2b). The majority of DHSs showed complex actuation patterns rather than simple cell-selective behaviour (Fig. 1e, Extended Data Fig. 2i), prompting us to develop a flexible approach for quantifying and annotating these patterns.

In principle, the actuation of any given index DHS across cell states can be summarized by a limited number of biological 'components' combined in a weighted fashion. Orthogonally, the same components can be used to summarize the DHS repertoire of an individual biosample. Because DHS-centric information can inform biosamples and vice versa, a key advantage of this approach is its potential to capture complex behaviours while providing biological interpretability.

A vocabulary for regulatory patterns

To simplify the matrix of 3,591,898 DHSs × 733 biosamples we applied non-negative matrix factorization[28] (NMF) (Extended Data Fig. 3a–d), a technique that was initially used in the field of computer vision for learning parts-based representations of objects and semantic features of text[29]. We represented each DHS by a large enough number of components ($k = 16$) to ensure accuracy—that is, the degree to which the original matrix can be reconstructed from the components—while retaining potential for interpretability via assignment of components to established biological contexts such as known cell lineage relationships, or cell states known to be specified by specific regulatory factors (Fig. 2c, Extended Data Fig. 3e–g, Methods).

To connect components with biological contexts, we identified the biosamples that were most strongly associated with each component, and the distribution of TF recognition sequences within DHSs that was most strongly associated with that component. For all components, the top contributing cell or tissue samples were notably coherent, enabling provisional assignment of a meaningful biological label to most components (Extended Data Fig. 4a–d, Methods). Enrichment of TF recognition sequences within the DHSs that were most strongly associated with each component revealed clear mappings between distinct sets of cell lineage- or state-specifying TFs and specific components (Extended Data Fig. 4e, f, Methods), orthogonal to the biosample-to-component mappings described above. Finally, we combined biosample-to-component mappings and TF-to-component mappings to create a regulatory 'vocabulary' that captures the actuation pattern of a DHS across cell types and states (Fig. 2d, Supplementary Note). Notably, the interpretation of components does not change with further induced model sparsity (Extended Data Fig. 5a–c) or changes in cell type representation (Extended Data Fig. 5d).

Biological annotation of individual DHSs

We next sought to annotate each DHS with a regulatory 'barcode' that captures its tissue manifestations. The cross-biosample actuation pattern of each DHS is captured by linear combinations of NMF components (Fig. 2c, Extended Data Fig. 3a–c), providing a de facto barcode of its biological spectrum (Fig. 2c, e). DHSs that are selective

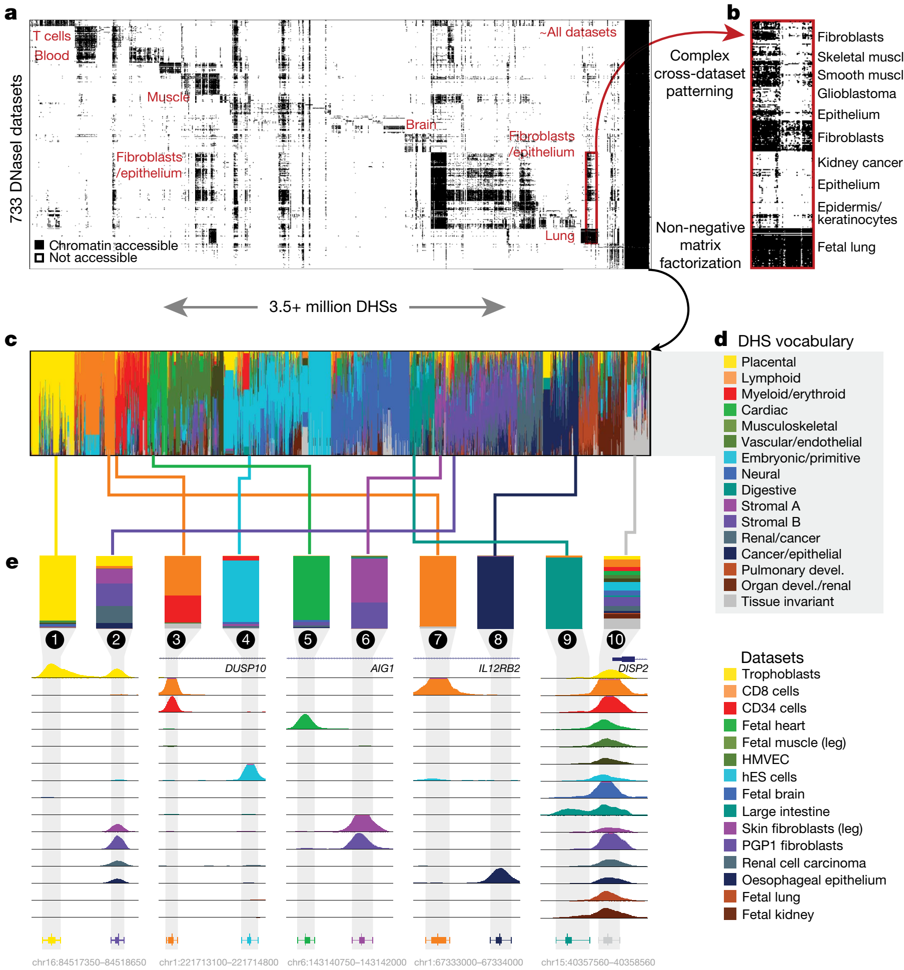

Fig. 2 | A simple vocabulary captures complex patterning of DHSs. a, DNA accessibility at 3.59 million consensus DHSs assayed across 733 biosamples encapsulated in a visually compressed DHS-by-biosample matrix. Recurring accessibility patterns indicate extensive sharing across cell contexts. Dark column (right) shows DHSs detected in (nearly) all datasets. **b**, Modular behaviour of DHS actuation illustrated by thousands of DHSs with similar cross-biosample accessibility patterns. **c**, Decomposition of DHS actuation patterns across 733 biosamples into 16 components using NMF. The cellular patterning of each DHS is described using a mixture of components, indicated by distinct colours. **d**, DHS component labels provide a regulatory vocabulary for DHSs. **e**, Component mixtures for ten example DHSs with varying degrees of component specificity. The biosample dataset most strongly associated with each component is shown. Bottom, annotation of individual DHSs with a single dominant component.

for a single cell type or state are annotated by a single majority component (Fig. 2e, columns 1, 4, 5, 7–9); DHSs that occur in multiple cellular contexts are described by combinations of components (Fig. 2e, columns 2, 3, 6, 10); and constitutive DHSs are annotated by mixtures of all components (Fig. 2e, column 10), including a component that describes tissue-invariant behaviour. In this schema, DHSs with similar cross-biosample actuation patterns exhibit similar mixtures of components. For analytical practicality and visual compactness, the annotation of each DHS can be further summarized using its strongest single component (Fig. 2e, bottom); we use this summary vocabulary for the analyses described below.

Dense encoding of regulatory information

The above results indicate that DHSs have the potential for surprisingly diverse biological regulatory patterns that combine coordinated positive (actuation) and negative (quiescent) behaviours. As the overwhelming majority of DHSs fall into a tight size range that stays roughly constant with increasing numbers of biosamples and does not vary with the complexity of component barcodes (Extended Data Fig. 2f), archetypal DHS elements must therefore encode regulatory information with extremely high linear density.

Regulatory annotation of human genes

The function of many genes is closely connected to their regulated expression across cells and tissues, and hence to the activity spectra of their cognate regulatory elements. We found that DHSs with similar component annotations were highly clustered along the genome (Extended Data Fig. 6a, b, Methods), particularly over gene bodies and their immediate flanking regions (Extended Data Fig. 6c), which collectively capture 65% of all DHSs (Extended Data Fig. 6d–g). We thus reasoned that integration of the components of DHSs overlying a given gene could be used to annotate its likely functional compartment(s). The existence of coordinately regulated DHSs in gene bodies cannot be ascribed to transcriptional activity per se, which produces only very minor changes in the general DNase I sensitivity baseline. Quantification of the enrichment of congruently annotated DHSs around 56,832 GENCODE genes (protein-coding and non-coding) genome-wide revealed 20,658 genes (5% FDR) with significant clustering along the genome of DHSs that belonged to the same component (Fig. 3a–d, Supplementary Table 2). Notably, the gene body-centric approach to annotation captured 70% more genes, and more genes that are likely to be biologically significant, than a TSS-centric approach (Extended Data Fig. 6h, i). Only a subset of gene body DHSs contributed to component

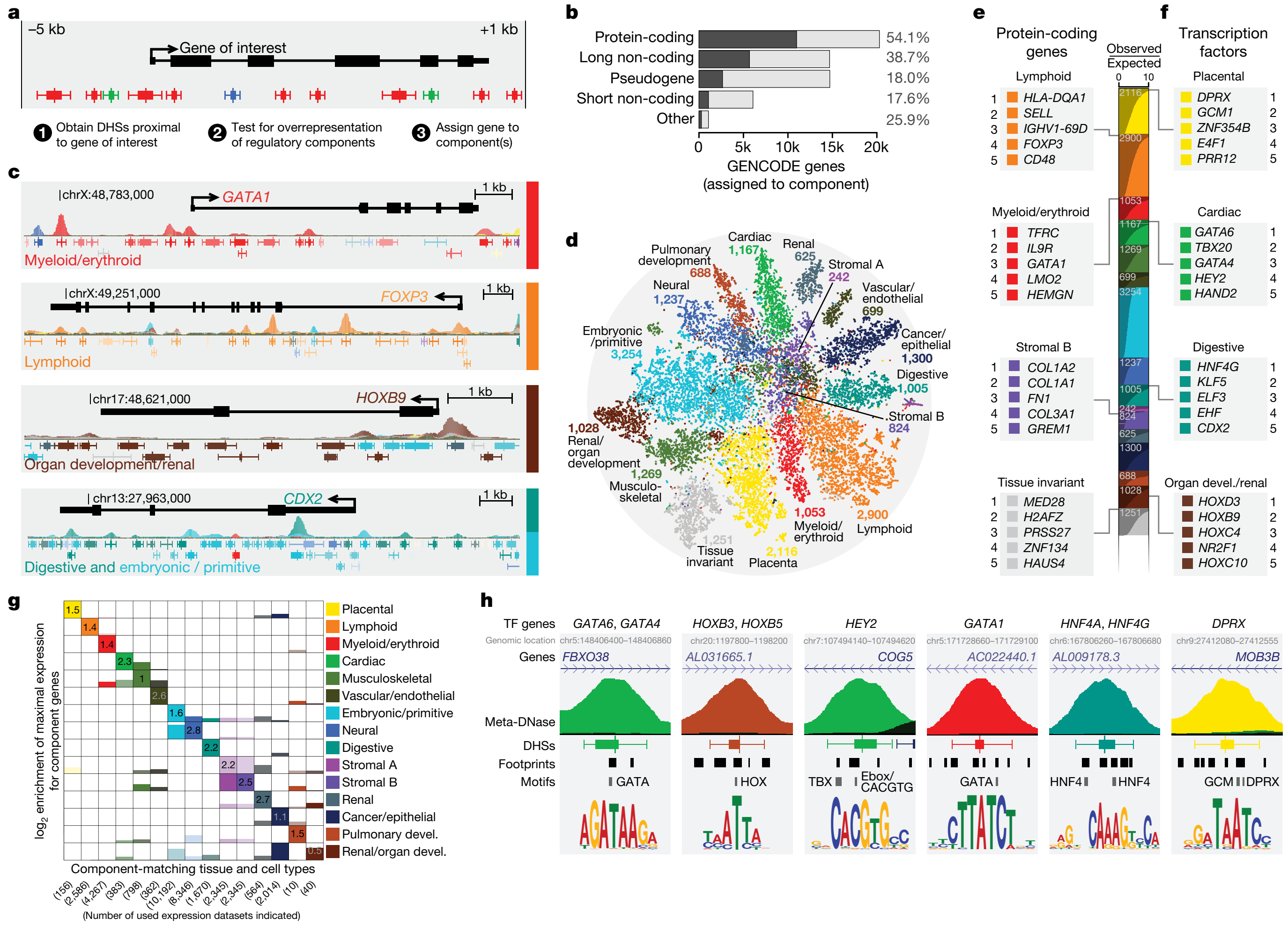

Fig. 3 | Regulatory annotation of human genes. a, Over-representation of DHS components in gene bodies and immediate flanks (maximum 5 kb upstream and 1 kb downstream). **b**, Percentage of genes annotated with DHS components (GENCODE gene categories). **c**, Regulatory annotation of *GATA1*, *FOXP3*, *HOXB9* and *CDX2* genes. **d**, Two-dimensional *t*-distributed stochastic neighbour embedding (*t*-SNE) projection of DHS component enrichment patterns across genes, coloured by dominant significant component (number of genes per component indicated). **e**, **f**, Summarized view of number of genes per component. Top five results for all protein-coding genes (**e**) and TF genes subset (**f**), for selected components. **g**, Correspondence between regulatory annotation and RNA expression shown using relative transcriptional activity across a panel of component-matched tissues and cell types ($\log_2$ observed/expected ratios). **h**, Putative TF-dependent regulatory elements defined by DHSs exclusively sharing regulatory components with genes encoding a given TF that also contain an occupied (footprinted) cognate TF motif.

assignments (median, 38%; IQR, 26–54%), consistent with the fact that many distal regulatory elements localize within the bodies of genes other than the ones that they regulate.

Of 20,291 GENCODE protein-coding genes, more than half (54.1%) could be assigned a regulatory component based on their overlying DHSs (Fig. 3b). To determine whether these assignments were concordant with other functional annotations, we assessed (i) whether the genes most confidently annotated by a given DHS component reflected their known function(s), and (ii) whether genes annotated with a particular component are maximally expressed in cell types that match or are closely related to those components. The top genes annotated by the lymphoid component are all involved in immune response and disease (Fig. 3e, Extended Data Fig. 7a). Similar relationships were observed for other categories of gene (Fig. 3e, Extended Data Fig. 7b–d), including those annotated by the myeloid/erythroid component (erythropoiesis or haematopoietic stem cell genes), a stromal component (collagen genes and fibronectin), and the tissue-invariant component (housekeeping genes). This phenomenon was particularly notable for TF-encoding genes[30] such as lineage-specifying master regulators of cardiac development (cardiac component; Fig. 3f, Extended Data Fig. 7f) or the development of other organ systems (Extended Data Fig. 7e–h).

To explore the concordance between DHS vocabulary annotations and gene expression across cell states, we investigated an independently generated compendium of more than 100,000 uniformly processed RNA sequencing (RNA-seq) datasets[31]. After matching DHS components with tissue-relevant expression datasets (Methods), we found strong correspondence between the vocabulary-based annotation of genes and the cell or tissue types in which they were maximally expressed (Fig. 3g). In many instances, DHS vocabulary annotation and gene expression offered different but complementary views of gene characteristics. For example, the transferrin receptor (TFRC) is responsible for cellular iron uptake and is required for erythropoiesis. *TFRC* RNA is most highly expressed in tissues from the placental component (Extended Data Fig. 7i), where TFRC is known to be involved in trophoblast membranes. From the perspective of regulation, however, *TFRC* is the most strongly associated gene in the myeloid/erythroid component (Fig. 3e, Extended Data Fig. 7b), in line with its core iron transport functionality. Analogously, the gene for HNF4G, a TF that is crucial for liver development, is the most strongly associated gene in the digestive component (Fig. 3e, Extended Data Fig. 7g); however, its RNA is expressed most highly in cells and tissues encompassed under the renal component (Extended Data Fig. 7i). DHS-centric annotations thus provide an orthogonal yet complementary view relative to expression data alone by providing a window into regulation. As DHSs greatly outnumber genes, DHS landscapes are in principle more information-rich than gene expression data alone.

Annotating genes with unknown functions

Despite intensive study, the function of many human genes remains obscure, particularly for those that are expressed at low levels or that have highly cell-selective expression patterns—for example, zinc-finger (ZNF) TFs[30,32] or long non-coding RNA genes[33]. Nearly half of ZNF TFs (43.7%) could be annotated with a DHS component (Extended Data Fig. 8a), indicating their likely biological sphere of activity. Among long non-coding RNA genes, 38.7% could be mapped to DHS components (Extended Data Fig. 8b), as could 18% of pseudogenes[34] (Extended Data Fig. 8c), which might reflect remnants of regulatory states that existed before ancient gene duplications. Beyond genes, we reasoned that entire pathways could be annotated using the DHS landscapes of their constituent genes (Extended Data Fig. 8d). For instance, the Kyoto Encyclopedia of Genes and Genomes (KEGG)[35] pathway 'allograft rejection' (a paradigmatic immune response) is strongly enriched for the lymphoid component (Extended Data Fig. 8e), consistent with the concept that genes involved in similar biological processes should share similar patterns of regulatory element activity.

Connecting DHS actuation to specific TFs

We reasoned that the coalescence of congruently annotated DHSs and genes, plus the availability of high-quality motif databases and newly available DNase I footprinting data[25], could enable the systematic discovery of regulatory regions for which actuation patterns were likely to be driven, at least in part, by particular TFs. We identified 454 TFs with known sequence recognition motifs for which the encoding genes were annotated by a DHS component. We next identified 189,318 DHSs genome-wide (per TF median 149, IQR 47–477 DHSs) that (i) were exclusively annotated by a component matching that of the TF gene, and (ii) showed occupancy of the cognate motif by footprinting[25] in a component-matched biosample (Fig. 3h). Such DHSs are likely to be highly functionally dependent on their associated TF, and should provide a rich substrate for experimental manipulations to investigate connections between TFs and regulatory functions.

Annotating genetic association signals

We next investigated whether DHS annotations could expand insights into the role(s) of genetic variation in regulatory DNA, and thus provide a more meaningful framework for interpreting the pathophysiological basis of disease and trait associations. A rank-based analysis of disease or trait against DHS component associations (explicitly controlling for large scale linkage disequilibrium (LD) structure; Methods) revealed increasingly strong component-specific enrichments of association signals across diverse traits (Fig. 4a, Extended Data Fig. 9a, b). In many cases these enrichments exceeded those obtained by considering only DHSs detected in biosamples most closely related to the relevant DHS component (for example, lymphoid cell biosamples versus lymphoid component; Fig. 4a, Extended Data Figs. 4a, 9c).

Quantifying the extent to which DHS annotations captured SNP-based trait heritability[36] (h_g^2) (Fig. 4b) revealed a strong increase in heritability enrichment for trait-relevant DHS components (Fig. 4b, coloured bars) relative to all index DHSs (Fig. 4b, grey bars) or to a large panel of 85 baseline annotations (Fig. 4b, white bars; top three annotations shown). Heritability was markedly enriched specifically within DHS 'core' regions, providing orthogonal evidence for the delineation and importance of this subcompartment (Fig. 4b).

To generalize these observations, we compiled more than 1,300 traits with SNP-based heritability of at least 1% from the UK Biobank project[37] and from curated published data[38]. Of these, 261 diseases and traits showed highly significant component-specific enrichment in heritability, particularly for pathophysiologically relevant DHS components (Fig. 4c, Extended Data Fig. 9d; 1% FDR). Restricting DHS delineations to 'core' regions again yielded significantly greater enrichment compared to full DHSs (Extended Data Fig. 9e, f).

To remove potentially confounding contributions from multiple genomic annotations that overlap the same SNP (for example, a DHS that overlaps a coding region of a gene annotated with a particular DHS component), we quantified the statistical significance of DHS component heritability contributions while controlling for the contribution of all other annotations (Methods). For virtually all reported traits, DHS component annotations significantly ($P < 0.01$) captured SNP-based trait heritability (Fig. 4d, black line).

We next performed cell type-specific heritability analyses[39] to quantify the concentration of trait-associated genetic signals in DHSs annotated by specific DHS components, relative to the full repertoire of DHSs mapped in disease- or trait-relevant cell types (Methods). Component-annotated DHSs produced significant improvements in capturing trait heritability compared to individual biosample maps ($P < 2.2 \times 10^{-16}$; Fig. 4d, grey solid line). At the level of specific traits, in 68 out of 261 cases (26%), DHS component annotations captured trait heritability better than individual DNase-seq datasets (Fig. 4e). We conclude that the current index of highly resolved consensus DHSs markedly sharpens disease and trait association and heritability signals.

Genetic signals span gene body DHSs

The observed clustering of concordantly regulated DHSs along gene bodies (Fig. 3) led us to speculate that such DHSs were more likely than other DHSs to contain relevant genetic signals. To test this idea, we quantified trait heritability separately for component-concordant DHSs (17% of DHSs) and component-discordant DHSs (34%) within gene bodies (Fig. 4f). Concordant DHSs strongly contributed to SNP-based trait heritability relative to DHSs that were found in the same genes but with component annotations discordant with the annotations of the underlying gene, despite having lower average DNase-seq signal levels (Extended Data Fig. 9g) and more specialized utilization patterns (occurring in an average of 15 versus 25 biosamples). DHSs that were proximal to genes not labelled by any DHS component showed the weakest heritability contributions, and intergenic DHSs contributed only modestly (Fig. 4f, Extended Data Fig. 9h). Rather than being confined to a small number of distal elements or promoters, it thus appears that genetic association signals are concentrated within congruently regulated sets of DHSs that decorate entire gene bodies.

Discussion

Here we have presented the most comprehensive and precise map of human DHSs, and a common coordinate system and vocabulary for regulatory DNA, creating a framework for global analyses of tissue-specific gene regulation and its intersection with human disease trait genetics. Regulation across cell types and states is a cardinal property of DHSs that is now captured in DHS components, greatly expanding the analytical horizon beyond cell type-agnostic annotations such as chromatin states[7,40]. Common reference coordinates should additionally facilitate comparisons between large experimental datasets, and between human and mouse DHSs, which can now be directly linked in a manner that is robust to future mouse assemblies[17].

Given the scale of the data, it is natural to ask how complete and stable our current maps are. New biosamples will add new DHSs and annotate

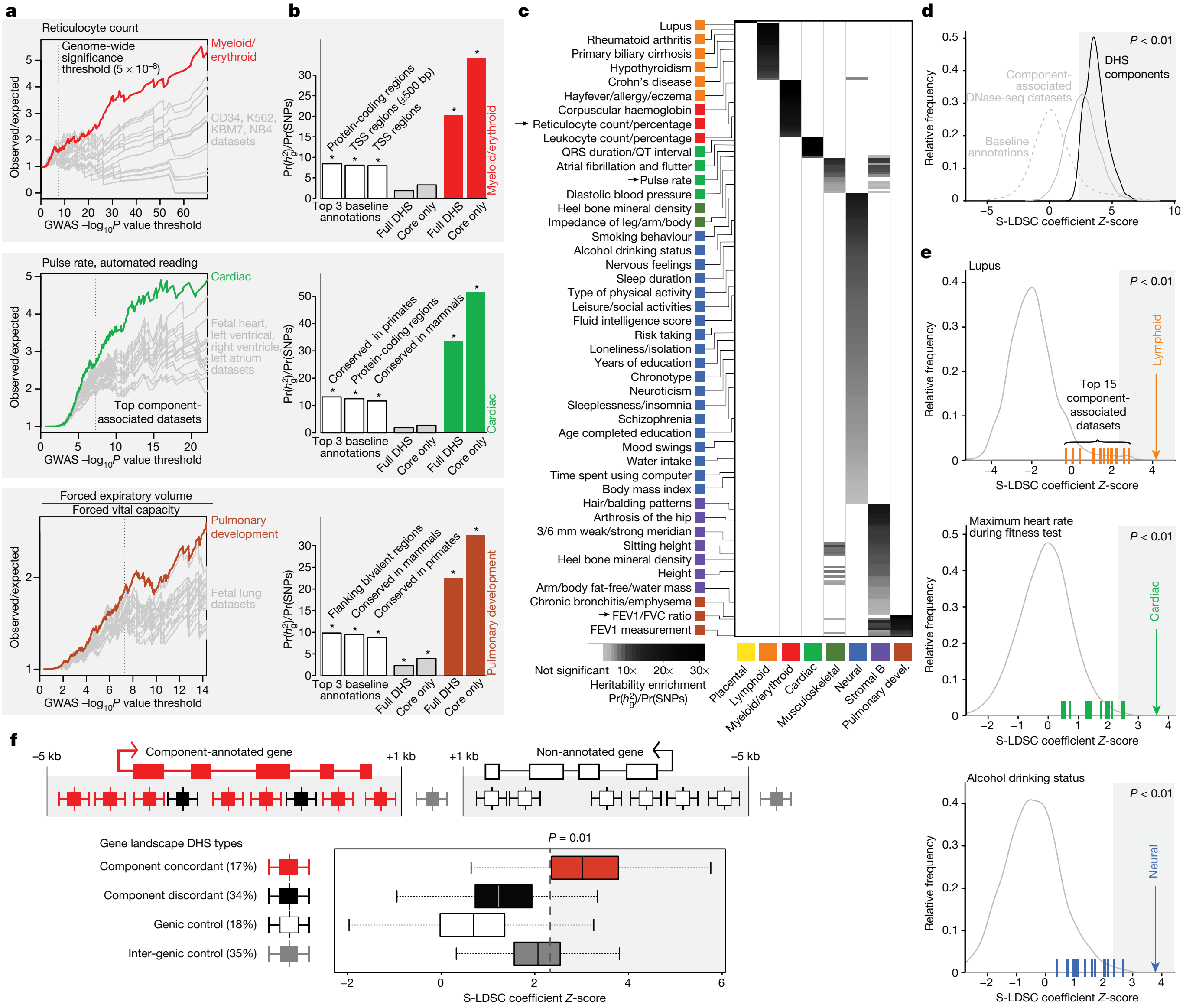

Fig. 4 | DHS components illuminate genetic associations and heritability. **a**, Association of DHSs with GWAS traits by component, shown as enrichment ratios for increasingly stringent subsets of variants (canonical genome-wide significance threshold of 5×10^{-8} indicated). Grey, enrichments for top 15 component-associated biosamples. **b**, Stratified LD-score regression (S-LDSC) for traits shown in **a** associates GWAS variants and DHS components. Heritability enrichment for the top three most enriched baseline annotations (white); the full DHS index (grey); and trait-relevant DHS components (red). *Statistically significant enrichment (one-sided test, 1% FDR). **c**, Enrichment of DHS component (*x*-axis) heritability across 261 GWAS traits (*y*-axis). Greyscale indicates heritability enrichment levels for statistically significant associations (one-sided tests, 1% FDR). Right, sampling of labels of enriched traits for each component. Arrows, traits from **a** and **b**. **d**, Distribution of S-LDSC coefficient *z*-scores across 261 GWAS traits, shown for all baseline annotations (dashed grey line), top 15 DHS component-associated biosamples (solid grey line) and DHS components (black line). **e**, S-LDSC coefficient *z*-scores for selected traits (lupus, $q = 0.002$; maximum heart rate during fitness, $q = 0.016$; alcohol drinking status, $q = 0.009$), shown for all biosamples (grey lines), top 15 component-associated biosamples (coloured ticks) and DHS components (coloured arrows). **f**, Stronger heritability contribution of component-concordant DHSs shown by stratifying S-LDSC *z*-scores by DHS types. Boxes, medians and IQRs (25–75%); whiskers, 1.5 × IQRs; $n = 261$ GWAS traits. Grey areas in **d**–**f** indicate S-LDSC *z*-scores (S-LDSC coefficients, normalized using estimated standard errors) with $P < 0.01$; FDR-corrected *q*-values shown for traits in **e**.

existing elements with ever higher precision. Adding 733 biosamples of equivalent biological breadth would increase the number of consensus DHSs by an average of 27%, with rapidly diminishing returns after that. From the current 21.55% it also is reasonable to predict that no more than 28% of the extant human reference sequence encodes *cis*-regulatory modalities that give rise to DHSs.

It should now be possible to triangulate the genetics-to-gene-regulation interface along three axes: (i) a genomic position axis, which is now finely resolved to consensus DHS summits (centroids); (ii) a cell/tissue-state axis now captured in DHS components; and (iii) a gene context axis that reflects the coherent co-localization of similarly regulated DHSs over gene bodies. The convergence of GWAS variants in coordinately regulated gene body DHSs suggests a fundamental feature of the genetic architecture of disease that has heretofore, to our knowledge, escaped notice. This finding resulted from combining the sharpened disease association and heritability signals enabled by high-precision annotation of regulatory DNA with the new ability to annotate the biological spectrum of each element, neither of which would have been possible without the large advances in biological scale and methodologies reported here. The fact that genetic association and heritability signals are concentrated across congruently regulated sets of DHSs that decorate entire gene bodies has important theoretical and practical implications for understanding both the genetic architecture of disease and the problem of connecting genetic signals with their target genes, which is critical for therapeutic translation.

More broadly, the framework we report represents a transition from an exploratory era focused on the discovery of novel elements, to a map-centric era with a focus on the detection of previously annotated elements within specific biological contexts (Extended Data Fig. 10a). The index framework may also obviate the need for peak calling (Extended Data Fig. 10b–e), and should prove particularly valuable for anchoring single-cell studies[41], which are presently at least 1,000-fold too sparse for robust delineation of regulatory DNA within individual cells.

Online content

Any methods, additional references, Nature Research reporting summaries, source data, extended data, supplementary information, acknowledgements, peer review information; details of author contributions and competing interests; and statements of data and code availability are available at https://doi.org/10.1038/s41586-020-2559-3.

1. Gross, D. S. & Garrard, W. T. Nuclease hypersensitive sites in chromatin. *Annu. Rev. Biochem*. **57**, 159–197 (1988).
2. McGhee, J. D., Wood, W. I., Dolan, M., Engel, J. D. & Felsenfeld, G. A 200 base pair region at the 5′ end of the chicken adult β-globin gene is accessible to nuclease digestion. *Cell* **27**, 45–55 (1981).
3. Mills, F. C., Fisher, L. M., Kuroda, R., Ford, A. M. & Gould, H. J. DNase I hypersensitive sites in the chromatin of human μ immunoglobulin heavy-chain genes. *Nature* **306**, 809–812 (1983).
4. Chung, J. H., Whiteley, M. & Felsenfeld, G. A 5′ element of the chicken β-globin domain serves as an insulator in human erythroid cells and protects against position effect in Drosophila. *Cell* **74**, 505–514 (1993).
5. Li, Q., Peterson, K. R., Fang, X. & Stamatoyannopoulos, G. Locus control regions. *Blood* **100**, 3077–3086 (2002).
6. Maurano, M. T. et al. Systematic localization of common disease-associated variation in regulatory DNA. *Science* **337**, 1190–1195 (2012).
7. Ernst, J. et al. Mapping and analysis of chromatin state dynamics in nine human cell types. *Nature* **473**, 43–49 (2011).
8. Gusev, A. et al. Partitioning heritability of regulatory and cell-type-specific variants across 11 common diseases. *Am. J. Hum. Genet*. **95**, 535–552 (2014).
9. Bell, O., Tiwari, V. K., Thomä, N. H. & Schübeler, D. Determinants and dynamics of genome accessibility. *Nat. Rev. Genet*. **12**, 554–564 (2011).
10. Wu, C. The 5′ ends of *Drosophila* heat shock genes in chromatin are hypersensitive to DNase I. *Nature* **286**, 854–860 (1980).
11. Stalder, J. et al. Tissue-specific DNA cleavages in the globin chromatin domain introduced by DNAase I. *Cell* **20**, 451–460 (1980).
12. Crawford, G. E. et al. Identifying gene regulatory elements by genome-wide recovery of DNase hypersensitive sites. *Proc. Natl Acad. Sci. USA* **101**, 992–997 (2004).
13. Sabo, P. J. et al. Discovery of functional noncoding elements by digital analysis of chromatin structure. *Proc. Natl Acad. Sci. USA* **101**, 16837–16842 (2004).
14. Boyle, A. P. et al. High-resolution mapping and characterization of open chromatin across the genome. *Cell* **132**, 311–322 (2008).
15. John, S. et al. Chromatin accessibility pre-determines glucocorticoid receptor binding patterns. *Nat. Genet*. **43**, 264–268 (2011).
16. Thurman, R. E. et al. The accessible chromatin landscape of the human genome. *Nature* **489**, 75–82 (2012).
17. Vierstra, J. et al. Mouse regulatory DNA landscapes reveal global principles of cis-regulatory evolution. *Science* **346**, 1007–1012 (2014).
18. Stergachis, A. B. et al. Conservation of trans-acting circuitry during mammalian regulatory evolution. *Nature* **515**, 365–370 (2014).
19. Shibata, Y. et al. Extensive evolutionary changes in regulatory element activity during human origins are associated with altered gene expression and positive selection. *PLoS Genet*. **8**, e1002789 (2012).
20. Song, L. et al. Open chromatin defined by DNaseI and FAIRE identifies regulatory elements that shape cell-type identity. *Genome Res*. **21**, 1757–1767 (2011).
21. Vierstra, J. et al. Functional footprinting of regulatory DNA. *Nat. Meth*. **12**, 927–930 (2015).
22. Klann, T. S. et al. CRISPR-Cas9 epigenome editing enables high-throughput screening for functional regulatory elements in the human genome. *Nat. Biotechnol*. **35**, 561–568 (2017).
23. Stergachis, A. B. et al. Developmental fate and cellular maturity encoded in human regulatory DNA landscapes. *Cell* **154**, 888–903 (2013).
24. Roadmap Epigenomics Consortium et al. Integrative analysis of 111 reference human epigenomes. *Nature* **518**, 317–330 (2015).
25. Vierstra, J. et al. Global reference mapping and dynamics of human transcription factor footprints. *Nature* https://doi.org/10.1038/s41586-020-2528-x (2020).
26. Jacques, P.-É., Jeyakani, J. & Bourque, G. The majority of primate-specific regulatory sequences are derived from transposable elements. *PLoS Genet*. **9**, e1003504 (2013).
27. Kellis, M. et al. Defining functional DNA elements in the human genome. *Proc. Natl Acad. Sci. USA* **111**, 6131–6138 (2014).
28. Stein-O'Brien, G. L. et al. Enter the matrix: factorization uncovers knowledge from omics. *Trends Genet*. **34**, 790–805 (2018).
29. Lee, D. D. & Seung, H. S. Learning the parts of objects by non-negative matrix factorization. *Nature* **401**, 788–791 (1999).
30. Lambert, S. A. et al. The human transcription factors. *Cell* **172**, 650–665 (2018).
31. Lachmann, A. et al. Massive mining of publicly available RNA-seq data from human and mouse. *Nat. Commun*. **9**, 1366 (2018).
32. Imbeault, M., Helleboid, P.-Y. & Trono, D. KRAB zinc-finger proteins contribute to the evolution of gene regulatory networks. *Nature* **543**, 550–554 (2017).
33. Mercer, T. R. et al. Targeted RNA sequencing reveals the deep complexity of the human transcriptome. *Nat. Biotechnol*. **30**, 99–104 (2011).
34. Pei, B. et al. The GENCODE pseudogene resource. *Genome Biol*. **13**, R51 (2012).
35. Kanehisa, M. & Goto, S. KEGG: Kyoto encyclopedia of genes and genomes. *Nucleic Acids Res*. **28**, 27–30 (2000).
36. Finucane, H. K. et al. Partitioning heritability by functional annotation using genome-wide association summary statistics. *Nat. Genet*. **47**, 1228–1235 (2015).
37. Bycroft, C. et al. The UK Biobank resource with deep phenotyping and genomic data. *Nature* **562**, 203–209 (2018).
38. Reshef, Y. A. et al. Detecting genome-wide directional effects of transcription factor binding on polygenic disease risk. *Nat. Genet*. **50**, 1483–1493 (2018).
39. Finucane, H. K. et al. Heritability enrichment of specifically expressed genes identifies disease-relevant tissues and cell types. *Nat. Genet*. **50**, 621–629 (2018).
40. Hoffman, M. M. et al. Unsupervised pattern discovery in human chromatin structure through genomic segmentation. *Nat. Methods* **9**, 473–476 (2012).
41. Giansanti, V., Tang, M. & Cittaro, D. Fast analysis of scATAC-seq data using a predefined set of genomic regions. *F1000Res*. **9**, 199 (2020).

Methods

Generation of DNase I hypersensitivity maps

DNase I assays were generally performed according to a protocol detailed previously[42]. This protocol involves treatment of intact nuclei with the small enzyme DNase I which is able to penetrate the nuclear pore and cleave exposed DNA. Small (<1 kb) fragments are isolated from lysed nuclei following DNase I treatment, linkers are added, and the resulting library is sequenced. Because tissue and cell culture, isolation, and handling protocols differ for different biosamples, these are indexed in Supplementary Table 1. Additional information on the procurement of biosample material and DNase-seq biosample selection and data processing is available in the Supplementary Methods.

Index of consensus human DHSs

DHSs were detected in individual biosample datasets and integrated across all 733 datasets to yield a set of 3.59 million consensus DHS delineations. These elements were subsequently annotated with estimates of their centre-of-mass, positional stability across datasets and confidence scores. A detailed explanation of this procedure is provided in the Supplementary Methods.

Overlap of the DHS index with genomic annotations. To assess the overlap of our DHS consensus elements with repetitive elements (Extended Data Fig. 2b), we obtained RepeatMasker[43] annotations downloaded from the University of California Santa Cruz (UCSC) Table Browser[44], and considered the various repeat classes and (sub) families as provided. To perform analogous analyses for human gene annotations (Extended Data Fig. 2c), we obtained GENCODE[45] v.28 Basic annotations. We defined exons as specified in the GENCODE annotation, promoters as the TSS of genes ±1 kb, and introns as the rest of the gene body. Intergenic regions were defined as those not covered by gene bodies or defined promoters. We assigned index DHSs to these annotations requiring at least a 1 bp overlap, choosing the annotation with the largest overlap in case of multiple overlapping annotations.

TOPMed within-human sequence variation data were obtained from the Bravo website (https://bravo.sph.umich.edu/freeze5/hg38/download, Freeze 5, hg38, VCF format). We converted 495.6 million single-base substitutions to nucleotide diversity scores (π), with a score of zero implied for every genomic base position with no variants. Per base, phyloP[46] sequence conservation scores were downloaded as-is (http://hgdownload.cse.ucsc.edu/goldenpath/hg38/phyloP100way/). Within-human sequence variation data ($\pi \times 10^4$) and phyloP conservation scores were aligned relative to DHS centroids using 20-bp non-overlapping windows tiled across a 1-kb region centred on each centroid (Extended Data Fig. 2g). For each window offset relative to the DHS centroid, genome-wide per-base scores were subsetted using bedops[47] and averaged with GNU datamash.

Saturation and extendability of DHS index. For random subsamples of sizes ranging from 1 to 733 biosamples, we estimated the mean number of novel DHSs added by a new dataset as a function of total number of datasets sampled (Extended Data Fig. 2h). To extrapolate these estimates to future biosample sets, we fitted a log-log model to the data. From the saturation analysis, we expect the overwhelming majority of DHSs identified in any new dataset to be represented already in the index, to which they will contribute additional confidence and precision. Incremental datasets can be added to the index by re-delineating DHSs using the original per-dataset DHS calls permanently recorded at the ENCODE DCC (Supplementary Table 1).

Construction of a DHS vocabulary

We used NMF[28,29] for the decomposition of a binary matrix consisting of the presence or absence calls of m DHSs across n DNase-seq datasets into a smaller set of k components. As with other dimensionality reduction methods, NMF does not guarantee a total recapitulation of the original data; instead we chose to allow information loss in exchange for a more interpretable result. Therefore, we considered using a much smaller number of k components than the lower of the two dimensions of our input matrix (733 DNase-seq datasets). To keep the reconstruction error in check, we used an objective function that is minimized subject to the Frobenius norm (Extended Data Fig. 3a). NMF typically uses a random initialization step, leading to unstable results. To alleviate this, we performed the initialization step using singular value decomposition (SVD)[48,49], leading to consistent results while maintaining a performance that is on par with randomly initialized instances. A more detailed rationale for the component-wise description of DHSs, as well as details on the implementation and execution of the decomposition, is provided in the Supplementary Methods.

Labelling of NMF components and DHSs. To aid interpretation of the 16 NMF-derived components, we used two orthogonal approaches to assign labels to components, based on (i) biosample properties and (ii) DHS sequence features.

First, for each component we selected the top biosamples based on component-specific NMF loadings present in their datasets (Extended Data Fig. 4a). These maximal NMF loadings across datasets were generally strong across components (Extended Data Fig. 4b). In general, a clear pattern emerged of shared properties of biosamples most strongly associated with specific components. To formalize this, we performed one-sided Mann–Whitney *U* tests to assess whether NMF loadings for biosamples sharing certain metadata categories (Supplementary Table 1) are greater than those for biosamples not in the given metadata category (Extended Data Fig. 4c). In particular, we assessed metadata categories corresponding to human organ systems and the cancer status of biosamples. *P* values were corrected for multiple hypothesis testing using the Bonferroni correction method. A post hoc analysis of biosample-to-component assignment for values of $k <$ 16 provided insight into the genesis of our $k = 16$ component model, showing junctures after which separate cell type lineages are captured by distinct components (Extended Data Fig. 4d).

Second, for each component we obtained DHSs with maximal NMF loadings for that component, and subsequently performed enrichment analyses for TF binding site motifs (Extended Data Fig. 4e). We used a wide array of TF motifs and used FIMO[50] (match threshold $P < 10^{-5}$), to search for motif instances in the human genome. We tested the association of motif occurrences with specific NMF components using Fisher's exact test. We used clusters of similar motifs (http://www.mauranolab.org/CATO/weblogos/main.html) for the purpose of summarization and visualization. The results show strong enrichments for component-specific motifs, suggesting preferential binding of component-relevant transcription factors (Extended Data Fig. 4f).

The strong associations of 1) biosample properties and 2) TF binding site occurrences with specific components enabled us to label each NMF component, resulting in a DHS vocabulary (Fig. 2d), further detailed in the Supplementary Note. For downstream analyses, we labelled each DHS with its strongest NMF component (Fig. 2e, bottom).

Robustness of component interpretation. To test the effect of inducing additional sparsity in the NMF model, we systematically increased the L1 penalization setting while tracking F1 scores and the fraction of non-zero parameters used in the model (Extended Data Fig. 5a–c). The top 15 component-contributing biosamples per component remain mostly consistent with Fig. 2e and Extended Data Fig. 4a without L1 penalization, indicating that enforcing additional sparsity does not impact the interpretation of model components.

To test the effect of possible over/under-representation of certain cell types, we removed 44 (40%) haematopoietic biosamples, consisting of the highest quality datasets representative of unique cellular conditions (Supplementary Table 1). After building a new NMF model, we observe that although the remaining (lower quality) haematopoietic biosamples are now captured by a single component instead of two, the interpretation of the remaining non-haematopoietic components does not change (Extended Data Fig. 5d).

Regulatory annotation of human genes

Per-component genomic distribution of DHSs. We compared the average distance between same-component DHSs against empirical distributions based on random assignment of component labels to DHSs and sampling the same number of DHSs 1,000 times (Extended Data Fig. 6a).

Per-component meta-DNase tracks. To illustrate the regional diversity of DHS component data, we generated meta-DNase tracks representing each of the 16 DHS components (Extended Data Fig. 6b) by averaging genome-wide DNase-seq signal profiles of the top 15 biosamples most strongly associated with each component (Extended Data Fig. 4a). For visual conciseness, we provide aggregate tracks that overlay the meta-DNase tracks of all DHS components (for example, Fig. 3c, Extended Data Figs. 6b, c, 7a–h, 8a–c).

Definition of regulatory landscapes. We defined the regulatory landscape of a gene as the set of DHSs within the gene body, plus DHSs in flanking regions of maximally 5 kb upstream and maximally 1 kb downstream of the gene body, or up until halfway through to the gene upstream, whichever value is smaller (Fig. 3a, Extended Data Fig. 6e–g). This captures approximately 65% of all DHSs (Extended Data Fig. 6d) and prevents flanking region DHSs from being routinely assigned to the regulatory landscapes of multiple genes, alleviating mixing of regulatory signals.

Association of genes with DHS components. We tested the association of all 56,832 annotated GENCODE genes (Fig. 3b) with each DHS component separately. Under the null hypothesis that DHS components are randomly distributed across gene regulatory landscapes, we used the binomial distribution to test whether the proportion of DHSs annotated with a given component is higher among DHSs within a particular gene regulatory landscape than outside. We controlled the FDR at 5% by calculating *q* values[51] across the total of all genes and components. Further details are provided in the Supplementary Methods. To study the differences between a gene-centric and TSS-centric approach, we calculated component associations for 10-kb regions centred around the TSS (that is, TSS ± 5 kb) and assessed the number and type of genes annotated (Extended Data Fig. 6h, i).

Annotations for GENCODE genes and pseudo-gene types. GENCODE v.28 (Basic) annotations were used for all analyses. For the purpose of labelling and visualizing genes, for each gene we used its longest transcript as its representative region. Pseudo-gene annotations were obtained from psiCube[52], http://pseudogene.org/psicube/data/gencode.v10.pgene.parents.txt.

Visualization of gene regulatory annotations. We used *t*-SNE to visualize the enrichment ratios of gene regulatory landscapes for DHS components (Fig. 3d, Extended Data Fig. 8a–c). Each dot shown represents a gene found to be significantly associated with one or more DHS components, and the union of these are the genes used to calculate the 2D embedding. The R (http://www.r-project.org) implementation as provided in the Rtsne package was used, with default parameters. Genes are coloured according to their (most strongly enriched) significant DHS component.

Construction and use of gene expression compendium dataset. We used the full human ARCHS4 dataset (downloaded 26 June 2018)[31] and selected relevant tissue and cell types for each DHS vocabulary component (Supplementary Methods). This resulted in a total of 33,733 unique gene expression datasets, with expression information for 35,238 genes. For each gene, we obtained the 95th percentile value across datasets selected for each DHS component as the representative value in that component, to not be led by outliers in the data, while still being sensitive for cell type selective expression levels. For each DHS component, we calculated average expression levels across genes labelled with that component (observed), as well as across all component-labelled genes (expected). Resulting values are reported as $\log_2$-transformed enrichment ratios (Fig. 3g).

Annotation and visualization of pathway labellings. A curated set of canonical pathways was obtained from the MSigDB Collections (http://software.broadinstitute.org/gsea/msigdb/genesets.jsp?collection=CP). Pathway enrichment analyses (Extended Data Fig. 8d, e) were performed analogously to gene enrichment analyses, by pooling DHSs in neighbourhoods of all pathway-associated genes. We used the KEGG[35] REST API (https://www.kegg.jp/kegg/rest/keggapi.html) to download and graphically annotate KEGG pathway representations.

Prioritization of TF-associated DHSs. We obtained DHSs with loadings for a single component only. For each component-labelled TF gene with a known sequence binding motif, we obtained the subset of DHSs that (i) are annotated with the same component as the TF, (ii) contain a TF-matching motif, and (iii) are footprinted in a biosample associated with the same component[25] (Fig. 3h). Although the above analysis identified a small minority of DHSs owing to stringent filtering, motifs with variable information content, and the smaller range of biosamples for which footprinting data are available, this approach could be recapitulated with less extreme parameters to identify larger sets of DHSs at reasonable confidence.

Genetic variation analyses

GWAS traits and summary statistics. We obtained GWAS summary statistics data from the UK Biobank project as processed by the Neale lab (http://www.nealelab.is/uk-biobank/). In addition, we obtained GWAS summary statistics calculated using BOLT-LMM v2.3[53], as used in recent work[38].

Estimates of SNP-based heritability. GWAS traits were curated by removing those with a narrow-sense SNP-based heritability[54] (h_g^2) of less than 1%. Although ideally we would quantify heritability by considering the true causal effects of variants, in reality we do not observe these. Instead, we are limited to GWAS summary statistics, which essentially describe the marginal trait-correlation for each variant, consisting of both causal effects and effects due to LD, plus statistical noise. Recently proposed methods such as LD score regression (LDSC)[55] are able to estimate heritability while explicitly considering the underlying LD structure. For continuous traits, in case both raw and inverse-ranked normalized (irnt) versions were available, we retained the latter only. This yielded a total of 1,316 traits for subsequent analyses with an h_g^2 of at least 1%.

Quantitative trait associations. For quantitative trait-versus-component analyses (Fig. 4a, Extended Data Fig. 9a–c), we assessed the correspondence between trait association strength (GWAS variant association *P* value) and the component annotations of variant-containing DHSs, for increasingly stringent subsets of GWAS variants. Enrichment *P* values were calculated using a binomial distribution, as done previously[6]. We explicitly control for large scale LD structure, using a form of LD clumping[56], by selecting a single variant-containing DHS for each of 1,708 approximately independent LD blocks[57]. Namely, for each LD block, the variant with the lowest GWAS association *P* value that overlaps a DHS was selected for subsequent analysis. In case multiple such variant-containing DHSs existed, we gave preference to the DHS with the highest confidence score (mean signal) in our DHS index.

Stratified LD-score regression. To estimate h_g^2 with maximal statistical power, we used LD score regression (LDSC)[55] to explicitly take into account LD structure. In particular, we used a stratified version of LDSC (S-LDSC)[36] to partition heritability estimates according to pre-defined sets of genome-wide annotations (Fig. 4b, c, Extended Data Fig. 9d, e), consisting of our annotated DHSs in addition to a wide range of 85 genome-wide functional 'baseline' annotations (baseline-LD model v.2.1). The v.2.1 baseline set consists of a total of 86 genome-wide annotations, building upon the 76 annotations used in the v.2.0 set and several additional annotations[58]. These 'baseline' annotations encode whether SNPs fall inside protein-coding or non-coding regions, regions with increased levels of evolutionary conservation, regions predicted or confirmed to have enhancer activity, and so on. Their breadth provides a robust[36] baseline model along which to test trait heritability contributions of our DHS components. We express the heritability enrichment of an annotation as the ratio of its proportion of per-trait h_g^2 and the proportion of SNPs covered by the annotation (Fig. 4b).

Variants included in the analysis are those registered in HapMap3, with a minimal minor allele frequency (MAF) of 5%, and excluding the human major histocompatibility complex (MHC) locus. Baseline LD scores were computed from 1000 Genomes Phase 3 data from European ancestry populations and corresponding allele frequencies (as used previously[58] and available from the LDSC reference downloads page, along with the baselineLD annotation set: https://data.broadinstitute.org/alkesgroup/LDSCORE/).

Heritability enrichments for DHS vocabulary components. We applied S-LDSC to our DHS vocabulary components as follows. In brief, each DHS was assigned to its majority DHS component and (when possible) assigned to overlapping variants. For the resulting vocabulary-based annotations, LD scores were calculated. We then performed S-LDSC separately for each of the selected 1,316 traits, relative to these vocabulary-based annotations and the baselineLD model described above. For each trait versus annotation combination, we obtained estimates of its heritability enrichment[36], expressed as the ratio of its proportion of h_g^2 and the proportion of SNPs covered by the annotation (Fig. 4b, c). We considered heritability enrichments statistically significant at an estimated FDR of less than 5% calculated across all considered traits and DHS components. This is more stringent than the commonly used per-trait correction for multiple hypothesis testing.

Unique per-annotation contributions to SNP-based heritability. Estimates of heritability enrichment can be confounded by contributions of multiple (overlapping) genomic annotations included in S-LDSC models. To quantify unique per-annotation contributions to heritability, we obtained the average per-SNP increase in heritability ascribed to that component, after controlling for all other annotations in the model (baseline annotations and DHS components)[36]. From the reported coefficients and their standard errors, we derived z-scores, one-sided P values and FDR-corrected q values for each trait-versus-component combination (Fig. 4d, e). For the heritability analysis in component concordant genic DHSs (Fig. 4f), we further stratified DHSs based on whether they are component concordant, component discordant, inside non-annotated genes (genic controls), or inter-genic. Figure 4f shows z-scores for the maximally enriched components identified in Fig. 4c.

To quantify the heritability contribution of per-dataset DHSs, we performed a variation on the standard S-LDSC procedure, as described previously[36]. Specifically, we built upon the baselineLD model by iteratively considering annotations derived from individual datasets only. These individual datasets were collected by selecting for each trait the 15 datasets most informative to each DHS component (Extended Data Fig. 4a). Annotations consist of DHSs observed in those datasets, as well as their complement, that is, the remainder of index DHSs. We report the contribution to heritability based on the former, expressed as z-scores (Fig. 4d, e).

Extendability of the DHS vocabulary

Addition of novel unseen datasets. New datasets may be added to the current NMF model while retaining the same interpretation of components (Extended Data Fig. 10a). In brief, 0.1% FDR variable-width peak calls are obtained from new datasets of interest, mapped to DHS index elements using bedops[47] and projected into the existing component space using standard NMF routines (see code for more details).

DHS index element identification without de novo peak identification. We used bedops[47] to look up DNase-seq signal levels of a dataset of interest over index elements, to determine whether a given element is actuated in the dataset. Expressed as a classification problem, using the existing 0.1% FDR variable-width peak calls as the groundtruth set, we assess precision and recall of peak recovery. For all 733 biosamples we find area under precision recall curve (AUPRC) values ranging from 0.33 to 0.83 (median, 0.71; IQR, 0.64–0.75), with a trophoblast biosample (ENCODE DCC identifier ENCBS576QRR) shown as an example (Extended Data Fig. 10a). The large difference between AUPRC values of matched versus non-matched biosamples allows the identification of the original biosample (Extended Data Fig. 10b), while showing that biosamples with similar AUPRC ranks share the same biological characteristics (Extended Data Fig. 10c). This procedure can also be followed for unseen datasets (Extended Data Fig. 10d), in particular datasets that are less deeply profiled or would otherwise be too sparse to call peaks on de novo—such as single cell chromatin profiling data.

Reporting summary

Further information on research design is available in the Nature Research Reporting Summary linked to this paper.

Data availability

All primary data are available from the ENCODE DCC portal. Biosample metadata are available in Supplementary Table 1 as well as in other formats via Zenodo (https://doi.org/10.5281/zenodo.3838751). The set of more than 3.5 million DHS delineations is available in tab-separated format from the ENCODE DCC portal (https://www.encodeproject.org/annotations/ENCSR857UZV/) and via Zenodo (https://doi.org/10.5281/zenodo.3838751). Data matrices describing the occurrence patterns of DHSs across biosamples are available in various formats via Zenodo (https://doi.org/10.5281/zenodo.3838751). There are no restrictions on data availability and (re)use. We additionally provide a specialized data browser (https://index.altius.org/) and a trackhub for the UCSC Genome Browser (https://genome.ucsc.edu/cgi-bin/hgTracks?db=hg38&hubUrl=https://resources.altius.org/~meuleman/DHS_Index_tracks/hub.txt). BED files documenting the coordinates and annotations of DHSs with evidence of being bound by specific transcription factors are available via Zenodo (https://doi.org/10.5281/zenodo.3838751), and top-scoring elements per TF can be explored in a browser (https://index.altius.org/?application=viewer&roiSet=TFassoc_Meuleman).

Code availability

Code is available on Github for building the index of consensus DHSs (https://github.com/Altius/Index), for constructing the DHS vocabulary and the addition of novel biosamples (https://github.com/Altius/Vocabulary).

42. John, S. et al. Genome-scale mapping of DNase I hypersensitivity. *Curr. Protoc. Mol. Biol. Ch.* **27**, Unit 21.27 (2013).
43. Smit, A. F. A., Hubley, R. & Green, P. RepeatMasker Open-4.0. http://www.repeatmasker.org (2015).
44. Karolchik, D. et al. The UCSC Table Browser data retrieval tool. *Nucleic Acids Res*. **32**, D493–D496 (2004).
45. Frankish, A. et al. GENCODE reference annotation for the human and mouse genomes. *Nucleic Acids Res*. **47** (D1), D766–D773 (2019).
46. Pollard, K. S., Hubisz, M. J., Rosenbloom, K. R. & Siepel, A. Detection of nonneutral substitution rates on mammalian phylogenies. *Genome Res*. **20**, 110–121 (2010).
47. Neph, S. et al. BEDOPS: high-performance genomic feature operations. *Bioinformatics* **28**, 1919–1920 (2012).
48. Boutsidis, C. & Gallopoulos, E. SVD based initialization: A head start for nonnegative matrix factorization. *Pattern Recognit*. **41**, 1350–1362 (2008).
49. Eckart, C. & Young, G. The approximation of one matrix by another of lower rank. *Psychometrika* **1**, 211–218 (1936).
50. Grant, C. E., Bailey, T. L. & Noble, W. S. FIMO: scanning for occurrences of a given motif. *Bioinformatics* **27**, 1017–1018 (2011).
51. Storey, J. D. & Tibshirani, R. Statistical significance for genomewide studies. *Proc. Natl Acad. Sci. USA* **100**, 9440–9445 (2003).
52. Sisu, C. et al. Comparative analysis of pseudogenes across three phyla. *Proc. Natl Acad. Sci. USA* **111**, 13361–13366 (2014).
53. Loh, P.-R. et al. Efficient Bayesian mixed-model analysis increases association power in large cohorts. *Nat. Genet*. **47**, 284–290 (2015).
54. Yang, J., Zeng, J., Goddard, M. E., Wray, N. R. & Visscher, P. M. Concepts, estimation and interpretation of SNP-based heritability. *Nat. Genet*. **49**, 1304–1310 (2017).
55. Bulik-Sullivan, B. K. et al. LD Score regression distinguishes confounding from polygenicity in genome-wide association studies. *Nat. Genet*. **47**, 291–295 (2015).
56. Purcell, S. et al. PLINK: a tool set for whole-genome association and population-based linkage analyses. *Am. J. Hum. Genet*. **81**, 559–575 (2007).
57. Berisa, T. & Pickrell, J. K. Approximately independent linkage disequilibrium blocks in human populations. *Bioinformatics* **32**, 283–285 (2016).
58. Gazal, S. et al. Functional architecture of low-frequency variants highlights strength of negative selection across coding and non-coding annotations. *Nat. Genet*. **50**, 1600–1607 (2018).

Acknowledgements We thank R. Senarighi for expert assistance with scientific illustration and T. Mercer and C. Lundberg for figure layout consultation. This work was supported by NIH grants U54HG007010 and UM1HG009444 and a charitable contribution to the Altius Institute for Biomedical Sciences by GlaxoSmithKline PLC.

Author contributions W.M. and J.S. initiated, coordinated and supervised the project. R.K. and J.H. supervised biosample collection and documentation of informed consent. J.H., K.L., D.B., M.D., D.D. and F.N. performed DNase-seq assays and generated sequencing libraries and data. J.N., A.J., M.F., M.B., R.S. and R.K. assisted with primary data processing and data management. W.M., A.M. and E.R. performed computational method development and analysed the data, with assistance from A.T., A.R., E.H. and J.V. W.M. generated figures. W.M. and J.S. wrote the manuscript.

Competing interests The authors declare no competing interests.

Additional information

Supplementary information is available for this paper at https://doi.org/10.1038/s41586-020-2559-3.

Correspondence and requests for materials should be addressed to W.M. or J.S.

Peer review information *Nature* thanks Guillaume Bourque, Hendrik Stunnenberg and the other, anonymous, reviewer(s) for their contribution to the peer review of this work.

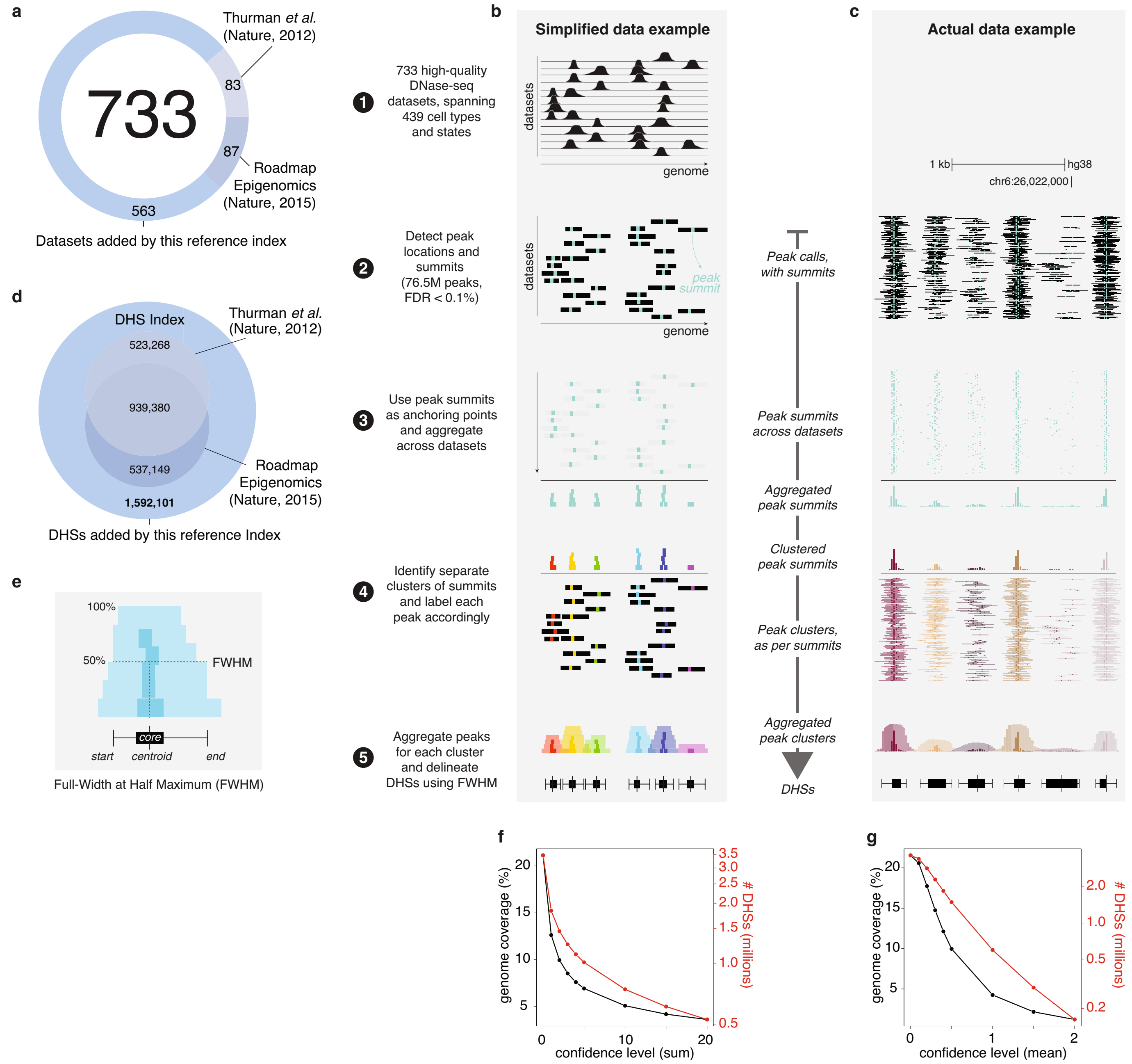

Extended Data Fig. 1 | Construction of a DHS index. a, Increase in number of DNase-seq datasets relative to previous efforts. **b**, **c**, Delineation of index DNase I hypersensitive sites (DHSs) from raw DNase-seq signal tracks, shown for simplified data (**b**) and actual data (**c**). Starting from individual DNase-seq datasets (step 1), we call peaks in each dataset (step 2), aggregate peak summits into clusters, indicating isolated accessibility events (step 3), group full peak coordinates according to these clusters (step 4), and delineate DHSs using full-width at half maximum (FWHM) (step 5). **d**, Increase in number of detected DHSs relative to previous efforts. **e.** Detailed view of FWHM delineation. **f**, **g**, Confidence scores based on DNase I signal strengths assigned to each DHS, allowing for pragmatic filtering using either summed (**f**) or mean (**g**) signal strength—the former assigning high confidence scores to DHSs with overall high signal levels across datasets, the latter providing a score normalized by the number of datasets in which a DHS was observed.

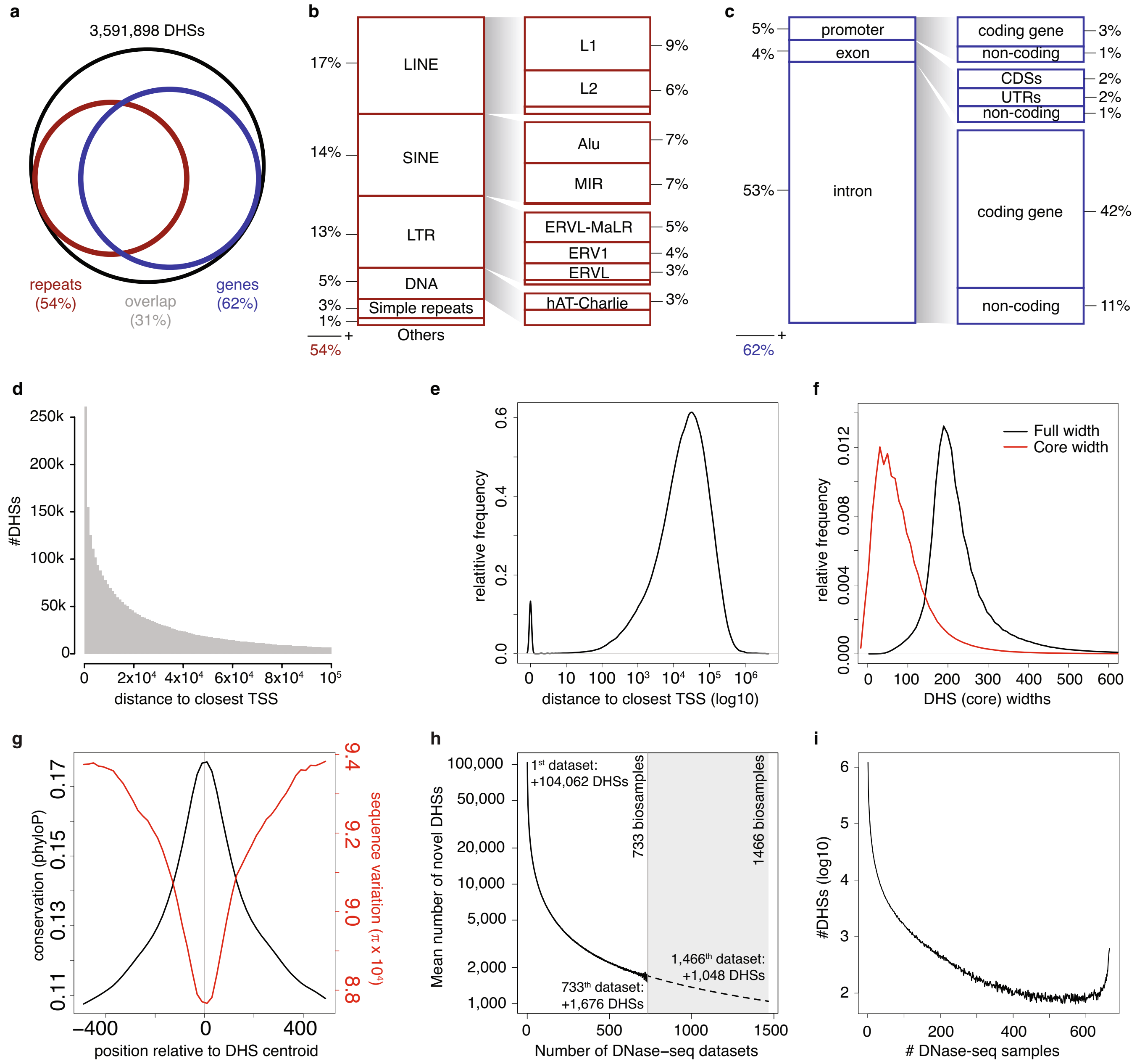

Extended Data Fig. 2 | Genomic context of DHS index elements. **a**, Overall coverage of 3.5M+ DHSs across genes and repetitive elements. **b**, Coverage of classes and families of repetitive elements. **c**, Coverage of annotated genic regions. **d**, Barplot of the number of DHSs as a function of distance to the nearest annotated transcription start site (TSS), up to 100,000 base pairs. **e**, Density plot of DHS distance to the closest TSS for all index DHSs, showing that the vast majority of DHSs are found distal to annotated promoters. **f**, Density plot of element widths for full DHSs and their core regions only, shown for DHSs observed in more than one biosample. Uniform 20 bp jitter added for smoothness. **g**, DHS centroids show an increase in sequence conservation (phyloP) and a decrease in within-human sequence variation (TOPMed, $\pi \times 10^4$). **h**, Mean number of new DHSs observed as a function of the *n*th DNase-seq dataset added, shown for the first 733 observed biosamples, as well as for an extrapolation to an additional future 733 new biosamples. **i**, Histogram indicating the variety in cell type selectivity of DHSs, ranging from single cell types to groups of 10s, 100s or even all assayed cellular conditions.

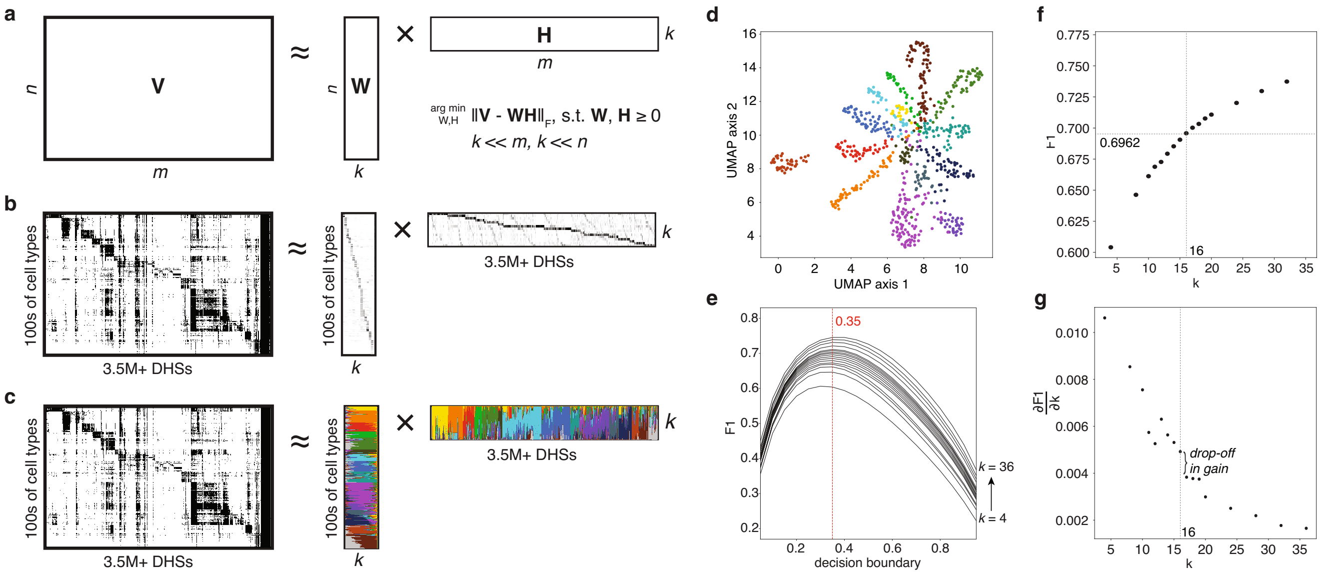

Extended Data Fig. 3 | NMF decomposition of DHS index. a, Schematic of non-negative matrix factorization (NMF) applied to an *n*-by-*m* matrix resulting in *k* components. The objective is to minimize the difference between the original matrix **(V)** and the product of **(W)** and **(H)**, such that all elements of **(W)** and **(H)** are non-negative. **b**, Depiction of NMF applied to our DNase-seq dataset of 733 biosample datasets and 3.5M+ DHSs, using *k* components. **c**, Colour-based view from the values shown in **b**. Colours indicate relative loadings of each NMF component, for both biosamples and DHSs. **d**, Two-dimensional UMAP projection of 733 biosamples coloured by their strongest representative NMF component. **e**, Choice of NMF decision boundary (0.35) based on maximal F1 score as a function of number of components *k* (4 to 36). **f**, F1 score as a function of the number of components *k*, with the chosen *k* = 16 and corresponding F1 score indicated. **g**, Gradient showing reduced gain in F1 score after *k* = 16.

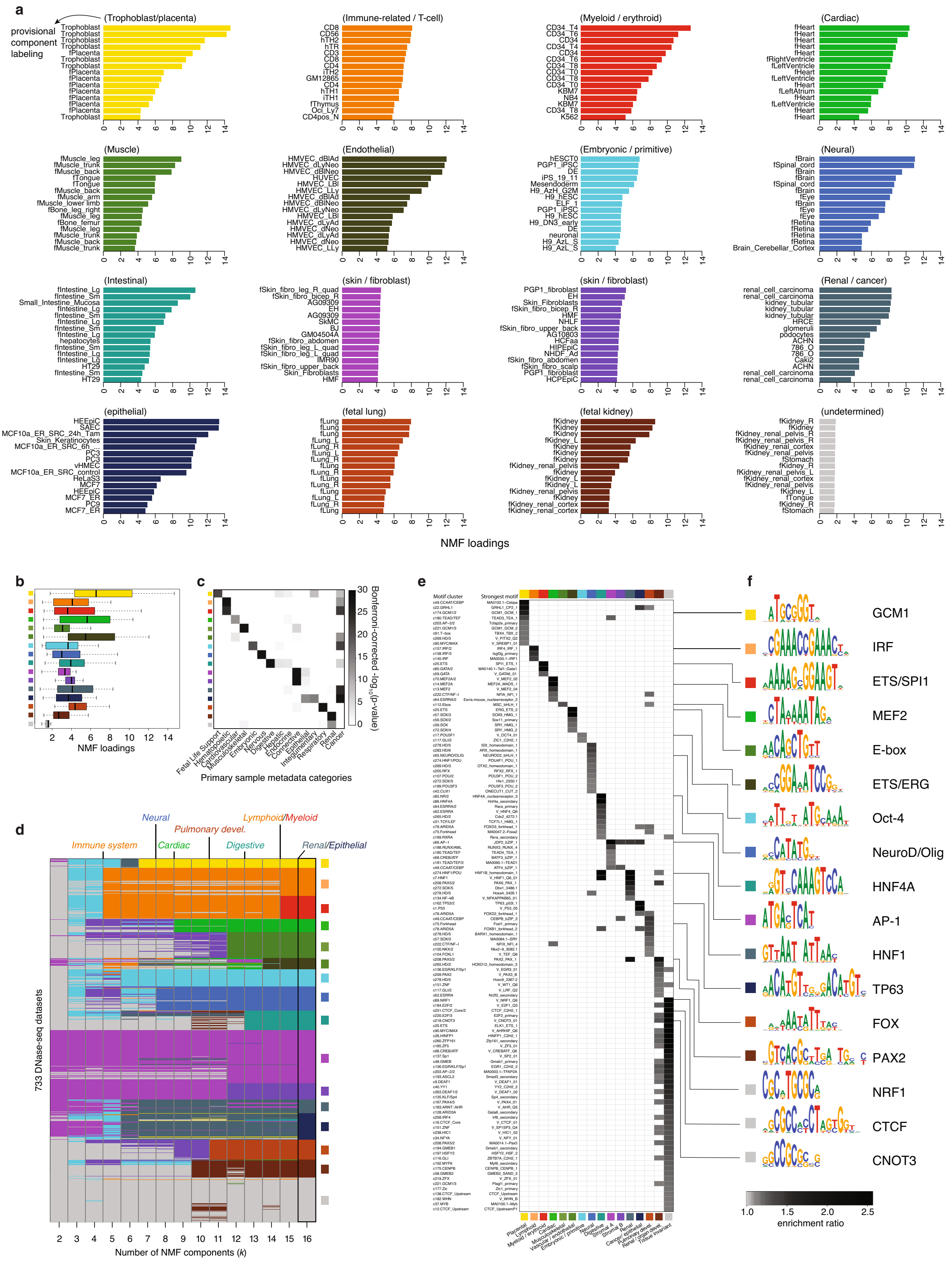

Extended Data Fig. 4 | See next page for caption.

Extended Data Fig. 4 | Association of DHS components with cellular conditions and TF motifs. a, Bar plots showing for each NMF component the top 15 DNase-seq datasets in terms of NMF loadings. NMF loading strength (*x*-axes) and dataset labelling (*y*-axes) are indicated. **b**, Box plots showing for each NMF component its loadings across those biosamples for which that component is maximally loaded. Boxes denote medians and interquartile ranges (IQRs, 25–75%), whiskers represent 1.5 × IQRs, $n = 18, 57, 46, 27, 52, 23, 34, 49, 40, 107, 33, 27, 54, 40, 36, 90$ biosamples, respectively. **c**, Beyond the top 15 biosamples for each component, general associations of components with annotations regarding human organ systems and cancer. Indicated are Bonferroni corrected *P* values, resulting from one-sided Mann–Whitney U tests. **d**, Distribution of biosamples across (maximal) NMF components, for the number of components (*k*) ranging from 2 to 16. Labels at the top indicate at which point distinct lineages became represented in corresponding components. **e**, Enrichment of transcription factor (TF) binding motifs in DHS components. Greyscale values indicate enrichment levels, only statistically significant results are included. DHS components shown on the *x*-axis, TF motif clusters with top representative motif on the *y*-axis. **f**, Top enriched TF motifs for each DHS component.

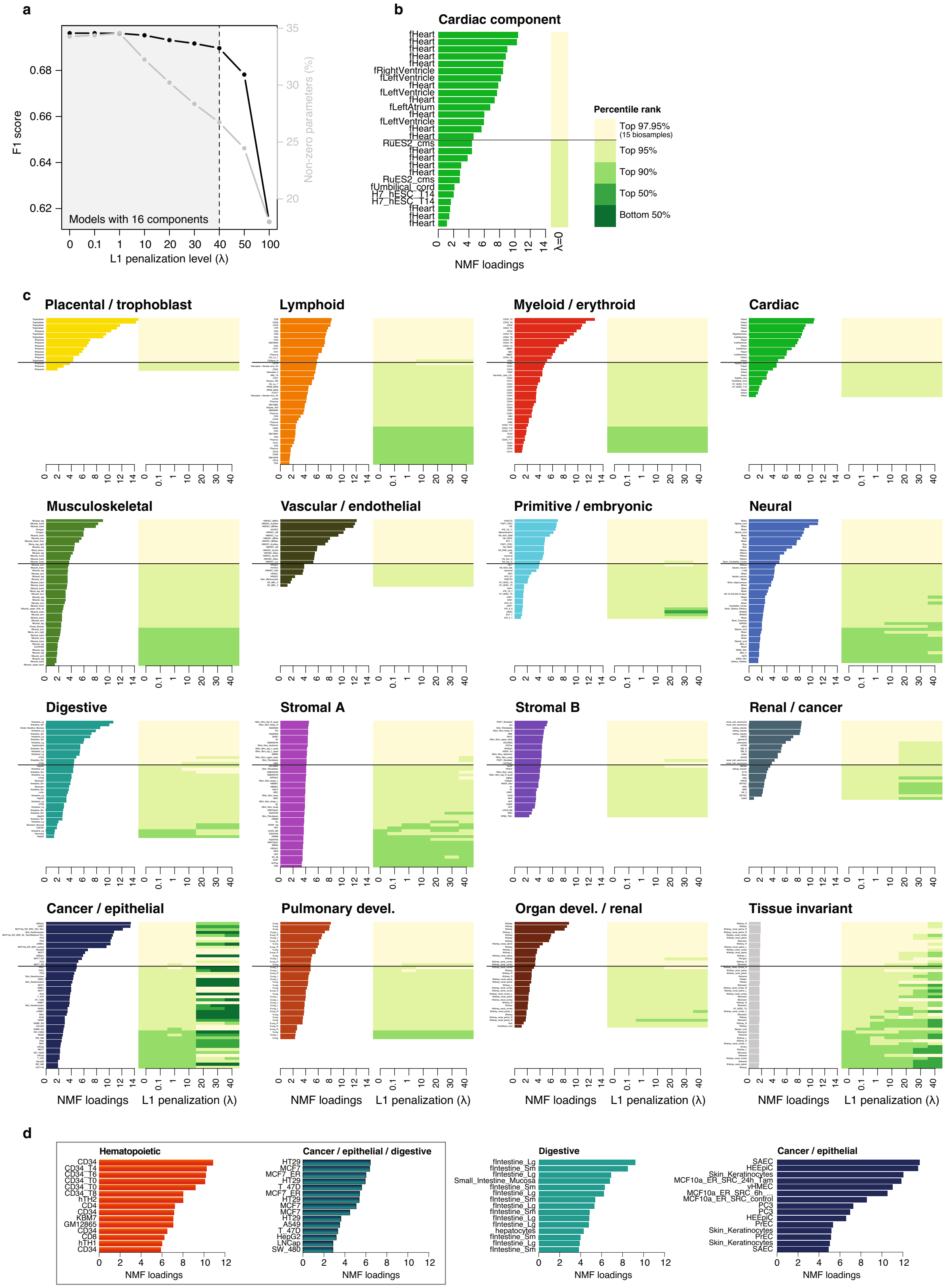

Extended Data Fig. 5 | See next page for caption.

Extended Data Fig. 5 | DHS component robustness. a, F1 score as a function of L1 penalization levels (λ), with separately indicated levels of sparsity reflected by the percentage of non-zero parameters in the resulting models. Shaded area represents penalization levels resulting in comparable 16-component models, as opposed to models with effectively less than 16 components, which are discarded in subsequent analyses. **b**, All biosamples with non-zero NMF loadings in the cardiac DHS component (for λ = 0). Horizontal line separates the top 15 biosamples (yellow shading) from the rest (shades of green), where green shading indicates quantile ranking in terms of component loading strength. **c**, Biosamples with non-zero NMF loadings for each DHS component, extended with agreement of quantile ranking as a function of L1 penalization levels, indicating that these rankings stay near constant for most components. **d**, Top 15 biosamples in terms of NMF loading per DHS component for an alternative NMF model resulting from a 40% downsampling of high-quality haematopoietic biosamples. NMF loading strength (*x*-axes) and dataset labelling (*y*-axes) are indicated, only for components that differ with the final model.

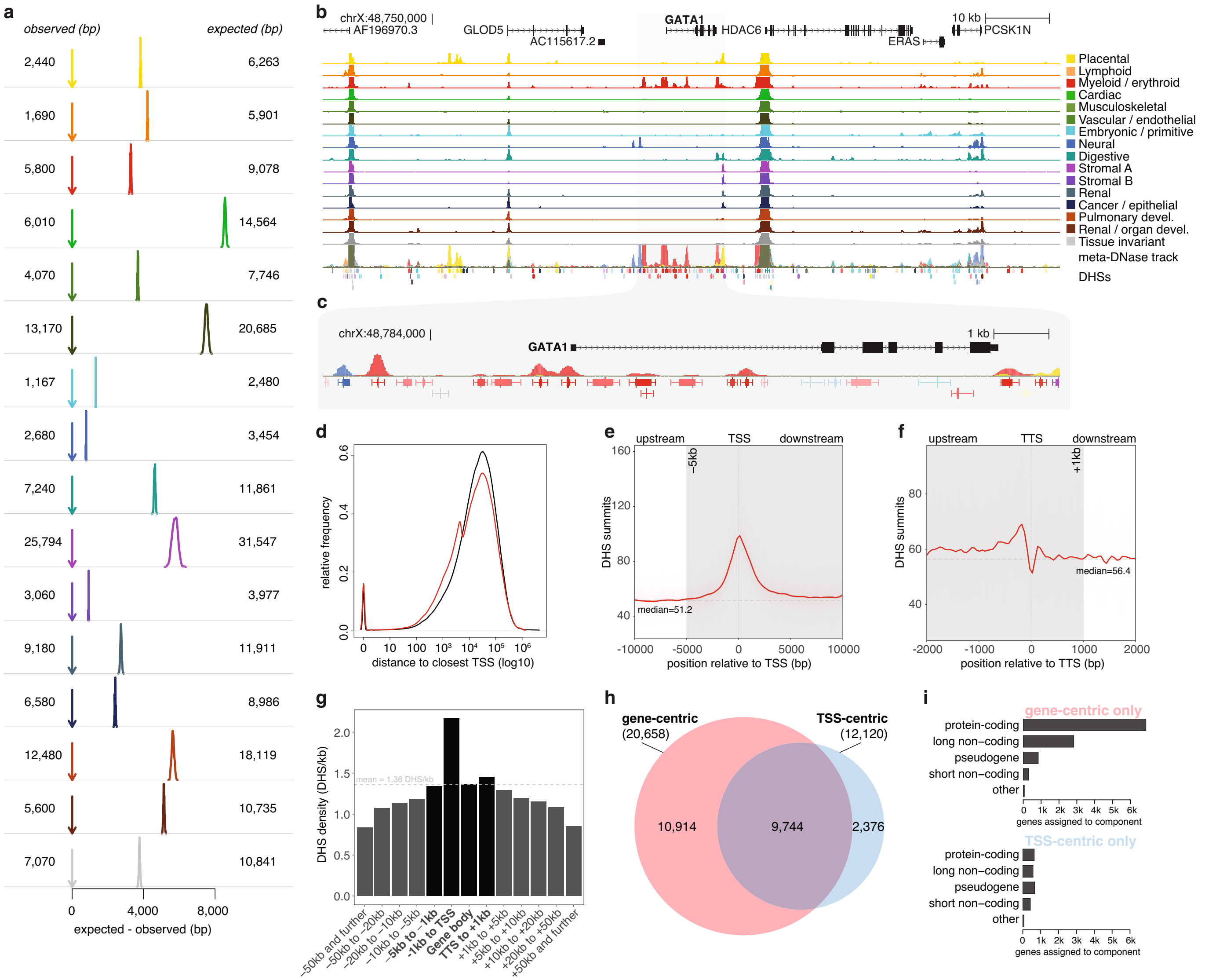

Extended Data Fig. 6 | Clustering of same-component DHSs near genes. **a**, Component-specific genomic clustering of DHSs, as shown by the median distance between same-component DHSs as compared to the median distance after random permutation of DHS-component labels. **b**, Regulatory landscape +/− 50kb around the *GATA1* gene, indicating GENCODE gene annotations, meta-DNase tracks for individual DHS components (Methods), and a meta-DNase overlay track. **c**, Detailed view, restricted to the *GATA1* regulatory landscape, including its delineated and annotated DHSs. Collectively, this landscape shows a statistical over-representation of DHSs associated with the myeloid/erythroid (red) component. **d**, Density plot of DHS distance to the closest TSS for all Index DHSs (black line) and the subset (65%) of DHSs considered for the purpose of annotating genes using DHS components. **e**, **f**, Alignment plots showing DHS summit density across the transcription start sites (TSSs, **e**) and transcription termination sites (TTSs, **f**) of annotated genes. Shaded areas indicate regions included for the purpose of annotating genes using DHS components. **g**, DHS density expressed in terms of number of DHSs per kilobase, indicating a general enrichment of DHSs in and immediately surrounding genes. **h**, Venn diagram showing the overlap between regulatory annotations based on the gene-centric approach described in this work and a TSS-centric approach (+/−5kb). The gene-centric approach captures the vast majority of genes annotated using the TSS-centric approach, while adding an additional approximately 11,000 genes. **i**, Type of genes annotated using a gene-centric versus TSS-centric approach, showing the former yielding larger fractions of protein-coding and long non-coding genes.

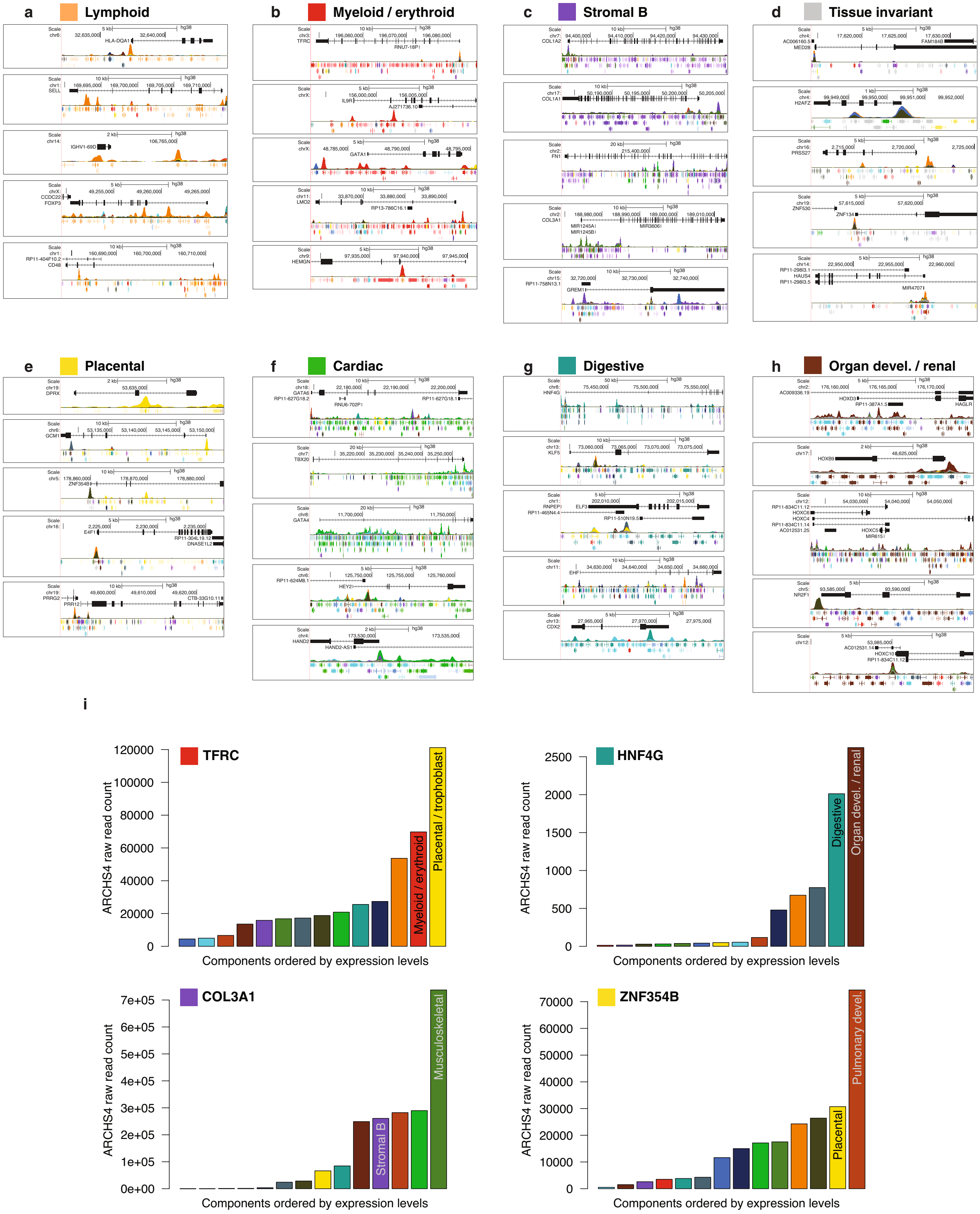

Extended Data Fig. 7 | Top labelled genes for selected components. **a**–**d**, Top-scoring protein-coding genes per DHS component reflect their functional roles, as shown for lymphoid (**a**), myeloid/erythroid (**b**), stromal (**c**) and tissue-invariant (**d**) components. **e**–**h**, Top-scoring transcription factor (TF) genes per DHS component reflect their functional roles, as shown for placental (**e**), cardiac (**f**), digestive (**g**) and organ developmental/renal (**h**) components. Full gene regulatory landscapes used for labelling are shown, with GENCODE gene annotations, meta-DNase overlay track, and DHSs. **i**, Examples of component-annotated genes with discordant expression patterns. Coloured squares next to gene names indicate relevant components, in this particular case discordant with cell and tissue types with maximal expression.

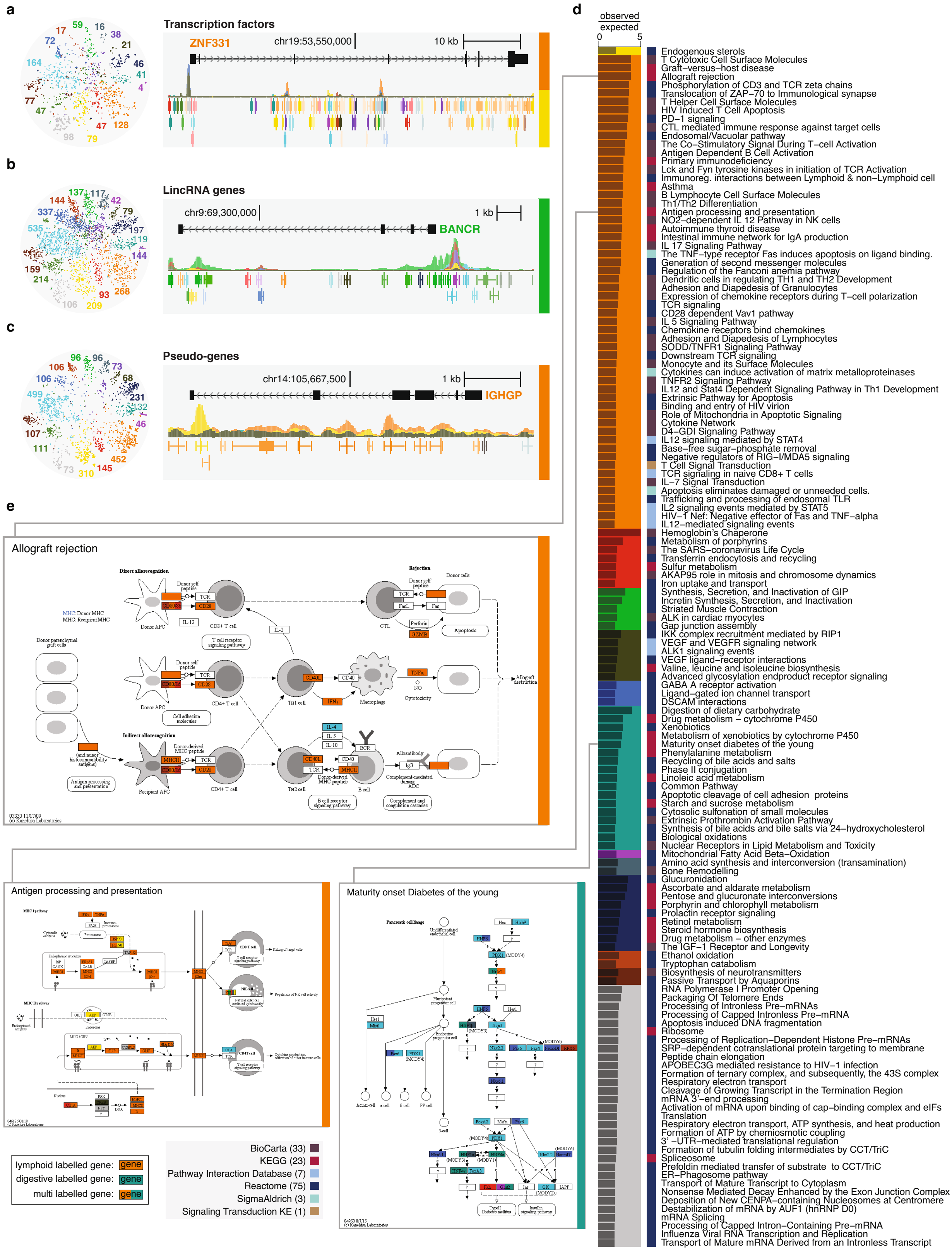

Extended Data Fig. 8 | See next page for caption.

Extended Data Fig. 8 | Annotation of genes with unknown function and pathways. **a**–**c**, Two-dimensional projection coordinates generated using *t*-SNE on all genes significantly associated with a DHS component and shown selectively for subsets of gene categories, namely transcription factors (TFs; diamonds: ZNF TF genes) (**a**), lincRNA genes (**b**) and pseudo-genes (**c**). Indicated are the number of labelled genes in each combination of gene category and DHS component. Examples of labelled genes are shown as follows. **a**, Regulatory landscape of *ZNF331*; a poorly annotated zinc-finger (ZNF) TF gene (lymphoid and placental components). **b**, Regulatory landscape of *BANCR*; a long intergenic non-coding RNA (lincRNA) gene, recently associated with cardiomyocyte migration. **c**, Regulatory landscape of the pseudo-gene *IGHGP* (lymphoid component). **d**, DHS component labelling of MSigDB canonical pathways, through the regulatory landscapes of constituent genes. Shown are pathways with a significant association (5% FDR) and an observed/expected ratio of at least 2. The most strongly associated components are indicated for each pathway, with their source databases. **e**, Examples of three component-associated pathways from the KEGG database, with genes coloured according to their majority component.

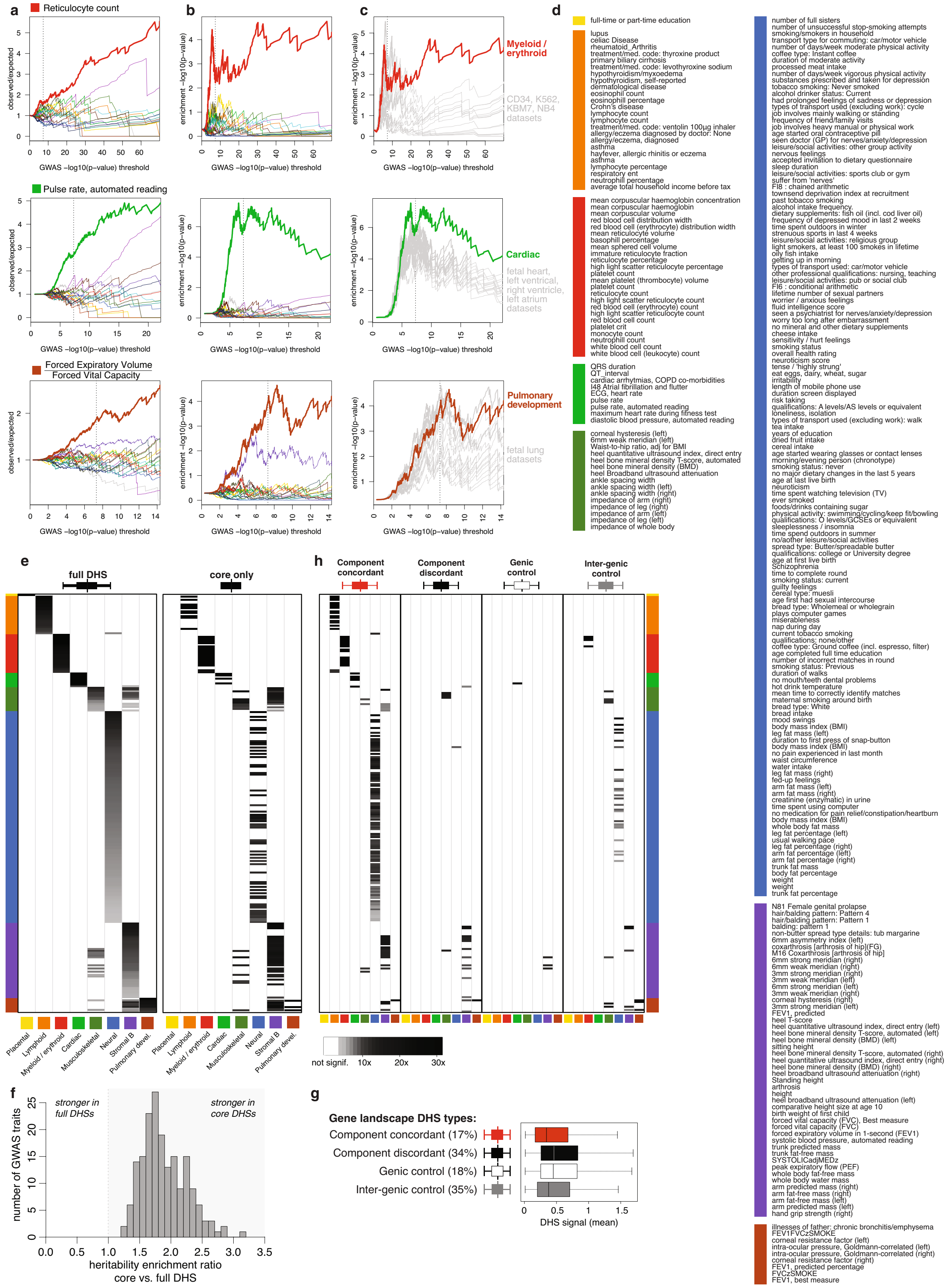

Extended Data Fig. 9 | See next page for caption.

Extended Data Fig. 9 | GWAS trait associations of DHS components. **a**–**c**, Quantitative association of component-DHSs with GWAS traits reticulocyte count, pulse rate, and FEV1/FVC ratio. Canonical genome-wide significance threshold indicated (5×10^{-8}). **a**, Enrichment ratios for increasingly stringent subsets of variants, per DHS component. **b**, Nominal enrichment $-\log_{10}$(*P* value) of a one-sided binomial test for each DHS component. **c**, Nominal enrichment $-\log_{10}$(p-value) of a one-sided binomial test for the strongest DHS component only, along with its strongest associated biosamples. **d**, GWAS traits associated with component-annotated index DHSs. **e**, Greyscale values, heritability enrichment levels for statistically significant (FDR 1%) traits based on the full delineated width of index DHSs (left) and restricted to index DHS 'core' regions (right). Row labelled as per **d**. **f**, Ratio of heritability enrichment values for 'core' versus 'full size' DHSs. **g**, DHS confidence scores (mean signal) stratified according to gene landscape DHS types. Boxes denote medians and interquartile ranges (IQRs, 25–75%), whiskers represent 1.5 x IQRs, $n = 261$ GWAS traits. **h**, Heritability enrichments stratified according to gene landscape DHS types. Greyscale indicates heritability enrichment levels for statistically significant associations (1% FDR).

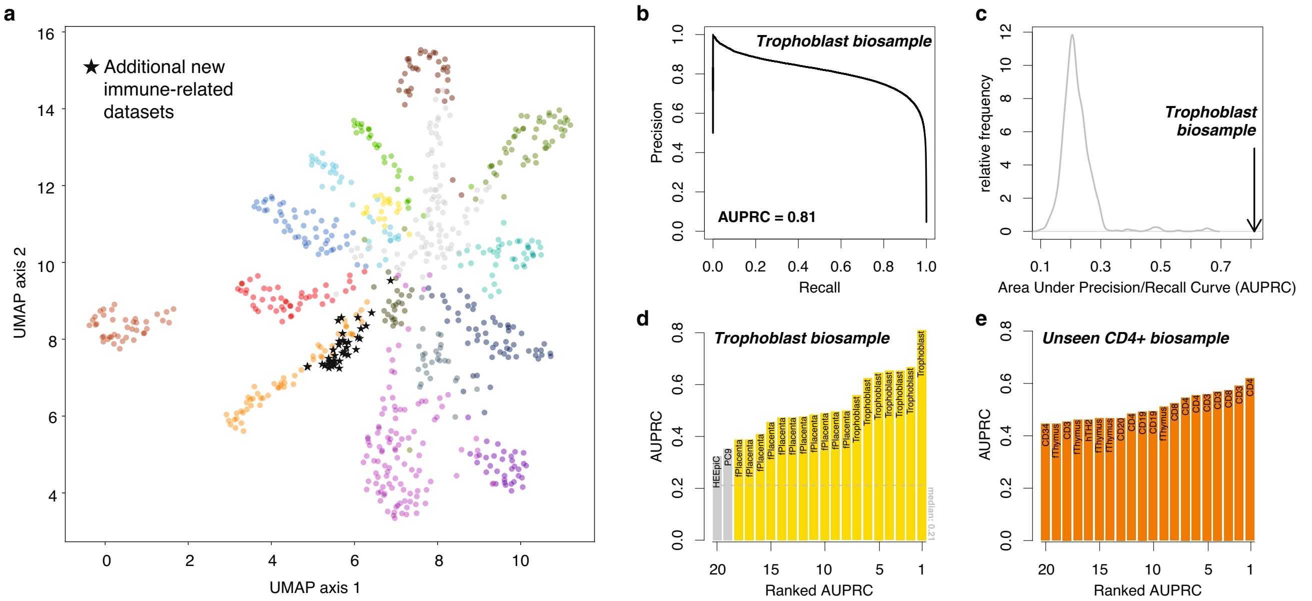

Extended Data Fig. 10 | Extendability of the DHS annotation framework. **a**, Two-dimensional UMAP projection of 733 biosamples by way of their index DHS utilization, coloured by their strongest representative NMF component. Stars indicate the embeddings of 38 previously unseen immune-related DNase-seq peak call datasets. **b**, Area under precision recall curve (AUPRC) values for predicting per-biosample DHSs from DNase-seq signal alone, shown for a trophoblast biosample. **c**, AUPRC values for the matching trophoblast versus all other 732 biosamples. **d**, Top 20 biosamples matching the aforementioned trophoblast biosample in terms of AUPRC values. **e**, Top 20 biosamples (out of 733) matching an unseen CD4+ biosample in terms of AUPRC values.

nature research

Corresponding author(s): Wouter Meuleman, John Stamatoyannopoulos

Last updated by author(s): Jun 28, 2020

Reporting Summary

Nature Research wishes to improve the reproducibility of the work that we publish. This form provides structure for consistency and transparency in reporting. For further information on Nature Research policies, see our Editorial Policies and the Editorial Policy Checklist.

Statistics

For all statistical analyses, confirm that the following items are present in the figure legend, table legend, main text, or Methods section.

n/a	Confirmed	
☐	☒	The exact sample size (*n*) for each experimental group/condition, given as a discrete number and unit of measurement
☐	☒	A statement on whether measurements were taken from distinct samples or whether the same sample was measured repeatedly
☐	☒	The statistical test(s) used AND whether they are one- or two-sided *Only common tests should be described solely by name; describe more complex techniques in the Methods section.*
☐	☒	A description of all covariates tested
☐	☒	A description of any assumptions or corrections, such as tests of normality and adjustment for multiple comparisons
☐	☒	A full description of the statistical parameters including central tendency (e.g. means) or other basic estimates (e.g. regression coefficient) AND variation (e.g. standard deviation) or associated estimates of uncertainty (e.g. confidence intervals)
☐	☒	For null hypothesis testing, the test statistic (e.g. *F*, *t*, *r*) with confidence intervals, effect sizes, degrees of freedom and *P* value noted *Give P values as exact values whenever suitable.*
☒	☐	For Bayesian analysis, information on the choice of priors and Markov chain Monte Carlo settings
☒	☐	For hierarchical and complex designs, identification of the appropriate level for tests and full reporting of outcomes
☒	☐	Estimates of effect sizes (e.g. Cohen's *d*, Pearson's *r*), indicating how they were calculated

Our web collection on statistics for biologists contains articles on many of the points above.

Software and code

Policy information about availability of computer code

Data collection	Data collection was assisted by the following pieces of software for read mapping and subsequent primary data processing: BWA (0.7.12), bedops (2.4.39), hotspot2 (2.1.1). All data collection and processing procedures are documented as part of the ENCODE DCC pipelines.
Data analysis	Data analysis was performed using R (version 3.6.1, using packages qvalue (v2.18.0), Matrix (v1.2.17), gplots (v3.0.3), Rtsne (v0.15)) and Python (version 3.6.4, using libraries numpy (v1.18.1), pandas (v1.0.3), sklearn (for NMF, v0.22.1), umap (v0.4.1)). Code is available on Github for building the index of consensus DHSs (https://github.com/Altius/Index), for constructing the DHS vocabulary and the addition of novel biosamples (https://github.com/Altius/Vocabulary), and for annotating DHSs relative to genes and repetitive elements (https://github.com/Altius/DHS_Annotations).

For manuscripts utilizing custom algorithms or software that are central to the research but not yet described in published literature, software must be made available to editors and reviewers. We strongly encourage code deposition in a community repository (e.g. GitHub). See the Nature Research guidelines for submitting code & software for further information.

Data

Policy information about availability of data

All manuscripts must include a data availability statement. This statement should provide the following information, where applicable:

- Accession codes, unique identifiers, or web links for publicly available datasets
- A list of figures that have associated raw data
- A description of any restrictions on data availability

All primary data are available from the ENCODE DCC portal. Biosample metadata are available in Supplementary Table 1 as well as in other formats via Zenodo (https://doi.org/10.5281/zenodo.3838751). The set of 3.5M+ DHS delineations is available in tab-separated format from the ENCODE DCC portal (https://www.encodeproject.org/annotations/ENCSR857UZV/) and via Zenodo (https://doi.org/10.5281/zenodo.3838751). Data matrices describing the occurrence patterns of DHSs across biosamples are available in various formats via Zenodo (https://doi.org/10.5281/zenodo.3838751). There are no restrictions on data availability and (re)use. We additionally provide a specialized data browser (https://index.altius.org/) and a trackhub for the UCSC Genome Browser (https://genome.ucsc.edu/cgi-bin/hgTracks?db=hg38&hubUrl=https://resources.altius.org/~meuleman/DHS_Index_tracks/hub.txt). BED files documenting the coordinates and annotations of DHSs with evidence of being bound by specific transcription factors are available via Zenodo (https://doi.org/10.5281/zenodo.3838751), and top-scoring elements per TF can be explored in a browser (https://index.altius.org/?application=viewer&roiSet=TFassoc_Meuleman). Various databases were consulted to obtain gene expression data (ARCHS4, https://amp.pharm.mssm.edu/archs4/download.html, accessed June 26, 2018), gene annotations (GENCODE v28 https://www.gencodegenes.org/human/release_28.html, psiCube http://pseudogene.org/psicube/data/gencode.v10.pgene.parents.txt) and pathway annotations (MSigDB v6.1 https://www.gsea-msigdb.org/gsea/msigdb/collections.jsp, KEGG v89.1 https://www.genome.jp/kegg/).

Field-specific reporting

Please select the one below that is the best fit for your research. If you are not sure, read the appropriate sections before making your selection.

☒ Life sciences ☐ Behavioural & social sciences ☐ Ecological, evolutionary & environmental sciences

For a reference copy of the document with all sections, see nature.com/documents/nr-reporting-summary-flat.pdf

Life sciences study design

All studies must disclose on these points even when the disclosure is negative.

Sample size	We determined sample size by considering exclusively high quality DNase-seq data with a SPOT score of at least 0.3 for our analyses, yielding a total of 733 DNase-seq datasets. Collectively, these data assay a total of 438 cell and tissue states spanning all human organ systems (Supplementary Table 1). This is currently the largest high-quality DNase I chromatin accessibility dataset available and as such its sample size is quite adequate.
Data exclusions	We removed DNase-seq samples with a SPOT score below 0.3, to ensure we only retain high quality data (Supplementary Table 1; Google Spreadsheet).
Replication	As part of the ENCODE data collection procedure, we have performed second replicate assays when enough material was available, and have retained replicates for analysis in case SPOT scores were at least 0.3, which is the case for 169 cell types and states. We do not have information on cases where our strict quality metrics were not achieved.
Randomization	Not applicable, as we are not performing any group-wise / cohort-wise comparisons.
Blinding	Not applicable, individual biosample data was obtained and jointly processed and analyzed.

Reporting for specific materials, systems and methods

We require information from authors about some types of materials, experimental systems and methods used in many studies. Here, indicate whether each material, system or method listed is relevant to your study. If you are not sure if a list item applies to your research, read the appropriate section before selecting a response.

Materials & experimental systems

n/a	Involved in the study	
☒	☐	Antibodies
☐	☒	Eukaryotic cell lines
☒	☐	Palaeontology and archaeology
☒	☐	Animals and other organisms
☐	☒	Human research participants
☒	☐	Clinical data
☒	☐	Dual use research of concern

Methods

n/a	Involved in the study	
☒	☐	ChIP-seq
☒	☐	Flow cytometry
☒	☐	MRI-based neuroimaging

Eukaryotic cell lines

Policy information about cell lines

Cell line source(s)	The source of all cell line material is described (when available) in Supplementary Table 1 and the online Google Spreadsheet. Cell lines were procured from appropriate commercial sources. h.ESC lines used were from NIH approved list and provided by laboratories with expertise in growing, characterizing and differentiating these cell types. (see ENCODE website for details and protocols).
Authentication	Authentication was provided by the commercial vendors from which the cell lines were procured and in accordance with ENCODE policies. Beyond this, no cell lines were further authenticated.
Mycoplasma contamination	Cell lines were not routinely checked for mycoplasma contamination.
Commonly misidentified lines (See ICLAC register)	One included cell line (SK-N-MC) appears on the ICLAC list, and we properly document this biosample as Ewing's sarcoma as opposed to a neuroepithelioma biosample.

Human research participants

Policy information about studies involving human research participants

Population characteristics	Population characteristics and other biosample metadata are described (when available) in Supplementary Table 1 and the online Google Spreadsheet. Human primary tissues were collected under IRB approved protocols using Open-access consents, as per NHGRI/ENCODE policies. Care was taken to ensure sex parity for tissues collected, to the extent possible. All primary tissues processed by our center were received as anonymized samples with minimal metadata information about tissue type, age, sex and ethnicity of the donor. As such, our institutional IRB reviewed our study using anonymized primary tissue and cell samples, and classified it as non-human subject studies.
Recruitment	Donors were recruited by collection centers (like Fred Hutch and dbGaP), using IRB approved Open-access consents. We received anonymized
Ethics oversight	University of Washington IRB

Note that full information on the approval of the study protocol must also be provided in the manuscript.

Rescue of oxytocin response and social behaviour in a mouse model of autism

https://doi.org/10.1038/s41586-020-2563-7

Received: 20 May 2019

Accepted: 25 May 2020

Hanna Hörnberg[1], Enrique Pérez-Garci[2], Dietmar Schreiner[1], Laetitia Hatstatt-Burklé[1], Fulvio Magara[3], Stephane Baudouin[4,6], Alex Matter[5], Kassoum Nacro[5], Eline Pecho-Vrieseling[2] & Peter Scheiffele[1]✉

A fundamental challenge in developing treatments for autism spectrum disorders is the heterogeneity of the condition. More than one hundred genetic mutations confer high risk for autism, with each individual mutation accounting for only a small fraction of cases[1–3]. Subsets of risk genes can be grouped into functionally related pathways, most prominently those involving synaptic proteins, translational regulation, and chromatin modifications. To attempt to minimize this genetic complexity, recent therapeutic strategies have focused on the neuropeptides oxytocin and vasopressin[4–6], which regulate aspects of social behaviour in mammals[7]. However, it is unclear whether genetic risk factors predispose individuals to autism as a result of modifications to oxytocinergic signalling. Here we report that an autism-associated mutation in the synaptic adhesion molecule *Nlgn3* results in impaired oxytocin signalling in dopaminergic neurons and in altered behavioural responses to social novelty tests in mice. Notably, loss of *Nlgn3* is accompanied by a disruption of translation homeostasis in the ventral tegmental area. Treatment of *Nlgn3*-knockout mice with a new, highly specific, brain-penetrant inhibitor of MAP kinase-interacting kinases resets the translation of mRNA and restores oxytocin signalling and social novelty responses. Thus, this work identifies a convergence between the genetic autism risk factor *Nlgn3*, regulation of translation, and oxytocinergic signalling. Focusing on such common core plasticity elements might provide a pragmatic approach to overcoming the heterogeneity of autism. Ultimately, this would enable mechanism-based stratification of patient populations to increase the success of therapeutic interventions.

Social recognition and communication are crucial elements in the establishment and maintenance of social relationships. Oxytocin and vasopressin are two evolutionarily conserved neuropeptides with important functions in the control of social behaviours, in particular pair-bonding and social recognition[7,8]. In humans, genetic variation of the oxytocin receptor (*OXTR*) gene is linked to individual differences in social behaviour[9]. Consequently, signalling modulators and biomarkers for the oxytocin or vasopressin system are being explored for conditions with altered social interactions such as autism spectrum disorders (ASDs)[5,6]. In mice, mutation of the genes encoding oxytocin or its receptor results in a loss of social recognition and social reward signalling[10–14]. Mutation of *Cntnap2*, a gene linked to ASD in humans, resulted in reduced levels of oxytocin in mice, and the addition of oxytocin improved social behaviour in this model[15]. However, the vast majority of genetic risk factors for autism have no known links to oxytocinergic signalling[1–3,16].

Here we explored oxytocin responses in mice that recapitulate a loss of function in the autism risk gene *Nlgn3*[17–19]. *Nlgn3* encodes a synaptic adhesion molecule[20–23], and *Nlgn3* mutant mice exhibit a range of behavioural alterations, including motor stereotypies[23,24], alterations in social novelty preference[25–28] (but see refs. [29,30]), social reward[31], and responses to social novelty tests[31]. Despite these alterations in social behaviours, adult *Nlgn3*-knockout ($Nlgn3^{KO}$) mice exhibit normal responses to inanimate objects[26,31]. In a five-trial social habituation/recognition task, we observed that the social novelty response phenotype is established already in juvenile $Nlgn3^{KO}$ mice (Fig. 1a–c, Extended Data Fig. 1a, b, Methods). The recognition and response to unfamiliar conspecifics depends on several neural circuit elements, including dopaminergic cells in the ventral tegmental area (VTA DA neurons)[7,31–33]. Re-expression of *Nlgn3* selectively in dopaminergic cells restored social novelty responses in juvenile $Nlgn3^{KO}$ mice (Fig. 1d–f, Extended Data Fig. 1c, d). By contrast, selective inactivation of *Nlgn3* in VTA DA neurons was sufficient to affect social novelty responses (Fig. 1g–i, Extended Data Fig. 1e–h). Social recognition in this assay depends on the function of the oxytocin receptor, as treatment of wild-type mice with the oxytocin receptor antagonist L-368,899 impaired recognition (Fig. 1j–l, Extended Data Fig. 1i, j).

---

[1]Biozentrum of the University of Basel, Basel, Switzerland. [2]Department of Biomedicine, University of Basel, Basel, Switzerland. [3]Centre for Psychiatric Neuroscience, Department of Psychiatry, Lausanne University Hospital, Lausanne, Switzerland. [4]Neuroscience Division, School of Biosciences, Cardiff University, Cardiff, UK. [5]Experimental Drug Development Centre, Singapore, Singapore. [6]Present address: Staticla, Geneva, Switzerland. ✉e-mail: peter.scheiffele@unibas.ch

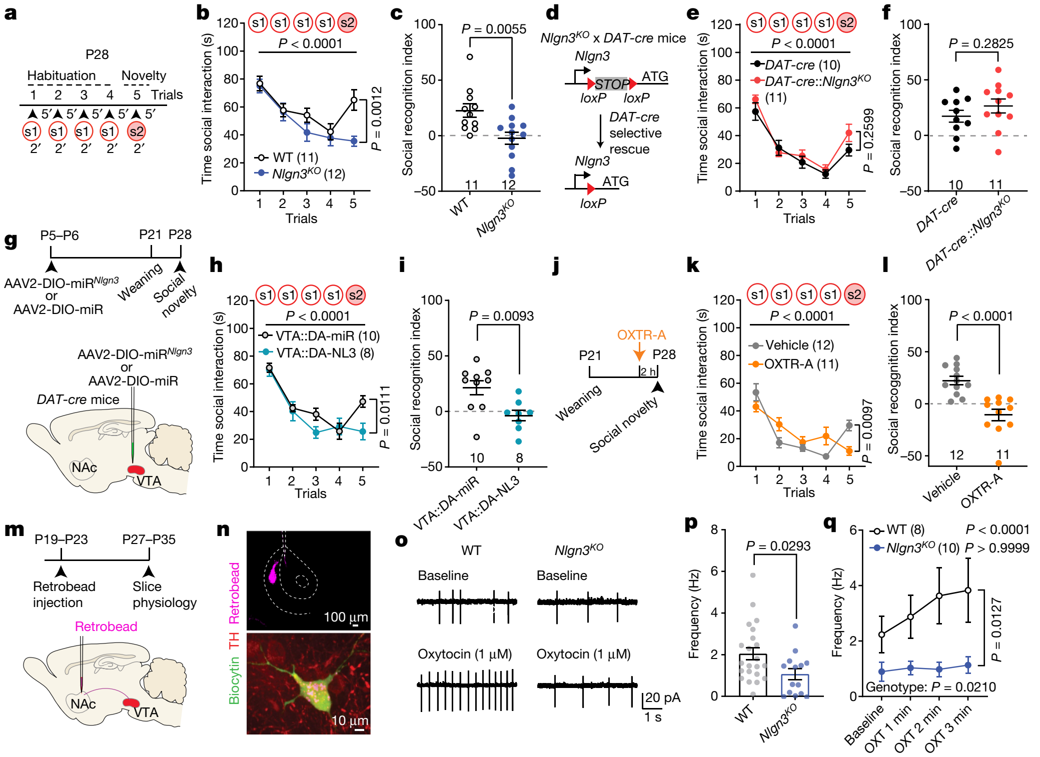

Fig. 1 | Oxytocin response is altered in VTA DA neurons lacking *Nlgn3*. **a**, Five-trial social habituation/recognition task. s1 and s2 denote first and second social stimulus, respectively; 2′ and 5′ denote 2 and 5 min. **b**, **c**, Mean social interaction time (**b**) and social recognition index (**c**) in wild-type (WT) and *Nlgn3*^{KO} mice. Numbers on graphs represent mice. **d**, *Nlgn3*^{KO} mutation containing a *loxP*-flanked transcriptional stop cassette. In *DAT-cre* mice, *Nlgn3* is selectively re-expressed in dopaminergic neurons. **e**, **f**, Mean social interaction time (**e**) and social recognition index (**f**) in *DAT-cre* and *DAT-cre*::*Nlgn3*^{KO} mice. **g**, VTA adeno-associated virus (AAV) injection in *DAT-cre* mice for microRNA-mediated knockdown of *Nlgn3* in VTA-DA neurons (VTA::DA-NL3). **h**, **i**, Mean social interaction time (**h**) and social recognition index (**i**) for VTA::DA-NL3 or control (VTA::DA-miR) mice. **j**, Treatment with the oxytocin receptor antagonist (OXTR-A) (L-368,899 10 mg kg^{-1} intraperitoneally in saline). **k**, **l**, Mean social interaction time (**k**) and social recognition index (**l**) for mice treated with OXTR-A or vehicle. **m**, Retrobeads were injected in the NAc medial shell, and tissues were prepared for slice physiology. **n**, Retrobead injection site in the NAc (top) and tyrosine hydroxylase (TH) immunoreactivity and retrobead labelling in biocytin-filled VTA neurons (bottom) after recording. **o**, Example traces of spontaneous firing at baseline (top) and after bath application of 1 μM OXT (bottom) in VTA DA neurons from wild-type (left) and *Nlgn3*^{KO} mice (right). **p**, Frequency at baseline in TH-positive wild-type and *Nlgn3*^{KO} VTA DA neurons. Wild type $n = 22$ cells from 12 mice; *Nlgn3*^{KO} $n = 14$ neurons from 8 mice. **q**, Average firing frequency (Hz) after bath application with OXT in retrobead-labelled TH-positive cells in the VTA of wild-type and *Nlgn3*^{KO} mice. The *P* values shown are from within group comparison of baseline versus OXT after 3 min. Wild type $n = 8$ cells from 7 mice; *Nlgn3*^{KO} $n = 10$ neurons from 7 mice. Error bars denote s.e.m. *P* values determined by repeated-measures two-way ANOVA followed by Bonferroni's post hoc test (**b**, **e**, **h**, **k**, **q**), unpaired two-sided *t*-test (**c**, **f**, **i**, **p**) or two-sided Mann–Whitney test (**l**). See Supplementary information for additional statistics.

The function of VTA DA neurons in social novelty responses and reinforcement is in part dependent on an oxytocin-induced increase in neuronal firing. Specifically, oxytocin released from axons that arise from hypothalamic nuclei increases the firing of VTA DA neurons projecting to the nucleus accumbens (NAc)[12,13]. Thus, we examined whether loss of *Nlgn3* might affect the response of this population of neurons to oxytocin. We marked VTA DA neurons projecting to the NAc medial shell and performed electrophysiological recordings from back-labelled neurons in acute slices of the VTA (Fig. 1m, n). Consistent with previous reports, back-labelled neurons showed low hyperpolarization-activated cation currents (I_h), and there was no significant difference between genotypes in I_h and other basic biophysical properties (Extended Data Fig. 2). In cell-attached recordings, the frequency of baseline firing of VTA DA neurons from *Nlgn3*^{KO} mice was slightly reduced compared with wild-type mice (Fig. 1p). Notably, bath application of 1 μM oxytocin significantly increased firing frequency in cells from wild-type mice but had no effect in slices from *Nlgn3*^{KO} mice (Fig. 1o, q). These findings uncover a requirement for the autism risk factor *Nlgn3* for oxytocin responses in the VTA.

A loss of oxytocinergic neurons has been reported in knockout mice for the autism risk factors *Cntnap2* and *Shank3b*[14,15]. In *Nlgn3*^{KO} mice, we did not detect any alteration in the density of oxytocinergic neurons in the paraventricular nucleus (one of the major oxytocinergic nuclei) or in the density of oxytocinergic fibres in the VTA (Fig. 2a, b, Extended Data Fig. 3a–c). Fluorescent in situ hybridization (FISH) analysis revealed a slight increase in *Oxtr* mRNA in VTA DA neurons from *Nlgn3*^{KO} mice compared with wild-type animals (Fig. 2c, d, Extended Data Fig. 3d–f). However, targeted proteomics (parallel reaction monitoring) on micro-dissected VTA tissue did not detect significant alterations in total oxytocin receptor protein, with no change in vasopressin 1A receptor mRNA (*Avpr1a*) or protein (Extended Data Fig. 3g–j, Supplementary Table 1). Thus, we performed shot-gun proteomics for an unbiased identification of molecular alterations in the VTA of *Nlgn3*^{KO} mice (Extended Data Fig. 4a–c, Supplementary Table 2). Gene Ontology (GO) and network-based functional classification analysis for proteins altered in *Nlgn3*^{KO} VTA identified protein transport, cell adhesion, and mRNA translation as main categories (Extended Data Fig. 4b, c). Dysregulation of membrane trafficking and G-protein-coupled receptor (GPCR) signalling components is consistent with the previously discovered roles for *Nlgn3* in synapse organization and GPCR signalling[22,23,34]. However, the alterations in regulators of translation were surprising. Alterations in mRNA translation have been linked to deficits in neuronal plasticity. We previously observed that behaviourally induced plasticity is altered in VTA DA neurons of *Nlgn3*^{KO} mice[31]. Thus, we compared translation in VTA

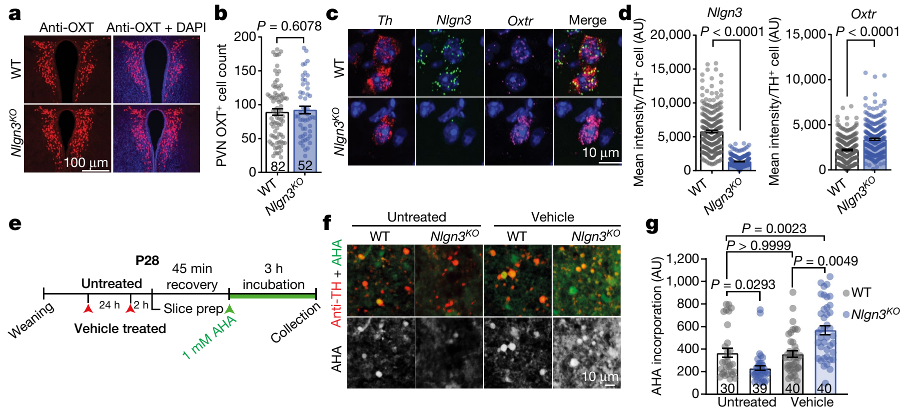

Fig. 2 | Disruption of translational regulation in the VTA of *Nlgn3*^{KO} mice. **a**, Representative image of OXT (red) and DAPI (blue) immunofluorescence in the PVN of wild-type and *Nlgn3*^{KO} mice. **b**, Mean OXT-positive cells per section in the PVN in wild-type and *Nlgn3*^{KO} mice. $n = 3$ mice per genotype; numbers on bars indicate sections analysed. **c**, Representative FISH images in the VTA from wild-type (top) and *Nlgn3*^{KO} (bottom) mice using probes for *Th* (red), *Nlgn3* (green) and *Oxtr* (magenta). **d**, Quantification of mean fluorescence intensity per *Th*$^{+}$ cell in the VTA from wild-type and *Nlgn3*^{KO} mice for *Nlgn3* (left) and *Oxtr* (right). *n*: wild type = 280 cells from 4 mice; *Nlgn3*^{KO} = 265 cells from 3 mice. AU, arbitrary units. **e**, Scheme for AHA incorporation on slice preparations from untreated and vehicle-treated mice. **f**, Representative images of acute slice measurements of protein synthesis in VTA visualized by AHA incorporation (green) with marking of TH-positive cells (red). **g**, Quantitative assessment of AHA incorporation in naive mice versus mice treated by oral gavage with vehicle. Wild-type untreated $n = 3$ mice; *Nlgn3*^{KO} untreated, *Nlgn3*^{KO} vehicle and wild-type vehicle $n = 4$ mice. Numbers on graph refer to the number of images analysed (8–20 VTA DA cells per image, approximately 10 images per mouse). All error bars are s.e.m. *P* values determined by two-sided Mann–Whitney test (**b**, **d**) or Kruskal–Wallis test followed by Dunn's multiple comparison test (**g**). See Supplementary information for additional statistics.

DA neurons of naive and behaviourally exposed wild-type and *Nlgn3*^{KO} mice. Incorporation of the methionine analogue azidohomoalanine (AHA)[35] in VTA DA neurons (marked by tyrosine hydroxylase) of acute mouse brain slices from naive *Nlgn3*^{KO} mice was reduced compared with wild-type mice (Fig. 2e–g, Extended Data Fig. 4d). Notably, the incorporation of AHA was increased in VTA DA neurons from *Nlgn3*^{KO} mice exposed to handling (Fig. 2e–g). This suggests a signalling-dependent disruption of translation homeostasis in the mutant mice.

Disruption of translation homeostasis is thought to broadly modify neuronal proteins resulting in impaired plasticity and neurodevelopmental conditions[36–40]. Thus, we sought to normalize translation in *Nlgn3*^{KO} mice and test whether this would restore oxytocin responses in VTA DA neurons. We focused on MAP kinase-interacting kinases (MNKs), which are crucial regulators of signalling-dependent modification of mRNA translation (Fig. 3a). Inhibition of MNK was reported to modify ribosomal protein levels and to ameliorate behavioural and plasticity alterations in *Fmr1* knockout (*Fmr1*^{KO}) mice[41–43]. We tested efficacy and brain penetrance of a series of highly specific MNK inhibitors originally developed for oncology applications[44]. One of these compounds, ETC-168, resulted in a dose-dependent reduction in phosphorylation of the MNK target eIF4E in cultured cortical mouse neurons without affecting protein levels of eIF4E or eIF4G or the activity of ERK1/2 (Fig. 3b, Extended Data Fig. 5a–e). In wild-type mice, orally administered ETC-168 had significant brain penetration (brain-to-plasma ratio 0.12) with a half-life of 4.3 h (Fig. 3d), and resulted in a reduction in eIF4E phosphorylation in the VTA and other brain areas (Fig. 3c, Extended Data Fig. 5f, l). Of note, phospho- or protein levels of eIF4E or MNK1 are unaltered in the VTA of *Nlgn3*^{KO} mice (Extended Data Fig. 5g–k). As a proof of concept, we probed the effectiveness of ETC-168 treatment in modifying a behavioural phenotype in *Fmr1*^{KO} mice. In a place-independent discrimination task, *Fmr1*^{KO} and wild-type mice learned a cue-reward contingency rule equally well, but *Fmr1*^{KO} mice were impaired on contingency reversal (Extended Data Fig. 6a, b). Treatment with ETC-168 during the reversal phase of the task significantly improved their performance (Extended Data Fig. 6c, d). Thus, ETC-168 is a highly selective, brain-penetrant inhibitor of MNK1/2 activity, which modifies cognitive behaviour in mice.

We then asked whether ETC-168 treatment would modify the translational machinery in the VTA of *Nlgn3*^{KO} mice. Using tandem mass tag (TMT)-based isobaric labelling, we verified the de-regulation of translational machinery in VTA tissue from *Nlgn3*^{KO} versus wild-type mice treated with vehicle (Extended Data Fig. 7a–d). Gene set enrichment analysis[45] uncovered an increase in core proteins of cytoplasmic but not mitochondrial ribosomes (Fig. 3e, Extended Data Fig. 7e, g). Inhibition of MNK with ETC-168 abolished the increase in core ribosomal proteins in *Nlgn3*^{KO} VTA (Fig. 3f, Extended Data Fig. 7f, h). In acute slices from *Nlgn3*^{KO} mice treated with ETC-168, incorporation of AHA was significantly reduced as compared with *Nlgn3*^{KO} mice treated with vehicle, resulting in similar AHA incorporation levels to slices from vehicle-treated wild-type mice (Fig. 3g–i).

We then tested whether ETC-168 treatment restored oxytocin responses and social novelty responses in *Nlgn3*^{KO} mice (Fig. 4a). Notably, short-term oral treatment (two applications of 5 mg kg^{-1} ETC-168 over 26 h) of *Nlgn3*^{KO} mice recovered the oxytocin-induced increase in firing frequency seen in wild-type mice (Fig. 4b, c). This treatment also fully restored social novelty responses, with no detectable effect on wild-type mice (Fig. 4a, d–f, Extended Data Fig. 8). This pharmacologically recovered social recognition behaviour was dependent on oxytocin receptor function (Extended Data Fig. 9). Notably, ETC-168 treatment was well tolerated and remained effective in a long-term treatment regime (Extended Data Figs. 7a–c, 10). Thus, modification of translation homeostasis in *Nlgn3*^{KO} mice by MNK inhibition restores oxytocin responses and social novelty responses.

This work uncovers an unexpected convergence between the genetic autism risk factor *Nlgn3*, translational regulation, oxytocinergic signalling, and social novelty responses. Although loss of *Nlgn3* impairs oxytocin responses in VTA DA neurons, the behavioural phenotype does not fully phenocopy genetic loss of oxytocin. Oxytocin knockout mice exhibit impaired habituation in the social recognition task[10], whereas *Nlgn3*^{KO} mice habituate normally but exhibit a selective deficit in the response to a novel conspecific. This is probably due to differential roles of *Nlgn3* and oxytocin across several neural circuits and over development. Moreover, *Nlgn3* loss-of-function also affects signalling through additional GPCRs[23].

We propose that pharmacological inhibition of MNKs may provide a new therapeutic strategy for neurodevelopmental conditions with altered translation homeostasis. Notably, MNK loss-of-function appears to be overall well tolerated. MNK1/2 double-knockout mice

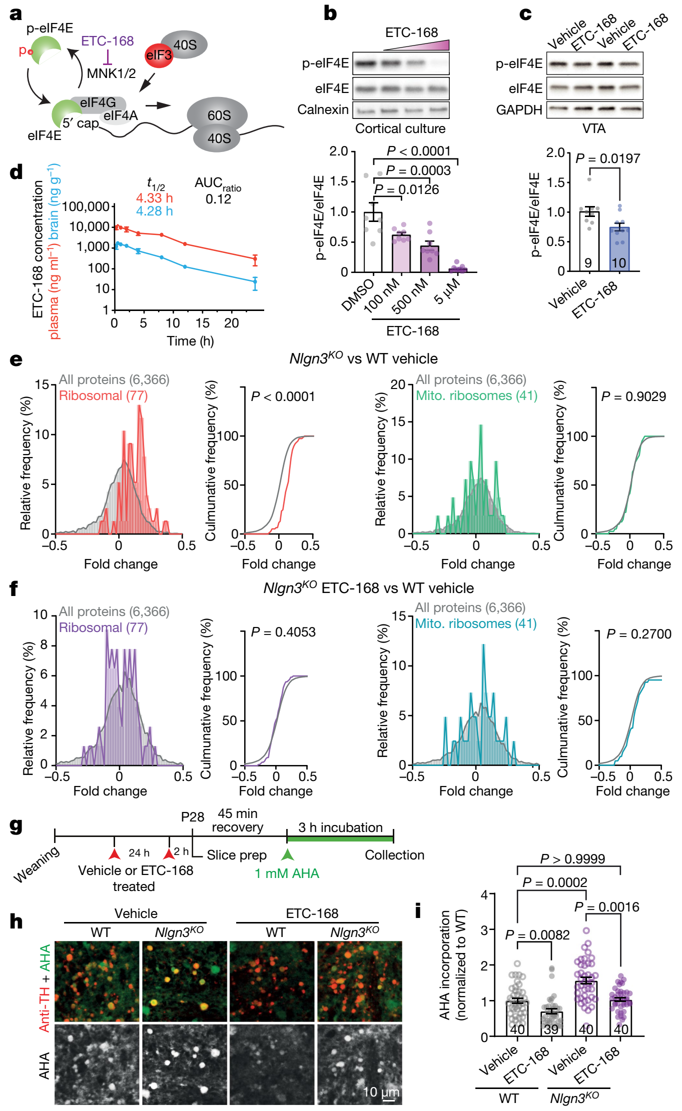

Fig. 3 | The novel MNK1/2 inhibitor ETC-168 rescues translation in *Nlgn3*^{KO} VTA. **a**, ETC-168 targets MNK1/2. Note that eIF4E phosphorylation decreases affinity of eIF4E for the mRNA 5′ cap structure **b**, Representative western blot (top) and quantification (bottom) of eIF4E phosphorylation in days in vitro 14 cortical neurons treated with DMSO or ETC-168 for 3 h. $n = 8$ replicates, 3 independent experiments. **c**, Representative western blot (top) and quantification (bottom) of eIF4E phosphorylation in VTA lysate from wild-type mice treated with vehicle or 5 mg kg^{-1} ETC-168. Numbers on graphs represent mice. **d**, Pharmacokinetic analysis of ETC-168 concentration in male mice ($n = 27$) after a single oral dose of 10 mg kg^{-1}. Plasma levels are in red, and brain levels are in blue. The half-life ($t_{1/2}$) and the brain-to-plasma exposure (AUC$_{ratio}$) are shown. **e**, Tandem mass tag (TMT) proteomic comparison of VTA from vehicle-treated mice ($n = 4$ mice per genotype and treatment). Relative frequency of log$_2$-transformed fold change in all detected proteins, cytosolic, or mitochondrial ribosomal protein abundance is plotted (*Nlgn3*^{KO} versus wild type). **f**, Comparison as in **e** for log$_2$-transformed fold change in protein abundance in ETC-168-treated *Nlgn3*^{KO} versus vehicle-treated wild-type mice. **g**, FUNCAT assay in acute slices from vehicle-treated or ETC-168-treated mice (5 mg kg^{-1} or vehicle by oral gavage). **h**, Representative examples of AHA incorporation (green) in TH-positive cells (red). **i**, Quantitative assessment of AHA incorporation in vehicle (as in Fig. 2g for comparison to untreated mice) versus ETC-168-treated wild-type and *Nlgn3*^{KO} mice. $n = 4$ mice per genotype and treatment. Numbers on graphs refer to number of images analysed. Error bars denote s.e.m. *P* values determined by one-way ANOVA followed by Bonferroni's post hoc test (**b**), two-sided unpaired *t*-test (**c**), Kolmogorov–Smirnov test (**e**, **f**), or Kruskal–Wallis test followed by Dunn's multiple comparison test (**i**). See Supplementary information for additional statistics.

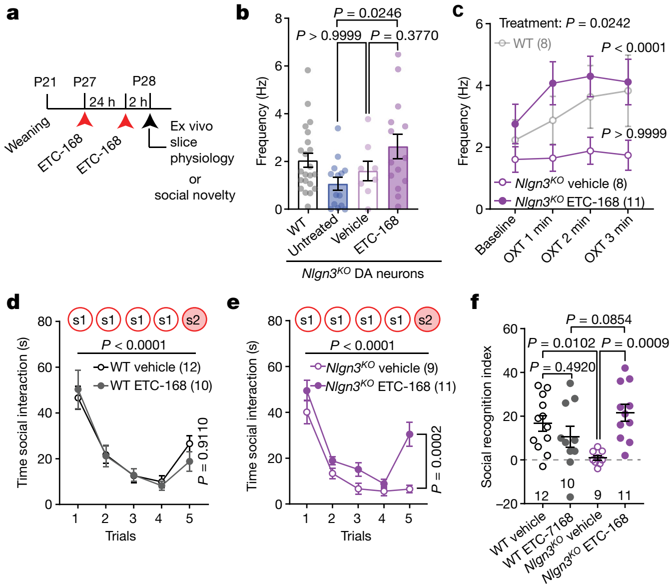

Fig. 4 | MNK inhibition restores social novelty responses in *Nlgn3*^{KO} mice. **a**, Scheme for drug treatment and analysis. **b**, Firing frequency at baseline in VTA DA neurons from *Nlgn3*^{KO} mice untreated (as previously shown in Fig. 1p), treated with vehicle, or treated with 5 mg kg^{-1} ETC-168. Untreated $n = 14$ neurons from 8 mice; vehicle $n = 8$ neurons from 4 mice; ETC-168 $n = 14$ neurons from 8 mice. The wild-type mouse data from Fig. 1p is presented for comparison ($n = 22$). **c**, OXT-induced frequency changes over time in VTA DA neurons from *Nlgn3*^{KO} mice treated with vehicle or 5 mg kg^{-1} ETC-168. Wild-type mice from Fig. 1q are presented for comparison. *P* values shown are for baseline versus OXT at 3 min. Vehicle-treated $n = 8$ cells from 4 mice; ETC-168-treated $n = 11$ neurons from 6 mice. **d**, **e**, Mean social interaction time in wild-type (**d**) and *Nlgn3*^{KO} (**e**) mice treated with vehicle or 5 mg kg^{-1} ETC-168. **f**, Social recognition index for wild-type and *Nlgn3*^{KO} mice treated with vehicle or 5 mg kg^{-1} ETC-168. Numbers in brackets indicate mice. All error bars are s.e.m. *P* values determined by one-way ANOVA followed by Bonferroni's post hoc test (**b**), repeated measures two-way ANOVA followed by Bonferroni's post hoc test (**c**), repeated measures two-way ANOVA between all genotype and treatment groups followed by Bonferroni's post hoc test (**d**, **e**), or repeated measures two-way ANOVA followed by Bonferroni's post hoc test for treatment and genotype (**f**). See Supplementary Information for additional statistics.

are viable[46] and several MNK inhibitors are entering clinical trials for cancer therapy[47]. Previously available MNK inhibitors were greatly limited by specificity and brain penetrance. Our work not only highlights a new class of highly-specific, brain-penetrant MNK inhibitors but also expands their application from fragile X syndrome[41] to a non-syndromic model of ASD. The common disruption in translational machinery and phenotypic rescue in two very different genetic models indicate that genetic heterogeneity of ASD might be reduced to a smaller number of cellular core processes. This raises the possibility that pharmacological interventions targeting such core processes may benefit broader subsets of patient populations.

Online content

Any methods, additional references, Nature Research reporting summaries, source data, extended data, supplementary information, acknowledgements, peer review information; details of author contributions and competing interests; and statements of data and code availability are available at https://doi.org/10.1038/s41586-020-2563-7.

1. de la Torre-Ubieta, L., Won, H., Stein, J. L. & Geschwind, D. H. Advancing the understanding of autism disease mechanisms through genetics. *Nat. Med.* **22**, 345–361 (2016).

2. O'Roak, B. J. et al. Sporadic autism exomes reveal a highly interconnected protein network of de novo mutations. *Nature* **485**, 246–250 (2012).
3. Iossifov, I. et al. De novo gene disruptions in children on the autistic spectrum. *Neuron* **74**, 285–299 (2012).
4. Yamasue, H., Aran, A. & Berry-Kravis, E. Emerging pharmacological therapies in fragile X syndrome and autism. *Curr. Opin. Neurol*. **32**, 635–640 (2019).
5. Bolognani, F. et al. A phase 2 clinical trial of a vasopressin V1a receptor antagonist shows improved adaptive behaviors in men with autism spectrum disorder. *Sci. Transl. Med*. **11**, eaat7838 (2019).
6. Parker, K. J. et al. A randomized placebo-controlled pilot trial shows that intranasal vasopressin improves social deficits in children with autism. *Sci. Transl. Med*. **11**, eaau7356 (2019).
7. Walum, H. & Young, L. J. The neural mechanisms and circuitry of the pair bond. *Nat. Rev. Neurosci*. **19**, 643–654 (2018).
8. Dölen, G., Darvishzadeh, A., Huang, K. W. & Malenka, R. C. Social reward requires coordinated activity of nucleus accumbens oxytocin and serotonin. *Nature* **501**, 179–184 (2013).
9. Cataldo, I., Azhari, A. & Esposito, G. A review of oxytocin and arginine-vasopressin receptors and their modulation of autism spectrum disorder. *Front. Mol. Neurosci*. **11**, 27 (2018).
10. Ferguson, J. N. et al. Social amnesia in mice lacking the oxytocin gene. *Nat. Genet*. **25**, 284–288 (2000).
11. Oettl, L. L. et al. Oxytocin enhances social recognition by modulating cortical control of early olfactory processing. *Neuron* **90**, 609–621 (2016).
12. Hung, L. W. et al. Gating of social reward by oxytocin in the ventral tegmental area. *Science* **357**, 1406–1411 (2017).
13. Xiao, L., Priest, M. F., Nasenbeny, J., Lu, T. & Kozorovitskiy, Y. Biased oxytocinergic modulation of midbrain dopamine systems. *Neuron* **95**, 368–384 (2017).
14. Sgritta, M. et al. Mechanisms underlying microbial-mediated changes in social behavior in mouse models of autism spectrum disorder. *Neuron* **101**, 246–259 (2019).
15. Peñagarikano, O. et al. Exogenous and evoked oxytocin restores social behavior in the Cntnap2 mouse model of autism. *Sci. Transl. Med*. **7**, 271ra8 (2015).
16. Ebert, D. H. & Greenberg, M. E. Activity-dependent neuronal signalling and autism spectrum disorder. *Nature* **493**, 327–337 (2013).
17. Sanders, S. J. et al. Multiple recurrent de novo CNVs, including duplications of the 7q11.23 Williams syndrome region, are strongly associated with autism. *Neuron* **70**, 863–885 (2011).
18. Gilman, S. R. et al. Rare de novo variants associated with autism implicate a large functional network of genes involved in formation and function of synapses. *Neuron* **70**, 898–907 (2011).
19. Tanaka, K. F. et al. Flexible Accelerated STOP Tetracycline Operator-knockin (FAST): a versatile and efficient new gene modulating system. *Biol. Psychiatry* **67**, 770–773 (2010).
20. Ichtchenko, K., Nguyen, T. & Südhof, T. C. Structures, alternative splicing, and neurexin binding of multiple neuroligins. *J. Biol. Chem*. **271**, 2676–2682 (1996).
21. Budreck, E. C. & Scheiffele, P. Neuroligin-3 is a neuronal adhesion protein at GABAergic and glutamatergic synapses. *Eur. J. Neurosci*. **26**, 1738–1748 (2007).
22. Chih, B., Afridi, S. K., Clark, L. & Scheiffele, P. Disorder-associated mutations lead to functional inactivation of neuroligins. *Hum. Mol. Genet*. **13**, 1471–1477 (2004).
23. Baudouin, S. J. et al. Shared synaptic pathophysiology in syndromic and nonsyndromic rodent models of autism. *Science* **338**, 128–132 (2012).
24. Rothwell, P. E. et al. Autism-associated neuroligin-3 mutations commonly impair striatal circuits to boost repetitive behaviors. *Cell* **158**, 198–212 (2014).
25. Tabuchi, K. et al. A neuroligin-3 mutation implicated in autism increases inhibitory synaptic transmission in mice. *Science* **318**, 71–76 (2007).
26. Radyushkin, K. et al. Neuroligin-3-deficient mice: model of a monogenic heritable form of autism with an olfactory deficit. *Genes Brain Behav*. **8**, 416–425 (2009).
27. Cao, W. et al. Gamma oscillation dysfunction in mPFC leads to social deficits in neuroligin 3 R451C knockin mice. *Neuron* **97**, 1253–1260 (2018).
28. Modi, B. et al. Possible implication of the CA2 hippocampal circuit in social cognition deficits observed in the neuroligin 3 knock-out mouse, a non-syndromic animal model of autism. *Front. Psychiatry* **10**, 513 (2019).
29. Chadman, K. K. et al. Minimal aberrant behavioral phenotypes of neuroligin-3 R451C knockin mice. *Autism Res*. **1**, 147–158 (2008).
30. Jaramillo, T. C. et al. Genetic background effects in Neuroligin-3 mutant mice: Minimal behavioral abnormalities on C57 background. *Autism Res*. **11**, 234–244 (2017).
31. Bariselli, S. et al. Role of VTA dopamine neurons and neuroligin 3 in sociability traits related to nonfamiliar conspecific interaction. *Nat. Commun*. **9**, 3173 (2018).
32. Hitti, F. L. & Siegelbaum, S. A. The hippocampal CA2 region is essential for social memory. *Nature* **508**, 88–92 (2014).
33. Gunaydin, L. A. et al. Natural neural projection dynamics underlying social behavior. *Cell* **157**, 1535–1551 (2014).
34. Xu, J. et al. Neuroligin 3 regulates dendritic outgrowth by modulating Akt/mTOR signaling. *Front. Cell. Neurosci*. **13**, 518 (2019).
35. Dieterich, D. C. et al. In situ visualization and dynamics of newly synthesized proteins in rat hippocampal neurons. *Nat. Neurosci*. **13**, 897–905 (2010).
36. Gkogkas, C. G. et al. Autism-related deficits via dysregulated eIF4E-dependent translational control. *Nature* **493**, 371–377 (2013).
37. Barnes, S. A. et al. Convergence of hippocampal pathophysiology in *Syngap*$^{+/-}$ and *Fmr1*$^{-/y}$ mice. *J. Neurosci*. **35**, 15073–15081 (2015).
38. Auerbach, B. D., Osterweil, E. K. & Bear, M. F. Mutations causing syndromic autism define an axis of synaptic pathophysiology. *Nature* **480**, 63–68 (2011).
39. Darnell, J. C. & Klann, E. The translation of translational control by FMRP: therapeutic targets for FXS. *Nat. Neurosci*. **16**, 1530–1536 (2013).
40. Asiminas, A. et al. Sustained correction of associative learning deficits after brief, early treatment in a rat model of Fragile X Syndrome. *Sci. Transl. Med*. **11**, eaao0498 (2019).
41. Gkogkas, C. G. et al. Pharmacogenetic inhibition of eIF4E-dependent Mmp9 mRNA translation reverses fragile X syndrome-like phenotypes. *Cell Rep*. **9**, 1742–1755 (2014).
42. Richter, J. D., Bassell, G. J. & Klann, E. Dysregulation and restoration of translational homeostasis in fragile X syndrome. *Nat. Rev. Neurosci*. **16**, 595–605 (2015).
43. Bramham, C. R., Jensen, K. B. & Proud, C. G. Tuning specific translation in cancer metastasis and synaptic memory: control at the MNK-eIF4E axis. *Trends Biochem. Sci*. **41**, 847–858 (2016).
44. Yang, H. et al. Optimization of selective mitogen-activated protein kinase interacting kinases 1 and 2 inhibitors for the treatment of blast crisis leukemia. *J. Med. Chem*. **61**, 4348–4369 (2018).
45. Lavallée-Adam, M., Rauniyar, N., McClatchy, D. B. & Yates, J. R. III. PSEA-Quant: a protein set enrichment analysis on label-free and label-based protein quantification data. *J. Proteome Res*. **13**, 5496–5509 (2014).
46. Ueda, T. et al. Combined deficiency for MAP kinase-interacting kinase 1 and 2 (Mnk1 and Mnk2) delays tumor development. *Proc. Natl Acad. Sci. USA* **107**, 13984–13990 (2010).
47. Xu, Y. et al. Translation control of the immune checkpoint in cancer and its therapeutic targeting. *Nat. Med*. **25**, 301–311 (2019).

Methods

Mice

Male wild-type, *Nlgn3*^{KO} (ref. 19) and *Fmr1*^{KO} (ref. 48) mice were used for this study. Note that this strain of *Nlgn3*^{KO} mice contains a transcriptional stop cassette[19] preventing genetic compensation events that might be triggered in mutants expressing truncated mRNAs[49]. For dopamine neuron-specific manipulations, *DAT-cre* BAC transgenic mice were used[50]. Mice were kept on a C57BL/6J background. All animals were group housed (weaning at postnatal day (P) 21–P23) under a 12 h light/dark cycle (06:00–18:00) with food and water ad libitum. All physiology and behaviour experiments were performed during the light cycle. Embryos for cortical cultures were obtained from NMRI mice (Janvier). All the procedures performed at University of Lausanne and Biozentrum complied with the Swiss National Institutional Guidelines on Animal Experimentation and were approved by the respective Swiss Cantonal Veterinary Office Committees for Animal Experimentation.

Pharmacokinetics of ETC-168

A group of 27 male C57BL/6 mice were administered with ETC-168 solution formulation in 7.5% NMP, 5% Solutol HS, 10% PG, 30% PEG-400, 47.5% normal saline at a dose of 10 mg kg^{-1}. Blood samples (approximately 60 µl) were collected under light isoflurane anaesthesia from retro orbital plexus at 0.25, 0.5, 1, 2, 4, 8, 12 and 24 h after drug administration. Plasma samples were separated by centrifugation of whole blood and stored below −70 °C until analysis. Immediately after collection of blood, brain samples were collected from each mouse at PD, 0.25, 0.5, 1, 2, 4, 8, 12 and 24 h. Brain samples were homogenized using ice-cold PBS (pH 7.4) and homogenates were stored below −70 °C until analysis. Total homogenate volume was three times the tissue weight. All samples were processed for analysis by protein precipitation using acetonitrile and analysed with fit-for-purpose LC–MS/MS method (lower limit of quantification (LLOQ): 2.00 ng ml^{-1} in plasma and 1.00 ng ml^{-1} in brain). Pharmacokinetic parameters were calculated using the non-compartmental analysis tool of Phoenix WinNonlin (v.6.3).

Pharmacological treatment

For in vitro experiments, ETC-168 was dissolved in DMSO. For in vivo treatment, ETC-168 was dissolved in 0.5% methylcellulose (Sigma, M7140) and 0.1% Tween-80 (Sigma, P5188) in MilliQ water to 1.25 mg ml^{-1}, and sonicated for 30 min. Animals were gavaged 24 h and 2 h before behavioural assessment or tissue collection for acute treatment. In the chronic treatment regime, animals were treated every 24 h, 2 h before start of the evaluation. The OXTR antagonist L-368,899 (Tocris, 2641) was dissolved in saline and 10 mg kg^{-1} was applied via i.p. injection 2 h before the start of behavioural assessments, or 15 min before the final dose of ETC-168.

Stereotaxic injection

Injections of diluted (1:4) Red Retrobead were done at P19–P23 and performed under isoflurane anaesthesia (Baxter AG). The mice were placed in a stereotaxic frame (Kopf Instrument) and a single craniotomy was made over the NAc medial shell at the following stereotaxic coordinates: ML ±0.55 mm, AP 1.5 mm, DV −4.05 mm from bregma. Injections were made with a 30-G Hamilton needle (Hamilton, 7762-03) for a total volume of 300 nl. Injection sites were confirmed post hoc by immunostaining. For electrophysiological experiments, the mice were left 5–8 days after injection before the start of experiment.

For *Nlgn3* conditional knockdown experiments, injections of purified AAV2-DIO-miR^{Nlgn3}-GFP and AAV2-DIO-miR-GFP were performed as previously described[31]. In brief, *DAT-cre* transgenic mice were injected at P5–P6 and a single craniotomy was made over the VTA at following stereotaxic coordinates: ML +0.15 mm, AP +0.2 mm, DV −4.2 mm from lambda for P5–P6. Injections were made with a 33-G Hamilton needle (Hamilton, 65460-02) for a total volume of 200 nl. Behavioural testing was performed at P28 and injections sites were confirmed post hoc by immunostaining as described previously[31]. In brief, VTA::DA^{NL3KD} mice were included if a minimum of 20% of TH-positive cells in the VTA were GFP-positive. Mice were excluded from the analysis if their body weight was less than 75% of the mean body weight at the start of behavioural trials or in case post hoc analysis revealed inefficient or off-target viral infection.

Habituation and novelty recognition task

Social recognition is considered to be commonly affected in individuals on the autism spectrum. Autistic individuals perform poorly on face identity recognition tasks, especially when a medium to high time delay (seconds to several minutes) between face presentation is applied[51,52]. To model social recognition in juvenile male mice, we adopted previous protocols that had been developed for adult rodents[10,53]. In this test, recognition between juvenile male mice (P26–P32) was tested with 5 min inter-trial intervals that mimic the timescales of recognition tasks from patient studies. An experimental cage similar to the animal's home cage was used with grid, food, and water removed. The experimental mice were acclimated in the cage for 30 min before the start of the test. At the start of the first trial, a novel same-sex mouse (stimulus mouse: C57BL/6J juvenile male mice, P21–P28) or an object (Lego block) was introduced into the cage for 2 min and mice were left to freely interact. This was repeated for 4 consecutive trials with 5 min in-between trial intervals to allow habituation to the stimulus mouse or object. On the fifth trial, a novel mouse (littermate to the stimulus mouse) or a novel object (dice) was introduced. For the social stimulus, interaction was scored when the experimental mouse initiated the action and when the nose of the animal was oriented towards the social stimulus mouse only. For the object stimulus, interaction was scored when the nose of the mouse was oriented 1 cm or less towards the object. The interaction time was used to calculate the recognition index as: (interaction trial 5) − (interaction trial 4). Social recognition in rodents has been reported to depend on oxytocin signalling[11,54]. To pharmacologically validate the recognition task, we treated mice with the oxytocin receptor antagonist (L-368,899 10 mg kg^{-1} injected intraperitoneally 2 h before testing). This treatment significantly suppressed recognition of novel conspecifics in this task (Fig. 1k, l).

Place-independent cue discrimination and reversal task

Adult male mice were used for this test. The test box (25 × 35 cm) was divided in a waiting and a reward zone by a gated plexiglass wall. Reward (condensed milk) was associated to one of the two lining patterns of a double tray (white tape versus brown sandpaper). The tray was turned in a pseudorandom fashion between trials in order to present the rewarded pattern on the right and the left 8 times within a daily session of 16 trials. Sliding lids were used to prevent nosepoke in the correct target after the mouse made a wrong choice, and to signal end of a trial and return to the waiting zone after the bait has been consumed. Before the start of the trial, mice were food deprived overnight and the reward was presented in the home cage to habituate to the reward. For the duration of the test, mice were food restricted overnight and receive food ad libitum after completion of the discrimination task. After the first night of food deprivation, mice were brought to the testing arena where they find condensed milk droplets (15 µl) in falcon lids similar to those used for the test. First day of habituation takes place in groups of cage mates, second day in individual session. Mice were shaped to shuttle to the waiting compartment of the arena after having consumed the reward. On day 1, mice were trained to find the reward only in one of two adjacent falcon lids that have been lined and mounted on little stages with a different pattern (brown sandpaper vs white tape). Each mouse undergoes 16 daily trials, with a cut-off of 20 min. Mice not completing 16 trials by the third testing day were excluded from further testing. Mice not attaining learning criterion for the first contingency (8 consecutive correct responses over two days) after 6 days of training did not go to the reversal learning step (or receive any treatment). Mice were trained for 6 consecutive days per week. Feeding was restricted to 1 g per mouse overnight. On day 7 (day 1 of reversal learning training), mice received ETC-168 5 mg kg^{-1} or vehicle by gavage 120 min before starting the tests for the duration of the reversal task. For the contingency reversal learning, mice were trained to nosepoke in the previously non-baited pattern in order to find reward. The training schedule was the same as before: 16 trials per day, until attainment of learning criterion (second day when 8 consecutive correct responses have been performed).

Open field and marble burying

Male mice were placed individually in the centre of a square open field arena (50 × 50 × 30 cm) made of grey plastic for 7 min. Velocity (cm s^{-1}) and time spend in center (s) was analysed using EthoVision10 system (Noldus). The arena was cleaned with 70% ethanol between trials. For the marble burying test, animals were placed in a standard type II cage with 5 cm bedding containing 20 identical black marbles distributed equally for 30 min. A marble was considered buried if at least two-thirds of the marble was covered.

Electrophysiology

Male mice (P28–P34) were deeply anaesthetized with isoflurane (4% in O_2, Vapour, Draeger) before decapitation and brain isolation. Acute horizontal brain slices (250 µm thick) from the midbrain were cut with a vibrating microslicer (Leica VT1200S) in ice-cold oxygenated sucrose-based cutting solution containing: NaCl (87 mM), $NaHCO_3$ (25 mM), KCl (2.5 mM), NaH_2PO_4 (1.25 mM) sucrose (75 mM), $CaCl_2$ (0.5), $MgCl_2$ (7mM) and glucose (10 mM) (equilibrated with 95% O_2, 5% CO_2). Slices were immediately transferred to a storage chamber containing artificial cerebral spinal fluid (ACSF) containing: NaCl (125 mM), $NaHCO_3$ (25 mM), KCl (2.5 mM), NaH_2PO_4 (1.25 mM), $MgCl_2$ (2 mM), $CaCl_2$ (2.5 mM) and glucose (11 mM), pH 7.4, constantly bubbled with 95% O_2 and 5% CO_2; 315–320 mOsm. Slices were maintained at 35 °C in ACSF for 60 min and then kept at room temperature before their transfer to the recording chamber. During the recordings, the slices were continuously perfused with ACSF at 35.0 ± 2.0 °C throughout the experiments. Neurons were visualized with a LNScope (Luigs & Neumann) equipped with an oblique illumination condenser, a 60x objective (LUMPplanFI, NA 0.9) and a reflected illuminator (Olympus). Slices were illuminated with a collimated LED infrared light source (Thorlabs) and wLS LED illumination unit (Q-imaging). The recorded neurons in the VTA were identified by their anatomical localization and recorded if they were labelled with red retrobeads (or by morphology for recording from non-retrobead labelled cells). Their dopaminergic identity was subsequently confirmed by immunohistochemistry. Neuronal activity was recorded at the somata with borosilicate glass pipettes (4–6 MΩ) filled with an intracellular solution containing: K-gluconate (125 mM), KCl (20 mM), HEPES (10 mM), EGTA (10 mM), $MgCl_2$ (2 mM), Na_2ATP (2 mM), Na_2-phosphocreatine (1 mM), Na_3GTP (0.3 mM), 0.2% biocytin, pH 7.2 (with KOH); 312.3 mOsm. Electrophysiological recordings were obtained using a Multiclamp 700B amplifier and digitized at 10 kHz. Recording of spontaneous firing activity in VTA in dopaminergic neurons was achieved in voltage clamp cell-attached configuration after formation of a gigaseal.

Baseline activity was recorded during 2 or 3 min (sweeps of 5 s duration were acquired every 10 s) before oxytocin (1 µM; TOCRIS, 1910) applied to the perfusion reached the recording chamber. Recordings in the presence of oxytocin were continued for 3 min. At the end of these recordings, a whole-cell configuration in voltage clamp (holding potential: −55 mV) was achieved by disruption of the gigaseal with gentle negative pressure applied through the recording pipette. A period of 5 min was then allowed for loading the neurons with biocytin. Finally, the recording pipette was carefully removed and the slice transferred to paraformaldehyde (4% in PBS) for subsequent anatomical analysis. All TH$^+$ cells, including cells negative for retrobeads, were used to analyse frequency. Only TH$^+$ and retrobead positive cells recorded for a minimum of 3 min after OXT application were used to analyse OXT response, and all data points represent an average per minute. I_h recordings were performed in whole-cell voltage-clamp configuration after compensating the pipette capacitance and the series resistance (R_s) (15–20 MΩ; 40–50%, bandwidth 3.5 kHz). R_s was monitored on-line and the experiments were discarded if the R_s changed >20%.

Neuronal input resistances (R_i) and membrane capacitances were evaluated for each neuron by injecting a voltage command of −5 mV for 200 ms duration, from a holding potential (HP) of −50 mV. The electrical capacitance of the neurons was determined by fitting a bi-exponential function to the capacitive current at the beginning of a −5 mV pulse (pipette capacitance was previously compensated during the cell-attached configuration prior whole-cell formation). The amplitude-weighted time constant (τ_{vc}) and measured current peak (I_{peak}) amplitude was inserted into the following formula to calculate the electrical capacitance.

$$C\ [pF] = \frac{\text{weighted } \tau_{vc}\ [\text{ms}] \times I_{\text{peak}}\ [\text{pA}]}{5\ [\text{mV}]}$$

Weighted τ_{vc} was calculated from the bi-exponential fitting as:

$$\tau_{vc} = \frac{(\text{A1} \times \tau_1) + (\text{A2} \times \tau_2)}{\text{A1} + \text{A2}}$$

I_h was evoked by injecting a series of 1.5 s duration hyperpolarizing voltage commands (V_{comm}) from a HP of −50 mV to −130 mV, in consecutive steps of 10 mV. $I_{h\text{-tail}}$ currents were evoked at −130 mV at the end of each V_{comm} before returning the HP to -50 mV. $I_{h\text{-tail}}$ voltage dependency was calculated by plotting their normalized amplitudes. Maximal $I_{h\text{-tail}}$ currents (I_{max}) as defined as recorded after the V_{comm} to −130 mV, was set to 1; minimal $I_{h\text{-tail}}$ currents (I_{min}) as recorded after the HP of −50 mV, was set to 0. A Boltzmann function was fitted: $I = I_{min} + (I_{max} - I_{min})/1 + \exp[(V_{50} - V_{comm})/s]$; in which V_{50} is the half-activation potential and s is the slope factor. After recording the I_h, each cell was switched to current clamp mode to record the resting membrane potential. The experimenter was blinded to the genotype and treatment condition.

Analysis of mRNA translation

Translation in the VTA was analysed using FUNCAT[55,56], in which AHA is incorporated into cells and then detected using an alkyne tagged to Alexa 488. Mice were anaesthetized at P28 and 250-µm thick horizontal slices were cut on a vibratome and placed in ACSF for 45 min at 35 °C to recover. The same cutting solution and ACSF as described for electrophysiology was used. Slices were moved to an incubation chamber and incubated for an additional 3 h with 1 mM AHA (Jena Bioscience, CLK-AA005). At the end of incubation, slices were transferred to ice-cold 4% paraformaldehyde (PFA) and left overnight at 4 °C. The next day, slices were incubated for 1.5 h in a blocking solution containing 5% BSA (Sigma), 5% normal donkey serum and 0.3% Trition X-100 in 1× PBS at agitation at room temperature. Slices were then washed 3 × 5 min followed by incubation over night with gentle agitation with 500 µl Click-iT reaction cocktail according to the manual instructions (Click-iT Cell Reaction Buffer Kit, Invirogen, C10269). Slices were then washed 3 × 10 min with 1× PBS followed by incubation with anti-TH (Millipor, AB1542, 1:1,000) primary antibody at room temperature for 2 h, washed three times in 1× PBS, followed by incubation for 2 h at room temperature with a secondary antibody. The sections were then washed three times in 1× PBS before mounted onto microscope slides with ProLong Gold antifade (Invitrogen, p36930). Images were taken on an Olympus SpinSR spinning disk with a UPL S APO 30× objective (NA 1.5). All images were taken with the same laser power, gain and exposure settings, and analysed using ImageJ. For analysis of AHA incorporation, 10 images were taken of the VTA and the Alexa-488 mean fluorescent intensity of 9–20 regions of interest (ROI) corresponding to TH$^+$ somas were measured. The mean fluorescent intensity of cells per image was used for analysis, and the experimenter was blinded to genotype and treatment. All images within each experiment were processed in parallel using identical settings in ImageJ (NIH) and Adobe Photoshop CS 8.0 (Adobe systems).

For puromycin incorporation, 400-µm thick coronal slices were cut on a vibratome and placed in ACSF (in mM: 125 NaCl, 2.5 KCl, 1 $MgCl_2$, 2 $CaCl_2$, 1.25 NaH_2PO_4, 20 glucose, 26 $NaHCO_3$, 95% O_2, 5% CO_2) for 30 min at room temperature followed by 2 h at 32 °C. Puromycin (5 µg µl^{-1}; Sigma) was added for 45 min to label newly synthesized proteins. Sections were snap frozen and subsequently lysed in 10 mM HEPES, 1% SDS, 1 mM NaF, 1 mM $NaVO_4$ containing protease and phosphatase inhibitor cocktail (Roche Applied Science), sonicated and incubated for 10 min at 95 °C. Puromycin incorporation was measured by western blot (see 'Western blot and AlphaLISA immunoassay') using mouse anti-puromycin antibody (EQ0001), Kerafast). The results were normalized to signal obtained with anti-calnexin antibodies run at the same time on a different blot.

Western blot and AlphaLISA immunoassay

Cortical neurons and brain tissue were homogenized in lysis buffer containing 137 mM NaCl, 2.7 mM KCl, 10 mM Na_2HPO_4, 1.8 mM KH_2PO_4, 5 mM EDTA, 1% Triton X-100 and complete protease and phosphatase inhibitors (Roche Applied Science). Immunoblotting was done with HRP-conjugated secondary antibodies and Pierce ECL Western Blotting Substrate. The following primary antibody was used in this study: p-eIF4E (Abcam, ab76256 1:1000), eIF4E (Abcam, ab47482 1:1,000), p-ERK1/2 (Cell Signaling, 4370S 1:1,000), ERK1/2 (Cell Signaling, 4695S 1:1,000), p-eIF4G (Cell Signaling, 2441S 1:1,000), eIF4G (Cell Signaling, 2498 1:1,000), p-MNK1 (Cell Signaling, 2111, 1:1,000), MNK1 (Cell Signaling, 2195S, 1:1,000), GAPDH (Cell Signaling, 5174 1:2,000) and calnexin (Stressgen, SPA-865 1:2,000). Loading controls were run on the same gel, and for some experiments Mini PROTEAN TGX Stain-Free Gels (Bio-Rad) were used as loading controls. Signals were acquired using an image analyser (Bio-Rad, ChemiDoc MP Imaging System) and images were analysed and prepared using ImageJ.

For additional measurements of eIF4E phosphorylation state, the AlphaLISA SureFire Ultra p-eIF4E (Ser209) Assay Kits (PerkinElmer) were used according to the manufactures protocol. AlphaLISA signals were measured using a Tecan SPARK plate reader on recommended settings.

Immunohistochemistry and imaging

Animals were transcardially perfused with fixative (4% paraformaldehyde in 100 mM phosphate buffer, pH 7.4) at P26–P32. Brains were post-fixed overnight at 4 °C, incubated in 30% sucrose in 1× PBS for 48 h, and snap frozen on dry ice. Tissues were sectioned at 35 µm on a cryostat (Microm HM650, Thermo Scientific). Floating sections were kept in 1× PBS before incubation with blocking solution containing 0.5% Triton X-100 in 1× TBS and 10% normal donkey serum. The slices were incubated with primary antibody at 4 °C overnight and washed three times in 1x TBS containing 0.5% Triton X-100, followed by incubation for 2 h at room temperature with a secondary antibody. The sections were washed three times in 1× TBS containing 0.5% Triton X-100 before mounted onto microscope slides with ProLong Gold antifade (Invitrogen, p36930). For post hoc confirmation of TH-positive cells after electrophysiology, the sections were fixed in the same fixative as described above, washed three times with 1× PBS before blocking and incubation with anti-TH antibody using same method as above. The following primary antibodies were used for this study: sheep anti-TH (Millipor, AB1542, 1:1,000) and mouse-anti neurophysin-1 (Millipore, MABN844, 1:2,000). Secondary antibodies used were: donkey anti-sheep IgG-Cy3 (713-165-147), donkey anti-sheep Cy5 (713-175-147), donkey anti-rabbit IgG Cy3 (711-165-152), goat anti-mouse Cy2 (714-225-150) all from Jackson ImmunoResearch. Streptavidin DyLight 488 (Thermo Scientific 21832, 1 mg ml^{-1}), was used to visualize biocytin. Hoechst dye was co-applied with the secondary antibody at a final concentration of 0.5 µg ml^{-1}. Images were acquired on a custom-made dual spinning disk microscope (Life Imaging Services GmbH) using 10× and 40× objectives. Images were taken bilaterally along the whole VTA and PVN dorso-ventral axis and images from at least four (VTA) or five (PVN) planes were analysed. OXT$^+$ cells in the PVN were counted manually. Neurophysin-1 area coverage and puncta intensity was measured using the particle measurement tool in ImageJ on sum projections. All images within each experiment were processed in parallel with identical settings using ImageJ and Adobe Photoshop CS 8.0 (Adobe systems).

FISH

Mice were deeply anaesthetized using isoflurane inhalation. Brains were quickly removed and snap frozen on dry ice before storage at −80 °C. Brains were cut on a cryostat into 10-µm sections, adhered to Superfrost ultra plus slides (Thermo Scientific) and stored at −80 °C. Sections were fixed for 30 min in 4% PFA before being processed using the RNAscope Fluorescent Multiplex Kit (ACD) according to the manufacturers instruction. The following probes were used: *Oxtr* (C3, 412171), *V1ar* (C3, 418061), *Th* (Slc6a3-C2, 315441) and *Nlgn3* (C1, 497661). Probes were combined as *Oxtr*/*Th*/*Nlgn3* or *V1ar*/*Th*/*Nlgn3*. Amp-4-Alt B were used for all combinations. Sections were imaged on a custom-made dual spinning disk microscope (Life Imaging Services GmbH) using 40× objective, with 12 section *z*-stacks with 0.2 µm in-between *z* sections. Images were processed in ImageJ by doing sum projection of the z-stacks, followed by analysis of fluorescent intensity and number of puncta. Cell types were identified based on the presence of *Th* and DAPI. A ROI was drawn around the cell to define the area using DAPI, and only cells with no adjacent DAPI staining was used to avoid false positives from signals from a second cell. Dots in the ROI were manually counted and fluorescent intensity was analysed using ImageJ. Images were assembled with identical settings using ImageJ and Adobe Photoshop CS 8.0 (Adobe systems).

Cell culture

Cortical cultures were prepared from E16.5 mouse embryos. Neocortices were dissociated by addition of papain (130 units, Worthington Biochemical LK003176) for 30 min at 37 °C. Cells were maintained in neurobasal medium (Gibco 21103-049) containing 2% B27 supplement (Gibco 17504-044), 1% Glutamax (Gibco 35050-038), and 1% penicillin/streptomycin (Sigma P4333). At DIV14, the cells were treated with either vehicle (DMSO) or different doses of ETC-168 for 3 h before collecting for western blot.

Proteomic analysis

VTA tissue was microdissected from coronal sections using anatomical landmarks. Dissected tissue was snap frozen in liquid nitrogen. Successful recovery of proteins from dopaminergic neurons was confirmed by quantitative assessment of enrichment of dopaminergic markers (dopamine transporter, tyrosine hydroxylase, dopamine decarboxylase) as compared to other brain regions (Extended Data Fig. 4a).

Sample preparation for LC–MS analysis. Tissue was washed twice with PBS and dissolved in 50 µl lysis buffer (1% sodium deoxycholate, 0.1 M ammonium bicarbonate), reduced with 5 mM TCEP for 15 min at 95 °C and alkylated with 10 mM chloroacetamide for 30 min at 37 °C. Samples were digested with trypsin (Promega) at 37 °C overnight (protein to trypsin ratio: 50:1). To each peptide samples an aliquot of a heavy reference peptide mix containing 10 chemically synthesized proteotypic peptides (Spike-Tides, JPT) was spiked into each sample at a concentration of 5 fmol of heavy reference peptides per 1 µg of total endogenous protein mass. Then, the peptides were cleaned up using iST cartridges

(PreOmics) according to the manufacturer's instructions. Samples were dried under vacuum and stored at −80 °C until further use.

Targeted PRM-LC–MS analysis of protein isoforms. In a first step, parallel reaction-monitoring (PRM) assays[57] were generated from a mixture containing 100 fmol of each heavy reference peptide and shotgun data-dependent acquisition (DDA) LC–MS/MS analysis on a Thermo Orbitrap Fusion Lumos platform (Thermo Fisher Scientific). The setup of the μRPLC-MS system was as described previously (Pubmed-ID: 27345528). Chromatographic separation of peptides was carried out using an EASY nano-LC 1200 system (Thermo Fisher Scientific), equipped with a heated RP-HPLC column (75 μm × 30 cm) packed in-house with 1.9 μm C18 resin (Reprosil-AQ Pur, Dr. Maisch). Peptides were analysed per LC–MS/MS run using a linear gradient ranging from 95% solvent A (0.15% formic acid, 2% acetonitrile) and 5% solvent B (98% acetonitrile, 2% water, 0.15% formic acid) to 45% solvent B over 60 min at a flow rate of 200 nl min^{-1}. Mass spectrometry analysis was performed on Thermo Orbitrap Fusion Lumos mass spectrometer equipped with a nanoelectrospray ion source (both Thermo Fisher Scientific). Each MS1 scan was followed by high-collision-dissociation (HCD) of the 10 most abundant precursor ions with dynamic exclusion for 20 s. Total cycle time was approximately 1 s. For MS1, 1×10^6 ions were accumulated in the Orbitrap cell over a maximum time of 100 ms and scanned at a resolution of 120,000 FWHM (at 200 *m*/*z*). MS2 scans were acquired at a target setting of 1×10^5 ions, accumulation time of 50 ms and a resolution of 30,000 FWHM (at 200 *m*/*z*). Singly charged ions and ions with unassigned charge state were excluded from triggering MS2 events. The normalized collision energy was set to 30%, the mass isolation window was set to 1.4 *m*/*z* and one microscan was acquired for each spectrum.

The acquired raw-files were database searched against a mouse database (Uniprot, download date: 19 April 2017, total of 34,490 entries) by the MaxQuant software (v.1.0.13.13). The search criteria were set as following: full tryptic specificity was required (cleavage after lysine or arginine residues); three missed cleavages were allowed; carbamidomethylation (C) was set as fixed modification; Arg10 (R), Lys8 (K) and oxidation (M) as variable modification. The mass tolerance was set to 10 ppm for precursor ions and 0.02 Da for fragment ions. The best six transitions for each peptide were selected automatically using an in-house software tool and imported to Skyline (v.1; https://brendanx-uw1.gs.washington.edu/labkey/project/home/software/Skyline/begin.view). A mass isolation lists containing all selected peptide ion masses were exported form Skyline, split into eight mass lists by charge, C-terminal amino acid and transition and precursor ions. The mass lists were then imported into the Lumos operating software for SureQuant analysis using the following settings: The resolution of the orbitrap was set to 30 k (120 k) FWHM (at 200 *m*/*z*) for heavy (light) peptide ions and the fill time was set to 54 (246) ms, respectively, to reach a target value of 1×10^6 ions. Ion isolation window was set to 0.4 thomson (Th) and the scan range was set to 150–1,500 Th. The mass window for triggering heavy PRM scans was set to 10 ppm and the depended PRM triggering threshold for the light channel was set to a minimum of 2 detected transitions. A MS1 scan using the same conditions are for DDA was included in each MS cycle. Each condition was analysed in biological quadruplicates or quintuplicates. All raw-files were imported into Skyline for protein / peptide quantification. To control for variation in sample amounts, the total ion chromatogram (only comprising peptide ions with two or more charges) of each sample was determined by Progenesis QI (v.2.0, Waters) and used for normalization. A summary of the peptides used is shown in Supplementary Table 1.

Global proteome analysis using shotgun proteomics

One microgram of peptides of each sample was subjected to LC–MS analysis using a using a Q-Exactive HF mass spectrometer connected to an electrospray ion source (both Thermo Fisher Scientific) as recently specified[58] and a custom-made column heater set to 60 °C. In brief, peptide separation was carried out using an EASY nLC-1000 system (Thermo Fisher Scientific) equipped with a RP-HPLC column (75 μm × 30 cm) packed in-house with C18 resin (ReproSil-Pur C18–AQ, 1.9 μm resin; Dr. Maisch GmbH) using a linear gradient from 95% solvent A (0.1% formic acid, 2% acetonitrile) and 5% solvent B (98% acetonitrile, 0.1% formic acid) to 45% solvent B over 60 min at a flow rate of 0.2 μl min^{-1}. A total of 3×10^6 and 1×10^5 ions were accumulated for MS1 and MS2, respectively, and scanned at a resolution of 60,000 and 15,000 FWHM (at 200 *m*/*z*). Fill time was set to 110 ms for MS1 and 50 ms for MS2 scans. For MS2, a normalized collision energy of 28% was used, the ion isolation window was set to 1.4 Th and the first mass was fixed to 100 Th. To determine changes in protein expressions across samples, a MS1 based label-free quantification was carried out. Therefore, the generated raw files were imported into the Progenesis QI software (Nonlinear Dynamics, v.2.0) and analysed using the default parameter settings. MS/MS-data were exported directly from Progenesis QI in mgf format and searched against a decoy database of the forward and reverse sequences of the predicted proteome from *Mus musculus* (Uniprot, download date: 18 April 2017, total of 34,490 entries) using MASCOT (v.2.4.1). The search criteria were set as following: full tryptic specificity was required (cleavage after lysine or arginine residues); three missed cleavages were allowed; carbamidomethylation (C) was set as fixed modification; oxidation (M) as variable modification. The mass tolerance was set to 10 ppm for precursor ions and 0.02 Da for fragment ions. Results from the database search were imported into Progenesis QI and the final peptide measurement list containing the peak areas of all identified peptides, respectively, was exported. This list was further processed and statically analysed using our in-house developed SafeQuant R script (SafeQuant; https://github.com/eahrne/SafeQuant[58]). The peptide and protein false discovery rate was set to 1% using the number of reverse hits in the data set. All quantitative analyses were performed in biological quintuplicates. Proteins with less than 1 peptide were excluded from the analysis.

The results details of the proteomics experiments carried out including identification scores, number of peptides quantified, normalized (by sum of all peak intensities) peak intensities, $\log_2$-transformed ratios, coefficients of variations and p-values for each quantified protein. A summary is displayed in Supplementary Table 2.

Global proteome analysis using tandem mass tags

Sample aliquots (prepared as described above) containing 10 μg of peptides were dried and labelled with tandem mass isobaric tags (TMTpro 16-plex, Thermo Fisher Scientific) according to the manufacturer's instructions. To control for ratio distortion during quantification, a peptide calibration mixture consisting of six digested standard proteins mixed in different amounts were added to each sample before TMT labelling as recently described[58]. After pooling the differentially TMT labelled peptide samples, peptides were again desalted on C18 reversed-phase spin columns according to the manufacturer's instructions (Macrospin, Harvard Apparatus) and dried under vacuum. TMT-labelled peptides were fractionated by high-pH reversed phase separation using a XBridge Peptide BEH C18 column (3.5 μm, 130 Å, 1 mm × 150 mm, Waters) on an Agilent 1260 Infinity HPLC system. Peptides were loaded on column in buffer A (ammonium formate (20 mM, pH 10) in water) and eluted using a two-step linear gradient starting from 2% to 10% in 5 min and then to 50% (v/v) buffer B (90% acetonitrile/10% ammonium formate (20 mM, pH 10) over 55 min at a flow rate of 42 μl min^{-1}. Elution of peptides was monitored with a UV detector (215 nm, 254 nm). A total of 36 fractions were collected, pooled into 12 fractions using a post-concatenation strategy as previously described[59], dried under vacuum.

Aliquots of 1 μg of peptides were analysed by LC–MS as previously described[58]. Chromatographic separation of peptides was carried out using an EASY nano-LC 1000 system (Thermo Fisher Scientific), equipped with a heated RP-HPLC column (75 µm × 37 cm) packed in-house with 1.9 µm C18 resin (Reprosil-AQ Pur, Dr. Maisch). Aliquots of 1 µg total peptides were analysed per LC–MS/MS run using a linear gradient ranging from 95% solvent A (0.15% formic acid, 2% acetonitrile) and 5% solvent B (98% acetonitrile, 2% water, 0.15% formic acid) to 30% solvent B over 90 min at a flow rate of 200 nl min^{-1}. Mass spectrometry analysis was performed on Q-Exactive HF mass spectrometer equipped with a nanoelectrospray ion source (both Thermo Fisher Scientific). Each MS1 scan was followed by high-collision-dissociation (HCD) of the 10 most abundant precursor ions with dynamic exclusion for 20 s. Total cycle time was approximately 1 s. For MS1, 3×10^6 ions were accumulated in the Orbitrap cell over a maximum time of 100 ms and scanned at a resolution of 120,000 FWHM (at 200 m/z). MS2 scans were acquired at a target setting of 1×10^5 ions, accumulation time of 100 ms and a resolution of 30,000 FWHM (at 200 m/z). Singly charged ions and ions with unassigned charge state were excluded from triggering MS2 events. The normalized collision energy was set to 35%, the mass isolation window was set to 1.1 m/z and one microscan was acquired for each spectrum.

The acquired raw-files were searched against a protein database containing sequences of the predicted SwissProt entries of *Mus musculus* (www.ebi.ac.uk, release date 27 March 2019), the six calibration mix proteins[58] and commonly observed contaminants (in total 17,412 sequences) using the SpectroMine software (Biognosys, v.1.0.20235.13.16424) and the TMT 16-plex default settings. In brief, the precursor ion tolerance was set to 10 ppm and fragment ion tolerance was set to 0.02 Da. The search criteria were set as follows: full tryptic specificity was required (cleavage after lysine or arginine residues unless followed by proline), 3 missed cleavages were allowed, carbamidomethylation (C), TMTpro (K and peptide n-terminus) were set as fixed modification and oxidation (M) as a variable modification. The false identification rate was set to 1% by the software based on the number of decoy hits. Proteins that contained similar peptides and could not be differentiated based on MS/MS analysis alone were grouped to satisfy the principles of parsimony. Proteins sharing significant peptide evidence were grouped into clusters. Acquired reporter ion intensities in the experiments were employed for automated quantification and statically analysis using a modified version of our in-house developed SafeQuant R script (v.2.3)[58]. This analysis included adjustment of reporter ion intensities, global data normalization by equalizing the total reporter ion intensity across all channels, summation of reporter ion intensities per protein and channel, calculation of protein abundance ratios and testing for differential abundance using empirical Bayes moderated t-statistics. Finally, the calculated P values were corrected for multiple testing using the Benjamini–Hochberg method. A summary is shown in Supplementary Table 3.

GO, network and gene set enrichment analysis

GO analysis was performed using DAVID classification system (https://david.ncifcrf.gov). Proteins significantly different between vehicle treated wild type and $Nlgn3^{KO}$ ($P < 0.05$) were compared to all proteins detected in the proteomic screen using the GO GOTERM_BP_DIRECT annotation dataset with minimum number of hits set to five and maximum P value threshold to 0.05 with Benjamini correction ($P < 0.05$). Network analysis was obtained using String v11 database[61]. Each node represents a protein altered in $Nlgn3^{KO}$ VTA compared to wild-type VTA in vehicle-treated conditions, and each edge show protein–protein interaction as determined by experiments and databases. The highest confidence (0.900) was used for interaction scores. Disconnected nodes and networks containing more than six proteins were removed. Gene set enrichment analysis for TMT proteomic data was performed using all proteins detected with at least two peptides with PSEA-Quant[45]. The list of GO terms with $Q < 0.01$ were summarized using REVIGO[62] with small (0.5) allowed similarity, and displayed using Cytoscape.

Statistical analysis

No statistical methods were used to predetermine sample size. The animals were randomly assigned to each group the moment of drug treatment, and a minimum of three independent cohorts were used for behavioural experiments. Statistical analysis was conducted with GraphPad Prism 8. The normality of sample distributions was assessed and when violated non-parametrical tests were used. When normally distributed, the data were analysed with unpaired t-test for comparison between two groups, while for multiple comparisons one-way ANOVA and repeated-measures ANOVA were used. For the analysis of variance with two factors (two-way ANOVA, repeated-measures two-way ANOVA and repeated measures two-way ANOVA by both factors), normality of sample distribution was assumed, and followed by Bonferroni post hoc test. Differences in frequency distribution were assessed using the Kolmogorov–Smirnov test. All the statistical tests adopted were two-sided. When comparing two samples distributions similarity of variances was assumed, therefore no corrections were adopted. Outliers were identified using ROUTS test on the most stringent setting ($Q = 0.1\%$). Data are represented as the mean ± s.e.m. and the significance was set at $P < 0.05$.

Reporting summary

Further information on research design is available in the Nature Research Reporting Summary linked to this paper.

Data availability

Raw mass spectrometry data associated with the manuscript have been deposited in to the ProteomeXchange Consortium via the PRIDE[60] partner repository with the dataset identifier PXD018808 and 10.6019/PXD018808. All renewable reagents and detailed protocols will be made available on request. Source data are provided with this paper.

48. The Dutch-Belgian Fragile X Consortium. Fmr1 knockout mice: a model to study fragile X mental retardation. *Cell* **78**, 23–33 (1994).
49. El-Brolosy, M. A. et al. Genetic compensation triggered by mutant mRNA degradation. *Nature* **568**, 193–197 (2019).
50. Turiault, M. et al. Analysis of dopamine transporter gene expression pattern — generation of DAT-iCre transgenic mice. *FEBS J.* **274**, 3568–3577 (2007).
51. Weigelt, S., Koldewyn, K. & Kanwisher, N. Face identity recognition in autism spectrum disorders: a review of behavioral studies. *Neurosci. Biobehav. Rev.* **36**, 1060–1084 (2012).
52. McPartland, J. C., Webb, S. J., Keehn, B. & Dawson, G. Patterns of visual attention to faces and objects in autism spectrum disorder. *J. Autism Dev. Disord.* **41**, 148–157 (2011).
53. Dantzer, R., Bluthe, R. M., Koob, G. F. & Le Moal, M. Modulation of social memory in male rats by neurohypophyseal peptides. *Psychopharmacology (Berl.)* **91**, 363–368 (1987).
54. Mitre, M., Minder, J., Morina, E. X., Chao, M. V. & Froemke, R. C. Oxytocin Modulation of Neural Circuits. *Curr. Top. Behav. Neurosci.* **35**, 31–53 (2018).
55. Tom Dieck, S. et al. Metabolic labeling with noncanonical amino acids and visualization by chemoselective fluorescent tagging. *Curr. Protoc. Cell Biol.* **Chapter 7**, Unit7.11 (2012).
56. Bowling, H. et al. BONLAC: A combinatorial proteomic technique to measure stimulus-induced translational profiles in brain slices. *Neuropharmacology* **100**, 76–89 (2016).
57. Peterson, A. C., Russell, J. D., Bailey, D. J., Westphall, M. S. & Coon, J. J. Parallel reaction monitoring for high resolution and high mass accuracy quantitative, targeted proteomics. *Mol. Cell. Proteomics* **11**, 1475–1488 (2012).
58. Ahrné, E. et al. Evaluation and improvement of quantification accuracy in isobaric mass tag-based protein quantification experiments. *J. Proteome Res.* **15**, 2537–2547 (2016).
59. Wang, Y. et al. Reversed-phase chromatography with multiple fraction concatenation strategy for proteome profiling of human MCF10A cells. *Proteomics* **11**, 2019–2026 (2011).
60. Vizcaíno, J. A. et al. 2016 update of the PRIDE database and its related tools. *Nucleic Acids Res.* **44** (D1), D447–D456 (2016).
61. Szklarczyk, D. et al. STRING v11: protein-protein association networks with increased coverage, supporting functional discovery in genome-wide experimental datasets. *Nucleic Acids Res.* **47** (D1), D607–D613 (2019).
62. Supek, F., Bošnjak, M., Škunca, N. & Šmuc, T. REVIGO summarizes and visualizes long lists of gene ontology terms. *PLoS One* **6**, e21800 (2011).
63. DiBenedictis, B. T., Nussbaum, E. R., Cheung, H. K. & Veenema, A. H. Quantitative mapping reveals age and sex differences in vasopressin, but not oxytocin, immunoreactivity in the rat social behavior neural network. *J. Comp. Neurol.* **525**, 2549–2570 (2017).

Acknowledgements We are grateful to A. Gomez, K. Tan, L. Traunmüller and F. Filice for comments on the manuscript and to members of the Scheiffele laboratory for discussions. We thank B. Boury Jamot for performing tests on $Fmr1^{KO}$ mice, F. Filice for experimental support, and A. Schmidt and the Biozentrum Proteomics Core Facility for conducting proteomics analysis. Funding: H.H. was supported by a Long-term Fellowship from the Human Frontiers Science Program. This work was supported by funds to P.S. from the Swiss National Science Foundation, a European Research Council Advanced Grant (SPLICECODE), EU-AIMS and AIMS-2-TRIALS which are supported by the Innovative Medicines Initiatives from the European Commission. The results leading to this publication has received funding from the Innovative Medicines Initiative 2 Joint Undertaking under grant agreement no. 777394. This Joint Undertaking receives support from the European Union's Horizon 2020 research and innovation programme and EFPIA and AUTISM SPEAKS, Autistica, SFARI. The Scheiffele Laboratory is an associate member of the Swiss National Science Foundation's National Competence Centre for Research (NCCR) RNA and Disease. F.M. was supported by NCCR SYNAPSY. Discovery of ETC-168 was financially supported by Biomedical Sciences Institutes (BMSI) and Joint Council Office (JCO Project 11 03 FG 07 05), Agency for Science, Technology and Research (A*STAR), Singapore.

Author contributions This work was jointly conceived by H.H. and P.S. and built on initial findings by S.B. and P.S. MNK inhibitors were developed by A.M. and K.N.; behavioural assays were developed by H.H. and F.M.; experimental procedures were performed by H.H., D.S., F.M., L.H.-B., S.B. and E.P.-G.; and data analysis was conducted by H.H., D.S., E.P.-G., F.M., P.S. and E.P.-V. The manuscript was jointly written by H.H. and P.S., with editing provided by E.-P.G., E.P.-V., S.B. and K.N.

Competing interests S.B. P.S. A.M. and K.N. have filed patents on the use of MNK inhibitors for treatment of neurodevelopmental disorders. A.M. and K.N. are current or former employees of the Experimental Drug Development Centre Singapore which has a commercial interest in the development of MNK1/2 inhibitors.

Additional information

Supplementary information is available for this paper at https://doi.org/10.1038/s41586-020-2563-7.

Correspondence and requests for materials should be addressed to P.S.

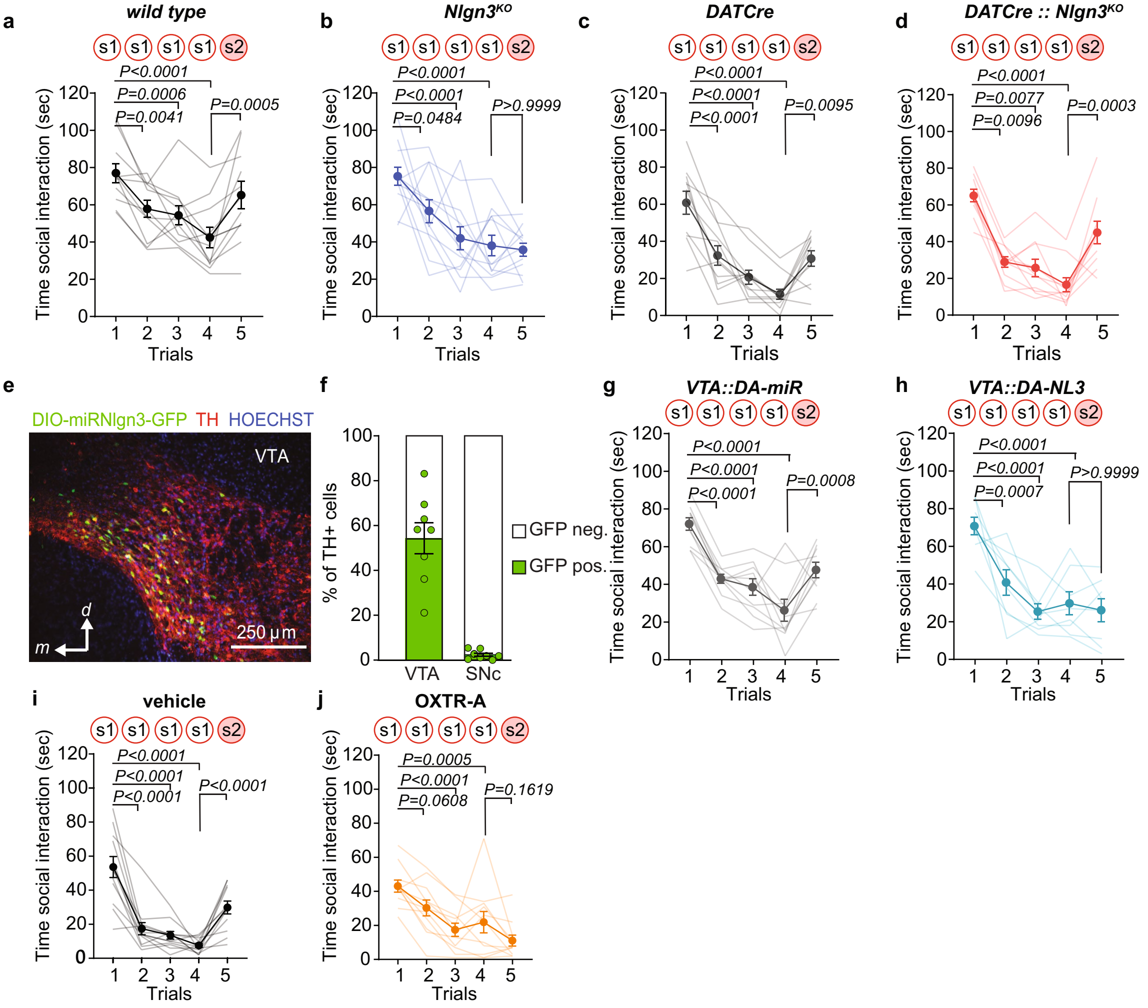

Extended Data Fig. 1 | Loss of social recognition in *Nlgn3*^{KO} mice. a, **b**, Mean social interaction time and data for individual mice in the social habituation/recognition test plotted for wild-type ($n = 11$) (**a**) and *Nlgn3*^{KO} (**b**) mice ($n = 12$). **c**, **d**, Mean social interaction time and data for individual mice plotted for *DAT-cre* control mice ($n = 10$) (**c**) and *DAT-cre::Nlgn3*^{KO} mice ($n = 11$) (**d**). **e**, Example for validation of targeted gene knockdown ($n = 8$ mice) from AAV2-DIO-miR^{Nlgn3}-GFP viruses (green) in TH-positive cells (red) in the VTA of *DAT-cre* mice. **f**, Quantification of percentage of TH-positive cells in VTA and SNc of *DAT-cre* mice that express GFP from the AAV2-DIO-miR-GFP vector ($n = 8$). **g**, **h**, Mean social interaction time and data for individual mice plotted for control mice (**g**, VTA::DA-miR, $n = 10$) and VTA DA-specific *Nlgn3* loss-of-function (**h**, VTA::DA-NL3, $n = 8$) in the social habituation/recognition test. **g**, Mean social interaction time and data for individual mice plotted for mice treated with vehicle ($n = 12$) (**i**) and OXTR-A ($n = 11$) (**j**). All error bars are s.e.m. Repeated-measures one-way ANOVA followed by Bonferroni's post hoc test for planned multiple comparison (**a**–**c**, **g**–**j**) or Friedman test followed by Dunn's post hoc test for planned multiple comparison (**d**). See Supplementary information for additional statistics.

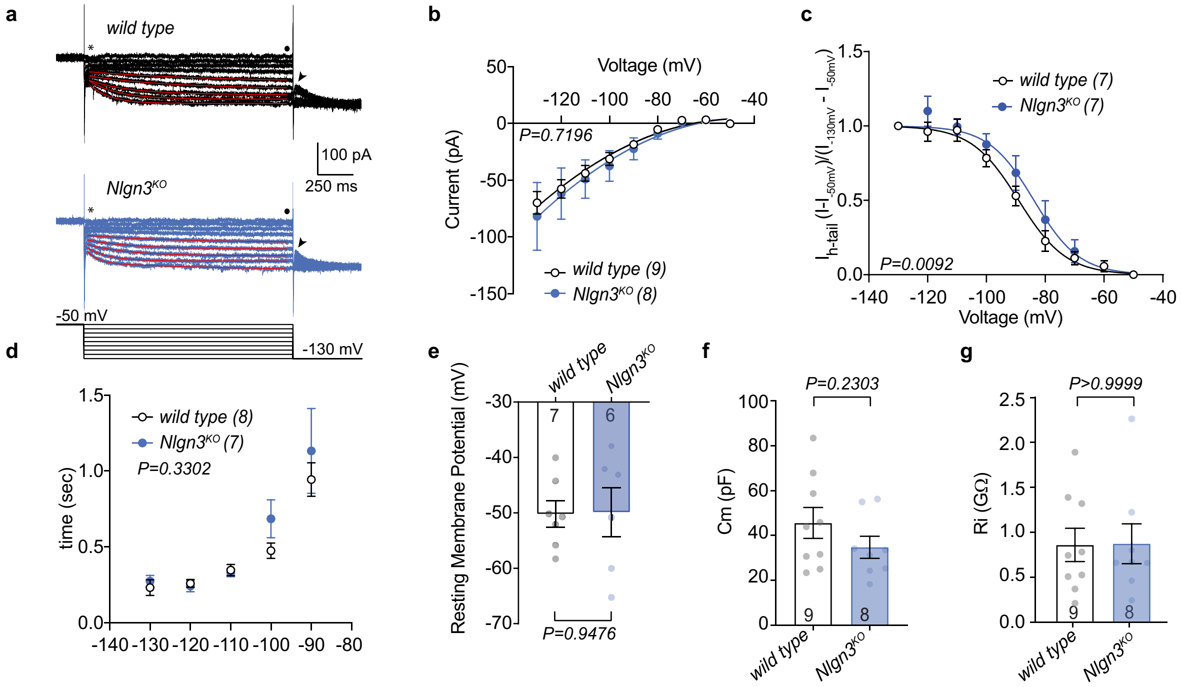

Extended Data Fig. 2 | Properties of NAc-projecting VTA DA neurons in wild-type and *Nlgn3*^{KO} mice. a, Representative I_h currents recorded from wild-type (black) and *Nlgn3*^{KO} (blue) neurons evoked by consecutive hyperpolarizing voltage steps of −10 mV from −50 to −130 mV (bottom). At the end of each voltage step, the voltage command was returned to −130 mV to evoke tail currents ($I_{h\text{-tail}}$, depicted with an arrowhead). Red lines show fit of a single exponential function used to assess the I_h activation kinetics. **b**, Averaged I_h amplitudes were plotted against the voltage step. I_h current amplitudes were measured at the steady state (indicated with a filled circle in **a**) and the leak current values, as defined as the amplitude of the instantaneous currents at the onset of voltage steps (indicated with an asterisk in **a**), subtracted. **c**, Voltage-dependency of $I_{h\text{-tail}}$ currents. $I_{h\text{-tail}}$ amplitudes were normalized relative to $I_{h\text{-tail}}$ at −50 mV and −130 mV. Solid lines show fits with a Boltzmann function for least square fit. The *P* value shows the difference in V50 between datasets. **d**, Activation kinetics of the I_h as determined by the τ values obtained from the exponential fitting, as a function of the voltage commands voltage. Only the values obtained from commands between −130 mV to −90 mV were evaluated. **e**, Comparison between groups of the resting membrane potential as assessed with current clamp recordings. **f**. Membrane capacitance (C_m) of wild-type and *Nlgn3*^{KO} DA neurons. **g**, Input resistant values (R_i) for wild-type and *Nlgn3*^{KO} mice. C_m and R_i values were obtained in voltage clamp mode by applying a −5 mV (200 ms) voltage command from a holding potential set at −50 mV. All error bars are s.e.m. The *P* value represents genotype differences. $n = 5$ mice per genotype, numbers on graphs represent cells. *P* values determined by repeated-measures two-way ANOVA (**b**), Boltzmann sigmoidal test (**c**), mixed-effects model (**d**), unpaired two-sided *t*-test (**e**, **f**), or two-sided Mann–Whitney test (**g**). See Supplementary Information for additional statistics.

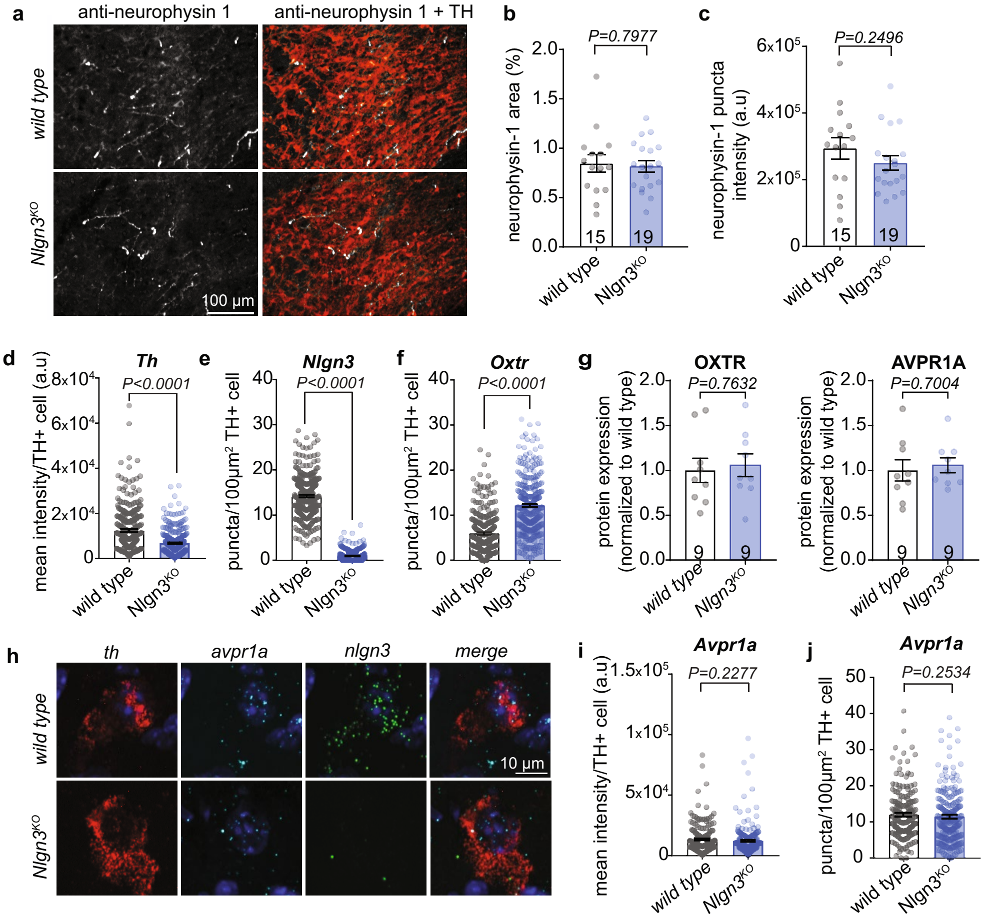

Extended Data Fig. 3 | Oxytocinergic innervation to VTA and *Avpr1a* mRNA levels are not affected in *Nlgn3*^{KO} mice. **a**, Representative images from 3 mice per genotype of neurophysin 1 (green), a cleavage product of the oxytocin neuropeptide precursor that is transported in vesicles together with oxytocin[63], and TH (red) immunofluorescence in the VTA of wild-type and *Nlgn3*^{KO} mice. Note that oxytocinergic axons arise from multiple hypothalamic nuclei, including the paraventricular nucleus. **b**, **c**, Mean VTA area coverage (**b**) and puncta fluorescence in the VTA (**c**) from wild-type and *Nlgn3*^{KO} mice. $n = 3$ mice per genotype. Numbers in brackets represent sections. **d**, Quantification of mean *Th* intensity per TH$^+$ cell. **e**, Quantification of *Nlgn3* puncta per 100 µm^2 TH$^+$ cell. **f**, Quantification of *Oxtr* puncta per 100 µm^2 TH$^+$ cell. n = WT: 280 cells from 4 mice; *Nlgn3*^{KO}: 265 cells from 3 mice (**d**–**f**). **g**, Targeted proteomic (PRM) measurements for oxytocin receptor (OXTR; left) and AVPR1A (right) proteins in VTA. Numbers on bars indicate mice. **h**, Representative images of FISH labelling of *Avrp1a* (cyan), *Th* (red) and *Nlgn3* (green) in the VTA from wild-type and *Nlgn3*^{KO} mice. Experiment was repeated independently twice. **i**, Quantification of mean *Avpr1a* intensity per TH$^+$ cell. **j**, Quantification of *Avpr1a* puncta per 100 µm^2 TH$^+$ cell from wild-type and *Nlgn3*^{KO} VTA. n = wild type: 169 cells from 4 animals; *Nlgn3*^{KO}: 200 cells from 3 mice (**i**, **j**). All error bars are s.e.m. *P* values determined by unpaired two-sided *t*-test (**b**, **c**, **g**), two-sided Mann–Whitney *U* test (**d**–**f**, **i**, **j**). See Supplementary Information for additional statistics.

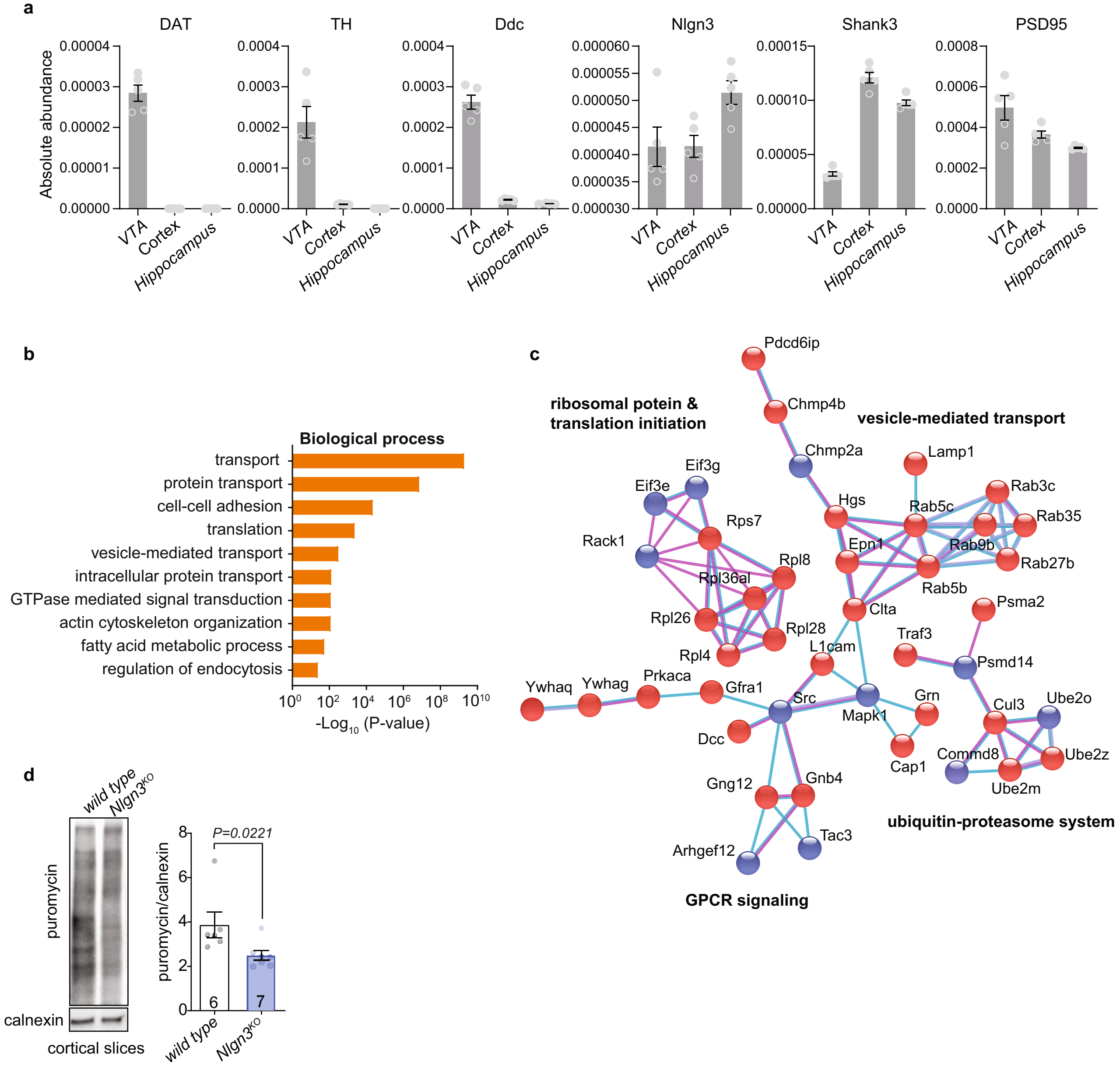

Extended Data Fig. 4 | Ribosomal proteins and translation processes are altered in *Nlgn3*^{KO} mice. a, TMT proteomics: graphs plotting abundance of dopamine markers and synaptic proteins from VTA, cortex and hippocampus. Dopaminergic markers are strongly enriched in VTA samples. $n = 5$ mice per brain region. **b**, **c**, Proteomic analysis of wild-type and *Nlgn3*^{KO} VTA, $n = 5$ mice per genotype. **b**, Enrichment of GO terms for biological processes for proteins significantly altered ($P < 0.05$) in *Nlgn3*^{KO} mice compared to wild-type mice. **c**, Network-based analysis of proteins altered in *Nlgn3*^{KO} VTA ($P < 0.01$). Blue nodes indicate downregulated proteins, red nodes upregulated proteins, light blue lines indicate interactions known from database and purple lines interactions experimentally determined. Disconnected nodes and nodes containing less than six proteins are not shown. See methods for additional information of statistics and analysis parameters. **d**, Mean puromycin incorporation in acute cortical slices from adult wild-type and *Nlgn3*^{KO} mice. All error bars are s.e.m. *P* values determined by two-sided Mann–Whitney *U* test. See Supplementary information for additional statistics.

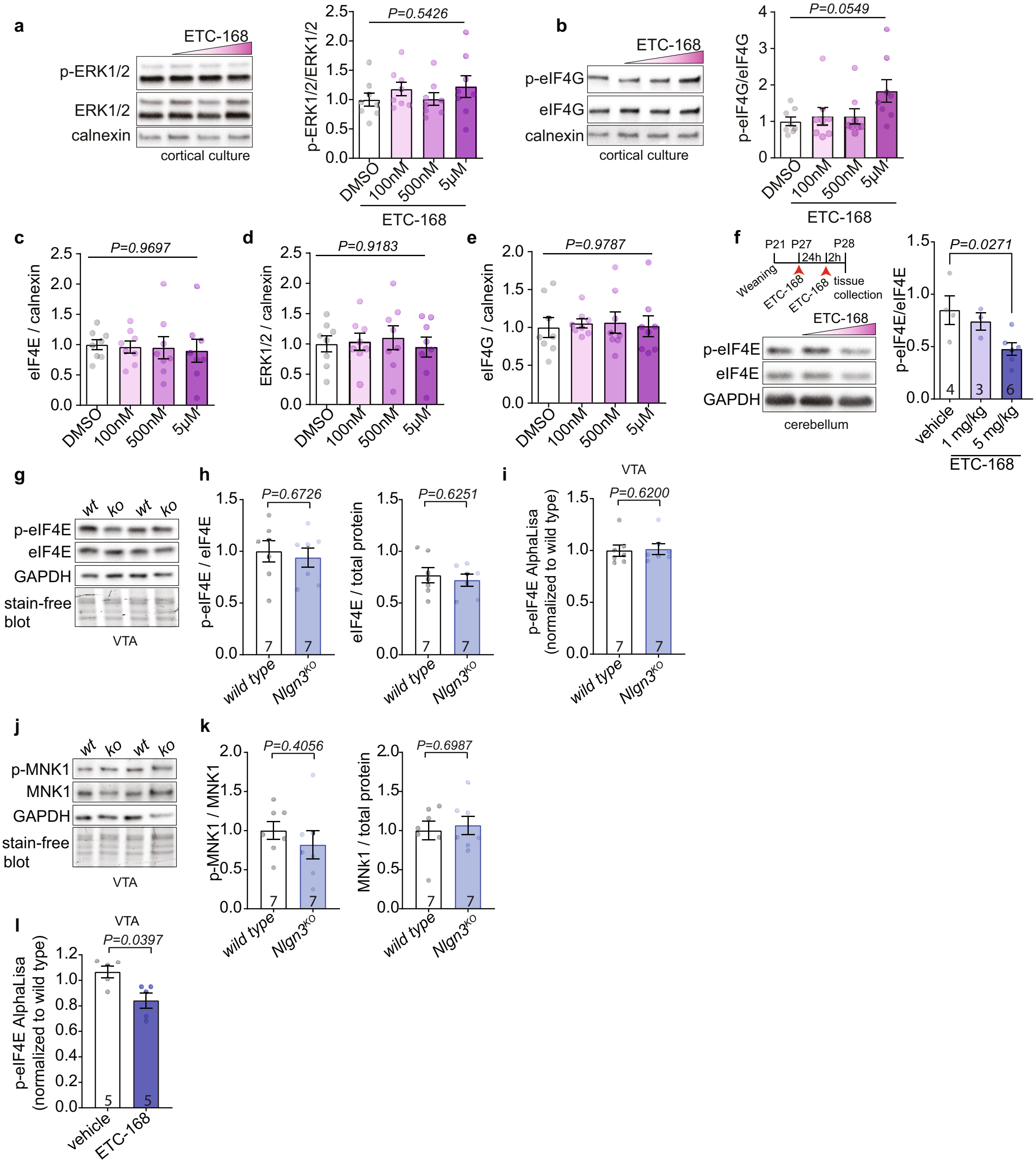

Extended Data Fig. 5 | Pharmacological profile of novel MNK1/2 inhibitor ETC-168. a, **b**, Quantification of p-ERK1/2 (**a**) and p-eIF4G (**b**) levels compared to non-phosphorylated protein in cortical neurons at DIV14 treated with ETC-168. *n* = 8 replicates from 3 independent experiments. **c**, **d**, Quantification of eIF4E (**c**), ERK1/2 (**d**) and eIF4G (**e**) levels normalized to calnexin in cortical neurons at DIV14 treated with ETC-168. *P* values determined by one-way ANOVA. *n* = 8 replicates from 3 independent experiments. **f**, Representative western blot of cerebellar lysate from wild-type mice treated with vehicle or ETC-168 and quantification of p-eIF4E levels compared to eIF4E. *n* = vehicle: 4; 1 mg kg^{-1}: 3; 5 mg kg^{-1}: 6. **g**, Representative western blot of VTA lysate from wild-type and *Nlgn3^{KO}* mice (*n* = 7 mice per genotype). **h**, Quantification of p-eIF4E compared with eIF4E levels in VTA of wild-type mice and *Nlgn3^{KO}* mice. *n* = 7 mice per genotype. **i**, Normalized p-eIF4E AlphaLisa counts from wild-type and *Nlgn3^{KO}* VTA lysate. *n* = 7 mice per genotype. **j**, **k**, Representative western blot (**j**) and quantification (**k**) of p-MNK1 and MNK1 levels in VTA lysate from wild-type mice and *Nlgn3^{KO}* mice. *n* = 7 mice per genotype. **l**, Normalized p-eIF4E AlphaLisa counts from VTA from wild-type treated with 5 mg kg^{-1} ETC-168 for 24 h +2 h. *n* = 5 mice per genotype. All error bars are s.e.m. *P* values determined by one-way ANOVA (**a**, **c**–**f**), Kruskal–Wallis test (**b**), unpaired two-sided *t*-test (**h**, **k**), or two-sided Mann–Whitney test (**i**, **l**). See Supplementary Information for additional statistics.

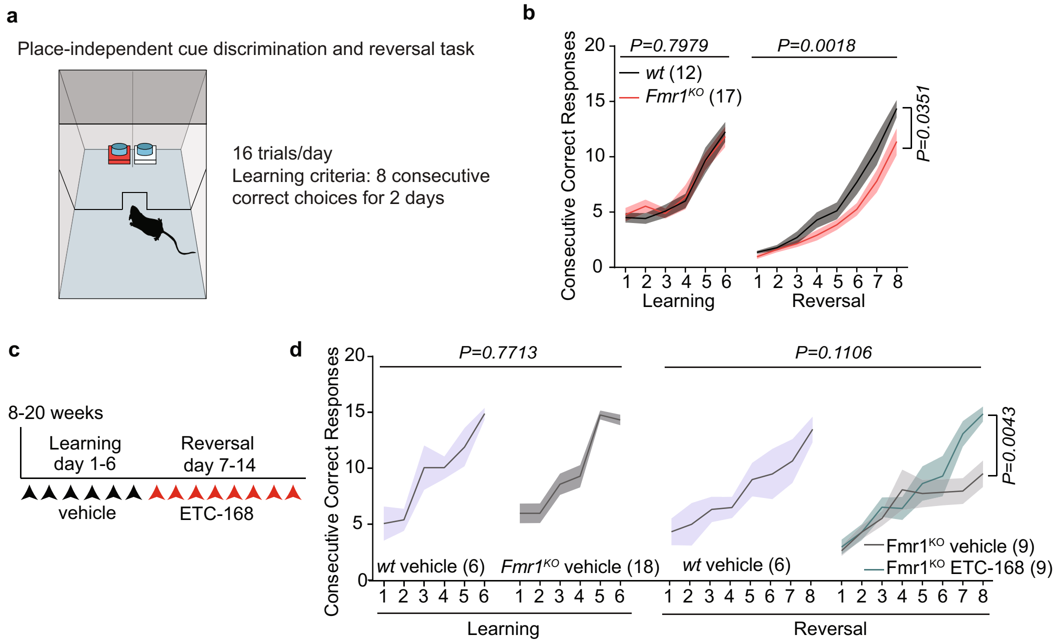

Extended Data Fig. 6 | ETC-168 treatment restores cognitive rigidity in *Fmr1*^{KO} mice. a, Schematics of the place-independent cue discrimination and reversal task. This task was chosen given that phenotypes in cognitive rigidity tasks have been replicated in several studies on this model. **b**, Mean consecutive correct responses plotted for *Fmr1*$^{WT/y}$ and *Fmr1*$^{KO/y}$ mice. **c**, Treatment schedule of *Fmr1*$^{WT/y}$ and *Fmr1*$^{KO/y}$ mice. Mice were treated daily with vehicle during the learning phase and with 5 mg kg^{-1} ETC-168 during the reversal phase 2 h before the start of the test. **d**, Mean conscutive correct responses plotted for vehicle treated *Fmr1*$^{WT/y}$ and vehicle or ETC-168 *Fmr1*$^{KO/y}$ mice. Numbers in brackets indicate mice. Error bars denote s.e.m. *P* values determined by repeated-measures two-way ANOVA followed by Bonferrroni's post hoc test. See Supplementary Information for additional statistics.

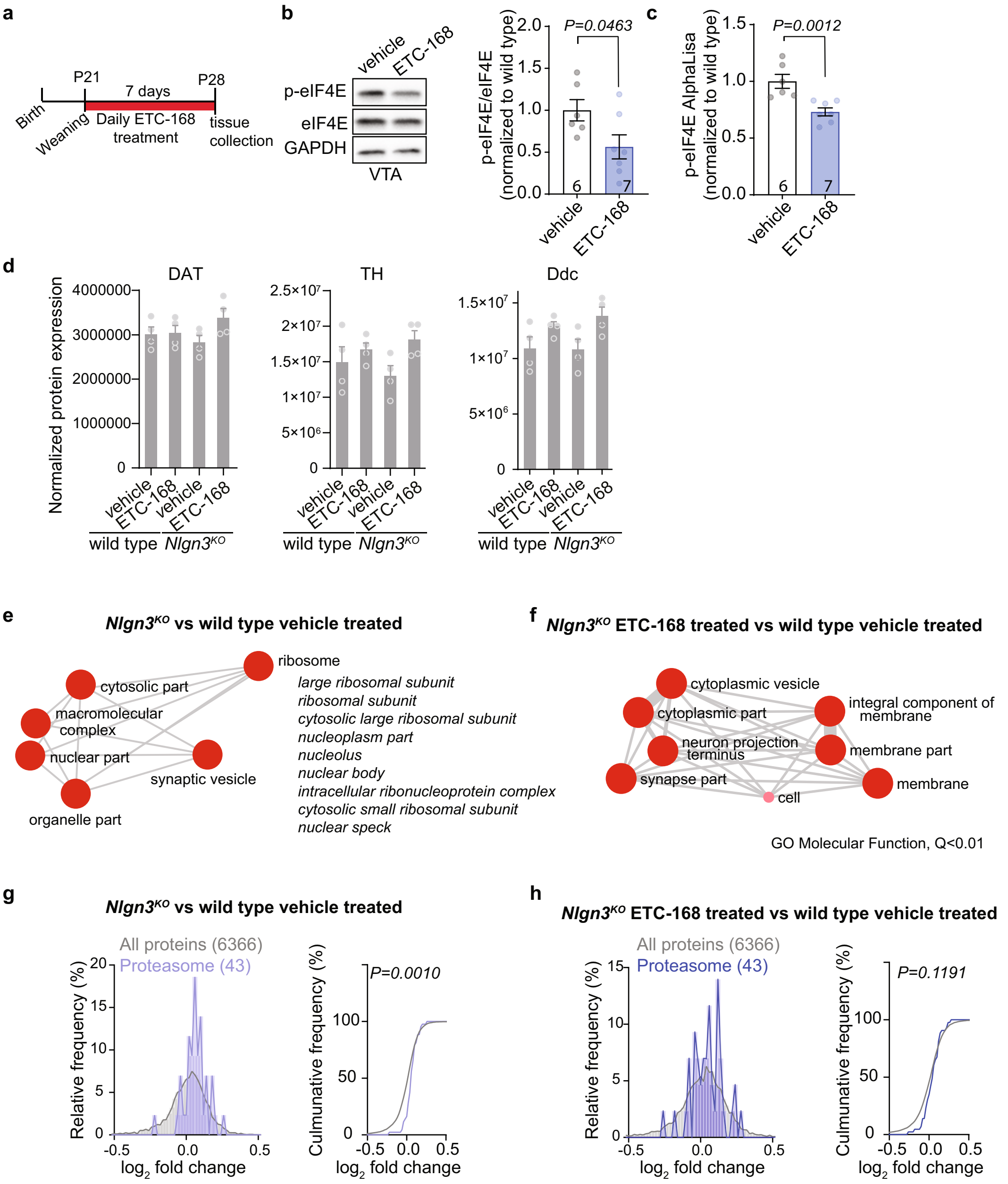

Extended Data Fig. 7 | Effect of ETC-168 treatment on protein abundance in wild-type and *Nlgn3*^{KO} mice. a, Experimental outline. **b**, Representative western blot and quantification of p-eIF4E compared to eIF4E levels in VTA lysate from wild-type mice treated with vehicle or 5 mg kg^{-1} ETC-168 for 7 consecutive days. n = vehicle: 6; ETC-168: 7. **c**, Normalized p-eIF4E AlphaLisa counts from wild-type mice VTA treated with vehicle or 5 mg kg^{-1} ETC-168 for 7 consecutive days. n = vehicle: 6; ETC-168: 7. **d**, Graphs plotting TMT proteomic-normalized protein expression of dopaminergic markers in VTA from wild-type and *Nlgn3*^{KO} mice treated with vehicle or ETC-168. Mice were treated for 7 days. n = 4 mice per genotype and treatment. **e**, **f**, Graphical representation of molecular function GO terms enriched in *Nlgn3*^{KO} versus wild-type mice treated with vehicle (**e**), and *Nlgn3*^{KO} mice treated with ETC-168 versus wild-type mice treated with vehicle (**f**). GO terms were summarized using REVIGO and only terms with $Q < 0.01$ are represented. **g**, **h**, TMT proteomic comparison of VTA from *Nlgn3*^{KO} versus wild-type mice treated with vehicle (**g**) and *Nlgn3*^{KO} mice treated with ETC-168 versus wild-type mice treated with vehicle (**h**). Relative frequency of log$_2$-transformed fold change in core proteasome abundance (*Nlgn3*^{KO}/wild type) is plotted. n = 4 mice per genotype and treatment. All error bars are s.e.m. P values determined by unpaired two-sided t-test (**b**), two-sided Mann–Whitney U test (**c**) or Kolmogorov–Smirnov test (**g**, **h**). See Methods and Supplementary Information for additional statistics.

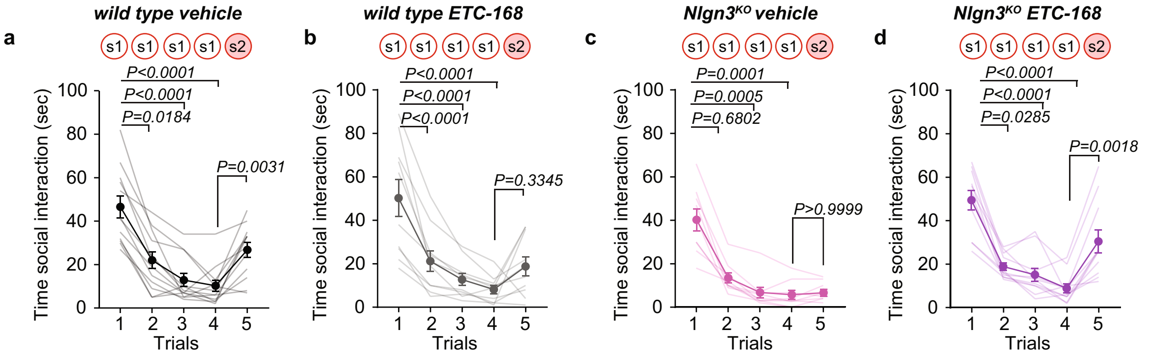

Extended Data Fig. 8 | Effect of short-term ETC-168 treatment on social recognition in wild-type and *Nlgn3*^{KO} mice. a–**d**, Time course of time interacting in the social habituation/recognition test for mice after short-term treatment with ETC-168. **a**, Wild-type mice treated with vehicle (*n* = 12). **b**, Wild-type mice treated with ETC-168 (*n* = 10). **c**, *Nlgn3*^{KO} mice treated with vehicle (*n* = 9). **d**, *Nlgn3*^{KO} mice treated with ETC-168 (*n* = 11). Error bars report s.e.m. *P* values determined by Friedman's test followed by Dunn's post hoc test for planned multiple comparison (**a**, **c**, **d**) or repeated-measures one-way ANOVA followed by Bonferroni's post hoc test for planned multiple comparison (**b**). See Supplementary Information for additional statistics.

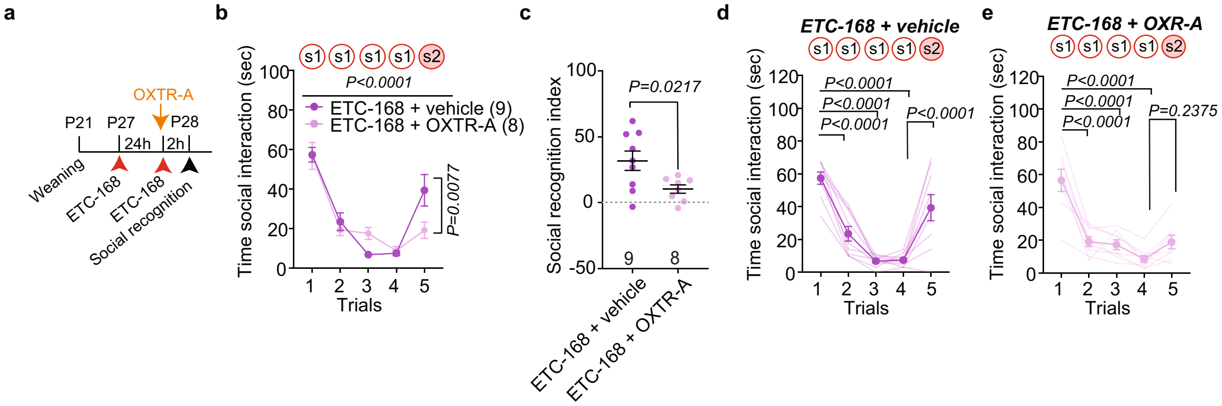

Extended Data Fig. 9 | Effect of ETC-168 treatment is dependent on the oxytocin receptor. a, Experimental outline. **b**, Mean social interaction time in *Nlgn3*^{KO} mice treated with 5 mg kg^{-1} ETC-168 and either vehicle or 10 mg kg^{-1} OXTR-A. Numbers in brackets indicate mice. **c**, Social recognition index for *Nlgn3*^{KO} mice treated with ETC-168 and vehicle, or ETC-168 and OXTR-A. Numbers on graph indicate mice. **d**, **e**, Individual values and mean of time interacting in the social habituation/recognition test after treatment with ETC-168 plus vehicle (*n* = 9) (**d**), or ETC-168 plus OXTR-A (*n* = 8) (**e**). Error bars report s.e.m. *P* values determined by repeated-measures two-way ANOVA followed by Bonferroni's post hoc test (**b**), unpaired two-sided *t*-test (**c**), repeated-measures one-way ANOVA followed by Bonferroni's post hoc test for planned multiple comparison (**d**, **e**). See Supplementary Information for additional statistics.

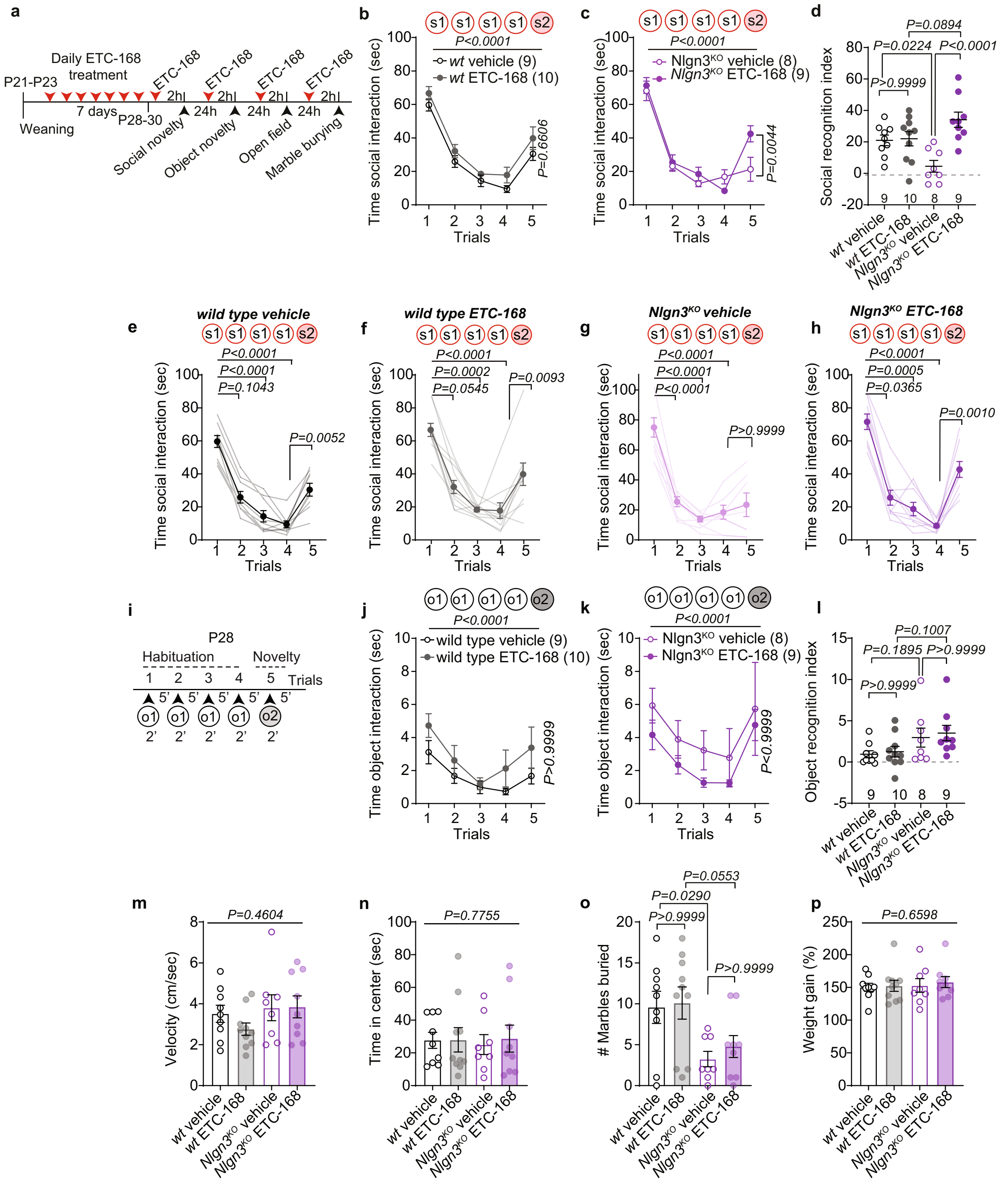

Extended Data Fig. 10 | Effect of long-term ETC-168 treatment on behaviour in wild-type and *Nlgn3*^{KO} mice. a, Experimental schematics of chronic ETC-168 treatment and behaviour schedule. Number of animals per treatment conditions for all behaviours in **b**–**p**: wild-type vehicle = 9, wild-type ETC-168 = 10, *Nlgn3*^{KO} vehicle = 8, *Nlgn3*^{KO} ETC-168 = 9. **b**, **c**, Mean social interaction time in wild-type (**b**) and *Nlgn3*^{KO} (**c**) mice treated for 8 days with vehicle or 5 mg kg^{-1} ETC-168. **d**, Social recognition index for wild-type and *Nlgn3*^{KO} mice treated with vehicle or 5 mg kg^{-1} ETC-168. Numbers in brackets indicate mice. **e**, **f**, Individual values and mean time interacting in the social habituation/recognition test after chronic treatment with ETC-168 for wild-type vehicle ($n = 9$) (**e**), wild-type ETC-168 ($n = 10$) (**f**), *Nlgn3*^{KO} vehicle ($n = 8$) (**g**), and *Nlgn3*^{KO} ETC-168 ($n = 9$) (**h**). **i**, Experimental schematics of object habituation/recognition test in juvenile mice. **j**–**l**, Mean object interaction time plotted for wild-type (**j**) and *Nlgn3*^{KO} (**k**) mice. *P* value above graphs report trial. **l**, Object recognition index. **m**, Mean velocity (cm s^{-1}) in an open field arena during 7 min. **n**, Time spend in centre of the open field arena. **o**, Number of marbles buried during a 30 min marble burying test. **p**, Percentage weight gain in wild-type and *Nlgn3*^{KO} mice treated with ETC-168 or vehicle. *P* value for treatment is displayed on graphs. Error bars report s.e.m. Repeated measures two-way ANOVA followed by Bonferroni's post hoc test for genotype and treatment (**b**, **c**, **j**, **k**); repeated-measures two-way ANOVA followed by Bonferroni's post hoc test for genotype and treatment (**d**, **l**, **o**), Friedman test followed by Dunn's post hoc test for planned multiple comparison (**e**, **f**, **h**), one-way ANOVA followed by Bonferroni's post hoc test for planned multiple comparison (**g**), or repeated-measures two-way ANOVA (**m**, **n**, **p**). See Supplementary Information for additional statistics.

nature research

Corresponding author(s): Peter Scheiffele

Last updated by author(s): Apr 22, 2020

Reporting Summary

Nature Research wishes to improve the reproducibility of the work that we publish. This form provides structure for consistency and transparency in reporting. For further information on Nature Research policies, see Authors & Referees and the Editorial Policy Checklist.

Statistics

For all statistical analyses, confirm that the following items are present in the figure legend, table legend, main text, or Methods section.

n/a	Confirmed	
☐	☒	The exact sample size (*n*) for each experimental group/condition, given as a discrete number and unit of measurement
☐	☒	A statement on whether measurements were taken from distinct samples or whether the same sample was measured repeatedly
☐	☒	The statistical test(s) used AND whether they are one- or two-sided *Only common tests should be described solely by name; describe more complex techniques in the Methods section.*
☐	☒	A description of all covariates tested
☐	☒	A description of any assumptions or corrections, such as tests of normality and adjustment for multiple comparisons
☐	☒	A full description of the statistical parameters including central tendency (e.g. means) or other basic estimates (e.g. regression coefficient) AND variation (e.g. standard deviation) or associated estimates of uncertainty (e.g. confidence intervals)
☒	☐	For null hypothesis testing, the test statistic (e.g. *F*, *t*, *r*) with confidence intervals, effect sizes, degrees of freedom and *P* value noted *Give P values as exact values whenever suitable.*
☒	☐	For Bayesian analysis, information on the choice of priors and Markov chain Monte Carlo settings
☒	☐	For hierarchical and complex designs, identification of the appropriate level for tests and full reporting of outcomes
☒	☐	Estimates of effect sizes (e.g. Cohen's *d*, Pearson's *r*), indicating how they were calculated

Our web collection on statistics for biologists contains articles on many of the points above.

Software and code

Policy information about availability of computer code

Data collection	EthoVision10 Metamorph 7.8.11.0 (Molecular Devises) Igor Po V.6.3.7.2 (WaveMetrics) CellSens V2.3 (Olympus) SparkControl V2.3 (Tecan)
Data analysis	Phoenix WinNonlin, version 6.3 (Certata) ImageJ, 1.49k (NHI) Progenesis QI Version 2.0 (Nonlinear Dymanics) MASCOT, version 2.4.1 (Matrix Science) DAVID 6.8 (NIAID/NIH) SpectroMine, 1.0.20235.13.16424 (Biognosys) String v11 (Elexir) Prism v8 (GraphPad) REVIGO (Rudjer Boskovic Institute) PSEA-Quant, October 11,2019 (Yates lab)

For manuscripts utilizing custom algorithms or software that are central to the research but not yet described in published literature, software must be made available to editors/reviewers. We strongly encourage code deposition in a community repository (e.g. GitHub). See the Nature Research guidelines for submitting code & software for further information.

Data

Policy information about availability of data

All manuscripts must include a data availability statement. This statement should provide the following information, where applicable:

- Accession codes, unique identifiers, or web links for publicly available datasets
- A list of figures that have associated raw data
- A description of any restrictions on data availability

Proteomic data will be deposited at PRIDE and will be made available upon acceptance of the manuscript. All renewable reagents and detailed protocols will be made available on request.

Field-specific reporting

Please select the one below that is the best fit for your research. If you are not sure, read the appropriate sections before making your selection.

☒ Life sciences ☐ Behavioural & social sciences ☐ Ecological, evolutionary & environmental sciences

For a reference copy of the document with all sections, see nature.com/documents/nr-reporting-summary-flat.pdf

Life sciences study design

All studies must disclose on these points even when the disclosure is negative.

Sample size	No statistical methods were used to predetermine the number of animals and cells. Suitable sample sizes were estimated based on previous experience and are similar to those generally employed in the field.
Data exclusions	For VTA-specific Nlgn3 knockdown experiments, animals were excluded by pre-established criteria if less then 20% of cells in the VTA were TH and GFP positive, or if the body weight was less than 75% of the mean body weight at the start of behavior trials. For Retrobead injected experiments, cells were excluded by pre-established critiera if post-hoc immunostaining for TH or retrobead was negative, or if biocytin labeling was unsuccessful (thus preventing post-hoc confirmation). Outliers were identified using ROUT test on the most stringent setting (Q=0.1%). This was used to exclude one DAT-Cre x Nlgn3KO mouse, and two data point for the FUNCAT experiments.
Replication	All animal experiments were done with a minimum of 3 cohorts with animals from several litters. Each cohort showed similar phenotypes. For immunostaining, western blot, FUNCAT and FISH experiments, a minimum of 3 animals per genotype was used to ensure reproducibility. For cell culture experiments, replicates from 3 independent experiments were used with similar results.
Randomization	Animals were randomly assigned to treatment groups at the moment of of viral injections, retrobead injections or behavioral tests and treatment.
Blinding	Experimenter was blinded to genotype for all experiments, and most analysis. The exception was FISH analysis where the presence of a Nlgn3 label made blinding impossible. For electrophysiological experiments, the experimenter was blinded for treatment and genotype. Blinding for treatment was not possible for behavioral experiments, as the experimenter had to administer the drug that had a different color to the vehicle treatment.

Reporting for specific materials, systems and methods

We require information from authors about some types of materials, experimental systems and methods used in many studies. Here, indicate whether each material, system or method listed is relevant to your study. If you are not sure if a list item applies to your research, read the appropriate section before selecting a response.

Materials & experimental systems

n/a	Involved in the study	
☐	☒	Antibodies
☒	☐	Eukaryotic cell lines
☒	☐	Palaeontology
☐	☒	Animals and other organisms
☒	☐	Human research participants
☒	☐	Clinical data

Methods

n/a	Involved in the study	
☒	☐	ChIP-seq
☒	☐	Flow cytometry
☒	☐	MRI-based neuroimaging

Antibodies

Antibodies used	p-eIF4E: Abcam, ab76256, EP2151Y, Lot#GR210598-1 eIF4E: Abcam, ab47482, Lot#GR100774-1 p-ERK1/2: Cell Signaling, 4370S, clone: 137F5, Lot#12

	ERK1/2: Cell Signaling, 4695S, clone: D13.14.4E, Lot#14 p-eIF4G: Cell Signaling, 2441S, Lot#4 eIF4G: Cell Signaling, 2498, Lot#4 p-MNK1: Cell Signaling, 2111, Lot#6 MNK1: Cell Signaling, 2195S, Lot#5 GAPDH: Cell Signaling, 5174, clone: D16H11, Lot#7 calnexin: Stressgen, SPA-865, Lot#01031711 puromycin: Kerafast, EQ0001, clone: 3RH11, Lot#2733311 TH: Millipor, AB1542, Lot#2982635 neurophysin-1: Millipor, MABN844, clone: PS38, Lot#3083532 donkey anti-sheep IgG-Cy3 Jackson ImmunoResearch 713-165-147 donkey anti-sheep Cy5 Jackson ImmunoResearch 713-175-147 donkey anti-rabbit IgG Cy3 Jackson ImmunoResearch 711-165-152 goat anti-mouse Cy2 Jackson ImmunoResearch 714-225-150
Validation	p-eIF4E: WB: validated using positive control 293 cell lysate treated with alkaline phosphatase and HEK293 cell lysate treated with Dexamethasone (abcam.com). eIF4E: evaluated by western blotting using Breast carcinoma tissue and NIH/3T3 cells extract (abcam.com) p-ERK1/2: evaluated by western blotting using extracts from COS cells, untreated or treated with either U0126 #9903 (10 µM for 1h) or TPA (cellsignal.com) ERK1/2: evaluated by western blotting using extracts from HeLa, NIH/3T3 and C6 cells (cellsignal.com) p-eIF4G: evaluated by western blotting using extracts from 293 cells expressing GST-eIF4GI Ser1192Ala or GST-eIF4GI Ser1108Ala mutant protein (cellsignal.com) eIF4G: evaluated by western blotting using extracts from various cell lines (cellsignal.com) p-MNK1: evaluated by western blotting in NIH/3T3 cells serum starved for 24h and then treated or untreated with serum for 30 min (cellsignal.com) MNK1: evaluated by western blot analysis of extracts from various cell lines (cellsignal.com) GAPDH: evaluated by western blotting using extracts from various cell lines (cellsignal.com) calnexin: evaluated by western blotting using MWM, Vero, 3T3, PC-12, and HeLa cell lines (enzolifesciences.com) puromycin: evaluated for western blotting (Kelleher, AR., et al. (2013). Am J Physiol Endocrinol Metab. 304(2):E229-236. TH: evaluated by Western Blot on mouse brain lysates (merckmillipore.com) neurophysin-1: evaluated for IHC (Ben-Barak, Y., et al. (1985). J. Neuroscie. 5(1):81-97)

Animals and other organisms

Policy information about studies involving animals; ARRIVE guidelines recommended for reporting animal research

Laboratory animals	Mice: C57BL/6j, male, P5-adult NMRI, male, female, E16.5
Wild animals	the study did not involve wild animals
Field-collected samples	the study did not involve field-collected samples
Ethics oversight	Basel Cantonal Veterinary Office Committees for Animal Experimentation Lausanne Cantonal Veterinary Office Committees for Animal Experimentation

Note that full information on the approval of the study protocol must also be provided in the manuscript.

Estimating the effects of non-pharmaceutical interventions on COVID-19 in Europe

https://doi.org/10.1038/s41586-020-2405-7

Received: 30 March 2020

Accepted: 22 May 2020

Seth Flaxman[1,7], Swapnil Mishra[2,7], Axel Gandy[1,7], H. Juliette T. Unwin[2], Thomas A. Mellan[2], Helen Coupland[2], Charles Whittaker[2], Harrison Zhu[1], Tresnia Berah[1], Jeffrey W. Eaton[2], Mélodie Monod[1], Imperial College COVID-19 Response Team*, Azra C. Ghani[2], Christl A. Donnelly[2,3], Steven Riley[2], Michaela A. C. Vollmer[2], Neil M. Ferguson[2], Lucy C. Okell[2] & Samir Bhatt[2,7]✉

Following the detection of the new coronavirus[1] severe acute respiratory syndrome coronavirus 2 (SARS-CoV-2) and its spread outside of China, Europe has experienced large epidemics of coronavirus disease 2019 (COVID-19). In response, many European countries have implemented non-pharmaceutical interventions, such as the closure of schools and national lockdowns. Here we study the effect of major interventions across 11 European countries for the period from the start of the COVID-19 epidemics in February 2020 until 4 May 2020, when lockdowns started to be lifted. Our model calculates backwards from observed deaths to estimate transmission that occurred several weeks previously, allowing for the time lag between infection and death. We use partial pooling of information between countries, with both individual and shared effects on the time-varying reproduction number (R_t). Pooling allows for more information to be used, helps to overcome idiosyncrasies in the data and enables more-timely estimates. Our model relies on fixed estimates of some epidemiological parameters (such as the infection fatality rate), does not include importation or subnational variation and assumes that changes in R_t are an immediate response to interventions rather than gradual changes in behaviour. Amidst the ongoing pandemic, we rely on death data that are incomplete, show systematic biases in reporting and are subject to future consolidation. We estimate that—for all of the countries we consider here—current interventions have been sufficient to drive R_t below 1 (probability $R_t < 1.0$ is greater than 99%) and achieve control of the epidemic. We estimate that across all 11 countries combined, between 12 and 15 million individuals were infected with SARS-CoV-2 up to 4 May 2020, representing between 3.2% and 4.0% of the population. Our results show that major non-pharmaceutical interventions—and lockdowns in particular—have had a large effect on reducing transmission. Continued intervention should be considered to keep transmission of SARS-CoV-2 under control.

Following the identification of the new coronavirus SARS-CoV-2 in Wuhan (China) in December 2019 and its global spread, large epidemics of COVID-19 have ensued in Europe. In response to the rising numbers of cases and deaths and to preserve health systems, European countries—as with those in Asia—have implemented measures to control their epidemics. These large-scale non-pharmaceutical interventions vary between countries, but include social distancing (such as banning large gatherings), border closures, school closures, measures to isolate symptomatic individuals and their contacts, and large-scale lockdowns of populations with all but essential internal travel banned. Understanding whether these interventions have had the desired effect of controlling the epidemic, and which interventions are necessary to maintain control, is critical given their large economic and social costs. The key aim of these interventions is to reduce R_t, a fundamental epidemiological quantity that represents the average number of infections generated at time t by each infected case over the course of their infection.

In China, strict movement restrictions and other measures (including case isolation and quarantine) began to be introduced from 23 January 2020, which achieved a downward trend in the number of confirmed new cases during February and resulted in zero new confirmed indigenous cases in Wuhan by 19 March 2020. Studies have estimated how the values of R_t changed during this time in different

---

[1] Department of Mathematics, Imperial College London, London, UK. [2] MRC Centre for Global Infectious Disease Analysis, Jameel Institute for Disease and Emergency Analytics, Imperial College London, London, UK. [3] Department of Statistics, University of Oxford, Oxford, UK. [7] These authors contributed equally: Seth Flaxman, Swapnil Mishra, Axel Gandy, Samir Bhatt. *A list of members and their affiliations appears at the end of the paper. ✉e-mail: s.bhatt@imperial.ac.uk

areas of China, from around 2–4 during the uncontrolled epidemic to below 1 (refs. [1,2]).

Estimating R_t for SARS-CoV-2 presents challenges, owing to the high proportion of infections that are not detected by health systems[1,3,4] and to the regular changes in testing policies, which resulted in different proportions of infections being detected over time and between countries. Initially, most countries had the capacity to test only a small proportion of suspected cases and reserved tests for severely ill patients or for high-risk groups (for example, the contacts of positively tested individuals).

An alternative way to estimate the course of the epidemic is to calculate backwards from observed deaths to the number of infections. We introduce a Bayesian mechanistic model linking the infection cycle to observed deaths, inferring the total population infected (attack rates) as well as R_t. We assess whether there is evidence that interventions have so far been successful at reducing R_t to values below 1. We simulate a hypothetical counterfactual scenario in which R_t remains at starting levels to estimate the deaths that would have occurred without interventions.

Reported deaths are likely to be far more reliable than case data—although reported death data still have limitations. First, early deaths attributable to COVID-19 may have been missed. Second, there is variation in the reporting of deaths by country and over time. Third, reporting delays are expected and can be both systematic and random in nature. We attempt to overcome these data limitations by using a consolidated data source, incorporating noise in our observational model, partially pooling of information between countries and performing a sensitivity analysis under scenarios of underreporting to test our conclusions (Supplementary Information).

Our model relies on fixed estimates of some epidemiological parameters, such as the onset-to-death distribution, the infection fatality rate and the generation distribution, that are based on previous work[5,6]; we perform a sensitivity analysis on these parameters. Our parametric form of R_t assumes that changes in R_t are an immediate response to interventions rather than gradual changes in behaviour, and it does not include importation or subnational variation. We assume that individual interventions have a similar effect in different countries, and that the efficacy of these interventions remains constant over time. Our framework infers R_t from mortality data, while accounting for time lags since infections occurred. As a result, even with perfect data and partial pooling, we cannot perfectly predict the current value of R_t. However, the credible intervals on R_t show the self-consistent behaviour that is a hallmark of a fully Bayesian analysis throughout the entire period we study, exhibiting appropriate shrinkage as more data become available (Supplementary Videos 1–3).

Italy was the first European country to begin major non-pharmaceutical interventions, and other countries followed soon afterwards (Extended Data Fig. 4). The onset of interventions ranged between 2 March and 29 March 2020. We analysed data on mortality from COVID-19 in 11 European countries until 4 May 2020, at which point lockdowns were relaxed in Italy and Spain. For each country, we model the number of infections, the number of deaths and R_t (Fig. 1). R_t is modelled as a piecewise constant function that changes only when an intervention occurs. Each country has its own individual starting R_t before interventions took place. For all countries, interventions are assumed to have the same relative effect on R_t and are informed by mortality data across all countries. The only exception is that we use partial pooling to introduce country-specific effects of the effectiveness of the last intervention introduced in the study period in a country (which is usually lockdown).

Estimated infections, R_t and effect sizes

In all countries, we estimate there are orders-of-magnitude fewer infections detected (Fig. 1, Extended Data Figs. 1, 2) than true infections, most likely owing to mild and asymptomatic infections as well as limited testing capacities and changes in testing policy. In Italy, our results suggest that—cumulatively—2.8 (2.2–3.5) million people (all parenthetical ranges refer to 95% credible intervals) have been infected as of 4 May 2020, which gives an attack rate of 4.6% (3.6–5.8%) of the population (Table 1). In Spain (which has also experienced a large number of deaths), we estimate that 5.5% of the population (2.6 (2.1–3.3) million people) have been infected to date. Germany, the most populous country in our study, is estimated to have one of the lowest attack rates at 0.85% with 710,000 (550,000–930,000) people infected. Belgium has the highest estimated attack rates of 8%, followed by Spain with 5.5%. Although there have been few reliable national serological studies[7], initial small-scale surveys in Austria[8] and Denmark[9] closely align with our estimates. A much larger study in Spain is very closely aligned with our estimates[10]. To some extent, these initial results validate our choice of infection fatality rate.

Averaged across all countries, we estimate the initial R_t to be 3.8 (2.4–5.6), consistent with previous analyses[1,11]. These estimates are informed by our choice of generation-interval distribution and the initial growth rate of observed deaths. A shorter assumed generation time results in lower starting R_t (Supplementary Discussion 3). The initial values of R_t are also uncertain, owing to (a) importation (rather than local transmission) being the dominant source of new infections in the early period of the epidemic and (b) possible under-ascertainment in deaths, particularly before testing became widespread. We perform sensitivity analyses around these parameters (Supplementary Discussions 10, 11).

We estimate large reductions in R_t in response to the combined non-pharmaceutical interventions. Our results—which are driven more by countries with advanced epidemics and larger numbers of deaths—suggest that these interventions have together had a substantial effect on transmission, as measured by changes in the estimated R_t. At the time of this study, we find current estimates of R_t to range from a posterior mean of 0.44 (0.26–0.61) for Norway to a posterior mean of 0.82 (0.73–0.93) for Belgium, with an average of 0.66 across the 11 countries—an 82% reduction compared to the pre-intervention values. For all countries, we find that current interventions have been sufficient to drive R_t below 1 (probability $R_t < 1.0$ is greater than 99% across all countries we consider) and achieve control of the epidemic. These conclusions are corroborated by studies from individual countries—France[12], Spain[13], Germany[14] and the UK[15]—over a similar period, which arrive at very similar estimates despite different methodologies and data. For example, a previous study[12] estimates an R_t of 0.67 for France using hospitalization records (we estimate 0.68); for Germany, the Robert Koch Institute reports R_t of 0.76 using electronically notified cases[14] (we estimate 0.71). The retrospective stability of our model (Supplementary Videos 1–3) is variable when the implementations of interventions are very dissimilar; an example of this is seen in Sweden, where interventions were dissimilar to other countries and led initially to large uncertainty. Our model uncertainty is also dependent on the magnitude of R_t; this occurs because infections are a nonlinear function of R_t and are sensitive to small increases. Uncertainty shrinks greatly when R_t is reduced. Examples of this effect are seen in all countries, but it is most pronounced in Belgium and France; these countries show large uncertainties in the number of infections in the early period of the epidemic. Our choice of parameterizing R_t using piecewise constant functions means that we cannot capture the fine-scale variation that could be achieved by using additional covariates.

Lockdown has an identifiable large effect on transmission (81% (75–87%) reduction) (Fig. 2). The close spacing of interventions in time (Extended Data Fig. 4) means that the individual effects of the other interventions are not identifiable (Fig. 2). Our partial pooling model requires only one country to provide a signal for the effect of a given intervention, and this effect is then shared across all countries. Although this sharing can potentially lead to initial over- or under-estimation of the effect of an intervention, it also means that a

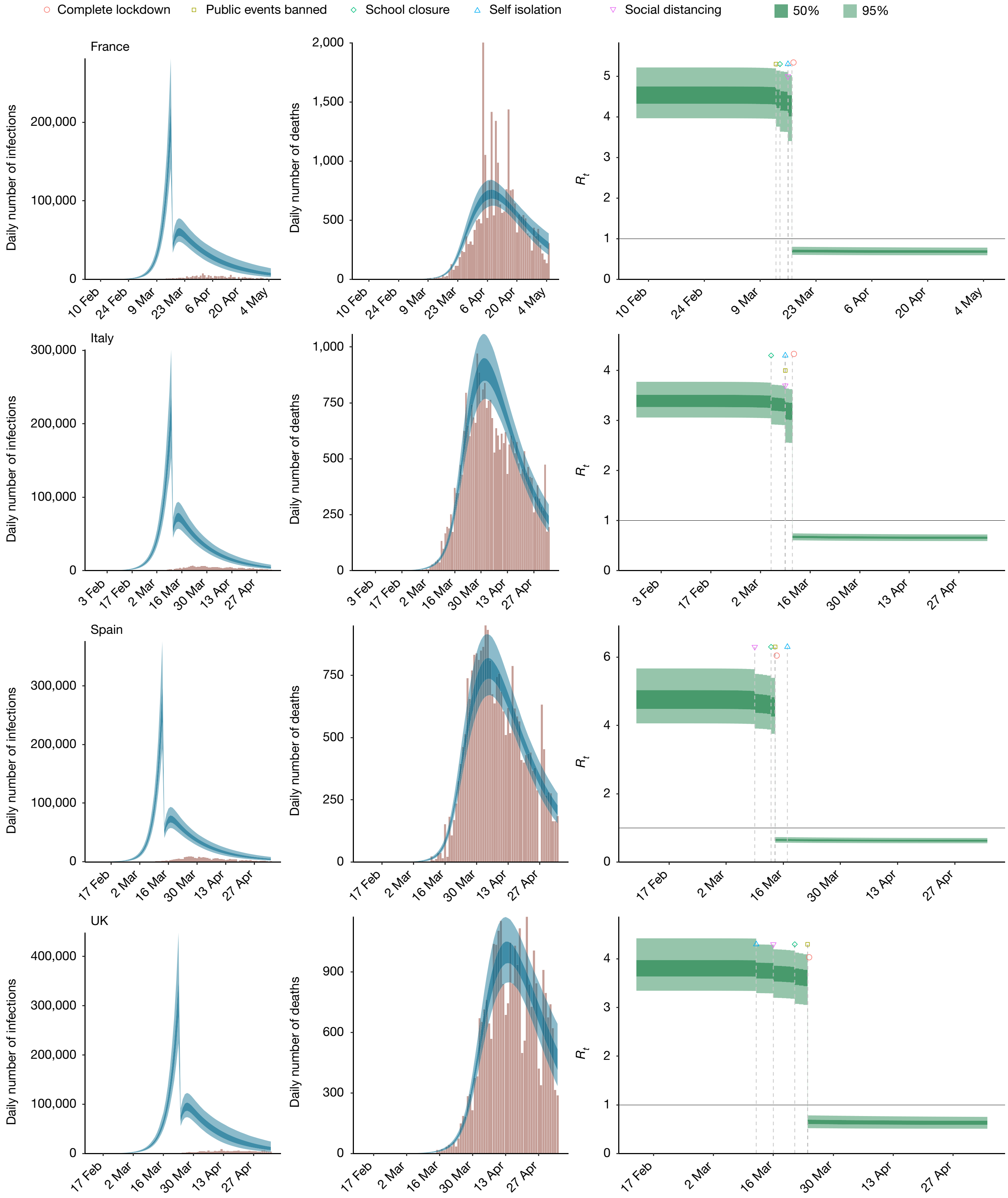

Fig. 1 | Country-level estimates of infections, deaths and R_t for France, Italy, Spain and the UK. Left, daily number of infections. Brown bars are reported infections; blue bands are predicted infections; dark blue, 50% credible interval; light blue 95% credible interval. The number of daily infections estimated by our model drops immediately after an intervention, as we assume that all infected people become immediately less infectious through the intervention. Afterwards, if R_t is above 1, the number of infections will start growing again. Middle, daily number of deaths. Brown bars are reported deaths; blue bands are predicted deaths; credible intervals are as in the left plot. Right, R_t. Dark green, 50% credible interval; light green, 95% credible interval. Icons are interventions, shown at the time at which they occurred.

Table 1 | Total population infected by country

Country	Percentage of total population infected (mean (95% credible interval))
Austria	0.76% (0.59–0.98%)
Belgium	8% (6.1–11%)
Denmark	1.0% (0.81–1.4%)
France	3.4% (2.7–4.3%)
Germany	0.85% (0.66–1.1%)
Italy	4.6% (3.6–5.8%)
Norway	0.46% (0.34–0.61%)
Spain	5.5% (4.4–7.0%)
Sweden	3.7% (2.8–5.1%)
Switzerland	1.9% (1.5–2.4%)
UK	5.1% (4.0–6.5%)

Posterior model estimates of the attack rate by country (percentage of total population infected) as of 4 May 2020. Results are derived from a model representing 11 countries with a total population of 375 million and 128,928 reported COVID-19-related deaths up to 4 May 2020.

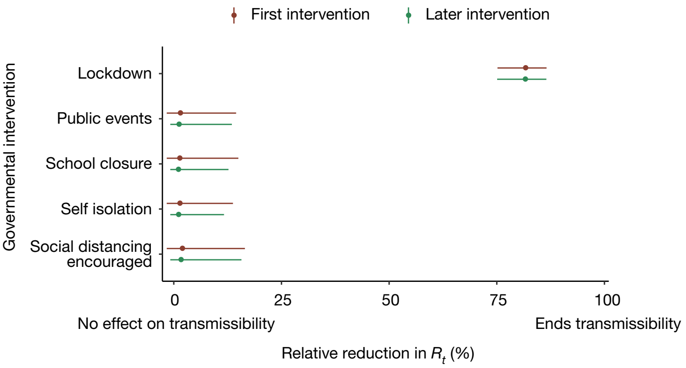

Fig. 2 | Effectiveness of interventions on R_t. Our model includes five covariates for governmental interventions, adjusting for whether the intervention was the first one undertaken by the government in response to COVID-19 (red) or was subsequent to other interventions (green). Mean relative percentage reduction in R_t is shown with 95% posterior credible intervals. If 100% reduction is achieved, $R_t = 0$ and there is no more transmission of COVID-19. Lockdown is significantly different from the other interventions; the other interventions are not significantly different from each other, probably owing to the fact that many interventions occurred on the same day or within days of each other (as shown in Extended Data Fig. 4). Results are derived from a model that represents 11 countries with a total population of 375 million and 128,928 reported COVID-19-related deaths up to 4 May 2020.

consistent signal for all countries can be estimated before that signal is present in data from an individual country[16]. Therefore, this sharing is potentially useful for generating early warnings, by leveraging what happened in countries with earlier epidemics to inform countries with more-recent epidemics.

Estimated effect of interventions on deaths

Extended Data Table 1 shows total deaths forecast from the beginning of the epidemic up to and including 4 May 2020 under our fitted model and under the counterfactual model, which predicts what would have happened if no interventions were implemented (and $R_t = R_0$; that is, the initial R_t estimated before interventions came into effect).

By comparing the deaths predicted under the model with no interventions to the deaths predicted in our intervention model, we calculated the total deaths averted in our study period. We find that across 11 countries 3.1 (2.8–3.5) million deaths have been averted owing to interventions since the beginning of the epidemic; Extended Data Fig. 5 compares the actual total deaths to the counterfactual total deaths. The counterfactual model without interventions is illustrative only, and reflects the assumptions of our model. We do not account for changes in behaviour; in reality, even in the absence of government interventions we would expect R_t to decrease and therefore would overestimate deaths in the no-intervention model. Conversely, we do not consider the effect on the infection fatality rate as a result of an overwhelmed health system in which patients may not be able to access critical care facilities, which would underestimate the number of counterfactual deaths. In the Supplementary Information, we show further counterfactual estimates under differing assumptions of the generation distribution and onset-to-death distribution and all scenarios broadly show the same trends. Given this agreement across differing scenarios, we believe our estimates for the counterfactual deaths averted to be plausible.

Discussion

During the ongoing transmission of SARS-CoV-2 in Europe, we analyse trends in the numbers of deaths to assess the extent to which transmission has been reduced. Representing the infection process associated with COVID-19 using a semi-mechanistic, joint Bayesian hierarchical model, we can reproduce trends observed in the data relating to deaths and produce empirically driven predictions that are valid over short time horizons.

We estimate that there have been many more infections than are currently reported. The high level of under-ascertainment of infections that we estimate here is probably due to the focus on testing in hospital settings, which misses milder or asymptomatic cases in the community. Despite this, we estimate that only a relatively small minority of individuals in each country have been infected (Table 1). Our estimates imply that the populations in Europe are not close to herd immunity (about 70% if R_0 is 3.8)[17]. Furthermore, with values of R_t below 1 in all countries, the rate of acquisition of herd immunity will slow down rapidly. Our estimates for attack rates during our study period are consistent with those reported from national serological studies[7]. Similarly, comparable studies estimating R_t all agree that the number as of 4 May 2020 is less than 1.

To our knowledge, our modelling approach is unique in pooling information from multiple countries at once. Using this approach means that we require a central consolidated data source (such as data from the European Centre of Disease Control (ECDC)), and also that trends in some countries will be affected by those countries with more data. We argue that this effect is beneficial, in that it helps to minimize idiosyncrasies in the data[16], as well as to improve consistency of estimates over time. Although our qualitative conclusions surrounding the effect of interventions and the finding that R_t is less than 1 are robust to our choice of whether to incorporate pooling or not, the ability to use a greater extent of available data and share information across countries in a statistically principled manner markedly improves the consistency of model predictions across the study period (Supplementary Videos 1–3).

Most interventions were implemented in rapid succession in many countries, and as such it is difficult to disentangle the individual effect sizes of each intervention. In our analysis, we find that only the effect of lockdown is identifiable, and that it has a substantial effect (81% (75–87%) reduction in R_t). Taking into account country-specific effects, the effect size of lockdown remains large across all countries (Supplementary Fig. 29).

We acknowledge the limitations of existing mortality data relating to COVID-19—in particular, deaths outside hospitals may be underreported. However, by using the ECDC data, we rely on a comprehensive data source that is refined and updated each day in a systematic process. Our sensitivity analysis of underreporting and statistical-measurement noise suggests that we may slightly underestimate the attack rates in some countries, but this does not change our overall conclusions pertaining to R_t. However, even if the data were complete, our method cannot surmount the time lag between infections and deaths and can only fully identify trends in infections 2–3 weeks earlier. Extensions of our model could use case, hospitalization or intensive care data, but reconciling the different biases inherent in these sources while ensuring parsimony is challenging and would require additional assumptions.

The modern understanding of infectious disease, combined with a global publicized response, has meant that nationwide interventions could be implemented with widespread adherence and support. Given the observed infection fatality ratios and the epidemiology of COVID-19, major non-pharmaceutical interventions have had an effect in reducing transmission in all of the countries we have considered. In all countries in this study, we find that these interventions have reduced R_t below 1, and have contained their epidemics at the current time. When looking at simplistic counterfactual models over the whole epidemic, the number of potential deaths averted is substantial. We cannot say for certain that the current measures will continue to control the epidemic in Europe; however, if current trends continue there is reason for optimism.

Online content

Any methods, additional references, Nature Research reporting summaries, source data, extended data, supplementary information, acknowledgements, peer review information; details of author contributions and competing interests; and statements of data and code availability are available at https://doi.org/10.1038/s41586-020-2405-7.

1. Li, R. et al. Substantial undocumented infection facilitates the rapid dissemination of novel coronavirus (SARS-CoV-2). *Science* **368**, 489–493 (2020).
2. Zhang, J. et al. Patterns of human social contact and contact with animals in Shanghai, China. *Sci. Rep*. **9**, 15141 (2019).
3. Zhao, A. J. et al. Antibody responses to SARS-CoV-2 in patients of novel coronavirus disease 2019. *Clin. Infect. Dis*. ciaa344 https://doi.org/10.1093/cid/ciaa344 (2020).
4. Jombart, T. et al. Inferring the number of COVID-19 cases from recently reported deaths. *Wellcome Open Research* **5**, 78 (2020).
5. Verity, R. et al. Estimates of the severity of coronavirus disease 2019: a model-based analysis. *Lancet* **20**, 669–677 (2020).
6. Bi, Q. et al. Epidemiology and transmission of COVID-19 in 391 cases and 1286 of their close contacts in Shenzhen, China: a retrospective cohort study. *Lancet Infect. Dis*. https://doi.org/10.1016/S1473-3099(20)30287-5 (2020).
7. Bobrovitz, N. et al. Lessons from a rapid systematic review of early SARS-CoV-2 serosurveys. Preprint at medRxiv https://doi.org/10.1101/2020.05.10.20097451 (2020).
8. Statistics Austria. *COVID-19 Prevalence Study: Maximum 0.15% of Austrian Population Infected with SARS-CoV-2* (Statistics Austria, 2020).
9. Erikstrup, C. et al. Estimation of SARS-CoV-2 infection fatality rate by real-time antibody screening of blood donors. *Clin. Infect. Dis*. ciaa849 https://doi.org/10.1093/cid/ciaa849 (2020).
10. Pollán, M. et al. Prevalence of SARS-CoV-2 in Spain (ENE-COVID): a nationwide, population-based seroepidemiological study. *Lancet* https://doi.org/10.1016/S0140-6736(20)31483-5 (2020).
11. Zhang, J. et al. Age profile of susceptibility, mixing, and social distancing shape the dynamics of the novel coronavirus disease 2019 outbreak in China. Preprint at medRxiv https://doi.org/10.1101/2020.03.19.20039107 (2020).
12. Salje, H. et al. Estimating the burden of SARS-CoV-2 in France. *Science* **369**, 208–211 (2020).
13. Hyafil, A. & Morina, D. Analysis of the impact of lockdown on the reproduction number of the SARS-Cov-2 in Spain. *Gac. Sanit*. https://doi.org/10.1016/j.gaceta.2020.05.003 (2020).
14. Robert Koch Institute. *Coronavirus Disease 2019 (COVID-19) Daily Situation Report of the Robert Koch Institute* (Robert Koch Institute, 2020).
15. Davies, N. G., Kucharski, A. J., Eggo, R. M., Gimma, A. & Edmunds, W. J. The effect of non-pharmaceutical interventions on COVID-19 cases, deaths and demand for hospital services in the UK: a modelling study. *Lancet* **5**, E375–E385 (2020).
16. Gelman, A. & Hill, J. *Data Analysis using Regression and Multilevel/Hierarchical Models* (Cambridge Univ. Press, 2006).
17. Miller, J. C. A note on the derivation of epidemic final sizes. *Bull. Math. Biol*. **74**, 2125–2141 (2012).

Imperial College COVID-19 Response Team

Pablo N. Perez-Guzman[2], Nora Schmit[2], Lucia Cilloni[2], Kylie E. C. Ainslie[2], Marc Baguelin[2], Adhiratha Boonyasiri[4], Olivia Boyd[2], Lorenzo Cattarino[2], Laura V. Cooper[2], Zulma Cucunubá[2], Gina Cuomo-Dannenburg[2], Amy Dighe[2], Bimandra Djaafara[2], Ilaria Dorigatti[2], Sabine L. van Elsland[2], Richard G. FitzJohn[2], Katy A. M. Gaythorpe[2], Lily Geidelberg[2], Nicholas C. Grassly[2], William D. Green[2], Timothy Hallett[2], Arran Hamlet[2], Wes Hinsley[2], Ben Jeffrey[2], Edward Knock[2], Daniel J. Laydon[2], Gemma Nedjati-Gilani[2], Pierre Nouvellet[2,5], Kris V. Parag[2], Igor Siveroni[2], Hayley A. Thompson[2], Robert Verity[2], Erik Volz[2], Caroline E. Walters[2], Haowei Wang[2], Yuanrong Wang[2], Oliver J. Watson[2,6], Peter Winskill[2], Xiaoyue Xi[1] & Patrick G. T. Walker[2]

[4]NIHR Health Protection Research Unit in Healthcare Associated Infections and Antimicrobial Resistance, Imperial College London, London, UK. [5]School of Life Sciences, University of Sussex, Brighton, UK. [6]Department of Laboratory Medicine and Pathology, Brown University, Providence, RI, USA.

Methods

Data

Our model uses daily consolidated death data from the ECDC for 11 European countries currently experiencing the COVID-19 epidemic: Austria, Belgium, Denmark, France, Germany, Italy, Norway, Spain, Sweden, Switzerland and the UK. The ECDC provides information on confirmed cases and deaths attributable to COVID-19. For population counts, we use the United Nations Population Division age-stratified counts[18].

We also catalogue data on the nature and type of major non-pharmaceutical interventions. We looked at the government webpages from each country as well as their official public health webpages to identify the latest advice or laws being issued by the government and public health authorities. We collected the following: school closure ordered; case-based measures; public events banned; social distancing encouraged; lockdown decreed; and the time of the first and last intervention. A full list of the timing of these interventions and the sources we have used is provided in the Supplementary Notes, Supplementary Table 2.

By using the ECDC data, we rely on a consolidated data source compiled by the ECDC, who include many sources of data each day, constantly refining and updating data using a comprehensive and systematic process. However, despite the rigorous protocols, countries may vary in the specifics of the data that they report to the ECDC. For example, there is variation in reporting (that is, community versus hospital) and time lags. Despite these issues, we use ECDC data to ensure as much consistency as possible across all countries.

Model

A visual summary of our model is presented in Extended Data Fig. 3; details are provided in the Supplementary Methods.

We fit our model to observed deaths according to ECDC data from 11 European countries. The modelled deaths are informed by an infection-to-death distribution (Supplementary Fig. 1; derived from assumptions about the time from infection to the onset of symptoms and about the time from the onset of symptoms to death), and the population-averaged infection fatality ratio (adjusted for the age structure and contact patterns of each country, as discussed in the Supplementary Methods, Supplementary Table 3).

Given these distributions and ratios, modelled deaths are a function of the number of infections. The number of infections is modelled as the product of R_t with a discrete convolution of the previous infections. Individual components of this convolution sum are weighted by the generation time distribution (the average time from the infection of one person to the time at which they infect another; Supplementary Fig. 2). In our work, we approximate the generation time distribution using the serial interval distribution. R_t is a function of the initial R_t before interventions and the effect sizes from interventions, in which interventions are modelled as piecewise constant functions.

Following the Bayesian hierarchy from bottom to top gives us a full framework to see how interventions affect infections, which can result in deaths. A schematic of our model is shown in Extended Data Fig. 3. To maximize the ability to observe the effect of interventions on deaths, we fit our model jointly for all 11 European countries, and use partial pooling of information between countries with both individual and shared effects on R_t. Partial pooling operates on the last intervention, which is—in most cases—lockdown. The effect of partial pooling can be seen in Supplementary Discussion 12, Supplementary Fig. 29. We chose a balanced prior that encodes the prior belief that interventions have an equal chance of having an effect or not, and ensure a uniform prior on the joint effect of all interventions (Supplementary Fig. 3). We evaluate the effect of our Bayesian prior distribution choices and evaluate our Bayesian posterior calibration to ensure our results are statistically robust.

We perform extensive model validation and sensitivity analyses. We validate our model by cross-validation over a 14-day period (Supplementary Discussion 1, Supplementary Table 1) and we show the fits for holdout samples in Supplementary Figs. 5–15. We check the convergence of the Markov chain Monte Carlo sampler (Supplementary Fig. 4). We consider the sensitivity of our estimates of R_t to the mean of the generation distribution (Supplementary Discussion 3, Supplementary Figs. 16, 17). We further show that the choice of generation distribution does not change our counterfactual conclusions (Supplementary Fig. 18). Using univariate analyses and uninformative priors, we find (Supplementary Fig. 19) that all effects on their own serve to decrease R_t (Supplementary Discussion 4). We compare our model to a non-parametric Gaussian Process model (Supplementary Discussion 5). To assess the effect of individual countries on the results, we perform a 'leave one country out' sensitivity analysis (Supplementary Discussion 6, Supplementary Figs. 20, 21). To validate our starting values of R_t, we compare our model against an exponential-growth linear model (Supplementary Discussion 7, Supplementary Fig. 22). Instead of a joint analysis, we consider fits of our model to individual countries (Supplementary Discussion 8, Supplementary Figs. 23–26). We perform a sensitivity analysis with respect to the onset-to-death distribution (Supplementary Discussion 9, Supplementary Fig. 27). We validate our probabilistic seeding scheme through an importance-sampling leave-one-out cross-validation (Supplementary Discussion 10). We consider a model extension with a constant, probabilistic under-reporting (Supplementary Discussion 11), finding that R_t does not change substantially (Supplementary Fig. 28).

Our model is different to other approaches (such as EpiEstim[19]) that use the discrete renewal equation. We use the renewal equation as a latent process to model infections and propose a generative mechanism to connect these infections to death data. Simply applying the renewal equation directly to death data requires positing a mechanism in which deaths in the past can cause future deaths (see, for example, ref. [20]). In addition, for R_t, we are able to use a functional relationship in which non-pharmaceutical interventions can have a direct effect on R_t.

Reporting summary

Further information on research design is available in the Nature Research Reporting Summary linked to this paper.

Data availability

Death counts for the 11 European countries for the time period in our study and the full set of posterior draws from our model are available at https://reshare.ukdataservice.ac.uk/854380/.

Code availability

All source code and data necessary for the replication of our results and figures are available at https://github.com/ImperialCollegeLondon/covid19model. An R package based on our method is available at https://imperialcollegelondon.github.io/epidemia/.

18. United Nations, Department of Economic and Social Affairs, Population Division. *World Population Prospects 2019: Data Booklet*, ST/ESA/SER.A/424. (United Nations, 2019).
19. Cori, A., Ferguson, N. M., Fraser, C. & Cauchemez, S. A new framework and software to estimate time-varying reproduction numbers during epidemics. *Am. J. Epidemiol.* **178**, 1505–1512 (2013).
20. Goldstein, E. et al. Reconstructing influenza incidence by deconvolution of daily mortality time series. *Proc. Natl Acad. Sci. USA* **106**, 21825–21829 (2009).

Acknowledgements S.B. acknowledges the NIHR BRC Imperial College NHS Trust Infection and COVID themes, the Academy of Medical Sciences Springboard award and the Bill and Melinda Gates Foundation. L.C.O. acknowledges funding from a UK Royal Society fellowship. Initial research on covariates in Supplementary Table 2 was crowdsourced; we thank a number of people across the world for help with this. This work was supported by Centre funding from the UK Medical Research Council under a concordat with the UK Department for International Development, the NIHR Health Protection Research Unit in Modelling Methodology and Community Jameel. We thank F. Valka for creating our website, and A. Gelman and the Stan team for helpful discussions. We acknowledge the resources provided by Cirrus UK National Tier-2 HPC Service at EPCC (http://www.cirrus.ac.uk) funded by the University of Edinburgh and EPSRC (EP/P020267/1), and cloud compute time donated by Microsoft and Amazon.

Author contributions S.B., S.F., S.M. and A.G. conceived and designed the study. S.B., S.F., S.M., A.G., H.C., H.J.T.U., T.A.M., M.A.C.V., J.W.E. and N.M.F. performed analysis. L.C.O., S.B., S.F., A.G., A.C.G., C.A.D., S.R. and N.M.F. wrote the first draft of the paper. S.B., S.F., H.C., C.W., P.W., T.B., P.N.P.G., N.S., L. Cilloni, M.A.C.V. and H.C. collected data. All authors discussed the results and contributed to the revision of the final manuscript.

Competing interests The authors declare no competing interests.

Additional information

Supplementary information is available for this paper at https://doi.org/10.1038/s41586-020-2405-7.

Correspondence and requests for materials should be addressed to S.B.

Peer review information *Nature* thanks David Earn and the other, anonymous, reviewer(s) for their contribution to the peer review of this work. Peer reviewer reports are available.

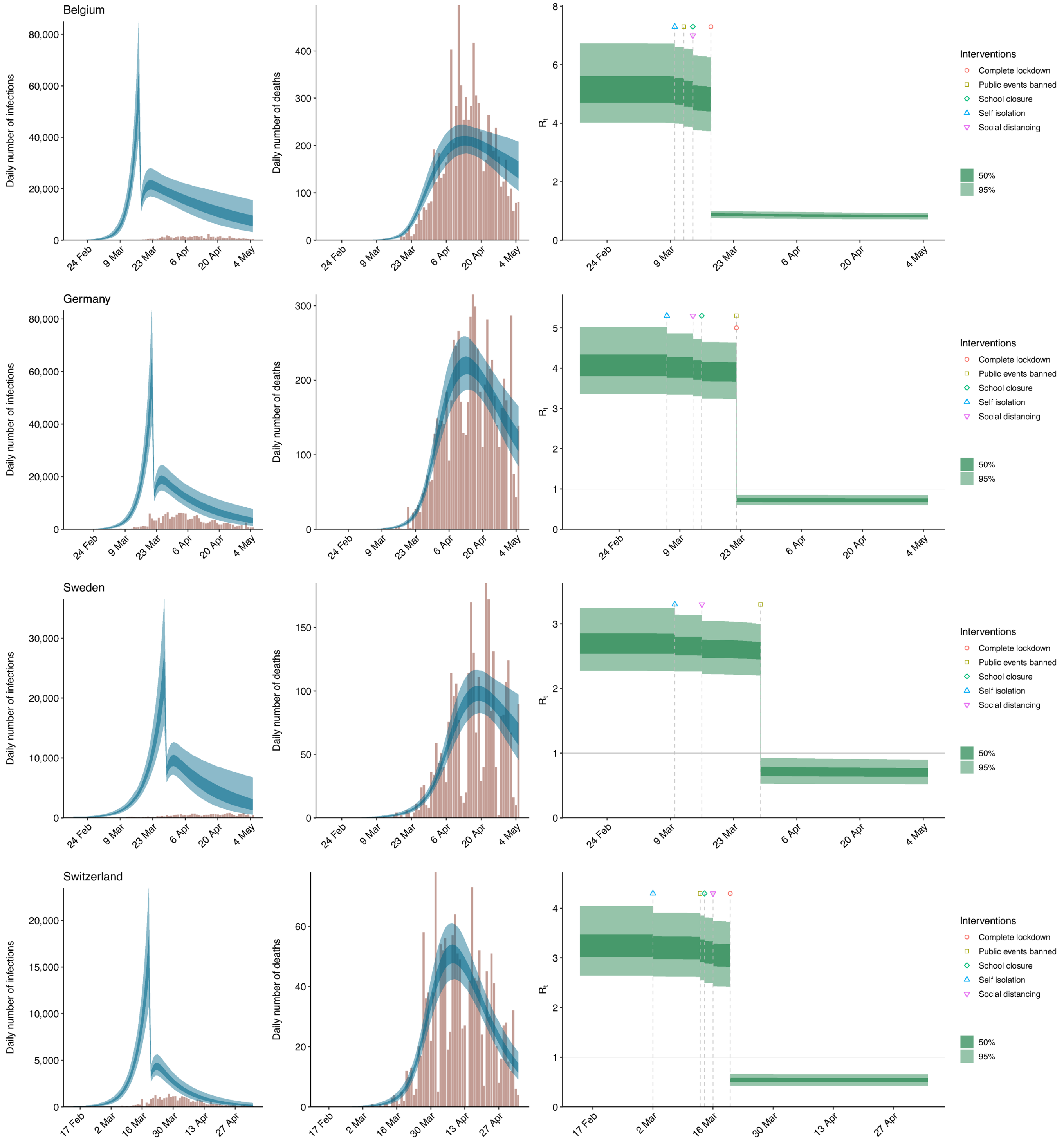

Extended Data Fig. 1 | Country-level estimates of infections, deaths and R_t for Belgium, Germany, Sweden and Switzerland. Left, daily number of infections. Brown bars are reported infections; blue bands are predicted infections; dark blue, 50% credible interval; light blue, 95% credible interval. The number of daily infections estimated by our model drops immediately after an intervention, as we assume that all infected people become immediately less infectious through the intervention. Afterwards, if R_t is above 1, the number of infections will starts growing again. Middle, daily number of deaths. Brown bars are reported deaths; blue bands are predicted deaths; credible intervals are as in the left plot. Right, R_t. Dark green, 50% credible interval; light green, 95% credible interval. Icons are interventions, shown at the time at which they occurred.

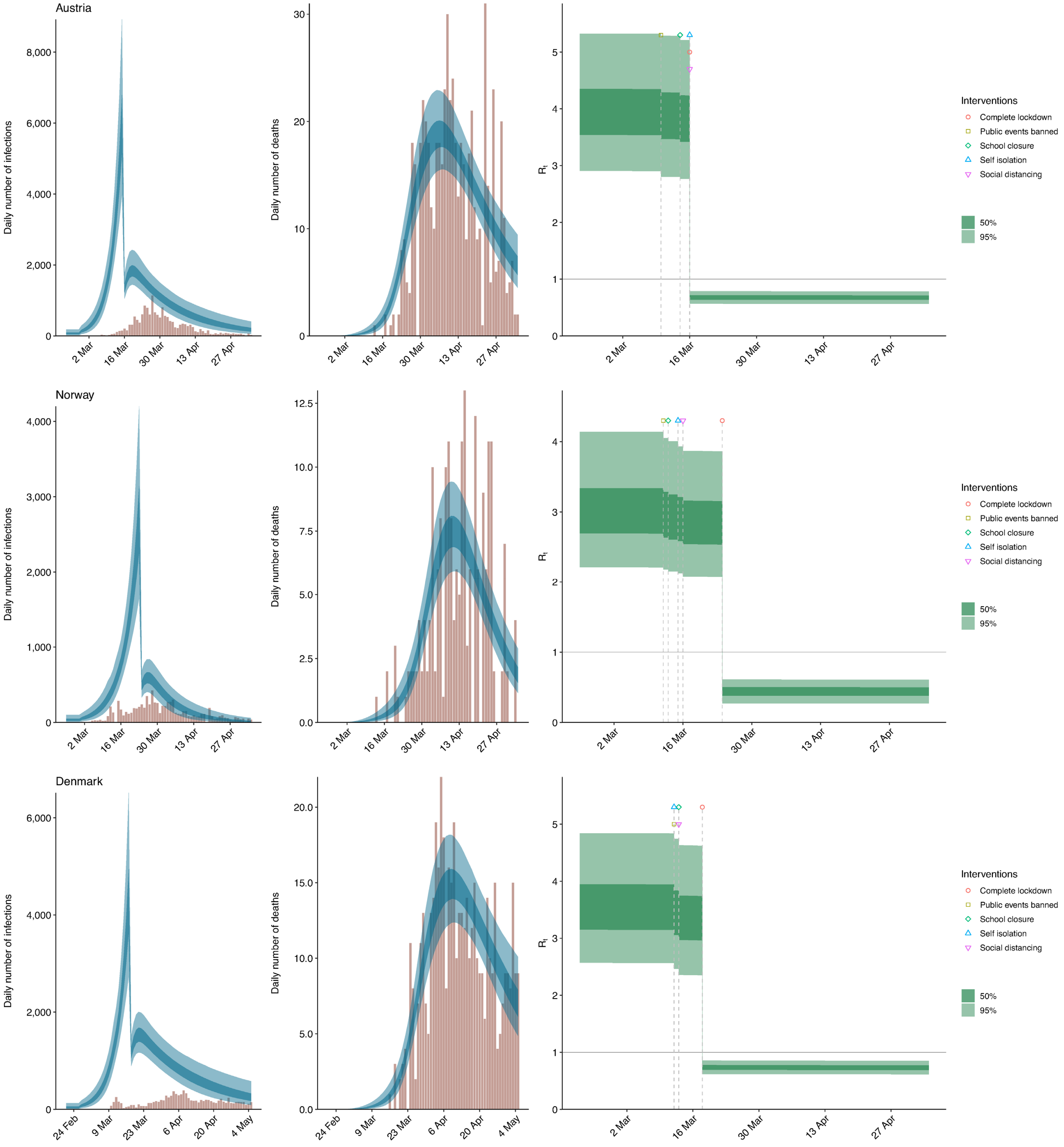

Extended Data Fig. 2 | Country-level estimates of infections, deaths and R_t for Austria, Norway and Denmark. Left, daily number of infections. Brown bars are reported infections; blue bands are predicted infections; dark blue, 50% credible interval; light blue, 95% credible interval. The number of daily infections estimated by our model drops immediately after an intervention, as we assume that all infected people become immediately less infectious through the intervention. Afterwards, if R_t is above 1, the number of infections will starts growing again. Middle, daily number of deaths. Brown bars are reported deaths; blue bands are predicted deaths; credible intervals are as in the left plot. Right, R_t. Dark green, 50% CI; light green, 95% CI. Icons are interventions, shown at the time at which they occurred.

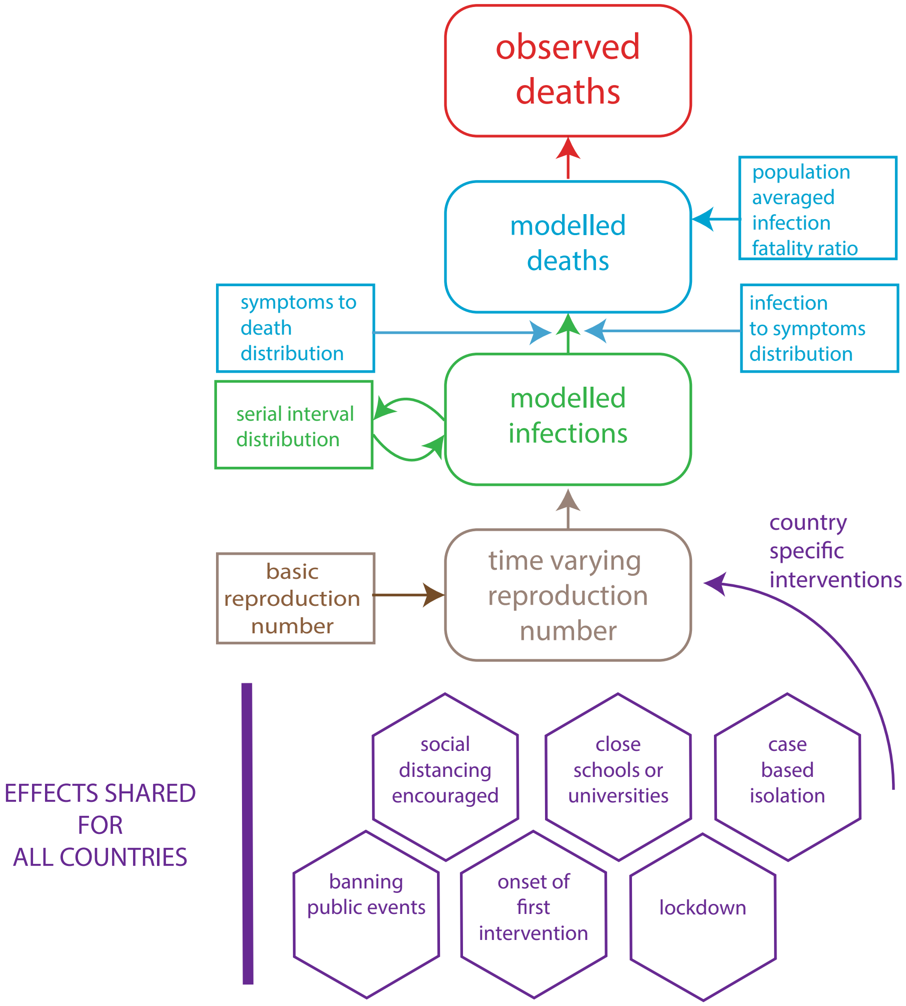

Extended Data Fig. 3 | Model summary. This figure shows a summary of the components of our model.

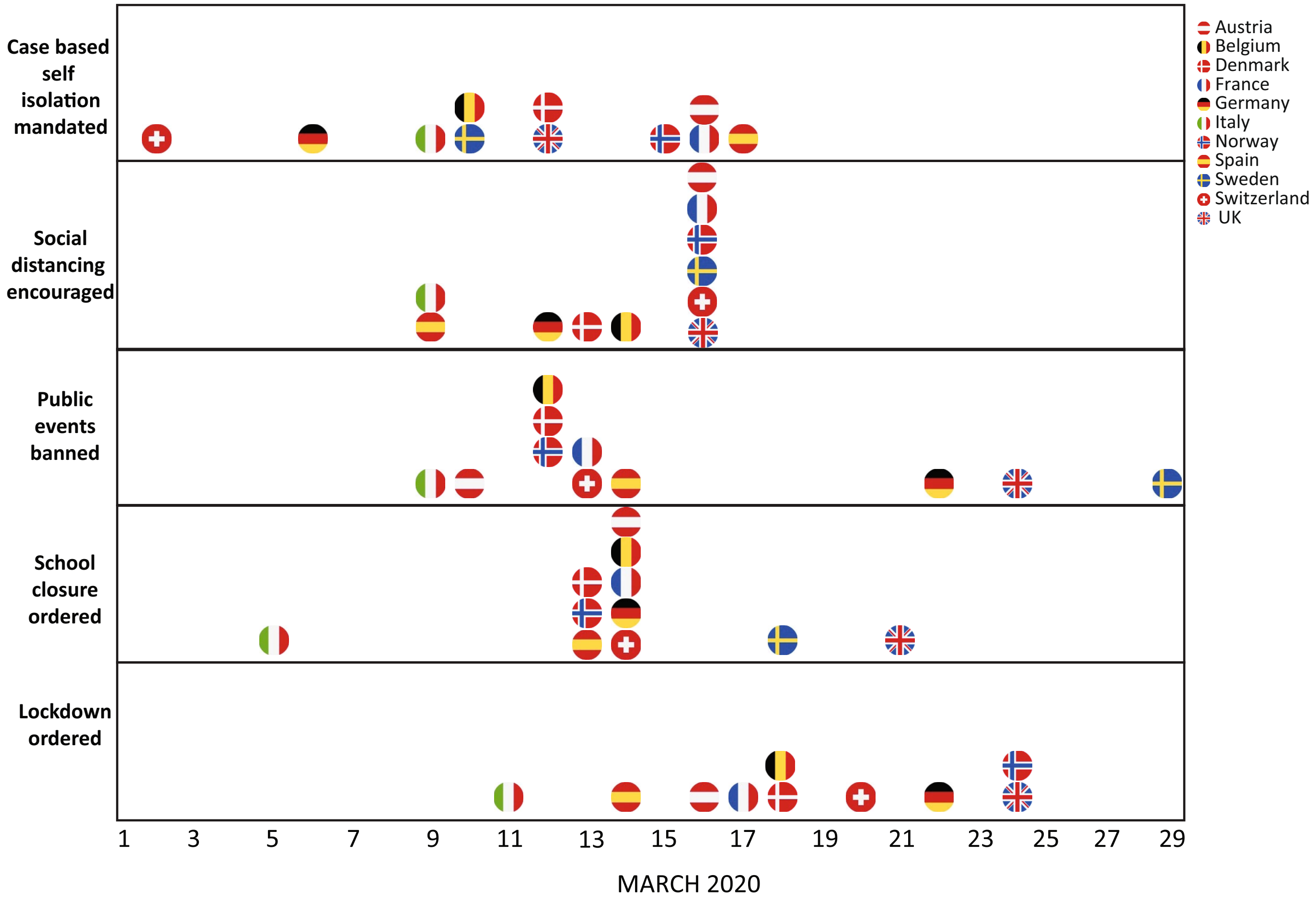

Extended Data Fig. 4 | Timings of interventions. Timings of interventions for the 11 European countries included in our analysis. For further details, see the Supplementary Information.

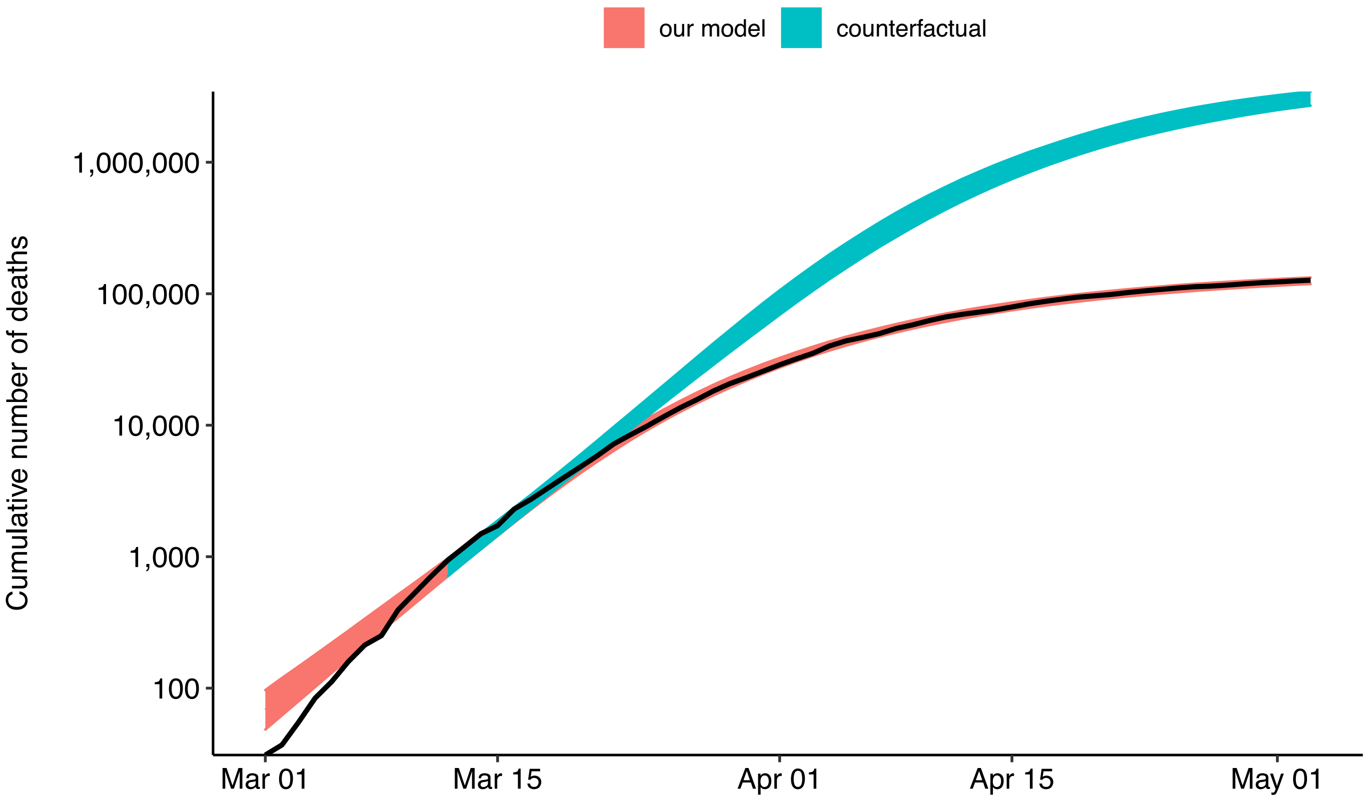

Extended Data Fig. 5 | Deaths averted owing to interventions. Lower and upper credible interval for the cumulative number of deaths for the 11 European countries in our model with interventions (pink) and the no-interventions counterfactual model (blue). Reported deaths are shown as a thick black line.

Extended Data Table 1 | Total forecasted deaths since the beginning of the epidemic up to 4 May 2020 in our model and in a counterfactual model that assumes no interventions had taken place

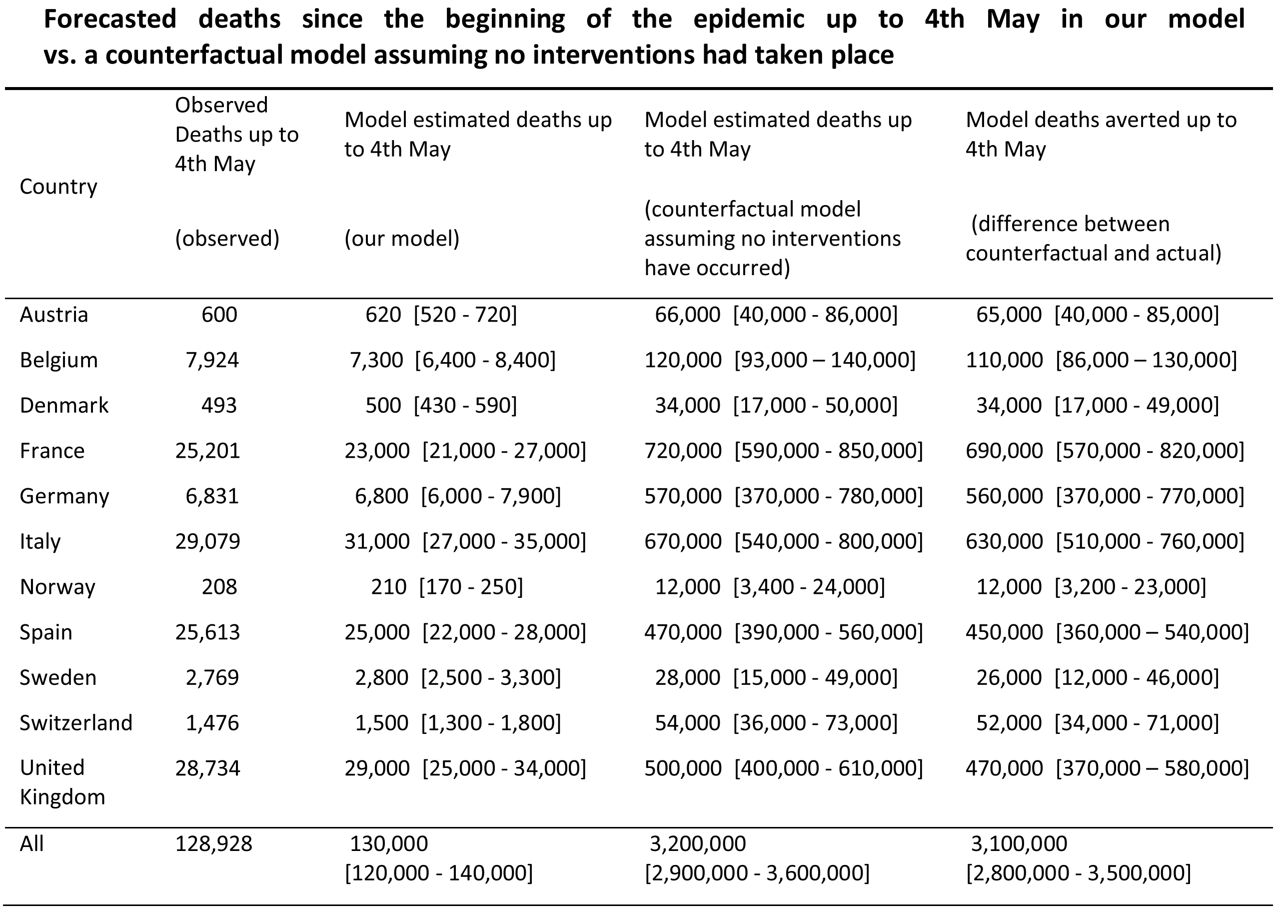

Forecasted deaths since the beginning of the epidemic up to 4th May in our model vs. a counterfactual model assuming no interventions had taken place

Country	Observed Deaths up to 4th May (observed)	Model estimated deaths up to 4th May (our model)	Model estimated deaths up to 4th May (counterfactual model assuming no interventions have occurred)	Model deaths averted up to 4th May (difference between counterfactual and actual)
Austria	600	620 [520 - 720]	66,000 [40,000 - 86,000]	65,000 [40,000 - 85,000]
Belgium	7,924	7,300 [6,400 - 8,400]	120,000 [93,000 – 140,000]	110,000 [86,000 – 130,000]
Denmark	493	500 [430 - 590]	34,000 [17,000 - 50,000]	34,000 [17,000 - 49,000]
France	25,201	23,000 [21,000 - 27,000]	720,000 [590,000 - 850,000]	690,000 [570,000 - 820,000]
Germany	6,831	6,800 [6,000 - 7,900]	570,000 [370,000 - 780,000]	560,000 [370,000 - 770,000]
Italy	29,079	31,000 [27,000 - 35,000]	670,000 [540,000 - 800,000]	630,000 [510,000 - 760,000]
Norway	208	210 [170 - 250]	12,000 [3,400 - 24,000]	12,000 [3,200 - 23,000]
Spain	25,613	25,000 [22,000 - 28,000]	470,000 [390,000 - 560,000]	450,000 [360,000 – 540,000]
Sweden	2,769	2,800 [2,500 - 3,300]	28,000 [15,000 - 49,000]	26,000 [12,000 - 46,000]
Switzerland	1,476	1,500 [1,300 - 1,800]	54,000 [36,000 - 73,000]	52,000 [34,000 - 71,000]
United Kingdom	28,734	29,000 [25,000 - 34,000]	500,000 [400,000 - 610,000]	470,000 [370,000 – 580,000]
All	128,928	130,000 [120,000 - 140,000]	3,200,000 [2,900,000 - 3,600,000]	3,100,000 [2,800,000 - 3,500,000]

Estimated averted deaths over this time period as a result of the interventions. Numbers in brackets are 95% credible intervals.

nature research

Corresponding author(s): Dr Samir Bhatt

Last updated by author(s): May 22, 2020

Reporting Summary

Nature Research wishes to improve the reproducibility of the work that we publish. This form provides structure for consistency and transparency in reporting. For further information on Nature Research policies, see our Editorial Policies and the Editorial Policy Checklist.

Statistics

For all statistical analyses, confirm that the following items are present in the figure legend, table legend, main text, or Methods section.

n/a	Confirmed	
☐	☒	The exact sample size (*n*) for each experimental group/condition, given as a discrete number and unit of measurement
☐	☒	A statement on whether measurements were taken from distinct samples or whether the same sample was measured repeatedly
☐	☒	The statistical test(s) used AND whether they are one- or two-sided *Only common tests should be described solely by name; describe more complex techniques in the Methods section.*
☐	☒	A description of all covariates tested
☐	☒	A description of any assumptions or corrections, such as tests of normality and adjustment for multiple comparisons
☐	☒	A full description of the statistical parameters including central tendency (e.g. means) or other basic estimates (e.g. regression coefficient) AND variation (e.g. standard deviation) or associated estimates of uncertainty (e.g. confidence intervals)
☒	☐	For null hypothesis testing, the test statistic (e.g. *F*, *t*, *r*) with confidence intervals, effect sizes, degrees of freedom and *P* value noted *Give P values as exact values whenever suitable.*
☐	☒	For Bayesian analysis, information on the choice of priors and Markov chain Monte Carlo settings
☐	☒	For hierarchical and complex designs, identification of the appropriate level for tests and full reporting of outcomes
☒	☐	Estimates of effect sizes (e.g. Cohen's *d*, Pearson's *r*), indicating how they were calculated

Our web collection on statistics for biologists contains articles on many of the points above.

Software and code

Policy information about availability of computer code

Data collection	No such software was used
Data analysis	RStan version 2.19.3 was used within R version 3.6.3

For manuscripts utilizing custom algorithms or software that are central to the research but not yet described in published literature, software must be made available to editors and reviewers. We strongly encourage code deposition in a community repository (e.g. GitHub). See the Nature Research guidelines for submitting code & software for further information.

Data

Policy information about availability of data

All manuscripts must include a data availability statement. This statement should provide the following information, where applicable:

- Accession codes, unique identifiers, or web links for publicly available datasets
- A list of figures that have associated raw data
- A description of any restrictions on data availability

All source code and data necessary for the replication of our results is available at https://github.com/ImperialCollegeLondon/covid19model
The full set of posterior draws from our model are available at https://reshare.ukdataservice.ac.uk/854380/

Field-specific reporting

Please select the one below that is the best fit for your research. If you are not sure, read the appropriate sections before making your selection.

☒ Life sciences ☐ Behavioural & social sciences ☐ Ecological, evolutionary & environmental sciences

For a reference copy of the document with all sections, see nature.com/documents/nr-reporting-summary-flat.pdf

Life sciences study design

All studies must disclose on these points even when the disclosure is negative.

Sample size	No samples were collected; data on the count of COVID-19-related deaths over time in 11 European countries was used.
Data exclusions	No data was excluded.
Replication	n/a
Randomization	n/a
Blinding	n/a

Reporting for specific materials, systems and methods

We require information from authors about some types of materials, experimental systems and methods used in many studies. Here, indicate whether each material, system or method listed is relevant to your study. If you are not sure if a list item applies to your research, read the appropriate section before selecting a response.

Materials & experimental systems

n/a	Involved in the study
☒	☐ Antibodies
☒	☐ Eukaryotic cell lines
☒	☐ Palaeontology and archaeology
☒	☐ Animals and other organisms
☒	☐ Human research participants
☒	☐ Clinical data
☒	☐ Dual use research of concern

Methods

n/a	Involved in the study
☒	☐ ChIP-seq
☒	☐ Flow cytometry
☒	☐ MRI-based neuroimaging

Article

The effect of large-scale anti-contagion policies on the COVID-19 pandemic

https://doi.org/10.1038/s41586-020-2404-8

Received: 22 March 2020

Accepted: 26 May 2020

Solomon Hsiang[1,2,3] ✉, Daniel Allen[1], Sébastien Annan-Phan[1,4], Kendon Bell[1,5], Ian Bolliger[1,6], Trinetta Chong[1], Hannah Druckenmiller[1,4], Luna Yue Huang[1,4], Andrew Hultgren[1,4], Emma Krasovich[1], Peiley Lau[1,4], Jaecheol Lee[1,4], Esther Rolf[1,7], Jeanette Tseng[1] & Tiffany Wu[1]

Governments around the world are responding to the coronavirus disease 2019 (COVID-19) pandemic[1], caused by severe acute respiratory syndrome coronavirus 2 (SARS-CoV-2), with unprecedented policies designed to slow the growth rate of infections. Many policies, such as closing schools and restricting populations to their homes, impose large and visible costs on society; however, their benefits cannot be directly observed and are currently understood only through process-based simulations[2–4]. Here we compile data on 1,700 local, regional and national non-pharmaceutical interventions that were deployed in the ongoing pandemic across localities in China, South Korea, Italy, Iran, France and the United States. We then apply reduced-form econometric methods, commonly used to measure the effect of policies on economic growth[5,6], to empirically evaluate the effect that these anti-contagion policies have had on the growth rate of infections. In the absence of policy actions, we estimate that early infections of COVID-19 exhibit exponential growth rates of approximately 38% per day. We find that anti-contagion policies have significantly and substantially slowed this growth. Some policies have different effects on different populations, but we obtain consistent evidence that the policy packages that were deployed to reduce the rate of transmission achieved large, beneficial and measurable health outcomes. We estimate that across these 6 countries, interventions prevented or delayed on the order of 61 million confirmed cases, corresponding to averting approximately 495 million total infections. These findings may help to inform decisions regarding whether or when these policies should be deployed, intensified or lifted, and they can support policy-making in the more than 180 other countries in which COVID-19 has been reported[7].

The COVID-19 pandemic is forcing societies worldwide to make consequential policy decisions with limited information. After containment of the initial outbreak failed, attention turned to implementing non-pharmaceutical interventions that are designed to slow the contagion of the virus. In general, these policies aim to decrease virus transmission by reducing contact among individuals within or between populations, such as by closing restaurants or restricting travel, thereby slowing the spread of COVID-19 to a manageable rate. These large-scale anti-contagion policies are informed by epidemiological simulations[2,4,8,9] and a small number of natural experiments during past epidemics[10]. However, the actual effects of these policies on infection rates in the ongoing pandemic are unknown. Because the modern world has never confronted this pathogen, nor deployed anti-contagion policies of such scale and scope, it is crucial that direct measurements of the effects of policies are used together with numerical simulations in current decision-making.

Societies around the world are considering whether the health benefits of anti-contagion policies are worth their social and economic costs. Many of these costs are clearly observed; for example, business restrictions increase unemployment and school closures affect educational outcomes. It is therefore not surprising that some populations have hesitated before implementing such policies, especially when their costs are visible while their health benefits—infections and deaths that would have occurred but are instead avoided or delayed—are unseen. Our objective is to measure the direct health benefits of these policies; specifically, how much these policies slowed the growth rate of infections. To do this, we compare the growth rate of infections within hundreds of subnational regions before and after each of these policies is implemented locally. Intuitively, each administrative unit observed immediately before a policy deployment serves as the 'control' for the same unit in the days after it receives a policy 'treatment' (see Supplementary Information for accounts of these deployments). Our hope is to learn from the recent experience of six countries in which the early spread of the virus triggered large-scale policy actions, in part so that societies and decision-makers everywhere can access this information.

---

[1]Global Policy Laboratory, Goldman School of Public Policy, UC Berkeley, Berkeley, CA, USA. [2]National Bureau of Economic Research, Cambridge, MA, USA. [3]Centre for Economic Policy Research, London, UK. [4]Agricultural & Resource Economics, UC Berkeley, Berkeley, CA, USA. [5]Manaaki Whenua – Landcare Research, Auckland, New Zealand. [6]Energy & Resources Group, UC Berkeley, Berkeley, CA, USA. [7]Electrical Engineering & Computer Science Department, UC Berkeley, Berkeley, CA, USA. ✉e-mail: shsiang@berkeley.edu

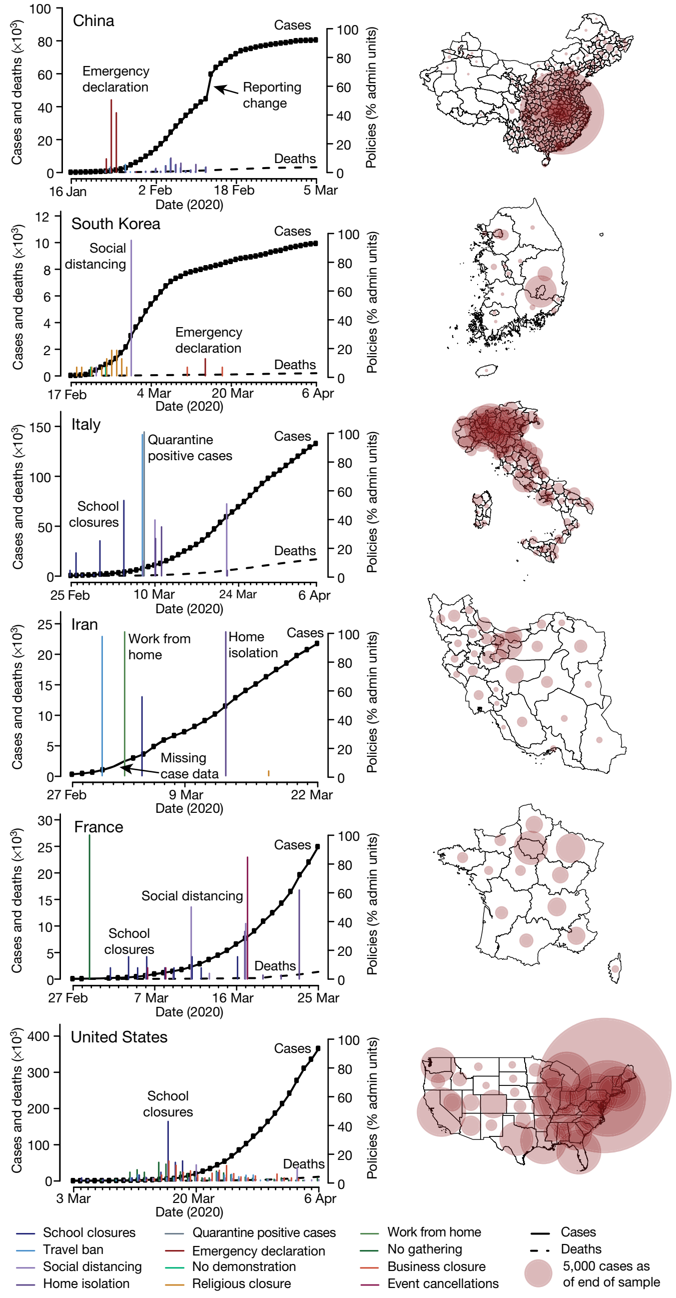

Fig. 1 | Data on COVID-19 infections and large-scale anti-contagion policies. Left, daily cumulative confirmed cases of COVID-19 (solid black line, left axis) and deaths (dashed black line) over time. Vertical lines are deployments of anti-contagion policies, for which the height indicates the number of administrative units that instituted a policy that day (right axis). For display purposes only, ≤5 policy types are shown per country and missing case data are imputed unless all subnational units are missing. Right, maps of cumulative confirmed cases by administrative unit on the last date of each sample.

Here we directly estimate the effects of 1,700 local, regional and national policies on the growth rate of infections across localities within China, South Korea, Italy, Iran, France and the United States (Fig. 1 and Supplementary Table 1). We compile subnational data on daily infection rates, changes in case definitions and the timing of policy deployments, including (1) travel restrictions, (2) social distancing through the cancellations of events and suspensions of educational, commercial and religious activities, (3) quarantines and lockdowns, and (4) additional policies such as emergency declarations and expansions of paid sick leave, from the earliest available dates to 6 April 2020 (Extended Data Fig. 1 and Supplementary Notes). During this period, populations remained almost entirely susceptible to COVID-19, causing the natural spread of infections to exhibit almost perfect exponential growth[11–13]. The rate of this exponential growth could change daily, determined by epidemiological factors, such as disease infectivity, as well as policies that alter behaviour[9,11]. Because policies were deployed while the epidemic unfolded, we can estimate their effects empirically. We examine how the daily growth rate of infections in each locality changed in response to the collection of ongoing policies applied to that locality on that day.

We use well-established reduced-form econometric techniques[5,14] that are commonly used to measure the effects of events[6,15] on economic growth rates. Similar to early COVID-19 infections, economic output generally increases exponentially with a variable rate that can be affected by policies and other conditions. Here, this technique aims to measure the total magnitude of the effect of changes in policy, without requiring explicit prior information about fundamental epidemiological parameters or mechanisms, many of which remain uncertain in the current pandemic. Instead, the collective influence of these factors is empirically recovered from the data without modelling their individual effects explicitly (see Methods). Previous research on influenza[16], for example, has shown that such statistical approaches can provide important complementary information to process-based models.

To construct the dependent variable, we transform location-specific, subnational time-series data on infections into first differences of their natural logarithm, which is the per-day growth rate of infections (see Methods). We use data from first- or second-level administrative units and data on active or cumulative cases, depending on availability (Supplementary Notes). We employ widely used panel regression models[5,14] to estimate how the daily growth rate of infections changes over time within a location when different combinations of large-scale policies are enacted (see Methods). Our econometric approach accounts for differences in the baseline growth rate of infections across subnational locations, which may be affected by time-invariant characteristics, such as demographics, socioeconomic status, culture and health systems; it accounts for systematic patterns in growth rates within countries unrelated to policy, such as the effect of the workweek; it is robust to systematic undersurveillance specific to each subnational unit; and it accounts for changes in procedures to diagnose positive cases (Methods and Supplementary Methods).

We estimate that in the absence of policies, early infection rates of COVID-19 grow 43% per day on average across these six countries (s.e.m. = 5%), implying a doubling time of approximately 2 days. Country-specific estimates range from 34% per day in the United States (s.e.m. = 7%) to 68% per day in Iran (s.e.m. = 9%). We cannot determine whether the high estimate for Iran results from true epidemiological differences, data-quality issues (see Methods), the concurrence of the initial outbreak with a major religious holiday and pilgrimage (Supplementary Notes) or sampling variability. Excluding Iran, the average growth rate is 38% per day (s.e.m. = 5%). Growth rates in all five other countries are independently estimated to be very near this value (Fig. 2a). These estimated values differ from observed average growth rates because the latter are confounded by the effects of policies. These growth rates are not driven by the expansion of testing or increasing rates of case detection (Methods and Extended Data Fig. 2) nor by data from individual regions (Extended Data Fig. 3).

Some previous analyses of pre-intervention infections in Wuhan have suggested that the growth rates were slower (doubling every 5–7 days)[17,18] using data collected before national standards for diagnosis and case definitions were first issued by the Chinese government on 15 January 2020[19]. However, case data in Wuhan from before this date contain multiple irregularities: the cumulative case count decreased on 9 January 2020; no new cases were reported for 9–15 January; and there were concerns that information about the outbreak was suppressed[20] (Supplementary Table 2). When we remove these data,

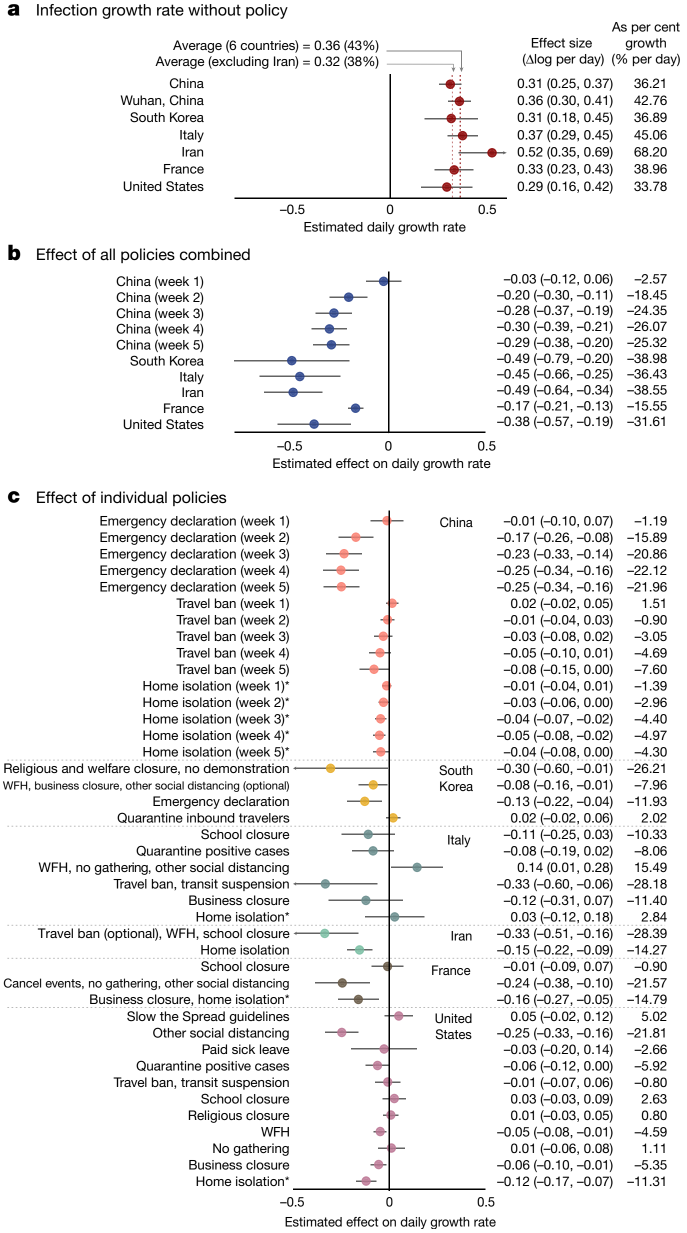

Fig. 2 | Empirical estimates of unmitigated COVID-19 infection growth rates and the effect of anti-contagion policies. Markers are country-specific estimates, whiskers show the 95% confidence interval. Columns report effect sizes as a change in the continuous-time growth rate (95% confidence intervals are shown in parentheses) and the day-over-day percentage growth rate. **a**, Estimates of daily COVID-19 infection growth rates in the absence of policy (dashed lines, averages with and without Iran, both excluding the Wuhan-specific estimate). **b**, Estimated combined effect of all policies on infection growth rates. **c**, Estimated effects of individual policies or policy groups on the daily growth rate of infections, jointly estimated and ordered roughly chronologically within each country. The asterisks indicate that the reported effect of 'home isolation' includes effects of other implied policies (see Methods). WFH denotes work from home policy. China, $n = 3{,}669$; South Korea, $n = 595$; Italy, $n = 2{,}898$; Iran, $n = 548$; France, $n = 270$; United States, $n = 1{,}238$.

using a shorter but more reliable pre-intervention time series from Wuhan (16–21 January), we recover a growth rate of 43% per day (s.e.m. = 3%), which corresponds to a doubling time of 2 days, consistent with results from all other countries except Iran (Fig. 2a).

During the early stages of an epidemic, a large proportion of the population remains susceptible to the virus, and if the spread of the virus is left uninhibited by changes in policies or behaviour, exponential growth continues until the fraction of the susceptible population decreases meaningfully[11,13,21,22]. After correcting for estimated rates of case detection[23], we compute that the minimum susceptible fraction across administrative units in our sample is 72% of the total population (Cremona, Italy) and 87% of administrative units would be likely to be in a regime of uninhibited exponential growth (that is, more than 95% of the population remains susceptible) if policies were removed on the last date of our sample.

Consistent with predictions from epidemiological models[2,10,24], we find that the combined effect of policies within each country reduces the growth rate of infections by a substantial and statistically significant amount (Fig. 2b and Supplementary Table 3). For example, a locality in France with a baseline growth rate of 0.33 (national average) that fully deployed all policy actions used in France would be expected to lower its daily growth rate by −0.17 to a growth rate of 0.16. In general, the estimated total effects of policy packages are large enough that they can in principle offset a large fraction of, or even eliminate, the baseline growth rate of infections—although in several countries, many localities have not deployed the full set of policies. Overall, the estimated effects of all policies combined are generally insensitive to withholding regional (that is, state- or province-level) blocks of data from the sample (Extended Data Fig. 3).

In China, only three policies were enacted across 115 cities early in a 7-week period, providing us with sufficient data to empirically estimate how the effects of these policies evolved over time without making assumptions about the timing of these effects (Fig. 2b and Methods). We estimate that the combined effect of these policies reduced the growth rate of infections by −0.026 (s.e.m. = 0.046) in the first week after they came into effect, increasing substantially in the second week to −0.20 (s.e.m. = 0.049), and essentially stabilizing in the third week around −0.28 (s.e.m. = 0.047). In other countries, we lack sufficient data to estimate these temporal dynamics explicitly and only report the average pooled effect of policies across all days after their deployment (Methods). If other countries have transient responses similar to China, we would expect that the effects in the first week after deployment are smaller in magnitude than the average effect that we report. We also explore how our estimates would change if we impose the assumption that policies cannot affect infection growth rates until after a fixed number of days (Extended Data Fig. 5a and Supplementary Methods section 3); however, we do not find evidence that this improves model fit.

The estimates described above (Fig. 2b) capture the superposition of all policies deployed in each country; that is, they represent the average effect of policies that we would expect to observe if all policies enacted anywhere in each country were implemented simultaneously in a single region of that country. We also estimate the effects of individual policies or clusters of policies (Fig. 2c) that are grouped based on either their similarity in goal (for example, library and museum closures) or timing (for example, policies deployed simultaneously). Our estimates for these individual effects tend to be statistically noisier than the estimates for all policies combined. Some estimates for the same policy differ between countries, perhaps because policies are not implemented identically or because populations behave differently. Nonetheless, 22 out of 29 point estimates indicate that individual policies are probably contributing to the reduction of the growth rate of infections. Seven policies (one in South Korea, two in Italy and four in the United States) have point estimates that are positive, six of which are small in magnitude (less than 0.1) and not statistically different from zero (5% level). Consistent with greater overall uncertainty in these disaggregated estimates, some of the estimates in China, South Korea, Italy and France are moderately more sensitive to withholding regional blocks of data (Extended Data Fig. 4), but remain broadly robust to the assumption of a constant delayed effect of all policies (Extended Data Fig. 5b).

On the basis of these results, we find that the deployment of anti-contagion policies in all six countries significantly slowed the

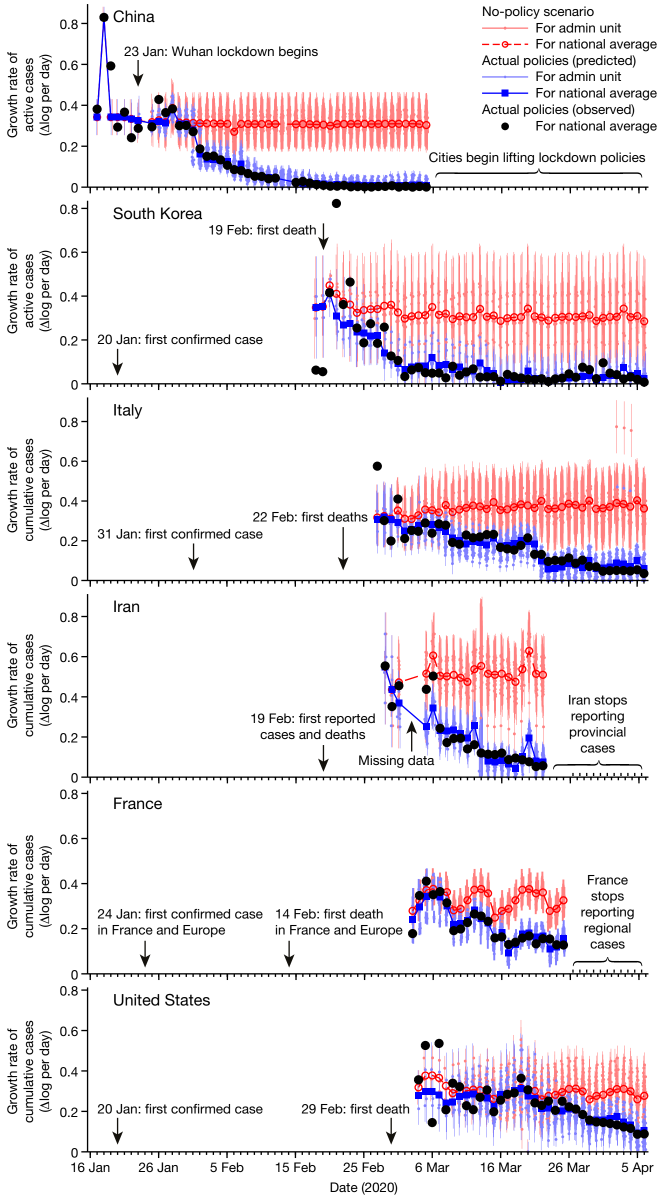

Fig. 3 | Estimated infection growth rates based on actual anti-contagion policies and in a no-policy counterfactual scenario. Predicted daily growth rates of active (China and South Korea) or cumulative (all others) COVID-19 infections based on the observed timing of all policy deployments within each country (blue) and in a scenario in which no policies were deployed (red). The difference between these two predictions is our estimated effect of actual anti-contagion policies on the growth rate of infections. Small markers are daily estimates for subnational administrative units (vertical lines are 95% confidence interval). Large markers are national averages. Black circles are observed daily changes in log(infections), averaged across administrative units. Sample sizes are the same as in Fig. 2.

pandemic. We combine the estimates above with our data on the timing of the 1,700 policy deployments to estimate the total effect of all policies across the dates in our sample. To do this, we use our estimates to predict the growth rate of infections in each locality on each day, given the actual policies in effect at that location on that date (Fig. 3). We then use the same model to predict what the counterfactual growth rates would be on that date if the effects of all policies were removed (Fig. 3), which we call the no-policy scenario. The difference between these two predictions is our estimate of the effect that all deployed policies had on the growth rate of infections. During our sample, we estimate that all policies combined slowed the average growth rate of infections by −0.252 per day (s.e.m. = 0.045, $P < 0.001$) in China, −0.248 (s.e.m. = 0.089, $P < 0.01$) in South Korea, −0.24 (s.e.m. = 0.068, $P < 0.001$) in Italy, −0.355 (s.e.m. = 0.063, $P < 0.001$) in Iran, −0.123 (s.e.m. = 0.019, $P < 0.001$) in France and −0.084 (s.e.m. = 0.03, $P < 0.01$) in the United States. These results are robust to modelling the effects of policies without grouping them (Extended Data Fig. 6a and Supplementary Table 4) or assuming a delayed effect of policy on infection growth rates (Supplementary Table 5).

The number of COVID-19 infections on a date depends on the growth rate of infections on all previous days. Thus, persistent reductions in growth rates have a compounding effect on infections, until growth is slowed by a shrinking susceptible population. To provide a sense of scale for our results, we integrate the growth rate of infections in each locality from Fig. 3 to estimate cumulative infections, both with actual anti-contagion policies and in the no-policy scenario. To account for the declining susceptible population in each administrative unit, we couple our econometric estimates of the effects of policies with a susceptible–infected–removed model[11,13] that adjusts the susceptible population in each administrative unit based on estimated case-detection rates[23,25] (see Methods). This allows us to extend our projections beyond the initial exponential growth phase of infections, a threshold that many localities cross in our no-policy scenario.

Our results suggest that anti-contagion policies have already substantially reduced the number of COVID-19 infections observed in the world at present (Fig. 4). Our central estimates suggest that there would be approximately 37 million more cumulative confirmed cases (corresponding to 285 million more total infections, including the confirmed cases by 5 March 2020) in China, 11.5 million more confirmed cases (38 million total infections by 6 April 2020) in South Korea, 2.1 million more confirmed cases (49 million total infections by 6 April 2020) in Italy, 4.9 million more confirmed cases (54 million total infections by 22 March 2020) in Iran, 280,000 more confirmed cases (9 million total infections by 25 March 2020) in France and 4.8 million more confirmed cases (60 million total infections by 6 April 2020) in the United States had these countries never enacted any anti-contagion policies since the start of the pandemic.The magnitudes of these impacts partially reflect the timing, intensity and extent of policy deployment (for example, how many localities deployed policies) and the duration for which they have been applied. Several of these estimates are subject to large statistical uncertainties (see intervals in Fig. 4). Sensitivity tests (Extended Data Fig. 7) that assume a range of plausible alternative parameter values relating to disease dynamics, such as incorporating a susceptible–exposed–infected–removed model, suggest that interventions may have reduced the severity of the outbreak by a total of 54–65 million confirmed cases over the dates in our sample (central estimates). Sensitivity tests in which the assumed infection–fatality ratio is varied (Supplementary Table 6) suggest a corresponding range of 46–77 million confirmed cases (490–580 million total infections).

Our empirical results indicate that large-scale anti-contagion policies have slowed the COVID-19 pandemic. Because infection rates in the countries that we studied would have initially followed rapid exponential growth had no policies been applied, our results suggest that these policies have provided large health benefits. For example, we estimate that there would be approximately 465× the observed number of confirmed cases in China, 17× the number in Italy and 14× the number in the United States by the end of our analysis if large-scale anti-contagion policies had not been deployed. Consistent with process-based simulations of COVID-19 infections[2,4,8,9,22,26], our analysis of existing policies indicates that seemingly small delays in policy deployment are likely to have produced markedly different health outcomes.

Although the limitations of available data pose challenges to our analysis, our aim is to use what data exist to estimate the first-order effects of unprecedented policy actions in an ongoing global crisis. As more data become available, related findings will become more

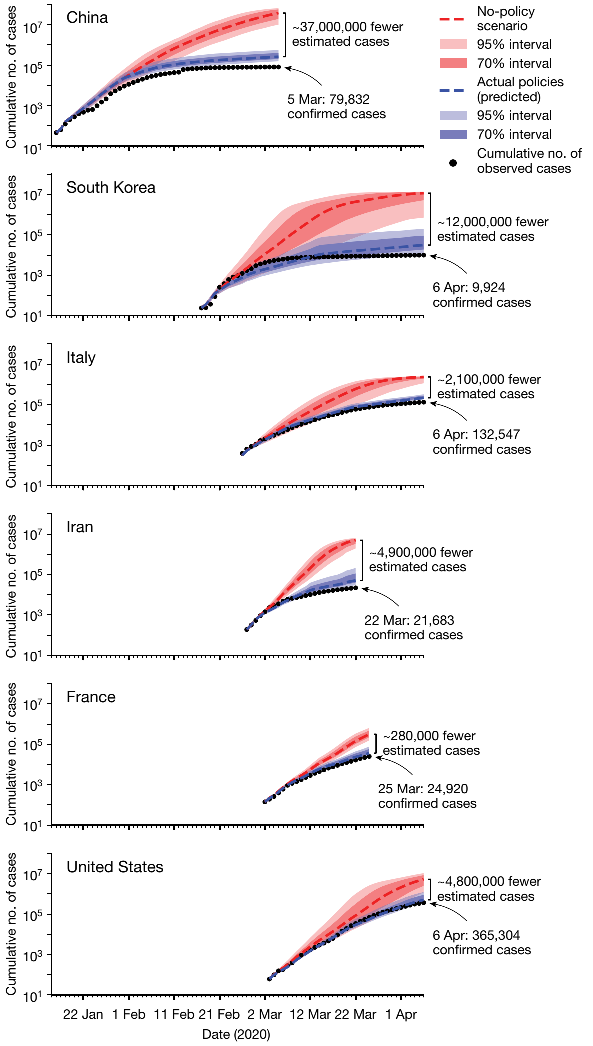

Fig. 4 | Estimated cumulative confirmed COVID-19 infections with and without anti-contagion policies. The predicted cumulative number of confirmed COVID-19 infections based on actual policy deployments (blue) and in the no-policy counterfactual scenario (red). Shaded areas show uncertainty based on 1,000 simulations for which empirically estimated parameters are resampled from their joint distribution (dark, inner 70% of predictions; light, inner 95%). Black dotted line is observed cumulative infections. Infections are not projected for administrative units that never report infections in the sample, but which might have experienced infections in a no-policy scenario.

precise and may capture more complex interactions. Furthermore, this analysis does not account for interactions between populations in nearby localities[13], nor mobility networks[3,4,8,9]. Nonetheless, we hope that these results can support critical decision-making, both in the countries that we study and in the more than 180 other countries in which COVID-19 infections have been reported[7].

A key advantage of our reduced-form top-down statistical approach is that it captures the real-world behaviour of affected populations without requiring that we explicitly model the underlying mechanisms and processes. This is useful in the current pandemic, for which many process-related parameters remain uncertain. However, our results cannot and should not be interpreted as a substitute for bottom-up process-based epidemiological models that are specifically designed to provide guidance in public health crises. Rather, our results complement existing models, for example, by helping to calibrate key model parameters. We believe both forward-looking simulations and backward-looking empirical evaluations should be used to inform decision-making.

Our analysis measures changes in local infection growth rates associated with changes in anti-contagion policies. A necessary condition for this association to be interpreted as the plausibly causal effect of these policies is that the timing of policy deployment is independent of infection growth rates[14]. This assumption is supported by established epidemiological theory[11,13,27] and evidence[28,29], which indicate that infections in the absence of policy will grow exponentially early in the epidemic, implying that pre-policy infection growth rates should be constant over time and therefore uncorrelated with the timing of policy deployment. Furthermore, scientific guidance to decision-makers early in the current epidemic explicitly projected constant growth rates in the absence of anti-contagion measures, limiting the possibility that anticipated changes in natural growth rates affected decision-making[2,22,30,31]. In practice, policies tended to be deployed in response to the high total numbers of cases (for example, in France)[32], in response to outbreaks in other regions (for example, in China, South Korea and Iran)[33], after delays due to political constraints (for example, in the United States and Italy) and often with timings that coincided with arbitrary events, such as weekends or holidays (see Supplementary Notes for detailed chronologies).

Our analysis accounts for documented changes in COVID-19 testing procedures and availability, as well as differences in case detection across locations; however, unobserved trends in case detection could affect our results (see Methods). We analyse estimated case-detection trends[23] (Extended Data Fig. 2) and find that this potential bias is small—possibly elevating our estimated no-policy growth rates by 0.026 (7%) on average.

It is also possible that changing public knowledge during the period of our study affects our results. If individuals alter their behaviour in response to new information unrelated to anti-contagion policies, such as seeking out online resources, this could alter the growth rate of infections and thus affect our estimates. If increasing availability of information reduces infection growth rates, it would cause us to overstate the effectiveness of anti-contagion policies. We note, however, that if public knowledge is increasing in response to policy actions, such as through news reports, then it should be considered a pathway through which policies alter infection growth, not a form of bias. Investigating these potential effects is beyond the scope of this analysis, but it is an important topic for future investigations.

Finally, our analysis focuses on confirmed infections, but other outcomes, such as hospitalizations or deaths, are also of policy interest. Future studies on these outcomes may require additional modelling approaches because they are relatively more context- and state-dependent. Nonetheless, we experimentally implement our approach on the daily growth rate of hospitalizations in France, the only country in our sample for which hospitalization data are available at the granularity of this study. We find that the total estimated effect of anti-contagion policies on the growth rate of hospitalizations is similar to our estimates for infection growth rates (Extended Data Fig. 6c).

Online content

Any methods, additional references, Nature Research reporting summaries, source data, extended data, supplementary information, acknowledgements, peer review information; details of author contributions and competing interests; and statements of data and code availability are available at https://doi.org/10.1038/s41586-020-2404-8.

1. Wu, F. et al. A new coronavirus associated with human respiratory disease in China. *Nature* **579**, 265–269 (2020).
2. Ferguson, N. M. et al. Report 9: Impact of non-pharmaceutical interventions (NPIs) to reduce COVID-19 mortality and healthcare demand. *Technical Report* (Imperial College London, 2020).
3. Chinazzi, M. et al. The effect of travel restrictions on the spread of the 2019 novel coronavirus (COVID-19) outbreak. *Science* **368**, 395–400 (2020).
4. Kraemer, M. U. G. et al. The effect of human mobility and control measures on the COVID-19 epidemic in China. *Science* **368**, 493–497 (2020).

5. Greene, W. H. *Econometric Analysis* (Prentice Hall, 2003).
6. Romer, C. D. & Romer, D. H. The macroeconomic effects of tax changes: estimates based on a new measure of fiscal shocks. *Am. Econ. Rev*. **100**, 763–801 (2010).
7. WHO. *WHO Coronavirus Disease (COVID-19) Dashboard*. https://covid19.who.int (accessed 13 April 2020).
8. Li, R. et al. Substantial undocumented infection facilitates the rapid dissemination of novel coronavirus (SARS-CoV-2). *Science* **368**, 489–493 (2020).
9. Tang, B. et al. Estimation of the transmission risk of the 2019-nCoV and its implication for public health interventions. *J. Clin. Med*. **9**, 462 (2020).
10. Hatchett, R. J., Mecher, C. E. & Lipsitch, M. Public health interventions and epidemic intensity during the 1918 influenza pandemic. *Proc. Natl Acad. Sci. USA* **104**, 7582–7587 (2007).
11. Ma, J. Estimating epidemic exponential growth rate and basic reproduction number. *Infect. Dis. Model*. **5**, 129–141 (2020).
12. Muniz-Rodriguez, K. et al. Doubling time of the COVID-19 epidemic by province, China. *Emerg. Infect. Dis*. **26**, https://doi.org/10.3201/eid2608.200219 (2020).
13. Chowell, G., Sattenspiel, L., Bansal, S. & Viboud, C. Mathematical models to characterize early epidemic growth: a review. *Phys. Life Rev*. **18**, 66–97 (2016).
14. Angrist, J. D. & Pischke, J.-S. *Mostly Harmless Econometrics: An Empiricist's Companion* (Princeton Univ. Press, 2008).
15. Burke, M., Hsiang, S. M. & Miguel, E. Global non-linear effect of temperature on economic production. *Nature* **527**, 235–239 (2015).
16. Kandula, S. et al. Evaluation of mechanistic and statistical methods in forecasting influenza-like illness. *J. R. Soc. Interface* **15**, 20180174 (2018).
17. Wu, J. T. et al. Estimating clinical severity of COVID-19 from the transmission dynamics in Wuhan, China. *Nat. Med*. **26**, 506–510 (2020).
18. Li, Q. et al. Early transmission dynamics in Wuhan, China, of novel coronavirus-infected pneumonia. *N. Engl. J. Med*. **382**, 1199–1207 (2020).
19. Tsang, T. K. et al. Impact of changing case definitions for COVID-19 on the epidemic curve and transmission parameters in mainland China. Preprint at medRxiv https://doi.org/10.1101/2020.03.23.20041319 (2020).
20. Wuhan pneumonia: 30 days from outbreak to out of control [in Chinese]. *BBC News* https://www.bbc.com/zhongwen/simp/chinese-news-51290945 (2020).
21. Fisman, D., Khoo, E. & Tuite, A. Early epidemic dynamics of the West African 2014 Ebola outbreak: estimates derived with a simple two-parameter model. *PLoS Curr*. **6** https://doi.org/10.1371/currents.outbreaks.89c0d3783f36958d96ebbae97348d571 (2014).
22. Maier, B. F. & Brockmann, D. Effective containment explains subexponential growth in recent confirmed COVID-19 cases in China. *Science* **368**, 742–746 (2020).
23. Russell, T. W. et al. Using a delay-adjusted case fatality ratio to estimate under-reporting. *Technical Report* (Centre for the Mathematical Modelling of Infectious Diseases, London School of Hygiene and Tropical Medicine, 2020).
24. Bootsma, M. C. J. & Ferguson, N. M. The effect of public health measures on the 1918 influenza pandemic in U.S. cities. *Proc. Natl Acad. Sci. USA* **104**, 7588–7593 (2007).
25. Meyerowitz-Katz, G. & Merone, L. A systematic review and meta-analysis of published research data on COVID-19 infection-fatality rates. Preprint at medRxiv https://doi.org/10.1101/2020.05.03.20089854 (2020).
26. Kucharski, A. J. et al. Early dynamics of transmission and control of COVID-19: a mathematical modelling study. *Lancet Infect. Dis*. **20**, 553–558 (2020).
27. Anderson, R. M. & May, R. M. *Infectious Diseases of Humans: Dynamics and Control* (Oxford Univ. Press, 1992).
28. Nishiura, H., Chowell, G., Safan, M. & Castillo-Chavez, C. Pros and cons of estimating the reproduction number from early epidemic growth rate of influenza A (H1N1) 2009. *Theor. Biol. Med. Model*. **7**, 1 (2010).
29. WHO Ebola Response Team. Ebola virus disease in West Africa—the first 9 months of the epidemic and forward projections. *N. Engl. J. Med*. **371**, 1481–1495 (2014).
30. Flaxman, S. et al. Report 13: Estimating the number of infections and the impact of non-pharmaceutical interventions on COVID-19 in 11 European countries. *Technical Report* (Imperial College London, 2020).
31. Lourenço, J. et al. Fundamental principles of epidemic spread highlight the immediate need for large-scale serological surveys to assess the stage of the SARS-CoV-2 epidemic. Preprint at medRxiv https://doi.org/10.1101/2020.03.24.20042291 (2020).
32. Préparation au Risque épidémique COVID-19 [in French]. https://solidarites-sante.gouv.fr/IMG/pdf/guide_methodologique_covid-19-2.pdf (2020).
33. Tian, H. et al. An investigation of transmission control measures during the first 50 days of the COVID-19 epidemic in China. *Science* **368**, 638–642 (2020).

Publisher's note Springer Nature remains neutral with regard to jurisdictional claims in published maps and institutional affiliations.

Methods

Data reporting

No statistical methods were used to predetermine sample size. The experiments were not randomized and the investigators were not blinded to allocation during experiments and outcome assessment.

Data collection and processing

We provide a brief summary of our data collection processes here; further details, including access dates are provided in the Supplementary Notes. Epidemiological data, case definitions/testing regimes and policy data for each of the six countries in our sample were collected from a variety of in-country data sources, including government public health websites, regional newspaper articles and crowd-sourced information on Wikipedia. The availability of epidemiological and policy data varied across the six countries, and preference was given to the collection of data at the most granular administrative unit level. The country-specific panel datasets are at the regional level in France, the state level in the United States, the province level in South Korea, Italy and Iran, and the city level in China. Owing to data availability, the sample dates differ across countries: in China we use data from 16 January to 5 March 2020; in South Korea from 17 February to 6 April 2020; in Italy from 26 February to 6 April 2020; in Iran from 27 February to 22 March 2020; in France from 29 February to 25 March 2020; and in the United States from 3 March to 6 April 2020. Our data sources are described in more detail below.

China. We acquired epidemiological data from an open-source GitHub project[34] that scrapes time series data from Ding Xiang Yuan, a Chinese website that integrates COVID-19 epidemiological data from various local governments. We extended this dataset back in time to 10 January 2020 by manually collecting official daily statistics from the central and provincial (Hubei, Guangdong and Zhejiang) Chinese government websites. We compiled policies by collecting data on the start dates of emergency declarations, travel bans and lockdowns at the city level from the '2020 Hubei lockdowns' Wikipedia page[35] and various other news reports. We suspect that most Chinese cities have implemented at least one anti-contagion policy due to their reported trends in infections; as such, we dropped cities for which we could not identify a policy deployment date to avoid miscategorizing the policy status of these cities. Thus our results are only representative for the sample of 115 cities for which we obtained policy data.

South Korea. We manually collected and compiled the epidemiological dataset for South Korea, based on provincial government reports, policy briefings and news articles. We compiled policy actions from news articles and press releases from the Korean Centers for Disease Control and Prevention, the Ministry of Foreign Affairs and websites of local governments.

Iran. We used epidemiological data from the table 'New COVID-19 cases in Iran by province'[36] in the '2020 coronavirus pandemic in Iran' Wikipedia article, which were compiled from data provided by the Iranian Ministry of Health website (in Persian). We relied on news reporting and two timelines of pandemic events in Iran[36,37] to collate policy data. From 2 March to 3 March 2020, Iran did not report subnational cases. Around this period, the country implemented three national policies: a recommendation against local travel (1 March), work from home for government employees (3 March) and school closure (5 March). As the effects of these policies cannot be distinguished from each other due to the data gap, we group them together for the purpose of this analysis.

Italy. We used epidemiological data from the GitHub repository[38] maintained by the Italian Department of Civil Protection (Dipartimento della Protezione Civile). For policies, we primarily relied on the English version of the COVID-19 dossier 'Chronology of main steps and legal acts taken by the Italian Government for the containment of the COVID-19 epidemiological emergency' written by the Dipartimento della Protezione Civile[39], and Wikipedia[40].

France. We used the region-level epidemiological dataset provided by the government website of France[41] and supplemented it with the number of confirmed cases by region on the public health website of France, which was previously updated daily until 25 March[42]. We obtained data on the policy response to the COVID-19 pandemic from the French government website, press releases from each regional public health site[43] and Wikipedia[44].

United States. We used state-level epidemiological data from usafacts.org[45], which are compiled from multiple sources. For policy responses, we relied on a number of sources, including the US Centers for Disease Control and the National Governors Association, as well as various executive orders from county- and city-level governments, and press releases from media outlets.

Policy data. Policies in administrative units were coded as binary variables, for which the policy was coded as either 1 (after the date that the policy was implemented and before it was removed) or 0 (otherwise) for the affected administrative units. When a policy only affected a fraction of an administrative unit (for example, half of the counties within a state), policy variables were weighted by the percentage of people within the administrative unit who were treated by the policy. We used the most recent population estimates we could find for the administrative units of countries (see the 'Population Data' section in the Supplementary Information). To standardize policy types across countries, we mapped each country-specific policy to one of the broader policy category variables in our analysis. In this exercise, we collected 168 policies for China, 59 for South Korea, 214 for Italy, 23 for Iran, 59 for France and 1,177 for the United States (Supplementary Table 1). There are some cases for which we encode policies that are necessarily in effect whenever another policy is in place, owing in particular to the far-reaching implications of home-isolation policies. In China, wherever home isolation is documented, we assume a local travel ban is enacted on the same day if we have not found an explicit local travel ban policy for a given locality. In France, we assume home isolation is accompanied by event cancellations, social distancing and no-gathering policies; in Italy, we assume home isolation entails no-gathering, local travel ban, work from home and social distancing policies; in the United States, we assume shelter-in-place orders indicate that non-essential business closures, work from home policies and no-gathering policies are in effect. For policy types that are enacted multiple times at increasing degrees of intensity within a locality, we add weights to the variable by escalating the intensity from 0 pre-policy in steps up to 1 for the final version of the policy (see the 'Policy Data' section in the Supplementary Information).

Epidemiological data. We collected information on cumulative confirmed cases, cumulative recoveries, cumulative deaths, active cases and any changes to domestic COVID-19-testing regimes, such as case definitions or testing methodology. For our regression analysis (Fig. 2), we use active cases when they are available (China and South Korea) and cumulative confirmed cases otherwise. We document quality-control steps in the Supplementary Information. For China and South Korea, we acquired more granular data than the data hosted on the Johns Hopkins University (JHU) interactive dashboard[46]; we confirm that the number of confirmed cases closely match between the two data sources (see Extended Data Fig. 1). To conduct the econometric analysis, we merge the epidemiological and policy data to form a single data set for each country.

Econometric analysis

Reduced-form approach. The reduced-form econometric approach that we apply here is a 'top-down' approach that describes the behaviour of aggregate outcomes y in data (in this case, infection rates). This approach can identify plausibly causal effects[5,14] induced by exogenous changes in independent policy variables z (for example, school closure) without explicitly describing all underlying mechanisms that link z to y, without observing intermediary variables x (for example, behaviour) that might link z to y, or without other determinants of y unrelated to z (for example, demographics), denoted w. Let $f(\cdot)$ describe a complex and unobserved process that generates infection rates y:

$$y = f(x_1(z_1, \ldots, z_K), \ldots, x_N(z_1, \ldots, z_K), w_1, \ldots, w_M) \tag{1}$$

Process-based epidemiological models aim to capture elements of $f(\cdot)$ explicitly, and then simulate how changes in z, x or w affect y. This approach is particularly important and useful in forward-looking simulations in which future conditions are likely to be different than historical conditions. However, a challenge faced by this approach is that we may not know the full structure of $f(\cdot)$, for example, if a pathogen is new and many key biological and societal parameters remain uncertain. We may not know the effect that large-scale policy (z) will have on behaviour ($x(z)$) or how this behaviour change will affect infection rates ($f(\cdot)$).

Alternatively, one can differentiate equation (1) with respect to the kth policy z_k:

$$\frac{\partial y}{\partial z_k} = \sum_{j=1}^{N} \frac{\partial y}{\partial x_j} \frac{\partial x_j}{\partial z_k} \tag{2}$$

which describes how changes in the policy affects infections through all N potential pathways mediated by $x_1, \ldots, x_N$. Usefully, for a fixed population observed over time, empirically estimating an average value of the local derivative on the left side in equation (2) does not depend on explicit knowledge of w. If we can observe y and z directly and estimate changes over time $\frac{\partial y}{\partial z_k}$ with data, then intermediate variables x also need not be observed nor modelled. The reduced-form econometric approach[5,14] thus attempts to measure $\frac{\partial y}{\partial z_k}$ directly, exploiting exogenous variation in policies z.

Model. Active infections grow exponentially during the initial phase of an epidemic, when the proportion of immune individuals in a population is near zero. Assuming a simple susceptible–infected–recovered (SIR) disease model[11], the growth in infections during the early period is

$$\frac{\mathrm{d}I_t}{\mathrm{d}t} = (S_t\beta - \gamma)I_t \underset{S_t \to 1}{=} (\beta - \gamma)I_t, \tag{3}$$

where I_t is the number of infected individuals at time t, β is the transmission rate (new infections per day per infected individual), γ is the removal rate (proportion of infected individuals recovering or dying each day) and S is the fraction of the population susceptible to the disease. The second equality holds in the limit $S \to 1$, which describes conditions during the beginning of the COVID-19 pandemic. The solution to this ordinary differential equation is the exponential function

$$\frac{I_{t_2}}{I_{t_1}} = \mathrm{e}^{g(t_2 - t_1)}, \tag{4}$$

where I_{t_1} is the initial condition. Taking the natural logarithm and rearranging, we have

$$\log(I_{t_2}) - \log(I_{t_1}) = g(t_2 - t_1). \tag{5}$$

Anti-contagion policies are designed to alter g, through changes to β, by reducing contact between susceptible and infected individuals. Holding the time step between observations fixed at one day ($t_2 - t_1 = 1$), we thus model g as a time-varying outcome that is a linear function of a time-varying policy

$$g_t = \log(I_t) - \log(I_{t-1}) = \theta_0 + \theta\text{policy}_t + \varepsilon_t, \tag{6}$$

where θ_0 is the average growth rate without a policy, policy_t is a binary variable describing whether a policy is deployed at time t, and θ is the average effect of the policy on growth rate g over all periods subsequent to the introduction of the policy, thereby encompassing any lagged effects of policies. ε_t is a mean-zero disturbance term that captures interperiod changes not described by policy_t. Using this approach, infections each day are treated as the initial conditions for integrating equation (4) through to the following day.

We compute the first differences $\log(I_t) - \log(I_{t-1})$ using active infections in countries for which they are available, otherwise we use cumulative infections, noting that they are almost identical during this early period (except in China, where we use active infections). We then match these data to policy variables that we construct using the novel datasets that we assembled and apply a reduced-form approach to estimate a version of equation (6), although the actual expression has additional terms detailed below.

Estimation. To estimate a multi-variable version of equation (6), we estimate a separate regression for each country c. Observations are for subnational units indexed by i observed for each day t. Because not all localities began testing for COVID-19 on the same date, these samples are unbalanced panels. To ensure data quality, we restrict our analysis to localities after they have reported at least ten cumulative infections.

A necessary condition for unbiased estimates is that the timing of policy deployment is independent of natural infection growth rates[14], a mathematical condition that should be true in the context of a new epidemic. In established epidemiological models, including the standard SIR model above, early rates of infection within a susceptible population are characterized by constant exponential growth. This phenomenon is well understood theoretically[13,27,47], has been repeatedly documented in past epidemics[28,29,48] as well as the current COVID-19 pandemic[11,12], and implies constant infection growth rates in the absence of policy intervention. Thus, we treat changes in infection growth rates as conditionally independent of policy deployments since the correlation between a constant variable and any other variable is zero in expectation.

We estimate a multiple regression version of equation (6) using ordinary least squares. We include a vector of subnational unit fixed effects $\boldsymbol{\theta}_0$ (that is, varying intercepts captured as coefficients to dummy variables) to account for all time-invariant factors that affect the local growth rate of infections, such as differences in demographics, socio-economic status, culture and health systems[5]. We include a vector of day-of-week fixed effects $\boldsymbol{\delta}$ to account for weekly patterns in the growth rate of infections that are common across locations within a country; however, in China, we omit day-of-week effects because we find no evidence they are present in the data—perhaps because of the fact that the outbreak of COVID-19 began during a national holiday and workers never returned to work. We also include a separate single-day dummy variable each time there is an abrupt change in the availability of COVID-19 testing or a change in the procedure to diagnose positive cases. Such changes generally manifest as a discontinuous jump in infections and a re-scaling of subsequent infection rates (for example, see China in Fig. 1), effects that are flexibly absorbed by a single-day dummy variable because the dependent variable is the first difference of the logarithm of infections. We denote the vector of these effects $\boldsymbol{\mu}$.

Lastly, we include a vector (length P_c) of country-specific policy variables (policy) for each location and day. These policy variables take on values between 0 and 1 (inclusive) where 0 indicates no policy action and 1 indicates a policy is fully enacted. In cases in which a policy variable captures the effects of collections of policies (for example, museum closures and library closures), a policy variable is computed for each, then they are averaged, so the coefficient on this type of variable is interpreted as the effect if all policies in the collection are fully enacted. There are also instances in which multiple policies are deployed on the same date in numerous locations, in which case we group policies that have similar objectives (for example, suspension of transit and travel ban, or cancelling of events and no gathering) and keep other policies separate (that is, business closure and school closure). The grouping of policies is useful for reducing the number of estimated parameters in our limited sample of data, allowing us to examine the impact of subsets of policies (Fig. 2c). However, policy grouping does not make a substantial difference to the estimated effect of all policies combined nor to the effect of actual policies, which we demonstrate by estimating a regression model in which no policies are grouped and these values are recalculated (Extended Data Fig. 6a and Supplementary Table 4).

In some cases (for Italy and the United States), policy data are available at a more spatially granular level than infection data (for example, city policies and state-level infections in the United States). In these cases, we code binary policy variables at the more granular level and use population weights to aggregate them to the level of the infection data. Thus, policy variables may take on continuous values between 0 and 1, with a value of 1 indicating that the policy is fully enacted for the entire population. Given the limited quantity of data currently available, we use a parsimonious model that assumes the effects of policies on infection growth rates are approximately linear and additively separable. However, future studies that comprise more data may be able to identify important nonlinearities or interactions between policies.

For each country, our general multiple regression model is thus

$$g_{cit} = \log(I_{cit}) - \log(I_{ci,t-1}) = \theta_{0,ci} + \delta_{ct} + \mu_{cit} + \sum_{p=1}^{P_c} (\theta_{pc}\mathrm{policy}_{pcit}) + \varepsilon_{cit} \quad (7)$$

where observations are indexed by country c, subnational unit i and day t. The parameters of interest are the country-by-policy specific coefficients θ_{cp}. We display the estimated residuals ε_{cit} in Extended Data Fig. 10, which are mean zero but not strictly normal (normality is not a requirement of our modelling and inference strategy), and we estimate uncertainty over all parameters by calculating our standard errors robust to error clustering at the day level[14]. This approach allows the covariance in ε_{cit} across different locations within a country, observed on the same day, to be non-zero. Such clustering is important in this context because idiosyncratic events within a country, such as a holiday or a backlog in testing laboratories, could generate nonuniform country-wide changes in infection growth for individual days that are not explicitly captured in our model. Thus, this approach nonparametrically accounts for both arbitrary forms of spatial autocorrelation or systematic misreporting in regions of a country on any given day (we note that it generates larger estimates for uncertainty than clustering by i). When we report the effect of all policies combined (Fig. 2b), we are reporting the sum of coefficient estimates for all policies $\sum_{p=1}^{P_c} \theta_{cp}$, accounting for the covariance of errors in these estimates when computing the uncertainty of this sum.

Note that our estimates of θ and θ_0 in equation (7) are robust to systematic underreporting of infections, a major concern in the ongoing pandemic, due to the construction of our dependent variable. This remains true even if different localities have different rates of underreporting, so long as the rate of underreporting is relatively constant. To see this, note that if each locality i has a medical system that reports only a fraction ψ_i of infections such that we observe $\tilde{I}_{it} = \psi_i I_{it}$ rather an actual infections I_{it}, then the left side of equation (7) will be

$$\begin{aligned}
&\log(\tilde{I}_{it}) - \log(\tilde{I}_{i,t-1}) = \log(\psi_i I_{it}) - \log(\psi_i I_{i,t-1})\\
&= \log(\psi_i) - \log(\psi_i) + \log(I_{it}) - \log(I_{i,t-1})\\
&= \log(I_{it}) - \log(I_{i,t-1}) = g_t
\end{aligned}$$

and is therefore unaffected by location-specific and time-invariant underreporting. Thus systematic underreporting does not affect our estimates for the effects of policy θ. As discussed above, potential biases associated with non-systematic underreporting that results from documented changes in testing regimes over space and time are absorbed by region–day-specific effects μ.

However, if the rate of underreporting within a locality is changing day-to-day, this could bias infection growth rates. We estimate the magnitude of this bias (Extended Data Fig. 2), and verify that it is quantitatively small. Specifically, if $\tilde{I}_{it} = \psi_{it} I_{it}$ where ψ_{it} changes day-to-day, then

$$\log(\tilde{I}_{it}) - \log(\tilde{I}_{i,t-1}) = \log(\psi_{it}) - \log(\psi_{i,t-1}) + g_t \quad (8)$$

where $\log(\psi_{it}) - \log(\psi_{i,t-1})$ is the day-over-day growth rate of the case-detection probability. Disease surveillance has evolved slowly in some locations as governments gradually expand testing, which would cause ψ_{it} to change over time, but these changes in testing capacity do not appear to significantly alter our estimates of infection growth rates. In Extended Data Fig. 2, we show one set of epidemiological estimates[23] for $\log(\psi_{it}) - \log(\psi_{i,t-1})$. Despite random day-to-day variations, which do not cause systematic biases in our point estimates, the mean of $\log(\psi_{it}) - \log(\psi_{i,t-1})$ is consistently small across the different countries: 0.05 in China, 0.064 in Iran, 0.019 in South Korea, −0.058 in France, 0.031 in Italy and 0.049 in the United States. The average of these estimates is 0.026, potentially accounting for 7.3% of our global average estimate for the no-policy infection growth rate (0.36). These estimates of $\log(\psi_{it}) - \log(\psi_{i,t-1})$ also do not display strong temporal trends, alleviating concerns that time-varying underreporting generates sizable biases in our estimated effects of anti-contagion policies.

Transient dynamics. In China, we are able to examine the transient response of infection growth rates following policy deployment because only three policies were deployed early in a seven-week sample period during which we observe many cities simultaneously. This provides us with sufficient data to estimate the temporal structure of policy effects without imposing assumptions regarding this structure. To do this, we estimate a distributed-lag model that encodes policy parameters using weekly lags based on the date that each policy is first implemented in locality i. This means the effect of a policy implemented one week ago is allowed to differ arbitrarily from the effect of that same policy in the following week, and so on. These effects are then estimated simultaneously and are displayed in Fig. 2b, c (see also Supplementary Table 3). Such a distributed lag approach did not provide statistically meaningful insights in other countries using the currently available data because there were fewer administrative units and shorter periods of observation (that is, smaller samples), and more policies (that is, more parameters to estimate) in all other countries. Future studies may be able to successfully explore these dynamics outside of China.

As a robustness check, we examine whether excluding the transient response from the estimated effects of policy substantially alters our results. We do this by estimating a 'fixed lag' model, in which we assume that policies cannot influence infection growth rates for L days, recoding a policy variable at time t as zero if a policy was implemented fewer than L days before t. We reestimate equation (7) for each value of L and present results in Extended Data Fig. 5 and Supplementary Table 5.

Alternative disease models. Our main empirical specification is motivated with an SIR model of disease contagion, which assumes zero latent period between exposure to COVID-19 and infectiousness. If we relax this assumption to allow for a latent period of infection, as in a susceptible–exposed–infected–recovered (SEIR) model, the growth of the outbreak is only asymptotically exponential[11]. Nonetheless, we demonstrate that SEIR dynamics have only a minor potential impact on the coefficients recovered by using our empirical approach in this context. In Extended Data Figs. 8, 9 we present results from a simulation exercise which uses equations (9)–(11), along with a generalization to the SEIR model[11] to generate synthetic outbreaks (see Supplementary Methods section 2). We use these simulated data to test the ability of our statistical model (equation (7)) to recover both the unimpeded growth rate (Extended Data Fig. 8) as well as the impact of simulated policies on growth rates (Extended Data Fig. 9) when applied to data generated by SIR or SEIR dynamics over a wide range of epidemiological conditions.

Projections

Daily growth rates of infections. To estimate the instantaneous daily growth rate of infections if policies were absent, we obtain fitted values from equation (7) and compute a predicted value for the dependent variable when all P_c policy variables are set to 0. Thus, these estimated growth rates $\hat{g}_{cit}^{\text{no policy}}$ capture the effect of all locality-specific factors on the growth rate of infections (for example, demographics), day-of-week effects, and adjustments based on the way in which infection cases are reported. This counterfactual does not account for changes in information that are triggered by policy deployment, as those should be considered a pathway through which policies affect outcomes, as discussed in the main text. Additionally, the ‘no policy’ counterfactual does not model previously unobserved changes in behaviour that might occur if fundamentally new behaviours emerge even in the absence of government intervention. When we report an average no-policy growth rate of infections (Fig. 2a), it is the average value of these predictions for all observations in the original sample. Location-and-day-specific counterfactual predictions $\left(\hat{g}_{cit}^{\text{no policy}}\right)$, accounting for the covariance of errors in estimated parameters, are shown as red markers in Fig. 3.

Cumulative infections. To provide a sense of scale for the estimated cumulative benefits of effects shown in Fig. 3, we link our reduced-form empirical estimates to the key structures in a simple SIR system and simulate this dynamical system over the course of our sample. The system is defined as the following:

$$\frac{\mathrm{d}S_t}{\mathrm{d}t} = -\beta_t S_t I_t \tag{9}$$

$$\frac{\mathrm{d}I_t}{\mathrm{d}t} = (\beta_t S_t - \gamma) I_t \tag{10}$$

$$\frac{\mathrm{d}R_t}{\mathrm{d}t} = \gamma I_t \tag{11}$$

where S_t is the susceptible population and R_t is the removed population. Here β_t is a time-evolving parameter, determined by our empirical estimates as described below. Accounting for changes in S becomes increasingly important as the size of cumulative infections ($I_t + R_t$) becomes a substantial fraction of the local subnational population, which occurs in some no-policy scenarios. Our reduced-form analysis provides estimates for the growth rate of active infections ($\hat{g}$) for each locality and day, in a regime where $S_t \approx 1$. Thus we know

$$\frac{\mathrm{d}I_t}{\mathrm{d}t} / I_t \,|_{S\approx 1} = \hat{g}_t = \beta_t - \gamma \tag{12}$$

but we do not know the values of either of the two right-side terms, which are required to simulate equations (9)–(11). To estimate γ, we note that the left-side term of equation (11) is

$$\frac{\mathrm{d}R_t}{\mathrm{d}t} \approx \frac{\mathrm{d}}{\mathrm{d}t}(\text{cumulative recoveries} + \text{cumulative deaths})$$

which we can observe in our data for China and South Korea. Computing first differences in these two variables (to differentiate with respect to time), summing them, and then dividing by active cases gives us estimates of γ (medians: China = 0.11, South Korea = 0.05). These values differ slightly from the classical SIR interpretation of γ, because in the public data that we are able to obtain, individuals are coded as ‘recovered’ when they no longer test positive for COVID-19, whereas in the classical SIR model this occurs when they are no longer infectious. We adopt the average of these two medians, setting $\gamma = 0.08$. We use medians rather than simple averages because low values for I_t induce a long right tail in daily estimates of γ and medians are less vulnerable to this distortion. We then use our empirically based reduced-form estimates of $\hat{g}$ (both with and without policy) combined with equations (9)–(11) to project total cumulative cases in all countries (Fig. 4). We simulate infections and cases for each administrative unit in our sample beginning on the first day for which we observe 10 or more cases (for that unit) using a time step of 4 h. Because we observe confirmed cases rather than total infections, we seed each simulation by adjusting observed I_t on the first day using country-specific estimates of case detection rates. We adjust existing estimates of case underreporting[23] to further account for asymptomatic infections assuming an infection–fatality ratio of 0.75%[25]. We assume $R_t = 0$ on the first day. To maintain consistency with the reported data, we report our output in confirmed cases by multiplying our simulated $I_t + R_t$ values by the aforementioned proportion of infections confirmed. We estimate uncertainty by resampling from the estimated variance–covariance matrix of all regression parameters. In Extended Data Fig. 7, we show sensitivity of this simulation to the estimated value of γ as well as to the use of an SEIR framework. In Supplementary Table 6, we show sensitivity of this simulation to the assumed infection–fatality ratio (see Supplementary Methods section 1).

Reporting summary

Further information on research design is available in the Nature Research Reporting Summary linked to this paper.

Data availability

The datasets generated and/or analysed during the current study are available at https://github.com/bolliger32/gpl-covid. Future updates and/or extensions to data or code will be listed at http://www.globalpolicy.science/covid19.

Code availability

For easier replication, we have created a CodeOcean ‘capsule’, which contains a pre-built computing environment in addition to the source code and data. This is available at https://codeocean.com/capsule/1887579/tree/v1. Future updates and/or extensions to data or code will be listed at http://www.globalpolicy.science/covid19.

34. Lin, J. *COVID-19/2019-nCoV Time Series Infection Data Warehouse*. https://github.com/BlankerL/DXY-COVID-19-Data (2020).
35. *COVID-19 Pandemic Lockdown in Hubei*. https://en.wikipedia.org/w/index.php?title=COVID-19_pandemic_lockdown_in_Hubei (Wikipedia, 2020).
36. *COVID-19 Pandemic in Iran*. https://en.wikipedia.org/w/index.php?title=COVID-19_pandemic_in_Iran (Wikipedia, 2020).
37. Kantis, C., Keirnan, S. & Bardi, J. S. Timeline of the coronavirus. *Think Global Health* https://www.thinkglobalhealth.org/article/updated-timeline-coronavirus (2020).
38. Presidenza del Consiglio dei Ministri Dipartimento della Protezione Civile. *Dati COVID-19 Italia*. https://github.com/pcm-dpc/COVID-19 (2020).
39. Presidenza del Consiglio dei Ministri Dipartimento della Protezione Civile. *Coronavirus Emergency* [in Italian]. http://www.protezionecivile.it/web/guest/home (Governo Italiano, 2020).
40. *COVID-19 Pandemic Lockdown in Italy*. https://en.wikipedia.org/w/index.php?title=COVID-19_pandemic_lockdown_in_Italy (Wikipedia, 2020).
41. Roussel, O. Fr-SARS-CoV-2. https://www.data.gouv.fr/en/datasets/fr-sars-cov-2 (2020).
42. Sante Publique France. *Coronavirus (COVID-19)*. https://www.santepubliquefrance.fr/ (2020).
43. Agence Régionale de Santé. *Agir pour la santé de tous*. https://www.ars.sante.fr/ (2020).
44. *COVID-19 Pandemic in France*. https://en.wikipedia.org/w/index.php?title=COVID-19_pandemic_in_France (Wikipedia, 2020).

45. *Coronavirus Locations: COVID-19 Map by County and State*. https://usafacts.org/visualizations/coronavirus-covid-19-spread-map/ (USA FACTS, 2020).
46. JHU CSSE. *COVID-19 Data Repository by the Center for Systems Science and Engineering (CSSE) at Johns Hopkins University*. https://github.com/CSSEGISandData/COVID-19 (2020).
47. Kermack, W. O. & McKendrick, A. G. A contribution to the mathematical theory of epidemics. *Proc. R. Soc. Lond. A* **115**, 700–721 (1927).
48. Mills, C. E., Robins, J. M. & Lipsitch, M. Transmissibility of 1918 pandemic influenza. *Nature* **432**, 904–906 (2004).

Acknowledgements We thank B. Chen for her role in initiating this work and A. Feller for his feedback. S.A.-P., E.K., P.L. and J.T. are supported by a gift from the Tuaropaki Trust. T.C. is supported by an AI for Earth grant from National Geographic and Microsoft. D.A., A.H. and I.B. are supported through joint collaborations with the Climate Impact Lab. K.B. is supported by the Royal Society Te Apārangi Rutherford Postdoctoral Fellowship. H.D. and E.R. are supported by the National Science Foundation Graduate Research Fellowship under grants DGE 1106400 and 1752814, respectively. Opinions, findings, conclusions or recommendations expressed in this material are those of the authors and do not reflect the views of supporting organizations.

Author contributions S.H. conceived and led the study. All authors designed analysis, interpreted results, designed figures and wrote the paper. D.A., S.A.-P., K.B., I.B., T.C., H.D., L.Y.H., A.H., E.K., P.L., J.L., E.R., J.T. and T.W. contributed equally and are listed alphabetically. China: L.Y.H. and T.W. collected health data, L.Y.H., T.W. and J.T. collected policy data, L.Y.H. cleaned data. South Korea: J.L. collected health data, T.C. and J.L. collected policy data, T.C. cleaned data. Italy: D.A. collected health data, P.L. collected policy data, D.A. cleaned data. France: S.A.-P. collected health data, S.A.-P., J.T. and H.D. collected policy data, S.A.-P. cleaned data. Iran: A.H. collected health data and policy data, A.H. and D.A. cleaned data. United States: E.R. and K.B. collected health data, E.K. collected policy data, E.R., D.A. and K.B. cleaned data. I.B. collected geographical and population data for all countries. S.H. designed the econometric model. S.H., S.A.-P. and J.T. conducted econometric analysis for all countries. K.B., I.B., A.H., E.R. and E.K. designed and implemented epidemiological models and projections. S.A.-P., K.B., I.B., J.T., A.H. and E.K. designed and implemented robustness checks. H.D. created Fig. 1, T.C. created Fig. 2, J.T. created Fig. 3, E.R. created Fig. 4, D.A. created Supplementary Table 1, L.Y.H. and J.L. created Supplementary Table 2, J.T. created Supplementary Tables 3, 4, S.A.-P. and J.T. created Supplementary Table 5, K.B. created Supplementary Table 6, L.Y.H. created Extended Data Figs. 1, 2, S.A.-P. created Extended Data Figs. 3–5, J.T. created Extended Data Fig. 6, K.B. created Extended Data Fig. 7, I.B. created Extended Data Figs. 8, 9, J.T. created Extended Data Fig. 10. D.A., I.B. and P.L. managed policy data collection and quality control. I.B. and TC managed the code repository. I.B. and P.L. ran project management. E.K., T.W., J.T. and P.L. managed literature review. L.Y.H., E.K. and T.W. managed references. P.L. managed Extended Data Figs. 1–10 and Supplementary Information.

Competing interests The authors declare no competing interests.

Additional information

Supplementary information is available for this paper at https://doi.org/10.1038/s41586-020-2404-8.

Correspondence and requests for materials should be addressed to S.H.

Peer review information *Nature* thanks Andrew Jones, Jeffrey Shaman and the other, anonymous, reviewer(s) for their contribution to the peer review of this work. Peer reviewer reports are available.

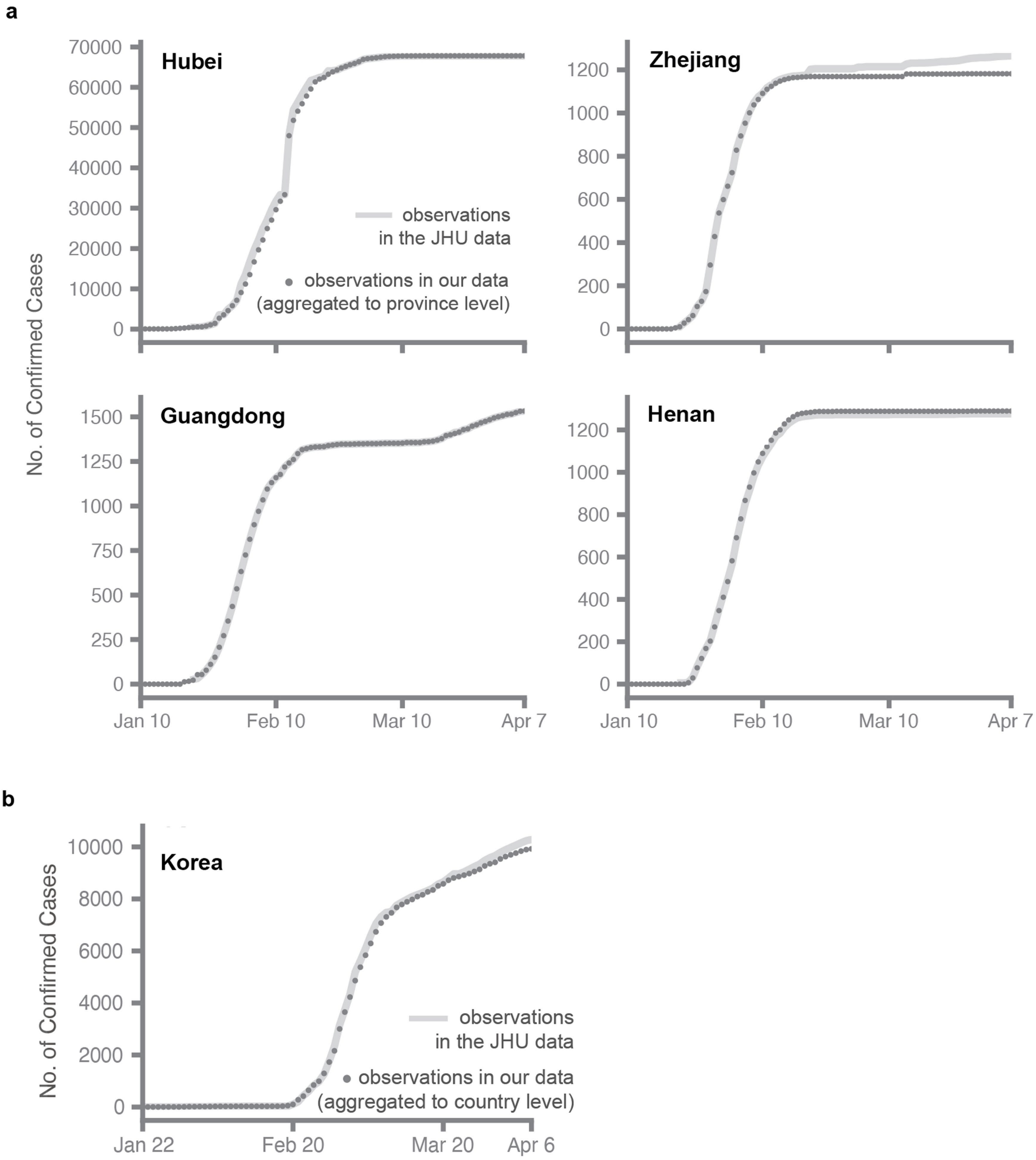

Extended Data Fig. 1 | Validating disaggregated epidemiological data against aggregated data from the JHU Center for Systems Science and Engineering. Comparison of cumulative confirmed cases from a subset of regions in our collated epidemiological dataset to the same statistics from the 2019 Novel Coronavirus COVID-19 (2019-nCoV) Data Repository by the Johns Hopkins Center for Systems Science and Engineering (JHU CSSE)[46]. We conducted this comparison for Chinese provinces and South Korea, for which the data we collected were from local administrative units that are more spatially granular than the data in the JHU CSSE database. **a**, In China, we aggregated our city-level data to the province level. **b**, In South Korea, we aggregated province-level data up to the country level. Small discrepancies, especially in later periods of the outbreak, are generally due to imported cases (international or domestic) that are present in national statistics but that we do not assign to particular cities (in China) or provinces (in Korea).

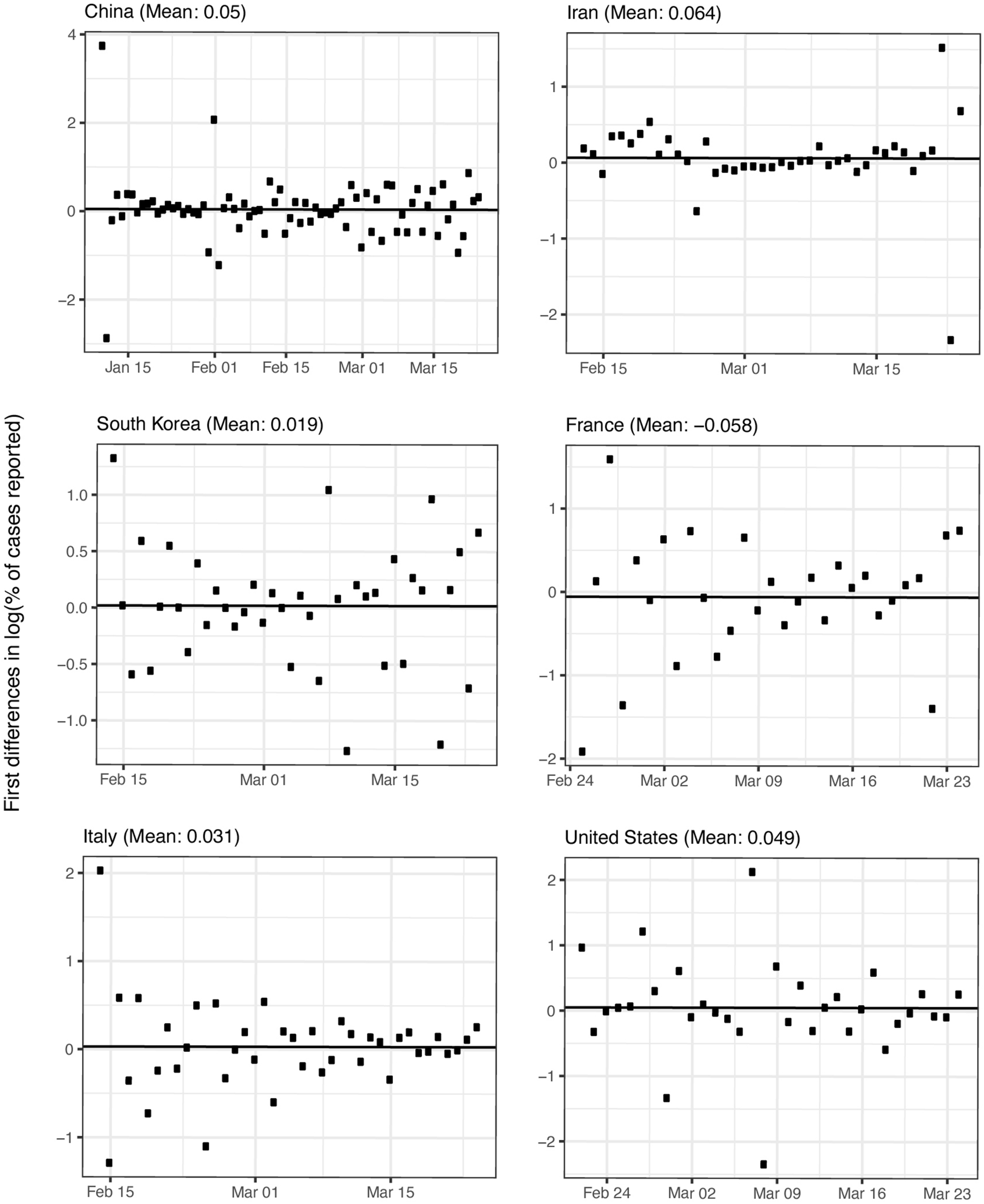

Extended Data Fig. 2 | Estimated trends in case detection over time within each country. Systematic trends in case detection may potentially bias estimates of no-policy infection growth rates (see equation (8)). We estimate the potential magnitude of this bias using data from the Centre for Mathematical Modelling of Infectious Diseases[23]. Markers indicate daily first differences in the logarithm of the fraction of estimated symptomatic cases reported for each country over time. The average value over time (solid line and value denoted in panel title) is the average growth rate of case detection, equal to the magnitude of the potential bias. For example, in the main text we estimate that the infection growth rate in the United States is 0.29 (Fig. 2a), of which growth in case detection might contribute 0.049 (this figure). Sample sizes are 75 in China, 41 in Iran, 40 in South Korea, 29 in France, 40 in Italy and 32 in the United States.

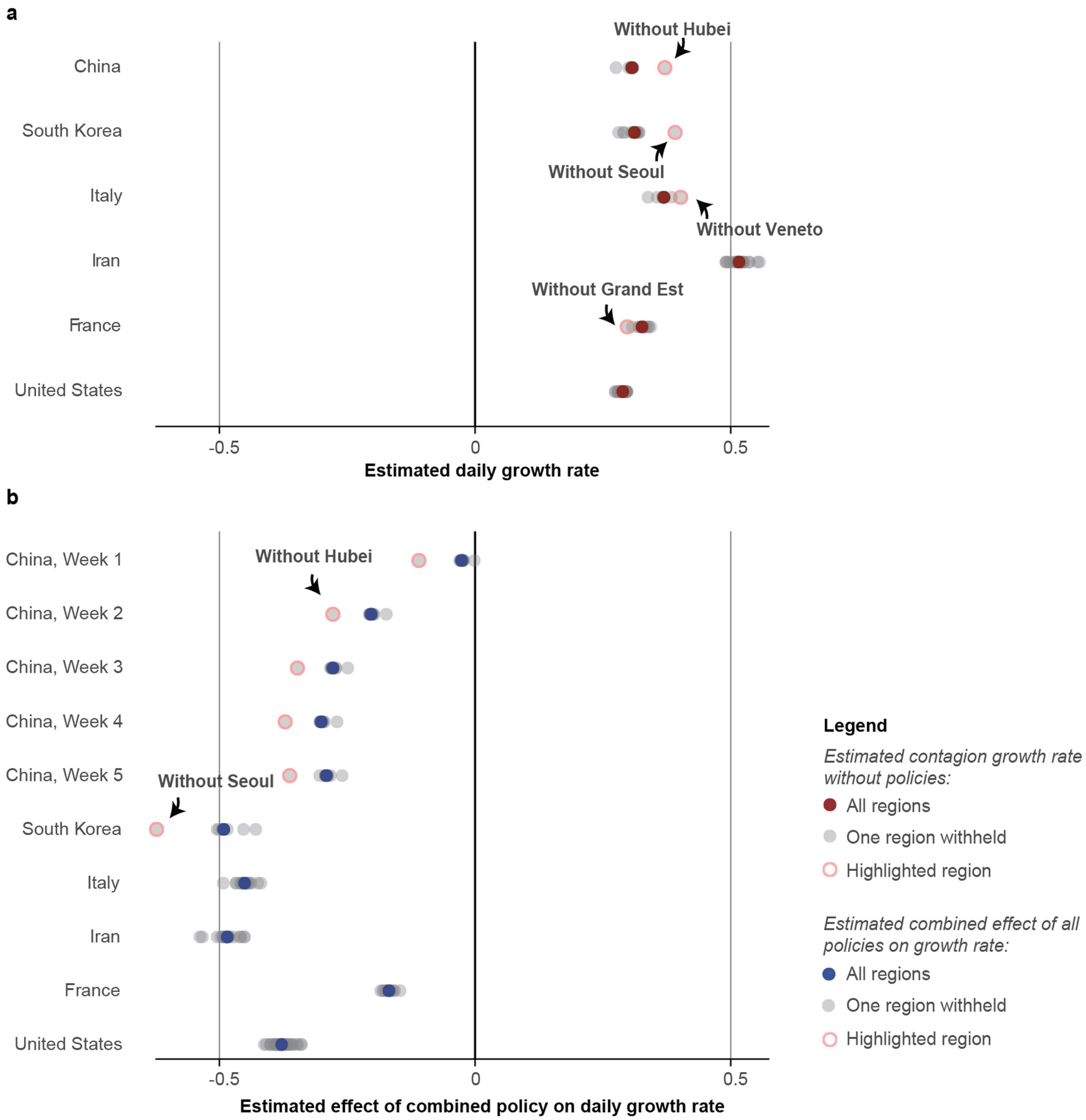

Extended Data Fig. 3 | Robustness of the estimated no-policy growth rate of infections and the combined effect of policies to withholding blocks of data from entire regions. a, **b**, For each country, we reestimated equation (7) using real data *k* times, each time withholding one of the *k* first-level administrative regions ('Adm1', that is, state or province) in that country. Each grey circle is either the estimated no-policy growth rate (**a**) or the total effect of all policies combined (**b**), from one of these *k* regressions. Red and blue circles show estimates from the full sample, identical to the results presented in Fig. 2a, b, respectively. For each country panel, if a single region is influential, the estimated value when it is withheld from the sample will appear as an outlier. Samples that omit an influential region are highlighted with an open pink circle. As in Fig. 2b, we estimate a distributed lag model for China and display each of the estimated weekly lag effects (where the pink circle is the same 'without Hubei' sample for lags). The full sample includes 3,669 observations in China, 595 in South Korea, 2,898 in Italy, 548 in Iran, 270 in France and 1,238 in the United States.

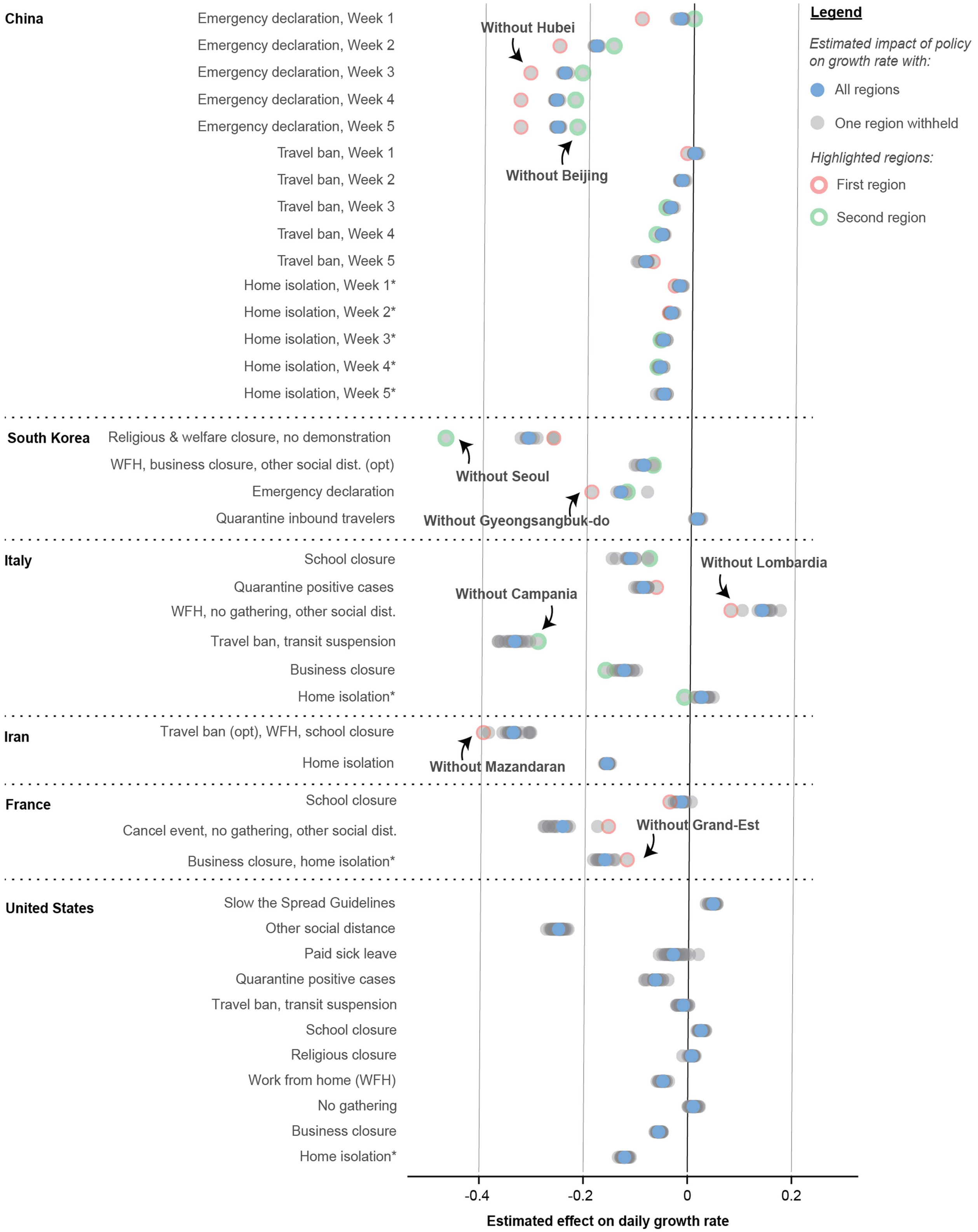

Extended Data Fig. 4 | Robustness of the estimated effects of individual policies to withholding blocks of data from entire regions. Same as Extended Data Fig. 3, but for individual policies (analogous to Fig. 2c). WFH denotes work from home policies; opt denotes optional policies. In cases in which two regions are influential, a second region is highlighted with an open green circle. The full sample includes 3,669 observations in China, 595 in South Korea, 2,898 in Italy, 548 in Iran, 270 in France and 1,238 in the United States.

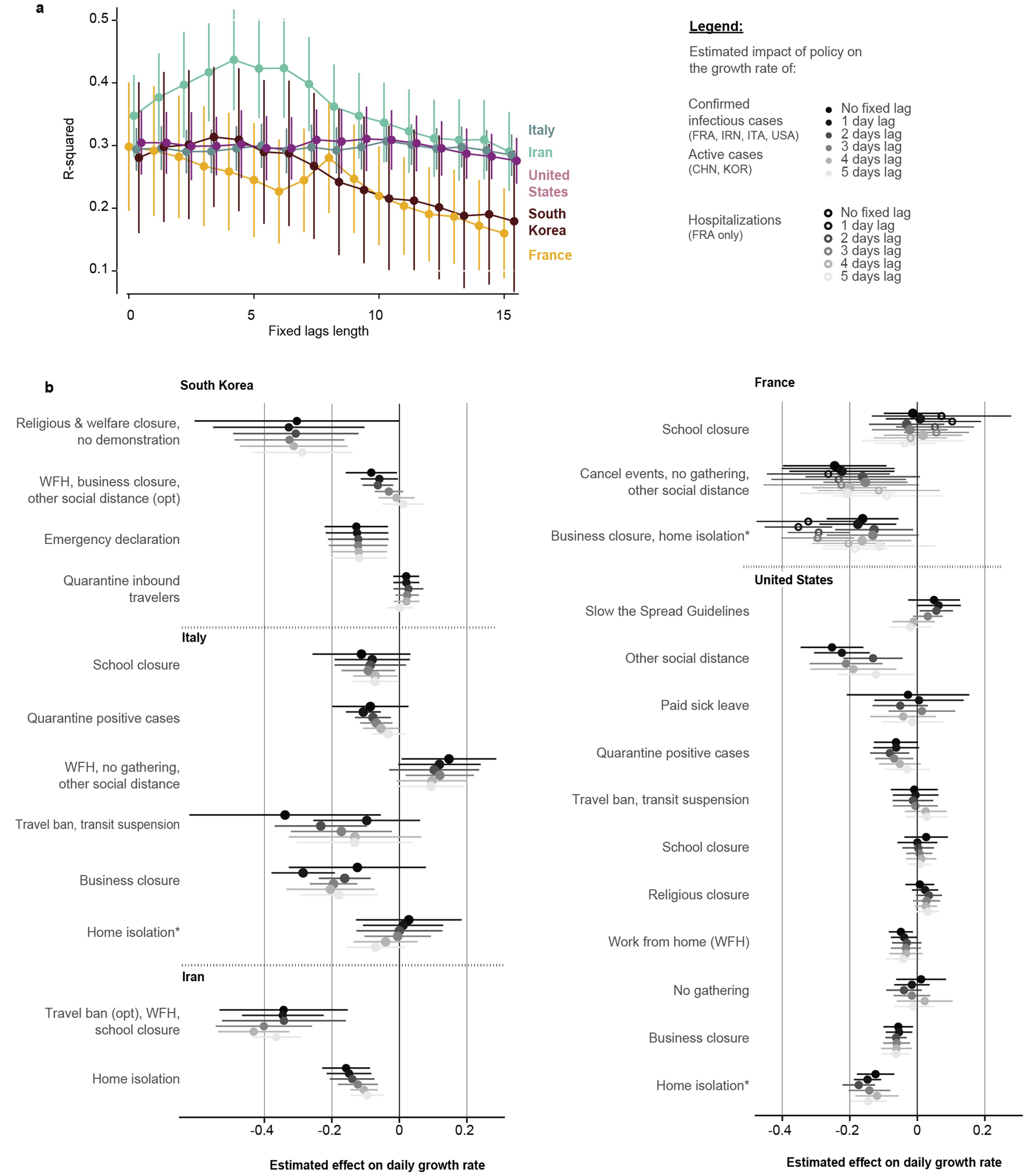

Extended Data Fig. 5 | See next page for caption.

Extended Data Fig. 5 | Evidence to support models in which policies affect infection growth rates in the days following deployment. Existing evidence has not demonstrated whether policies should affect infection growth rates in the days immediately after deployment. It is therefore not clear ex ante whether the policy variables in equation (7) should be encoded as 'on' immediately following a policy deployment. We estimate 'fixed-lag' models in which a fixed delay between the deployment of a policy and its effect is assumed (see Supplementary Methods section 3). If a delay model is more consistent with real world infection dynamics, these fixed lag models should recover larger estimates for the impact of policies and exhibit better model fit. **a**, R^2 values associated with fixed-lag lengths varying from 0 to 15 days. Centre values represent the R^2 value in our sample, whiskers are 95% confidence interval computed through resampling with replacement. In-sample fit generally declines or remains unchanged if policies are assumed to have a delay longer than 4 days. **b**, Estimated effects for no lag (the model reported in the main text) and for fixed lags between 1 and 5 days. Centre values represent the point estimate, error bars are 95% confidence intervals. Estimates generally are unchanged or shrink towards zero (for example, home isolation in Iran), consistent with mis-coding of post-policy days as no-policy days. The sample size is 595 in South Korea, 2,898 in Italy, 548 in Iran, 270 in France and 1,238 in the United States.

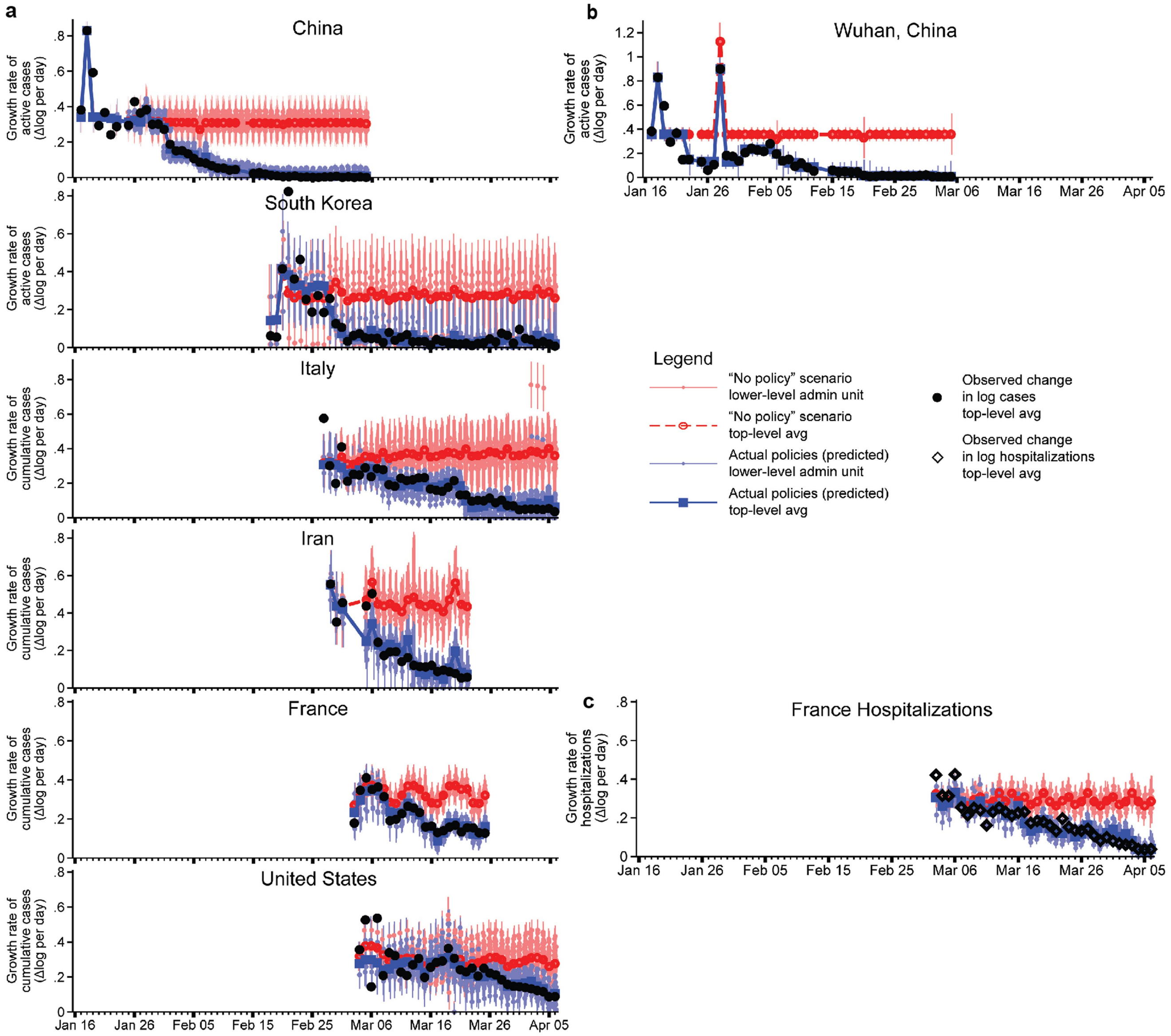

Extended Data Fig. 6 | Estimated infection or hospitalization growth rates with actual anti-contagion policies and in a no-policy counterfactual scenario. a, The estimated daily growth rates of active (China and South Korea) or cumulative (all others) infections based on the observed timing of all policy deployments within each subnational unit (blue) and in a scenario in which no policies were deployed (red). Identical to Fig. 3, but using an alternative disaggregated encoding of policies that does not group any policies into policy packages. The sample size is 3,669 in China, 595 in South Korea, 2,898 in Italy, 548 in Iran, 270 in France and 1,238 in the United States. **b**, Same as Fig. 3, but equation (7) is implemented for a single example administrative unit: Wuhan, China. The sample size is 46 observations. **c**, Same as Fig. 3, but using hospitalization data from France rather than cumulative cases (the French government stopped reporting cumulative cases after 25 March 2020). The sample size is 424 observations. For all panels, the difference between the with- and no-policy predictions is our estimated effect of actual anti-contagion policies on the growth rate of infections (or hospitalizations). The markers are daily estimates for each subnational administrative unit (vertical lines are 95% confidence intervals). Black circles are observed changes in log(infections) (or diamonds for log(hospitalizations)), averaged across observed administrative units.

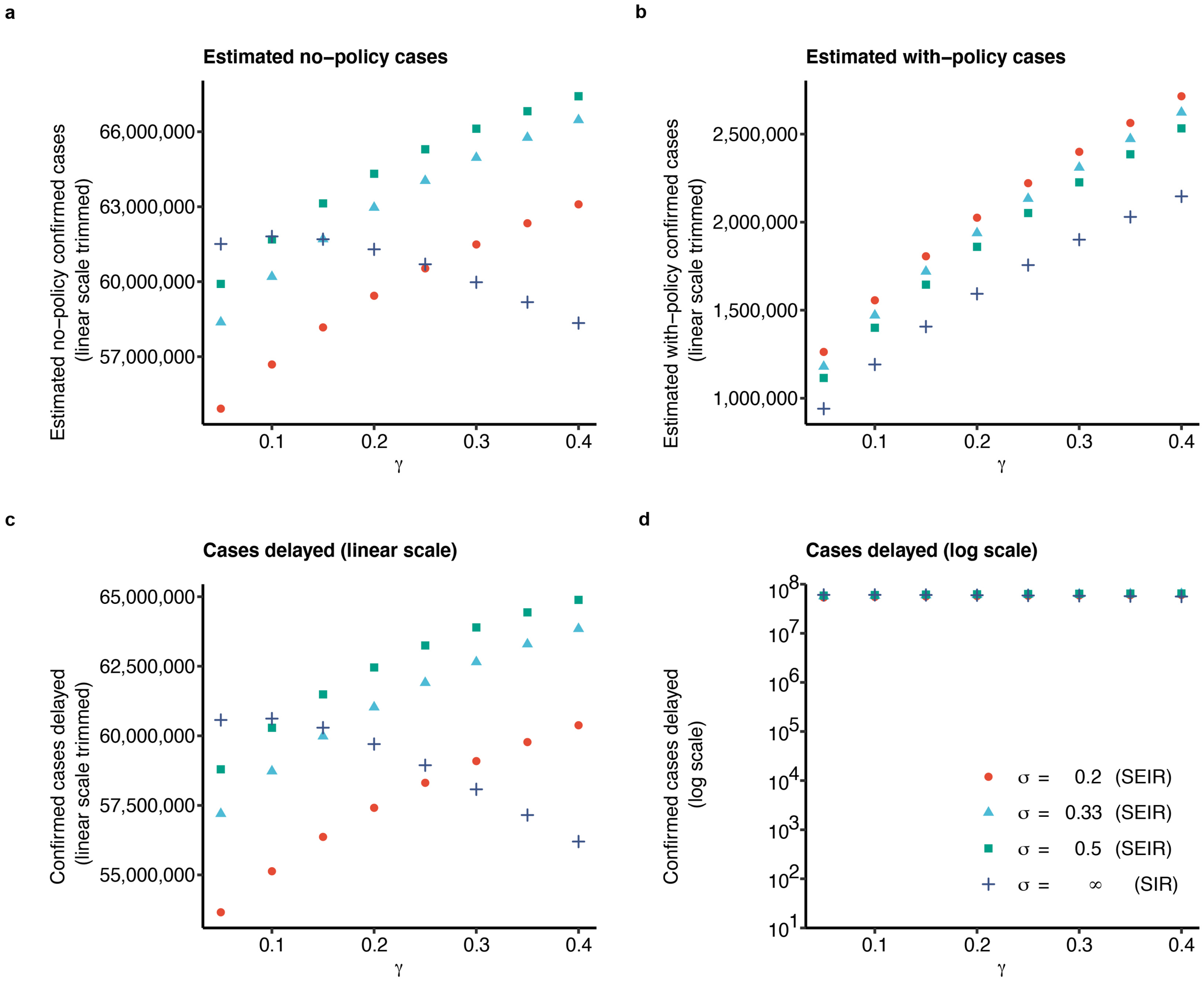

Extended Data Fig. 7 | Sensitivity of estimated averted/delayed infections to the choice of γ and σ in an SIR/SEIR framework. The sensitivity of total averted/delayed cases presented in Fig. 4 to alternative modelling assumptions. We compute total cases across the respective final days in our samples for the six countries presented in our analysis. The figure displays how these totals vary with eight values of γ (0.05–0.4) and four values of σ (0.2, 0.33, 0.5, ∞), where the final value of σ (∞) corresponds to the SIR model. **a**, The simulated total number of infections under no policy. **b**, Same as in **a**, but using actual policies. **c**, The difference between **a** and **b**, which is the total number of averted/delayed infections. **d**, Same as **c**, but on a logarithmic scale similar to Fig. 4 (**a**–**c** are on a linear scale, trimmed to show details). Figure 4 uses $\gamma = 0.079$, which we calculate using empirical recovery/death rates in countries for which we observed them (China and South Korea; see Methods). If we assume a 14-day delay between infected individuals becoming non-infectious and being reported as ‘recovered’ in the data, we would calculate $\gamma = 0.18$. Figure 4 assumes $\sigma = \infty$.

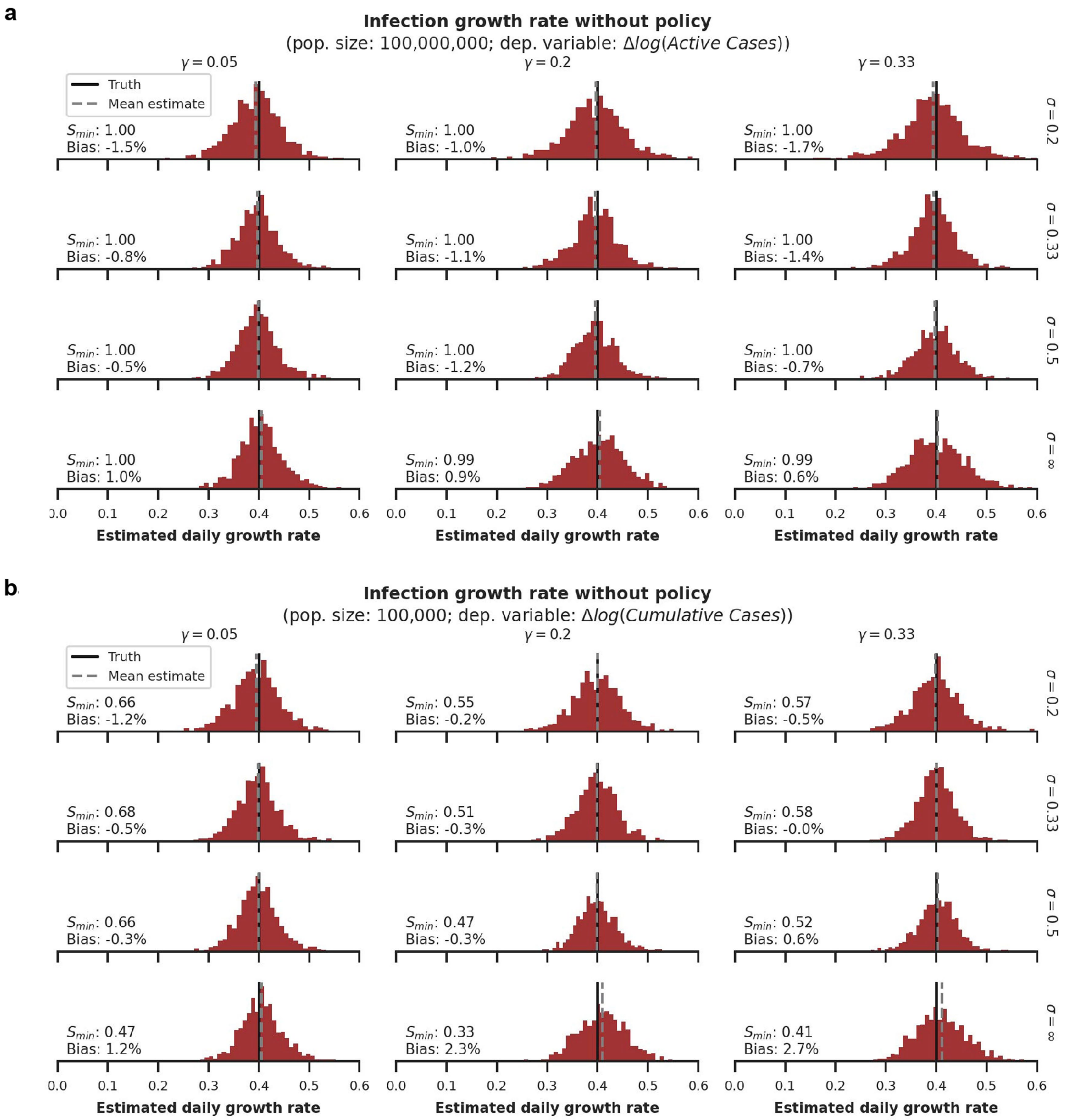

Extended Data Fig. 8 | Simulating reduced-form estimates for the no-policy growth rate of infections for different population regimes and disease dynamics. We examine the performance of reduced-form econometric estimators through simulations in which different underlying disease dynamics are assumed (see Supplementary Methods section 2). Each histogram shows the distribution of econometrically estimated values across 1,000 simulated outbreaks. Estimates are for the no-policy infection growth rate (analogous to Fig. 2a) when three different policies are deployed at random moments in time. The black line shows the correct value imposed on the simulation and the red histogram shows the distribution of estimates using the regression in equation (7), applied to data output from the simulation. The grey dashed line shows the mean of this distribution. The 12 subpanels describe the results when various values are assigned to the mean infectious period (γ^{-1}) and mean latency period (σ^{-1}) of the disease. $\sigma = \infty$ is equivalent to SIR disease dynamics. In each panel, $S_{\min}$ is the minimum susceptible fraction observed across all 1,000 45-day simulations shown in each panel. In the real datasets used in the main text, after correcting for country-specific underreporting, $S_{\min}$ across all units analysed is 0.72 and 95% of the analysed units finish with $S_{\min} > 0.91$. Bias refers to the distance between the dashed grey and black line as a percentage of the true value. **a**, Simulations in near-ideal data conditions in which we observe active infections within a large population (such that the susceptible fraction of the population remains high during the sample period, similar to those in our data for Chongqing, China). **b**, Simulations in a non-ideal data scenario in which we are only able to observe cumulative infections in a small population (similar to those in our sample for Cremona, Italy).

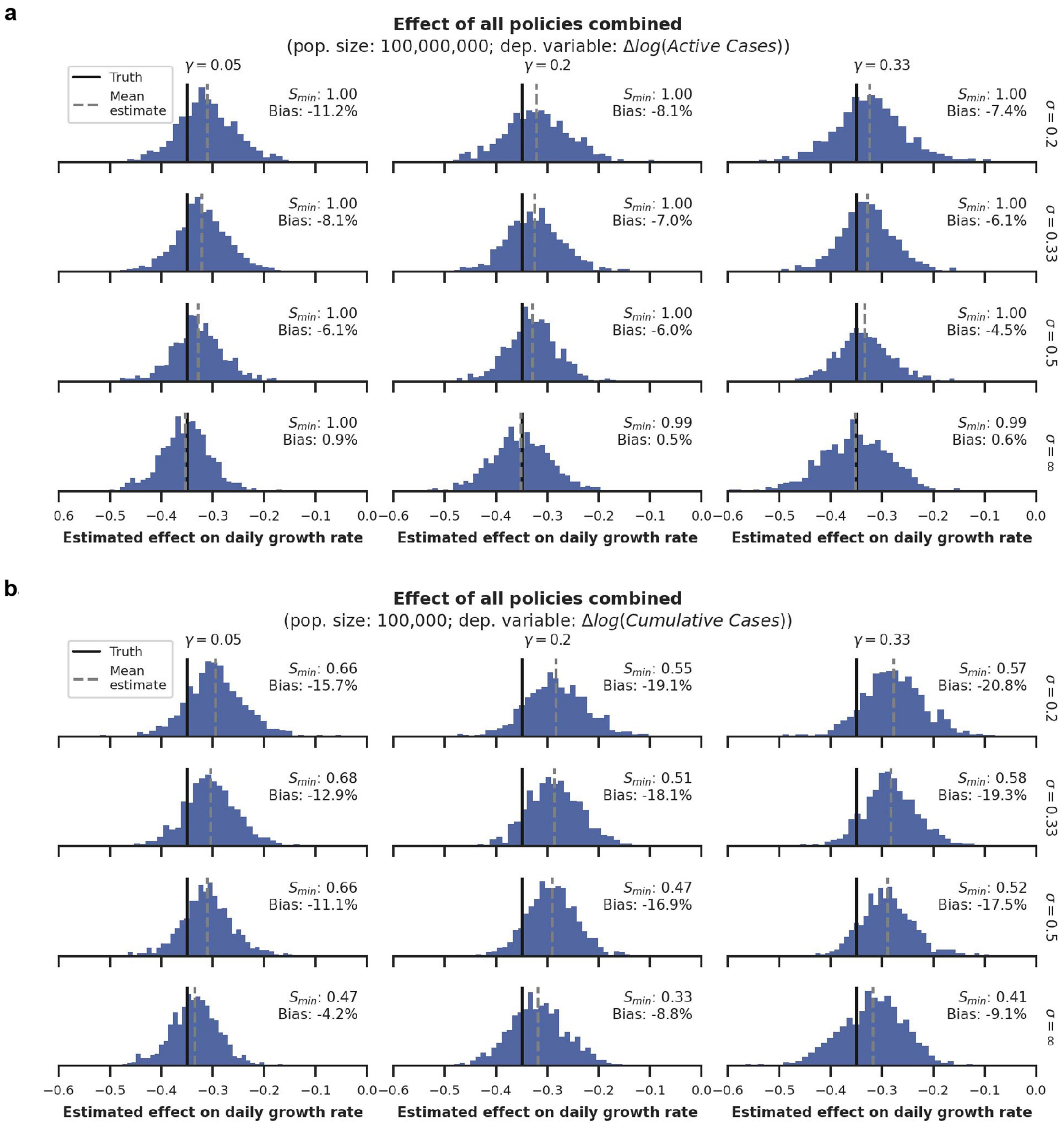

Extended Data Fig. 9 | Simulating reduced-form estimates for anti-contagion policy effects for different population regimes and assumed disease dynamics. Same as Extended Data Fig. 8, but estimates are for the combined effect of three different policies (analogous to Fig. 2b) that are deployed at random moments in time. **a**, Simulations in near-ideal data conditions in which we observe active infections within a large population (such that the susceptible fraction of the population remains high during the sample period, similar to those in our data for Chongqing, China). **b**, Simulations in a non-ideal data scenario in which we are only able to observe cumulative infections in a small population (similar to those in our sample for Cremona, Italy).

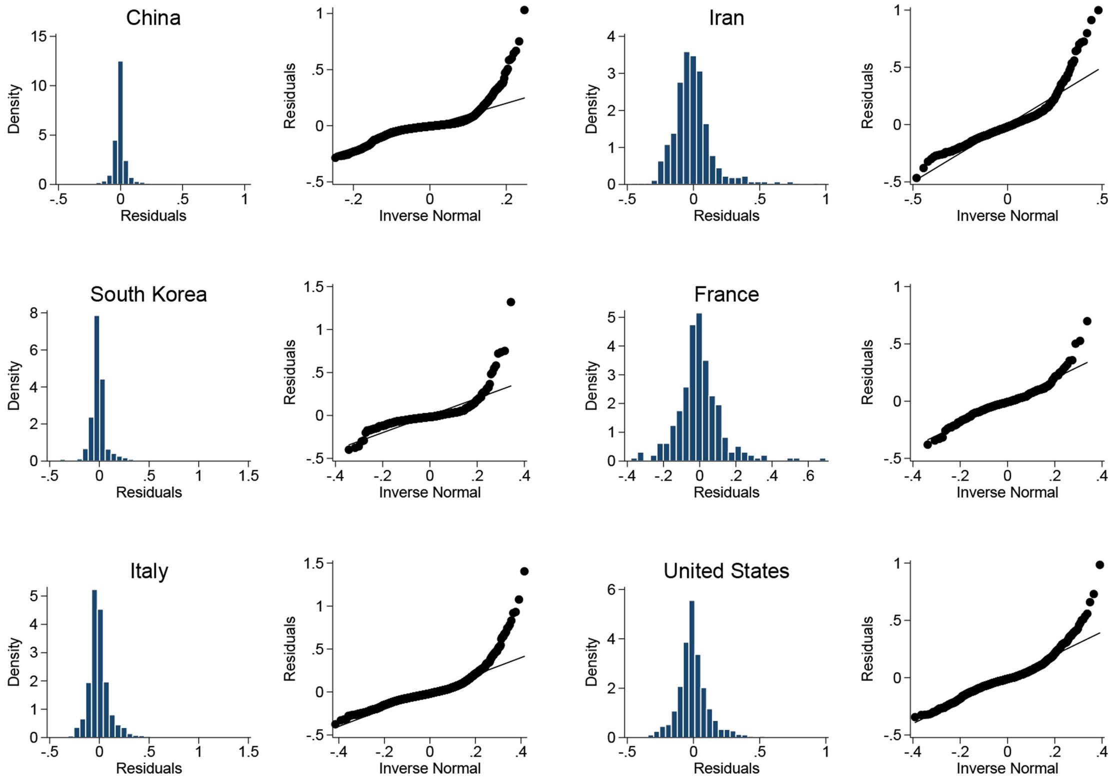

Extended Data Fig. 10 | Regression residuals for the growth rates of COVID-19 by country. These plots show the estimated residuals from equation (7) for each country-specific econometric model. Histograms (left) show the estimated unconditional probability density function. Quantile plots (right) show quantiles of the cumulative density function (*y* axis) plotted against the same quantiles for a normal distribution. For additional details, see Fig. 3 and the 'Econometric analysis' section of the Methods.

nature research

Corresponding author(s): Solomon Hsiang

Last updated by author(s): May 13, 2020

Reporting Summary

Nature Research wishes to improve the reproducibility of the work that we publish. This form provides structure for consistency and transparency in reporting. For further information on Nature Research policies, see Authors & Referees and the Editorial Policy Checklist.

Statistics

For all statistical analyses, confirm that the following items are present in the figure legend, table legend, main text, or Methods section.

n/a	Confirmed	
☐	☒	The exact sample size (*n*) for each experimental group/condition, given as a discrete number and unit of measurement
☐	☒	A statement on whether measurements were taken from distinct samples or whether the same sample was measured repeatedly
☐	☒	The statistical test(s) used AND whether they are one- or two-sided *Only common tests should be described solely by name; describe more complex techniques in the Methods section.*
☐	☒	A description of all covariates tested
☐	☒	A description of any assumptions or corrections, such as tests of normality and adjustment for multiple comparisons
☐	☒	A full description of the statistical parameters including central tendency (e.g. means) or other basic estimates (e.g. regression coefficient) AND variation (e.g. standard deviation) or associated estimates of uncertainty (e.g. confidence intervals)
☐	☒	For null hypothesis testing, the test statistic (e.g. *F*, *t*, *r*) with confidence intervals, effect sizes, degrees of freedom and *P* value noted *Give P values as exact values whenever suitable.*
☒	☐	For Bayesian analysis, information on the choice of priors and Markov chain Monte Carlo settings
☐	☒	For hierarchical and complex designs, identification of the appropriate level for tests and full reporting of outcomes
☐	☒	Estimates of effect sizes (e.g. Cohen's *d*, Pearson's *r*), indicating how they were calculated

Our web collection on statistics for biologists contains articles on many of the points above.

Software and code

Policy information about availability of computer code

Data collection	Computer code was not used to collect data.
Data analysis	Python version 3.8, R version 3.5, Stata MP

For manuscripts utilizing custom algorithms or software that are central to the research but not yet described in published literature, software must be made available to editors/reviewers. We strongly encourage code deposition in a community repository (e.g. GitHub). See the Nature Research guidelines for submitting code & software for further information.

Data

Policy information about availability of data

All manuscripts must include a data availability statement. This statement should provide the following information, where applicable:

- Accession codes, unique identifiers, or web links for publicly available datasets
- A list of figures that have associated raw data
- A description of any restrictions on data availability

All data used in this analysis is from free, publicly available sources, and can be accessed at https://github.com/bolliger32/gpl-covid

Field-specific reporting

Please select the one below that is the best fit for your research. If you are not sure, read the appropriate sections before making your selection.

☐ Life sciences ☒ Behavioural & social sciences ☐ Ecological, evolutionary & environmental sciences

For a reference copy of the document with all sections, see nature.com/documents/nr-reporting-summary-flat.pdf

Behavioural & social sciences study design

All studies must disclose on these points even when the disclosure is negative.

Study description	The study analyzes six different countries with varying policy implementations to estimate the impact of these anti-contagion policies on the growth rate of infections.
Research sample	The research sample consists of COVID-19 case counts from China, Korea, Italy, France, Iran, and the United States.
Sampling strategy	We chose countries to analyze among those that accounted for the majority of the global confirmed caseload at the beginning of our analysis (3/14/2020). We chose a selection of countries based on global interest and the languages spoken by the authors (for ease of data collection). Within each country, we collected all available data on active infections (where available) and cumulative infections, in addition to all available policy data. No sampling was required.
Data collection	Data collection is detailed in the appendix.
Timing	Data collection began on March 14, 2020 and ended on April 12, 2020.
Data exclusions	Case data were excluded from dates with < 10 confirmed cases because of concerns about statistical reliability.
Non-participation	No participants dropped out or declined participation because this study did not directly involve them.
Randomization	Randomization was not possible for this study because the paper investigates the growth rate of COVID-19 cases with policy interventions or in the absence thereof.

Reporting for specific materials, systems and methods

We require information from authors about some types of materials, experimental systems and methods used in many studies. Here, indicate whether each material, system or method listed is relevant to your study. If you are not sure if a list item applies to your research, read the appropriate section before selecting a response.

Materials & experimental systems

n/a	Involved in the study
☒	☐ Antibodies
☒	☐ Eukaryotic cell lines
☒	☐ Palaeontology
☒	☐ Animals and other organisms
☒	☐ Human research participants
☒	☐ Clinical data

Methods

n/a	Involved in the study
☒	☐ ChIP-seq
☒	☐ Flow cytometry
☒	☐ MRI-based neuroimaging

Mechanisms of stretch-mediated skin expansion at single-cell resolution

https://doi.org/10.1038/s41586-020-2555-7

Received: 19 February 2019

Accepted: 19 June 2020

Mariaceleste Aragona[1], Alejandro Sifrim[2,3], Milan Malfait[1], Yura Song[1], Jens Van Herck[2,3], Sophie Dekoninck[1], Souhir Gargouri[1], Gaëlle Lapouge[1], Benjamin Swedlund[1], Christine Dubois[1], Pieter Baatsen[4], Katlijn Vints[4], Seungmin Han[5,6], Fadel Tissir[7], Thierry Voet[2,3], Benjamin D. Simons[5,6,8] ✉ & Cédric Blanpain[1,9] ✉

The ability of the skin to grow in response to stretching has been exploited in reconstructive surgery[1]. Although the response of epidermal cells to stretching has been studied in vitro[2,3], it remains unclear how mechanical forces affect their behaviour in vivo. Here we develop a mouse model in which the consequences of stretching on skin epidermis can be studied at single-cell resolution. Using a multidisciplinary approach that combines clonal analysis with quantitative modelling and single-cell RNA sequencing, we show that stretching induces skin expansion by creating a transient bias in the renewal activity of epidermal stem cells, while a second subpopulation of basal progenitors remains committed to differentiation. Transcriptional and chromatin profiling identifies how cell states and gene-regulatory networks are modulated by stretching. Using pharmacological inhibitors and mouse mutants, we define the step-by-step mechanisms that control stretch-mediated tissue expansion at single-cell resolution in vivo.

In shaping tissue architecture, cells are subject to mechanical forces arising intrinsically through the cytoskeleton, by cell–cell adhesion, and from the microenvironment through interaction with the extracellular matrix (ECM)[4,5]. Cells sense and respond to these cues via the integrated activation of different signalling pathways. This process of mechanotransduction eventually leads to changes in cell shape, gene expression and cell fate[6]. Although studies have shown that mechanotransduction can dictate cell behaviour in vitro[7], the underlying mechanisms that allow organs to sense and mediate mechanical cues in vivo are only beginning to be revealed.

As the first barrier against the environment, the skin is highly exposed to mechanical stress. The skin must resist and respond to physical insults, as well as adapt its shape and size to maintain vital barrier functions[8].

Mechanical stretch-mediated tissue expansion is a procedure commonly used in plastic surgery to generate extra skin to repair birth defects, remove scars or for breast reconstruction[1]. In this procedure, an inflatable 'skin expander' is inserted below the skin and inflated, causing the expansion of the overlaying skin[1]. During the course of expansion, an excess of cells must be produced. But do all proliferative cells respond equally to stretch, or do subpopulations respond differentially? How is mechanosensation linked to gene transcription, and which transcription factors relay mechanical stress to control expansion?

Hydrogel induces mouse skin expansion

To study the cellular and molecular mechanisms that regulate stretch-mediated expansion in vivo, we established a mouse model that mimics the procedure used in humans, in which a self-inflating hydrogel is introduced underneath the skin. The hydrogel is designed to inflate to a predefined shape and size[9]. The 4-ml hydrogel devices expanded rapidly, reaching their maximum volume after one day (Extended Data Fig. 1a–d). During the first two days following expansion, the cell area was increased and cell density decreased, consistent with stretch. After four days, these parameters returned to their homeostatic values, indicating the production of new tissue. At day 2, BrdU incorporation increased twofold, and after day 4, BrdU incorporation decreased progressively, reaching control levels by day 14 after expansion (Fig. 1a–e).

To investigate whether the differentiation rate was affected, we assessed the production of keratin 1$^+$ (Krt1$^+$) and Krt10$^+$ suprabasal cells following expansion. From day 4 onwards, we observed an increase in the number of Krt1$^+$Krt10$^+$ suprabasal layers, demonstrating that stretch-mediated proliferation couples renewing divisions with differentiation (Fig. 1f, g).

During morphogenesis and in in vitro cell culture, stretch is commonly associated with rearrangement of cell–cell junctions[10]. Transmission electron microscopy (TEM) showed that stretch induced intercellular spacing and thicker keratin bundles. Desmosomes and hemidesmosomes remained unchanged (Extended Data Fig. 1e–q). Despite cellular remodelling, the integrity of the skin barrier was maintained, as assessed by transepithelial water loss (TEWL) (Extended Data Fig. 1r). Moreover, the expression of adherens-junction and tight-junction proteins was unchanged (Fig. 1h, i, Extended Data Figs. 1s–w and 2a–d). However, following expansion, the tension-sensitive epitope of α-catenin (a18)[11] was increasingly accessible, and vinculin expression

---

[1]Laboratory of Stem Cells and Cancer, Université Libre de Bruxelles, Brussels, Belgium. [2]Department of Human Genetics, University of Leuven, KU Leuven, Leuven, Belgium. [3]Sanger Institute–EBI Single-Cell Genomics Centre, Wellcome Trust Sanger Institute, Hinxton, UK. [4]Electron Microscopy Platform of VIB Bio Imaging Core, Leuven, Belgium. [5]The Wellcome Trust–Cancer Research UK Gurdon Institute, University of Cambridge, Cambridge, UK. [6]Wellcome Trust–Medical Research Council Stem Cell Institute, University of Cambridge, Cambridge, UK. [7]Université Catholique de Louvain, Institute of Neuroscience, Developmental Neurobiology, Brussels, Belgium. [8]Department of Applied Mathematics and Theoretical Physics, Centre for Mathematical Sciences, University of Cambridge, Cambridge, UK. [9]WELBIO, Université Libre de Bruxelles, Brussels, Belgium. ✉e-mail: bds10@cam.ac.uk; cedric.blanpain@ulb.ac.be

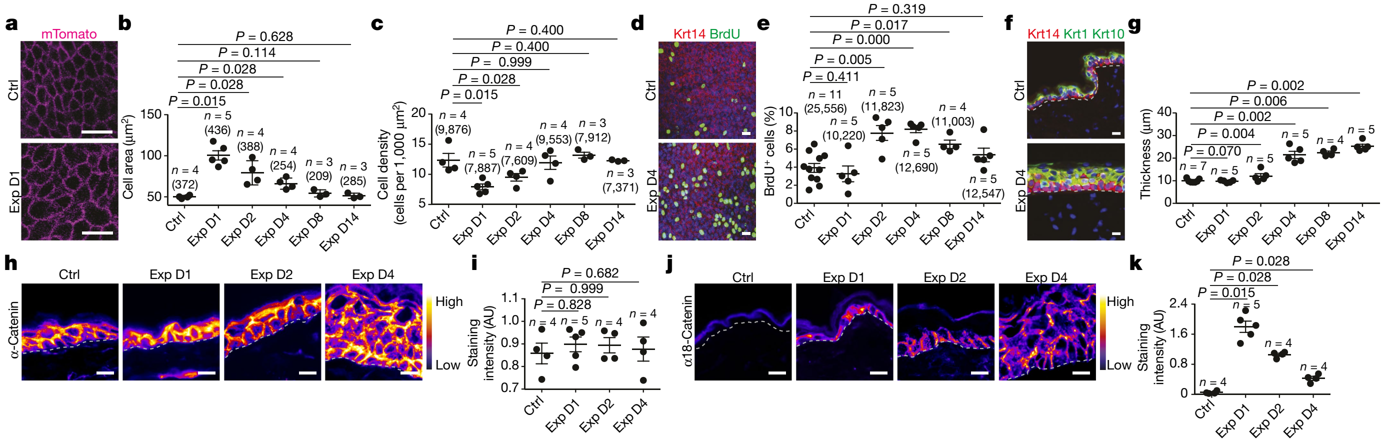

Fig. 1 | Inflated hydrogel mediates skin expansion. a, Membranous signal (pink), from paraformaldehyde-perfused *Rosa26*$^{mT/mG}$ mice in the control condition (Ctrl) and day 1 (D1) of the expansion condition (Exp). Scale bars, 15 µm. **b**, Area of basal cells measured from **a**. **c**, Basal cell density. Number of nuclei per 1,000 µm^2 (five different independent areas of 40,000 µm^2 per mouse). **d**, Immunostaining for Krt14 (red), BrdU incorporation (green) and Hoechst staining (nuclei, blue) on whole-mount epidermis. Scale bars, 20 µm. **e**, BrdU-positive cells from **d**. **f**, Immunostaining for Krt14 (red), Krt1 and Krt10 (green), and Hoechst staining (blue) on tissue sections. Scale bars, 20 µm. **g**, Tissue thickness; three independent measurements from at least two sections per mouse. **h**, **j**, Staining of the adherens-junction component α-catenin (**h**) and the α18 tension-sensitive epitope of α-catenin (α18-catenin) (**j**) colour-coded for signal intensity with ImageJ. Protein expression is visualized as a colour gradient with black indicating no expression and yellow indicating maximum expression. Scale bars, 10 µm. **i**, **k**, Average integrated density signal for α-catenin (**i**) and α18-catenin (**k**). Each data point is the average of five measurements per mouse. AU, arbitrary units. In **f**, **h j**, the dashed line indicates the basal lamina. In **b**, **c**, **e**, numbers of cells are in parentheses and *n* = number of mice. Two-tailed Mann–Whitney test; mean per mouse ± s.e.m.

was enriched at the adhesion sites, showing that adherens junctions are remodelled following stretch (Fig. 1j, k, Extended Data Fig. 2e, f).

Although inflammation occurred following expansion, blocking inflammation by dexamethasone administration did not decrease proliferation (Extended Data Fig. 2g–m), suggesting that inflammation is not essential to mediate cell proliferation.

Stretching promotes stem cell renewal

To define the fate dynamics of epidermal cells during stretch-mediated skin expansion, we performed clonal analysis on *Krt14-creER-Rosa*^{Confetti} mice. As described previously[12–14], the steady increase in basal (and total) clone size over the two-week time course was compensated by a decrease in clone persistence, such that the total labelled cell fraction remained constant over time. Furthermore, the clone size distributions showed an exponential-like dependence (Fig. 2a–f, Extended Data Fig. 3a, b), consistent with the dynamics of a single equipotent cell population maintained through population asymmetric self-renewal, as found in other compartments of skin epidermis[12–15].

During stretch-mediated expansion, the average clone size was increased by 3.4-fold in the basal and 6.8-fold in the total cell content, twofold larger than under control conditions. However, in this case, the expansion in basal clone size was not compensated by a decrease in clone persistence (Fig. 2g–k, Methods), indicating that tissue expansion does not simply increase proliferation, but also changes the balance between renewal and differentiation.

To understand the changes that take place in cell fate during expansion, we first considered the homeostatic control condition. Despite its exponential form, detailed inspection of the clone size distribution revealed evidence of a statistically significant bias towards clones bearing an even number of basal cells (65 ± 5% (mean ± s.d.) at day 14), a feature that was also present in the total clone size distribution (57 ± 4% at day 14) (Fig. 2b). Remarkably, this feature was greatly enhanced in 12-*O*-tetradecanoylphorbol-13-acetate (TPA)-treated (Extended Data Fig. 3d–g) and expansion conditions (Fig. 2g, Extended Data Fig. 3h–j), for both basal (80 ± 11% and 84 ± 6%, respectively, at day 14) and total (78 ± 11% and 81 ± 6%, respectively, at day 14) clone size, suggesting that it did not derive from statistical noise or synchrony of division, but may originate from a niche-like organization of tissue. To develop this idea, we considered an arrangement in which back-skin interfollicular epidermis (IFE) comprised a mosaic of units, each of which hosts two basal cells organized in a stem–progenitor cell-like hierarchy with one basal cell belonging to a renewing (stem cell) compartment and the other a progenitor cell committed to differentiation through terminal division and stratification (Fig. 2l, Supplementary Note). To ensure the prevalence of even cell numbers in clones, we posited that the terminal division and stratification of progenitor cells is compensated predominantly by the asymmetric division of stem cells within the same unit. Further, to account for the expansion of clones beyond two basal cells, we proposed that correlated cell loss and replacement must also occur between neighbouring units. From a fit to the clonal data, we found that this model could predict the distributions of basal and total clone size with a division rate of once per 4.6 days, while around 4 out of 5 divisions of renewing cells result in asymmetric fate outcome, a similar figure to that found in other skin compartments on the basis of a model of intrinsic fate choice[12–16]. Notably, we found that a ‘one-progenitor’ model based on the correlated differentiation and divisions of neighbours[17] could not reproduce the fine features of the data (Fig. 2l, Extended Data Fig. 3k–p, Supplementary Note).

In common with control and TPA data, the distribution of clone sizes during expansion also showed convergence towards an exponential size dependence (Fig. 2k). We therefore investigated whether a minimal adjustment of the homeostatic model could predict the clone dynamics. Taking as an input the measured proliferation rate on the basis of BrdU incorporation (Fig. 1e), we found that a continuous adjustment of fate imbalance could account for the average clone size increase, as well as the enrichment of even-sized clones, providing evidence that progenitor heterogeneity is conserved during expansion (Extended Data Fig. 4a–g, Supplementary Note).

To further challenge the two-progenitor model and the transient changes in cell fate following skin expansion, we marked cells during division using a BrdU single-pulse-chase assay. We assessed the fate of proliferative cells during stretch, discriminating between daughter cells biased for renewal (Krt14$^+$Krt10$^-$) and those committed to differentiation (Krt14$^+$Krt10$^+$). We found that stretching increased the proportion of BrdU$^+$Krt14$^+$Krt10$^-$ cells, consistent with the model, demonstrating

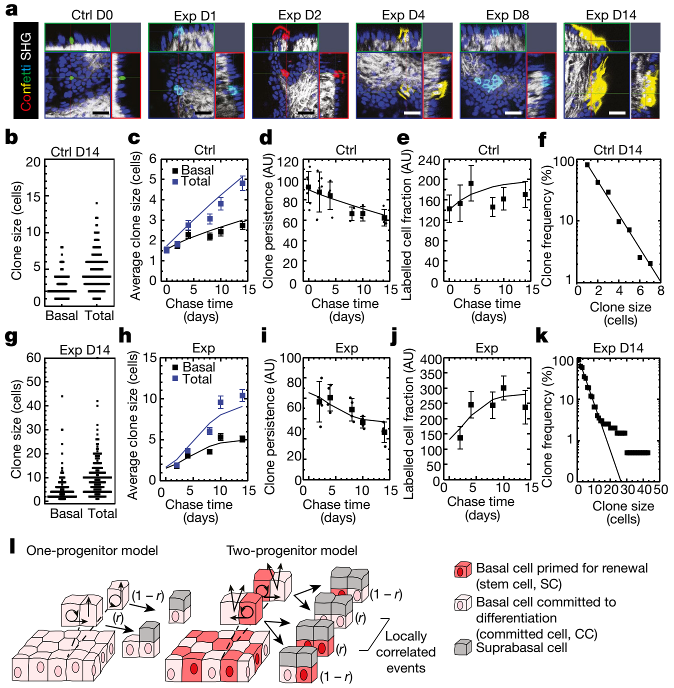

Fig. 2 | Clonal analysis of epidermal stem cells during stretch-mediated skin expansion. a, *Krt14-creER-Rosa*^{Confetti} clones ($n = 4$ independent experiments). Second harmonic generation (SHG) imaging visualizes collagen fibres (white). Nuclei stained with 7-aminoactinomycin D (7AAD) (blue). Scale bars, 50 µm. **b**–**k**, Clonal analysis in control and expansion conditions. **b**, **g**, Distribution of clone sizes at day 14 based on basal and total cell number. **c**, **h**, Average clone size based on basal (black) and total (blue) cell content. **d**, **i**, Clone persistence. **e**, **j**, Average labelled cell fraction. **f**, **k**, Cumulative clone size distribution at day 14 showing an approximate exponential size dependence (lines). In **b**–**f**: day 0, 115 clones from $n = 7$ mice; day 2, 175 clones from $n = 7$ mice; day 4, 136 clones from $n = 5$ mice; day 8, 159 clones from $n = 3$ mice; day 10, 146 clones from $n = 3$ mice; day 14, 195 clones from $n = 4$ mice. In **g**–**k**: day 2, 231 clones from $n = 4$ mice; day 4, 197 clones from $n = 4$ mice; day 8, 199 clones from $n = 4$ mice; day 10, 157 clones from $n = 4$ mice; day 14, 199 clones from $n = 4$ mice. **l**, Schematic showing the cellular organization in a one-progenitor model and the proposed two-progenitor model of back-skin IFE. In the two-progenitor model, the epidermis contains renewing stem cells, committed cells and suprabasal cells. In homeostasis, stem cells divide at an average rate λ. This division has a probability of $1 - r$ of an asymmetric fate outcome, leading to the replacement of the partner committed cell, which in turn is lost through terminal division and stratification from the basal layer. The remaining divisions lead to the correlated loss and replacement of renewing cells through symmetric cell divisions. Probability is shown in parentheses. In **c**–**f**, **h**–**k**, data are mean ± s.d. In **c**–**e**, **h**–**j**, points show data and lines show results of a two-progenitor model (see Supplementary Note).

that expansion promotes an imbalance of the renewing population towards cell duplication (Extended Data Fig. 4h, i).

Molecular features related to stretch

To define the changes in gene expression following expansion, we performed microarray analysis on basal cells isolated by fluorescence-activated cell sorting (FACS) in different conditions (Extended Data Fig. 5a). Genes upregulated in both expanded and TPA conditions comprise those regulating cell cycle, DNA replication, cell survival and cytoskeleton remodelling (Extended Data Fig. 5b, c). Many of these genes are also upregulated during wound healing[18], suggesting that they represent a common transcription program linked to cellular stress and proliferation.

Genes that were preferentially upregulated in the expanded condition were enriched for those related to cell–cell and cell–ECM adhesion, small GTPase, regulators of the actomyosin cytoskeleton (Fig. 3a) and genes regulating proliferation, including *Egfr*, *Ras*, mitogen-activated protein kinase (MAPK), activator protein 1 (AP1), transcription factors *Junb*, *Fos*, *Fosb* and *Fosl1*, and components of the YAP–TEAD pathway (for example, *Tead1* and the canonical YAP target gene *Cyr61*) (Fig. 3b). Consistently, we found changes in the expression of some of these adhesion and cytoskeleton proteins by immunostaining and FACS analysis (Extended Data Fig. 5d–f).

To unravel the changes in the chromatin landscape that are associated with expansion, we used an assay for transposase-accessible chromatin using sequencing (ATAC-seq) to identify the chromatin regions that were remodelled at day 2 following expansion. To define the transcription factors associated with chromatin remodelling, we performed motif-discovery analyses on the chromatin-remodelled regions. The most frequent motifs associated with open chromatin regions corresponded to AP1, p63, STAT, ETS, CEBP, AP2A and GRHL2 (Fig. 3c, Extended Data Fig. 5g–k, Supplementary Tables 1, 2). Immunostaining confirmed overexpression of members of the AP1 transcription factor family such as FOSL1, FOS and JUN, as well as p63, pSTAT3 and KLF4 in the basal and early suprabasal cells (Fig. 3d–f, Extended Data Fig. 5l–t). These results show that stretch-mediated skin expansion is regulated by the EGFR–Ras–MAPK pathway, leading to the activation of JUN and FOS[19] transcription factors, transcription factors such as p63 that mediate epidermal stem cell renewal[20], as well as transcription factors associated with differentiation such as CEBP[21], KLF4[22] and GRHL2[23], allowing skin expansion while maintaining skin barrier functions.

scRNA-seq during stretching

To assess whether all basal cells respond equally to stretch, we performed single-cell RNA sequencing (scRNA-seq) on FACS-isolated cells enriched for basal IFE, infundibulum, sebaceous gland and basal upper hair follicle cells in control conditions ($n = 4{,}659$), after TPA treatment ($n = 4{,}342$) and following expansion (day 1, $n = 4{,}934$ and day 4, $n = 2{,}716$) (Extended Data Fig. 5a). Using graph-based clustering, we identified different subpopulations on the basis of marker gene expression. These different clusters were found in all conditions (Extended Data Fig. 6a–l), and were similar to the clusters described in a previous study[24,25].

On the basis of the clonal analysis, we first questioned whether the scRNA-seq data supported the existence of proliferative heterogeneity in the IFE. When only IFE cells were analysed in control conditions, we identified a population of undifferentiated cells with a stem cell-like signature, a population of proliferative basal committed cells co-expressing basal and early differentiation markers such as Krt1 and Krt10, and a population of non-cycling cells expressing differentiation markers (Fig. 3g). The same IFE populations were found in all conditions, although the proliferative activity of stem cells and committed cells were proportionately increased in expansion and TPA conditions (Fig. 3g, Extended Data Fig. 7a–f, Supplementary Table 3).

In addition, cell states expressing genes associated with stress and hyperproliferation (for example, *Krt6a*, *Sprr1a*, *S100a8*, *Klk10*) were found in the expanded condition (Fig. 3g, Extended Data Fig. 7g). Notably, the stem cell-like 'stretch' cluster appearing on day 1 following expansion—identified by the expression of basal markers (for example, *Krt14*, *Itgb1*) and higher expression of *Ly6a*, *H2-K1*, *Thy1* and *Mt2* (Fig. 3g–i, Extended Data Fig. 7h)—presented increased activity of transcription factors regulating proliferation and immediate early genes (for example, *E2f1* and *Egr1*) as well as AP1 transcription factors (for example, *Fos*, *Junb* and *Jund*), inflammation (for example, *Stat1* and *Stat3*) and commitment or differentiation (for example, *Klf4*), as analysed by SCENIC analysis[26] (Fig. 3j, Extended Data Fig. 8a, Supplementary Tables 4–6), suggesting that only a fraction of basal cells respond transcriptionally to mechanical stress.

To determine the lineage trajectories among the different subpopulations, we performed pseudotemporal ordering of cells using

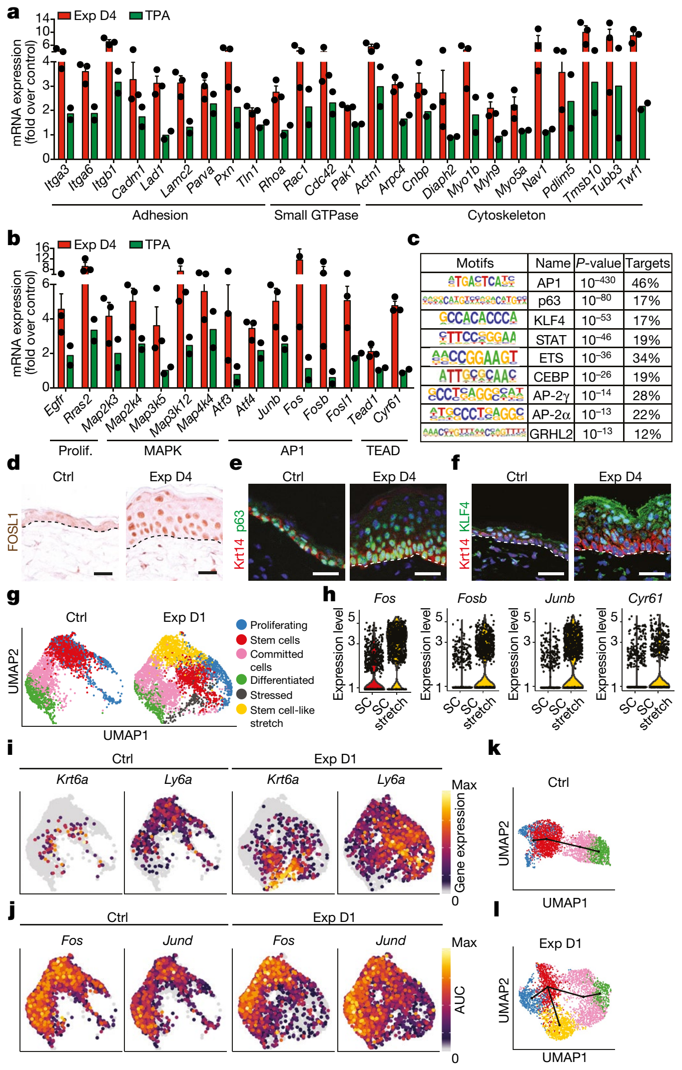

Fig. 3 | Transcriptional and chromatin remodelling associated with stretch-mediated skin expansion. **a**, **b**, mRNA expression of genes upregulated in day 4 of expansion conditions ($n = 3$) compared with TPA-treated cells ($n = 2$). Bars are mean with s.e.m. of the fold change over the average value of the control ($n = 3$). *Cyr61* is also known as *Ccn1*. Prolif., proliferation. **c**, Transcription factor motifs enriched in the ATAC-seq peaks that were upregulated on day 2 of expansion conditions compared with control ($n = 3{,}262$ target sequences, 46,200 background sequences) as determined by Homer analysis using known motif search. **d**, Immunohistochemistry for FOSL1. **e**, **f**, Immunofluorescence for p63 (**e**) or KLF4 (**f**) and Krt14, and Hoechst staining. In **d**–**f**, dashed lines delineate the basal lamina. Scale bars, 20 μm. $n = 3$ independent experiments. **g**, Uniform manifold approximation and projection (UMAP) graphic of the clustering analysis for scRNA-seq of the control ($n = 3{,}142$ cells) and expansion day 1 ($n = 3{,}756$ cells) IFE projected on an integrated embedding of the dataset. **h**, Violin plots of the indicated genes at expansion day 1 in the stem cell (SC) ($n = 700$ cells) and stem cell-like stretch (SC stretch) ($n = 801$ cells) clusters (see Source Data). **i**, UMAP plots coloured by normalized gene expression values for the indicated genes in the control and expansion day 1 IFE. Gene expression is visualized as a colour gradient with grey indicating no expression (that is, expression below the 50th percentile across each respective sample) and yellow indicating maximum (max) expression. **j**, UMAP plots coloured by the degree of regulon activation for transcription factors differentially activated (area under the curve (AUC) rank-sum test FDR corrected P-value < 0.05) in the different conditions. Colour scaling represents the normalized AUC value of target genes in the regulon being expressed as computed using SCENIC. **k**, **l**, Lineage trajectories (black lines) computed using Slingshot. Clusters are coloured as in **g**. In **i**–**l**, $n = 3{,}142$ cells (control) and $n = 3{,}756$ cells (expansion day 1).

Slingshot[27] in control and expansion day 1 conditions. In all conditions, we found a trajectory starting from undifferentiated basal stem cells, passing through the progenitor state, and terminating with the most differentiated cells (Fig. 3k, l, Extended Data Fig. 8b). In expansion day 1 conditions, we resolved another differentiation pathway involving progression through the stress states, delineating the different responses to mechanical cues (Fig. 3l, Extended Data Fig. 8c, d). Together, these data show that stem cells present a rapid and profound response to stretch.

Mechanosensing at adherens junctions

The results of TEM and molecular analysis suggested that stretching induces remodelling of the cytoskeleton, as well as an increase at the transcription level of several genes encoding remodellers of the actomyosin cytoskeleton, such as *Diaph2* and *Diaph3*, and formin-like proteins involved in actin regulation[28] (Fig. 3a, Extended Data Fig. 1e–g, k, Extended Data Fig. 5c, k). To test whether rearrangements of actin organization are essential to mediate the response to stretch, we studied the consequence of *Diaph3* deletion (*Diaph3* conditional knockout (cKO)). The increase in the number of cells presenting F-actin structures on their apical surface on day 1 of expansion was reduced, and no increase in cell proliferation following stretch was observed in *Diaph3* cKO mice (Fig. 4a, Extended Data Fig. 9a–g).

Mechanical stretch has been shown to promote the phosphorylation of myosin II, relaying mechanotransduction in cell lines in vitro[2] and in the *Drosophila* wing disc[29]. Consistently, following conditional ablation of *Myh9*, a key subunit of myosin IIA (*Myh9* cKO), proliferation was not increased in response to stretch (Fig. 4b, Extended Data Fig. 9h–l).

As basal cells sense stretching by remodelling the traction at adherens junctions, we assessed whether *Diaph3* and *Myh9* cKO prevent adhesion remodelling. The accessibility of the α-catenin tension-sensitive epitope and vinculin staining were not increased following stretching in *Diaph3* and *Myh9* cKO mice (Extended Data Fig. 9m–r). Deletion of *Diaph3* and *Myh9* following expansion resulted in the incapacity of the epidermis to adapt to stretch, causing a barrier defect (Fig. 4c).

MEK–ERK–AP1 regulate expansion

Previous studies demonstrated that in vitro mechanical stretching induces proliferation by activation of MEK signalling[30], and that ERK is activated on stress fibres in a myosin II-dependent manner[31]. To assess whether pharmacological inhibition of the MEK–ERK pathway could impair the cellular behaviour following skin stretching, we treated mice with the MEK inhibitors trametinib and pimasertib. Both inhibitors reduced phosphorylation of ERK and resulted in a decrease of cell proliferation and the number of differentiated cells induced by stretching (Extended Data Fig. 10a–g), demonstrating the importance of MEK–ERK–AP1 signalling in the regulation of the stretch response in vivo.

YAP and MAL regulate skin stretching

Previous studies have shown that YES-associated protein 1 (YAP1), the downstream coeffector of Hippo signalling, and megakaryoblastic leukaemia/myocardin-like 1 (MAL, also known as MRTFA or MKL1), the co-factor of serum response factor (SRF), are induced in response to mechanical stimuli[32,33]. In the skin, YAP–TAZ and SRF pathways are essential for epidermal development and wound repair, but are dispensable for homeostasis[34,35]. In vitro studies have demonstrated the role of MAL–SRF in the survival and differentiation of keratinocytes cultured on micropatterned surfaces[36], and that of YAP as a driver of proliferation in stretched cultured cells in vitro[37].

To test whether and when YAP and MAL are activated in vivo, we assessed their subcellular localization at different times during expansion. Whereas YAP and MAL were localized preferentially in the

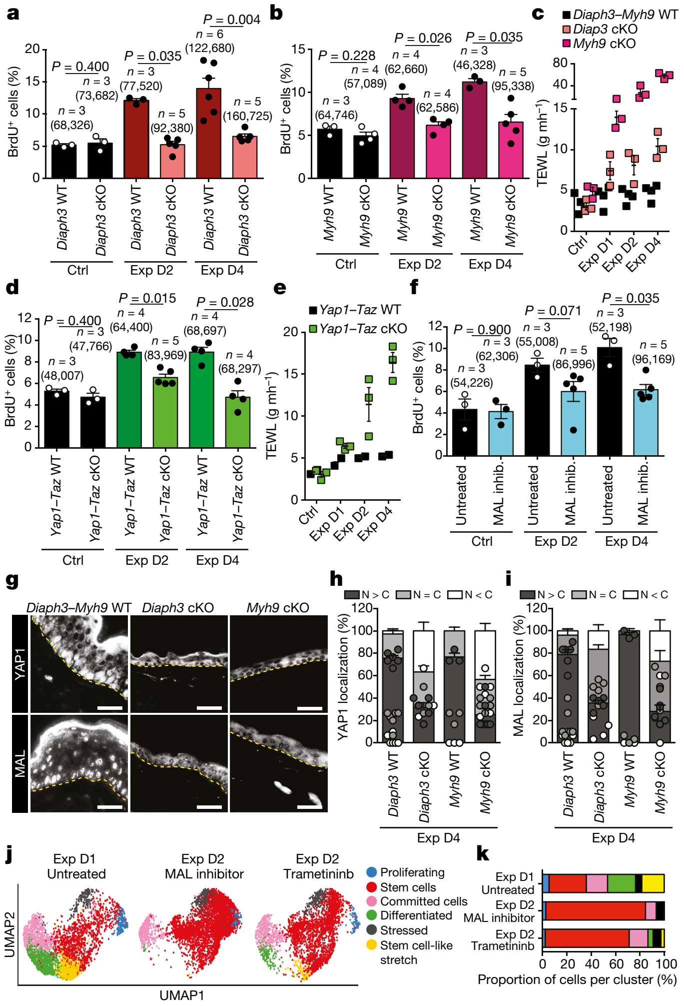

Fig. 4 | Molecular regulation of stretch-mediated skin expansion. a, BrdU-positive cells in control and expansion conditions in *Diaph3* wild-type (WT) or cKO mice. **b**, BrdU-positive cells in control and expansion conditions in *Myh9* WT and cKO mice. **c**, TEWL measurements from $n = 2$ *Diaph3* WT, $n = 2$ *Myh9* WT (black), $n = 3$ *Diaph3* cKO (pink) and $n = 3$ *Myh9* cKO mice (violet). **d**, BrdU-positive cells in control and expansion conditions in *Yap1–Taz* WT or cKO mice. **e**, TEWL measurements from $n = 2$ *Yap1–Taz* WT mice (black) and $n = 3$ *Yap1–Taz* cKO mice (green). **f**, BrdU-positive cells in untreated or treated mice with the MAL inhibitor in control and expansion conditions. **g**, Immunostaining for YAP1 (top) and MAL (bottom) on skin sections of *Diaph3* cKO and *Myh9* cKO mice at expansion day 4. The control images are from a *Diaph3* WT (top) mouse and a *Myh9* WT (bottom) mouse. Dashed lines delineate the basal lamina. Scale bars, 20 μm. **h**, **i**, YAP1 (**h**) and MAL (**i**) subcellular localization in skin sections represented in **g**. Data are mean ± s.e.m. N > C, more protein in nucleus than in cytoplasm; N = C, similar level of protein in nucleus as in cytoplasm; N < C, less protein in nucleus than in cytoplasm. $n = 150$ cells per condition. **j**, UMAP computed on the integrated single-cell RNA-seq dataset coloured for the different cellular clusters in IFE. $n = 3{,}869$ cells (expansion day 1 untreated); $n = 4{,}762$ cells (expansion day 2 MAL inhibitor); $n = 3{,}254$ cells (expansion day 2 trametininb). **k**, Quantification of the cellular clusters in **j**. In **a**–**f**, data are mean ± s.e.m.; n = number of mice; total numbers of cells analysed are indicated in parentheses. In **a**, **b**, **d**, **f**, two-tailed Mann–Whitney test. In **c**, **e**, each data point represents the average of 30 individual subsequently recorded measurements at the probe head.

cytoplasm in the control, they gradually translocated to the nucleus of basal cells during expansion (Extended Data Fig. 10h–k). These data reveal that YAP and MAL are activated immediately following stretching, but only in a subset of basal cells, similar to AP1 family members (Extended Data Fig. 10l).

To define the functional role of YAP, we induced deletion of *Yap1* and *Taz* specifically in the epidermis (*Yap1–Taz* cKO) and assessed their role during stretch. A significant decrease in BrdU incorporation was observed already by day 2 in *Yap1–Taz* cKO epidermis, as well as a reduction in epidermal thickness (Fig. 4d, Extended Data Fig. 10m–q). In addition, the deletion of *Yap1* and *Taz* following hydrogel expansion caused a barrier defect (Fig. 4e).

To assess the role of MAL activity, we treated the mice immediately after surgery with the pharmacological MAL–SRF inhibitor CCG203971[38], and found a significant decrease of BrdU incorporation and epidermal thickness at day 4 (Fig. 4f, Extended Data Fig. 10r–u). Notably, inhibition of both pathways completely blocked the response to stretch (Extended Data Fig. 11a–d).

As *Diaph3* and *Myh9* control adhesion remodelling upon stretching, we tested whether they act upstream of YAP1 and MAL. In *Diaph3* cKO and *Myh9* cKO epidermis, YAP1 and MAL were not translocated into the nucleus following stretch (Fig. 4g–i, Extended Data Fig. 11e, f), demonstrating the essential role of *Diaph3* and *Myh9* in regulating canonical mechanotransducers. Together, these experiments demonstrate that mechanical stretch couples cytoskeletal contractility with the nuclear effectors of mechanotransduction and stem cell activation in vivo.

scRNA-seq after MEK and MAL inhibition

To define the consequences of the inhibition of the signalling pathways that control stretch-induced proliferation on the cellular heterogeneity and stem cell dynamics in vivo, we performed short-term lineage tracing of basal cells using BrdU pulse-chase combined with immunohistochemistry. The results showed a decrease in renewing divisions (BrdU$^+$Krt14$^+$Krt10$^-$) in the *YAP–TAZ* cKO mice and upon inhibition of MAL–SRF or MEK–ERK–AP1 (Extended Data Fig. 11g–l). In addition, short-term genetic lineage tracing in the presence of MAL–SRF or MEK–ERK–AP1 inhibition showed suppression of the increase of clone size following skin expansion (Extended Data Fig. 12a–f). scRNA-seq at day 2 after expansion in the presence of the MEK–ERK–AP1 and MAL–SRF inhibitors showed that, although the inhibition of both pathways led to a similar decrease in cell proliferation, the proportion of cells in different states differed between treatments. Cellular heterogeneity was relatively well conserved following the inhibition of the MEK–ERK–AP1 pathway, whereas the MAL–SRF inhibitor diminished the abundance of stem cells with stress characteristics and decreased the heterogeneity of basal cells (Fig. 4j, k, Extended Data Fig. 12g, h, Supplementary Tables 7–9), suggesting that while the MEK–ERK–AP1 pathway controls only proliferation induced by stretching, the MAL–SRF pathway controls cellular heterogeneity in the basal layer and stretch sensing.

Discussion

We have dissected the cellular and molecular spatiotemporal mechanisms that control the behaviour of epidermal stem cells in response to mechanical stretch. Quantitative modelling of clonal data suggests that proliferation and differentiation of basal cells in back-skin epidermis is spatially and temporally linked, as has been suggested during homeostasis[17,39]. During stretch-mediated skin expansion, a transient shift of stem cell fate towards renewal allows the basal population to expand while differentiation is maintained. These results were supported by results of scRNA-seq, which revealed the existence of different cell states within the basal layer, identifying the molecular signature of stem and committed cells in the mouse back skin, and highlighting the heterogeneous response of basal cells to stretching.

Mechanistically, we found that regulators of the actomyosin cytoskeleton, including formin-like proteins and non-muscle myosin, are essential for sensing skin stretching in vivo, and act upstream of canonical mechanotransducers such as YAP1 and MAL. Of note, the same signalling pathways are activated during embryonic pancreas development[40] and in the fly notum upon mechanical compression[41], suggesting that these signalling pathways and transcriptional regulators have a conserved role in mechanotransduction across the animal kingdom and between embryonic development and adult tissue regeneration.

Online content

Any methods, additional references, Nature Research reporting summaries, source data, extended data, supplementary information, acknowledgements, peer review information; details of author contributions and competing interests; and statements of data and code availability are available at https://doi.org/10.1038/s41586-020-2555-7.

1. Zöllner, A. M., Holland, M. A., Honda, K. S., Gosain, A. K. & Kuhl, E. Growth on demand: reviewing the mechanobiology of stretched skin. *J. Mech. Behav. Biomed. Mater*. **28**, 495–509 (2013).
2. Le, H. Q. et al. Mechanical regulation of transcription controls Polycomb-mediated gene silencing during lineage commitment. *Nat. Cell Biol*. **18**, 864–875 (2016).
3. Nava, M. M. et al. Heterochromatin-driven nuclear softening protects the genome against mechanical stress-induced damage. *Cell* **181**, 800–817 (2020).
4. Iskratsch, T., Wolfenson, H. & Sheetz, M. P. Appreciating force and shape—the rise of mechanotransduction in cell biology. *Nat. Rev. Mol. Cell Biol*. **15**, 825–833 (2014).
5. LeGoff, L. & Lecuit, T. Mechanical forces and growth in animal tissues. *Cold Spring Harb. Perspect. Biol*. **8**, a019232 (2016).
6. Kirby, T. J. & Lammerding, J. Emerging views of the nucleus as a cellular mechanosensor. *Nat. Cell Biol*. **20**, 373–381 (2018).
7. Vining, K. H. & Mooney, D. J. Mechanical forces direct stem cell behaviour in development and regeneration. *Nat. Rev. Mol. Cell Biol*. **18**, 728–742 (2017).
8. Blanpain, C. & Fuchs, E. Plasticity of epithelial stem cells in tissue regeneration. *Science* **344**, 1242281 (2014).
9. Obdeijn, M. C., Nicolai, J. P. & Werker, P. M. The osmotic tissue expander: a three-year clinical experience. *J. Plast. Reconstr. Aesthet. Surg*. **62**, 1219–1222 (2009).
10. Wickström, S. A. & Niessen, C. M. Cell adhesion and mechanics as drivers of tissue organization and differentiation: local cues for large scale organization. *Curr. Opin. Cell Biol*. **54**, 89–97 (2018).
11. Yonemura, S., Wada, Y., Watanabe, T., Nagafuchi, A. & Shibata, M. α-Catenin as a tension transducer that induces adherens junction development. *Nat. Cell Biol*. **12**, 533–542 (2010).
12. Clayton, E. et al. A single type of progenitor cell maintains normal epidermis. *Nature* **446**, 185–189 (2007).
13. Mascré, G. et al. Distinct contribution of stem and progenitor cells to epidermal maintenance. *Nature* **489**, 257–262 (2012).
14. Sánchez-Danés, A. et al. Defining the clonal dynamics leading to mouse skin tumour initiation. *Nature* **536**, 298–303 (2016).
15. Lim, X. et al. Interfollicular epidermal stem cells self-renew via autocrine Wnt signaling. *Science* **342**, 1226–1230 (2013).
16. Rompolas, P. et al. Spatiotemporal coordination of stem cell commitment during epidermal homeostasis. *Science* **352**, 1471–1474 (2016).
17. Mesa, K. R. et al. Homeostatic epidermal stem cell self-renewal is driven by local differentiation. *Cell Stem Cell* **23**, 677–686 (2018).
18. Aragona, M. et al. Defining stem cell dynamics and migration during wound healing in mouse skin epidermis. *Nat. Commun*. **8**, 14684 (2017).
19. Eferl, R. & Wagner, E. F. AP-1: a double-edged sword in tumorigenesis. *Nat. Rev. Cancer* **3**, 859–868 (2003).
20. Botchkarev, V. A. & Flores, E. R. p53/p63/p73 in the epidermis in health and disease. *Cold Spring Harb. Perspect. Med*. **4**, a015248 (2014).
21. Lopez, R. G. et al. C/EBPα and β couple interfollicular keratinocyte proliferation arrest to commitment and terminal differentiation. *Nat. Cell Biol*. **11**, 1181–1190 (2009).
22. Segre, J. A., Bauer, C. & Fuchs, E. Klf4 is a transcription factor required for establishing the barrier function of the skin. *Nat. Genet*. **22**, 356–360 (1999).
23. Hopkin, A. S. et al. GRHL3/GET1 and trithorax group members collaborate to activate the epidermal progenitor differentiation program. *PLoS Genet*. **8**, e1002829 (2012).
24. Joost, S. et al. Single-cell transcriptomics reveals that differentiation and spatial signatures shape epidermal and hair follicle heterogeneity. *Cell Syst*. **3**, 221–237 (2016).
25. Joost, S. et al. Single-cell transcriptomics of traced epidermal and hair follicle stem cells reveals rapid adaptations during wound healing. *Cell Rep*. **25**, 585–597 (2018).
26. Aibar, S. & Gonzalez-Blas, C. B. SCENIC: single-cell regulatory network inference and clustering. *Nat. Methods* **14**, 1083–1086 (2017).
27. Street, K. et al. Slingshot: cell lineage and pseudotime inference for single-cell transcriptomics. *BMC Genomics* **19**, 477 (2018).
28. Rottner, K., Faix, J., Bogdan, S., Linder, S. & Kerkhoff, E. Actin assembly mechanisms at a glance. *J. Cell Sci*. **130**, 3427–3435 (2017).
29. Duda, M. et al. Polarization of myosin ii refines tissue material properties to buffer mechanical stress. *Dev. Cell* **48**, 245–260 (2019).
30. Yang, K. et al. YAP and ERK mediated mechanical strain-induced cell cycle progression through RhoA and cytoskeletal dynamics in rat growth plate chondrocytes. *J. Orthop. Res*. **34**, 1121–1129 (2016).
31. Hirata, H. et al. Actomyosin bundles serve as a tension sensor and a platform for ERK activation. *EMBO Rep*. **16**, 250–257 (2015).
32. Panciera, T., Azzolin, L., Cordenonsi, M. & Piccolo, S. Mechanobiology of YAP and TAZ in physiology and disease. *Nat. Rev. Mol. Cell Biol*. **18**, 758–770 (2017).
33. Posern, G. & Treisman, R. Actin' together: serum response factor, its cofactors and the link to signal transduction. *Trends Cell Biol*. **16**, 588–596 (2006).
34. Rognoni, E. & Walko, G. The roles of YAP/TAZ and the Hippo pathway in healthy and diseased skin. *Cells* **8**, 411 (2019).
35. Luxenburg, C., Pasolli, H. A., Williams, S. E. & Fuchs, E. Developmental roles for Srf, cortical cytoskeleton and cell shape in epidermal spindle orientation. *Nat. Cell Biol*. **13**, 203–214 (2011).
36. Connelly, J. T. et al. Actin and serum response factor transduce physical cues from the microenvironment to regulate epidermal stem cell fate decisions. *Nat. Cell Biol*. **12**, 711–718 (2010).
37. Aragona, M. et al. A mechanical checkpoint controls multicellular growth through YAP/TAZ regulation by actin-processing factors. *Cell* **154**, 1047–1059 (2013).
38. Whitson, R. J. et al. Noncanonical hedgehog pathway activation through SRF–MKL1 promotes drug resistance in basal cell carcinomas. *Nat. Med*. **24**, 271–281 (2018).
39. Miroshnikova, Y. A. et al. Adhesion forces and cortical tension couple cell proliferation and differentiation to drive epidermal stratification. *Nat. Cell Biol*. **20**, 69–80 (2018).
40. Mamidi, A. et al. Mechanosignalling via integrins directs fate decisions of pancreatic progenitors. *Nature* **564**, 114–118 (2018).
41. Moreno, E., Valon, L., Levillayer, F. & Levayer, R. Competition for space induces cell elimination through compaction-driven ERK downregulation. *Curr. Biol*. **29**, 23–28 (2019).

Methods

Mouse strains

Krt14-creER (ref. [42]) and *Krt14-cre* (ref. [43]) transgenic mice were provided by E. Fuchs (Rockefeller University). *Rosa*^{Confetti} mice[44] mice were provided by H. Clevers (Hubrecht Institute). *Yap1*$^{fl/fl}$ and *Taz*$^{fl/fl}$ mice[45] were obtained from G. Halder (KU Leuven) who received them from R. Johnson at the MD Anderson Cancer Center, Houston. *Diaph3*$^{fl/fl}$ mice[46] were produced by F. Tissir (UCLouvain) and *Myh9*$^{fl/fl}$ mice[2] were a gift from S. Wickström (University of Helsinki). *Rosa26*$^{mT/mG}$ (ref. [47]) mice were provided form I. Migeotte (Université Libre de Bruxelles). Mouse colonies were maintained in a certified animal facility in accordance with European guidelines. The experiments were approved by the local ethical committee (CEBEA) under protocols #604 and #605. The study is compliant with all relevant ethical regulations regarding animal research.

Expander experiments

Mice were anaesthetized (5% xylazine 10% ketamine in PBS) and the dorsal skin was disinfected with 10% iso-Betadine (Meda Pharma), an incision was created in the most caudal part of the dorsal skin to minimize any tension in the wound as the expansion progressed and to maximise the distance from the access wound, to the location of the expander. A subcutaneous pocket was created with forceps and a 4-ml Hemispher Self-inflating tissue expander (Osmed) was placed in the most rostral part under the dorsal skin in proximity of the neck. Stiches were used to close the subcutaneous pocket, to limit the hydrogel movement and to close the access incision.

All analyses were performed in the area on the top of the dome of the hemisphere induced by the skin expander, since this region experiences the highest strain. The hemispherical architecture of the hydrogel has, by its geometric nature, a higher degree of mechanical load at the apex of the hemisphere with isotropic stress[48] and only the skin overlying the very upper part of the hydrogel was studied.

Sample size, randomization and blinding

The sample size was chosen based on previous experience in the laboratory, for each experiment to yield high power to detect specific effects. No statistical methods were used to predetermine sample size. The experiments were not randomized. All animals used were of similar age (60–90 days after birth) and between 28 and 33 g of weight. The investigators were not blinded to allocation during experiments and outcome assessment.

Skin whole-mount

For skin whole-mount confocal microscopy on induced *Krt14-creER-Rosa*^{Confetti} mice, pieces of entire skin of around 1 cm^2 were cleared with Sca/eCUBIC-1 and Sca/eCUBIC-2 solutions as described in[49]. The pieces were fixed overnight in 4% paraformaldehyde, incubated 3 days at 37 °C in Sca/eCUBIC-1 solution and incubated at room temperature in Sca/eCUBIC-2 solution for at least 2 days before their analysis. Counterstaining of nuclei was performed with 7AAD (1/1000, Thermo Fisher Scientific). Images were acquired at LiMiF (Université Libre de Bruxelles, Faculté de Médecine, Campus Erasme) on a LSM780NLO confocal system fitted on an Observer Z1 inverted microscope (Zeiss) equipped with a Chameleon Vision II 690-1064 nm multiphoton laser (Coherent Europe) using a Plan Apochromat 20×/0.8 dry objective or LD C Apochromat 40×/1.1 water immersion objective (Zeiss). Spectral images were acquired in lambda mode with a single excitation wavelength at 920 nm and a GaAsp spectral detector (Zeiss). Images 512 by 512 pixels were acquired as a *z*-stack across the thickness of the object. Fluorochromes were separated by linear unmixing using ZEN2012 software (Zeiss). Settings were kept identical for all conditions; this does not apply to the depth (*z* stack) that was adjusted individually to encompass the region of interest. Single plane images were displayed using Zen2012 (Black Edition) software (Zeiss) and exported as uncompressed TIFF images.

Clonal induction in *Krt14-creER-Rosa*^{Confetti} mice

For lineage tracing experiment, *Krt14-creER-Rosa*^{Confetti} mice were induced at 2 months of age with Tamoxifen (Sigma) (0.1 mg/g diluted in 10% vol/vol Ethanol and sunflower seed oil, Sigma) by intraperitoneal injection.

Inducing *Yap1*–*Taz* and *Myh9* deletion

For *Yap1-Taz* deletion in *Krt14-creER Yap1*$^{fl/fl}$*Taz*$^{fl/fl}$ mice and for *Myh9* deletion in *Krt14-creER Myh9*$^{fl/fl}$ mice, animals received a daily dose of 2.5 mg of tamoxifen (Sigma-Aldrich), for 30 g of body weight, diluted in a mixture of 10% ethanol (VWR) 90% sunflower oil (Sigma-Aldrich) by intraperioneal administration, for 5 consecutive days and every other day after surgery.

Mouse treatments

For TPA treatments, TPA (200 µl of 0.02 mg/ml solution in acetone) was administered daily to shaved mouse back skin for 2 days. To inhibit MEK1/2 activity, mice were treated with Trametinib 2 mg per kg body weight by daily oral gavage, Pimasertib 20 mg per kg body weight daily by oral gavage for at least 7 consecutive days before analysis or as indicated in the figures. To inhibit MAL activity, mice received drug treatment via intraperitoneal injection daily using 100 mg CCG203971 (Cayman Chemical) per kg body weight for 2 or 4 days as indicated in the figures. For the dexamethasone experiments, dexamethasone powder (Sigma) was resuspended at 1 mg ml^{-1} in ethanol 100% and diluted 5× in sterile PBS. The mice were injected intraperitoneally once per day at the dose of 1 mg kg^{-1}. The treatment started 2 days before the surgery to place the expander and was sustained until the end of the experiment.

Monitoring hydrogel expansion, skin growth, quantification of clone size and persistence

To measure the increase in the hydrogel volume, the height or radius of the expander (r) was measured every day (D) from D0 to D14 and the volume calculated as the volume of a half sphere with the formula $V = (2/3) \times \pi r^3$.

To measure basal cell area, whole-mount tissues were obtained from *Rosa26*$^{mT/mG}$ mice that were fixed by paraformaldehyde perfusion. Images were acquired by two-photon confocal microscopy (40× objective, $z = 1\,\mu$m). Basal cells were identified based on the orthogonal view and if their basal side was in direct contact with the signal of the second harmonic generation. Cell area was measured using ImageJ after manually drawing the contour of each cell revealed by the fluorescence on the membrane on the *Rosa26*$^{mT/mG}$ mice in the x–y plane.

To define the clone persistence, hair follicles were used as landmarks to calibrate the degree of expansion. During expansion, the total number of hair follicles is not changed, implying that, for an area expansion by a factor ε, the hair follicle density must fall by a factor $1/\varepsilon$. If the area a of each hair follicle remains unchanged during the expansion, for a patch of tissue of area A containing hair follicles spanning an area A_{HF}, the fractional increase in area during the expansion is given by $\varepsilon = A^0_{\mathrm{HF}}/A_{\mathrm{HF}}$, where A^0_{HF} is the corresponding area of hair follicles in the control animal. Then, with an average of n clones in an area A, the clonal fractional change in clonal persistence is given by $\varepsilon n/n_0$, where n_0 represents the corresponding clone number in the control animals. For clonal persistence, large areas of tissue (at least 1 cm^2 per animal) were acquired using the 25× objective and the number of basally attached clones was quantified on the two-photon confocal images in a fixed area of 4 mm^2 across the different time points.

To quantify the size of the clone, whole-mounts obtained from *Krt14-creER-Rosa*^{Confetti} mice were imaged by two-photon confocal microscopy. Orthogonal view was used to see in 3 dimensions RFP, YFP, mCFP or nGFP-positive cells and quantify the number of basal and total cells per clone. Cells were considered as basal when their basal side was in direct contact with the signal of the second harmonic generation.

Epidermal whole-mount and immunostaining

Almost the entire back skin was dissected from the animal, the fat was removed by mechanical scraping with a scalpel and the remaining tissue was cut in pieces of around 2 cm^2 and incubated in PBS/EDTA (20 mM) on a rocking plate at 37 °C for 90 min. Epidermis was separated from the dermis using forceps as an intact sheet and washed 2 times with PBS. Pieces of epidermis were pre-fixed in 4% paraformaldehyde for 1 h at room temperature. Epidermis was rinsed 2 times with PBS for 5 min and conserved in PBS with 0.2% azide at 4 °C. For immunofluorescence staining, entire pieces of epidermis were incubated in blocking buffer (1% BSA, 5% horse serum, 0.8% Triton in PBS) for 3 h at room temperature on a rocking plate (100 rpm). The samples were incubated in primary antibody with anti-Integrin β4 (rat, 1:200, BD Biosciences) overnight at 4 °C. Samples were then washed 3 times in PBS with 0.2% Tween for 1 h and incubated in appropriate secondary antibodies diluted 1:400 in blocking buffer for 1 h at room temperature on the rocking plate. For BrdU staining, samples were incubated in HCl 1M at 37 °C for 35 min, washed with PBS 0.2% tween, stained with anti-BrdU (rat, 1:200, Abcam) in blocking buffer and with appropriate secondary antibody. The following secondary antibodies were used: anti-rat conjugated to AlexaFluor488 (Molecular Probes), to Rhodamine Red-X or to Cy5 (Jackson Immuno Research). Alexa488 or Alexa633 conjugated phalloidin (Thermo Fisher Scientific) was used 1:200 in blocking buffer to visualize F-actin microfilaments. Nuclei were stained in Hoechst solution diluted 1:5000 for 30 min and mounted in DAKO mounting medium supplemented with 2.5% Dabco (Sigma). All confocal images were acquired at room temperature with a LSM780 confocal system fitted on an AxioExaminer Z1 upright microscope equipped with C-Apochromat 40×/1.1 or Plan Apochromat 25×/0.8 water immersion objectives (Zeiss, Iena, Germany). Optical sections 512 × 512 pixels were collected sequentially for each fluorochrome. The datasets generated were merged and displayed with ZEN2012 software (Zeiss).

Histology and immunostaining on sections

Skin epidermis was embedded in OCT and kept at −80 °C. Sections of 6 μm were cut using a CM3050S Leica cryostat (Leica Mycrosystems). After fixation in 4% paraformaldehyde for 10 min at room temperature, tissues were washed 3 times in PBS for 5 min and incubated in blocking buffer (1% BSA, 5% horse serum, 0.2% Triton in PBS) for 1 h at room temperature. Primary antibodies were incubated overnight at 4 °C. Sections were rinsed 3 times in PBS and incubated with secondary antibodies and Hoechst in blocking buffer for 1 h at room temperature. Sections were again washed three times with PBS. The following primary antibodies were used: anti-Krt14 (chicken, 1:20,000, custom batch, Thermo Fisher); anti-Krt1 (rabbit, 1:4,000, Covance/IMTEC, PRB-165P); anti-Krt10 (rabbit, 1:4,000, Covance/IMTEC, PRB-159P); anti-c-JUN (rabbit, 1:200; Proteintech, 24909-1-AP); anti-p63 (rabbit, 1:100 Abcam, ab124762); anti-KLF4 (rabbit, 1:100 Abcam, ab129473); anti-pSTAT3 (rabbit, 1:100 Cell signaling, 9145); anti-YAP1 (rabbit, 1:100 Proteintech, 13584-1-AP); anti-MAL (rabbit, 1:100, Sigma, HPA030782); anti-α-catenin (rabbit, 1:1000 Sigma, C2081); anti-α18-catenin (rat monoclonal, 1:20,000, a gift form A. Nagafuchi, Kumamoto University); anti-Vinculin (mouse, 1:200 Millipore MAB3574); anti-p120-catenin (rabbit, 1:1000 Invitrogen PA5-82545); anti-E-cadherin (rat, 1:500, ebioscience 14-3249-82); anti-ZO-1(rabbit, 1:200 Invitrogen 61-7300); anti-Claudin-1 (rat, 1:100 Thermo Scientific 51-9000); anti-Paxillin (rabbit, 1:100 Abcam 32084); anti-CD45 (rat, 1:500, BD Biosciences 553081); anti-CD68 (rabbit, 1:100 Abcam ab125212).

The following secondary antibodies were used diluted to 1:400: anti-mouse, anti-rat, anti-rabbit, anti-chicken conjugated to Alexa Fluor 488 (Molecular Probes), to rhodamine Red-X (Jackson Immunoresearch) or to Cy5 (Jackson Immunoresearch). Nuclei were stained in Hoechst solution (1:2000) and slides were mounted in DAKO mounting medium supplemented with 2.5% Dabco (Sigma). All images of section immunostaining were acquired using the Axio Imager M1 Microscope, the AxioCamMR3 or MrC5 camera and using the Axiovision software (Carl Zeiss). Acquisitions were performed at room temperature using 20× numerical aperture (NA) 0.4 (Carl Zeiss).

Immunofluorescence intensity measurements

To quantify the intensity of the immunostaining for proteins at the adherens junctions (α-catenin, α18-catenin, β-catenin, p120-catenin) and Paxillin, ImageJ was used to measure the integrated density, a well-established method of measuring fluorescence intensity that accounts for differences in area[50] of the signal in the basal layer of the skin (labelled by Krt14). To quantify the integrated density of the signal of the tight junction proteins ZO-1 and Claudin-1, the measurements were taken on the upper suprabasal layers. Images are shown with the pseudo-colour Fire from ImageJ after they have been contrasted equally and background was uniformly removed with Adobe Photoshop.

Immunohistochemistry

For staining on paraffin sections, 4μm paraffin sections were deparaffinized and rehydrated. Antigen unmasking was performed for 20 min at 98 °C in citrate buffer (pH 6) using the PT module. Endogenous peroxidase was blocked using 3% H_2O_2 (Merck) in methanol for 10 min at room temperature. Endogenous avidin and biotin were blocked using the Endogenous Blocking kit (Invitrogen) for 20 min at room temperature. Nonspecific antigen blocking was performed using blocking buffer. Rabbit anti-YAP (1:200, Santa Cruz Biotechnology, sc-15407), rabbit anti-TAZ (1:100, Sigma-Aldrich, HPA007415), rabbit anti-cFOS (1:100, Proteintech, 26192-1-AP), rabbit anti-MYH9 (1:500, Sigma, HPA001644), rabbit anti-pERK (1:200, Cell signaling, 4370S) were incubated overnight at 4 °C. For anti-FOSL1 (1:500, Santa Cruz Biotechnology, sc-28310) and anti-β-catenin (mouse, 1:1,000 Abcam ab6301) tissue were also blocked with Mouse on Mouse (M.O.M.) Blocking Reagent (Vector Laboratories). Anti-rabbit biotinylated with blocking buffer, anti-mouse biotinylated with blocking buffer, Standard ABC kit, and ImmPACT DAB (Vector Laboratories) were used for the detection of horseradish peroxidase (HRP) activity. Slides were then dehydrated and mounted using SafeMount (Labonord).

Proliferation experiments

For BrdU experiments, mice were injected with a single intraperitoneal injection of BrdU (50 mg/kg in PBS) at different time points and killed 4 h after. For the quantification an area of at least 1.5 mm^2 per mouse was analysed with Zen2012 (Black Edition) software (Zeiss) to determine the percentage of BrdU-positive cells.

Trans-epithelial water loss measurement

TEWL was measured on back skin of isoflurane-sedated mice using a TEWA meter TM210 (Courage and Khazaka). Every measurement represents the average of 30 individual subsequently recorded measurements at the probe head.

Transmission electron microscopy

The skin was cut into pieces of approximately 1 cm^2 and pre-fixed 2 h at room temperature in the fixative solution composed of 4% paraformaldehyde (Sigma-Aldrich) and 2.5% of electron microscopy grade glutaraldehyde (Sigma-Aldrich) diluted in 0.1M cacodylate buffer pH 7.4 (Sigma). Subsequently the pieces were cut again to reach an approximate size of 1 mm^2 and immersed in the fixative solution at 4 °C overnight. After washing 6 times for 10 min in 0.1 M cacodylate buffer on ice under slow rotation, the samples were post-fixed for 2 h in 2% osmium tetroxide and again washed 6 times for 10 min in water. Samples were then stained with 0.5% uranyl acetate overnight at 4 °C in the dark. The following day the samples were washed 6 times for

10 min in water and incubated with lead aspartate (Walton's lead aspartate composed of 0.02 M lead nitrate in 0.03 M sodium aspartate pH 5.5) for 45 min at 60 °C in the dark. After the samples were washed in water (6 × 10 min) and dehydrated in a graded ethanol series of 50, 70 and 90% on ice (20 min steps) and 100% ethanol (3 × 20 min) before being placed in propylene oxide (2 × 20 min). The samples were infiltrated in a mixture of 2:1 propylene oxide/epoxy resin (Agar) for 1 h at room temperature and in a mixture of 1:1 propylene oxide/epoxy resin for 1 h at room temperature before being left overnight in 1:2 propylene oxide/epoxy resin mixture with open lid to allow evaporation of propylene oxide. The next morning, samples were placed in 100% epoxy resin that was changed every 2 h and embedded at the end of the day in 100% fresh resin. They were incubated overnight at 45 °C and at 60 °C for 2 days to allow polymerization. Samples were processed into 50–70 nm ultrathin sections using a Leica Ultracut UCT ultra-microtome. Micrographs were taken in a JEOL JEM1400 transmission electron microscope equipped with an Olympus Quemesa 11 Mp camera at 80 kV accelerating voltage.

Dissociation of epidermal cells, cell sorting and microarray analysis

The mice were shaved with an electric shaver, the back skin was dissected, and the fat and underlying subcutis were removed with a scalpel. The samples were placed in 0.25% Trypsin (Gibco, Thermo Fisher Scientific) in DMEM (Gibco, Thermo Fisher Scientific) and 2mM EDTA (Thermo Fisher Scientific) overnight at 4 °C. The epidermis was separated from the dermis and the trypsin was neutralized by adding DMEM medium supplemented with 2% Chelex Fetal Calf Serum (FCS). Samples were filtrated on 70 and 40 µm filters (Falcon). Single-cell suspensions were incubated in 2% FCS/PBS with primary antibodies for 30 min on ice, protected from the light, with shaking every 10 min. Primary antibodies were washed with 2% FCS/PBS and cells incubated for 30 min in APC-conjugated streptavidin (BD Biosciences), on ice, with shaking every 10 min. Living epidermal cells were gated by forward scatter, side scatter and negative staining for Hoechst dye. Basal IFE and infundibulum cells were stained using PE-conjugated anti-α6-integrin (clone GoH3, 1:200, ebioscience) or FITC- conjugated anti-α6-integrin (clone GoH3, 1:200, ebioscience) and bulge cells were stained with biotinylated CD34 (clone RAM34; 1:50, BD Biosciences). Basal cells from the IFE were targeted using CD34 negative and α6 integrin positive gating. The geometric mean fluorescence intensity of Itgβ1 (FITC-coniugated anti-β1-integrin, 1:100, BD Bioscience 555005) and Itga2 (PE-coniugated anti-α2-integrin, 1:100, BD Bioscience 553858) was measured on the α6-integrin^{high}CD34^{-} population.

Fluorescence-activated cell sorting analysis was performed using FACSAria I at high pressure (70 psi) and FACSDiva software (BD Biosciences). Sorted cells (300 cells per sample) were harvested directly in 45 µl of lysis buffer (20 mM DTT, 10 mM Tris.HCl ph 7.4, 0.5% SDS, 0.5 µg/µl proteinase K). Samples were then lysed at 65 °C for 15 min and frozen. RNA isolation, amplification and microarray were performed in the Functional Genomics Core, Barcelona. cDNA synthesis, library preparation and amplification were performed as described in[51]. Microarrays were then performed on Mouse Genome 430 p.m. strip Affymetrix array. The data were normalized using RMA algorithm. The entire procedure was repeated in three technical independent samples for the control and the EXP D4 condition and in two technical independent samples for the TPA treatment. Genetic signatures were obtained by considering genes presenting a fold change greater or smaller than 2 or −2, respectively in both biological replicates.

RNA extraction and quantitative PCR

Fresh-frozen pieces of mouse skin were reduced to powder with a mortar and RNA extraction was then carried out with the RNAeasy Microkit from Quiagen according to the manufacturer's protocol. Purified RNA was used to synthesize the first-strand complementary DNA using SuperScript II (Invitrogen) with random hexamers (Roche). Quantitative PCR analyses were carried out with Light Cycler 96 (Roche). Primers used: TNFα-5′: ACCACGCTCTTCTGTCTACT, TNFα-3′: AGGAGGTTGACTTTCTCCTG, IFNγ-5′: TCAAGTGGCATAGATGTGGAA, IFNγ-3′: CACTCGGATGAGCTCATTGA, CCL2-5′: CAGGTCCCTGTCATGCTTCT, CCL2-3′: GTCAGCACAGACCTCTCTCT, CCL5-5′: ACCATGAAGATCTCTGCAGC, CCL5-3′: TGAACCCACTTCTTCTCTGG. Normalizers: HPRT-5′: GCAGTACAGCCCCAAAATGG, HPRT-3′: TCCAACAAAGTCTGGCCTGT, Gapdh-5′: CGTGTTCCTACCCCCAATGT, Gapdh-3′: GTGTAGCCCAAGATGCCCTT.

ATAC sequencing

For ATAC-seq, 100000 sorted basal cells were collected in 1 ml PBS supplemented with 3% FBS at 4 °C. Cells were centrifuged and cell pellets were resuspended in 100 µl lysis buffer (TrisHCl 10 mM, NaCl 10 mM, MgCl2 3 mM, Igepal 0.1%) and centrifuged at 500*g* for 25 min at 4 °C. Supernatant was carefully discarded and nuclei were resuspended in 50 µl reaction buffer (Tn5 transposase 2.5 µl, TD buffer 22.5 µl, from Nextera DNA sample preparation kit, Illumina, and 25 µl $H_2$0). The reaction was performed at 37 °C for 30 min and was stopped by adding 5 µl clean up buffer (NaCl 900 mM, EDTA 300 mM). DNA was purified using the MiniElute purification kit (QIAGEN) following the manufacturer's protocol. DNA libraries were PCR amplified (Nextera DNA Sample Preparation Kit, Illumina), and size selected from 200 to 800 bp (BluePippin, Sage Sciences), following the manufacturer's recommendations.

ATAC-seq analysis

Adaptor sequences were removed with TrimmomaticPE using options 'HEADCROP:10 CROP:70 ILLUMINACLIP:adaptor.file:2:30:10 LEADING:3 TRAILING:3 SLIDINGWINDOW:4:15 MINLEN:60' . ATAC−seq paired-end reads were then aligned to mouse genome Grcm38 using Bowtie2 (v.2.2.6)[52] using options '-X 2000−fr−very-sensitive−no-discordant−no-unal−no-mixed −non-deterministic'. Mitochondrial reads, reads from unmapped or random counting and reads with a mapping quality <20 were removed using SAMtools[53]. Duplicate reads were removed by Picard tools (http://broadinstitute.github.io/picard/).

Peak calling was performed on each individual sample by MACS2 (v.2.1.0.20151222)[54] using options '-f BAMPE -g mm −nomodel−call-summits -B −SPMR', q-value 0.0001. Peaks from the different subpopulations were merged for downstream analysis.

Reads counts of each merged peak for each individual sample were calculated by HTSeq-count[55] using options '-f bam -r pos -m intersection-nonempty'. These counts were normalized for one million mapped reads in merged peaks and fold-change was calculated compared to control. Peaks were associated to genes with GREAT software[56] with the following parameters: 5.0 kb in proximal upstream, 1.0 kb in proximal downstream and 100.0 kb in distal. For most of the analysis, only peaks annotated to at least one gene were kept.

Differential peaks are defined as peaks having at least a twofold change compared to control and being called peak in the expanded condition and contain at least 3 reads per million.

De novo motif search was performed using findMotifsGenome.pl program in HOMER software[57] searching for motifs of 6 to 12 bp in a region of 500 bp around the peak centre.

Single-cell RNA sequencing

Single basal cells from the back skin were FACS sorted (Integrin alpha 6 high, Cd34 negative) after dissociation. 6000 cells were loaded onto each channel of the Chromium Single Cell 3′ microfluidic chips (V2-chemistry, PN-120232, 10X Genomics) and barcoded with a 10X Chromium controller according to the manufacturer's recommendations (10X Genomics). RNA from the barcoded cells was subsequently reverse transcribed, followed by amplification, shearing 5′ adaptor and sample index attachment. The Libraries were prepared using the Chromium Single Cell 3′ Library Kit (V2-chemistry, PN-120233, 10X

Genomics) and sequenced on an Illumina HiSeq 4000 (paired-end 100bp reads).

Single-cell transcriptomic data analysis

Sequencing reads were aligned and annotated with the mm10-1.2.0 reference dataset as provided by 10X Genomics and demultiplexed using CellRanger (v.2.1.1) with default parameters. Further downstream analyses were carried out individually for each of the four samples (*CTRL, EXP. D1, EXP.D4* and *TPA*). Quality control was performed using the *scater* R package (v.1.10.0)[58]. For each sample, all of the cells passed the following criteria: had more than 4,000 UMI counts, showed expression of more than 1,500 unique genes and had less than 10% UMI counts belonging to mitochondrial sequences. Read counts were normalized using deconvoluted cell-specific size factors with the *scran* R package (v.1.10.2)[59]. Cell-cycle phases were assigned using the *cyclone* function from *scran*[60]. Dimensional reduction and clustering were performed using the *Seurat* R package (v.3.1.1). A PCA for each sample was calculated using the scaled expression data of the most variable genes (identified as outliers on a mean/variability plot, implemented in the *FindVariableGenes* function from *Seurat*). To remove unwanted sources of variability caused by differences in cycling stages but retaining the distinction between cycling and non-cycling cells, the differences between S-phase and GS/M-phase scores (determined by *cyclone*) were regressed out during scaling (by setting the *vars.to.regress* parameter of the *ScaleData* function in *Seurat*). UMAP[61] calculation and graph-based clustering were done for each sample using the appropriate functions from *Seurat* (default parameters) with the respective PCA results as input. Different values of the *resolution* parameter were tested for the clustering. We set the final resolution to 0.6 (after testing a range from 0.3–1.2) first in the control sample, and then applied the same parameters to the other samples. Given that the obtained clustering sensitivity for a given resolution is dependent on the number of cells of that subpopulation in each respective sample, we swept over the same range of resolutions for the other samples, to assure the presence/absence of described clusters in all samples. This resolution best reflected the biological heterogeneity that emerged from the lineage tracing and the analysis of the clonal data, identifying a progenitor population (characterized by intermediate levels of *Krt5*, *Krt14*, *Krt1* and *Krt10*) that emerged as an intermediate cluster between the stem cells (that expressed high levels of *Krt14*, *Krt15* and integrins) and the differentiated population (highly enriched in *Krt1* and *Krt10*). A Wilcoxon rank-sum test was used to define marker genes for each cluster. Benjamini–Hochberg FDR correction for potential cluster marker genes across all samples ($n = 10{,}651$) using the p.adjust method in R and only markers expressed in at least 25% of cells of the cluster, having an average log-fold change of at least 0.25 were reported. Differentially expressed genes and regulons between the CTRL SCs and EXP D1 STRETCH SCs and SCs clusters were computed as two-sided Wilcoxon ranked sum tests using the *FindMarkers* function in *Seurat* and p-values were FDR adjusted for the total number of comparisons ($n = 542$ and $n = 571$ respectively). Pseudotime ordering of cells was calculated using *slingshot* (v.1.1.0)[27]. We checked the robustness of the resulting trajectories by performing the analysis on PCA and UMAP reductions and also on downsampled subsets of the data to half the dataset size, these different reductions and permutations did not affect the described trajectories. Gene regulatory network analysis was performed using SCENIC[26] with default parameters. Differentially activated regulons for each cluster were determined by performing a Wilcoxon rank-sum test on the normalized regulon AUC values of cells in the various clusters, p-values were FDR-adjusted using the Benjamini–Hochberg method and regulons with an adjusted p-value less than 0.05 were considered differentially activated. For visualization purposes we integrated the CTRL, EXP D1, EXP D2 and TPA samples using the *Seurat* package's standard CCA-MNN based data integration workflow. Feature selection was performed using the *FindVariableFeatures* function fom *Seurat* with default parameters, selecting the 2,000 most variable genes. Canonical correlation analysis (CCA) followed by integration anchors selection was then performed on the selected features using the *FindIntegrationAnchors* function from *Seurat*, taking the first 20 dimensions from the CCA into account, as described by the *Seurat* authors[62]. These anchors were then used to integrate the data with the *IntegrateData* function.

To compare the single-cell RNA-seq data from the treated EXP D2 samples (*EXP D2-Trametinib* and *EXP D2-MAL inhibitor*), data integration was performed with the *EXP D1* sample following the approach implemented in *Seurat*[62]. The samples with the treatments were sequenced at a different time point than the *EXP D1* sample and had in general lower UMI count distributions. Therefore, the UMI counts matrix of the *EXP D1* sample was first downsampled, using the *downsampleMatrix* function from the *DropletUtils* package (https://bioconductor.org/packages/release/bioc/html/DropletUtils.html), such that its total number of counts was the same as the average of the total number of counts of the treatment samples. QC filtering and pre-processing was then performed as described before for each individual sample before integration. Further downstream analyses such as dimensionality reduction and clustering were all performed as described before using the integrated data. Cell-cycle phase prediction and differential expression analysis were performed on the uncorrected data to avoid interfering with the underlying distribution assumptions of these statistical methods. Cluster annotation was mainly performed by comparing the overlap of the new clusters of the integrated data with the original cell type annotations of the *EXP D1* sample and by studying the expression of known marker genes. Differentially expressed genes and regulons between the EXP D1 SCs and the EXP D2 SC clusters were computed as two-sided Wilcoxon ranked sum tests using the *FindMarkers* function in *Seurat* and p-values were FDR adjusted for the total number of comparisons ($n = 13{,}786$ and $n = 758$ respectively). Subpopulations that are not associated with the IFE (infundibulum and sebaceous gland) were removed for the final analysis.

Statistical analysis

Two-tailed Student's t-test, two-tailed Mann–Whitney U-test and Wilcoxon signed-rank test were performed using GraphPad Prism v.7.00 for Mac (GraphPad Software). Bar graphs and dot plots were generated by GraphPad Prism and show mean ± s.e.m. unless otherwise indicated.

Reporting summary

Further information on research design is available in the Nature Research Reporting Summary linked to this paper.

Data availability

Data associated with this study have been deposited in the NCBI Gene Expression Omnibus under accession numbers GSE126231, GSE126734 and GSE146637, respectively, for the microarray, ATAC-seq and scRNA-seq. Data supporting the findings of this study are available within the Article (and its Supplementary Information files). Source data are provided with this paper.

Code availability

Custom computer code and algorithms used to generate results that are reported in the paper are available within the article (and its Supplementary Information files) and from the corresponding authors on reasonable request. The code used for the modelling of the clonal data has been deposited in GitHub (available at https://github.com/BenSimonsLab/Aragona_Nature_2020).

42. Vasioukhin, V., Degenstein, L., Wise, B. & Fuchs, E. The magical touch: genome targeting in epidermal stem cells induced by tamoxifen application to mouse skin. *Proc. Natl Acad. Sci. USA* **96**, 8551–8556 (1999).

43. Vasioukhin, V., Bauer, C., Degenstein, L., Wise, B. & Fuchs, E. Hyperproliferation and defects in epithelial polarity upon conditional ablation of alpha-catenin in skin. *Cell* **104**, 605–617 (2001).
44. Snippert, H. J. et al. Intestinal crypt homeostasis results from neutral competition between symmetrically dividing Lgr5 stem cells. *Cell* **143**, 134–144 (2010).
45. Xin, M. et al. Hippo pathway effector Yap promotes cardiac regeneration. *Proc. Natl Acad. Sci. USA* **110**, 13839–13844 (2013).
46. Damiani, D., Goffinet, A. M., Alberts, A. & Tissir, F. Lack of Diaph3 relaxes the spindle checkpoint causing the loss of neural progenitors. *Nat. Commun*. **7**, 13509 (2016).
47. Muzumdar, M. D., Tasic, B., Miyamichi, K., Li, L. & Luo, L. A global double-fluorescent Cre reporter mouse. *Genesis* **45**, 593–605 (2007).
48. Tepole, A. B., Gart, M., Purnell, C. A., Gosain, A. K. & Kuhl, E. The incompatibility of living systems: characterizing growth-induced incompatibilities in expanded skin. *Ann. Biomed. Eng*. **44**, 1734–1752 (2016).
49. Susaki, E. A. et al. Whole-brain imaging with single-cell resolution using chemical cocktails and computational analysis. *Cell* **157**, 726–739 (2014).
50. Ellis, S. J. et al. Distinct modes of cell competition shape mammalian tissue morphogenesis. *Nature* **569**, 497–502 (2019).
51. Gonzalez-Roca, E. et al. Accurate expression profiling of very small cell populations. *PLoS ONE* **5**, e14418 (2010).
52. Langmead, B. & Salzberg, S. L. Fast gapped-read alignment with Bowtie 2. *Nat. Methods* **9**, 357–359 (2012).
53. Li, H. et al. The Sequence Alignment/Map format and SAMtools. *Bioinformatics* **25**, 2078–2079 (2009).
54. Zhang, Y. et al. Model-based analysis of ChIP-Seq (MACS). *Genome Biol*. **9**, R137 (2008).
55. Anders, S., Pyl, P. T. & Huber, W. HTSeq—a Python framework to work with high-throughput sequencing data. *Bioinformatics* **31**, 166–169 (2015).
56. McLean, C. Y. et al. GREAT improves functional interpretation of cis-regulatory regions. *Nat. Biotechnol*. **28**, 495–501 (2010).
57. Heinz, S. et al. Simple combinations of lineage-determining transcription factors prime cis-regulatory elements required for macrophage and B cell identities. *Mol. Cell* **38**, 576–589 (2010).
58. McCarthy, D. J., Campbell, K. R., Lun, A. T. & Wills, Q. F. Scater: pre-processing, quality control, normalization and visualization of single-cell RNA-seq data in R. *Bioinformatics* **33**, 1179–1186 (2017).
59. Lun, A. T., Bach, K. & Marioni, J. C. Pooling across cells to normalize single-cell RNA sequencing data with many zero counts. *Genome Biol*. **17**, 75 (2016).
60. Scialdone, A. et al. Computational assignment of cell-cycle stage from single-cell transcriptome data. *Methods* **85**, 54–61 (2015).
61. Becht, E. et al. Dimensionality reduction for visualizing single-cell data using UMAP. *Nat. Biotechnol*. **37**, 38–44 (2019).
62. Stuart, T. et al. Comprehensive integration of single-cell data. *Cell* **177**, 1888–1902 (2019).

Acknowledgements We acknowledge the animal facility at ULB (Erasme campus), the ULB genomic core facility (F. Libert and A. Lefort), J.-M. Vanderwinden and LiMiF for the help with confocal microscopy, T. Van Brussel for help with 10X genomics, B. Gilbert, W. Declercq and P. Vieugue for helping with the TEWL assay, A. De Groote for performing mice perfusion, and colleagues who provided reagents mentioned in the text. scRNA-seq was performed at the Brussels Interuniversity Genomics High Throughput core and the Genomics Core Leuven. C.B. is an investigator of WELBIO. M.A. is supported by a long-term postdoctoral fellowship of the HFSPO (LT000380/2015-L) and an FNRS fellowship. B.D.S. is supported by a Royal Society EP Abraham Research Professorship and a Wellcome Trust Senior Investigator Award (098357/Z/12/Z). S.H. is supported by a long-term fellowship of the HFSPO (LT000092/2016-L). B.D.S and S.H. acknowledge core funding to the Gurdon Institute from the Wellcome Trust (092096) and CRUK (C6946/A14492). A.S., J.V.H. and T.V. are supported by KU Leuven SymBioSys, Stiching Tegen Kanker, FWO postdoctoral fellowship number 12W7318N and Marie Skłodowska-Curie fellowship number 12O5617N. F.T. is a research director at the FNRS. This work was supported by the FNRS, TELEVIE, the PAI programme, a research grant from the Fondation Contre le Cancer, the ULB foundation, the foundation Bettencourt Schueller, the foundation Baillet Latour and a consolidator grant of the European Research Council (ERC-EXPAND, 616333).

Author contributions M.A. and C.B. designed the experiments. M.A., B.D.S. and C.B. performed data analysis. M.M., A.S., J.V.H. and T.V. performed scRNA-seq and analysis. S.H. helped with data analysis. S.D., S.G. and G.L. helped with experiments and animal follow-up. Y.S. and B.S. performed ATAC-seq analysis. C.D. helped with FACS. P.B. and K.V. performed TEM. F.T. contributed with genetic tools. M.A., B.D.S. and C.B. wrote the manuscript. All authors read and approved the final manuscript.

Competing interests The authors declare no competing interests.

Additional information

Supplementary information is available for this paper at https://doi.org/10.1038/s41586-020-2555-7.

Correspondence and requests for materials should be addressed to B.D.S. or C.B.

Peer review information *Nature* thanks Carien Niessen, Nathan Salomonis and the other, anonymous, reviewer(s) for their contribution to the peer review of this work.

Reprints and permissions information is available at http://www.nature.com/reprints.

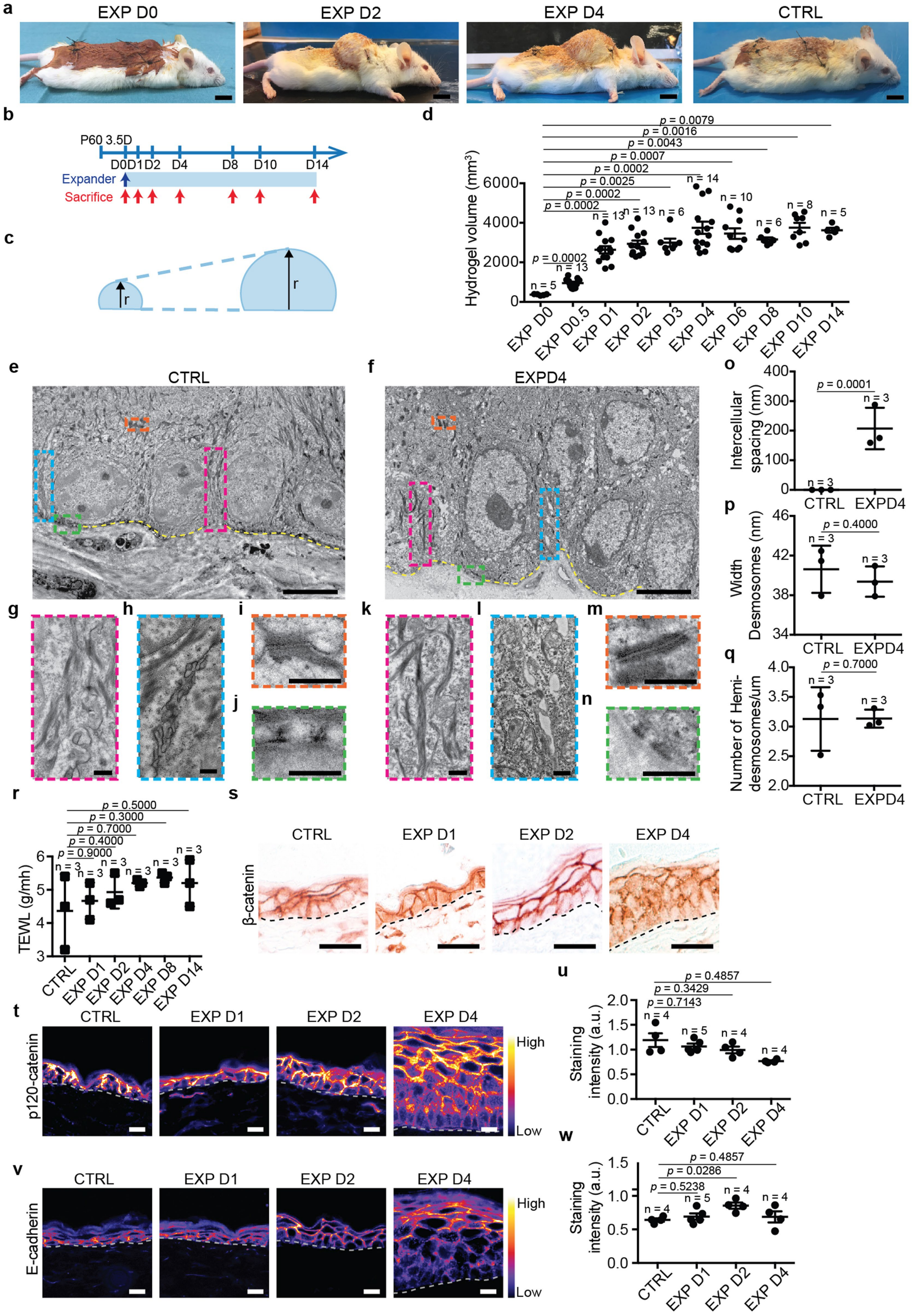

Extended Data Fig. 1 | See next page for caption.

Extended Data Fig. 1 | A mouse model of mechanical stretch-mediated skin expansion. a, Representative photographs of mice with the skin expander immediately after surgery at day (D) D0, D2, D4 and in control (CTRL) condition. Scale bars, 10 mm. The device was implanted on the back skin of the animals, close to the neck where the rigidity of the proximate cervical spines allows the hydrogel to stretch the skin during the inflation of the expander. Control mice were operated upon similarly but without introducing the hydrogel. **b**, Timeline of the experiment. CD1 mice were operated to place the expander and followed over time. **c**, Scheme showing the growth of the hydrogel. The arrows indicate the radius of the hemisphere. **d**, Hydrogel volume (measured by the height of the hydrogel and calculated as the volume of a hemisphere, see Methods, $n = 5$ D0, $n = 13$ D0.5, $n = 13$ D1, $n = 13$ D2, $n = 7$ D3, $n = 13$ D4, $n = 10$ D6, $n = 6$ D8, $n = 8$ D10, $n = 5$ D14 mice). **e**–**n**, TEM of ultrathin sections of control (**e**, **g**–**j**) and expanded (**f**, **k**–**n**) epidermis. In **e** and **f**, dashed yellow lines denote dermal-epidermal boundary and boxed area in pink, cerulean, orange and green are shown at higher magnification, respectively, in **g** and **k**, **h** and **l**, **i** and **m**, **j** and **n**. Scale bars, 5 µm. **g**, **k**, Keratin bundles. **h**, **l**, Ultrastructural analysis of cell–cell adhesion. **i**, **m**, Desmosomes. **j**, **n**, Hemidesmodomes. **o**, Quantification of the intercellular spacing on images as in **h** and **l**. Wilcoxon signed-rank test, two-sided. **p**, Quantification of the width of the desmosomes as in **i** and **m**. **q**, Quantification of the width of the number of hemidesmosomes per µm in **j** and **n**. **r**, TEWL measurements from $n = 3$ CD1 mice in CTRL and at different time point during expansion. **s**, Immunohistochemistry for the adherens junctions (AJ) component β-catenin, $n = 3$ independent experiments. **t**, **v**, Representative images of AJ component p120-catenin (**t**) and E-cadherin (**v**) colour-coded for the signal intensity with ImageJ. Protein expression is visualized as a colour gradient going from black to yellow, with black as indicator of no expression and yellow as indicator of maximal expression. Scale bars, 10 µm. **u**, **w**, Quantification of the average integrated density signal for p120-catenin (**u**) and E-cadherin (**w**). Each data point is the average of 3 sections per mouse ($n = 3$ mice per condition). **o**–**q**, The quantifications are made on $n = 3$ different animals per condition on 10 different samples per mouse and represented as mean + s.e.m. **g**–**n**, Scale bars, 500 nm. **d**, **p**–**r**, **u**, **w**, Two-tailed Mann–Whitney test, mean + s.e.m.

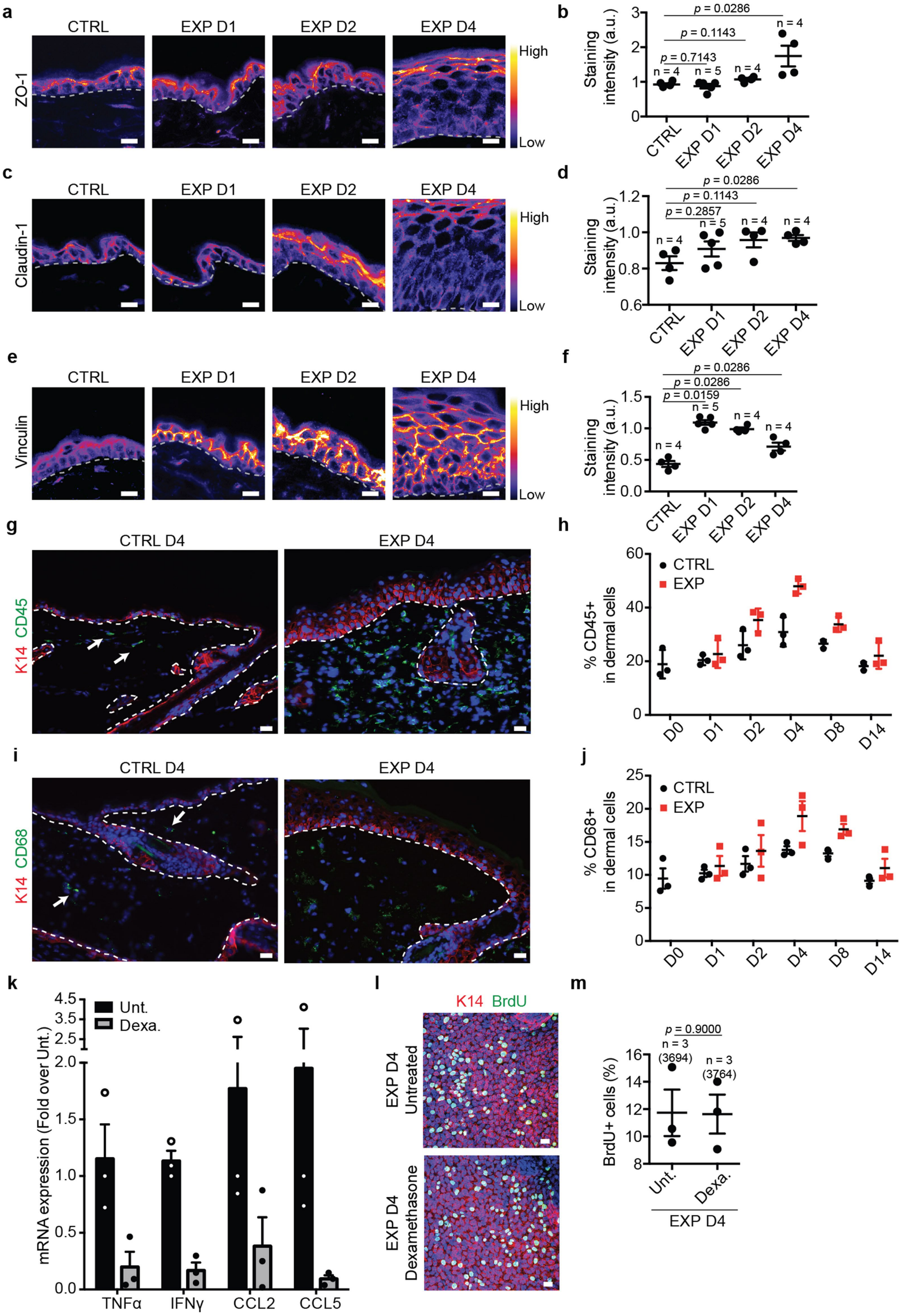

Extended Data Fig. 2 | Adhesion remodelling and inflammatory response during stretch-mediated skin expansion. **a**, **c**, **e**, Representative images of the tight junction (TJ) components ZO-1 (**a**) and Claudin-1 (**c**) and of Vinculin (**e**) colour-coded for the signal intensity with ImageJ. Protein expression is visualized as a colour gradient going from black to yellow, with black as indicator of no expression and yellow as indicator of maximal expression. Scale bars, 10 µm. **b**, **d**, **f**, Quantification of the average integrated density signal for ZO-1 (**b**), Claudin-1 (**d**) and Vinculin (**f**). The number of mice per condition is indicated. **g**, **i**, Immunostaining for K14 (red), inflammatory cells stained with CD45 (**g**) and macrophages stained with CD68 (**i**) (green) and Hoechst for nuclei (blue) on tissue sections. Scale bars, 10 µm. White arrows indicate positive cells, *n* = 3 independent experiments. **h**, **j**, Percentage of CD45 (**h**) and CD68 (**j**) positive cells on the total dermal cells quantified based on the nuclear staining, *n* = 3 mice per condition, mean per mouse + s.e.m. **k**, mRNA expression analysis for the indicated gene in Untreated (Unt., black) skin and skin treated with Dexamethasone (Dexa., grey). Fold change is expressed compared to one Unt. sample, *n* = 3 mice per condition, mean per mouse + s.e.m. **l**, Maximum intensity projection of confocal pictures showing immunostaining for K14 (red), BrdU (green) and Hoechst for nuclei (blue) 4 h following BrdU administration on whole mount epidermis. Scale bars, 10 µm. **m**, Proportion of basal cells that are BrdU positive (*n* = 3,694 cells counted from 3 mice for Untreated and *n* = 3,764 cells from 3 mice for the Dexamethasone treatment). **a**, **c**, **e**, **g**, **i**, Dashed lines indicate the basal lamina. **b**, **d**, **f**, **m**, Two-tailed Mann–Whitney test, mean per mouse + s.e.m.

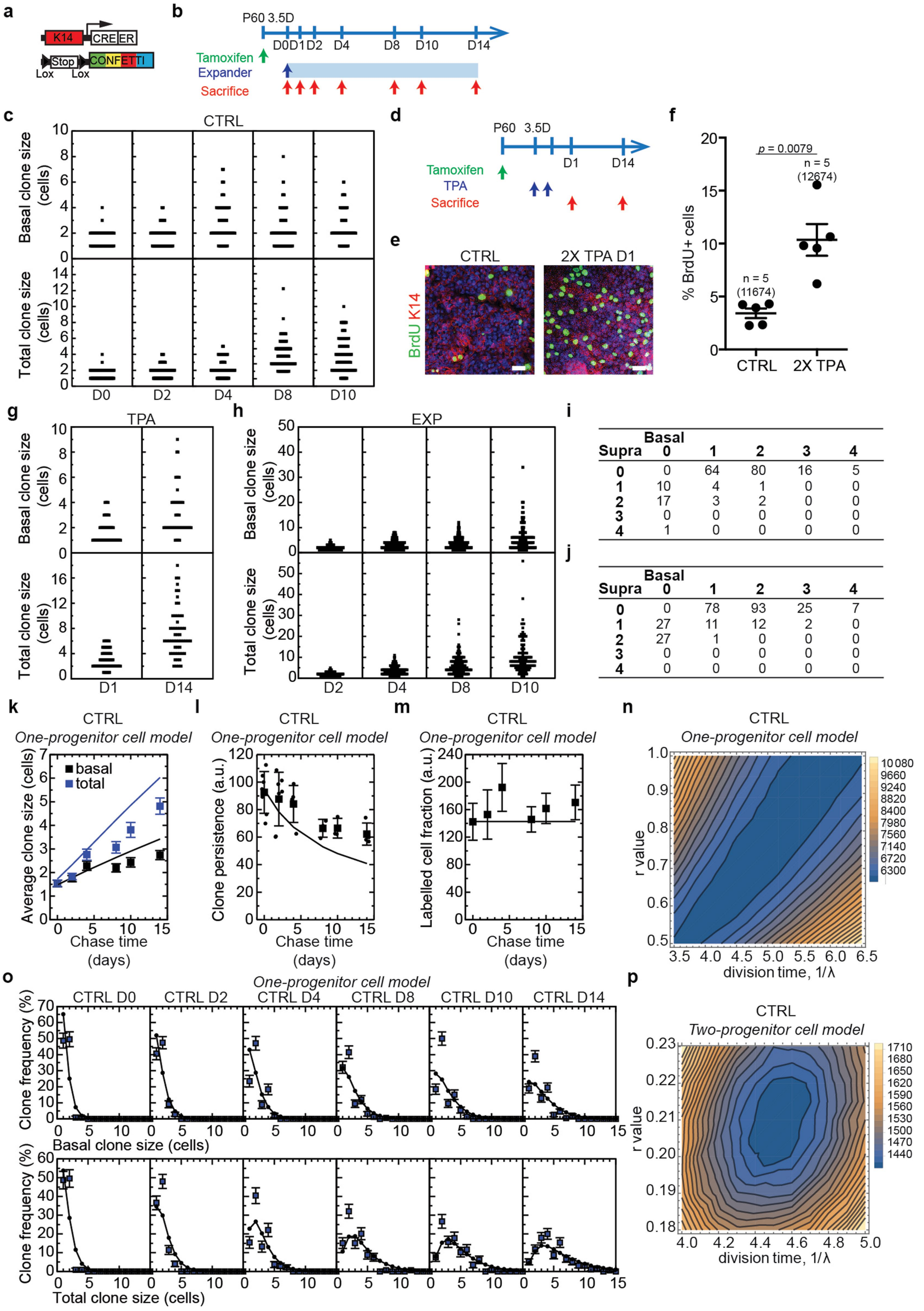

i

Supra	Basal 0	1	2	3	4
0	0	64	80	16	5
1	10	4	1	0	0
2	17	3	2	0	0
3	0	0	0	0	0
4	1	0	0	0	0

j

Supra	Basal 0	1	2	3	4
0	0	78	93	25	7
1	27	11	12	2	0
2	27	1	0	0	0
3	0	0	0	0	0
4	0	0	0	0	0

Extended Data Fig. 3 | See next page for caption.

Extended Data Fig. 3 | Clonal analysis of epidermal stem cells during homeostasis, TPA treatment and stretch-mediated skin expansion. **a**, Genetic labelling strategy used to trace K14 IFE SC in the back skin during homeostasis and stretch-mediated tissue expansion. **b**, Timeline of the experiment. *Krt14-creER-Rosa*^{Confetti} mice were induced with Tamoxifen at 2 months of age and operated upon 3.5 days after to place the expander. The samples were collected 0, 1, 2, 4, 8, 10 and 14 days after surgery. **c**, Raw distribution of clone size taken from mouse back skin under normal homeostatic conditions (CTRL) at different time points based on basal (top) and total (bottom) cell number. Note that times are calibrated so that the "day 0" time-point is acquired 3.5 days after Tamoxifen injection, requiring effective chase times to be calibrated accordingly, see **b**. D0: 115 clones from $n = 7$ mice; D2: 175 clones from $n = 7$ mice; D4: 136 clones from $n = 5$ mice; D8: 159 clones from $n = 3$ mice; D10: 146 clones from $n = 3$ mice. **d**, Time line of the experiment to perform clonal tracing upon TPA treatment. *Krt14-creER-Rosa*^{Confetti} mice were induced with Tamoxifen at 2 months of age and after 3.5 days topically treated with 12-*O*-Tetradecanoylphorbol-13-acetate (TPA) for 2 consecutive days. The samples were collected 1 and 14 days after treatment. **e**, Maximum intensity projection of representative confocal pictures showing immunostaining for K14 (red) and BrdU (green) following BrdU administration on whole mount epidermis form mice treated with TPA or with vehicle (CTRL). Hoechst nuclear staining in blue. Scale bars, 20 µm. **f**, Percentage of BrdU positive cells in control and mice treated with TPA at D1 ($n = 5$). Two-tailed Mann–Whitney test, mean + s.e.m. **g**, Raw distribution of clone size taken from mouse back skin during TPA treatment (TPA) based on basal (top) and total (bottom) cell number. D1: 85 clones from $n = 4$ mice; D14: 54 clones from $n = 5$ mice. **h**, Raw distribution of clone size taken from mouse back skin under stretch-mediated tissue expansion (EXP) at different time points based on basal (top) and total (bottom) cell number. As with control, note that times are calibrated so that the "day 0" time-point is acquired 3.5 days after Tamoxifen injection, requiring effective chase times to be calibrated accordingly. D2: 231 clones from $n = 4$ mice; D4: 197 clones from $n = 4$ mice; D8: 199 clones from $n = 4$ mice; D10: 157 clones from $n = 4$ mice. **i**, Table showing the abundance (raw counts) of clones by their basal and suprabasal cell composition from the CTRL D2 condition (that is, 5 days post-induction), $n = 203$ clones from 7 mice. **j**, Table showing the abundance (raw counts) of clones by their basal and suprabasal cell composition from the EXPD2 condition, $n = 283$ clones from 4 mice. **k**, Fit of the one-progenitor model to the average size of persisting clones in control conditions based on the basal (black) and total (blue) cell content. Points show data and lines are the results of the fit to a one-compartment model (see Methods). **l**, **m**, **o**, Fit to the one-progenitor cell model. Clone persistence (**l**), labelled cell fraction (**m**), and the distribution of basal (upper) and total (lower) clone size (**o**). Points show data and lines are the results of the fit to a one-progenitor model. **k**–**m**, **o**, D0: 115 clones from $n = 7$ mice; D2: 175 clones from $n = 7$ mice; D4: 136 clones from $n = 5$ mice; D8: 159 clones from $n = 3$ mice; D10: 146 clones from $n = 3$ mice; D14: 195 clones from $n = 4$ mice. **n**, **p**, Sensitivity analysis of the model fits depicted as a map of the total square-differences of the experimental basal/total clone size data and the respective model predictions as a function of the average division time, $1/\lambda$, and the degree of imbalance towards stem cell loss/replacement, r, (see Methods). Panel **n** shows the results of one-progenitor model and the CTRL data, **p** shows the results of two-progenitor model and the CTRL data. These results show both the enhanced accuracy of the two-progenitor model over the one-progenitor model, despite involving the same number of fit parameters. **k**–**m**, Mean + s.d. **o**, Mean + s.e.m.

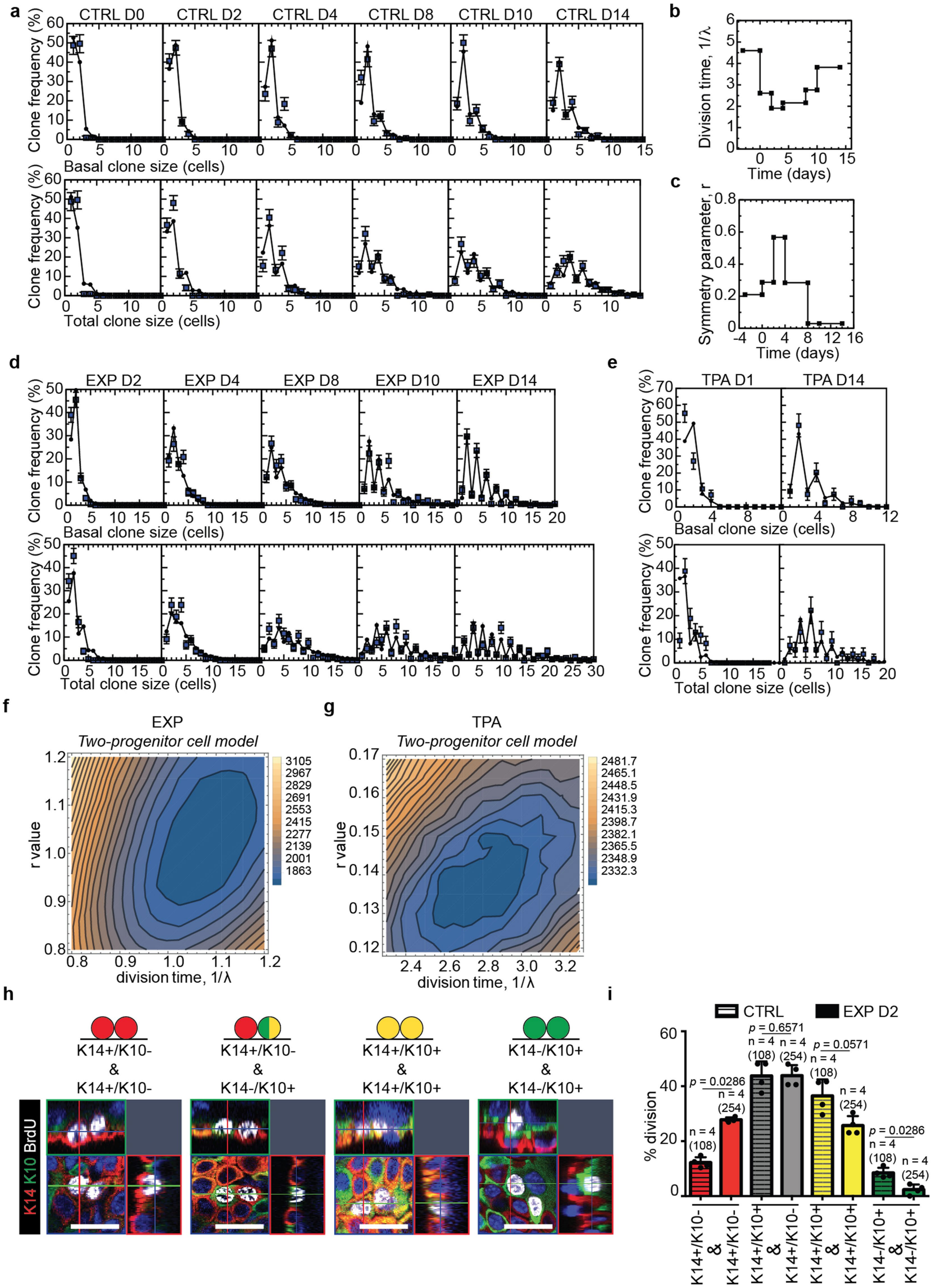

Extended Data Fig. 4 | See next page for caption.

Extended Data Fig. 4 | Fit of the data to the two-progenitor model. a, Fit of the model to the clone size distribution under homeostatic control conditions. Note that, with $1/\lambda = 4.6$ days and $r = 0.21$, the model faithfully reproduces both the exponential-like clone size distribution and the predominance of clones bearing an even number of basal and total cell numbers. Mean + s.e.m. D0: $n = 115$ clones from 7 mice; D2: $n = 175$ clones from 7 mice; D4: $n = 136$ clones from 5 mice; D8: $n = 159$ clones from 3 mice; D10: $n = 146$ clones from 3 mice; D14: $n = 195$ clones from 4 mice. **b**, Change of division time ($1/\lambda$) during stretch-mediated expansion as parameterised from the measured rate of BrdU incorporation, Fig. 1e. **c**, Change in the probability of symmetric division (parameter, r) during stretch-mediated skin expansion obtained from a fit of the two-compartment model to the clone size data (for details, see Supplementary Note). **d**, Corresponding fit of the two-compartment model to the clone size distribution during stretch-mediated expansion. The model accurately reproduces both the exponential-like clone size distribution and the predominance of clones bearing an even number of basal and total cell numbers. Notably, the sharp increase in even-sized clones at long times can only be recovered by limiting the frequency of renewing divisions well below that of the control value. Mean + s.e.m. D2: $n = 231$ clones from 4 mice; D4: $n = 197$ clones from 4 mice; D8: $n = 199$ clones from 4 mice; D10: $n = 157$ clones from 4 mice. **e**, Fit of the model to the clone size distribution at D14 under TPA treatment. Note that with $1/\lambda = 2.3$ days and $r = 0.15$, the model faithfully reproduces both the exponential-like clone size distribution and the predominance of clones bearing an even number of basal and total cell numbers. Mean + s.e.m. D1: $n = 85$ clones from 4 mice; D14: $n = 54$ clones from 5 mice. **f**, **g**, Sensitivity analysis of the model fits depicted as a map of the total square-differences of the experimental basal/total clone size data and the respective model predictions as a function of the average division time, $1/\lambda$, and the degree of imbalance towards stem cell loss/replacement, r, (see Methods). Panels (**f**) shows the results of the results of two-progenitor model and the EXP data, and (**g**) shows the results of two-progenitor model and the TPA data. For the EXP data (**f**), we have imposed the measured relative variation of the proliferation rate (as inferred from BrdU incorporation) (Fig. 1e and panel (**b**)) and an inferred relative variation of the r parameter as obtained from a model fit (**c**), while the two parameters in panel (**f**) represent variation in the net rates. **h**, Representative orthogonal confocal sections immunostained for Krt14 (red), Krt10 (green) following short-term BrdU (white) incorporation identifying cells biased for renewal (Krt14^{+}Krt10^{-}), cells primed for differentiation (Krt14^{+}Krt10^{+}) and differentiated cells (Krt14^{-}Krt10^{+}). **i**, Percentage of the type of divisions in CTRL (108 divisions from $n = 4$ mice) and EXP D2 (254 divisions from $n = 4$ mice) based on short-term BrdU tracing and staining as in **h**. Two-tailed Mann–Whitney test, mean + s.e.m.

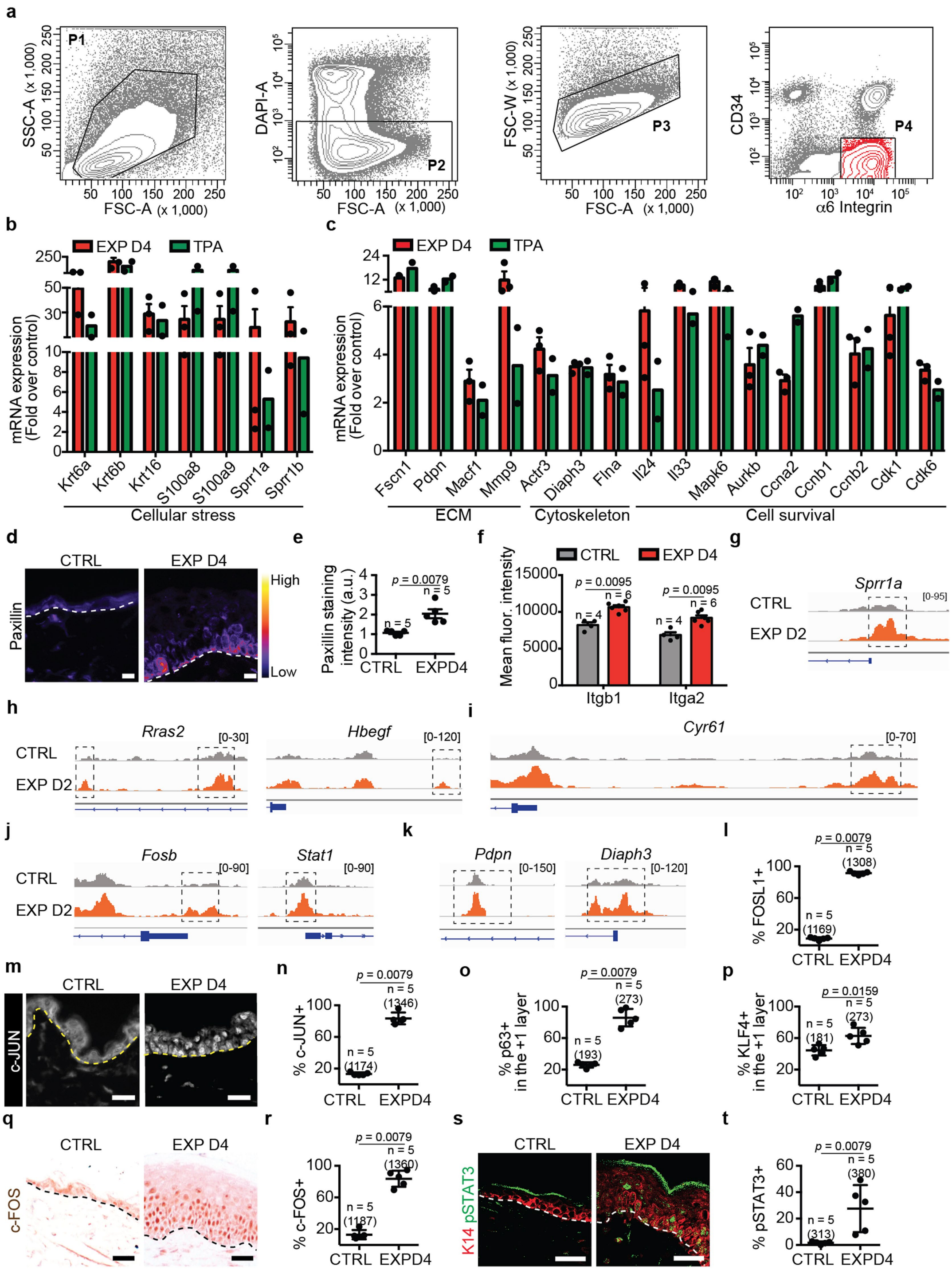

Extended Data Fig. 5 | See next page for caption.

Extended Data Fig. 5 | Genetic signature of TPA-treated and expanded epidermis. **a**, Representative FACS plots showing the strategy used to isolate basal cells. Single living cells were gated by debris exclusion (P1), DAPI exclusion (P2), doublet elimination (P3) and basal IFE Integrin-α6^{high} CD34^{neg} cell were sorted (P4). *n* = 10 independent experiments. **b**, **c**, mRNA expression of genes that were upregulated in basal cells at EXP D4 (*n* = 3) and in cells treated with TPA (*n* = 2). These genes are related to a generic stress signature (**b**), regulating ECM remodelling and cytoskeleton, important for cell survival and cell cycle (**c**). Bars are mean with s.e.m. **d**, Representative images of Paxillin immunostaining colour-coded for the signal intensity with ImageJ. Protein expression is visualized as a colour gradient going from black to yellow with black as indicator of no expression and yellow as indicator of maximal expression. Scale bars, 10 μm **e**, Quantification of the average integrated density signal for Paxillin as in **d**. Each data point is the average of 3 sections per mouse (*n* = 3 mice per condition). **f**, Geometric mean fluorescence intensity for the indicated integrin in CTRL (grey, *n* = 4 mice) and EXP D4 (red, *n* = 6 mice) from FACS analysis of basal IFE Integrin-α6^{high} CD34^{neg} cells. **g**–**k**, ATAC-seq profiles showing increasing accessibility of chromatin regions that are specifically remodelled during mechanical expansion (CTRL in grey and EXP D2 in orange). **l**, Quantification of the number of cells FOSL1+ in the basal layer related to Fig. 3d. **m**, Immunostaining on skin sections for JUN (white) in control and EXP D4. **n**, Quantification of the number of cells JUN+ in the basal layer related to **m**. **o**, Quantification of the number of cells p63+ in the +1 layer related to Fig. 3e. **p**, Quantification of the number of cells KLF4+ in the +1 layer related to Fig. 3f. **q**, Immunohistochemistry on paraffin sections for c-FOS in control and EXPD4. Scale bars, 20 μm. **r**, Quantification of the number of cells c-FOSL+ in the basal layer related to **q**. **s**, Immunofluorescence on tissue sections for pSTAT3 in green and K14 (red) to identified the epidermis. Scale bars, 20 μm. **t**, Quantification of the number of cells positive for pSTAT3 in the basal layer related to **s**. **l**, **n**, **o**, **p**, **r**, **t**, 3 sections quantified per *n* = number of mice and total number of cells indicated in parentheses **d**, **m**, **q**, **s**, Dashed lines delineate the basal lamina. **e**, **f**, **l**, **n**–**p**, **r**, **t**, Two-tailed Mann–Whitney test, Mean + s.e.m.

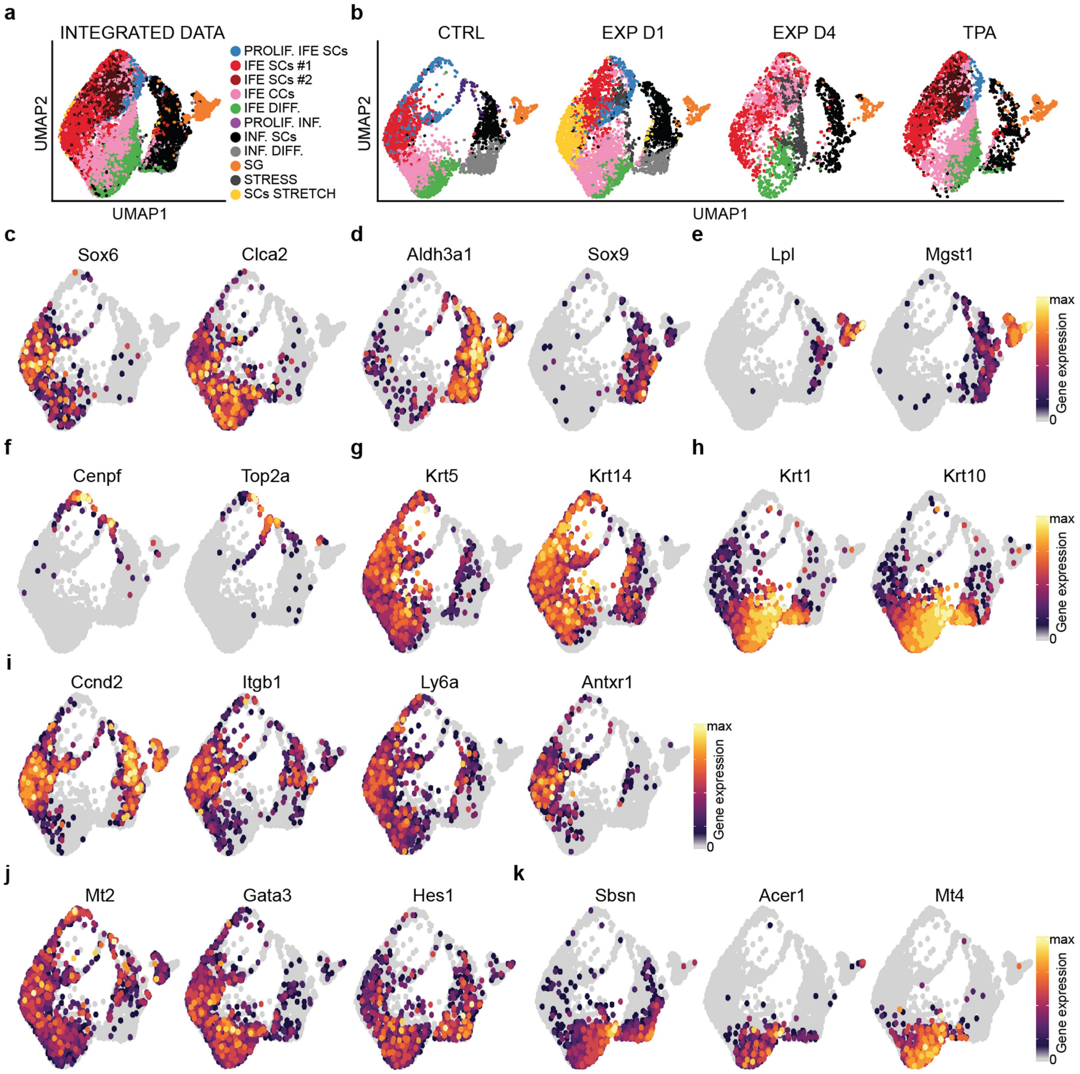

CLUSTER	CLUSTER SPECIFIC GENES
IFE SCs	Krt5^{high}, Krt14^{high}, Krt15^{high}, Itga6, Itgb1, Itgb4, Ccnd2, Ly6a, Sparc, Smoc2, Postn, Antrx1, Fth1, Dst
IFE CCs	Krt5^{mid}, Krt14^{mid},Krt1^{mid}, Krt10^{mid},Mt2, Gata3, Hes1, Ly6d
IFE DIFF.	Krt1^{high}, Krt10^{high}, Sbsn, Acer1, Cdnk1a, Irf6, Mt4, Ly6g6c
INF. SCs	Krt5^{mid}, Krt14^{mid}, Ccnd2, Lrig1, Sox9, Plet1, Foxc1, Sostdc1, Fam132a, Aldh3a1, Fst1, ApoE
INF. DIFF	Krt5^{low}, Krt14^{low}, Krt17, Krt79, Defb6, Gata6, Ppr1a, Ly6g6c
SG	Scd1, Lnc2, Lpl, Mgst1, Ldhb, Nrp2
SCs STRETCH	Krt15^{high}, Ccnd2, Sparc, Smoc2, Lamb3, Fth1, Fos, Fosb, Jun, Junb, Cyr61
STRESS	Krt6b, Krt16, Sprr1a, Sprr1b, Sprr2d, Klk10, S100a8, S100a9, Fosl1
PROLIF.	Cenpf, Top2a, Mki67, Cdc20, Stmn1, Tubb5, Hmgb2, Birc5

Extended Data Fig. 6 | Single-cell RNA sequencing clustering analysis. **a**, UMAP graphic representation of the CTRL, EXP D1, EXP D4 and TPA single-cell RNA-seq data, showing the graph-based clustering results annotated by cell type. The proliferating IFE stem cells (PROLIF. IFE SCs) are in light blue, the IFE stem cells cluster are in red (IFE SCs#1) and dark red (IFE SCs#2), the IFE committed cells (IFE CCs) cluster is in pink and the differentiated IFE cells (IFE DIFF.) are in green. The differentiated cells from the infundibulum (INF. DIFF.) are in grey, the stem cells of the infundibulum (INF. SCs.) are in black, the proliferating cells of the infundibulum (PROLIF. INF.) are in plum and the sebaceous gland cluster (SG) is in orange. The IFE stress cells (STRESS) are in dark grey and the cluster of stem cells stretch (SCs STRETCH) in yellow. *n* = 16,651 cells. **b**, UMAP of the different samples (CTRL, EXP D1, EXP D4, TPA) using the same integrated projection. *n* = 4,659 cells CTRL, *n* = 4,934 cells EXP D1, *n* = 2,716 cells EXP D4, *n* = 4,342 cells TPA. **c**–**k**, UMAP plot of the CTRL sample colored by normalized gene expression values for genes identifying the IFE (**c**) versus infundibulum (**d**), the sebaceous gland (**e**) and the proliferating cells (**f**). Undifferentiated (**g**) and more differentiated cells (**h**) in the IFE identified the SCs cluster (**i**), the CCs cluster (**j**) and the differentiated stage (**k**). Gene expression is visualized as a colour gradient going from grey to yellow with grey as indicator of no expression (that is, expression values below or equal to the 50th percentile for that sample) and yellow as indicator of maximal expression. **c**–**k**, *n* = 16,651 cells. **l**, Table showing the specific marker genes used to annotate the different clusters.

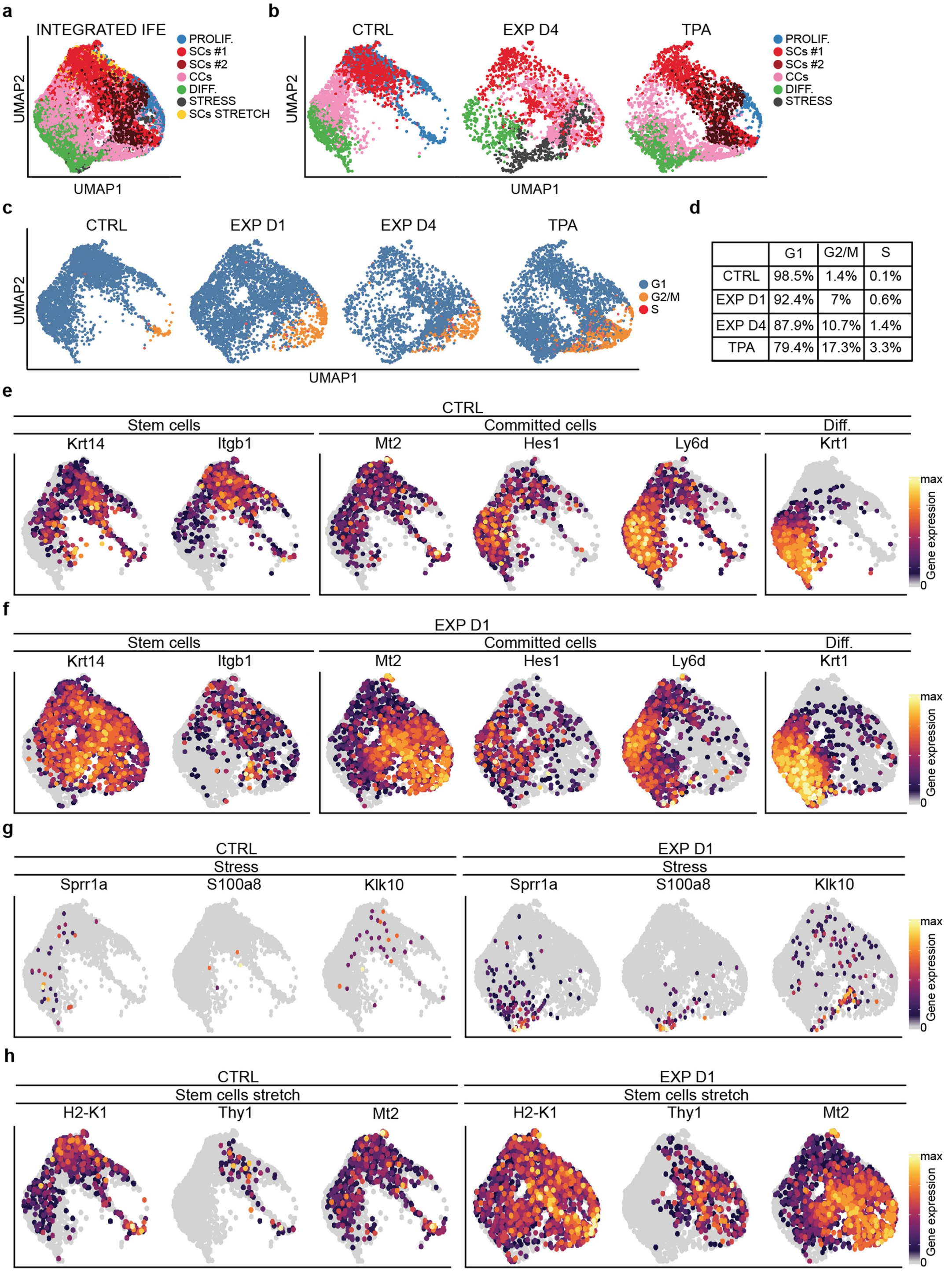

	G1	G2/M	S
CTRL	98.5%	1.4%	0.1%
EXP D1	92.4%	7%	0.6%
EXP D4	87.9%	10.7%	1.4%
TPA	79.4%	17.3%	3.3%

Extended Data Fig. 7 | Single-cell RNA sequencing clustering analysis on the IFE cells. a, Integrated UMAP graphic representation of the IFE cells in CTRL, EXP D1, EXP D4 and TPA single-cell RNA-seq data, showing the graph-based clustering results annotated by cell type. The proliferating stem cells (PROLIF.) are in light blue, the stem cells clusters are in red and dark red (SCs#2), the committed cells (CCs) cluster is in pink and the differentiated cells (DIFF.) are in green. The stress cells (STRESS) are in dark grey and the cluster of stem cells stretch (SCs STRETCH) in yellow. *n* = 12,747 cells. **b**, UMAP of the different samples (CTRL, EXP D1, EXP D4, TPA). **c**, Predicted cell-cycle phases assigned using the *cyclone* function from *scran* tool and visualized in the UMAP. Cells in G1 are in light blue, cells in G2/M are in orange and cells in S phase are in red. **b**–**d**, *n* = 3,142 cells CTRL, *n* = 3,756 cells EXP D1, *n* = 2,145 cells EXP D4, *n* = 3,704 cells TPA. **d**, Percentage of cells in the different cycling phase calculated on the total number of cells. **e**–**h**, UMAP plot colored by normalized gene expression values for the indicated gene and in the indicated sample. Gene expression is visualized as a colour gradient going from grey to yellow with grey as indicator of no expression and yellow as indicator of maximal expression. *n* = 3,142 cells CTRL, *n* = 3,756 cells EXP D1.

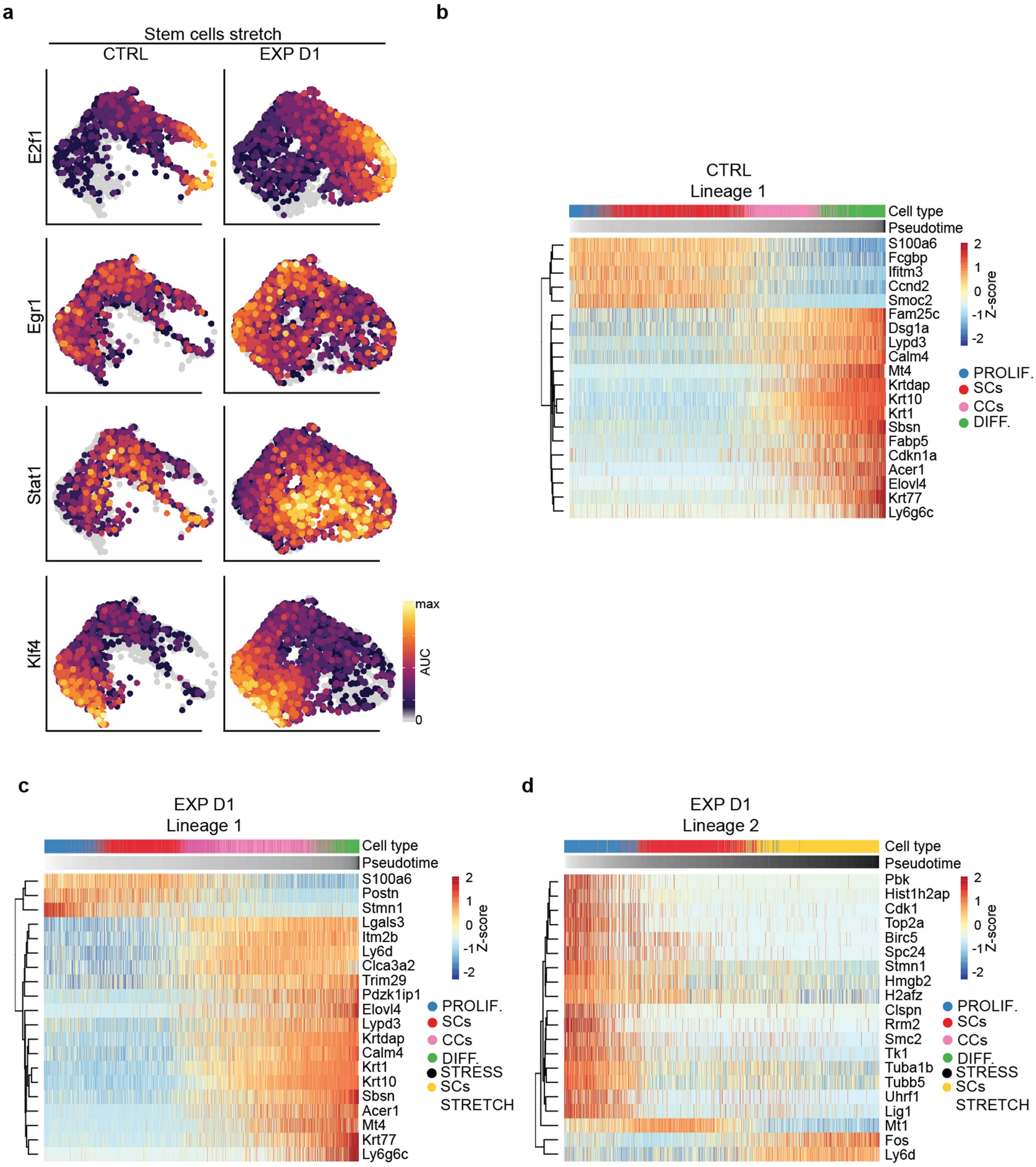

Extended Data Fig. 8 | Pseudotime analysis for single-cell RNA sequencing. **a**, UMAP plots coloured by the degree of regulon activation for TFs differentially activated (AUC rank-sum test FDR corrected p-value <0.05) in the different conditions. Colour scaling represents the normalized AUC value of target genes in the regulon being expressed as computed by SCENIC. **b**, Heat map representation of the top 20 gene expression changes along the inferred pseudotime trajectory computed with Slingshot for the CTRL IFE. **c**, Heat map representation of the top 20 gene expression changes along the inferred pseudotime homeostatic trajectory computed with Slingshot for the EXP D1 IFE. **d**, Heat map representation of the top 20 gene expression changes along the inferred pseudotime trajectory computed with Slingshot characterizing the stress state for the EXP D1 IFE. **b**–**d**, Columns represent cells ordered by their position along the pseudotime trajectory; rows represent genes whose expression profiles show highest correlation (FDR-correted p-value <0.01) with the pseudotime variable, calculated using a generalized additive model (GAM). The colour scaling of the cells represents the normalized expression value of a gene in a particular cell, scaled by Z-score. **a**–**d**, *n* = 3,142 cells CTRL, *n* = 3,756 cells EXP D1.

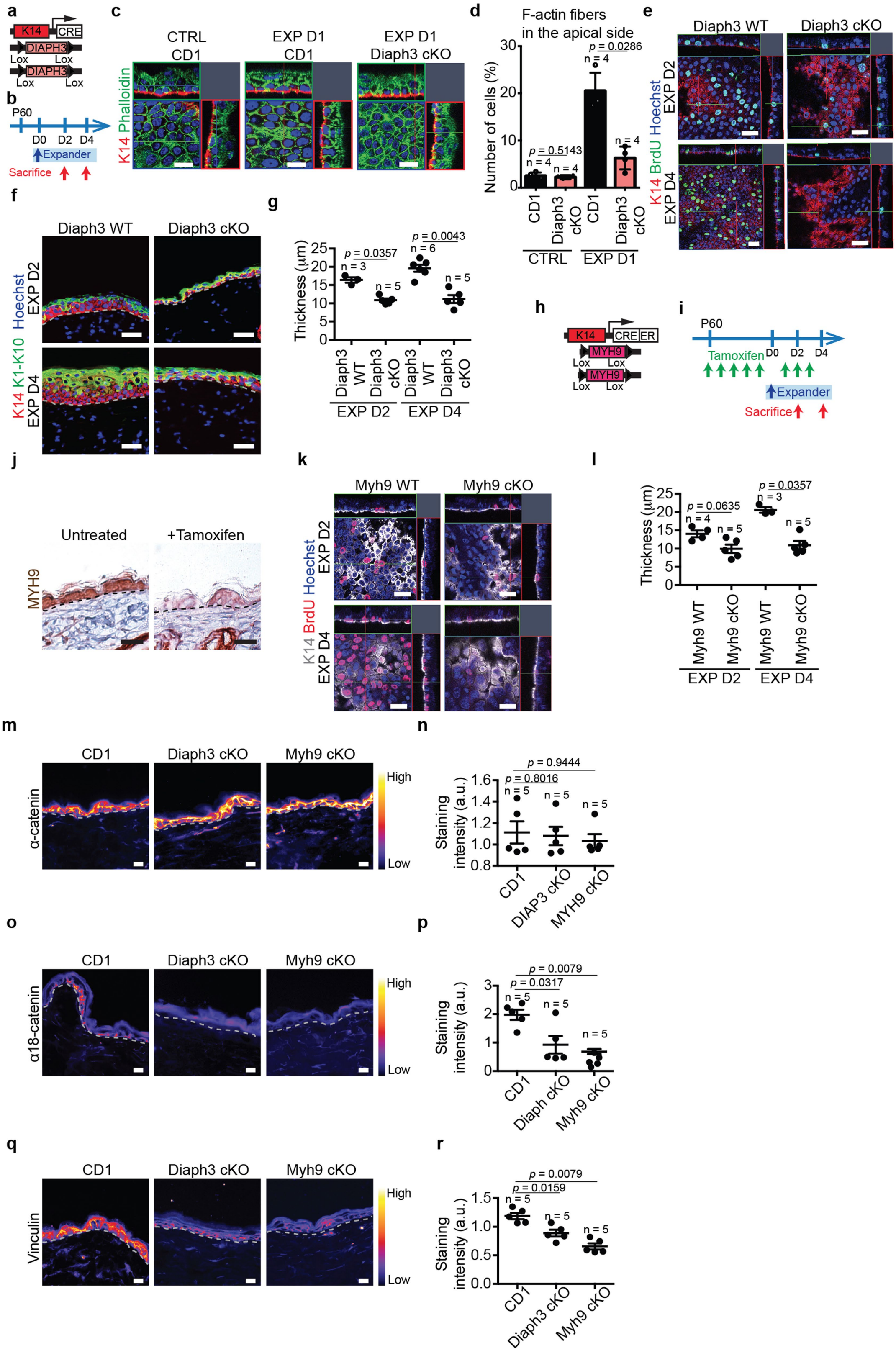

Extended Data Fig. 9 | See next page for caption.

Extended Data Fig. 9 | Cell contractility in stretch-mediated tissue expansion. a, Scheme of the genetic strategy to delete *Diaph3* in the epidermis. **b**, Protocol to delete *Diaph3* during stretch-mediated tissue expansion. **c**, Orthogonal views of confocal analysis of immunostaining for K14 (red) marking basal cells and Phalloidin (green) to visualize F-actin and Hoechst for nuclei (blue) in whole mounts of IFE in CTRL from a CD1 mouse, EXP D1 from a CD1 or *Krt14-cre-DIAPH3fl/fl* (*Diaph3* cKO) mouse. Scale bars, 10 µm. **d**, Percentage of cells with F-actin fibres in the apical side of basal cells related to **c** ($n = 4$ mice per condition). **e**, Orthogonal views of confocal analysis of immunostaining for K14 (red) marking basal cells, BrdU (green) and Hoechst for nuclei (blue) in whole mounts of IFE from *Krt14-cre-DIAPH3fl/+* (*Diaph3* WT) and *Krt14-cre-DIAPH3fl/fl* (*Diaph3* cKO) mice during expansion. Scale bars, 20 µm. Epidermal *Diaph3* cKO were born at a Mendelian ratio and did not present obvious pathological phenotypes. $n = 3$ independent experiments. **f**, Immunostaining for the basal marker K14 (red) and the suprabasal markers K1 and K10 (green) in *Diaph3* WT and *Diaph3* cKO mice in EXP D2 and EXP D4. Scale bars, 20 µm. **g**, Epidermal thickness of *Diaph3* WT and *Diaph3* cKO mice in EXP D2 and EXP D4 (three measurements taken with ImageJ on two sections per mouse, $n =$ at least 3 mice for the different conditions). **h**, Scheme of the genetic strategy to delete *Myh9* in the epidermis. **i**, Protocol to delete *Myh9* during stretch-mediated tissue expansion. **j**, Immunohistochemistry for MYH9 in untreated and Tamoxifen induced *Krt14-creER-MYH9fl/fl* mice. Scale bars, 20 µm. $n = 3$ independent experiments. **k**, Orthogonal views of confocal analysis of immunostaining for K14 (white), BrdU (red) and Hoechst for nuclei (blue) in whole mounts of IFE in *Myh9* WT and *Myh9* cKO mice during expansion. Scale bars, 20 µm. **l**, Epidermal thickness of *Myh9* WT and *Myh9* cKO mice in EXP D2 and EXP D4 (three measurements taken with ImageJ on two sections per mouse, $n =$ at least 3 mice for the different conditions). **m**–**r**, Analysis of adherens junctions in *Diaph3* cKO and *Myh9* cKO mice. **m**, **o**, **q**, Representative images of adherens junction (AJ) component α-catenin (**m**), the α18 tension sensitive form of α-catenin (α18-catenin) (**o**) and Vinculin (**q**), colour-coded for the signal intensity with ImageJ. Protein expression is visualized as a colour gradient going from black to yellow, with black as indicator of no expression and yellow as indicator of maximal expression. Dashed lines indicate the basal lamina. Scale bars, 10 µm. **n**, **p**, **r**, Quantification of the average integrated density signal for α-catenin (**n**), α18-catenin (**p**) and Vinculin (**r**). Each data point is the average of 3 sections per mouse ($n = 5$ mice per condition). **d**, **g**, **l**, **n**, **p**, **r**, Two-tailed Mann–Whitney test, mean + s.e.m.

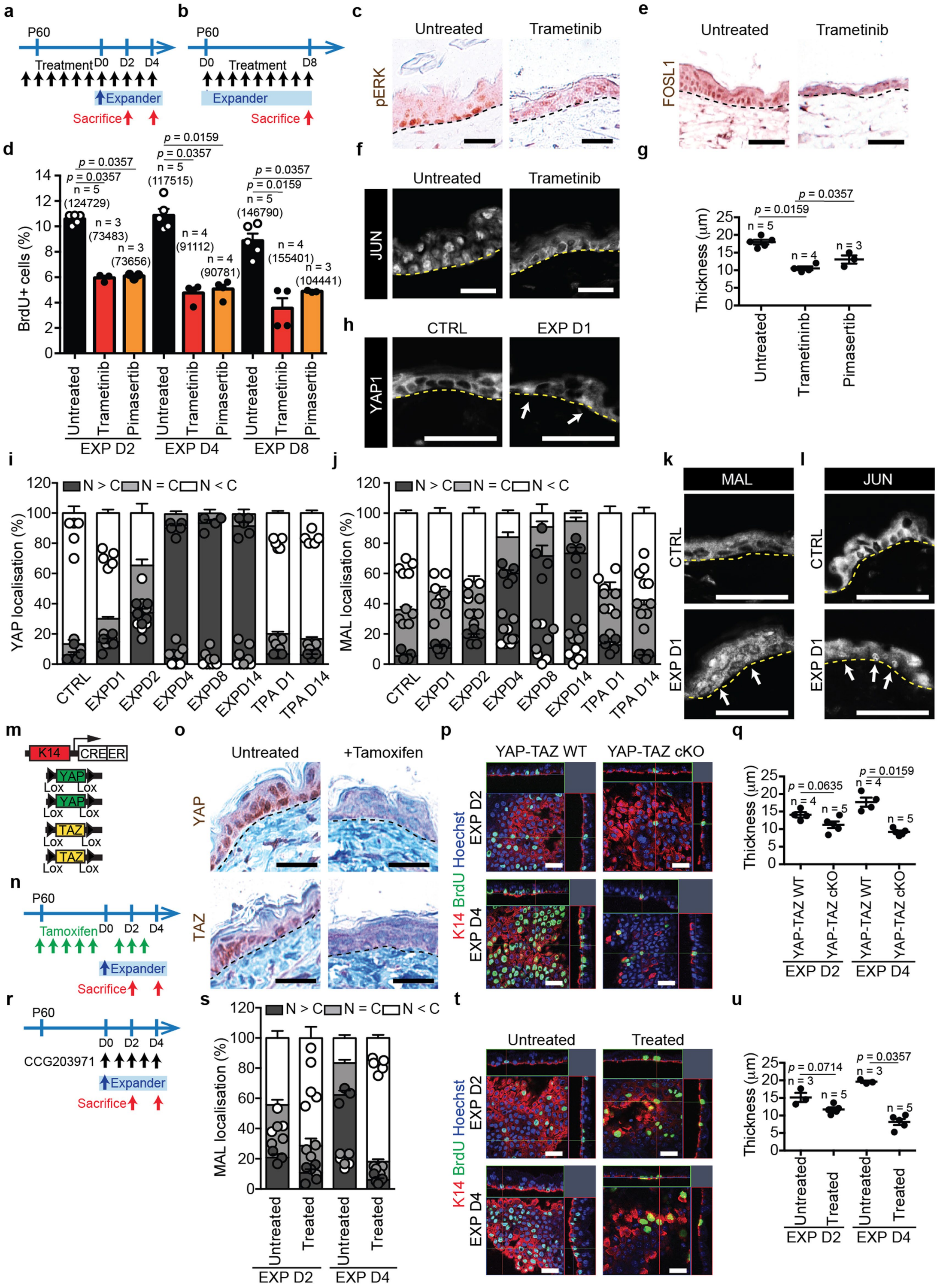

Extended Data Fig. 10 | See next page for caption.

Extended Data Fig. 10 | MEK/ERK/AP1, YAP-TAZ and MAL/SRF regulate stretch-mediated proliferation. **a**, **b**, Protocol for Trametinib or Pimasertib treatment in CD1 mice operated to place the expander and scarified at D2, D4 (**a**) and D8 (**b**) after surgery. **c**, Immunohistochemistry for pERK on paraffin sections of epidermis form CD1 mice untreated or treated with the indicated drug at EXP D2. **d**, Quantification of the proportion of BrdU positive cells during expansion at the indicated time point in CD1 mice untreated or treated with Trimatenib or Pimasertib (n = at least 3 mice per condition as indicated, total number of cells analysed indicated in parentheses). **e**, **f**, Immunohistochemistry for FOSL1 (**e**) and immunofluorescence for JUN (**f**) on sections of epidermis from CD1 mice untreated or treated with the indicated drug at EXP D2. **g**, Epidermal thickness measured with ImageJ on tissue sections at EXP D8 in CD1 mice untreated or treated with the indicated drug ($n = 5$ mice untreated, $n = 4$ mice Trametinib, $n = 3$ mice Pimasertib, 3 measurements on at least 2 sections per mouse). **h**, Immunostaining (white) for YAP1 on skin sections in the control and in EXP D1. White arrows indicate nuclear localization. **i**, Quantification of YAP1 subcellular localization, bars and error bars represent the mean and s.e.m. Nuclear (N) > Cytosplasm (C), more YAP1 in nucleus than in cytoplasm, N = C, similar level of YAP1 in nucleus than in cytoplasm, N < C, less YAP1 in nucleus than in cytoplasm ($n = 150$ cells for all samples except $n = 120$ for EXP D8). **j**, Quantification of MAL subcellular localization, presented as mean and s.e.m. N > C, more MAL in nucleus than in cytoplasm, N = C, similar level of MAL in nucleus than in cytoplasm, N < C, less MAL in nucleus than in cytoplasm ($n = 150$ cells for all samples except $n = 120$ for EXP D8). **k**, **l**, Immunostaining (white) for MAL (**k**) and JUN (**l**) on skin sections in the control and in EXP D1. White arrows indicate nuclear localization. **m**, **n**, Scheme of the genetic strategy to delete YAP-TAZ in the epidermis (**m**) and protocol to delete YAP and TAZ in stretch-mediated tissue expansion (**n**). **o**, Immunohistochemistry for YAP (top) and TAZ (bottom) in *Krt14-creER-YAP-TAZfl/fl* mice before and after Tamoxifen administration. **p**, Orthogonal views of confocal analysis of immunostaining for K14 (red) marking basal cells, BrdU (green) and Hoechst for nuclei (blue) in whole mounts of IFE in *YAP-TAZfl/fl* (*YAP-TAZ* WT) or *Krt14-creER-YAP-TAZfl/fl* (*YAP-TAZ* cKO) mice at the indicated time point following expansion. **q**, Epidermal thickness of *YAP-TAZ* WT and *YAP-TAZ* cKO mice in EXP D2 and EXP D4 (three measurements taken with ImageJ on two sections per mouse, n = at least 4 mice per condition). **r**, Protocol to inhibit MAL with the CCG203971 small molecule during stretch-mediated tissue expansion. **s**, Quantification of MAL subcellular localization in EXP D2 and EXP D4 mice treated or not with the MAL inhibitor. N > C, more MAL in nucleus than in cytoplasm, N = C, similar level of MAL in nucleus than in cytoplasm, N < C, less MAL in nucleus than in cytoplasm ($n = 150$ cells per condition). Data are presented as mean and s.e.m. **t**, Orthogonal views of confocal analysis of immunostaining for K14 (red) marking basal cells, BrdU (green) and Hoechst for nuclei (blue) in whole mounts of IFE in mice treated with the MAL inhibitor or with vehicle control (untreated) at the indicated time point following expansion. **u**, Epidermal thickness of CD1 mice in EXP D2 and EXP D4 treated or not with the MAL inhibitor (three measurements taken with ImageJ on two sections per mouse, $n = 3$ for untreated mice, $n = 5$ for treated animals). **c**, **e**, **f**, **h**, **k**, **l**, **o**, **p**, **t**, Scale bars, 20 µm. $n = 3$ independent experiments. **c**, **e**, **f**, **h**, **k**, **l**, **o**, Dashed lines delineate the basal lamina. **d**, **g**, **q**, **u**, Two-tailed Mann–Whitney test, mean + s.e.m.

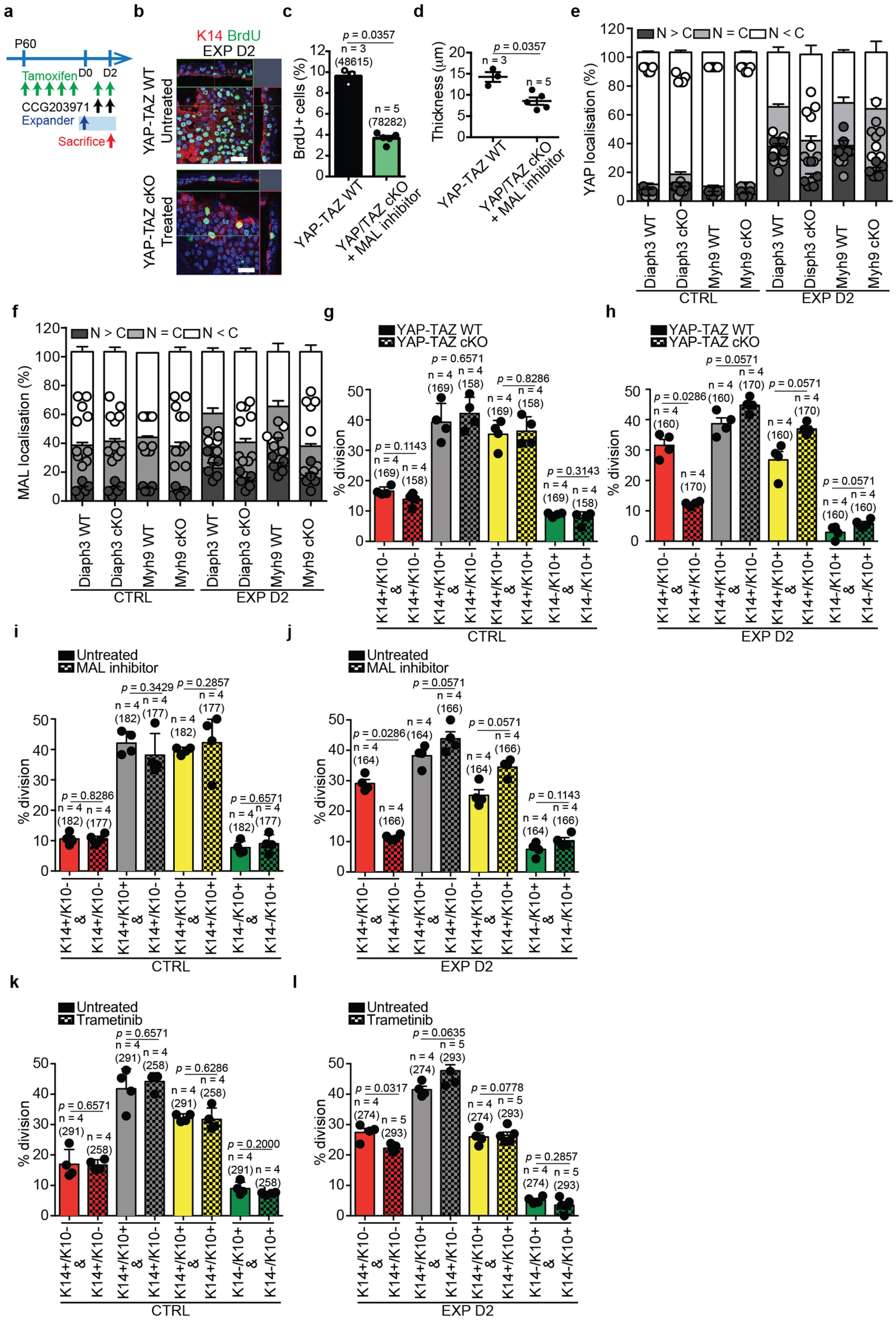

Extended Data Fig. 11 | See next page for caption.

Extended Data Fig. 11 | Pathways associated with stretch-mediated tissue expansion. **a**, Protocol used to delete YAP and TAZ and to inhibit MAL with CCG203971 treatment in *Krt14-creER-YAP-TAZfl/fl* mice in EXP D2. **b**, Orthogonal views of immunostaining for K14 (red) to mark basal cells, BrdU (green) and Hoechst for nuclei (blue) on whole mounts of IFE in *YAP-TAZ* WT untreated mice and *YAP-TAZ* cKO mice treated with the MAL inhibitor at 2 days after the expander placement. Scale bars, 20 µm. **c**, Proportion of BrdU positive cells in untreated *YAP-TAZ* WT mice (48,615 cells from 3 mice) and in *YAP-TAZ* cKO mice treated with the MAL inhibitor (78,282 cells from 5 mice). Two-tailed Mann–Whitney test, mean + s.e.m. **d**, Epidermal thickness of *YAP-TAZ* WT untreated ($n = 3$) and *YAP-TAZ* cKO treated with the MAL inhibitor in EXP D2 ($n = 5$), three measurements taken with ImageJ on two sections per mouse. Two-tailed Mann–Whitney test, mean + s.e.m. **e**, **f**, Quantification of YAP1 (**e**) and MAL (**f**) subcellular localization, presented as mean and s.e.m. in CTRL and EXP D2. N > C, more protein in nucleus than in cytoplasm, N = C, similar level of protein in nucleus than in cytoplasm, N < C, less protein in nucleus than in cytoplasm ($n = 150$ cells per condition). **g**, **h**, Percentage of the type of divisions in CTRL (**g**) and EXP D2 (**h**) in *YAP-TAZ* WT mice and *YAP-TAZ* cKO mice based on the short-term BrdU tracing and staining as in Extended Data Fig. 4h. **i**, **j**, Percentage of the type of divisions in CTRL (**i**) and EXP D2 (**j**) in Untreated mice and with MAL inhibitor based on the short-term BrdU tracing and staining as in Extended Data Fig. 4h. **k**, **l**, Percentage of the type of divisions in CTRL (**k**) and EXP D2 (**l**) in Untreated mice and with Trametinib based on the short-term BrdU tracing and staining as in Extended Data Fig. 4h. **g**–**l**, The number of counted divisions is indicated in parenthesis from n = number of mice. Two-tailed Mann–Whitney test, mean + s.e.m.

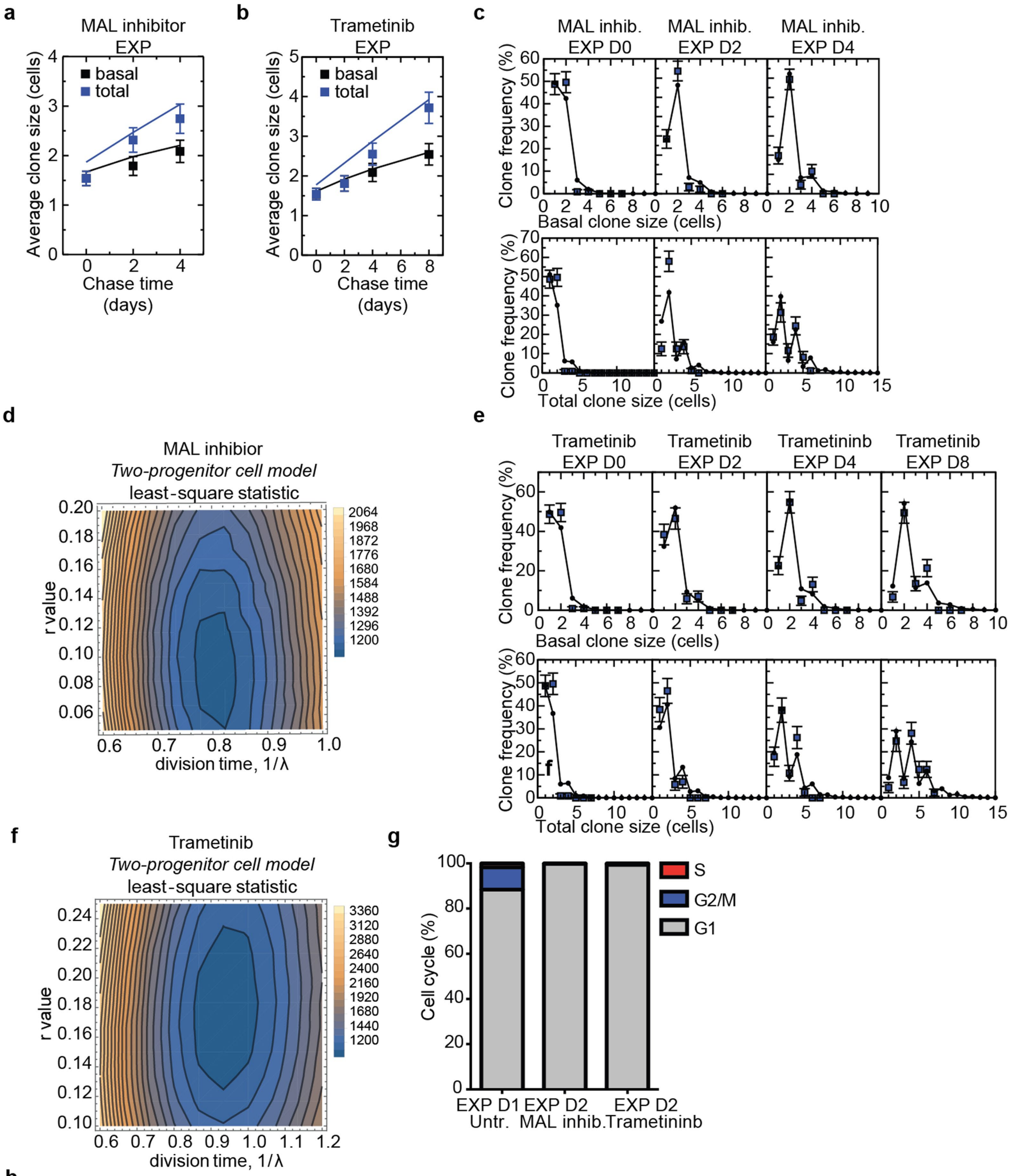

h

	EXP D1 Untreated	EXP D2 MAL inhib.	EXP D2 Trametininb
SCs STRETCH	18.4%	0.0%	2.7%
STRESS	5.1%	6.3%	6.3%
DIFF.	22.9%	0.2%	4.2%
CCs	17.4%	8.7%	15.4%
SCs	30.6%	81.8%	68.8%
PROLIF.	5.4%	2.7%	2.3%

Extended Data Fig. 12 | Single-cell data analysis after MEK and MAL inhibition. a, Average size of persisting clones in mice treated with MAL inhibitor during expansion, based on the basal (black) and total (blue) cell content. Points show data and lines denote the results from the fit to the two-compartment model (see main text and Methods). D0: $n = 115$ clones from 7 mice; D2: $n = 86$ clones from 3 mice; D4: $n = 83$ clones from 3 mice. **b**, Average size of persisting clones in mice treated with Trametinib during expansion, based on the basal (black) and total (blue) cell content. Points show data and lines denote the results from the fit to the two-compartment model (see main text and Methods). D0: $n = 115$ clones from 7 mice; D2: $n = 84$ clones from 3 mice; D4: $n = 80$ clones from 4 mice; D8: $n = 81$ clones from 3 mice. **c**, Fit of the model to the clone size distribution during expansion upon MAL inhibition with $1/\lambda = 3.8$ days and $r = 0.08$. D0: $n = 115$ clones from 7 mice; D2: $n = 86$ clones from 3 mice; D4: $n = 83$ clones from 3 mice. **d**, Least-square values indicate the sensitivity of the fit parameters in **c**. **e**, Fit of the model to the clone size distribution during expansion upon Trametininb treatment with $1/\lambda = 4.3$ days and $r = 0.17$. D0: $n = 115$ clones from 7 mice; D2: $n = 84$ clones from 3 mice; D4: $n = 80$ clones from 4 mice; D8: $n = 81$ clones from 3 mice. **f**, Least-square values indicate the sensitivity of the fit parameters in **e**. **g**, Predicted cell-cycle phases assigned using the *cyclone* function from *scran* tool of EXP D1 Untreated IFE, EXP D2 IFE treated with the MAL inhibitor and EXP D2 IFE treated with Trametinib. Cells in G1 are in grey, cells in G2/M are in blue and cells in S phase are in red. The percentage of cells in the different cycling phases is calculated on the total number of cells. **h**, Table showing the values of the percentage of the different cellular clusters in Fig. 4j, k. **a**, **b**, Mean + s.d. **c**, **e**, Mean + s.e.m.

nature research

Corresponding author(s): Cédric Blanpain, Benjamin D. Simons

Last updated by author(s): 16/06/2020

Reporting Summary

Nature Research wishes to improve the reproducibility of the work that we publish. This form provides structure for consistency and transparency in reporting. For further information on Nature Research policies, see Authors & Referees and the Editorial Policy Checklist.

Please do not complete any field with "not applicable" or n/a. Refer to the help text for what text to use if an item is not relevant to your study.
For final submission: please carefully check your responses for accuracy; you will not be able to make changes later.

Statistics

For all statistical analyses, confirm that the following items are present in the figure legend, table legend, main text, or Methods section.

n/a	Confirmed	
☐	☒	The exact sample size (*n*) for each experimental group/condition, given as a discrete number and unit of measurement
☐	☒	A statement on whether measurements were taken from distinct samples or whether the same sample was measured repeatedly
☐	☒	The statistical test(s) used AND whether they are one- or two-sided *Only common tests should be described solely by name; describe more complex techniques in the Methods section.*
☒	☐	A description of all covariates tested
☒	☐	A description of any assumptions or corrections, such as tests of normality and adjustment for multiple comparisons
☐	☒	A full description of the statistical parameters including central tendency (e.g. means) or other basic estimates (e.g. regression coefficient) AND variation (e.g. standard deviation) or associated estimates of uncertainty (e.g. confidence intervals)
☒	☐	For null hypothesis testing, the test statistic (e.g. F, t, r) with confidence intervals, effect sizes, degrees of freedom and P value noted *Give P values as exact values whenever suitable.*
☒	☐	For Bayesian analysis, information on the choice of priors and Markov chain Monte Carlo settings
☒	☐	For hierarchical and complex designs, identification of the appropriate level for tests and full reporting of outcomes
☒	☐	Estimates of effect sizes (e.g. Cohen's d, Pearson's r), indicating how they were calculated

Our web collection on statistics for biologists contains articles on many of the points above.

Software and code

Policy information about availability of computer code

Data collection	Microscope: Axio Imager M1, Axiovision 4.8.2, Zeiss. Confocal: LSM 780, Zeiss, ZEN2012, Zeiss. Flow cytometry: FACSAria, FACS DiVa, BD Biosciences,8.0.1, 2014, firmware 1.4, CST 3.0.1, PLA 2.0. TEWL: TM210,Courage and Khazaka. TEM: JEOL JEM1400. qPCR: Light Cycler 96 (Roche). Single-cells: Chromium Single Cell 3' (V2-chemistry, PN-120232, 10X Genomics), 10X Chromium controller (10x Genomics).
Data analysis	Microscope and confocal: ZEN 2012 (Zeiss), ImageJ (1.46r). Statistical analysis: Excel (14.4.3), GraphPad Prism (7.00). ATAC-seq: R software (v3.5.1), Bowtie2 (2.2.6), MACS2 (2.1.0.20151222), GREAT (3.0.0), HOMER (10). Single-cells analysis: 10X Genomics, CellRanger (2.1.1) , R package (1.10.0), R package (1.10.2), Seurat R package (3.1.1). Slingshot (1.1.0), SCENIC.

For manuscripts utilizing custom algorithms or software that are central to the research but not yet described in published literature, software must be made available to editors/reviewers. We strongly encourage code deposition in a community repository (e.g. GitHub). See the Nature Research guidelines for submitting code & software for further information.

Data

Policy information about availability of data

All manuscripts must include a data availability statement. This statement should provide the following information, where applicable:

- Accession codes, unique identifiers, or web links for publicly available datasets
- A list of figures that have associated raw data
- A description of any restrictions on data availability

Data associated with this study have been deposited in the NCBI Gene Expression Omnibus under accession number GSE126231, GSE126734 and GSE146637 respectively for the microarray, ATAC-seq and single-cell RNA-seq. Data supporting the findings of this study are available within the article (and its Supplementary Information files). Source data behind Figures 1-4 Extended Data Figures 1-12 are available within the manuscript files.

Field-specific reporting

Please select the one below that is the best fit for your research. If you are not sure, read the appropriate sections before making your selection.

☒ Life sciences ☐ Behavioural & social sciences ☐ Ecological, evolutionary & environmental sciences

For a reference copy of the document with all sections, see nature.com/documents/nr-reporting-summary-flat.pdf

Life sciences study design

All studies must disclose on these points even when the disclosure is negative.

Sample size	No statistical methods were used to predetermine sample size. All experiments were repeated at least three times. In microarray, TPA was repeated twice with reproducible results. Single-cell: the results for each mouse were grouped and analyzed together in all conditions. The number of animals has been reduced for ethical reasons.
Data exclusions	No animals were excluded from the analysis.
Replication	All experiments were repeated at least three times (3 biological independent experiments/mice) showing similar results, except for microarray analysis for which one condition experiment (TPA) was repeated twice (2 biological independent experiments/mice) and single cell for which we analysed one mouse per condition (1 biological independent experiment/mouse). All attempts at replication were successfull and are shown, n is described in legends.
Randomization	The experiments were not randomized. The mice included in this study were selected according to their correct genotype. The mice received tamoxifen injection/s when they were 2 months old. Sex-specific differences were minimized by including similar number of male and female animals.
Blinding	The investigators were not blinded to allocation during experiments and outcome assessment. Blinding was not possible as the same investigator processed the animals and analysed the data.

Reporting for specific materials, systems and methods

We require information from authors about some types of materials, experimental systems and methods used in many studies. Here, indicate whether each material, system or method listed is relevant to your study. If you are not sure if a list item applies to your research, read the appropriate section before selecting a response.

Materials & experimental systems

n/a	Involved in the study	
☐	☒	Antibodies
☒	☐	Eukaryotic cell lines
☒	☐	Palaeontology
☐	☒	Animals and other organisms
☒	☐	Human research participants
☒	☐	Clinical data

Methods

n/a	Involved in the study	
☒	☐	ChIP-seq
☐	☒	Flow cytometry
☒	☐	MRI-based neuroimaging

Antibodies

Antibodies used	For immunofluorescence and ISH the following primary antibodies were used: anti-B4-integrin (Rat, 1:200, BD, clone346-11A, ref.553745, lot.5239648), anti-Keratin10 (rabbit, 1/3000, Covance, ref.PRB-159P-0100), anti-Keratin1 (rabbit, 1/3000, Covance, ref.PRB-165P-0100), anti-Keratin-14 (rabbit, 1/3000, Thermofisher), anti-BrdU (mouse, 1/200, BD, clone 3D4,ref. 560209, lot.4293550), anti-MAL (rabbit,1/200, Sigma, ref.HPA030782,lot.C106712), anti-c-JUN (rabbit, 1/200; Proteintech, 24909-1-AP); anti-p63 (rabbit, 1/100 Abcam, ab124762); anti-KLF4 (rabbit, 1/100 Abcam, ab129473); anti-pSTAT3 (rabbit, 1/100 Cell signaling, 9145); anti-YAP1 (rabbit, 1/100 Proteintech, 13584-1-AP); rabbit anti-YAP (1:200, Santa Cruz Biotechnology, sc-15407), rabbit anti-TAZ (1:100, Sigma-Aldrich, HPA007415), rabbit anti-cFOS (1:100, Proteintech, 26192-1-AP), rabbit anti-MYH9 (1:500, Sigma, HPA001644), rabbit anti-pERK (1:200, Cell signaling, 4370S), anti-FOSL1 (1:500, Santa Cruz Biotechnology, sc-28310), anti-β-catenin (mouse, 1:1000 Abcam ab6301), anti-α-catenin (rabbit, 1:1000 Sigma, C2081); anti-α18-catenin (rat monoclonal, 1:20000) was a generous gift form Akira Nagafuchi, Kumamoto University; anti-Vinculin (mouse, 1:200 Millipore MAB3574); anti-p120-catenin (rabbit, 1:1000 Invitrogen PA5-82545); anti-E-cadherin (rat, 1:500, ebioscience 14-3249-82); anti-ZO-1(rabbit, 1:200 Invitrogen 61-7300); anti-Claudin-1 (rat, 1:100Thermo Scientific 51-9000); anti-Paxillin (rabbit, 1:100 Abcam 32084); anti-CD45 (rat, 1:500, BD Biosciences 553081); anti-CD68 (rabbit, 1:100 Abcam ab125212); anti-SOX6 (rabbit, 1:400 Sigma HPA001923); anti-NFIB (rabbit, 1:200 Sigma HPA003956). The following secondary antibodies were used: anti-rabbit, anti-rat, anti-goat, anti-chicken, anti-mouse conjugated to AlexaFluor488 (Molecular Probes) and to rhodamine Red-X and Cy5 (JacksonImmunoResearch).
Validation	As positive control for immunostaining, tissues with known expression of the marker were used on mouse sections. As negative control, for immunostaining, staining omitting the primary antibody was performed.

Animals and other organisms

Policy information about studies involving animals; ARRIVE guidelines recommended for reporting animal research

Laboratory animals	K14CREER and K14CRE transgenic mice were kindly provided by E. Fuchs, Rockefeller University, USA. Rosa-Confetti mice were provided by H. Clevers. YAPfl/fl and TAZfl/fl mice were obtained from Georg Halder (KU Leuven) who received them from Randy Johnson at the MD Anderson Cancer Center, Houston. Diap3fl/fl mice were obtained from Fadel Tissil (UCL) and MYH9fl/fl mice were a kindly gift from Sara Wickström (University of Helsinki). Rosa26-mT/mG mice were provided form Isabelle Migeotte (Université Libre de Bruxelles). Mice included in this study were from mixed genetic background. Female and male animals have been used for all experiments and equal animal gender ratios have been respected in the majority of the analysis. Mice were included in the study when they were 2 months old when the tamoxifen was administred.
Wild animals	No wild animals were used in this study.
Field-collected samples	No field-collected samples were used in this study.
Ethics oversight	Mice colonies were maintained in a certified animal facility in accordance with European guidelines. The experiments were approved by the local ethical committee (CEBEA) under protocols #604 and #605.The study is compliant with all relevant ethical regulations regarding animal research.

Note that full information on the approval of the study protocol must also be provided in the manuscript.

Flow Cytometry

Plots

Confirm that:

☒ The axis labels state the marker and fluorochrome used (e.g. CD4-FITC).

☒ The axis scales are clearly visible. Include numbers along axes only for bottom left plot of group (a 'group' is an analysis of identical markers).

☒ All plots are contour plots with outliers or pseudocolor plots.

☒ A numerical value for number of cells or percentage (with statistics) is provided.

Methodology

Sample preparation	The mice were shaved with an electric shaver, the back skin was dissected from the mice, fat and underlying subcutis were removed with a scalpel. The samples were placed in 0,25% Trypsin (Gibco, Thermo Fisher Scientific) in DMEM-Dulbecco's modified Eagle's medium (Gibco, Thermo Fisher Scientific) and 2mM EDTA (Thermo Fisher Scientific) overnight at 4°C. The epidermis was separated form the dermis and the trypsin was neutralized by adding DMEM medium supplemented with 2% Chelex Fetal Calf Serum (FCS). Samples were filtrated on 70 and 40µm filter (Falcon). Single cells suspension were incubated in 2% FCS/PBS with primary antibodies for 30 min on ice, protected from the light, with shaking every 10 min. Primary antibodies were washed with 2% FCS/PBS and cells incubated for 30 min in APC-conjugated streptavidin (BD Biosciences), on ice, with shaking every 10 min. Living epidermal cells were gated by forward scatter, side scatter and negative staining for Hoechst dye. Basal IFE and infundibulum cells were stained using PE-conjugated anti-α6-integrin (clone GoH3; 1/200, ebioscience) and bulge cells were stained with biotinylated CD34 (clone RAM34; 1:50, BD Biosciences). Basal cells from the interfollicular epidermis were targeted using CD34 negative and α6 integrin positive gating. The geometric mean fluorescence intensity of Itgβ1 (FITC-coniugated anti-β1-integrin, 1:100, BD Bioscience 555005) and Itga2 (PE-coniugated anti-α2-integrin, 1:100, BD Bioscience 553858) was measured on the α6-integrinhigh/CD34neg population.
Instrument	FACSAria III (BD Bioscience)
Software	FACSDiva Software 8.0.1 (BD Bioscience)
Cell population abundance	The proportion of the relevant cell populations is depicted in Extended Data Fig.3a
Gating strategy	Living cells were selected by forward scatter, side scatter, doublets discrimination and by Hoechst dye exclusion. Basal epidermal cells were selected based on the expression of Integrin-alhap6-high-PE and Cd34-APC negative.

☒ Tick this box to confirm that a figure exemplifying the gating strategy is provided in the Supplementary Information.

Mucosal or systemic microbiota exposures shape the B cell repertoire

https://doi.org/10.1038/s41586-020-2564-6

Received: 19 February 2019

Accepted: 18 May 2020

Hai Li[1,6], Julien P. Limenitakis[1,6], Victor Greiff[2], Bahtiyar Yilmaz[1], Olivier Schären[3], Camilla Urbaniak[4], Mirjam Zünd[1], Melissa A. E. Lawson[1], Ian D. Young[1], Sandra Rupp[1], Mathias Heikenwälder[5], Kathy D. McCoy[1], Siegfried Hapfelmeier[3], Stephanie C. Ganal-Vonarburg[1,6]✉ & Andrew J. Macpherson[1,6]✉

Colonization by the microbiota causes a marked stimulation of B cells and induction of immunoglobulin, but mammals colonized with many taxa have highly complex and individualized immunoglobulin repertoires[1,2]. Here we use a simplified model of defined transient exposures to different microbial taxa in germ-free mice[3] to deconstruct how the microbiota shapes the B cell pool and its functional responsiveness. We followed the development of the immunoglobulin repertoire in B cell populations, as well as single cells by deep sequencing. Microbial exposures at the intestinal mucosa generated oligoclonal responses that differed from those of germ-free mice, and from the diverse repertoire that was generated after intravenous systemic exposure to microbiota. The IgA repertoire—predominantly to cell-surface antigens—did not expand after dose escalation, whereas increased systemic exposure broadened the IgG repertoire to both microbial cytoplasmic and cell-surface antigens. These microbial exposures induced characteristic immunoglobulin heavy-chain repertoires in B cells, mainly at memory and plasma cell stages. Whereas sequential systemic exposure to different microbial taxa diversified the IgG repertoire and facilitated alternative specific responses, sequential mucosal exposure produced limited overlapping repertoires and the attrition of initial IgA binding specificities. This shows a contrast between a flexible response to systemic exposure with the need to avoid fatal sepsis, and a restricted response to mucosal exposure that reflects the generic nature of host–microbial mutualism in the mucosa.

Mammalian immunoglobulins are composed of heavy (H) and light (L) chains, each of which is assembled from one of many $V_{H/L}$, (D_H) and $J_{H/L}$ gene segments during B cell development. The resulting genetic and structural diversity of the immunoglobulin repertoire, and antigen recognition possibilities, are further increased by additional nucleotide insertion during recombination, later somatic mutation or class-switch recombination from IgM and/or IgD to IgG, IgE or IgA. The selection and clonal expansion of particular B cells with appropriate immunoglobulin specificity endows the system with the ability to respond to a huge variety of antigens. Comparisons of colonized and germ-free mice show that the number of B cells and immunoglobulin levels (especially those of IgG and IgA) are considerably amplified by colonization with a microbiota, some members of which penetrate mucous membranes to prime systemic secondary lymphoid structures even in healthy hosts[4,5]. B cell repertoires have so far been shown to be largely unique to each individual[1,2], although whether this is caused by differences in microbiota composition or the sequence of colonization in each individual is unknown.

Using localized time-limited exposures of defined doses of single benign microbial taxa in germ-free mice[3], here we address how the B cell repertoire is shaped by microbiota exposure at mucous membranes or in systemic lymphoid tissues, and how interactions between different exposure sites or subsequent exposures to different taxa affect the outcome.

Distinct repertoires depend on exposure site

We used standardized doses of the live non-replicating *Escherichia coli* strain HA107 to transitorily expose germ-free mice to live microorganisms, either confined within the intestine or via the blood stream. After exposure, all mice rapidly return to germ-free status, owing to HA107 auxotrophy for the essential bacterial amino acids D-alanine and diaminopimelic acid[3]. We found distinct antibody repertoires computed on the basis of CDR3 heavy-chain amino acid identity[6] from entire IgA, IgG and IgM repertoires, depending on whether the exposure was mucosal or systemic (Fig. 1a–c, Extended Data Fig. 1a). Clonotype overlap was significantly greater within each exposure condition compared with different conditions (right panels of Fig. 1a–c) and different exposure conditions segregated in unsupervised tree clustering (bottom panels of Fig. 1a–c). We also found a clear separation according to microbial exposure condition, with shared clonotypes computed as sequences

---

[1]Maurice Müller Laboratories (DBMR), Universitätsklinik für Viszerale Chirurgie und Medizin Inselspital, University of Bern, Bern, Switzerland. [2]Department of Immunology, University of Oslo, Oslo, Norway. [3]Institute for Infectious Diseases, University of Bern, Bern, Switzerland. [4]McMaster University Medical Centre, Hamilton, Ontario, Canada. [5]Division of Chronic Inflammation and Cancer, German Cancer Research Center (DKFZ), Heidelberg, Germany. [6]These authors contributed equally: Hai Li, Julien P. Limenitakis, Stephanie C. Ganal-Vonarburg, Andrew J. Macpherson. ✉e-mail: stephanie.ganal@dbmr.unibe.ch; andrew.macpherson@dbmr.unibe.ch

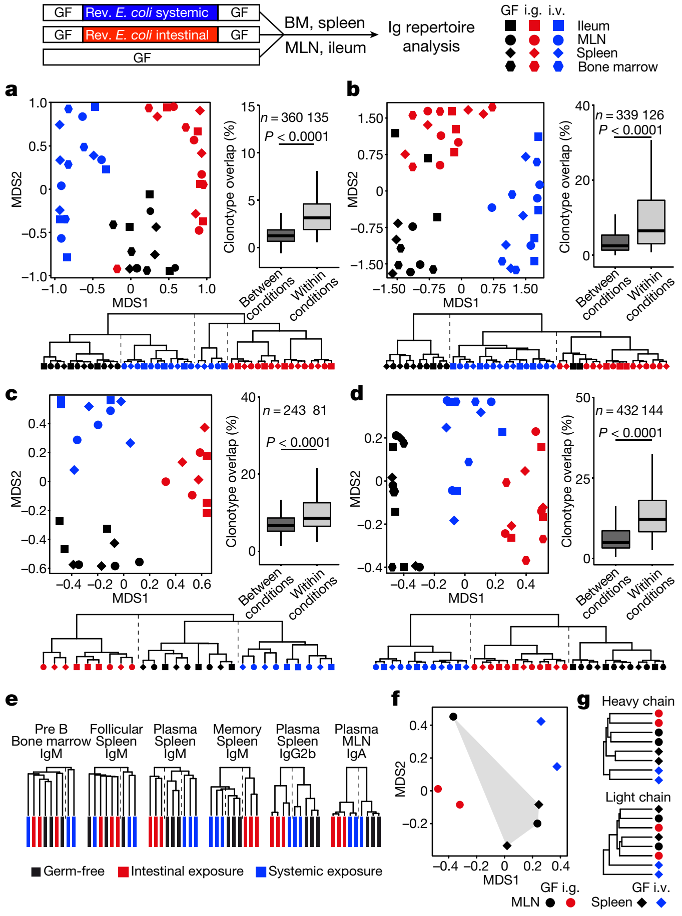

Fig. 1 | Antibody repertoires in mucosal and systemic tissues after transitory oral or systemic exposure to a commensal microorganism. **a**–**g**, Germ-free mice (GF) were orally or systemically primed three times every other day by intragastric (i.g.) (10^{10} colony-forming units (CFU)) or intravenous (i.v.) (10^8 CFU) *E. coli* HA107 (**a**–**c**, **e**–**g**), or *C. orbiscindens* (**d**), and compared with germ-free control mice. Sequencing of the immunoglobulin repertoire at 21 d for IgA (**a**, **d**), IgG2b (**b**) and IgM (**c**) in the ileum, mesenteric lymph nodes (MLN), bone marrow (BM) and spleen was performed. In **a**–**d**, the left panels show multidimensional scaling (MDS) plots based on immunoglobulin heavy-chain CDR3 amino acid sequences of the entire repertoire. In **a**–**d**, the right panels show Tukey plots of clonal overlap between samples of different priming conditions or the same priming condition (sample comparisons from the same mouse were excluded), shown with arithmetic mean and whiskers extending to 1.5× interquartile range. Two-sided Wilcoxon rank–sum tests were performed with adjusted *P* values as shown. The bottom panels in **a**–**d** show hierarchical clustering. Dendrogram branch lengths show the distance between repertoires on the basis of CDR3 amino acid sequence similarity; vertical dotted lines designate principal unbiased separations. **e**, IgM, IgA and IgG2b of indicated sorted B cell populations at 21 d. In the hierarchical clustering dendrograms from the indicated sorted cell populations, branch length shows the distance between CDR3 amino acid repertoires. **f**, **g**, Single-cell VDJ repertoire sequencing analysis. **f**, MDS plot of distance between repertoires on the basis of combined immunoglobulin heavy- and light-chain CDR3 amino acid sequences. Grey shading visually indicates germ-free repertoires. **g**, Hierarchical clustering of single-cell heavy- or light-chain immunoglobulin repertoires from mesenteric lymph nodes and spleen. Data are representative of nine (**a**–**c**), two (**d**, **e**) or three (**f**, **g**) independent experiments. All data points represent organs from individual mice. Rev., reversible.

encoded by the same V_H and J_H segments and an identical nucleotide sequence in the CDR3 region[7] (Extended Data Fig. 1b–g).

We used *Clostridium orbiscindens* (German Collection of Microorganisms and Cell Cultures (DSMZ) accession 8061) as a second transitory colonizing taxon to confirm that the repertoires depend on the route of microbial exposure (Fig. 1d, Extended Data Fig. 1h). Flow cytometric sorting before analysis with standardized numbers of subsets of B cells showed that the distinct effects of different routes of microbial exposure occurred in the memory and plasma cells (Fig. 1e). Although single-cell experiments currently only capture a fraction of the clonotype repertoire compared with bulk analysis (in our case, 14 ± 6%, $\bar{x} \pm$ s.d., $n = 8$ independent samples from 6 mice), a multidimensional scaling plot that combines the heavy- and light-chain information also segregated according to exposure route (Fig. 1f). Subsequent analysis that considered single-cell heavy- and light-chain clonotypes individually showed that the selective effects of the route of microbial exposure segregate with the immunoglobulin heavy chain (Fig. 1g).

Using bacterial-specific flow cytometry, we verified a preferential isotype class switch to IgG2b after systemic exposure, or to IgA after mucosal exposure[3] (Extended Data Fig. 1i, j). Consistent with previous reports[8–12], we also found that mucosal exposure could generate a small serum IgG response (red symbols in Extended Data Fig. 1k). Conversely, exclusive systemic exposure generated a specific secretory IgA response in the intestine (blue symbols in Extended Data Fig. 1l), which confirms that both the mucosal and the systemic immune systems can be primed by microbial exposure from either route.

Alternative approaches are being used by different laboratories to avoid the over estimation of clonal frequencies owing to sequencing errors. We carried out a series of control experiments to confirm that equivalent biological clustering results were obtained with either computational consolidation or the use of unique molecular identifier barcodes (Extended Data Fig. 2a–c). Although each set of bulk sequencing results in this Article are from samples processed together in a batch, we also verified the technical reproducibility of the same sample processed on different occasions (Extended Data Fig. 2d).

Priming thresholds differ by exposure route

In our system of non-replicating transitory exposures, in germ-free mice, test doses can be calibrated without further expansion in vivo. We showed that mucosal doses of 10^6–10^8 colony-forming units were needed to reshape the mucosal IgH repertoire (Extended Data Fig. 3a, e, f), consistent with the high doses that are known to induce specific IgA binding[3] (Extended Data Fig. 3b). By contrast, the systemic IgH repertoire was reshaped by as little as 10,000 colony-forming units (Extended Data Fig. 3c, g, h). The doses required for detectable humoral responses were generally at least an order of magnitude greater than those required for repertoire programming (Extended Data Fig. 3b, d).

Exposure route affects B cell targeting

To explore whether repertoires of immunoglobulin heavy-chain clonotypes differed according to mucosal or systemic microbial exposure, we investigated the targets for bacterial-antigen binding according to exposure route. Intestinal IgA bound most effectively to the purified bacterial membrane fraction of *E. coli*, whereas serum IgG bound to both membrane and cytoplasmic fractions (Fig. 2a). Ribosomal proteins of *E. coli* dominated the cytoplasmic binding of serum IgG antibodies, and were confirmed in a second context by proteomic analysis in specific-pathogen-free mice that were systemically exposed to *Enterobacter cloacae* (Extended Data Fig. 4a–c). Increased exposure of bacterial membranes relative to the cytoplasmic contents in the mesenteric lymph nodes after intestinal treatment was shown by higher lipopolysaccharide/16S ribosome ratios compared with the spleen after systemic treatment (Extended Data Fig. 4d). These differences may be caused by the intestinal efficiency of bacterial lipid uptake compared with bacterial cytoplasmic protein contents, whereas systemic exposure would prime equivalent immune responses to membrane and cytoplasmic fractions after opsonization and phagocytosis[13,14].

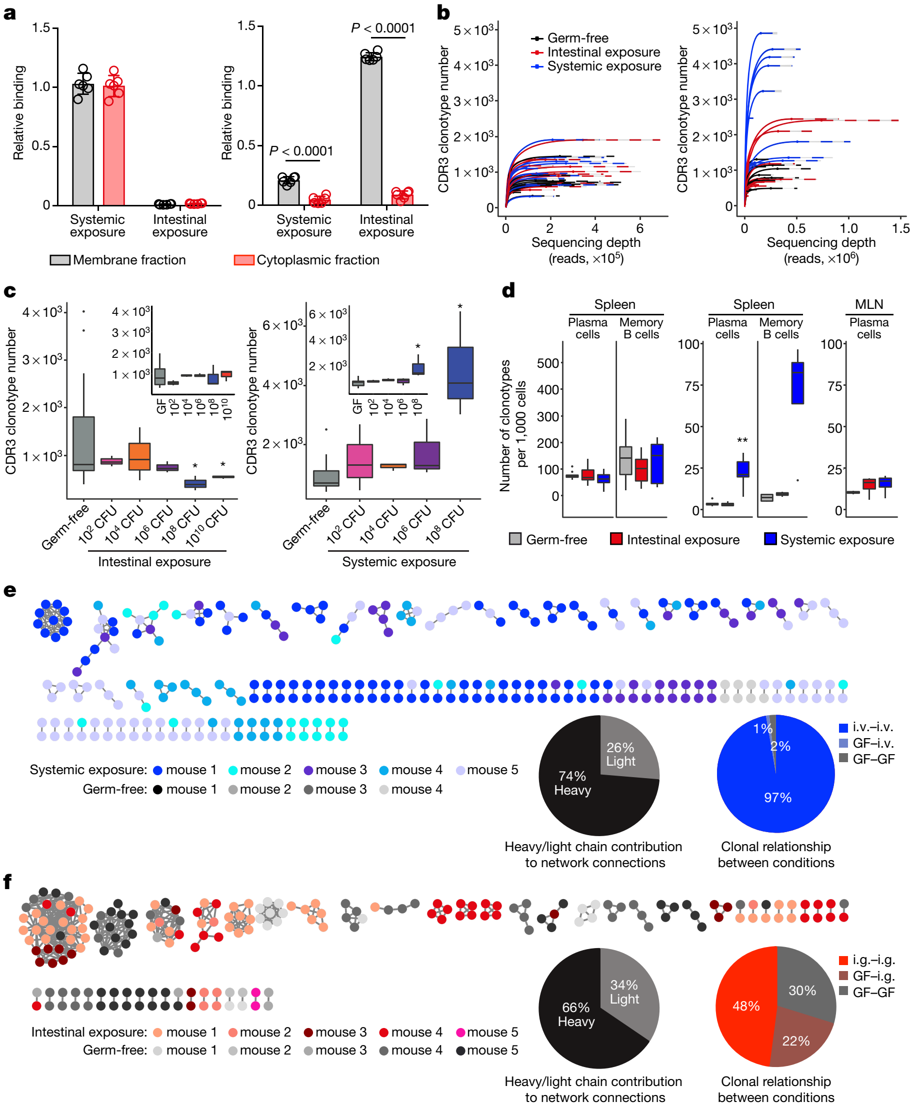

Fig. 2 | Differences between B cell repertoires after systemic or mucosal exposure. Germ-free mice were treated orally or systemically with *E. coli* HA107 at the indicated doses, as in Fig. 1. **a**, Binding of systemic or intestinal antibodies (left, serum IgG2b; right, intestinal wash IgA) to *E. coli* membrane versus cytoplasmic fractions evaluated using enzyme-linked immunosorbent assay ($\bar{x}$ ± s.d., $n = 6$ mice, two-sided unpaired t-test). **b**, Rarefaction plots of immunoglobulin heavy-chain sequencing at 21 d for IgA (left) and IgG2b (right) in mesenteric lymph nodes and spleen. **c**, Immunoglobulin heavy-chain sequencing at 21 d for IgA in mesenteric lymph nodes (left) and spleen (left inset), and IgG2b in spleen (right) and mesenteric lymph nodes (right inset) ($n = 3$ mice for each bacterial exposure group and each defined dose, $n = 15$ germ-free control mice, $^{*}P = 0.036$ mesenteric lymph node IgA (both cases), $P = 0.046$ spleen, $P = 0.036$ mesenteric lymph node IgG2b, two-sided Wilcoxon rank-sum test). **d**, IgM (left), IgG2b (middle) and IgA (right) heavy-chain sequencing of splenic sorted B cell populations at 21 d, $n = 6$ mice for each condition. Tukey plots indicate the calculated number of clonotypes per 1,000 cells in B cell populations. $^{**}P = 0.003$, two-sided Wilcoxon rank–sum test. **e**, **f**, Single-cell sequencing analysis. Networks built on combined heavy- and light-chain CDR3 amino acid sequences each from single spleen IgG-expressing (**e**) or mesenteric lymph node IgA-expressing (**f**) B cells (singlets excluded; $n = 1{,}601$ and 670 for **e** and **f**, respectively). Edges show Levenshtein distance = 1 or 2. Networks show immunoglobulin sequence relationships within and between different mice in the same experiment, colour-coded according to mouse and treatment. Left pie charts indicate the percentage of edge connections that are based on Levenshtein distance 1 on the light chain compared to the heavy chain; right pie charts indicate the distribution of edge connections between individual B cells within or between exposure conditions. Corresponding networks for naive B cells are shown in Extended Data Fig. 6a, b for **e**, **f**, respectively. Tukey plots in **c**, **d** are shown with arithmetic mean and whiskers of 1.5× interquartile range. Data are representative of two independent experiments. All data points are from individual mice.

In support of this, repertoires of B cell clonotypes after systemic—but not mucosal—challenge with ultrasound-lysed bacteria overlapped with the repertoires after exposure with intact bacteria (Extended Data Fig. 4e, f). Conversely, in the absence of local anatomical processing, the intrinsic antigen-specific and -nonspecific responses to membrane or cytoplasmic bacterial antigens presented directly in vitro did not differ depending on mesenteric or splenic origin of the B cells (Extended Data Fig. 4g). We conclude that the different repertoires from mucosal and systemic B cell priming are a consequence of the way in which microbial membrane and cytoplasmic antigens are processed and presented in the different anatomical compartments.

Exposure context shapes IgA or IgG diversity

IgA has previously been found to be oligoclonal[15,16]. We next followed how repertoire expansion or restriction developed according to isotype, exposure route and dose. Whereas IgG diversity generally increased considerably after systemic exposure, no increase in IgA diversity was found

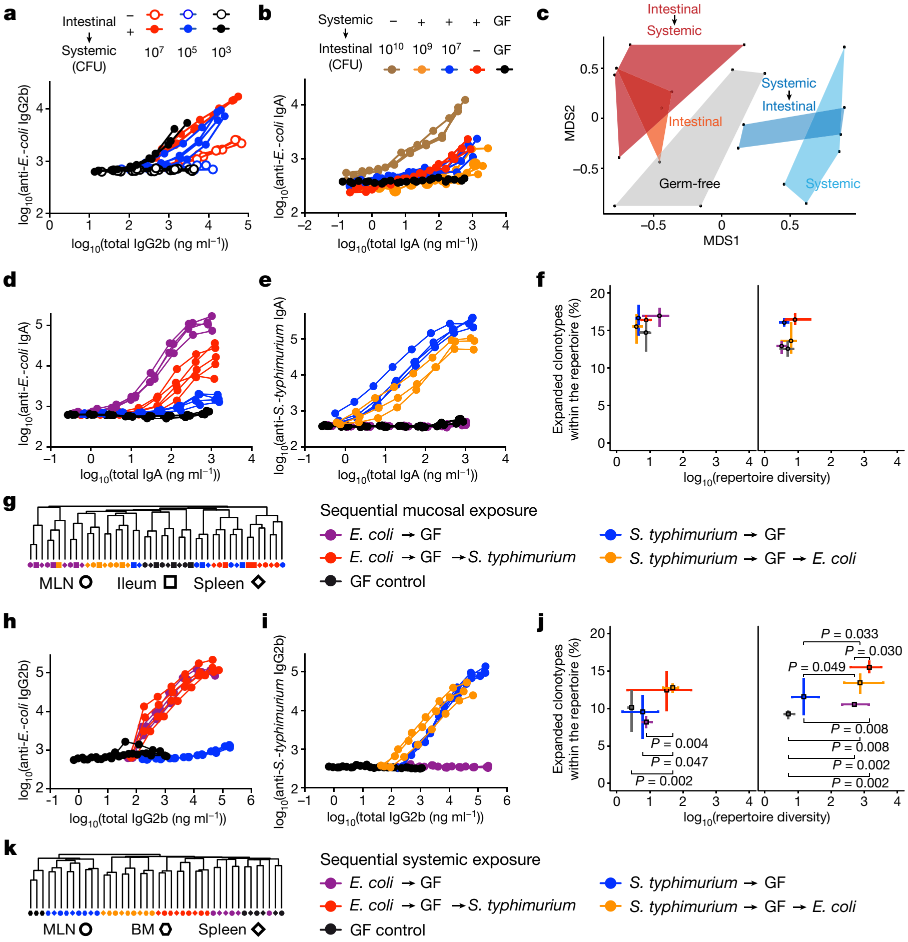

Fig. 3 | Antimicrobial antibody responses after combined mucosal and systemic exposure or exposure to two different microbial taxa. **a**, **b**, Germ-free mice were intestinally (**a**) or systemically (**b**) exposed to *E. coli* HA107 on alternate days, or remained germ-free throughout. On day 21, all mice were intravenously (**a**) or intestinally (**b**) exposed to the indicated doses of HA107 (schema shown in Extended Data Fig. 7a, b). Flow cytometric analysis of specific bacterial binding of serum IgG2b (**a**) or intestinal IgA (**b**) on day 42. **c**, Germ-free mice were primed as in **a**, **b**. Immunoglobulin sequencing for IgM of sorted splenic plasma cells. MDS plot of repertoire separation. **d**–**g**, Germ-free mice were mucosally primed with three doses of *E. coli* HA107 or *S. typhimurium* HA218, or remained germ free. At day 21, half of each group received a second schedule of priming with the opposite taxon. *n* = 3 for each condition (schema shown in Extended Data Fig. 8a). **d**, **e**, Bacterial flow cytometry of *E.-coli*-HA107-specific (**d**) or *S.-typhimurium*-HA218-specific (**e**) intestinal IgA at day 42. **f**, Comparisons of mean repertoire diversity and median percentage of expanded clonotypes within the IgA repertoires in the spleen (right) and mesenteric lymph nodes (left). **g**, Hierarchical clustering of full-length IgA heavy-chain sequences. **h**–**k**, Experimental design as in **d**–**g**, except both reversible taxa given systemically. *n* = 3 for each condition (schema shown in Extended Data Fig. 8b). **h**, **i**, Bacterial flow cytometry for serum IgG bacterial binding. **j**, Comparisons of mean repertoire diversity and median percentage of expanded clonotypes within the IgG2b repertoires in the spleen (right) and mesenteric lymph nodes (left). **k**, Hierarchical clustering of full-length IgG2b heavy-chain sequences. **f**, **j**, Unpaired two-tailed *t*-test was performed on the number of expanded clonotypes. Bars show ranges for each dimension. Data are representative of three (**a**) or two (**b**–**j**) independent experiments. All data points are from individual mice.

in any tissue after maximal mucosal exposure (Fig. 2b)—and the diversity of both IgG and IgA was considerably less than that of IgM (Extended Data Fig. 5a). As the dose for mucosal exposure increased, the diversity of CDR3 clonotypes in the IgA heavy chain became more restricted, particularly in the mesenteric lymph nodes (Fig. 2c). By comparison, diversity of the IgG heavy chain in both the spleen and the mesenteric lymph nodes was maintained or further increased with higher levels of systemic exposure (Fig. 2c). We also confirmed directly in sorted cells that repertoire diversity is increased after systemic microbial exposure in IgG memory and plasma cells, but not after either route of exposure in IgA plasma cells (Fig. 2d). Transitory exposure by both the systemic and the mucosal routes generated only small numbers of somatic mutations, which were not substantially increased by increasing the transitory exposure doses (Extended Data Fig. 5b, c). The converse of the breadth of the isotype repertoires is the degree of clonal relatedness, which was higher for IgA than for IgG2b (Extended Data Fig. 5d, e). Mucosal and systemic exposures clearly have different physical constraints in terms of the epithelial barrier and scalability of local antigen processing and presentation to B cells. Nevertheless, our experiments show that increased doses of mucosal microorganisms only narrow the IgA repertoire, whereas the systemic IgG repertoire is progressively diversified as the exposure dose is increased.

To compare directly how immunoglobulin heavy- and light-chain sequences evolve in different mice during microbial exposure at the different sites, we analysed single-cell networks of paired heavy and light chains in naive and class-switched B cells. As shown in Figs. 1g, 2e, f and Extended Data Fig. 6a, b, light-chain diversity made only a minor contribution to the networks. IgA in the mesenteric lymph nodes after intestinal exposure predominantly showed heavy-chain connectivity (including between germ-free and mucosally stimulated mice), whereas IgG networks from the spleen of systemically exposed mice had very few germ-free sequences (Fig. 2e, f). By contrast, germ-free immunoglobulin sequences were present in our analysis of naive B cells and intercalated into the networks of both mucosally and systemically exposed mice (Extended Data Fig. 6a, b). There was spontaneous activation and class-switch recombination to IgA (even in the mesenteric lymph nodes of germ-free mice), whereas splenic B cells became significantly activated after systemic microbial exposure (Extended Data Fig. 6c–f). We conclude that there are clear relationships of class-switched immunoglobulin sequences between mice exposed to different microorganisms in both the mesenteric lymph nodes and the spleen. In diversely colonized mice, polyspecific antibodies have previously been shown to arise from specificities in the germ-free repertoire[16]. We show here that the developing IgA repertoire that is characteristic of mucosal exposure is related to the class-switched immunoglobulin sequences present in germ-free mice.

Oral sensitization of systemic responses

Because mucosal or systemic microbial exposures generate different responses in the B cell repertoire at different thresholds, we asked whether exposure at one site could determine the characteristics of a secondary response at the other. The real-world situation is that there are variable degrees of sequential exposure in both mucosal and systemic compartments.

Oral feeding of a soluble protein antigen tolerizes subsequent B and T cell responses to systemic exposure with the same antigen[17]. By contrast, a sequence of microbial mucosal exposure followed by systemic exposure reduced the threshold for the systemic response by several orders of magnitude compared with intestinal exposure alone (Fig. 3a, Extended Data Fig. 7a). This effect is T-cell-dependent, as shown by the fact that the enhanced systemic response could be abrogated through CD4 T cell depletion at the time of the initial intestinal exposure (Extended Data Fig. 7c–f). Although systemic responses were sensitized by prior mucosal exposure to the same microorganism, this did not work the other way around; systemic exposure did not reduce the subsequent high threshold for mucosal IgA responses primed by the mucosal route (Fig. 3b, Extended Data Fig. 7b).

Given that individual mucosal and systemic exposures lead to different B cell repertoires, we asked whether the order of sequential exposure (systemic to mucosal, or vice versa) makes a difference. Our results showed that, for splenic IgM plasma cells, the site of first exposure determined the resulting repertoire even after subsequent exposure at a different site (Fig. 3c), although the priming may be dominated by the site of first exposure.

Functional effects of sequential exposures

Our final question was how IgA and IgG repertoires build up with successive transitory exposures to different microorganisms. Mucosal exposure to the non-replicating *Salmonella typhimurium* strain HA218 (engineered from a non-invasive, non-virulent parent strain on the same principles as those for *E. coli* HA107[18]) attenuated an established mucosal IgA response to *E. coli* HA107, or vice versa with the opposite order (Fig. 3d, e, Extended Data Fig. 8a). By contrast, the broader systemic IgG response to either microorganism given systemically was unrestricted, irrespective of exposure order (Fig. 3h, i, Extended Data Fig. 8b). The repertoires of CDR3 clonotypes were also biased by the most recent mucosal exposure, whereas after sequential systemic exposures the clustering was distinct regardless of exposure order (Fig. 3g, k). The clonal relatedness and diversity of IgA showed no significant increase after successive treatments, by contrast with the increased IgG clonal diversity and relatedness in the spleen as successive systemic treatments were administered (Fig. 3f, j). These results are consistent with a greater flexibility of new systemic IgG specificities to accommodate a response to another microorganism (in order to avoid systemic sepsis), whereas IgA mucosal protection requires more generic—and probably lower—affinity responses[2,16] that adapt sequentially to many different varieties of overlapping antigen exposure[2,19–21].

Here we have shown that the route and order of exposures to microbial antigens determine the repertoire and functional outcome for B cell immune responses. In general, the systemic exposure thresholds are lower, but trigger responses that expand and diversify the B cell repertoire (as compared with mucosal exposure). This is consistent with the IgA repertoire building on an evolutionarily determined baseline, as some of the clonotypes overlap with immunoglobulin sequences from defined natural antimicrobial specificities (Extended Data Table 1). These different functional demands from B cell immunity offer an explanation for the different characteristics of responses of the B cell system against challenges from the microbiota in different host compartments, the expansion of the same B cell clone in multiple Peyer's patches[22] and poor responses to the mucosal route for vaccination, where limited hygiene results in an increased burden of environmental microorganisms and recurrent mucosal infections[23,24].

Online content

Any methods, additional references, Nature Research reporting summaries, source data, extended data, supplementary information, acknowledgements, peer review information; details of author contributions and competing interests; and statements of data and code availability are available at https://doi.org/10.1038/s41586-020-2564-6.

1. Lindner, C. et al. Age, microbiota, and T cells shape diverse individual IgA repertoires in the intestine. *J. Exp. Med.* **209**, 365–377 (2012).
2. Lindner, C. et al. Diversification of memory B cells drives the continuous adaptation of secretory antibodies to gut microbiota. *Nat. Immunol.* **16**, 880–888 (2015).
3. Hapfelmeier, S. et al. Reversible microbial colonization of germ-free mice reveals the dynamics of IgA immune responses. *Science* **328**, 1705–1709 (2010).
4. Berg, R. D. Bacterial translocation from the gastrointestinal tract. *Adv. Exp. Med. Biol.* **473**, 11–30 (1999).
5. Lockhart, P. B. et al. Bacteremia associated with toothbrushing and dental extraction. *Circulation* **117**, 3118–3125 (2008).
6. Xu, J. L. & Davis, M. M. Diversity in the CDR3 region of V_H is sufficient for most antibody specificities. *Immunity* **13**, 37–45 (2000).
7. Soto, C. et al. High frequency of shared clonotypes in human B cell receptor repertoires. *Nature* **566**, 398–402 (2019).
8. Koch, M. A. et al. Maternal IgG and IgA antibodies dampen mucosal T helper cell responses in early life. *Cell* **165**, 827–841 (2016).
9. Gomez de Agüero, M. et al. The maternal microbiota drives early postnatal innate immune development. *Science* **351**, 1296–1302 (2016).
10. Zeng, M. Y. et al. Gut microbiota-induced immunoglobulin G controls systemic infection by symbiotic bacteria and pathogens. *Immunity* **44**, 647–658 (2016).
11. Chen, Y. et al. Microbial symbionts regulate the primary Ig repertoire. *J. Exp. Med.* **215**, 1397–1415 (2018).
12. Wilmore, J. R. et al. Commensal microbes induce serum IgA responses that protect against polymicrobial sepsis. *Cell Host Microbe* **23**, 302–311 (2018).
13. Pepys, M. B. Role of complement in induction of antibody production in vivo: effect of cobra factor and other C3-reactive agents on thymus-dependent and thymus-independent antibody responses. *J. Exp. Med.* **140**, 126–145 (1974).
14. Sörman, A., Zhang, L., Ding, Z. & Heyman, B. How antibodies use complement to regulate antibody responses. *Mol. Immunol.* **61**, 79–88 (2014).
15. Stoel, M. et al. Restricted IgA repertoire in both B-1 and B-2 cell-derived gut plasmablasts. *J. Immunol.* **174**, 1046–1054 (2005).
16. Bunker, J. J. et al. Natural polyreactive IgA antibodies coat the intestinal microbiota. *Science* **358**, eaan6619 (2017).
17. Mowat, A. M., Faria, A. M. & Weiner, H. L. in *Mucosal Immunology* Vol. 1 (eds J. Mestecky et al.) 487–537 (Elsevier, 2005).
18. Pfister, S. P. et al. Uncoupling of invasive bacterial mucosal immunogenicity from pathogenicity. *Nat. Commun.* **11**, 1978 (2020).
19. Boursier, L., Dunn-Walters, D. K. & Spencer, J. Characteristics of IgV_H genes used by human intestinal plasma cells from childhood. *Immunology* **97**, 558–564 (1999).
20. Casola, S. et al. B cell receptor signal strength determines B cell fate. *Nat. Immunol.* **5**, 317–327 (2004).
21. Dunn-Walters, D. K., Boursier, L. & Spencer, J. Hypermutation, diversity and dissemination of human intestinal lamina propria plasma cells. *Eur. J. Immunol.* **27**, 2959–2964 (1997).
22. Bergqvist, P. et al. Re-utilization of germinal centers in multiple Peyer's patches results in highly synchronized, oligoclonal, and affinity-matured gut IgA responses. *Mucosal Immunol.* **6**, 122–135 (2013).
23. Levine, M. M. Immunogenicity and efficacy of oral vaccines in developing countries: lessons from a live cholera vaccine. *BMC Biol.* **8**, 129 (2010).
24. Valdez, Y., Brown, E. M. & Finlay, B. B. Influence of the microbiota on vaccine effectiveness. *Trends Immunol.* **35**, 526–537 (2014).

Methods

No statistical methods were used to predetermine sample size. The experiments were not randomized and investigators were not blinded to allocation during experiments and outcome assessment.

Mice

Germ-free C57BL/6 mice (males or females, 8–16 weeks of age) were bred and maintained in flexible-film isolators at the Clean Mouse Facility (University of Bern). Sex balance was ensured in all experimental groups and germ-free status was routinely monitored by culture-dependent and -independent methods. All mouse experiments were performed in accordance with Swiss Federal regulations approved by the Commission for Animal Experimentation of Kanton Bern. Group sample sizes of ≥3 mice were determined from preliminary experiments that indicated sufficient power to discriminate repertoire effects. Computational analysis, but not experimental processing, was blinded to the treatment of each animal.

Bacterial culture

Escherichia coli HA107 and non-invasive non-virulent *S. typhimurium* HA218 (UK-1 Δ*asd*, Δ*alr*, Δ*dadX*, Δ*metC::tetRA*, Δ*ssaV::camR*, Δ*invC::aphT*) were cultured overnight in LB medium containing 100 μg/ml meso-DAP and 400 μg/ml D-alanine at 37 °C, shaking at 200 rpm[3]. A full description of in vivo characteristics of the reversible *Salmonella* strain has been published separately[18]. *Enterobacter cloacae* was cultured in LB medium at 37 °C, 200 rpm. *Clostridium orbiscindens* (DSMZ 8061) was cultured in BHI medium with additional haemin and vitamin K at 37 °C in a Whitley MG500 anaerobic incubator gassed with 10% (v/v) H_2, 10% CO_2 and 80% N_2. Reversible colonisations with *C. orbiscindens* (DSMZ 8061) were confirmed through culture-dependent and -independent methods to return to germ-free status after live exposure. To prepare gavage solutions or intravenous injections, bacteria were centrifuged for 10 min at 4,000*g* and washed twice with sterile PBS. The required dose was resuspended in 500 μl of sterile PBS and administered to germ-free mice by oral gavage or injection into the tail vein.

Preparation of *E. coli* HA107 lysates and subfractions

Overnight culture of *E. coli* HA107 was collected, washed with PBS and resuspended at 10^{10} CFU/ml in PBS. Bacterial cells were disrupted by ultrasound using the Bioruptor system for 15 min at 4 °C (Diagenode, 30-s on/30-s off mode). The lysate was centrifuged at 10,000*g* for 10 min, diluted and sterilized by 0.2-μm filtration before in vivo treatment or further fractionation. The lysate was fractionated into membrane and cytoplasmic fractions by ultracentrifugation (Optima MAX-TL benchtop ultracentrifuge, Beckman) for 10 min, 100,000*g*. The cytoplasmic supernatant was collected and the pellet containing membranes was resuspended in PBS. An 18-h ultracentrifugation at 100,000*g* was performed on the cytoplasmic fraction to separate the ribosomal fraction from the non-ribosomal fraction[25]. Protein concentrations were quantified using the Pierce BCA assay kit (Thermo Fisher Scientific).

Systemic and intestinal exposure to live reversible *E. coli* HA107

For systemic exposure, germ-free mice were aseptically transferred to a laminar flow hood. Doses (10^2–10^8 CFU, as shown) of *E. coli* HA107 were administered into the tail vein. For intestinal exposure, mice received 10^2–10^{10} CFU of *E. coli* HA107 by oral gavage within germ-free isolators[3]. When multiple doses were administered, mice received three doses on alternate days. Mice were analysed two weeks after administration of the last exposure dose.

Systemic and intestinal priming of immune responses with *E. coli* HA107 lysate

The preparation of bacterial lysates was performed as described in 'Preparation of *E. coli* HA107 lysates and subfractions'. Germ-free mice were treated with bacterial lysates (dose equivalent to 10^8 intact bacteria) either systemically or orally on alternate days. Mice were analysed two weeks after administration of the last priming dose.

Combined intestinal and systemic priming with *E. coli* HA107

Germ-free C57BL/6 mice were divided into two groups. In the first scenario, a group of mice was treated with three doses of 10^{10} CFU of HA107 orally on days 0, 2 and 4, and the other group were unprimed controls. Both groups of mice (intestinally primed with 3 doses of 10^{10} CFU of *E. coli* HA107 and control mice) received an intravenous injection of 10^3–10^7 CFU (as shown) of *E. coli* HA107 on day 21.

In the second, converse scenario, a group of mice was treated 3 times with 10^8 CFU of HA107 systemically on days 0, 2 and 4 and the other group were unprimed controls. Both groups of mice subsequently received 3 intragastric doses of 10^7–10^9 CFU (as shown) of *E. coli* HA107 on days 21, 23 and 25. All mice from both scenarios were analysed on day 42.

Combined priming with *E. coli* HA107 and *S. typhimurium* HA218

For mucosal priming, germ-free mice received 10^{10} CFU of *E. coli* HA107 by gavage on days 0, 2 and 4, or were unprimed controls. Subsequently, half the mice in both groups received 3 doses of 10^{10} CFU *S. typhimurium* HA218 on days 21, 23 and 25 by gavage, and the other half received no further priming. Within the same experiment further groups received the opposite treatment sequence of *S. typhimurium* HA218 to *E. coli* HA107. Systemic priming was carried out using groups of germ-free mice with the above schedule in both treatment orders, except that 3 doses of 10^8 CFU of *E. coli* HA107 or *S. typhimurium* HA218 by intravenous injection were used instead of the intestinal treatments for mucosal priming. Recovery of germ-free status was verified at each stage. All mice were analysed on day 42.

Priming with cholera toxin subunit B

Germ-free mice each received 3 doses of intragastric (15 μg) or intravenous (15 μg) cholera toxin B (CTB) on alternate days and were analysed 3 weeks after the last priming dose. For intragastric delivery, CTB was dissolved in 0.1 M sodium bicarbonate (pH 9); systemic delivery was in PBS.

Bacterial fluorescence-activated cell sorting

Bacterial FACS was performed as described previously[3], with the following refinements. *E. coli* HA107 was incubated with serum or intestinal washes with starting dilutions at 1/10 for serum, or undiluted for intestinal washes: in each sample the concentrations of different immunoglobulin isotypes had been measured separately by ELISA, as detailed below. After incubation and washing to remove unbound antibodies, the samples were incubated further at 4 °C for 2 h either with secondary anti-mouse IgA–FITC (BD Biosciences C10-3) or anti-mouse IgG2b–FITC (BD Biosciences R12-3). Bacteria were acquired on a BD FACSArray using FSC and SSC parameters in logarithmic mode. The FACS data were analysed using FlowJo software (TreeStar), and the levels of bacteria-specific antibodies present in the samples were expressed as the geometric mean against the absolute immunoglobulin concentration in the sample.

ELISA

Immunoglobulin-specific ELISAs were performed as previously described[26] using goat anti-mouse IgA, IgM, IgG1, IgG2b, IgG2c, IgG3 coating antibodies from SouthernBiotech. Antibody standards were purified mouse myeloma immunoglobulin of the required isotype with peroxidase-coupled secondary antibodies as previously detailed. The same protocol was used for antigen-specific ELISA, except that ELISA plates were first coated overnight with 10 μg/ml of HA107 membrane, cytoplasmic, ribosomal or non-ribosomal fractions.

Immunoblotting

Bacterial (*E. cloacae*) cytoplasmic proteins (10 μg/ml) were loaded to 12% SDS–PAGE and electrophoresed for 45 min at 90V; subsequently they were either stained directly for proteins or transferred to a nitrocellulose membrane. After blocking with 3% BSA, the membrane was incubated with intravenous primed mouse serum diluted at 1:30 in PBS for 1 h at room temperature. Peroxidase-conjugated goat anti-mouse IgG catalysis of 3, 3′-diaminobenzidine was used to detect bound IgG[27].

LPS versus 16S rRNA measurements

Germ-free mice were treated either systemically with 10^8 CFU of *E. coli* HA107 or mucosally with 10^{10} CFU of *E. coli* HA107. Mice were dissected 18 h later. Spleen and MLN were collected and disaggregated on baked 40-μm metal cell strainers using PBS. Samples were then split into two portions for either LPS or 16S rRNA estimation.

LPS measurements. Samples were centrifuged (350*g*, 5 min) to remove intact cells. Supernatants were heated at 70 °C for 30 min and cleared by centrifugation at 10,000*g*. LPS was quantified using the EndoZyme II Recombinant Factor C Endotoxin Detection Assay (Hyglos, BioMérieux no. 890030) according to the manufacturer's instructions, using tenfold dilutions to circumvent interference. After incubation at 37 °C for 90 min fluorescence was measured at an excitation of 380 nm and an emission of 445 nm (Infinite Pro 200, Tecan). End-point fluorescent measurements with blank corrections and standards from 0.005–5 EU/ml were used. Standard curve generation and regression analysis performed in GraphPad Prism were used to estimate LPS concentrations in samples, with extrapolation of the standard curve based on the regression parameters. Samples and standards were measured in duplicate.

16S measurements. Total RNA was extracted from samples using the DNA-RNA all prep kit (Qiagen), and real-time PCR was performed on synthesized cDNA using forward (5′-ATG CGT AGA GAT CTG GAG G-3′) and reverse primers (5′-CAA CCT CCA AGT CGA CAT C-3′) for 16S ribosomal gene amplification.

Lymphocyte isolation

To isolate lymphocytes from spleens, lymph nodes and Peyer's patches, tissues were cut into small pieces and digested in IMDM (2% FCS) containing collagenase type IA (1 mg/ml, Sigma) and DNase I (10 U/ml, Roche) at 37 °C for 30 min. Cellular suspensions were passed through a cell strainer (40 μm) and washed with IMDM (2% FCS, 2mM EDTA). Erythrocytes in splenic suspensions were lysed using 0.84% NH_4Cl for 2 min at room temperature. Cells were finally resuspended in FACS buffer and counted in a Neubauer chamber.

Flow cytometry

After isolation, cells were washed once with PBS before staining with fixable viability dye diluted in PBS (eBisocience) for 30 min on ice. Single-cell suspensions were sequentially incubated with primary biotin- or fluorescence-coupled antibodies diluted in FACS buffer. The following mouse-specific conjugated antibodies were used: B220–FITC (RA3-6B2, Biolegend), BCL6–AlexaFluor647 (K112-91, BD Biosciences), CD3–BV785 (17A2, Biolegend), CD4–PE (RM4-5, Biolegend), CD11b–PEcy7 (M1/70, Biolegend), CD19–AF700 (6D5, Biolegend), CD21–FITC (7E9, Biolegend), CD22–FITC (OX-97, Biolegend), CD23–PerCPcy5.5 (B3B4, Biolegend), CD25–PerCP–cy5.5 (PC61, Biolegend), CD43–FITC (1B11, Biolegend), CD80–PerCPcy5.5 (16-10A1, Biolegend), CD86–BV421 (GL-1, Biolegend), CD93–PEcy7 (AA4.1, Biolegend), CD138–PE (281-2, Biolegend), CD273–APC (TY25, Biolegend), CXCR5–biotin (2G8, BD Biosciences), IgA–FITC (C10-3, BD Biosciences), IgG2b–FITC (R12-3, BD Biosciences), IgM–PEcy7 (RMM-1, Biolegend), Ly77–BV421 (GL-7, BD Biosciences) and PD-1–PE (RMP1-30, Biolegend). Streptavidin–APC (BD Biosciences) was used together with biotin-coupled antibodies. Data were acquired on an LSRFortessa (BD Biosciences) and analysed using FlowJo software (Tree Star). In all experiments, FSC-H versus FSC-A was used to gate singlets, and to exclude dead cells using the fluorescence-coupled fixable viability dye (eBisocience). B lineage subsets were stained for flow cytometry cell sorting as: pre B cells from bone marrow (live/dead$^-$CD3$^-$CD19$^+$CD138$^-$IgM$^-$CD25$^+$), plasma cells from bone marrow (live/dead$^-$CD3$^-$CD138$^+$CD19$^-$CD22$^-$), transitional B cells from spleen (live/dead$^-$CD3$^-$CD19$^+$CD138$^-$GL7$^-$CD93$^+$), splenic IgM$^+$ plasma cells (live/dead$^-$CD3$^-$CD19$^-$CD138$^+$IgM$^+$), splenic IgG2b$^+$ plasma cells (live/dead$^-$CD3$^-$CD19$^-$GL7$^-$CD138$^+$IgG2b$^+$), follicular splenic B cells (live/dead$^-$CD3$^-$CD19$^+$CD93$^-$CD138$^-$CD23^{high}CD21^{low}), splenic marginal zone B cells (live/dead$^-$CD3$^-$CD19$^+$CD93$^-$CD138$^-$CD23^{low}CD21^{high}), splenic IgM$^+$ memory cells (live/dead$^-$CD3$^-$CD19$^+$CD138$^-$CD80$^+$CD273$^+$IgM$^+$)[28], splenic IgG2b$^+$ memory cells (live/dead$^-$CD3$^-$CD19$^+$GL7$^-$CD138$^-$IgG2b$^+$), peritoneal B2 cells (live/dead$^-$CD3$^-$CD19$^+$CD23$^+$CD43$^-$), peritoneal B1a cells (live/dead$^-$CD3$^-$CD19$^+$CD23$^-$CD43$^+$B220^{low}IgM^{high}), peritoneal B1b cells (live/dead$^-$CD3$^-$CD19$^+$CD23$^-$CD11b$^+$B220^{high}IgM^{low}) and splenic/MLN IgA$^+$ plasma cells (live/dead$^-$CD3$^-$CD19$^-$GL7$^-$CD138$^+$IgA$^+$).

In vitro primary cell culture

Primary cells were isolated from spleen, Peyer's patches and MLN from germ-free or *E.-coli*-HA107-conditioned mice. Tissues were disaggregated through 40-μm cell strainers and flushed with 10 ml IMDM + GlutaMax (GIBCO) supplemented with 10% FCS (Invitrogen). Cell suspensions were centrifuged (350*g*, 5 min, 4 °C) and erythrocyte lysis from splenic samples was performed as described in 'Lymphocyte isolation'.

For the estimation of IgA and IgG2b production by B cells, cells were centrifuged again and resuspended in complete IMDM medium IMDM + GlutaMAX (GIBCO), supplemented with 10% FCS (Invitrogen), 10,000 μg/ml streptomycin (GIBCO), 10,000 U/ml penicillin (GIBCO), 50 μM 2-mercaptoethanol (Merck). The cell suspensions were seeded at a density of 10^6 cells/ml in 200 μl of complete IMDM medium per well, in 96-well round-bottom tissue culture plates. The cell cultures were incubated at 37 °C, 5% CO_2. Viability of the cultured cells was controlled daily microscopically. Supernatants were collected after five days and antibody concentrations were determined using ELISA as described in 'ELISA'.

For the assessment of repertoire reprogramming to antigen exposure, an aliquot of cells was collected and CD86$^+$CD138$^+$ antigen-experienced plasma cells were sorted and used as pre-treatment controls. Remaining cells were seeded at a density of 10^6 cells/ml in RPMI 1640 medium supplemented with FCS, streptomycin, penicillin and β-mercaptoethanol as above, with the addition of 10 ng/ml recombinant IL-4 (Peprotech) in a 48-well flat-bottomed plate. *Escherichia coli* cytoplasmic and membrane fractions were added at 5 μg/ml (protein equivalent) to culture wells. The culture conditions were as detailed above. On day 6, cells were collected, and CD86$^+$CD138$^+$ plasma cells were FACS-sorted for repertoire analysis.

CD4 T cell depletion

Germ-free mice were injected intraperitoneally either with 250 μg of anti-CD4 antibody (clone GK5.1, Bioexcel) or an isotype control (clone LTF-2, Bioexcel) diluted in 250 μl of PBS on day −3 before intestinal exposure with 3×10^{10} CFU *E. coli* HA107 on days 0, 2 and 4. T cell depletion and recovery were confirmed by flow cytometry on blood samples taken on days 0 and 21, respectively. All mice received a single intravenous dose of 10^7 CFU *E. coli* HA107 on day 21. Mice were analysed on day 42.

Immunoglobulin repertoire bulk sequencing

Tissues were removed and snap-frozen in Trizol reagent using liquid nitrogen. Thawed tissues were immediately homogenized (Retsch bead-beater) in 1 ml of Trizol reagent (Life Technologies). Chloroform

(200 µl) was added, samples were mixed, and centrifuged (12,000*g*, 15 min, 4 °C). The upper phase was collected, and RNA was precipitated with ice-cold isopropanol by centrifugation (12,000*g*, 10 min, 4 °C). The RNA pellet was washed with 75% (v/v) ethanol, dried and resuspended in RNase-free water. RNA concentrations and purity were analysed using a Nanodrop2000 (Thermo Scientific).

For IgA, cDNA synthesis was performed by mixing 700 ng of RNA, 1 µl of 2 µM gene-specific primer mix[1], 1 µl of 10 mM of dATP, dCTP, dGTP and dTTP (Invitrogen), with dH_2O to a total volume of 13 µl. For IgM and IgG2b heavy chains and light chains, oligo(dT) primers were used for cDNA synthesis. Samples were then heated to 65 °C for 5 min, after which they were put on ice for a minimum of 1 min. Tubes were shortly centrifuged to collect contents, and in a second reaction step, 4 µl 5× first strand buffer (Invitrogen), 1 µl 0.1 M DTT (Invitrogen), 1 µl RNaseOUT (Invitrogen) and 1µl Superscript III RT enzyme (Invitrogen) were added to the reaction, mixed and incubated at 55 °C for 50 min. The reaction was terminated by heat inactivation at 70 °C for 15 min followed by cooling at 4 °C. Samples were stored at −20 °C until further processing.

Amplicon PCR for IgA, IgM or IgG2b heavy chains and κ or λ light chains was performed by mixing 5 µl of 10× PlatinumTaq PCR buffer (Qiagen), 1 µl of 10 mM mixed dNTPs, 0.2 µl of PlatinumTaq DNA Polymerase (Qiagen), 1.5 µl of 50 mM $MgCl_2$, 1 µl of each 100 µM forward primer mix and reverse primers (see sequences in Supplementary Table E, according to chain and isotype), 5 µl template cDNA, in a total volume of 50 µl. The forward primers consisted of a degenerative mix of 19 different primers binding into FR1 as previously described[29,30]. Reverse primers were complementary to the constant region of each isotype (see sequences in Supplementary Table E). All primers used in the study are detailed in the Supplementary Information.

PCR products were loaded onto a 1.5% (w/v) agarose gel and purified with the QIAquick Gel Extraction kit (Qiagen) according to the manufacturer's instructions. The purified DNA was tested for quality and quantity using a 2100 Bioanalyzer (Agilent) and Qbit (Thermofisher). A second PCR was performed to attach sample indices and sequencing adapters using the Nextera XT Index Kit (Illumina). Subsequent sample sizes and quality were tested with a Fragment Analyzer (Advanced Analytical), normalized and libraries were pooled for sequencing on the MiSeq Illumina sequencer in the paired 250-bp mode, or the 300-bp mode for experiments containing UMIs.

Repertoire sequencing and pre-processing

Antibody variable heavy-chain (V_H) libraries were prepared as previously described[31], and sequenced on the Illumina MiSeq platform (2 × 250 cycles, paired-end) with 10% PhiX control library. Mean base-call quality of all samples was in the range of Phred score 30. The resulting FASTQ files were pre-processed (VDJ alignment, clonotyping) using the MiXCR software package v.2.1.12 (clonotype formation by CDR3 amino acid region annotated using C57BL/6J germline gene data[32] (available at http://mixcr.milaboratory.com/ and https://github.com/milaboratory/mixcr/)).

MIXCR considers sequence quality and corrects PCR and sequencing errors in the alignment step to the reference V, D and J germline segments. The error correction is done by assembling the clonotypes with a heuristic multilayer clustering, which can be summarized as follows. The algorithm consists of two steps: (a) a *k*-mer chaining algorithm is used, then—to find the optimal reference sequence—a heuristic search is performed to maximize a scoring function that takes into account variations (deletions, insertions and mutations) in the sequence reads. (b) Subsequently, multiple candidate alignments are built and a classical alignment score (scoring matrix and penalties for indels) is calculated. Reads are filtered on the basis of these values. Then, clonotypes are assembled and those presenting errors are further removed by clustering similar sequences on the basis of a defined similarity threshold (clonotyping). Finally, MIXCR rescues low-quality reads in a later step by mapping them to previously assembled high-quality clonotypes to preserve maximal quantitative information. Singletons (supported by only a single read) were excluded from clonotype output[29,32], as previously described[33].

For all analyses, except where nucleotide analysis combined with V and J segment information is specified, clones were defined by 100% amino acid sequence identity of CDR3 regions. CDR3 regions were defined by MiXCR according to the nomenclature of the Immunogenetics database (IMGT)[34].

Clonal analysis and quantification of repertoire convergence

MIXCR output files were further processed in VDJtools post-analysis framework[35] (available at https://github.com/mikessh/vdjtools) to further analyse clonotype diversity, V gene use and sample clustering on the basis of CDR3 abundance. Further filtering was applied to keep only in-frame, productive sequences. Basic statistic segment use was calculated, and weighted variable use profiles were hierarchically clustered and visualized as heat maps. Repertoire overlap was measured by calculating the geometric mean of relative overlap frequencies between variable segment use profiles or CDR3 amino acid sequence use. The relative overlap similarity was represented as hierarchical clustering or MDS plots. Heat maps following the top100 clonotypes (ranked by abundance) present in at least 2 samples were generated on the basis of an all-versus-all intersection between chosen samples with settings = 'strict', meaning intersections had to contain the identical nucleotide sequence (CD3nt sequence + V gene + J gene). The corresponding CDR3 amino acid sequences are provided in the Supplementary Tables, numbered respective to the figures in which each heat map is found.

Technical replicate sequencing and UMI pre-processing

Technical reproducibility as previously described[29,31] was tested on cDNA derived from 9 C57BL/6 mice. cDNA was split into three portions and library preparation was performed in parallel with different Illumina indices according to the manufacturer's instructions and protocol. Replicate samples were sequenced with the same sequencing depth. cDNA was amplified using primers with the alternative primer design approaches of 15 nucleotide unique molecular identifiers (UMI_1)[36] or with UMI with fixed positions preventing secondary structures (UMI_2)[37] by PCR in a multiplex reaction using primer sets as described for the Illumina protocol above. Raw reads were demultiplexed and exported without the sample barcodes or Illumina clustering adapters. Pre-processing of the raw demultiplexed reads was carried out using pRESTO[38]. Reads with a mean Phred quality score below 20 were removed, then those without valid forward (V-region) and reverse (isotype specific constant region) primer sequence matches were removed (match error rate of 0.2). The forward primer regions were masked (with Ns) and the reverse primer regions were deleted from the sequence. Reads with identical UMIs were collapsed into a single consensus sequence for each UMI. UMI read groups with a nucleotide diversity score exceeding 0.1 were discarded. Finally, corrected consensus sequence read pairs were assembled into full length sequences with a maximum allowed error rate of 0.2 and *P* value threshold of 0.1. All unique sequences that were not represented by at least two raw reads were removed from further analysis and duplicate full-length sequences were discarded. Following pre-processing, sequences were further processed using MIXCR as described in 'Repertoire sequencing and pre-processing' with the computational correction of PCR errors option turned off (-OcloneClusteringParameters = null).

Mutation and N-joints

To resolve junctional and N-joint regions, the V, N1, D, N2 and J subregions were defined on the sequences exported using MIXCR. Normalized CDR3 subregion (V, N1, D, N2 and J) lengths (median) of clonotypes by B cell subpopulation were calculated. Mutation analysis was performed on the annotated sequences exported using MIXCR excluding N-joint regions. Each mutation was reported at the amino acid level for V and J segments counted per sequence. The median number of mutations per sequence over a given repertoire is reported.

Rarefaction plots

To explore the relationship between sample size and diversity coverage, rarefaction and extrapolation sampling curves were generated using the iNEXT R package[39].

Determination of sequence similarity among clones within a repertoire

The Levenshtein distance between all pairwise CDR3 amino acid sequence combinations of identical CDR3 amino acids was calculated, and each Levenshtein distance was subsequently normalized by the sequence length of the respective sequence combination. Levenshtein distances were computed using the stringdist package in R[40].

Network construction and analysis

The networks were constructed by representing each unique amino acid CDR3 sequence (clone) as nodes. Clones that were exactly one amino acid substitution, insertion or deletion (Levenshtein distance = 1) apart were connected by edges as previously described[41]. An antibody repertoire network is an undirected graph $G = (V, E)$ described as a set of nodes (CDR3 vertices, V) together with a set of connections (similarity edges, E), representing the adjacency matrix A of pairwise Levenshtein distances (LD) between CDR3 amino acids.

Degrees (number of similar CDR3 sequences to a specific CDR3 sequence) were calculated for each similarity layer LD1 for each CDR3 sequence in each sample. CDR3 with zero degrees that were not similar to any other CDR3 in the network were excluded to fit degree distributions. The contribution of expanded clonotypes within a given repertoire consisted of the sum of clonotypes with a degree ≥ 1 on a Levenshtein distance 1 network over the size of the repertoire. The networks were visualized employing Cytoscape or the Fruchterman–Reingold layout and Kamada–Kawai layout algorithms using the igraph R package[42]. For networks based on single-cell data, concatenated heavy- and light-chain amino acid CDR3 sequences from the same cell were analysed.

Single-cell transcriptomics and repertoire sequencing

Germ-free mice were mucosally exposed to 3×10^{10} CFU *E. coli* HA107, systemically exposed to 3×10^{8} CFU *E. coli* HA107 or maintained as germ-free controls. Spleens and mesenteric lymph nodes were removed on day 21 and disaggregated to single-cell suspensions. Cells were enriched for CD138$^+$ plasma cells by magnetic cell sorting. Cells were washed once and resuspended in PBS/0.05% (w/v) BSA. The 10x Genomics platform was used to perform concurrent B cell V(D)J repertoire sequencing and single cell 5′ gene expression analysis. Prepared libraries were sequenced on an Illumina NovaSeq 6000 (2 × 150 cycles, paired-end mode).

V(D)J immunoglobulin single-cell sequencing analysis

Processing raw sequencing data. The CellRanger software version 3.0.1 was used to process the raw sequencing data produced by the 10x Chromium direct immunoglobulin enrichment. The 10x Genomics mouse genome GRCm38.93 3.0.0 release was used as reference for the alignments. The 'filtered contigs' files were subsequently used for downstream analyses.

V(D)J annotation of BCR contigs. Following pre-processing, sequences were further analysed using MIXCR v.2.1.12 as described in 'Repertoire sequencing and pre-processing' with the computational correction of PCR errors option turned off (-OcloneClusteringParameters = null). V(D)J alignment and annotation was performed against C57BL/6J germline gene data. CDR3 regions were defined by MIXCR according to the nomenclature of the Immunogenetics database (IMGT). Clonotypes were defined by 100% amino acid sequence identity of CDR3 regions.

Filtering and display of relationships between exposure conditions in B cell receptor repertoire contigs and cells. As with bulk Repseq analyses, only productively rearranged clonotypes were used. Cells with one heavy chain contig paired with one light chain contig were kept for downstream analysis. Cells remaining were checked to have a transcriptomic profile consistent with B-cells (cells with any one of the following markers: CD19, CD138 or the isotype-encoding genes with a positive log-normalized expression level). Given the limited output at single-cell level, repertoire overlap was relaxed from 100% to 90% amino acid identity incorporating a length correction[2]. The relative overlap was normalized for the resulting repertoire size and similarity was represented as hierarchical clustering or MDS plots.

Statistical significance

Statistical significance was tested either using Student *t*-test or the Wilcoxon rank–sum test followed by a Benjamini–Hochberg correction for false discovery rate. Results were considered significant for adjusted $P < 0.05$.

Availability of biological materials

The bacterial strains for reversible germ-free colonisation can be obtained without restriction from A.J.M. and S.H. following a material transfer agreement with the University of Bern.

Reporting summary

Further information on research design is available in the Nature Research Reporting Summary linked to this paper.

Data availability

The raw files for the datasets generated during this study are available on the Sequence Read Archive, Bioproject accession PRJNA625440. The pre-processed files (clonotype list and properties) are available on the GitHub repository https://github.com/Mucosal-Immunology-Bern/Manuscript-microbiota-and-B-cell-repertoire.

Code availability

The associated codes for the analysis using R packages can be found at https://github.com/Mucosal-Immunology-Bern/Manuscript-microbiota-and-B-cell-repertoire.

25. Rivera, M. C., Maguire, B. & Lake, J. A. Isolation of ribosomes and polysomes. *Cold Spring Harb. Protoc.* **2015**, pdb.prot081331 (2015).
26. Slack, E. et al. Innate and adaptive immunity cooperate flexibly to maintain host-microbiota mutualism. *Science* **325**, 617–620 (2009).
27. Macpherson, A. J. et al. A primitive T cell-independent mechanism of intestinal mucosal IgA responses to commensal bacteria. *Science* **288**, 2222–2226 (2000).
28. Tomayko, M. M., Steinel, N. C., Anderson, S. M. & Shlomchik, M. J. Cutting edge: hierarchy of maturity of murine memory B cell subsets. *J. Immunol.* **185**, 7146–7150 (2010).
29. Greiff, V. et al. Quantitative assessment of the robustness of next-generation sequencing of antibody variable gene repertoires from immunized mice. *BMC Immunol.* **15**, 40 (2014).
30. Krebber, A. et al. Reliable cloning of functional antibody variable domains from hybridomas and spleen cell repertoires employing a reengineered phage display system. *J. Immunol. Methods* **201**, 35–55 (1997).
31. Menzel, U. et al. Comprehensive evaluation and optimization of amplicon library preparation methods for high-throughput antibody sequencing. *PLoS ONE* **9**, e96727 (2014).
32. Bolotin, D. A. et al. MiXCR: software for comprehensive adaptive immunity profiling. *Nat. Methods* **12**, 380–381 (2015).
33. Greiff, V. et al. Systems analysis reveals high genetic and antigen-driven predetermination of antibody repertoires throughout B cell development. *Cell Rep.* **19**, 1467–1478 (2017).
34. Lefranc, M. P. et al. IMGT, the international ImMunoGeneTics database. *Nucleic Acids Res.* **27**, 209–212 (1999).
35. Shugay, M. et al. VDJtools: unifying post-analysis of T cell receptor repertoires. *PLoS Comput. Biol.* **11**, e1004503 (2015).

36. Stern, J. N. et al. B cells populating the multiple sclerosis brain mature in the draining cervical lymph nodes. *Sci. Transl. Med.* **6**, 248ra107 (2014).
37. Khan, T. A. et al. Accurate and predictive antibody repertoire profiling by molecular amplification fingerprinting. *Sci. Adv.* **2**, e1501371 (2016).
38. Vander Heiden, J. A. et al. pRESTO: a toolkit for processing high-throughput sequencing raw reads of lymphocyte receptor repertoires. *Bioinformatics* **30**, 1930–1932 (2014).
39. Hsieh, T., Ma, K. & Chao, A. iNEXT: an R package for rarefaction and extrapolation of species diversity (Hill numbers). Methods *Ecol. Evol.* **7**, 1451–1456 (2016).
40. van der Loo, M. The stringdist package for approximate string matching. *R Journal* **6**, 111–122 (2014).
41. Miho, E., Roškar, R., Greiff, V. & Reddy, S. T. Large-scale network analysis reveals the sequence space architecture of antibody repertoires. *Nat. Commun.* **10**, 1321 (2019).
42. Csardi, G. & Nepusz, T. The igraph software package for complex network research. *Interjournal Complex Syst.*, **2006**, 1695 (2006).

Acknowledgements We thank M. Gomez de Agüero, T. Leeb, P. Nicholson, M. Geuking and D. Candinas. The Clean Mouse Facility is supported by the Genaxen Foundation, Inselspital and the University of Bern. This work was funded by the Swiss National Science Foundation (SNSF CRSII5_177164, SNSF 310030_179479) and the European Research Council (H2020 ERC-2016-ADG HHMM_Neonates, Grant Agreement: 742195) to A.J.M. S.C.G.-V. was funded by a Marie Curie Intra-European Fellowship (FP7-PEOPLE-2013-IEF project no. 627206), a long-term fellowship from the European Molecular Biology Organization and the Peter Hans Hofschneider Endowed Professorship by Stiftung Experimentelle Biomedizin. V.G. acknowledges the support of UiO:LifeSciences Convergence Environment Immunolingo and EU H2020 iReceptorplus (no. 825821). S.H. was funded by SNSF grant 169791 and ERC StG 281904. K.D.M. was funded by the ERC StG 281785. M.H. was funded by an ERC CoG (HepatoMetaboPath). J.P.L. was supported by a SystemsX Transition Postdoc Fellowship (TPdF2013/139).

Author contributions H.L., J.P.L., S.C.G.-V. and A.J.M. conceived the study, interpreted data and wrote the manuscript. H.L. and S.C.G.-V. performed most experiments. J.P.L. and V.G. carried out computational analysis. B.Y., M.A.E.L., S.R., M.H. and K.D.M. helped with repertoire experiments. O.S. and S.H. contributed bacterial strains and culture preparation. C.U., M.Z. and I.D.Y. helped with ex-vivo analyses of bacterial fractions and cellular responses.

Competing interests The authors declare no competing interests.

Additional information
Supplementary information is available for this paper at https://doi.org/10.1038/s41586-020-2564-6.
Correspondence and requests for materials should be addressed to S.C.G.-V. or A.J.M.
Peer review information *Nature* thanks Rodney Newberry, Duane R. Wesemann and the other, anonymous, reviewer(s) for their contribution to the peer review of this work.

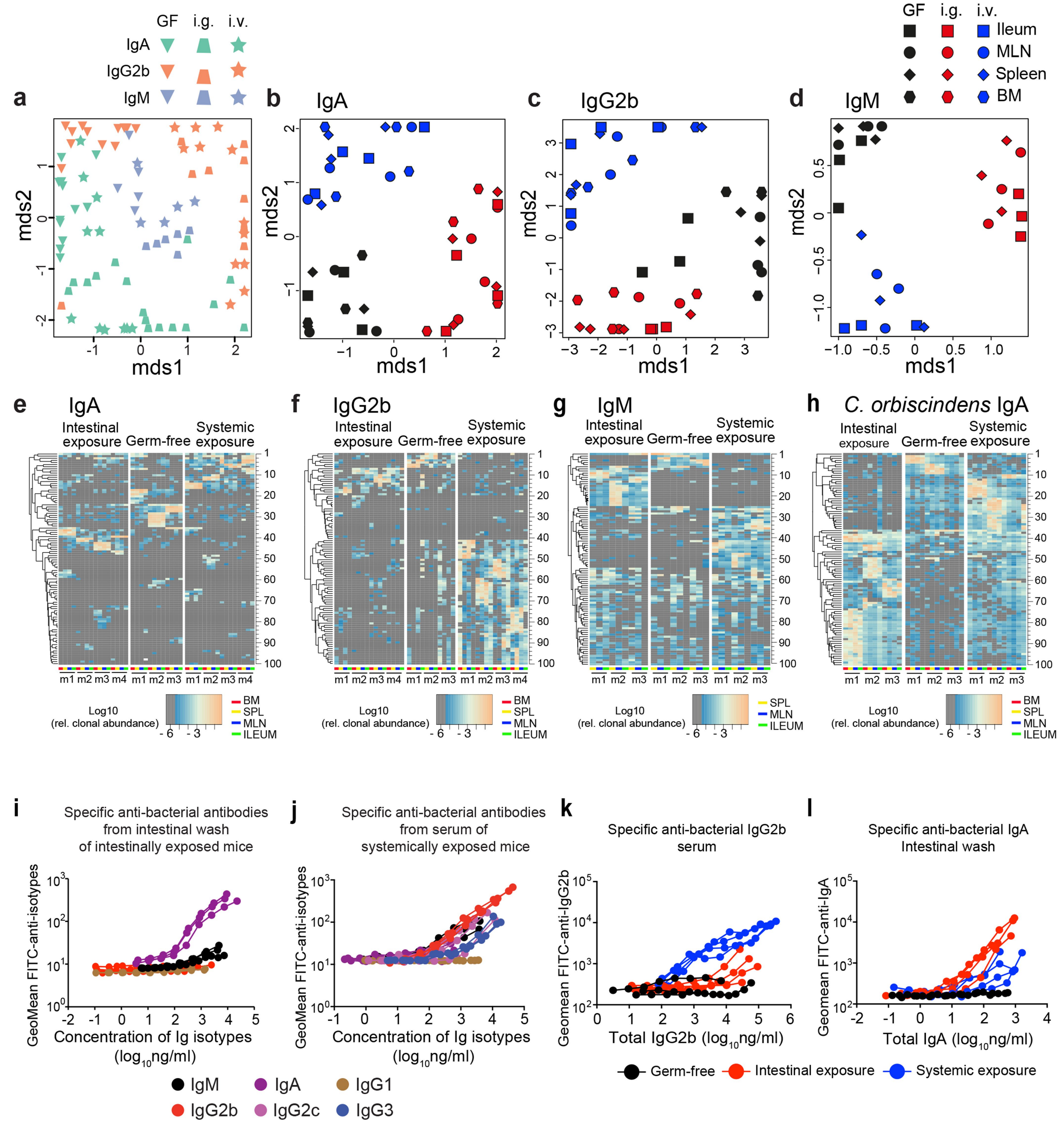

Extended Data Fig. 1 | Mucosal and systemic exposure differentially shape the repertoires of the various immunoglobulin isotypes. **a**–**h**, Germ-free mice were either orally or systemically primed three times every other day by intragastric (10^{10} CFU) or intravenous (10^8 CFU) delivery of *E. coli* HA107 (**a**–**g**) or *Clostridium orbicindens* (**h**) and compared with germ-free control mice. Immunoglobulin heavy-chain-repertoire clonotypes at day 21 are defined by V and J segment use in combination with CDR3 nucleotide sequences, except for **a**, in which clonotypes are based on CDR3 amino acid sequences as in Fig. 1. **a**, MDS plot of IgA, IgG2b and IgM showing distinct isotype repertoires (in each case all isotypes were sequenced from each individual sample from at least 3 mice). **b**–**d**, MDS plot from ileum, MLN, bone marrow (BM) or spleen (SPL) of immunoglobulin repertoire sequencing for IgA (**b**), IgG2b (**c**) and IgM (**d**). **e**–**h**, Heat maps showing the 100 most abundant non-unique clonotypes for IgA (**e**, **h**), IgG2b (**f**) and IgM (**g**). Clonotype specifics for each panel are shown in the Supplementary Information. Samples of ileum, BM, MLN and SPL from each mouse are included. Individual mice are colour-coded on the *x*-axis of heat maps. **i**, **j**, Immunoglobulins from intestinal wash of intestinally exposed mice (**i**) or from serum of systemically exposed mice (**j**) on day 21 were assessed in bacterial flow cytometry for specific IgM, IgG1, IgG2b, IgG2c, IgG3 or IgA binding to *E. coli* HA107. **k**, **l**, *E. coli* HA107 was incubated with day 21 serum or intestinal wash immunoglobulin of the three groups of mice followed by detection of bound mouse IgG2b (**k**) or IgA (**l**) by flow cytometry. All data points are from organs of individual mice.

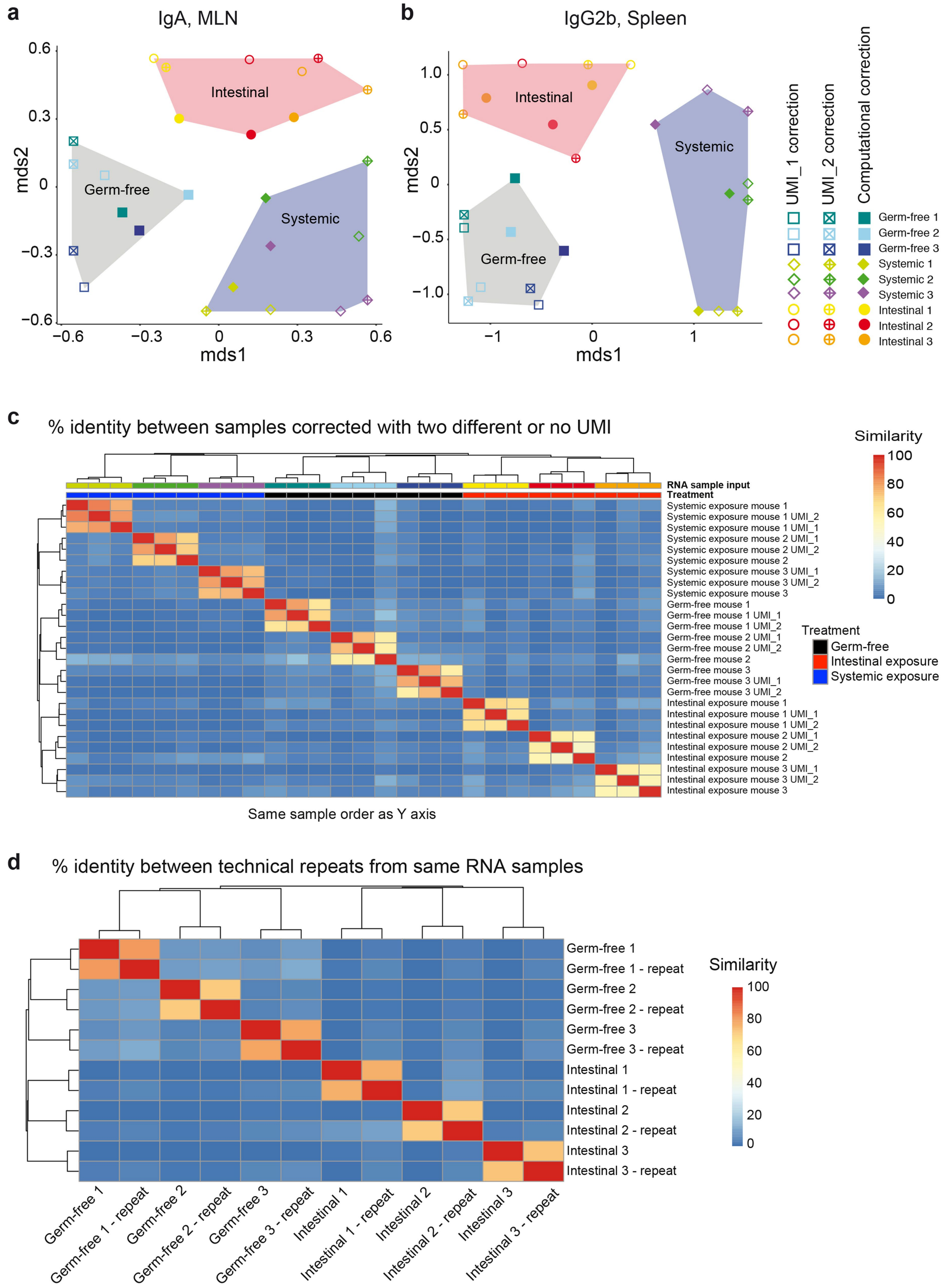

Extended Data Fig. 2 | See next page for caption.

Extended Data Fig. 2 | Comparison of computational correction method with UMIs for PCR artefacts and sequencing reproducibility on different occasions. Germ-free mice were either orally or systemically primed three times every other day by intragastric (10^{10} CFU) or intravenous (10^{8} CFU) exposure to *E. coli* HA107 and compared with germ-free control mice. Immunoglobulin repertoire sequencing at 21 days for IgA in MLN and IgG2b in spleen was performed in parallel from the same RNA samples with two different primers containing different UMIs or primers without UMIs. **a**, **b**, MDS plot of MLN IgA (**a**) or spleen IgG2b (**b**) repertoires showing Euclidean distance between points representing the similarity between results whether computational correction (filled symbols) or UMI correction (open and cross symbols for the different UMIs) was used. **c**, Heat map based on CDR3 sequence identity reflecting similarity between UMI-corrected and computational-corrected IgG2b repertoires. **d**, Identity matrix based on CDR3 sequences of technical replicates of the same biological sample that had been used on two separate occasions for the entire pipeline of cDNA preparation, IgA amplicon PCR, library preparation and MiSeq sequencing. The distinctions between replicate mice and technical repeats are shown in the diagram.

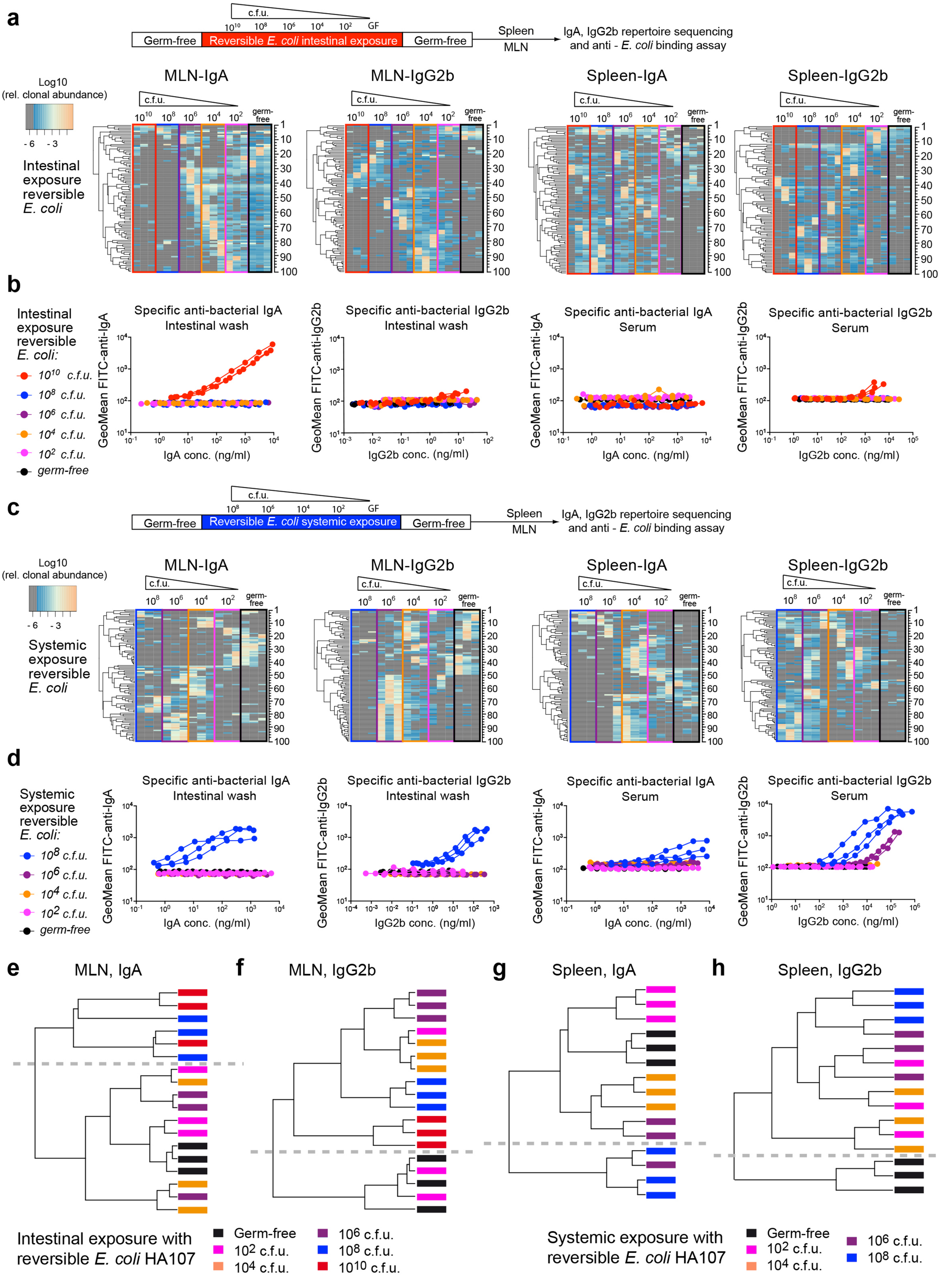

Extended Data Fig. 3 | See next page for caption.

Extended Data Fig. 3 | Threshold differences for shaping systemic or mucosal B cell repertoires and induction of antibody responses. Reversible *E. coli* HA107 was given to germ-free mice at the indicated doses orally (**a**, **b**, **e**, **f**) or systemically (**c**, **d**, **g**, **h**), as in the legend to Fig. 1. **a**, **c**, Immunoglobulin repertoire analysis at 21 days showing heat maps of the top 100 non-unique clonotypes for IgA and IgG2b in MLN and spleen based on V, J segment use combined with CDR3 nucleotide sequences. **b**, **d**, Flow cytometric analysis of *E.-coli*-specific immunoglobulin binding from intestinal or serum samples from the corresponding mice in **a** and **c**, respectively. **e**–**h**, Hierarchical clustering of the indicated immunoglobulin repertoires. Dendrogram of samples, branch length shows the distance between repertoires based on CDR3 amino acid sequence similarity of entire B cell repertoires. The dotted lines indicate the principal separations in unsupervised analyses as an independent assessment of thresholds of exposure required for repertoire shaping. Each column within the heat maps or each dilution series from antibody-binding bacterial flow cytometry are from individual mice; in every case, three mice were used for every experimental condition studied.
The Supplementary Information contains a table specifying the top 100 clonotypes in each case for **a**, **c**. Data are representative of two independent experiments.

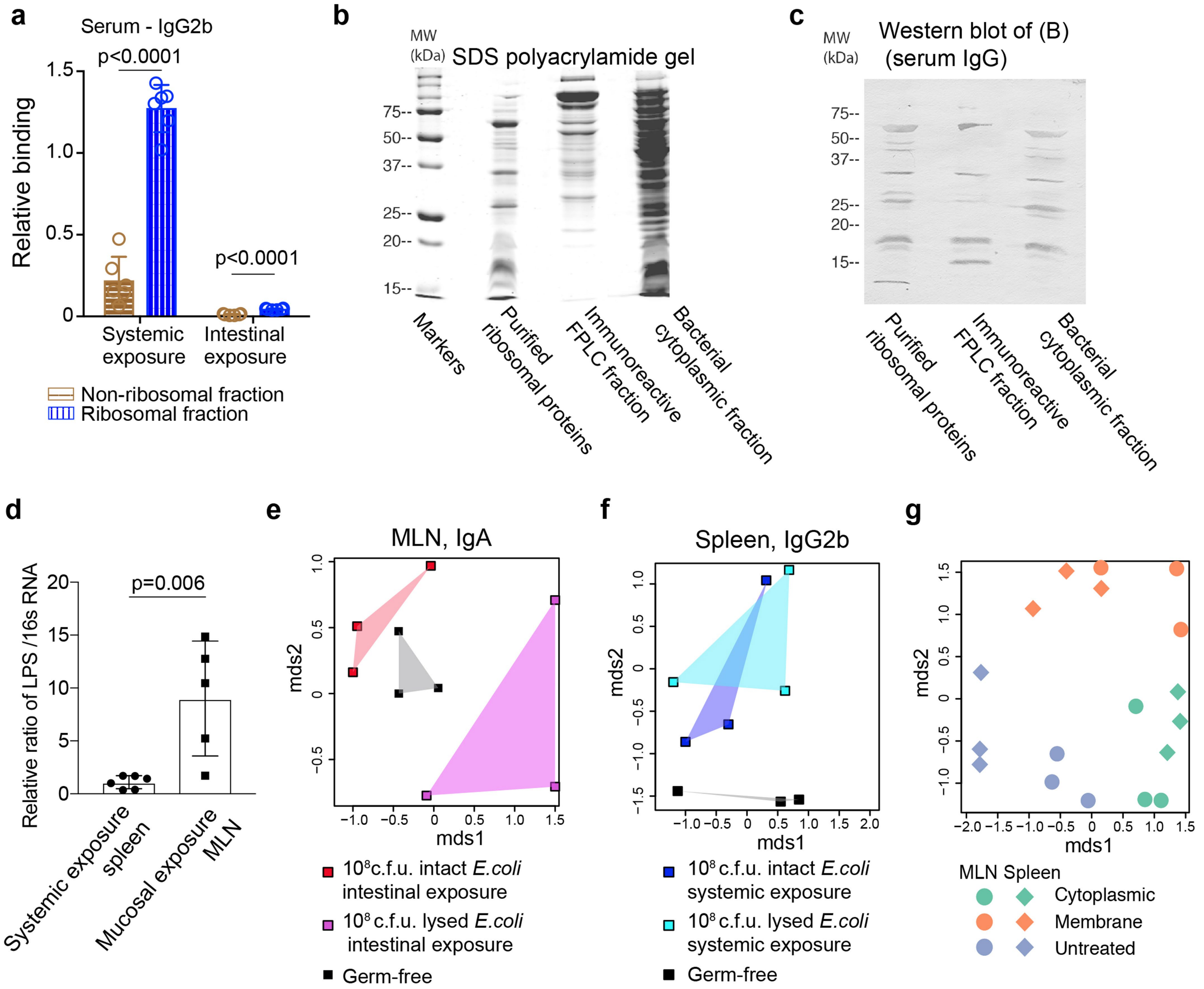

Extended Data Fig. 4 | Differences in processing of microbial antigens, and presentation in the mucosal and systemic compartments. **a**, Reversible *E. coli* HA107 were given to germ-free mice at the indicated doses orally or systemically, as in the legend to Fig. 1. Binding of systemic or intestinal antibodies to *E. coli* non-ribosomal versus ribosomal proteins of the cytoplasmic fraction evaluated using ELISA ($\bar{x}$ ± s.d., *n* = 6, two-sided unpaired *t*-test). **b**, **c**, *Enterobacter cloacae* proteins were either separated by FPLC or subject to ribosomal protein purification, before 12% SDS-polyacrylamide gel electrophoresis. Silver stain for total protein (**b**). Western blot for immunoreactivity against serum IgG raised from specific pathogen-free C57BL/6 mice injected with 10^8 CFU *E. cloacae* 20 days previously (**c**). Control experiments verified previously published data[27] that un-manipulated control mice showed no immunoreactivity against this dominant intestinal aerobe. Proteomic analysis of extracted bacterial ribosomal proteins confirmed identities as follows: 50SL24, 50SL11, 50SL4, 50SL3, 50SL1, 30SS4 and 30SS1. **d**, Germ-free mice were orally (*n* = 6) or systemically (*n* = 5) exposed once by intragastric (10^{10} CFU) or intravenous (10^8 CFU) delivery of *E. coli* HA107. Mesenteric lymph nodes and spleens were analysed 18 h later for LPS levels and 16S rRNA ($\bar{x}$ ± s.d., two-sided unpaired *t*-test). **e**, **f**, Indicated doses of intact or ultrasound-lysed *E. coli* HA107 were administered orally (**e**) or systemically (**f**) three times to germ-free mice every other day and compared to germ-free control mice. Immunoglobulin heavy-chain repertoire analysis at 21 days for IgA in mesenteric lymph nodes (**e**) or IgG2b in the spleen (**f**). **g**, In vitro culture of leukocytes from the mesenteric lymph nodes or spleen of germ-free mice stimulated with either cytoplasmic or membrane fractions of *E. coli* HA107. Activated B cells were sorted on day 5 after stimulation and IgM heavy chain sequencing was carried out. **e**–**g**, In all cases, Euclidean distance in MDS plots reflects the distance between indicated repertoires based on CDR3 amino acid sequences of the entire B cell repertoire. **a**–**d**, Data are representative of two independent experiments. **e**–**g**, Data are from two single experiments. Each data point is from the organ of an individual mouse.

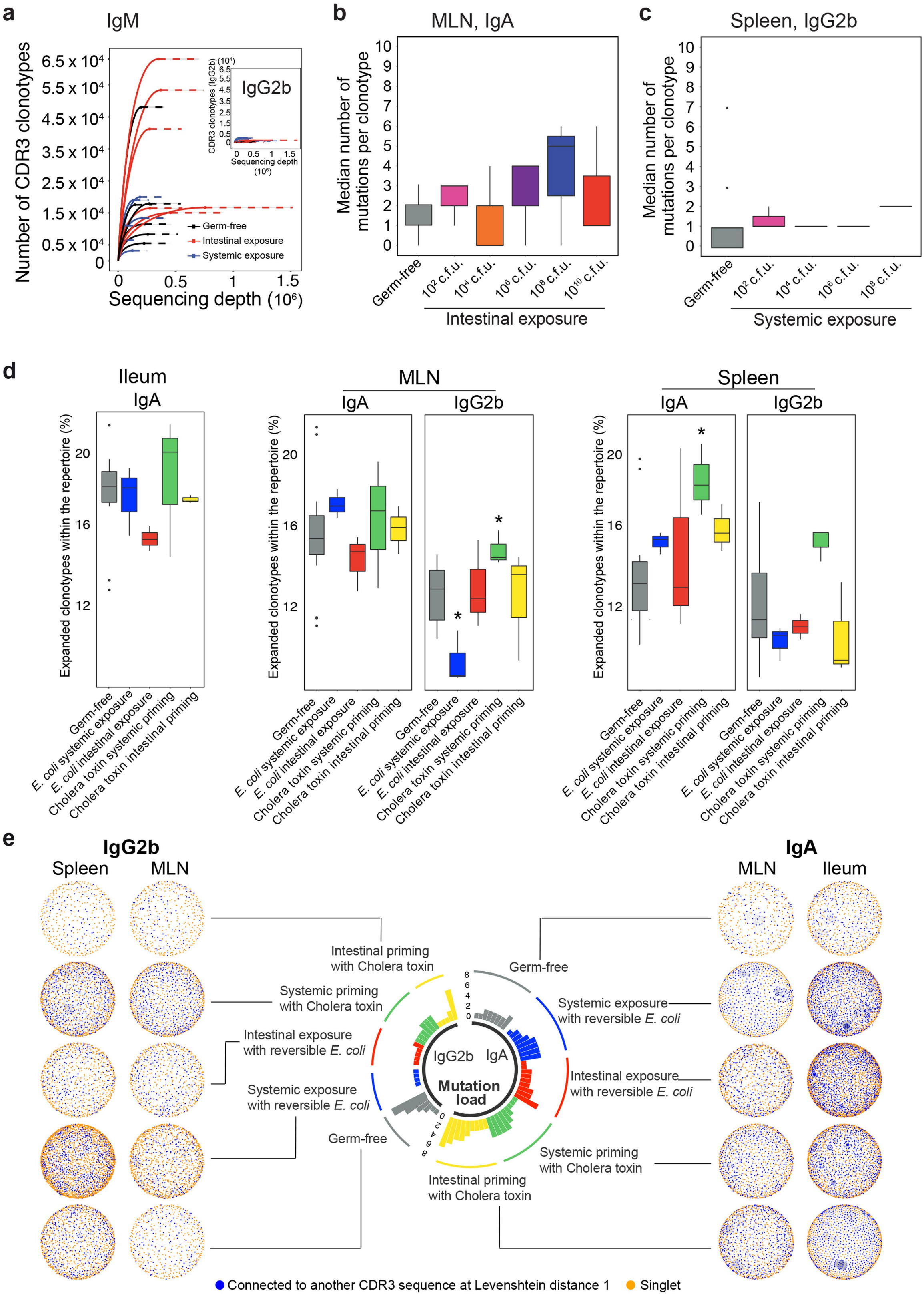

Extended Data Fig. 5 | See next page for caption.

Extended Data Fig. 5 | Network formation of different isotypes depending on transitory microbial treatment, and comparison with strong cholera toxin immunogen. Germ-free mice were orally or systemically primed three times every other day by a range of intragastric (10^2–10^{10} CFU) or intravenous (10^2–10^8 CFU) doses of *E. coli* HA107, compared with priming by cholera toxin or to germ-free control mice. **a**, Rarefaction plots of immunoglobulin repertoire sequencing at 21 days for IgM or IgG2b (inset shows same data as in Fig. 2b, but different *y*-axis scale) in MLN and spleen. Colour coding indicates the route of exposure. **b**, **c**, Median number of mutations per clonotype for IgA in the MLN (**b**) or IgG2b in splenic B cells (**c**). Tukey plots in each case are shown with whiskers at 1.5× interquartile range ($n = 3$ for each condition). **d**, **e**, Germ-free mice were orally or systemically primed three times every other day by intragastric (10^{10} CFU) or intravenous (10^8 CFU) delivery of *E. coli* HA107, or by intragastric (15 µg) or intravenous (15 µg) delivery of cholera toxin B (CTB) and compared with germ-free control mice. Immunoglobulin repertoire sequencing was carried out for IgA, IgM and IgG2b at 21 days. **d**, Tukey plots with whiskers at 1.5× interquartile range indicate proportions of expanded clonotypes (excluding singletons) within the entire CDR3 amino acid IgA repertoire in ileum, MLN and spleen, or within the IgG2b repertoire in MLN and spleen after the indicated exposures ($n = 3$ mice in each bacterial or cholera toxin priming group, $n = 12$ germ-free control mice, two-sided Wilcoxon rank-sum test). Adjusted *P* values as shown. **e**, Radial plot showing median values for mutational levels in MLN, ileum and spleen in individual mice. Peripheral displays of representative network structures of clonotypes showing relatedness with edges representing Levenshtein distance 1 (blue). Singletons are shown in orange. **d**, **e**, All conditions were repeated over 10 times, except for cholera toxin intravenous priming, which was carried out once, and cholera toxin intestinal priming, which was carried out twice. All data points are from individual mice.

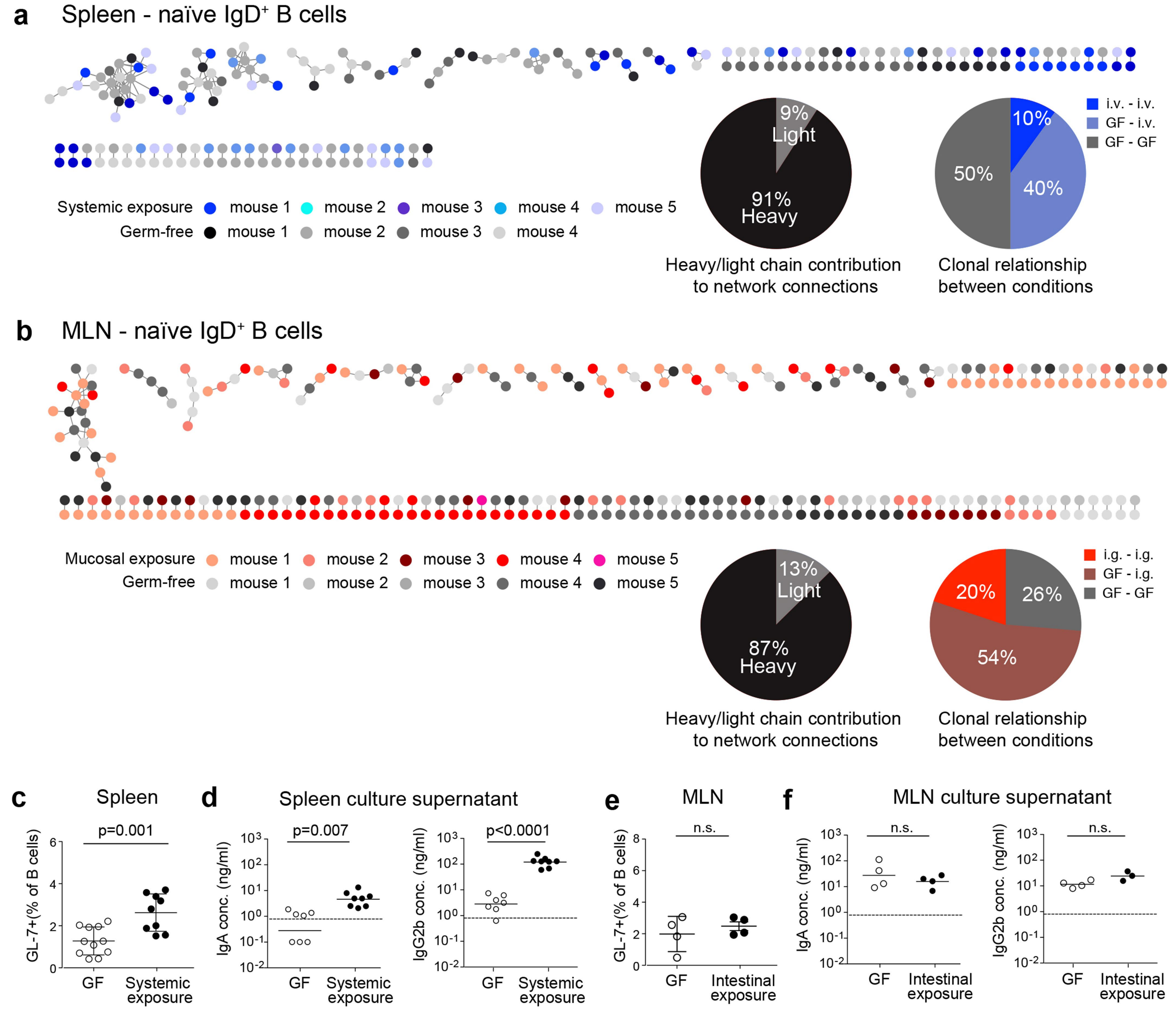

Extended Data Fig. 6 | Characteristics of naive B cell repertoires following systemic or mucosal exposure and sites of B cell activation. **a**, **b**, Characteristics of naive single-cell B cell repertoires corresponding to class-switched single-cell repertoires shown in Fig. 2e, f, respectively. Germ-free mice were orally or systemically primed three times every other day by intragastric (10^{10} CFU) or intravenous (10^{8} CFU) delivery of *E. coli* HA107 and compared with germ-free control mice. Single-cell VDJ sequencing analysis on day 21. Network built on combined heavy- and light-chain CDR3 amino acid sequences each from a single splenic (**a**) or MLN (**b**) naive IgD-expressing B cell, excluding singlets (*n* = 4,272 or 5,672 for **a** and **b**, respectively). Edges show Levenshtein distance 1 or 2. Networks show the immunoglobulin sequence relationships within and between different mice in the same experiment, colour-coded according to mouse and treatment. Left pie charts indicate the percentage of edge connections that are based on a Levenshtein distance of 1 on the light chain compared to the heavy chain; right pie charts indicate the distribution of edge connections between individual B cells within or between exposure conditions. **c**, **d**, Germ-free mice were systemically (i.v.) primed with two doses of 10^{8} CFU *E. coli* HA107, 7 days apart, and compared with germ-free control mice. Lymphocytes from spleen were isolated 18 h after the intravenous injection, stained with fluorescent-labelled antibodies and analysed by flow cytometry. **c**, Overall quantifications ($\bar{x}$ ± s.d., *n* = 11 germ-free and 9 systemic exposure) of live GL7$^+$CD19$^+$ lymphocytes as a proportion of all CD19$^+$ lymphocytes from two independent experiments. **d**, Lymphocytes from spleen were isolated 3 d after the last injection for culture. IgA and IgG2b antibody levels were determined in culture supernatants at 5 d by ELISA. Plots show pooled data from two experiments (geometric mean, *n* = 7 germ-free and 8 systemic exposure for both isotypes). **e**, **f**, Germ-free mice were reversibly exposed with 3 gavage doses of 10^{10} CFU *E. coli* HA107 and compared with germ-free control mice. **e**, Overall quantifications ($\bar{x}$ ± s.d., *n* = 4 for each condition) of live GL7$^+$BCL6$^+$CD19$^+$ lymphocytes as a proportion of all CD19$^+$ lymphocytes from MLN 24 h after the last gavage ($\bar{x}$ ± s.d.). **f**, Lymphocytes from MLN were isolated 3 d after the last injection for culture. IgA and IgG2b antibody levels were determined at 5 d in culture supernatants by ELISA. Geometric means, *n* = 4 for each condition, except IgG2b intestinal exposure = 3. **c**–**f**, *P* values with unpaired *t*-test are indicated as shown in the figure. All data points are from individual mice.

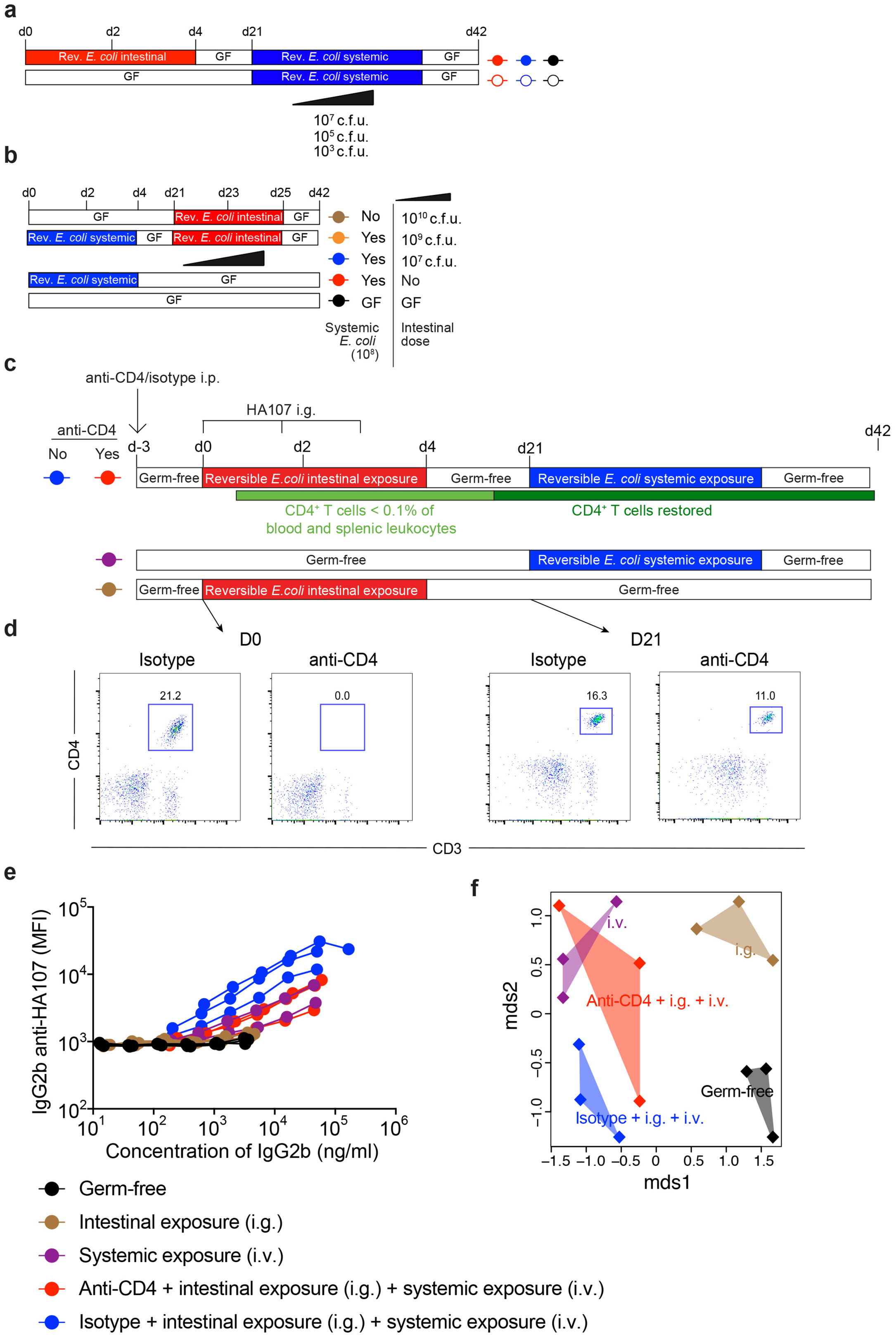

Extended Data Fig. 7 | See next page for caption.

Extended Data Fig. 7 | CD4 T cells are required for systemic immune memory following intestinal exposure to reversible *E. coli* HA107. **a**, **b**, Schematic experimental designs to Figs. 3a–c. **a**, Germ-free mice were intestinally exposed to 10^{10} CFU reversible *E. coli* HA107 on alternate days or remained germ-free throughout. On day 21, all mice were reversibly intravenously exposed to 10^3–10^7 CFU HA107, as shown. Mice were analysed on day 42. **b**, As in **a**, except that the initial reversible exposure was given systemically with subsequent reversible intestinal exposures at different doses. **c**, Germ-free mice were mucosally exposed to 3 doses of 10^{10} CFU *E. coli* HA107 on days 0, 2 and 4, or left germ-free. In both groups, half the mice were treated with anti-CD4 depleting antibody intraperitoneally on day −3; the other half received a control isotype. CD4$^+$ T cells were absent (<0.1% of blood leukocytes) from day 0 until at least day 10, but were shown to have recovered by day 21. On day 21, mice were intravenously primed with 10^7 CFU *E. coli* HA107. Control groups included intestinally only exposed mice and untreated germ-free mice. **d**, Representative dot plots of flow cytometric analysis of the blood on days 0 and 21 in both the isotype and anti-CD4 antibody treated groups. **e**, Bacterial flow cytometry at day 42 analysing specific bacterial surface binding against *E. coli* HA107 from serum IgG2b of the indicated groups. **f**, Immunoglobulin repertoire sequencing for IgG2b in the spleen on day 42. Euclidean distance in the MDS plot reflects the distance based on CDR3 amino acid sequences of the entire repertoires. Data in **c**–**f** are representative of two independent experiments. Each dilution series (**e**) or data points (**f**) are from individual mice.

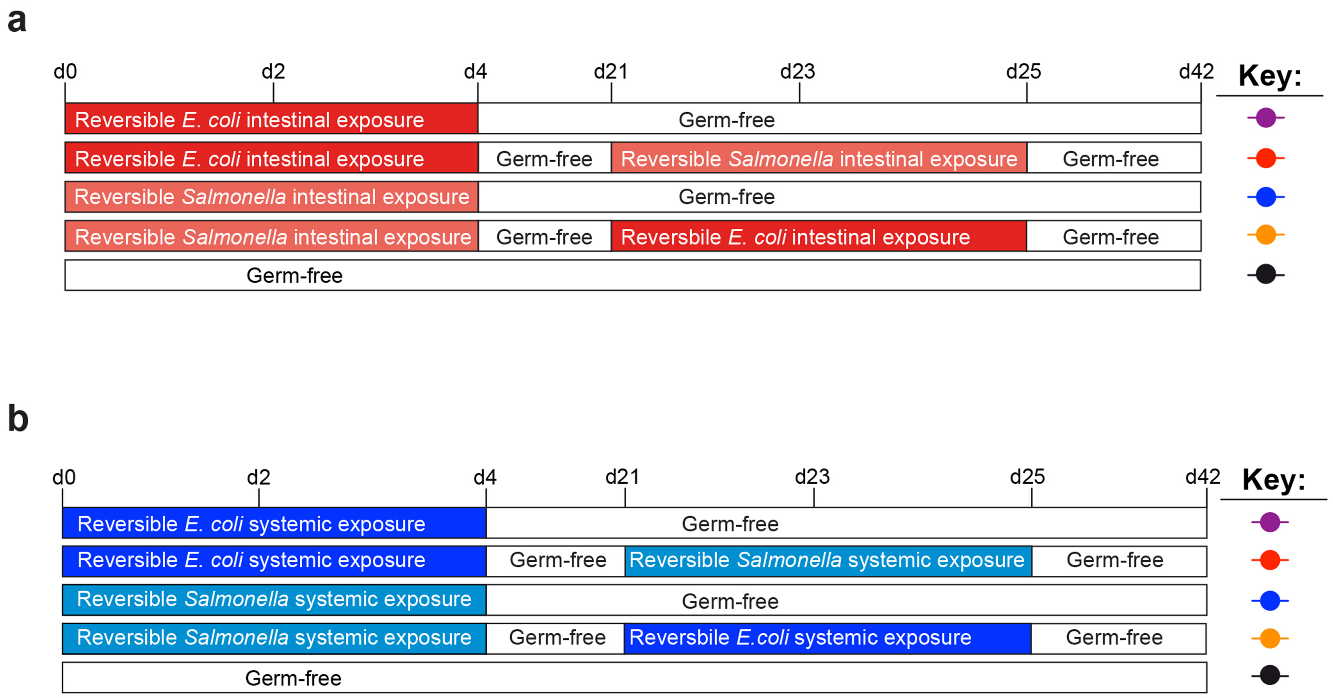

Extended Data Fig. 8 | Experimental schemes. This figure relates to Fig. 3. **a**, Schematic experimental design, related to Fig. 3d–g. Germ-free mice were mucosally primed with three doses of 10^{10} CFU *E. coli* HA107 or reversible *S. typhimurium* HA218 on alternate days or remained germ-free. At day 21, half of each group received a second schedule of priming, but with the opposite taxon. Recovery of germ-free status was verified after each stage. **b**, Schematic experimental design, related to Fig. 3h–k. As in **a**, except that both reversible taxa were given systemically at doses of 10^8 CFU, as shown.

Extended Data Table 1 | Comparison of B cell receptor CDR3 sequences assessed in this study with previously reported data

CDR3 in this study also found before	Accession (Heavy Chain)	Antigen	Database
CARGFDYW	1229	ANTI-ALPHA 1,6 DEXTRAN HYBRIDOMA	Abysis
CARLNYGSSYFDYW	1512	ANTI-ALPHA 1,6 DEXTRAN HYBRIDOMA	Abysis
CARGGFDYW	1674	ANTI-RNA AUTOANTIBODY, ANTI-POLY(G,C) HYBRIDOMA	Abysis
CARGGYYYTMDYW	2392	ANTI-PHOSPHORYLCHOLINE HYBRIDOMA	Abysis
CARYYYGSSYAMDYW	AAA37996.1	E. coli	Abysis
CARGGYYYAMDYW	AAB94776.1	anti-phosphocholine/Streptococcus pneumoniae	Abysis
CAREGFVYW	AAD12890.1	4-hydroxy-3-nitrophenyl)acetyl (NP)	Abysis
CARYYGNYFDYW	AAD26737.1	N/A	Abysis
CATGFAYW	AAF61546.1	N/A	Abysis
CARYYYGSSYFDYW	AAF68209.1	IgM auto-antibody	Abysis
CARNWDWYFDVW	AAO18855.1	N/A	Abysis
CASYYGSSYWYFDVW	AAO18959.1	N/A	Abysis
CARDYYGSSYYAMDYW	AAO19008.1	N/A	Abysis
CARSDYAMDYW	AAO19026.1	N/A	Abysis
CAREGFAYW	AAO40666.1	N/A	Abysis
CARDYYGSSYDWYFDVW	AAX20781.1	N/A	Abysis
CARTGFDYW	ABF68094.1	N/A	Abysis
CARGGNYYFDYW	ABF68200.1	N/A	Abysis
CARDYYGSSYWYFDVW	ABF68373.1	N/A	Abysis
CARGGFAYW	ACI62104.1	B1a IgM	Abysis
CARGGDYW	ACS35898.1	N/A	Abysis
CARWDYW	ACS35899.1	N/A	Abysis
CASSSYAMDYW	ADI86860.1	B-1b	Abysis
CARDYGSSYWYFDVW	ADI86862.1	B-1b	Abysis
CARHYGSSYFDYW	ADI86986.1	B-2	Abysis
CARYYYGSSFDYW	ADI87022.1	B-2	Abysis
CARDYYGSSWYFDVW	ADI87036.1	B-2	Abysis
CARSGYAMDYW	AEC22989.1	autoreactive B cells	Abysis
CARDYYGSDYW	AEK05503.1	4-hydroxy-3-nitrophenyl acetyl (NP)-chicken γ-globulin	Abysis
CARRYFDVW	BAU30148.1	(4-hydroxy-3-nitrophenyl) acetyl hapten	Abysis
CTGLGFDYW	NA	Polyreactive High Microbiota Reactive antigen	Bunker et al. [16]
CARDYYGSSYYFDYW	NA	Non-Polyreactive Low Microbiota Reactive antigen	Bunker et al. [16]
CARYYDYFDYW	1213	Germ-line IgM	Abysis+Bunker et al. [16]
CARGDYW	ABV01849.1	N/A	Abysis+Bunker et al. [16]

nature research

Corresponding author(s): Andrew Macpherson

Last updated by author(s): 25/04/20

Reporting Summary

Nature Research wishes to improve the reproducibility of the work that we publish. This form provides structure for consistency and transparency in reporting. For further information on Nature Research policies, see Authors & Referees and the Editorial Policy Checklist.

Statistics

For all statistical analyses, confirm that the following items are present in the figure legend, table legend, main text, or Methods section.

n/a	Confirmed	
☐	☒	The exact sample size (*n*) for each experimental group/condition, given as a discrete number and unit of measurement
☐	☒	A statement on whether measurements were taken from distinct samples or whether the same sample was measured repeatedly
☐	☒	The statistical test(s) used AND whether they are one- or two-sided *Only common tests should be described solely by name; describe more complex techniques in the Methods section.*
☒	☐	A description of all covariates tested
☐	☒	A description of any assumptions or corrections, such as tests of normality and adjustment for multiple comparisons
☐	☒	A full description of the statistical parameters including central tendency (e.g. means) or other basic estimates (e.g. regression coefficient) AND variation (e.g. standard deviation) or associated estimates of uncertainty (e.g. confidence intervals)
☐	☒	For null hypothesis testing, the test statistic (e.g. *F*, *t*, *r*) with confidence intervals, effect sizes, degrees of freedom and *P* value noted *Give P values as exact values whenever suitable.*
☐	☒	For Bayesian analysis, information on the choice of priors and Markov chain Monte Carlo settings
☐	☒	For hierarchical and complex designs, identification of the appropriate level for tests and full reporting of outcomes
☐	☒	Estimates of effect sizes (e.g. Cohen's *d*, Pearson's *r*), indicating how they were calculated

Our web collection on statistics for biologists contains articles on many of the points above.

Software and code

Policy information about availability of computer code

Data collection	Flow cytometry data were acquired using BD FACSDIVA (v6.0) or FCAP ARRAY (v1.0.2) software. ELISA plates were read using the Tecan 1-control software. MiSeq control software (v2.6.2.1) was used to control sequence instrument operation; Real Time Analysis software (v. 1.18.54) to perform image anaylsis, base calling and quality assignment; MiSeq Reporter software (v. 2.6.2) for demultiplexing and FASTQ generation; and Sequencing analysis viewer (v. 1.10.2) for quality control. Sequencing data were downloaded using LIMS (http://vetsrv03.campus.unibe.ch/).
Data analysis	Data analysis was carried out with FlowJo v9 and 10, MiXCR v2.1.12, VDJtools v1.2.1, CellRanger v3.0.1, Prism v7, Microsoft Excel 2018 and R v3.5.0. The code for analysis can be found in the github repository (https://github.com/Mucosal-Immunology-Bern/Manuscript-microbiota-and-B-cell-repertoire).

For manuscripts utilizing custom algorithms or software that are central to the research but not yet described in published literature, software must be made available to editors/reviewers. We strongly encourage code deposition in a community repository (e.g. GitHub). See the Nature Research guidelines for submitting code & software for further information.

Data

Policy information about availability of data

All manuscripts must include a data availability statement. This statement should provide the following information, where applicable:

- Accession codes, unique identifiers, or web links for publicly available datasets
- A list of figures that have associated raw data
- A description of any restrictions on data availability

The raw files for the datasets generated during this study will be available on the SRA repository (bioproject PRJNA625440). The pre-processed files (clonotype list and properties) will be deposit on the github repository (https://github.com/Mucosal-Immunology-Bern/Manuscript-microbiota-and-B-cell-repertoire). The associated codes for the analysis using R packages can be found in the same github repository. The list of figures that have associated raw data are given in the supplementary information table, specicially Figure 1a-g, Figure 2 b-f, Figure 3 c,f,g,j,k, Ext. data 1 a-h, Ext. data 2a-d, Ext. data 3 a,c,e-h, Ext.data 4e-g, Ext.data 5 a-e, Ext. data 6 a,d, Ext. data 7 f. There are no restrictions on data availability.

Field-specific reporting

Please select the one below that is the best fit for your research. If you are not sure, read the appropriate sections before making your selection.

☒ Life sciences ☐ Behavioural & social sciences ☐ Ecological, evolutionary & environmental sciences

For a reference copy of the document with all sections, see nature.com/documents/nr-reporting-summary-flat.pdf

Life sciences study design

All studies must disclose on these points even when the disclosure is negative.

Sample size	In vivo experiments using germ-free or reversibly colonized germ-free mice were performed using 3-5 mice per group which was the maximum number of mice that could be handled simultaneously under strict axenic conditions. We determined that these sample sizes were sufficient to discriminate repertoire shaping according to the site and dose of transitory microbial exposure in preliminary experiments. Given that many repeats of the repertoire experiments (as specified in the paper) yielded consistent results, we concluded that these sample sizes were sufficiently powered for the study.
Data exclusions	No data points were excluded from the analysis.
Replication	Each experiment was repeated at least once, but usually more than twice. The exceptions were only for the experiment shown in panels e-g of Ext data figure 4, and the cholera toxin i.v. treatment in Ext.data figure 5d. Other treatments in Ext. data Figure 5d were all repeated 2 or more times. All replication attempts throughout the paper were successful.
Randomization	No randomization of mice. 1. The nature of germ-free work is to eliminate all possible confounding covariates through use of inbred animals and strict standardisation of animal husbandry conditions in aseptic isolators maintained under strict dark-light cycles, sterilised food and water. 2. Since the experimental manipulations are to transitorily alter hygiene conditions, we cannot have different treatments in the same cage. Therefore, we needed to keep the different hygiene conditions (e.g. transitory mucosal colonisation and germ-free throughout) separated. Given the litter sizes of offspring separated at weaning, full randomisation would therefore necessitate large numbers of changes of cage mates (as opposed to subdividing a cage with offspring of one gender of a single weaned litter) at the onset of experiments, which we needed to avoid to minimise animal stress.
Blinding	Blinding was present during the bioinformatic analysis. Blinding during data collection was not relevant to our study because all biological replicates were subjected to identical experimental conditions.

Reporting for specific materials, systems and methods

We require information from authors about some types of materials, experimental systems and methods used in many studies. Here, indicate whether each material, system or method listed is relevant to your study. If you are not sure if a list item applies to your research, read the appropriate section before selecting a response.

Materials & experimental systems

n/a	Involved in the study	
☐	☒	Antibodies
☒	☐	Eukaryotic cell lines
☒	☐	Palaeontology
☐	☒	Animals and other organisms
☒	☐	Human research participants
☒	☐	Clinical data

Methods

n/a	Involved in the study	
☒	☐	ChIP-seq
☐	☒	Flow cytometry
☒	☐	MRI-based neuroimaging

Antibodies

Antibodies used	FACS staining antibodies: B220-FITC (Biolegend; cat. 103206; clone no. RA3-6B2; lot no. B208579, B141300; dilution no. 1 in 100); Bcl-6-AlexaFluor647 (BD Biosciences, clone no. K112-91; lot no. 7055649; dilution no. 1 in 100); CD3-BV785 (Biolegend; cat. 100232; clone no. 17A2; lot no. B23796, B279058; dilution no. 1 in 100); CD4-PE (Biolegend; cat no. 100512; clone no. RM4-5; lot no. B259958; dilution no. 1 in 100); CD11b-PEcy7 (Biolegend; cat no. 101216; clone no. M1/70; lot no. B213161, B259668; dilution no. 1 in 100); CD19-AF700 (Biolegend; cat no. 115528; clone no. 6D5; lot no. B261756, B249811, dilution no. 1 in 100); CD21-FITC (Biolegend; cat no. 123408; clone no. 7E9; lot no. B226773; dilution: 1 in 100); CD22-FITC (Biolegend; cat no. 126106; clone no. OX-97; lot no. ; dilution: 1 in 100); CD23-PerCPcy5.5 (Biolegend; cat no. 101618; clone no. B3B4; lot no. B206794; dilution no. 1 in 100); CD25-PerCP-cy5.5 (Biolegend; cat no. 102030; clone no. PC61, lot no. B145989; dilution: 1 in 100); CD43-FITC (Biolegend; cat no. 121206; clone no. 1B11, lot no. B121194; dilution: 1 in 100); CD80-PerCPcy5.5 (Biolegend; cat no. 104722; clone no. 16-10A1, lot no. B250658, B127414; dilution: 1 in 100); CD86-BV421 (Biolegend; cat no. 105032; clone no. GL-1; lot no. B187225; dilution: 1 in 100); CD93-PE-cy7 (Biolegend; cat no. 136506; clone no. AA4.1; lot no. B236661; dilution: 1 in 100); CD138-PE (Biolegend; cat

	no. 142504; clone no. 281-2; lot no. B203320, B182142; dilution: 1 in 100); CD273-APC (Biolegend; cat no. 107210; clone no. TY25; lot no. B268265; dilution: 1 in 100), CXCR5-biotin (BD Biosciences, clone no. 2G8; lot no. 8080503, dilution no. 1 in 50); IgA-FITC (BD Biosciences, cat no. 559354; clone no. C10-3, lot no. 5089919, 7128897; dilution: 1 in 100); IgG2b-FITC (BD Biosciences; cat no. 553395; clone no. R12-3, lot no. 5099651; dilution: 1 in 100), IgM-PEcy7 (Biolegend; cat no. 406514; clone no. RMM-1; lot no. B172064; dilution: 1 in 100), Ly-77-BV421 (BD Biosciences; cat no. 562967; clone no. GL-7; lot no. B275586; dilution: 1 in 100), PD-1-PE (Biolegend; cat no. 109104; clone no. RMP1-30, lot no. B142661; dilution: 1 in 100); Streptavidin-APC (BD Bioscience; cat no. 554063; dilution: 1 in 300) ELISA antibody: Coating antibody: Goat anti-mouse IgM (Southern biotech; cat no. 1020-01); Goat anti-mouse IgG1 1070-01 (Southern biotech; cat no. 1070-01); Goat anti-mouse IgG2b (Southern biotech; cat no. 1090-01); Goat anti-mouse IgG3 (Southern biotech; cat no. 1100-01); Goat anti-mouse IgA (Southern biotech; cat no. 1040-01). Standards: Purified mouse myeloma IgM (Zymed; cat no. 02-6800); Purified mouse myeloma IgG1 (Zymed; cat no. 02-6100); Purified mouse myeloma IgG2b (Zymed; cat no. 02-6300); Purified mouse myeloma IgG3 (Pharmingen; cat no. 553486); Purified mouse IgA (PharMingen; cat no. 553476). Secondary antibodies: Anti-mouse IgM μ chain specific-peroxidase conjugated (Sigma; A8786); Anti-mouse IgG γ chain specific-peroxidase conjugated (Sigma; A3673); Anti-mouse IgA α chain specific-peroxidase conjugated (Sigma; A4789). anti-CD4 depleting antibody (BioXCell, Cat. no. BE0003-1; lot no. 62831701)
Validation	Antibodies have been validated using serial titration of the antibody in combination with either an isotype or a fluoresence minus one control.

Animals and other organisms

Policy information about studies involving animals; ARRIVE guidelines recommended for reporting animal research

Laboratory animals	Mice used in this study were housed in the Clean Mouse Facility of the University of Bern. All mice were born and raised sterilely and kept in sterile fexible film isolators. C57BL/6 mice were used (8-16 weeks of age of mixed gender).
Wild animals	The study did not involve wild animals.
Field-collected samples	The study did not involve samples collected from field studies.
Ethics oversight	All mouse experiments were performed in accordance with Swiss Federal and Cantonal regulations. Permission was granted by the Commission for animal experimentation of the Kanton Bern.

Note that full information on the approval of the study protocol must also be provided in the manuscript.

Flow Cytometry

Plots

Confirm that:

☒ The axis labels state the marker and fluorochrome used (e.g. CD4-FITC).

☒ The axis scales are clearly visible. Include numbers along axes only for bottom left plot of group (a 'group' is an analysis of identical markers).

☒ All plots are contour plots with outliers or pseudocolor plots.

☒ A numerical value for number of cells or percentage (with statistics) is provided.

Methodology

Sample preparation	The single cell suspensions were collected by smashing mesenteric lymph nodes, spleen or bone from freshly sacrificed mice.
Instrument	BD FACS Array, Aria III, Fortessa and CytoFlex.
Software	BD FACSDiva (v6.0) for collection and FlowJo (versions 9 and 10) for analysis.
Cell population abundance	Purity of each sorted sample was over 90% as confirmed by re-acquisation on the sorter (Aria III).
Gating strategy	Relevant gating strategies were described in Methods. We have not provided a separate figure given the standard settings, but could do so.

☒ Tick this box to confirm that a figure exemplifying the gating strategy is provided in the Supplementary Information.

Position-specific oxidation of miR-1 encodes cardiac hypertrophy

https://doi.org/10.1038/s41586-020-2586-0

Received: 9 April 2019

Accepted: 6 May 2020

Heeyoung Seok[1], Haejeong Lee[1,2], Sohyun Lee[1], Seung Hyun Ahn[1], Hye-Sook Lee[1], Geun-Woo D. Kim[1,2], Jongjin Peak[1], Jongyeun Park[1], You Kyung Cho[1], Yeojin Jeong[2], Dowoon Gu[1], Yeahji Jeong[1], Sangkyeong Eom[1], Eun-Sook Jang[1] & Sung Wook Chi[1,2] ✉

In pathophysiology, reactive oxygen species oxidize biomolecules that contribute to disease phenotypes[1]. One such modification, 8-oxoguanine[2] (o^8G), is abundant in RNA[3] but its epitranscriptional role has not been investigated for microRNAs (miRNAs). Here we specifically sequence oxidized miRNAs in a rat model of the redox-associated condition cardiac hypertrophy[4]. We find that position-specific o^8G modifications are generated in seed regions (positions 2–8) of selective miRNAs, and function to regulate other mRNAs through o^8G•A base pairing. o^8G is induced predominantly at position 7 of miR-1 (7o^8G-miR-1) by treatment with an adrenergic agonist. Introducing 7o^8G-miR-1 or 7U-miR-1 (in which G at position 7 is substituted with U) alone is sufficient to cause cardiac hypertrophy in mice, and the mRNA targets of o^8G-miR-1 function in affected phenotypes; the specific inhibition of 7o^8G-miR-1 in mouse cardiomyocytes was found to attenuate cardiac hypertrophy. o^8G-miR-1 is also implicated in patients with cardiomyopathy. Our findings show that the position-specific oxidation of miRNAs could serve as an epitranscriptional mechanism to coordinate pathophysiological redox-mediated gene expression.

The oxidation of guanine within nucleic acids produces 8-oxoguanine (o^8G)[2], which can pair with adenine and induce guanine-to-thymine (G>T) mutations in DNA[5,6]. Despite receiving less attention, RNA is more vulnerable than DNA to this modification[3], and o^8G is formed in RNA during the pathogenesis of various diseases[3,7,8]. miRNAs are post-transcriptional regulators that recognize their mRNA targets through base-pairing to their seed regions (positions 2–8); each miRNA can suppress hundreds of mRNA molecules by reducing their stability and/or translation[9]. In an indication that the oxidation of miRNAs might be related to the redox state of the cell, extensive oxidation of miR-184 was identified in the rat cardiomyoblast cell line H9c2 under oxidative stress, targeting the antiapoptotic proteins BCL-XL and BCL-W and resulting in increased death of cardiomyocyte cells[10].

Cardiac hypertrophy—an enlargement and thickening of the heart muscle that can lead to heart failure—can be induced by stress, injury or extracellular stimuli[4]. Oxidative stress is known to be involved, and has also been implicated in adrenergic hypertrophy[1]. Numerous cardiac miRNAs have been found to function as negative (for example, miR-1[11–13] and miR-133[11]) or positive (for example, miR-155[14] and miR-22[15]) regulators of cardiac hypertrophy. miR-1 is critical for cardiac function[16,17], cardiogenesis[18] and the prevention of cardiac hypertrophy[11–13]. However, during ischaemia reperfusion, the ectopic expression of miR-1 exacerbates arrhythmogenesis[19,20] and injury[21]. Although it is likely that o^8G•A base pairing could occur under such conditions, so far o^8G has been regarded only as a consequence of oxidative damage, and its potent epitranscriptional roles have not been investigated.

Oxidation of miRNA in cardiac hypertrophy

Initially, we investigated whether hypertrophic stimulation by an adrenergic receptor agonist could generate reactive oxygen species (ROS) and oxidize miRNAs in H9c2 cells. Using flow cytometry, we detected a rapid increase in ROS$^+$ cells after treatment with phenylephrine (Fig. 1a). Of the 33.5% of cells that were enlarged, 93% produced ROS—representing a 1.8-fold increase in the total proportion of ROS-producing cells after treatment (31.2%) compared with before treatment (17.3%) (Fig. 1b). The abundance of ROS in phenylephrine-induced hypertrophy was sustained for up to 48 h, as confirmed in an independent batch of H9c2 cells (Extended Data Fig. 1a, b). In addition, serum starvation—a precondition for stimulating adrenergic hypertrophy—enhanced the enlargement phenotype with a high basal ROS level (Extended Data Fig. 1c).

Treatment with the antioxidant *N*-acetylcysteine (NAC) diminished the phenylephrine-induced hypertrophy of MF20$^+$ cardiomyocytes (Fig. 1c, d); such redox dependency was also confirmed in H9c2 cells (Fig. 1e, Extended Data Fig. 1d–f) and in the AC16 human ventricular cardiomyocyte cell line (Extended Data Fig. 1g, h) using flow cytometry. Further expanding to an in vivo mouse model, we used chronic administration of isoproterenol (ISO) (Extended Data Fig. 1i) to induce cardiac hypertrophy (hearts were enlarged by approximately 15%) (Fig. 1f, g), which was confirmed by echocardiogram (Extended Data Fig. 1j, k) and was found to generate ROS (Extended Data Fig. 1l). Consistent with the cell line results, co-treatment with NAC alleviated ISO-induced hypertrophy (Fig. 1f, g, Extended Data Fig. 1k). Fluorometric analysis using the probe dihydroethidium (DHE) showed that the largest increase in

---

[1]Department of Life Sciences, Korea University, Seoul, Korea. [2]Division of Life Sciences, College of Life Sciences and Biotechnology, Korea University, Seoul, Korea. ✉e-mail: chi13@korea.ac.kr

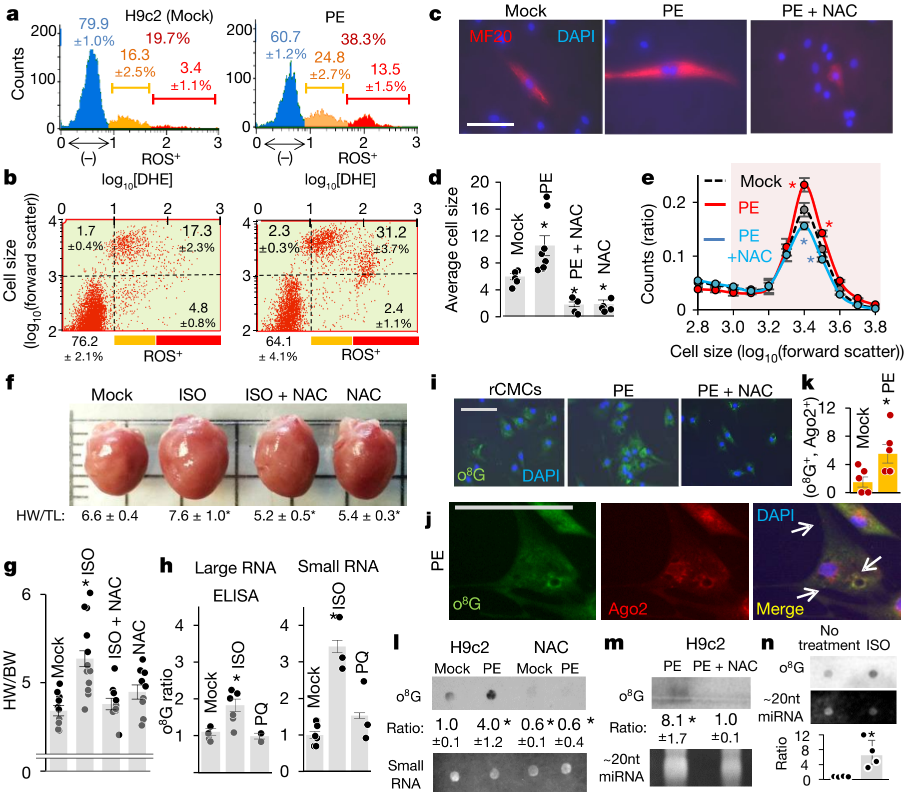

Fig. 1 | Redox-dependent cardiac hypertrophy induces miRNA oxidation. **a**, **b**, Measurement of ROS in H9c2 cells by flow cytometry after treatment with phenylephrine (PE) (*n* = 10,000 cells). Blue, ROS$^-$; orange and red, ROS$^+$. After 10 min treatment, the increase in hypertrophic ROS$^+$ cells was substantial. **c**–**e**, Cardiomyocytes (MF20$^+$) in phenylephrine- and/or NAC-treated H9c2 cells. **c**, Inverted fluorescence microscopy images; scale bar, 50 µm. **d**, Average cell size (units of 5,148 pixels; *n* ≥ 4 measurements, 100 cells, ImageJ); **P* = 0.038 (PE), 1.0×10^{-4} (PE + NAC) and 0.001 (NAC) compared with mock. **e**, Distribution of cell sizes; **P* = 0.031, 0.041 (phenylephrine, left to right), 0.036 and 0.049 (phenylephrine + NAC, left to right), respectively (mock with each condition). **f**, **g**, Mouse hearts after treatment with ISO and/or NAC (*n* ≥ 9). **f**, Photographs of mouse hearts after the indicated treatments; the scale on the ruler is 1 mm and the squares are 25 mm^2. HW/TL, heart weight per tibia length (mg mm^{-1}). **P* = 0.032 (ISO), 7.4×10^{-5} (ISO + NAC) and 1.3×10^{-5} (NAC) compared with mock. **g**, Heart weight as a proportion of body weight (HW/BW; mg/g) after the indicated treatments. **P* = 4.2×10^{-4}. **h**, Quantification of o^{8}G in ISO-treated mouse hearts by ELISA; large RNA, >200 nt (5 µg); small RNA, <200 nt (0.4 µg). Large RNA, **P* = 0.014; small RNA, **P* = 7.0×10^{-5}. **i**, Immunofluorescence staining of o^{8}G in rCMCs treated with phenylephrine and with phenylephrine + NAC. Scale bar, 100 µm. **j**, Immunofluorescence staining of o^{8}G and Ago2 in phenylephrine-treated rCMCs. Scale bar, 100 µm. Arrows indicate colocalized puncta (o^{8}G$^+$, Ago2$^+$). **k**, Ratio of colocalization (o^{8}G$^+$, Ago2$^+$) for each condition compared with mock (*n* = 6 measurements, 100 cells); **P* = 0.023. **l**, **m**, Dot blot (**l**) and northwestern analysis (**m**) of o^{8}G in small RNAs from H9c2 cells treated with phenylephrine and/or NAC. Ratio, o^{8}G intensity divided by RNA input (*n* = 4); In **l**, **P* = 0.01 (H9c2 PE), 0.0007 (mock NAC) and 0.011 (NAC PE). In **m**, **P* = 0.019. **n**, Dot blot analysis of o^{8}G in gel-extracted approximately 20-nt miRNA, qualified in Extended Data Fig. 2l; from untreated or ISO-treated mouse hearts. Ratio, o^{8}G intensity divided by RNA input. **P* = 0.03. Data are mean ± s.d. All *P* values are obtained from two-sided *t*-tests; repeated with biologically independent samples. All graphs show data as mean ± s.e.m. unless otherwise indicated.

ROS was associated with hypertrophy in phenylephrine-treated H9c2 cells (Extended Data Fig. 2a).

Next, separating RNAs by size (200 nucleotides (nt)), we measured o^{8}G by enzyme-linked immunosorbent assay (ELISA) (Fig. 1h) in mouse hearts after treatment with ISO. We found that o^{8}G accumulated in small RNAs (3.2-fold increase after treatment) to a greater extent than in large RNAs (1.8-fold increase); higher than the values obtained under oxidative stress induced by paraquat (Fig. 1h). RNA oxidation was also supported by the detection of redox-dependent cytoplasmic staining of o^{8}G in ISO-treated and in phenylephrine-treated H9c2 cells (Extended Data Fig. 2b) as well as in phenylephrine-treated primary rat cardiomyocytes (rCMCs) (Fig. 1i). We then further refined the analysis by measuring the amount of o^{8}G in miRNAs, based on the colocalization of o^{8}G with Argonaute 2 (Ago2) (Fig. 1j, Extended Data Fig. 2c). We found increased amounts of o^{8}G in miRNAs of phenylephrine-treated rCMCs (increase of approximately 3-fold after treatment) (Fig. 1k) and in miRNAs of phenylephrine-treated or ISO-treated H9c2 cells (Extended Data Fig. 2d, e).

Consistent with the above findings, dot blotting with an o^{8}G-specific antibody revealed increasing oxidation of small RNAs from phenylephrine-treated H9c2 cells (Fig. 1l, Extended Data Fig. 2f) and phenylephrine-treated rCMCs (Extended Data Fig. 2g) in a redox-dependent manner. Northwestern blotting of phenylephrine-treated H9c2 cells (Fig. 1m, Extended Data Fig. 2h, i) and ISO-injected mouse hearts (Extended Data Fig. 2j, k) showed that o^{8}G occurred in miRNAs of approximately 20 nt in size, a finding that was also supported by dot blotting of gel-extracted miRNAs of this size (Fig. 1n, Extended Data Fig. 2l, m).

Sequencing of o^{8}G in cardiac miRNAs

We next attempted to develop a sequencing method for o^{8}G in miRNAs, which we termed o^{8}G-miSeq, by optimizing the immunoprecipitation technique and the o^{8}G-induced G>T transversion[22] (Fig. 2a). Using cross-linking immunoprecipitation (CLIP)[23,24] conditions, the immunoprecipitation process was improved substantially (Extended Data Fig. 3a)—yielding, on average, a 3,500-fold enrichment of o^{8}G relative to G (Fig. 2b). The occurrence of the G>T mutation in cDNA[22] was 50–60%, which was validated by cleavage of an acquired restriction enzyme site (Fig. 2c) and by sequencing (Fig. 2d, Extended Data Fig. 3b–d).

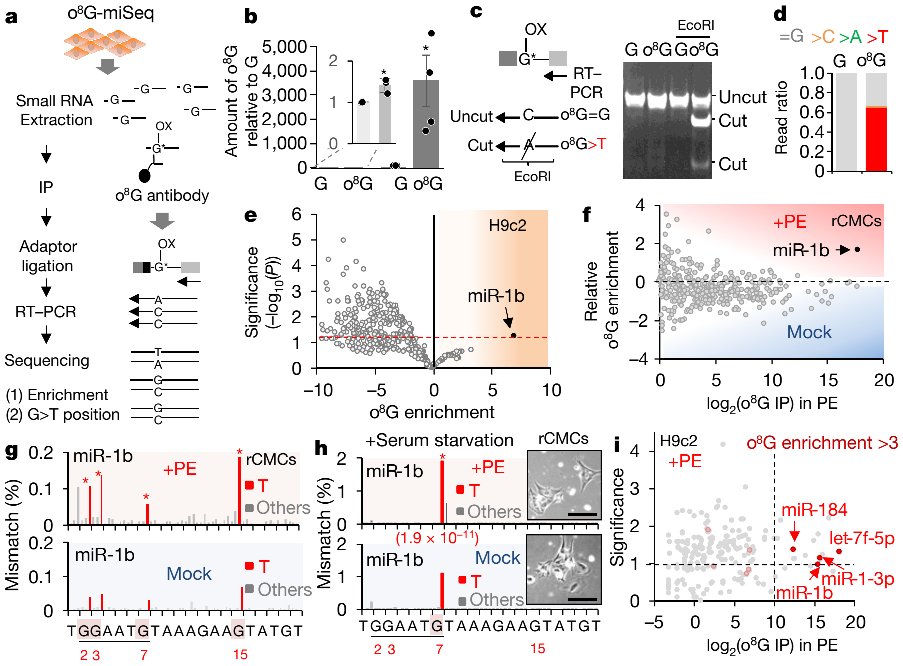

Fig. 2 | o^{8}G-miSeq for cardiac miRNAs. a, Schematic of the o^{8}G-miSeq process. **b**, Analysis of o^{8}G by immunoprecipitation, showing the amount of oxidized spike-in RNA (o^{8}G) relative to the non-oxidized control (G); $n \geq 3$. Immunoprecipitation experiments were carried out under previously reported conditions[8,10]. Inset, $^*P = 0.037$; optimized condition (right), $P = 0.015$. **c**, **d**, G>T mutation induced by o^{8}G•A base pairing during RT–PCR (**c**, left); checked by susceptibility (GAA**o^{8}G**TC > GAA**T**TC) to EcoRI cleavage (**c**, right) and sequencing (**d**). **e**, Results of o^{8}G-miSeq analysis of H9c2 cells. o^{8}G enrichment is calculated as log$_2$(IP/input), normalized o^{8}G by input read-count. The dashed red line indicates $P = 0.05$. **f**, **g**, Results of o^{8}G-miSeq analysis of phenylephrine-treated rCMCs. **f**, Relative o^{8}G enrichment is calculated as the o^{8}G enrichment difference between phenylephrine-treated cells versus mock-treated cells; log$_2$(o^{8}G-IP) is a measure of the amount of o^{8}G. **g**, Positional sequence variation of miR-1b, represented as a normalized mismatch (%); Fisher's exact test; $^*P = 2.3 \times 10^{-39}$, 6.9×10^{-53}, 5.6×10^{-14} and 4.0×10^{-75} (left to right). **h**, Same analyses as in **g** except for miRNA-seq in hypertrophic rCMCs under serum starvation. $^*P = 1.9 \times 10^{-11}$. Scale bars, 100 μm. **i**, Results of o^{8}G-miSeq analysis of phenylephrine-treated H9c2 cells. The red dots with arrows indicate the selected oxidized miRNAs; faint red dots indicate miRNAs for which o^{8}G enrichment >3. The dashed lines indicate o^{8}G in phenylephrine treatment > 10 (x axis), and statistical significance > 1 ($P < 0.1$) (y axis). All P values are obtained from two-sided t-tests; data are mean ± s.e.m. unless otherwise indicated.

The o^{8}G-miSeq method was then applied to H9c2 cells (Supplementary Table 1a), revealing miR-1b as the most extensively oxidized miRNA relative to its expression (o^{8}G enrichment, log$_2$(IP/input) = 7) (Fig. 2e). No bias from either the amount of miRNA or the G-content of the miRNAs was detected (Extended Data Fig. 3e). o^{8}G-miSeq analysis of rCMCs (Supplementary Table 1b) revealed that miR-1b was preferentially oxidized over other miRNAs in response to phenylephrine treatment (relative o^{8}G enrichment) (Fig. 2f, Extended Data Fig. 3f). Oxidation to o^{8}G in miR-1b predominantly occurred in the seed regions (Extended Data Fig. 3g), with an increase at positions 2, 3, 7 and 15 after phenylephrine treatment (Fig. 2g).

Notably, when phenylephrine-treated rCMCs were serum-starved, position 7 of miR-1b was oxidized exclusively (Fig. 2h): miRNA sequencing analysis (Supplementary Table 1c) indicated an approximately 2-fold increase of G>T transversion only at this position, and o^{8}G-miSeq revealed that the oxidation of miR-1b was most extensive upon treatment with phenylephrine (Extended Data Fig. 3h). Considerable oxidation of other miRNAs—including miR-184, let-7f-5p and miR-1-3p—was detected in phenylephrine-treated H9c2 cells (o^{8}G enrichment >3, determined relative to untreated cells), with a substantial amount of o^{8}G overall (log$_2$(o^{8}G IP) > 10) (Fig. 2i, Supplementary Table 1d). Notably, the oxidation of miR-184 after treatment with H$_2$O$_2$ has previously been observed[10] (Extended Data Fig. 3i).

Oxidized miR-1 silences targets via o^{8}G•A

We next validated the oxidation of the miRNAs miR-1b, miR-1-3p, miR-184 and let-7f by confirming their significant increase during the o^{8}G immunoprecipitation experiment after treatment with an adrenergic agonist (Fig. 3a, b). Notably, oxidized miR-1 was enriched in the hearts of ISO-treated mice, despite decreased total levels upon ISO treatment (Fig. 3b, Extended Data Fig. 3j). Focusing on miR-1, we further examined whether the identified o^{8}G positions in seed regions (positions 2, 3 and 7; denoted 2o^{8}G-miR-1, 3o^{8}G-miR-1 and 7o^{8}G-miR-1) enable miR-1 to recognize corresponding new target sites (2oxo, 3oxo and 7oxo sites) via o^{8}G•A base pairing (Fig. 3c). Luciferase reporter assays showed that the o^{8}G-miR-1s could silence targets through cognate oxo sites (Fig. 3d). The oxo sites were responsive to phenylephrine but derepressed by NAC treatment in rCMC cells (Fig. 3e), as well as in AC16 cells after treatment with phenylephrine or H$_2$O$_2$ (Extended Data Fig. 3k, l); this indicates that the level of endogenous o^{8}G-miR-1 was sufficient to redirect target recognition and achieve silencing.

To exclude the compounding effect of cellular heterogeneity, we performed flow cytometry analyses with dual fluorescent protein (dFP) reporters: we expressed a green fluorescent protein (GFP) gene that includes miRNA target sites, and a red fluorescent protein (RFP) gene that does not have the target site (Fig. 3f). We were therefore able to detect o^{8}G-miR-1-dependent repression at the level of individual H9c2 cells (Extended Data Fig. 4a), despite a low global level of endogenous miR-1 (Extended Data Fig. 4b). As a result, every miR-1 oxo reporter was endogenously suppressed by the basal level of o^{8}G-miR-1, which was confirmed by either transfecting miR-1 inhibitor or cognate miR-1 variants (Extended Data Fig. 4c). Significant phenylephrine-dependent repression of the 7oxo reporter was observed (Extended Data Fig. 4d, e), as measured by the cumulative distribution function (CDF) of relative activities ($P = 1.56 \times 10^{-5}$; Kolmogorov–Smirnov test) (Fig. 3f).

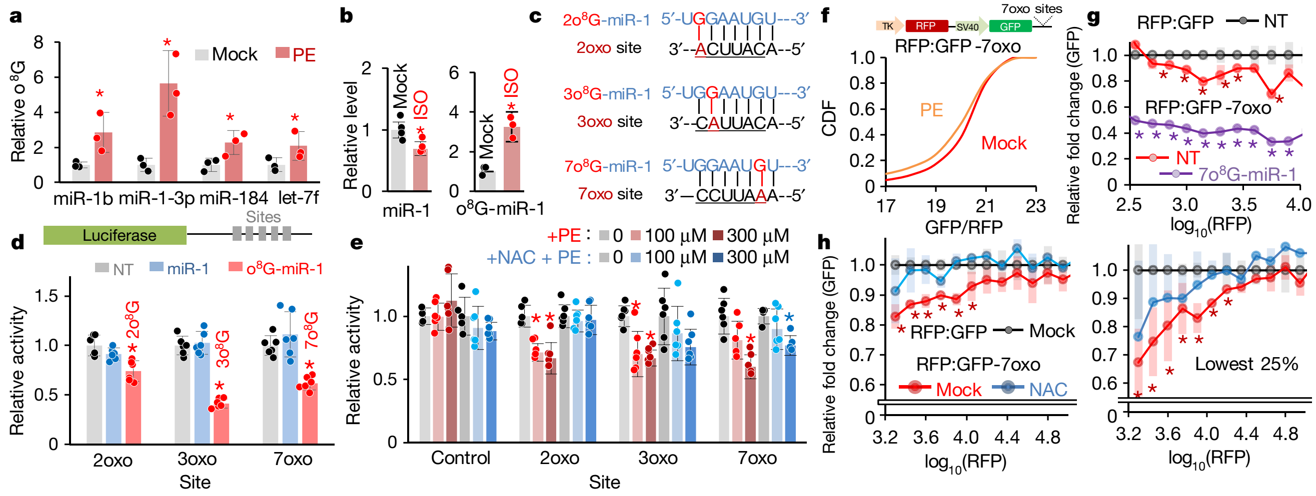

Fig. 3 | o^{8}G-miR-1 redirects target repression via o^{8}G•A base pairing. **a**, **b**, Validation of miRNA oxidation in phenylephrine-treated rCMCs (**a**) and ISO-treated mouse hearts (**b**) using o^{8}G immunoprecipitation followed by qPCR. In **a**, relative o^{8}G is the amount of o^{8}G normalized to the o^{8}G-containing spike-in control. $^*P = 0.051$ (miR-1b), 0.013 (miR-1-3p), 0.048 (miR-184), 0.1 (let-7f) comparing phenylephrine and mock treatments. Data are mean ± s.e.m. In **b**, relative level is the amount of o^{8}G normalized to U6. miR-1 levels were analysed by qPCR only. $^*P = 0.03$ (miR-1), 0.003 (o^{8}G-miR-1) comparing mock and ISO treatments. Data are mean ± s.e.m. **c**, New target sites of oxidized miR-1 as a result of redirection by o^{8}G•A base pairing. **d**, Luciferase reporter assays for 2oxo, 3oxo and 7oxo sites using synthesized o^{8}G-miR-1 (2o^{8}G, 3o^{8}G or 7o^{8}G); activity is reported relative to non-targeting control (NT). $^*P = 0.002$ (2o^{8}G-miR-1), 8.4×10^{-8} (3o^{8}G-miR-1), 1.6×10^{-5} (7o^{8}G-miR-1) relative to NT. **e**, Luciferase reporter assays for the oxo sites responding to phenylephrine treatment or phenylephrine + NAC treatment in rCMCs. The control site is a seed site with a mismatch at position 6 (pivot)[32], impairment of which abrogates seed-mediated target repression[33]. $^*P = 1.7 \times 10^{-4}$, 0.7×10^{-4}, 0.004, 1.3×10^{-5}, 4.5×10^{-4} and 1.7×10^{-3}, respectively. **f**, The dFP reporter with 7oxo sites in GFP (RFP:GFP-7oxo, top) and CDF results in phenylephrine-treated H9c2 cells (bottom; $n \geq 3$). $P = 1.56 \times 10^{-5}$, two-sided Kolmogorov–Smirnov test. **g**, **h**, Relative fold change (GFP, 7oxo site versus no site; $n \geq 3$) in individual H9c2 cells responding to 7o^{8}G-miR-1 (**g**) and NAC treatment (**h**, left), plotted depending on the level of dFP reporter expression (estimated by $\log_{10}$(RFP)). The right graph in **h** shows the reanalysed results considering only the lowest 25% of GFP signals (within a similar range to RFP). The flow cytometer was equipped with a blue laser (**f**) or with two separate lasers (**g**, **h**; to maximize the excitation of both GFP and RFP). $n = 3$; repeated with biologically independent samples. In **h**, $^*P < 0.05$ (see Source Data for individual values). Unless stated, all P values were obtained from two-sided t-tests. Data are mean ± s.d. unless otherwise indicated.

We further examined these results by calculating the fold changes in fluorescence relative to the dFP reporter with no site (Extended Data Fig. 4f, g), to confirm the repression of the 7oxo site by the endogenous 7o^{8}G-miR-1 (RFP:GFP-7oxo versus RFP:GFP, non-targeting (NT)) (Fig. 3g) and its derepression by NAC (RFP:GFP-7oxo, mock versus NAC) (Fig. 3h, Extended Data Fig. 4h). Notably, relative repression increased when only the lowest 25% of reporter fluorescence values (GFP-7oxo) were considered (Fig. 3h, right), suggesting the existence of a cell population with a high level of 7o^{8}G-miR-1. In support of this, we observed similar results by switching the fluorescent proteins in the dFP reporter, resulting in more sensitive detection (Extended Data Fig. 4i–l). In addition, oxidized miR-1 was able to suppress seed sites, albeit less potently than unoxidized miR-1 (Extended Data Fig. 4m)—presumably owing to retained activity of the o^{8}G•C base pairing.

o^{8}G-miR-1 induces cardiac hypertrophy

Although miR-1 expression has been reported to induce atrophy[11,13], treatment with phenylephrine impaired the miR-1-induced atrophy of rCMCs (Fig. 4a, b, Extended Data Fig. 5a). Motivated by the detection of o^{8}G-miR-1, we introduced synthetic 2o^{8}G-miR-1, 3o^{8}G-miR-1 or 7o^{8}G-miR-1 to rCMCs and observed a greater induction of hypertrophy than was found after treatment with phenylephrine (Fig. 4b–d, Extended Data Fig. 5b). This effect was found to be dependent on o^{8}G•A base pairing, because substitution of o^{8}G with U (forming 2U-miR-1, 3U-miR-1 and 7U-miR-1)—which could suppress only cognate oxo sites (Extended Data Fig. 5c, d)—caused the same hypertrophic phenotype (Fig. 4d, e, Extended Data Fig. 5e). Concordant results were obtained using H9c2 cells (Extended Data Fig. 5f). Specifically, hypertrophy induced by 7o^{8}G-miR-1 or 7U-miR-1 substantially increased the expression of atrial natriuretic peptide (ANP), a cardiac hypertrophy marker (Fig. 4f, g), and enlargement of cells was confirmed by time-lapse imaging of rCMCs (Fig. 4h, Supplementary Videos 1, 2) and of H9c2 cells (Extended Data Fig. 5g) with cytometric quantification (Extended Data Fig. 5h).

Next, we administered 7o^{8}G-miR-1 to mice (Fig. 4i) and confirmed its delivery to the heart by quantitative PCR (qPCR) (Extended Data Fig. 6a). At least 10% of the heart increased significantly in size (Fig. 4i, Extended Data Fig. 6b), with cardiomyocytes in the interventricular septum increasing in size by approximately 19% (Fig. 4j, k, Extended Data Fig. 6c), and ANP was significantly upregulated (Fig. 4l). Injection of synthetic 7U-miR-1 (Extended Data Fig. 6d) also induced cardiac hypertrophy in mice (Extended Data Fig. 6d, e), as did the delivery of 7U-miR-1 as a cardiomyocyte-specific expression vector (α-MHC promoter) in the presence of basal ROS levels (Extended Data Fig. 6f–h).

We then generated cardiomyocyte-specific transgenic mice, in which the expression of 7U-miR-1 led to exacerbated hypertrophic phenotypes (Fig. 4m, Extended Data Fig. 6i); this was in contrast to transgenic mice expressing miR-1, in which no change was observed (Fig. 4n, Extended Data Fig. 6j–l). Transgenic mice expressing 7U-miR-1 had decreased survival rates (Extended Data Fig. 6m) and displayed cardiac hypertrophy (Fig. 4o); the extent of the cardiac hypertrophy phenotype was correlated with the level of 7U-miR-1 expression in three independent transgenic lines throughout generations (Extended Data Fig. 6n–u). The hearts of transgenic mice expressing 7U-miR-1 had enlarged cardiomyocytes in the interventricular septa (Fig. 4o–q, Extended Data Fig. 6q, s) and showed progression towards myocardial fibrosis (Fig. 4r, Extended Data Fig. 6r).

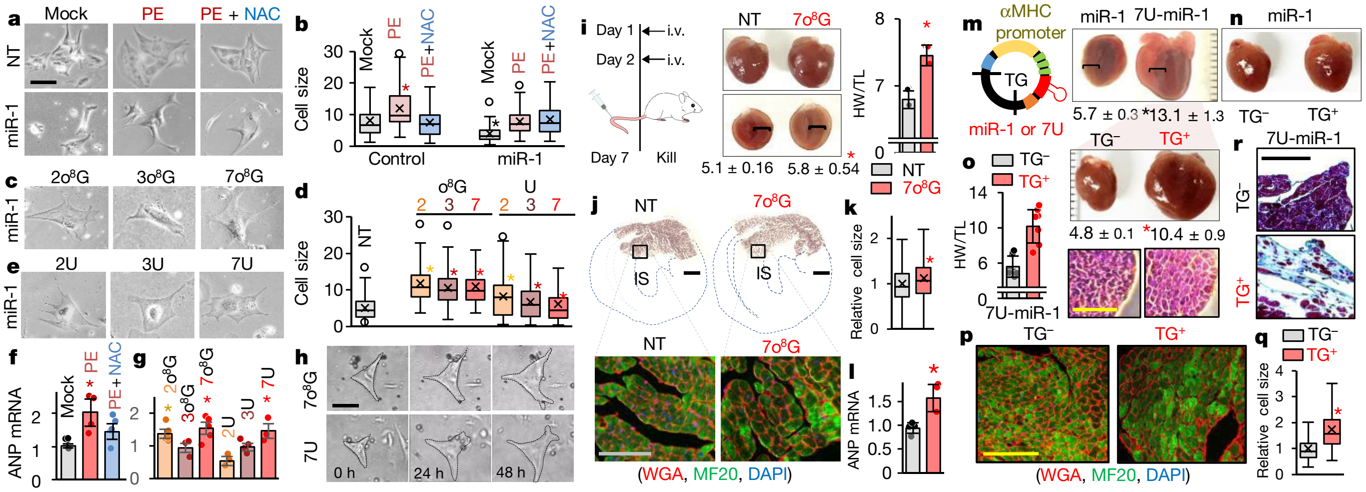

Fig. 4 | o^{8}G-miR-1 generates cardiac hypertrophy. **a**–**e**, Morphology of rCMCs after transfection of miR-1 (**a**, **b**; treatment with phenylephrine or with phenylephrine + NAC), o^{8}G-miR-1 (**c**, **d**; 2o^{8}G, 3o^{8}G or 7o^{8}G) or U-miR-1 (**d**, **e**; 2U, 3U or 7U). Cell size was quantified using ImageJ (a unit of 5,148 pixels, $n \geq 59$), relative to mock treatment (transfection with non-targeting control miRNA (**b**, **d**)). In box plots, the lines represent the median, first and third quartiles, the whiskers denote the minima and maxima, and 'x' marks the mean value. In **b**, $^*P = 1.3 \times 10^{-5}$ (mock vs PE, control) and 2.4×10^{-10} (mock, control vs miR-1). In **d**, $^*P = 4.3 \times 10^{-36}$ (2o^{8}G), 1.9×10^{-38} (3o^{8}G), 1.7×10^{-25} (7o^{8}G), 2.1×10^{-11} (2U), 2.0×10^{-5} (3U) and 0.012 (7U), compared with NT. **f**, **g**, ANP mRNA levels, measured by qPCR ($n \geq 3$) relative to mock. Data are mean ± s.d. In **f**, $^*P = 0.007$. In **g**, $^*P = 0.021$ (2o^{8}G), 0.012 (7o^{8}G) and 0.034 (7U). **h**, Time-lapse bright-field microscopy images of rCMCs transfected with 7o^{8}G-miR-1 or 7U-miR-1 (Supplementary Videos 1, 2). $n \geq 3$. **i**, Left, procedure for the intravenous (i.v.) administration of 7o^{8}G-miR-1 into mice. Middle, Photographs of mouse hearts after the administration of 7o^{8}G-miR-1. The values denote HW/BW (mg g^{-1}); $^*P = 0.05$. Right, HW/TL (mg mm^{-1}) after administration of 7o^{8}G-miR-1 (with 25% of non-targeting) or non-targeting control; $^*P = 0.002$. **j**, Tissue sections from mouse hearts after the administration of 7o^{8}G-miR-1. Top, haematoxylin and eosin (H&E) staining; bottom, immunofluorescence staining. MF20, cardiomyocytes; WGA (wheat germ agglutinin), cell border; DAPI, nucleus. **k**, Quantification of relative cell size of cardiomyocytes (MF20$^+$; $n = 500$) in **j** by ImageJ; $^*P = 3.4 \times 10^{-3}$. **l**, Expression of ANP mRNA as measured in **f**, **g**; $^*P = 0.009$. **m**–**o**, Results from cardiomyocyte-specific transgenic (TG) mice expressing 7U-miR-1 (**m**, **o**) or miR-1 (**m**, **n**); TG$^-$, without transgenic cassette; TG$^+$, with transgenic cassette. **m**, Left, use of the α-MHC promoter vector; right, images of hearts from F$_0$ TG$^+$ mice. The values given are HW/BW; $^*P = 4.2 \times 10^{-5}$. **n**, Images of hearts from F$_1$ (founder line 33) miR-1-expressing TG$^-$ and TG$^+$ mice. **o**, Left, HW/TL for 7U-miR-1-expressing TG$^+$ and TG$^-$ mice, $^*P = 4.8 \times 10^{-5}$; top right, images of hearts from 7U-miR-1-expressing TG$^+$ and TG$^-$ mice, values are HW/BW, $^*P = 2.1 \times 10^{-6}$; bottom right, visualization of the interventricular septum by H&E staining. **p**, **q**, Cardiomyocytes in the interventricular septum of TG$^-$ and TG$^+$ mice expressing 7U-miR-1, stained (**p**) and quantified (**q**) as in **j**, **k**. In **q**, $n \geq 294$; $^*P = 2.89 \times 10^{-41}$. **r**, Masson's trichrome staining of the interventricular septum; the blue areas in the bottom image indicate fibrosis. $n \geq 3$. All scale bars are 100 μm (except **j**, top, 1 mm). All P values are obtained from two-sided t-tests; $^*P < 0.05$; $n \geq 3$; similar results with biologically independent samples; data are mean ± s.e.m. unless otherwise indicated.

o^{8}G-miR-1 globally redirects target repression

We used RNA sequencing to assess the transcriptome-wide effects of miR-1 oxidation in mouse hearts into which 7o^{8}G-miR-1 had been delivered (Fig. 5a, Supplementary Table 2a). According to CDF analysis, putative target mRNAs containing the 6mer 7oxo site (position 2–7) in the 3′ untranslated regions (3′UTR) showed significant propensity for downregulation (Fig. 5a, Extended Data Fig. 7a). The same results were observed for 7mer 7oxo targets (positions 2–8) in each replicate or in combination (Extended Data Fig. 7b, c). Among putative 7oxo targets that were identified as differentially expressed genes (DEGs) (Fig. 5b), downregulated genes were predominant ($n = 596$ downregulated versus $n = 22$ upregulated genes). The downregulated DEGs were significantly enriched in gene ontologies related to heart function—such as cardiac morphogenesis, contraction and calcium ion transport ($P < 0.05$) (Fig. 5c). Gene set enrichment analysis (GSEA) and gene ontology analysis also revealed the enrichment of genes from biological pathways related to cardiac hypertrophy (Extended Data Fig. 7d–g)—for example antihypertrophic factors *Gata4* and *Gsk3b*[4,25], and a pivotal calcium regulator *Atp2a2*[1,4] (also known as *Serca2*). The 7o^{8}G-miR-1-mediated repression of *Atp2a2*, *Gata4* and *Gsk3b*—the 3′UTRs of which contain conserved 7oxo sites (Supplementary Table 3a)—was further validated in rCMCs by qPCR. (Fig. 5d).

Similar results were obtained for 7o^{8}G-miR-1 in H9c2 cells (Supplementary Table 2b), as shown by CDF analysis (Extended Data Fig. 8a, b) and by volcano plots (Fig. 5e). Notably, CDF analysis also revealed seed sites in 7o^{8}G-miR-1-mediated downregulation—although the extent of the repression was marginal (Extended Data Fig. 8c, d). The 7oxo targets were also enriched in gene ontologies of heart development and morphogenesis function ($P < 0.05$) (Extended Data Fig. 8e). Extending the analysis to 2o^{8}G-miR-1 and 3o^{8}G-miR-1 (Supplementary Table 2c, d), RNA sequencing and CDF analysis revealed that these miRNAs induced significant repression of cognate targets (Extended Data Fig. 8f–h) and the functions of these targets in gene ontologies of heart morphogenesis (2oxo targets), blood circulation (2oxo and 3oxo targets) and heart contraction (3oxo targets; Extended Data Fig. 8i, j). Some 7oxo targets in rCMCs were further confirmed by qPCR (Fig. 5f): *Gja1*, *Dram1* and *Pon2*, both 7oxo and seed sites (Supplementary Table 3b); and *Pcgf6* and *Bicd2*, 7oxo site only (Supplementary Table 4a, b). Additionally, *Fbxo32* (also known as atrogin 1)[26], *Pten*[25] and *Usp18*[27]—reported to be negative regulators of cardiac hypertrophy—were also validated as targets of 7o^{8}G-miR-1 (Extended Data Fig. 8k), because they contain conserved 7oxo sites in 3′UTRs (Supplementary Table 4c).

Next, we used RNA-seq (Supplementary Table 5a) to examine the finding that o^{8}G-miR-1 targets are globally repressed in ISO-induced hypertrophic hearts (positions 2, 3 and 7) (Extended Data Fig. 8l): this was especially evident in 7oxo targets (Fig. 5g) and was somewhat evident in 3oxo targets (Extended Data Fig. 8m). Genes that were downregulated in ISO-treated hearts (log$_2$ ratio < 0) were significantly enriched upon 7o^{8}G-miR-1-dependent repression (GSEA; Fig. 5h) but only marginally enriched during 2o^{8}G-miR-1-dependent repression (Extended Data Fig. 8n). Finally, targets of 7o^{8}G-miR-1 were experimentally validated to be suppressed in either phenylephrine-treated rCMCs (*Gja1*, *Atp2a2* and *Gsk3b*, Fig. 5i; *Bicd2*, Extended Data Fig. 9a) or ISO-treated

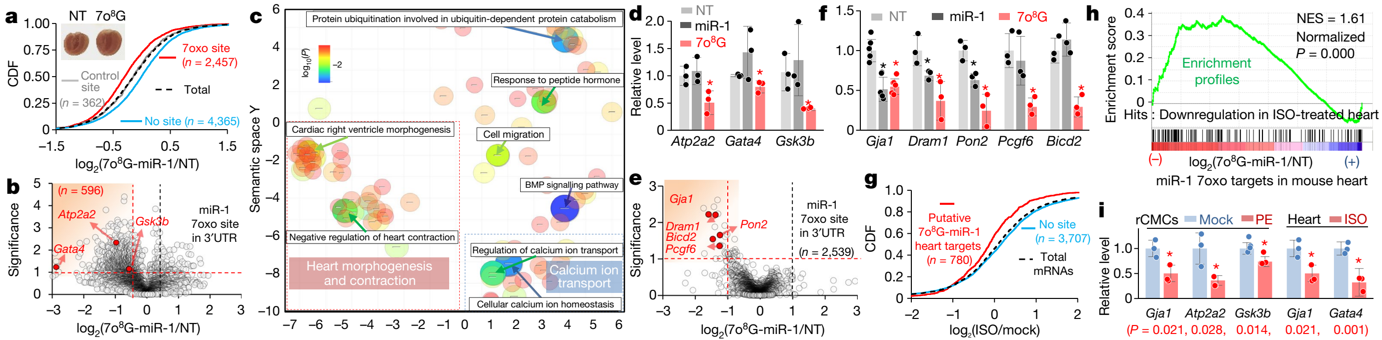

Fig. 5 | Transcriptome-wide target repression by o^8G-miR-1 in cardiac hypertrophy. **a**, **b**, RNA-seq analysis of hypertrophic mouse hearts after the administration of $7o^8G$-miR-1, presented as a CDF plot (**a**) and a volcano plot (**b**). The inset of **a** shows images of hearts administered with $7o^8G$-miR-1 or a non-targeting control miRNA. 7oxo site, 6mer (**a**, positions 2–7) or 6mers (**b**, positions 2–8, $n = 3{,}804$) in 3′UTRs; control site, mismatch site at position 6 of miR-1 in 3′UTRs[32] but no 7oxo site in the transcript; no site, neither a 7oxo site nor a seed site (6mers in positions 2–8). In **a**, $P = 5.4 \times 10^{-28}$ (7oxo site compared with total), two-sided Kolmogorov–Smirnov test (more results are shown in Extended Data Fig. 7a), compared with total mRNAs. **b**, Downregulated DEGs ($n = 596$, 7oxo site) are selected by cutoffs (red dotted lines) in statistical significance (>1, *y* axis; $P < 0.1$, two-sided *t*-test) and fold change ($\log_2$ ratio <-0.5, *x*-axis); critical target genes are highlighted in red and labelled with arrows. **c**, Gene ontology analysis of the downregulated DEGs. Downregulated DEGs are displayed in semantic space as cluster representatives; the colour and proportional size of circles indicate $\log_{10}$(*P* value). *P* values were obtained using Database for Annotation, Visualization and Integrated Discovery (DAVID) (Supplementary Methods). **d**, Experimental validation of the downregulated DEGs in $7o^8G$-miR-1- or miR-1-transfected rCMCs using qPCR; relative level indicates levels of the transcripts under $7o^8G$-miR-1 versus non-targeting control expression; *$P = 0.038$ (*Atp2a2*), 0.034 (*Gata4*) and 0.025 (*Gsk3b*). **e**, H9c2 cells ($n = 4$) transfected with $7o^8G$-miR-1 were analysed by RNA-seq as in **b**; cutoffs for downregulated DEGs are shown by the dotted lines (significance >1, median $\log_2$ ratio <-1). **f**, Targets of $7o^8G$-miR-1 identified in **e** were validated as in **d**; *$P = 1.8 \times 10^{-4}$ (*Gja1* miR-1), 6.6×10^{-5} (*Gja1* $7o^8G$), 0.052 (*Dram1* miR-1), 0.024 (*Dram1* $7o^8G$), 0.014 (*Pon2* miR-1), 0.006 (*Pon2* $7o^8G$), 0.007 (*Pgcf6* $7o^8G$) and 0.004 (*Bicd2* $7o^8G$). **g**, RNA-seq analysis of ISO-treated mouse hearts, analysed for putative $7o^8G$-miR-1 targets ($\log_2$ ratio < 0 in **a**, 7oxo site in 3′UTR) by CDF (7mer, position 2–8) as in **a**. $P = 3.16 \times 10^{-12}$ (targets compared with total mRNAs). **h**, GSEA for gene expression profiles of 7oxo targets (6mers, position 2–8); hits (shown as lines) are the transcripts showing downregulation in ISO-treated hearts ($\log_2$ ratio < 0). NES, normalized enrichment score. **i**, qPCR analysis of $7o^8G$-miR-1 targets in phenylephrine-treated rCMCs or ISO-treated mouse hearts; for sequences of miR-1 7oxo sites, see Supplementary Table 3, 4. $P = 0.021$ (*Gja1* PE), 0.028 (*Atp2a2* PE), 0.014 (*Gsk3b* PE), 0.021 (*Gja1* ISO), 0.001 (*Gata4* ISO), compared with mock treatment. All *P* values from two-sided *t*-tests; $n \geq 3$; repeated with biologically independent samples; data are mean ± s.d. unless otherwise indicated.

hypertrophic mouse hearts (*Gja1* and *Gata4*, Fig. 5i; *Bicd2* and *Atp2a2*, Extended Data Fig. 9b).

$7o^8G$-miR-1 in cardiomyopathy and its loss of function

We then broadened our investigation to the hearts of patients with cardiomyopathy. We retrieved and analysed data from the high-throughput sequencing of Ago-associated RNA[28], isolated from the left ventricles of human hearts by crosslinking immunoprecipitation (Ago HITS-CLIP) ($n = 6$; Supplementary Table 5b–d). Although the rate of G>T mutations was low, the same pattern (positions 2, 3 and 7) was detected as in o^8G-miR-1 (Fig. 6a). The G>T mutations were strongly clustered into two groups: one comprising a group of patients (1, 2, 4 and 5) with the highest frequency of mutations at position 7, along with some mutations at other positions (positions 2, 3 and 12) (Fig. 6b); the other (patients 3 and 6) with the highest frequency of mutations exclusively at position 2 (Fig. 6b). In Ago-mRNA clusters[28], miR-1 oxo sites were overrepresented more than expected (Fig. 6c), equivalent to an average of around 18% of seed sites, exceeding the G•U pairing (around 10%) and control sites (around 7%). Moreover, validated $7o^8G$-miR-1 targets—such as *ATP2A2*, *GSK3B*, *BICD2*, *GJA1*, *GATA4*, *DRAM1*, *PTEN* and *FBXO32* (Extended Data Fig. 9c–j) and *HSPB7* (Fig. 6d)—were found to map the 7oxo sites in Ago-mRNA peaks (CLIPick[29]), which were confirmed to be functional by a luciferase reporter assay (Fig. 6e, Extended Data Fig. 9k).

Independently, by conducting covalent ligation of endogenous Argonaute-bound RNAs with cross-linking and immunoprecipitation (CLEAR-CLIP)[24] experiments that produce ligated chimaera reads between miR-1 and target sites (Extended Data Fig. 9l, Supplementary Table 6a), we found that *HSPB7*—which has been identified as a risk gene for idiopathic dilated cardiomyopathy[30]—also had a 7oxo site (Fig. 6d). We observed that the frequency of Ago binding in 7oxo sites was increased in ISO-treated mouse hearts, in contrast to a decrease in its binding in seed sites (Extended Data Fig. 9m, n). The 7oxo site in *HSPB7* (Fig. 6d, Extended Data Fig. 9o) was further validated by qPCR (Extended Data Fig. 9p). We also checked the activity of the 7oxo site in conjunction with the seed site in *GJA1*[19], and observed combinatorial cooperativity for target repression in luciferase reporters (Extended Data Fig. 9q).

Finally, adapting the concept of miRNA sponges[31], the physiological relevance of $7o^8G$-miR-1 was evaluated using a loss-of-function study, in which competitive inhibitors against miR-1 (anti-seed) and $7o^8G$-miR-1 (anti-7oxo) were prepared to contain a tandem repeat of cognate target sites (Extended Data Fig. 10a). After validating their specificity using a luciferase reporter assay (Extended Data Fig. 10b, c) and RNA sequencing (Supplementary Table 6b, Extended Data Fig. 10d), we introduced anti-7oxo (4 sites; 4×) to rCMCs and observed the attenuation of phenylephrine-induced hypertrophy (Extended Data Fig. 10e). Next, several transgenic mouse lines expressing anti-7oxo in cardiomyocytes (α-MHC promoter, 13×) (Fig. 6f) were generated (Extended Data Fig. 10f, g) and confirmed to show specific expression of anti-7oxo (Extended Data Fig. 10h, Supplementary Table 6c) and global derepression of $7o^8G$-miR-1 targets (Fig. 6g, Extended Data Fig. 10i). There was no difference in basal heart size, but ISO-induced hypertrophy was significantly prevented in all different transgenic lines of both F_0 and F_1 generations (Fig. 6h, Extended Data Fig. 11a–e) without enlargement of cardiomyocytes (Extended Data Fig. 11f–h). Overall, we conclude that position-specific oxidation of miR-1—in particular to form $7o^8G$-miR-1—serves as an endogenous driver of cardiac hypertrophy and diseases.

Discussion

Here we demonstrate that the activation of adrenergic receptors generates ROS and leads to the formation of o^8G in the seed region of miR-1. miR-1 is thus redirected to repress new targets that function in cardiac

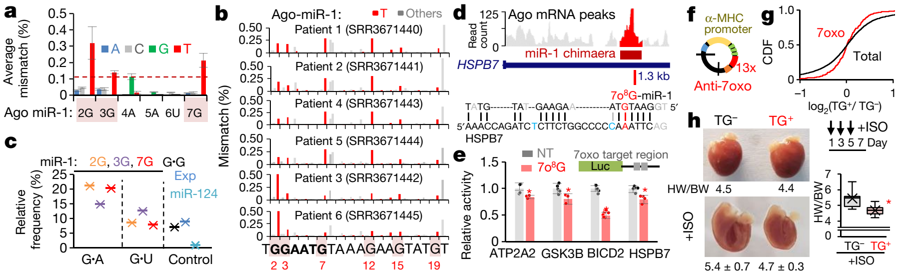

Fig. 6 | 7o^{8}G-miR-1 is implicated in cardiomyopathy and its loss of function. **a**, **b**, Sequence variation in Ago-associated miR-1, either mismatch rate (%) in seed as average (**a**) or the individual rate (%) (**b**) for each position. The Ago-associated RNA data, obtained by HITS-CLIP from the left ventricle of human hearts, are from ref. [28]. **c**, Relative frequency (%) of miR-1 oxo sites (G•A at position 2G, 3G or 7G) relative to seed sites in the normalized Ago-mRNA clusters[28]. G•U, wobble pairing sites; control, control sites (G•G, no pairing; Exp, expected frequency; miR-124, seed site of miR-124, not expressed in heart). **d**, miR-1 7oxo site in 3′UTRs of *HSPB7* (top), overlapping with the Ago-mRNA peaks ($P < 0.05$, CLIPick[29]; red). Other peaks are shown in grey. The sequences of the site are shown at the bottom; 7oxo sites in other genes in Extended Data Fig. 9c–j. **e**, Validation of the 7oxo sites by luciferase reporter assay. Half-maximal inhibitory concentrations (IC$_{50}$) of *GATA4*, *ATP2A2* and *BICD2* are stated in Extended Data Fig. 9k; sequences of the sites are provided in Supplementary Tables 3, 4. *$P = 0.05$ (*ATP2A2*), 0.016 (*GSK3B*), 9.4×10^{-11} (*BICD2*) and 0.003 (*HSPB7*). **f**, Anti-7oxo (a competitive inhibitor of 7o^{8}G-miR-1; α-MHC, 13× 7oxo sites) was used to generate transgenic mice (Extended Data Fig. 10f–h). **g**, Derepression of 7oxo targets (red line) in hearts of ISO-treated TG^{+} mice (F$_{0}$; founder line 68) was confirmed by RNA-seq (Supplementary Table 6c), compared with total transcripts (black line). $P = 0.002$, two-sided Kolmogorov–Smirnov test; details in Extended Data Fig. 10i. **h**, Heart sizes of anti-7oxo TG^{-} mice compared with those of TG^{+} mice in response to ISO administration (F$_{1}$; $n \geq 7$); in the box plot, the lines represent the median, first and third quartiles, the whiskers denote the minima and maxima, and 'x' marks the mean value. *$P = 0.019$. For further details, including HW/TL, see Extended Data Fig. 11c–e. All *P* values are obtained from two-sided *t*-tests unless otherwise stated; $n = 3$; repeated with biologically independent samples; data are mean ± s.d. unless otherwise indicated.

hypertrophy pathways (Extended Data Fig. 11i, Supplementary Discussion). Levels of o^{8}G-miR-1 immediately increase upon treatment with an adrenergic agonist and are sustained for up to a week in hypertrophic hearts (Extended Data Fig. 11j). Furthermore, sequences of the miR-1 oxo sites are evolutionally conserved in 3′UTRs (Extended Data Fig. 11k). Our findings suggest that the formation of o^{8}G in miRNA could be the general epitranscriptional mechanism by which ROS—under pathophysiological conditions—can impart fine-tuning of gene expression, as a part of redox signalling that ultimately leads to phenotypic alterations.

Online content

Any methods, additional references, Nature Research reporting summaries, source data, extended data, supplementary information, acknowledgements, peer review information; details of author contributions and competing interests; and statements of data and code availability are available at https://doi.org/10.1038/s41586-020-2586-0.

1. Burgoyne, J. R., Mongue-Din, H., Eaton, P. & Shah, A. M. Redox signaling in cardiac physiology and pathology. *Circ. Res.* **111**, 1091–1106 (2012).
2. Kasai, H. & Nishimura, S. Hydroxylation of deoxyguanosine at the C-8 position by ascorbic acid and other reducing agents. *Nucleic Acids Res.* **12**, 2137–2145 (1984).
3. Simms, C. L. & Zaher, H. S. Quality control of chemically damaged RNA. *Cell. Mol. Life Sci.* **73**, 3639–3653 (2016).
4. Frey, N. & Olson, E. N. Cardiac hypertrophy: the good, the bad, and the ugly. *Annu. Rev. Physiol.* **65**, 45–79 (2003).
5. Freudenthal, B. D. et al. Uncovering the polymerase-induced cytotoxicity of an oxidized nucleotide. *Nature* **517**, 635–639 (2015).
6. Shibutani, S., Takeshita, M. & Grollman, A. P. Insertion of specific bases during DNA synthesis past the oxidation-damaged base 8-oxodG. *Nature* **349**, 431–434 (1991).
7. Nunomura, A. et al. RNA oxidation is a prominent feature of vulnerable neurons in Alzheimer's disease. *J. Neurosci.* **19**, 1959–1964 (1999).
8. Chang, Y. et al. Messenger RNA oxidation occurs early in disease pathogenesis and promotes motor neuron degeneration in ALS. *PLoS ONE* **3**, e2849 (2008).
9. Seok, H., Ham, J., Jang, E. S. & Chi, S. W. MicroRNA target recognition: insights from transcriptome-wide non-canonical interactions. *Mol. Cells* **39**, 375–381 (2016).
10. Wang, J. X. et al. Oxidative modification of miR-184 enables it to target Bcl-xL and Bcl-w. *Mol. Cell* **59**, 50–61 (2015).
11. Carè, A. et al. MicroRNA-133 controls cardiac hypertrophy. *Nat. Med.* **13**, 613–618 (2007).
12. Karakikes, I. et al. Therapeutic cardiac-targeted delivery of miR-1 reverses pressure overload-induced cardiac hypertrophy and attenuates pathological remodeling. *J. Am. Heart Assoc.* **2**, e000078 (2013).
13. Li, Q. et al. Attenuation of microRNA-1 derepresses the cytoskeleton regulatory protein twinfilin-1 to provoke cardiac hypertrophy. *J. Cell Sci.* **123**, 2444–2452 (2010).
14. Seok, H. Y. et al. Loss of microRNA-155 protects the heart from pathological cardiac hypertrophy. *Circ. Res.* **114**, 1585–1595 (2014).
15. Huang, Z. P. et al. MicroRNA-22 regulates cardiac hypertrophy and remodeling in response to stress. *Circ. Res.* **112**, 1234–1243 (2013).
16. Zhao, Y. et al. Dysregulation of cardiogenesis, cardiac conduction, and cell cycle in mice lacking miRNA-1-2. *Cell* **129**, 303–317 (2007).
17. Heidersbach, A. et al. microRNA-1 regulates sarcomere formation and suppresses smooth muscle gene expression in the mammalian heart. *eLife* **2**, e01323 (2013).
18. Zhao, Y., Samal, E. & Srivastava, D. Serum response factor regulates a muscle-specific microRNA that targets *Hand2* during cardiogenesis. *Nature* **436**, 214–220 (2005).
19. Yang, B. et al. The muscle-specific microRNA miR-1 regulates cardiac arrhythmogenic potential by targeting *GJA1* and *KCNJ2*. *Nat. Med.* **13**, 486–491 (2007).
20. Su, X. et al. Over-expression of microRNA-1 causes arrhythmia by disturbing intracellular trafficking system. *Sci. Rep.* **7**, 46259 (2017).
21. Pan, Z. et al. miR-1 exacerbates cardiac ischemia-reperfusion injury in mouse models. *PLoS ONE* **7**, e50515 (2012).
22. Alenko, A., Fleming, A. M. & Burrows, C. J. Reverse transcription past products of guanine oxidation in RNA leads to insertion of A and C opposite 8-oxo-7,8-dihydroguanine and A and G opposite 5-guanidinohydantoin and spiroiminodihydantoin diastereomers. *Biochemistry* **56**, 5053–5064 (2017).
23. Chi, S. W., Zang, J. B., Mele, A. & Darnell, R. B. Argonaute HITS-CLIP decodes microRNA–mRNA interaction maps. *Nature* **460**, 479–486 (2009).
24. Moore, M. J. et al. miRNA-target chimeras reveal miRNA 3′-end pairing as a major determinant of Argonaute target specificity. *Nat. Commun.* **6**, 8864 (2015).
25. Crackower, M. A. et al. Regulation of myocardial contractility and cell size by distinct PI3K–PTEN signaling pathways. *Cell* **110**, 737–749 (2002).
26. Li, H. H. et al. Atrogin-1/muscle atrophy F-box inhibits calcineurin-dependent cardiac hypertrophy by participating in an SCF ubiquitin ligase complex. *J. Clin. Invest.* **114**, 1058–1071 (2004).
27. Ying, X. et al. Novel protective role for ubiquitin-specific protease 18 in pathological cardiac remodeling. *Hypertension* **68**, 1160–1170 (2016).
28. Spengler, R. M. et al. Elucidation of transcriptome-wide microRNA binding sites in human cardiac tissues by Ago2 HITS-CLIP. *Nucleic Acids Res.* **44**, 7120–7131 (2016).
29. Park, S. et al. CLIPick: a sensitive peak caller for expression-based deconvolution of HITS-CLIP signals. *Nucleic Acids Res.* **46**, 11153–11168 (2018).
30. Stark, K. et al. Genetic association study identifies *HSPB7* as a risk gene for idiopathic dilated cardiomyopathy. *PLoS Genet.* **6**, e1001167 (2010).
31. Ebert, M. S. & Sharp, P. A. MicroRNA sponges: progress and possibilities. *RNA* **16**, 2043–2050 (2010).
32. Chi, S. W., Hannon, G. J. & Darnell, R. B. An alternative mode of microRNA target recognition. *Nat. Struct. Mol. Biol.* **19**, 321–327 (2012).
33. Lee, H. S. et al. Abasic pivot substitution harnesses target specificity of RNA interference. *Nat. Commun.* **6**, 10154 (2015).
34. Choi, Y. J., Gibala, K. S., Ayele, T., Deventer, K. V. & Resendiz, M. J. E. Biophysical properties, thermal stability and functional impact of 8-oxo-7,8-dihydroguanine on oligonucleotides of RNA-a study of duplex, hairpins and the aptamer for preQ1 as models. *Nucleic Acids Res.* **45**, 2099–2111 (2017).
35. Kim, S. K., Lee, S. H., Kwon, O. S. & Moon, B. J. DNA·RNA heteroduplex containing 8-oxo-7,8-dihydroguanosine: base pairing, structures, and thermodynamic stability. *J. Biochem. Mol. Biol.* **37**, 657–662 (2004).

Reporting summary

Further information on research design is available in the Nature Research Reporting Summary linked to this paper.

Data availability

All raw sequencing data from o^{8}G-miSeq (SRP189806, SRP189807, SRP189808, SRP226125), RNA-seq (SRP189813, SRP189117, SRP189812, SRP189811, SRP189809, SRP213998, SRP228274) and CLEAR-CLIP (SRP189810) were deposited to the Sequence Read Archive (SRA). All FASTQ files are available at http://clip.korea.ac.kr/oxog/, including sequencing data of o^{8}G IP with spike-in. Source data are provided with this paper.

Code availability

The Python scripts used in this work are available at http://clip.korea.ac.kr/oxog/.

Acknowledgements We thank all members of the Chi laboratory for help and discussions. We thank in particular M.-H. Chung for sharing research experiences with H. Kasai and S. Nishimura, which inspired us to initiate this project; the late S.-D. Yoo for scientific discussions; the late Y.-S. Lee for initial help on this work; D.-Z. Wang for providing the pJG/ALPHA MHC vector; J. Han, H.-W. Lee and W. J. Park for providing AC16 cells and Y. W. Chung for H9c2 cells, which were used for preliminary studies; Samsung Medical Center for echocardiograms; J. Im and J. W. Park for initial help with the HPLC analysis to confirm the o^{8}G immunoprecipitation; E. S. Cho for help in analysing sequence conservation of miR-1 oxo sites; D. H. Lee and W. Lee for initial help with the project; and the staff of Gyerim Experimental Animal Resource Center for animal care and technical assistance. This work was supported by Samsung Research Funding and Incubation Center of Samsung Electronics under project number SRFC-MA1801-10 and Korea University Grant.

Author contributions H.S., H.L. and S.L. performed the major experiments. H.S., H.L., S.L., G.-W.D.K., S.H.A., E.-S.J. and S.W.C analysed the data. H.S., H.L., S.L., H.-S.L., J. Park, D.G. and S.E. performed the biochemical and molecular biology experiments. H.S. and H.L. conducted flow cytometry analyses. H.S. and H.L. performed the o^{8}G-miSeq. H.S., H.L. and Yeojin Jeong conducted the experiments to demonstrate o^{8}G>T mutation. H.S., H.L., S.L., Y.K.C., Yeahji Jeong and G.-W.D.K. performed the RNA-seq. J. Peak conducted the CLEAR-CLIP analysis. S.H.A., Y.K.C. and S.W.C. performed the bioinformatics analyses. H.S., H.L., S.L., H.-S.L. and J. Park conducted the luciferase reporter assays. H.S., S.L. and G.-W.D.K. performed the mouse experiments. H.S., E.-S.J. and S.W.C. conceived, designed and supervised the research. H.S., E.-S.J. and S.W.C. wrote the manuscript.

Competing interests Korea University has filed a Korean patent application (10-2019-0156147) covering part of the work presented in this Article, listing H.S. and S.W.C. as inventors.

Additional information

Supplementary information is available for this paper at https://doi.org/10.1038/s41586-020-2586-0.

Correspondence and requests for materials should be addressed to S.W.C.

Peer review information *Nature* thanks Marino Resendiz, Eva van Rooij and the other, anonymous, reviewer(s) for their contribution to the peer review of this work.

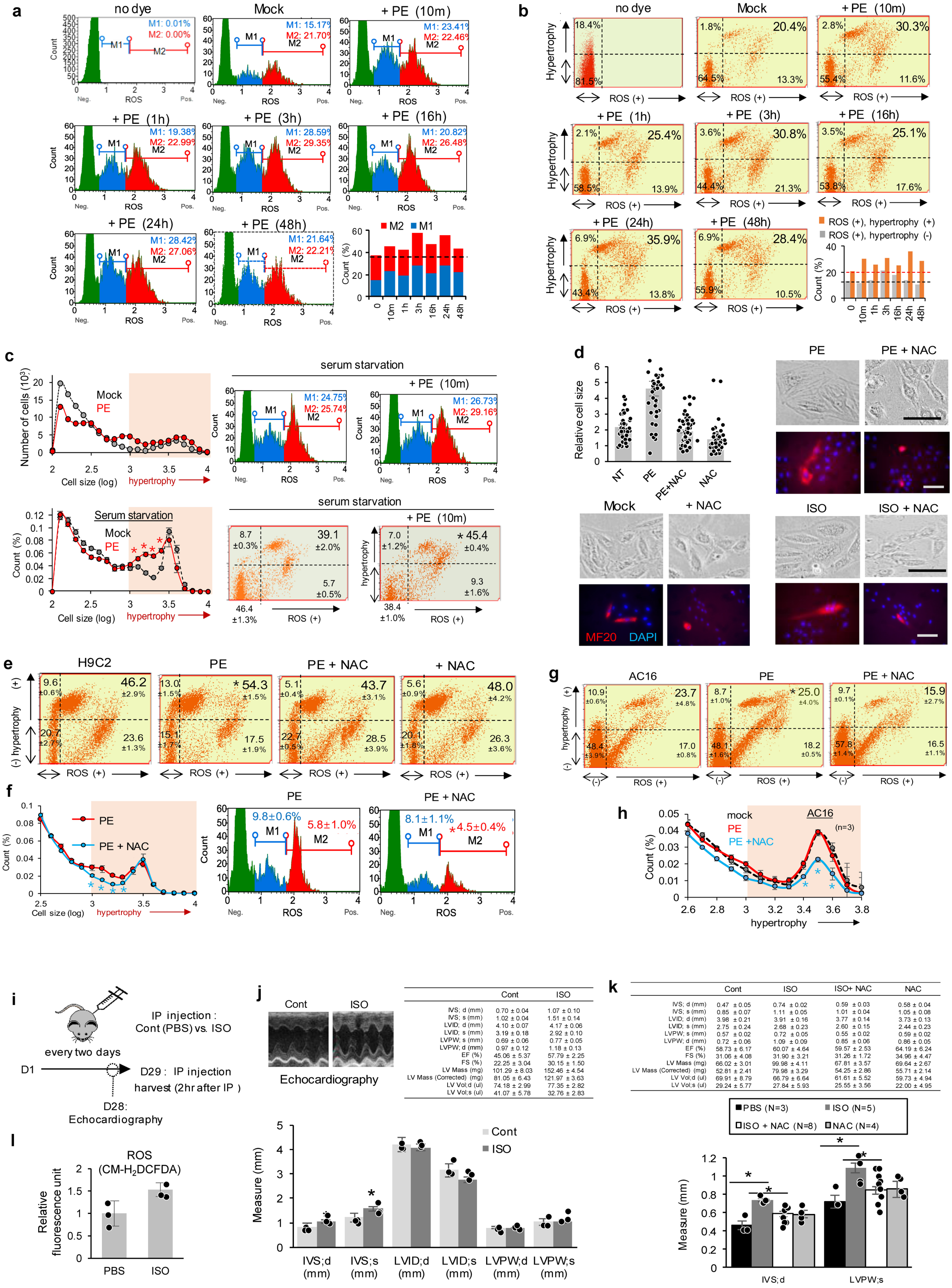

	Cont	ISO
IVS; d (mm)	0.70 ± 0.04	1.07 ± 0.10
IVS; s (mm)	1.02 ± 0.04	1.51 ± 0.14
LVID; d (mm)	4.10 ± 0.07	4.17 ± 0.06
LVID; s (mm)	3.19 ± 0.18	2.92 ± 0.10
LVPW; s (mm)	0.69 ± 0.06	0.77 ± 0.05
LVPW; d (mm)	0.97 ± 0.12	1.18 ± 0.13
EF (%)	45.06 ± 5.37	57.79 ± 2.25
FS (%)	22.25 ± 3.04	30.15 ± 1.50
LV Mass (mg)	101.29 ± 8.03	152.46 ± 4.54
LV Mass (Corrected) (mg)	81.05 ± 6.43	121.97 ± 3.63
LV Vol;d (ul)	74.18 ± 2.99	77.35 ± 2.82
LV Vol;s (ul)	41.07 ± 5.78	32.76 ± 2.83

	Cont	ISO	ISO+ NAC	NAC
IVS; d (mm)	0.47 ± 0.05	0.74 ± 0.02	0.59 ± 0.03	0.58 ± 0.04
IVS; s (mm)	0.85 ± 0.07	1.11 ± 0.05	1.01 ± 0.04	1.05 ± 0.08
LVID; d (mm)	3.98 ± 0.21	3.91 ± 0.16	3.77 ± 0.14	3.73 ± 0.13
LVID; s (mm)	2.75 ± 0.24	2.68 ± 0.23	2.60 ± 0.15	2.44 ± 0.23
LVPW; s (mm)	0.57 ± 0.02	0.72 ± 0.05	0.55 ± 0.02	0.59 ± 0.02
LVPW; d (mm)	0.72 ± 0.06	1.09 ± 0.09	0.85 ± 0.06	0.86 ± 0.05
EF (%)	58.73 ± 6.17	60.07 ± 4.64	59.57 ± 2.53	64.19 ± 6.24
FS (%)	31.06 ± 4.08	31.90 ± 3.21	31.26 ± 1.72	34.96 ± 4.47
LV Mass (mg)	66.02 ± 3.01	99.98 ± 4.11	67.81 ± 3.57	69.64 ± 2.67
LV Mass (Corrected) (mg)	52.81 ± 2.41	79.98 ± 3.29	54.25 ± 2.86	55.71 ± 2.14
LV Vol;d (ul)	69.91 ± 8.79	66.79 ± 6.64	61.61 ± 5.52	59.73 ± 4.94
LV Vol;s (ul)	29.24 ± 5.77	27.84 ± 5.93	25.55 ± 3.56	22.00 ± 4.95

Extended Data Fig. 1 | See next page for caption.

Extended Data Fig. 1 | Adrenergic cardiac hypertrophy depends on ROS. **a**, **b**, ROS measurement in H9c2 cells after phenylephrine treatment in a time-dependent manner, detected by fluorescent ROS dye (DHE) and flow cytometry (10,000 cells); M1 (blue), cells with moderate ROS; M2 (red), cells with high level of ROS (**a**). The results were further analysed for cell size; $\log_{10}$(forward scatter), *y* axis; hypertrophy, cell size >3 (**b**). **c**, Same analysis as in **a**, **b** except subjecting to serum starvation and showing distribution of cell size in left panels; number of cells or counts (%), *y* axis (left); $n = 3$ biologically independent experiments. **d**, Morphology of H9c2 cells in the presence of phenylephrine and/or NAC treatment, quantified for their average cell size relative to NAC treatment ($n \geq 40$ cells, ImageJ; top left graph); NT versus phenylephrine, $P = 9.5 \times 10^{-7}$; error bars, s.e.m. Immunofluorescence staining of cardiomyocytes, discriminated by staining of sarcomeric isoforms of myosin heavy chain (MF20, a marker of cardiomyocyte differentiation). Notably, differentiated cardiomyocyte lineage cells ($MF20^+$) were quantified owing to different extent of fate heterogeneity in H9c2 cardiomyoblast cells; the same batch of H9c2 cells used in **a**–**c**; scale bar, 50 μm. **e**–**h**, Same analyses as in **c** except examining the effect of NAC treatment in H9c2 cells (**e**, **f**) and using AC16 cells (**g**, **h**); $n = 3$ biologically independent experiments; H9c2 cells in all of these figures (**a**–**h**) were obtained from Korean Cell Line Bank. Of note, prevention of ISO induced cardiac hypertrophy by NAC treatment indicates that ROS production is probably upstream of the hypertrophic phenotype. **i**, **j**, Chronic intraperitoneal (IP) injection of 75 mg kg^{-1} ISO and PBS (used as control) was conducted for mice ($n = 7$ biologically independent mice) in every two days for 29 days (**i**) and their echocardiography results ($n = 3$ biologically independent mice) were obtained (**j**); IVS, interventricular septum; LVID, left ventricular internal diameter; LVPW, left ventricular posterior wall; EF, ejection fraction (%); FS, fractional shortening (%); LV, left ventricular; d, diastolic; s, systolic; $^*P = 0.024$ (IVS;d, ISO versus Cont) and 0.027 (IVS;s, ISO versus Cont), respectively; data are mean ± s.e.m. **k**, Same experiments as performed in **i**, **j**, except treating NAC and using echocardiography at day 21; $^*P = 0.001$, 0.004, 0.031 and 0.033, respectively; $n \geq 3$ biologically independent mice; data are mean ± s.e.m. **l**, Measurement of ROS in lysate (100 μg proteins) from the ISO-induced hypertrophic mouse hearts by using fluorescent ROS dye, CM-H_2DCFDA. $^*P = 0.046$. All *P* values from two-sided *t*-test; $^*P < 0.05$; $n \geq 3$ biological independent samples; data are mean ± s.d. unless otherwise indicated.

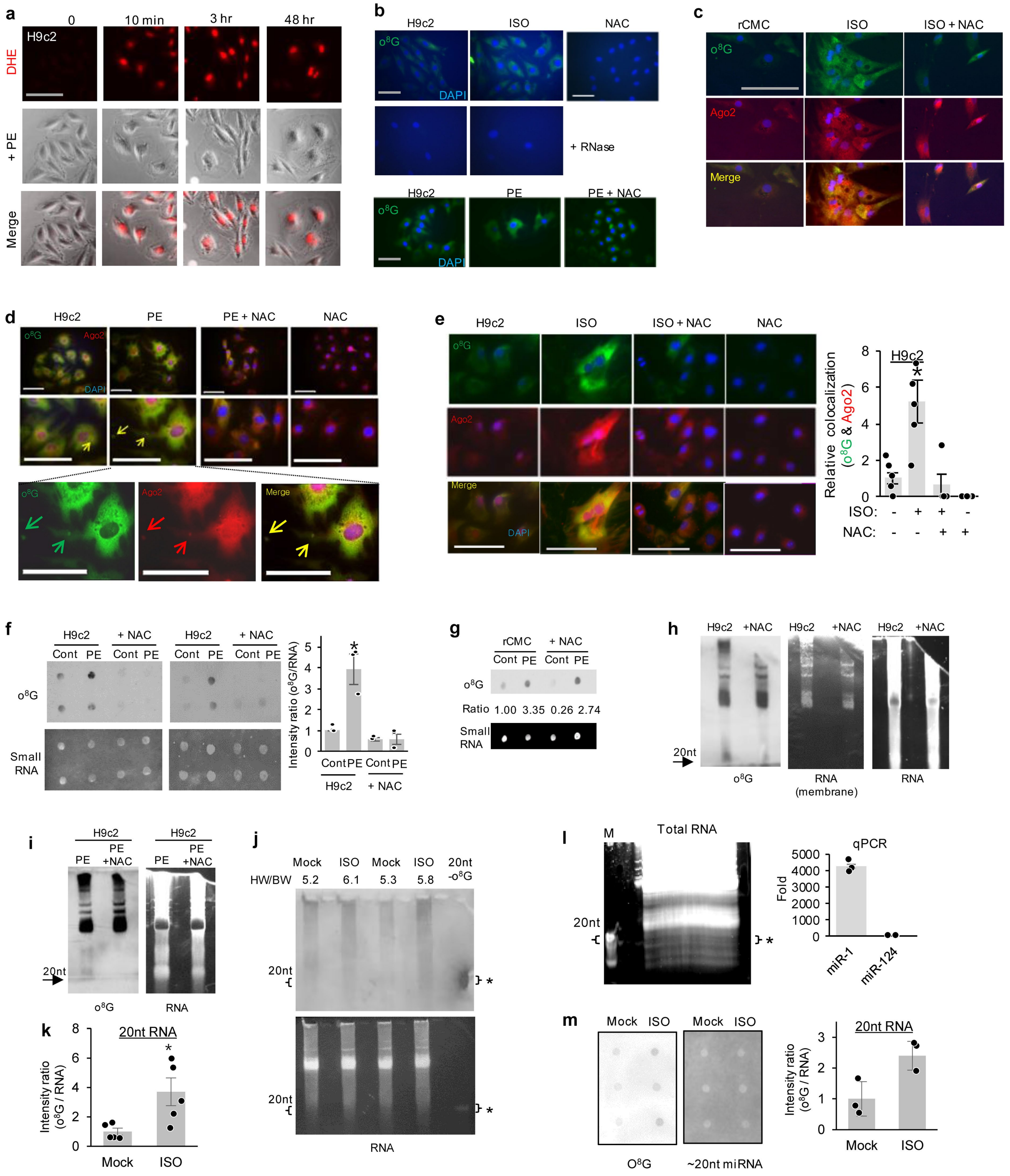

Extended Data Fig. 2 | See next page for caption.

Extended Data Fig. 2 | Adrenergic cardiac hypertrophy oxidizes miRNAs. **a**, Extent of ROS and alteration of cell size was monitored by using ROS fluorescence dye (DHE) in phenylephrine-treated H9c2 cells in time-dependent manner; scale bar, 50 µm. Notably, sustained elevation of ROS was also observed (up to 48 h) by flow cytometry (Extended Data Fig. 1a, b). **b**, Immunofluorescence staining of oxidized nucleic acids in ISO- and/or NAC-treated H9c2 cells by using o^8G-specific antibody (top). Cytoplasmic pattern of o^8G staining disappeared upon treating with RNase, confirming that o^8G occurs in RNA (middle). Phenylephrine-treated H9c2 cells were also examined (bottom); scale bar, 50 µm. **c**–**e**, Immunofluorescence staining of o^8G and Ago2 in ISO- and/or NAC-treated rCMCs (**c**), phenylephrine- and/or NAC-treated H9c2 cells (**d**), and ISO- and/or NAC-treated H9c2 cells where their colocalization was quantified (**e**); coloured arrow, cytoplasmic puncta stained as both Ago2 and o^8G (**d**); $n \geq 4$; $^*P = 0.012$ (**e**, right); Scale bars, 100 µm (**c**) or 50 µm (**d**, **e**). Every independent experiment ($n \geq 3$) showed similar results (**a**–**e**). **f**, Dot blot analyses of o^8G for small RNA, extracted from phenylephrine- and/or NAC-treated H9c2 cells (top left) with quantification (relative to small RNA input in lower left panel; right); $n = 3$; $^*P = 0.009$. **g**, Same analyses performed in phenylephrine- and/or NAC-treated rCMCs as in **f**. **h**–**k**, Northwestern blotting of o^8G for total RNA (20 µg), extracted from NAC-treated H9c2 cells (**h**), phenylephrine- and/or NAC-treated H9c2 cells (**i**) and ISO-injected mouse hearts (**j**) with quantification of normalized intensity (intensity ratio, o^8G signal per amount of RNA; **k**) in 20 nt RNA (indicated with arrow or asterisk); $n = 5$ biological independent mice; Mock, a control set with injection of PBS; HW/BW, heart weight per body weight (**j**); 20 nt-o^8G, synthesized 20-nt-long RNA with o^8G used as a size marker; $^*P = 0.024$ (**k**). **l**, miRNA was isolated from total RNA in mouse hearts based on their ~20 nt size (left; *), where existence of muscle-specific miR-1 was confirmed by qPCR with no detection of a brain-specific miRNA, miR-124 (right); M, synthesized 20-nt-long RNA used as a size marker; $P = 4.24 \times 10^{-5}$ (miR-1 versus miR-124). **m**, Dot blot analysis of o^8G was performed for the gel-extracted miRNAs (40 ng), derived from ISO-treated hypertrophic mouse hearts (left) and the results were quantified as in **k** (right); error bars, s.d.; $^*P = 0.029$; $n = 3$ biologically independent samples. All P values from two-sided t-test; $^*P < 0.05$; $n \geq 3$ biological independent samples; data are mean ± s.e.m. unless otherwise indicated.

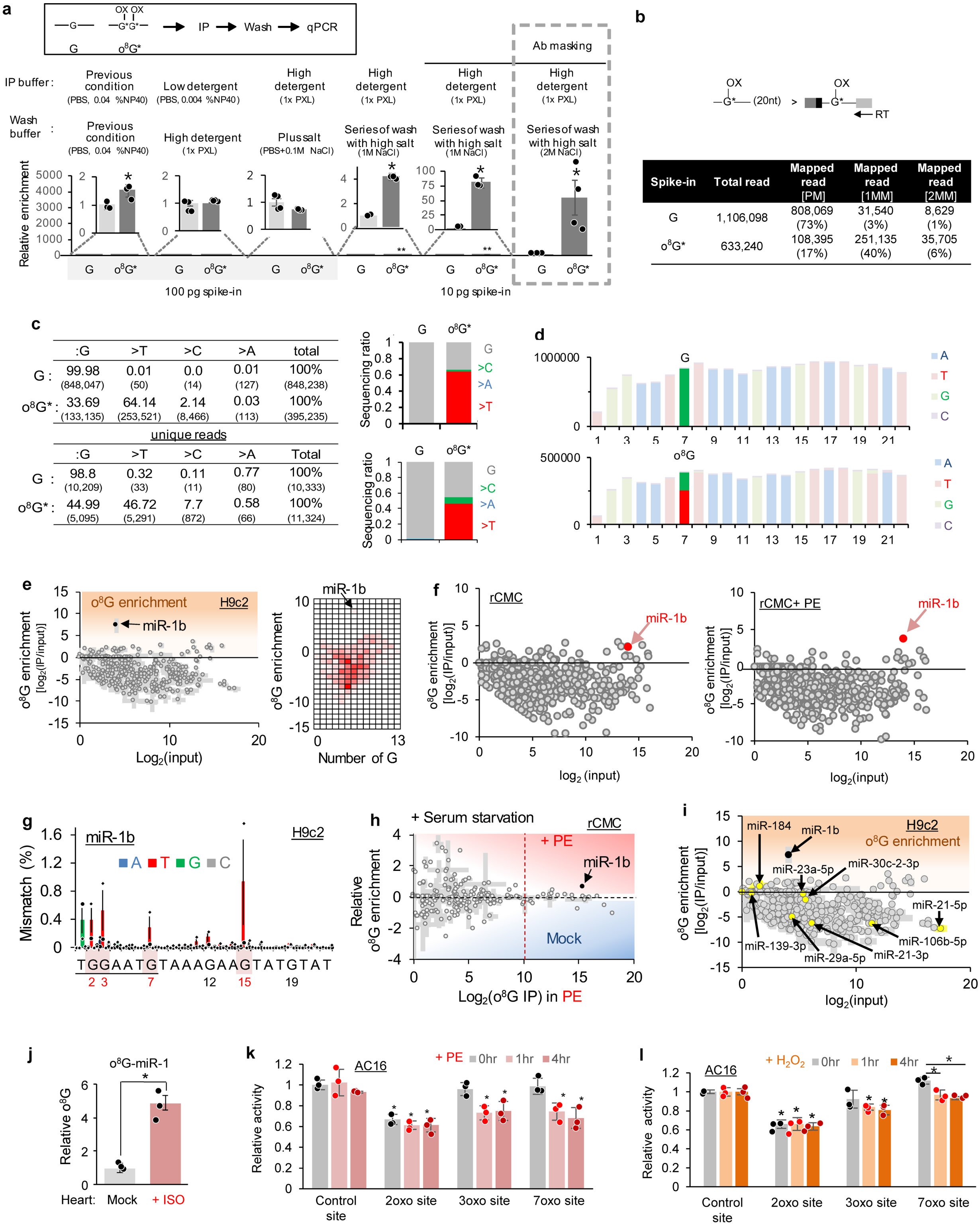

Spike-in	Total read	Mapped read [PM]	Mapped read [1MM]	Mapped read [2MM]
G	1,106,098	808,069 (73%)	31,540 (3%)	8,629 (1%)
o^8G^*	633,240	108,395 (17%)	251,135 (40%)	35,705 (6%)

	:G	>T	>C	>A	total
G :	99.98 (848,047)	0.01 (50)	0.0 (14)	0.01 (127)	100% (848,238)
o^8G^* :	33.69 (133,135)	64.14 (253,521)	2.14 (8,466)	0.03 (113)	100% (395,235)

unique reads

	:G	>T	>C	>A	Total
G :	98.8 (10,209)	0.32 (33)	0.11 (11)	0.77 (80)	100% (10,333)
o^8G^* :	44.99 (5,095)	46.72 (5,291)	7.7 (872)	0.58 (66)	100% (11,324)

Extended Data Fig. 3 | See next page for caption.

Extended Data Fig. 3 | Development of o^{8}G-miSeq to identify oxidized miRNA and o^{8}G position for cardiac hypertrophy. a, Optimization of o^{8}G IP by adjusting IP and wash condition, estimated by using synthesized RNA containing o^{8}G as spike-in control (100 pg or 10 pg) followed by qPCR; relative enrichment, amount of o^{8}G RNA per non-oxidized RNA. "Ab masking" denotes preincubation of o^{8}G antibody with non-oxidized G; $^*P = 0.04$, 1.6×10^{-6}, 1.3×10^{-4} and 0.02, respectively; $n \geq 3$; error bars, s.e.m. The detailed process and the composition of buffers are described in Supplementary Methods. **b**–**d**, Sequencing results of cDNA, reverse transcribed from synthesized o^{8}G RNA (Fastq files, http://clip.korea.ac.kr/oxog/; **b**). Sequencing reads with ≤2 mismatches (2MM) were analysed for the frequency of variation, found in the introduced position of o^{8}G; based on raw counts (**c**, top); based on unique reads, to exclude artificial bias derived from PCR amplification (**c**, bottom; discriminated by degenerative barcode, details in Supplementary Methods). Numbers of variation in every position of synthesized RNA were also represented; G (**d**, top) versus o^{8}G (**d**, bottom), position 7; read-count, *y* axis. Of note, ~50–60% G>T variation rate is in agreement with thermal denaturation transitions obtained from RNA:DNA duplexes[34,35]. **e**, o^{8}G-miSeq results from H9c2 cells. o^{8}G enrichment, log ratio of o^{8}G IP normalized to the input read counts for miRNAs, was plotted depending on the miRNA abundance (input; **e**, left), number of G in sequences as heat map density (**e**, right). **f**, o^{8}G enrichment ($\log_2$(IP/input)) was analysed depending on the level of miRNA ($\log_2$ value of read-count from miRNA-seq) in the absence (left) versus presence of phenylephrine treatment (right); miR-1b, red dot indicated by red arrow. **g**, The positional sequence variation of miR-1b is represented as a normalized mismatch (%) in o^{8}G-miSeq results from H9c2 cells; error bars, s.e.m. The o^{8}G in miR-1b was found to be enriched predominantly in seed region (positions 2, 3 and 7) based on G>T mutation rate. Notably, o^{8}G at position 15 was also observed to be comparable to that of the other positions in seed. **h**, o^{8}G-miSeq in phenylephrine-treated rCMCs with serum starvation. Relative o^{8}G enrichment was plotted for miRNAs depending on the extent of phenylephrine-induced oxidation ($\log_2$(o^{8}G IP) in phenylephrine). Of note, miR-1b showed the most marked phenylephrine-induced oxidation (relative o^{8}G enrichment = 0.8) with a considerable level of o^{8}G ($\log_2$(o^{8}G-IP)>10, dotted red line). **i**, o^{8}G-miSeq result of H9c2 cells was compared with previous results of oxidized miRNAs in H_2O_2-treated H9c2 cells[10], which were identified by using o^{8}G IP and microarray. The previous results were represented inside of the current o^{8}G-miSeq data, highlighted as a yellow circle with indicated arrow in the plot of o^{8}G enrichment (amount in o^{8}G IP relative to abundance) and abundance of miRNA ($\log_2$(input)). Notably, except miR-184, the previously identified oxidized miRNAs were not so much enriched in the o^{8}G-miSeq results, presumably due to disregarding background from different abundance of miRNA or lack of o^{8}G IP optimization in the previous trial. The discrepancy also could be caused by heterogeneity of H9c2 cell lines, which behave differently depending on culture condition and batches. **j**, Relative o^{8}G of miR-1 in ISO-treated mouse heart (chronic injection) was measured by o^{8}G IP and qPCR; the amount of miR-1 in o^{8}G IP was normalized by the amount of o^{8}G-contained spike-in control; error bars, s.e.m.; $^*P = 0.002$. miR-1 showed the most dramatic enhancement (fivefold). Of note, elevation of o^{8}G-miR-1 in chronic injection of ISO implicated that o^{8}G-miR-1 could persist during chronic stress for cardiac hypertrophy. **k**, **l**, Luciferase reporter assays with oxo sites of miR-1 as performed in Fig. 3e except for AC16 with phenylephrine (**k**) or H_2O_2 treatment (**l**); $^*P = 0.001$, 6.1×10^{-3}, 0.001, 0.025, 0.027, 0.034 and 0.012, respectively (**k**); $^*P = 2.3 \times 10^{-4}$, 0.002, 0.001, 0.007, 0.018, 2.0×10^{-3} and 1.2×10^{-4}, respectively (**l**). All *P* values from two-sided *t*-test; $^*P < 0.05$; $n = 3$ biological independent samples; data are mean ± s.d. unless otherwise indicated.

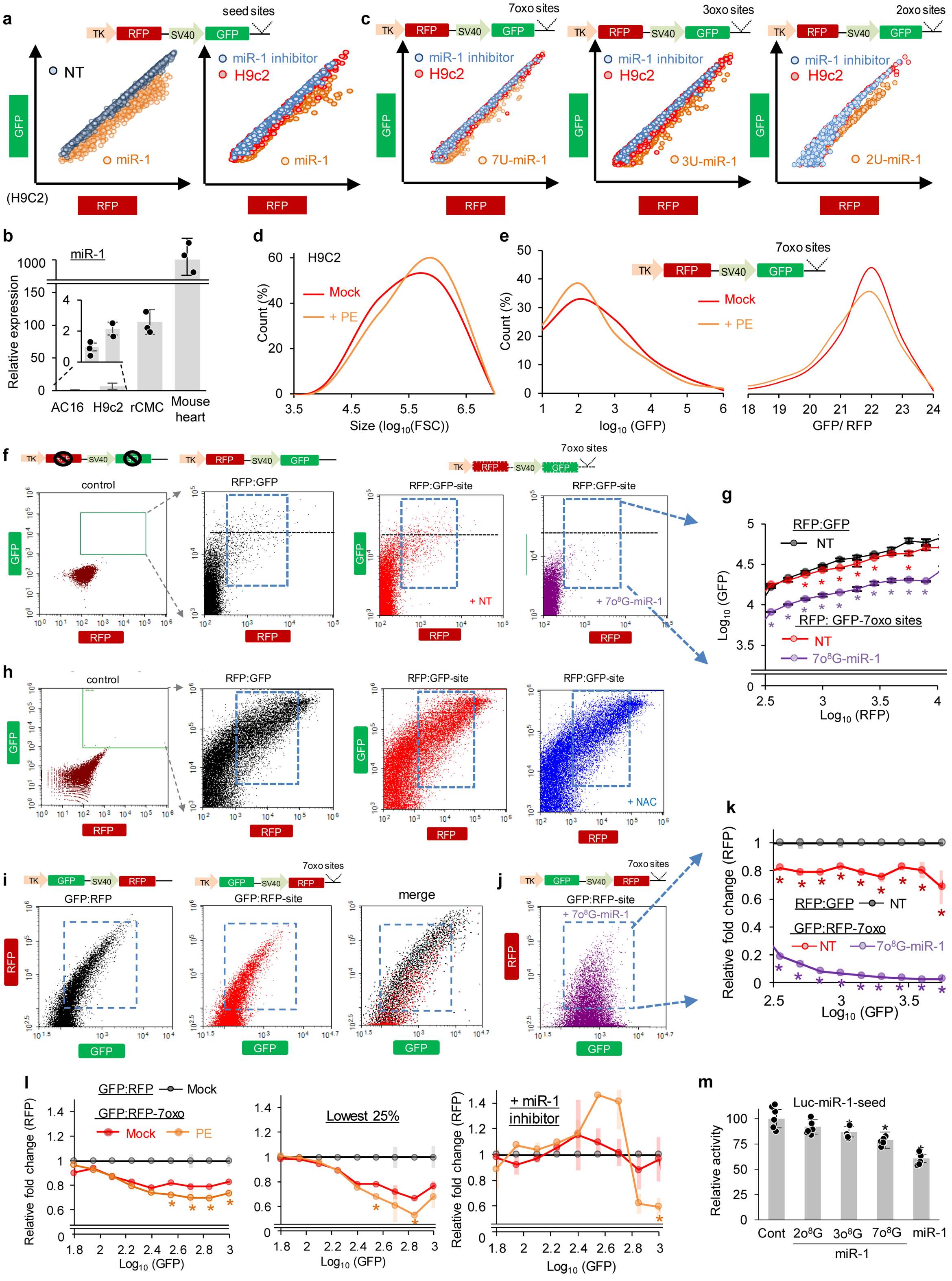

Extended Data Fig. 4 | See next page for caption.

Extended Data Fig. 4 | Oxidized miR-1 silences new target sites via o^{8}G•A base pairing. **a**, dFP (dual fluorescent proteins) reporter with miR-1 seed sites in GFP (top) was validated to detect miR-1 dependent repression at the endogenous level of individual H9c2 cells; NT, non-targeting control; miR-1, synthesized miR-1 used as positive control; miR-1 inhibitor for blocking endogenous miR-1. **b**, Expression level of miR-1 in AC16 cells, H9c2 cells, rCMCs and mouse heart, measured by qPCR relatively to U6; error bars, s.e.m. Notably, heterogeneity of AC16 and H9c2 cells could result in low global level of miR-1 in total small RNAs, implicating the worth of examining miR-1 at individual cell level. **c**, Same dFP reporter analyses as performed in **a** except for 7oxo, 3oxo and 2oxo sites; 7U-miR-1, 3U-miR-1 or 2U-miR-1, used as positive control. Of note, every miR-1 oxo site (7oxo, 3oxo and 2oxo site) in the dFP reporters was endogenously suppressed with sensitivity to detect the repression mediated by the basal level of o^{8}G-miR-1, confirmed by either transfecting miR-1 inhibitor or cognate miR-1 variants. **d**, Phenylephrine-dependent enlargement of H9c2 cells, measured by size ($\log_{10}$(FSC)) using flow cytometer. **e**, Distribution of GFP value ($\log_{10}$(GFP)) in dFP reporter, of which GFP contains miR-1 7oxo sites (left). Relative repression ($\log_{10}$(GFP/RFP)) was calculated by averaging the reporter fluorescence values (GFP-7oxo) with a similar range of control fluorescence values (RFP) in the cells (right). The relative repression was also examined in phenylephrine-treated H9c2 cells. Of note, flow cytometry in **a**, **c**–**e** used a blue laser for the excitation. **f**, **g**, Quantification of dFP reporter in H9c2 cells by flow cytometry. Based on scatter plot of GFP versus RFP (**f**), GFP value ($\log_{10}$(GFP)) with 7oxo sites (RFP:GFP-site; red) was examined by averaging GFP values derived from similar range of control RFP values in the cells (**g**), further normalized as relative fold change (Fig. 3g), normalized by dFP reporter with no site (RFP:GFP-no site; black); 7o^{8}G-miR-1, used as positive control (purple). Vectors with no fluorescence protein gene (control) were used to measure level of autofluorescence. **h**, Same analyses as in **f** except for considering NAC treatment. Of note, 10 times greater amount of reporter vector was used in **h** than in **f**, resulting in fewer transfected cells in **f**. **i**–**k**, Flow cytometry analysis using switched dFP protein reporter, of which fluorescent proteins were interchanged in **i**, top, resulting in sensitive detection of the suppression of miR-1 7oxo site by the endogenous level of 7o^{8}G-miR-1 (**i**, **j**); experiments with positive control, 7o^{8}G-miR-1 (**j**). Repressive propensity of RFP with 7oxo site (GFP:RFP-site; **i**, middle) was shown in merge (**i**, right), relative to RFP with no site (GFP:RFP-no site; **i**, left), showing similar tendency of shifting; relative fold change, normalized RFP values denominated by dFP reporter with no site (RFP:GFP-no site; black). **l**, Same analysis as in **i**–**k** with switched dFP reporter except using phenylephrine (left) and miR-1 inhibitor (right). Of note, phenylephrine-induced repression of miR-1 7oxo sites became more substantial when only a limited cell population, for which reporter values (RFP) were in the lowest 25%, was considered (middle). Observation of the restored reporter activity (RFP) by introducing miR-1 inhibitor (right) further confirmed that phenylephrine-dependent repression of miR-1 7oxo sites was mediated by miR-1. The flow cytometer used in **f**–**l** was equipped with two separate lasers to maximize the excitation of both GFP and RFP, resulting in increased sensitivity of the detection. **m**, Luciferase reporter assays with miR-1 seed sites in the presence of 5 nM of control (cont; NT), 2o^{8}G-miR-1, 3o^{8}G-miR-1, 7o^{8}G-miR-1 and miR-1; $^*P = 0.005$, 0.4×10^{-3} and 0.1×10^{-4}; error bars, s.e.m.; $n = 6$ biological independent samples. Notably, introduction of oxidized miR-1 (2o^{8}G, 3o^{8}G and 7o^{8}G) could also suppress seed sites in luciferase reporter albeit less potent than unoxidized miR-1, presumably because of retained activity of o^{8}G•C base pairing. All *P* values from two-sided *t*-test; $^*P < 0.05$; $n = 3$ biological independent samples; data are mean ± s.d. unless otherwise indicated.

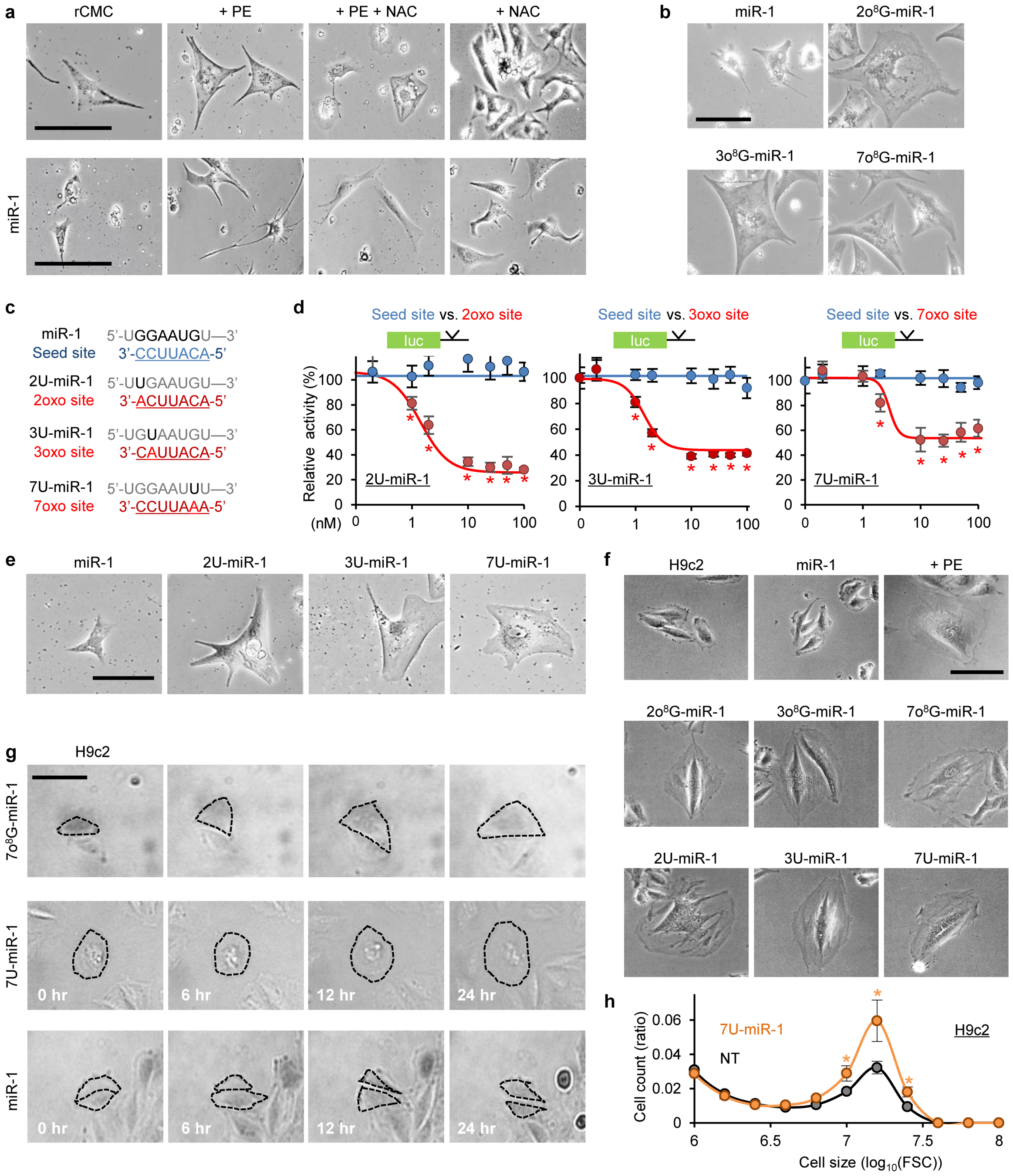

Extended Data Fig. 5 | Oxidized miR-1 elicits hypertrophy of cardiomyocyte through o^{8}G•A base pairing. a, Effect of miR-1 expression on rCMCs in the presence of phenylephrine and/or NAC treatment; scale bar, 100 μm. **b**, Morphology of rCMCs after the transfection of oxidized miR-1 (2o^{8}G, 3o^{8}G or 7o^{8}G); scale bar, 100 μm. Every independent experiment ($n \geq 3$) showed similar results (**a**, **b**). **c**, Sequences of o^{8}G-miR-1 mimics, of which o^{8}G was substituted with U (2U-miR-1, 3U-miR-1 and 7U-miR-1), and its cognate sites (2oxo, 3oxo and 7oxo site). **d**, Luciferase reporter assays with different concentration of 2U-miR-1, 3U-miR-1 or 7U-miR-1 for its cognate 2oxo, 3oxo or 7oxo site (red), compared with miR-1 seed site (blue). Of note, U-miR-1 (2U, 3U or 7U) cannot repress seed site. **e**, rCMC with transfection of miR-1, 2U-miR-1, 3U-miR-1 or 7U-miR-1; scale bar, 100 μm. **f**, H9c2 cells with transfection of miR-1, oxidized miR-1 (2o^{8}G, 3o^{8}G or 7o^{8}G) or U-miR-1 (2U, 3U or 7U). Phenylephrine treatment was used as a positive control inducing hypertrophy; scale bar, 50 μm. **g**, Time lapse images of H9c2 cells transfected with 7o^{8}G-miR-1, 7U-miR-1 or miR-1; scale bar, 50 μm. Every independent experiment ($n \geq 3$) showed similar results (**e**–**g**). **h**, Distribution of H9c2 cell size after 7U-miR-1 transfection (flow cytometry, 10,000 cells, $n = 3$); NT, non-targeting miRNA control. *P* values from two-sided *t*-test, (**d**, **h**); *$P < 0.05$; $n \geq 3$ biological independent samples; data are mean ± s.d. unless otherwise indicated.

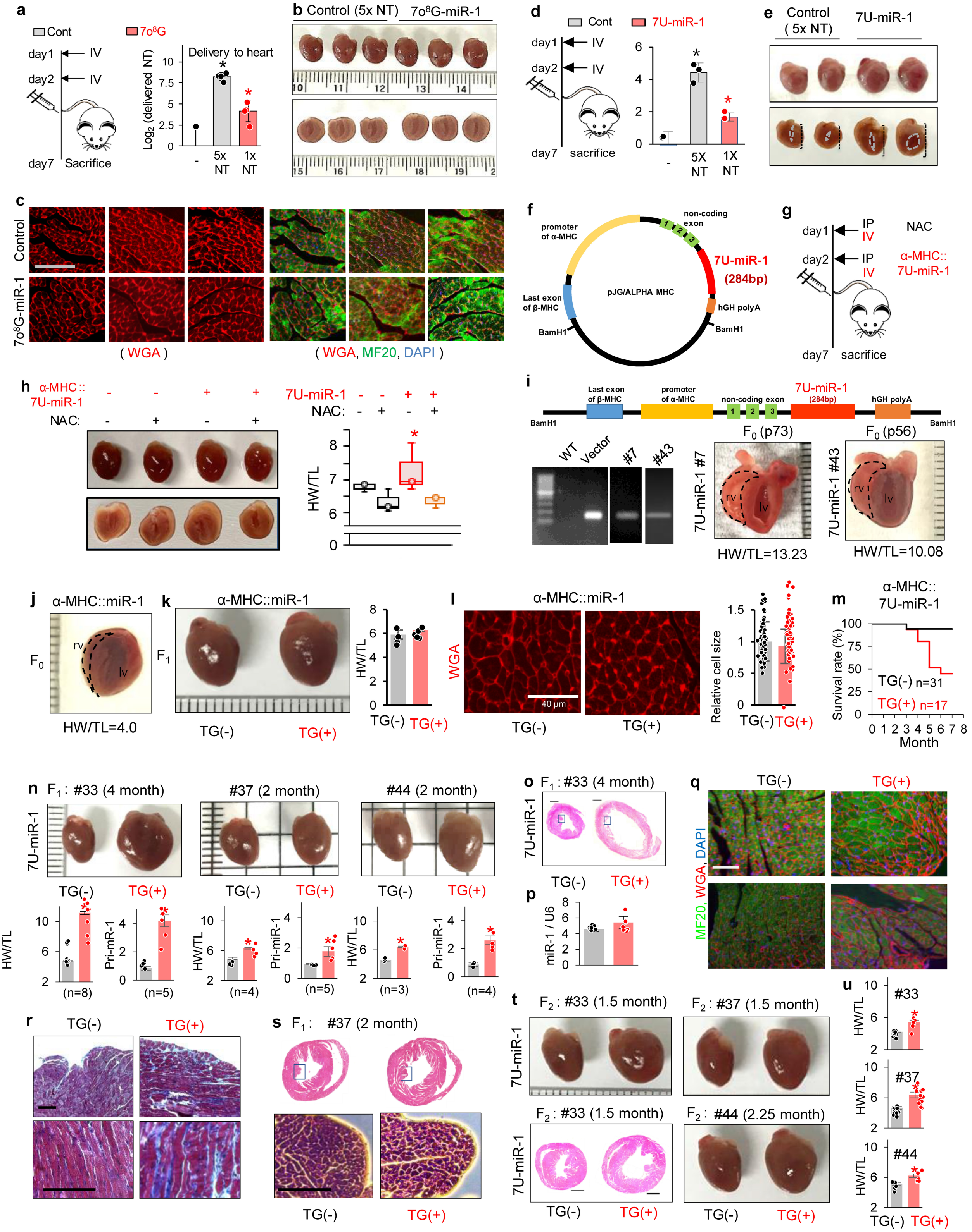

Extended Data Fig. 6 | See next page for caption.

Extended Data Fig. 6 | 7o^{8}G-miR-1 induces cardiac hypertrophy in vivo. **a**, **b**, In vivo injection of 7o^{8}G-miR-1 as polyethylenimine (PEI) complex. Non-targeting control (NT) was injected together to check the delivery; "Cont", 5×NT (100% NT); "7o^{8}G", 1×NT (1:4; 25% NT, 75% 7o^{8}G-miR-1); 5 mg kg^{-1} (left); IV, intravenous tail injection. The delivery rates were estimated by qPCR (log$_2$ ratio relative to the negative control (−), normalized to U6, $n = 4$ biological independent mice); error bars, s.d.; $^*P = 7.2 \times 10^{-5}$ and 0.017, respectively (**a**, right). The mouse hearts were displayed in **b**. **c**, Immunofluorescence staining of interventricular septum from 7o^{8}G-miR-1 delivered mouse hearts; wheat germ agglutinin (WGA), cell border, red; MF20, cardiomyocyte, green; DAPI, nucleus, blue; scale bar, 100 μm. Every independent experiment ($n \geq 3$) showed similar results. **d**, **e**, Same experiments as in **a**, **b** except using 7U-miR-1 as mixture of NT (1:4, 5mg kg^{-1}) and PEI (N/P ratio = 8); $^*P = 0.002$ and 0.029, respectively (**d**, right); representative mouse hearts (**e**). **f**, Cardiomyocyte-specific expression vector (pJG/ALPHA MHC), which contains α-MHC (alpha myosin heavy chain) promoter to drive cardiomyocyte specific expression of 7U-miR-1 (α-MHC::7U-miR-1). **g**, Injection of α-MHC::7U-miR-1 plasmid (1.9 mg kg^{-1}) as complex with PEI (N/P ratio = 8) into PBS- or NAC-administrated mice (100 mg kg^{-1}, IP injection; time interval of ~8 h at the same day). Delivery of the plasmid to heart tissue was confirmed by qPCR of hGH poly (A) in the plasmid. **h**, α-MHC::7U-miR-1 delivered mouse hearts (left) and the quantification of their size (HW/TL; right); box plots with median line, first and third quartile; whiskers, minima and maxima (right); $n \geq 4$ biological independent mice; $^*P = 0.022$ (7U-miR-1 versus others). Of note, expression of 7U-miR-1 in cardiomyocyte promoted enlargement of hearts only in the absence of NAC treatment, implicating that basal level of ROS is required for 7o^{8}G-miR-1-induced cardiac hypertrophy. **i**, Generation of cardiomyocyte-specific transgenic mouse with expression of 7U-miR-1 (7U-miR-1 TG); transgene cassette, generated from α-MHC::7U-miR-1 plasmid by treating BamHI (top). Genotyping results of two independent founders (F$_0$; #7, #43; bottom left) and section of their hearts (bottom right) at the age of p73 (#7) and p56 (#43). Of note, both 7U-miR-1 TG showed marked increase in heart size (HW/TL = 13.23 and 10.08, relative to average size of HW/TL = ~5.0), especially evident in the size of right ventricle (rv); lv, left ventricle. **j**–**l**, Generation of cardiomyocyte-specific transgenic mice of miR-1 (α-MHC::miR-1 TG) following the same process as used in **i**. Notably, there was no change in heart size of α-MHC::miR-1 TG; F$_0$ (HW/TL = 4.0; **j**); F$_1$, TG(−) versus TG(+) (**k**, left); HW/TL, $n \geq 4$ (**k**, right). WGA staining of heart tissue from α-MHC::miR-1 TG (TG(−) versus TG(+)), showing no difference in cell size (**l**, left); 40 μm; quantification of relative cell size ($n = 70$), ImageJ (**l**, right). **m**, Survival rate (%) of α-MHC::7U-miR-1 TG (F$_1$). **n**, Hearts of 7U-miR-1 TG (F$_1$; TG(−) versus TG(+)), derived from 3 independent founders (#33, #37, #44; top); HW/TL (bottom). Expression of pri-miR-1 was examined by qPCR to infer the copy number of transgene; relative expression ("pri-miR-1", bottom); $^*P = 4.8 \times 10^{-5}$, 0.0009, 0.014, 0.009, 0.0007 and 0.002, respectively; $n \geq 3$ biologically independent mice. **o**, Ventricle region of 7U-miR-1 TG heart (F$_1$, #33, TG(−) versus TG(+); H&E staining); scale bar, 1 mm. **p**, Measurement of total miR-1 level, contributed by expressing 7U-miR-1 transgene (7U-miR-1 TG, F$_1$, #33); TG(+) vs TG(−); qPCR results normalized by U6 abundance (miR-1/U6); $n \geq 9$. Of note, expression of 7U-miR-1 transgene added negligible amount to endogenous miR-1 in hearts, implicating physiological relevance of 7U-miR-1 transgenic mouse.

q, **r**, Immunofluorescence staining of cardiomyocytes in the interventricular septum of 7U-miR-1 TG (F$_1$, #33, **q**) and their Masson's trichrome staining (**r**); WGA, red; MF20, green; DAPI, blue; scale bar, 100 μm. **s**, H&E staining of heart section of 7U-miR-1 TG (F$_1$, #37, TG(−) versus TG(+); top). Enlargement of cells in 7U-miR-1 TG was observed (bottom); rectangular part of the top panel is represented; H&E staining; scale bar, 100 μm. **t**, Hearts of 7U-miR-1 TG (F$_2$; TG(−) versus TG(+)), derived from 3 independent founders (#33, #37, #44). Section of 7U-miR-1 TG heart (F$_2$, #33, TG(−) versus TG(+); H&E staining) was also displayed (**t**, bottom left); scale bar, 1 mm. **u**, The heart size was quantified for 7U-miR-1 TG (F$_2$; TG(−) versus. TG(+); #33 ($n = 11$ versus 6), #37 ($n = 13$ versus 12), #44 ($n = 5$ versus 7)); HW/TL; $^*P = 0.0001$, 8.6×10^{-6} and 0.009, respectively. All P values from two-sided t-test; $^*P < 0.05$; $n \geq 3$ biological independent samples; data are mean ± s.e.m. unless otherwise indicated.

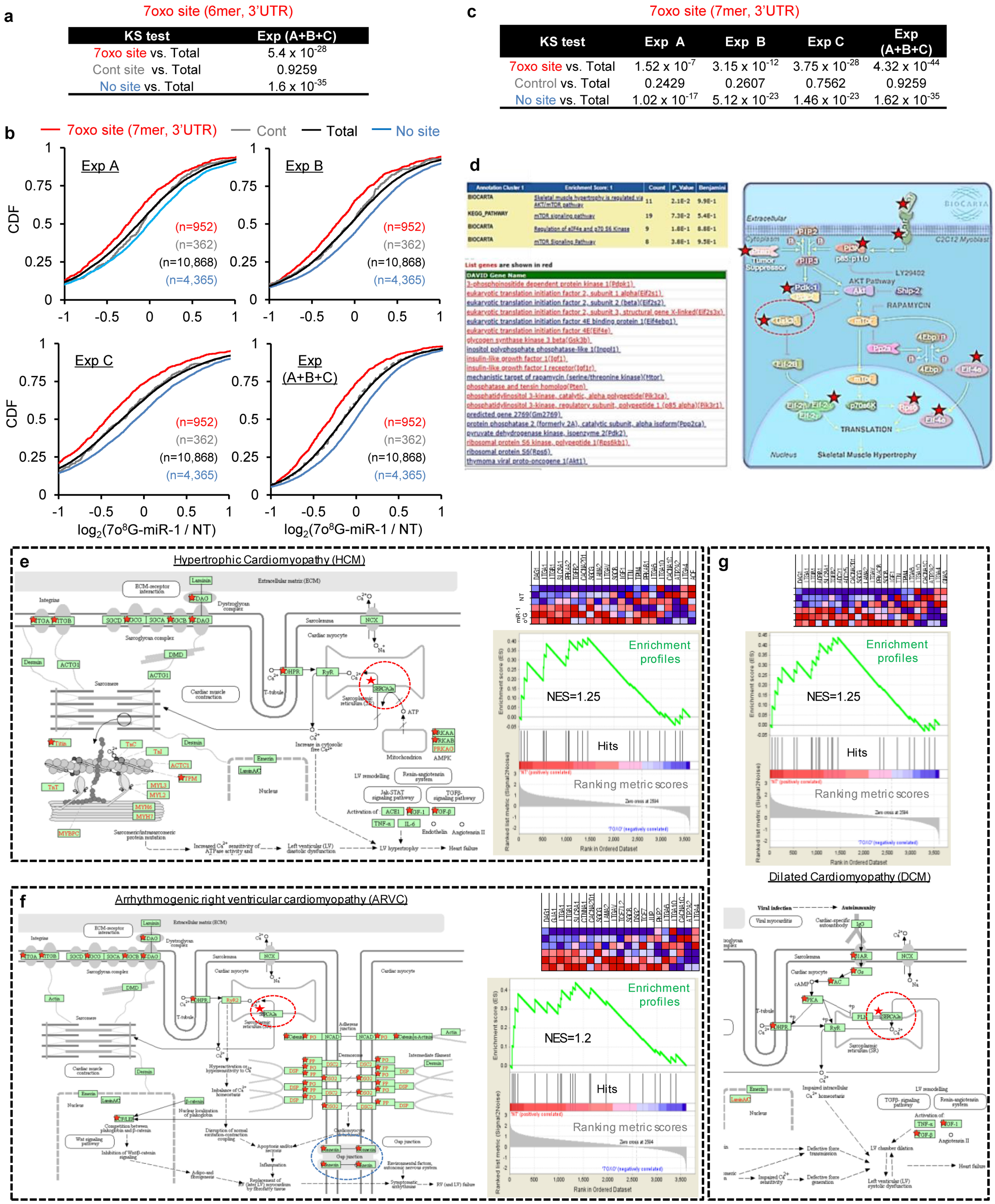

a 7oxo site (6mer, 3'UTR)

KS test	Exp (A+B+C)
7oxo site vs. Total	5.4×10^{-28}
Cont site vs. Total	0.9259
No site vs. Total	1.6×10^{-35}

c 7oxo site (7mer, 3'UTR)

KS test	Exp A	Exp B	Exp C	Exp (A+B+C)
7oxo site vs. Total	1.52×10^{-7}	3.15×10^{-12}	3.75×10^{-28}	4.32×10^{-44}
Control vs. Total	0.2429	0.2607	0.7562	0.9259
No site vs. Total	1.02×10^{-17}	5.12×10^{-23}	1.46×10^{-23}	1.62×10^{-35}

d

Annotation Cluster 1	Enrichment Score: 1	Count	P_Value	Benjamini
BIOCARTA	Skeletal muscle hypertrophy is regulated via AKT/mTOR pathway	11	2.1E-2	9.9E-1
KEGG_PATHWAY	mTOR signaling pathway	19	7.3E-2	5.4E-1
BIOCARTA	Regulation of eIF4e and p70 S6 Kinase	9	1.8E-1	8.8E-1
BIOCARTA	mTOR Signaling Pathway	8	3.8E-1	9.5E-1

List genes are shown in red

DAVID Gene Name
3-phosphoinositide dependent protein kinase 1(Pdpk1)
eukaryotic translation initiation factor 2, subunit 1 alpha(Eif2s1)
eukaryotic translation initiation factor 2, subunit 2 (beta)(Eif2s2)
eukaryotic translation initiation factor 2, subunit 3, structural gene X-linked(Eif2s3x)
eukaryotic translation initiation factor 4E binding protein 1(Eif4ebp1)
eukaryotic translation initiation factor 4E(Eif4e)
glycogen synthase kinase 3 beta(Gsk3b)
inositol polyphosphate phosphatase-like 1(Inppl1)
insulin-like growth factor 1(Igf1)
insulin-like growth factor 1 receptor(Igf1r)
mechanistic target of rapamycin (serine/threonine kinase)(Mtor)
phosphatase and tensin homolog(Pten)
phosphatidylinositol 3-kinase, catalytic, alpha polypeptide(Pik3ca)
phosphatidylinositol 3-kinase, regulatory subunit, polypeptide 1 (p85 alpha)(Pik3r1)
predicted gene 2769(Gm2769)
protein phosphatase 2 (formerly 2A), catalytic subunit, alpha isoform(Ppp2ca)
pyruvate dehydrogenase kinase, isoenzyme 2(Pdk2)
ribosomal protein S6 kinase, polypeptide 1(Rps6kb1)
ribosomal protein S6(Rps6)
thymoma viral proto-oncogene 1(Akt1)

Extended Data Fig. 7 | See next page for caption.

Extended Data Fig. 7 | Transcriptome-wide analysis of 7o^{8}G-miR-1-delivered mouse hearts. **a**, Kolmogorov–Smirnov test results for Fig. 5a. There are significant downregulation ($P = 5.4 \times 10^{-23}$) of mRNAs with 7oxo site (6mer, positions 2–7, in 3′UTR) and significant upregulation ($P = 1.6 \times 10^{-35}$) of mRNAs with no site (neither miR-1 7oxo site nor seed site, 6mers) depending on 7o^{8}G-miR-1 expression, relative to total (total mRNAs). But, mRNA with control site ("cont site", mismatched site at position 6 of miR-1 in 3′UTRs but no 7oxo site in the transcript, previously reported to be unrecognized by miRNA[32]) showed no significance. **b**, CDF analysis for mRNAs with miR-1 7oxo site (7mer, position 2-8, in 3′UTR, $n = 952$, red line) depending on 7o^{8}G-miR-1-mediated fold change (log2 ratio, x-axis), conducted for each replicate pairs (Exp A, B and C; Supplementary Table 2a) and also for combined results (Exp(A+B+C)). **c**, Kolmogorov–Smirnov test results for **b**, relative to total. **d**, Functional annotation results for downregulated DEG with miR-1 7oxo site in Fig. 5b, performed by DAVID (https://david.ncifcrf.gov) using BIOCARTA and KEGG pathways (top left). The most significantly enriched pathway, "skeletal mouse hypertrophy regulated via AKT/mTOR pathway" ($P = 0.02$) in BIOCARTA were indicated with other components of hits in the table (red; bottom left) and pathway map (red star; right). GSK3B is highlighted with red dotted circle. Notably, activation of GSK3B has been reported to suppress cardiac hypertrophy[25]. **e**–**g**, Concentrating on heart-related pathways in the Kyoto Encyclopedia of Genes and Genomes (KEGG) database, the normalized enrichment score (NES) from gene set enrichment analysis (GSEA) elucidated "hypertrophic cardiomyopathy" (HCM, NES = 1.25; **e**, right), "arrhythmogenic right ventricular cardiomyopathy" (ARVC, NES = 1.20; **f**, right), and "dilated cardiomyopathy" (DCM, NES = 1.25; **g**, top) as pathways regulated by 7o^{8}G-miR-1. Heat maps on the top indicate the mRNAs in the corresponding pathway with measured expression; red, downregulation; blue, upregulation; order of results from top, NT ($n = 3$), 7o^{8}G-miR-1 ($n = 3$). Hits from downregulated DEG with miR-1 7oxo site in Fig. 5b were also displayed as red stars in HCM (**e**, left), ARVC (**f**, left) and DCM (only a distinct part from HCM and ARVC is displayed; **g**, bottom). *ATP2A2* (*SERCA2*) is highlighted with red dotted circle and *GJA1* (*CX43*) with blue dotted circle.

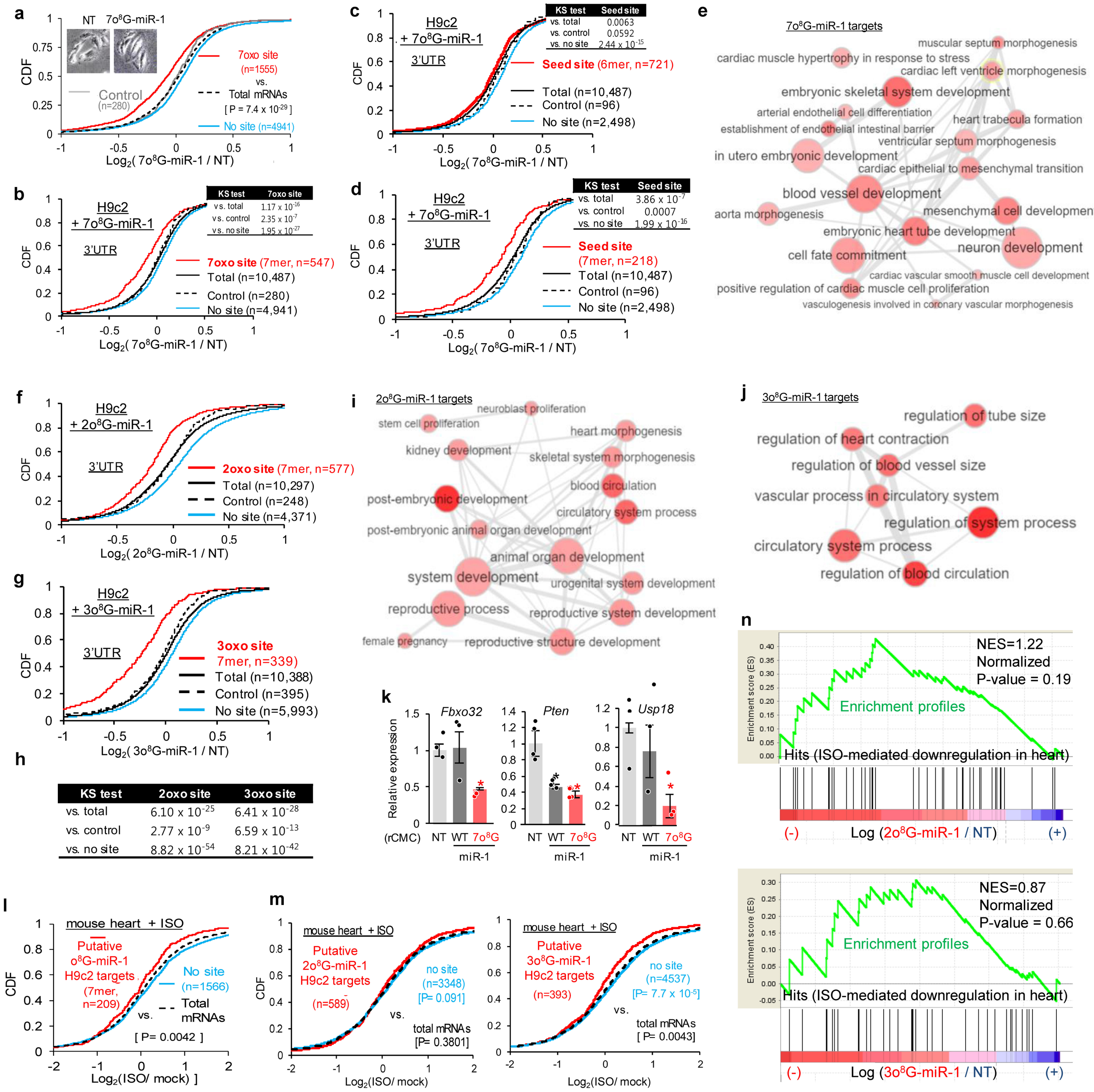

Extended Data Fig. 8 | Transcriptome-wide analysis of o^{8}G-miR-1 transfected H9c2 cells. **a**, **d**, CDF analysis as performed in Fig. 5a except for 7o^{8}G-miR-1-transfected H9c2 cells; all 7oxo sites (**a**), 7mer 7oxo site (positions 2–8; **b**), 6mer seed site (positions 2–7; **c**) and 7mer seed site (positions 2–8; **d**). Kolmogorov–Smirnov test (two sided) results were displayed in the table (**b**, **c**, **d**, top right table); mean. Control in **c**, **d** denotes mismatched site at position 6 of miR-1 in 3′UTRs but no seed site in the transcript. **e**, Gene Ontology analysis results of 7o^{8}G-miR-1 targets identified in H9c2 cells (Fig. 5c); intensity of bubble colour, *P* value (derived from DAVID); bubble size, frequency of the Gene Ontology term. Highly similar Gene Ontology terms are linked by edges in the graph, where the line width indicates the degree of similarity. Of note, only Gene Ontology terms in biological process were used in this analysis. **f**–**h**, CDF analysis as in **a**–**d** except for 2o^{8}G-miR-1 (**f**) or 3o^{8}G-miR-1 (**h**) by using RNA-seq results (Supplementary Table 2c, d); Kolmogorov–Smirnov test (two sided) results in **h**. **i**, **j**, Gene Ontology analysis results as performed in **e** except for 2o^{8}G-miR-1 (**i**) and 3o^{8}G-miR-1 (**j**); $P < 0.05$ (derived from DAVID), $n = 176$ (2o^{8}G-miR-1), $n = 34$ (3o^{8}G-miR-1). 2o^{8}G-miR-1 targets and 3o^{8}G-miR-1 targets were selected as containing 6mer sites (position 2–9) in 3′UTR and showing log$_2$ ratio <−0.8 in **f**, **g**. The biggest cluster was displayed as representative (**i**, **j**). **k**, Validation of putative 7o^{8}G-miR-1 targets by qPCR in 7o^{8}G-miR-1-transfected rCMC as performed in Fig. 5d, f. As control, GAPDH (for FBXO32 and PTEN) or ACTB (for USP18) was also measured for normalization. FBXO32, PTEN and USP18, of which 3′UTRs contain 7oxo sites (Supplementary Table 4c) were examined; *t*-test, two-sided; $^*P = 0.003$, 5.4×10^{-4}, 2.1×10^{-4} and 0.044, respectively; $n \geq 3$ biological independent samples; data are mean ± s.e.m. Notably, PTEN also contains a miR-1 seed site in its 3′UTR. **l**, **m**, CDF analyses as conducted in Fig. 5g except for all o^{8}G-miR-1 targets (2oxo, 3oxo or 7oxo sites; **l**) or only for 2o^{8}G-miR-1 (**m**, left panel) or 3o^{8}G-miR-1 targets (**m**, right). **n**, GSEA results performed as in Fig. 5h except using 2o^{8}G-miR-1 (top) and 3o^{8}G-miR-1 (bottom) dependent changes of putative cognate mRNA targets (6mers, 3′UTR) in H9c2 cells (Supplementary Table 2c, d) for the enrichment of ISO-dependent downregulation (log ratio < 0); NES, normalized enrichment score; *P* value, adjusted *P* value derived from GSEA.

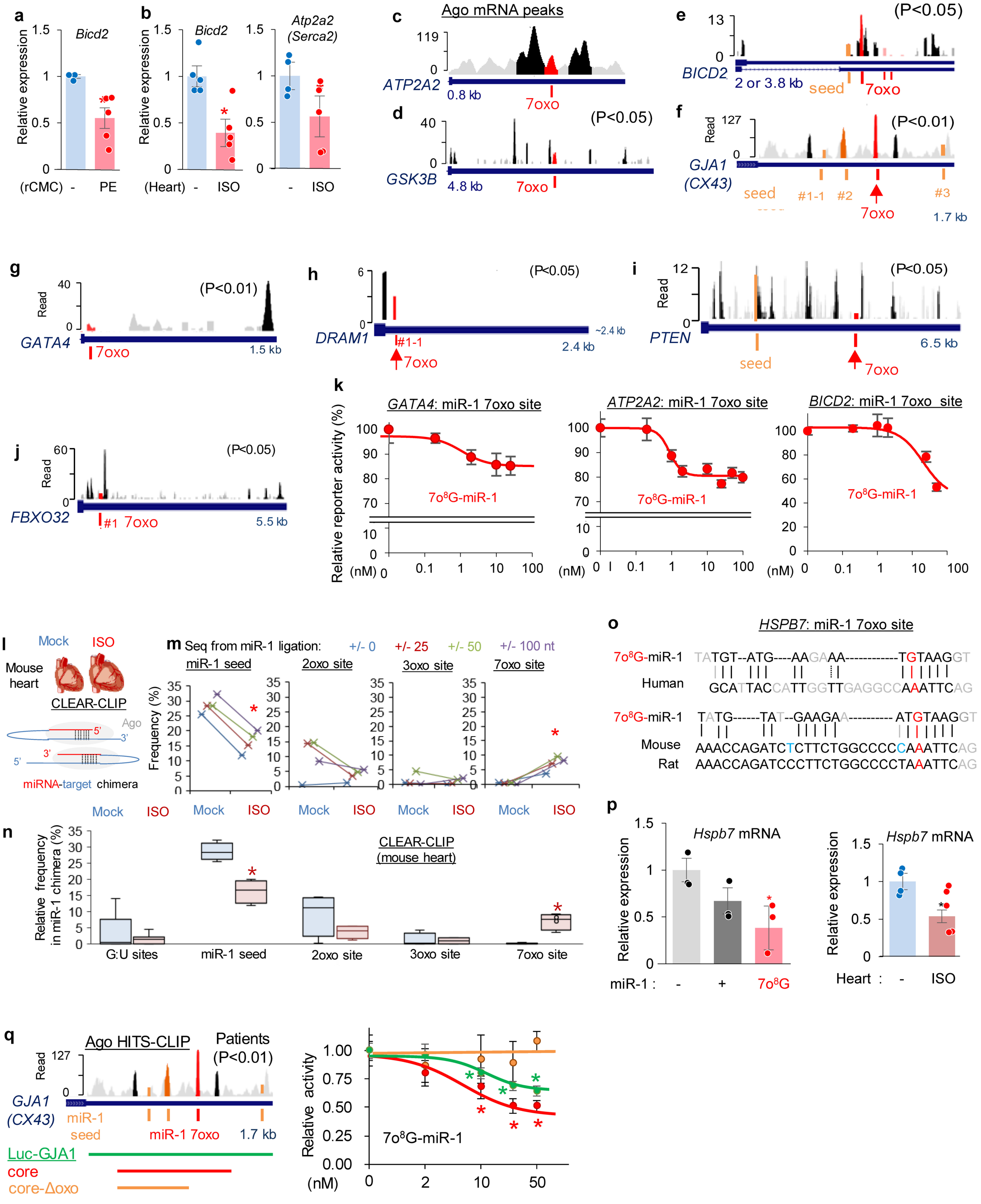

Extended Data Fig. 9 | See next page for caption.

Extended Data Fig. 9 | Identification of 7o^{8}G-miR-1 targets and their 7oxo sites during adrenergic cardiac hypertrophy and cardiomyopathy. **a**, Experimental validation of *Bicd2* as 7o^{8}G-miR-1 target (7oxo site) in phenylephrine-treated rCMCs. Relative expression was measured by qPCR, normalized by *Actb*; *$P = 0.024$; $n \geq 3$ biological independent samples; error bars, s.e.m. **b**, Same validation experiments as in **a** except using ISO-treated mouse hearts for *Bicd2* (left, normalized by *Actb*) and *Atp2a2* (right, normalized by *Gapdh*); *$P = 0.005$ and 0.06, respectively; $n \geq 4$ biological independent samples; error bars, s.e.m. **c**–**j**, miR-1 7oxo sites (red) in Ago bound regions (3′UTR) of patients with heart disease for *ATP2A2* (**c**), *GSK3B* (**d**), *BICD2* (**e**), *GJA1* (**f**), *GATA4* (**g**), *DRAM1* (**h**), *PTEN* (**i**) and *FBXO32* (**j**), represented as in Fig. 6d; identified in the Ago-mRNA peaks (red; sequences in Supplementary Tables 3 and 4) with significant peak height ($P < 0.05$ or 0.01, CLIPick[29], black); with miR-1 seed site (orange). **k**, Luciferase reporter assays with different concentrations of 7o^{8}G-miR-1 for 7oxo sites, derived from *GATA4*, *ATP2A2* and *BICD2*. Half-maximal inhibitory concentration (IC$_{50}$) was calculated. Of note, repression mediated by miR-1 7oxo site in *GATA4* (IC$_{50}$ = 1.2 nM) or *ATP2A2* (IC$_{50}$ = 0.7 nM) was efficient, albeit the maximum repression was only ~15–20% (left and middle). By contrast, miR-1 7oxo site in *BICD2* exerted better maximum repression (52%) with low efficiency (IC$_{50}$ = 11nM; right). **l**–**n**, CLEAR-CLIP analysis for ISO induced hypertrophic mouse hearts, yielding miRNA-target chimaera reads (**l**). miR-1 containing chimaera reads were aligned and analysed for the frequency of miR-1 seed, 2oxo, 3oxo, and 7oxo sites depending on ISO treatment, examined by expanding the size of the sequences from the miR-1 ligated site (±0, 25, 50 or 100 nt; **m**); box plots with median line, first and third quartile; whiskers, minima and maxima (**n**). Although only limited number of chimaera reads were yielded for miR-1 (Supplementary Table 6a), global propensity of its target interaction could be analysed for their changes depending on ISO-treatment. **o**, Sequence of conserved miR-1 7oxo site in *HSPB7*, which overlapped with miR-1 chimaeras in ISO-treated mouse hearts and Ago-mRNA peaks of patients with cardiomyopathy (Fig. 6d). **p**, Validation of *Hspb7* as miR-1 7oxo target by performing qPCR in 7o^{8}G-miR-1 transfected rCMC (normalized by *Gapdh*, left) and ISO-injected mouse heart by qPCR (normalized by *Actb*, right).–, NT transfection (left) or mock (right); *$P = 0.04$ and 0.01, respectively; $n = 3$ (left) or 5 (right) biologically independent samples; error bars, s.e.m. **q**, Ago-bound miR-1 seed and 7oxo sites identified in the 3′UTR of *GJA1* in patients with cardiomyopathy, as represented in **c**–**j**; left. Activity of luciferase reporters, containing the indicated regions (left), were examined depending on the concentration of 7o^{8}G-miR-1 (right). Of note, despite containing the miR-1 seed site, core-Δoxo completely lost repression by 7o^{8}G-miR-1, implicating the importance of 7oxo site to execute miR-1 dependent repression of *GJA1*. All *P* values from two-sided *t*-test, *$P < 0.05$; $n \geq 3$ biological independent samples; data are mean ± s.d. unless otherwise indicated.

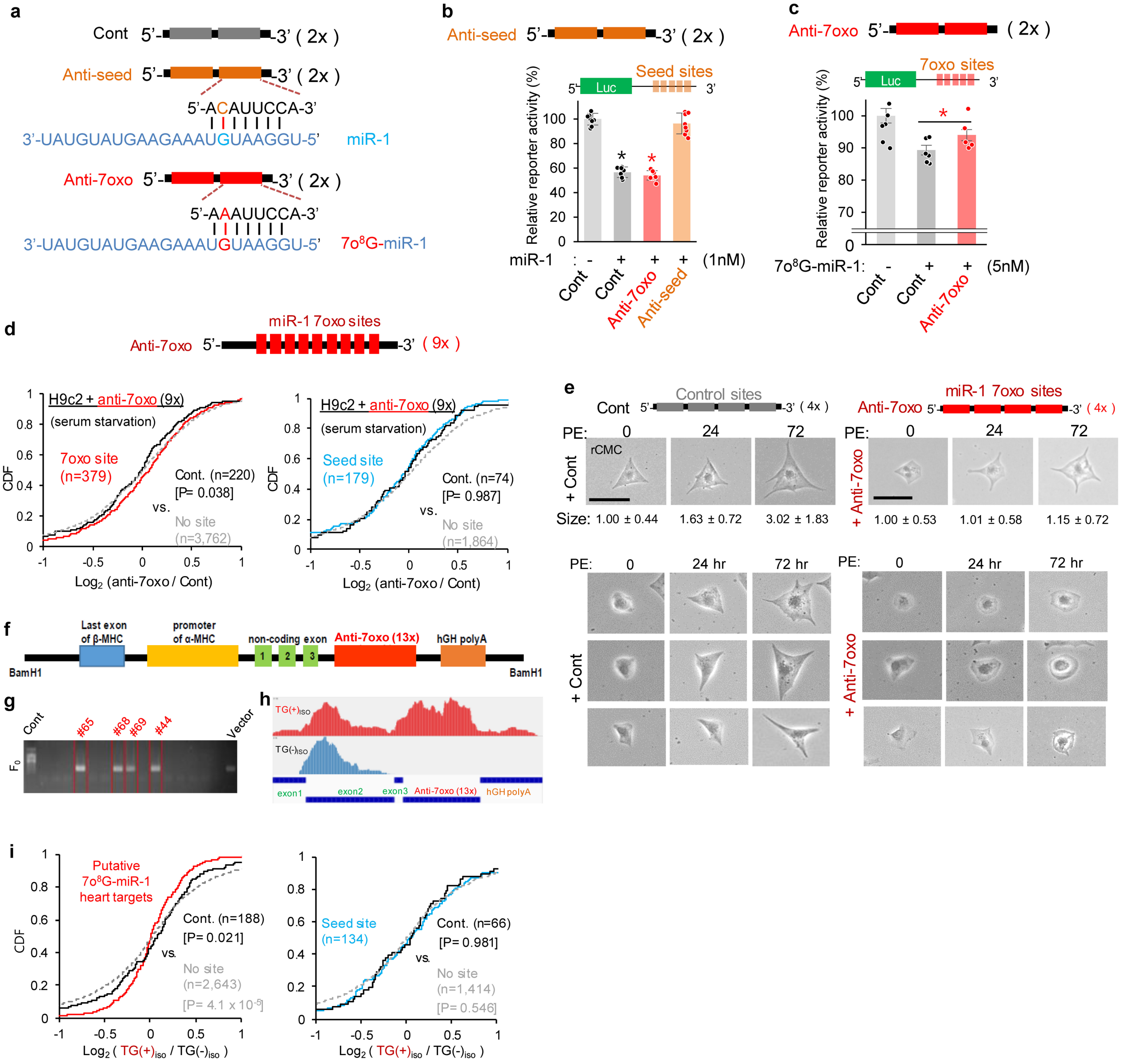

Extended Data Fig. 10 | Specific inhibition of 7o^{8}G-miR-1 by competitive inhibitors, anti-7oxo. a, Schematics of competitive miRNA inhibitors, which consist of tandem repeats of miRNA target sites (7mer, position 2–8) in RNA oligonucleotide; "Cont", NT seed sites (2×); anti-seed, miR-1 seed sites (2×); Anti-7oxo, miR-1 7oxo sites (2×). Base pairing of miR-1 or 7o^{8}G-miR-1 with cognate target site (seed or 7oxo site) was represented. **b**, **c**, Luciferase reporter assays used to validate activity and specificity of competitive miRNA inhibitors (anti-seed and anti-7oxo) in **a**. Luciferase reporter vector containing miR-1 seed sites or 7oxo sites was constructed and used to confirm derepression of the reporters by anti-seed (**b**) and by anti-7oxo (**c**); "Cont", anti-NT (containing seed sites of NT); –, NT; *$P = 1.87 \times 10^{-11}$ and 5.08×10^{-12}, respectively; $n = 8$ biologically independent samples (**b**); *$P = 0.038$; $n \geq 5$ biologically independent samples (**c**); error bars, s.e.m. Of note, anti-7oxo significantly derepressed 7oxo site mediated target repression, albeit the extent was somewhat marginal. This is possibly because of containing only two repeats of target sites in the inhibitor. Notably, anti-7oxo showed no effect on seed site mediated target repression, confirming the specificity of anti-7oxo (**c**). **d**, CDF analysis to globally confirm derepression of 7oxo targets by anti-7oxo (9×); "7oxo site", mRNAs with 7oxo site (7mer, position 2–8, in 3′UTR); "No site", mRNAs with neither 7oxo site nor seed site (6mers, positions 2–8, in 3′UTR); "Cont", transcripts with a mismatch site at position 6 of miR-1 (negative control; 7mer, positions 2–8, in 3′UTR) but without 7oxo (left) or seed site (right). Expressed transcripts (FPKM >1 in both samples, valid status from Cuffdiff, $n = 7{,}958$) from RNA-seq (Supplementary Table 6b) were used for the analysis. Notably, anti-7oxo (9×) significantly derepressed miR-1 7oxo sites ($P = 0.038$, relative to control; Kolmogorov–Smirnov test, two sided; left) but not miR-1 seed sites ($P = 0.987$, relative to control, Kolmogorov–Smirnov test, two sided; right). **e**, Time-lapse images of rCMC, transfected with either cont (anti-NT (4×); left) or anti-7oxo (4×; right) after phenylephrine treatment (with serum starvation); scale bar, 100 µm. Introduction of anti-7oxo to rCMCs attenuated phenylephrine-induced hypertrophy. **f**, Generation of cardiomyocyte-specific transgenic mice (TG) with expression of anti-7oxo (13×); transgene cassette, generated from α-MHC::anti-7oxo (13×) plasmid by BamHI. **g**, Genotyping results of four independent founders (F_0; #65, #68, #69, #44). **h**, Mapping result of RNA-seq reads (Supplementary Table 6c) for the anti-7oxo transgene cassette, expressed in hearts of ISO-treated TG (F_0, #68). Notably, TG(+) showed sufficient expression of anti-7oxo (13×) sequences in heart tissue. **i**, CDF analyses of RNA-seq results (Supplementary Table 6c) to confirm anti-7oxo (13×) mediated derepression of 7o^{8}G-miR-1 targets (7oxo sites) as analysed in **d**. Notably, significant derepression of 7o^{8}G-miR-1 targets (as measured by $\log_2(\mathrm{TG}(+)_{\mathrm{ISO}}/\mathrm{TG}(-)_{\mathrm{ISO}})$) was observed ($P = 0.021$, relative to "Cont", Kolmogorov–Smirnov test, two sided ; $P = 4.1 \times 10^{-5}$, relative to "no site"); by contrast there was no change for miR-1 seed targets (right). All P values from t-test, two-sided; *$P < 0.05$; $n \geq 3$ biological independent samples; data are mean ± s.d. unless otherwise indicated.

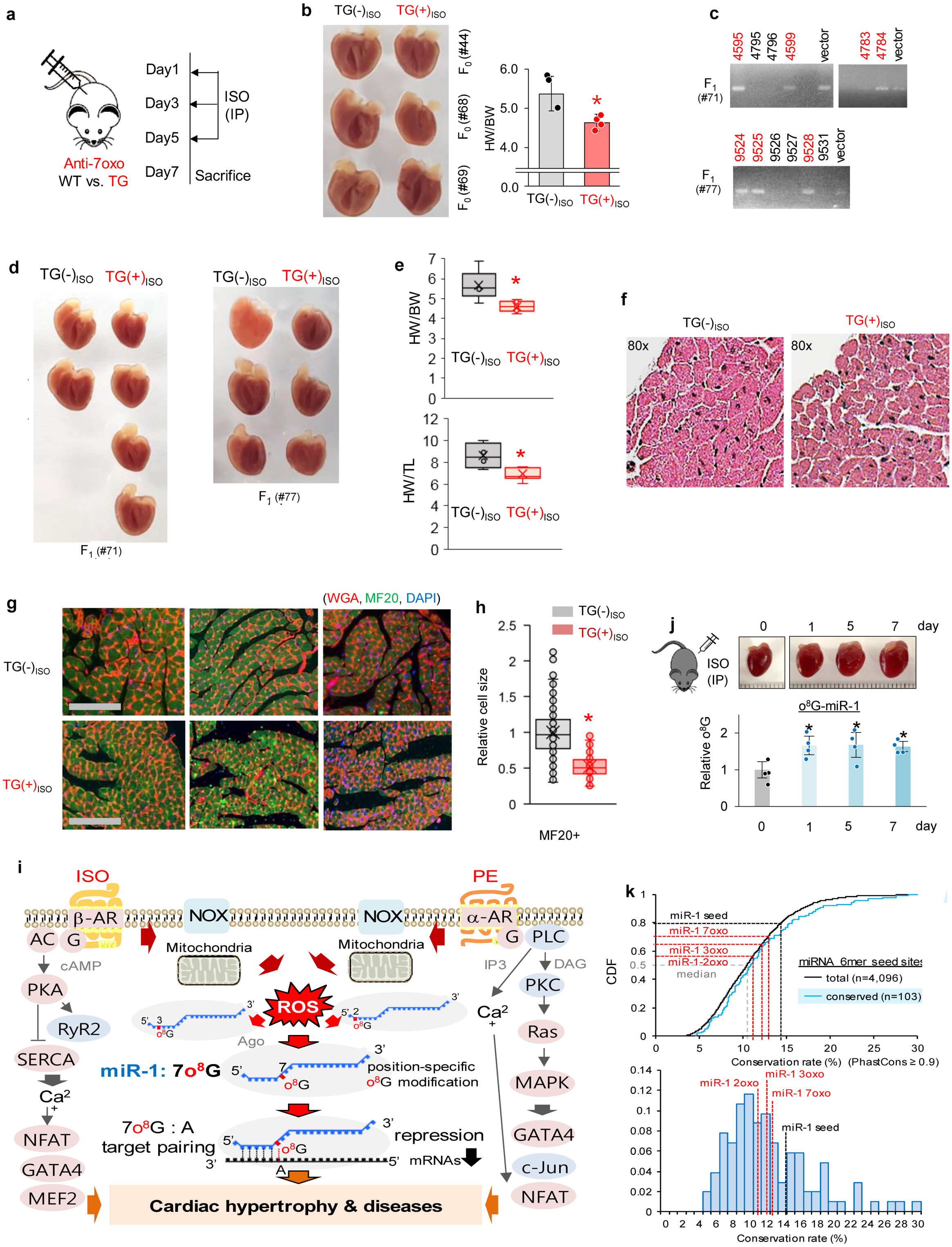

Extended Data Fig. 11 | See next page for caption.

Extended Data Fig. 11 | Loss-of-function study of 7o^{8}G-miR-1 in vivo by establishing an anti-7oxo transgenic mouse. a, The ISO treatment schedule for anti-7oxo TG, cardiomyocyte-specific transgenic mice with expression of anti-7oxo (a specific sponge inhibitor against 7o^{8}G-miR-1); intraperitoneal (IP) injection. **b**, Heart size of anti-7oxo TG(−) versus TG(+) in the presence of ISO administration (three independent F_0 lines, #69, #68, #44; left); HW/BW; error bars, s.d.; $*P = 0.014$; $n \geq 3$ (right). **c**, Genotyping results of F_1, generated from two different F_0 lines (#71, top; #77, bottom). **d**, Section of hearts from littermates of two different lines (#71, left; #77, right); TG(−) versus TG(+) under ISO treatment. **e**, Heart size in **d** was quantified as HW/TL (bottom) or HW/BW (top); box plots with median line, first and third quartile; whiskers, minima and maxima; x, mean; $*P = 0.007$ and 0.013. Of note, ISO-induced hypertrophy is prevented in anti-7oxo TG (F_1). **f**, H&E stained tissue sections of interventricular septum (IS) of anti-7oxo TG (F_0); $n = 3$; each experiment was repeated independently with similar results. **g**, Immunofluorescence staining of cardiomyocytes in IS of anti-7oxo TG (F_0); wheat germ agglutinin (WGA) for refining the cell border; MF20 for cardiomyocytes; DAPI for nuclear staining; scale bar, 100 μm. **h**, Relative cell size of MF(+) in **g** was quantified ($n = 200$, ImageJ; $*P = 3.2 \times 10^{-59}$); box plots with median line, first and third quartile; whiskers, minima and maxima; "x", mean. Notably, size of cardiomyocyte was maintained in anti-7oxo TG even in the presence of ISO treatment. **i**, A schematic model of the position-specific oxidation of miR-1; 7o^{8}G-miR-1 targets identified in the adrenergic receptor (AR) pathway, red; others, blue. **j**, Quantification of o^{8}G-miR-1 in ISO-injected mice in time-dependent manner. After IP injection of ISO, hearts were collected at different time points (0, 1, 5 and 7 days; top), of which small RNA was used to measure relative amount of o^{8}G-miR-1 to o^{8}G spike-in control by performing o^{8}G IP and qPCR (miR-1; bottom). Notably, sustained oxidation of miR-1 was observed up to 7 days from ISO treatment; $*P = 0.01$, 0.03 and 0.01, respectively; $n = 4$ biologically independent mice; error bars, s.e.m. **k**, Sequence conservation of o^{8}G-miR-1 target sites in 3′UTR. Conservation rates for miR-1 oxo sites (2oxo, 3oxo and 7oxo sites) including seed site were indicated in cumulative graph (left) and distribution (right) of seed sites of conserved miRNAs (conserved; blue line) and all heptamers (total; black line). Notably, sequences of miR-1 2oxo, 3oxo and 7oxo sites were evolutionally conserved in 3′UTR (11.3, 13.0 and 12.3%, respectively) as much as seed sites of conserved miRNAs in mammals—higher than median conservation rate (10.5%, 6mers) but lower than miR-1 seed site (14.5%). All *P* values from two-sided *t*-test, two-sided; $n \geq 3$ biological independent samples; data show the mean unless otherwise indicated.

nature research

Corresponding author(s): Sung Wook Chi

Last updated by author(s): Mar 2, 2020

Reporting Summary

Nature Research wishes to improve the reproducibility of the work that we publish. This form provides structure for consistency and transparency in reporting. For further information on Nature Research policies, see Authors & Referees and the Editorial Policy Checklist.

Statistics

For all statistical analyses, confirm that the following items are present in the figure legend, table legend, main text, or Methods section.

n/a	Confirmed	
☐	☒	The exact sample size (*n*) for each experimental group/condition, given as a discrete number and unit of measurement
☐	☒	A statement on whether measurements were taken from distinct samples or whether the same sample was measured repeatedly
☐	☒	The statistical test(s) used AND whether they are one- or two-sided *Only common tests should be described solely by name; describe more complex techniques in the Methods section.*
☐	☒	A description of all covariates tested
☐	☒	A description of any assumptions or corrections, such as tests of normality and adjustment for multiple comparisons
☐	☒	A full description of the statistical parameters including central tendency (e.g. means) or other basic estimates (e.g. regression coefficient) AND variation (e.g. standard deviation) or associated estimates of uncertainty (e.g. confidence intervals)
☐	☒	For null hypothesis testing, the test statistic (e.g. *F*, *t*, *r*) with confidence intervals, effect sizes, degrees of freedom and *P* value noted *Give P values as exact values whenever suitable.*
☒	☐	For Bayesian analysis, information on the choice of priors and Markov chain Monte Carlo settings
☒	☐	For hierarchical and complex designs, identification of the appropriate level for tests and full reporting of outcomes
☒	☐	Estimates of effect sizes (e.g. Cohen's *d*, Pearson's *r*), indicating how they were calculated

Our web collection on statistics for biologists contains articles on many of the points above.

Software and code

Policy information about availability of computer code

Data collection	Muse 1.5 software (FACS data collection and analysis) BD accuri C6 Plus 1.0.23.1 software (FACS data collection and analysis) Attune NxT software version 3.1 (FACS data collection and analysis) Leica Application Suite V3.3 (for fluorescence image acquisition and analysis) iBright FL100 Imaging System (dot blot) GloMax-Multi detection system software version 1.3.2 (Luciferase reporter assays) SRA toolkit (ver. 2.8.2) was used for downloading raw sequencing files from SRA database.
Data analysis	ImageJ (https://imagej.nih.gov/ij/) Bowtie with allowance of 2 mismatches (Bowtie --norc -l 7 –n 2 -a –f)), where the collapsed sequencing reads were indexed (using bowtie-build indexer with default parameter). Treeview (http://rana.lbl.gov/EisenSoftware.htm) for heat-map analyses ImageJ (https://imagej.nih.gov/) for image quantitation RNA-Seq analysis was performed by using Tuxedo Suite; TopHat2 (http://ccb.jhu.edu/software/tophat), Cufflinks and Cuffdiff (http://cole-trapnell- lab.github.io/cufflinks/). Bowtie (http://bowtie-bio.sourceforge.net) for mapping sequencing reads to miRNAs CLIPick (http://clip.korea.ac.kr/clipick/) for Peak analysis of CLIP data GO analysis was performed by using DAVID (http://david.abcc.ncifcrf.gov/) with default parameters unless otherwise indicated, visualized with REVIGO (http://revigo.irb.hr/). Enrichment of functional annotation was analyzed by using GSEA (http://software.broadinstitute.org/gsea/). Python scripts for o8G-miSeq and Spike-in (http://clip.korea.ac.kr/oxog/).

For manuscripts utilizing custom algorithms or software that are central to the research but not yet described in published literature, software must be made available to editors/reviewers. We strongly encourage code deposition in a community repository (e.g. GitHub). See the Nature Research guidelines for submitting code & software for further information.

Data

Policy information about availability of data

All manuscripts must include a data availability statement. This statement should provide the following information, where applicable:

- Accession codes, unique identifiers, or web links for publicly available datasets
- A list of figures that have associated raw data
- A description of any restrictions on data availability

Raw sequencing data were deposited to SRA; SRP189806, SRP189807, SRP189808,SRP189813, SRP189117, SRP189812, SRP189811, SRP189809,SRP189810, SRP213998, SRP214400, SRP226125, SRP228274

Field-specific reporting

Please select the one below that is the best fit for your research. If you are not sure, read the appropriate sections before making your selection.

☒ Life sciences ☐ Behavioural & social sciences ☐ Ecological, evolutionary & environmental sciences

For a reference copy of the document with all sections, see nature.com/documents/nr-reporting-summary-flat.pdf

Life sciences study design

All studies must disclose on these points even when the disclosure is negative.

Sample size	No power analyses were used to predetermine sample sizes. However, sample sizes were chosen based on prior studies using similar experimental procedures. For most qPCR analyses we analyzed 3 sets of biological samples. The variability between the three biological replicates was very minimal and therefore did not require increasing the sample size.
Data exclusions	No data were excluded from the analyses
Replication	For in vivo experiments, biological replicates as well as independent cohorts of mice were used. For in vitro experiments, technical triplicates as well as independent experiments on separate days were performed to ensure reproducibility. All other data were replicated in at least two independent experiments as stated in figure legends All attempts at replication were successful.
Randomization	No randomization was used in this study. For in vitro experiments, indicated celllls were transfected with indicated plasmids or RNAs, or treated with indicated drugs. For in vivo mice experiments, mice were grouped according to the drug treatment
Blinding	There was no blinding to group allocation. However, staffs, who did drug or RNA injection to mouse, had no idea of expecting outcome.

Reporting for specific materials, systems and methods

We require information from authors about some types of materials, experimental systems and methods used in many studies. Here, indicate whether each material, system or method listed is relevant to your study. If you are not sure if a list item applies to your research, read the appropriate section before selecting a response.

Materials & experimental systems

n/a	Involved in the study	
☐	☒	Antibodies
☐	☒	Eukaryotic cell lines
☒	☐	Palaeontology
☐	☒	Animals and other organisms
☒	☐	Human research participants
☒	☐	Clinical data

Methods

n/a	Involved in the study	
☒	☐	ChIP-seq
☐	☒	Flow cytometry
☒	☐	MRI-based neuroimaging

Antibodies

Antibodies used	Anti-o8G antibody (15A3), QED Bioscience, Cat# 12501, lot# 102411 (1:1000 for Immunofluorescence staining, 1:2000 for dot or Northwestern blotting, 1.25-1.78µg/RNA (µg) for immunoprecipitation) Anti-Ago2 antibody, Abcam (ab5072), Cat# ab32381, Lot# GR71413-1 (1:200 for Immunofluorescence staining) Anti-Ago2 antibody (2A8), DIAGENODE, Cat# C15200167-100, Lot# 003 (10µg for CLEAR-CLIP) Anti-Ago2 antibody (2E12), Abnova, Cat# H00027161-K; Lot# H5221-S2

(10µg for CLEAR-CLIP)
Anti MYH1E antibody, Developmental Studies Hybridoma Bank, Cat# MF20, Lot#:12/7/17
(1:1000 for Immunofluorescence staining)

Validation

Anti-o8G antibody (15A3); eukaryotic; ELISA, IHC, AP, IP; PLoS One 3, e2849, 1183 (2008): J Biol Chem 280, 20978-20986, (2005): FASEB J 21, 2753-2764, (2007): Mol Cell 59, 50-61, (2015); IF, IB, IP data were provided in the current manuscript.
Anti-Ago2 antibody (Abcam); ChIP grade; mouse, rat, human; IP, IHC-P, ChIP, RIP, WB, ICC/IF; Nature 565:500-504 (2019): Nat Struct Mol Biol 25, 1019-1027 (2018); IF data were provided in the current manuscript
Anti-Ago2 antibody (2A8); human, mouse, other (wide range); IP, HITS-CLIP, WB, IF, IHC; Nucleic Acids Res 42, 4629–4639 (2014); HITS-CLIP data were provided in the current manuscript.
Anti-Ago2 antibody (2E12); ChIP grade; human, mouse, rat; IB, IP; Nature 465, 584-9 (2010); HITS-CLIP data were provided in the current manuscript
Anti MYH1E antibody (MF20); human, mouse, rat, chicken; ELISA, FACS, FFPE, IF, IC, IP, IB; J Biol Chem. 283, 26484-9 (2008): Development, 141: 4320-4331 (2014): Scientific reports 8, 2678 (2018); IF data were provided in the current manuscript

Eukaryotic cell lines

Policy information about cell lines

Cell line source(s)

H9c2: ATCC (H9c2(2-1); CRL-1446) or Korean Cell Line Bank
AC16: gift from Drs. J. Han (purchased from Milipore; scc109, terminated product) or H.-W. Lee and W.J. Park (originated as gift from Dr. M.M Davidson; Columbia Univ.)
HeLa: ATCC (CCL-2) or Korean Cell Line Bank

Authentication

H9c2 and HeLa were obtained from ATCC or Korean Cell Line Bank, of which cell lines have been thoroughly tested and authenticated. For each cell line used here, we always check its shape, growth condition and any contaminants by observing microscope. General cell maintenance is around 48 hr interval, suggesting normal cell proliferation. Moreover, by performing RNA-Seq frequently in each cell line, we have confirmed the identity of cell lines with features including its own species of orgin. In this current study, we also did replicate experiments with multiple batches from different provider to see whether the results were reproducible.

Mycoplasma contamination

Confirm that all cell lines were tested as negative for mycoplasma contamination

Commonly misidentified lines
(See ICLAC register)

None

Animals and other organisms

Policy information about studies involving animals; ARRIVE guidelines recommended for reporting animal research

Laboratory animals

C57BL/6 mouse, male & female, 8-12 weeks old
Transgenic mice of C57BL/6 (α-MHC:miR-1, α-MHC :miR-1-7U, α-MHC: anti-7oxo), male & female, 5-12 weeks old
Sprague Dawley rat, male & female, neonatal (day1)

Wild animals

This study did not involved in the wild animals.

Field-collected samples

The study did not involve samples collected from the field.

Ethics oversight

Korea University Institutional Animal Care and Use Committee (AICUC)

Note that full information on the approval of the study protocol must also be provided in the manuscript.

Flow Cytometry

Plots

Confirm that:

☒ The axis labels state the marker and fluorochrome used (e.g. CD4-FITC).

☒ The axis scales are clearly visible. Include numbers along axes only for bottom left plot of group (a 'group' is an analysis of identical markers).

☒ All plots are contour plots with outliers or pseudocolor plots.

☒ A numerical value for number of cells or percentage (with statistics) is provided.

Methodology

Sample preparation

Fluorescence protein reporter-transfected H9c2 cell or drug-treated H9c2 cells were collected by treating 1x trypsin-EDTA for 3 minutes and neutralizing with DMEM with 10% FBS. Collected cells are dissolved in 1x PBS (Biosesang) with 4% BSA (Bovogen) and 5mM EDTA (Sigma) and analyzed by flow cytometers.
For using Muse Cell Analyzer, H9c2 and AC16 cells were prepared as the method suggested by manufacturer.

Instrument	BD accuri C6 Plus (BD Biosciences, equipped with blue(488nm) laser), Attune NxT flow cytometer (Invitrogen, equipped with blue(488nm) and yellow(561nm) laser) Muse Cell Analyzer (Millipore)
Software	BD accuri C6 Plus software (data collection and analysis) Attune NxT software (data collection and analysis) Muse Software (data collection and analysis) NovoExpress software (ACEA Biosciences; for data analysis and conversion to csv), Excel
Cell population abundance	Cells (n=10,000) were examined. Flow cytometry was used for quantification purposes only (no postsorting fractions were collected)
Gating strategy	For all experiments FSC-A/ SSC-A gates of the cell population were used to discriminate viable cells from debris. Singlet and doublet cells were discriminated using FSC-A/ FSC-H gating. Psicheck2 vector (no fluorescence protein expressed) is used for distinguish autofluorescence and expressed fluorescence proteins. Then, scatter plots of GFP vs. RFP signals (n=10,000 cells) were analyzed. An example for gating strategy is presented in Extended Data Fig. 4i-k.

☒ Tick this box to confirm that a figure exemplifying the gating strategy is provided in the Supplementary Information.

Dichotomous engagement of HDAC3 activity governs inflammatory responses

https://doi.org/10.1038/s41586-020-2576-2

Received: 6 March 2019

Accepted: 12 May 2020

Hoang C. B. Nguyen[1,2], Marine Adlanmerini[1,2], Amy K. Hauck[1,2] & Mitchell A. Lazar[1,2]✉

The histone deacetylases (HDACs) are a superfamily of chromatin-modifying enzymes that silence transcription through the modification of histones. Among them, HDAC3 is unique in that interaction with nuclear receptor corepressors 1 and 2 (NCoR1/2) is required to engage its catalytic activity[1–3]. However, global loss of HDAC3 also results in the repression of transcription, the mechanism of which is currently unclear[4–8]. Here we report that, during the activation of macrophages by lipopolysaccharides, HDAC3 is recruited to activating transcription factor 2 (ATF2)-bound sites without NCoR1/2 and activates the expression of inflammatory genes through a non-canonical mechanism. By contrast, the deacetylase activity of HDAC3 is selectively engaged at ATF3-bound sites that suppress Toll-like receptor signalling. Loss of HDAC3 in macrophages safeguards mice from lethal exposure to lipopolysaccharides, but this protection is not conferred upon genetic or pharmacological abolition of the catalytic activity of HDAC3. Our findings show that HDAC3 is a dichotomous transcriptional activator and repressor, with a non-canonical deacetylase-independent function that is vital for the innate immune system.

In contrast to the lethality conferred by the global loss of HDAC3, genetic inactivation of its enzymatic activity by disruption of the deacetylase-activating domain (DAD) of NCoR1 and NCoR2 is compatible with life with no overt physiological abnormalities[3]. Such evidence highlights the importance of the non-enzymatic functions of HDAC3, which remain poorly characterized and have critical implications for the development of deacetylase-targeting drugs such as suberoylanilide hydroxamic acid (SAHA), an HDAC inhibitor that has been approved by the Food and Drug Administration for the treatment of cancer and is being tested for efficacy in other diseases[9–13]. Loss of HDAC3 diminishes the Toll-like receptor 4 (TLR4)-mediated hyperinflammatory response to lipopolysaccharide (LPS) in macrophages owing to the impaired activation of pro-inflammatory genes; however, the mechanism is unknown[4]. Here we identify a non-canonical mechanism in which HDAC3 switches between its two enzymatic states to contribute to both repression and activation of gene transcription in a single cell type.

To determine whether HDAC3 has functions that are independent of its deacetylase activity, we used mouse bone-marrow-derived macrophages (BMDM) with myeloid-specific loss of HDAC3 (MHD3KO) that were cultured in vitro after retrovirally mediated expression of an empty control vector, the catalytically dead HDAC3(Y298F) mutant (containing a tyrosine-to-phenylalanine substitution at residue 298) or wild-type HDAC3 (WT-rescue)[5,14]. The expression of HDAC3(Y298F) was titrated such that amounts of both the mRNA (Fig. 1a) and the protein (Fig. 1b) were comparable to those of endogenous HDAC3. The deacetylase activity of HDAC3 immunoprecipitated from HDAC3(Y298F)-expressing cells was markedly reduced, to a level indistinguishable from that of MHD3KO macrophages (Fig. 1c).

We next investigated the role of the catalytic activity of HDAC3 in the transcriptional response to acute LPS challenge in vitro. As expected, LPS induced substantial changes in control macrophages, including the upregulation of classic inflammatory markers such as *Il6*, *Il1a*, *Il1b* and *Nos2*. Approximately one-third of the genes that were differentially expressed after LPS stimulation (762/2,152) were not differentially expressed in the MHD3KO macrophages (Fig. 1d, Extended Data Fig. 1a–c). The transcriptome of MHD3KO macrophages is shifted towards an alternatively activated phenotype[5], which could affect the response to LPS. Nevertheless, expression of more than half of the HDAC3-dependent, LPS-responsive genes (385/762) was rescued by the HDAC3(Y298F) mutant (referred to hereafter as deacetylase (DA)-independent genes), and these genes highly overlapped with those expressed in control and WT-rescue macrophages under LPS stimulation (Extended Data Fig. 1d).

We focused in particular on the 174 genes that were upregulated by LPS in a manner that was dependent on HDAC3 but not on its enzymatic activity (Fig. 1e). The profile included pro-inflammatory genes, such as those encoding cytokine production and activation of NF-κB signalling (Fig. 1f). By contrast, expression of the 142 genes that were downregulated upon LPS stimulation in an HDAC3-dependent manner was not rescued by the HDAC3(Y298F) mutant (Extended Data Fig. 1e, f; referred to hereafter as DA-dependent genes). These genes were functionally most notable for downregulation of TLR signalling—including *Tlr4* gene transcription (Extended Data Fig. 1g)—which suggests a potential negative feedback mechanism in response to endotoxin[15]. Overall, the HDAC3(Y298F) mutant phenocopied the inflammatory transcriptional response to LPS stimulation of wild-type HDAC3, whereas the transcriptional response to the anti-inflammatory cytokine IL4 was enzyme-dependent (Extended Data Fig. 1h), indicating that the enzyme-independent activity of HDAC3 was highly specific to the LPS response.

To understand the mechanisms that underlie the DA-independent and DA-dependent transcriptomes, we performed chromatin

---

[1]Institute for Diabetes, Obesity, and Metabolism, Perelman School of Medicine at the University of Pennsylvania, Philadelphia, PA, USA. [2]Division of Endocrinology, Diabetes, and Metabolism, Department of Medicine, Perelman School of Medicine at the University of Pennsylvania, Philadelphia, PA, USA. ✉e-mail: lazar@pennmedicine.upenn.edu

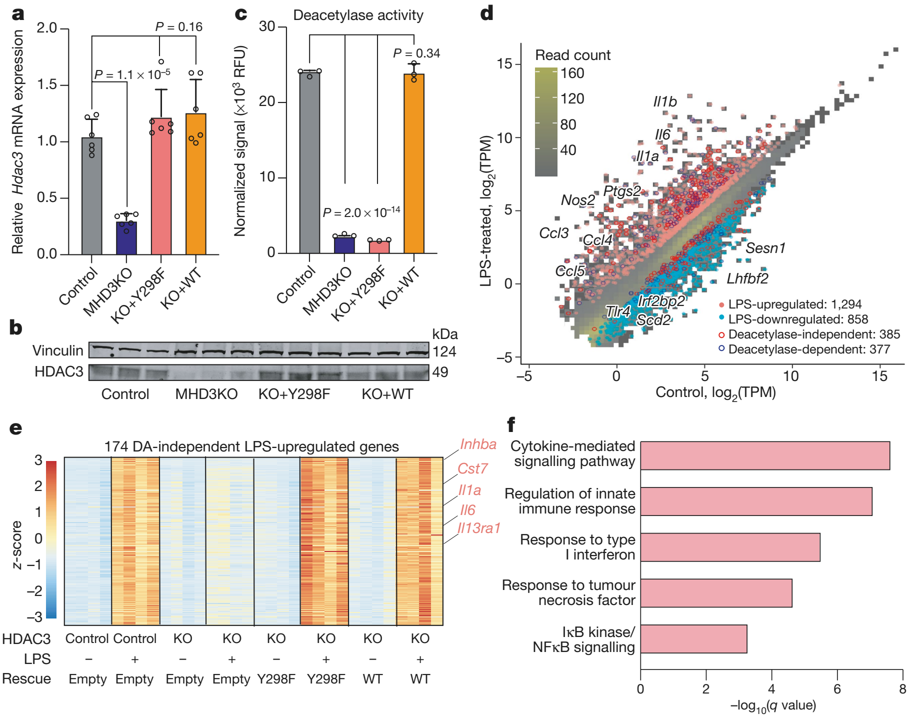

Fig. 1 | HDAC3 activates LPS-stimulated inflammatory gene expression in a DA-independent manner. a, *Hdac3* mRNA levels in control, MHD3KO, HDAC3(Y298F)-rescue (KO+Y298F) and WT-rescue (KO+WT) macrophages as quantified by quantitative PCR (qPCR). Data are mean ± s.d. ($n = 6$ biological replicates), *P* values calculated by one-way ANOVA. **b**, Western blot (performed independently twice, $n = 3$ biological replicates) of HDAC3 protein levels in control, MHD3KO, HDAC3(Y298F)-rescue and WT-rescue macrophages, with vinculin as loading control. **c**, Deacetylase activity of HDAC3 immunoprecipitated from control, MHD3KO, HDAC3(Y298F)-rescue and WT-rescue macrophages, as measured by the fluorescent signal of the enzymatically cleaved substrate. Data are mean ± s.d. ($n = 3$ biological replicates). *P* values calculated by one-way ANOVA. **d**, Scatter plot of RNA-seq data showing transcripts-per-kilobase-million (TPM)-transformed average read counts from vehicle (control) or LPS-treated control macrophages ($n = 4$ biological replicates, TPM > 0.1) and HDAC3-regulated LPS-responsive genes (pink, upregulated; light blue, downregulated; differential expression (DE) cutoff: $|\log_2(\text{fold change (FC)})| > 1$, two-sided Benjamini–Hochberg-adjusted false discovery rate (FDR) < 0.05, as determined by edgeR likelihood ratio test). DA-independent (red hollow circle) are genes for which LPS-stimulated changes were rescued by HDAC3(Y298F) and wild-type HDAC3. Deacetylase-dependent (blue hollow circle) are genes for which LPS-stimulated changes were rescued by wild-type HDAC3 but not by HDAC3(Y298F). **e**, Heat map showing 174 LPS-upregulated, HDAC3-dependent differentially expressed genes that were rescued by HDAC3(Y298F) and wild-type HDAC3 (DA-independent genes: $n = 4$ biological replicates, DE cutoff: $|\log_2\text{FC}| > 1$, two-sided Benjamini–Hochberg-adjusted FDR < 0.05 as determined by edgeR likelihood ratio test). **f**, Gene ontology analysis of 174 LPS-upregulated DA-independent genes ($n = 4$ biological replicates). *q* values represent Benjamini–Hochberg-adjusted one-sided hypergeometric *P* values for over-representation as determined by Enrichr.

immunoprecipitation followed by high-throughput sequencing (ChIP–seq) analyses for HDAC3 (Extended Data Fig. 2a, b). LPS stimulation substantially increased HDAC3 genomic occupancy within 100 kilobases (kb) of the transcription start sites of previously identified DA-independent genes (Fig. 2a), whereas HDAC3 binding was unchanged near DA-dependent genes (Fig. 2b).

We next assessed the functionality of HDAC3 binding sites using two independent measures of enhancer activity, namely Global Run-On sequencing (GRO-seq) and acetylated histone H3 lysine 27 (H3K27Ac) ChIP–seq. Globally, neither loss of HDAC3 nor LPS stimulation perturbed enhancer RNA (eRNA) production (Extended Data Fig. 2c) or H3K27Ac levels (Extended Data Fig. 2d, e). However, at HDAC3 binding sites near DA-independent genes, LPS stimulated a marked increase in eRNA production (Fig. 2c, Extended Data Fig. 2f) as well as H3K27Ac levels (Fig. 2d), which were attenuated in the MHD3KO macrophages. Conversely, enhancer activity (Fig. 2e, Extended Data Fig. 2g) and H3K27Ac abundance (Fig. 2f) proximal to DA-dependent genes were reduced by LPS stimulation and considerably induced upon loss of HDAC3; this is consistent with HDAC3 functioning as a repressor via histone deacetylation at these sites. Although functional enhancers might not always regulate the nearest genes[16], the transcriptional congruity between HDAC3-regulated enhancers and HDAC3-regulated genes supports a direct enhancer–promoter regulatory relationship.

Because HDAC3 does not have intrinsic DNA-binding capability, we considered whether the selective engagement of its catalytic activity was determined by transcription factors that facilitate genomic recruitment. De novo motif exploration of HDAC3-bound LPS-stimulated enhancers revealed the canonical motifs bound by the macrophage lineage determinant PU.1 and by NF-κB-p65, as expected (Extended Data Fig. 2h). Application of a transcription factor binding analysis (TBA)[17] based on machine learning to DA-independent and DA-dependent HDAC3-bound genomic regions revealed that DNA-sequence features intrinsic to these distinct genomic regions could predict different outcomes (Extended Data Fig. 3a). Specifically, TBA identified ATF2 as the most statistically significant positive cobinding partner at DA-independent sites, whereas ATF3 was predicted as the transcription factor most likely to be responsible for the outcome of DA-dependent genes (Fig. 3a). Notably, ATF2 was predicted to be negatively correlated with HDAC3 binding at DA-dependent sites, whereas ATF3 might negatively influence the binding of HDAC3 at DA-independent sites (Fig. 3a); other members of the AP-1 family did not display such robust differential binding affinity (Fig. 3b, Extended Data Fig. 3b, c). Moreover, HDAC3-bound eRNAs were more abundantly transcribed when the region contained the ATF2 motif than when it contained the ATF3 motif (Extended Data Fig. 3d).

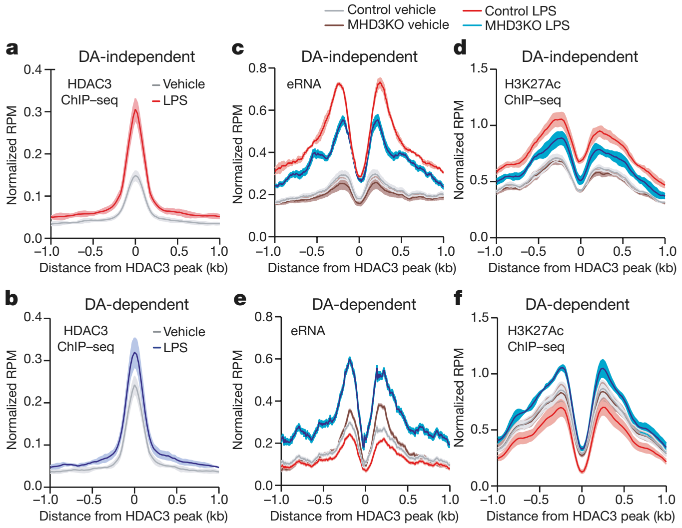

Fig. 2 | Differential recruitment and transcriptional functions of HDAC3 at DA-independent and DA-dependent LPS-responsive genes. a, **b**, Average density profiles in reads per million (RPM) of HDAC3 ChIP–seq data (mean ± s.e.m.; $n = 3$ biological replicates) at enhancers near DA-independent genes (two-sided Wilcoxon's $P = 2.6 \times 10^{-15}$) (**a**) or DA-dependent genes (two-sided Wilcoxon's $P = 0.084$) in vehicle or LPS-treated macrophages (**b**). **c**, **d**, Average density profiles in RPM (mean ± s.e.m.; $n = 3$ biological replicates) of bidirectional eRNA transcription measured by GRO-seq (control LPS-treated versus MHD3KO LPS-treated; two-sided Wilcoxon's $P = 7.7 \times 10^{-25}$) (**c**) or H3K27Ac levels measured by ChIP–seq (control LPS-treated versus MHD3KO LPS-treated; two-sided Wilcoxon's $P = 4.2 \times 10^{-7}$) (**d**) at HDAC3-bound sites near DA-independent genes in control and MHD3KO macrophages, with or without LPS. **e**, **f**, Average density profiles in RPM (mean ± s.e.m.; $n = 3$ biological replicates) of bidirectional eRNA transcription measured by GRO-seq (control LPS-treated versus MHD3KO LPS-treated; two-sided Wilcoxon's $P = 3.2 \times 10^{-126}$) (**e**) or H3K27Ac levels measured by ChIP–seq (control LPS-treated versus MHD3KO LPS-treated; two-sided Wilcoxon's $P = 6.4 \times 10^{-12}$) (**f**) at HDAC3-bound sites near DA-dependent genes in control and MHD3KO macrophages, with or without LPS. DA-independent sites = 172, DA-dependent sites = 141.

To test whether these predicted motifs were sufficient to differentially determine the engagement of the catalytic activity of HDAC3 for transcription, we transfected macrophages with reporter genes consisting of enhancer elements upstream of either *Clec2d* (a DA-independent gene containing the ATF2 motif) (Extended Data Fig. 3e) or *Gas6* (a DA-dependent gene containing the ATF3 motif) (Extended Data Fig. 3f). LPS markedly stimulated the transcriptional activity of the ATF2 reporter in an HDAC3-dependent manner—which was rescued by the HDAC3(Y298F) mutant—only in the presence of endogenous ATF2, and independent of ATF3 (Extended Data Fig. 3g). Moreover, mutating the ATF2 motif to the ATF3 motif abrogated the LPS-stimulated induction of luciferase transcription (Extended Data Fig. 3g). By contrast, the ATF3 reporter had strong basal activity that was repressed by LPS in an HDAC3-dependent manner and was unaffected by depletion of ATF2; this repression was rescued only by catalytically active wild-type HDAC3 (Extended Data Fig. 3h). However, loss of either ATF3 or the ATF3 binding motif de-repressed luciferase transcription, phenocopying the loss of HDAC3 (Extended Data Fig. 3h).

These results predicted that ATF2 would be more abundant at DA-independent HDAC3-regulated sites whereas ATF3 would be preferentially associated with enzyme-active HDAC3, and this was confirmed by comparison of their respective cistromes (Extended Data Fig. 4a). ATF2 was more abundant at DA-independent HDAC3-regulated sites in LPS-treated macrophages (Fig. 3c), whereas ATF3 was more enriched at HDAC3-bound sites near DA-dependent genes (Fig. 3d). Depletion of ATF2 or ATF3 with multiple independent short interfering RNAs (siRNAs) (Extended Data Fig. 4b, c) did not induce significant transcriptional changes at the baseline (Extended Data Fig. 4d). However, loss of ATF2—but not ATF3—reduced HDAC3 recruitment (Fig. 3e, Extended Data Fig. 4e) and specifically abolished HDAC3 DA-independent transcriptional activation of LPS-induced genes (Fig. 3f). By contrast, loss of ATF3—but not ATF2—specifically diminished HDAC3 recruitment to DA-dependent enhancers (Fig. 3g, Extended Data Fig. 4f), resulting in de-repression of LPS-downregulated genes (Fig. 3h). These results suggest that differences in the enrichment of ATF2 and ATF3 genomic occupancy determine the dichotomous functions of HDAC3 transcriptional regulation in response to LPS.

To gain insight into the mechanism of ATF2-mediated transcriptional activation by HDAC3, we performed cistromic profiling for the transcription factor p65. p65 has previously been implicated in HDAC3-dependent LPS signalling[18–20], and its motif is enriched at HDAC3-bound enhancers. LPS induced genomic binding of p65 at DA-independent sites (Extended Data Fig. 4g) more robustly than at DA-dependent sites (Extended Data Fig. 4h). p65 binding was enhanced by the loss of HDAC3 only at DA-dependent sites (Extended Data Fig. 4h), which is consistent with literature reports showing that p65 is a direct substrate of HDAC3[20–22] and that deacetylation triggers the nuclear export of p65[21,22]. p65 depletion did not alter HDAC3 genomic binding (Fig. 3e, g), but attenuated the induction of DA-independent genes (Fig. 3f) upon LPS stimulation without affecting DA-dependent genes (Fig. 3h); this suggests a specific role for p65 recruitment in DA-independent activation of pro-inflammatory genes.

Because the catalytic activity of HDAC3 requires activation by co-repressor complexes, we next tested whether the selective requirement of HDAC3 deacetylase functions could be explained by the differential recruitment of NCoR1/2. Notably, genomic colocalization of NCoR1/2 with HDAC3 was diminished at DA-independent enhancers of genes activated by HDAC3 (Fig. 3i, Extended Data Fig. 4i) relative to their robust recruitment to DA-dependent targets that were repressed by HDAC3 (Fig. 3j, Extended Data Fig. 4j). Quantitatively, NCoR1/2 were enriched at sites of ATF3 binding relative to sites of ATF2 binding (Extended Data Fig. 4k–n), providing a plausible mechanism for the reported immunosuppressive functions of ATF3[23–26], including ATF3-dependent repression of *Tlr4*[25,27]. Conversely, the depletion of NCoR1/2 at ATF2- and HDAC3-binding sites contributes to the physiological basis for DA-independent gene activation.

We next tested the importance of the DA-independent functions of HDAC3 in regulating acute systemic inflammation. A knock-in HDAC3(Y298F) mouse was not available; however, we used mice in which HDAC3 showed reduced catalytic activity owing to mutations in the deacetylase-activating domain (DAD) of NCoR1/2 that abolish their activation of HDAC3 (NSDAD mice[3]). A dose of LPS that we empirically determined to be lethal to around 50% of wild-type C57BL/6 mice within 24–120 h (Extended Data Fig. 5a) was lethal to NSDAD mice within 28 h of injection (Fig. 4a), similar to previous findings in NCoR1-DAD mutant mice[28]. Correspondingly, circulating levels of pro-inflammatory cytokines IL6 and TNF were markedly increased in NSDAD mice 6 h after LPS exposure (Extended Data Fig. 5b). By contrast, MHD3KO mice were largely protected from acute endotoxin lethality (Fig. 4a) and had lower levels of circulating pro-inflammatory cytokines compared with control mice (Extended Data Fig. 5b). Endogenous HDAC3 therefore contributes to LPS susceptibility, an effect that is magnified in the absence of its catalytic activity; this indicates that the DA-independent and DA-dependent functions of HDAC3 have opposing roles in the toxicity of LPS.

To better understand the differential LPS sensitivities of MHD3KO and NSDAD mice, we evaluated the transcriptomes and HDAC3 cistromes of their peritoneal macrophages 6 h after endotoxin exposure in vivo. Gene expression analysis (Extended Data Fig. 5c) revealed that the in vivo DA-independent transcriptome was highly correlated with its in vitro counterpart (Extended Data Fig. 5d). Loss of HDAC3 abrogated the activation of LPS-stimulated DA-independent genes in both control and NSDAD mice (Fig. 4b, Extended Data Fig. 5e), and these bore

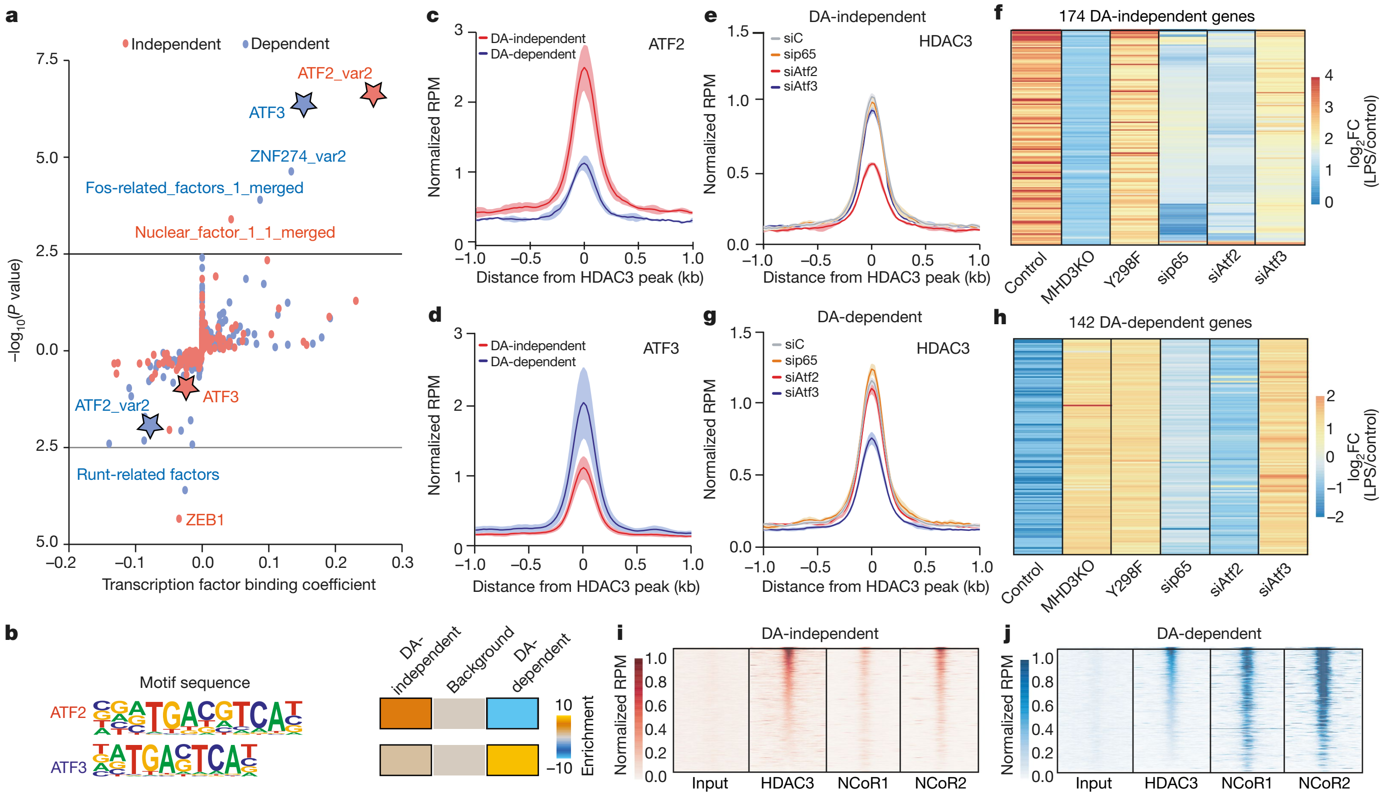

Fig. 3 | Engagement of HDAC3 enzyme activity is determined by its differential recruitment by ATF2 and ATF3. a, Machine-learning-based TBA applied to HDAC3-bound 200-bp genomic regions ($n = 3$ biological replicates) near DA-independent and DA-dependent genes. DNA motifs are ranked on the basis of binding coefficient (negative or positive correlation with HDAC3 binding) and significance of the motifs based on likelihood ratio test. **b**, Differential enrichment of TGACGTCA (ATF2 motif: 44/172 independent, 0/141 dependent) or TGACTCA (ATF3 motif: 24/172 independent, 97/141 dependent) motifs at HDAC3-bound sites near DA-independent and DA-dependent genes. **c**, **d**, Average density profiles in RPM of ATF2 (two-sided Wilcoxon's $P = 3.6 \times 10^{-19}$) (**c**) and ATF3 (two-sided Wilcoxon's $P = 1.9 \times 10^{-10}$) (**d**) ChIP–seq data (mean ± s.e.m.; $n = 3$ biological replicates) at HDAC3-bound sites near either DA-independent or DA-dependent genes in LPS-treated control macrophages. **e**, **g**, Average density profiles in RPM of HDAC3 ChIP–seq data (mean ± s.e.m.; $n = 2$ biological replicates) for control (siC), ATF2-depleted (siAtf2), ATF3-depleted (siAtf3) or p65-depleted (sip65; *p65* is also known as *Rela*) LPS-treated macrophages at HDAC3-bound sites near DA-independent (**e**) or DA-dependent (**g**) genes. **f**, **h**, Heat map showing LPS-induced transcriptional changes—as a function of $\log_2$(FC) comparing LPS-treated and vehicle control ($n = 3$ biological replicates)—of DA-independent (**f**) or DA-dependent (**h**) genes in control, MHD3KO, HDAC3(Y298F), ATF2-depleted (siAtf2), ATF3-depleted (siAtf3) or p65-depleted (sip65) macrophages. **i**, **j**, Heat maps of input, HDAC3, NCoR1 and NCoR2 ChIP–seq data showing average signal ($n = 3$ biological replicates) in RPM at HDAC3-bound sites near (**i**) DA-independent (**i**) or DA-dependent (**j**) genes. DA-independent sites = 172, DA-dependent sites = 141.

the signature of the pro-inflammatory response (Fig. 4c). By contrast, the catalytic activity of HDAC3 was required at in vivo DA-dependent genes (Extended Data Fig. 5f, g), where it exerted negative feedback on TLR4 signalling (Extended Data Fig. 5h). Moreover, as previously observed in vitro, LPS stimulated the genomic recruitment of HDAC3 in vivo to sites near DA-independent genes (Extended Data Fig. 5i) but not DA-dependent genes (Extended Data Fig. 5j). Taken together, these results suggest that inhibition of the catalytic activity of HDAC3 might be detrimental, owing to persistent HDAC3-dependent activation of inflammatory gene expression that must be reduced to enhance survival[29–31].

Because HDAC inhibitors are used in the clinic for several therapeutic indications, we compared the effects of pharmacological and genetic inhibition of the catalytic activity of HDAC3 on LPS toxicity. Consistent with previous reports of its anti-inflammatory benefits[13,32–34], low doses of SAHA (25–100 mg kg^{-1}) conferred a protective effect against severe septic shock (Extended Data Fig. 6a). This is opposite to the phenotype of the NSDAD mice, in which HDAC3 is present but without deacetylase activity, and may reflect the fact that SAHA is a more potent inhibitor of other class I HDACs than of HDAC3[35]. By contrast, daily administration of a higher, yet non-toxic dose of SAHA (400 mg kg^{-1}) sensitized mice to LPS, similar to the phenotype of the NSDAD mice (Fig. 4d). MHD3KO mice subjected to the same treatment were protected (Fig. 4d), suggesting that genetic or pharmacological inhibition of the enzymatic activity of HDAC3 might sensitize mice to endotoxic shock through HDAC3-mediated hyperactivation of DA-independent pro-inflammatory mediators. Indeed, the transcriptome of LPS-stimulated was similar to that of macrophages from NSDAD mice exposed to LPS (Extended Data Fig. 6b). Moreover, this dose-dependent transcriptional activation was accompanied by LPS-stimulated HDAC3 recruitment to DA-independent genes (Extended Data Fig. 6c, d) that did not occur at DA-dependent genes (Extended Data Fig. 6e, f).

Although classically associated with transcriptional repression, a growing body of evidence suggests that HDAC3 might also function as a coactivator[4,6–8,36]. Here we have demonstrated selective enzymatic engagement of HDAC3 as a function of its differential association with co-repressor complexes NCoR1 and NCoR2, selectively coordinated by either ATF3 or ATF2 (Fig. 4e). Our results implicate HDAC3 as a critical integrator of pathogenic stimuli to orchestrate well-balanced inflammatory responses. Efforts to attenuate class I HDAC enzymatic activity for immunomodulation should carefully consider the paradoxical intensification of enzyme-independent, pro-inflammatory activities of HDAC3.

Online content

Any methods, additional references, Nature Research reporting summaries, source data, extended data, supplementary information,

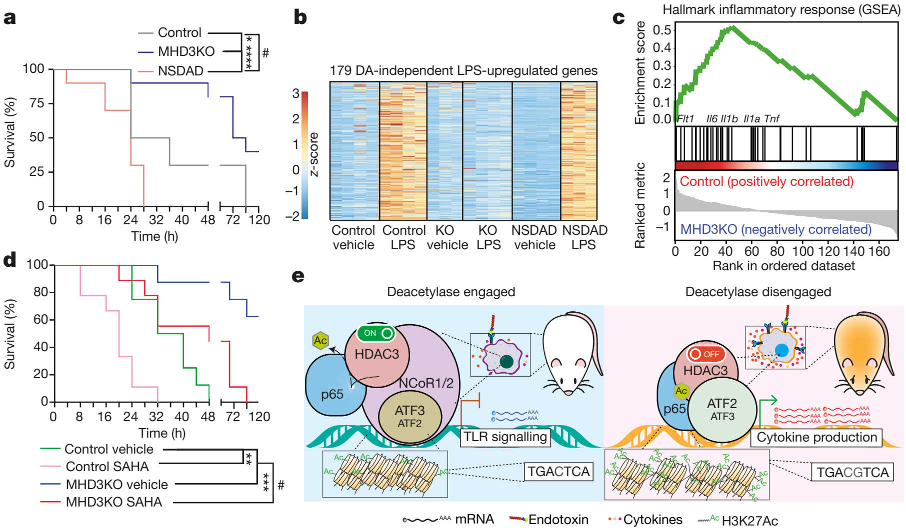

Fig. 4 | Dichotomous functions of HDAC3 orchestrate the inflammatory response to endotoxin in vivo. a, Kaplan–Meier survival curves of control, MHD3KO and NSDAD mice ($n = 10$ independent mice) subjected to 10 mg kg^{-1} purified LPS by intraperitoneal injection. #$P = 0.014$, *$P = 0.024$, ****$P = 7.1 \times 10^{-5}$, calculated using a two-sided Mantel–Cox test. **b**, Heat map showing 179 LPS-upregulated, HDAC3-dependent differentially expressed genes in vivo that were rescued by NSDAD (DA-independent genes: $n = 4$ biological replicates, except for KO vehicle and NSDAD LPS with $n = 3$ biological replicates, DE cutoff: $|\log_2 FC| > 1$, two-sided Benjamini–Hochberg-adjusted FDR < 0.05 as determined by edgeR likelihood ratio test). **c**, Gene set enrichment analysis (GSEA) for the in vivo DA-independent transcriptome (179 genes) showing enrichment of hallmark inflammatory response genes that were more upregulated in peritoneal macrophages from LPS-treated control mice than from LPS-treated MHD3KO mice ($n = 4$ biological replicates). **d**, Kaplan–Meier survival curves of control and MHD3KO mice subjected to 10 mg kg^{-1} of purified LPS by intraperitoneal injection, with co-administration of either vehicle control (10% DMSO in PBS, $n = 8$ independent mice) or 400 mg kg^{-1} of SAHA ($n = 9$ independent mice). #$P = 0.0013$, **$P = 0.0014$, ***$P = 0.00052$, calculated using a two-sided Mantel–Cox test. **e**, Dichotomous functions of HDAC3 orchestrate the inflammatory response to endotoxin.

acknowledgements, peer review information; details of author contributions and competing interests; and statements of data and code availability are available at https://doi.org/10.1038/s41586-020-2576-2.

1. Guenther, M. G., Barak, O. & Lazar, M. A. The SMRT and N-CoR corepressors are activating cofactors for histone deacetylase 3. *Mol. Cell. Biol.* **21**, 6091–6101 (2001).
2. Watson, P. J., Fairall, L., Santos, G. M. & Schwabe, J. W. R. Structure of HDAC3 bound to co-repressor and inositol tetraphosphate. *Nature* **481**, 335–340 (2012).
3. You, S. H. et al. Nuclear receptor co-repressors are required for the histone-deacetylase activity of HDAC3 in vivo. *Nat. Struct. Mol. Biol.* **20**, 182–187 (2013).
4. Chen, X. et al. Requirement for the histone deacetylase Hdac3 for the inflammatory gene expression program in macrophages. *Proc. Natl Acad. Sci. USA* **109**, E2865–E2874 (2012).
5. Mullican, S. E. et al. Histone deacetylase 3 is an epigenomic brake in macrophage alternative activation. *Genes Dev.* **25**, 2480–2488 (2011).
6. Greer, C. B. et al. Histone deacetylases positively regulate transcription through the elongation machinery. *Cell Rep.* **13**, 1444–1455 (2015).
7. Lewandowski, S. L., Janardhan, H. P. & Trivedi, C. M. Histone deacetylase 3 coordinates deacetylase-independent epigenetic silencing of transforming growth factor- β1 (TGF-β1) to orchestrate second heart field development. *J. Biol. Chem.* **290**, 27067–27089 (2015).
8. Emmett, M. J. et al. Histone deacetylase 3 prepares brown adipose tissue for acute thermogenic challenge. *Nature* **546**, 544–548 (2017).
9. Mann, B. S., Johnson, J. R., Cohen, M. H., Justice, R. & Pazdur, R. FDA approval summary: vorinostat for treatment of advanced primary cutaneous T-cell lymphoma. *Oncologist* **12**, 1247–1252 (2007).
10. Gryder, B. E., Sodji, Q. H. & Oyelere, A. K. Targeted cancer therapy: giving histone deacetylase inhibitors all they need to succeed. *Future Med. Chem*. **4**, 505–524 (2012).
11. De Souza, C. & Chatterji, B. P. HDAC inhibitors as novel anti-cancer therapeutics. *Recent Pat. Anticancer Drug Discov*. **10**, 145–162 (2015).
12. Kazantsev, A. G., & Leslie, M. T. Therapeutic application of histone deacetylase inhibitors for central nervous system disorders. *Nat. Rev. Drug Discov.* **10**, 854–868 (2008).
13. Leoni, F. et al. The antitumor histone deacetylase inhibitor suberoylanilide hydroxamic acid exhibits antiinflammatory properties via suppression of cytokines. *Proc. Natl Acad. Sci. USA* **99**, 2995–3000 (2002).
14. Sun, Z. et al. Deacetylase-independent function of HDAC3 in transcription and metabolism requires nuclear receptor corepressor. *Mol. Cell* **52**, 769–782 (2013).
15. Marinelli, C. et al. Ligand engagement of Toll-like receptors regulates their expression in cortical microglia and astrocytes. *J. Neuroinflammation* **12**, 244 (2015).
16. Gasperini, M. et al. A genome-wide framework for mapping gene regulation via cellular genetic screens. *Cell* **176**, 377–390.e19 (2019).
17. Fonseca, G. J. et al. Diverse motif ensembles specify non-redundant DNA binding activities of AP-1 family members in macrophages. *Nat. Commun.* **10**, 414 (2019).
18. Barish, G. D. et al. Bcl-6 and NF-kappaB cistromes mediate opposing regulation of the innate immune response. *Genes Dev.* **24**, 2760–2765 (2010).
19. Chen, S. et al. Valproic acid attenuates traumatic spinal cord injury-induced inflammation via STAT1 and NF-κB pathway dependent of HDAC3. *J. Neuroinflammation* **15**, 150 (2018).
20. Ziesché, E. et al. The coactivator role of histone deacetylase 3 in IL-1-signaling involves deacetylation of p65 NF-κB. *Nucleic Acids Res.* **41**, 90–109 (2012).
21. Chen, L.-f., Fischle, W., Verdin, E. & Greene, W. C. Duration of nuclear NF-κB action regulated by reversible acetylation. *Science* **293**, 1653–1657 (2001).
22. Kiernan, R. et al. Post-activation turn-off of NF-κ B-dependent transcription is regulated by acetylation of p65. *J. Biol. Chem.* **278**, 2758–2766 (2003).
23. Khuu, C. H., Barrozo, R. M., Hai, T. & Weinstein, S. L. Activating transcription factor 3 (ATF3) represses the expression of CCL4 in murine macrophages. *Mol. Immunol.* **44**, 1598–1605 (2007).
24. De Nardo, D. et al. High-density lipoprotein mediates anti-inflammatory reprogramming of macrophages via the transcriptional regulator ATF3. *Nat. Immunol.* **15**, 152 (2014).
25. Luo, H. et al. ATF3 inhibits tenascin-C-induced foam cell formation in LPS-stimulated THP-1 macrophages by suppressing TLR-4. *J. Atheroscler. Thromb.* **22**, 1214–1223 (2015).
26. Bambouskova, M. et al. Electrophilic properties of itaconate and derivatives regulate the IκBζ–ATF3 inflammatory axis. *Nature* **556**, 501–504 (2018).
27. Labzin, L. I. et al. ATF3 is a key regulator of macrophage IFN responses. *J. Immunol*. **195**, 4446–4455 (2015).
28. Yan, Q. et al. Nuclear factor-κB binding motifs specify Toll-like receptor-induced gene repression through an inducible repressosome. *Proc. Natl Acad. Sci. USA* **109**, 14140–14145 (2012).
29. Copeland, S., Warren, H. S., Lowry, S. F., Calvano, S. E. & Remick, D. Acute inflammatory response to endotoxin in mice and humans. *Clin. Diagn. Lab. Immunol.* **12**, 60–67 (2005).
30. Honore, P. M. et al. Cytokine removal in human septic shock: where are we and where are we going? *Ann. Intensive Care* **9**, 56 (2019).
31. Wheeler, D. S., et al. Induction of endotoxin tolerance enhances bacterial clearance and survival in murine polymicrobial sepsis. *Shock* **30**, 267–273 (2008).
32. Roger, T. et al. Histone deacetylase inhibitors impair innate immune responses to Toll-like receptor agonists and to infection. *Blood* **117**, 1205–1217 (2011).
33. Lin, H.-S. et al. Anti-rheumatic activities of histone deacetylase (HDAC) inhibitors in vivo in collagen-induced arthritis in rodents. *Br. J. Pharmacol.* **150**, 862–872 (2007).
34. Hu, Q. & Mao, D. Histone deacetylase inhibitor SAHA attenuates post-seizure hippocampal microglia TLR4/MYD88 signaling and inhibits TLR4 gene expression via histone acetylation. *BMC Neurosci*. **17**, 22 (2016).
35. Huber, K. et al. Inhibitors of histone deacetylases: correlation between isoform specificity and reactivation of HIV type 1 (HIV-1) from latently infected cells. *J. Biol. Chem.* **286**, 22211–22218 (2011).
36. Kuang, Z. et al. The intestinal microbiota programs diurnal rhythms in host metabolism through histone deacetylase 3. *Science* **365**, 1428–1434 (2019).

Publisher's note Springer Nature remains neutral with regard to jurisdictional claims in published maps and institutional affiliations.

Methods

Animal studies

MHD3KO mice[5] and NSDAD mice[3] were generated as previously described. Mice were housed in a temperature-controlled specific-pathogen-free facility under 12-h light/dark cycles. Adult male mice of 8 weeks old were used in all experiments. Age-matched wild-type C57BL/6 mice were purchased from Jackson Laboratories. No calculation was performed to pre-determine the sample size. Animal care and use procedures followed the guidelines of the Institutional Animal Care and Use Committee of the University of Pennsylvania in accordance with the guidelines of the National Institutes of Health. All experimental procedures were performed according to institutional pain class C protocol.

In vivo endotoxic shock study

All procedures were performed according to institutional pain class C protocol. Mice were intraperitoneally injected with 10 mg kg^{-1} of purified LPS (Sigma *Escherichia coli* O111:B4) and closely observed continuously every 4 h for the first 48 h post endotoxin exposure, for a total of 120 h. SAHA administration (Peprotech; 25–400 mg kg^{-1} every 24 h, or 10% DMSO in PBS vehicle control) was started 1 day before LPS injection and continued daily until the experimental end point. Mice of different genetic backgrounds or treatments were randomized, and identities were blinded from the experimenter until the final census. All surviving animals were humanely euthanized 120 h after injection. Experiments were performed independently twice.

ELISA

Circulating cytokine levels from mouse serum collected 6 h after administration of endotoxin were measured with Mouse Quantikine ELISA kits (TNF, MTA00B; IL6, M6000B) according to the manufacturer's instructions. Chemiluminescence was measured at a wavelength of 450 nm using a Synergy HT plate reader (BioTek) and cytokine concentrations were quantified using a four-parameter fit curve.

In vivo transcription profiling

Eight-week-old wild-type C57BL/6, MHD3KO and NSDAD mice and their control littermates were intraperitoneally injected with either phosphate-buffered saline (PBS, Sigma) or 10 mg kg^{-1} of purified LPS (Sigma *E. coli* O111:B4) at 16:00. Without thioglycolate stimulation, peritoneal macrophages were collected 6 h after LPS or PBS injection at 22:00 and passed through pre-separation filters (Miltenyi Biotec, 130-041-407) to obtain a single-cell suspension. Peritoneal macrophages were then isolated by magnetic-activated cell sorting as previously described[37], following the manufacturer's instructions (Miltenyi Biotec, 130-110-434) and using MiniMACS columns (Miltenyi Biotec, 130-042-201). RNA was isolated from purified cells using TRIzol (Invitrogen) with the RNeasy Micro kit (Qiagen).

Cell culture

BMDM were collected and cultured as previously described[5]. In brief, DMEM supplemented with 30% L929 (Sigma, 8501) conditioned medium, 10% fetal bovine serum (Tissue Culture Biologics), 100 U ml^{-1} penicillin and 100 μg ml^{-1} streptomycin (Invitrogen) was used to culture and differentiate cells for 7 days in Petri plates, with fresh medium replaced on the fourth day and replating on the sixth day after collection. Cells were then treated with PBS (vehicle), 10 ng ml^{-1} IL-4 (Peprotech) for 24 h, or 5 ng ml^{-1} LPS (Sigma) for 4 h. For HDAC inhibitor studies, a 4-h pre-treatment of either vehicle control (10% DMSO) or 25–400 nM SAHA (Peprotech) before the addition of vehicle or LPS was performed. All cell cultures were maintained at 37 °C in 5% CO_2 incubators. No cell line authentication or mycoplasma contamination testing was performed.

Retroviral expression of exogenous HDAC3 mutant

Sequencing-confirmed wild-type HDAC3 (WT-rescue) and HDAC3(Y298F) cDNAs were cloned into a murine stem cell virus (MSCV) retroviral construct. Retroviruses were produced in HEK-293FT (Invitrogen, R70007) cells by co-transfection of MSCV containing either no insert (empty vector), HDAC3(Y298F) or WT-rescue and pCL-Eco vectors with FuGENE 6 (Promega), and supernatants were collected 72 h after transfection. Supernatants from three 15-cm^2 tissue culture dishes (1.0×10^7 cells per dish) were passed through a 0.20-μm filter (Corning) before viral concentration with PEG-it Virus Precipitation Solution (System Biosciences) at 4 °C to a final stock volume of 600 μl. Concentrated retrovirus was added to 1.0×10^6 differentiating macrophages on day 4 (of the 7-day period) in DMEM containing 2 μg ml^{-1} polybrene. Fresh medium containing 1 μg ml^{-1} puromycin was added 48 h later for selection of successful viral transduction, which occurred over the next 4 days. We empirically determined that using 300 μl (titration was performed at 50, 100, 200, 300, 400, 500 μl) of the concentrated viral stock allows re-expression of exogeneous HDAC3 and the HDAC3(Y298F) mutant to a level comparable to that of endogenous HDAC3. To control for viral transduction, control and MHD3KO macrophages were also transduced with retroviruses carrying the empty vector.

DsiRNA-mediated gene silencing

After the 7-day period of macrophage differentiation as described in 'Cell culture', 5.0×10^6 cells were plated overnight in 10-cm tissue culture dishes. The media was replaced with 10 ml of serum-free, antibiotic-free DMEM for maximum transfection efficiency. For each target gene, 3 different siRNAs (dicer-substrate RNA (Dsi-RNA), IDT) were used as independent biological replicates. Transfection was done with Lipofectamine RNAiMax and siRNAs, or transfection control per manufacturer's protocol, with total RNAi concentration held constant at 50 nM. At 48 h post-transfection, transfected BMDM were collected. Knockdown of specific genes was confirmed by qPCR and western blot before downstream experiments. Gene-specific siRNA sequences can be found in Supplementary Table 1.

Dual luciferase assays

For unbiased selection of enhancer elements for reporter genes, first, consensus sequences for 200-bp DNA-sequences of enhancer elements upstream of DA-independent genes (171) and DA-dependent genes (142) were obtained using Clustal Omega multiple-alignment tool. The 200-bp enhancer element 14-kb upstream of *Clec2d* was selected for ATF2 reporter gene assay because it mapped best to the consensus sequence of 171 enhancer elements (multi-mapping score 151/200 bp, allowing gaps) for DA-independent genes. Similarly, the 200-bp enhancer element 16-kb upstream of *Gas6* was computationally selected for ATF3 reporter gene assay (multi-mapping score 177/200 bp, allowing gaps) because it mapped best to the consensus sequence of 142 enhancer elements for DA-dependent genes. A mutant reporter gene was generated by mutating the intrinsic ATF2 motif to an ATF3 motif for the ATF2 reporter, and vice versa for the ATF3 reporter. Unique flanking 5′ and 3′ extensions allowing for enzyme restriction digest were added as PCR anchor points. DNA cassettes were purchased as Ultramers from IDT, PCR-amplified, and subcloned into the pGL4.24 vector (Promega) with a minimal promoter using the restriction enzymes KpnI and XhoI (NEB). Full-length sequences for each multimerized motif are available in Supplementary Table 1. For luciferase assays, BMDM were seeded at 1.0×10^4 cells per well in a 96-well plate, co-transfected with 10 ng of luciferase reporter construct, 4 ng of CMV-Renilla plasmid, using 0.3 μl of Lipofectamine 2000 per well, in a reverse transfection protocol. Cells were lysed in passive lysis buffer (Promega Dual Luciferase Kit) 48 h post-transfection. Luminescence was read using a Synergy HT plate reader (Biotek). Four biological replicates were used in each condition.

Firefly luciferase signal was normalized to *Renilla* luciferase signal to account for transfection efficiency.

Gene expression measurement

RNA was isolated from cells using TRIzol (Invitrogen) and purified with the RNeasy minikit (Qiagen). qPCR was performed using 500 ng–1 µg of RNA (Applied Biosystems) following the manufacturer's instructions. qPCR was performed on cultured macrophages using the primers listed in Supplementary Table 1, with SYBR Green Master Mix (Applied Biosystems) on the QuantStudio 6 Flex Real-Time PCR system (Applied Biosytems). qPCR analysis was performed using the standard curve method, and all genes were normalized to the housekeeping gene *36b4* (also known as *Rplp0*). All qPCR experiments were performed with at least 3 biological replicates per condition. For RNA-seq, RNA integrity was examined using Agilent RNA 6000 Nano kit. RNA samples with RNA integrity number >7 (1 µg) were used for RNA cleanup and library preparation with Illumina Truseq Stranded Total RNA Library Prep kit according to the manufacturer's instructions. All barcoded libraries were quantified by KAPA Library Quantification Kit (Roche), and equimolarly pooled for subsequent sequencing. All RNA-seq experiments were performed with at least three biological replicates per condition. For each biological replicate, macrophages were pooled from at least three or four different mice.

RNA-seq data processing

All RNA-seq libraries were sequenced on Illumina HiSeq2000, Hiseq4000, Nextseq500, or Novaseq6000 platforms. Sequencing reads were aligned to the UCSC mm10 genome using STAR(v.2.6.0a)[38] with the following parameters: –outFilterMultimapNmax 1–outSAMtype BAM SortedByCoordinate–readFilesCommand zcat–outSAMstrandField intronMotif. Read counts were then obtained from mapped bam files with featureCounts (v.1.5.3)[39] with the following parameters: -t exon -g gene_id -s 1 -T 20. To filter out lowly expressed genes, raw read counts were transformed into transcripts per kilobase million (TPM) and only genes with TPM > 0.1 in at least two of the biological replicates were kept in the count matrix for further downstream differential expression analyses. edgeR[40] estimateDisp() and calcNormFactor() functions were used to estimate intrinsic dispersion and calculation normalization factors, respectively, to account for variations in sequencing depth. Normalized read counts were fit to a negative binomial generalized log-linear model with glmFit(). To account for changes in two variables simultaneously—for example, LPS and HDAC3—multi-variable design matrices were used. Differentially expressed (DE) genes (cut-off defined as $|\log_2 FC| > 1$, two-sided Benjamini–Hochberg-adjusted $FDR < 0.05$) were identified using edgeR likelihood ratio test glmLRT().

To identify the DA-independent transcriptome, first, LPS-stimulated differentially expressed genes ($|\log_2 FC| > 1$, $FDR < 0.05$) were identified from (a) the difference between HDAC3(Y298F) versus MHD3KO: [(Y298F LPS − Y298F vehicle) − (MHD3KO LPS − MHD3KO vehicle)]; (b) the difference between control versus MHD3KO: [(control LPS − control vehicle) − (MHD3KO LPS − MHD3kO vehicle)]; c) the difference between WT-rescue versus MHD3KO: [(WT-rescue LPS − WT-rescue vehicle) − (MHD3KO LPS − MHD3KO vehicle)]. DA-independent genes were classified as those that fit the null hypothesis of equality (that is, no difference, FDR > 0.05) for the HDAC3(Y298F)-rescue contrasts of [(Y298F versus MHD3KO) − (control versus MHD3KO)] and [(Y298F versus MHD3KO) − (WT-rescue versus MHD3KO)]. Similarly, the DA-dependent transcriptome fit the null hypothesis of equality for the contrasts of [(Y298F versus control) − (MHD3KO versus control)] and [(Y298F versus WT-res) − (MHD3KO versus WT-res)]. As such, for DA-independent genes, the HDAC3(Y298F) transcriptome was statistically modelled to be overlapping with both control and WT-rescue, while maximally distant to MHD3KO. Meanwhile, for DA-dependent genes, the HDAC3(Y298F) transcriptome was statistically modelled to be overlapping with MHD3KO, while maximally distant to both control and WT-rescue. Cumulative distribution function (CDF) plots for DA-independent and DA-dependent transcriptomes were generated with the R package latticeExtra function ecdfplot(). Heat maps were generated with the R package pheatmap using z-transformed TPM or $\log_2$(FC) values across all biological replicates and treatment conditions. Gene ontology analyses of DA-independent, LPS-upregulated and DA-dependent, LPS-downregulated genes were performed using Enrichr[41,42] reporting terms with the most significant reported q values (<0.05). Gene set enrichment analyses were performed with GSEA software[43,44] using gene sets provided directly from https://software.broadinstitute.org/gsea/.

GRO-seq and data processing

GRO-seq was performed as previously described[45,46] with the following modifications: BMDM were collected from control and MHD3KO using three independent biological replicates per condition. For each biological replicate, BMDM from 10 different mice were pooled together before being treated with either PBS control or 5 ng ml^{-1} of LPS for 4 h before collection. Cells were washed twice with ice-cold PBS, then put in cold swelling buffer (10 mM Tris at pH 7.5, 2 mM $MgCl_2$, 3 mM $CaCl_2$) for 5 min on ice. Cells were scraped off and centrifuged at 400g for 10 min. The nuclei were then extracted using lysis buffer (swelling buffer with 10% glycerol and 1% Igepal). After two washes with lysis buffer, nuclei were resuspended in freezing buffer (50 mM Tris pH 8.3, 40% glycerol, 5 mM $MgCl_2$, 0.1 mM EDTA). Nuclei (1.0×10^7) were used for each library. The nuclear run-on reaction was incubated in run-on buffer (10 mM Tris pH 8.0, 5 mM $MgCl_2$, 1 mM DTT, 300 mM KCl, 200 U ml^{-1} Superase-In, 1% Sarkosyl, 500 mM ATP, GTP and Br-UTP, 2 mM CTP) for 7 min at 30 °C. Nascent transcripts were enriched with anti-BrUTP antibodies. After 10 min of RNA hydrolysis and reverse transcription, all products were used for GRO-seq library preparations in parallel to reduce batch effect.

GRO-seq libraries were barcoded and sequenced on the Illumina HiSeq4000 platform. Bidirectional eRNA identification was performed as previously described[8,47]. HDAC3-colocalized eRNAs were identified by overlapping all HDAC3 genomic sites with all bidirectional eRNA sites using bedtools[48] intersectBed. Bidirectional eRNA signal densities at specific HDAC3 peak regions were obtained with annotatepeaks.pl with a 2-kb window from the centre of the HDAC3 peak, using the option -size 2000 -hist with a 25-bp bin size. Average density profiles were generated with mean signal in normalized reads per million (RPM) and error bands for biological replicates. Density profile statistics were calculated with a Wilcoxon rank sum test using the R function wilcox.test(), for two independent samples with no assumption of normal distribution and a null hypothesis of equal medians ($x - y = \mu = 0$).

Western blot

Cellular lysates were prepared by lysing cells ($0.5–1.0 \times 10^7$) in ice-cold RIPA buffer containing protease and phosphatase inhibitors (Roche). For the H3K27Ac immunoblot, HDAC3 inhibitor cocktail (sodium butyrate, nicotinamide and trichostatin A) was also added to the lysis buffer. Cellular debris was removed by centrifugation (21,000g) for 20 min at 4 °C. Protein concentration was measured with Pierce BCA Protein Assay Kit (Fisher, 23225) and all samples were normalized to the same input protein concentration. Samples were denatured in loading buffer, separated using SDS–PAGE, transferred to a polyvinylidene difluoride membrane (Pierce), blocked with Odyssey TBS Blocking Buffer (LICOR 927-50100), and probed using target-specific primary antibodies (listed in Supplementary Table 1) at 1:1,000 dilution. Bound primary antibodies were detected by species-specific LICOR fluorescent IRDye secondary antibodies (IRDye 800CW goat anti-mouse 925-32210, lot C70712-11, 1:20,000 dilution; IRDye 680RD donkey anti-rabbit 926-68073, lot C90129-15, 1:20,000 dilution). Immunoblots were imaged with the Odyssey Sa Infrared Imaging System according to the manufacturer's instructions. Dual-channel colour (red/green) blots were converted to greyscale for colour-blind-friendly visualization purposes. Blots were cut appropriately by molecular weight whenever cross-species antibodies were used to reduce background (resulting from using mouse-derived antibodies in mouse-derived tissues. Raw blots can be found in Supplementary Fig. 1.

Immunoprecipitation

Fully differentiated BMDM or peritoneal macrophages were lysed with ChIP buffer (50 nM Tris-HCl pH 7.5, 500 mM NaCl, 1 mM EDTA, 1% Triton-X 100, 0.1% sodium deoxycholate, 0.1% SDS, supplemented with cOmplete Protease Inhibitor, Roche, for H3K27Ac, HDAC3 inhibitor cocktail with sodium butyrate, nicotinamide and trichostatin A was also added), incubated on ice for 30 min, and centrifuged at maximum speed for 30 min to collect cell debris at 4 °C. Of the cleared lysates, 5% were saved as input. Lysates were subjected to BCA protein quantification to normalize the amount of input material subjected to immunoprecipitation. Lysates were then incubated with antibody overnight at 4 °C, followed by immunoprecipitation with Protein A Sepharose CL-4B beads (30 µl wet beads/ IP) for 6 h at 4 °C. Beads were subsequently subjected to a 5-min wash with ChIP-buffer, a 5-min wash with ChIP-buffer with additional 500 nM NaCl, and a 5-min wash with wash buffer (10 nM Tris-HCl pH 8.0, 250 mM LiCl, 0.5% NP-40, 10% sodium deoxycholate, 1 mM EDTA).

HDAC activity assay

Using the HDAC Assay Kit (Active Motif 56200) according to the manufacturer's instructions, the deacetylase activity of immunoprecipitated HDAC3 (as described in 'Immunoprecipitation') from control, MHD3KO, HDAC3(Y298F) or WT-rescue BMDM with 1 mg of starting material using anti-HDAC3 antibody (Abcam 7030). Substrate solution containing short peptides with acetylated lysine residues were added directly to the HDAC3-antibody–Protein A bead slurry complex. After incubation with developing solution, fluorescent signals from standards and samples were detected using a plate reader system (Biotek Synergy HT), and deacetylase activity was determined by the standard curve method.

ChIP–seq and data processing

All reported ChIP–seq experiments were performed in three independent biological replicates, except for HDAC3 ChIP–seq in ATF2-, ATF3- or p65-depleted cells, for which there were two independent biological replicates per condition. For each biological replicate, BMDM were pooled from at least five different mice for sufficient input material. BMDM (1.0×10^7) were crosslinked on a Petri plate with 1% formaldehyde for 15 min at room temperature, then quenched with 2.5 M glycine for 5 min. Crosslinked cells were then scraped off the plates in PBS, collected by centrifugation (1,000*g* for 5 min) and lysed in 1 ml ChIP buffer (as described in 'Immunoprecipitation') and placed on ice for 10 min. Chromatin fragmentation was performed with a microtip probe sonicator (Fisher Scientific, FB705 Sonic Dismembrator) at 4 °C with the following settings: 3× 10% amplitude for 10 s, followed by 3× 15% amplitude for 15 s, with a 30-s pause in between each sonication. Chromatin was then cleared with centrifugation at maximum speed for 30 min at 4 °C, 5% saved for input, and incubated with antibodies (listed in Supplementary Table 1) overnight at 4 °C. Immunoprecipitation of ChIP DNA was similar to the immunoprecipitation procedure described in the above section, except for reversal of crosslinking overnight at 65 °C with elution buffer (50 mM Tris-HCl pH 8.0, 10 mM EDTA, 1% SDS) before treatment with 0.33 mg ml^{-1} RNase A (Fisher EN0531) and 0.5 mg ml^{-1} Proteinase K (Fisher 2546) at 37 °C for 1 h. DNA was isolated with phenol/chloroform followed by overnight ethanol precipitation at −20 °C. ChIP DNA was prepared for sequencing according to the amplification protocol provided by Illumina.

All ChIP–seq libraries were barcoded and sequenced on NextSeq500 or HiSeq4000. Sequencing reads were aligned to the UCSC mm10 genome using Bowtie2 (v.2.2.6)[49] with the following parameters -p 20 -N 1. Mapped reads were processed into tag counts, filtered for PCR duplicates, corrected for read-depth bias, and fragment lengths for each biological replicate with HOMER[50] functions makeTagDirectory -tbp 1 -fragLength 150 -totalReads 2e7. For peak calling, findPeaks function was used with parameter -size 200 to resize all peaks to a uniform size of 200 bp. As background, input samples were used, except for HDAC3 for which MHD3KO was used. Peaks were called independently for each replicate. Only peaks that are present in at least two biological replicates are considered 'true' peaks. Peaks are defined as foldchange IP/input(KO) > 4, FDR < 0.0001. Genome browser tracks were generated with HOMER function makeUCSCfile -bigWig -fsize 1e20 and corrected for variations in read-depth with -norm 2e7. For identification of HDAC3 peaks near DA-independent and DA-dependent genes, bedtools window -l 1e5 was used on genomic location of respective transcription start sites (obtained from https://genome.ucsc.edu) and HDAC3 peaks. For each gene, only the closet peak was counted. For peaks that happened to be close to both a DA-independent gene and a DA-dependent gene, whichever one was closer to the peak was assigned. ChIP–seq signal densities at specific peak regions were obtained with annotatepeaks.pl with a 2-kb window from the peak centre, using the option -size 2000 -hist (for histograms) or -ghist (for heat maps) with 25-bp bin size. Average density profiles were generated with mean signal in normalized reads per million (RPM) and error bands for biological replicates. Density profile statistics were calculated with a Wilcoxon rank sum test using the R function wilcox.test(), for two independent samples with no assumption of normal distribution and a null hypothesis of equal medians ($x - y = \mu = 0$). De novo motif analyses were performed with the HOMER function findMotifsGenome.pl. For identification of motifs specific to DA-independent and DA-dependent sites, a machine-learning-based TBA[17] was applied to HDAC3-bound genomic regions near DA-independent genes and DA-dependent genes. TBA (v.1.0) was operated under recommended parameters (https://github.com/jenhantao/tba) with multi-threading and option –p to test for significance with a likelihood ratio test. For differential motif enrichment, DA-independent and DA-dependent genomic sites were cross-compared against each other as input and background, and vice versa. An enrichment score heat map was generated using $-\log_{10}$(hypergeomtric *P* value) for enrichment and $\log_{10}$(hypergeometric *P* value) for depletion. ChIP–seq quality controls—including the number of mapped reads, peak counts, and FRiP score—are provided in Supplementary Table 2. Statistically significant motifs from HOMER de novo motif discovery for HDAC3, ATF2, ATF3, p65, NCoR1 and NCoR2 are listed in Supplementary Table 3.

Statistics and reproducibility

All data were presented with individual biological replicates shown when appropriate. RStudio (v.1.0.153) with the R packages edgeR (v.3.26.8), ggplot2 (v.3.3.0), latticeExtra (v.0.6-29), pheatmap (v.1.0.12) softwares and GraphPad Prism (v.8.0) were used for graphing and statistical analysis. Genome-browser tracks were visualized with IGV 2.3.92[51]. All statistical tests are fully described in the figure legends. In general, *P* values were calculated using two-tailed Student's *t*-test for pairwise comparisons and one-way ANOVA for multiple comparisons. All statistical tests were adjusted using the Holm–Sidak method for multiple testing, with a 95% confidence interval. Hypergeometric testing was either reported by HOMER (v.4.11)[50] or Enrichr (v.2.1)[41,42], or was performed with the R function phyper(). Statistics reported by Enrichr (*q* values) were adjusted using the Benjamini–Hochberg method. Correlations with associated *P* values from two-sided *t*-tests were calculated using the R function cor().

The following experiments were performed independently twice with similar results: Fig. 1a, b (HDAC3 gene and protein expression), Extended Data Fig. 2e (H3K27Ac western blot) and Extended Data Fig. 6a (in vivo endotoxin susceptibility in SAHA-treated mice).

The following experiments were performed once: Fig. 1c (HDAC3 catalytic activity), Fig. 1d–f and Extended Data Fig. 1a–h (RNA-seq), Figs. 2a, b, 3a, b and Extended Data Figs. 2a, b, h, 3a, b (HDAC3 ChIP–seq), Fig. 2c, e and Extended Data Figs. 2c, f, g, 3d (GRO-seq), Fig. 2d, f and Extended Data Fig. 2a, d (H3K27Ac ChIP–seq), Fig. 3c, d and Extended Data Fig. 4a, m, n (ATF2 and ATF3 ChIP–seq), Fig. 3e–h and Extended Data Fig. 4d–f (HDAC3 ChIP–seq and RNA-seq in siAtf2/siAtf3/sip65 macrophages), Fig. 3i, j and Extended Data Fig. 4i–l (NCoR1/2 ChIP–seq), Extended Data Fig. 3e–h (luciferase assays), Extended Data Fig. 4b, c (ATF2/ATF3/p65 expression), Extended Data Fig. 4g, h (p65 ChIP–seq), Fig. 4a (in vivo endotoxin susceptibility in genetic mouse models), Fig. 4b, c and Extended Data Fig. 5c–j (in vivo RNA-seq and HDAC3 ChIP–seq), Fig. 4d (SAHA endotoxin susceptibility in genetic model), Extended Data Fig. 5a, b (endotoxin susceptibility and cytokine measurement), Extended Data Fig. 6b–f (HDAC3 ChIP–seq and RNA-seq in SAHA treated macrophages).

Reporting summary

Further information on research design is available in the Nature Research Reporting Summary linked to this paper.

Data availability

All sequencing data from RNA-seq, ChIP–seq and GRO-seq analyses have been deposited to the Gene Expression Omnibus under accession number GSE140611. ChIP–seq data for Fos, JunB, JunD and CREB in LPS-stimulated BMDMs were obtained from GSE99895. All other data are available from the corresponding author upon reasonable request.

37. Lee, M. S. et al. Genome-wide profiling of in vivo LPS-responsive genes in splenic myeloid cells. *Mol. Cells* **35**, 498–513 (2013).
38. Dobin, A. et al. STAR: ultrafast universal RNA-seq aligner. *Bioinformatics* **29**, 15–21 (2013).
39. Liao, Y., Smyth, G. K. & Shi, W. featureCounts: an efficient general purpose program for assigning sequence reads to genomic features. *Bioinformatics* **30**, 923–930 (2014).
40. Robinson, M. D., McCarthy, D. J. & Smyth, G. K. edgeR: a Bioconductor package for differential expression analysis of digital gene expression data. *Bioinformatics* **26**, 139–140 (2010).
41. Chen, E. Y. et al. Enrichr: interactive and collaborative HTML5 gene list enrichment analysis tool. *BMC Bioinformatics* **14**, 128 (2013).
42. Kuleshov, M. V. et al. Enrichr: a comprehensive gene set enrichment analysis web server 2016 update. *Nucleic Acids Res.* **44**, W90–W97 (2016).
43. Subramanian, A. et al. Gene set enrichment analysis: a knowledge-based approach for interpreting genome-wide expression profiles. *Proc. Natl Acad. Sci.* **102**, 15545–15550 (2005).
44. Mootha, V. K. et al. PGC-1α-responsive genes involved in oxidative phosphorylation are coordinately downregulated in human diabetes. *Nat. Genet.* **34**, 267–273 (2003).
45. Wang, D., et al. Reprogramming transcription by distinct classes of enhancers functionally defined by eRNA. *Nature* **474**, 390–394 (2011).
46. Kaikkonen, M. U. et al. Remodeling of the enhancer landscape during macrophage activation is coupled to enhancer transcription. *Mol. Cell* **51**, 310–325 (2013).
47. Fang, B. et al. Circadian enhancers coordinate multiple phases of rhythmic gene transcription in vivo. *Cell* **159**, 1140–1152 (2014).
48. Quinlan, A. R. & Hall, I. M. BEDTools: a flexible suite of utilities for comparing genomic features. *Bioinformatics* **26**, 841–842 (2010).
49. Langmead, B. & Salzberg, S. L. Fast gapped-read alignment with Bowtie 2. *Nat. Methods* **9**, 357–359 (2012).
50. Heinz, S. et al. Simple combinations of lineage-determining transcription factors prime *cis*-regulatory elements required for macrophage and B cell identities. *Mol. Cell* **38**, 576–589 (2010).
51. Robinson, J. T. et al. Integrative genomics viewer. *Nat. Biotechnol.* **29**, 24–26 (2011).

Acknowledgements We thank D. Steger and H. Goodarzi for discussions, J. Marinis and J. DiSpirito for help with setting up the macrophage system, and the Functional Genomics Core of the Penn Diabetes Research Center (National Institutes of Health (NIH) P30 19525) for next-generation sequencing. This work was supported by NIH R01 DK43806 (M.A.L.), NIH T32 DK07314 (A.K.H.), American Diabetes Association 1-18-PDF-126 (M.A.) and the JPB Foundation.

Author contributions H.C.B.N. and M.A.L. conceived the project, designed experiments, analysed results and wrote the manuscript; H.C.B.N. performed animal experiments and LPS susceptibility assays on genetic mouse models, tissue culture, HDAC3/ATF2/ATF3/p65 immunoblots, RNA-seq, HDAC3/ATF2/NCor1/NCoR2 ChIP–seq, and GRO-seq experiments, as well as bioinformatic analyses. M.A. performed isolation of peritoneal macrophages from the LPS-injected genetic mouse model for RNA-seq/ChIP–seq analyses, and the LPS susceptibility assay on C57BL/6, control and MHD3KO mice treated with different doses of SAHA. A.K.H. performed the H3K27Ac immunoblot, and ChIP–seq analyses for H3K27Ac, ATF3 and p65.

Competing interests M.A.L. receives research support from Pfizer for unrelated work, serves as an advisory board member for Pfizer, has consulted for Novartis, Madrigal, Calico and Third Rock, and holds equity in KDAC Therapeutics.

Additional information
Supplementary information is available for this paper at https://doi.org/10.1038/s41586-020-2576-2.
Correspondence and requests for materials should be addressed to M.A.L.
Peer review information *Nature* thanks Gioacchino Natoli, Inez Rogatsky and the other, anonymous, reviewer(s) for their contribution to the peer review of this work.

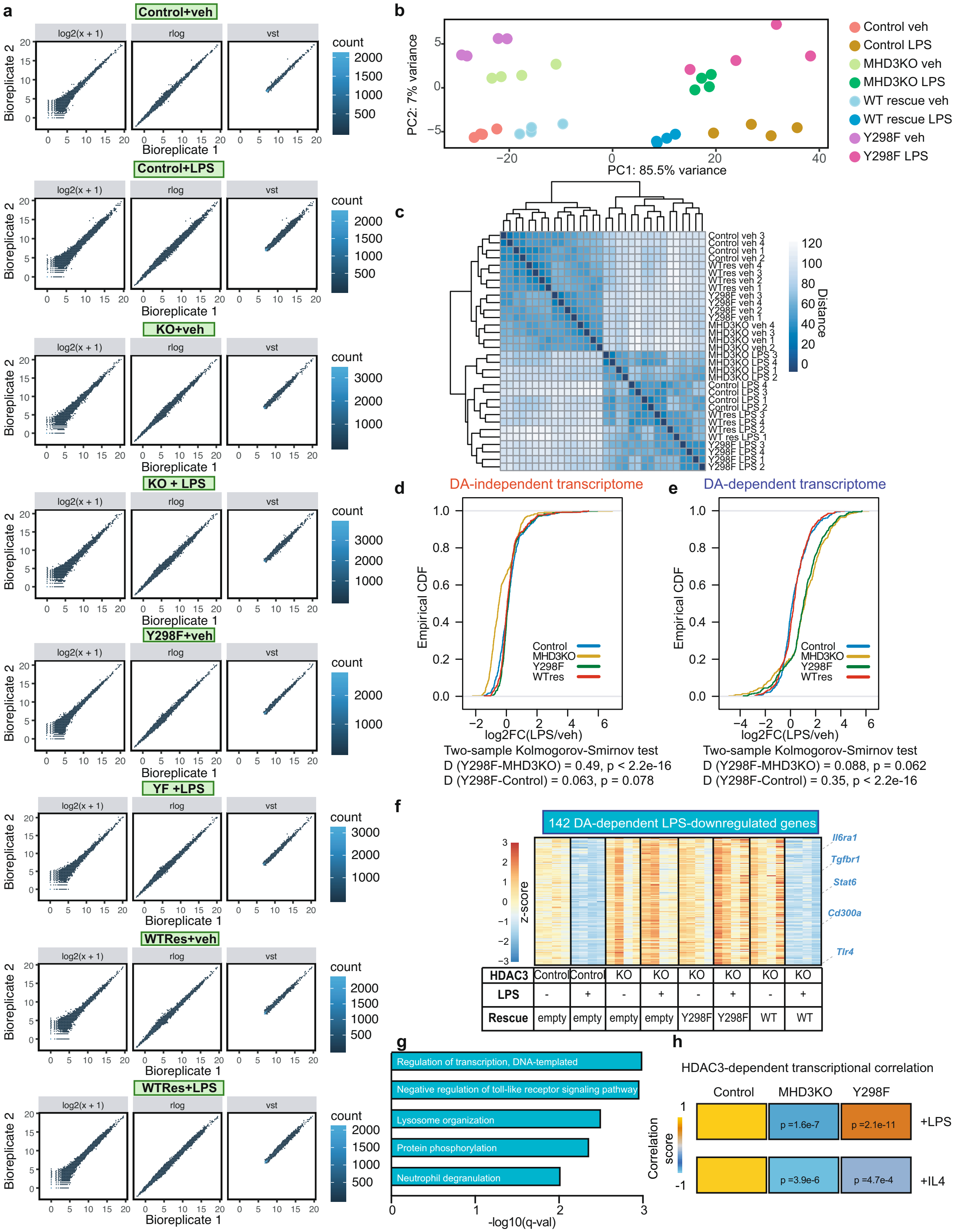

Extended Data Fig. 1 | See next page for caption.

Extended Data Fig. 1 | DA-independent and DA-dependent functions of HDAC3 in the inflammatory response to LPS. a, Scatter plots of RNA-seq experiments in control, MHD3KO, HDAC3(Y298F) and WT-rescue BMDM, with or without LPS, showing correlation between biological replicates using either $\log_2$ transformation ($\log_2(x+1)$), variance stabilizing transformation (vst), or regularized-logarithm transformation (rlog) of normalized read counts. **b**, Principal component analysis (PCA) plot using the vst values from RNA-seq experiments in control, MHD3KO, HDAC3(Y298F) and WT-rescue BMDM, with or without LPS ($n = 4$ biological replicates). **c**, Heat map of sample-to-sample distances using the vst values from RNA-seq experiments in control, MHD3KO, HDAC3(Y298F) and WT-rescue BMDM, with or without LPS ($n = 4$ biological replicates). **d**, Empirical cumulative distribution function (CDF) and associated two-sided Kolmogorov–Smirnov test *D* statistics of LPS-stimulated changes in statistically modelled DA-independent gene expression (385 genes) for control, MHD3KO, HDAC3(Y298F) and WT-rescue BMDM ($n = 4$ biological replicates). **e**, Empirical CDF and associated two-sided Kolmogorov–Smirnov test *D* statistics of LPS-stimulated changes in statistically modelled DA-dependent gene expression (377 genes) for control, MHD3KO, HDAC3(Y298F) and WT-rescue BMDM ($n = 4$ biological replicates). **f**, Heat map showing 142 LPS-downregulated genes that were rescued by wild-type HDAC3 but not by HDAC3(Y298F) (DA-dependent genes: $n = 4$ biological replicates, DE cutoff: $|\log_2 FC| > 1$, two-sided Benjamini–Hochberg-adjusted FDR < 0.05 as determined by edgeR likelihood ratio test). **g**, Gene ontology analysis of 142 LPS-downregulated genes ($n = 4$ biological replicates). *q*-values represent Benjamini–Hochberg-adjusted one-sided hypergeometric *P* values for over-representation as determined by Enrichr. **h**, LPS-stimulated (762 genes) and IL4-stimulated (405 genes) transcriptomic correlation of MHD3KO and HDAC3(Y298F), compared with control BMDM ($n = 4$ biological replicates). Heat map showing Spearman's correlation ρ values with corresponding two-sided *P* values calculated by *t*-tests.

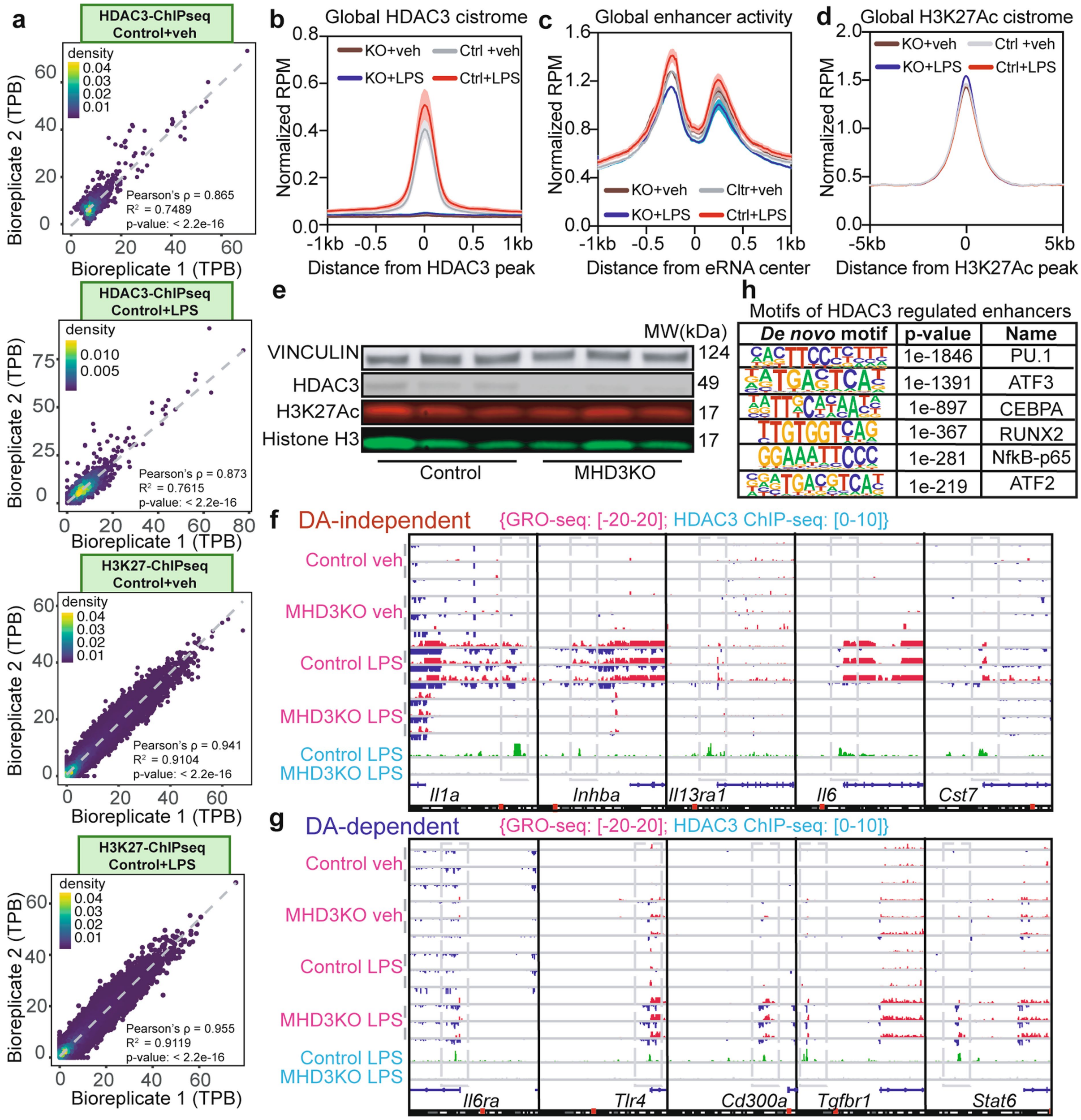

Extended Data Fig. 2 | Differential recruitment and enhancer activity of HDAC3 at LPS-responsive genes. a, Scatter plots of ChIP–seq experiments for HDAC3 and H3K27Ac in vehicle or LPS-treated control BMDM (*n* = 3 biological replicates) showing correlation between biological replicates using tag counts per base-pair (TPB) at identified peak regions. Pearson's *P* values were calculated with two-sided *t*-tests. **b**, Average density profiles in RPM of HDAC3 ChIP–seq showing mean ± s.e.m. (*n* = 3 biological replicates) at all identified HDAC3 peaks (10,966 total) in control and MHD3KO macrophages, with or without LPS. **c**, Average density profiles in RPM of GRO-seq showing mean ± s.e.m. (*n* = 3 biological replicates) at all identified eRNAs (12,192 total) in control and MHD3KO BMDM, with or without LPS. **d**, Average density profiles in RPM of H3K27Ac showing mean ± s.e.m. (*n* = 3 biological replicates) at all identified H3K27Ac peaks (50,247 total) in control and MHD3KO macrophages, with or without LPS. **e**, Western blot (performed independently twice) of HDAC3 and H3K27Ac protein levels in control and MHD3KO macrophages, with vinculin and histone H3 as loading controls. **f**, **g**, Genome-browser tracks showing three biologically replicated examples of enhancer and gene body activity as measured by GRO-seq relative to HDAC3 ChIP–seq peaks in control and MHD3KO macrophages, with or without LPS near DA-independent (**f**) or DA-dependent (**g**) genes. **h**, Top de novo enriched motifs at HDAC3-bound genomic regions (10,966 sites from *n* = 3 biological replicates). Statistics were determined by HOMER with one-sided hypergeometric *P* values for over-representation.

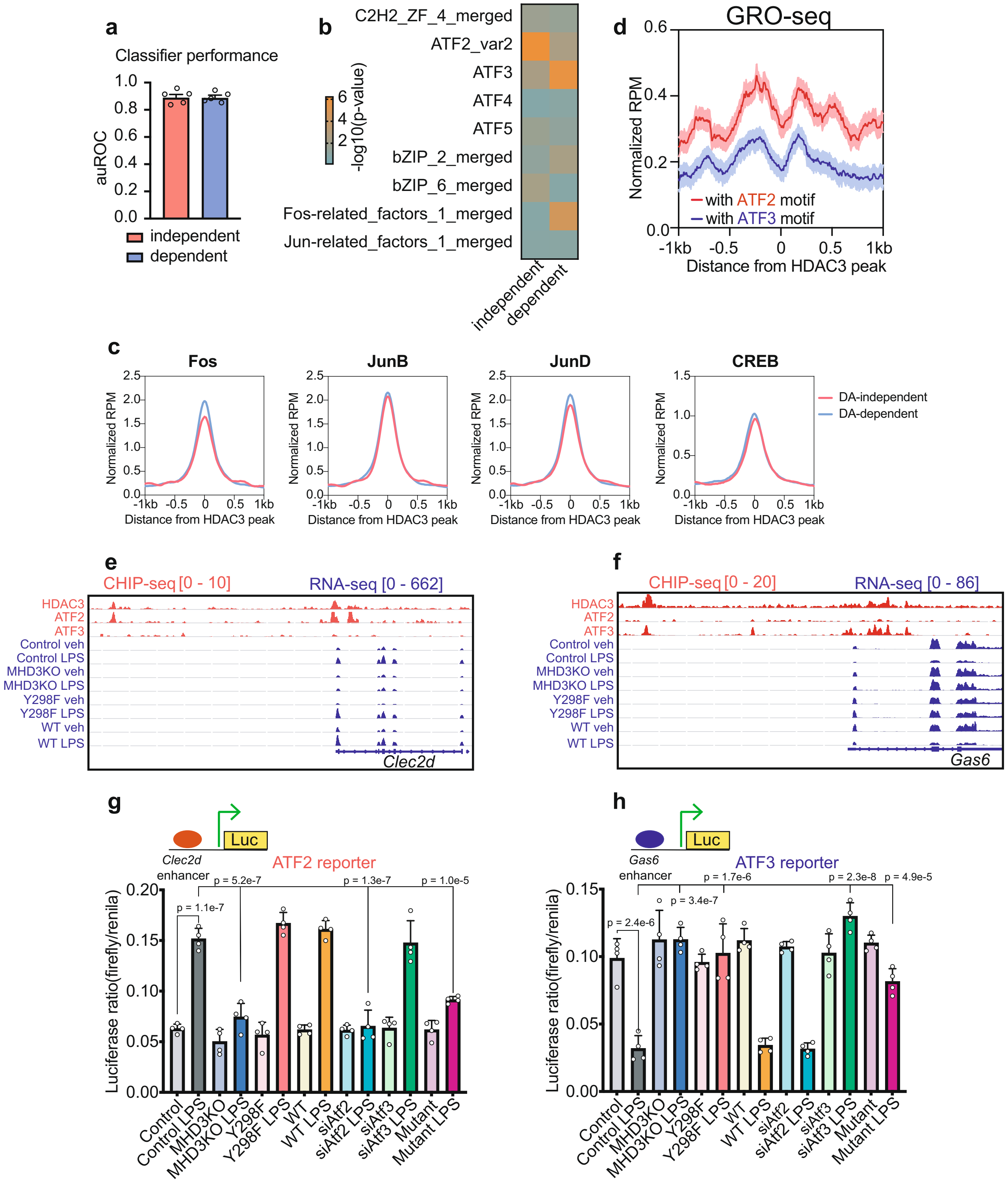

Extended Data Fig. 3 | See next page for caption.

Extended Data Fig. 3 | ATF2 and ATF3 differentially mediate HDAC3 transcriptional effects at DA-independent and DA-dependent sites, respectively. **a**, Comparison of the performance of TBA classifiers modelled against DA-independent and DA-dependent 200-bp-DNA sequences as measured by the area under the receiver operating characteristic curve (auROC, $n = 5$ independent train-test iterations, data shown as mean ± s.d.). **b**, Heat map showing relative enrichment of several AP-1 family member DNA motifs as determined by TBA with likelihood ratio test against DA-independent and DA-dependent 200-bp-DNA sequences across 5 train-test iterations. The non-redundant, merged motifs from TBA include ATF1, 4, 5, 6, 7, Jun family, Fos family, and other related bZIP factors. **c**, Average density profiles in RPM of Fos, JunB, JunD and CREB ChIP–seqs obtained from Gene Expression Omnibus database at HDAC3-bound sites near either DA-independent or DA-dependent genes in LPS-treated BMDM. **d**, Average density profiles in RPM of bidirectional eRNA transcription measured by GRO-seq showing mean ± s.e.m. ($n = 3$ biological replicates) at HDAC3-bound enhancers with ATF2 motif (1,680 sites) or ATF3 motif (3,673 sites) (two-sided Wilcoxon's $P = 8.6 \times 10^{-127}$) in LPS-treated BMDM. **e**, **f**, Genome-browser tracks showing HDAC3, ATF2 and ATF3 ChIP–seq peaks at enhancer elements upstream of *Clec2d* (**e**) or *Gas6* (**f**), as well as gene body activity as measured by RNA-seq in control, MHD3KO, HDAC3(Y298F) and WT rescue macrophages, with or without LPS. **g**, **h**, Dual-luciferase assays of transcription driven by the *Clec2d* (**g**) or *Gas6* (**h**) enhancers in control, MHD3KO, HDAC3(Y298F) rescue, WT-rescue (WT), ATF2-depleted and ATF3-depleted BMDM, with or without LPS stimulation. Data shown are mean ± s.d., $n = 4$ biological replicates. P values were calculated by one-way ANOVA. DA-independent sites = 172, DA-dependent sites = 141.

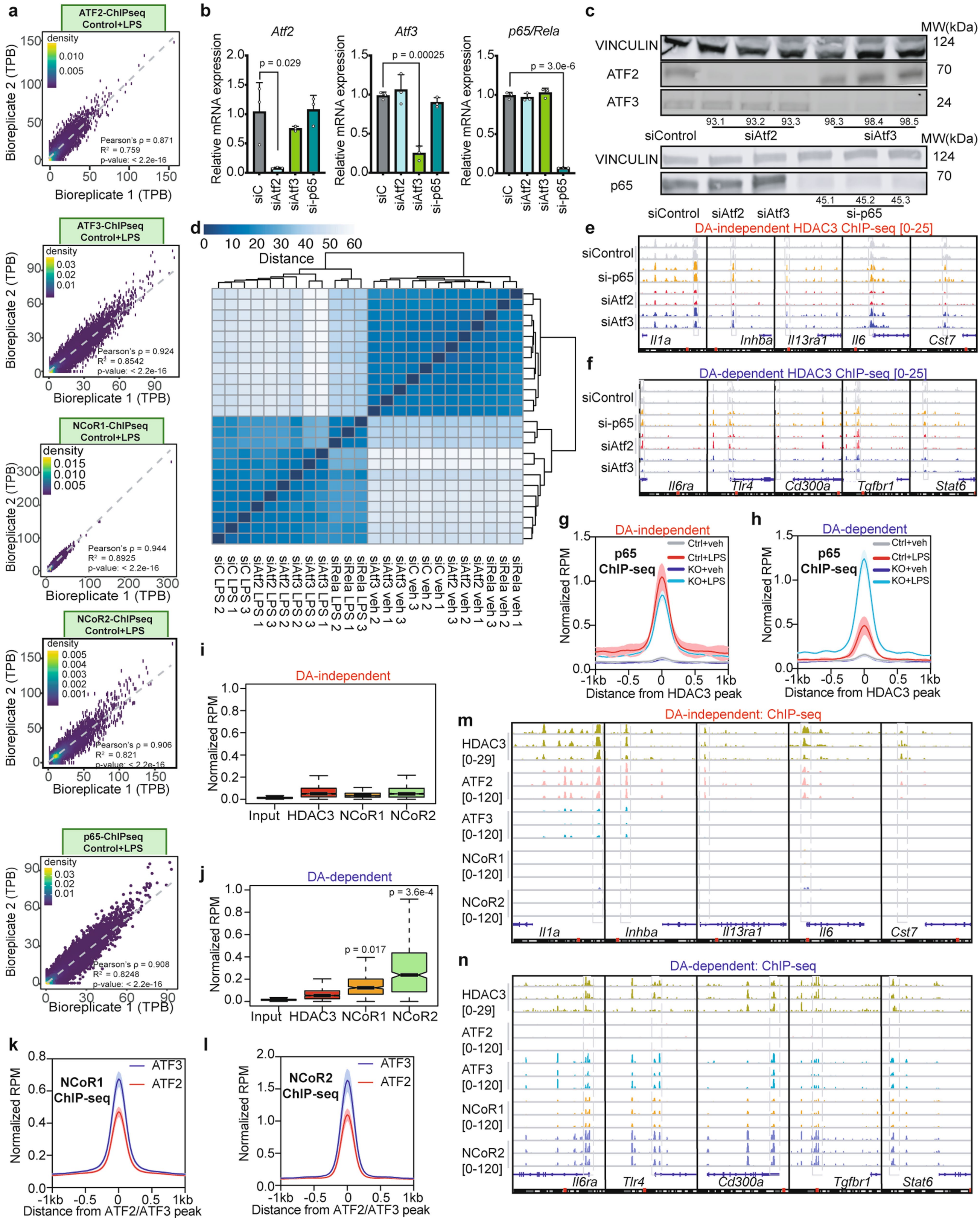

Extended Data Fig. 4 | See next page for caption.

Extended Data Fig. 4 | ATF2 and ATF3 recruit HDAC3 to sites near DA-independent and DA-dependent genes, respectively. a, Scatter plots of ChIP–seq experiments for ATF2, ATF3, NCoR1, NCoR2 and p65 in LPS-treated BMDM ($n = 3$ biological replicates) showing correlation between biological replicates using average tag counts per base-pair (TPB) at identified peak regions. Pearson's P values were calculated with two-sided t-tests. **b**, Relative gene expression levels of *Atf2*, *Atf3* and *p65* (also known as *Rela*) as measured by qPCR in control (siC), ATF2-depleted (siAtf2), ATF3-depleted (siAtf3), or p65-depleted (sip65) BMDM ($n = 3$ biological replicates). Data shown mean ± s.d., P values calculated by two-sided Student's t-test. **c**, Western blots (performed once) of ATF2, ATF3 and p65 protein levels with vinculin as loading control for control (siControl), ATF2-depleted (siAtf2), ATF3-depleted (siAtf3) or p65-depleted (sip65) BMDM, each with 3 independent siRNAs. **d**, Heat map of sample-to-sample distances using the vst values from RNA-seq experiments in control (siC), ATF2-depleted (siAtf2), ATF3-depleted (siAtf3) or p65-depleted (sip65) BMDM, with or without LPS ($n = 3$). **e**, **f**, Genome-browser tracks showing biologically replicated examples of HDAC3 ChIP–seq peaks in control (siControl), ATF2-depleted (siAtf2), ATF3-depleted (siAtf3) or p65-depleted (sip65) LPS-stimulated BMDM near DA-independent (**e**) or DA-dependent (**f**) genes. **g**, **h**, Average density profiles in RPM of p65 ChIP–seq showing mean ± s.e.m. ($n = 3$ biological replicates) at HDAC3-bound sites near DA-independent genes (Control LPS versus MHD3KO LPS two-sided Wilcoxon's $P = 0.063$) (**g**) or DA-dependent genes (Control LPS versus MHD3KO LPS two-sided Wilcoxon's $P = 2.4 \times 10^{-16}$) in control and MHD3KO BMDM, with or without LPS (**h**). **i**, **j**, Box-and-whisker plot showing minimum, maximum, median, first quartile and third quartile from quantification of average ChIP–seq signal ($n = 3$ biological replicates) in RPM for input, HDAC3, NCoR1 and NCoR2 at HDAC3-bound sites near DA-independent (**i**) or DA-dependent (**j**) genes. P values were calculated with two-sided Mann–Whitney test. **k**, **l**, Average density profiles in RPM showing mean ± s.e.m. ($n = 3$ biological replicates) of NCoR1 (two-sided Wilcoxon's $P = 4.7 \times 10^{-4}$) (**k**) and NCoR2 (two-sided Wilcoxon's $P = 1.2 \times 10^{-5}$) (**l**) genomic colocalization with either ATF2 (19,594 peaks) or ATF3 (57,041 peaks). **m**, **n**, Genome-browser tracks showing three biologically replicated examples of ChIP–seq peaks for HDAC3, ATF2, ATF3, NCoR1, and NCoR2 in LPS-stimulated BMDM near DA-independent (**k**) or DA-dependent (**l**) genes. DA-independent sites = 172, DA-dependent sites = 141.

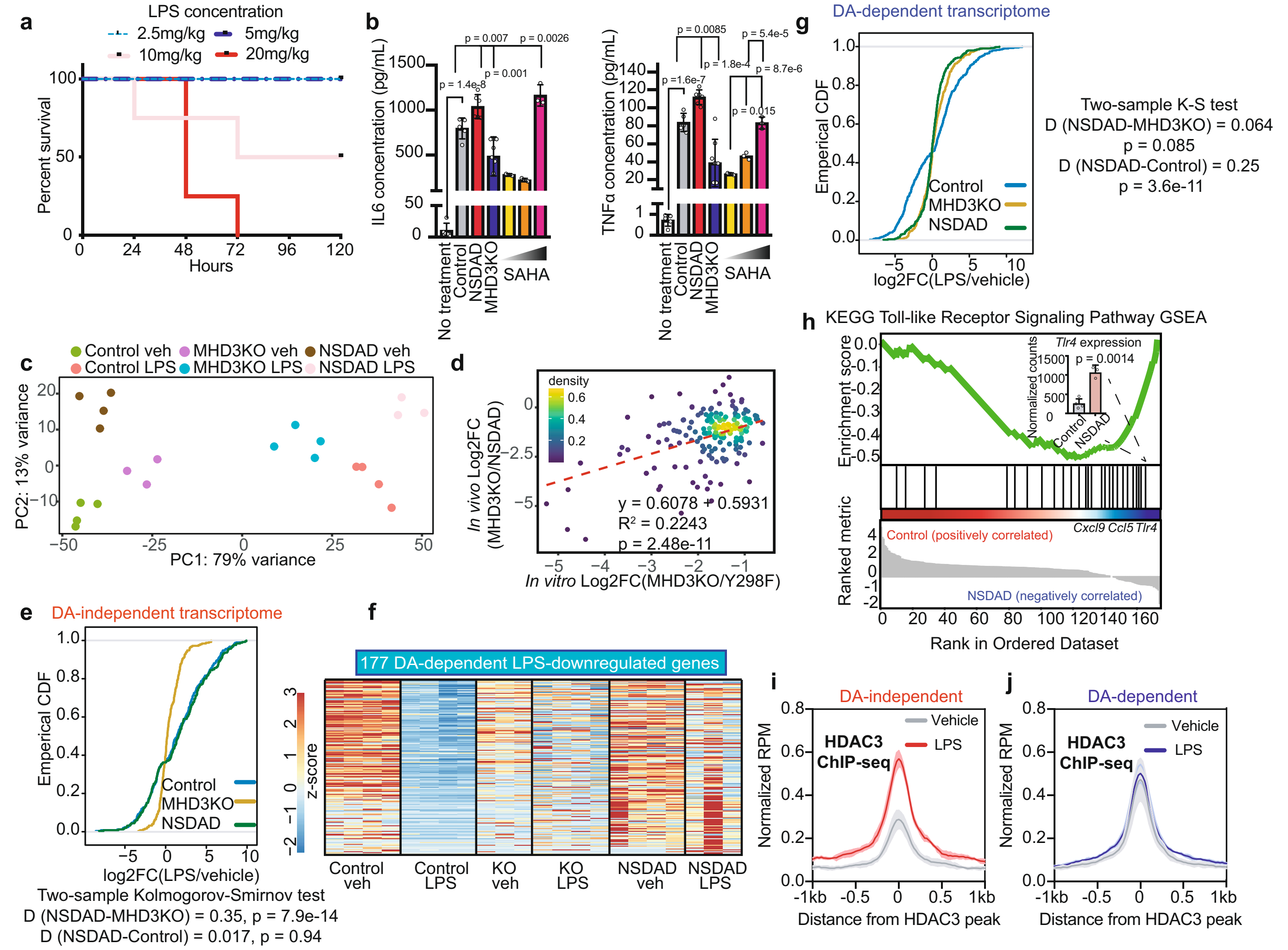

Extended Data Fig. 5 | Loss of HDAC3 protein but not deacetylase activity protects mice from acute endotoxic shock. a, Kaplan–Meier curves of wild-type C57BL/6 mice injected with increasing doses of LPS and observed for 120 h ($n = 4$ independent mice). **b**, Serum cytokine concentrations measured by ELISA for IL6 and TNF in 10 mg kg^{-1} LPS-injected control, MHD3KO, NSDAD, C57BL/6 mice ($n = 5$ independent mice) administered with increasing doses of SAHA (25, 100, 400 mg kg^{-1}), and untreated control ($n = 3$ independent mice). Data shown mean ± s.d. *P* values calculated by one-way ANOVA. **c**, PCA plot using the vst values from RNA-seq experiments of in vivo peritoneal macrophages from control, MHD3KO and NSDAD mice injected with vehicle control (PBS) or 10 mg kg^{-1} LPS ($n = 4$ biological replicates, except for KO vehicle and NSDAD LPS with $n = 3$ biological replicates). **d**, Scatter plot showing correlation between in vitro ($n = 4$ biological replicates) and in vivo ($n = 3$ biological replicates) DA-independent differential gene expression (174 genes). Pearson's *P* value was calculated with two-sided *t*-test. **e**, Empirical CDF and associated two-sided Kolmogorov–Smirnov test *D* statistics of LPS-stimulated changes in statistically modelled DA-independent in vivo gene expression (251 genes) for peritoneal macrophages from control ($n = 4$ biological replicates), MHD3KO ($n = 4$ biological replicates) and NSDAD ($n = 3$ biological replicates). **f**, Heat map showing 177 LPS-downregulated, HDAC3-dependent differentially expressed genes in vivo that were not rescued by NSDAD (DA-dependent genes: $n = 4$ biological replicates, except for KO vehicle and NSDAD LPS with $n = 3$ biological replicates; DE cutoff: $|\log_2 FC| > 1$, two-sided Benjamini–Hochberg-adjusted FDR < 0.05 as determined by edgeR likelihood ratio test). **g**, Empirical CDF and associated two-sided Kolmogorov–Smirnov test *D* statistics of LPS-stimulated changes in statistically modelled DA-dependent in vivo gene expression (404 genes) for peritoneal macrophages from control ($n = 4$ biological replicates), MHD3KO ($n = 4$ biological replicates) and NSDAD ($n = 3$ biological replicates). **h**, Gene set enrichment analysis (GSEA) for the in vivo DA-dependent transcriptome (177 genes) showing enrichment of KEGG Toll-like receptor signalling pathway that was more upregulated in peritoneal macrophages from LPS-treated NSDAD mice ($n = 3$ biological replicates) than from LPS-treated control mice ($n = 4$ biological replicates). Bar graph showing *Tlr4* gene expression level in normalized counts of peritoneal macrophages from control and NSDAD treated with LPS. Data shown mean ± s.d., two-sided *P* value was calculated by Student's *t*-test. **i**, **j**, Average density profiles in RPM of HDAC3 ChIP–seq showing mean ± s.e.m. ($n = 3$ biological replicates) at HDAC3-bound sites near 167 in vivo DA-independent genes (two-sided Wilcoxon's $P = 1.7 \times 10^{-23}$) (**i**) or 165 DA-dependent genes (two-sided Wilcoxon's $P = 0.153$) (**j**) in peritoneal macrophages from vehicle- or LPS-treated control mice.

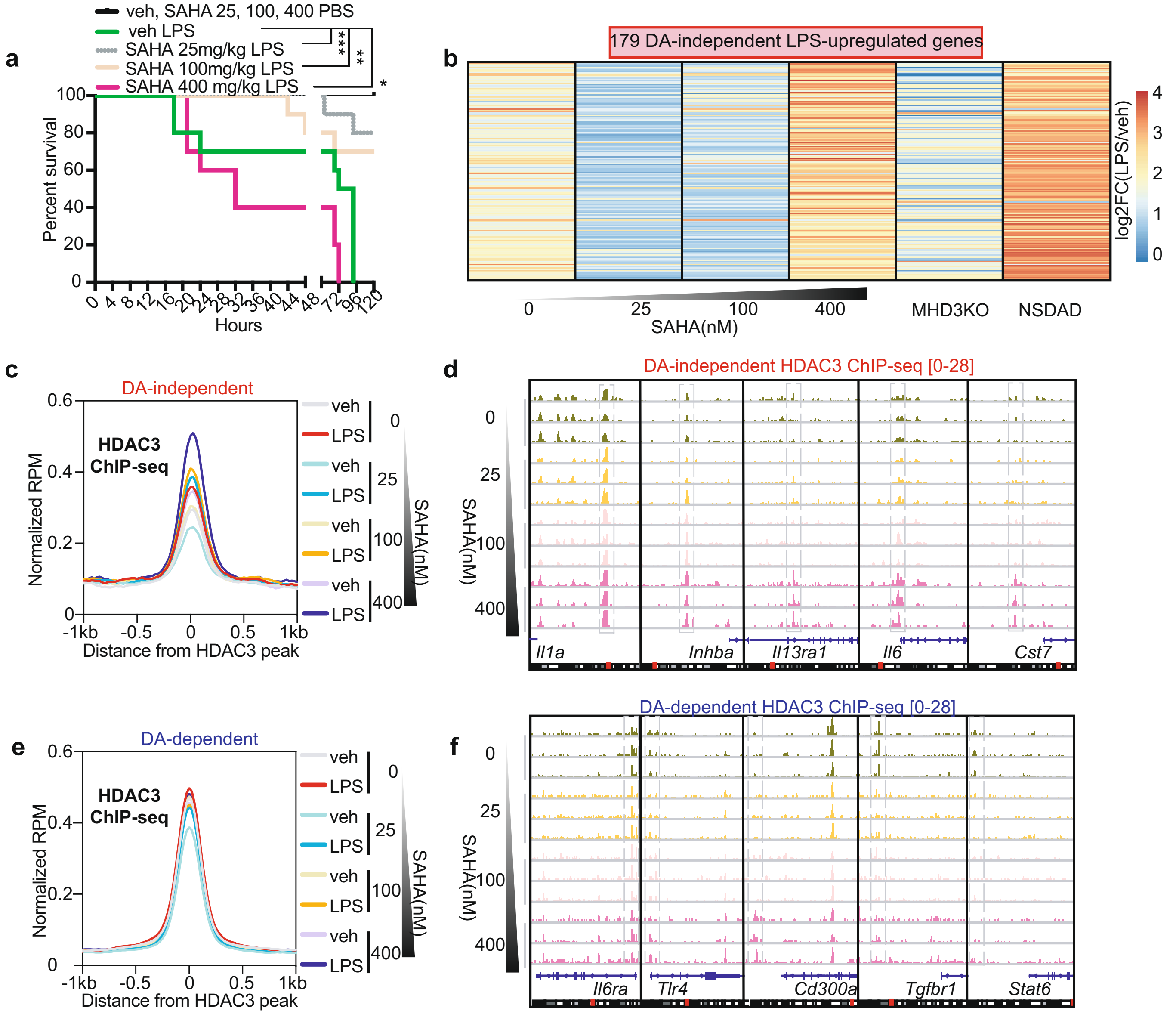

Extended Data Fig. 6 | Dose-dependent effects of HDAC inhibitor SAHA on endotoxin susceptibility. a, Kaplan–Meier curves of C57BL/6 mice subjected to 10 mg kg^{-1} of intraperitoneal injection of purified LPS, with increasing doses of SAHA (25, 100, 400 mg kg^{-1}). SAHA vehicle (veh), 10% DMSO in PBS. *$P = 0.036$, **$P = 0.001$, ***$P = 0.00065$, $n = 10$ independent mice, calculated by two-sided Mantel–Cox test. **b**, Heat map showing LPS-induced transcriptional changes as a function of log$_2$(fold change) (log$_2$FC) of 179 in vivo DA-independent genes in LPS-exposed BMDM treated with increasing dose of SAHA (25, 100, 400 nM, $n = 3$ biological replicates) and peritoneal macrophages from LPS-exposed MHD3KO ($n = 4$ biological replicates) and NSDAD mice ($n = 3$ biological replicates). **c**, Average density profiles in RPM of HDAC3 ChIP–seq showing means of 3 biological replicates at HDAC3-bound sites near 172 DA-independent genes. **d**, Genome-browser tracks showing 3 biologically replicated examples of ChIP–seq peaks for HDAC3 in LPS-stimulated BMDM treated with increasing dose of SAHA (25, 100, 400 nM) near DA-independent genes. **e**, Average density profiles in RPM of HDAC3 ChIP–seq showing means of 3 biological replicates at HDAC3-bound sites near 141 DA-dependent genes. **f**, Genome-browser tracks showing 3 biologically replicated examples of ChIP–seq peaks for HDAC3 in LPS-stimulated BMDM treated with increasing dose of SAHA (25, 100, 400 nM) near DA-dependent genes.

nature research

Corresponding author(s): Mitchell A. Lazar

Last updated by author(s): Apr 30, 2020

Reporting Summary

Nature Research wishes to improve the reproducibility of the work that we publish. This form provides structure for consistency and transparency in reporting. For further information on Nature Research policies, see Authors & Referees and the Editorial Policy Checklist .

Statistics

For all statistical analyses, confirm that the following items are present in the figure legend, table legend, main text, or Methods section.

n/a	Confirmed	
☐	☒	The exact sample size (*n*) for each experimental group/condition, given as a discrete number and unit of measurement
☐	☒	A statement on whether measurements were taken from distinct samples or whether the same sample was measured repeatedly
☐	☒	The statistical test(s) used AND whether they are one- or two-sided *Only common tests should be described solely by name; describe more complex techniques in the Methods section.*
☐	☒	A description of all covariates tested
☐	☒	A description of any assumptions or corrections, such as tests of normality and adjustment for multiple comparisons
☐	☒	A full description of the statistical parameters including central tendency (e.g. means) or other basic estimates (e.g. regression coefficient) AND variation (e.g. standard deviation) or associated estimates of uncertainty (e.g. confidence intervals)
☐	☒	For null hypothesis testing, the test statistic (e.g. *F*, *t*, *r*) with confidence intervals, effect sizes, degrees of freedom and *P* value noted *Give P values as exact values whenever suitable.*
☒	☐	For Bayesian analysis, information on the choice of priors and Markov chain Monte Carlo settings
☒	☐	For hierarchical and complex designs, identification of the appropriate level for tests and full reporting of outcomes
☒	☐	Estimates of effect sizes (e.g. Cohen's *d*, Pearson's *r*), indicating how they were calculated

Our web collection on statistics for biologists contains articles on many of the points above.

Software and code

Policy information about availability of computer code

Data collection	Sequencing data, including RNA-seq, GRO-seq, and ChIP-seq, were prepared according to previously published and cited methodology with detailed description of any modification in Methods section, and generated with Illumina Hiseq2000, Hiseq4000, Nextseq500, or Novaseq 6000. Western blot images were scanned and analyzed by LICOR ImageStudioLite (v 5.2.5)
Data analysis	Graphpad Prism (v8.0) and RStudio (v1.0.153) softwares were used for graphing and statistical analysis. Genome-browser tracks were generated with IGV (v2.3.92). R packages used in this study: edgeR(v3.26.8), latticeExtra(v0.6-29), pheatmap (v1.0.12), ggplot2(v3.3.0). STAR(v2.6.0a) was used for RNA-seq mapping. FeatureCounts (v1.5.3) was used for counting reads assigned to exons. GSEA (v4.0.3) was used for gene-set enrichment analysis. Bowtie2(v2.2.6) was used for ChIP-seq mapping. HOMER (v4.11) was used for ChIP-seq and GRO-seq peak calling, motif analysis, as well as obtaining read density from processed bed files. Bedtools (v2.25.0) was used to intersect bed files of genomic regions. TBA (v1.0) was used for machine learning-based motif prediction analysis. Gene ontology analyses were performed with Enrichr(v2.1). Every step of the analyses was done according instructions provided with each package, with detailed description provided in Methods section without any custom codes or algorithms.

For manuscripts utilizing custom algorithms or software that are central to the research but not yet described in published literature, software must be made available to editors/reviewers. We strongly encourage code deposition in a community repository (e.g. GitHub). See the Nature Research guidelines for submitting code & software for further information.

Data

Policy information about availability of data

All manuscripts must include a data availability statement. This statement should provide the following information, where applicable:

- Accession codes, unique identifiers, or web links for publicly available datasets
- A list of figures that have associated raw data
- A description of any restrictions on data availability

All sequencing data, including RNA-seq, ChIP-seq, and GRO-seq were deposited to Gene Expression Omnibus under accession number GSE140611 with access code available to reviewers upon request.

Field-specific reporting

Please select the one below that is the best fit for your research. If you are not sure, read the appropriate sections before making your selection.

☒ Life sciences ☐ Behavioural & social sciences ☐ Ecological, evolutionary & environmental sciences

For a reference copy of the document with all sections, see nature.com/documents/nr-reporting-summary-flat.pdf

Life sciences study design

All studies must disclose on these points even when the disclosure is negative.

Sample size	At least 3 biological replicates were used for each experiment. In our experience, this number is the minimum required to account for the variability commonly observed in the murine bone-marrow derived macrophages, which is commonly accepted in the field. In cases where a large amount of input material or consistency of experimental conditions was required, as in the case of RNA-seq, GRO-seq and ChIP-seq, we had to pool materials from 3-10 mice, as detailed in Methods section, for each biological replicate. For animal studies, 8-10 mice were used for each experimental group, as detailed in the figure legends for each experiment as well as Method section. No calculation was performed to pre-determine the sample size.
Data exclusions	For RNA-seq, genes that are < 0.1 TPM were discarded as too lowly expressed. For ChIP-seq, all peaks have a required cut-off of 1 RPM. For GRO-seq, we also discarded reads mapped to highly abundant transcripts such as rRNA, as those rarely represents true nascent transcription of target of interest. Reads that mapped twice to the same regions were also removed, as they are likely artifacts of PCR amplification. All of these exclusion criteria were pre-established as previously published (Fang et al., Cell 2014; Emmet et al., Nature 2017). All samples were subjected to the same normalization pipeline to minimize variability in sequencing depth. We did not otherwise discard any data from any other experiments in this study.
Replication	All experiments were performed in at least 3 independent biological replicates, and repeated at least one more time independently except for the case of RNA-seq, ChIP-seq and GRO-seq, where we only profiled the independent biological replicates once due to cost and material constraints. However, we did cross-compare our data with publicly available datasets from other labs and observed significant overlaps.
Randomization	For in vivo studies, we randomized mice of different genetic backgrounds as well as treatment conditions into different groups to account for variability in treatment exposure and stress level in each group.
Blinding	The author was blinded from the identities of mice used in the in vivo experiments by an independent lab member until final mortality census of the animals. For preparation of high-throughput sequencing libraries, the author processed the samples in a random order without blinding as all samples were subjected to the same library preparation procedure, and hence blinding at this step was irrelevant. For each study, all samples were processed at the same time to reduce bias and batch effect.

Reporting for specific materials, systems and methods

We require information from authors about some types of materials, experimental systems and methods used in many studies. Here, indicate whether each material, system or method listed is relevant to your study. If you are not sure if a list item applies to your research, read the appropriate section before selecting a response.

Materials & experimental systems

n/a	Involved in the study	
☐	☒	Antibodies
☐	☒	Eukaryotic cell lines
☒	☐	Palaeontology
☐	☒	Animals and other organisms
☒	☐	Human research participants
☒	☐	Clinical data

Methods

n/a	Involved in the study	
☐	☒	ChIP-seq
☒	☐	Flow cytometry
☒	☐	MRI-based neuroimaging

Antibodies

Antibodies used	List of antibodies used can also be found in Supplementary Table 1. HDAC3(Abcam, monoclonal 7030, lot# GR121157-6, 1:200 dilution for IP, 1:1000 dilution for WB), p65 (Cell signaling, monoclonal D14E12, lot# 13, 1:200 dilution for IP, 1:1000 dilution for WB), Vinculin (Sigma, monoclonal V9131, lot#128M4852V, 1:2000 dilution for WB), H3K27Ac (Abcam 4729, lot# GR251958-1, 1:200 dilution for IP, 1:1000 dilution for WB), ATF2 (Cell Signaling,D4L2X, lot# 1, 1:200 dilution for IP, 1:1000 dilution for WB), ATF3 (Cell Signaling,D2Y5W, lot# 1, 1:200 dilution for IP, 1:1000 dilution for WB) , NCoR1 (Cell Signaling, E4S4N, lot# 1, 1:200 dilution for IP), NCoR2 (Millipore AntiSMRTe 06-891, lot# 2982400, 1:200 dilution for IP), Histone H3(Abcam, 24834, lot# GR236539, 1:1000 dilution for WB)
Validation	HDAC3 (Abcam 7030) was validated to work for both Western Blot (WB) and Chromatin immuno precipitation (ChIP) in mouse cell lines as detailed on the manufacturer's website (https://www.abcam.com/hdac3-antibody-chip-grade-ab7030.html), as well as previously published for WB and ChIP in mouse tissues from our lab such as BAT (Emmet et al., Nature 2017), pancreas (Remsberg et al., Mol metabolism 2017), liver (Armour et al, Nat Comm 2017) p65 (Cell signaling D14E12) was validated to work with WB in multiple human and mouse cell lines and ChIP in Hela cell as detailed on the manufacturer's website (https://www.cellsignal.com/products/primary-antibodies/nf-kb-p65-d14e12-xp-rabbit-mab/8242). ATF2 (Cell Signaling D4L2X) was validated to work in human cell lines for WB and ChIP as detailed on the manufacturer's website (https://www.cellsignal.com/products/primary-antibodies/atf-2-d4l2x-xp-rabbit-mab/35031), and was reported to work with mouse RAW264 cell line for WB (Kim et al., BMC Complementary and Alternative Medicine 2019) ATF3 (Cell Signaling,D2Y5W) was validated to work in human cell lines for WB and ChIP as detailed on the manufacturer's website (https://www.cellsignal.com/products/primary-antibodies/atf-3-d2y5w-rabbit-mab/33593), and was reported to work with human breast cancer cell line for WB (Subbaramaiah et al., JBC 2019) NCoR1 (Cell Signaling, E4S4N) was validated to work in LS180 human cell line for ChIP as detailed on the manufacturer's website (https://www.cellsignal.com/products/primary-antibodies/ncor1-e4s4n-rabbit-mab/34271) NCoR2 (Millipore AntiSMRTe 06-891) was validated to work in human Hela cell line for ChIP as detailed on the manufacturer's website (https://www.emdmillipore.com/US/en/product/Anti-SMRTe-Antibody,MM_NF-06-891#documentation) H3K27Ac (Abcam 4729) was validated to work in mouse MEF cell line for WB and human Hela cell line for ChIP as detailed on the manufacturer's website (https://www.abcam.com/histone-h3-acetyl-k27-antibody-chip-grade-ab4729.html), as well as previously published for WB and ChIP in mouse tissues from our lab such as BAT (Emmet et al., Nature 2017) Histone H3 was reported to work in human Hela cell line, and mouse embryonic fibroblast and testis cell lines for WB as detailed on the manufacturer's website (https://www.abcam.com/histone-h3-antibody-mabcam-24834-nuclear-loading-control-and-chip-grade-ab24834.html), as as well as previously published for WB and ChIP in mouse tissues such as BAT (Emmet et al., Nature 2017) Vinculin (Abcam, 24834) was reported to work for WB in multiple human and mouse cell lines as detailed on the manufacturer's website (https://www.sigmaaldrich.com/catalog/product/sigma/v9131?lang=en&region=US) as well as previously published for WB in mouse tissues from our lab such as BAT (Emmet et al., Nature 2017), liver and embryonic stem cell (Adlanmerini et al., PNAS 2019, Dierickx et al., 2019)

Eukaryotic cell lines

Policy information about cell lines

Cell line source(s)	Primary murine bone-marrow derived macrophages, HEK-293FT from Invitrogen (R70007), L929 (Sigma, 8501).
Authentication	No authentication was used.
Mycoplasma contamination	We do not test for mycoplasma as we mostly work with murine-derived primary tissues that do not have high passage number.
Commonly misidentified lines (See ICLAC register)	No commonly misidentified cell lines were used.

Animals and other organisms

Policy information about studies involving animals; ARRIVE guidelines recommended for reporting animal research

Laboratory animals	Mice were housed in a temperature-controlled specific-pathogen-free facility under 12h light/dark cycles. Adult male mice of 8 weeks old were used in all experiments. Age-matched WT C57Bl6 mice were purchased from Jackson lab.
Wild animals	Study did not involve any wild animals.
Field-collected samples	No samples were collected from the field.
Ethics oversight	Animal care and use procedures followed the guidelines of the Institutional Animal Care and Use Committee of the University of Pennsylvania in accordance with the guidelines of the National Institutes of Health. All procedures were performed according to institutional pain class C protocol.

Note that full information on the approval of the study protocol must also be provided in the manuscript.

ChIP-seq

Data deposition

☒ Confirm that both raw and final processed data have been deposited in a public database such as GEO.

☒ Confirm that you have deposited or provided access to graph files (e.g. BED files) for the called peaks.

Data access links *May remain private before publication.*	https://www.ncbi.nlm.nih.gov/geo/query/acc.cgi?acc=GSE140581
Files in database submission	HDAC3_KO_1 HDAC3_KO_2 HDAC3_KO_3 HDAC3_KO_LPS_1 HDAC3_KO_LPS_2 HDAC3_KO_LPS_3 HDAC3_WT_1 HDAC3_WT_2 HDAC3_WT_3 HDAC3_WT_LPS_1 HDAC3_WT_LPS_2 HDAC3_WT_LPS_3 HDA3_Y298F_1 HDA3_Y298F_2 HDA3_Y298F_3 HDAC3_Y298F_LPS_1 HDAC3_Y298F_LPS_2 HDAC3_Y298F_LPS_3 H3K27_KO1 H3K27_KO2 H3K27_KO3 H3K27_KO_lps_1 H3K27_KO_lps_2 H3K27_KO_lps_3 H3K27_wt1 H3K27_wt2 H3K27_wt3 H3K27_wt_lps_1 H3K27_wt_lps_2 H3K27_wt_lps_3 ATF2_1 ATF2_2 ATF2_3 ATF2_LPS_1 ATF2_LPS_2 ATF2_LPS_3 ATF3_wt1 ATF3_wt2 ATF3_wt3 ATF3_wt_lps_1 ATF3_wt_lps_2 ATF3_wt_lps_3 NCoR1_1 NCoR1_2 NCoR1_3 NCOR1_LPS1 NCOR1_LPS2 NCOR1_LPS3 NCOR1_LPS4 NCoR2_Ctrl_1 NCoR2_Ctrl_2 NCoR2_Ctrl_3 NCoR2_LPS1 NCoR2_LPS2 NCoR2_LPS3 p65_KO1 p65_KO2

p65_KO3
KO_P65_ChIP_LPS_1
KO_P65_ChIP_LPS_2
KO_P65_ChIP_LPS_3
p65_wt1
p65_wt2
p65_wt3
WT_P65_ChIP_LPS_1
WT_P65_ChIP_LPS_2
WT_P65_ChIP_LPS_3
0nM_1_SAHA_LPS_HDAC3_ChIP_seq
0nM_1_SAHA_HDAC3_ChIP_seq
0nM_2_SAHA_LPS_HDAC3_ChIP_seq
0nM_2_SAHA_HDAC3_ChIP_seq
0nM_3_SAHA_LPS_HDAC3_ChIP_seq
0nM_3_SAHA_HDAC3_ChIP_seq
100nM_1_SAHA_LPS_HDAC3_ChIP_seq
100nM_1_SAHA_HDAC3_ChIP_seq
100nM_2_SAHA_LPS_HDAC3_ChIP_seq
100nM_2_SAHA_HDAC3_ChIP_seq
100nM_3_SAHA_LPS_HDAC3_ChIP_seq
100nM_3_SAHA_HDAC3_ChIP_seq
25nM_1_SAHA_LPS_HDAC3_ChIP_seq
25nM_1_SAHA_HDAC3_ChIP_seq
25nM_2_SAHA_LPS_HDAC3_ChIP_seq
25nM_2_SAHA_HDAC3_ChIP_seq
25nM_3_SAHA_LPS_HDAC3_ChIP_seq
25nM_3_SAHA_HDAC3_ChIP_seq
400nM_1_SAHA_LPS_HDAC3_ChIP_seq
400nM_1_SAHA_HDAC3_ChIP_seq
400nM_2_SAHA_LPS_HDAC3_ChIP_seq
400nM_2_SAHA_HDAC3_ChIP_seq
400nM_3_SAHA_LPS_HDAC3_ChIP_seq
400nM_3_SAHA_HDAC3_ChIP_seq
siATF2_1_LPS_HDAC3_ChIP_seq
siATF2_1_NA_HDAC3_ChIP_seq
siATF2_2_LPS_HDAC3_ChIP_seq
siATF2_2_NA_HDAC3_ChIP_seq
siATF3_1_LPS_HDAC3_ChIP_seq
siATF3_1_NA_HDAC3_ChIP_seq
siATF3_2_LPS_HDAC3_ChIP_seq
siATF3_2_NA_HDAC3_ChIP_seq
siC_1_LPS_HDAC3_ChIP_seq
siC_1_NA_HDAC3_ChIP_seq
siC_2_LPS_HDAC3_ChIP_seq
siC_2_NA_HDAC3_ChIP_seq
sip65_1_LPS_HDAC3_ChIP_seq
sip65_1_NA_HDAC3_ChIP_seq
sip65_2_LPS_HDAC3_ChIP_seq
sip65_2_NA_HDAC3_ChIP_seq
CHIP_seq_ATF2_input_LPS
CHIP_seq_ATF2_input_veh
CHIP_seq_ATF3_input_LPS
CHIP_seq_ATF3_input_veh
CHIP_seq_H3K27Ac_input_LPS
CHIP_seq_H3K27Ac_input_veh
CHIP_seq_HDAC3_input_LPS
CHIP_seq_HDAC3_input_veh
CHIP_seq_NCoR1_input_veh
CHIP_seq_NCoR2_input_LPS
CHIP_seq_NCoR2_input_veh
CHIP_seq_p65_input_LPS
CHIP_seq_p65_input_veh
ChIP_seq_NCoR1_input_LPS
invivo_LPS1_HDAC3_ChIP_seq
invivo_LPS2_HDAC3_ChIP_seq
invivo_LPS3_HDAC3_ChIP_seq
invivo_vehicle1_HDAC3_ChIP_seq

invivo_vehicle2_HDAC3_ChIP_seq
invivo_vehicle3_HDAC3_ChIP_seq

Genome browser session
(e.g. UCSC)

Please download xml session from below link and load on IGV
https://dm.genomespace.org/datamanager/file/Home/Public/cavalryman7992/ChIP_seq_Nguyen_Lazar_2019.xml

Methodology

Replicates

Three biological replicates macrophages (BMDM or peritoneal) pooled from 3-5 mice

Sequencing depth

Each library contains at least 20 million reads

Antibodies

HDAC3 (Abcam7030), H3K27Ac (Abcam 4729), ATF2 (Cell Signaling,D4L2X), ATF3 (Cell Signaling,D2Y5W) ,p65 (Cell Signaling,D14E12), NCoR1 (Cell Signaling, E4S4N), NCoR2 (Millipore AntiSMRTe 06-891)

Peak calling parameters

Peak calling parameters were set at
Fold over input required = 4.00
Poisson p-value over input required = 1.00e-04
Poisson p-value over local region required = 1.00e-04
size of region used for local filtering = 10000
100% of reported peaks passed this threshold

Data quality

All sequencing runs had >70-80% Q30 with >70% Cluster PF. All data were mapped to mm10 with at least 80-90% of reads mapped.

Software

Bowtie2 version 2.2.6
HOMER v4.11
bedtools v2.25
TBA Transcription factor binding analysis v1.0

Lysosome-targeting chimaeras for degradation of extracellular proteins

https://doi.org/10.1038/s41586-020-2545-9

Received: 1 May 2019

Accepted: 22 June 2020

Steven M. Banik[1], Kayvon Pedram[1], Simon Wisnovsky[1], Green Ahn[1], Nicholas M. Riley[1] & Carolyn R. Bertozzi[1,2] ✉

The majority of therapies that target individual proteins rely on specific activity-modulating interactions with the target protein—for example, enzyme inhibition or ligand blocking. However, several major classes of therapeutically relevant proteins have unknown or inaccessible activity profiles and so cannot be targeted by such strategies. Protein-degradation platforms such as proteolysis-targeting chimaeras (PROTACs)[1,2] and others (for example, dTAGs[3], Trim-Away[4], chaperone-mediated autophagy targeting[5] and SNIPERs[6]) have been developed for proteins that are typically difficult to target; however, these methods involve the manipulation of intracellular protein degradation machinery and are therefore fundamentally limited to proteins that contain cytosolic domains to which ligands can bind and recruit the requisite cellular components. Extracellular and membrane-associated proteins—the products of 40% of all protein-encoding genes[7]—are key agents in cancer, ageing-related diseases and autoimmune disorders[8], and so a general strategy to selectively degrade these proteins has the potential to improve human health. Here we establish the targeted degradation of extracellular and membrane-associated proteins using conjugates that bind both a cell-surface lysosome-shuttling receptor and the extracellular domain of a target protein. These initial lysosome-targeting chimaeras, which we term LYTACs, consist of a small molecule or antibody fused to chemically synthesized glycopeptide ligands that are agonists of the cation-independent mannose-6-phosphate receptor (CI-M6PR). We use LYTACs to develop a CRISPR interference screen that reveals the biochemical pathway for CI-M6PR-mediated cargo internalization in cell lines, and uncover the exocyst complex as a previously unidentified—but essential—component of this pathway. We demonstrate the scope of this platform through the degradation of therapeutically relevant proteins, including apolipoprotein E4, epidermal growth factor receptor, CD71 and programmed death-ligand 1. Our results establish a modular strategy for directing secreted and membrane proteins for lysosomal degradation, with broad implications for biochemical research and for therapeutics.

Unlike the proteasomal pathway, the lysosomal pathway for protein degradation is not limited to proteins that have intracellular domains. Families of cell-surface lysosome-targeting receptors (LTRs) have been reported that facilitate the transport of proteins to lysosomes[9]. We proposed that chimeric molecules capable of binding both a cell-surface LTR and an extracellular protein might induce internalization and lysosomal degradation of the target, offering a means to accelerate the degradation of proteins by using binders that act in the extracellular space. The prototypical LTR is the cation-independent mannose-6-phosphate receptor (CI-M6PR, also called IGF2R), which endogenously transports proteins bearing N-glycans capped with mannose-6-phosphate (M6P) residues to lysosomes[10]. The receptor cycles constitutively between endosomes, the cell surface and the Golgi complex. CI-M6PR shuttles cargo efficiently to prelysosomal compartments, where a lowered pH enables cargo to dissociate and progress to the lysosome while CI-M6PR is recycled. On the basis of its ability to efficiently deliver proteins to lysosomes and its expression in a range of different tissue types, CI-M6PR has been exploited to deliver therapeutic enzymes for the treatment of lysosomal storage disorders[11]. Here we present lysosome-targeting chimaeras—which we term LYTACs (Fig. 1a)—that enable the depletion of secreted and membrane-associated proteins via a mechanism of action that is orthogonal and complementary to that of existing technologies[12], and which does not rely on an extracellular protease for efficacy[13]. We show that LYTACs can serve as biochemical probes for the study of receptor trafficking and protein degradation, and can mediate the degradation of both secreted and membrane-associated proteins of therapeutic interest.

---

[1]Department of Chemistry, Stanford University, Stanford, CA, USA. [2]Howard Hughes Medical Institute, Stanford, CA, USA. ✉e-mail: bertozzi@stanford.edu

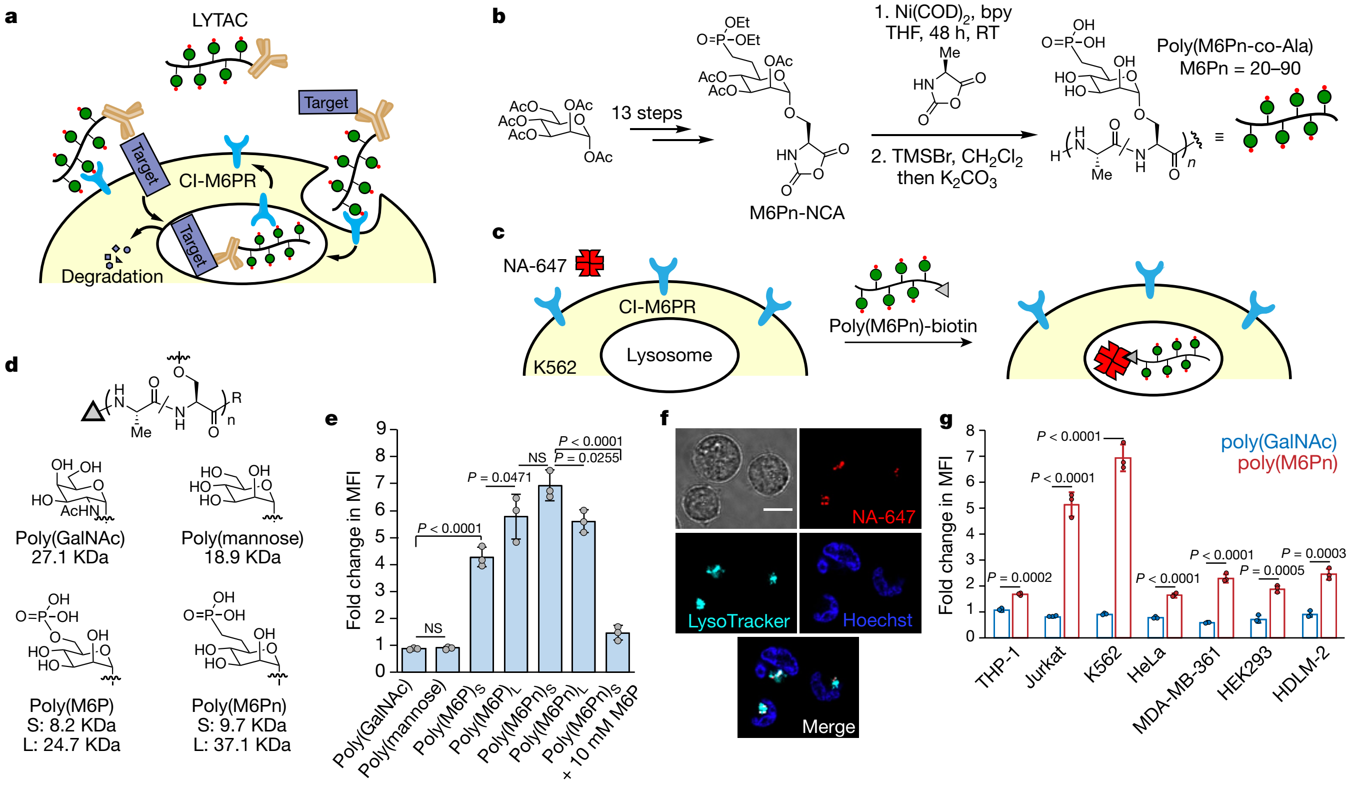

Fig. 1 | LYTACs using CI-M6PR traffic proteins to lysosomes. a, The concept of LYTACs, in which a glycopolypeptide ligand for CI-M6PR is conjugated to an antibody to traffic secreted and membrane-associated proteins to lysosomes. **b**, Synthesis of M6Pn glycopolypeptide ligands for CI-M6PR. bpy, bipyridyl; COD, cyclooctadiene; RT, room temperature; THF, tetrahydrofuran; TMS, trimethylsilyl. **c**, Assay for the internalization of NA-647 by biotin-based LYTACs. **d**, Panel of synthetic M6P and M6Pn glycopolypeptides and controls. L, long; S, short. **e**, Fold changes in mean fluorescence intensity (MFI) for K562 cells incubated at 37 °C for 1 h with 500 nM NA-647 or 500 nM NA-647 and 2 μM biotinylated glycopolypeptide in complete growth media. MFI was determined by live-cell flow cytometry. **f**, Live-cell confocal microscopy images of K562 cells treated as in **e**, then labelled with LysoTracker Green for 30 min. Scale bar, 10 μm. **g**, Panel of cell lines for NA-647 uptake experiments, performed as in **e**. For **e**, **g**, data are mean ± s.d. of three independent experiments. For **f**, images are representative of two independent experiments. *P* values were determined by unpaired two-tailed *t*-tests; fold changes are reported relative to incubation with protein targets alone. NS, not significant.

To develop ligands for CI-M6PR, we leveraged precedents aimed at enhancing lysosomal enzyme replacement therapies and drug delivery platforms. This previous work included biosynthetic engineering of M6P-bearing glycans[14] as well as chemical synthesis of oligomeric M6P-containing scaffolds[15]. A recurring design parameter from these studies was the requirement for a multivalent ligand, in order to achieve optimal CI-M6PR agonism[16–18]. Previous work had also revealed that the 6-phosphoester could undergo hydrolysis in human serum[19], leading to rapid endocytosis by macrophages bearing mannose receptors[20]. We reasoned that *N*-carboxyanhydride (NCA)-derived glycopolypeptides[21] bearing multiple serine-*O*-mannose-6-phosphonate (M6Pn) residues[22] would enable multivalent presentation on a biocompatible, phosphatase-inert[23] and modular scaffold. We synthesized M6Pn glycopolypeptides starting with the conversion of mannose pentaacetate to M6Pn-NCA in 13 steps (Fig. 1b, Extended Data Fig. 1a). Subsequent copolymerization of M6Pn-NCA and alanine-NCA (1:1 ratio, for the purpose of spacing and polymerization kinetics) provided access to M6Pn glycopolypeptides (post-deprotection dispersity, $Đ = 1.3$–1.5) of various lengths, including short (20 M6Pn) and long (90 M6Pn) variants, to test in protein degradation assays. We also synthesized the corresponding M6P-containing copolymers bearing the natural phosphorylated glycan structure (Extended Data Fig. 1b), with similar molecular weights and dispersities to those obtained with M6Pn monomers.

To demonstrate the feasibility of CI-M6PR-driven LYTACs, we designed an in cellulo assay to measure the uptake of NeutrAvidin-647 (NA-647), an Alexa Fluor-647 (AF647)-labelled protein to which biotin binds (Fig. 1c). We synthesized and biotinylated poly(M6P) and poly(M6Pn) polypeptides, as well as poly(*N*-acetylgalactosamine) (poly(GalNAc)) and poly(mannose) as controls (Fig. 1d, Extended Data Figs. 1c, d, 2a). K562 cells were incubated with either NA-647 or NA-647 and biotinylated glycopolypeptide for one hour, then washed and analysed by flow cytometry. Co-incubation with M6P and M6Pn polypeptides increased cellular fluorescence by 5–6-fold compared with the background, with only minor differences in uptake efficiency observed as a result of glycopolypeptide length (short versus long, Fig. 1e). M6Pn polypeptides showed performance that was equivalent or superior to that of M6P polypeptides of similar length, whereas incubation with mannose- or GalNAc-containing glycopolypeptides showed no marked change in fluorescence compared with the background. NA-647 uptake mediated by poly(M6Pn) was attenuated by co-incubation with excess exogenous M6P. Furthermore, uptake remained continuous over time (Extended Data Fig. 2b), suggesting that surface-receptor recycling was the rate-limiting step[24]. AF647 is reported to be stable in endosomes and lysosomes[25], with a steadily increasing fluorescent signal arising from intracellular fluorophore accumulation. Live-cell fluorescence microscopy experiments revealed that the AF647 signal co-localized with acidic endosomes and lysosomes after only 1 h (Fig. 1f, Extended Data Figs. 2c, d). Finally, biotinylated LYTACs mediated NA-647 uptake in various cell lines, demonstrating the breadth of CI-M6PR-targeting (Fig. 1g) as well as the ability to use small molecules as LYTAC 'warheads'.

We next performed a CRISPR interference (CRISPRi) pooled genetic screen with the aim of identifying genes for which knockdown ablates the delivery of NA-647 by biotinylated LYTACs[26,27] (Fig. 2a). K562 cells expressing dCas9-KRAB were transduced with a genome-wide library

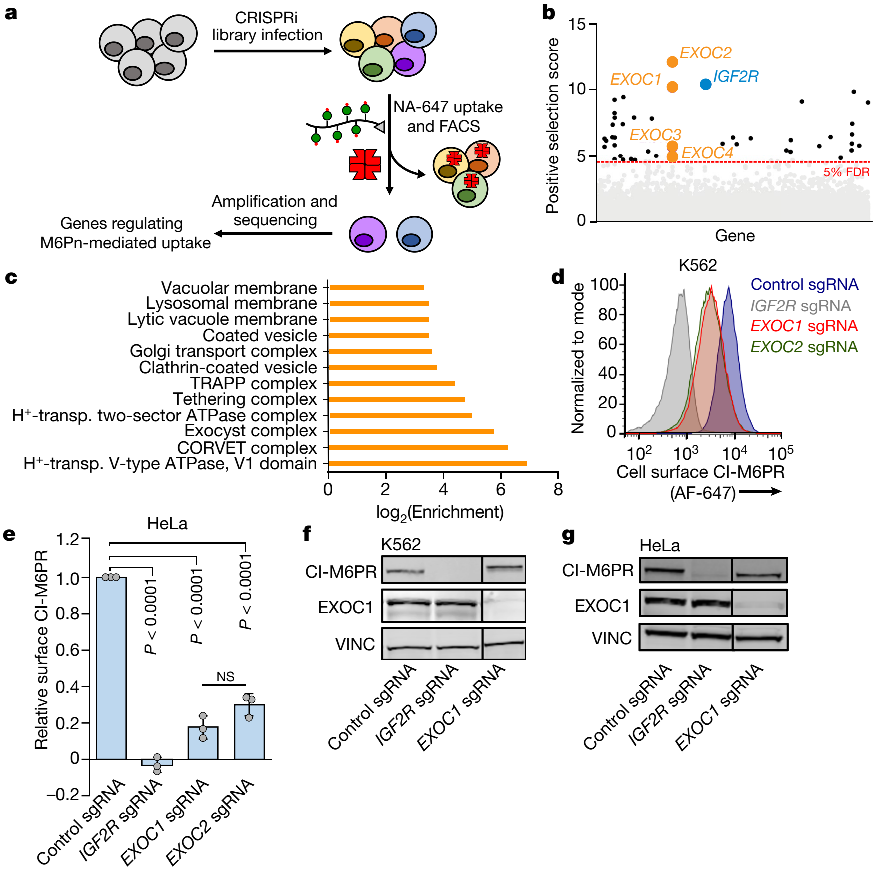

Fig. 2 | CRISPRi screen identifies key cellular machinery for LYTACs. **a**, Schematic of a CRISPRi screen in K562 cells stably expressing dCas9-KRAB and a library of sgRNAs with genome-wide coverage. **b**, Selected gene hits for regulation of NA-647 internalization by LYTACs. **c**, Gene ontology (GO) annotation for significant hits (<5% FDR). **d**, **e**, Cell surface expression levels of CI-M6PR in dCas9-KRAB K562 cells (**d**) or dCas9-KRAB HeLa cells (**e**) transfected with control sgRNA, *IGF2R*-targeting sgRNA, *EXOC1*-targeting sgRNA or *EXOC2*-targeting sgRNA. Cells were stained for CI-M6PR and subjected to live-cell flow cytometry. **f**, **g**, Western blot analysis of EXOC1 and CI-M6PR in K562 (**f**) and HeLa (**g**) CRISPRi knockdown lines. For **c**, analysis is representative of two replicates; **d**, **f**, **g** are representative of two independent experiments. K562 cells rapidly lost the exocyst knockdown phenotype after two passages. For **e**, data are mean ± s.d. of three independent experiments in HeLa and normalized to non-targeting sgRNA. *P* values were determined by unpaired two-tailed *t*-tests.

of CRISPRi single guide RNAs (sgRNAs) and incubated with LYTAC and NA-647. A population of cells that exhibited a substantial decrease in NA-647 labelling was isolated by fluorescence-activated cell sorting (FACS), and next-generation sequencing was performed to identify sgRNAs that were overrepresented in this population. Guide RNAs to *IGF2R* (which encodes CI-M6PR) were highly enriched in the sorted pool, providing unbiased confirmation of selective receptor targeting (Fig. 2b; for the full dataset, see Supplementary Information). Other significantly enriched guide RNAs (false discovery rate (FDR) < 5%) targeted genes that regulate endosomal acidification, vesicle trafficking, endosome–lysosome fusion and clathrin-dependent endocytosis (Fig. 2c), consistent with a CI-M6PR-driven endocytic pathway to lysosomes[10]. Components of the exocyst complex—which is reported to mediate vesicle localization to the plasma membrane[28]—were also identified as essential for the M6Pn-mediated internalization of NA-647. We proposed that the exocyst complex could be involved in the presentation of CI-M6PR on the cell surface, a biochemical pathway which is yet to be elucidated[10]. We performed CRISPRi knockdown of *EXOC1* and *EXOC2* (which encode the exocyst complex components 1 and 2, respectively) in K562 cells using CRISPRi library guides, and measured cell-surface CI-M6PR levels by flow cytometry. A 60% decrease in cell-surface CI-M6PR levels was observed (Fig. 2d). We replicated these results in HeLa cells (75% decrease, Fig. 2e), and found that total CI-M6PR levels did not change upon knockdown of *EXOC1* in either cell line (Fig. 2f, g, respectively). Further, we observed no change in surface expression of epidermal growth factor receptor (EGFR) on HeLa cells (Extended Data Fig. 3), indicating that the global trafficking of cell-surface proteins remained unperturbed. Together these data indicate that the surface presentation of CI-M6PR is mediated in part by the exocyst complex, and—more broadly—that LYTACs can be used to study the molecular pathways involved in the regulation of cell-surface receptors.

We next sought to determine whether conjugation of a poly(M6Pn)-bearing glycopolypeptide to an antibody would reprogramme the antibody to rapidly direct extracellular agents to the lysosome. As a proof-of-principle experiment, we non-specifically labelled lysine residues on a polyclonal anti-mouse IgG with bicyclononyne-*N*-hydroxysuccinimide (BCN-NHS), and subsequently conjugated this antibody to azide-terminated M6Pn glycopolypeptides via copper-free strain-promoted azide–alkyne cycloaddition (Fig. 3a), generating the LYTAC **Ab-1**. The conjugation reaction could be readily monitored by native gel electrophoresis, because the covalent attachment of the anionic polypeptides caused a characteristic enhancement in migration compared with antibodies conjugated with non-charged polypeptides (that is, poly(GalNAc)) (Fig. 3b). Incubation of K562 cells with **Ab-1** and a mouse IgG labelled with Alexa Fluor-488 (AF488) (Extended Data Fig. 4a) resulted in a 40-fold increase in lysosomal AF488 signal relative to that of controls (Extended Data Fig. 4b, c).

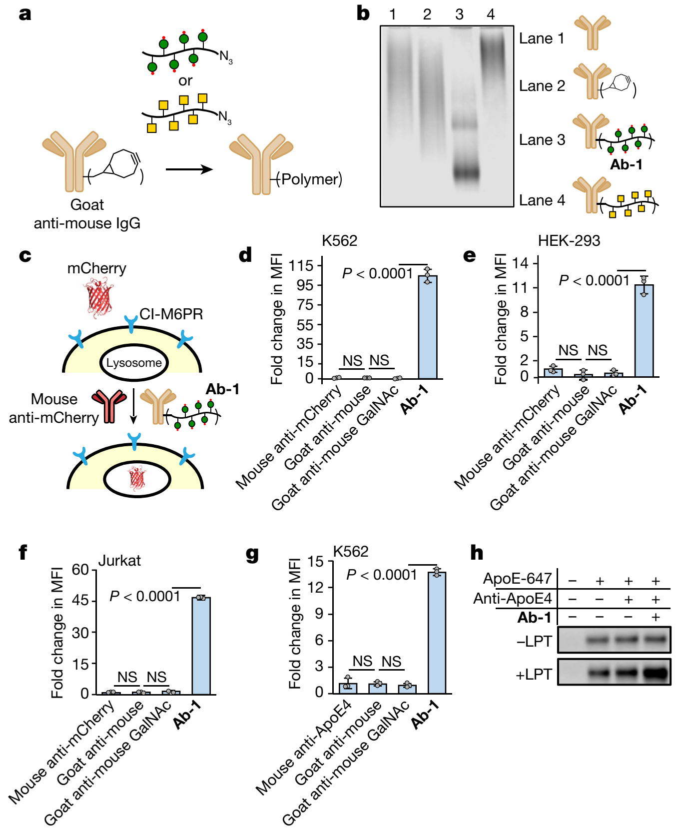

Fig. 3 | LYTACs target soluble proteins to lysosomes for degradation. **a**, Synthetic scheme for antibody-based LYTACs with a goat anti-mouse IgG. **b**, Native gel (with Coomassie staining) of polyclonal goat anti-mouse IgG conjugates. **c**–**f**, Uptake of mCherry antigen and its antibody by a LYTAC, into K562 cells (**d**), HEK-293 cells (**e**) or Jurkat cells (**f**) with 50 nM mCherry, and 25 nM mouse anti-mCherry or 25 nM mouse anti-mCherry with 25 nM goat anti-mouse or conjugates after 1 h at 37 °C. Mean fluorescence intensity (MFI) was measured by live-cell flow cytometry. **g**, Uptake of ApoE4-647 into K562 cells; experiments were performed analogously to **d**. Median fluorescence intensity (MFI) was measured by live-cell flow cytometry. **h**, Cells were incubated as in **g** for 8 h in the presence or absence of 0.1 mg ml^{-1} leupeptin (LPT), then lysed. Lysates were separated by SDS–PAGE, and ApoE4-647 was detected via in-gel fluorescence. Results are representative of two (**h**) or three (**b**) independent experiments. Data are mean ± s.d. of three independent experiments (**d**–**g**). *P* values were determined by unpaired two-tailed *t*-tests.; fold changes are reported relative to incubation with protein targets alone.

Given that **Ab-1** efficiently trafficked IgG molecules to lysosomes, we reasoned that it could function as a LYTAC for a primary IgG antibody bound to its antigen (Fig. 3c). Co-incubation of cells with mCherry, mouse anti-mCherry and **Ab-1** resulted in increases in uptake of between 10-fold and 100-fold relative to non-M6Pn-bearing antibodies in cell lines (Fig. 3d–f). We next aimed to expand this strategy to a clinically relevant target, selecting apolipoprotein E4 (ApoE4), which has been implicated in the pathogenesis of neurodegenerative disease[29]. A 13-fold increase in uptake of ApoE4-647 was observed using **Ab-1** and a mouse anti-ApoE4 primary antibody (Fig. 3g), and uptake was continuous over the course of the incubation (Extended Data Fig. 4d). Co-localization of the AF-647 signal with lysosomes was observed at both 1 h and 24 h (Extended Data Fig. 4g), replicating our findings with NeutrAvidin and IgG. Notably, non-specific inhibition of serine and cysteine proteases resulted in the accumulation of intracellular ApoE4-647, and this accumulation was substantially increased in the presence of anti-ApoE4 with **Ab-1** (Fig. 3h, Extended Data Fig. 4e, f). These data demonstrate that LYTAC-mediated target enrichment in the lysosome is coupled with target degradation. More broadly, conjugation of a lysosome-targeting ligand to an antibody can reprogramme the antibody to direct an extracellular antigen for degradation.

We next asked whether LYTACs could be used to accelerate the degradation of membrane-bound extracellular proteins. In principle, this requires simultaneous binding of a surface-associated protein and engagement of CI-M6PR, an interaction which would also benefit from increased effective molarity upon target binding (Fig. 4a). We first targeted EGFR, a known driver of cancer proliferation that can perform multiple scaffolding functions regardless of inhibition of its receptor tyrosine kinase activity. LYTACs were constructed using cetuximab (ctx)—an EGFR-blocking antibody approved by the Food and Drug Administration (FDA)—using a similar scheme to **Ab-1** (Extended Data Fig. 5a). HeLa cells were incubated for 24 h with 100 nM ctx, ctx functionalized with either long or short M6Pn glycopolypeptides, or GalNAc-functionalized ctx as a control. Cells were then lysed and assayed for total EGFR levels (Extended Data Fig. 5b). Substantial degradation of EGFR was observed only with ctx conjugates bearing M6Pn glycopolypeptides (greater than 70% degradation, comparable to EGF-induced downregulation), while no changes in CI-M6PR levels were observed. There was no apparent difference in degradation ability between LYTACs bearing short or long M6Pn glycopolypeptides. To demonstrate that depletion of EGFR is mediated by CI-M6PR, we compared the degradation performance of ctx-M6Pn **Ab-2** (Extended Data Fig. 5c) to that of unmodified ctx in dCas9-KRAB HeLa lines stably expressing a non-targeting or an *IGF2R*-targeting sgRNA. Degradation of EGFR was observed only in HeLa cells that expressed non-targeting sgRNA, whereas knockdown of *IGF2R* completely abrogated the degradation mediated by **Ab-2** (Fig. 4b). Equivalent results were obtained with concentrations of **Ab-2** of between 100 nM and 10 nM (Extended Data Fig. 5e). EGFR degradation was observed after 3 h and reached a maximum between 12 h and 24 h, persisting for at least 72 h (Extended Data Fig. 5f, g). Exogenous M6P inhibited the degradation of EGFR (Fig. 4c) in the presence of **Ab-2**, whereas treatment of cells with chloroquine prevented **Ab-2**-promoted degradation, demonstrating a dependency both on M6P binding and on lysosomal acidification. To rule out the possibility that EGFR crosslinking by ctx contributes to target downregulation[30,31], we digested ctx with papain to obtain ctx-Fab—which binds EGFR in a monovalent fashion—and conjugated it to poly(M6Pn) to generate **Fab-1** (Extended Data Fig. 5d). **Fab-1** accelerated the degradation of EGFR, in a CI-M6PR-dependent manner, to levels comparable with those obtained using **Ab-2** (Fig. 4d); this demonstrates that monovalent target binders can be used as LYTACs. In a mixed cell assay with HeLa (CI-M6PR$^+$EGFR$^+$) and Jurkat (CI-M6PR$^+$EGFR$^-$) cells, the ctx–M6Pn conjugate exhibited a similar binding profile to that of ctx alone, suggesting that LYTACs with dual affinities for the target and CI-M6PR can maintain high on-target specificity (Extended Data Fig. 6). EGFR degradation was also observed in breast cancer (BT474 and MDA-MB-361) and hepatocellular carcinoma (Hep3B and HepG2) cell lines (Fig. 4h, Extended Data Fig. 7a).

Next, we used quantitative mass spectrometry to perform a proteome-wide characterization of LYTAC degradation specificity in cells treated with ctx or **Ab-2**. A significant reduction of EGFR levels was promoted by **Ab-2**, whereas ctx did not affect EGFR levels (Fig. 4e). CI-M6PR levels were unchanged, further supporting that the degradation of EGFR is catalytic in terms of CI-M6PR. Changes in the expression levels of other proteins as a result of EGFR degradation were also observed (Extended Data Table 1; for the full dataset, see Supplementary Information). These co-degraded proteins may represent EGFR interaction partners or co-regulated molecules. For example, treatment with **Ab-2** caused significant downregulation of dihydropteridine reductase, 7,8-dihydro-8-oxoguanine triphosphatase and transcription factor DP-1, and resulted in the upregulation of glucose-1,6-bisphosphate synthase and coordinator of PRMT5 and differentiation stimulator (COPRS). Although the precise mechanism

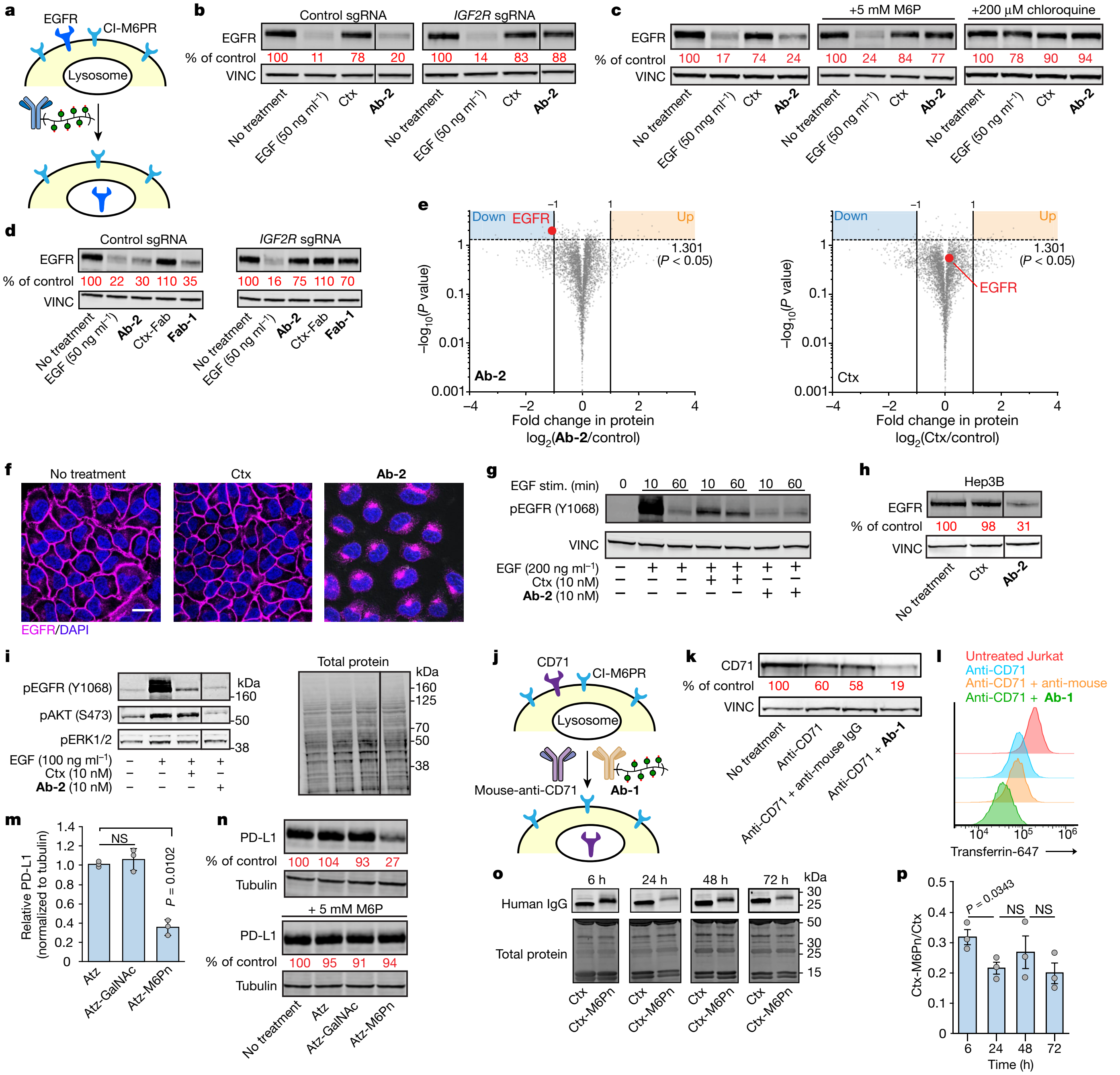

Fig. 4 | LYTACs accelerate degradation of membrane proteins. a, Schematic of EGFR degradation using LYTACs. **b**, EGFR levels after treatment with 10 nM **Ab-2** for 24 h in dCas9-KRAB HeLa cells expressing a control sgRNA or sgRNA targeting *IGF2R*. **c**, EGFR levels after treatment with 10 nM **Ab-2** for 48 h in dCas9-KRAB HeLa cells expressing a control sgRNA in the presence of 5 mM mannose-6-phosphate (M6P) or 200 µM chloroquine. **d**, EGFR levels after treatment with **Fab-1** in dCas9-KRAB HeLa cells expressing a control sgRNA or sgRNA targeting *IGF2R*. **e**, Fold change in the abundance of 3,877 HeLa proteins detected by quantitative proteomics analysis after 24-h treatment with either 10 nM **Ab-2** (left) or ctx (right) relative to untreated cells, data are the mean of three biological replicates. **f**, Cellular localization of EGFR after treatment with ctx or **Ab-2** for 48 h. Scale bar, 20 µm. **g**, Levels of pEGFR in dCas9-KRAB HeLa cells expressing a control sgRNA after 24-h incubation with 10 nM ctx or **Ab-2**, then incubation with EGF for 10 min or 60 min. **h**, Levels of EGFR after treatment with 10 nM **Ab-2** in Hep3B cells for 48 h. **i**, Levels of pEGFR, pAkt and pERK1/2 in Hep3B cells after 48 h incubation with 10 nM ctx or **Ab-2**, then incubation with EGF for 30 min. **j**, Degradation of CD71 mediated by a primary antibody and **Ab-1**. **k**, CD71 levels after treatment with 50 nM anti-CD71 or anti-CD71 and **Ab-1** in Jurkat cells after 24 h. **l**, Uptake of transferrin-647 in Jurkat cells treated with anti-CD71 or anti-CD71 and **Ab-1** for 24 h. **m**, PD-L1 levels in HDLM-2 cells after treatment with 25 nM atezolizumab (atz) or atz-LYTAC for 48 h. **n**, Levels of PD-L1 degradation with 25 nM atz-LYTAC after 48 h in HDLM-2 cells in the presence of 5 mM M6P. **o**, Serum levels of ctx or ctx-LYTAC in BALB/c mice injected intraperitoneally at 5 mg kg^{-1}. **p**, Quantification of serum ctx-M6Pn relative to ctx after intraperitoneal injection. Data are representative of two (**c**, **d**, **f**, **g**, **l**, **n**) or three (**b**, **h**, **i**, **k**, **o**) independent experiments or mice (**o**). Data are mean ± s.d. (**m**) or mean ± s.e.m. (**p**) of three independent experiments (**m**, one of which is shown in **n**) or mice (**p**). *P* values were determined by unpaired two-tailed *t*-tests. Relative values were calculated via densitometry and normalized to loading control (**b**–**d**, **h**, **k**, **m**, **n**) or relative to ctx levels (**p**).

for these changes remains to be elucidated, these data suggest that LYTACs may provide a means to monitor cellular changes in response to targeted protein degradation.

We compared the functional consequences of LYTAC-mediated degradation to those of EGFR inhibition by ctx. Immunofluorescent microscopy revealed marked relocalization of EGFR from the plasma membrane to intracellular vesicles upon treatment with **Ab-2** compared to treatment with ctx alone (Fig. 4f). To assess the consequences of degradation and removal from the plasma membrane, we incubated cells with ctx or **Ab-2**, then washed and treated them with EGF. In cells left untreated by ctx or **Ab-2**, we observed rapid phosphorylation of Tyr1068 of EGFR that decreased over time—this is consistent with EGF-induced downregulation of EGFR (Fig. 4g). Cells treated with ctx exhibited modest levels of phosphorylation that were sustained for the course of the EGF incubation. The sustained levels of phosphorylation are consistent with the ability of EGFR to engage in autophosphorylation and thus enhance stimulatory ligand-binding events through oligomerization[32,33]. However, degradation of EGFR with **Ab-2** reduced phosphorylation, demonstrating the advantages of receptor removal. This effect was dependent on CI-M6PR (Extended Data Fig. 5h). Because downstream kinase phosphorylation is independent of EGFR phosphorylation in non-starved HeLa cells[34], we used Hep3B hepatocellular carcinoma cells. **Ab-2** facilitated robust EGFR degradation in Hep3B cells (Fig. 4h), and this degradation desensitized cells to EGF stimulation (Fig. 4i). Notably, although ctx treatment inhibited EGFR phosphorylation, levels of downstream phosphorylated Akt (pAkt) were similar between ctx and untreated cells. Only with **Ab-2** treatment was downstream pAkt reduced to the levels observed in unstimulated cells. Proliferation of HepG2 cells is known to be stimulated by EGF[35]. We showed that **Ab-2** inhibited the proliferative effects of EGF stimulation in HepG2 cells, relative to treatment with ctx alone (Extended Data Fig. 7a, b).

To demonstrate the scope of the LYTAC platform, we targeted several additional membrane-associated proteins for degradation. CD71 (transferrin receptor-1)—a therapeutic cancer target that is progressing towards clinical trials—is known to cycle between early endosomes and the cell surface, avoiding trafficking to the lysosome for degradation[36]. Upon incubation of Jurkat cells with a mouse anti-CD71 antibody and **Ab-1** (Fig. 4j), degradation of CD71 was observed (greater than 80%; Fig. 4k), which was dependent on M6Pn recognition (Extended Data Fig. 8g). Note that the anti-CD71 antibody alone is reported to induce partial CD71 downregulation[37]. After 24-h incubation, cells treated with anti-CD71 and **Ab-1** internalized less transferrin-647 than did untreated cells or cells treated with non-M6Pn-bearing antibodies (Fig. 4l), further highlighting the functional consequences of target degradation.

Additionally, we investigated whether LYTACs could degrade PD-L1, a driver of cancer cell immune evasion. For PD-L1 to undergo accelerated degradation, the LYTAC must overcome the PD-L1 recycling pathway[38]. MDA-MB-231 cells—which are PD-L1-positive—were treated with anti-PD-L1, anti-PD-L1 functionalized with GalNAc glycopolypeptides or anti-PD-L1-M6Pn LYTAC (**Ab-3**, Extended Data Fig. 8a). Treatment with **Ab-3** resulted in a significant decrease (average 33%) in cell-surface PD-L1 levels compared to treatment with unfunctionalized anti-PD-L1 or anti-PD-L1-poly(GalNAc) (Extended Data Fig. 8b, c). As MDA-MB-231 cells express low levels of CI-M6PR, we tested the degradation of PD-L1 in the Hodgkin's lymphoma cell line HDLM-2, which expresses higher levels of CI-M6PR. After 36 h of treatment with **Ab-3**, 50% downregulation of total PD-L1 was observed (Extended Data Fig. 8d, e). When treated with a LYTAC derived from atezolizumab (the active ingredient in Tecentriq) (Extended Data Fig. 8f)—an FDA-approved PD-L1-blocking antibody—we observed a greater extent of PD-L1 degradation (average 70% degradation, Fig. 4m), which was dependent on M6Pn-recognition (Fig. 4n). Thus, LYTACs can override the endogenous recycling programs of cell-surface proteins and accelerate their lysosomal degradation.

Finally, we asked how M6Pn conjugation might affect antibody clearance in vivo. BALB/c mice were injected intraperitoneally with 5 mg kg^{-1} ctx or ctx-M6Pn, and serum antibody levels were assayed by western blotting. Six hours after injection, we observed a threefold reduction in serum ctx-M6Pn relative to ctx, suggesting a rapid clearance phase post-injection (Fig. 4o, p). However, between 6 h and 72 h we observed only a moderate decrease in serum ctx-M6Pn relative to ctx, and no substantial accumulation in either the liver or the spleen (Extended Data Fig. 9). These data suggest two regimes of clearance: a rapid initial phase and a slower, more sustained clearance. Modulating these two regimes will be important for tailoring the in vivo efficacy of any individual combination of LYTAC and target protein.

In summary, the LYTAC platform enables targeting of extracellular and membrane-associated proteins directly for lysosomal degradation. The success of a particular LYTAC is likely to result from a combination of factors—including the endogenous kinetics of protein trafficking and turnover, the amount of surface localization, the inherent susceptibility to lysosomal transportation through clathrin-mediated endocytosis and the stoichiometry relative to the lysosome-targeting receptor. Although the LYTACs described above take advantage of CI-M6PR, in principle other shuttling receptors could be co-opted, reducing the potential for resistance to develop when targeting oncoproteins. We have demonstrated that both small molecules and larger peptides can be used as protein target binders in LYTACs. Modulating the pharmacokinetic properties to control off-target clearance and stoichiometries of a given LYTAC necessary to effectively degrade a membrane protein will remain a key challenge for further translational applications. We anticipate that the chemical tunability and modularity of LYTACs will offer new opportunities to manipulate these parameters for targeted protein degradation of secreted and membrane proteins, both for research and for potential therapeutics.

Online content

Any methods, additional references, Nature Research reporting summaries, source data, extended data, supplementary information, acknowledgements, peer review information; details of author contributions and competing interests; and statements of data and code availability are available at https://doi.org/10.1038/s41586-020-2545-9.

1. Sakamoto, K. M. et al. Protacs: chimeric molecules that target proteins to the Skp1-Cullin-F box complex for ubiquitination and degradation. *Proc. Natl Acad. Sci. USA* **98**, 8554–8559 (2001).
2. Winter, G. E. et al. Phthalimide conjugation as a strategy for in vivo target protein degradation. *Science* **348**, 1376–1381 (2015).
3. Nabet, B. et al. The dTAG system for immediate and target-specific protein degradation. *Nat. Chem. Biol.* **14**, 431–441 (2018).
4. Clift, D. et al. A method for the acute and rapid degradation of endogenous proteins. *Cell* **171**, 1692–1706.e18 (2017).
5. Fan, X., Jin, W. Y., Lu, J., Wang, J. & Wang, Y. T. Rapid and reversible knockdown of endogenous proteins by peptide-directed lysosomal degradation. *Nat. Neurosci.* **17**, 471–480 (2014).
6. Naito, M., Ohoka, N. & Shibata, N. SNIPERs—hijacking IAP activity to induce protein degradation. *Drug Discov. Today Technol.* **31**, 35–42 (2019).
7. Uhlén, M. et al. Tissue-based map of the human proteome. *Science* **347**, 1260419 (2015).
8. Brown, K. J. et al. The human secretome atlas initiative: implications in health and disease conditions. *Biochim. Biophys. Acta* **1834**, 2454–2461 (2013).
9. Coutinho, M. F., Prata, M. J. & Alves, S. A shortcut to the lysosome: the mannose-6-phosphate-independent pathway. *Mol. Genet. Metab.* **107**, 257–266 (2012).
10. Ghosh, P., Dahms, N. M. & Kornfeld, S. Mannose 6-phosphate receptors: new twists in the tale. *Nat. Rev. Mol. Cell Biol.* **4**, 202–213 (2003).
11. Gary-Bobo, M., Nirdé, P., Jeanjean, A., Morère, A. & Garcia, M. Mannose 6-phosphate receptor targeting and its applications in human diseases. *Curr. Med. Chem.* **14**, 2945–2953 (2007).
12. Igawa, T., Haraya, K. & Hattori, K. Sweeping antibody as a novel therapeutic antibody modality capable of eliminating soluble antigens from circulation. *Immunol. Rev.* **270**, 132–151 (2016).
13. Alon, R., Bayer, E. A. & Wilchek, M. Affinity cleavage of cell surface antibodies using the avidin–biotin system. *J. Immunol. Methods* **165**, 127–134 (1993).
14. Liu, L., Lee, W.-S., Doray, B. & Kornfeld, S. Engineering of GlcNAc-1-phosphotransferase for production of highly phosphorylated lysosomal enzymes for enzyme replacement therapy. *Mol. Ther. Methods Clin. Dev.* **5**, 59–65 (2017).

15. Zhu, Y. et al. Conjugation of mannose 6-phosphate-containing oligosaccharides to acid α-glucosidase improves the clearance of glycogen in Pompe mice. *J. Biol. Chem.* **279**, 50336–50341 (2004).
16. Beljaars, L. et al. Albumin modified with mannose 6-phosphate: a potential carrier for selective delivery of antifibrotic drugs to rat and human hepatic stellate cells. *Hepatology* **29**, 1486–1493 (1999).
17. Berkowitz, D. B., Maiti, G., Charette, B. D., Dreis, C. D. & MacDonald, R. G. Mono- and bivalent ligands bearing mannose 6-phosphate (M6P) surrogates: targeting the M6P/insulin-like growth factor II receptor. *Org. Lett.* **6**, 4921–4924 (2004).
18. Das, S., Parekh, N., Mondal, B. & Gupta, S. S. Controlled synthesis of end-functionalized mannose-6-phosphate glycopolypeptides for lysosome targeting. *ACS Macro Lett.* **5**, 809–813 (2016).
19. Jeanjean, A., Garcia, M., Leydet, A., Montero, J.-L. & Morère, A. Synthesis and receptor binding affinity of carboxylate analogues of the mannose 6-phosphate recognition marker. *Bioorg. Med. Chem.* **14**, 3575–3582 (2006).
20. Sly, W. S. et al. Enzyme therapy in mannose receptor-null mucopolysaccharidosis VII mice defines roles for the mannose 6-phosphate and mannose receptors. *Proc. Natl Acad. Sci. USA* **103**, 15172–15177 (2006).
21. Kramer, J. R., Onoa, B., Bustamante, C. & Bertozzi, C. R. Chemically tunable mucin chimeras assembled on living cells. *Proc. Natl Acad. Sci. USA* **112**, 12574–12579 (2015).
22. Vidal, S., Montero, J.-L., Leydet, A. & Morère, A. A flexible route to mannose 6-phosphonate functionalized derivatives. *Phosphorus Sulfur Silicon Relat. Elem.* **177**, 2363–2377 (2002).
23. Jeanjean, A. et al. Synthesis of new sulfonate and phosphonate derivatives for cation-independent mannose 6-phosphate receptor targeting. *Bioorg. Med. Chem. Lett.* **18**, 6240–6243 (2008).
24. Ritter, T. E., Fajardo, O., Matsue, H., Anderson, R. G. & Lacey, S. W. Folate receptors targeted to clathrin-coated pits cannot regulate vitamin uptake. *Proc. Natl Acad. Sci. USA* **92**, 3824–3828 (1995).
25. Johnson, D. E., Ostrowski, P., Jaumouillé, V. & Grinstein, S. The position of lysosomes within the cell determines their luminal pH. *J. Cell Biol.* **212**, 677–692 (2016).
26. Kampmann, M., Bassik, M. C. & Weissman, J. S. Functional genomics platform for pooled screening and generation of mammalian genetic interaction maps. *Nat. Protocols* **9**, 1825–1847 (2014).
27. Horlbeck, M. A. et al. Compact and highly active next-generation libraries for CRISPR-mediated gene repression and activation. *eLife* **5**, e19760 (2016).
28. Heider, M. R. & Munson, M. Exorcising the exocyst complex. *Traffic* **13**, 898–907 (2012).
29. Yamazaki, Y., Painter, M. M., Bu, G. & Kanekiyo, T. Apolipoprotein E as a therapeutic target in Alzheimer's disease: a review of basic research and clinical evidence. *CNS Drugs* **30**, 773–789 (2016).
30. Li, J. Y. et al. A biparatopic HER2-targeting antibody–drug conjugate induces tumor regression in primary models refractory to or ineligible for HER2-targeted therapy. *Cancer Cell* **29**, 117–129 (2016).
31. Spangler, J. B. et al. Combination antibody treatment down-regulates epidermal growth factor receptor by inhibiting endosomal recycling. *Proc. Natl Acad. Sci. USA* **107**, 13252–13257 (2010).
32. Huang, Y. et al. Molecular basis for multimerization in the activation of the epidermal growth factor receptor. *eLife* **5**, e14107 (2016).
33. Needham, S. R. et al. EGFR oligomerization organizes kinase-active dimers into competent signalling platforms. *Nat. Commun.* **7**, 13307 (2016).
34. Zhu, J., Blenis, J. & Yuan, J. Activation of PI3K/Akt and MAPK pathways regulates Myc-mediated transcription by phosphorylating and promoting the degradation of Mad1. *Proc. Natl Acad. Sci. USA* **105**, 6584–6589 (2008).
35. Huang, P. et al. The role of EGF–EGFR signalling pathway in hepatocellular carcinoma inflammatory microenvironment. *J. Cell. Mol. Med.* **18**, 218–230 (2014).
36. Shen, Y. et al. Transferrin receptor 1 in cancer: a new sight for cancer therapy. *Am. J. Cancer Res.* **8**, 916–931 (2018).
37. Weissman, A. M., Klausner, R. D., Rao, K. & Harford, J. B. Exposure of K562 cells to anti-receptor monoclonal antibody OKT9 results in rapid redistribution and enhanced degradation of the transferrin receptor. *J. Cell Biol.* **102**, 951–958 (1986).
38. Burr, M. L. et al. CMTM6 maintains the expression of PD-L1 and regulates anti-tumour immunity. *Nature* **549**, 101–105 (2017).

Methods

Data reporting

No statistical methods were used to predetermine sample size. The experiments were not randomized and the investigators were not blinded to allocation during experiments and outcome assessment.

General synthetic chemistry procedures

All reactions were performed in standard, dry glassware fitted with rubber septa under an inert atmosphere of nitrogen unless otherwise described. Reagents were purchased in reagent grade from commercial suppliers and used as received, unless otherwise described. Anhydrous solvents (acetonitrile, benzene, dichloromethane, diethyl ether, *N*,*N*-dimethylformamide, tetrahydrofuran and toluene) were prepared by passing the solvent through an activated alumina column. See the Supplementary Information for detailed synthetic procedures and characterization of all new compounds.

Cell lines

Cells were grown in T75 flasks (Thermo Fisher) and maintained at 37 °C and 5% CO_2. K562 and Jurkat cells were grown in RPMI supplemented with 10% fetal bovine serum (FBS) and 1% penicillin/streptomycin. THP-1 cells were grown in RPMI supplemented with 10% FBS, 1% penicillin/streptomycin, and 0.05 mM 2-mercaptoethanol. HeLa, MDA-MB-361, HEK-293, HEK-293T, Hep3B and MDA-MB-231 cells were grown in DMEM supplemented with 10% FBS and 1% penicillin/streptomycin. HepG2 cells were grown in low-glucose DMEM supplemented with 10% FBS and 1% penicillin/streptomycin. BT474 cells were grown in RPMI supplemented with 10% FBS and 1% penicillin/streptomycin with 0.023 U ml^{-1} insulin. HDLM-2 cells were grown in RPMI supplemented with 20% heat-inactivated FBS and 1% penicillin/streptomycin. HeLa and K562 cells stably expressing dCas9-KRAB were a gift from M. Bassik. Jurkat, HeLa, MDA-MB-361, MDA-MB-231, THP-1, K562, HEK-293, HEK-293T, Hep3B, HepG2 and BT474 cells were obtained from the American Type Culture Collection (ATCC), HDLM-2 cells were obtained from the laboratory of T. Waldmann. Cell lines were authenticated by the supplier. Cell lines were verified to be mycoplasma-negative using a Lonza MycoAlert Mycoplasma Detection Assay.

General procedure for NeutrAvidin-647 uptake experiments

Cells (70% confluent in 24-well plate for adherent cells, 1×10^6 cells per ml for suspension cells) were incubated in complete growth medium supplemented with 500 nM NA-647, or NA-647 and 2 μM glycopolypeptide. Addition was performed sequentially, with NA-647 added first followed by glycopolypeptide and immediate transfer to 37 °C.

General procedure for protein uptake and degradation experiments

Cells (70% confluent in 24-well plate for adherent cells, 2×10^6 cells per ml for suspension cells) were incubated in complete growth medium supplemented with 50 nM target protein, or 50 nM target protein and 25 nM of each antibody. Addition was performed sequentially, with target protein added first followed by secondary antibodies, followed by primary antibodies, and subsequent immediate transfer to 37 °C. Recombinant proteins were expressed in-house (mCherry) or purchased from Abcam (human apolipoprotein E4, ab50243) and labelled with commercially available fluorescent dyes.

CRISPRi screen procedure

The hCRISPRi-v2 library was a gift from J. Weissman (Addgene ID 83969). K562 cells stably expressing dCas9-KRAB were infected with the 104,535 sgRNA library described previously[27], targeting the transcriptional start sites of 18,905 annotated genes at a redundancy of 5 sgRNA per start site. Infectivity was titrated such as to transduce the library at a multiplicity of infection of 0.3–0.4. Cells were selected with puromycin for 96 h and then allowed to expand in puromycin-free media for 48 h. Staining and FACS was performed within seven days of completion of puromycin selection. On the day of sorting, two replicates of 50×10^6 library-infected cells (4×10^6 cells per ml) were incubated with NA-647 (500 nM) and poly(M6Pn)$_{long}$ (2 μM) for 1 h at 37 °C. Cells were washed three times with PBS at 4 °C. Cells were then resuspended in PBS with SYTOX Green (according to the manufacturer's specifications) and sorted by FACS using a BD Aria II. Intact, viable cells were selected by gating on FSC/SSC and SYTOX Green channels. A population of cells representing the bottom 15% of the fluorescence distribution in the NA-647 channel was then selected for and sorted. Sorting was conducted until 25×10^6 events had been processed, corresponding to an approximately 250-fold library coverage. Sorted cells were then pelleted and frozen for subsequent downstream processing. Aliquots of 50×10^6 unsorted cells from each replicate were also pelleted and frozen down in parallel for normalization.

CRISPRi screen DNA extraction and data analysis

Frozen cell pellets were thawed and genomic DNA extraction was performed using either the QIAamp DNA Blood Maxi Kit (for unsorted samples) or the Sigma GeneElute Mammalian Genomic DNA Miniprep kit (for sorted samples) according to manufacturer's specifications. The sgRNA-encoding regions were amplified via nested PCR and sequenced on an Illumina NextSeq500. Alignment of sequencing reads to the sgRNA library and statistical comparison of positively selected genes in sorted versus unsorted samples was performed using MaGeCK[39]. MaGeCK returned a statistical score for gene enrichment in the sorted population and genes were ranked by a positive selection score corresponding to the −log(PosScore). GO enrichment analysis was performed using GOrilla[40].

Generation of CRISPRi-knockdown cell lines

K562 or HeLa cells stably expressing dCas9-KRAB were infected with lentivirus-encoding sgRNAs identified from the CRISPRi screen. Lentivirus was produced by co-transfection of HEK-293T cells with a lentiviral transfer vector and packaging plasmids (pGag/pol, pREV, pTAT, pVSVG). Transfection was performed using Lipofectamine 2000 reagent as recommended by the manufacturer. Viral supernatants were collected 48 h after transfection, filtered through a 0.45-μm filter, and added to target cells (400 μl viral supernatant per well in a 6-well plate) along with polybrene (8 μg per ml). Then, 48 h post infection, cell media was replaced and cells were placed under puromycin selection (2 μg ml^{-1}).

sgRNA guides: *IGF2R* 5′-GAGGTGAGCGCGGCTCGACT-3′; *EXOC1* 5′-GGGCGGACAGACGAGCTGAC-3′; *EXOC2* 5′-GGGCGGAAGTGAGGTGCCGG-3′; non-targeting (*GAL4*) 5′-GTTGGAGCACTGTCCTCCGAACGT-3′.

Flow cytometry for surface staining and uptake measurements

For protein uptake experiments in suspension cell lines, cells were incubated for the indicated time with proteins and conjugates, then washed 3 times with PBS at 4 °C. Cells were then incubated with either SYTOX Green or SYTOX Red according to the manufacturer's specifications for 15 min on ice. For protein uptake experiments in adherent cell lines, cells were incubated for the indicated time with proteins and conjugates, then washed two times quickly with PBS and lifted with trypsin. Cells were transferred to a 96-well V-bottom plate and washed 3 times with PBS, then incubated with either SYTOX Green or SYTOX Red according to the manufacturer's specifications for 15 min on ice. For surface-staining experiments, adherent cells were lifted with non-enzymatic cell dissociation buffer (Gibco) and transferred to a 96-well V-bottom plate, and suspension cells were transferred to a 96-well V-bottom plate. After washing 3 times with 0.5% BSA in PBS, cells were incubated with primary antibody for 30 min on ice. Cells were subsequently washed 3 times with 0.5% BSA in PBS, then incubated with secondary antibodies for 30 min on ice. After incubation, cells were washed 3 times with 0.5% BSA in PBS and incubated with either SYTOX Green or SYTOX Red according to the manufacturer's specifications for 15 min on ice. Flow cytometry was performed on either a BD-Accuri C6 Plus or DxP FACScan flow cytometer, and analysis was performed using the FlowJo software package. Gating was performed on single cells and live cells.

Cell surface degradation experiment

Adherent cells (70% confluency for 24-h experiments, 50% confluency for 48-h experiments) were treated with antibodies or conjugates in complete growth medium. At the indicated time, cells were washed three times with Dulbecco's phosphate-buffered saline (DPBS), then lysed as detailed below. Suspension cells were suspended in complete growth media in a flat bottom plate, and at the indicated time transferred to a 96-well V-bottom plate and washed three times with PBS, then lysed as detailed in 'Western blotting'.

Competitive EGF stimulation experiment

Adherent cells (70% confluency for 24-h experiments, 50% confluency for 48-h experiments) were treated with antibodies or conjugates in complete growth medium. At the indicated time, cells were washed three times with DPBS, then incubated with EGF in fresh complete growth medium. After incubation, cells were washed three times with DPBS, then lysed as detailed in 'Western blotting'.

Western blotting

Cell culture experiments with adherent cells conducted in 24-well plates were washed 3 times with DPBS, then lysed with RIPA buffer supplemented with protease inhibitor cocktail (Roche), phosphatase inhibitor cocktail (Cell Signaling Technologies) and 0.1% benzonase (Millipore-Sigma) on ice for 30 min. The lysates were spun at 21,000*g* for 15 min at 4 °C and protein concentration was determined using BCA assay (Pierce). Suspension cell lines were transferred to a 96-well V-bottom plate, washed 3 times with PBS, then lysed with RIPA buffer supplemented as above. Adherent cells in 6-well plates were washed three times with DPBS then lysed with 1X Laemmli buffer containing protease inhibitor cocktail (Roche) and phosphatase inhibitor cocktail (Cell Signaling Technologies). Lysates were then sonicated on ice using a microtip sonicator for 30 s, with 10 s sonication intervals and rest intervals, and protein concentration was determined using BCA assay (Pierce). Equal amounts of lysates were separated by SDS–PAGE (4–12% Bis-Tris gel or 10% Bis-Tris gel), then transferred to a nitrocellulose membrane. After transfer, the membrane was stained for total protein using REVERT Total Protein Stain (LI-COR), then blocked in TBS-T with 5% non-fat dried milk or Odyssey Blocking Buffer (TBS) (LI-COR) for 1 h at room temperature with gentle shaking. Membranes were incubated overnight with primary antibodies at 4 °C with gentle shaking, then washed three times with TBS-T for five minutes each. The membrane was then incubated with 800CW goat anti-mouse IgG, 800CW goat anti-rabbit IgG, 800CW donkey anti-goat IgG, 680LT goat anti-rabbit IgG or 680LT goat anti-mouse IgG secondary antibodies (1:10,000) in Odyssey Blocking Buffer (TBS) for 1 h at room temperature with gentle shaking. Membranes were washed three times with TBS-T, then imaged using an OdysseyCLxImager (LI-COR). Quantification of band intensities was performed using Image Studio Software (LI-COR).

Confocal microscopy

A Nikon A1R confocal microscope equipped with a Plan Fluor 60× oil immersion 1.30–numerical aperture objective was used. This instrument is equipped with a 405-nm violet laser, a 488-nm blue laser, a 561-nm green laser and a 639-nm red laser.

Mass spectrometry

Sample preparation. Samples were prepared for proteomic analysis using a previously described method with methanol precipitation to extract proteins, followed by tryptic digestion[41]. In brief, HeLa cells from each treatment condition were lysed by suspension in 6 M guanidine, total protein concentration was measured using BCA (Thermo Fisher Scientific), and 100 µg of protein was extracted via precipitation in 90% methanol for each sample. Supernatants were decanted and protein pellets were suspended in a buffer comprising 8 M urea, 100 mM Tris pH 8, 10 mM tris(2-carboxyethyl)phosphine and 40 mM chloroacetamide. After incubation at room temperature for 30 min, samples were diluted to 1.5 M urea with 100 mM Tris pH 8 and digested with trypsin (50:1 protein to enzyme, Promega) overnight. Sample cleanup was performed by first quenching with formic acid to a final pH of around 2, followed by desalting over a polystyrene–divinylbenzene solid phase extraction (PS–DVB SPE) cartridge (Phenomenex). Samples were dried with vacuum centrifugation after desalting, and peptide mass was assayed using a peptide colorimetric assay (Fisher).

LC–MS/MS. All samples were resuspended in 0.2% formic acid in water at around 500 ng µl^{-1}, and 500 ng of total peptide mass was injected on column for each sample. Peptides were separated over a 25-cm EasySpray reversed phase LC column (75 µm inner diameter packed with 2 µm, 100 Å, PepMap C18 particles, Thermo Fisher Scientific). The mobile phases (A: water with 0.2% formic acid and B: acetonitrile with 0.2% formic acid) were driven and controlled by a Dionex Ultimate 3000 RPLC nano system (Thermo Fisher Scientific). Gradient elution was performed at 300 nl min^{-1}. Mobile phase B was increased to 5% over 6 min, followed by an increase to 40% at 76 min, a ramp to 90% B at 77 min, and a wash at 90% B for 10 min. Flow was then ramped back to 0% B over the course of 1 min, and the column was re-equilibrated at 0% B for 12 min, for a total analysis of 100 min. Eluted peptides were analysed on an Orbitrap Fusion Tribrid MS system (Thermo Fisher Scientific). Precursors were ionized using an EASY-Spray ionization source (Thermo Fisher Scientific) source held at +2.2 kV compared to ground, and the column was held at 40 °C. The inlet capillary temperature was held at 275 °C. Survey scans of peptide precursors were collected in the Orbitrap from 350-1500 Th with an automatic gain control target of 1,000,000, a maximum injection time of 50 ms and a resolution of 120,000 at 200 *m*/*z*. Monoisotopic precursor selection was enabled for peptide isotopic distributions, precursors of $z = 2–5$ were selected for data-dependent MS/MS scans for 2 s of cycle time, and dynamic exclusion was set to 45 s with a ±10 ppm window set around the precursor monoisotope. An isolation window of 0.7 *m*/*z* was used to select precursor ions with the quadrupole. MS/MS scans were collected using high-energy collisional dissociation at 30 normalized collision energy (nce) with an automatic gain control target of 30,000 and a maximum injection time of 25 ms. Mass analysis was performed in the linear ion trap using the 'Rapid' scan speed while scanning from 200–1,500 *m*/*z*.

Data analysis. Raw data were processed using MaxQuant version 1.6.3.4[42], and tandem mass spectra were searched with the Andromeda search algorithm[43]. Oxidation of methionine and protein N-terminal acetylation were specified as variable modifications, while carbamidomethylation of cysteine was set as a fixed modification. A precursor ion search tolerance of 20 ppm and a product ion mass tolerance of 0.3 Da were used for searches, and two missed cleavages were allowed for full trypsin specificity. Peptide spectral matches were made against a target-decoy human reference proteome database downloaded from Uniprot. Peptides were filtered to a 1% FDR and a 1% protein FDR was applied according to the target-decoy method[44]. Proteins were identified and quantified using at least one peptide (razor + unique), where razor peptide is defined as a non-unique peptide assigned to the protein group with the most other peptides (Occam's razor principle). Proteins were quantified and normalized using MaxLFQ[45] with a label-free quantification (LFQ) minimum ratio count of 1. LFQ intensities were calculated using the match between runs feature, and MS/MS spectra were required for LFQ comparisons. For quantitative comparisons, protein intensity values were $\log_2$-transformed before further analysis, and missing values were imputed from a normal distribution with width 0.3 and downshift value of 1.8 (that is, default values) using the Perseus software suite[46]. Significance calculations were performed using a two-tailed *t*-test with heteroscedastic variance (performed in Microsoft Excel).

Antibody in vivo clearance study

Mouse experiments were performed in compliance with ethical regulations approved by the Administrative Panel on Laboratory Animal Care (APLAC) at Stanford University under protocol 31511. Female BALB/c mice (6–8 weeks old, from the Jackson Laboratory) were treated with 5 mg kg^{-1} of either antibody or conjugate via intraperitoneal injection (3 mice per group). The initial grouping of mice was random, after which no additional randomization or blinding was used. At the indicated time, blood was sampled from the tail using anti-coagulant capillary tubes, and serum was separated after centrifugation at 700*g* at 4 °C for 15 min. To analyse the presence of human antibody in serum, 2 µl serum was diluted into 30 µl LDS loading buffer and separated by SDS–PAGE (4–12% or 10% Bis-Tris gel), then transferred to a nitrocellulose membrane. Liver and spleen were collected after 72 h, homogenized and lysed with RIPA buffer supplemented with protease inhibitor cocktail and 0.1% benzonase, and 50 ug of organ lysate were separated by SDS–PAGE (4–12% Bis-Tris gel). The presence of cetuximab was detected using 800CW goat anti-human IgG secondary antibody (1:1,000).

Reporting summary

Further information on research design is available in the Nature Research Reporting Summary linked to this paper.

Data availability

CRISPRi screen results are provided in Supplementary Table 1, quantitative proteomics results are provided in Supplementary Table 2. The flow cytometry gating strategy is provided in the Supplementary Information. All data that supported the findings of this study are included and are also available from the corresponding author upon request. Source data are provided with this paper.

39. Li, W. et al. MAGeCK enables robust identification of essential genes from genome-scale CRISPR/Cas9 knockout screens. *Genome Biol*. **15**, 554 (2014).
40. Eden, E., Navon, R., Steinfeld, I., Lipson, D. & Yakhini, Z. GOrilla: a tool for discovery and visualization of enriched GO terms in ranked gene lists. *BMC Bioinformatics* **10**, 48 (2009).
41. Hebert, A. S. et al. Improved precursor characterization for data-dependent mass spectrometry. *Anal. Chem*. **90**, 2333–2340 (2018).
42. Tyanova, S., Temu, T. & Cox, J. The MaxQuant computational platform for mass spectrometry-based shotgun proteomics. *Nat. Protocols* **11**, 2301–2319 (2016).
43. Cox, J. et al. Andromeda: a peptide search engine integrated into the MaxQuant environment. *J. Proteome Res*. **10**, 1794–1805 (2011).
44. Elias, J. E. & Gygi, S. P. Target-decoy search strategy for increased confidence in large-scale protein identifications by mass spectrometry. *Nat. Methods* **4**, 207–214 (2007).
45. Cox, J. et al. Accurate proteome-wide label-free quantification by delayed normalization and maximal peptide ratio extraction, termed MaxLFQ. *Mol. Cell. Proteomics MCP* **13**, 2513–2526 (2014).
46. Tyanova, S. et al. The Perseus computational platform for comprehensive analysis of (prote)omics data. *Nat. Methods* **13**, 731–740 (2016).

Acknowledgements We thank M. Bassik for the CRISPRi library and dCas9-KRAB-expressing cell lines; T. Waldmann for a gift of the HDLM-2 cell line and E. Appel for use of aqueous gel permeation chromatography equipment. This work was supported in part by National Institutes of Health (NIH) grant P30CA124435 using the Stanford Cancer Institute Proteomics/Mass Spectrometry Shared Resource and by NIH grant R01CA227942 to C.R.B. S.M.B was supported by a National Institute of General Medical Sciences F32 Postdoctoral Fellowship. K.P. was supported by a National Science Foundation Graduate Research Fellowship, a Stanford Graduate Fellowship, and the Stanford ChEM-H Chemistry/Biology Interface Predoctoral Training Program. S.W. was supported by a Banting Postdoctoral Fellowship from the Canadian Institutes of Health. G.A. was supported by a National Science Foundation Graduate Research Fellowship. N.M.R. was supported by NIH grant K00CA21245403.

Author contributions S.M.B., K.P. and C.R.B. conceived the project. S.M.B., K.P., S.W., G.A. and N.M.R. carried out experiments and interpreted data. S.M.B. and C.R.B. wrote the manuscript with input from all authors. C.R.B. provided supervision.

Competing interests C.R.B. is a co-founder and scientific advisory board member of Lycia Therapeutics, Palleon Pharmaceuticals, Enable Bioscience, Redwood Biosciences (a subsidiary of Catalent) and InterVenn Biosciences, and a member of the board of directors of Eli Lilly & Company. S.M.B. is a consultant for Lycia Therapeutics. Stanford University has filed patent applications related to this work which are licensed to Lycia Therapeutics, listing S.M.B., K.P., G.A. and C.R.B. as inventors.

Additional information

Supplementary information is available for this paper at https://doi.org/10.1038/s41586-020-2545-9.

Correspondence and requests for materials should be addressed to C.R.B.

Peer review information *Nature* thanks Nathanael Gray and the other, anonymous, reviewer(s) for their contribution to the peer review of this work.

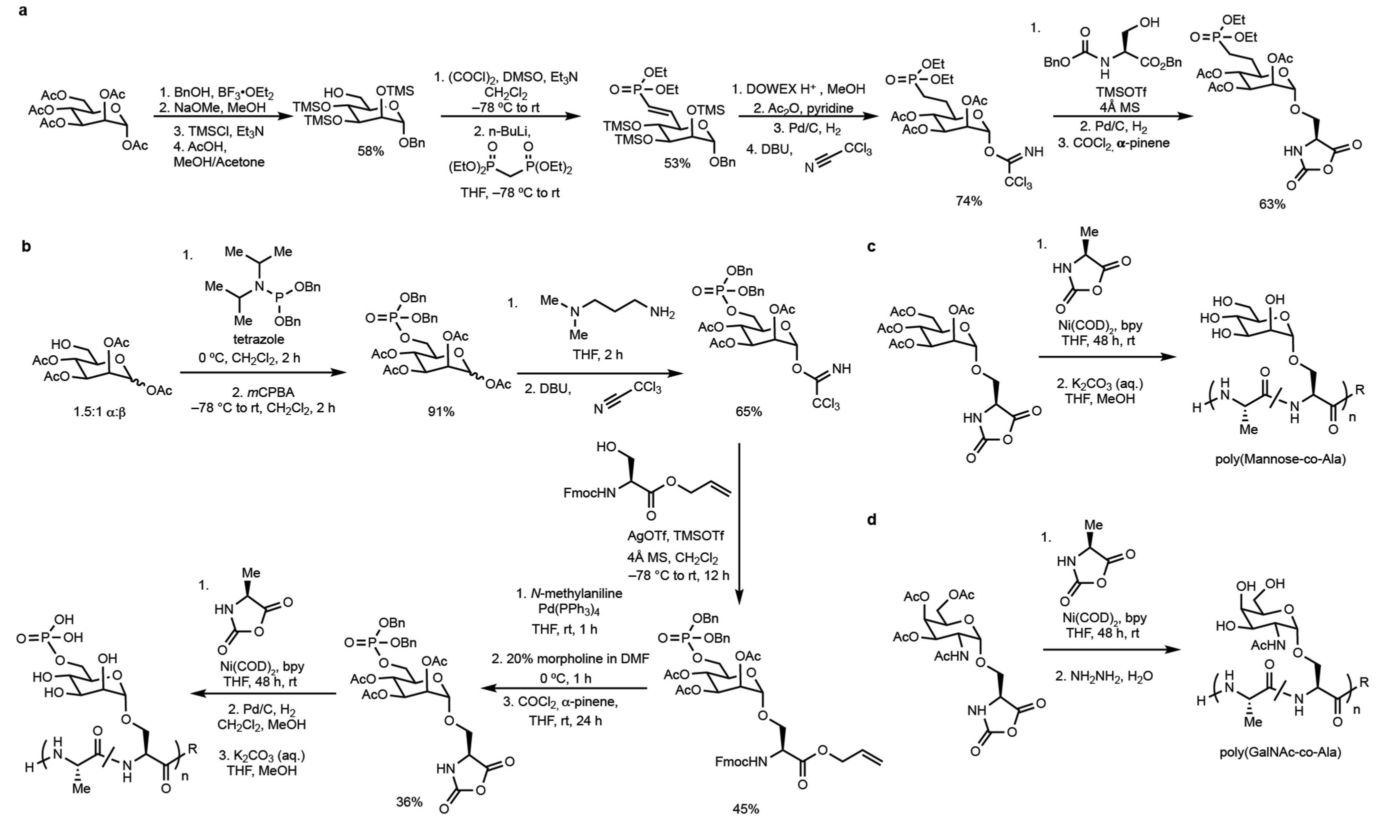

Extended Data Fig. 1 | Synthesis of M6Pn-NCA, poly(mannose-6-phosphate-co-Ala), poly(mannose-co-Ala) and poly(GalNAc-co-Ala). **a**, Synthetic route to mannose-6-phosphonate-serine *N*-carboxyanhydride (NCA). **b**, Synthetic route to M6P-NCA, followed by Ni-catalysed polymerization. Polymerization reactions were carried out in a N$_2$ glovebox for 48 h in tetrahydrofuran. **c**, **d**, General synthetic schemes for the polymerization of mannose-NCA (**c**) and GalNAc-NCA (**d**). DBU, 1,8-diazabicyclo[5.4.0]undec-7-ene; Fmoc, fluorenylmethyloxycarbonyl; mCPBA, *meta*-chloroperoxybenzoic acid; OTf, triflate.

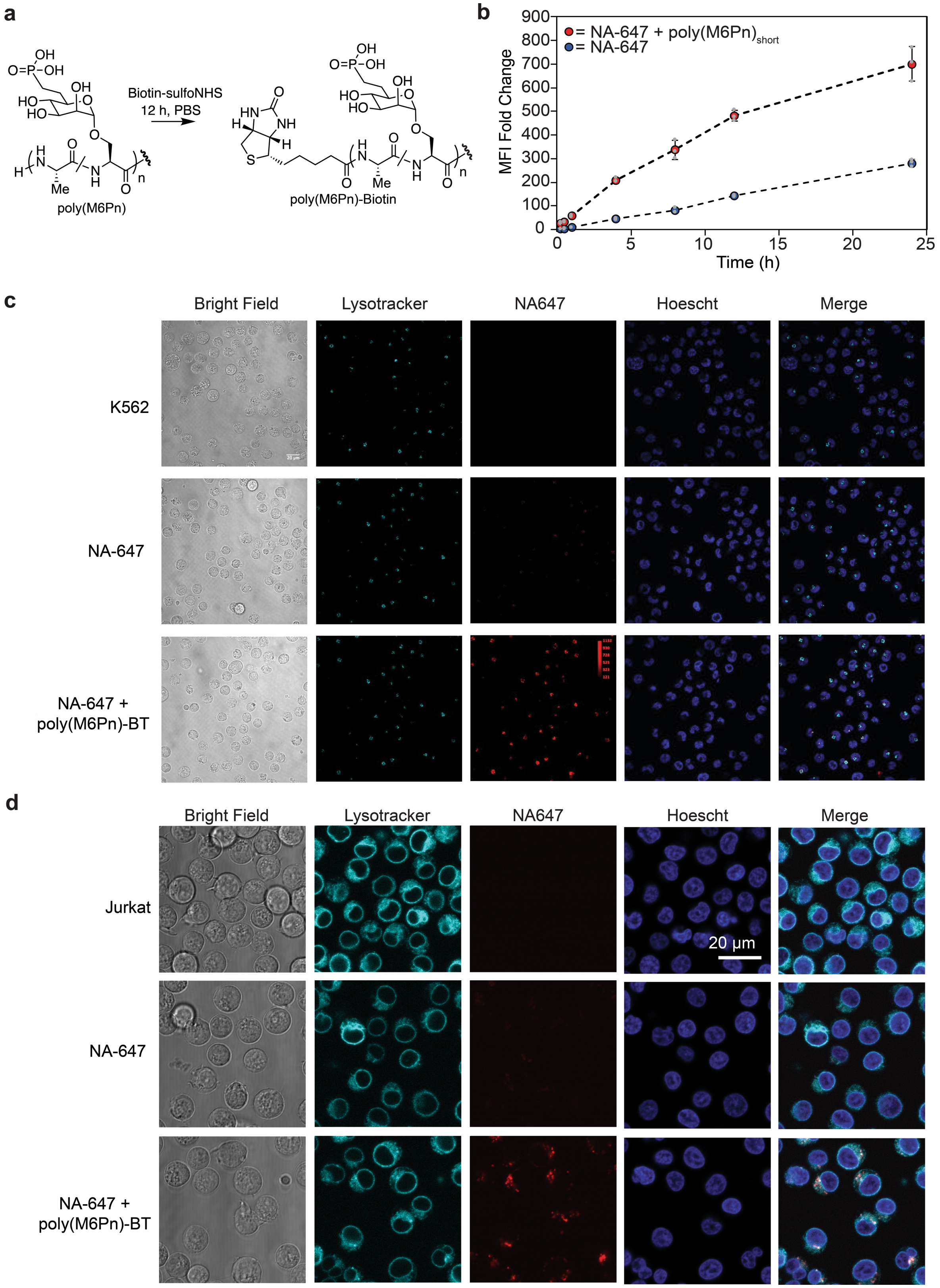

Extended Data Fig. 2 | See next page for caption.

Extended Data Fig. 2 | Biotin-poly(M6Pn) LYTACs direct NA-647 to lysosomes. a, General scheme for biotinylation of glycopolypeptides with sulfo-NHS biotin. Biotinylation reactions were performed in 1× PBS at room temperature overnight. **b**, Biotin–LYTAC-mediated NA-647 uptake is continuous over time in K562 cells. K562 cells were incubated at 37 °C in complete growth medium with 500 nM NA-647 or 500 nM NA-647 and 2 μM poly(M6Pn)$_{\text{short}}$ for the indicated time, then washed and analysed by live-cell flow cytometry. The MFI (mean fluorescence intensity) was measured relative to background fluorescence from untreated K562 cells. **c**, **d**, Biotinylated poly(M6Pn) LYTACs direct NA-647 to lysosomes in K562 cells (**c**) and Jurkat cells (**d**). Cells were incubated with PBS, 500 nM NA-647, or 500 nM NA-647 and 2 μM biotinylated poly(M6Pn)$_{\text{short}}$ for 0.5–1 h in complete growth medium. NA-647 (red) colocalized with acidic endosomes and lysosomes as labelled with LysoTracker Green (turquoise). Scale bar, 20 μm. Fluorescence intensity is normalized in the NA-647 channel for all images. For **c**, **d**, data are representative of two independent experiments. For **b**, data are mean ± s.d. of three independent experiments.

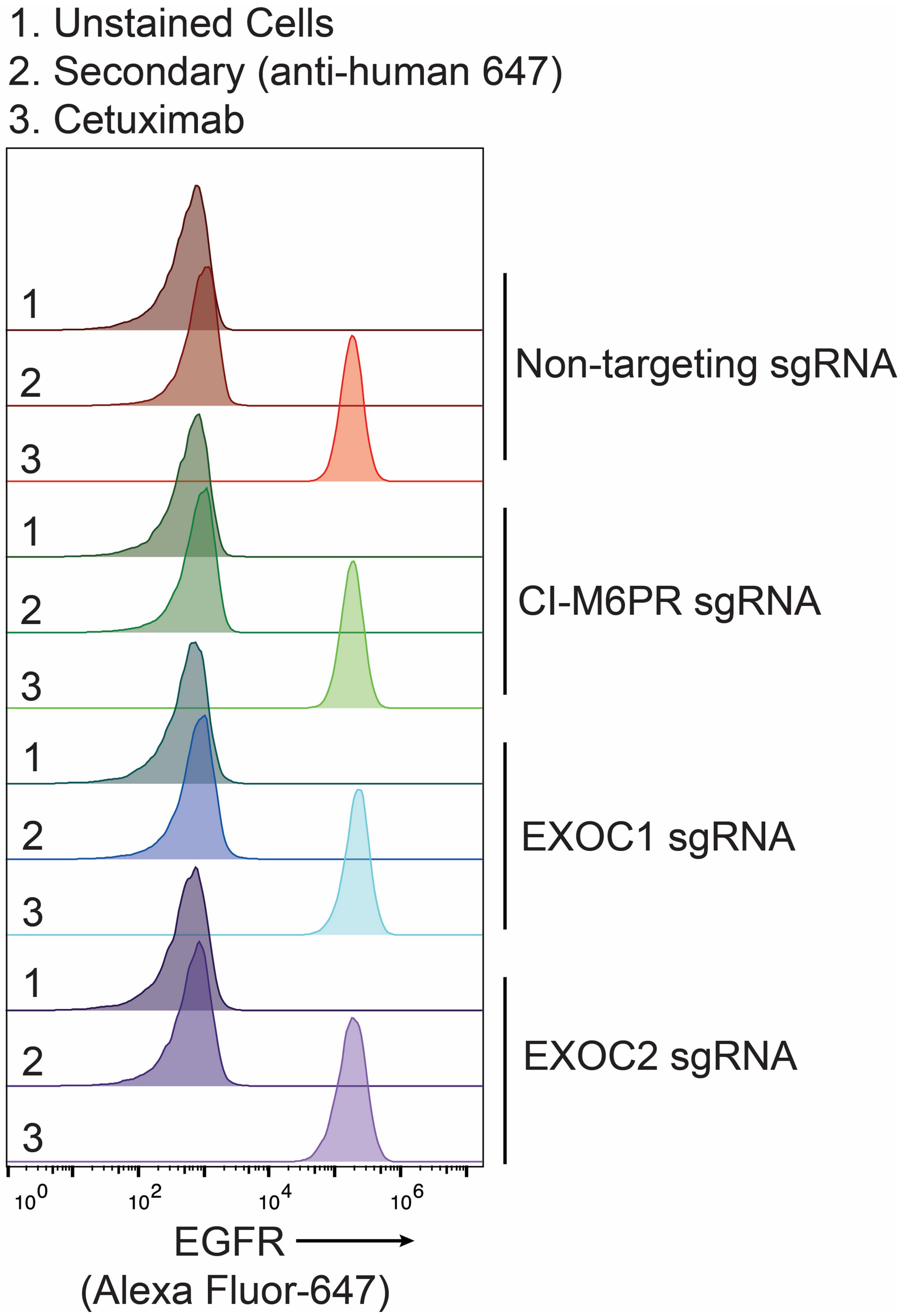

Extended Data Fig. 3 | EGFR surface levels are unchanged upon *EXOC1* and *EXOC2* knockdown in HeLa cells. Cetuximab binds equally to dCas9-KRAB HeLa cells transfected with non-targeting sgRNA and cells transfected with sgRNA targeting *IGF2R*, *EXOC1* or *EXOC2*, indicating no change in EGFR surface levels. Cells were subjected to live-cell flow cytometry using cetuximab followed by an anti-human Alexa Fluor-647-conjugated anti-human (anti-human 647) secondary antibody. Data are representative of two independent experiments.

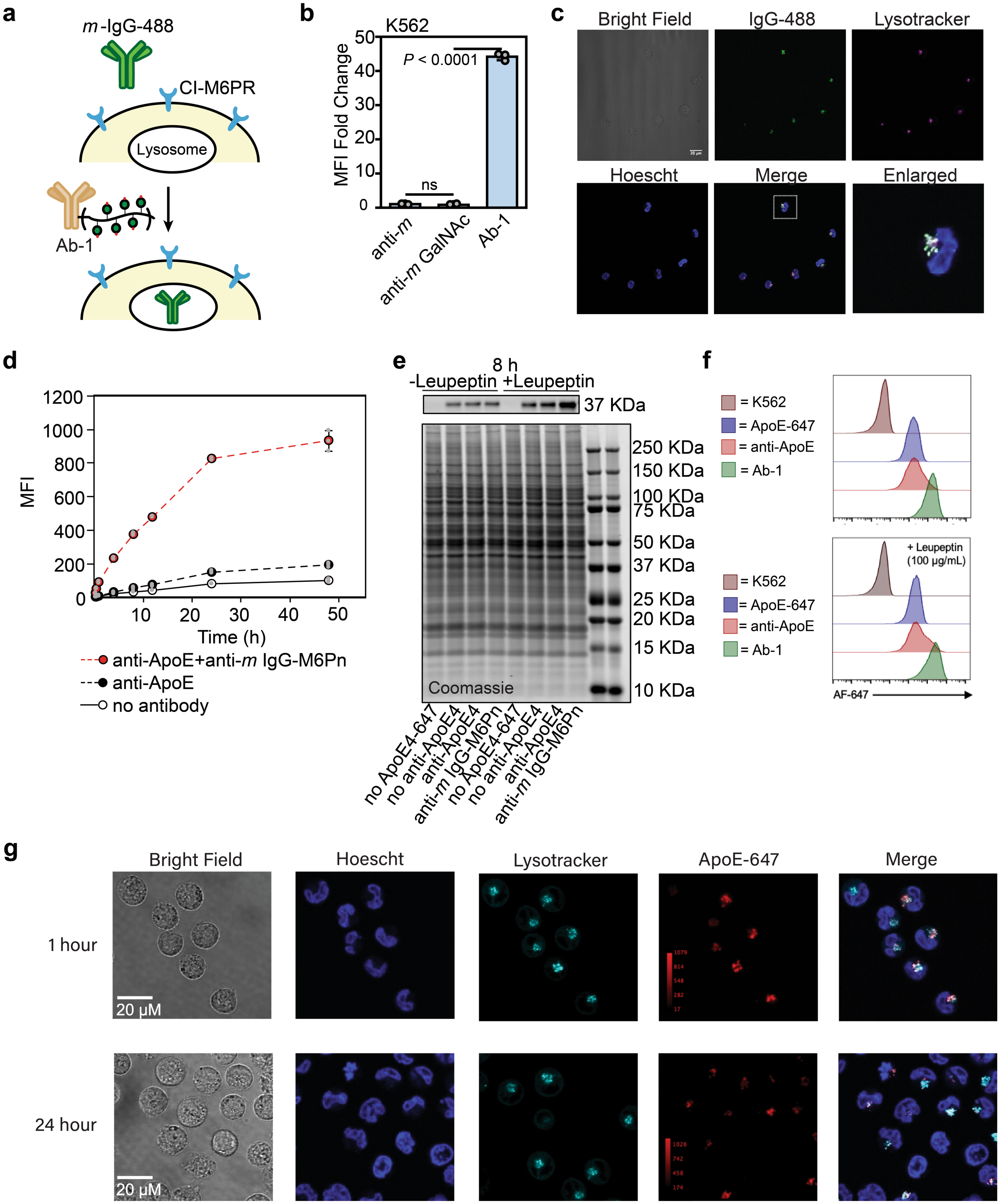

Extended Data Fig. 4 | See next page for caption.

Extended Data Fig. 4 | Ab-1 mediates uptake of soluble proteins to lysosomes. a, Uptake of an Alexa Fluor-488 (AF488)-labelled mouse IgG (*m*-IgG-488) into cells using antibody LYTACs. **b**, Uptake of *m*-IgG-488 using **Ab-1**. Mean fluorescence intensity (MFI) fold change over background uptake measured by live-cell flow cytometry. K562 cells were incubated at 37 °C for 1 h with 50 nM IgG-488 or 50 nM IgG and 25 nM of anti-mouse or **Ab-1**. **c**, AF488 signal (green) colocalized with acidic endosomes and lysosomes as labelled with LysoTracker Red (magenta). Expanded view shows a cell containing IgG-488 and LysoTracker Red. Scale bar, 20 µm. **d**, ApoE4-647 uptake over time. K562 cells were incubated with 50 nM ApoE4-647 in the presence or absence of 25 nM anti-ApoE4 and **Ab-1**. At the indicated time point, cells were aliquoted and median fold intensity (MFI) measurements were measured by live-cell flow cytometry. **e**, Total protein levels for leupeptin inhibition of apoE4 degradation in K562 cells, corresponding to lanes shown in Fig. 3h. Total protein was visualized by Coomassie stain. **f**, Flow cytometry plots of ApoE4-647 uptake over time, with or without leupeptin inhibition. **g**, Uptake of ApoE4-647 to lysosomes. K562 cells were incubated with PBS, 50 nM ApoE4-647, 25 nM anti-ApoE4 and 25 nM Ab-1 for 1 h or 24 h in complete growth media at 37 °C. Alexa Fluor-647 signal (red) colocalizes with acidic endosomes and lysosomes as labelled with LysoTracker Green (turquoise). Data are representative of two (**c**, **e**–**g**) independent experiments. Data are mean ± s.d. of three independent experiments (**b**, **d**). *P* values were determined by unpaired two-tailed *t*-tests; fold changes are reported relative to incubation with protein targets alone (**b**) or background fluorescence (**d**).

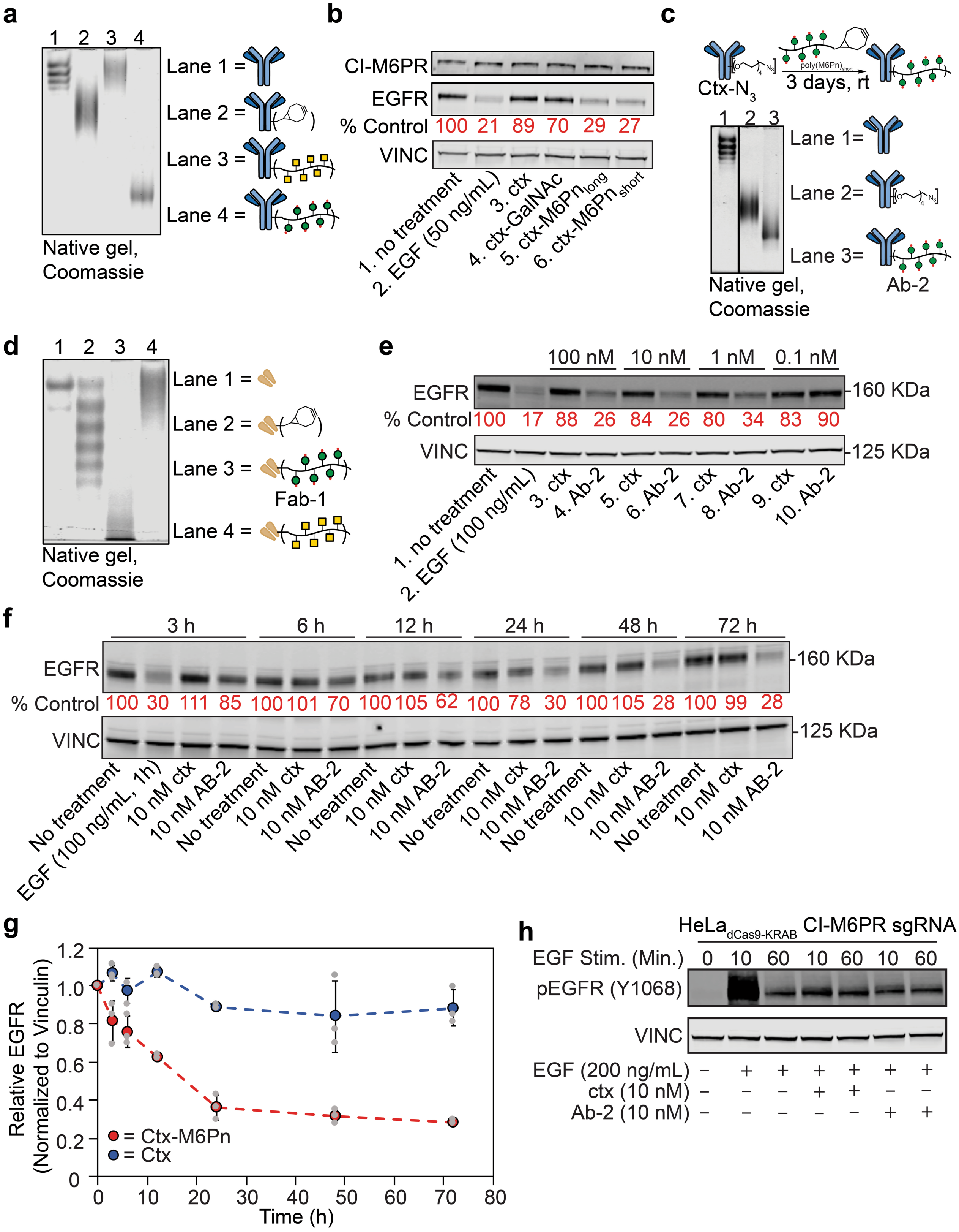

Extended Data Fig. 5 | See next page for caption.

Extended Data Fig. 5 | Optimization of LYTAC-mediated EGFR degradation. **a**, Native gel of cetuximab (ctx)-based LYTACs. **b**, Levels of EGFR in HeLa cells treated with 100 nM ctx (lane 3), ctx-GalNAc (lane 4), ctx-M6Pn$_{long}$ (lane 5) or ctx-M6Pn$_{short}$ (lane 6) for 24 h in complete growth medium. EGF stimulation is a positive control for EGFR downregulation. **c**, Synthesis of linker-swapped **Ab-2**. Ctx was labelled with NHS-PEG$_4$-N$_3$, then incubated with BCN-functionalized poly(M6Pn)$_{short}$ for 3 days at room temperature. Reaction progress was monitored by native gel electrophoresis and visualized with Coomassie stain. **d**, Native gel of ctx-Fab-based LYTACs. **e**, EGFR levels in dCas9-KRAB HeLa cells transfected with non-targeting sgRNA against *GAL4* after incubation with 100 nM, 10 nM,1 nM, or 0.1 nM conjugates for 36 h in complete growth medium. **f**, EGFR levels in dCas9-KRAB HeLa cells transfected with non-targeting *GAL4* sgRNA incubated with **Ab-2** or ctx for the indicated time. **g**, Quantification of LYTAC or ctx-mediated EGFR degradation in dCas9-KRAB HeLa expressing *GAL4* sgRNA over time as read out by western blot relative to untreated cells. **h**, Levels of pEGFR in dCas9-KRAB HeLa cells expressing an sgRNA targeting *IGF2R* after 24 h incubation with 10 nM ctx or **Ab-2**, then incubation with EGF for 10 or 60 min. Data are representative of two (**a**–**e**, **h**) or three (**f**) independent experiments. For **g**, data are mean ± s.d. of three independent experiments, one of which is shown in **f**. Per cent control was calculated by densitometry and normalized to loading control (**b**, **e**, **f**).

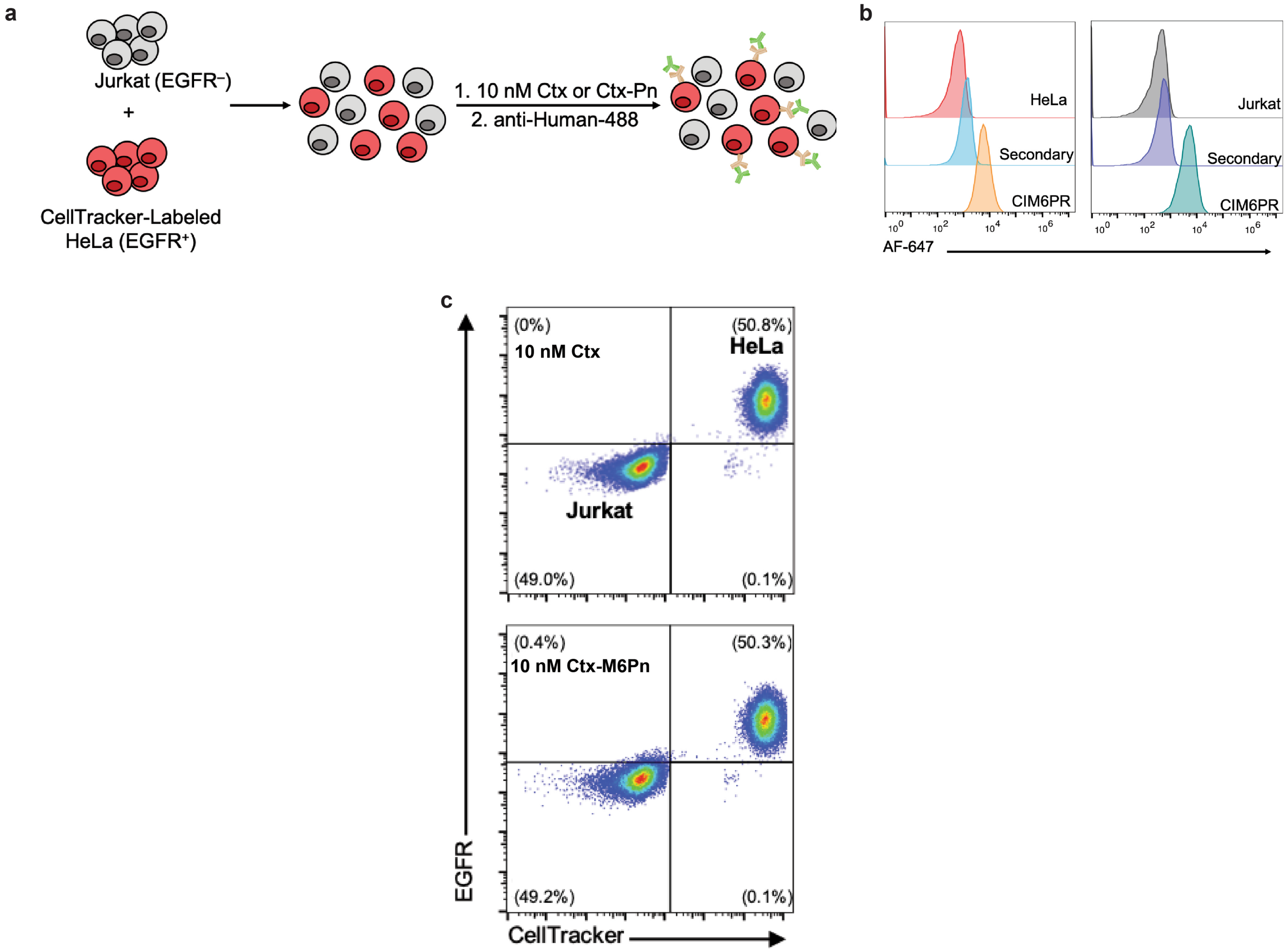

Extended Data Fig. 6 | Mixed-cell assay demonstrates that binding specificity is comparable between ctx-M6Pn and ctx. a, Scheme for mixed cell assay. HeLa cells were lifted and labelled with CellTracker Deep Red, then mixed in a 1:1 ratio with Jurkat cells. The mixed cell sample was stained with either 10 nM ctx or ctx-M6Pn conjugate, followed by anti-human 488, then subjected to live-cell flow cytometry. **b**, Cell surface CI-M6PR levels on HeLa cells (CIM6PR$^+$EGFR$^+$) and Jurkat cells (CIM6PR$^+$EGFR$^-$) were measured by live-cell flow cytometry. HeLa and Jurkat cells exhibited similar levels of cell-surface CI-M6PR. **c**, Ctx and ctx-M6Pn exhibit equivalent binding to HeLa cells, and ctx-M6Pn exhibits minimal increased binding to Jurkat cells relative to ctx. Data are representative of two independent experiments (**b**) or two experimental replicates (**c**).

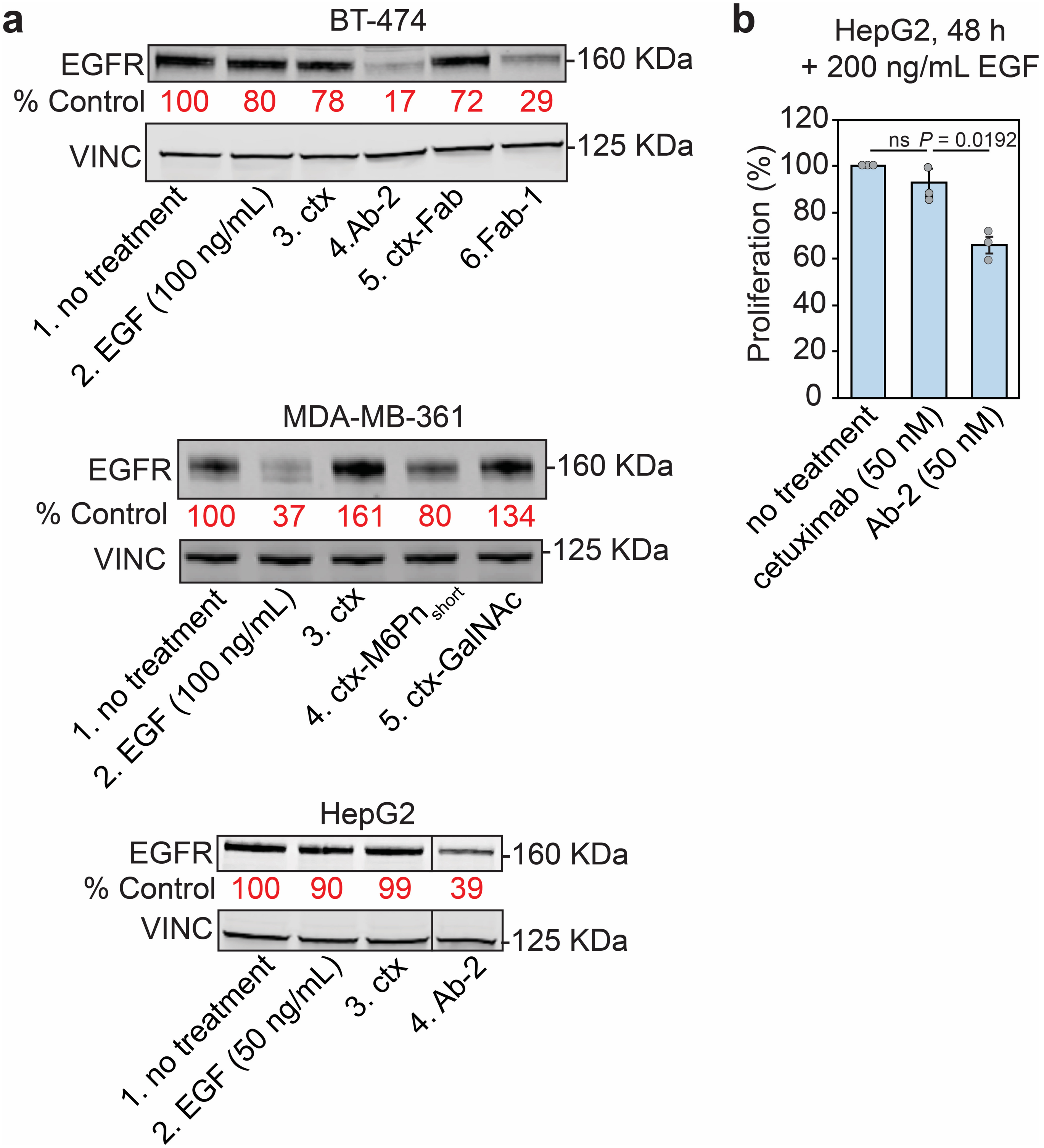

Extended Data Fig. 7 | LYTACs mediate EGFR degradation in multiple cell lines. **a**, EGFR levels in BT-474, MDA-MB-361, or HepG2 cells after incubation with 10–20 nM conjugates. **b**, Proliferation of HepG2 cells in the presence of EGF (200 ng ml^{-1}) and 50 nM cetuximab or **Ab-2**. Cells were incubated with EGF and antibodies for 48 h, and proliferation measured using an MTS assay. Data are representative of three independent experiments (**a**). For **b**, data are mean ± s.e.m. of three independent experiments. *P* values were determined by unpaired two-tailed *t*-tests. Per cent control was calculated by densitometry and normalized to loading control.

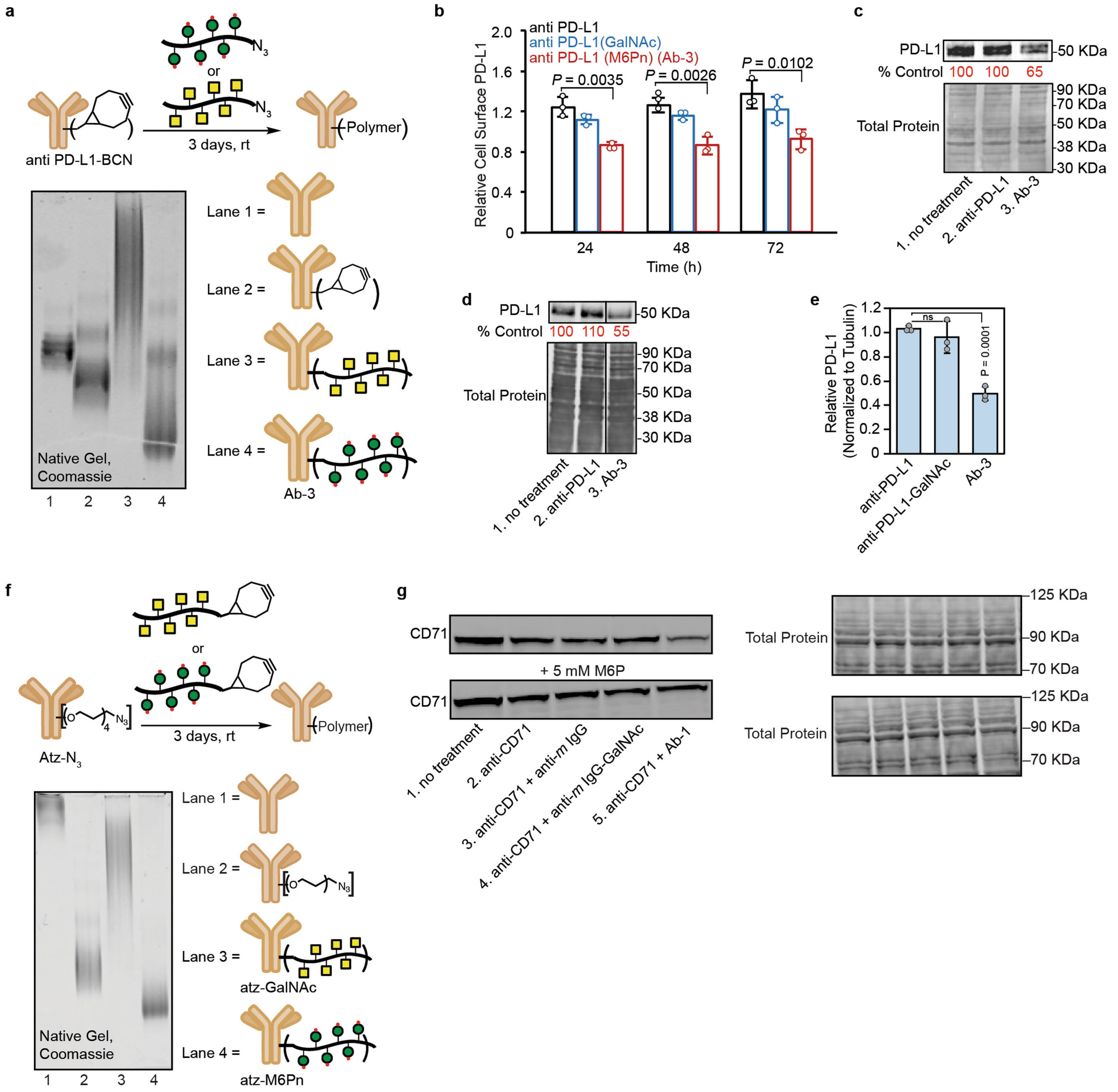

Extended Data Fig. 8 | Synthesis of anti PD-L1 glycopolypeptide conjugates, PD-L1 degradation, and CD71 degradation depends on M6P binding. **a**, Anti-PD-L1 was non-specifically labelled with BCN, then incubated with poly(M6Pn)$_{short}$ for 3 days at room temperature. Reaction progress was monitored by native gel electrophoresis and visualized by Coomassie stain. **b**, Cell-surface PD-L1 determined by live-cell flow cytometry after incubation with anti-PD-L1 or conjugates (50 nM). At each time point, cells were washed, lifted, brought to 4 °C, then stained for PD-L1 using excess unconjugated anti-PD-L1 (1 μM). **c**, PD-L1 levels in MDA-MB-231 cells after 48-h incubation with anti-PD-L1 or **Ab-3**. **d**, PD-L1 levels in HDLM-2 cells after 36 h incubation with anti-PD-L1 or **Ab-3**. **e**, Quantification of PD-L1 degradation in HDLM-2 cells with **Ab-3**. **f**, Atezolizumab was non-specifically labelled with NHS-(PEG)$_4$-N$_3$, then incubated with poly(M6Pn)$_{short}$-BCN for 3 days at room temperature. Reaction progress was monitored by native gel electrophoresis and visualized by Coomassie stain. **g**, Levels of CD71 in Jurkat cells after 24 h in the presence of 5 mM M6P. Data are representative of two (**a**, **c**, **f**, **g**) independent experiments. For **b**, data are mean ± s.d. of three independent experiments, and cell surface levels are relative to untreated cells. For **e**, data are mean ± s.d. of three independent experiments, one of which is shown in **d**. Per cent control was calculated by densitometry and normalized to loading control.

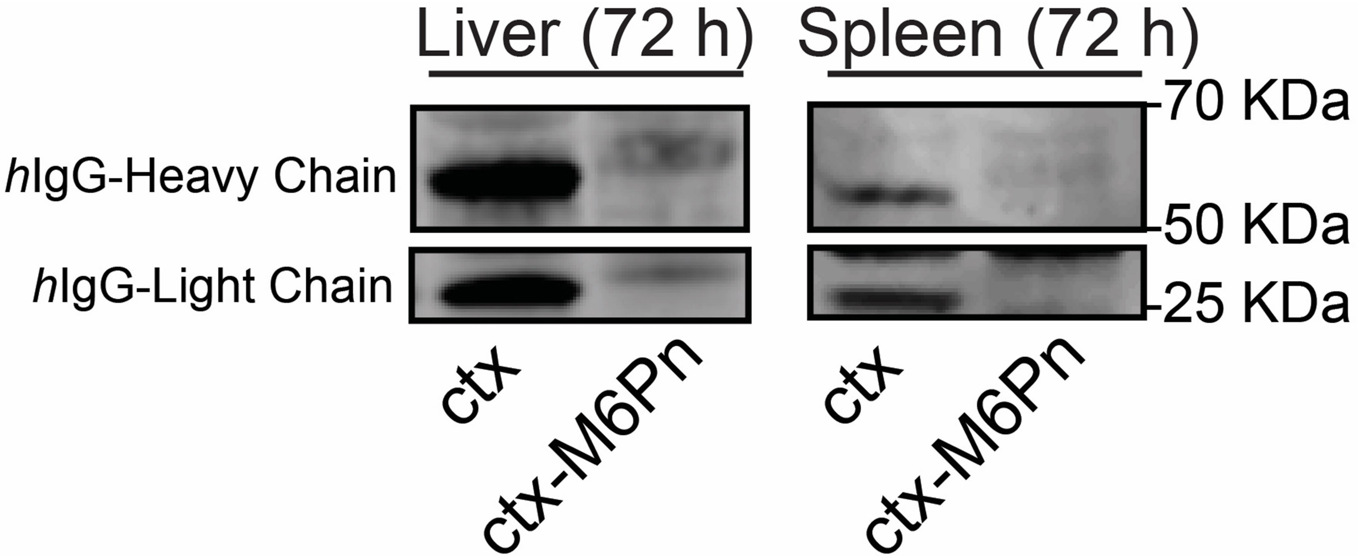

Extended Data Fig. 9 | Human IgG in select mouse tissues. Livers and spleens were collected from mice 72 h after intraperitoneal injection of ctx or ctx-M6Pn. Data are representative of three independent groups, one mouse per treatment per group.

Extended Data Table 1 | Selected examples of proteins with differential abundance after treatment of HeLa cells with ctx or Ab-2

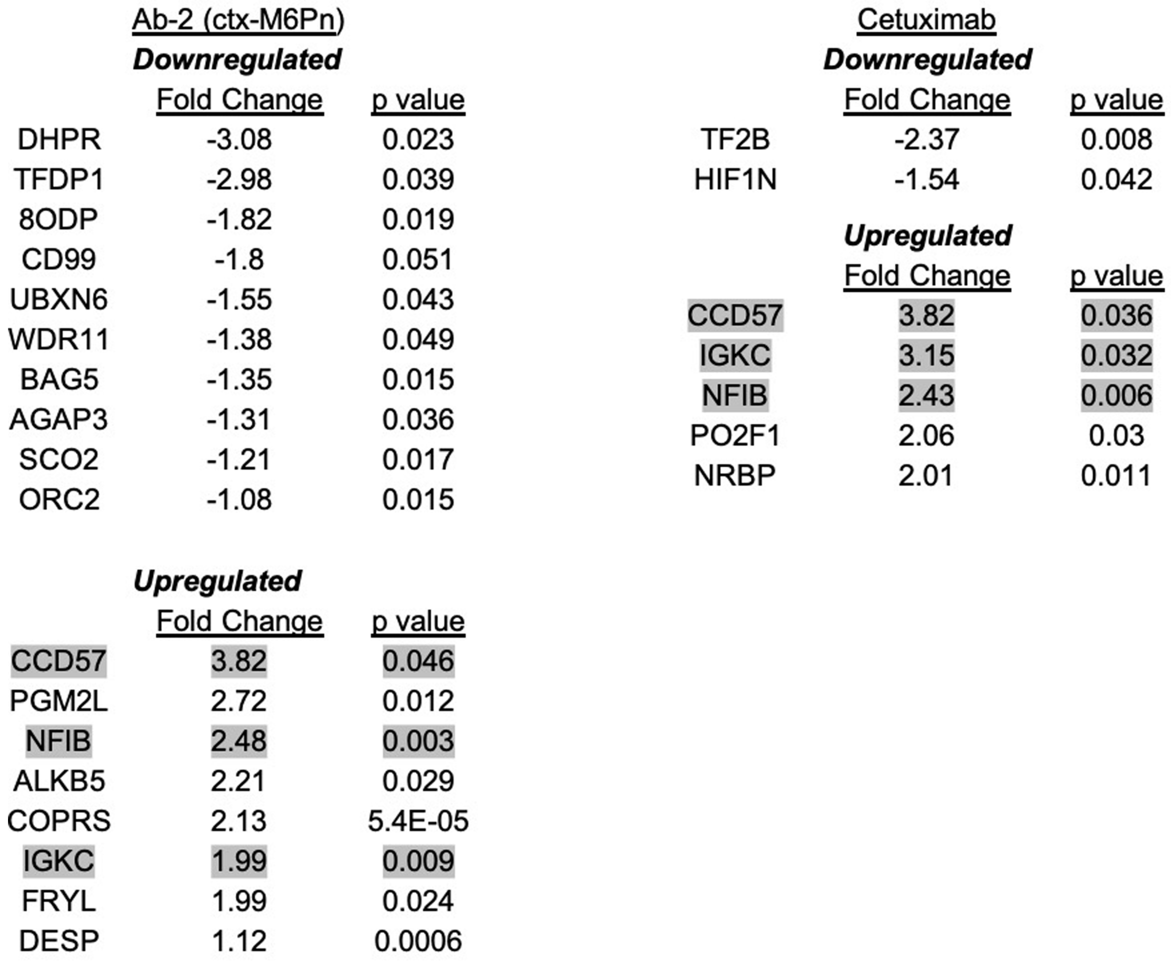

Ab-2 (ctx-M6Pn)

Downregulated

	Fold Change	p value
DHPR	-3.08	0.023
TFDP1	-2.98	0.039
8ODP	-1.82	0.019
CD99	-1.8	0.051
UBXN6	-1.55	0.043
WDR11	-1.38	0.049
BAG5	-1.35	0.015
AGAP3	-1.31	0.036
SCO2	-1.21	0.017
ORC2	-1.08	0.015

Upregulated

	Fold Change	p value
CCD57	3.82	0.046
PGM2L	2.72	0.012
NFIB	2.48	0.003
ALKB5	2.21	0.029
COPRS	2.13	5.4E-05
IGKC	1.99	0.009
FRYL	1.99	0.024
DESP	1.12	0.0006

Cetuximab

Downregulated

	Fold Change	p value
TF2B	-2.37	0.008
HIF1N	-1.54	0.042

Upregulated

	Fold Change	p value
CCD57	3.82	0.036
IGKC	3.15	0.032
NFIB	2.43	0.006
PO2F1	2.06	0.03
NRBP	2.01	0.011

Untreated, ctx-treated, or **Ab-2**-treated HeLa cells were lysed, digested, and analysed by quantitative proteomics. Depicted are exemplary hits with fold change values reported relative to untreated samples. Proteins highlighted in grey were found in both ctx and **Ab-2** treated cells. For a full list, see Supplementary Information. Data are mean of three biological replicates. *P* values were determined by unpaired two-tailed *t*-tests with untreated cells.

nature research

Corresponding author(s): Carolyn R. Bertozzi

Last updated by author(s): Jun 3, 2020

Reporting Summary

Nature Research wishes to improve the reproducibility of the work that we publish. This form provides structure for consistency and transparency in reporting. For further information on Nature Research policies, see Authors & Referees and the Editorial Policy Checklist.

Statistics

For all statistical analyses, confirm that the following items are present in the figure legend, table legend, main text, or Methods section.

n/a	Confirmed	
☐	☒	The exact sample size (*n*) for each experimental group/condition, given as a discrete number and unit of measurement
☐	☒	A statement on whether measurements were taken from distinct samples or whether the same sample was measured repeatedly
☐	☒	The statistical test(s) used AND whether they are one- or two-sided *Only common tests should be described solely by name; describe more complex techniques in the Methods section.*
☒	☐	A description of all covariates tested
☐	☒	A description of any assumptions or corrections, such as tests of normality and adjustment for multiple comparisons
☐	☒	A full description of the statistical parameters including central tendency (e.g. means) or other basic estimates (e.g. regression coefficient) AND variation (e.g. standard deviation) or associated estimates of uncertainty (e.g. confidence intervals)
☐	☒	For null hypothesis testing, the test statistic (e.g. *F*, *t*, *r*) with confidence intervals, effect sizes, degrees of freedom and *P* value noted *Give P values as exact values whenever suitable.*
☒	☐	For Bayesian analysis, information on the choice of priors and Markov chain Monte Carlo settings
☒	☐	For hierarchical and complex designs, identification of the appropriate level for tests and full reporting of outcomes
☒	☐	Estimates of effect sizes (e.g. Cohen's *d*, Pearson's *r*), indicating how they were calculated

Our web collection on statistics for biologists contains articles on many of the points above.

Software and code

Policy information about availability of computer code

Data collection	BD CSampler Plus or FACS Diva (v 8.0) were used for flow cytometry data acquisition. Wyatt ASTRA software package (v 7.0.1.24) was used for GPC data acquisition. Image Studio Software (v 5.2) was used for Western blot scanning. NIS Elements (v 5.11.00) was used for fluorescence microscopy image acquisition. Excalibur (v 4.2) was used for MS data acquisition.
Data analysis	MaxQuant (1.6.3.4) and the Andromeda search algorithm along with Perseus (1.6.22) were used for MS data analysis. MestReNova (v 12.0.3) was used for all chemical NMR analysis. The Wyatt ASTRA software package (v 7.0.1.24) was used for analysis of aqueous GPC data. Microsoft Excel (v 16.23) and Graphpad Prism (v 5.0) were used for data analysis. FlowJo (v 10.0) was used for flow cytometry data analysis. ImageJ (v 1.0) was used for fluorescence microscopy image analysis. Image Studio Software (v 5.2) was used for Western blot quantification.

For manuscripts utilizing custom algorithms or software that are central to the research but not yet described in published literature, software must be made available to editors/reviewers. We strongly encourage code deposition in a community repository (e.g. GitHub). See the Nature Research guidelines for submitting code & software for further information.

Data

Policy information about availability of data

All manuscripts must include a data availability statement. This statement should provide the following information, where applicable:

- Accession codes, unique identifiers, or web links for publicly available datasets
- A list of figures that have associated raw data
- A description of any restrictions on data availability

All data relevant to the manuscript are included, including full data sets from CRISPRi screens and proteomics and source data. Further details and information are available from the corresponding author upon request.

Field-specific reporting

Please select the one below that is the best fit for your research. If you are not sure, read the appropriate sections before making your selection.

☒ Life sciences ☐ Behavioural & social sciences ☐ Ecological, evolutionary & environmental sciences

For a reference copy of the document with all sections, see nature.com/documents/nr-reporting-summary-flat.pdf

Life sciences study design

All studies must disclose on these points even when the disclosure is negative.

Sample size	No statistical method was used to determine sample size. Sample size choice was based on our experience with variability in these assays and our ability to detect meaningful differences between treatments. Variability was low based on our experience with western blot analysis and flow cytometry quantification experiments of protein uptake, degradation experiments, and surface measurement experiments. The sample size for mouse experiments was chosen based on previous experience with respect to the observed variability differences among groups when using western blot analysis of mouse serum to detect meaningful differences between treatments.
Data exclusions	There were no data exclusions except those resulting from technical errors making data interpretation impossible (torn gels, blots, poor gel transfers).
Replication	All data were successfully replicated with multiple biological replicates as indicated in the Figure legends. Experiments in Extended Data Fig. 6c were performed once with two experimental replicates. After two passages post-selection of dCas9-CRISPRi with EXOC1 sgRNA, K562 cells lost the EXOC1 phenotype. Data in Fig. 2 were obtained within one passage of one another.
Randomization	Initial choice of mouse for injection of antibody or conjugate was random. The order of analysis in flow cytometry experiments was randomized. No further formal randomization was employed as internal controls were employed for quantitative comparisons.
Blinding	Sample treatments and subsequent MS sample processing and MS analysis were blinded from one another. No additional blinding was employed for western blot analysis or flow cytometry analysis in order to make comparisons between specific treatments.

Reporting for specific materials, systems and methods

We require information from authors about some types of materials, experimental systems and methods used in many studies. Here, indicate whether each material, system or method listed is relevant to your study. If you are not sure if a list item applies to your research, read the appropriate section before selecting a response.

Materials & experimental systems

n/a	Involved in the study	
☐	☒	Antibodies
☐	☒	Eukaryotic cell lines
☒	☐	Palaeontology
☐	☒	Animals and other organisms
☒	☐	Human research participants
☒	☐	Clinical data

Methods

n/a	Involved in the study	
☒	☐	ChIP-seq
☐	☒	Flow cytometry
☒	☐	MRI-based neuroimaging

Antibodies

Antibodies used

Atezolizumab (A1305, Biovision, lot 4K23A13050, usage varied)

Rabbit anti-pAKT (S473) (9271, Cell Signaling Technologies, lot 14, 1:1000)

Rabbit anti-pEGFR (Y1068) (2234, Cell Signaling Technologies, lot 21, 1:1000)

Rabbit anti-p44/42 MAPK (4376, Clone 20G11, lot 18, Cell Signaling Technologies, 1:1000)

Rabbit anti-EGFR (4267, Clone D38B1, lot 19, Cell Signaling Technologies, 1:1000)

Goat anti-EGFR (AF231, R&D Systems, lot AUC1217071, 1 µg/mL)

Mouse anti-sCD71 (VMA00037, Bio-Rad, lot 09071, 1:1000)

Rabbit anti-PD-L1 (13684, Clone E1L3N, Cell Signaling Technologies, lot 7, 1:500)

Mouse anti-Vinculin (MCA465GA,Clone V284, Bio-Rad, lot 1806, 1:1000)

Mouse anti-alpha-Tubulin (T5168, Clone B-5-1-2, Millipore Sigma, 1:5000)

Rabbit anti-EXOC1 (ab118798, Abcam, 1:2500)

Rabbit anti-CIM6PR (14364, Clone D3V8C, Cell Signaling Technologies, lot 1, 1:1000)

Mouse anti-CD71 (BE0023, Clone OKT-9, BioXCell, usage varied)

Mouse anti-PD-L1 (BE0285, Clone 29E.2A3, BioXCell, usage varied)

Mouse anti-mCherry (orb66657, Clone 5A12A7H10, Biorbyt, usage varied)

Mouse anti-ApoE4 (NBP1-49529, Clone 4E4, Novus Biologicals, lot E-2, usage varied)

Goat anti-Mouse IgG (115-005-062, Jackson ImmunoResearch, usage varied)

Mouse anti-biotin-Alexa Fluor 488 (200-542-211, Jackson ImmunoResearch, lot 119967, usage varied)

Cetuximab, obtained from Eli Lilly (usage varied, 0.1 µM when used for flow cytometry staining, batch IMF406)

Mouse anti-CIM6PR Abcam (ab2733, Clone 2G11, Abcam, lot GR310738-6, 1:500)

Goat anti-mouse IgG-Alexa Fluor 488 (115-545-008, Jackson ImmunoResearch, 1:375)

Goat anti-mouse IgG-Alexa Fluor 647 (115-605-071, Jackson ImmunoResearch, 1:375)

Goat anti-human IgG-Alexa Fluor 647 (109-605-003, Jackson ImmunoResearch, 1:375)

Goat anti-Rabbit IgG 800CW (926-32211, LI-COR, 1:10000)

Goat anti-Mouse IgG 800CW (926-32210, LI-COR, 1:10000)

Donkey anti-Goat IgG 800CW (926-32214, LI-COR, 1:10000)

Goat anti-Rabbit IgG 680LT (926-68021, LI-COR, 1:10000)

Goat anti-Mouse IgG 680LT (926-68020, LI-COR, 1:10000)

Goat anti-Human IgG 800CW (926-32232, LI-COR, 1:1000)

Validation

All antibodies were used for applications validated by antibody suppliers per quality assurance provided by each supplier.

Atezolizumab (A1305, Biovision): https://www.biovision.com/anti-pd-l1-atezolizumab-humanized-antibody.html. Tecentriq is the United States FDA-approved antibody against PD-L1. Binding to PD-L1 verified by knockdown measured by blot with E1L3N (Cell Signaling Technologies) in Fig.4.

anti-pAKT (S473) (9271, Cell Signaling Technologies): https://www.cellsignal.com/products/primary-antibodies/phospho-akt-ser473-antibody/9271. Validated from manufacturer's website and citations therein, validation included stimulation with AKT activating ligands (i.e. PDGF) as well transfection with phospho-inactive AKT mutants.

anti-pEGFR (Y1068) (2234, Cell Signaling Technologies): https://www.cellsignal.com/products/primary-antibodies/phospho-egf-receptor-tyr1068-antibody/2234. Validated from manufacturer's website and citations therein, validation included stimulation with EGF.

anti-p44/42 MAPK (4376, Clone 20G11, Cell Signaling Technologies): https://www.cellsignal.com/products/primary-antibodies/phospho-p44-42-mapk-erk1-2-thr202-tyr204-20g11-rabbit-mab/4376. Validated from manufacturer's website and citations therein. Validation included comparison with p38 and protein levels in the presence and absence of MAPK activating ligands.

anti-EGFR (4267, Clone D38B1, Cell Signaling Technologies): https://www.cellsignal.com/products/primary-antibodies/egf-receptor-d38b1-xp-rabbit-mab/4267. Validated from manufacturer's website and citations therein, validation included EGFR knock-out.

anti-EGFR (AF231, R&D Systems): https://www.rndsystems.com/products/human-egfr-antibody_af231#product-details. Validated from manufacturer's website and citations therein, results cross-validated with anti-EGFR D38B1 (Cell Signaling Technologies) by comparison with Extended Data Fig. 5.

anti-sCD71 (VMA00037, Bio-Rad): https://www.bio-rad-antibodies.com/monoclonal/human-cd71-soluble-antibody-vma00037.html?f=antibody%20only&thirdPartyCookieEnabled=false. Validated from manufacturer's website. Manufacturer's statement: "The PrecisionAb label is reserved for antibodies that meet the defined performance criteria within Bio-Rad's ongoing antibody validation programme."

anti-PD-L1 (13684, Clone E1L3N, Cell Signaling Technologies): https://www.cellsignal.com/products/primary-antibodies/pd-l1-

e1l3n-xp-rabbit-mab/13684. Validated from manufacturer's website and citations therein, validation included demonstration of PD-L1 increases in the presence of absence of IFN-γ.

anti-Vinculin (MCA465GA,Clone V284, Bio-Rad): https://www.bio-rad-antibodies.com/monoclonal/human-vinculin-antibody-v284-mca465.html?f=purified&thirdPartyCookieEnabled=false. Validated from manufacturer's website and citations therein.

anti-alpha-Tubulin (T5168, Clone B-5-1-2, Millipore Sigma): https://www.sigmaaldrich.com/catalog/product/sigma/t5168?lang=en&region=US. Validated from manufacturer's website and citations therein.

anti-EXOC1 (ab118798, Abcam): https://www.abcam.com/exoc1-antibody-ab118798.html. Validated from manufacturer's website and citations therein, validated with CRISPRi knockdown in Fig. 2 of this work.

anti-CIM6PR (14364, Clone D3V8C, Cell Signaling Technologies): https://www.cellsignal.com/products/primary-antibodies/igf-ii-receptor-ci-m6pr-d3v8c-rabbit-mab/14364. Validated from manufacturer's website and citations therein, validated with CRISPRi knockdown in Fig. 2 of this work.

anti-CD71 (BE0023, Clone OKT-9, BioXCell): https://bxcell.com/product/h-cd71/. Validated from manufacturer's website and citations therein.

anti-PD-L1 (BE0285, Clone 29E.2A3, BioXCell): https://bxcell.com/product/invivomab-anti-human-pd-l1-b7-h1/. Validated from manufacturer's website and citations therein.

anti-mCherry (orb66657, Clone 5A12A7H10, Biorbyt): https://www.biorbyt.com/mcherry-antibody-orb66657.html. Validated from manufacturer's website and citations therein. Validated by uptake of recombinant mCherry in Fig. 3.

anti-ApoE4 (NBP1-49529, Clone 4E4, Novus Biologicals): https://www.novusbio.com/products/apoe4-antibody-4e4_nbp1-49529. Validated from manufacturer's website and citations therein.

goat anti-Mouse IgG (115-005-062, Jackson ImmunoResearch): https://www.jacksonimmuno.com/catalog/products/115-005-062. Validated from manufacturer's website and citations therein.

mouse anti-biotin-Alexa Fluor 488 (200-542-211, Jackson ImmunoResearch): https://www.jacksonimmuno.com/catalog/products/200-542-211. Validated from manufacturer's website and citations therein, validated by investigators performing uptake experiments with anti-mouse IgG (Extended Data Fig. 4).

Cetuximab (anti-EGFR) is an United States FDA-approved antibody against EGFR.

anti-CIM6PR (ab2733, Clone 2G11, Abcam): https://www.abcam.com/m6pr-cation-independent-antibody-2g11-ab2733.html. Validated from manufacturer's website and citations therein, validated in Fig. 2 by CRISPRi knockdown.

Goat anti-mouse IgG-Alexa Fluor 488 (115-545-008, Jackson ImmunoResearch): https://www.jacksonimmuno.com/catalog/products/115-545-008. Validated from manufacturer's website and citations therein.

Goat anti-mouse IgG-Alexa Fluor 647 (115-605-071, Jackson ImmunoResearch): https://www.jacksonimmuno.com/catalog/products/115-605-071. Validated from manufacturer's website and citations therein.

Goat anti-human IgG-Alexa Fluor 647 (109-605-003, Jackson ImmunoResearch): https://www.jacksonimmuno.com/catalog/products/109-605-003. Validated from manufacturer's website and citations therein.

Goat anti-Rabbit IgG 800CW (926-32211, LI-COR): https://www.licor.com/bio/reagents/irdye-800cw-goat-anti-rabbit-igg-secondary-antibody. Validated from manufacturer's website.

Goat anti-Mouse IgG 800CW (926-32210, LI-COR): https://www.licor.com/bio/reagents/irdye-800cw-goat-anti-mouse-igg-secondary-antibody. Validated from manufacturer's website.

Donkey anti-Goat IgG 800CW (926-32214, LI-COR, 1:10000): https://www.licor.com/bio/reagents/irdye-800cw-donkey-anti-goat-igg-secondary-antibody. Validated from manufacturer's website.

Goat anti-Rabbit IgG 680LT (926-68021, LI-COR, 1:10000): https://www.licor.com/bio/reagents/irdye-680lt-goat-anti-rabbit-igg-secondary-antibody. Validated from manufacturer's website.

Goat anti-Mouse IgG 680LT (926-68020, LI-COR, 1:10000): https://www.licor.com/bio/reagents/irdye-680lt-goat-anti-mouse-igg-secondary-antibody. Validated from manufacturer's website.

Goat anti-Human IgG 800CW (926-32232, LI-COR, 1:1000): https://www.licor.com/bio/reagents/irdye-800cw-goat-anti-human-igg-secondary-antibody. Validated from manufacturer's website.

Eukaryotic cell lines

Policy information about cell lines

Cell line source(s)	Jurkat, HeLa, MDA-MB-361, MDA-MB-231, THP-1, K562, HEK293, Hep3B, HepG2 and BT474 were obtained from the American Tissue Culture Collection (ATCC), HDLM-2 were obtained from the laboratory of Dr. Thomas Waldmann (NIH), CRISPRi cell lines were obtained from Dr. Michael Bassik's laboratory (Stanford University)

Authentication	Cell lines were authenticated by the supplier, HDLM-2 and CRISPRi lines were not subjected to additional authentication.
Mycoplasma contamination	Cell lines were verified to be mycoplasma negative by Lonza MycoAlert Mycoplasma Detection Assay.
Commonly misidentified lines (See ICLAC register)	No commonly misidentified lines were used.

Animals and other organisms

Policy information about studies involving animals; ARRIVE guidelines recommended for reporting animal research

Laboratory animals	BALB/c mice, female, 6-8 weeks old
Wild animals	No wild animals were involved in this study.
Field-collected samples	This study did not involve collecting samples from the field.
Ethics oversight	IACUC and Stanford APLAC approval# 31511

Note that full information on the approval of the study protocol must also be provided in the manuscript.

Flow Cytometry

Plots

Confirm that:

☒ The axis labels state the marker and fluorochrome used (e.g. CD4-FITC).

☒ The axis scales are clearly visible. Include numbers along axes only for bottom left plot of group (a 'group' is an analysis of identical markers).

☐ All plots are contour plots with outliers or pseudocolor plots.

☒ A numerical value for number of cells or percentage (with statistics) is provided.

Methodology

Sample preparation	For protein uptake experiments in suspension cell lines, cells were incubated for the indicated time with proteins and conjugates, then washed three times with PBS at 4 °C. Cells were then incubated with either Sytox Green or Sytox Red according to the manufacturer's specifications for 15 minutes on ice. For protein uptake experiments in adherent cell lines, cells were incubated for the indicated time with proteins and conjugates, then washed two times quickly with PBS and lifted with trypsin. Cells were transferred to a 96-well V-bottom plate and washed three times with PBS, then incubated with either Sytox Green or Sytox Red according to the manufacturer's specifications for 15 minutes on ice. For surface staining experiments, adherent cells were lifted with non-enzymatic cell dissociation buffer (Gibco) and transferred to a 96-well V-bottom plate, and suspension cells were transferred to a 96-well V-bottom plate. After washing three times with 0.5% BSA in PBS, cells were incubated with primary antibody for 30 minutes on ice. Cells were subsequently washed three times with 0.5% BSA in PBS, then incubated with secondary antibodies for 30 minutes on ice. After incubation, cells were washed three times with 0.5% BSA in PBS and incubated with either Sytox Green or Sytox Red according to the manufacturer's specifications for 15 minutes on ice.
Instrument	BD-Accuri C6 Plus and DxP FACScan for analysis, BD Aria II for sorthing
Software	BD CSampler Plus or FACS Diva were used for data collection, data analysis was performed using the FlowJo software package.
Cell population abundance	N/A
Gating strategy	Gating was based on FSC and SSC area, followed by dead cell removal using a Sytox stain, and doublet removal using FSC-H vs FSC-A.

☒ Tick this box to confirm that a figure exemplifying the gating strategy is provided in the Supplementary Information.

Structural basis of the activation of a metabotropic GABA receptor

https://doi.org/10.1038/s41586-020-2408-4

Received: 16 October 2019

Accepted: 7 April 2020

Hamidreza Shaye[1,2], Andrii Ishchenko[1,2], Jordy Homing Lam[1,3], Gye Won Han[1,2], Li Xue[4], Philippe Rondard[4], Jean-Philippe Pin[4], Vsevolod Katritch[1,2,3], Cornelius Gati[5,6]✉ & Vadim Cherezov[1,2,3]✉

Metabotropic γ-aminobutyric acid receptors ($GABA_B$) are involved in the modulation of synaptic responses in the central nervous system and have been implicated in neuropsychological conditions that range from addiction to psychosis[1]. $GABA_B$ belongs to class C of the G-protein-coupled receptors, and its functional entity comprises an obligate heterodimer that is composed of the GB1 and GB2 subunits[2]. Each subunit possesses an extracellular Venus flytrap domain, which is connected to a canonical seven-transmembrane domain. Here we present four cryo-electron microscopy structures of the human full-length GB1–GB2 heterodimer: one structure of its inactive apo state, two intermediate agonist-bound forms and an active form in which the heterodimer is bound to an agonist and a positive allosteric modulator. The structures reveal substantial differences, which shed light on the complex motions that underlie the unique activation mechanism of $GABA_B$. Our results show that agonist binding leads to the closure of the Venus flytrap domain of GB1, triggering a series of transitions, first rearranging and bringing the two transmembrane domains into close contact along transmembrane helix 6 and ultimately inducing conformational rearrangements in the GB2 transmembrane domain via a lever-like mechanism to initiate downstream signalling. This active state is stabilized by a positive allosteric modulator binding at the transmembrane dimerization interface.

γ-Aminobutyric acid (GABA) is the principal inhibitory neurotransmitter in the central nervous system, counteracting the main excitatory neurotransmitter glutamate and exerting its function via two types of receptor: ionotropic $GABA_A$ receptors, which mediate fast responses[3], and metabotropic G-protein-coupled $GABA_B$ receptors, which elicit slow, prolonged activity—primarily through $G_{i/o}$ proteins[1,4]. $GABA_B$ functions both pre-synaptically to inhibit the release of neurotransmitters, and post-synaptically, which leads to hyperpolarization of the neuron[5,6]. Given the central role of $GABA_B$ in neurobiology, it has previously been linked to various neurological diseases, pain regulation and addiction[7] and represents a major pharmacological target[8]. Therapeutic drugs that target $GABA_B$—such as baclofen (sold under the brand name Lioresal) and β-phenyl-γ-aminobutyric acid (also known as phenibut)—have been used to treat spasticity[9], alcohol addiction[10,11], anxiety and insomnia[12]. Auto-antibodies that target $GABA_B$ have previously been identified at the origin of epilepsies and encephalitis[13], and mutations in *GABBR2* (which encodes GB2) have previously been associated with Rett syndrome and epileptic encephalopathies[14–16].

$GABA_B$ belongs to class C of the G-protein-coupled receptors (GPCRs), along with calcium sensing (CaS), metabotropic glutamate (mGlu) and taste 1 (TAS1) receptors[17]. As opposed to mGlu and CaS receptors (which function in homodimeric forms), the association of two distinct subunits—GB1 and GB2—is required for $GABA_B$ function, although the formation of higher-order $GABA_B$ oligomers has also previously been proposed[2,18]. The heterodimeric assembly is stabilized by the interaction of the two subunits through an intracellular coiled-coil domain, which masks the di-leucine internalization (^{886}EKSRLL^{891}) and endoplasmic reticulum retention (^{923}RSRR^{926}) signals of GB1 and thus allows the trafficking of the heterodimer to the cell surface[19,20]. $GABA_B$ heterodimers use a unique allosteric mechanism for signal transduction, in which the binding of an agonist in the extracellular Venus flytrap domain (VFT) of GB1 leads to G protein activation through a rearrangement of the intracellular interface of the transmembrane domain (TMD) of GB2[21,22]. The structural basis of this allosteric mechanism has previously been studied by X-ray crystallography of soluble VFT heterodimers, which has revealed molecular rearrangements within the VFTs upon ligand binding[23]. Although this information is instrumental for our understanding of $GABA_B$ signal transduction[24], it lacks key insights into the mechanism of TMD transitions associated with receptor activation.

Here we used single-particle cryo-electron microscopy (cryo-EM) to obtain full-length $GABA_B$ structures in four distinct conformations (Fig. 1) along the receptor activation path from an inactive apo state to the active state, stabilized by both an agonist and a positive allosteric modulator (PAM). These structures reveal how the agonist-induced transformations at the level of the VFT heterodimer lead to conformational changes of the TMDs to trigger intracellular signalling.

---

[1]Bridge Institute, USC Michelson Center for Convergent Biosciences, University of Southern California, Los Angeles, CA, USA. [2]Department of Chemistry, University of Southern California, Los Angeles, CA, USA. [3]Department of Biological Sciences, University of Southern California, Los Angeles, CA, USA. [4]Institut de Génomique Fonctionnelle (IGF), CNRS, INSERM, Université de Montpellier, Montpellier, France. [5]Biosciences Division, SLAC National Accelerator Laboratory, Menlo Park, CA, USA. [6]Department of Structural Biology, Stanford University, Stanford, CA, USA. ✉e-mail: cgati@stanford.edu; cherezov@usc.edu

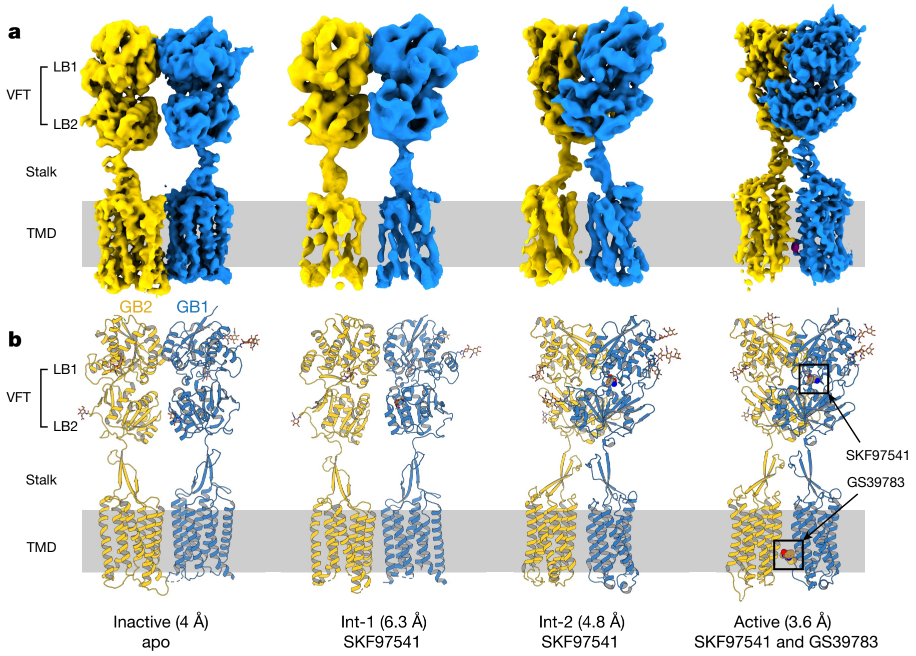

Inactive (4 Å)
apo

Int-1 (6.3 Å)
SKF97541

Int-2 (4.8 Å)
SKF97541

Active (3.6 Å)
SKF97541 and GS39783

Fig. 1 | Cryo-EM maps and models of the GABA$_B$ heterodimer. a, **b**, Maps (**a**) and models (**b**) are shown for four different conformations of GABA$_B$, including active and inactive states and two intermediate conformations. The numbers in parentheses indicate the estimated resolution of the cryo-EM maps. GB1 and GB2 are coloured in blue and yellow, respectively. The agonist (SKF97541)- and PAM (GS39783)-bound state is labelled as active, with a caveat that the fully active state can only be observed in complex with a G protein or other transducer.

Determining the cryo-EM structure

After establishing expression and purification protocols using the co-expression of both GB1 and GB2 subunits in insect cells (Extended Data Fig. 1), we collected an initial dataset of the GB1–GB2 heterodimer in digitonin micelles in the presence of 3-aminopropyl(methyl) phosphinic acid (SKF97541), a GABA$_B$ agonist that is ten times more potent than baclofen. SKF97541 has previously been shown to penetrate the central nervous system[25], and has demonstrated antidepressant activity in vivo[26]. We verified that both ligand binding and the signalling response of the GABA$_B$ construct we used for determining the cryo-EM structure are identical to those of the wild-type receptor (Fig. 2e, f). Our cryo-EM data revealed two substantially different conformations of GABA$_B$, one at a resolution of 6.3 Å and the other at 4.8 Å (Fig. 1, Extended Data Figs. 2, 3, Extended Data Table 1). The first reconstruction showed poorly resolved TMDs, whereas the VFTs adopted a conformation that was intermediate between the previously described apo and agonist-bound crystal structures[23]. The second reconstruction showed an active-like form, in which the two TMDs were in contact with each other, and the VFTs matched the agonist-bound crystal structure (Protein Data Bank code (PDB) 4MS3) within a root mean square deviation (r.m.s.d.) of 2.1 Å. We attributed the limited resolution of these structures to the fact that the agonist-bound receptor was in a dynamic equilibrium between the two states, which we dubbed intermediate state 1 and 2 (int-1 and int-2), and could not be locked in a fully active conformation without a G protein or another allosteric partner.

In an attempt to stabilize the receptor in its active state, we collected a second dataset of GABA$_B$ in the presence of both the agonist SKF97541 and the PAM GS39783, which has previously demonstrated anxiolytic activity without the side effects that are associated with baclofen[27]. Indeed, we observed a single receptor conformation that achieved an overall resolution of 3.6 Å (Figs. 1, 3a, Extended Data Figs. 3, 4, Extended Data Table 1), enabling confident modelling of most amino acid side chains.

Finally, we collected a third dataset of the ligand-free (apo) form of the receptor at 4 Å resolution. This structure differs markedly from all of the ligand-bound states we reconstructed, and represents the starting point of the activation pathway (Figs. 1, 2a, Extended Data Figs. 3, 5, Extended Data Table 1).

Overall structure of GABA$_B$ heterodimer

The overall GABA$_B$ structure reveals a heterodimeric arrangement of the two subunits (Figs. 1, 2a), in which each subunit contains an extracellular VFT attached to the canonical TMD via a stalk domain. Both VFTs consist of two lobes (which we refer to as LB1 and LB2) connected by a hinge that allows the sampling of a range of conformations, from fully open to fully closed. The heterodimeric association of the VFTs is mediated by the two LB1s interacting with each other in a side-by-side orientation, facing opposite directions. The structure of the stalk is distinct from the cysteine-rich domain that connects the VFT and TMD domains in other class-C GPCRs[28]. The stalk consists of a twisted three-stranded β-sheet that bundles the linker between the VFT and TMD with the long extracellular loop 2 (ECL2) of the TMD (Fig. 2c). This secondary structure element ensures a strong pairing between the two main domains, by directly connecting the VFT with transmembrane helices TM1, TM4 and TM5, as well as with TM3 through a conserved disulfide bond (C^{ECL2}–$C^{3.29}$; superscript refers to generic residue numbering in class-C GPCRs[29]). The junction sites between the stalks and the VFTs in both subunits are strengthened by ionic interactions between positively and negatively charged residues, which sustained throughout our molecular dynamics simulations—despite fluctuations of the VFTs (Fig. 2c, d). Bending and twisting modes of the VFTs were observed in the inactive and active states, respectively, and there were stronger ionic contacts and smaller amplitudes of motion in the active state (Extended Data Fig. 6a, b, d, e).

Effects of agonist binding

Our apo structure at 4 Å resolution allowed us to model the majority of side chains and detailed arrangements within the main structural domains of GB1–GB2 (Fig. 2a). We observed that in the apo state the two GABA$_B$ subunits interact through their LB1s and the intracellular

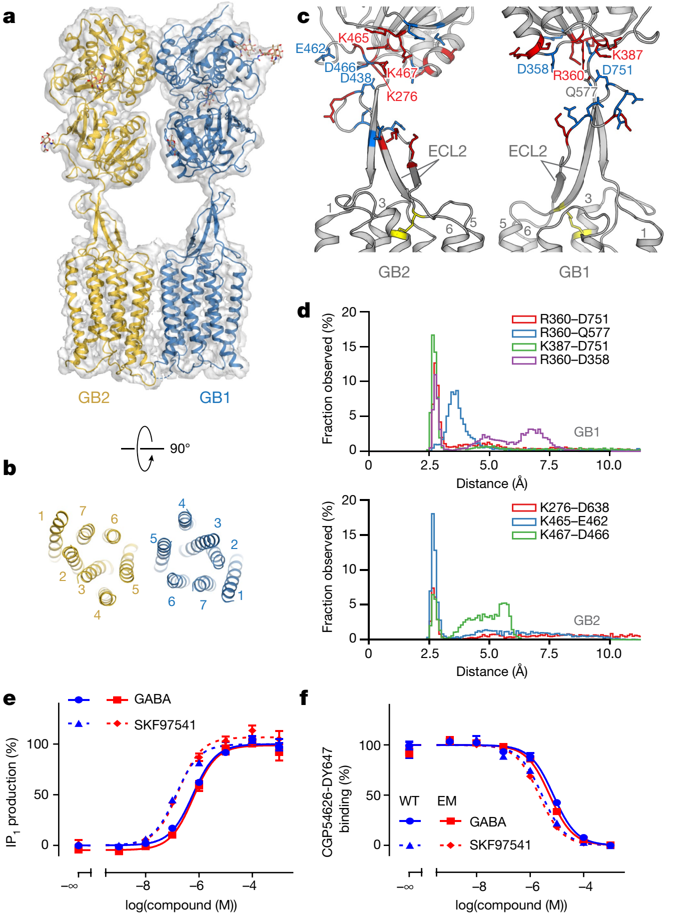

Fig. 2 | Structural details of GABA$_B$ in the inactive apo state. **a**, Overall view of the apo GABA$_B$ model and map. **b**, Extracellular view of the GABA$_B$ TMD in the inactive apo state. **c**, Structure of the stalk domains. The junctions between the stalks and the VFTs are stabilized by a network of electrostatic interactions between positively (red) and negatively (blue) charged residues. The disulfide bond between ECL2 and TM3 is shown as yellow sticks. **d**, Distribution of distances for ionic interactions between the stalk and VFT in GB1 and GB2 obtained from molecular dynamics simulations of apo GABA$_B$. **e**, IP$_1$ production mediated by the wild-type receptor (blue) or the construct used for cryo-EM (red) upon stimulation with GABA (solid line) or SKF97541 (dotted line). **f**, Displacement of the non-permeant antagonist CGP54626-DY647 by GABA (solid line) or SKF97541 (dotted line) from the wild-type receptor (WT, blue) or the construct used for cryo-EM (EM, red). Data shown in **e** and **f** are normalized by the wild-type response and presented as mean ± s.e.m. of four biologically independent experiments.

tips of TM3 and TM5 (Extended Data Figs. 5i, 6c). Consistent with the crystal structure of the soluble heterodimeric apo VFT (PDB 4MQE) (r.m.s.d. = 1.3 Å) (Extended Data Fig. 7a), both VFTs are in a fully open conformation with a maximal separation of 47.6 Å between the C-terminal ends of the LB2s.

Agonist binding results in two intermediate states that exist in a dynamic equilibrium (Fig. 1, Supplementary Video 1). In the int-1 state, the VFT of GB1 is partially closed at about 20% of the total amplitude, as compared to the fully closed and fully open crystal structures. This closure is accompanied by a rotation of both VFTs with respect to the TMDs (Fig. 4a). At the same time, the two LB2s remain separated and the TMDs face each other via TM5. In addition, the TM3–TM5 interaction between the TMDs is probably released in the int-1 state, which would result in a more dynamic conformation—this is underlined by the substantially lower resolution of this structure.

The int-2 state shows a complete closure of the VFT of GB1, consistent with the previous crystal structures of the agonist-bound VFTs[23].

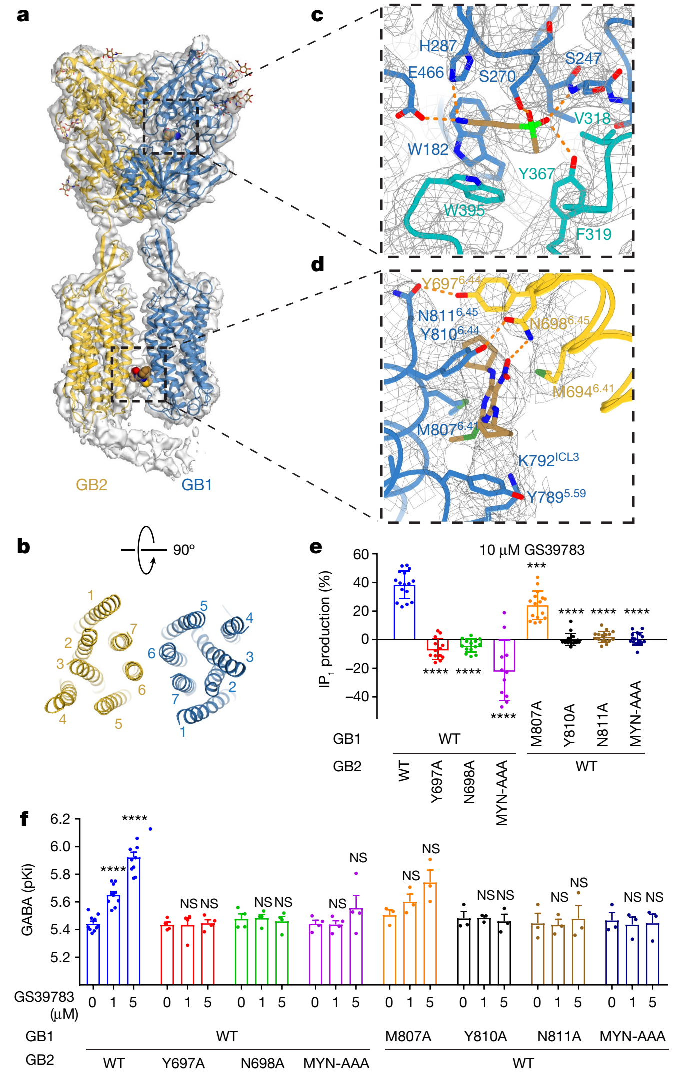

Fig. 3 | Structure of the active-state GABA$_B$, and details of agonist and PAM binding. **a**, Overall view of GABA$_B$ model and map in the active agonist- and PAM-bound conformation. Elongated density interacting with the intracellular part of GB2 resembles the coiled-coil domain. **b**, Extracellular view of GABA$_B$ TMD in the active conformation. **c**, Enlarged view of the ligand-binding pocket in the VFT of GB1. SKF97541 activates GABA$_B$ by interacting with LB1 (blue) and LB2 (teal) of GB1. **d**, Binding of the PAM (GS39783) further stabilizes the GABA$_B$ active state by interacting with TMD residues from both GB1 and GB2. SKF97541 and GS39783 are shown as sticks with carbon atoms coloured in sand; oxygen in red; nitrogen in blue; phosphorus in light green; and sulfur in dark green. **e**, IP$_1$ production induced by 10 μM GS39783 in intact HEK293 cells that express the indicated subunit combinations. Values are mean ± s.d. from seven biologically independent experiments. Data are normalized by GABA response and analysed using one-way analysis of variance (ANOVA) with Dunnett's multiple comparison test to determine significance (compared with wild type), with ****$P < 0.0001$ for all, except for GB1(M807A) (***$P = 0.013$). **f**, pKi values for GABA, determined from displacement of CGP54626-DY647 binding in intact cells that express the indicated subunit combinations in the absence or presence of 1 or 5 μM GS39783. The number of biologically independent experiments is given in Extended Data Table 2. Data were analysed using one-way ANOVA with Dunnett's multiple comparison test to determine significance (compared with no GS39783 for the same combined subunits). ****$P \leq 0.0001$; not significant (NS), $P > 0.05$. For 1 μM or 5 μM GS39783, $P = 0.9994$ or 0.8166, respectively, for GB2(Y697A); 0.9672 or 0.8849, respectively, for GB2(N698A); 0.9934 or 0.4946, respectively, for GB2(MYN-AAA); 0.5504 or 0.2972, respectively, for GB1(M807A); 0.9981 or 0.5843, respectively, for GB1(Y810A); 0.9605 or 0.7139, respectively, for GB1(N811A); and 0.8819 or 0.9318, respectively, for GB1(MYN-AAA). In **e**, **f**, GB1(MYN-AAA) refers to a triple mutant (M807A/Y810A/N811A) of GB1, and GB2(MYN-AAA) refers to a triple mutant (M694A/Y697A/N698A) of GB2.

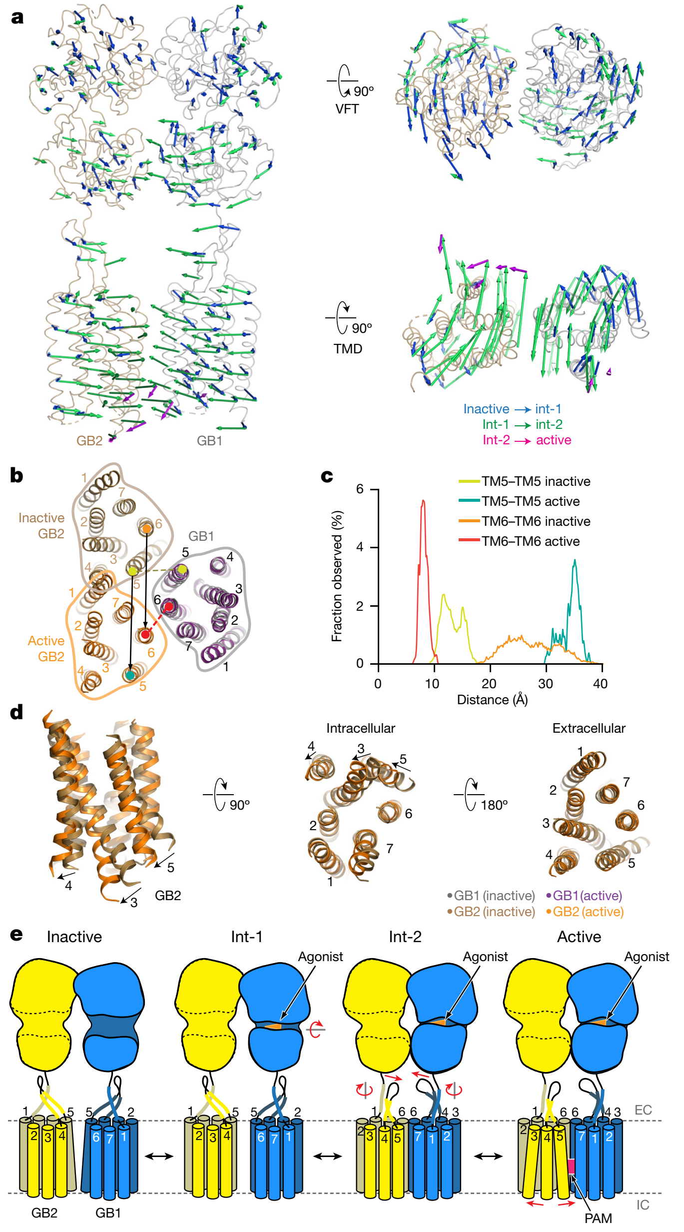

Fig. 4 | Activation-related transitions in GABA$_B$. **a**, Overall view of apo GABA$_B$, indicating the conformational changes from inactive apo through two intermediate agonist-bound to active agonist- and PAM-bound states. Activation, initiated by the agonist binding and a closure of the VFT of GB1 (blue arrows), propagates to large-scale translations of the TMDs in the int-2 state (green arrows). PAM binding induces an additional conformational change within the TMD of GB2 (magenta arrows). **b**, Extracellular view of the GABA$_B$ TMDs in the inactive and active states aligned by the GB1 TMD demonstrates an approximately 30 Å (black arrows) relative movement of the GB2 TMD. During this transition, the interface between TMDs changes from TM5 (inactive state) to TM6 (active state); the TM6–TM6 distance (red dash) decreases from 30.3 Å to 8.4 Å and the TM5–TM5 distance (olive dash) increases from 13.1 Å to 37 Å, consistent with previously published cross-linking data[30]. **c**, Distribution of the TM5–TM5 and TM6–TM6 distances in the inactive apo and active agonist- and PAM-bound states as observed in molecular dynamics simulations. **d**, Shifts of TM3 and TM5 by about 6 Å on the intracellular side of GB2 upon agonist and PAM binding open a cleft for the engagement of a G protein. **e**, Cartoon illustrates activation-related transitions from the inactive apo state, through the agonist-bound intermediate states, to the agonist- and PAM-bound active state. In the inactive state, both VFTs adopt fully open conformations, and their LB2s are well-separated. Agonist binding closes the VFT of GB1, bringing the LB2s in contact. These transformations at the level of VFTs propagate through the stalks towards the TMDs, resulting in their mutual reorientation and formation of a contact interface along TM6. PAM binding further stabilizes the active state, leading to substantial shifts of the intracellular ends of TM3 and TM5, which open up a cleft for the engagement of G proteins or other transducers. EC, extracellular; IC, intracellular.

This closure brings the two LB2s in contact, and decreases the distance between their C-terminal ends from 42 to 32 Å (Fig. 4a). This conformational rearrangement of the VFTs propagates through the stalks, which leads to a relative motion of the TMDs that can be presented as a 30 Å translation of the TMD of GB2 with respect to the stationary TMD of GB1 (Fig. 4a, b). As a result of these transformations, the two TMDs come in direct contact through an interface along TM6 (Extended Data Fig. 4g), consistent with previous cross-linking studies[30]. A similar interaction along TM6 has also previously been observed in the agonist-bound mGlu5 homodimer structure[28]. The conformational rearrangement of the TMDs completely changes not only the heterodimer interface (Fig. 4b), but also the overall dynamics of the receptor domains, as observed in our molecular dynamics simulations and normal mode analyses (Figs. 2d, 4c, Extended Data Fig. 6d, e).

PAM stabilizes the active-state conformation

The addition of a PAM along with the orthosteric agonist stabilized the receptor conformation in a state similar to int-2 (r.m.s.d. = 1.0 Å), which resulted in a reconstruction with an overall resolution of 3.6 Å (Fig. 3a) and enabled us to observe activation-related transitions within the TMD of GB2.

The high-resolution structure also revealed the binding details of the orthosteric agonist SKF97541, a close analogue of GABA in which the carboxylic acid moiety is replaced by methylphosphinic acid. Similar to the interactions of GABA in its complex with the VFT of GB1 (PDB 4MS3), binding of SKF97541 is largely defined by its acidic and basic groups. The basic amino moiety of SKF97541 forms polar and ionic interactions with H287 and E466, and the phosphinic acid of SKF97541 makes key hydrogen bonds to S247, S270 and Y367 (Fig. 3c, Supplementary Video 2). The ligand is also sandwiched between the bulky aromatic side chains of W182 and W395. Our molecular dynamics simulations confirmed the stability of these interactions (Extended Data Fig. 6f, j). Most residues interacting with SKF97541 and GABA belong to LB1 of the VFT of GB1, but two of them—Y367 and W395—reside on LB2 and shift by about 2 Å between the int-1 and int-2 states.

The most substantial differences between the agonist-bound (int-2) structure and the agonist- and PAM-bound structure occur within the TMD of GB2, in which TM3 and TM5 straighten and shift on the intracellular side by about 6 Å whereas TM6, which is considered a hallmark of activation in class-A and -B GPCRs, does not move substantially (Fig. 4a, d). By contrast, the conformation of the TMD of GB1 remains mostly unchanged (Extended Data Fig. 7c–f). Notably, the first three structures of the activation cycle (the apo, int-1, and int-2 states) show the same conformation of TM3 and TM5 in the TMD of GB2. The ionic lock between K$^{3.50}$ and D$^{6.35}$, which is highly conserved among class-C GPCRs and is observed in all inactive mGlu crystal structures[24], is intact in GB1 but broken in GB2 in the PAM-bound state. These conformational changes in the TMD of GB2 are most probably required to accommodate binding of the G$_{i/o}$ protein for the initiation of intracellular signalling. This mechanism is further supported by the local resolution and *B*-factor comparison of GB2 (Extended Data Fig. 4e, f), which demonstrates that the intracellular ends of TM3, TM4 and TM5 are the most dynamic parts of the structure. Directly connected to these helices, the intracellular loop 2 (ICL2) and ICL3 of GB2 have previously been identified as crucial for downstream signalling[22,31].

PAM binding site at the heterodimer interface

GS39783 has previously been characterized as a PAM of GABA_B; however, little is known about its binding site and its mechanism of action[32]. We confirmed a positive allosteric effect of GS39783 on both ligand binding and the signalling response of GABA. Additionally, using highly amplified inositol monophosphate (IP_1) assays, we observed that GS39783 alone behaves as an agonist (Extended Data Fig. 1c, d, Extended Data Table 2). After building and refining the agonist- and PAM-bound GABA_B model, we identified two putative binding sites for GS39783 with unexplained residual density. Site 1 is located inside the TMD of GB2 and site 2 is observed at the interface between the TMDs of GB1 and GB2 (Fig. 3d, Supplementary Video 3). Mutations of residues in site 1 inside the TMD of GB2 did not affect either the allosteric or the agonist action of GS39783, which suggests that this is not the main binding site for GS39783 (Extended Data Figs. 8, 9).

On the other hand, the mutation of residues in site 2—which is located at the TM6 heterodimer interface—unambiguously confirmed it as the site of action for GS39783 (Fig. 3e, f, Extended Data Figs. 8, 9). TM6 has a major role in the activation of GABA_B as the sole interface between TMDs, and the binding of GS39783 in between the TM6s can stabilize this interaction. In this site, GS39783 fits well in the experimental density and is anchored by a hydrogen bond with $\text{N698}^{6.45}$ of GB2 and a stacking interaction with $\text{Y810}^{6.44}$ of GB1 (Fig. 3d). Other residues that shape the pocket and interact with GS39783 include $\text{Y789}^{5.59}$, $\text{K792}^{5.62}$, and $\text{M807}^{6.41}$ of GB1, as well as $\text{M694}^{6.41}$ and $\text{Y697}^{6.44}$ of GB2. These interactions are largely preserved in the molecular dynamics simulations of the complex (Extended Data Fig. 6f, i).

We therefore propose that GS39783 has a dual role in GABA_B activation by stabilizing the TM6-mediated dimerization interface[33] and facilitating conformational transitions within the TMD of GB2.

Discussion

In this work, we have determined the 3D structure of the pharmacologically important GABA_B in four distinct conformations along its activation trajectory from an inactive apo to an agonist- and PAM-stabilized active state (Supplementary Video 1), enabling us to propose a model of signal transduction by GABA_B and its modulation by a PAM (Fig. 4e). Upon binding of an agonist, a compaction of the VFTs brings the two TMDs closer together and reorients them to allow direct contact along TM6, consistent with the proposed model based on TMD cross-linking experiments[30] (Fig. 4b). Overall, the observed domain rearrangements associated with the activation of GABA_B resemble the previously published structures of mGlu5[28], which suggests that this activation mechanism is probably conserved among class-C GPCRs. However, there are three major differences between mGlu receptors and GABA_B: GABA_B is a mandatory heterodimer of two noncovalently associated subunits, whereas mGlu receptors function as homodimers with two identical subunits linked via a disulfide bond; although GABA binding in a single subunit (GB1) is sufficient to fully activate the receptor, glutamate binding in both mGlu subunits is required for full activation[34]; and GABA_B lacks a cysteine-rich domain, which is present in each mGlu subunit and connects the VFT with the TMD, increasing the overall size of the receptor. Notably, our GABA_B structures revealed the presence of a relatively rigid stalk composed of the ECL2 hairpin and the linker connecting the VFT with TMD. Similar to the cysteine-rich domain in mGlu receptors, this stalk probably transduces the signal from the VFTs to the TMDs, acting as a lever.

In contrast to the mGlu5 study[28] (in which no conformational changes within the TMDs were reported), we succeeded in reaching an additional activation-related step and captured a PAM-stabilized state of GABA_B with marked changes within the TMD of GB2. Unlike class-A and -B GPCRs (in which receptor activation is associated with a pronounced outward movement of TM6), the amplitude of TM6 motion in GABA_B is constrained by the heterodimeric interface between two subunits. Instead, we observed notable movements of TM3, TM4 and TM5 that opened a cleft on the intracellular side of GB2, potentially to engage a G protein or other transducers. This conformational change may be favoured by the interaction between TM6 from each subunit resulting from the reorientation of the TMDs upon receptor activation, which possibly explains the role proposed for the TMD of GB1 in the activation process[30,33]. We identified the location of a binding site for GS39783 at the interface between the TMDs of the two subunits. GABA_B PAMs can be attractive alternatives to orthosteric agonists owing to their therapeutic potential; however, the lack of knowledge about their binding and mechanism of action has hindered progress in their development.

Our results provide detailed insights into the structural transformations that are associated with the activation of GABA_B, shedding light on the intrinsically asymmetric allosteric mechanism in which the binding of a ligand in the VFT of GB1 translates via the stalks into marked rearrangements of the TMD of GB2. Such an asymmetric transition underlines the unique activation process of GABA_B. Finally, the structural differences between each of the states give important insights into the pharmacological intervention of this receptor, and could potentially result in the design of new allosteric modulators.

Online content

Any methods, additional references, Nature Research reporting summaries, source data, extended data, supplementary information, acknowledgements, peer review information; details of author contributions and competing interests; and statements of data and code availability are available at https://doi.org/10.1038/s41586-020-2408-4.

1. Bowery, N. G. et al. International Union of Pharmacology. XXXIII. Mammalian γ-aminobutyric acid_B receptors: structure and function. *Pharmacol. Rev*. **54**, 247–264 (2002).
2. Comps-Agrar, L. et al. The oligomeric state sets GABA_B receptor signalling efficacy. *EMBO J*. **30**, 2336–2349 (2011).
3. Sieghart, W. Structure, pharmacology, and function of GABA_A receptor subtypes. *Adv. Pharmacol*. **54**, 231–263 (2006).
4. Gassmann, M. & Bettler, B. Regulation of neuronal GABA_B receptor functions by subunit composition. *Nat. Rev. Neurosci*. **13**, 380–394 (2012).
5. Lüscher, C., Jan, L. Y., Stoffel, M., Malenka, R. C. & Nicoll, R. A. G protein-coupled inwardly rectifying K^+ channels (GIRKs) mediate postsynaptic but not presynaptic transmitter actions in hippocampal neurons. *Neuron* **19**, 687–695 (1997).
6. Schuler, V. et al. Epilepsy, hyperalgesia, impaired memory, and loss of pre- and postsynaptic GABA_B responses in mice lacking $\text{GABA}_{\text{B(1)}}$. *Neuron* **31**, 47–58 (2001).
7. Cousins, M. S., Roberts, D. C. S. & de Wit, H. GABA_B receptor agonists for the treatment of drug addiction: a review of recent findings. *Drug Alcohol Depend*. **65**, 209–220 (2002).
8. Vacher, C. M. & Bettler, B. GABA_B receptors as potential therapeutic targets. *Curr. Drug Targets CNS Neurol. Disord*. **2**, 248–259 (2003).
9. Chang, E. et al. A review of spasticity treatments: pharmacological and interventional approaches. *Crit. Rev. Phys. Rehabil. Med*. **25**, 11–22 (2013).
10. de Beaurepaire, R. Suppression of alcohol dependence using baclofen: a 2-year observational study of 100 patients. *Front. Psychiatry* **3**, 103 (2012).
11. Addolorato, G. et al. Baclofen efficacy in reducing alcohol craving and intake: a preliminary double-blind randomized controlled study. *Alcohol Alcohol*. **37**, 504–508 (2002).
12. Lapin, I. Phenibut (β-phenyl-GABA): a tranquilizer and nootropic drug. *CNS Drug Rev*. **7**, 471–481 (2001).
13. Dalmau, J. & Graus, F. Antibody-mediated encephalitis. *N. Engl. J. Med*. **378**, 840–851 (2018).
14. Hamdan, F. F. et al. High rate of recurrent de novo mutations in developmental and epileptic encephalopathies. *Am. J. Hum. Genet*. **101**, 664–685 (2017).
15. Vuillaume, M.-L. et al. A novel mutation in the transmembrane 6 domain of *GABBR2* leads to a Rett-like phenotype. *Ann. Neurol*. **83**, 437–439 (2018)
16. Yoo, Y. et al. *GABBR2* mutations determine phenotype in Rett syndrome and epileptic encephalopathy. *Ann. Neurol*. **82**, 466–478 (2017).
17. Kniazeff, J., Prézeau, L., Rondard, P., Pin, J.-P. & Goudet, C. Dimers and beyond: the functional puzzles of class C GPCRs. *Pharmacol. Ther*. **130**, 9–25 (2011).
18. Stewart, G. D., Comps-Agrar, L., Nørskov-Lauritsen, L. B., Pin, J. P. & Kniazeff, J. Allosteric interactions between GABA_{B1} subunits control orthosteric binding sites occupancy within GABA_B oligomers. *Neuropharmacology* **136**, 92–101 (2018).
19. White, J. H. et al. Heterodimerization is required for the formation of a functional GABA_B receptor. *Nature* **396**, 679–682 (1998).
20. Margeta-Mitrovic, M., Jan, Y. N. & Jan, L. Y. A trafficking checkpoint controls GABA_B receptor heterodimerization. *Neuron* **27**, 97–106 (2000).
21. Galvez, T. et al. Allosteric interactions between GB1 and GB2 subunits are required for optimal GABA_B receptor function. *EMBO J*. **20**, 2152–2159 (2001).

22. Robbins, M. J. et al. $GABA_{B2}$ is essential for G-protein coupling of the $GABA_B$ receptor heterodimer. *J. Neurosci*. **21**, 8043–8052 (2001).
23. Geng, Y., Bush, M., Mosyak, L., Wang, F. & Fan, Q. R. Structural mechanism of ligand activation in human $GABA_B$ receptor. *Nature* **504**, 254–259 (2013).
24. Pin, J.-P. & Bettler, B. Organization and functions of mGlu and $GABA_B$ receptor complexes. *Nature* **540**, 60–68 (2016).
25. Howson, W., Mistry, J., Broekman, M. & Hills, J. M. Biological activity of 3-aminopropyl (methyl) phosphinic acid, a potent and selective $GABA_B$ agonist with CNS activity. *Bioorg. Med. Chem. Lett*. **3**, 515–518 (1993).
26. Frankowska, M., Filip, M. & Przegaliński, E. Effects of $GABA_B$ receptor ligands in animal tests of depression and anxiety. *Pharmacol. Rep*. **59**, 645–655 (2007).
27. Cryan, J. F. et al. Behavioral characterization of the novel $GABA_B$ receptor-positive modulator GS39783 (*N*,*N*′-dicyclopentyl-2-methylsulfanyl-5-nitro-pyrimidine-4,6-diamine): anxiolytic-like activity without side effects associated with baclofen or benzodiazepines. *J. Pharmacol. Exp. Ther*. **310**, 952–963 (2004).
28. Koehl, A. et al. Structural insights into the activation of metabotropic glutamate receptors. *Nature* **566**, 79–84 (2019).
29. Isberg, V. et al. Generic GPCR residue numbers – aligning topology maps while minding the gaps. *Trends Pharmacol. Sci*. **36**, 22–31 (2015).
30. Xue, L. et al. Rearrangement of the transmembrane domain interfaces associated with the activation of a GPCR hetero-oligomer. *Nat. Commun*. **10**, 2765 (2019).
31. Duthey, B. et al. A single subunit (GB2) is required for G-protein activation by the heterodimeric $GABA_B$ receptor. *J. Biol. Chem*. **277**, 3236–3241 (2002).
32. Urwyler, S. et al. *N*,*N*′-Dicyclopentyl-2-methylsulfanyl-5-nitro-pyrimidine-4,6-diamine (GS39783) and structurally related compounds: novel allosteric enhancers of γ-aminobutyric $acid_B$ receptor function. *J. Pharmacol. Exp. Ther*. **307**, 322–330 (2003).
33. Monnier, C. et al. *Trans*-activation between 7TM domains: implication in heterodimeric $GABA_B$ receptor activation. *EMBO J*. **30**, 32–42 (2011).
34. Kniazeff, J. et al. Closed state of both binding domains of homodimeric mGlu receptors is required for full activity. *Nat. Struct. Mol. Biol*. **11**, 706–713 (2004).

Methods

No statistical methods were used to predetermine sample size. The experiments were not randomized and investigators were not blinded to allocation during experiments and outcome assessment.

Expression of GABA$_B$

This study used two separate constructs with cleavable N- and C-terminal tags for GB1 and GB2. Human GB1 isoform 1A (UniProt: Q9UBS5, residues 165–920) was modified to include an N-terminal influenza haemagglutinin signal sequence and a C-terminal eGFP tag. Additionally, human GB2 (UniProt: O75899, residues 42–821) was modified to include an N-terminal influenza haemagglutinin signal sequence following a 3× Flag epitope. The N- and C-terminal tags are removable by tobacco etch virus protease (TEV) and human rhinovirus 3C protease (PreX), respectively. The overall strategy of designing the constructs was to keep the topology of VFT and coiled-coil domain intact and also to provide the ability of pulling down the heterodimeric species.

Each construct was cloned into a pFastBac1 vector (Invitrogen) and expressed in *Spodoptera frugiperda* Sf9 insect cells (ATCC CRL-1711, authenticated by supplier using morphology and growth characteristics, certified mycoplasma-free) using the Bac-to-Bac system (Invitrogen). Cells were co-infected with baculovirus at a density of $2.5–3 \times 10^6$ cells ml^{-1} in ESF921 medium containing 2% (v/v) production boost additive (PBA, Expression Systems) at a multiplicity of infection (MOI) of 8 for both GB1 and GB2 constructs. After 48 h cells were collected, washed in PBS, and stored at −80 °C until further use.

Purification of GABA$_B$

Cells were thawed in low salt wash buffer containing 20 mM HEPES-NaOH pH 7.5, 10 mM MgCl$_2$, 20 mM KCl and protease inhibitor cocktail (made in-house). One round of dounce homogenization followed by centrifugation at 200,000*g* was carried out to disrupt intact cells and to remove unwanted soluble proteins. Further homogenization and centrifugation were done in the presence of 1 M NaCl for two rounds to remove cell nuclei and membrane-associated proteins. The washed membranes were resuspended and solubilized in buffer containing 100 mM HEPES-NaOH pH 7.5, 800 mM NaCl, 10% (v/v) glycerol, 1% (w/v) *n*-dodecyl-β-D-maltopyranoside (DDM, Anatrace), 0.2% (w/v) cholesteryl hemisuccinate (CHS, Sigma-Aldrich) for 2.5 h at 4 °C. Purification was carried out in the presence of 50 μM SKF97541 (Tocris Bioscience) for preparation of the agonist-bound sample, and without adding ligands for the agonist- and PAM-bound and apo sample. Solubilized membranes were spun down at 200,000*g* for 50 min, and the resulting supernatant was incubated with anti-Flag M2 affinity gel (MilliporeSigma) overnight at 4 °C. The resin was washed with 15 column volumes of wash buffer I containing 25 mM HEPES-NaOH pH 7.5, 300 mM NaCl, 0.1% (w/v) DDM, 0.02% (w/v) CHS and incubated overnight in the same buffer with the addition of 100 μg ml^{-1} Flag peptide and TEV protease (GenScript) at 4 °C. The eluted protein was then incubated with anti-GFP nanobody resin (made in-house) and washed with 5 column volumes wash buffer I and 10 column volumes wash buffer II containing 25 mM HEPES-NaOH pH 7.5, 300 mM NaCl, 0.02% (w/v) DDM, 0.004% (w/v) CHS and exchanged to digitonin (MilliporeSigma) by incubating the resin with the same buffer containing 1% digitonin for 1 h. Elution was performed overnight by incubating the resin with PreX protease (GenScript) at 4 °C. The protein was finally purified by size-exclusion chromatography (SEC) on a Superose 6 Increase 10/300 GL column (GE Healthcare) in SEC buffer containing 25 mM HEPES-NaOH pH 7.5, 300 mM NaCl, 0.1% (w/v) digitonin. Dimeric fractions were pooled, supplemented with 100 μM SKF97541 (for the agonist sample) or with 100 μM SKF97541 and 100 μM GS39783 (for the agonist and PAM sample, Tocris Bioscience), stored at 4 °C overnight and concentrated to 10 mg ml^{-1} using a 100-kDa cut-off concentrator (Amicon) immediately before applying the sample to cryo-EM grids.

Cryo-EM data acquisition and processing

For the preparation of cryo-EM grids, Quantifoil grids (Au 1.2/1.3, 200 mesh, Quantifoil) were glow-discharged for 40 s at 30 mA (EasiGlo, Ted Pella). A total of 2.5 μl of concentrated GABA$_B$ sample was applied to each grid in a plunge-freezer (Leica GP3), blotted for 5 s at 95% relative humidity at 20 °C and plunge-frozen into liquid ethane. Frozen grids were transferred to liquid nitrogen and stored for data acquisition.

The first two datasets (agonist- and agonist- and PAM-bound receptor) described in this study were collected on a Titan Krios (Thermo Fisher), equipped with a K3 direct-electron detector (Gatan), without energy filter, operated at 300 kV. Each movie had a total exposure time of 3.5 s with 70 ms per frame readout, at a dose-rate of about 15 e Å^{-2} s^{-1}, corresponding to a total dose of about 50 e Å^{-2}. High-magnification images were collected in super-resolution mode, with a corresponding pixel size of 0.426 Å. Automated data collection was performed using SerialEM[35], with a strategy of applying image shifts to collect data from 9 holes (with 3 images per hole) after each stage movement, to increase throughput. The third, apo dataset was collected on a Titan Krios (Thermo Fisher) equipped with an energy filter and K2 direct-electron detector (Gatan), operated at 300 kV. The data collection procedure was similar to the previous two datasets, with the difference of a nominal pixel size of 1.08 Å, a dose rate of about 8 e Å^{-2} s^{-1}, 200-ms exposure time per frame, a total of 8-s exposures with the energy filter set to 20 eV slit size and only one acquisition per hole.

The first dataset (SKF97541-bound GABA$_B$) had a total of 14,271 micrographs (3.5 d of data collection), the second dataset (SKF97541- and GS39783-bound GABA$_B$) of 10,917 micrographs (2.5 d of data collection) and the third dataset (apo GABA$_B$) 5,947 micrographs (2 d of data collection). Beam-induced motion correction was performed using MotionCor2[36] and included binning of the super-resolution images by a factor of 2 for the first two K3 datasets. CTF estimation was done using CTFFIND4[37]. Corrected images for the first dataset were imported into the RELION 3.0 software package[38], following established processing pipelines. After initial template-based autopicking, 2D classification resulted in classes from two distinctly different conformations of GABA$_B$ (Extended Data Fig. 2). Three-dimensional classification in RELION was used to separate particles into two classes. The particles from each class were then transferred to the cryoSPARC software package[39] for detergent belt subtraction, followed by several rounds of ab-initio reconstruction, heterogeneous refinement, non-uniform refinement and local refinement, resulting in two reconstructions at 6.3 and 4.8 Å (Extended Data Fig. 2). The second dataset (SKF97541- and GS39783-bound GABA$_B$) was directly imported into cryoSPARC; 2D classification resulted in 124,575 particles. A final set of 89,001 particles resulted in a reconstruction of 3.6 Å resolution, based on the Fourier shell correlation (FSC) = 0.143 criterion (Extended Data Figs. 4, 5g). The third dataset (GABA$_B$ apo) was also only processed with cryoSPARC, with a final set of 113,093 particles resulting in a reconstruction at 4.0 Å resolution (Extended Data Fig. 5).

GABA$_B$ structure determination and refinement

The initial model for the agonist- and PAM-bound GABA$_B$ was composed of a TMD model generated by homology from the crystal structure of mGlu1 (PDB 4OR2) using SWISS-MODEL[40] and a VFT model derived from the previously published crystal structure of GABA$_B$ VFT in complex with GABA (PDB 4MS3). Both models were first manually docked into the cryo-EM density map using UCSF ChimeraX[41] and further improved by using phenix.dock_in_map in PHENIX v.1.17.1[42]. The pseudosymmetry of the GABA$_B$ heterodimer was addressed by both docking known VFT crystal structures and pinpointing asymmetries in the glycosylation sites, most prominently seen on N440 of GB1. The model was then subjected to iterative manual building in Coot[43] and real-space refinement in PHENIX against sharpened 3.6 Å resolution map using global minimization, local rotamer fitting and restrained group ADP refinement with secondary structure restraints and a nonbonded weight of 500. In this structure, we observed an extensive elongated density next to ICL2 of the TMD of GB2, stretching out in the intracellular space at an angle of about 20° to the plane of the membrane (Fig. 3a). Owing to the poor local resolution, it was not possible to unambiguously model this domain. However, based on its topology, we tentatively assigned it to the intracellular coiled-coil domain.

The fully refined agonist- and PAM-bound $GABA_B$ TMDs along with a VFT model derived from the crystal structure of $GABA_B$ VFT in the apo state (PDB 4MQE) were used as an initial template for the apo state model by fitting into the cryo-EM density map and further improved by iterative manual building in Coot and real-space refinement in PHENIX against the sharpened 4.0 Å resolution map using global minimization, local rotamer fitting and restrained ADP refinement with secondary structure restraints and a non-bonded weight of 500.

The initial model for the int-1 state was generated by fitting two TMDs from the fully refined apo $GABA_B$ structure, as well as LB1 and LB2, of the VFT of GB1 and a whole VFT of GB2 from the crystal structure (PDB 4MS3) in the map in ChimeraX followed by rigid-body refinement in PHENIX. After manual adjustments in Coot, which included connecting separate domains and trimming most side chains and intracellular loops in TMDs, the model was subjected to real-space refinement in PHENIX against the sharpened 6.3 Å resolution int-1 map using global minimization, local rotamer fitting and restrained group ADP refinement with secondary structure and reference model (apo structure) restraints and a non-bonded weight of 500. Although the agonist is probably bound to the receptor in the int-1 state, it was not included in the model because of insufficient resolution.

The initial model for the int-2 state was generated by fitting two TMDs from the fully refined apo $GABA_B$, as well as two VFTs from the GABA-bound crystal structure (PDB 4MS3) in the map in ChimeraX followed by rigid-body refinement in PHENIX. After manual adjustments in Coot, which included connecting separate domains and trimming some side chains and intracellular loops in the TMDs, the model was subjected to real-space refinement in PHENIX against the sharpened 4.8 Å resolution int-2 map using global minimization, local rotamer fitting and restrained group ADP refinement with secondary structure and reference model (agonist- and PAM-bound structure) restraints and a non-bonded weight of 500. Cryo-EM data collection and refinement statistics are shown in Extended Data Table 1.

Molecular dynamics simulations

All molecular dynamics simulations were conducted with Gromacs[44] v.2018 simulation engine under Charmm36 force field parameters and topologies[45]. Missing loops and side chains were modelled using loop modelling and optimization tools in ICM-Pro[46] v.3.8.7b. The resulting structures were then uploaded to the Charmm-GUI webserver[47] to generate input files for the simulation. All structures were embedded into a bilayer of POPC lipids; initial membrane coordinates were assigned by the PPM server[48] via the Charmm-GUI interface. The 'Ligand Reader & Modeller' of Charmm-GUI[49] was invoked to generate Charmm36 force field parameters and topologies for GS39783 and SKF97541. The apo system contained 375 POPC lipids, 61,663 water molecules, 167 sodium and 186 chloride ions, and the ligand-bound system contained 385 POPC lipids, 66,825 water molecules, 181 sodium and 200 chloride ions. After initial energy minimizations, both systems were equilibrated for 20 ns, followed by production runs of up to 800 ns for the apo system and 500 ns for the SKF97541- and GS39783-bound system. The simulations were performed either on NVIDIA P100 GPU enabled nodes made available by the Google Cloud Platform or with GPU clusters at the High-Performance Computing Center of the University of Southern California. Molecular dynamics trajectories were analysed using MDAnalysis package[50].

Normal mode analysis

Normal modes of the apo and SKF97541- and GS39783-bound structures were assessed using the ProDy package[51]. Two independent anisotropic network models (ANM), with respect to apo and SKF97541- and GS39783-bound structures, were defined in the presence of an explicit POPC lipid bilayer. Coordinates of the lipids were taken from Charmm-GUI output. Network nodes include Cα atoms from the proteins and heavy atoms from the lipids. The slowest modes of each ANM model were compared to the principal components of corresponding molecular dynamics trajectories by evaluating correlations between eigenvectors on corresponding Cα atoms[52].

Molecular pharmacology methods

The pRK5 plasmids encoding the wild-type human $GB1_a$ with the signal peptide of mGlu5, followed by a HA tag and a Halo tag at the N terminus, upstream of residue G18, or the wild-type human GB2 with the signal peptide of mGlu5, a Flag tag followed by SNAP tag at the N terminus, upstream of W42, were obtained from the laboratory of J. Liu. Human GB1 and GB2 constructs used for cryo-EM analysis were subcloned into these pRK5 plasmids to obtain a HA- and Halo-tagged GB1 construct (between the Mlu-I and Hind-III unique sites), and the Flag- and SNAP-tagged GB2 construct (between the Not-I and Hind-III unique sites). The mutations of GB1 and GB2 in the pRK5 plasmids were generated by site-directed mutagenesis using the QuikChange mutagenesis protocol (Agilent Technologies).

HEK293 cells (ATCC CRL-1573, authenticated by supplier using morphology and growth characteristics, certified mycoplasma-free) were cultured in Dulbecco's modified Eagle's medium (DMEM) supplemented with 10% FBS and transfected by electroporation. Ten million cells were transfected with 260 V voltage and 800 μF capacitance using the Gene Pulser Xcell MicroPulser Electroporator (Bio-Rad), and then distributed into a 96-well plate (Greiner Bio-one). Eventually, Lipofectamine 2000 (Thermo Fisher Scientific) was used according to the manufacturer protocol for transfection. One hundred thousand cells were transfected with 20 ng GB1 plasmid and 40 ng GB2 plasmid either alone or simultaneously for 1 well in a 96-well plate. For the IP_1 detection, cells were also co-transfected with 10 ng chimeric G protein $G\alpha q_{i9}$ to allow efficient coupling of the receptor to the phospholipase C pathway[21]. IP_1 accumulation in HEK293 cells was measured using the IP-One HTRF kit (Cisbio) according to the manufacturer's recommendations.

Ligand-binding assay

HEK293 cells were co-transfected with pRK5 plasmids encoding wild-type or mutant GB1 and GB2 in 96-well plates. Intact cells were washed once with Tag-lite buffer (Cisbio) 48 h later and incubated with both 5 nM CGP54626-DY647 (Cisbio) and increasing concentrations of GABA for 3 h at 4 °C in Tag-lite buffer. After three washes with Tag-lite buffer, fluorescence was measured as the specific DY647 emission spectrum (665 nm) with an Infinite F500 reader (Tecan).

Cell-surface quantification of receptor with SNAP tag or Halo tag

For SNAP tag and Halo tag detection, HEK293 cells from 96-well plates were incubated at 37 °C with 100 nM of SNAP-Lumi4-Tb or 100 nM of Halo-Lumi4-Tb for 1 h, 48 h after transfection. After labelling, cells were washed three times with Tag-lite buffer (Cisbio), and fluorescence of Lumi4-Tb (excitation at 337 nm, emission at 620 nm, 60 μs delay, and 400 ms integration time) was read using Infinite F500 reader (Tecan).

Figures and graphical illustration

Pymol v. 2.3.3 (Schroedinger), UCSF ChimeraX v. 0.9, and ICM-Pro v. 3.8.7b (Molsoft) were used to make figures and videos. All cryo-EM maps shown in the manuscript were masked to hide densities arising from the detergent belt. All reported r.m.s.d. values were calculated using the align command in Pymol. The distances between the C-terminal ends of the GB1 and GB2 VFTs in Extended Data Fig. 7a, b were measured between Cα atoms of residues D576 (cryo-EM models) or D459 (X-ray models) in GB1 and D466 (cryo-EM and X-ray models) in GB2. The TM5–TM5 and TM6–TM6 distances in Fig. 4b, c were measured between Cα atoms of residues G771$^{5.41}$ and V822$^{6.56}$ in GB1 and residues G658$^{5.41}$ and V709$^{6.56}$ in GB2 to compare with cross-linking data[30]. The shifts of TM3 and TM5 of GB2 in Fig. 4d were measured for Cα atoms of residues I581$^{3.57}$ and T678$^{5.61}$. The GABA$_B$ heterodimer interface areas in Extended Data Figs. 4g, 5i were calculated using the program PISA[53].

Reporting summary

Further information on research design is available in the Nature Research Reporting Summary linked to this paper.

Data availability

The cryo-EM density maps and corresponding coordinates have been deposited in the Electron Microscopy Data Bank (EMDB) and the PDB, respectively, under the following accession codes: EMD-20822 and 6UO8 (SKF97541- and GS39783-bound GABA$_B$), EMD-20823 and 6UO9 (SKF97541-bound GABA$_B$, int-2 state), EMD-20824 and 6UOA (SKF97541-bound GABA$_B$, int-1 state), and EMD-21219 and 6VJM (apo GABA$_B$).

Source data are provided with this paper. Supplementary Figure 1 contains the uncropped gel shown in Extended Data Fig. 1f. All other data are available from the authors on reasonable request.

35. Schorb, M., Haberbosch, I., Hagen, W. J. H., Schwab, Y. & Mastronarde, D. N. Software tools for automated transmission electron microscopy. *Nat. Methods* **16**, 471–477 (2019).
36. Zheng, S. Q. et al. MotionCor2: anisotropic correction of beam-induced motion for improved cryo-electron microscopy. *Nat. Methods* **14**, 331–332 (2017).
37. Rohou, A. & Grigorieff, N. CTFFIND4: fast and accurate defocus estimation from electron micrographs. *J. Struct. Biol.* **192**, 216–221 (2015).
38. Zivanov, J. et al. New tools for automated high-resolution cryo-EM structure determination in RELION-3. *eLife* **7**, e42166 (2018).
39. Punjani, A., Rubinstein, J. L., Fleet, D. J. & Brubaker, M. A. cryoSPARC: algorithms for rapid unsupervised cryo-EM structure determination. *Nat. Methods* **14**, 290–296 (2017).
40. Waterhouse, A. et al. SWISS-MODEL: homology modelling of protein structures and complexes. *Nucleic Acids Res.* **46**, W296–W303 (2018).
41. Goddard, T. D. et al. UCSF ChimeraX: meeting modern challenges in visualization and analysis. *Protein Sci.* **27**, 14–25 (2018).
42. Adams, P. D. et al. PHENIX: a comprehensive Python-based system for macromolecular structure solution. *Acta Crystallogr. D* **66**, 213–221 (2010).
43. Emsley, P. & Cowtan, K. Coot: model-building tools for molecular graphics. *Acta Crystallogr. D* **60**, 2126–2132 (2004).
44. Abraham, M. J. et al. GROMACS: high performance molecular simulations through multi-level parallelism from laptops to supercomputers. *SoftwareX* **1–2**, 19–25 (2015).
45. Huang, J. & MacKerell, A. D. Jr. CHARMM36 all-atom additive protein force field: validation based on comparison to NMR data. *J. Comput. Chem.* **34**, 2135–2145 (2013).
46. Abagyan, R., Totrov, M. & Kuznetsov, D. ICM: a new method for protein modeling and design: Applications to docking and structure prediction from the distorted native conformation. *J. Comput. Chem.* **15**, 488–506 (1994).
47. Jo, S., Kim, T., Iyer, V. G. & Im, W. CHARMM-GUI: a web-based graphical user interface for CHARMM. *J. Comput. Chem.* **29**, 1859–1865 (2008).
48. Lomize, M. A., Pogozheva, I. D., Joo, H., Mosberg, H. I. & Lomize, A. L. OPM database and PPM web server: resources for positioning of proteins in membranes. *Nucleic Acids Res.* **40**, D370–D376 (2012).
49. Kim, S. et al. CHARMM-GUI ligand reader and modeler for CHARMM force field generation of small molecules. *J. Comput. Chem.* **38**, 1879–1886 (2017).
50. Michaud-Agrawal, N., Denning, E. J., Woolf, T. B. & Beckstein, O. MDAnalysis: a toolkit for the analysis of molecular dynamics simulations. *J. Comput. Chem.* **32**, 2319–2327 (2011).
51. Bakan, A., Meireles, L. M. & Bahar, I. ProDy: protein dynamics inferred from theory and experiments. *Bioinformatics* **27**, 1575–1577 (2011).
52. Gur, M., Zomot, E. & Bahar, I. Global motions exhibited by proteins in micro- to milliseconds simulations concur with anisotropic network model predictions. *J. Chem. Phys.* **139**, 121912 (2013).
53. Krissinel, E. Stock-based detection of protein oligomeric states in jsPISA. *Nucleic Acids Res.* **43**, W314–W319 (2015).

Acknowledgements We thank K. Villers, C. Hanson, F. Nasertorabi, J. Velasquez and M. Barekatain for technical support; S. Roux for the help with collecting functional data; E. Montabana for microscope support; Y.-T. Li and N. Patel for support with computing resources; and Y. Kadyshevskaya for help with illustrations. This research was supported by the National Institutes of Health (NIH) grant R35 GM127086 (V.C.), by the Department of Energy, Laboratory Directed Research and Development program at SLAC National Accelerator Laboratory, under contract DE-AC02-76SF00515, and by the Fondation pour la Recherche Médicale (DEQ20170336747, to J.-P.P.). We acknowledge the SLAC-Stanford Cryo-EM center (SLAC National Accelerator Laboratory) for microscope time. Functional experiments were performed at the ARPEGE (Pharmacology Screening-Interactome) facility, Institut de Génomique Fonctionnelle. We acknowledge Google Cloud Platform credits and USC High Performance Computing Center for computer resources used in molecular dynamics simulations.

Author contributions H.S. expressed and purified GABA$_B$ heterodimers for cryo-EM data collection. A.I. helped with the development of protocols for receptor expression and purification. C.G. performed cryo-EM sample preparation, data collection and image processing. L.X. performed ligand-binding and functional experiments. G.W.H. helped with the structure refinement and quality control. J.H.L, and V.K. performed molecular dynamics and ANM modelling. P.R., J.-P.P., J.H.L. and V.K. analysed data. H.S., C.G. and V.C. conceived the project, analysed data, and wrote the manuscript with contributions from all authors. V.C. supervised the project.

Competing interests The authors declare no competing interests.

Additional information

Supplementary information is available for this paper at https://doi.org/10.1038/s41586-020-2408-4.

Correspondence and requests for materials should be addressed to C.G. or V.C.

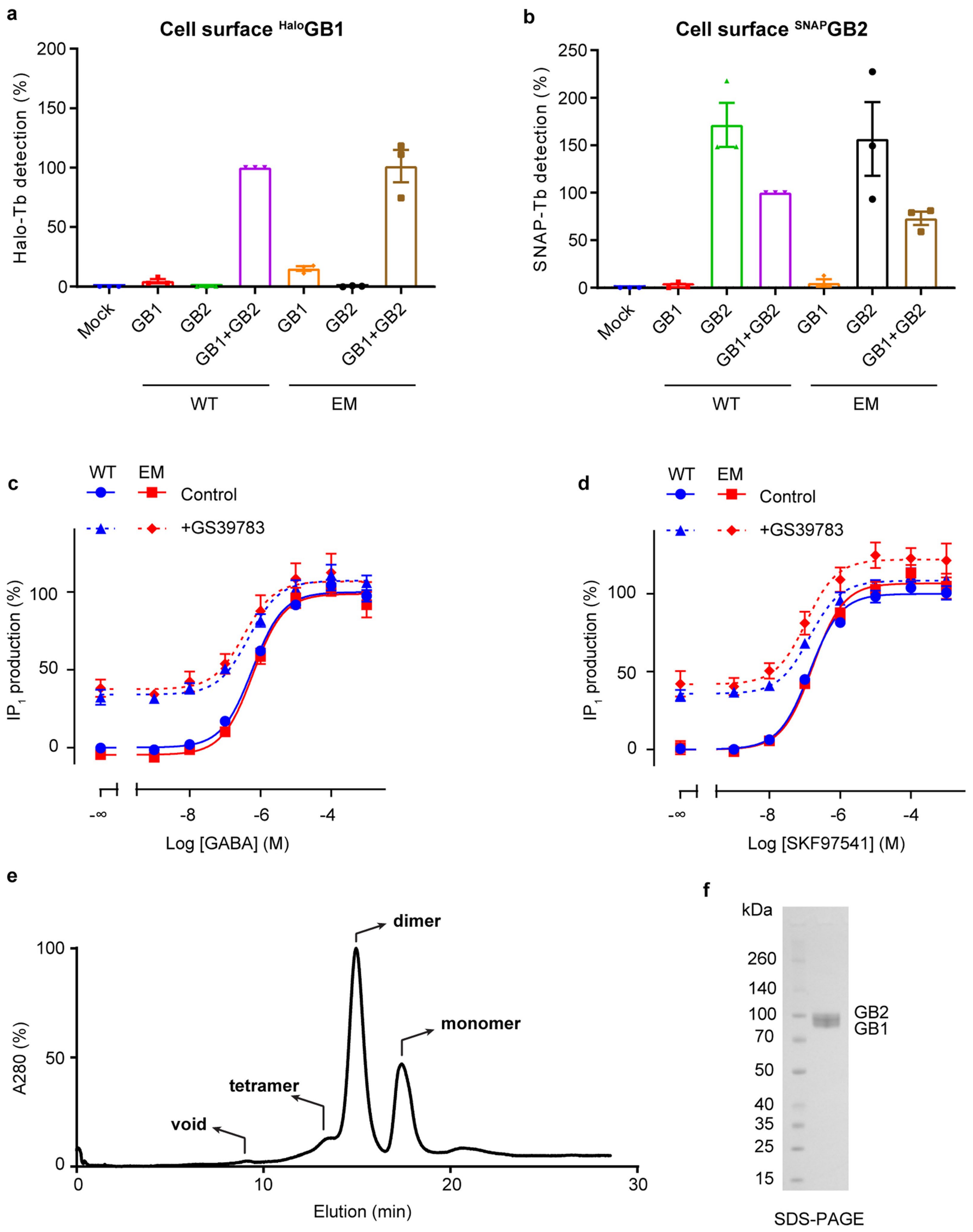

Extended Data Fig. 1 | Expression, characterization and purification of GABA_B. a, **b**, Cell surface expression of Halo–GB1 (**a**) and SNAP–GB2 (**b**), transfected alone or cotransfected with the second subunit, measured by the fluorescence emission of the Lumi4-Tb bound to the Halo (**a**) or SNAP tag (**b**). Values are normalized by the wild-type GB1 cotransfected with wild-type GB2 (purple bar) and shown as mean ± s.d. of three biologically independent experiments. GABA_B constructs for cryo-EM are expressed and function similarly to the wild-type receptor. **c**, **d**, Positive allosteric effect of GS39783 (5 µM) on IP_1 accumulation in cells expressing wild-type or cryo-EM constructs of GABA_B heterodimers and activated either by GABA (**c**) or SKF97541 (**d**). Data are normalized by the wild-type response in absence of GS39783 (control) and shown as mean ± s.e.m. of three biologically independent experiments (4 for wild type). **e**, Representative SEC profile of apo GABA_B in digitonin micelles. Dimeric fractions were pooled, supplemented with ligand and concentrated for cryo-EM imaging. **f**, Coomassie stained SDS–PAGE profile shows two distinct bands for GB1 (86 kDa) and GB2 (88 kDa). For gel source data, see Supplementary Fig. 1.

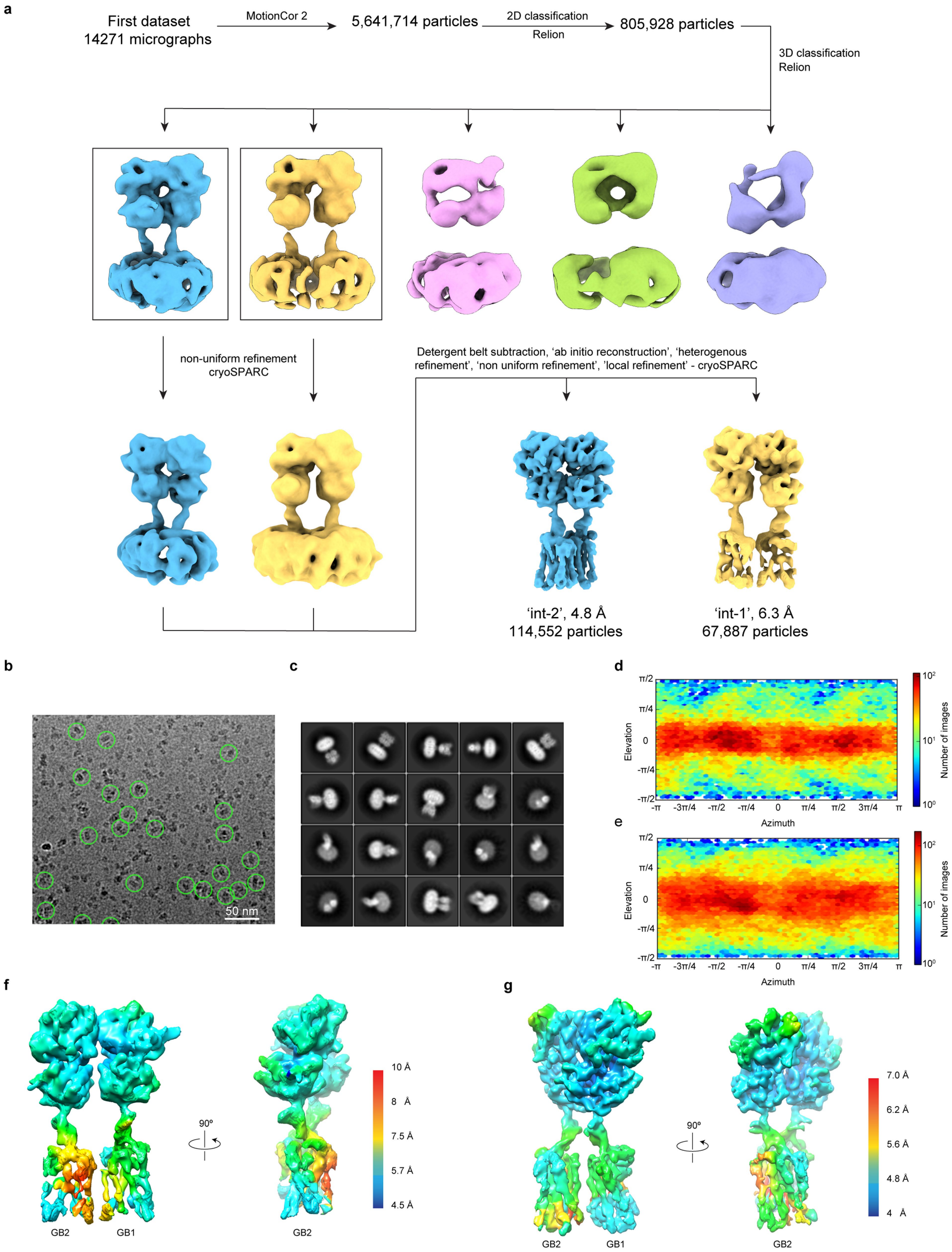

Extended Data Fig. 2 | Cryo-EM data processing for SKF97541-bound GABA$_B$. **a**, Single-particle cryo-EM data processing scheme using RELION and cryoSPARC. **b**, Representative micrograph showing picked particles. **c**, Representative 2D class averages. **d**, Angular distribution of particles included in the final cryo-EM reconstruction for the int-1 state. **e**, The same as **d** but for the int-2 state. **f**, **g**, Density maps for int-1 (**f**) and int-2 (**g**) states coloured by local resolution, showing higher resolution at the VFT interface.

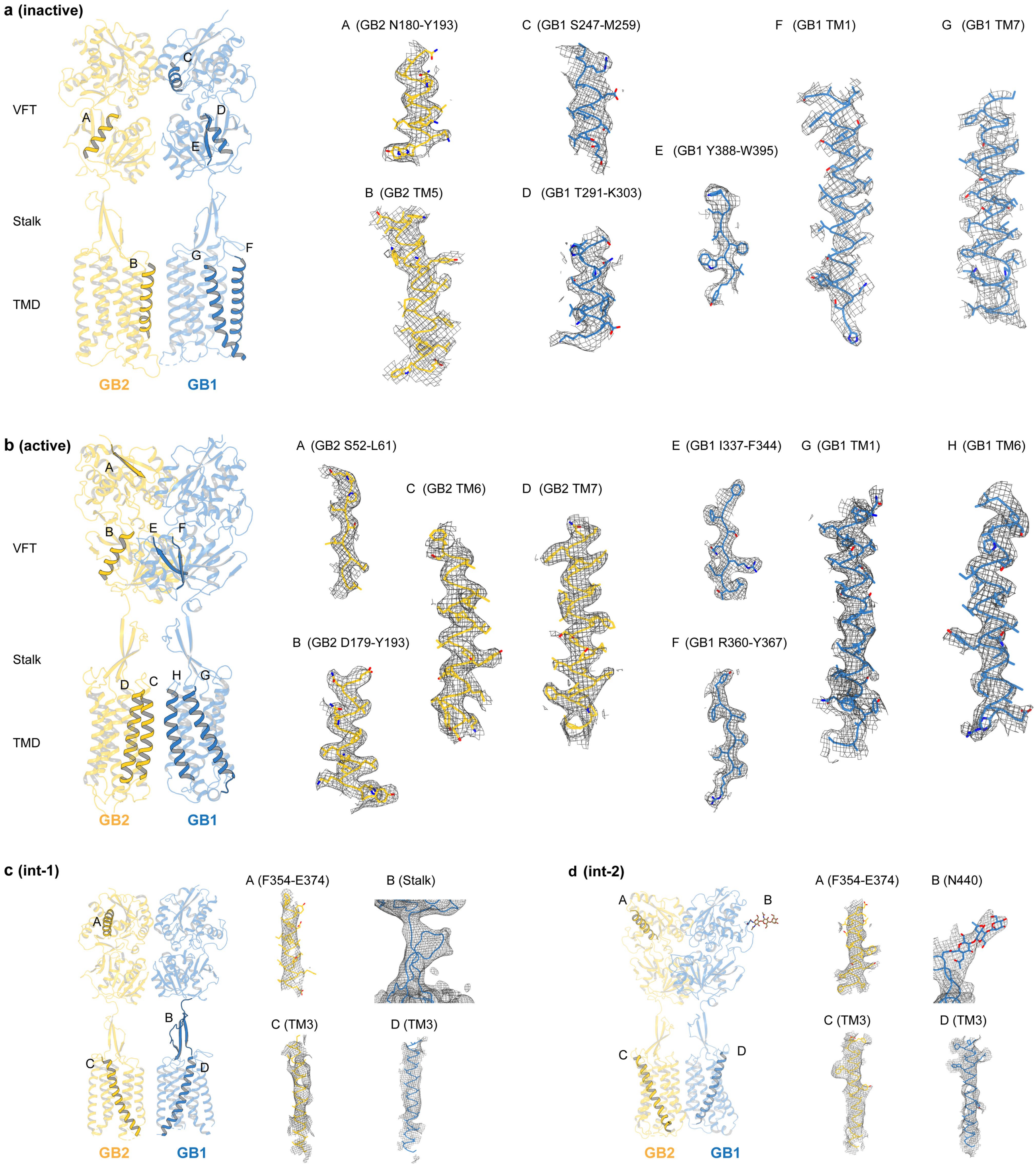

Extended Data Fig. 3 | Cryo-EM map quality. a–d, Representative densities and fitted atomic models are shown for GABA$_B$ in the inactive apo state (**a**), active agonist- and PAM-bound state (**b**), and two intermediate int-1 (**c**) and int-2 states (**d**).

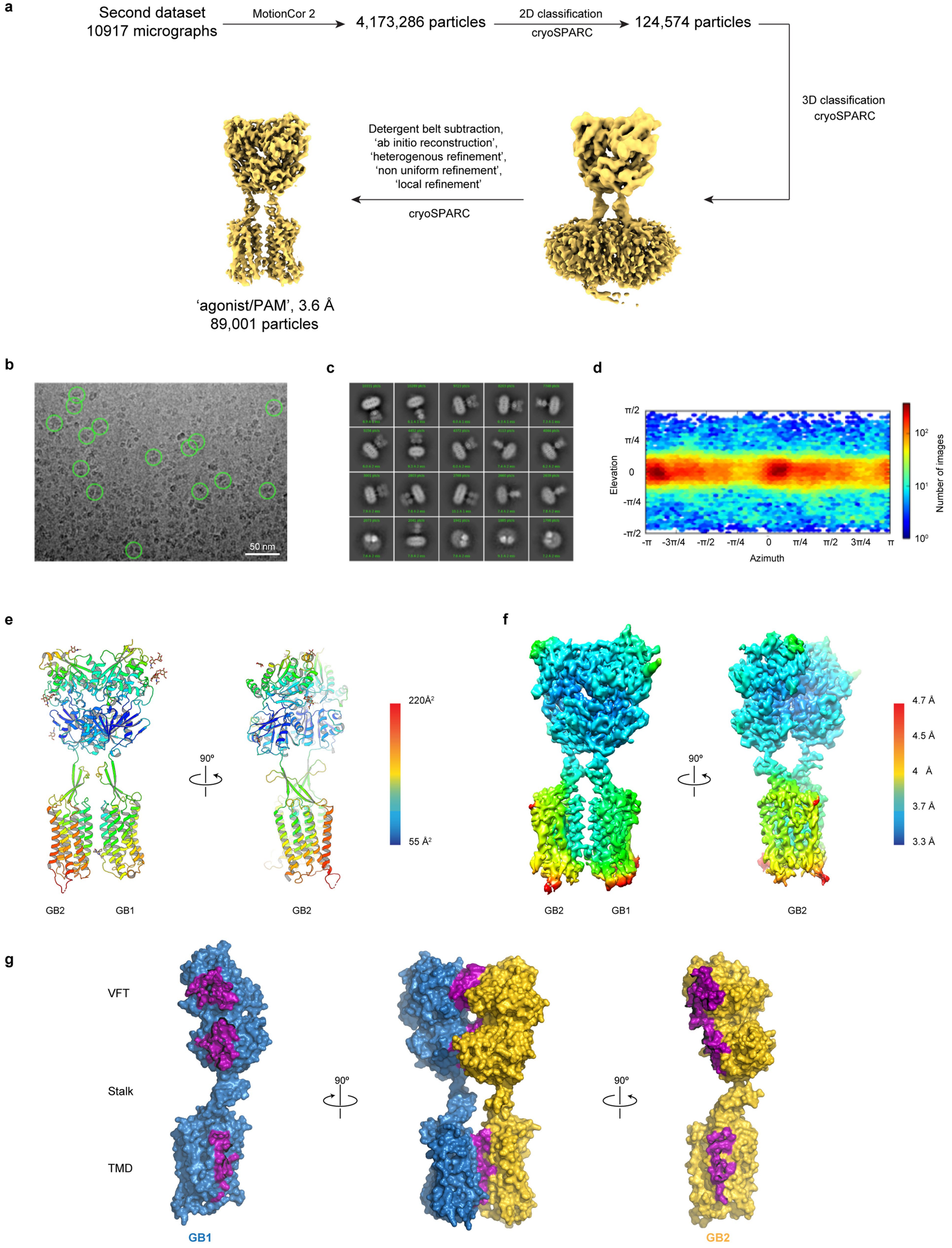

Extended Data Fig. 4 | Cryo-EM data processing for SKF97541- and GS39783-bound GABA$_B$. **a**, Single-particle cryo-EM data processing scheme using cryoSPARC. **b**, Micrograph showing picked particles. **c**, Representative 2D class averages show distinct secondary structure features. **d**, Particle angular distribution of the final cryo-EM reconstruction. **e**, Structural model shown in cartoon representation and coloured by the *B*-factors. **f**, Density map coloured by local resolution, showing higher resolution at the interface between GB1 and GB2. **g**, The heterodimer interface includes both LB1 and LB2, as well as TM6, with a total interface area of 1,930 Å^2. Residues involved in dimerization contacts are coloured in purple.

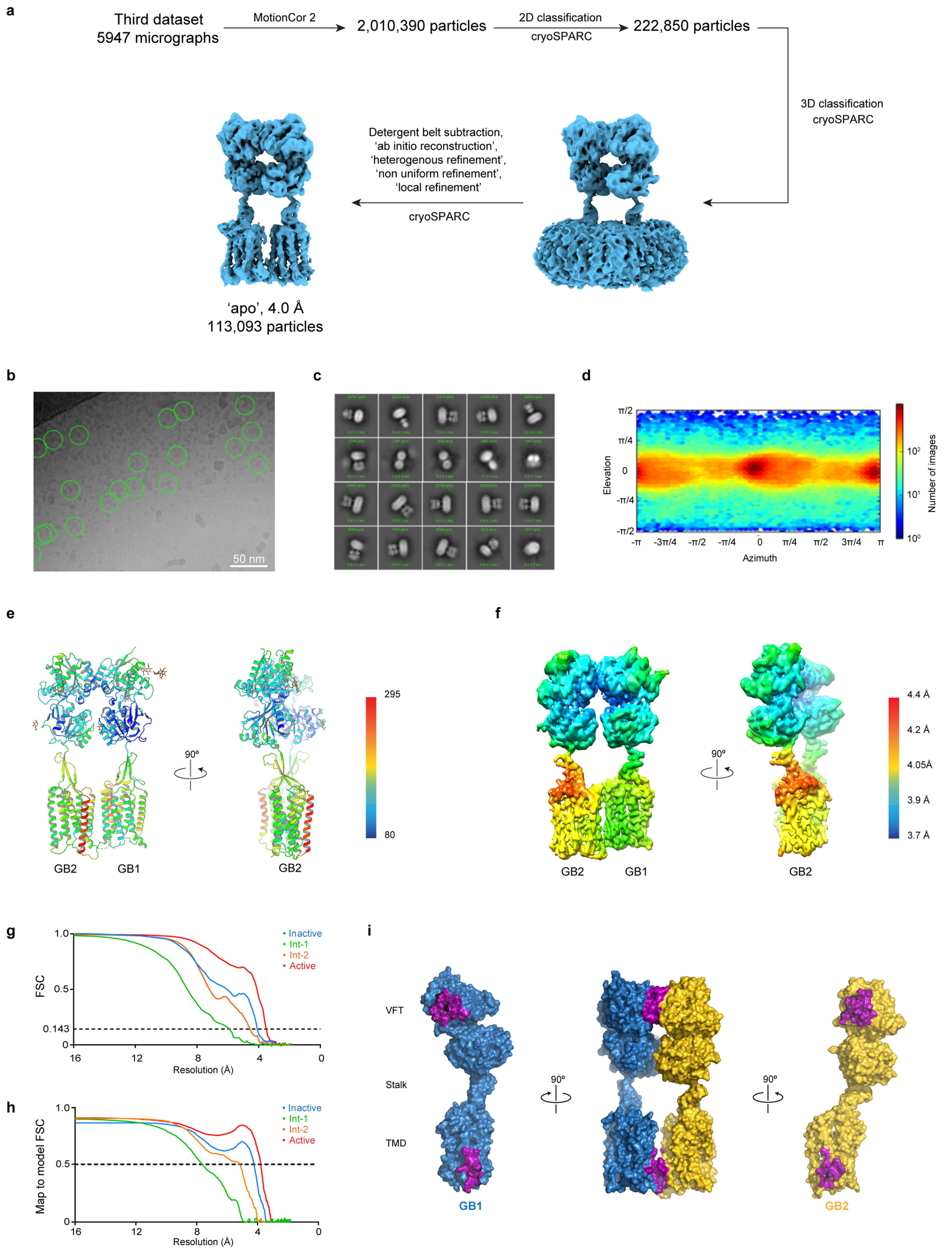

Extended Data Fig. 5 | Cryo-EM data processing for apo GABA$_B$. **a**, Single-particle cryo-EM data processing scheme using cryoSPARC. **b**, Micrograph showing picked particles. **c**, Representative 2D class averages show distinct secondary structure features. **d**, Particle angular distribution of the final cryo-EM reconstruction. **e**, Structural model shown in cartoon representation and coloured by the *B*-factors. **f**, Density map coloured by local resolution, showing higher resolution at the interface of GB1 and GB2. **g**, Gold-standard FSC curves from cryoSPARC. **h**, Map-to-model FSC curve between each refined model and the corresponding sharpened electron potential maps. **i**, GB1 and GB2 interact through LB1s and intracellular tips of TM3 and TM5, with a total interface area of 963 Å^2. Residues involved in dimerization contacts are coloured in purple.

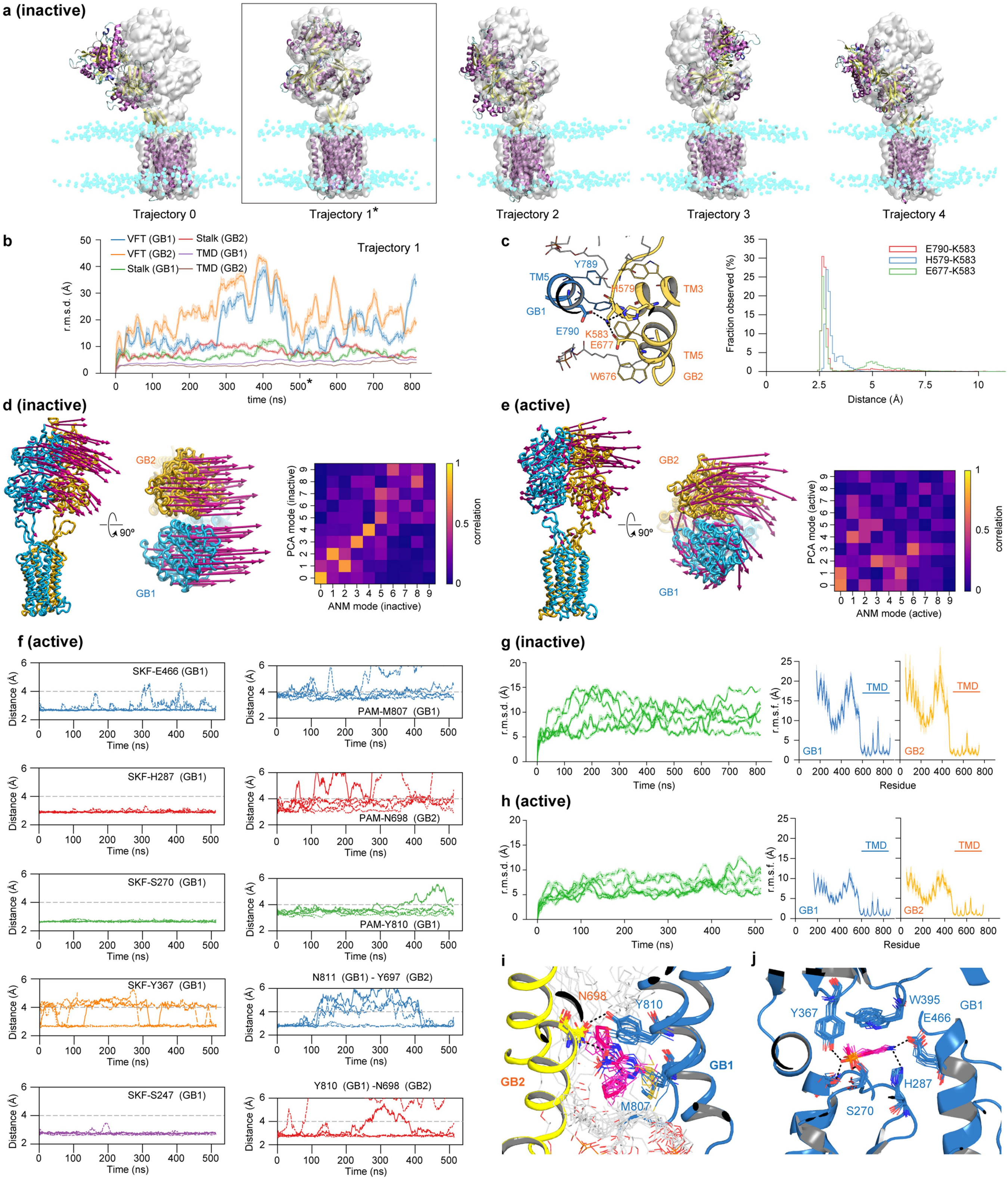

Extended Data Fig. 6 | See next page for caption.

Extended Data Fig. 6 | Molecular dynamics simulations of inactive (apo) and active (agonist- and PAM-bound) states. a, VFT fluctuations in the inactive state are illustrated by comparing molecular dynamics snapshots at 500 ns for all 5 trajectories (cartoon, purple for α-helices and yellow for β-strands) against the cryo-EM structure (grey surface). Cyan spheres indicate nitrogen of hydrophilic heads of the POPC lipid bilayer. Asterisk corresponds to trajectory 1. **b**, Traces of Cα r.m.s.d. for different domains in trajectory 1. The structures in the trajectory were aligned by TMDs against the cryo-EM structure. **c**, Distribution of distances for ionic interactions between TM3 and TM5 at the intracellular side of the apo $GABA_B$, as observed in molecular dynamics simulations. **d**, **e**, Membrane-coupled ANM analysis of the inactive (**d**)- and active (**e**)-state cryo-EM structures. Eigenvectors of the slowest mode are drawn on every eighth Cα as magenta arrows. In the inset heat map, overall dynamics of the protein as observed in molecular dynamics simulations are compared against that predicted from ANM analysis on electron microscopy structures; correlations between eigenvectors of the ten slowest ANM modes and the principal components of Cα motions in molecular dynamics simulations are calculated, showing concurrence between the two. **f**, Distance plots as observed in agonist- and PAM-bound trajectories for interactions between SKF97541 (SKF) and various contact residues in the GB1 pocket (left column), interactions between GS39783 (PAM) and its contact residues at the TMD interface (right column, rows 1–3) and interactions between GB1 and GB2 residues (right column, rows 4 and 5). **g**, **h**, Traces of Cα r.m.s.d. on the overall structure for individual molecular dynamics trajectories (green) and plots of root mean square fluctuations (r.m.s.f.) per residue in GB1 (blue) and GB2 (yellow) subunits as observed in molecular dynamics simulations for inactive (**g**) and active (**h**) states. **i**, **j**, Stacked snapshots of GS39783 (**i**) and SKF97541 (**j**) binding site for one of the trajectories, taken every 50 ns and spanning 500 ns. In traces of Cα r.m.s.d. (**b**, **g**, **h**), data (solid line) are presented as an average within a sliding window of 500 ps; shading refers to 95% confidence interval ($n = 500$). In plots of r.m.s.f. (**g**, **h**), data (solid line) are shown as an average of 5 independent trajectories at each residue position; shading refers to 95% confidence interval ($n = 5$).

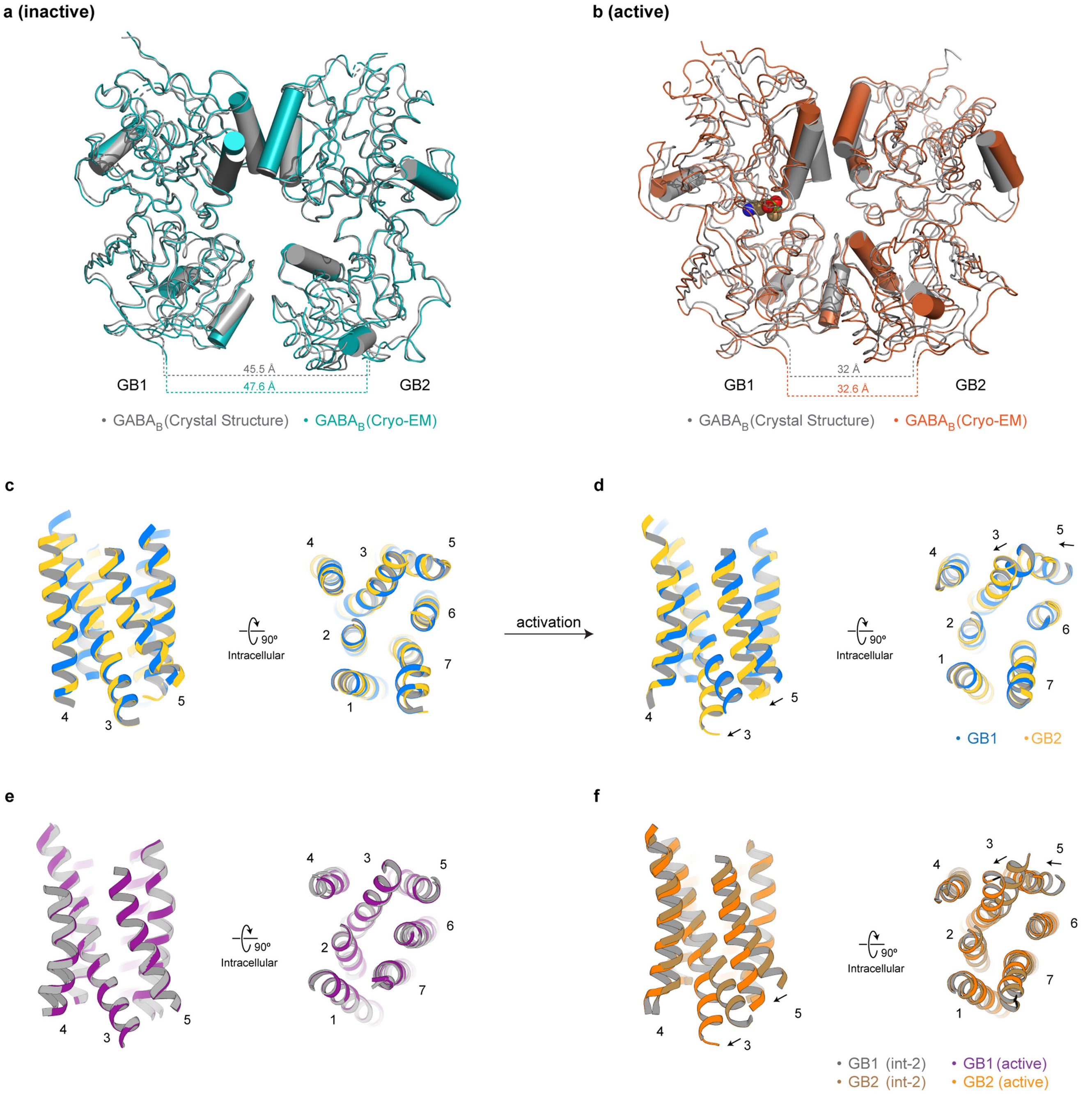

Extended Data Fig. 7 | Comparisons with previous crystal structures and additional details of activation-related transitions in GABA$_B$. **a**, Comparison of the VFTs between the apo cryo-EM structure (teal) and the apo crystal structure (PDB 4MQE, grey). **b**, Comparison of the VFTs between the active agonist- and PAM-bound cryo-EM structure (orange) and the GABA-bound crystal structure (PDB 4MS3, grey). **c**, Comparison between GB1 and GB2 TMDs in the inactive apo state demonstrates no substantial difference between the subunits. **d**, Comparison between GB1 and GB2 TMDs in the active agonist- and PAM-bound state illustrates the differences between the subunits upon activation. **e**, The TMD of GB1 remains unchanged between the int-2 and the active agonist- and PAM-bound states. **f**, Shifts of TM3 and TM5 at the intracellular side of the TMD of GB2 between the int-2 and active states open up a cleft for the engagement of a G protein.

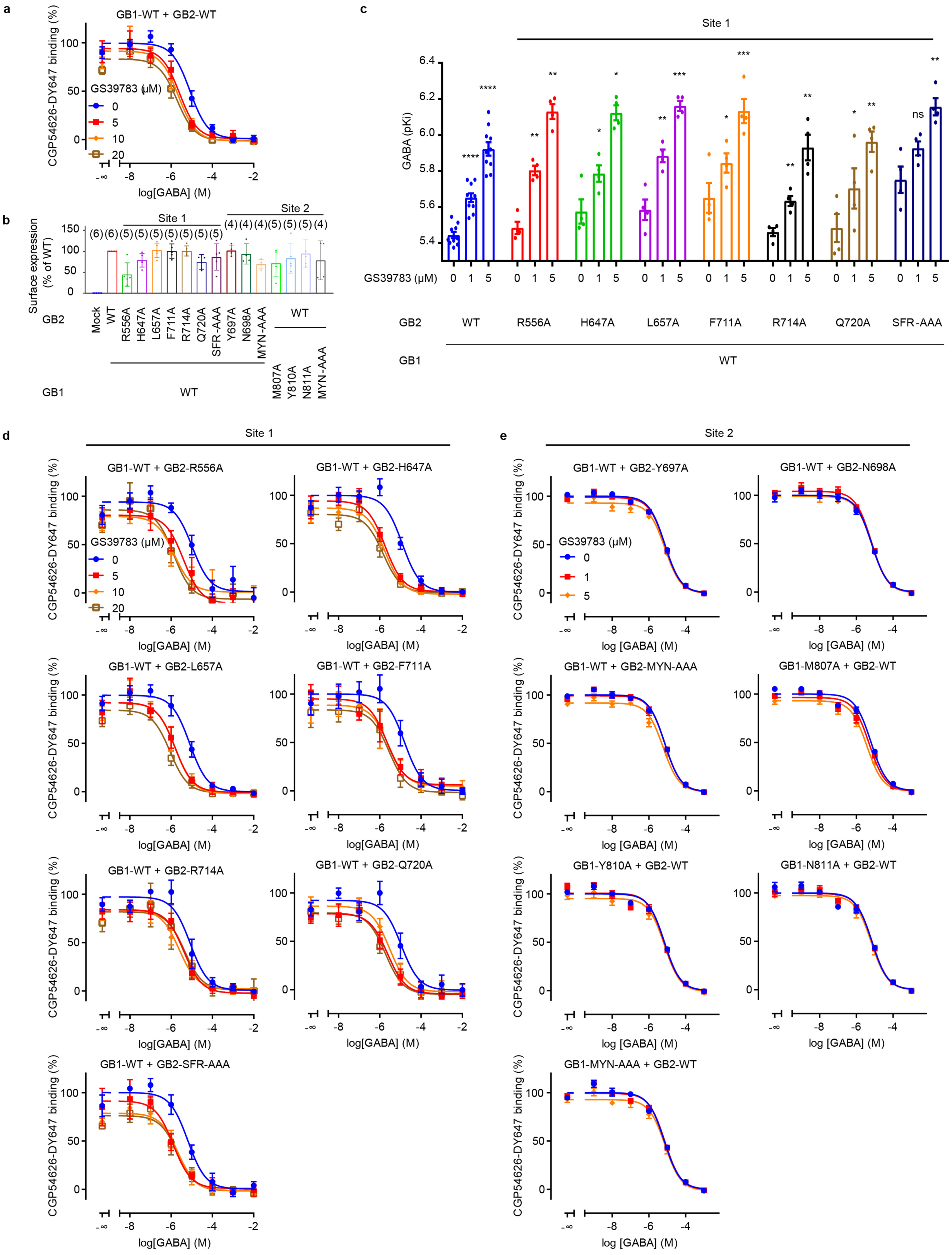

Extended Data Fig. 8 | See next page for caption.

Extended Data Fig. 8 | Effects of a PAM on the orthosteric ligand binding in the site-1 and -2 mutants of GABA$_B$. a, Displacement of the CGP54626-DY647 by GABA in intact cells expressing the wild-type GABA$_B$ receptor in the absence (blue) or presence of 5 μM (red), 10 μM (orange) or 20 μM (sand) GS39783. **b**, Cell-surface expression of site-1 and -2 mutants, measured by cotransfecting Halo–GB1 with GB2 and recording fluorescence emission of Halo–Lumi4-Tb. Data are normalized by the wild-type expression and shown as mean ± s.d. The numbers of biologically independent experiments are shown in parentheses. **c**, pKi values for GABA were determined from displacement of CGP54626-DY647 binding in intact cells expressing the indicated subunit combinations in the absence or presence of 1 μM or 5 μM GS39783. Values are mean ± s.e.m. of 4 (10 for wild type) biologically independent experiments. Data are analysed using one-way ANOVA with Dunnett's multiple comparison test to determine significance (compared with no GS39783 for the same combined subunits), with $^{****}P \leq 0.0001$, $^{***}P \leq 0.001$, $^{*}P \leq 0.01$ and NS (not significant) $P > 0.05$. For 1 μM (5 μM) GS39783, $P = 0.0030$ (0.0045) for GB2(R556A), 0.0205 (0.0157) for GB2(H647A), 0.0084 (0.0009) for GB2(L657A), 0.0436 (0.0003) for GB2(F711A), 0.0013 (0.0053) for GB2(R714A), 0.0373 (0.0056) for GB2(Q720A), and 0.0735 (0.0019) for GB2(SFR-AAA). GB2(SFR-AAA) refers to a triple mutant (S710A/F711A/R714A) of GB2. **d**, **e**, Displacement of the CGP54626-DY647 by GABA in intact cells expressing the indicated mutants in site 1 (**d**) and site 2 (**e**), in the absence or presence of the indicated concentrations of GS39783 as in **a**. Data are normalized by the signal in absence of GS39783 and shown as mean ± s.e.m. of three biologically independent experiments.

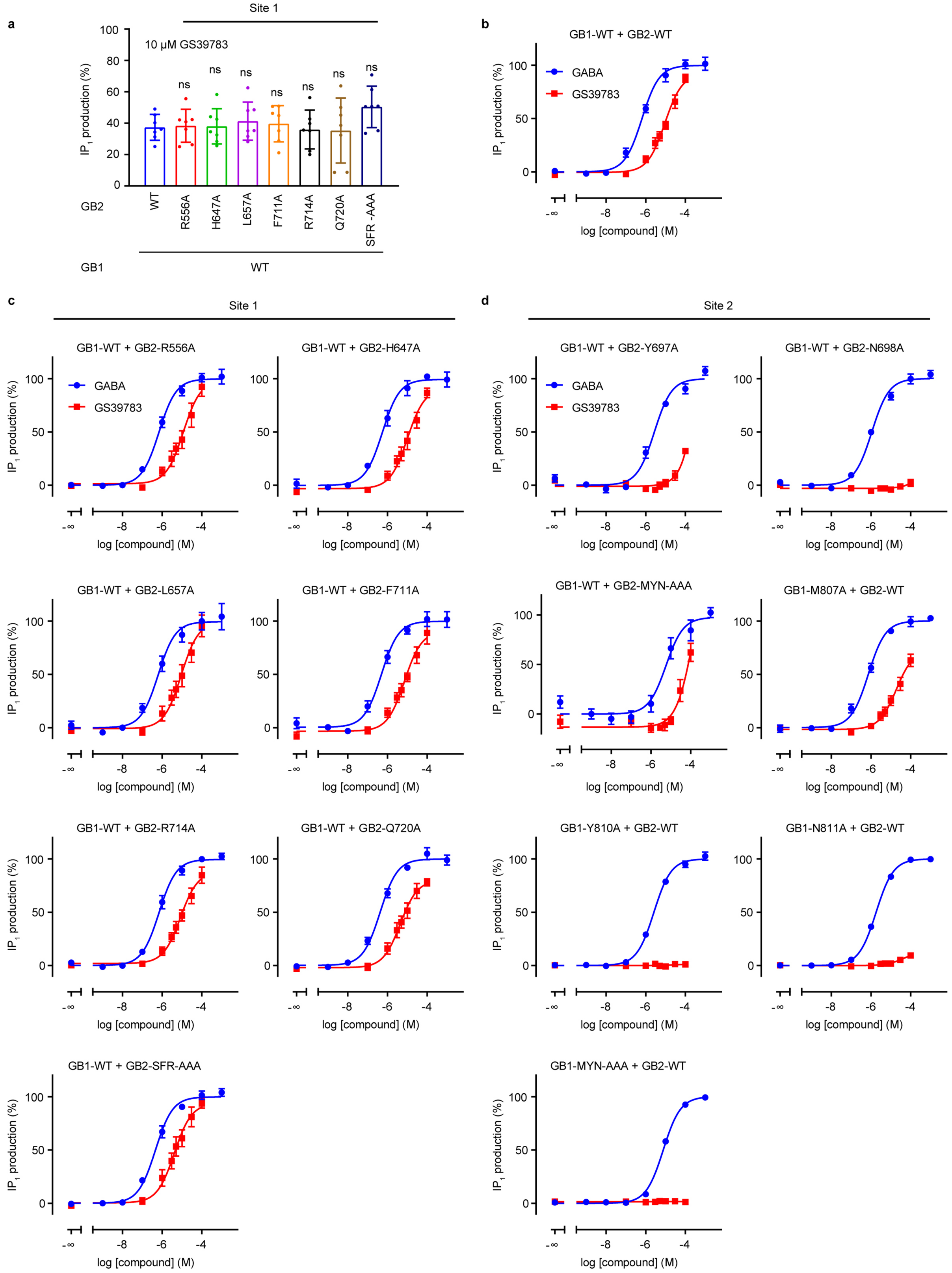

Extended Data Fig. 9 | The effects of a PAM on signalling of the site-1 and -2 mutants of GABA$_B$. **a**, IP$_1$ production induced by 10 μM GS39783 in intact cells expressing the indicated site-1 GB2 mutants co-expressed with the wild-type GB1. Data are normalized by the GABA response and shown as mean ± s.d. of 7 (10 for wild type) biologically independent experiments. Data are analysed using one-way ANOVA with Dunnett's multiple comparison test to determine significance (compared with wild type), with $P = 0.9998$ for GB2(R556A), 0.9999 for GB2(H647A), 0.9907 for GB2(L657A), 0.9995 for GB1(F711A), 0.9997 for GB2(R714A), 0.9996 for GB2(Q720A), and 0.2807 for GB2(SFR-AAA). **b**–**d**, IP$_1$ production induced by GABA (blue) or GS39783 (red) in intact cells expressing the wild-type receptor (**b**) or the indicated mutant of the site 1 (**c**) or site 2 (**d**). Data are normalized by the GABA response and shown as mean ± s.e.m. of four biologically independent experiments.

Extended Data Table 1 | Cryo-EM data collection, refinement and validation statistics

	GABA$_B$ apo (EMDB-21219) (PDB 6VJM)	GABA$_B$/SKF97541 Int-1 (EMDB-20824) (PDB 6UOA)	GABA$_B$/SKF97541 Int-2 (EMDB-20823) (PDB 6UO9)	GABA$_B$/SKF97541/ GS39783 (EMDB-20822) (PDB 6UO8)
Data collection and processing				
Magnification	135,000	29,000	29,000	29,000
Voltage (kV)	300	300	300	300
Electron exposure (e^{-}/Å^2)	8	15	15	15
Defocus range (μm)	-1.5 - -2.5	-1.5 - -3.0	-1.5 - -3.0	-1.5 - -3.0
Pixel size (Å)	1.08	0.8521	0.8521	0.8521
Symmetry imposed	C1	C1	C1	C1
Initial particle images (no.)	2,010,390	5,641,714	5,641,714	4,173,286
Final particle images (no.)	113,093	48,600	114,552	89,001
Map resolution (Å)	4.0	6.3	4.8	3.6
FSC threshold	0.143	0.143	0.143	0.143
Map resolution range (Å)	3.7 - 4.6	5.7 - 12.2	4.5 - 7.3	3.4 - 7.0
Refinement				
Initial model used (PDB code)	4MQE, 6UO8	4MQE, 6VJM	4MS3, 6UO8	4MS3, 4OR2
Model resolution (Å)	4.2	7.6	5.2	3.8
FSC threshold	0.5	0.5	0.5	0.5
Model resolution range (Å)	29.1 - 3.4	29.3 - 1.8	34.3 - 3.5	33.7 - 3.0
Map sharpening *B* factor (Å^2)	-143.0	-378.1	-230.7	-125.8
Model composition				
Non-hydrogen atoms	10,629	9,153	9,915	10,958
Protein residues	1,369	1,323	1,365	1,385
Ligands	0	0	1	2
N-glycans	11	11	13	13
B factors (Å^2)				
Protein	147.4	361.4	209.8	116.0
Ligands	N/A	N/A	141.0	120.8
N-glycans	191.8	421.3	260.1	145.3
R.m.s. deviations				
Bond lengths (Å)	0.005	0.006	0.006	0.004
Bond angles (°)	0.912	1.300	1.360	0.713
Validation				
MolProbity score	1.86	1.87	1.86	1.68
Clashscore	6.77	6.80	6.36	4.16
Poor rotamers (%)	0.19	1.14	1.07	0.00
Ramachandran plot				
Favored (%)	91.75	92.94	92.03	92.23
Allowed (%)	8.25	7.06	7.97	7.77
Disallowed (%)	0.0	0.0	0.0	0.0

Extended Data Table 2 | Mutation study of GABA_B

	GB1 + GB2	GABA pK_i ± S.D. [GS] (n)	GABA pEC_{50} ± S.D. (n)	GS39783 pEC_{50} ± S.D. (n)	GS39783 Emax (% Emax GABA) ± S.D. (n)
	WT + WT	5.44 ± 0.06 [0] (10)	6.19 ± 0.08 (4)	5.03 ± 0.08 (4)	91.9 ± 4.8 (4)
		5.65 ± 0.08 [1] (10)			
		5.92 ± 0.12 [5] (10)			
		5.95 ± 0.16 [10] (7)			
		6.02 ± 0.15 [20] (7)			
Site 1	WT + R556A	5.48 ± 0.07 [0] (4)	6.16 ± 0.07 (4)	4.93 ± 0.14 (4)	98.5 ± 8.7 (4)
		5.80 ± 0.05 [1] (4)			
		6.13 ± 0.08 [5] (4)			
		6.16 ± 0.25 [10] (4)			
		6.18 ± 0.24 [20] (4)			
	WT + H647A	5.58 ± 0.13 [0] (4)	6.26 ± 0.09 (4)	5.00 ± 0.11 (4)	90.8 ± 6.6 (4)
		5.79 ± 0.09 [1] (4)			
		6.12 ± 0.08 [5] (4)			
		6.06 ± 0.14 [10] (4)			
		6.15 ± 0.17 [20] (4)			
	WT + L657A	5.59 ± 0.11 [0] (4)	6.2 ± 0.13 (4)	5.04 ± 0.14 (4)	99.5 ± 8.6 (4)
		5.88 ± 0.07 [1] (4)			
		6.16 ± 0.06 [5] (4)			
		6.10 ± 0.16 [10] (4)			
		6.35 ± 0.14 [20] (4)			
	WT + F711A	5.65 ± 0.16 [0] (4)	6.3 ± 0.1 (4)	5.14 ± 0.11 (4)	90.7 ± 6.4 (4)
		5.84 ± 0.11 [1] (4)			
		6.13 ± 0.14 [5] (4)			
		5.88 ± 0.26 [10] (4)			
		5.86 ± 0.23 [20] (4)			
	WT + R714A	5.46 ± 0.05 [0] (4)	6.15 ± 0.06 (4)	5.08 ± 0.1 (4)	88.2 ± 5.5 (4)
		5.63 ± 0.06 [1] (4)			
		5.93 ± 0.14 [5] (4)			
		5.92 ± 0.16 [10] (3)			
		5.65 ± 0.20 [20] (3)			
	WT + Q720A	5.48 ± 0.16 [0] (4)	6.37 ± 0.07 (4)	5.35 ± 0.11 (4)	80.1 ± 4.7 (4)
		5.70 ± 0.22 [1] (4)			
		5.96 ± 0.11 [5] (4)			
		5.82 ± 0.16 [10] (3)			
		6.03 ± 0.18 [20] (3)			
	WT + SFR-AAA	5.75 ± 0.15 [0] (4)	6.34 ± 0.06 (4)	5.39 ± 0.12 (4)	93.7 ± 5.9 (4)
		5.93 ± 0.08 [1] (4)			
		6.16 ± 0.10 [5] (4)			
		5.98 ± 0.18 [10] (3)			
		5.98 ± 0.19 [20] (3)			
Site 2	WT + Y697A	5.43 ± 0.04 [0] (4)	5.56 ± 0.09 (3)	N.D.	N.D.
		5.43 ± 0.10 [1] (4)			
		5.45 ± 0.05 [5] (4)			
	WT + N698A	5.48 ± 0.07 [0] (4)	5.96 ± 0.06 (3)	N.E.	N.E.
		5.48 ± 0.05 [1] (4)			
		5.46 ± 0.07 [5] (4)			
		5.30 ± 0.16 [10] (3)			
		5.18 ± 0.16 [20] (3)			
	WT + MYN-AAA*	5.44 ± 0.05 [0] (4)	5.25 ± 0.16 (3)	N.E.	N.E.
		5.44 ± 0.05 [1] (4)			
		5.56 ± 0.18 [5] (4)			
	M807A + WT	5.51 ± 0.06 [0] (3)	6.14 ± 0.06 (3)	4.72 ± 0.12 (3)	73.5 ± 6.6 (3)
		5.60 ± 0.09 [1] (3)			
		5.74 ± 0.15 [5] (3)			
	Y810A + WT	5.48 ± 0.09 [0] (3)	5.59 ± 0.04 (3)	N.E.	N.E.
		5.49 ± 0.03 [1] (3)			
		5.46 ± 0.09 [5] (3)			
	N811A + WT	5.45 ± 0.12 [0] (3)	5.74 ± 0.03 (3)	N.E.	N.E.
		5.43 ± 0.07 [1] (3)			
		5.48 ± 0.16 [5] (3)			
	MYN-AAA + WT	5.47 ± 0.10 [0] (3)	5.12 ± 0.03 (3)	N.E.	N.E.
		5.44 ± 0.09 [1] (3)			
		5.45 ± 0.11 [5] (3)			

Apparent affinities for GABA (pK_i) in the presence of indicated concentrations of GS39783 (0, 1, 5, 10 or 20 μM) and functional data for the GABA or GS39783 alone. N.E., no effect (absence of response); N.D., not determined (value cannot be calculated). The number of biologically independent experiments (*n*) is shown in parentheses.

*Mutation MYN-AAA in GB2 refers to a triple mutant (M694A/Y697A/N698A).

nature research

Corresponding author(s): Cornelius Gati, Vadim Cherezov

Last updated by author(s): Mar 29, 2020

Reporting Summary

Nature Research wishes to improve the reproducibility of the work that we publish. This form provides structure for consistency and transparency in reporting. For further information on Nature Research policies, see Authors & Referees and the Editorial Policy Checklist.

Statistics

For all statistical analyses, confirm that the following items are present in the figure legend, table legend, main text, or Methods section.

n/a	Confirmed	
☐	☒	The exact sample size (*n*) for each experimental group/condition, given as a discrete number and unit of measurement
☐	☒	A statement on whether measurements were taken from distinct samples or whether the same sample was measured repeatedly
☐	☒	The statistical test(s) used AND whether they are one- or two-sided *Only common tests should be described solely by name; describe more complex techniques in the Methods section.*
☒	☐	A description of all covariates tested
☒	☐	A description of any assumptions or corrections, such as tests of normality and adjustment for multiple comparisons
☐	☒	A full description of the statistical parameters including central tendency (e.g. means) or other basic estimates (e.g. regression coefficient) AND variation (e.g. standard deviation) or associated estimates of uncertainty (e.g. confidence intervals)
☐	☒	For null hypothesis testing, the test statistic (e.g. *F*, *t*, *r*) with confidence intervals, effect sizes, degrees of freedom and *P* value noted *Give P values as exact values whenever suitable.*
☒	☐	For Bayesian analysis, information on the choice of priors and Markov chain Monte Carlo settings
☒	☐	For hierarchical and complex designs, identification of the appropriate level for tests and full reporting of outcomes
☒	☐	Estimates of effect sizes (e.g. Cohen's *d*, Pearson's *r*), indicating how they were calculated

Our web collection on statistics for biologists contains articles on many of the points above.

Software and code

Policy information about availability of computer code

Data collection	Cryo-EM data were collected automatically on a Titan Krios (FEI) using SerialEM v.3.8beta.
Data analysis	The following software was used in this study: MotionCor2, CTFFIND v4.1.10, RELION v. 3.0, CryoSparc v. 2.11, UCSF ChimeraX v. 0.7.0, Coot v. 0.8.9, PyMOL v. 2.3.3, Phenix v 1.17.1-3660, ccp4 v. 7.0.078, ICM-Pro v. 3.8.7b, ProDy v. 1.10.10, MDAnalysis v. 0.20.1, Gromacs v. 2018, Graphpad Prism v6, Swiss Model webserver (https://swissmodel.expasy.org), Charmm-GUI webserver (http://www.charmm-gui.org/).

For manuscripts utilizing custom algorithms or software that are central to the research but not yet described in published literature, software must be made available to editors/reviewers. We strongly encourage code deposition in a community repository (e.g. GitHub). See the Nature Research guidelines for submitting code & software for further information.

Data

Policy information about availability of data

All manuscripts must include a data availability statement. This statement should provide the following information, where applicable:

- Accession codes, unique identifiers, or web links for publicly available datasets
- A list of figures that have associated raw data
- A description of any restrictions on data availability

The cryo-EM density maps and corresponding coordinates have been deposited in the Electron Microscopy Data Bank (EMDB) and the Protein Data Bank (PDB), respectively, under the following accession codes: EMD-20822 and 6UO8 (GABAB bound to SKF97541 and GS39783), EMD-20823 and 6UO9 (GABAB bound to SKF97541, int-2 state), EMD-20824 and 6UOA (GABAB bound to SKF97541, int-1 state), and EMD-21219 and 6VJM (GABAB in the apo state).
Figs. 2e, f, 3e, f and Extended Data Figs. 1a-d, 8, 9 have associated raw data. Supplementary information file contains the uncropped gel shown in Extended Data Fig. 1f. All other data are available from the authors on reasonable request.

Field-specific reporting

Please select the one below that is the best fit for your research. If you are not sure, read the appropriate sections before making your selection.

☒ Life sciences ☐ Behavioural & social sciences ☐ Ecological, evolutionary & environmental sciences

For a reference copy of the document with all sections, see nature.com/documents/nr-reporting-summary-flat.pdf

Life sciences study design

All studies must disclose on these points even when the disclosure is negative.

Sample size	No statistical methods were used to predetermine sample size. Pharmacological assays were conducted at least in n=3 biologically independent experiments and are comparable to other published studies. Wild-type constructs were used as internal controls, resulting in larger number of independent repeats. Sample size for cryo-EM experiments was determined by availability of microscope time and to ensure refining a high-resolution structure that allowed us to obtain a high-resolution reconstruction within the confines of limited microscope time.
Data exclusions	No pharmacological data were excluded. There were no pre-established criteria for exclusion of cryo-EM data. However, the process of generating 3D maps from cryo-EM particles involves sorting for particles that are damaged, have low signal, or are in minority conformations that are unlikely to refine correctly. This is implemented in Relion 3.0 and CryoSparc 2.11.
Replication	All pharmacological measurements were done at least in triplicates. All attempts at replication were successful and included in the final data. There was no attempt to replicate cryo-EM data. Each dataset includes averaging of tens of thousands of particles.
Randomization	This study did not allocate experimental groups thus no randomization was required for the reported experiments.
Blinding	The researchers were not blinded to allocation during experiments and outcome assessment. Blinding was not required for the reported experiments because all functional and structural data were analyzed using the same methods, and results are not subjective.

Reporting for specific materials, systems and methods

We require information from authors about some types of materials, experimental systems and methods used in many studies. Here, indicate whether each material, system or method listed is relevant to your study. If you are not sure if a list item applies to your research, read the appropriate section before selecting a response.

Materials & experimental systems

n/a	Involved in the study	
☐	☒	Antibodies
☐	☒	Eukaryotic cell lines
☒	☐	Palaeontology
☒	☐	Animals and other organisms
☒	☐	Human research participants
☒	☐	Clinical data

Methods

n/a	Involved in the study	
☒	☐	ChIP-seq
☒	☐	Flow cytometry
☒	☐	MRI-based neuroimaging

Antibodies

Antibodies used	Anti-FLAG M2 antibody gel. Supplier MilliporeSigma, Catalog number A2220, M2 monoclonal, Lot number SLCD7154, no dilution. Anti-GFP nanobody resin, cAbGFP4, no dilution, made in-house using protocols from Kubala et al. "Structural and thermodynamic analysis of the GFP: GFP-nanobody complex." Protein Science 19.12 (2010): 2389-2401.
Validation	Anti-FLAG M2 antibody gel, full validation report is available on the supplier website. Anti-GFP nanobody, validation was reported by Kubala et al. in "Structural and thermodynamic analysis of the GFP: GFP-nanobody complex." Protein Science 19.12 (2010): 2389-2401.

Eukaryotic cell lines

Policy information about cell lines

Cell line source(s)	Cell lines were purchased from the American Type Culture Collection (ATCC). Insect Sf9 cell line: ATCC CRL-1711. Human HEK293 cell line: ATCC-CRL-1573.
Authentication	The cell line was authenticated by the supplier (ATCC) using morphology and growth characteristics.

Mycoplasma contamination	Cells have been tested and shown to be free from mycoplasma (Hoechst DNA strain and Direct Culture methods employed).
Commonly misidentified lines (See ICLAC register)	No commonly misidentified cell lines were used.

Structure of human GABA_B receptor in an inactive state

https://doi.org/10.1038/s41586-020-2452-0

Received: 8 October 2019

Accepted: 1 May 2020

Jinseo Park[1,19], Ziao Fu[2,19], Aurel Frangaj[1,19], Jonathan Liu[1,19], Lidia Mosyak[1,19], Tong Shen[3,19], Vesna N. Slavkovich[4], Kimberly M. Ray[1], Jaume Taura[5], Baohua Cao[1], Yong Geng[1,6], Hao Zuo[1], Yongjun Kou[6], Robert Grassucci[2], Shaoxia Chen[7], Zheng Liu[2], Xin Lin[8,9], Justin P. Williams[10], William J. Rice[11], Edward T. Eng[11], Rick K. Huang[12], Rajesh K. Soni[13], Brian Kloss[14], Zhiheng Yu[12], Jonathan A. Javitch[1,8,9,10], Wayne A. Hendrickson[2,10,14], Paul A. Slesinger[5], Matthias Quick[8,9], Joseph Graziano[4], Hongtao Yu[15], Oliver Fiehn[3], Oliver B. Clarke[10,16] ✉, Joachim Frank[2,17] ✉ & Qing R. Fan[1,18] ✉

The human GABA_B receptor—a member of the class C family of G-protein-coupled receptors (GPCRs)—mediates inhibitory neurotransmission and has been implicated in epilepsy, pain and addiction[1]. A unique GPCR that is known to require heterodimerization for function[2–6], the GABA_B receptor has two subunits, GABA_B1 and GABA_B2, that are structurally homologous but perform distinct and complementary functions. GABA_B1 recognizes orthosteric ligands[7,8], while GABA_B2 couples with G proteins[9–14]. Each subunit is characterized by an extracellular Venus flytrap (VFT) module, a descending peptide linker, a seven-helix transmembrane domain and a cytoplasmic tail[15]. Although the VFT heterodimer structure has been resolved[16], the structure of the full-length receptor and its transmembrane signalling mechanism remain unknown. Here we present a near full-length structure of the GABA_B receptor, captured in an inactive state by cryo-electron microscopy. Our structure reveals several ligands that preassociate with the receptor, including two large endogenous phospholipids that are embedded within the transmembrane domains to maintain receptor integrity and modulate receptor function. We also identify a previously unknown heterodimer interface between transmembrane helices 3 and 5 of both subunits, which serves as a signature of the inactive conformation. A unique 'intersubunit latch' within this transmembrane interface maintains the inactive state, and its disruption leads to constitutive receptor activity.

We assembled the heterodimeric human GABA_B receptor by using baculovirus-infected mammalian cells. Each subunit was truncated at the carboxy-terminal end according to the domain boundary of the intracellular coiled-coil[17], in order to eliminate flexible regions (Supplementary Fig. 1). Upon extraction and purification with detergent (Extended Data Fig. 1a, b and Supplementary Fig. 2), the complex bound to radioactive [^{3}H]GABA with a dissociation constant comparable to the GABA affinity reported for native receptors[3,4,7] (Extended Data Fig. 1c). Functional analysis incorporating a chimaeric $\text{G}\alpha_\text{qi5}$ protein and inositol phosphate assay[18] in mammalian cells showed that the agonist baclofen activated the C-terminally truncated and full-length receptor with similar potency and efficacy, indicating that the deleted regions in the GABA_B1b and GABA_B2 cytoplasmic tails are not required for ligand-mediated G-protein activation (Extended Data Fig. 1d).

We determined the structure of the heterodimeric GABA_B receptor by cryo-electron microscopy (cryo-EM) to an overall resolution of 3.3 Å (Extended Data Fig. 2a–e and Supplementary Table 1). The global density map displayed directional anisotropy owing to linker flexibility (Extended Data Fig. 2f). Performing local refinement separately on the extracellular domains (ECDs) and transmembrane domains yielded reconstructions at resolutions of 3.1 Å and 3.4 Å, respectively (Extended Data Fig. 2g, h). We used a composite map that combined the ECD and

---

[1]Department of Pharmacology, Columbia University, New York, NY, USA. [2]Department of Biochemistry and Molecular Biophysics, Columbia University, New York, NY, USA. [3]NIH West Coast Metabolomics Center, University of California Davis, Davis, CA, USA. [4]Department of Environmental Health Sciences, Columbia University, New York, NY, USA. [5]Nash Family Department of Neuroscience, Friedman Brain Institute, Icahn School of Medicine at Mount Sinai, New York, NY, USA. [6]Key Laboratory of Receptor Research, Center for Structure and Function of Drug Targets, Shanghai Institute of Materia Medica, Chinese Academy of Sciences, Shanghai, China. [7]MRC Laboratory of Molecular Biology, Cambridge, UK. [8]Department of Psychiatry, Columbia University, New York, NY, USA. [9]Division of Molecular Therapeutics, New York State Psychiatric Institute, New York, NY, USA. [10]Department of Physiology and Cellular Biophysics, Columbia University, New York, NY, USA. [11]National Resource for Automated Molecular Microscopy, Simons Electron Microscopy Center, New York Structural Biology Center, New York, NY, USA. [12]Janelia Research Campus, Howard Hughes Medical Institute, Ashburn, VA, USA. [13]Proteomics Shared Resource, Herbert Irving Comprehensive Cancer Center, Columbia University, New York, NY, USA. [14]Center on Membrane Protein Production and Analysis, New York Structural Biology Center, New York, NY, USA. [15]Howard Hughes Medical Institute, Department of Pharmacology, University of Texas Southwestern Medical Center, Dallas, TX, USA. [16]Department of Anesthesiology and the Irving Institute for Clinical and Translational Research, Columbia University, New York, NY, USA. [17]Department of Biological Sciences, Columbia University, New York, NY, USA. [18]Department of Pathology and Cell Biology, Columbia University, New York, NY, USA. [19]These authors contributed equally: Jinseo Park, Ziao Fu, Aurel Frangaj, Jonathan Liu, Lidia Mosyak, Tong Shen. ✉e-mail: oc2188@cumc.columbia.edu; jf2192@cumc.columbia.edu; qf13@cumc.columbia.edu

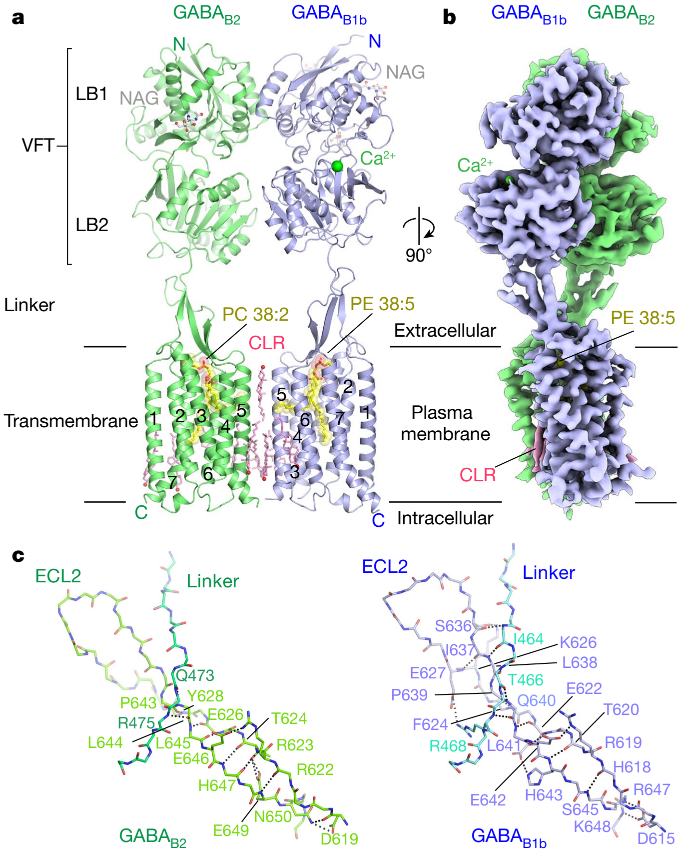

Fig. 1 | Cryo-EM structure of human GABA$_B$ receptor. a, Ribbon representation of the GABA$_B$-receptor structure, composed of GABA$_{B1b}$ (blue) and GABA$_{B2}$ (green) subunits. Ca^{2+} is shown as a green sphere; phospholipids (PE 38:5 and PC 38:2) are shown as yellow space-filling models; N-linked glycans (NAGs) and cholesterols (CLRs) are shown, respectively, as grey and pink ball-and-stick models. Transmembrane helices 1–7 are marked for each subunit. **b**, Cryo-EM density map of the GABA$_B$ receptor, composed of local reconstructions for extracellular (3.1 Å) and transmembrane (3.4 Å) domains, in an orthogonal view from **a**. **c**, Linker domains of GABA$_{B1b}$ and GABA$_{B2}$, showing the main-chain and side-chain hydrogen-bonding patterns between the linker region and ECL2.

transmembrane reconstructions for model building and refinement (Extended Data Fig. 3). By applying three-dimensional variability analysis to the data, we found that the receptor is in dynamic motion, and that its functional state corresponds to a continuum of conformations along multiple dimensions (Supplementary Videos 1–4).

The heterodimeric GABA$_B$ receptor is assembled when GABA$_{B1b}$ and GABA$_{B2}$ subunits interact side-by-side while facing in opposite directions (Fig. 1a, b and Extended Data Fig. 4). Both the VFT and the transmembrane components of the two subunits are related by pseudo-twofold axes. Extracellular and intracellular loops (ECLs and ICLs) that interconnect adjacent helices within each transmembrane domain are visible in the density map, except for ICL2. The cytoplasmic tail including the coiled-coil domain is disordered, possibly because of its flexible attachment to the transmembrane domain.

The elongated peptide linker that joins the VFT to the transmembrane domain is buttressed through its interaction with a β-hairpin formed by ECL2 (Fig. 1c). ECL2 twists across the linker, forming a united mechanical junction that transmits the conformational changes in the VFT to the transmembrane domain and vice versa. Additionally, the ECD and transmembrane domains of the receptor spontaneously flex back and forth about the linker, exhibiting the region's intrinsic flexibility (Supplementary Video 1).

Given that no ligand was added during protein purification, we expected the receptor to be in an apo form and an inactive conformation. To our surprise, we observed several ligands bound to the receptor. GABA$_{B1b}$ contains a Ca^{2+} ion at the interdomain cleft of VFT. In addition, an endogenous phospholipid is bound within the transmembrane pocket of each subunit, with a phosphatidylethanolamine (PE 38:5) in GABA$_{B1b}$, and a phosphatidylcholine (PC 38:2) in GABA$_{B2}$. Finally, ten cholesterol or cholesteryl hemisuccinate molecules, which we modelled as cholesterol (see Methods), are distributed around the exterior of the transmembrane complex, including two that interface with both subunits.

Inactive conformation of GABA$_B$ receptor

The cryo-EM structure of the GABA$_B$ receptor appears to occupy an inactive conformation, given its similarity to known crystal structures of the GABA$_B$ VFT in its apo and antagonist-bound states[16]. First, the VFT module, composed of the lobe-shaped LB1 and LB2 domains, adopts an open interdomain conformation in both subunits (Extended Data Fig. 5a, b). Second, although an amino-terminal LB1–LB1 dimer interface is present in all functional states, the distinct lack of a heterodimer interface between the membrane-proximal LB2 domains is shared by the near full-length cryo-EM structure and inactive-state VFT structures (Extended Data Fig. 5c, d). By contrast, a hallmark of the active-state VFT structures is a unique heterodimer interface between LB2 domains, which results from agonist-induced GABA$_{B1b}$ closure[16].

Using conformational variability analysis, we observed that the LB2 domains of both subunits fluctuate by approaching and withdrawing from the central vertical axis of the heterodimer, yet never make contact as they do in active-state VFT crystal structures (Supplementary Videos 2, 3). The motion exhibited by the LB2 domains and their associated linkers suggests that the inactive functional state corresponds to an ensemble of conformations, where the separation between the membrane-proximal regions falls within a small range around the coordinates of our structure.

Inactive transmembrane heterodimer interface

We identified a hitherto unknown heterodimer interface between the transmembrane TM5 and TM3 helices of both subunits that embodies the signature of the GABA$_B$ receptor's inactive conformation (Fig. 2a). A TM5–TM5 contact has previously been detected through crosslinking of the GABA$_B$ receptor[19], but transmembrane dimer interfaces of any kind are yet to be found in other inactive class C GPCRs, including the recent inactive metabotropic glutamate receptor mGlu$_5$ structure[20] (Extended Data Fig. 5e).

Positioned at 30° from the extracellular dimer interface, the transmembrane dimer interactions bury approximately 740 Å^2 of surface area and exhibit high shape complementarity (Extended Data Fig. 5f). The pair of TM5 helices scissor at their central residues before contacting the transverse TM3 of opposing subunits at their intracellular ends (Fig. 2a). TM5 extracellular ends display conformational variance wherein they approach and withdraw but fail to make contact (Supplementary Video 4). All direct heterodimer interactions occur near the cytoplasmic membrane surface and can be divided into three core layers (I–III) along the helical path of TM5 (Fig. 2a).

The surface layer I caps the extracellular end of the transmembrane heterodimer interface. It is composed of hydrophobic contacts between four leucine residues of both subunits. The middle layer II lies directly beneath layer I, and consists of three phenylalanine residues packing against one another, as well as their neighbouring leucine residues. Both layers solely incorporate TM5 residues.

Layer III, consisting of sections IIIa and IIIb, completes the interface at the intracellular end. IIIa possesses a network of salt bridges that tether the cytoplasmic ends of GABA$_{B1b}$ and GABA$_{B2}$ transmembrane domains.

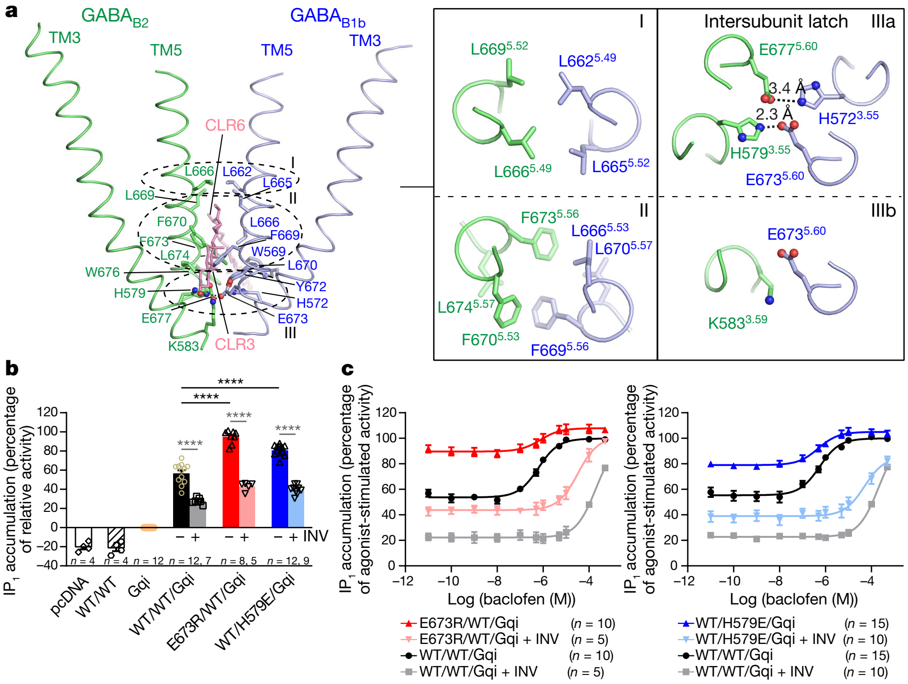

Fig. 2 | Transmembrane heterodimer interface of the $\mathrm{GABA_B}$ receptor. **a**, The transmembrane heterodimer interface formed by TM5 and TM3 of both subunits. Three layers (I, II and III) of interfacial contacts are identified by dotted circles. Direct heterodimer contacts within each layer are shown on the right. **b**, **c**, Functional analysis of the 'intersubunit latch'. Basal activity (**b**) and dose-dependent baclofen-stimulated receptor response (**c**) in cells transiently expressing a $G\alpha_{qi5}$ chimaera (abbreviated as Gqi) with different combinations of $\mathrm{GABA_B}$ wild-type subunits (WT) and mutant subunits ($\mathrm{GABA_{B1b}}$ E673R, abbreviated as E673R; $\mathrm{GABA_{B2}}$ H579E, abbreviated as H579E). Inositol-1-phosphate ($\mathrm{IP_1}$) accumulation was measured in the presence or absence of 20 µM CGP54626 (abbreviated as INV). Cells transfected with empty pcDNA3.1 vector (abbreviated as pcDNA), $G\alpha_{qi5}$ alone, or WT $\mathrm{GABA_B}$ subunits in the absence of $G\alpha_{qi5}$ were used as controls. Relative activity is expressed as percentage of maximum wild-type activity induced by baclofen relative to the activity of $G\alpha_{qi5}$ alone. Data points represent averages ± s.e.m. of multiple experiments (*n* values shown), each with quadruplicate measurements. $^{****}P < 0.0001$; one-way analysis of variance (ANOVA) with Bonferroni's post hoc test was used to calculate statistical differences in basal activity (**b**). The level of cell surface expression was 90% for E673R/WT and 76% for WT/H579E mutants in comparison with the WT/WT heterodimer.

This critical interaction is mediated by a quartet of charged residues from the TM3 and TM5 helices (His $572^{3.55}$ and Glu $673^{5.60}$ in $\mathrm{GABA_{B1b}}$; His $579^{3.55}$ and Glu $677^{5.60}$ in $\mathrm{GABA_{B2}}$; Supplementary Table 2), a feature that we refer to as the 'intersubunit latch' for securing the transmembrane orientation of the two subunits in the inactive conformation. One of the 'intersubunit latch' residues shares nonpolar contacts with a lysine of $\mathrm{GABA_{B2}}$ TM5, establishing the accessory site IIIb.

In addition, the central layers of direct heterodimer contacts are flanked on each side by a cholesterol molecule. One mediates the interaction between TM5 helices of both subunits (CLR3), while the other bridges TM3 of $\mathrm{GABA_{B1b}}$ and TM5 of $\mathrm{GABA_{B2}}$ (CLR6) (Extended Data Fig. 5g).

The 'intersubunit latch'

To determine the importance of the 'intersubunit latch' in controlling the inactive state of the $\mathrm{GABA_B}$ receptor, we examined the effect of single charge-repelling mutations ($\mathrm{GABA_{B1b}}$ E673R and $\mathrm{GABA_{B2}}$ H579E) within the motif. Wild-type $\mathrm{GABA_B}$ receptor exhibited basal activity in the absence of agonist (Fig. 2b), as reported previously[14]. Both mutants substantially increased basal activity when compared to the wild type, suggesting that each mutation promotes agonist-independent constitutive activity (Fig. 2b). The basal activity displayed by these mutants reached approximately 80–90% of the maximal agonist-dependent wild-type response (Fig. 2b, c). Application of the agonist baclofen raised receptor activity further to the highest wild-type level (Fig. 2c). Neither mutation altered the agonist potency. After each construct was treated with the inverse agonist CGP54626, the basal activity of mutants still remained higher than that of the wild type, providing further evidence that the 'intersubunit latch' mutations serve to shift the conformational equilibrium of $\mathrm{GABA_B}$ towards an active state. Taken together, our mutational data indicate that the 'intersubunit latch' is fundamental to maintaining the inactive state of the receptor.

Endogenous ligands bound to $\mathrm{GABA_{B1b}}$ VFT

We identified a new potential $\mathrm{Ca^{2+}}$-binding site in the vicinity of the orthosteric ligand-binding cleft on the LB2 surface of $\mathrm{GABA_{B1b}}$ (Fig. 3a and Extended Data Fig. 6a, b). The metal ion density has remarkable peak height in the cryo-EM density map (10σ) and is surrounded by residues that are chemically favourable for $\mathrm{Ca^{2+}}$ coordination. The $\mathrm{Ca^{2+}}$ is anchored by the carboxylate groups of three acidic residues (Asp 281, Glu 309 and Glu 423) and by the backbone carbonyl atoms of two additional residues (Gly 277 and Tyr 279) (Fig. 3b). The $\mathrm{Ca^{2+}}$–O bond distances are between 3.0 Å and 4.6 Å, suggesting that the ion is in a hydrated state. The $\mathrm{Ca^{2+}}$ location in $\mathrm{GABA_{B1b}}$ is different from any of the four sites found in the calcium-sensing (CaS) receptor[21], another class C GPCR (Fig. 3c).

Using inductively coupled plasma mass spectroscopy, we detected the presence of Ca and Cu above background level in purified $\mathrm{GABA_B}$ receptor. The amounts of other metal elements were negligible (Supplementary Table 3). The molar ratios of Ca and Cu relative to the receptor protein (0.43:1 and 0.51:1) suggest partial occupancy of the ion-binding sites. An unmodelled density within the interdomain cleft, coordinated by tryptophan and histidine, may serve as a potential $\mathrm{Cu^{2+}}$-binding site but lacks sufficient signal to be labelled confidently.

In exploring the functional role of the bound ion, we found that the $\mathrm{Ca^{2+}}$ chelator EGTA substantially reduced $\mathrm{GABA_B}$ basal activity, and that mutating specific coordinating residues ($\mathrm{GABA_{B1b}}$ E309K and $\mathrm{GABA_{B1b}}$

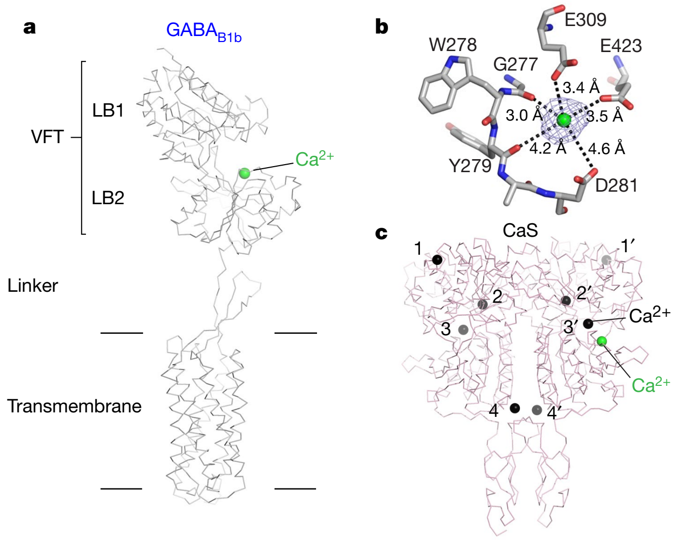

Fig. 3 | Ca^{2+} binding in GABA$_{B1b}$. **a**, Ribbon representation of the GABA$_{B1b}$ subunit, showing the location of the Ca^{2+}-binding site at the interdomain crevice of VFT. **b**, Specific interactions between GABA$_{B1b}$ and Ca^{2+}. The mesh represents the cryo-EM density map contoured at 7.5σ surrounding Ca^{2+}. **c**, Crystal structure of the CaS receptor extracellular domain (Protein DataBank (https://www.rcsb.org) code 5K5S), highlighting its bound Ca^{2+} (black spheres, numbered 1–4 and 1′–4′ in the two protomers) and the corresponding location of the Ca^{2+}-binding site in GABA$_{B1b}$ (green sphere).

E423R) had similar, although less drastic, effects (Extended Data Fig. 6c, d). Consistent with previous findings, these data suggest that Ca^{2+} may act as a positive allosteric modulator of the GABA$_B$ receptor[22,23]. Our structure implies that Ca^{2+} stabilizes residues adjacent to the critical agonist-binding residue Trp 278, thereby indirectly reinforcing its conformation (Fig. 3b).

We also found density in the orthosteric agonist-binding site of GABA$_{B1b}$, and its shape suggests a GABA-like endogenous ligand (Extended Data Fig. 6a, b). GABA is a potential candidate because it fits the density and was detected in the lysate of cells used to express the receptor (Extended Data Fig. 6e, f). This GABA-like endogenous ligand bound in an inactive receptor conformation may reflect a preactivation state; however, further investigation is required.

Discovery of endogenous phospholipid ligands

Our structure revealed endogenous phospholipids within the transmembrane domains of both GABA$_B$ subunits. Using the CaS receptor as a control in mass spectrometry, we identified two phospholipids specifically bound to the GABA$_B$ receptor, PE 38:5 and PC 38:2 (Fig. 4a–d). Both lipids consist of two long-chain fatty acyl moieties of 18 and 20 carbons. We further assigned PE 38:5 to GABA$_{B1b}$ and PC 38:2 to GABA$_{B2}$ on the basis of the size difference between the phosphoethanolamine and phosphocholine head groups of the two lipids (Extended Data Fig. 7a, b). The lipid density in the GABA$_{B2}$ transmembrane domain has a bulkier head group that can better accommodate the larger choline moiety of PC 38:2.

Mirroring the amphipathicity of phospholipids, the lipid-binding pocket of each GABA$_B$ subunit retains a hydrophilic trunk and two lipophilic branches for binding the lipid polar head and nonpolar tails, respectively. The trunk consists of a negatively charged patch covering the amine moiety, and a positively charged area surrounding the phosphate (Extended Data Fig. 7c, d). The lipid-binding pockets are notably deep, extending from the extracellular membrane surface to the centre of the transmembrane domain (Fig. 4e, f). Each lipid occupies nearly the entire range of ligand-binding positions in class A, B, C and F GPCRs (Extended Data Fig. 7e–h).

Each GABA$_B$ subunit makes extensive contacts with the bound lipid, using a majority of the transmembrane helices, including TM2, 3, 5, 6 and 7 (Extended Data Fig. 7a, b, i, j). Approximately 2,400 Å^2 of surface area is buried by either lipid–subunit pair. In addition, ECL2 directly contacts PE 38:5 in GABA$_{B1b}$, while the linker and all three ECLs interact with PC 38:2 in GABA$_{B2}$.

Key elements of the lipid–receptor interactions are conserved in GABA$_{B1b}$ and GABA$_{B2}$ (Fig. 4g–j, Extended Data Fig. 7i, j and Supplementary Fig. 3). First, the hydrophilic head of each lipid is anchored through interactions with conserved histidine and arginine residues (His 643 of ECL2 and Arg 549$^{3.32}$ in GABA$_{B1b}$; His 647 of ECL2 and Arg 556$^{3.32}$ in GABA$_{B2}$) (Fig. 4g, h). GABA$_{B2}$ also incorporates Arg 714 of ECL3, rendering the lipid-binding pocket more electropositive than that of GABA$_{B1b}$ (Fig. 4h).

Second, the 20-carbon fatty acyl chain of both lipids follows a perpendicular turn to pass between two aromatic residues (Phe 557$^{3.40}$ and Tyr 657$^{5.44}$ in GABA$_{B1b}$; Tyr 564$^{3.40}$ and Tyr 661$^{5.44}$ in GABA$_{B2}$) (Fig. 4i, j). A *cis* double bond in each fatty acyl chain forms π interactions with the aromatic side chains. The bend is further buttressed by extensive nonpolar contacts with the aliphatic part of a conserved lysine (GABA$_{B1b}$ Lys 660$^{5.47}$; GABA$_{B2}$ Lys 664$^{5.47}$) lying parallel to the chain. Finally, the 18-carbon fatty acyl chain of both lipids is relatively straight, extending towards the cytoplasm in a binding pocket lined by small aliphatic residues on TM2, TM3 and TM7 (Fig. 4i, j).

The GABA$_B$ receptor's transmembrane domains are covered by the linker and ECLs, which form a lid over the lipid-binding pocket. Phospholipids may access the lipid-binding pocket of designated subunits laterally through gaps between TM5 and TM6 (Extended Data Fig. 8a–d). One of the fatty acyl tails of each phospholipid even protrudes through this opening. The lipid-binding sphingosine-1-phosphate (S1P$_1$) receptor possesses a similar gap between TM1 and TM7 (ref. [24]; Extended Data Fig. 8e, f). The endogenous lipids of other GPCRs can be readily replaced[24], but the size and engagement of the endogenous lipids bound to the GABA$_B$ receptor suggest that they are essential for maintaining receptor integrity and stability.

To explore the physiological relevance of the endogenous phospholipids, we mutated residues that hydrogen bonded with the phosphate head group. We identified R714A in GABA$_{B2}$ ECL3, which displayed a small gain of function despite reduced cell surface expression (Extended Data Fig. 8g, h). This mutation is expected to enhance the movement of PC 38:2 within GABA$_{B2}$ by eliminating a critical interaction with the lid. Our results suggest that PC 38:2 may act as a negative allosteric modulator of GABA$_B$ receptor by stabilizing the inactive conformation of GABA$_{B2}$.

Comparison of subunits with other GPCRs

The GABA$_{B1b}$ and GABA$_{B2}$ subunits have highly similar VFT and transmembrane components but differ in their relative orientation (Extended Data Fig. 9a, b). Each subunit differs from all other class C GPCRs in possessing an extended peptide linker between the VFT and transmembrane domains instead of a cysteine-rich domain (Fig. 1c).

GABA$_B$ subunits also display distinct helix positions in the seven-helix bundles among inactive GPCRs (Extended Data Fig. 9c–f). However, these differences are minor compared with the dramatic movement of TM6 in class A and B GPCRs when activated by G-protein coupling[25,26]. This corroborates our conclusion that we have captured an inactive conformation of the GABA$_B$ receptor.

The GABA$_B$ receptor presents unique variations of conserved transmembrane motifs (Extended Data Fig. 10a, b). In most class A GPCRs such as rhodopsin[27], the 'ionic lock' tethers TM3 and TM6 to stabilize the inactive state of an individual transmembrane domain[27] (Extended Data Fig. 10c). The 'ionic locks' of both GABA$_B$ subunits consist of an aspartate from ICL3 and a lysine from TM3 (Lys$^{3.50}$) (Extended Data Fig. 10a, b). Although only the Lys/Asp pair in GABA$_{B1b}$ are within hydrogen-bond distance, their backbone Cα–Cα separations (9.3–9.4 Å) are comparable

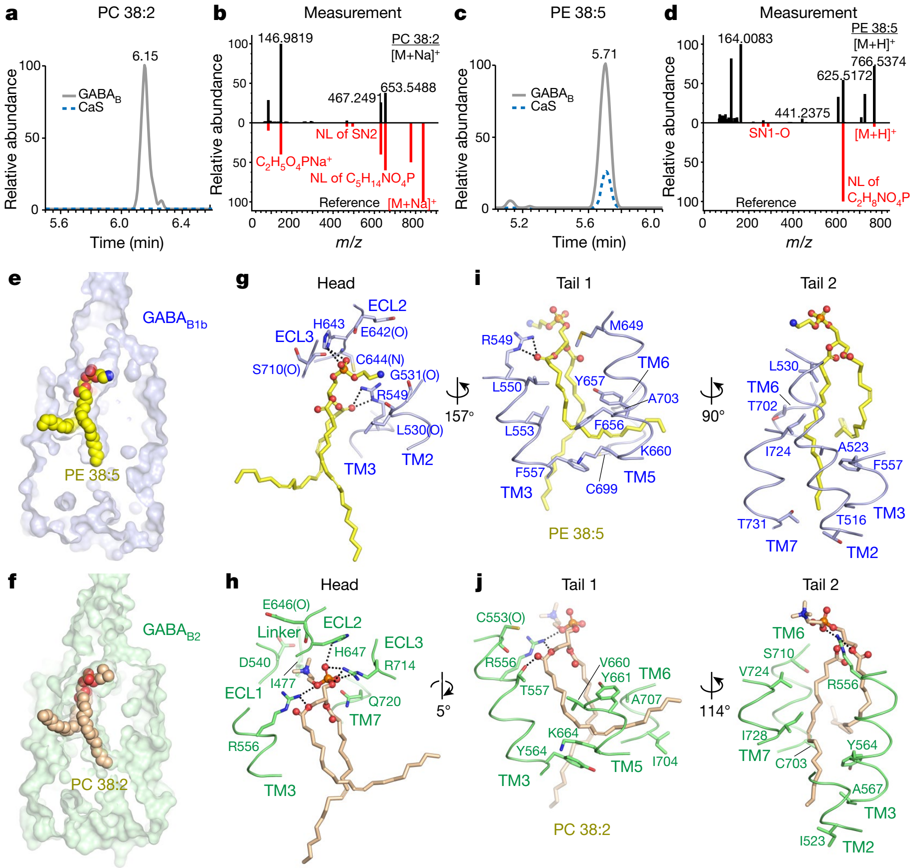

Fig. 4 | Identification of endogenous phospholipid ligands of the GABA$_B$ receptor. **a**, **c**, Liquid chromatography with tandem mass spectrometry (LC-MS/MS) analysis of phospholipids bound to the GABA$_B$ receptor ($n = 1$). The LC traces show the abundance of phospholipids PC 38:2 (**a**) and PE 38:5 (**c**) in GABA$_B$ preparation relative to a CaS receptor control. **b**, **d**, High-resolution MS spectra of the peaks in **a**, **c** (black) matched with standard spectra of PC 38:2 (**b**) and PE 38:5 (**d**) in red. NL, neutral loss: a fragment in a neutral charge state during collision-induced dissociation; SN1 and SN2, stereospecific numbering of glycerophospholipids, marking the fatty acyl groups at respectively the first and second carbons of the glycerol. **e**, **f**, Molecular surface of the GABA$_{B1b}$ (**e**) and GABA$_{B2}$ (**f**) transmembrane domains, showing the binding pockets for PE 38:5 and PC 38:2, respectively. **g**–**j**, Three views of the specific interactions between phospholipids and each GABA$_B$ subunit. Contacts are shown between the phospholipid head group and residues from GABA$_{B1b}$ (**g**) and GABA$_{B2}$ (**h**), and between phospholipid fatty acyl chains and GABA$_{B1b}$ (**i**) and GABA$_{B2}$ (**j**).

to that of rhodopsin[27] (8.7 Å) and inactive mGlu receptors[28,29] (10.9–11.2 Å), indicating that the 'ionic lock' is intact within both GABA$_B$ subunits (Extended Data Fig. 10a–e).

The 'ionic lock' in each GABA$_B$ subunit resides in close proximity to an FxPKxx sequence in TM7, which is the counterpart of the NPxxY(x)$_{5,6}$F motif in class A GPCRs[25]. Specifically, the conserved Lys$^{7.51}$ participates in a network of hydrophilic contacts with the 'ionic lock' through Asn$^{2.39}$ and a serine in ICL1 (Extended Data Fig. 10a, b and Supplementary Fig. 3). These interactions unite the 'ionic lock' and FxPKxx motif into a larger and integral system for maintaining the inactive transmembrane conformation of individual GABA$_B$ subunits.

Conclusion

The combination of our previous VFT structures and present cryo-EM data supports the occurrence of three essential events during activation of the GABA$_B$ receptor: first, agonist-induced closure of the GABA$_{B1b}$ VFT; second, association of membrane-proximal LB2 domains; and third, dissociation of the 'intersubunit latch' and ensuing rearrangement of the transmembrane heterodimer interface. This hypothesis is consistent with our finding that an inverse agonist bound to the extracellular domain can inhibit the constitutive activity stemming from the spontaneous closure of the GABA$_{B1b}$ VFT, but not that resulting from direct 'downstream' disruption of the 'intersubunit latch'.

The GABA$_B$-receptor structure also yields surprising findings regarding its endogenous ligand composition. We suspect that the phospholipids discovered well inside each transmembrane cavity are necessary structural components, as they are prebound within each subunit and their interactions with the receptor are extensive. These endogenous lipids may be unique to the GABA$_B$ receptor, as the lipid-binding residues are not conserved among class C GPCRs (Supplementary Fig. 3). Preoccupation of the transmembrane pocket suggests that GABA$_B$ allosteric modulators may bind to yet unknown sites, with the heterodimer interface being a potential location. An active structure of the GABA$_B$ receptor would confirm whether the phospholipids are integral receptor components or functional modifiers.

Online content

Any methods, additional references, Nature Research reporting summaries, source data, extended data, supplementary information, acknowledgements, peer review information; details of author contributions and competing interests; and statements of data and code availability are available at https://doi.org/10.1038/s41586-020-2452-0.

1. Bettler, B., Kaupmann, K., Mosbacher, J. & Gassmann, M. Molecular structure and physiological functions of $GABA_B$ receptors. *Physiol. Rev.* **84**, 835–867 (2004).
2. Jones, K. A. et al. $GABA_B$ receptors function as a heteromeric assembly of the subunits $GABA_BR1$ and $GABA_BR2$. *Nature* **396**, 674–679 (1998).
3. Kaupmann, K. et al. $GABA_B$-receptor subtypes assemble into functional heteromeric complexes. *Nature* **396**, 683–687 (1998).
4. White, J. H. et al. Heterodimerization is required for the formation of a functional $GABA_B$ receptor. *Nature* **396**, 679–682 (1998).
5. Kuner, R. et al. Role of heteromer formation in $GABA_B$ receptor function. *Science* **283**, 74–77 (1999).
6. Ng, G. Y. et al. Identification of a $GABA_B$ receptor subunit, gb2, required for functional $GABA_B$ receptor activity. *J. Biol. Chem.* **274**, 7607–7610 (1999).
7. Kaupmann, K. et al. Expression cloning of $GABA_B$ receptors uncovers similarity to metabotropic glutamate receptors. *Nature* **386**, 239–246 (1997).
8. Malitschek, B. et al. The N-terminal domain of γ-aminobutyric $acid_B$ receptors is sufficient to specify agonist and antagonist binding. *Mol. Pharmacol.* **56**, 448–454 (1999).
9. Galvez, T. et al. Allosteric interactions between GB1 and GB2 subunits are required for optimal $GABA_B$ receptor function. *EMBO J.* **20**, 2152–2159 (2001).
10. Margeta-Mitrovic, M., Jan, Y. N. & Jan, L. Y. Function of GB1 and GB2 subunits in G protein coupling of $GABA_B$ receptors. *Proc. Natl Acad. Sci. USA* **98**, 14649–14654 (2001).
11. Robbins, M. J. et al. $GABA_{B2}$ is essential for G-protein coupling of the $GABA_B$ receptor heterodimer. *J. Neurosci.* **21**, 8043–8052 (2001).
12. Duthey, B. et al. A single subunit (GB2) is required for G-protein activation by the heterodimeric $GABA_B$ receptor. *J. Biol. Chem.* **277**, 3236–3241 (2002).
13. Havlickova, M. et al. The intracellular loops of the GB2 subunit are crucial for G-protein coupling of the heteromeric γ-aminobutyrate B receptor. *Mol. Pharmacol.* **62**, 343–350 (2002).
14. Monnier, C. et al. Trans-activation between 7TM domains: implication in heterodimeric $GABA_B$ receptor activation. *EMBO J.* **30**, 32–42 (2011).
15. Pin, J. P. & Bettler, B. Organization and functions of mGlu and $GABA_B$ receptor complexes. *Nature* **540**, 60–68 (2016).
16. Geng, Y., Bush, M., Mosyak, L., Wang, F. & Fan, Q. R. Structural mechanism of ligand activation in human $GABA_B$ receptor. *Nature* **504**, 254–259 (2013).
17. Burmakina, S., Geng, Y., Chen, Y. & Fan, Q. R. Heterodimeric coiled-coil interactions of human $GABA_B$ receptor. *Proc. Natl Acad. Sci. USA* **111**, 6958–6963 (2014).
18. Conklin, B. R., Farfel, Z., Lustig, K. D., Julius, D. & Bourne, H. R. Substitution of three amino acids switches receptor specificity of $G_q\alpha$ to that of $G_i\alpha$. *Nature* **363**, 274–276 (1993).
19. Xue, L. et al. Rearrangement of the transmembrane domain interfaces associated with the activation of a GPCR hetero-oligomer. *Nat. Commun.* **10**, 2765 (2019).
20. Koehl, A. et al. Structural insights into the activation of metabotropic glutamate receptors. *Nature* **566**, 79–84 (2019); correction **567**, **E**10 (2019).
21. Geng, Y. et al. Structural mechanism of ligand activation in human calcium-sensing receptor. *eLife* **5**, e13662 (2016).
22. Wise, A. et al. Calcium sensing properties of the $GABA_B$ receptor. *Neuropharmacology* **38**, 1647–1656 (1999).
23. Galvez, T. et al. Ca^{2+} requirement for high-affinity gamma-aminobutyric acid (GABA) binding at $GABA_B$ receptors: involvement of serine 269 of the $GABA_BR1$ subunit. *Mol. Pharmacol.* **57**, 419–426 (2000).
24. Hanson, M. A. et al. Crystal structure of a lipid G protein-coupled receptor. *Science* **335**, 851–855 (2012).
25. Rasmussen, S. G. et al. Crystal structure of the β_2 adrenergic receptor-Gs protein complex. *Nature* **477**, 549–555 (2011).
26. Thal, D. M., Glukhova, A., Sexton, P. M. & Christopoulos, A. Structural insights into G-protein-coupled receptor allostery. *Nature* **559**, 45–53 (2018).
27. Palczewski, K. et al. Crystal structure of rhodopsin: a G protein-coupled receptor. *Science* **289**, 739–745 (2000).
28. Doré, A. S. et al. Structure of class C GPCR metabotropic glutamate receptor 5 transmembrane domain. *Nature* **511**, 557–562 (2014).
29. Wu, H. et al. Structure of a class C GPCR metabotropic glutamate receptor 1 bound to an allosteric modulator. *Science* **344**, 58–64 (2014).

Methods

No statistical methods were used to predetermine sample size. The experiments were not randomized and investigators were not blinded to allocation during experiments and outcome assessment.

Protein expression and purification

Human GABA_{B1b} (UniProt (https://www.uniprot.org) code Q9UBS5-2) and GABA_{B2} (UniProt code O75899) subunits were each cloned into a modified pEG BacMam vector[30] for coexpression in baculovirus-infected mammalian cells. GABA_{B1a} and GABA_{B1b} are two major isoforms of GABA_{B1}, and have identical pharmacological profiles[7]. Different C-terminal truncations of each receptor subunit were tested for heterodimeric receptor assembly. The optimal GABA_{B1b} expression construct consisted of residues 1–802 (GABA_{B1b}(1–802)), while the GABA_{B2} construct included residues 1–819 (GABA_{B2}(1–819)). This allowed the heterodimeric construct to be transported to the cell membrane, as it retained the intracellular coiled-coil region present in the intracellular tail of each subunit[31,32]. Signal peptides for GABA_{B1b} and GABA_{B2} occupied residues 1–29 and 1–41, respectively. A Flag tag was engineered at the C terminus of each subunit to facilitate affinity purification.

Human embryonic kidney (HEK) 293 GnTI^- cells[33] were grown in suspension culture at 37 °C in 8% CO_2 using 293 freestyle media (Life Technology, Carlsbad, CA). The cells were coinfected with recombinant baculoviruses carrying the GABA_{B1b}(1–802) and GABA_{B2}(1–819) genes at 37 °C. To enhance the expression level, we added 10 mM sodium butyrate 18 h post infection, and incubated the cells for a further 72 h at 30 °C before harvest.

Cell membrane was isolated by differential centrifugation. The cells were lysed using an EmulsiFlex-C3 high pressure homogenizer (Avestin, Ottawa, Canada) in a buffer containing 50 mM HEPES, pH 7.5, 150 mM NaCl, 10% glycerol and a cocktail of protease inhibitors (Roche, Basel, Switzerland). Cell debris was removed by centrifugation of the lysed cell suspension at 10,000 r.p.m. The cell membrane was then pelleted by ultracentrifugation at 45,000 r.p.m.

The GABA_{B} receptor was extracted from the cell membrane with 50 mM HEPES, pH 7.5, 150 mM NaCl, 10% glycerol, 1% lauryl maltose neopentyl glycol (LMNG) (Anatrace, Maumee, OH) and 0.2% cholesteryl hemisuccinate (CHS) (MilliporeSigma, St. Louis, MO) at 4 °C overnight. After the insoluble matter was removed by centrifugation, the supernatant was applied to an anti-Flag M2 antibody affinity column (MilliporeSigma, St. Louis, MO). The column was washed stepwise with decreasing concentrations of detergent, from 0.1% to 0.002% LMNG. The heterodimeric GABA_{B1b}(1–802)–GABA_{B2}(1–819) complex was then eluted with 50 mM HEPES, pH 7.5, 50 mM NaCl, 0.002% LMNG, 0.0004% CHS and 0.2 mg ml^{-1} Flag peptide.

The receptor was further purified by Mono Q (GE Healthcare, Chicago, IL) ion-exchange chromatography using a linear salt gradient from 50 mM to 1 M NaCl in 50 mM HEPES, pH 7.5, 0.002% LMNG and 0.0004% CHS. Finally, the assembled GABA_{B} receptor was subjected to Superose 6 (GE Healthcare, Chicago, IL) size-exclusion chromatography in 50 mM HEPES, pH 7.5, 50 mM NaCl, 0.002% LMNG and 0.0004% CHS.

HEK 293 GnTI^- cells were purchased from and authenticated by the American Type Culture Collection (ATCC catalogue number CRL-3022). Cell morphology was examined for each passage of cells. The cells were certified by ATCC to be free of mycoplasma contamination, but they were not tested again during culturing.

Cryo-EM specimen preparation and data acquisition

Specimens were composed of vitrified GABA_{B} protein samples occupying UltraAuFoil R 0.6/1, 300-mesh holey Au/Au grids (Quantifoil Micro Tools, Jena, Germany). The surfaces of the grids were rendered hydrophilic by glow-discharging using H_2 and O_2 for 25 s at 10 W with a Solarus 950 plasma cleaner system (Gatan, Pleasanton, CA). For vitrification, 3 µl of purified GABA_{B} receptor at a concentration of approximately 0.3 mg ml^{-1} was applied to each grid, blotted for 4 s at a blot force of 3 inside a Vitrobot Mark IV (Thermo Fisher Scientific, Waltham, MA), and plunge-frozen in a liquid propane:ethane mixture (63:37, *v*/*v*) cooled with liquid nitrogen.

Data collection was performed on a Titan Krios transmission electron microscope (Thermo Fisher Scientific, Waltham, MA) equipped with a K2 Summit direct electron detection camera (Gatan, Pleasanton, CA) in counting mode and a post-column GIF Quantum energy filter (Gatan) in zero-energy-loss mode with a slit width of 20 eV. Micrographs were accrued at a calibrated pixel size of 1.06 Å and with nominal defocus range of −0.5 to −2 µm. Each micrograph consisted of 60 frames collected over a 12-s exposure at a dose rate of roughly 8 electrons per pixel per second for a total dose of roughly 85 electrons per Å^2. A total of 3,435 micrographs were acquired as dose-fractionated image stacks.

Cryo-EM image processing

Image processing began with frame alignment and dose-weighting of the image stacks using the CPU-based implementation of MotionCor2 (ref. [34]) in Relion 3.0 (ref. [35]). Estimation of contrast transfer function (CTF) for each non-dose-weighted micrograph was determined by Gctf[36] version 1.06. After visual inspection of the micrographs and their power spectra, 3,334 were selected for further processing.

Approximately 3,000 particles were manually picked in Relion 3.0 (ref. [35]), and extracted from a 4× binned data set with a pixel size of 4.24 Å. These data produced an initial set of two-dimensional (2D) classes that were used as templates to select 1,048,241 particles automatically, all of which were subsequently imported into cryoSPARC version 2 (ref. [37]) for extensive 2D classification. After elimination of unfit classes, a total of 312,840 particles from the high-quality 2D classes were combined to produce an ab initio three-dimensional (3D) reference in cryoSPARC version 2 (ref. [37]). On the basis of the ab initio model, particles were re-extracted at full scale from the unbinned data set with a pixel size of 1.06 Å in Relion 3.0 (ref. [35]), and re-introduced into cryoSPARC version 2 (ref. [37]) for 3D refinement. Homogeneous refinement of the ab initio 3D model against the unbinned set of particles yielded a density map with nominal resolution of 3.6 Å according to the Fourier shell correlation (FSC) = 0.143 gold standard criterion[38]. Heterogenous refinement of multiple models obtained before and after homogeneous refinement allowed removal of additional poor-quality particles and reduced the particle count to 233,737. Nonuniform refinement then improved the resolution to 3.5 Å. At this point, CTF refinement and Bayesian polishing were conducted in Relion 3.0 (ref. [35]), followed by an additional round of nonuniform refinement in cryoSPARC version 2 (ref. [37]), further improving the resolution to 3.3 Å.

Although the transmembrane domains of the GABA_{B} receptor exhibit pseudo twofold symmetry, bulky carbohydrate densities that are visible only in the ECD of the GABA_{B1b} subunit resulted in sufficient low-resolution asymmetry to prevent particle misalignment. These densities include partial carbohydrate densities attached to Asn 323 and Asn 365 of GABA_{B1b} that do not have counterparts in GABA_{B2}.

The global density map exhibited directional anisotropy[39] that is caused by interdomain movement about a flexible linker. To eliminate the adverse effect of such movement on map quality, we performed local refinement of the ECD and transmembrane domains of the GABA_{B} receptor independently. A mask was created covering each region, and the nonuniform refinement algorithm was used as implemented in cryoSPARC version 2 (ref. [37]). The resulting reconstructions for the individual ECD and transmembrane domains reached 3.1 Å and 3.4 Å resolution, respectively. A composite map was generated in UCSF Chimera[40] by taking the maximum values pointwise from the two locally refined maps after alignment to the global reconstruction ('vop maximum' command in UCSF Chimera[40]). This composite map was used for subsequent model building and refinement.

Resolutions of cryo-EM reconstructions were determined using a cutoff value of 0.143 in gold standard half-map FSC curves[38].

We carried out 3D variability analysis[41] in cryoSPARC version 2 (ref. [37]) using the 233,737 particles from global nonuniform refinement as input. Calculations were performed for the entire receptor, the ECDs and the transmembrane domains, respectively. In each case, multiple modes of variability were solved, and represented as eigenvectors along which conformational changes occur. To visualize the transformation of density, we calculated five reconstructions along each eigenvector, with a filter resolution of 4.5 Å. A movie that combines these reconstructions as frames was generated in Chimera[40] for each dimension of motion.

Model building and refinement

Model building was carried out in COOT[42]. The crystal structure of a complex of human GABA$_{\text{B1b}}$ VFT and GABA$_{\text{B2}}$ VFT in the apo form (Protein DataBank code 4MQE) was used as the initial model for the extracellular domain of the receptor. The VFT modules of GABA$_{\text{B1b}}$ and GABA$_{\text{B2}}$ were separately placed into density as rigid bodies. Individual residues were then adjusted to optimize the fit. The linker and transmembrane domain of each subunit were traced de novo based on the density. The final model contained residues 48–368, 377–576 and 588–747 of GABA$_{\text{B1b}}$, and 54–294, 302–376, 385–584 and 595–749 of GABA$_{\text{B2}}$.

In addition to the polypeptide chains, we built models for a Ca^{2+} ion in the extracellular domain of GABA$_{\text{B1b}}$, and for one phospholipid (PE 38:5 in GABA$_{\text{B1b}}$ and PC 38:2 in GABA$_{\text{B2}}$) within the transmembrane domain of each subunit. Density for carbohydrate was observed at three N-linked glycosylation sites on GABA$_{\text{B1b}}$ (Asn 365, Asn 385 and Asn 397) and one site on GABA$_{\text{B2}}$ (Asn 404). An N-glucosamine residue was modelled at each of these glycosylation sites. Continuous density was also identified for ten cholesterol or CHS molecules surrounding the transmembrane domains of both GABA$_{\text{B}}$ subunits. Cholesterols were modelled to optimize the fit with density; however, these densities may belong to CHS molecules with disordered parts. Density for an endogenous ligand was found at the interdomain cleft of the GABA$_{\text{B1b}}$ VFT. Although this density could be fit with GABA, it was not modelled because the origin and identity of the ligand remained ambiguous without confirmation by an independent method.

The entire structure was refined by the real-space refinement algorithm and validated with the comprehensive validation application as implemented in Phenix[43]. Ramachandran statistics were calculated using MolProbity[44]. The refined model also has an overall EMRinger[45] score of 2.7, while the extracellular and transmembrane domains have scores of 3.4 and 1.8, respectively. The final model revealed that VFT and transmembrane components are related to their counterparts in the other subunit by 177° and 179° rotations about the vertical axis, respectively.

Pairwise structural alignment was performed using LSQMAN[46]. Figures were generated using Pymol Molecular Graphics System version 2.3 (Schrödinger), UCSF Chimera[40] and UCSF ChimeraX[47]. Software installation support was provided by SBGrid[48].

Scintillation proximity assay

Binding of [^{3}H]GABA (60 Ci mmol^{-1}; American Radiolabelled Chemicals, St. Louis, MO) to the GABA$_{\text{B}}$ receptor was measured with a scintillation proximity assay (SPA)[49,50]. Purified GABA$_{\text{B1b}}$(1–802)–GABA$_{\text{B2}}$(1–819) complex (100 ng) was extensively dialysed against the purification buffer to remove any residual endogenous ligand. The dialysed protein was then immobilized to yttrium silicate (YSi) protein A SPA beads (62.5 μg; PerkinElmer, Waltham, MA) using anti-Flag M2 antibody (12.5 pg; Millipore Sigma, St. Louis, MO), and incubated at 4 °C for 30 min in the same buffer as used for the final step of protein purification (50 mM Hepes, pH 7.5, 50 mM NaCl, 0.002% LMNG, 0.004% CHS). Increasing concentrations (ranging from 0.2 μM to 25 μM) of [^{3}H]GABA (2.5 Ci mmol^{-1} final specific radioactivity) were added to the protein/antibody/SPA-bead mixture, and the samples were allowed to reach equilibrium at 4 °C for 16 h. A reaction performed with an antibody/SPA-bead mixture in the absence of GABA$_{\text{B}}$ receptor was used to determine the nonproximity signal originating from nonspecific interaction between the radioligand and SPA beads.

All samples were counted in a Microbeta counter (PerkinElmer, Waltham, MA) in counts per minute (c.p.m.) in the SPA mode. The efficiency of detection was calculated with a standard curve of known [^{3}H] GABA concentrations, and this was used to transform c.p.m. into pmol. Specific binding was determined by subtracting the nonproximity signal (nonspecific binding) from the total binding signal and was plotted as a function of free radioligand concentration. Nonlinear regression fitting of the data was performed in SigmaPlot 13.0 to obtain the dissociation constant (K_d) and the molar ratio of GABA-to-receptor binding.

Identification of phospholipid ligands and GABA

Identification of bound endogenous lipids was conducted as described[51] with modifications. Briefly, intact GABA$_{\text{B}}$ and control CaS receptor were digested with trypsin overnight at 37 °C. Digested proteins were dried and extracted with 1 ml of ice-cold methanol:water (9:1, *v*/*v*). The supernatants were dried and resuspended with methanol:toluene (9:1, *v*/*v*) to an equivalent concentration of 2 μM. For LC-MS/MS analysis[52], the lipid extracts were separated on a Waters Acquity UPLC CSH C18 column (100 × 2.1 mm; 1.7 μm) (Waters, Milford, MA) coupled to an Acquity UPLC CSH C18 VanGuard precolumn (5 × 2.1 mm; 1.7 μm) (Waters). The column was maintained at 65 °C at a flow rate of 0.6 ml min^{-1}. The mobile phases consisted of A, acetonitrile:water (60:40, *v*/*v*) with ammonium formate (10 mM) and formic acid (0.1%), and B, 2-propanol:acetonitrile (90:10, *v*/*v*) with ammonium formate (10 mM) and formic acid (0.1%). The 15-min separation was conducted under the following gradient: 0 min 15% B; 0–2 min 30% B; 2–2.5 min 48% B; 2.5–11 min 82% B; 11–12 min 99% B; 12–15 min 15% B. A Q Exactive HF mass spectrometer (Thermo Fisher Scientific, Waltham, MA) was operated in electrospray ionization (ESI) in positive mode with the following parameters: mass range 100–1,500 *m*/*z*; spray voltage +3.6 kV; sheath gas (nitrogen) flow rate 60 units; auxiliary gas (nitrogen) flow rate 25 units; capillary temperature 320 °C; full scan MS1 mass resolving power 60,000; data-dependent MS/MS acquisition (dd-MS/MS) four scans per cycle; dd-MS/MS mass resolving power 15,000. The mass features that were differentially higher in the GABA$_{\text{B}}$ receptor were subjected to targeted MS/MS in reinjections to acquire tandem mass spectra. Thermo Xcalibur version 4.0.27.19 was used for data acquisition. Data processing and identification were performed in MS-DIAL version 3.40. Identification was conducted by matching accurate mass, tandem mass spectra and chromatographic retention time with built-in lipid library LipidBlast[53]. The identified endogenous lipids bound to GABA$_{\text{B}}$ receptor include phosphatidylcholine (PC) 38:2 (PC(18:1_20:1); International Chemical Identifier (InChI) key: QLEJPADMSQQACL-WWUFLCHTSA-N), and phosphatidylethanolamine (PE) 38:5 (PE(18:1_20:4); InChIKey VFUVYNGTMNUBMF-ZRVIQYDLSA-N). Although many isoforms exist for these lipids, both phospholipids share two long-chain fatty acyl moieties of 18 and 20 carbons based on mass spectrometry fragmentation pattern and biological relevance.

Identification of GABA was conducted with targeted LC-MS/MS. Briefly, cell supernatant, cell lysate, culture media and lysis buffer controls were dried from 1 ml and extracted with 1 ml of ice-cold methanol:water (9:1, *v*/*v*). The supernatants were dried and resuspended with 200 μl of acetonitrile:water (8:2, *v*/*v*). The extracts were separated on a Waters Acquity UPLC BEH Amide column (150 × 2.1 mm; 1.7 μm) (Waters, Milford, MA) coupled with an Acquity UPLC BEH Amide VanGuard precolumn (5 × 2.1 mm; 1.7 μm) (Waters). The column was maintained at 45 °C at a flow rate of 0.4 ml min^{-1}. Mobile phase A was water with ammonium formate (10 mM) and formic acid (0.125%) while B was acetonitrile:water (95:5, *v*/*v*) with ammonium formate (10 mM) and formic acid (0.125%). Separation was conducted using the gradient: 0–2 min 100% B; 2–7.7 min 70% B; 7.7–9.5 min 40% B; 9.5–12.5 min

30% B; 10.25–12.75 100% B, 12.75–16.75 100% B. A Q Exactive HF mass spectrometer was operated with the same parameters as above. A GABA standard was injected along with the samples to confirm its spectrum and retention time. The responses of GABA in samples were normalized to that of GABA standard with known concentration.

Cell surface expression

Full-length human GABA$_{B1b}$ and GABA$_{B2}$ were each cloned into a pcDNA3.1(+) vector (Life Technologies, Carlsbad, CA), with a Flag tag inserted after the signal peptide of GABA$_{B1b}$, and a haemagglutinin (HA) tag after the signal peptide of GABA$_{B2}$. Similar constructs were also generated for the C-terminally truncated GABA$_{B1b}$(1–802) and GABA$_{B2}$(1–819). Single mutants of full-length GABA$_{B1b}$ (E673R, E309K and E423R) and GABA$_{B2}$ (H579E and R714A) were constructed using the QuikChange mutagenesis system (Agilent Technologies, Santa Clara, CA).

The cell surface expression levels of wild-type and mutant GABA$_{B}$ receptor were measured as described[17]. Briefly, HEK293 T/17 cells (ATCC) were cultured in monolayer in DMEM/F12 media (Life Technology, Carlsbad, CA) supplemented with 10% fetal bovine serum (FBS) at 37 °C in the presence of 5% CO_2. The cells were co-transfected with GABA$_{B1b}$ and GABA$_{B2}$ plasmids using Lipofectamine 3000 (Life Technologies, Carlsbad, CA). Each GABA$_{B1b}$ and GABA$_{B2}$ mutant was paired with its wild-type partner. Given that GABA$_{B1b}$ is retained inside the cells unless it is chaperoned by GABA$_{B2}$, we used the surface expression level of GABA$_{B1b}$ on intact cells to measure the amount of assembled heterodimeric GABA$_{B}$ receptor on the cell surface. The amount of surface GABA$_{B1b}$ protein detected for each pair of constructs was normalized with the cell count in each experiment. The cell surface expression level of each mutant is calculated as a percentage of the wild-type receptor.

After blocking with 1% BSA, the cells were incubated with mouse anti-Flag M1 antibody (MilliporeSigma, St. Louis, MO) as the primary antibody to measure GABA$_{B1b}$ expression, followed by donkey anti-mouse IRDye 800-labelled antibody (Li-Cor Biosciences, Lincoln, NE) as the secondary antibody. Fluorescent signals were measured with an Odyssey Infrared Imager (Li-Cor Biosciences). Each experiment was performed in triplicate.

HEK 293 T/17 cells were purchased from and authenticated by ATCC (catalogue number CRL-11268). Cell morphology was examined for each passage of cells. The cells were certified by ATCC to be free of mycoplasma contamination, but they were not tested again during culturing.

Inositol phosphate measurement

HEK293 T/17 cells were cotransfected with plasmids encoding GABA$_{B1b}$, GABA$_{B2}$, and Gα$_{qi5}$. The Gα$_{qi5}$ chimaera was constructed by replacing the five C-terminal amino acids of murine Gα$_{q}$ with those of murine Gα$_{i}$ (ref. [18]). Exchanging the C-terminal end of Gα$_{q}$ with that of Gα$_{i/o}$ permits it to couple with the GABA$_{B}$ receptor and allows the functional activity of the receptor to be tracked through the activity of phospholipase C (PLC). Control experiments were conducted using cells transfected with an empty pcDNA3.1(+) vector, Gα$_{qi5}$ alone, or wild-type GABA$_{B1b}$ and GABA$_{B2}$ in the absence of Gα$_{qi5}$.

Inositol phosphate accumulation was quantified with the homogenous time-resolved fluorescence (HTRF) IP-one Tb kit (Cisbio Bioassays, Codolet, France), which measures the accumulation of inositol-1-monophosphate (IP$_1$), a metabolite of inositol-1,4,5-triphosphate (IP$_3$). One day after transfection, the cells were stimulated with increasing concentrations of baclofen for one hour at 37 °C. The stimulated cells were lysed, and the native IP$_1$ that had been produced was incubated with a d2 fluorophore-labelled IP$_1$ analogue (the acceptor) to compete for binding to an Eu Cryptate-coupled anti-IP1 monoclonal antibody (the donor). Fluorescence data were collected at 620 nm and 665 nm with a PHERAstar FS plate reader (BMG Labtech, Cary, NC) after laser excitation at 320 nm. The fluorescence resonance energy transfer (FRET) signal was calculated as the fluorescence ratio (665 nm/620 nm) and is inversely proportional to the concentration of native IP$_1$ produced following GABA$_{B}$ activation through a chimaeric Gα$_{qi5}$ G protein. The agonist-induced receptor response of each mutant was calculated as a percentage of the maximum activity of wild-type receptor relative to the activity observed for Gα$_{qi5}$ alone. Basal activity was determined in the absence of baclofen stimulation and calculated similarly to the agonist-dependent receptor response. Data analysis was performed using the nonlinear regression algorithms in Prism (GraphPad Software, San Diego, CA). Data points represent averages ± s.e.m. of multiple experiments, each consisting of quadruplicate measurements.

Application of a known antagonist, CGP54626, reduced agonist potency as expected. In addition, the compound lowered the basal activity of the GABA$_{B}$ receptor, indicating that it has inverse agonist activity, as previously reported[54]. Therefore, we refer to the compound as an inverse agonist.

Inductively coupled plasma mass spectrometry

Purified GABA$_{B}$ receptor (200 μl, 11.1 μg μl^{-1} or 57.7 μM) was collected in metal-free tubes and digested overnight by adding 1 ml of concentrated nitric acid (HNO_3) (Fisher Scientific, Hampton, NH; Optima grade). The digested protein was then diluted to a total volume of 10 ml with 8.7 ml of deionized water supplemented with 500 μg l^{-1} of gold (Au) and 100 μl of an internal standard solution containing 500 μg l^{-1} each of gallium (Ga) and rhodium (Rh) in 2% HNO_3. The protein purification buffer (200 μl), containing 10 mM HEPES, pH 7.5, 50 mM NaCl, 0.002% LMNG and 0.0004% CHS, was similarly mock digested and diluted for analysis.

Inductively coupled plasma mass spectrometry (ICP-MS) was conducted using a NexION 350S ICP-MS instrument (Perkin Elmer, Waltham, MA) equipped with dynamic reaction cell (DRC) feature and a SC-4 DX FAST Autosampler (Elemental Scientific, Omaha, NE). The DRC-ICP-MS experimental method was developed from published procedures[55,56] and a laboratory protocol for multi-element DCR-ICP-MS from the Centers for Disease Control (CDC) (https://www.cdc.gov/nchs/data/nhanes/nhanes_13_14/UM_UMS_UTAS_UTASS_H_MET.pdf). The concentrations of magnesium (Mg), calcium (Ca), manganese (Mn), iron (Fe), cobalt (Co), nickel (Ni), copper (Cu), zinc (Zn) and strontium (Sr) in the digested protein and buffer samples were measured. Data points represent averages ± coefficient of variance from eight measurements within two experiments.

One multi-element calibration standard was prepared from concentrated single-element stocks, and used for instrument calibration. The calibration standard was diluted to various concentrations using a solution containing 10% HNO_3 and 500 μg l^{-1} of Au to cover the expected concentration range of each analyte in the protein sample: 0.01, 0.02, 0.05, 0.1, 0.2 μg l^{-1} for Co and Sr; 0.05, 0.1, 0.25, 0.5, 1.0 μg l^{-1} for Mn and Ni; 0.25, 0.5, 1.25, 2.5, 5.0 μg l^{-1} for Mg and Cu; 0.5, 1.0, 2.5, 5.0, 10.0 μg l^{-1} for Fe and Zn; and 2.5, 5.0, 12.5, 25, 50 μg l^{-1} for Ca.

The instrument was also calibrated against a set of blank solutions, including commercially available quality controls containing digested hair samples from Public Health Expertise and Reference Center, Quebec (INSPQ, Quebec, Canada), and a water sample containing a broad range of metals from the National Institute of Technology (NIST, Gaithersburg, MD).

Special attention was paid to correction for matrix-induced interferences. Matrix suppression was compensated by the selection of suitable internal standards, which were matched to masses and, if possible, to ionization properties of the analytes. The internal standards were added to each calibration standard and quality control sample to the same final concentration as that in the protein sample and buffer (5 μg l^{-1} each of Ga and Rh). The elements Mg, Ca, Mn, Fe, Co, Ni, Cu, and Zn were corrected with Ga, while Sr was corrected with Rh. Polyatomic interferences were suppressed with the instrument's DRC technology feature, using ammonia as a second gas for Mn and Fe, while Mg, Ca, Sr, Co, Ni, Cu, and Zn were measured in standard mode without a second gas.

Matrix-assisted laser desorption/ionization

Purified GABA_{B1b}(1–802)–GABA_{B2}(1–819) complex (0.3 mg ml^{-1}, 1 µl) was mixed with 1 µl sinapinic acid matrix solution (Bruker Daltonics, Billerica, MA) containing 10 mg of sinapinic acid in 1 ml of 2.5% trifluoroacetic acid (MilliporeSigma, St. Louis, MO) and 50% acetonitrile (MilliporeSigma). The protein–matrix suspension (2 µl) was added to the ground-steel matrix-assisted laser desorption/ionization (MALDI) target plate and dried at room temperature. Mass spectra were collected using a UltrafleXtreme MALDI time-of-flight (TOF)/TOF mass spectrometer (Bruker Daltonics) operated with FlexControl software in linear positive mode—that is, using a mass range of 30,000–120,000 daltons. The instrument was externally calibrated with a Proteins MALDI-MS calibration kit (MilliporeSigma, St. Louis, MO). Each individual mass spectrum was analysed and adjusted for smoothness and baseline using FlexAnalysis software 3.0 (Bruker Daltonics). We determined the molecular mass of the heterodimeric GABA_{B1b}(1–802)–GABA_{B2}(1–819) complex to be 192,647.967 daltons.

Reporting summary

Further information on research design is available in the Nature Research Reporting Summary linked to this paper.

Data availability

All data are included in this paper and its Supplementary Information. Cryo-EM density maps of the GABA_{B} receptor have been deposited in the Electron Microscopy Data Bank (https://www.ebi.ac.uk/pdbe/emdb/) under accession code EMD-21685. Atomic coordinates for the GABA_{B} receptor structure have been deposited in the RCSB Protein Data Bank under accession code 6WIV. Raw cryo-EM images have been deposited in the Electron Microscopy Public Image Archive (https://www.ebi.ac.uk/pdbe/emdb/empiar/) under accession code EMPIAR-10410.

30. Goehring, A. et al. Screening and large-scale expression of membrane proteins in mammalian cells for structural studies. *Nat. Protocols* **9**, 2574–2585 (2014).
31. Margeta-Mitrovic, M., Jan, Y. N. & Jan, L. Y. A trafficking checkpoint controls GABA_{B} receptor heterodimerization. *Neuron* **27**, 97–106 (2000).
32. Pagano, A. et al. C-terminal interaction is essential for surface trafficking but not for heteromeric assembly of GABA_{B} receptors. *J. Neurosci*. **21**, 1189–1202 (2001).
33. Reeves, P. J., Callewaert, N., Contreras, R. & Khorana, H. G. Structure and function in rhodopsin: high-level expression of rhodopsin with restricted and homogeneous N-glycosylation by a tetracycline-inducible N-acetylglucosaminyltransferase I-negative HEK293S stable mammalian cell line. *Proc. Natl Acad. Sci. USA* **99**, 13419–13424 (2002).
34. Zheng, S. Q. et al. MotionCor2: anisotropic correction of beam-induced motion for improved cryo-electron microscopy. *Nat. Methods* **14**, 331–332 (2017).
35. Scheres, S. H. RELION: implementation of a Bayesian approach to cryo-EM structure determination. *J. Struct. Biol*. **180**, 519–530 (2012).
36. Zhang, K. Gctf: real-time CTF determination and correction. *J. Struct. Biol*. **193**, 1–12 (2016).
37. Punjani, A., Rubinstein, J. L., Fleet, D. J. & Brubaker, M. A. cryoSPARC: algorithms for rapid unsupervised cryo-EM structure determination. *Nat. Methods* **14**, 290–296 (2017).
38. Scheres, S. H. & Chen, S. Prevention of overfitting in cryo-EM structure determination. *Nat. Methods* **9**, 853–854 (2012).
39. Tan, Y. Z. et al. Addressing preferred specimen orientation in single-particle cryo-EM through tilting. *Nat. Methods* **14**, 793–796 (2017).
40. Pettersen, E. F. et al. UCSF Chimera—a visualization system for exploratory research and analysis. *J. Comput. Chem*. **25**, 1605–1612 (2004).
41. Punjani, A. & Fleet, D. J. 3D variability analysis: directly resolving continuous flexibility and discrete heterogeneity from single particle cryo-EM images. *bioRxiv* https://doi.org/10.1101/2020.04.08.032466 (2020).
42. Emsley, P., Lohkamp, B., Scott, W. G. & Cowtan, K. Features and development of Coot. *Acta Crystallogr. D* **66**, 486–501 (2010).
43. Adams, P. D. et al. PHENIX: a comprehensive Python-based system for macromolecular structure solution. *Acta Crystallogr. D* **66**, 213–221 (2010).
44. Chen, V. B. et al. MolProbity: all-atom structure validation for macromolecular crystallography. *Acta Crystallogr. D* **66**, 12–21 (2010).
45. Barad, B. A. et al. EMRinger: side chain-directed model and map validation for 3D cryo-electron microscopy. *Nat. Methods* **12**, 943–946 (2015).
46. Novotny, M., Madsen, D. & Kleywegt, G. J. Evaluation of protein fold comparison servers. *Proteins* **54**, 260–270 (2004).
47. Goddard, T. D. et al. UCSF ChimeraX: meeting modern challenges in visualization and analysis. *Protein Sci*. **27**, 14–25 (2018).
48. Morin, A. et al. Collaboration gets the most out of software. *eLife* **2**, e01456 (2013).
49. Geng, Y. et al. Structure and functional interaction of the extracellular domain of human GABA_{B} receptor GBR2. *Nat. Neurosci*. **15**, 970–978 (2012).
50. Quick, M. & Javitch, J. A. Monitoring the function of membrane transport proteins in detergent-solubilized form. *Proc. Natl Acad. Sci. USA* **104**, 3603–3608 (2007).
51. Gupta, K. et al. Identifying key membrane protein lipid interactions using mass spectrometry. *Nat. Protocols* **13**, 1106–1120 (2018).
52. Mafu, S. et al. Biosynthesis of the microtubule-destabilizing diterpene pseudolaric acid B from golden larch involves an unusual diterpene synthase. *Proc. Natl Acad. Sci. USA* **114**, 974–979 (2017).
53. Kind, T. et al. LipidBlast in silico tandem mass spectrometry database for lipid identification. *Nat. Methods* **10**, 755–758 (2013).
54. Mukherjee, R. S., McBride, E. W., Beinborn, M., Dunlap, K. & Kopin, A. S. Point mutations in either subunit of the GABA_{B} receptor confer constitutive activity to the heterodimer. *Mol. Pharmacol*. **70**, 1406–1413 (2006).
55. Chen, K. L. B., Amarasiriwardena, C. J. & Christiani, D. C. Determination of total arsenic concentrations in nails by inductively coupled plasma mass spectrometry. *Biol. Trace Elem. Res*. **67**, 109–125 (1999).
56. Pruszkowski, E., Neubauer, K. & Thomas, R. An overview of clinical applications by inductively coupled plasma mass spectrometry. *Atomic Spectroscopy* **19**, 111–115 (1998).
57. Hollenstein, K. et al. Structure of class B GPCR corticotropin-releasing factor receptor 1. *Nature* **499**, 438–443 (2013).
58. Wang, C. et al. Structure of the human smoothened receptor bound to an antitumour agent. *Nature* **497**, 338–343 (2013).

Acknowledgements We thank R. Henderson for early-stage cryo-EM investigation and critical reading of the manuscript; C. S. Zuker for advice and financial support; C. Karan and R. Realubit for assistance with the EnVision plate reader at Columbia Genome Center; A. Sobolevsky, K. Saotome and E. Cao for BacMam vectors; Y. H. Wong for a $\text{G}\alpha_{\text{qi5}}$ chimera plasmid; and B. K. Kobilka and B. Skiniotis for advice. Titan Krios data collection was performed at the Simons Electron Microscopy Center, directed by B. O. Carragher and C. Potter, supported by grants from the Simons Foundation (SF349247), NYSTAR and the National Institutes of Health (NIH; GM103310). This work was supported by NIH grants R01GM088454 (to Q.R.F.), R01GM125801 (to Q.R.F., P.A.S. and M.Q.), R01GM107462 (to W.A.H.), P41GM116799 (to W.A.H.), and U2C ES030158 for lipid identification (to O.F.). Q.R.F. was an Irma Hirschl Career Scientist, Pew Scholar, McKnight Scholar and Schaefer Scholar.

Author contributions J.P., J.L., Q.R.F. and K.M.R. cultured cells and purified protein; Z.F. and A.F. prepared cryo-EM grids; Z.F., A.F., Q.R.F. and O.B.C. collected cryo-EM data; Z.F. and A.F. performed initial image processing; O.B.C. processed cryo-EM data to high resolution; L.M. and Q.R.F. built and refined models; Q.R.F., L.M., A.F., J.P. and Z.F. analysed structures; T.S. and O.F. identified phospholipids and GABA by mass spectrometry; V.N.S. and J.G. conducted elemental analysis; Q.R.F, J.L., J.P., A.F., J.T., X.L. and J.P.W. performed mutagenesis and cell-based functional assays; M.Q. performed and analysed radioligand binding studies; B.C, Y.G., H.Z. and Y.K. generated expression plasmids and carried out early protein purification trials; R.G., W.J.R., E.T.E., R.K.H. and Z.Y. assisted with cryo-EM data collection; S.C., Z.L., W.J.R. and E.T.E. performed initial cryo-EM characterization; R.K.S. measured molecular mass; B.K. screened detergents; W.A.H. contributed to structural analysis; Q.R.F., P.A.S. and J.A.J. supervised functional analyses; J.F., O.B.C. and H.Y. supervised cryo-EM studies; Q.R.F. and A.F. wrote the paper; T.S., V.N.S., M.Q., Z.F. and R.K.S. contributed Methods sections; all authors contributed to revision of the manuscript; Q.R.F., A.F., J.P., O.B.C., T.S., Z.F., J.L. and M.Q. prepared figures; Q.R.F. conceived and supervised the project.

Competing interests The authors declare no competing interests.

Additional information
Supplementary information is available for this paper at https://doi.org/10.1038/s41586-020-2452-0.
Correspondence and requests for materials should be addressed to O.B.C., J.F. or Q.R.F.
Peer review information *Nature* thanks Ryan Hibbs, Bernhard Bettler and the other, anonymous, reviewer(s) for their contribution to the peer review of this work.
Reprints and permissions information is available at http://www.nature.com/reprints.

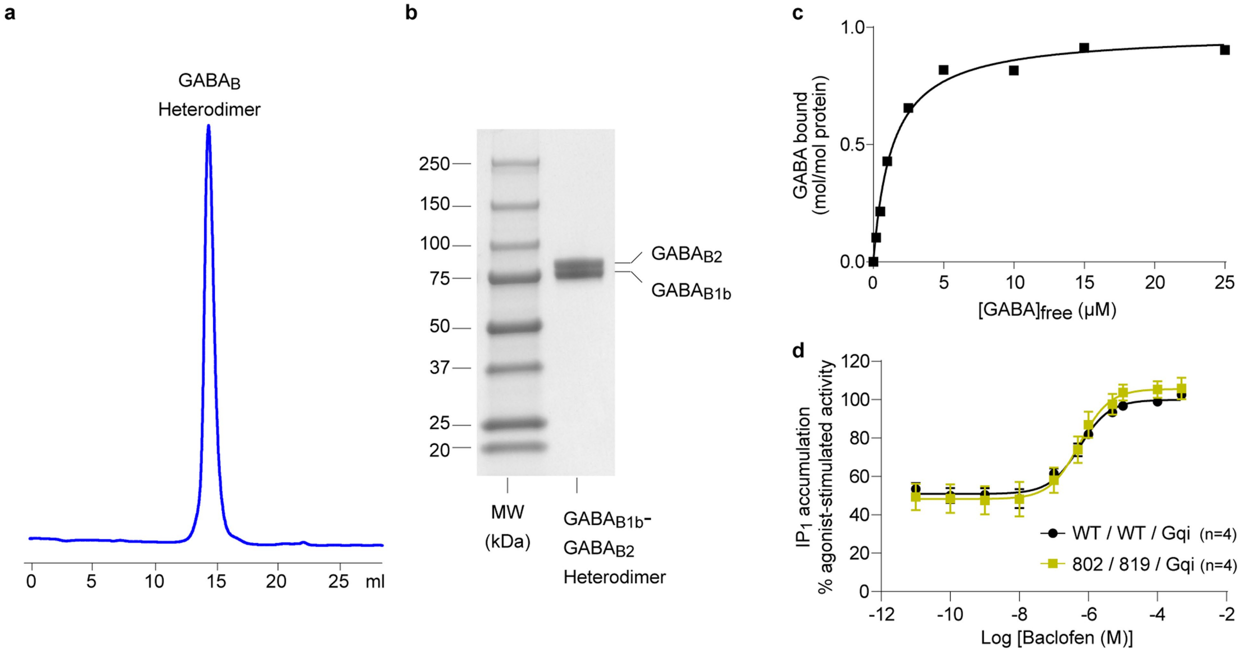

Extended Data Fig. 1 | Purification and functional analysis of the human GABA$_B$ receptor. a, Superose 6 size-exclusion chromatography profile of detergent-purified GABA$_{B1b}$(1–802)–GABA$_{B2}$(1–819) complex. **b**, SDS PAGE gel of the size-exclusion peak fraction from **a** under reducing conditions. For gel source data, see Supplementary Fig. 2. **c**, Dose-dependent [^{3}H]GABA binding to purified GABA$_{B1b}$(1–802)–GABA$_{B2}$(1–819) complex, reaching maximum molar ratios of GABA-to-receptor binding at 0.98 ± 0.03 mol mol^{-1}. Each data point represents the mean of triplicate measurements from a typical experiment. The experiment was repeated four times with similar results. Data were subjected to nonlinear regression fitting, and the dissociation constant (K_d = 1.3 ± 0.16 μM) is reported as means ± s.e.m. of the fit. **d**, Functional analysis comparison of full-length and truncated WT GABA$_B$ receptor. Shown is the dose-dependent baclofen-stimulated receptor response in cells transiently expressing Gα_{qi5} (abbreviated as Gqi) with full-length GABA$_B$ heterodimer or the C-terminally truncated GABA$_{B1b}$(1–802)–GABA$_{B2}$(1–819) complex. Cells transfected with Gα_{qi5} alone were used as a negative control. Relative agonist-stimulated activity was measured by IP$_1$ accumulation, and is expressed as a percentage of maximum wild-type activity induced by baclofen relative to the activity of Gα_{qi5} alone. Data points represent averages ± s.e.m. of multiple experiments (*n*), each with quadruplicate measurements. Cell surface expression level was 106% for the GABA$_{B1b}$(1–802)–GABA$_{B2}$(1–819) complex in comparison with the full-length WT/WT heterodimer.

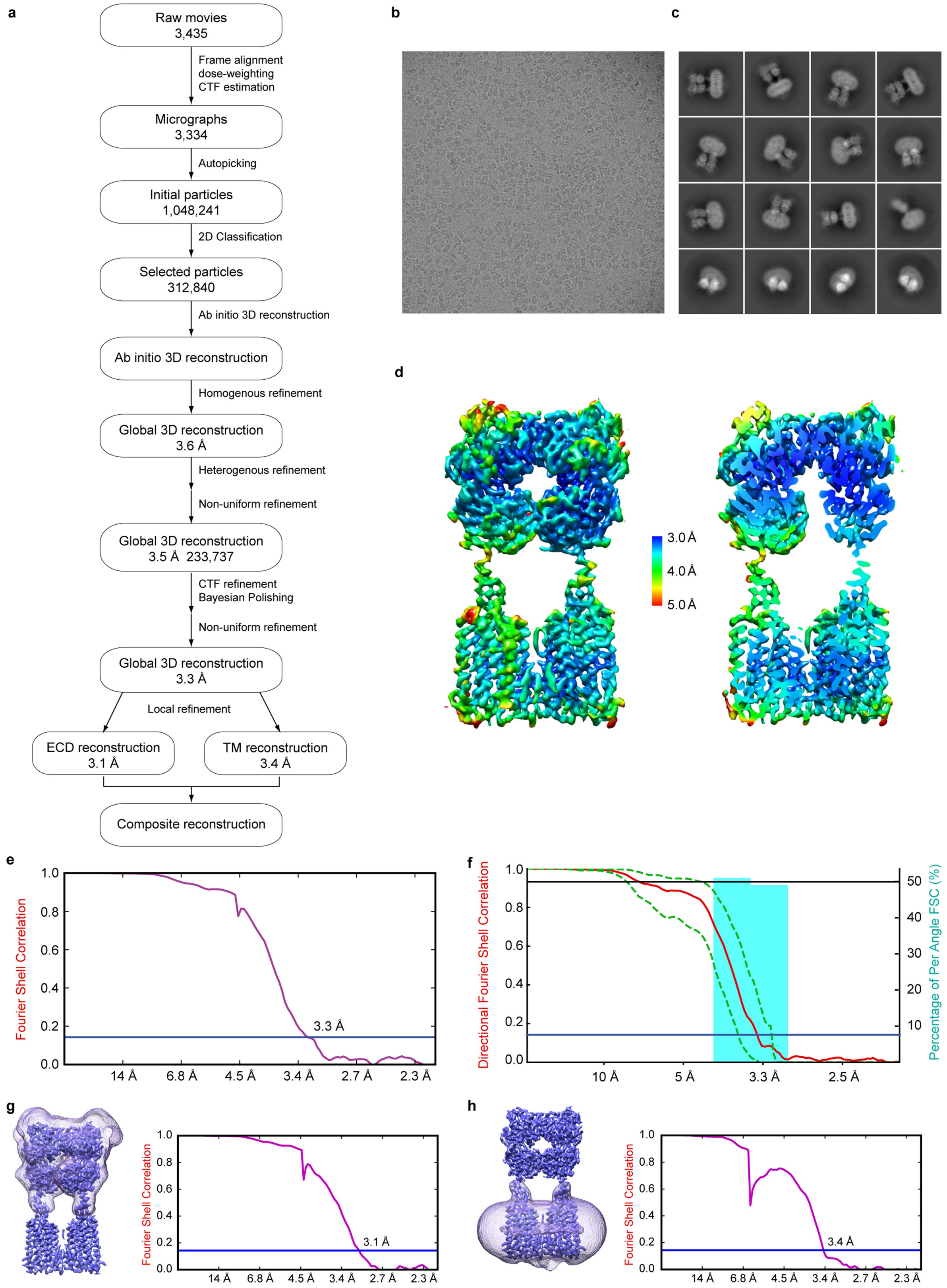

Extended Data Fig. 2 | See next page for caption.

Extended Data Fig. 2 | Cryo-EM imaging of human GABA$_B$ receptor. **a**, Workflow of cryo-EM data processing. **b**, A representative motion-corrected cryo-electron micrograph of the GABA$_B$ receptor. **c**, Reference-free 2D class averages, highlighting clear density for transmembrane helices. **d**, Global density map, coloured according to local resolution, in full and clipped views perpendicular to the plane of the membrane. **e**, Global FSC curve (purple) corrected by high-resolution noise substitution. The overall resolution as determined by an FSC cut-off value of 0.143 (blue line) is 3.3 Å. **f**, 3D FSC curves, measuring directional resolution anisotropy. Plots show the global half-map FSC (red solid line; left-hand *y*-axis), together with the spread of directional resolution values within ± 1 standard deviation of the mean (area encompassed by green dashed lines), and a histogram (turquoise; right-hand *y*-axis) of 100 such directional resolution values sampled evenly over the 3D FSC threshold value of 0.143 (blue line). The sphericity value reported by 3D FSC is 0.958 out of 1. **g**, **h**, Separate FSC curves for the locally refined reconstructions of ECDs **g**) and transmembrane domains (**h**). The blue lines mark the resolution corresponding to an FSC value of 0.143 (ECD, 3.1 Å; transmembrane region, 3.4 Å). The adjacent diagrams show the masks (translucent surface) used for each local refinement.

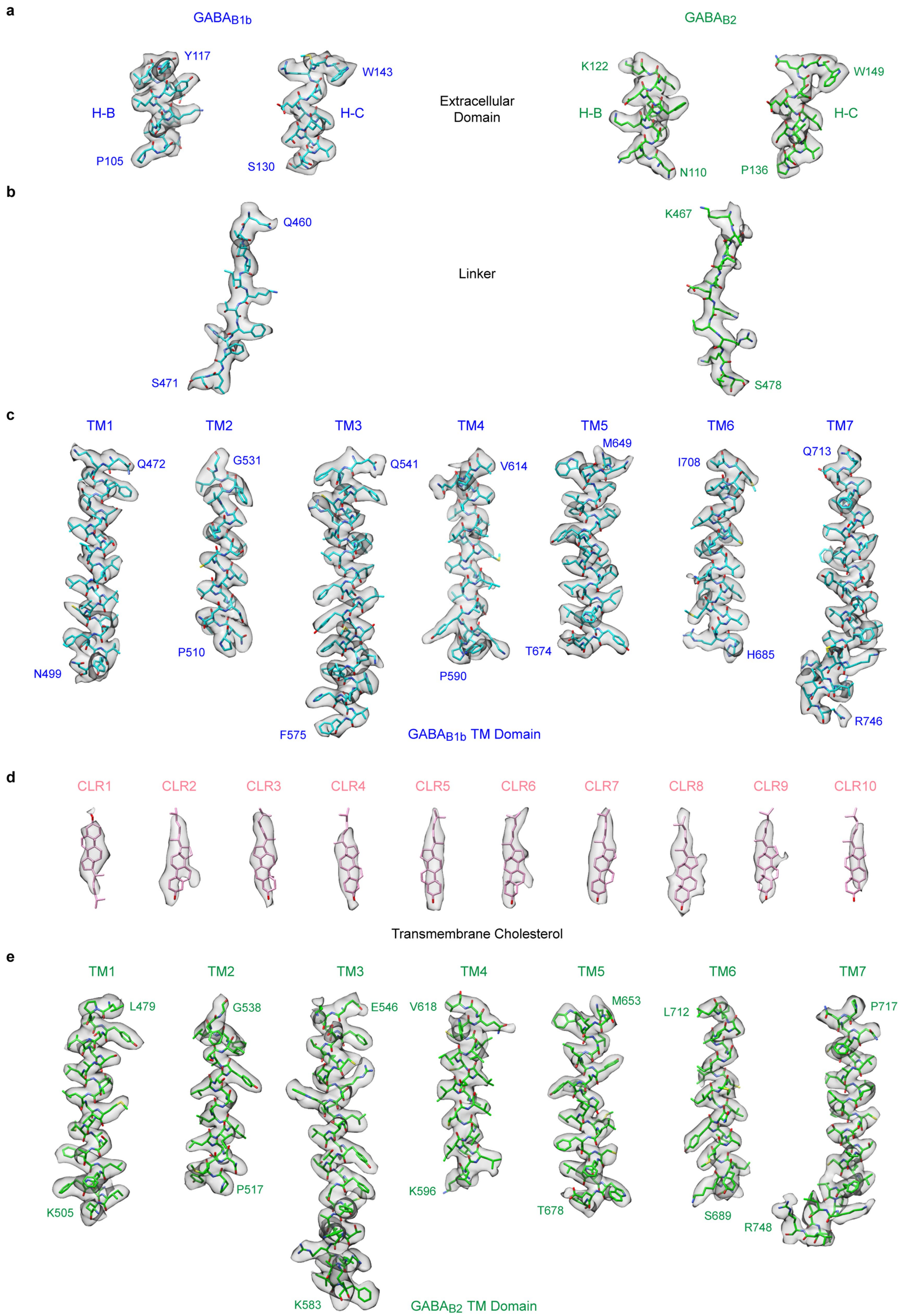

Extended Data Fig. 3 | Structural model of the GABA$_B$ receptor fit within the cryo-EM map. a–d, Cryo-EM density maps and refined models for the LB1 interface helices (H–B and H–C) in the extracellular VFT (**a**), the linker between the VFT and transmembrane domains (**b**), all seven transmembrane helices of the GABA$_{B1b}$ subunit (**c**), the ten modelled transmembrane cholesterols (**d**) and all seven transmembrane helices of the GABA$_{B2}$ subunit (**e**). The density map is a composite of the locally refined reconstructions for the ECD and transmembrane domains. The N- and C-terminal residues of each helix are labelled.

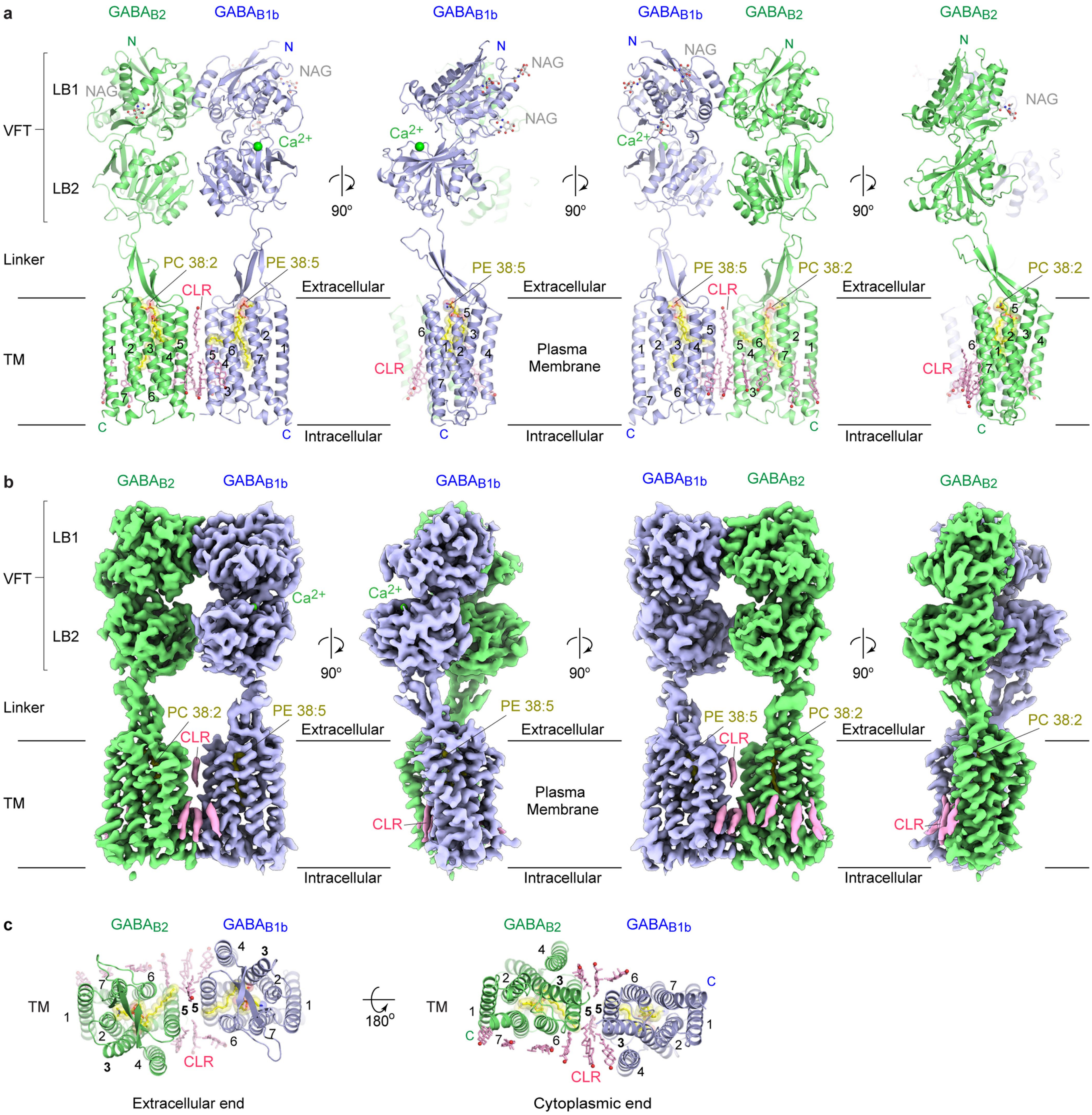

Extended Data Fig. 4 | Architecture of the GABA$_B$ receptor. **a**, Structure of the GABA$_B$ receptor in four views related by 90° rotations about an axis perpendicular to the membrane. GABA$_{B1b}$ (blue) and GABA$_{B2}$ (green) are rendered as ribbons; Ca^{2+} is shown as a green sphere; phospholipids (PE 38:5 and PC 38:2) are presented as yellow space-filling models; the observed N-linked glycans (NAGs) and cholesterols (CLRs) are shown respectively as grey and pink ball-and-stick models. Transmembrane helices 1–7, along with N and C termini, are marked for each subunit. **b**, Cryo-EM density map of the GABA$_B$ receptor, in the same orientations and colour scheme as in **a**. The map is composed of local reconstructions for the ECD and transmembrane domain, which were independently refined to 3.1 Å and 3.4 Å, respectively. **c**, Linker and transmembrane domain of the GABA$_B$ receptor viewed from the extracellular and intracellular sides.

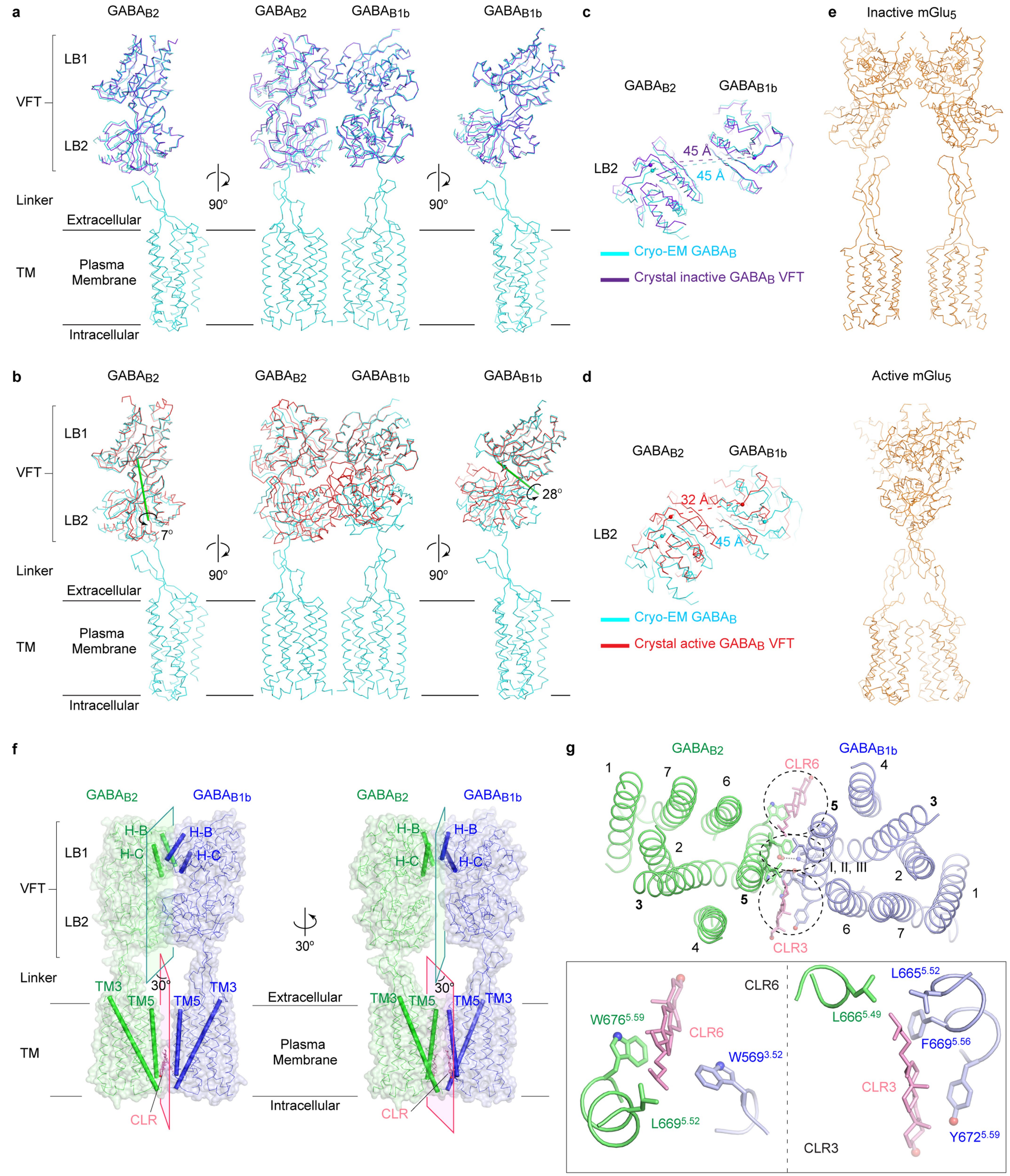

Extended Data Fig. 5 | See next page for caption.

Extended Data Fig. 5 | Heterodimer conformation and interface features of the GABA$_B$ receptor. a, **b**, Cryo-EM structure of near full-length GABA$_B$ receptor (cyan) superimposed with the crystal structure of its extracellular VFT module in the inactive state (PDB code 4MQE; purple) (**a**) or active state (PDB code 4MS3; red) (**b**). The middle panel shows the heterodimeric receptor structures superimposed based on the LB1 domain of the GABA$_{B1b}$ subunit. The two side panels show superpositions of individual GABA$_{B1b}$ and GABA$_{B2}$ subunits on the basis of their respective LB1 domains. In **b**, the green line denotes the axis of rotation that relates the LB2 domains of near full-length and VFT structures of GABA$_{B1b}$ (rotation $\chi = 28°$; screw translation $\tau_\chi = 0.6$ Å), or near full-length and VFT structures of GABA$_{B2}$ (rotation $\chi = 7°$; screw translation $\tau_\chi = 0.3$ Å). **c**, **d**, Extracellular LB2 domains viewed from the C-terminal end. Superposition of near full-length (cyan) and VFT structures (**c**, inactive state, purple; **d**, active state, red) based on the LB1 domain of the GABA$_{B1b}$ subunit. Within each heterodimeric complex, the C termini of the LB2 domains in the GABA$_{B1b}$ and GABA$_{B2}$ subunits are shown as spheres, and the distance between the two C termini is marked by dotted lines. **e**, Cryo-EM structure of full-length mGlu$_5$ in the inactive (PDB code 6N52) and active (PDB code 6N51) conformations[20]. **f**, Molecular surface of the GABA$_{B1b}$–GABA$_{B2}$ complex, showing the plane of the heterodimer interface for the extracellular and transmembrane domains. Structural elements involved in heterodimer formation are highlighted in cartoon format (ectodomain, H–B and H–C helices; transmembrane domain, TM5 and TM3 helices). **g**, The GABA$_B$ transmembrane domain viewed from the extracellular side, comparing the locations of core (I, II, IIIa, IIIb) versus peripheral cholesterol-mediated heterodimer contacts from different layers. Heterodimer contacts mediated by two cholesterols (CLR6 and CLR3) are shown at the bottom.

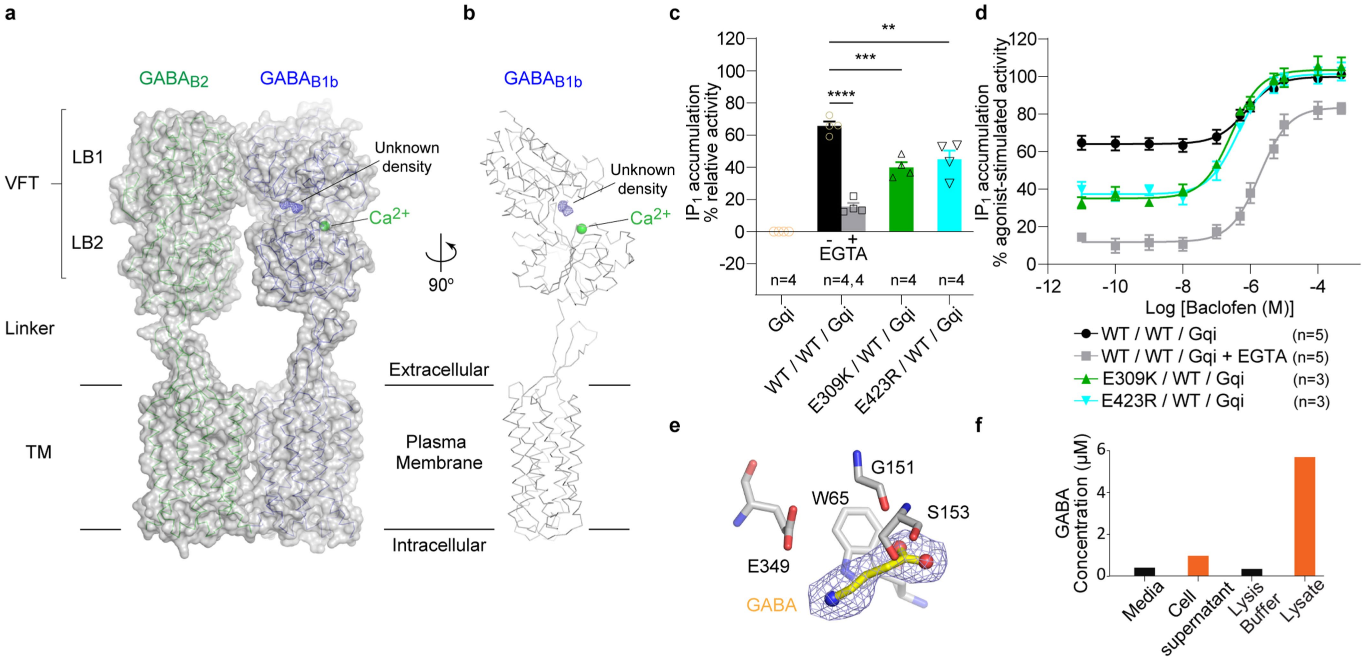

Extended Data Fig. 6 | Extracellular ligand binding in GABA$_{B1b}$. **a**, **b**, Molecular surface (**a**) and ribbon representation (**b**) of the GABA$_{B1b}$ subunit, showing the location of the Ca^{2+}-binding site and an unmodelled density at the interdomain crevice of VFT. **c**, **d**, Functional analysis of the impact of endogenous Ca^{2+}. Basal activity (**c**) and dose-dependent baclofen-stimulated receptor response (**d**) in cells transiently expressing the $G\alpha_{qi5}$ subunit (abbreviated as Gqi) with different combinations of WT and mutant GABA$_B$-receptor subunits (GABA$_{B1b}$ E309K, abbreviated as E309K; GABA$_{B1b}$ E423R, abbreviated as E423R). IP$_1$ accumulation by the WT/WT heterodimer was measured in the presence and absence of 2.5 mM EGTA. Cells transfected with $G\alpha_{qi5}$ alone were used as negative controls. Relative activity in both graphs is expressed as a percentage of the maximum wild-type activity induced by baclofen relative to the activity of $G\alpha_{qi5}$ alone. Data points represent averages ± s.e.m. of multiple experiments (*n*), each with quadruplicate measurements. $^{**}P = 0.0016$, $^{***}P = 0.0002$, $^{****}P < 0.0001$; one-way ANOVA with Bonferroni's post hoc test was used to calculate statistical differences in basal activity (**c**). Cell surface expression level was 107% for E309K/WT and 87% for E423R/WT mutants in comparison with the WT/WT heterodimer. **e**, Fitting of GABA into the extra density (contoured at 7.0σ) at the orthosteric ligand-binding site and its potential interaction with GABA$_{B1b}$. **f**, Concentration of endogenous GABA in the supernatant and lysate of HEK 293 GnTI$^-$ cells after recombinant expression of the GABA$_B$ receptor, as well as cell culture medium and lysis buffer controls, as detected by mass spectrometry.

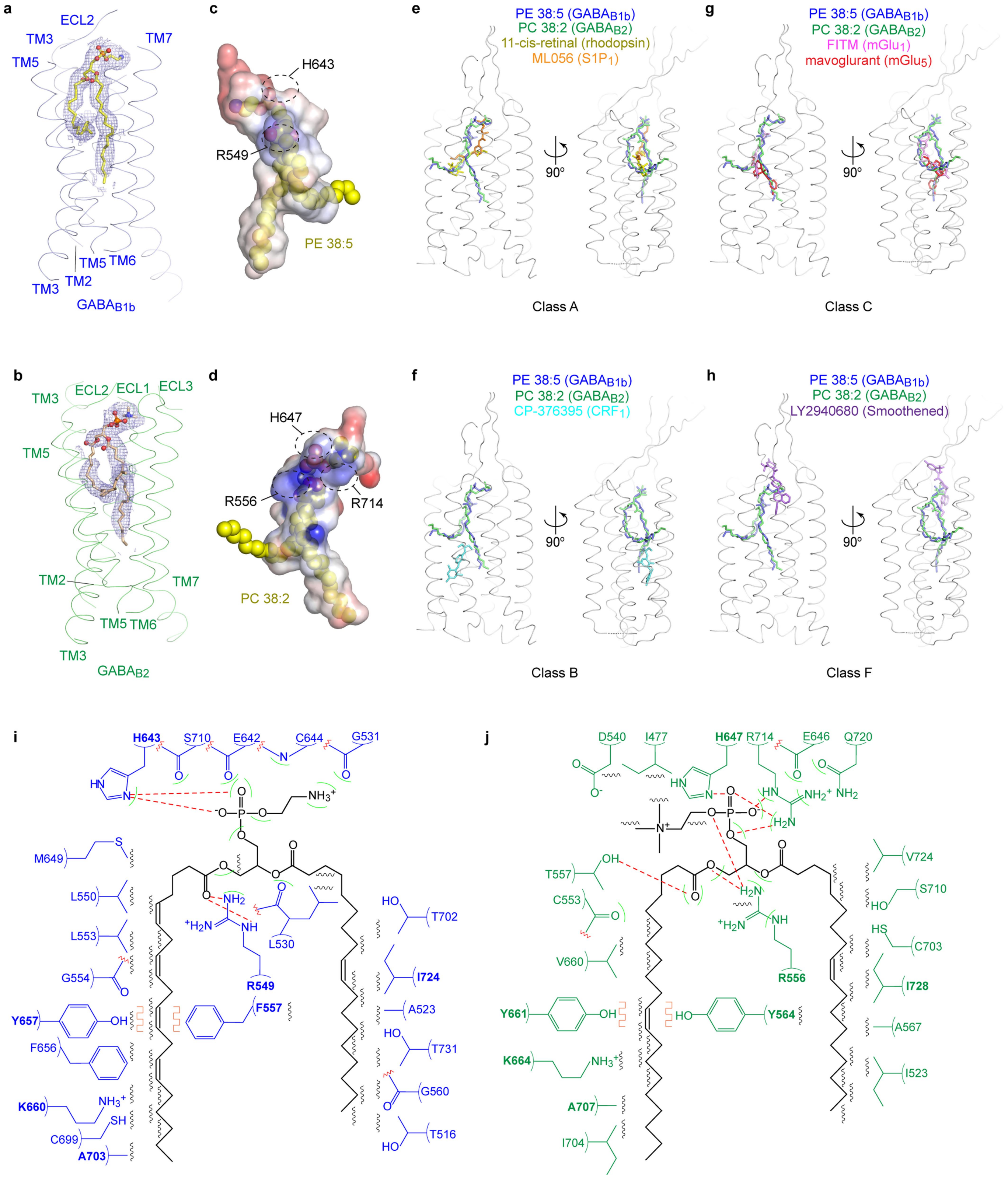

Extended Data Fig. 7 | See next page for caption.

Extended Data Fig. 7 | Endogenous phospholipid-binding sites of the GABA$_B$ receptor. a, **b**, Ribbon representation of the GABA$_{B1b}$ (**a**) and GABA$_{B2}$ (**b**) transmembrane domains, highlighting the cryo-EM density for phospholipids contoured at 4.0σ. Phospholipids are rendered in ball-and-stick representation. **c**, **d**, Electrostatic potential surface of the lipid-binding pocket in GABA$_{B1b}$ (**c**) and GABA$_{B2}$ (**d**). The phospholipids are shown as spheres. Charged residues that directly contact the phosphate group of each lipid are marked. **e**–**h**, Comparison of phospholipids bound to GABA$_B$ subunits with ligands bound to the class A GPCRs rhodopsin[27] (PDB code 1F88) and S1P$_1$ receptor[24] (PDB code 3V2Y) (**e**), the class B GPCR corticotropin-releasing factor receptor 1 (CRF$_1$; ref. [57]; PDB code 4K5Y) (**f**), the class C GPCRs mGlu$_1$ (ref. [29]; PDB code 4OR2) and mGlu$_5$ (ref. [28]; PDB code 4OO9) (**g**), and the class F GPCR Smoothened[58] (PDB code 4JKV) (**h**). In each panel, the Cα trace of the GABA$_{B1b}$ linker and transmembrane domain is shown in two orthogonal views in grey, and the superimposed GABA$_B$ ligands PE 38:5 and PC 38:2 are shown as blue and green stick models, respectively. Various GPCRs were overlapped onto the transmembrane domain of GABA$_{B1b}$ to bring their bound ligands into superposition. **i**, **j**, Schematic diagrams of the specific contacts between GABA$_{B1b}$ and PE 38:5 (**i**), and between GABA$_{B2}$ and PC 38:2 (**j**). Selected contacts between residues and phospholipids are highlighted; hydrogen bonds, red dotted lines; hydrophobic contacts, black wiggled lines; polar interactions, green curved lines; pi-stacking interactions, orange box wave. Red zigzags indicate contacts that are mediated by main-chain atoms. Lipid-interacting residues that are conserved in the two subunits are highlighted in bold and include: (1) head group (GABA$_{B1b}$, His 643 and Arg 549$^{3.32}$; GABA$_{B2}$, His 647 and Arg 556$^{3.32}$); (2) 20-carbon fatty acyl chain (GABA$_{B1b}$, Phe 557$^{3.40}$, Tyr 657$^{5.44}$ and Ala 703$^{6.54}$; GABA$_{B2}$, Tyr 564$^{3.40}$, Tyr 661$^{5.44}$ and Ala 707$^{6.54}$); (3) 18-carbon fatty acyl chain (GABA$_{B1b}$, Ile 724$^{7.36}$; GABA$_{B2}$ Ile728$^{7.36}$).

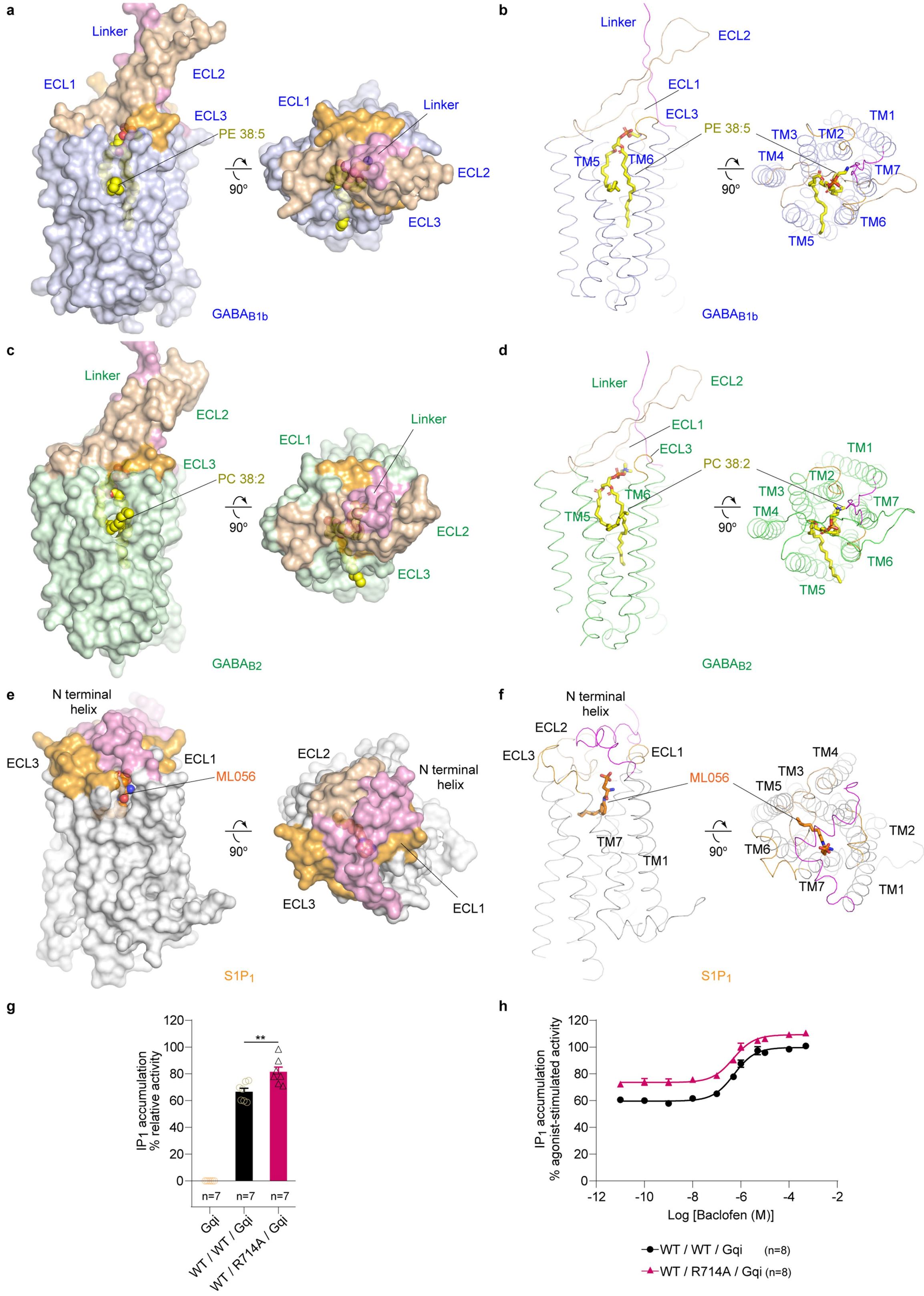

Extended Data Fig. 8 | See next page for caption.

Extended Data Fig. 8 | Endogenous phospholipid interactions with GABA$_{\mathrm{B}}$ receptor. a, **c**, **e**, Orthogonal views of a potential access channel in GABA$_{\mathrm{B1b}}$, GABA$_{\mathrm{B2}}$ and S1P$_1$ in molecular surface representation, along with phospholipids PE 38:5, PC 38:2 or the sphingolipid mimic ML056, in space-filling representation. Side views (left) show an opening between helices TM5 and TM6 in GABA$_{\mathrm{B1b}}$ (**a**) and GABA$_{\mathrm{B2}}$ (**c**), and between TM1 and TM7 in S1P$_1$ (**e**), while top views (right) highlight the blocked entrance to the lipid-binding pocket from the extracellular side. In all cases, ECL1 and ECL3 (orange), ECL2 (pale brown), the linker of GABA$_{\mathrm{B}}$-receptor subunits (pink) and the N-terminal helix of S1P$_1$ (pink) are distinguished by colour. **b**, **d**, **f**, The same information as in **a, c, e** but with ribbon models for GABA$_{\mathrm{B1b}}$ (**b**), GABA$_{\mathrm{B2}}$ (**d**), and S1P$_1$ (ref. [24]) (PDB code 3V2Y) (**f**). Lipids are in stick format. **g**, **h**, Functional effect of a GABA$_{\mathrm{B2}}$ lipid-binding site mutation. Basal activity (**g**) and dose-dependent baclofen-stimulated receptor response (**h**) in cells transiently expressing Gα_{qi5} (Gqi) with WT GABA$_{\mathrm{B}}$ receptor or WT GABA$_{\mathrm{B1b}}$ and mutant GABA$_{\mathrm{B2}}$ R714A (R714A) heterodimer. Cells transfected with Gα_{qi5} alone were used as negative controls. Relative activity in both graphs was measured by IP$_1$ accumulation, and expressed as a percentage of the maximum wild-type activity induced by baclofen relative to the activity of Gα_{qi5} alone. Data points represent averages ± s.e.m. of multiple experiments (*n*), each with quadruplicate measurements. $^{**}P = 0.0016$; one-way ANOVA with Bonferroni's post hoc test was used to calculate statistical differences in basal activity (**g**). Cell surface expression level was 77% for the WT/R714A mutant in comparison with the WT/WT heterodimer.

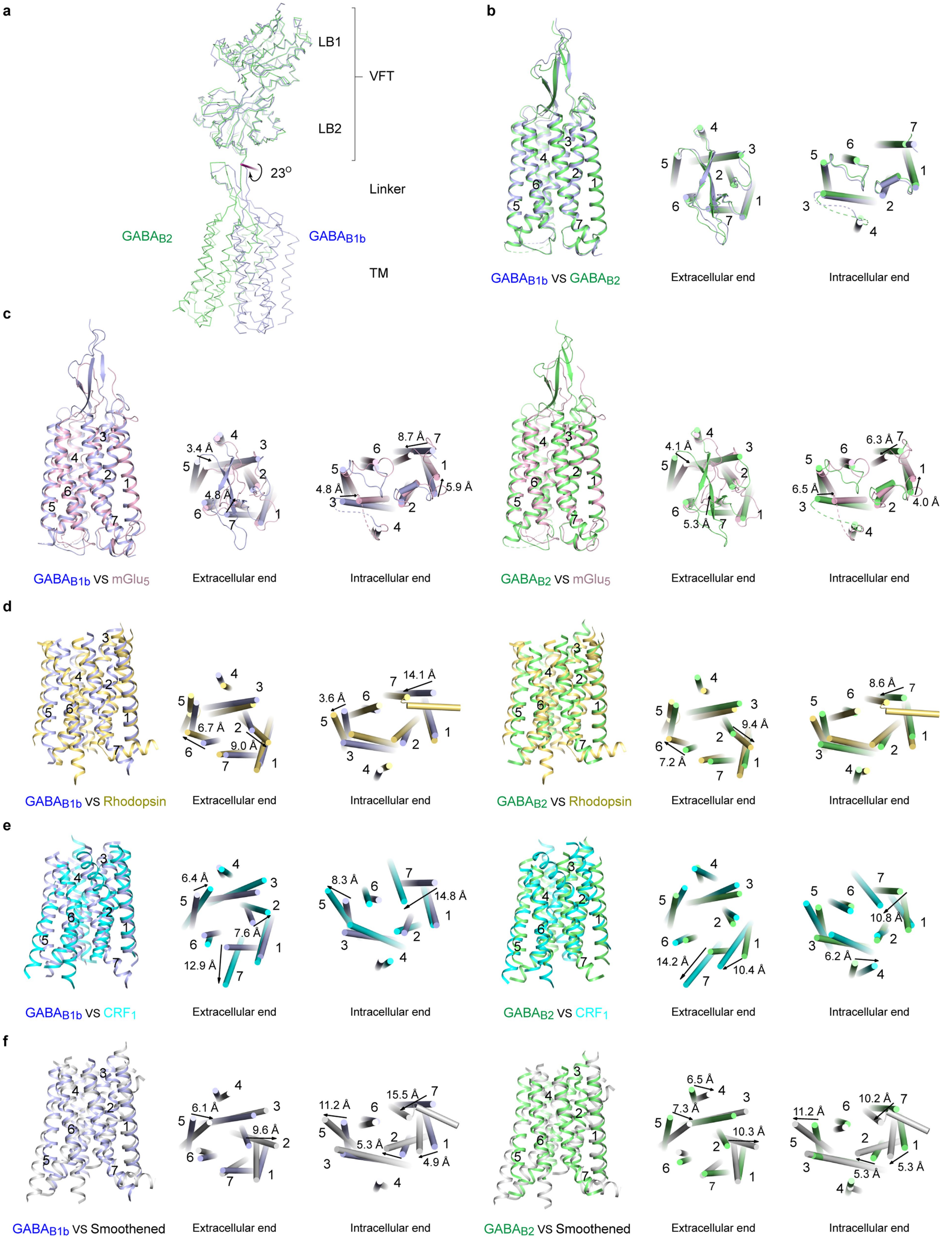

Extended Data Fig. 9 | See next page for caption.

Extended Data Fig. 9 | Comparison of the GABA$_B$ transmembrane domain with other GPCRs. a, Superposition of GABA$_{B1b}$ and GABA$_{B2}$ subunits based on their VFT modules. The short purple line denotes the axis of rotation that relates the linker and transmembrane domains of GABA$_{B1b}$ and GABA$_{B2}$ (rotation $\chi = 23°$; screw translation $\tau_\chi = 0.01$ Å). **b**, Superposition of the linker and transmembrane domains of the GABA$_{B1b}$ and GABA$_{B2}$ subunits. **c**, Superposition of the linker and transmembrane domains of each GABA$_B$ subunit with the class C GPCR mGlu$_5$ (ref. [20]; PDB code 6N52) in three different views, with arrows revealing inward extracellular shifts in TM5 and TM7, as well as an inward intracellular shift in TM3, in mGlu$_5$ compared with either GABA$_B$ subunit. **d**–**f**, Superposition of the transmembrane helices of each GABA$_B$ subunit with the class A GPCR rhodopsin[27] (PDB code 1F88) (**d**), the class B GPCR CRF$_1$ (ref. [57]; PDB code 4K5Y) (**e**), and the class F GPCR Smoothened[58] (PDB code 4JKV) (**f**). Arrows indicate large shifts in transmembrane helix positions between GABA$_B$ subunits and other GPCRs, such as outward extracellular movements in class A (TM2 and TM6), class B (TM1, TM2 and TM7), and class F (TM2, TM4 and TM5). There are also inward intracellular shifts in TM7 in all comparisons, and outward intracellular shifts in TM5 in class A, B and F.

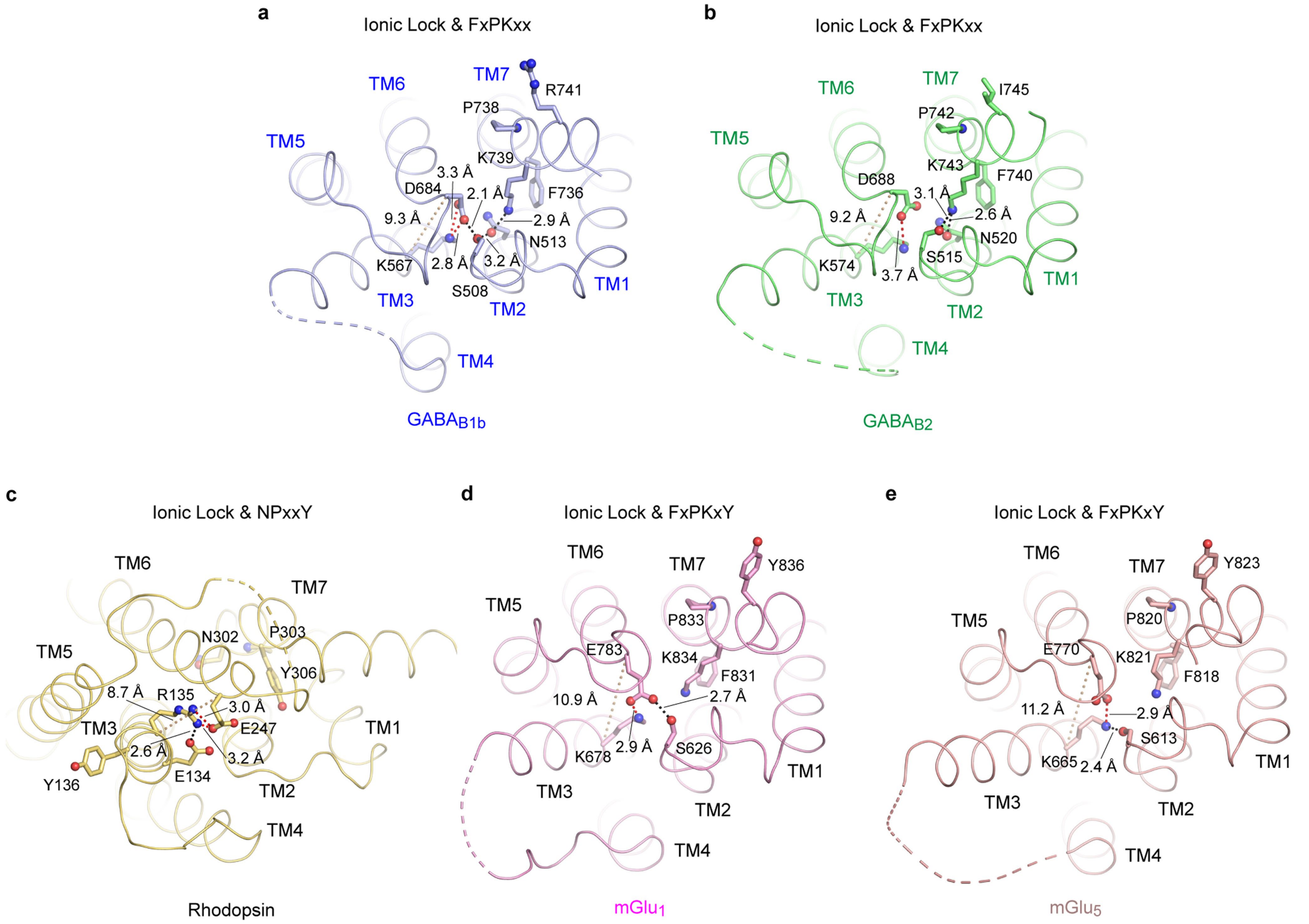

Extended Data Fig. 10 | Conserved motifs in GABA$_B$, rhodopsin and mGlu receptors. a, **b**, The 'ionic lock' and FxPKxx motifs in the GABA$_{B1b}$ (**a**) and GABA$_{B2}$ (**b**) subunits. The 'ionic locks' consist of Asp 684 of ICL3 and Lys 567$^{3.50}$ in GABA$_{B1b}$, and Asp 688 of ICL3 and Lys 574$^{3.50}$ in GABA$_{B2}$. The FxPKxx motifs include the conserved Lys 739$^{7.51}$ of GABA$_{B1b}$ and Lys 743$^{7.51}$ of GABA$_{B2}$, which interact with the 'ionic locks' through Asn$^{2.39}$ (GABA$_{B1b}$ N513$^{2.39}$; GABA$_{B2}$ N520$^{2.39}$) and a serine (GABA$_{B1b}$ S508; GABA$_{B2}$ S515) in ICL1. **c**, The 'ionic lock' and NPxxY motifs in class A rhodopsin[27]. **d**, **e**, The 'ionic lock' and FxPKxY motifs in the class C receptors mGlu$_1$ (ref. [29]; **d**) and mGlu$_5$ (ref. [28]; **e**), which are in close proximity as in GABA$_B$ subunits. Key residues of the motifs are displayed as stick models. Hydrogen bonds are indicated by black dotted lines. Interactions between participating residues of the 'ionic lock' are denoted by red dotted lines with distances labelled. Distances between the Cα atoms of the 'ionic lock' residues are marked by brown dotted lines.

nature research

Corresponding author(s): Oliver B. Clarke, Joachim Frank, Qing R. Fan

Last updated by author(s): 04/08/2020

Reporting Summary

Statistics

For all statistical analyses, confirm that the following items are present in the figure legend, table legend, main text, or Methods section.

n/a	Confirmed	
☐	☒	The exact sample size (*n*) for each experimental group/condition, given as a discrete number and unit of measurement
☐	☒	A statement on whether measurements were taken from distinct samples or whether the same sample was measured repeatedly
☐	☒	The statistical test(s) used AND whether they are one- or two-sided *Only common tests should be described solely by name; describe more complex techniques in the Methods section.*
☒	☐	A description of all covariates tested
☒	☐	A description of any assumptions or corrections, such as tests of normality and adjustment for multiple comparisons
☐	☒	A full description of the statistical parameters including central tendency (e.g. means) or other basic estimates (e.g. regression coefficient) AND variation (e.g. standard deviation) or associated estimates of uncertainty (e.g. confidence intervals)
☐	☒	For null hypothesis testing, the test statistic (e.g. *F*, *t*, *r*) with confidence intervals, effect sizes, degrees of freedom and *P* value noted *Give P values as exact values whenever suitable.*
☒	☐	For Bayesian analysis, information on the choice of priors and Markov chain Monte Carlo settings
☒	☐	For hierarchical and complex designs, identification of the appropriate level for tests and full reporting of outcomes
☒	☐	Estimates of effect sizes (e.g. Cohen's *d*, Pearson's *r*), indicating how they were calculated

Our web collection on statistics for biologists contains articles on many of the points above.

Software and code

Policy information about availability of computer code

Data collection	Cryo-EM: Leginon 3.2, Gatan Microscopy Suite 3.3; LC-MS/MS: Thermo Xcalibur v4.0.27.19; ICP-MS: Syngistix v1.1. Cell-based functional assay data collection: PHERAstar FS v3.10 R3; MALDI-MS: FlexControl3.4.135.
Data analysis	Cryo-EM: MotionCor2 v2.1, Gctf v1.06, Relion 3.0, cryoSPARC v2.4, UCSF Chimera v1.13.1; Model building and refinement: COOT v0.8.9.0, Phenix v1.14, Molprobity, EMRinger; Structural alignment: LSQMAN v9.7.9; Figures: Pymol v1.8.6.0 and v2.3.1, UCSF Chimera v1.13.1; UCSF ChimeraX v0.9; Cell-based functional assay data analysis: PRISM v8.2.0; SPA binding data analysis: SigmaPlot v13.0; LC-MS/MS: MS-DIAL v3.40, LipidBlast v49.

For manuscripts utilizing custom algorithms or software that are central to the research but not yet described in published literature, software must be made available to editors/reviewers. We strongly encourage code deposition in a community repository (e.g. GitHub). See the Nature Research guidelines for submitting code & software for further information.

Data

Policy information about availability of data

All manuscripts must include a data availability statement. This statement should provide the following information, where applicable:

- Accession codes, unique identifiers, or web links for publicly available datasets
- A list of figures that have associated raw data
- A description of any restrictions on data availability

All data are included in this article and its Supplementary Information. Cryo-EM density maps of GABA(B) receptor have been deposited in the Electron Microscopy

Data Bank under accession codes EMD-21685. Atomic coordinates for the GABA(B) receptor structure are deposited in the RCSB Protein Data Bank under the accession number 6WIV.

Field-specific reporting

Please select the one below that is the best fit for your research. If you are not sure, read the appropriate sections before making your selection.

☒ Life sciences ☐ Behavioural & social sciences ☐ Ecological, evolutionary & environmental sciences

For a reference copy of the document with all sections, see nature.com/documents/nr-reporting-summary-flat.pdf

Life sciences study design

All studies must disclose on these points even when the disclosure is negative.

Sample size	No sample size calculation was performed. Cell-based IP accumulation data represent average of multiple experiments (n = 3 - 15), each consisting of quadruplicate measurements. ICP-MS data represent average of eight measurements within two experiments.
Data exclusions	No data was excluded from analysis.
Replication	Cell-based IP accumulation experiments were repeated three to fifteen times. ICP-MS experiments were repeated twice.
Randomization	Randomization was not relevant to the experiments in our study.
Blinding	Blinding was not relevant to the experiments in our study since no subjective allocation was involved.

Reporting for specific materials, systems and methods

We require information from authors about some types of materials, experimental systems and methods used in many studies. Here, indicate whether each material, system or method listed is relevant to your study. If you are not sure if a list item applies to your research, read the appropriate section before selecting a response.

Materials & experimental systems

n/a	Involved in the study	
☐	☒	Antibodies
☐	☒	Eukaryotic cell lines
☒	☐	Palaeontology
☒	☐	Animals and other organisms
☒	☐	Human research participants
☒	☐	Clinical data

Methods

n/a	Involved in the study	
☒	☐	ChIP-seq
☒	☐	Flow cytometry
☒	☐	MRI-based neuroimaging

Antibodies

Antibodies used	1. Mouse monoclonal ANTI-FLAG® M2 Affinity Gel, Milliporesigma A2220. 2. Mouse monoclonal ANTI-FLAG® M1 antibody, MilliporeSigma F3040, clone M1, 1:300 dilution. 3. IRDye® 800CW Goat anti-Mouse IgG Secondary Antibody, Li-Cor Biosciences 926-32210, 1:4,000 dilution.
Validation	1. Mouse monoclonal ANTI-FLAG® M2 Affinity Gel: Validation by Milliporesigma; application included purification of FLAG fusion proteins. 2. Mouse monoclonal ANTI-FLAG® M1 antibody: Validation by Milliporesigma for detection of proteins with an N-terminal FLAG marker; application included immunocytochemistry (on-cell western).

Eukaryotic cell lines

Policy information about cell lines

Cell line source(s)	1. HEK293S GnTI- (ATCC® No. CRL-3022™); 2. HEK 293T/17 (ATCC® No. CRL-11268™).
Authentication	Cell lines were authenticated by ATCC. Cellular morphology was checked by microscope for each passage of cells.
Mycoplasma contamination	Cell lines were certified by ATCC, but not tested again for mycoplasma contamination during culturing.

Commonly misidentified lines (See ICLAC register)	None.

Article

Structures of metabotropic GABA$_B$ receptor

https://doi.org/10.1038/s41586-020-2469-4

Received: 11 March 2020

Accepted: 16 June 2020

Makaía M. Papasergi-Scott[1,2,4], Michael J. Robertson[1,2,4], Alpay B. Seven[1,2], Ouliana Panova[1,2], Jesper M. Mathiesen[3] & Georgios Skiniotis[1,2]✉

Stimulation of the metabotropic GABA$_B$ receptor by γ-aminobutyric acid (GABA) results in prolonged inhibition of neurotransmission, which is central to brain physiology[1]. GABA$_B$ belongs to family C of the G-protein-coupled receptors, which operate as dimers to transform synaptic neurotransmitter signals into a cellular response through the binding and activation of heterotrimeric G proteins[2,3]. However, GABA$_B$ is unique in its function as an obligate heterodimer in which agonist binding and G-protein activation take place on distinct subunits[4,5]. Here we present cryo-electron microscopy structures of heterodimeric and homodimeric full-length GABA$_B$ receptors. Complemented by cellular signalling assays and atomistic simulations, these structures reveal that extracellular loop 2 (ECL2) of GABA$_B$ has an essential role in relaying structural transitions by ordering the linker that connects the extracellular ligand-binding domain to the transmembrane region. Furthermore, the ECL2 of each of the subunits of GABA$_B$ caps and interacts with the hydrophilic head of a phospholipid that occupies the extracellular half of the transmembrane domain, thereby providing a potentially crucial link between ligand binding and the receptor core that engages G proteins. These results provide a starting framework through which to decipher the mechanistic modes of signal transduction mediated by GABA$_B$ dimers, and have important implications for rational drug design that targets these receptors.

The neurotransmitter GABA is primarily responsible for synaptic inhibition throughout the nervous system, via activation of GABA$_A$ ion channels and pre- and postsynaptic GABA$_B$ receptors. GABA$_B$ stimulation of the G$_{i/o}$ class of heterotrimeric G proteins results in a prolonged decrease in neuronal excitability via the inhibition of adenylyl cyclase and voltage-gated Ca^{2+} channels, as well as the opening of G protein-coupled inward-rectifying potassium channels[2,3,6]. Abnormal execution of GABA$_B$ signalling is responsible for several neuropsychiatric diseases, and the receptor is an attractive drug target for a range of disorders, including drug addiction, pain, epilepsy, spasticity, anxiety and gastro-oesophageal reflux disease[7,8].

There are about 20 G-protein-coupled receptors (GPCRs) in family C, including GABA$_B$, the metabotropic glutamate receptors (mGlu1 to mGlu8), the calcium-sensing receptor, two taste receptors and several orphan receptors[9,10]. These receptors operate as obligate dimers, in which each subunit is composed of a bilobed extracellular ligand-binding domain (termed the Venus flytrap (VFT)) and a 7-transmembrane domain (7TM) that are connected via a linker region[11]. Previous crystallographic studies of the VFT from various members of family C (including GABA$_B$) have shown that agonist binding rearranges the VFT in a way that would bring the linker regions into close proximity[12,13]. All GPCRs in family C contain a cysteine-rich domain within the linker region—with the exception of GABA$_B$, which has a relatively short linker. Recent structures of mGlu5 have shown that the cysteine-rich domain interacts with ECL2 of the transmembrane region, thereby transducing conformational changes 120 Å away from the ligand-binding site on the VFT to the 7TM (where G-protein activation occurs)[14]. Given that GABA$_B$ lacks a cysteine-rich domain, the structural communication between an agonist-bound VFT and the 7TM remains unclear.

Furthermore, unlike other GPCRs in family C, GABA$_B$ is an obligate heterodimer of dissimilar subunits—GABA$_{B1}$ and GABA$_{B2}$[15]. Agonist binding occurs only on the VFT of GABA$_{B1}$, and G-protein coupling and activation occurs exclusively through GABA$_{B2}$[4,5]. Therefore, besides its pharmacological interest, GABA$_B$ presents an ideal model system to study *trans*-activation mechanisms of dimeric family C GPCRs. However, such studies have been limited by the lack of structural information on full-length GABA$_B$, restricting our ability to understand how agonist binding to GABA$_{B1}$ results in G-protein activation on the intracellular side of GABA$_{B2}$. Here we use single-particle cryo-electron microscopy (cryo-EM), atomistic simulations and cellular signalling assays to obtain structural and mechanistic insights into full-length GABA$_B$ receptor complexes.

For structural studies, we co-expressed recombinant constructs of human GABA$_{B1b}$ and GABA$_{B2}$ in insect cells and purified the GABA$_B$ heterodimer by tandem affinity chromatography in the presence of the inverse agonist CGP55845[16]. We determined the structure of the inactive detergent-solubilized GABA$_B$ heterodimer at a global indicated resolution of 3.6 Å (Fig. 1, Extended Data Figs. 1, 2a, Extended Data Table 1). Our cryo-EM map resolved the entire GABA$_B$ apart from the C-terminal coil–coil domain, which appears to be flexible in relation to the transmembrane regions. Additionally, our focused map

---

[1]Department of Molecular and Cellular Physiology, Stanford University School of Medicine, Stanford, CA, USA. [2]Department of Structural Biology, Stanford University School of Medicine, Stanford, CA, USA. [3]Department of Drug Design and Pharmacology, Faculty of Health and Medical Sciences, University of Copenhagen, Copenhagen, Denmark. [4]These authors contributed equally: Makaía M. Papasergi-Scott, Michael J. Robertson. ✉e-mail: yiorgo@stanford.edu

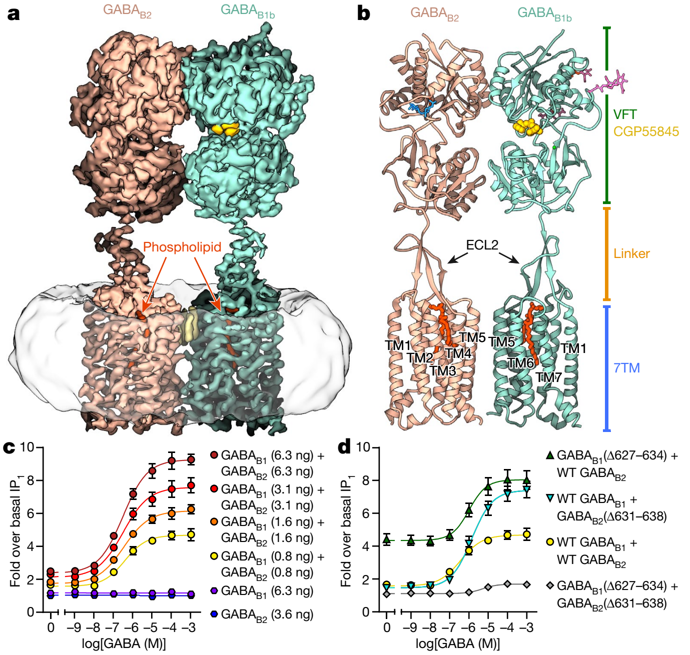

Fig. 1 | Cryo-EM map and model of the full-length GABA$_B$ receptor heterodimer in inactive state. **a**, **b**, GABA$_B$ receptor cryo-EM map (**a**) and ribbon diagram (**b**) (GABA$_{B1b}$, teal; GABA$_{B2}$, tan; GDN micelle, white; CGP55845, gold; phospholipids, orange; glycosylation, blue and pink). Elongated densities at the 7TM interface are probably lipid or detergent molecules (yellow). **c**, GABA E_{max} increases with higher levels of cotransfected GABA$_{B1}$ and GABA$_{B2}$ plasmid DNA. **d**, ECL2 truncation of either subunit of GABA$_B$ increases E_{max} of GABA-stimulated response when compared to cotransfected wild-type (WT) receptors of similar surface expression (Extended Data Fig. 6a); ECL2 shortening of both protomers inhibits activity. For sample sizes, replicability, sample collection and descriptions of error bars for all figures, see 'Statistics and reproducibility' in Methods.

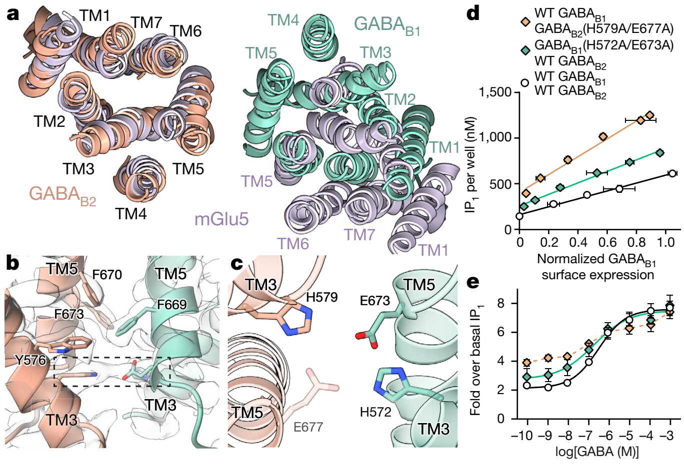

Fig. 2 | TM3 and TM5 stabilize an inactive-state dimer interface of GABA$_B$ 7TM. **a**, Inactive-state GABA$_B$ 7TMs (GABA$_{B1}$, teal; GABA$_{B2}$, tan) are in closer proximity than those of inactive mGlu5 (purple) (PDB 6N52[14]), top-down view. **b**, The GABA$_{B1}$ and GABA$_{B2}$ interface is stabilized through hydrophobic interactions along the TM5 helices, and by polar residues on the intracellular side of TM3 and TM5 (boxed). **c**, Polar interaction residues from the intracellular side of the receptor. GABA$_{B2}$ E677 is shown for perspective; however, the map density for this residue was insufficient for high-confidence modelling of its side chain. IP$_1$ accumulation assays illustrate differences in the basal activity (**d**) and GABA response (**e**) of GABA$_B$ TM3 and TM5 mutants.

of the extracellular region at a resolution of 3.5 Å provided improved density for the linker regions, and assisted with modelling (Extended Data Fig. 1). The asymmetric protomers (GABA$_{B1}$ and GABA$_{B2}$) share a similar secondary structure and arrangement, but are distinguished by differential glycosylation and a well-resolved ligand density within the GABA$_{B1}$ VFT that is absent in GABA$_{B2}$ (Fig. 1, Extended Data Figs. 3, 4a). The upper VFT lobes of GABA$_B$ form a junction, whereas the lower VFT lobes are separated by about 20 Å (Fig. 1, Extended Data Fig. 3). The CGP55845 ligand adopts a horseshoe-like conformation (which was confirmed by GemSpot[17]) that closely resembles the crystal structure of the GABA$_{B1}$ VFT in complex with the inhibitor CGP54626[12,16] (Extended Data Fig. 3). We also observe a small spherical density in GABA$_{B1}$ that appears to be interacting with the backbone carbonyl of G277, in addition to several anionic groups and a tyrosine, which raises the possibility that a divalent cation resides in that location (Extended Data Fig. 3e).

Inactive GABA$_B$ assumes an overall morphology similar to that of the apo-state structure of mGlu5[14]; the most substantial differences between these two arise within the linker region (Fig. 1b). Bridging the VFT and 7TM, an approximately 20-residue linker forms a β-sheet in conjunction with the ECL2. Notably, the length of the GABA$_B$ receptor ECL2 is nearly twice that of mGlu5 (Fig. 1, Extended Data Fig. 4b). In the absence of cysteine-rich domains, the β-sheet structure of the GABA$_B$ linker in complex with ECL2 orders this region, with the additional ECL2 length thus allowing coupling between the 7TM and VFT for signal transduction. Our molecular dynamics simulations support the structural stabilization of the linker through the β-sheet formation. After 200 ns, in all simulations the linker and ECL2 continued to adopt a stable structure even in the absence of the VFTs, although we did observe a slight downward rotation in β-sheet orientation (Extended Data Fig. 5). To further examine the involvement of ECL2 in receptor activation, we used a functional assay with a chimeric G$\alpha_{o/q}$, in which the $G_{i/o}$-coupled GABA$_B$ receptor can couple to the PLC pathway[3,18]. We measured the accumulation of the downstream metabolite inositol monophosphate (IP$_1$) by LiCl using an established assay[19], and thereby monitored the GABA-stimulated and basal receptor activity (Fig. 1c). ECL2 shortening was generally inhibitory to the proper membrane trafficking of the subunits of GABA$_B$. Accordingly, we normalized the transfected DNA to obtain similar expression levels between constructs (Extended Data Fig. 6a). The partial deletion of the ECL2 of GABA$_{B1}$ (residues 627–634)—comprising the unstructured tip of the loop nearest the VFT—produced an increase in basal activity, but did not affect the GABA maximal response (E_{max}) when expressed with wild-type GABA$_{B2}$ (Fig. 1d). These findings indicate that abrogating the ECL2–linker allows flexibility in the GABA$_{B1}$ VFT relative to the rest of the receptor dimer, resulting in activation through the GABA$_{B2}$ VFT–7TM route in the absence of agonist[20]. By contrast, the partial deletion of the ECL2 of GABA$_{B2}$ (residues 631–638) did not affect basal activity, but produced an increase in GABA E_{max} and a decrease in GABA potency when compared to wild-type receptor expressed at similar levels at the cell surface—indicating that the ECL2 of GABA$_{B2}$ may be partially inhibitory (Fig. 1d, Extended Data Fig. 6a). When both receptors contain a truncated ECL2, we observed a decrease in GABA E_{max}, which suggests that at least one VFT must be structurally coupled through the extended ECL2–linker for full activation (Fig. 1d). Collectively, these data support a bimodal transactivation mechanism of GABA$_B$, in which agonist binding on the GABA$_{B1}$ receptor can proceed from the GABA$_{B1}$ VFT down to the GABA$_{B1}$ 7TM region to enact changes in GABA$_{B2}$ that promote G-protein activation, and also activate the GABA$_{B2}$ 7TM directly through the GABA$_{B2}$ VFT.

Besides those of the VFT and the C-terminal coiled–coil, we observe that inactive GABA$_B$ forms an additional dimer interface between transmembrane (TM)3 and TM5 from each monomer of the heterodimer (Figs. 1, 2). The interface is formed by ionic interactions between residues on the intracellular side of each receptor—H572 in TM3 and E673 in TM5 of GABA$_{B1}$, and H579 in TM3 and E677 in TM5 of GABA$_{B2}$—and is

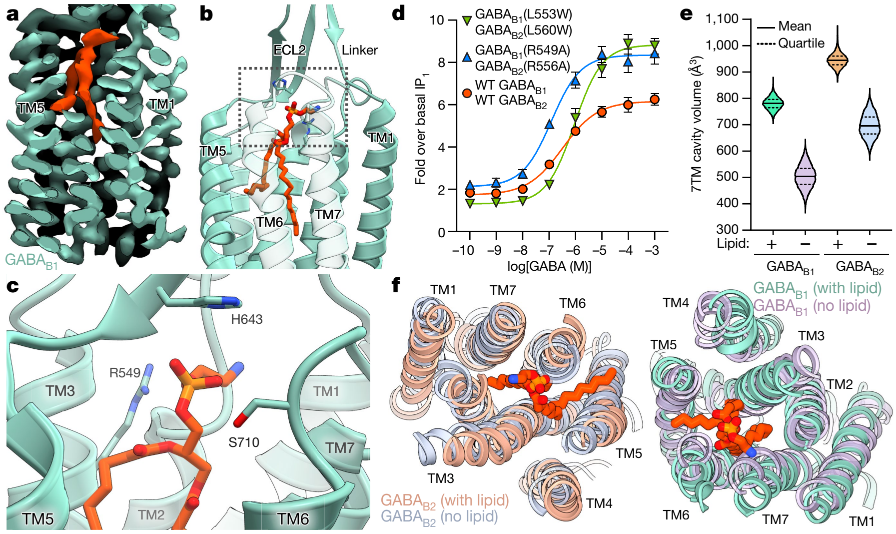

Fig. 3 | Phospholipid binds within the transmembrane cores of GABA$_B$. **a**, Electron microscopy map clipped to show the location of phospholipid within GABA$_{B1}$ of the heterodimer. **b**, **c**, Ribbon representation of phosphatidylethanolamine within GABA$_{B1}$ (**b**), with boxed region (**c**) to show the structural environment of the headgroup. **d**, GABA concentration response for wild-type GABA$_B$ (red), and mutants designed to displace phospholipid (green) or de-stabilize the phospholipid headgroup (blue). **e**, **f**, Molecular dynamics simulations show a collapse of the transmembrane cavity when lipid is absent. **e**, Violin plot of cavity-volume ensemble data. **f**, Representative top-down view of the GABA$_B$ ribbon and stick model from molecular dynamics simulations at 200 ns.

further stabilized through aromatic residues along the same helices (Fig. 2b, c). We also observed elongated densities, probably corresponding to glyco-diosgenin (GDN) and/or cholesteryl hemisuccinate (which were used in purification), packed between the extracellular sides of the two 7TM regions, which may also stabilize the interface (Fig. 1a, Extended Data Fig. 2i). The dimer interface contrasts with that of the inactive mGlu5 receptor, in which a distance of about 16 Å separates the two 7TM regions[14] (Fig. 2a). To probe the importance of these interactions, we mutated the TM3–TM5 interface and performed IP$_1$ accumulation assays (Fig. 2d, e, Extended Data Fig. 6). Notably, mutation of either H579 or E677 on GABA$_{B2}$ to alanine, or mutation of both E673 and H572 on GABA$_{B1}$ to alanine, increased the basal activity of the receptor, which suggests that the TM3–TM5 interface is inhibitory to signalling in the absence of agonist, which further supports the transactivation mechanism described above (Fig. 2, Extended Data Fig. 6b–e). When expressed at the cell surface alone, GABA$_{B2}$(H579A/E677A) exhibited a slight increase in basal activity compared to GABA$_{B2}$ alone (Extended Data Fig. 6d). These findings further support a role of an intraprotomer H579–E677 interaction in GABA$_{B2}$ to assist stabilizing an auto-inhibited state, and are consistent with the lack of constitutive activity by the GABA$_{B2}$(Δ631–638) mutant.

The most unexpected observation in the transmembrane region of both monomers of GABA$_B$ is a wishbone-shaped density that occupies the extracellular half of each 7TM core. The bifurcated density, which is better resolved within the GABA$_{B1}$ helical bundle, corresponds to a phospholipid (Fig. 3, Extended Data Fig. 2). Our consideration of the size and shape of the density, the surrounding amino acid environment within the 7TM core and the known phospholipid composition in *Spodoptera frugiperda* (Sf9) insect cells led us to infer that the density in GABA$_{B1}$, and probably GABA$_{B2}$, corresponds to phosphatidylethanolamine (Fig. 3, Extended Data Fig. 7). However, it is possible that the observed density is the result of a heterogeneous mixture of phospholipids. The observation of the phospholipid is particularly intriguing, as—to our knowledge—no other GPCR structure has revealed a two-chained phospholipid within this space. Although a lipid-activated subfamily within family A GPCRs exists, known ligands are single-acyl-chain lipids, eicosanoids and sterols[21]. Notably, GABA$_B$ residues in the extracellular loops (including ECL2) and TM3 of GABA$_B$ coordinate the polar headgroup of the phospholipid, resulting in a 'lid' over the 7TM cavity that resembles the lipid-binding GPCRs of family A. The remaining hydrophilic atoms in the lipid appear solvent-exposed, whereas the lipid tails are buried deep into the hydrophobic portion of the transmembrane cavity (Fig. 3b, c). The presence of the 7TM lipid in our cryo-EM structures suggests it is bound tightly, as is also suggested by its retention during detergent solubilization of the receptor. Additionally, a conserved TM6 tryptophan—which acts as an activating 'toggle-switch' in other GPCRs of family C[22,23]—is replaced by cysteine in both GABA$_{B1}$ and GABA$_{B2}$ (Extended Data Fig. 4c, d). This replacement is essential, as any probable tryptophan rotamer at that position would clash sterically with the bound phospholipid.

The presence of lipid in the 7TM core suggests this lipid may have a physiological role in the structural and functional integrity of the transmembrane bundles, occupying a region that corresponds to the ligand-binding site in other classes of GPCR (Extended Data Fig. 4). Moreover, given the role of the ECL2 in coupling the VFT to the 7TM regions, it is conceivable that interactions of the phospholipid with the ECL2 are essential for increasing the stability of the linker region and also participate in relaying structural transitions from the VFT to the 7TM core. Mutations designed to displace lipid tails in the 7TM core (GABA$_{B1}$(L553W) and GABA$_{B2}$(L560W)) decrease basal activity and potency of GABA while increasing GABA E_{max}, whereas mutation of the arginine that coordinates the headgroup of the phospholipids (GABA$_{B1}$(R549A) and GABA$_{B2}$(R556A)) results in increases in both GABA$_B$ basal activity and receptor response to GABA (Fig. 3d, Extended Data Fig. 6f, g). Collectively, these results indicate that destabilization of phospholipid in the core affects receptor activation, and it is thus conceivable that the lipid directly modulates receptor activity as a result of ECL2 movements in native GABA$_B$. To further probe the role of phospholipid, we used a range of atomistic simulations with the GABA$_B$ receptor system. We initiated simulations of the GABA$_B$ 7TM and linker with the VFT removed, both with and without lipid. The simulations revealed that without lipid the transmembrane helices begin to collapse into the core, with mean decreases in cavity volume of about 30% (Fig. 3, Extended Data Fig. 5, Supplementary Data 1, 2); this suggests a strongly coupled interplay between the phospholipid and 7TM core. Alternatively, multiple simulations that started without

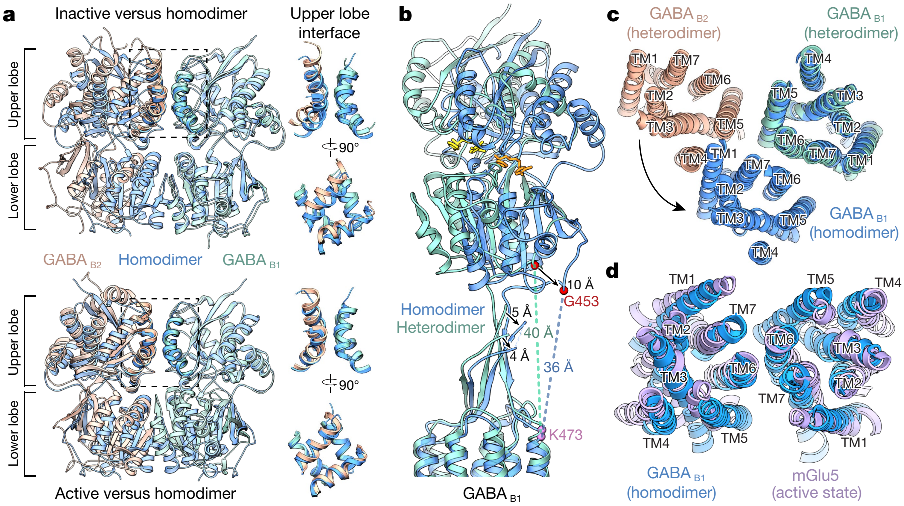

Fig. 4 | Inhibitor-bound $\mathrm{GABA_{B1}}$ homodimers adopt a VFT orientation similar to that of active $\mathrm{GABA_B}$ heterodimer, and a 7TM interface similar to that of active mGlu5. a, VFT overlay of structures of $\mathrm{GABA_B}$ heterodimer (tan and teal) in inactive (top) and active (bottom) state (PDB 4MS4[12]), with the model of $\mathrm{GABA_{B1}}$ homodimer (blue). The upper-lobe interaction interface (boxed) of the $\mathrm{GABA_{B1}}$ homodimer matches that of the active-state heterodimer. **b**, The $\mathrm{GABA_{B1}}$ subunit of the heterodimer (teal) and homodimer (blue) were aligned to the 7TM, revealing differences in VFT and linker positioning. **c**, Top-down view of superposed 7TM of $\mathrm{GABA_B}$ heterodimer (tan and teal) and homodimer (blue), showing the marked difference in the protomer interface. **d**, Top-down view of superimposed 7TM of agonist-bound mGlu5 (purple) (PDB 6N51[14]) and $\mathrm{GABA_{B1}}$ homodimer (blue).

lipid in the transmembrane helices showed lipid tails from the bilayer entering the receptor hydrophobic cavity below residue Y661, at a site akin to that at which the tail protrudes in our cryo-EM structure. Peripheral lipid-tail insertion in simulations correlated with circumvention of the collapse of the 7TM cavity (Extended Data Fig. 5). In one simulation, after 200 ns we observed a lipid that had inserted both of its hydrocarbon tails into the receptor core. Extending the simulation by an additional 100 ns revealed the headgroup had moved over the top of the receptor, indicating lipid entry may occur as a stepwise process in which the lipid-tail enters by sliding between TM5 and TM6, and is followed by the entire lipid (Extended Data Fig. 5). Although it is probable that lipid insertion into the 7TM core occurs concurrently with helix insertion into the membrane during protein folding, these results suggest a clear tendency for phospholipids to insert at that position in a mature receptor.

Pharmaceutical agents targeting the $\mathrm{GABA_B}$ receptor and other GPCRs of family C are proposed to function either at the orthosteric ligand-binding site or allosterically within the transmembrane core, as with orthosteric ligands of family A GPCRs. However, the bound phospholipid appears to occlude the binding of allosteric modulators analogous to those used to target other family C receptors[24]. Consequently, potential allosteric modulators of $\mathrm{GABA_B}$ would need to either displace the core lipid or bind at an alternative site peripheral to the bundle.

Although we obtained pure $\mathrm{GABA_B}$ heterodimer by tandem affinity purification of receptor constructs with distinct tags, when both subunits contain an N-terminal Flag tag we also purified a considerable fraction (>40%) of $\mathrm{GABA_{B1}}$ homodimers. In cells, an endoplasmic-reticulum retention signal within the $\mathrm{GABA_{B1}}$ coil–coil domain prevents $\mathrm{GABA_{B1}}$ from reaching the plasma membrane, unless this domain is masked by the $\mathrm{GABA_{B2}}$ C terminus or other interacting partners[25,26]. Thus, the presence of $\mathrm{GABA_{B1}}$ homodimer in our preparation is probably due to the persistence of internal membranes during the purification procedure. However, multiple studies have previously suggested a physiological role for $\mathrm{GABA_{B1}}$ homodimers within some cell types of the nervous system and gastrointestinal tract that express $\mathrm{GABA_{B1}}$ isoforms in the absence of $\mathrm{GABA_{B2}}$[27–32]. Although it is as yet unclear how homodimeric $\mathrm{GABA_{B1}}$ functions in the absence of $\mathrm{GABA_{B2}}$ G-protein coupling, we sought to obtain further mechanistic insights into the $\mathrm{GABA_B}$ system and obtained the structure of the $\mathrm{GABA_{B1b}}$ homodimer at a global indicated resolution of 3.2 Å (Fig. 4, Extended Data Figs. 2, 8, Extended Data Table 1).

The structure of the $\mathrm{GABA_{B1}}$ homodimer shows that both of the VFTs are liganded, and that the monomers assume a roughly two-fold symmetric arrangement. The individual lobes of each VFT are in an open conformation, and are superimposable with the $\mathrm{GABA_{B1}}$ subunit VFT in the inactive heterodimer (Fig. 4b). Despite the conformation of the individual protomers, the VFT homodimer adopts the same overall conformation as the crystal structure of agonist-bound $\mathrm{GABA_B}$ VFT (Protein Data Bank (PDB) code 4MS4)[12], owing to an almost-identical upper lobe interaction interface (Fig. 4b). Correspondingly, the lower lobes of the receptor are brought into proximity and the receptor adopts a more-compact state that shortens the distance between the VFTs and the 7TMs (Fig. 4). Compared to the heterodimer, the 7TMs in the $\mathrm{GABA_{B1}}$ homodimer are rotated to form a TM6–TM6 interface (Fig. 4c). This is consistent with previous cross-linking experiments that identified a TM6–TM6 interaction upon agonist-induced stimulation of the heterodimer[33], and agrees with structural rearrangements of mGlu5 upon stimulation with agonist[14] (Fig. 4d). Furthermore, the relative arrangement of the VFT and transmembrane regions are notably similar to those of the activated state of near-full-length mGlu5[14] (Extended Data Fig. 8). Thus, the conformation observed in the $\mathrm{GABA_{B1}}$ homodimer may provide valuable hints into the architecture of the active-state $\mathrm{GABA_B}$ receptor (Fig. 4). Previous $\mathrm{GABA_B}$ chimaera studies have shown that replacement of one of the 7TMs of the $\mathrm{GABA_{B1}}$ homodimer with that of the $\mathrm{GABA_{B2}}$ receptor (thus enabling G-protein coupling) produces a constitutively active receptor that is not additionally stimulated by GABA[34,35]. Hence, the relative positioning of the VFT—as observed in the structure of the $\mathrm{GABA_{B1}}$ homodimer—appears to be sufficient to stabilize an active conformation, presumably through the linkage of VFT to 7TM to reorient the helical interface. Because $\mathrm{GABA_{B1}}$ in the homodimer is bound to an inverse agonist, the adoption of an ‘active-like’ global conformation of the VFT must be irrespective of the ligand, probably owing to differences in the interaction interface of the VFT N-terminal lobes in comparison to the same interface in the heterodimer.

Collectively, our structures, cellular signalling assays and atomistic simulations provide crucial insights into mechanistic aspects of $\mathrm{GABA_B}$ signalling. The extended ECL2 and its interaction with the linker region appears to compensate for the lack of a cysteine-rich domain in

GABA$_B$ compared to all other family C receptors, and thus also transduce conformational changes from the VFT to the 7TM regions. The phospholipid that occupies the 7TM core is important for the integrity of the transmembrane domains in both subunits of GABA$_B$, while also structurally coordinating the critical ECL2 region. Our findings support a model in which agonist binding to GABA$_{B1}$ results in VFT dimer compaction that reorients the protomers via the linker–ECL2. Such a conformational change would drive the 7TMs to twist away from an auto-inhibited state mediated by the inactive TM3–TM5 interface, thereby forming a new TM6 helical interface. Although currently unclear, the activating transitions within the GABA$_{B2}$ 7TM are probably mediated both through the newly formed TM6–TM6 interface and propagation through its own ECL2, as supported by our functional assays. An intriguing possibility is that the phospholipid may act as a sensor of changes in VFT and ECL2 conformations that would result in activating transitions within the 7TM of GABA$_{B2}$ to prime it for G-protein engagement. Addressing these questions will require detailed structural studies of the active-state heterodimer alone, and in complex with a G protein engaging the receptor core. The present work—along with recent studies on mGlu5—forms a starting structural framework for deciphering the signal transduction mechanism of GABA$_B$ and family C GPCRs in the context of full-length receptors.

Online content

Any methods, additional references, Nature Research reporting summaries, source data, extended data, supplementary information, acknowledgements, peer review information; details of author contributions and competing interests; and statements of data and code availability are available at https://doi.org/10.1038/s41586-020-2469-4.

1. Bettler, B., Kaupmann, K., Mosbacher, J. & Gassmann, M. Molecular structure and physiological functions of GABA$_B$ receptors. *Physiol. Rev*. **84**, 835–867 (2004).
2. Mannoury la Cour, C., Herbelles, C., Pasteau, V., de Nanteuil, G. & Millan, M. J. Influence of positive allosteric modulators on GABA$_B$ receptor coupling in rat brain: a scintillation proximity assay characterisation of G protein subtypes. *J. Neurochem*. **105**, 308–323 (2008).
3. Franek, M. et al. The heteromeric GABA-B receptor recognizes G-protein α subunit C-termini. *Neuropharmacology* **38**, 1657–1666 (1999).
4. Robbins, M. J. et al. GABA$_{B2}$ is essential for G-protein coupling of the GABA$_B$ receptor heterodimer. *J. Neurosci*. **21**, 8043–8052 (2001).
5. Galvez, T. et al. Mutagenesis and modeling of the GABA$_B$ receptor extracellular domain support a Venus flytrap mechanism for ligand binding. *J. Biol. Chem*. **274**, 13362–13369 (1999).
6. Hepler, J. R. & Gilman, A. G. G proteins. *Trends Biochem. Sci*. **17**, 383–387 (1992).
7. Enna, S. J. GABAB receptor agonists and antagonists: pharmacological properties and therapeutic possibilities. *Expert Opin. Investig. Drugs* **6**, 1319–1325 (1997).
8. Malcangio, M. GABA$_B$ receptors and pain. *Neuropharmacology* **136** (Pt A), 102–105 (2018).
9. Pin, J. P., Galvez, T. & Prézeau, L. Evolution, structure, and activation mechanism of family 3/C G-protein-coupled receptors. *Pharmacol. Ther*. **98**, 325–354 (2003).
10. Bräuner-Osborne, H., Wellendorph, P. & Jensen, A. A. Structure, pharmacology and therapeutic prospects of family C G-protein coupled receptors. *Curr. Drug Targets* **8**, 169–184 (2007).
11. Chun, L., Zhang, W. H. & Liu, J. F. Structure and ligand recognition of class C GPCRs. *Acta Pharmacol. Sin*. **33**, 312–323 (2012).
12. Geng, Y., Bush, M., Mosyak, L., Wang, F. & Fan, Q. R. Structural mechanism of ligand activation in human GABA$_B$ receptor. *Nature* **504**, 254–259 (2013).
13. Geng, Y. et al. Structural mechanism of ligand activation in human calcium-sensing receptor. *eLife* **5**, e13662 (2016).
14. Koehl, A. et al. Structural insights into the activation of metabotropic glutamate receptors. *Nature* **566**, 79–84 (2019).
15. Margeta-Mitrovic, M., Jan, Y. N. & Jan, L. Y. A trafficking checkpoint controls GABA$_B$ receptor heterodimerization. *Neuron* **27**, 97–106 (2000).
16. Mukherjee, R. S., McBride, E. W., Beinborn, M., Dunlap, K. & Kopin, A. S. Point mutations in either subunit of the GABA$_B$ receptor confer constitutive activity to the heterodimer. *Mol. Pharmacol*. **70**, 1406–1413 (2006).
17. Robertson, M. J., van Zundert, G. C. P., Borrelli, K. & Skiniotis, G. GemSpot: a pipeline for robust modeling of ligands into cryo-EM maps. *Structure* **28**, 707–716 (2020).
18. Conklin, B. R., Farfel, Z., Lustig, K. D., Julius, D. & Bourne, H. R. Substitution of three amino acids switches receptor specificity of G$_q$α to that of G$_i$α. *Nature* **363**, 274–276 (1993).
19. Trinquet, E. et al. D-*myo*-Inositol 1-phosphate as a surrogate of D-*myo*-inositol 1,4,5-tris phosphate to monitor G protein-coupled receptor activation. *Anal. Biochem*. **358**, 126–135 (2006).
20. Liu, J. et al. Molecular determinants involved in the allosteric control of agonist affinity in the GABA$_B$ receptor by the GABA$_{B2}$ subunit. *J. Biol. Chem*. **279**, 15824–15830 (2004).
21. Audet, M. & Stevens, R. C. Emerging structural biology of lipid G protein-coupled receptors. *Prot. Sci*. **28**, 292–304 (2019).
22. Doré, A. S. et al. Structure of class C GPCR metabotropic glutamate receptor 5 transmembrane domain. *Nature* **511**, 557–562 (2014).
23. Frangaj, A. & Fan, Q. R. Structural biology of GABA$_B$ receptor. *Neuropharmacology* **136** (Pt A), 68–79 (2018).
24. Gasparini, F. & Spooren, W. Allosteric modulators for mGlu receptors. *Curr. Neuropharmacol*. **5**, 187–194 (2007).
25. Pagano, A. et al. C-terminal interaction is essential for surface trafficking but not for heteromeric assembly of GABA$_B$ receptors. *J. Neurosci*. **21**, 1189–1202 (2001).
26. Balasubramanian, S., Teissére, J. A., Raju, D. V. & Hall, R. A. Hetero-oligomerization between GABA$_A$ and GABA$_B$ receptors regulates GABA$_B$ receptor trafficking. *J. Biol. Chem*. **279**, 18840–18850 (2004).
27. Hyland, N. P. & Cryan, J. F. A gut feeling about GABA: focus on GABA$_B$ receptors. *Front. Pharmacol*. **1**, 124 (2010).
28. Ng, T. K. & Yung, K. K. Differential expression of GABA$_B$R1 and GABA$_B$R2 receptor immunoreactivity in neurochemically identified neurons of the rat neostriatum. *J. Comp. Neurol*. **433**, 458–470 (2001).
29. Burman, K. J. et al. GABA$_B$ receptor subunits, R1 and R2, in brainstem catecholamine and serotonin neurons. *Brain Res*. **970**, 35–46 (2003).
30. Calver, A. R. et al. The expression of GABA$_{B1}$ and GABA$_{B2}$ receptor subunits in the cNS differs from that in peripheral tissues. *Neuroscience* **100**, 155–170 (2000).
31. Gassmann, M. et al. Redistribution of GABA$_{B}$(1) protein and atypical GABA$_B$ responses in GABA$_{B(2)}$-deficient mice. *J. Neurosci*. **24**, 6086–6097 (2004).
32. Margeta-Mitrovic, M., Jan, Y. N. & Jan, L. Y. Ligand-induced signal transduction within heterodimeric GABA$_B$ receptor. *Proc. Natl Acad. Sci. USA* **98**, 14643–14648 (2001).
33. Xue, L. et al. Rearrangement of the transmembrane domain interfaces associated with the activation of a GPCR hetero-oligomer. *Nat. Commun*. **10**, 2765 (2019).
34. Binet, V. et al. The heptahelical domain of GABA$_{B2}$ is activated directly by CGP7930, a positive allosteric modulator of the GABA$_B$ receptor. *J. Biol. Chem*. **279**, 29085–29091 (2004).
35. Galvez, T. et al. Allosteric interactions between GB1 and GB2 subunits are required for optimal GABA$_B$ receptor function. *EMBO J*. **20**, 2152–2159 (2001).

Methods

No statistical methods were used to predetermine sample size. The experiments were not randomized and investigators were not blinded to allocation during experiments and outcome assessment.

Cloning

The cDNA clone for human GABA$_{B2}$ receptor (accession NM_005458) in pcDNA3.1$^+$ was obtained from the cDNA Resource Center (www.cdna.org); and the cDNA clone for human GABA$_{B1b}$ was purchased from Horizon Discovery (accession BC050532, clone ID 5732186). Primers were designed to include a haemagglutinin (HA) signal sequence[36] in the place of authentic signal sequences of each receptor, thus removing the first 29 residues of GABA$_{B1}$ and 41 residues of GABA$_{B2}$. Both the authentic signal sequence and the HA sequence are cleaved during processing; therefore, the substitution does not result in a change of sequence in the mature receptor. For purification of receptors for cryo-EM studies, GABA$_B$ constructs were subcloned into the pFastBacDual vector (Invitrogen) with N-terminal Flag epitope (DYKDDDD) following the HA signal sequence and/or C-terminal hexa-histidine (His6) tags, so that the following constructs were produced: HA–Flag–GABA$_{B1}$(30–844)–His6, HA–GABA$_{B1}$(30–844)–His6 and HA–Flag–GABA$_{B2}$(41–941). For signalling assays, the HA–Flag–GABA$_{B1}$(30–844)–His6 and a HA–HA–GABA$_{B2}$(41–941)-construct (in which the Flag tag was replaced by the HA epitope tag YPYDVPDYA) were subcloned into pcDNA3.1(+). The primers (Integrated DNA Technologies) used to subclone GABA$_B$ included: EcoRI-HA-Flag-GABA$_{B1}$, 5′-GCGCGCGAATTCATGAAGACGATCATC GCCCTGAGCTACATCTTCTGCCTGGTGTTCGCCGATTACAAGGACGACGATGACAAGTCCACTCCCCCCATCTCCCG-3′; GABA$_{B1}$-His6-SalI, 5′-GCGCGCGTCGACTTAATGATGATGATGATGGTGCTTATAAAGCAAATGCAC-3′; GABA$_{B1}$-SalI 5′- GCGCGCGTCGACTTACTT ATAAAGCAAATGCAC-3′; EcoRI-HA-FLAG-GABA$_{B2}$, 5′-GCGCGCGAATTCATGAAGACGATCATCGCCCTGAGCTACATCTTCTGCCTGGTGTTCGCCGATTACAAGGACGACGATGACAAGTGGGCGCGGGGCGCCCCC-3′; GABA$_{B2}$-His6-SalI, 5′-GCGCGCGTCGACTTAATGATGATGATGATGGTGCAGGCCCGAGACCATGAC-3′; and GABA$_{B2}$-SalI, 5′- GCGCGCGTCGACTTACAGGCCCGAGACCATGAC-3′. To generate GABA$_B$ mutants, PCR reactions were conducted with either PfuTurbo or Q5 polymerase using the following pairs of primers and pcDNA3.1$^+$neo containing either HA–Flag–GABA$_{B1b}$ or HA–HA–GABA$_{B2}$: GABA$_{B1b}$(H572A), 5′-GGTGGGTCGCCACGGTCTTC-3′ and 5′-GAAGACCGTGGCGACCCACC-3′; GABA$_{B1b}$(E673A), 5′- CTTGCTTATGCTACCAAGAG-3′ and 5′-CTCTTGGTAGCATAAGCAAG-3′; GABA$_{B2}$(H579A), 5′-CTGGAGAGTCGCTGCCATCTTCAA-3′ and 5′- TTGAAGATGGCAGCGACTCTCCAG-3′; GABA$_{B2}$(E677A), 5′- CTTAGCTTGGGCTACCCGCAAC-3′ and 5′- GTTGCGGGTAGCCCAAGCTAAG-3′; GABA$_{B1}$(Δ627–634), 5′- CTTGGCAAATGTCTCAATGGTC-3′ and 5′-GTCTCTATTCTGCCCCAGC-3′; GABA$_{B2}$(Δ631–638), 5′-ATCTCCATCCGCCCTCTCC-3′ and 5′-CATGCTGTACTTCTCCACTG-3′; GABA$_{B1}$(R549A), 5′- CTGCCAGGCCGCCCTCTGGCTCCTG-3′ and 5′-ACGAAAGGGAACTGG-3′; GABA$_{B2}$(R556A), 5′- GCACCGTCGCTACCTGGATTCTC-3′ and 5′- AAAGTGTTTCAAAGG-3′; GABA$_{B1}$(L553W), 5′- CTCTGGCTCTGGGGCCTGGGCTTTAG-3′ and 5′-GCGGGCCTGGCAGACG-3′; GABA$_{B2}$(L560W), 5′-GGACCTGGATTTGGACCGTGGGCTAC-3′ and 5′-TGACGGTGCAAAGTG-3′.

Expression and purification

Sf9 insect cells (Expression Systems) were coinfected at a density of about 2.0×10^6 cells/ml with HA-Flag-GABA$_{B2}$ baculovirus and either HA-Flag-GABA$_{B1b}$-His6 or HA-GABA$_{B1b}$-His6 baculovirus at a multiplicity of infection between 3.0 and 5.0. During expression, cells were treated with 5 μM CGP55845 (Hello Bio). At 48 h post-infection, cells were collected by centrifugation, washed once with phosphate-buffered saline containing protease inhibitors (leupeptin, soybean trypsin inhibitor, *N-p*-tosyl-L-phenylalanine chloromethyl ketone, tosyl-L-lysyl-chloromethane hydrochloride, phenylmethylsulfonyl fluoride, aprotinin, bestatin and pepstatin) and 5 μM CGP55845. Cell lysis was achieved through nitrogen cavitation in buffer containing 20 mM HEPES, pH 7.5, 150 mM NaCl, 1 mM EDTA, 10 μM CGP55845, 2 mM MgCl$_2$, nuclease and protease inhibitors. The whole-cell lysate was centrifuged at 1,000*g* to remove nuclei and unbroken cells. The supernatant was centrifuged at 100,000*g* to isolate the membrane fraction. Membranes were resuspended by Dounce homogenization in buffer containing 20 mM HEPES, pH 7.5, 150 mM NaCl, 2 mM MgCl$_2$, 1 mM EDTA, 2 mg/ml iodoacetamide, 10 μM CGP55845, 1% *n*-dodecyl β-D-maltoside (DDM), 0.2% sodium cholate, 0.2% cholesterol hemisuccinate (CHS), nuclease and protease inhibitors. Solubilized membranes were clarified by centrifugation at 100,000*g*, and the supernatant was loaded onto a pre-equilibrated column of anti-DYKDDDDK G1 affinity resin (Genscript). The resin was washed with buffer A (20 mM HEPES, pH7.5, 150 mM NaCl, 10 μM CGP55845 and protease inhibitors) with 0.1% DDM and 0.02% CHS. Protein was eluted with buffer A containing 0.1% DDM, 0.02% CHS and 0.2 mg/ml DYKDDDDK peptide. The eluate was then loaded onto a pre-equilibrated Nickel-NTA column. Resin was washed with buffer A containing 0.1% DDM and 0.02% CHS; and the buffer was exchanged in six steps to buffer A supplemented with 0.2% GDN, 0.02% CHS, followed by a two-step exchange into buffer A containing 0.004% GDN and 0.0004% CHS. Protein was eluted from the Ni-NTA resin with buffer A containing 0.004% GDN, 0.0004% CHS and 500 mM imidazole. The resulting eluate was concentrated by centrifugal filtration with a 50-kDa molecular-weight cut off, and subsequently run on a Superose 6 size-exclusion column (GE Healthcare). Samples were pre-screened for sample quality by negative-stain transmission electron microscopy and then immediately prepared on cryo-EM grids.

Cryo-EM data collection

For the GABA$_{B1b}$–GABA$_{B2}$ heterodimer, 3.5 μl of sample was applied at a concentration of 3–5 mg/ml to glow-discharged holey carbon grids (Quantifoil R1.2/1.3). The grids were blotted using an FEI Vitrobot Mark IV (Thermo Fisher Scientific) at 18 °C and 100% humidity, and plunge-frozen into liquid ethane. Two datasets were used to produce the final structure. For both data collections, cryo-EM imaging was performed on a Titan Krios (Thermo Fisher Scientific) electron microscope equipped with a K3 Summit direct electron detector (Gatan). The microscope was operated at 300 kV accelerating voltage, at a magnification of 57,050× in counting mode resulting in a magnified pixel size of 0.8521 Å. For the first dataset, movies were obtained at an exposure rate of 14.19 electrons per Å^2 per s with defocus ranging from −1.5 to −2.7 μm. The total exposure time was 3.985 s over 57 frames per movie stack. For the second dataset, movies were obtained at an exposure rate of 21.43 electrons per Å^2 per s with defocus ranging from −1.2 to −2.5 μm. The total exposure time was 2.996 s including 50 frames per movie stack.

Cryo-EM grids for the GABA$_{B1b}$ homodimer at a concentration 5.0 mg/ml were prepared similarly to the heterodimer. Cryo-EM imaging was performed on a Titan Krios electron microscope equipped with a post-column energy filter and a K2 Summit direct electron detector (Gatan). The microscope was operated at 300 kV accelerating voltage, at a magnification of 47,198× in counting mode, resulting in a pixel size of 1.06 Å. Movies were obtained at an exposure rate of 6.212 electrons per Å^2 per s with defocus ranging from −0.9 to −2.5 μm. The total exposure time was 8.0 s over 40 frames per movie stack. Automatic data acquisition was performed using SerialEM[37] for all datasets.

Image processing and 3D reconstructions

Dose-fractionated image stacks were subjected to beam-induced motion correction and dose-weighting using MotionCor2[38]. Contrast transfer function (CTF) parameters for each non-dose weighted micrograph were determined by Gctf[39] for the homodimer and dataset 1 of the heterodimer, and by CTFFIND-4.1[40] for dataset 2 of the heterodimer. For all datasets, particle selection, 2D and 3D classification were performed on a binned dataset (pixel size 1.72 Å and 4.24 Å for the heterodimer and homodimer, respectively) using RELION (versions 3.0 and 3.1)[41]. The two datasets for the heterodimer were processed individually before being combined following a Bayesian polishing step. A total of 538,957 particles from 1,324 micrographs and 2,062,083 particles from 8,991 micrographs were extracted using semi-automated particle selection for the heterodimer datasets 1 and 2, respectively. Both particle sets were then separately subjected to three rounds of 2D classification and two rounds of 3D classification. Particles in both sets were subjected to Bayesian polishing individually and then combined for a total of 286,140 particles. The merged dataset was fit for CTF parameters (per particle defocus and astigmatism, per micrograph *B*-factor) and estimated for anisotropic magnification and beam-tilt. A final 3D refinement was followed by post-processing using a mask that excluded the GDN micelle density. A focused refinement was also carried out using a mask encompassing the VFT and linker regions of GABA$_B$. For the GABA$_{B1b}$ homodimer structure, a total of 2,278,113 particles were extracted from 5,602 micrographs using semi-automated particle selection. Particles were subjected to multiple rounds of 2D and 3D classification, until a subset of 282,811particles was selected for the final map. The particle set underwent multiple rounds of CTF parameter fitting and was subjected to Bayesian polishing before 3D refinement and post-processing of the final map. UCSF Chimera[42] was used for map and model visualization.

Model building

The initial model for the VFT was taken from the inactive-state VFT crystal structure (PDB 4MR7[12]) and the initial structure of the transmembrane domain of GABA$_{B1b}$ was generated as a homology model from the inactive cryo-EM structure of mGlu5 (PDB 6N52[14]) (38% sequence similarity to GABA$_{B1}$) using Schrödinger's Prime homology modelling[43]. Both components were placed into the GABA$_B$ cryo-EM map using 'fit-in-map' function of Chimera. The linker, intracellular loops and extracellular loops of GABA$_{B1}$ were interactively adjusted into the electron microscopy map using Coot (version 0.8.9.1el)[44] and the resulting model of the GABA$_B$ linker–7TM was then used to generate a homology model of GABA$_{B2}$ using Schrodinger's Prime homology modelling, which was also placed into the map in Chimera. Iterative rounds of interactive model adjustment in Coot followed by real-space refinement in Phenix (version 1.17.1-3660)[45], using secondary structure restraints in addition to the default restraints, were performed to improve the modelling. The resulting structure of GABA$_{B1}$ was sufficiently different to the original homology model such that that the root mean square deviation (r.m.s.d.) between the homology model and the final model is non-trivial (about 2.0 Å in the transmembrane helices alone). Once confidence in the side-chain placement was reached for the ligand-binding cleft on GABA$_{B1}$, the GemSpot pipeline[17] was used to model the inhibitor, CGP55845, into the map. After further improvement, 1-palmitoyl-2-oleoyl-*sn*-glycero-3-phosphoethanolamine (POPE) was modelled in the transmembrane pocket of GABA$_{B1}$ and GABA$_{B2}$ with GemSpot. Final model refinement was performed with Phenix[45].

Molecular dynamics simulations and analysis

To prepare the system for molecular dynamics simulations, the low-resolution features of the map were used to manually build intracellular loop 2 (ICL2) into the model of the GABA$_{B1}$–GABA$_{B2}$ inactive heterodimer using Coot. The system was then prepared in Maestro, version 2019-4 (Schrödinger) to build any stubbed side chains and determine protonation states. The VFTs were removed from the heterodimer to produce a truncated construct starting at residues T461 for GABA$_{B1b}$ and T468 for GABA$_{B2}$, thus containing only the linkers and the transmembrane domains. The Orientations of Proteins in Membranes (OPM)[46] webserver was used to orient the system with respect to a membrane plane and the CHARMM-GUI[47] was used to generate a PDB file of the system in either a 1-palmitoyl-2-oleoyl-*sn*-glycero-3 -phosphocholine (POPC) and cholesterol bilayer or a 3:1 POPC:POPE and cholesterol bilayer. Approximate dimensions for the system were 105 × 105 × 110 Å for a total of 240 lipid and 7 cholesterol molecules. This bilayer was then solvated in TIP3P water with 150 mM sodium chloride ions balanced to achieve charge neutrality. The salt concentration of 150 mM is consistent with the conditions at which the receptor was purified. POPE was used for the lipid in the transmembrane binding sites of GABA$_{B1}$ and GABA$_{B2}$.

The PDB file for the full solvated system was prepared in VMD (version 1.9.3)[48] for simulation in NAMD (version 2.13)[49] to produce a protein structure file (psf). The OPLS-AA/M[50] force field was used for the protein, and OPLS-AA[50] was used for the lipids, cholesterol and ions. Disulfide bonds were placed between C546 and C644 in GABA$_{B1}$ and C553 and C648 in GABA$_{B2}$ and both the N and C termini were blocked with capping groups, acetylated N termini and N-methylamide C termini. NAMD was used to run molecular dynamics simulations, in which all phases used periodic boundary conditions with nonbonded interactions smoothed starting at 10 Å to 12 Å, with long-range interactions treated with the particle mesh Ewald method. Systems were minimized for 2,000 steps and then slowly heated in the NPT ensemble with a Langevin thermostat and a Nosé–Hoover Langevin piston barostat set at 1 atm with a period of 50 fs and a decay of 25 fs. A 2-fs time-step was used with the SHAKE[51] and SETTLE[52] algorithms. Heating occurred from 0 to 310 K in increments of 20 K with 0.4 ns of simulation at each increment. Harmonic restraints of 1 kcal per mol per Å^2 were used during heating on all non-hydrogen atoms of the protein and lipids. The system was then equilibrated with 1 kcal per mol per Å^2 harmonic restraints on all protein and lipid non-hydrogen atoms for 10 ns followed by another 10 ns of equilibration with 1 kcal per mol per Å^2 harmonic restraints on non-hydrogen backbone atoms. Finally, 1 kcal per mol per Å^2 harmonic restraints were applied to only Cα atoms for 2 ns before being stepped down to 0.5 kcal per mol per Å^2 for 2 ns, 0.3 kcal per mol per Å^2 for 2 ns, and then removed. The first 30 ns of unrestrained molecular dynamics were also discarded as equilibration.

All trajectories were downsampled by 10× for analysis. Cavity volume was calculated with Epock (1.0.5)[53] in VMD[48] on trajectories that had been aligned to either GABA$_{B1}$ or GABA$_{B2}$ from the starting structure. The cavity region was defined to include the binding region of the hydrophobic tails of the lipid. Transmembrane–transmembrane distances were calculated in VMD based on the Cα position of residues: 3.33, 4.50, 5.40, 6.54, and 7.28 in the Ballesteros–Weinstein[54] numbering scheme.

Transfection and seeding of cells for signalling assays

HEK293 cells (ATCC CRL-1573) were transfected with expression vector DNAs encoding the two GABA$_B$ receptor protomers and a chimeric G$\alpha_{q/o5}$ subunit (five C-terminal amino acids of Gα_q were exchanged with those of Gα_o) to allow the G$\alpha_{i/o}$-coupled GABA$_B$ receptor to activate PLC and induce IP$_3$ and intracellular Ca^{2+} release[3]. Before transfection, cells were brought into suspension by trypsinization and resuspension to 0.18 million cells per ml in growth medium (D-MEM, Gibco 10566016; supplemented with 10% fetal bovine serum, Gibco 10270106; 1% sodium pyruvate, Gibco 11360039; 1% MEM non-essential amino acids, Gibco 11140068; and 1% penicillin–streptomycin Solution, Gibco 15140122).

For each 1 ml of cell suspension transfected, a total of 1 μg DNA in 25 μl OptiMEM (Gibco 51985) was incubated for 20 min with a mixture of 57 μl OptiMEM and 3 μl FuGene6 (Promega E2692). After FuGene6–DNA complex formation, the mixture was added directly to the cell suspension, mixed thoroughly and cells seeded with 100 μl cell suspension in appropriate 96-well plates. Of the 1 μg DNA per ml cell suspension, the amount of expression vector DNA encoding the chimeric G$\alpha_{q/o5}$ was 0.5 μg/ml cell suspension in all experiments. The amount of GABA$_B$ encoding DNA was varied between 7.8 ng and 0.25 μg for each of the GABA$_B$-receptor protomer DNAs depending on the assay and mutants tested. Empty vector DNA was added to give a total amount of 1 μg DNA per ml cell suspension transfected. For characterization of basal activity of the TM3 and TM5 protomer mutants, a typical gene dose experiment was performed. DNA corresponding to 62.5 ng DNA per ml cell suspension of each of the protomers (wild type or mutants) were mixed and serially diluted twofold 5 times, typically down to 3.9 ng DNA per ml cell suspension. The transfected cell suspension was seeded at 100 µg/ml both in clear poly-L-lysine coated 96-well plates for IP_1 accumulation assays and in white poly-L-lysine coated 96-well plates for cell-surface enzyme-linked immunosorbent assay (ELISA) assays.

IP_1 accumulation assays

The IP_1 assays for wild-type and mutant receptors were performed essentially as previously described[14]. Forty-eight hours after transfection, the growth medium was replaced with HBSS buffer (HBSS (Gibco 14025), 20 mM HEPES pH 7.5, 1 mM $CaCl_2$, 1 mM $MgCl_2$ and 0.1% BSA) supplemented with BSA to 0.5% and incubated at 37 °C for 3–4 h.

For characterization of the TM3–TM5 protomer-interface mutants for basal activity, the HBSS + 0.5% BSA buffer was replaced with 100 µl HBSS buffer, followed by addition of 50 µl HBSS buffer containing LiCl (150 mM) to give a final concentration of 50 mM LiCl. After incubation for 1 h at 37 °C the IP_1 accumulation was stopped by addition of 40 µl CisBio IP-One Tb HTRF Kit (CisBio, 62IPAPEC) lysis buffer. The accumulated IP_1 levels were determined according to the manufacturer's instructions and as previously described[14].

For the generation of GABA concentration–response curves, the compounds were diluted in three times the final concentration in HBSS buffer containing 60 mM LiCl. The assay was started, first by replacing the HBSS + 0.5% BSA buffer with 100 µl HBSS buffer, followed by addition of 50 µl of the above compound dilutions to give a final LiCl concentration of 20 mM. The IP_1 accumulation assay was stopped and assayed as described above after incubation for 1 h at 37 °C. Data were calculated as the amount of IP_1 formed per well or normalized to the basal IP_1 level, and fitted by nonlinear regression using GraphPad Prism. Results and description of statistical analyses used in this Article can be found in Supplementary Table 1.

Cell-surface ELISA assay

Surface expression levels of wild-type and mutant $GABA_B$ receptors were determined using a direct ELISA against the N-terminal $GABA_{B1b}$ Flag tag and the N-terminal $GABA_{B2}$ HA tag, as previously described[55]. Transfected cells were seeded in white poly-D-lysine-coated 96-well plates. Forty-eight hours after transfection, cells were washed once with 100 µl per well DPBS + 1 mM $CaCl_2$ (wash buffer). Following fixation with 50 µl per well 4% paraformaldehyde solution for 5 min at room temperature, cells were washed twice with 100 µl wash buffer and blocked with 100 µl per well blocking solution (3% dry milk, 1 mM $CaCl_2$, 50 mM Tris-HCl, pH 7.5) for 30 min at room temperature, followed by addition of 75 µl per well HRP-conjugated anti-Flag antibody (Sigma Aldrich, A8592), or HRP-conjugated anti-HA antibody (R&D systems HAM0601), both diluted 1:2,000 in blocking solution, and allowed to incubate for 1 h at room temperature. The plates were then washed four times with 100 µl per well blocking solution followed by four washes with wash buffer. The amount of surface-expressed receptors was detected by adding 60 µl wash buffer and 20 µl HRP substrate (Bio-Rad, 170-5060) per well, incubating for 10 min and measuring of luminescence in an EnVision plate reader (Perkin Elmer).

Statistics and reproducibility

Detailed results and description of statistical analyses used in this Article can be found in Supplementary Table 1. Data and error bars in Figs. 1c, d are mean ± s.e.m. from at least five independent experiments. In Fig. 1c, data of co-expressed wild-type $GABA_{B1}$ (6.3 ng) with wild-type $GABA_{B2}$ (6.3 ng), wild-type $GABA_{B1}$ (3.1 ng) with wild-type $GABA_{B2}$ (3.1 ng), and wild-type $GABA_{B1}$ (1.6 ng) with wild-type $GABA_{B2}$ (1.6 ng) represent $n = 7$ independent experiments; data of co-expressed wild-type $GABA_{B1}$ (0.8 ng) with wild-type $GABA_{B2}$ (0.8 ng), solely expressed wild-type $GABA_{B1}$ (6.3 ng), solely expressed wild-type $GABA_{B2}$ (3.1 ng), and untransfected HEK293 cells represent $n = 6$ independent experiments. In Fig. 1d, data of co-expressed $GABA_{B1}$(Δ627–634) with wild-type $GABA_{B2}$, and wild-type $GABA_{B1}$ with $GABA_{B2}$(Δ631–638) represent $n = 7$ independent experiments; and co-expressed $GABA_{B1}$(Δ627–634) with $GABA_{B2}$(Δ631–638) represent $n = 5$ independent experiments. Data in Fig. 2d are representative of one experiment performed in triplicate and repeated independently at least three times with similar results ($n = 3$), data points and error bars are mean ± s.e.m. Data in Fig. 2e are mean ± s.e.m. from at least three independent experiments; data for co-expressed $GABA_{B1}$(H572A/E673A) with wild-type $GABA_{B2}$, and wild-type $GABA_{B1}$with $GABA_{B2}$(H579A/E677A) represent $n = 3$ independent experiments; and data for wild-type $GABA_{B1}$ with wild-type $GABA_{B2}$ represent $n = 7$ independent experiments. Data in Fig. 3d are mean ± s.e.m. from at least four independent experiments; co-expressed $GABA_{B1}$(L553W) with $GABA_{B2}$(L560W) represent $n = 5$ independent experiments, and $GABA_{B1}$(R549A) with $GABA_{B2}$(R556A) represent $n = 4$ independent experiments, and data for wild-type $GABA_{B1}$ with wild-type $GABA_{B2}$ represent $n = 7$ independent experiments. Ensemble data in Fig. 3e represent distribution over a 200-ns time course, for 5 simulations per condition; each violin represents $n = 37{,}500$ time points.

External computational resource use

The Extreme Science and Engineering Discovery Environment (XSEDE)[56] resource comet-gpu through sdsc-comet allocation TG-MCB190153 was used in preparation of this Article.

Reporting summary

Further information on research design is available in the Nature Research Reporting Summary linked to this paper.

Data availability

All data generated or analysed during this study are included in the Article and its Supplementary Information. Cryo-EM maps of $GABA_B$ heterodimer and $GABA_{B1b}$ homodimer have been deposited in the Electron Microscopy Data Bank under accession codes EMD-21533 and EMD-21534, respectively. The atomic coordinates of $GABA_B$ heterodimer and $GABA_{B1b}$ homodimer have been deposited in the Protein Data Bank under the accession codes 6W2X and 6W2Y, respectively.

36. Guan, X. M., Kobilka, T. S. & Kobilka, B. K. Enhancement of membrane insertion and function in a type IIIb membrane protein following introduction of a cleavable signal peptide. *J. Biol. Chem*. **267**, 21995–21998 (1992).
37. Mastronarde, D. N. Automated electron microscope tomography using robust prediction of specimen movements. *J. Struct. Biol*. **152**, 36–51 (2005).
38. Zheng, S. Q. et al. MotionCor2: anisotropic correction of beam-induced motion for improved cryo-electron microscopy. *Nat. Methods* **14**, 331–332 (2017).
39. Zhang, K. Gctf: real-time CTF determination and correction. *J. Struct. Biol*. **193**, 1–12 (2016).
40. Rohou, A. & Grigorieff, N. CTFFIND4: fast and accurate defocus estimation from electron micrographs. *J. Struct. Biol*. **192**, 216–221 (2015).
41. Zivanov, J. et al. New tools for automated high-resolution cryo-EM structure determination in RELION-3. *eLife* **7**, e42166 (2018).
42. Pettersen, E. F. et al. UCSF Chimera—a visualization system for exploratory research and analysis. *J. Comput. Chem*. **25**, 1605–1612 (2004).
43. Jacobson, M. P. et al. On the role of the crystal environment in determining protein side-chain conformations. *J. Mol. Biol*. **320** (3), 597–608 (2002).
44. Emsley, P., Lohkamp, B., Scott, W. G. & Cowtan, K. Features and development of Coot. *Acta Crystallogr. D* **66**, 486–501 (2010).
45. Liebschner, D. et al. Macromolecular structure determination using X-rays, neutrons and electrons: recent developments in Phenix. *Acta Crystallogr. D* **75**, 861–877 (2019).
46. Lomize, M. A., Pogozheva, I. D., Joo, H., Mosberg, H. I. & Lomize, A. L. OPM database and PPM web server: resources for positioning of proteins in membranes. *Nucleic Acids Res*. **40**, D370–D376 (2012).
47. Jo, S., Kim, T., Iyer, V. G. & Im, W. CHARMM-GUI: a web-based graphical user interface for CHARMM. *J. Comput. Chem*. **29**, 1859–1865 (2008).
48. Humphrey, W., Dalke, A. & Schulten, K. VMD: visual molecular dynamics. *J. Mol. Graph*. **14**, 33–38 (1996).
49. Phillips, J. C. et al. Scalable molecular dynamics with NAMD. *J. Comput. Chem*. **26**, 1781–1802 (2005).
50. Robertson, M. J., Tirado-Rives, J. & Jorgensen, W. L. Improved peptide and protein torsional energetics with the OPLSAA force field. *J. Chem. Theory Comput*. **11**, 3499–3509 (2015).

51. Ryckaert, J.-P., Ciccotti, G. & Berendsen, H. J. C. Numerical integration of the cartesian equations of motion of a system with constraints: molecular dynamics of *n*-alkanes. *J. Comput. Phys.* **23**, 327–341 (1977).
52. Miyamoto, S. & Kollman, P. A. Settle – an analytical version of the shake and rattle algorithm for rigid water models. *J. Comput. Chem.* **13**, 952–962 (1992).
53. Laurent, B. et al. Epock: rapid analysis of protein pocket dynamics. *Bioinformatics* **31**, 1478–1480 (2015).
54. Ballesteros, J. A. & Weinstein, H. in *Methods in Neurosciences* **vol. 25** (ed. Sealfon, S. C.) 366–428 (Academic, 1995).
55. Hilger, D. et al. Structural insights into ligand efficacy and activation of the glucagon receptor. Preprint at https://www.biorxiv.org/content/10.1101/660837v1 (2019).
56. Towns, J. et al. XSEDE: accelerating scientific discovery. *Comput. Sci. Eng.* **16**, 62–74 (2014).
57. Scheres, S. H. Processing of structurally heterogeneous cryo-EM data in RELION. *Methods Enzymol.* **579**, 125–157 (2016).
58. Afonine, P. V. et al. New tools for the analysis and validation of cryo-EM maps and atomic models. *Acta Crystallogr. D* **74**, 814–840 (2018).
59. Kato, K., Goto, M. & Fukuda, H. Regulation by divalent cations of ^{3}H-baclofen binding to GABA^B sites in rat cerebellar membranes. *Life Sci.* **32**, 879–887 (1983).
60. Bowery, N. G., Hill, D. R. & Hudson, A. L. Characteristics of GABA^B receptor binding sites on rat whole brain synaptic membranes. *1983. Br. J. Pharmacol.* **120** (Suppl), 452–467, discussion 450–451 (1997).
61. Haga, K. et al. Structure of the human M2 muscarinic acetylcholine receptor bound to an antagonist. *Nature.* **482**, 547–551 (2012).
62. Marheineke, K., Grünewald, S., Christie, W. & Reiländer, H. Lipid composition of *Spodoptera frugiperda* (Sf9) and *Trichoplusia ni* (Tn) insect cells used for baculovirus infection. *FEBS Lett.* **441**, 49–52 (1998).
63. Ma, J. C. & Dougherty, D. A. The cation–π interaction. *Chem. Rev.* **97**, 1303–1324 (1997).

Acknowledgements This work is supported by National Institutes of Health (NIH) grant R01 NS092695 (G.S. and J.M.M.) and used the Extreme Science and Engineering Discovery Environment (XSEDE)[56] resource comet-gpu through sdsc-comet allocation TG-MCB190153, which is supported by National Science Foundation grant number ACI-1548562. We thank Q. Qu for advice and assistance with cryo-EM.

Author contributions M.M.P.-S. designed and cloned GABA$_B$ constructs, expressed and purified all proteins and collected and processed cryo-EM data. M.J.R. built and refined the structure from cryo-EM density maps and set up, performed and analysed molecular simulations. A.B.S. and O.P. assisted with cryo-EM data collection and processing. J.M.M. performed and analysed cellular signalling experiments. M.M.P.-S., M.J.R., J.M.M. and G.S. interpreted results. M.M.P.-S., M.J.R., J.M.M. and G.S. wrote the manuscript with O.P. and A.B.S. providing input. G.S. supervised the project.

Competing interests The authors declare no competing interests.

Additional information

Supplementary information is available for this paper at https://doi.org/10.1038/s41586-020-2469-4.

Correspondence and requests for materials should be addressed to G.S.

Peer review information *Nature* thanks Ryan Hibbs and the other, anonymous, reviewer(s) for their contribution to the peer review of this work. Peer reviewer reports are available.

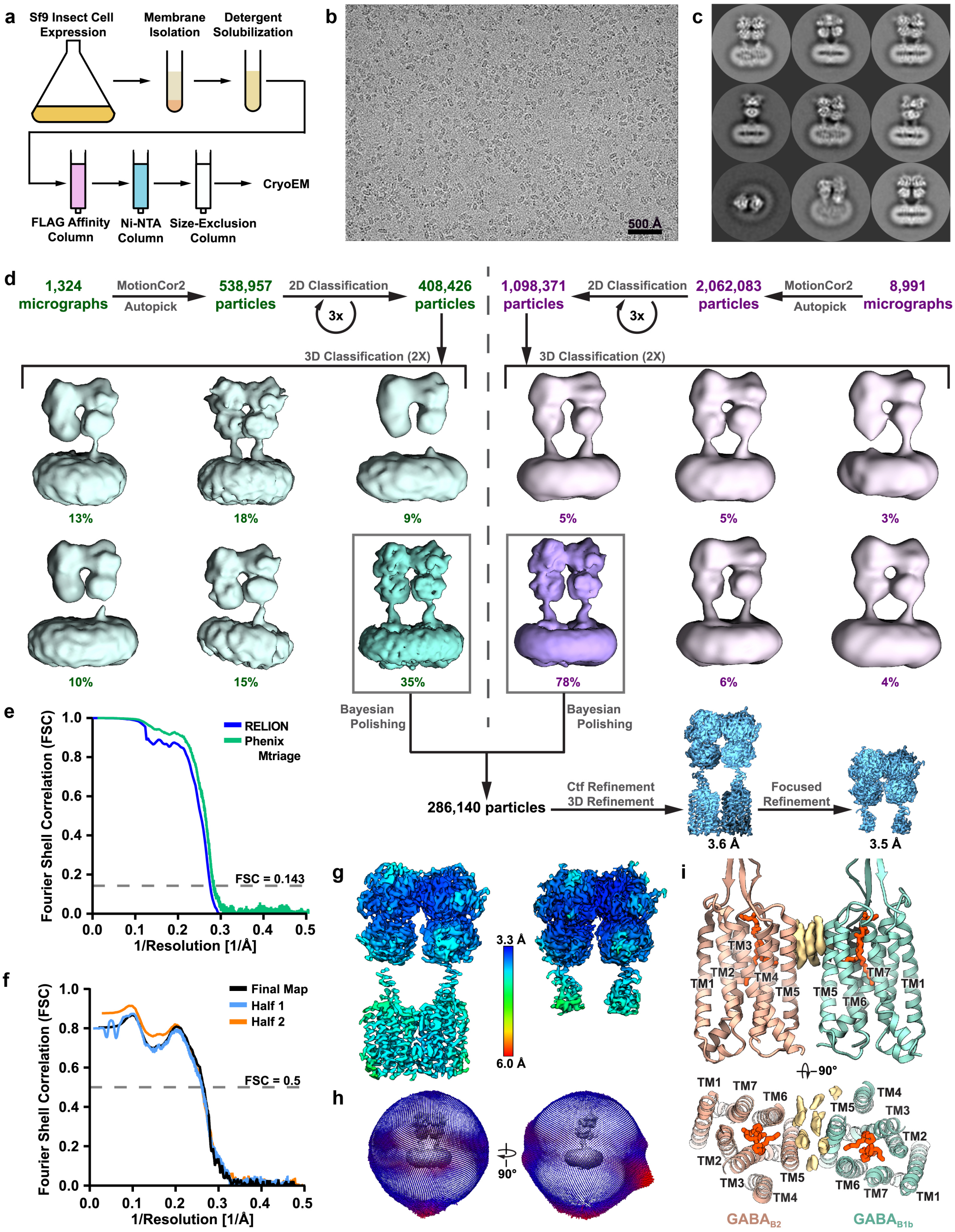

Extended Data Fig. 1 | Sample preparation, cryo-EM processing and reconstruction of GABA$_B$ heterodimer. **a**, Purification scheme for GABA$_B$. **b**, **c**, Representative cryo-EM micrograph of 10,315 collected (**b**) and 2D class averages (**c**) of GABA$_B$ dimers. **d**, Flow chart outlining the cryo-EM processing workflow using RELION[57], the global resolutions of the full-length structure and VFT focused structures were 3.6 Å and 3.5 Å, respectively, at 0.143 Fourier shell correlation (FSC) as calculated by RELION. **e**, **f**, Gold-standard FSC curve of half-maps calculated using RELION and Phenix Mtriage[58] (**e**), and map-to-model validation curves generated through Phenix Mtriage (**f**). **g**, Local resolution of cryo-EM maps. **h**, Angular distribution of projections used in final cryo-EM reconstruction. **i**, Ordered cryo-EM densities (light yellow), probably corresponding to GDN and/or cholesteryl hemisuccinate, are found at the TM5 interface of GABA$_{B1}$ and GABA$_{B2}$.

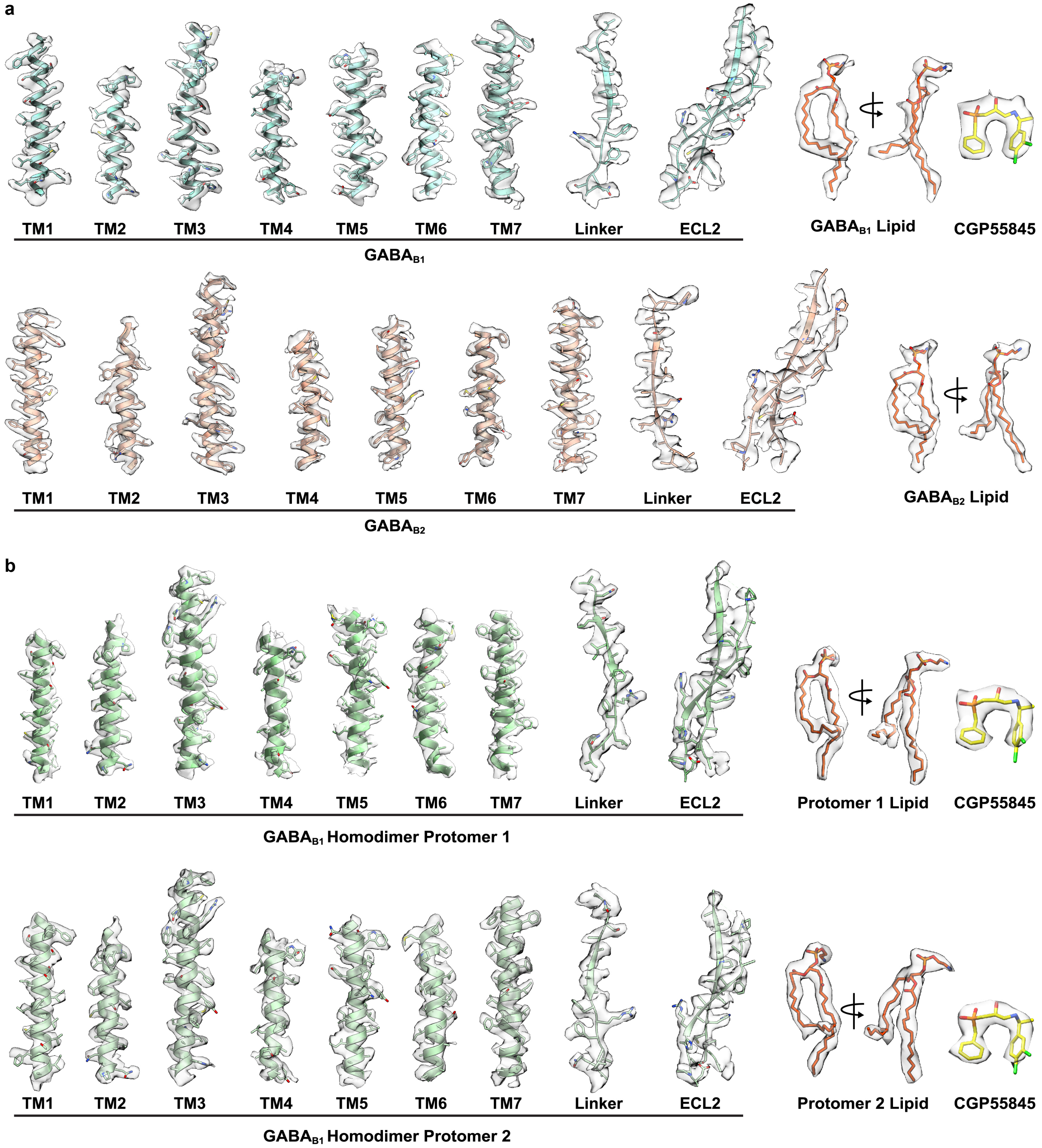

Extended Data Fig. 2 | Agreement between cryo-EM map and model. **a**, Electron microscopy density and model for GABA$_B$ heterodimer complex; transmembrane helices of GABA$_{B1}$, transmembrane helices of GABA$_{B2}$, linker region, bound phosphatidylethanolamine (PE) and ligand CGP55845. Densities visualized within UCSF Chimera[42] and zoned at 2.2 with threshold set to 0.0142, with the exception of the following: GABA$_{B1}$-bound lipid, GABA$_{B1}$-bound CGP55845 and GABA$_{B2}$ linker, in which thresholds of 0.01, 0.0189 and 0.0127 were used, respectively. **b**, Electron microscopy density and model for GABA$_{B1}$ homodimer; transmembrane helices and linker region of both protomers, 7TM-bound PE and ligand CGP55845. Densities were zoned at 2.2 and threshold set to 0.016, apart from CGP55845 and the ECL2 in both protomers, in which a threshold of 0.03 or 0.02 was used, respectively.

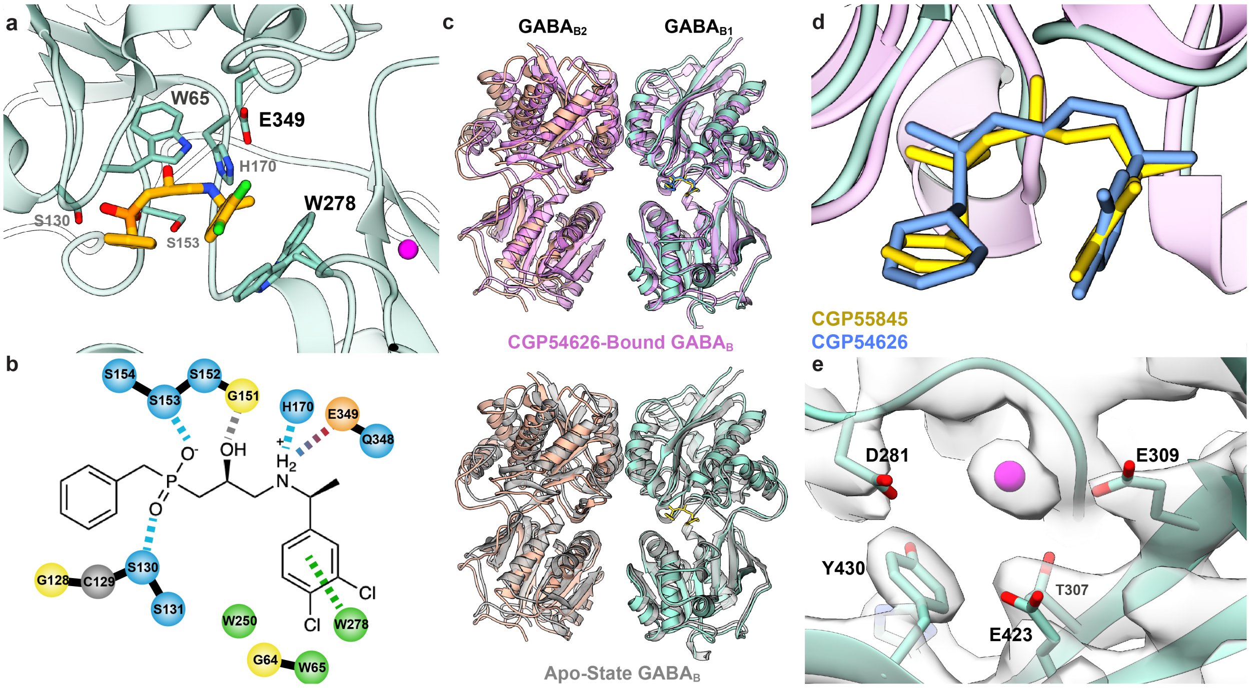

Extended Data Fig. 3 | Binding of CGP55845 and cation to GABA$_{B1}$ VFT. **a**, Model of CGP55845 within the VFT of GABA$_{B1b}$. The entire ligand is confined by W65 and W278 of GABA$_{B1}$, which form hydrophobic interactions with the chlorinated ring of CGP55845. **b**, Schematic of interacting residues on GABA$_{B1b}$ with the inhibitor, CGP55845. GABA$_{B1b}$ residues S153 and S130 form hydrogen bonds with oxygen atoms of the phosphate group, and H170 and E349 form a hydrogen bond and a salt bridge with the amine group of the ligand, respectively. π–π stacking occurs between the chlorinated ring structure of CGP55845 and W278, and W65 provides hydrophobic packing on the opposing side of the ring. S130, H170, E349 and W65 are all substantially different residues in GABA$_{B2}$, precluding ligand binding. Residues are colour-coded corresponding to their properties: light blue, hydrophilic; orange, anionic; green, hydrophobic; yellow, glycine; and grey, cysteine. Interaction lines are also colour-coded according to their type: light blue, side-chain hydrogen bonding; grey, backbone hydrogen bonding; blue–red gradient, salt bridge; and green, π–π stacking. **c**, Overlay of CGP55845-bound GABA$_B$ cryo-EM structure (tan and teal) with CGP54626-bound GABA$_B$ crystal structure (pink) (PDB 4MR7) or apo-state GABA$_B$ crystal structure (grey) (PDB 4MQE), resulting in r.m.s.d. values of 1.30 Å and 1.28 Å, respectively[12]. **d**, Comparison of ligand pose between CGP55845 (yellow) and CGP54626 (blue), which differs from CGP55845 only in a substitution of an aromatic ring in place of cyclohexane. **e**, Spherical density surrounded by anionic residues within the VFT supports a cation (magenta) at that site. The presence of a metal ion would be consistent with the observation that calcium and other divalent ions affect ligand affinity[59,60], and examination of the deposited scattering factors for the high-resolution VFT crystal structure (PDB 4MR7[12]) reveals positive difference density also consistent with a cation at this site.

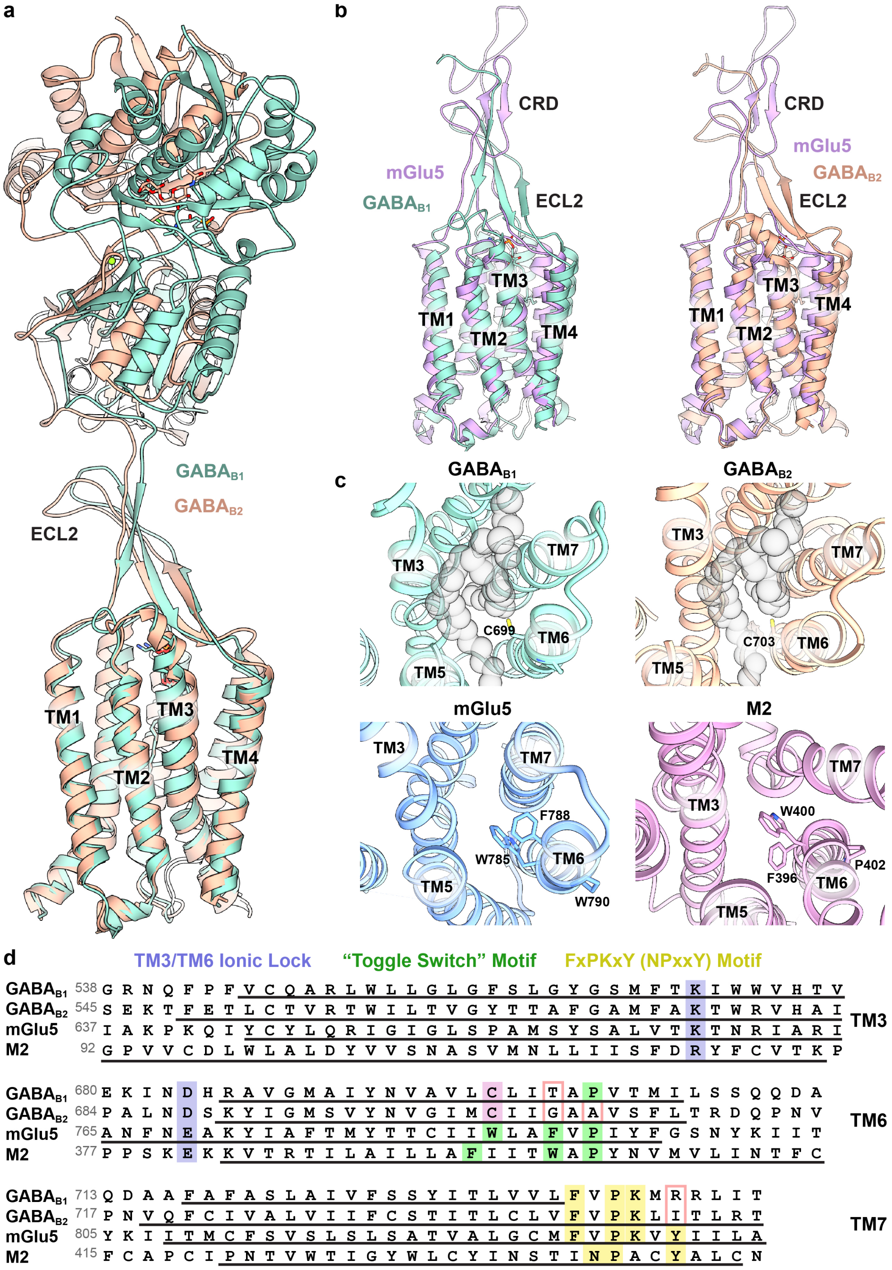

Extended Data Fig. 4 | Comparison of structures across GPCR classes. **a**, GABA$_B$ protomers share similar secondary and overall structure. **b**, Comparison of mGlu5 and GABA$_B$ 7TM and ECL2–linker shown from side view. **c**, Top-down view of GABA$_{B1}$, GABA$_{B2}$, mGlu5 (PDB 6N52[14]) and family A M2 acetylcholine receptor (PDB 3UON[61]) with sidechains corresponding to the toggle-switch motif shown. Phospholipid space-filling model is included in grey within GABA$_{B1}$ and GABA$_{B2}$. **d**, Sequence alignment of human GABA$_B$ receptors with mGlu5 and M2 receptors, comparing canonical GPCR activation motifs: TM3–TM6 ionic lock (blue), toggle-switch motif (green) and FXPKXY motif (yellow). Sequences are aligned to motifs within each transmembrane helix and transmembrane helical secondary structure is underlined. Residues in GABA$_B$ sequences differing from canonical motifs are outlined in pink. The cysteine residue that replaces the toggle-switch tryptophan is highlighted in pink.

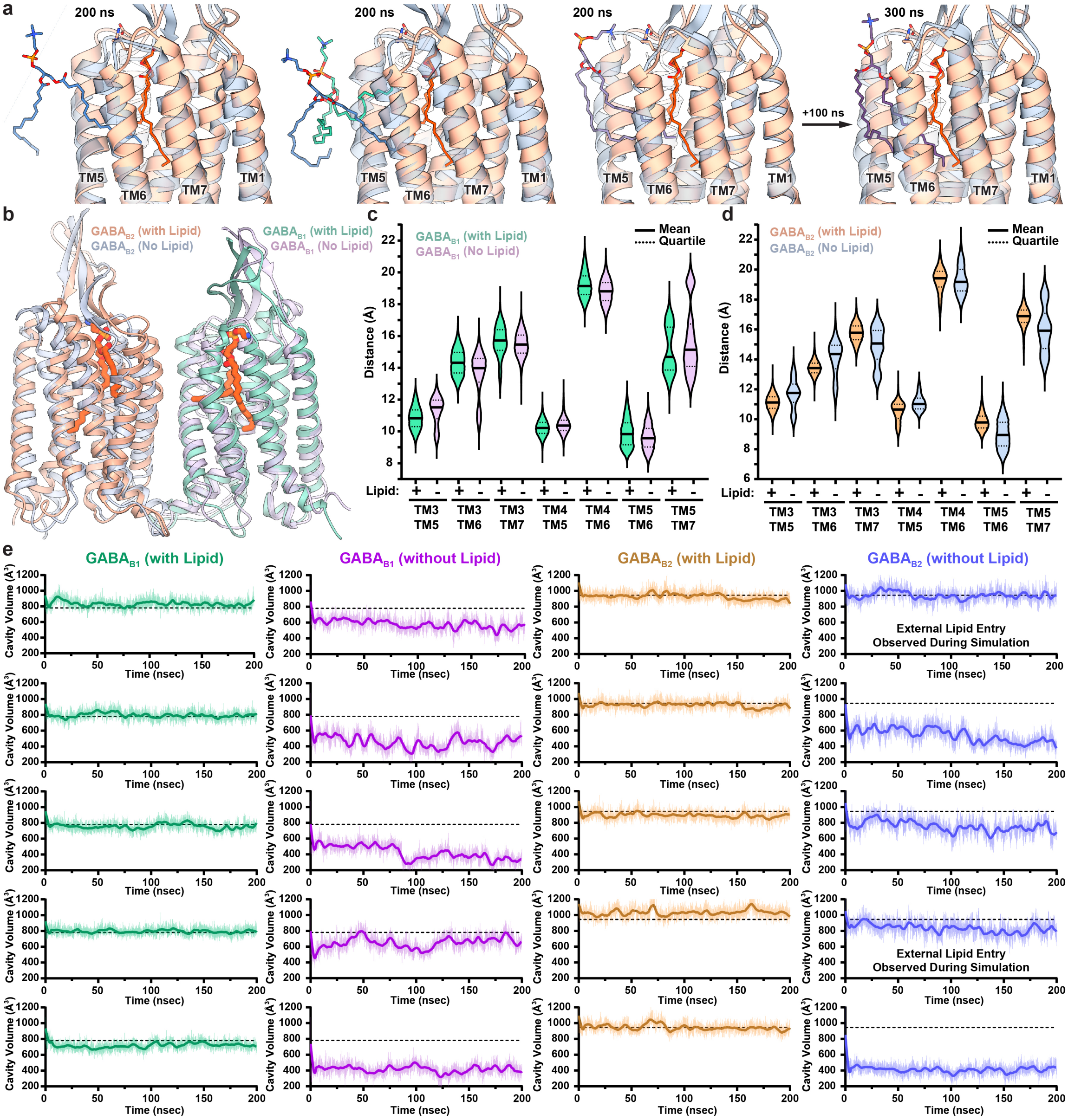

Extended Data Fig. 5 | Atomistic simulations of phospholipid structural stabilization and entry. **a**, The results of three out of seven total simulations of GABA$_B$ 7TM and linker in the absence of core-bound lipid after 200 ns. The results show the extent of lipid (green and purple) entry in GABA$_{B2}$ (grey) in the simulations versus the experimental structure (tan) with PE (orange). One of the trajectories was extended an additional 100 ns (rightmost panel) and lipid entry was observed to progress towards the core. **b**, Representative side view of the GABA$_B$ ribbon and stick model from simulations at 200 ns, showing persistence of the ECL2 and β-sheet structure even in absence of the VFTs. **c**, **d**, Violin plots of ensemble distances between GABA$_{B1}$ (**d**) and GABA$_{B2}$ (**e**) TM helices in simulations with and without core-bound lipid. Distances were measured from the Cα atoms of the following residues in GABA$_{B1}$: L550 (TM3), W611 (TM4), L653 (TM5), M707 (TM6) and A716 (TM7); and the following residues in GABA$_{B2}$: T557 (TM3), W615 (TM4), L657 (TM5), F711 (TM6) and Q720 (TM7). Simulations were run over 200 ns and violin plots represent *n* = 37,500 data points and 5 simulations per condition. **e**, 7TM cavity volume measured over time for individual simulations. Average cavity volume of phospholipid-bound receptor is shown as dashed line, thick lines indicate rolling averages of 5.33 ns and thin lines represent raw data.

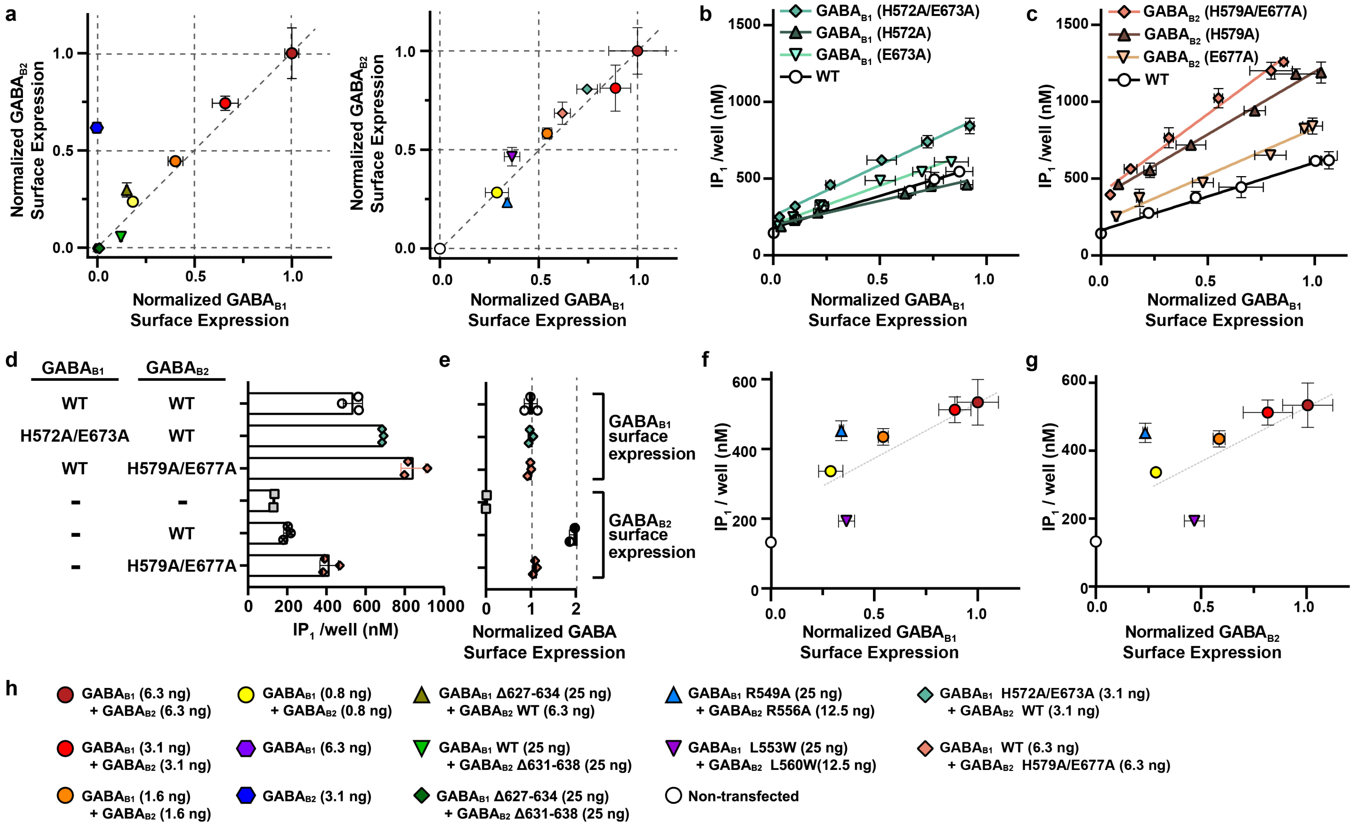

Extended Data Fig. 6 | Functional analysis of GABA$_B$ mutants. **a**, Comparative normalized surface-expression levels of constructs. Surface-expression levels of wild-type and mutant GABA$_B$ receptors were determined using a direct ELISA against the N-terminal GABA$_{B1}$ Flag tag and the N-terminal GABA$_{B2}$ HA tag. Surface-expression levels were normalized to the surface expression of a wild-type GABA$_B$ receptor when 6.3 ng Flag-tagged GABA$_{B1}$ and 6.3 ng HA-tagged GABA$_{B2}$ DNA was used for transfection. The line $x = y$ indicates similar surface expression of GABA$_B$ subunits as evident from transfection with lower amounts of Flag-tagged GABA$_{B1}$ and HA-tagged GABA$_{B2}$. Values above the line have greater GABA$_{B2}$ surface expression relative to GABA$_{B1}$, and values below the line have greater GABA$_{B1}$ surface expression relative to GABA$_{B2}$. GABA$_{B1}$ did not reach the cell surface (data point hidden behind triangle at the coordinate (0,0) in the left subpanel). **b**, **c**, Mutations of ionic residues forming the interface of GABA$_{B1}$ (**b**) and GABA$_{B2}$ (**c**) result in increased constitutive activity of the receptor. To achieve a range of expression levels of the mutants in **b** and **c**, the DNA amounts transfected were serially diluted twofold from 3.3 ng (mutants in **b**) or 6.3 ng (mutants in **c**) of each subunit, respectively. **d**, **e**, GABA$_{B2}$(H579A/E677A) expressed without GABA$_{B1}$ shows a moderate increase in basal activity over wild-type GABA$_{B2}$ expressed alone (**d**), although surface expression (**e**) of the wild-type GABA$_{B2}$ subunit was higher than of GABA$_{B2}$(H579A/E677A). **f**, **g**, Mutation of lipid coordinating residues (blue triangle) increase the constitutive activity of GABA$_{B1}$ (**f**) and GABA$_{B2}$ (**g**), whereas mutations displacing the lipid tails from the 7TM core (purple triangle) result in decreased basal activity of the receptor when compared to wild-type receptor of similar receptor surface expression. **h**, Key to colours and symbols used in **a**, **f**, and **g** with DNA transfection amounts indicated in parentheses. Data are representative of one experiment performed in triplicate and repeated independently at least three times with similar results ($n = 3$ independent experiments), error bars represent mean ± s.e.m.

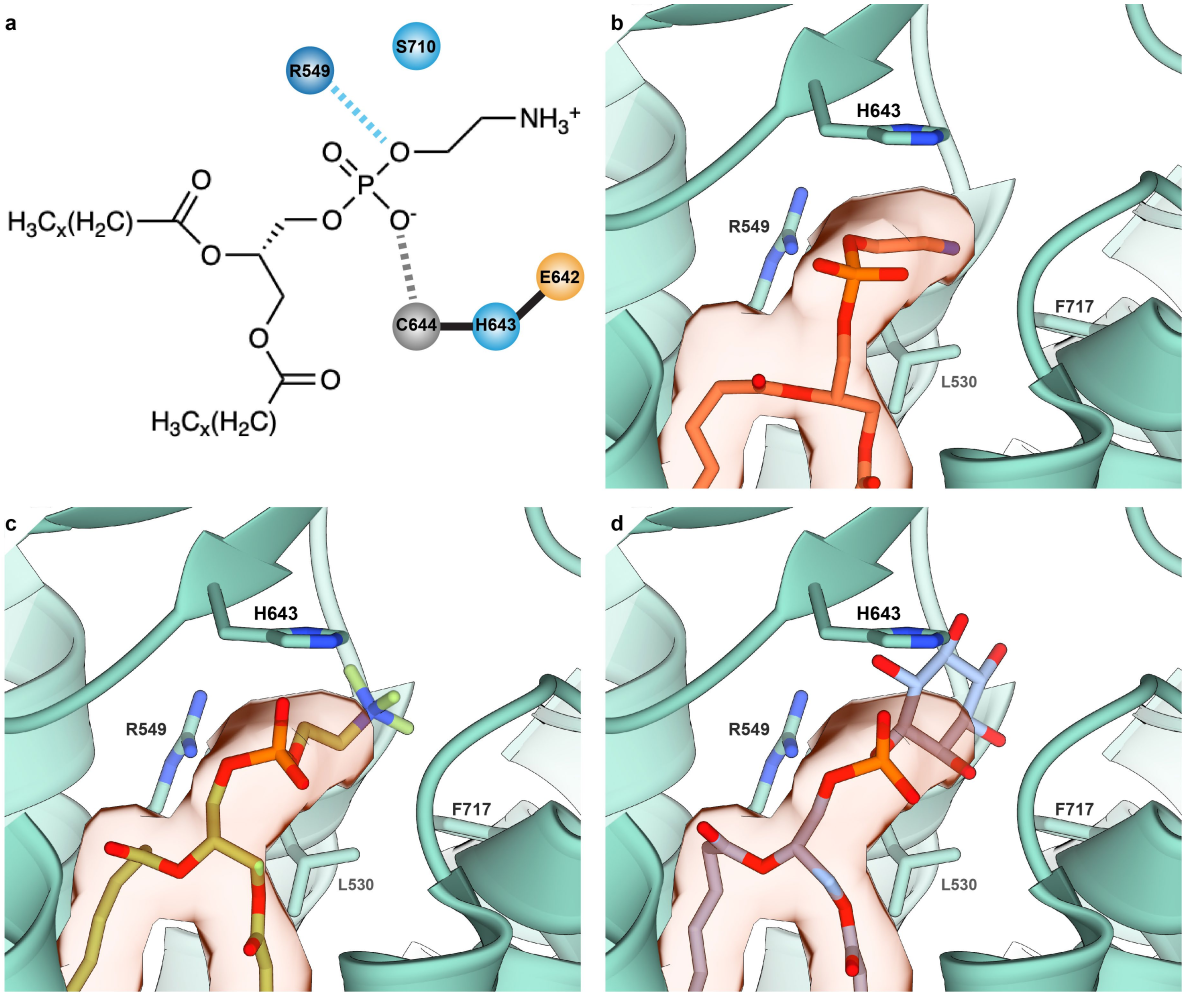

Extended Data Fig. 7 | Modelling of phospholipid into GABA$_B$. **a**, Schematic of GABA$_{B1}$ residues interacting with the polar headgroup of PE. The terminal amine (-NH^{3+}) forms a salt bridge with residue D714 in ECL3, and the phosphate group is coordinated by S710 of ECL3, R549 of TM3 and the backbone nitrogen of the C644 of ECL2. **b**–**d**, As our receptor purification did not contribute additional lipid, we considered the known lipid composition of Sf9 insect cells. Four primary phospholipids are present in Sf9 insect cells: phosphatidylcholine (43%), phosphatidylethanolamine (32%), phosphatidylinositol (23%) and cardiolipin (4%)[62]. It was apparent from the map that the lipid had only two carbon chains, immediately excluding cardiolipin as it has four hydrocarbon tails. A comparison of the map and the binding site residues led to the decision to model PE (**b**) into the pocket using the GemSpot pipeline[17], which produced good cross-correlation with favourable interactions. To further confirm our selection, analysis of overlays of phosphatidylcholine (**c**) and phosphatidylinositol (**d**) over the docked model revealed phosphatidylcholine is unlikely given that the interactions with the cation appear to be primarily salt bridges, rather than the cation–π interactions that more commonly coordinate choline in proteins[63]. Although phosphatidylinositol may make favourable interactions, our map does not appear to support such a large moiety in the headgroup position. Thus, PE is the most likely lipid to reside in the structure and was therefore used in the models.

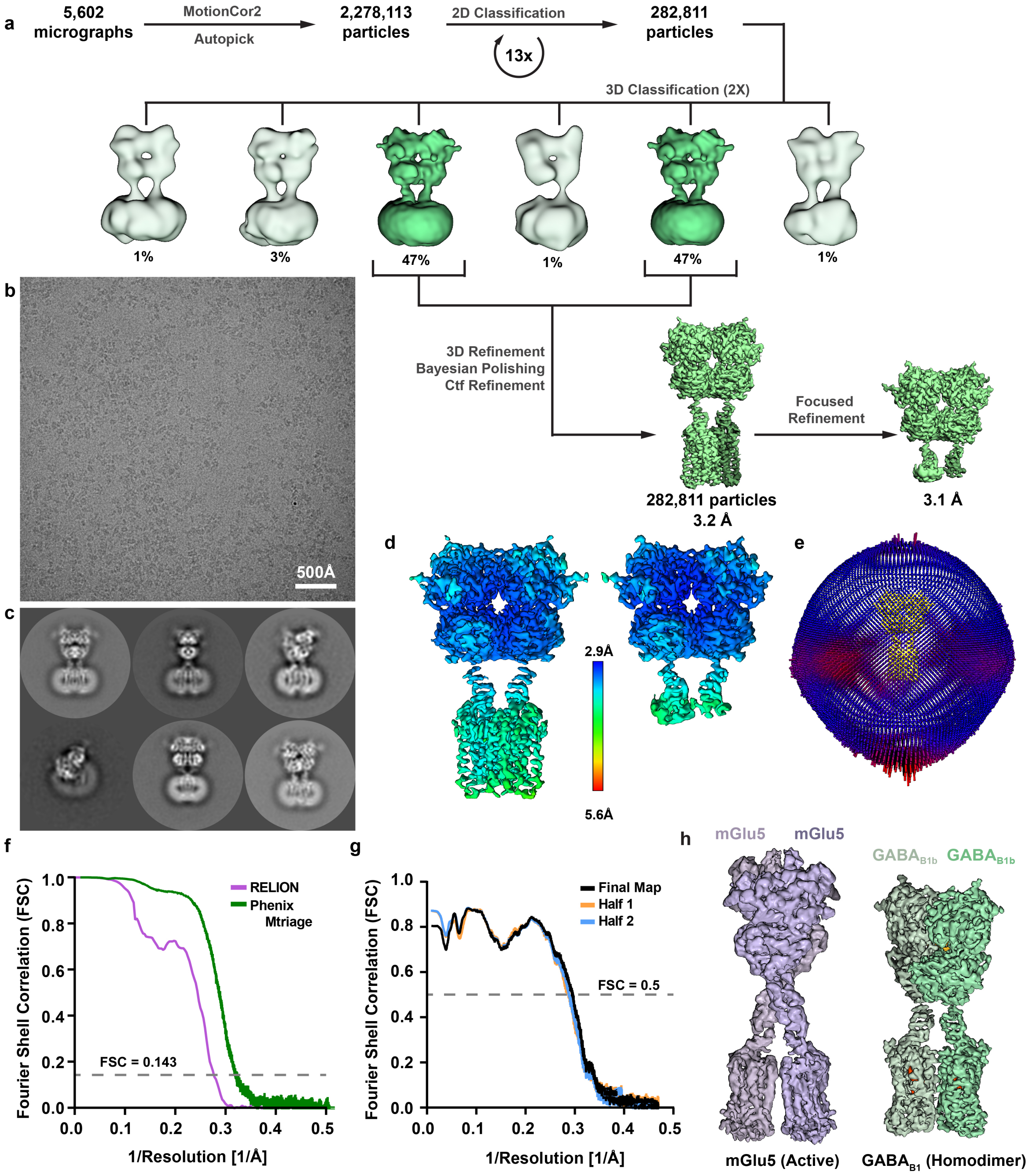

Extended Data Fig. 8 | Cryo-EM processing workflow of GABA$_{B1b}$ homodimer. **a**, Flow chart outlining the cryo-EM processing of the GABA$_B$ homodimer. **b**, **c**, Representative micrograph of 5,602 collected (**b**) and 2D class averages (**c**). **d**, Local resolution of cryo-EM maps. **e**, Angular distribution of projections used in the final cryo-EM reconstruction. **f**, **g**, Gold-standard FSC curve of half-maps calculated using RELION and Phenix Mtriage[58] (**f**), and map-to-model validation curves generated through Phenix Mtriage (**g**). Global indicated resolutions of the full-length structure and VFT structure were 3.2 Å and 3.1 Å, respectively, at 0.143 FSC as calculated by RELION. **h**, Electron microscopy maps of active mGlu5 (purple) (EMD-0345[14]), and homodimeric GABA$_{B1}$ (green). The GABA$_{B1}$ homodimer adopts an overall architecture similar to that of active mGlu5.

Extended Data Table 1 | Cryo-EM data collection, refinement and validation statistics

	GABA$_{\text{B1b}}$/GABA$_{\text{B2}}$ Heterodimer (EMDB-21533) (PDB-6W2X)		**GABA$_{\text{B1b}}$ Homodimer (EMDB-21534) (PDB-6W2Y)**
Data collection and processing	**Data Set #1**	**Data Set #2**	
Magnification (x)	57,050	57,050	47,198
Voltage (kV)	300	300	300
Electron exposure (e–/Å^2)	56.5	64.2	49.7
Defocus range (μm)	-1.5 - -2.7	-1.2 - -2.5	-0.9 - -2.5
Pixel size (Å)	0.8521	0.8521	1.06
Symmetry imposed	C1	C1	C1
Initial particle images (no.)	538,957	2,062,083	2,278,113
Final particle images (no.)	286,140 (Combined Data Sets)		282,811
Map resolution (Å)	3.6 Å		3.2 Å
FSC threshold	0.143		0.143
Map resolution range (Å)	3.3 - 4.4		3.0 - 4.4
Map sharpening *B* factor (Å^2)	-183.273		-84.088
Refinement			
Initial model used (PDB code)	4MR7, 6N52 Homology		GABA$_{\text{B1b}}$ of 6W2X (this work)
Model resolution (Å)	3.7		3.4
FSC threshold	0.5		0.5
Model composition			
Non-hydrogen atoms	9860		9721
Protein residues	1345		1327
Ligands	3		4
B factors (Å^2)			
Protein	15.17		57.57
Ligand	28.97		59.82
R.m.s. deviations			
Bond lengths (Å)	0.004		0.007
Bond angles (°)	0.608		0.763
Validation			
MolProbity score	1.75		2.02
Clashscore	5.55		9.98
Poor rotamers (%)	0.00		0.12
Ramachandran plot			
Favored (%)	92.92		91.66
Allowed (%)	7.08		8.34
Disallowed (%)	0.00		0.00

nature research

Corresponding author(s): Georgios Skiniotis

Last updated by author(s): 03/11/2020

Reporting Summary

Nature Research wishes to improve the reproducibility of the work that we publish. This form provides structure for consistency and transparency in reporting. For further information on Nature Research policies, see Authors & Referees and the Editorial Policy Checklist.

Statistics

For all statistical analyses, confirm that the following items are present in the figure legend, table legend, main text, or Methods section.

n/a	Confirmed	
☐	☒	The exact sample size (n) for each experimental group/condition, given as a discrete number and unit of measurement
☐	☒	A statement on whether measurements were taken from distinct samples or whether the same sample was measured repeatedly
☐	☒	The statistical test(s) used AND whether they are one- or two-sided *Only common tests should be described solely by name; describe more complex techniques in the Methods section.*
☒	☐	A description of all covariates tested
☒	☐	A description of any assumptions or corrections, such as tests of normality and adjustment for multiple comparisons
☐	☒	A full description of the statistical parameters including central tendency (e.g. means) or other basic estimates (e.g. regression coefficient) AND variation (e.g. standard deviation) or associated estimates of uncertainty (e.g. confidence intervals)
☐	☒	For null hypothesis testing, the test statistic (e.g. F, t, r) with confidence intervals, effect sizes, degrees of freedom and P value noted *Give P values as exact values whenever suitable.*
☒	☐	For Bayesian analysis, information on the choice of priors and Markov chain Monte Carlo settings
☒	☐	For hierarchical and complex designs, identification of the appropriate level for tests and full reporting of outcomes
☒	☐	Estimates of effect sizes (e.g. Cohen's d, Pearson's r), indicating how they were calculated

Our web collection on statistics for biologists contains articles on many of the points above.

Software and code

Policy information about availability of computer code

Data collection	CryoEM Data was collected automatically on a Titan Krios (FEI) using SerialEM.
Data analysis	The following software were used in this study: MotionCor2, Gctf, CTFFind-4.1, Relion3.0, Relion3.1, USCF Chimera 1.14, Coot (0.8.9.1el), Phenix (1.17.1-3660), GemSpot, Maestro (2019-4), OPM, CHARMM-GUI, VMD (1.9.3), NAMD (2.13), Epock (1.0.5), GraphPad Prism 8.

For manuscripts utilizing custom algorithms or software that are central to the research but not yet described in published literature, software must be made available to editors/reviewers. We strongly encourage code deposition in a community repository (e.g. GitHub). See the Nature Research guidelines for submitting code & software for further information.

Data

Policy information about availability of data

All manuscripts must include a data availability statement. This statement should provide the following information, where applicable:

- Accession codes, unique identifiers, or web links for publicly available datasets
- A list of figures that have associated raw data
- A description of any restrictions on data availability

All data generated or analyzed during this study are included in this article and the Supplementary Information. CryoEM maps of GABAB heterodimer and GABAB1b homodimer have been deposited in the Electron Microscopy Data Bank under accession codes EMD-21533 and EMD-21534, respectively. The atomic coordinates of GABAB heterodimer and GABAB1b homodimer have been deposited in the Protein Data Bank under the accession codes 6W2X and 6W2Y, respectively.

Field-specific reporting

Please select the one below that is the best fit for your research. If you are not sure, read the appropriate sections before making your selection.

☒ Life sciences ☐ Behavioural & social sciences ☐ Ecological, evolutionary & environmental sciences

For a reference copy of the document with all sections, see nature.com/documents/nr-reporting-summary-flat.pdf

Life sciences study design

All studies must disclose on these points even when the disclosure is negative.

Sample size	Sample sizes were not predetermined by statistical methods. For cryoEM data, sample sizes were determined/limited by time availability of the microscope.
Data exclusions	No data was systematically excluded. Generation of maps from cryo-EM particles involves use of Relion (3.0 or 3.1) to sort particles, and remove damaged or poor quality particles to achieve a high-resolution final reconstruction.
Replication	Cellular signaling assays were replicated in at least three independent experiments for each condition tested. All replication attempts were successful.
Randomization	No randomization was attempted or needed.
Blinding	No blinding was attempted or needed.

Reporting for specific materials, systems and methods

We require information from authors about some types of materials, experimental systems and methods used in many studies. Here, indicate whether each material, system or method listed is relevant to your study. If you are not sure if a list item applies to your research, read the appropriate section before selecting a response.

Materials & experimental systems

n/a	Involved in the study
☐	☒ Antibodies
☐	☒ Eukaryotic cell lines
☒	☐ Palaeontology
☒	☐ Animals and other organisms
☒	☐ Human research participants
☒	☐ Clinical data

Methods

n/a	Involved in the study
☒	☐ ChIP-seq
☒	☐ Flow cytometry
☒	☐ MRI-based neuroimaging

Antibodies

Antibodies used	HRP-conjugated anti-FLAG antibody (Sigma Aldrich, A8592) and HRP-conjugated anti-HA antibody (R&D systems HAM0601),
Validation	Antibodies are validated by supplier. No additional validation was conducted by authors of this study.

Eukaryotic cell lines

Policy information about cell lines

Cell line source(s)	HEK293 cells (ATCC® CRL-1573™) Sf9, Expression Systems, Cat 94-001S
Authentication	Cell lines are maintained by the supplier. No additional authentication was performed by the authors of this study.
Mycoplasma contamination	Cell lines are tested by manufacturer for contamination and no additional testing was performed by the authors of this study.
Commonly misidentified lines (See ICLAC register)	None used.

Author Correction: Structural insights into μ-opioid receptor activation

https://doi.org/10.1038/s41586-020-2542-z

Correction to: *Nature* https://doi.org/10.1038/nature14886

Weijiao Huang, Aashish Manglik, A. J. Venkatakrishnan, Toon Laeremans, Evan N. Feinberg, Adrian L. Sanborn, Hideaki E. Kato, Kathryn E. Livingston, Thor S. Thorsen, Ralf C. Kling, Sébastien Granier, Peter Gmeiner, Stephen M. Husbands, John R. Traynor, William I. Weis, Jan Steyaert, Ron O. Dror & Brian K. Kobilka

In this Article, the configuration of BU72 at the benzylic amine was mistakenly reported as (*S*). Re-fitting this stereocentre to (*R*) improved the fit of the observed density in the X-ray structure. The (*S*)-configuration was originally assigned on the basis of the expected stereochemistry from ref.[1]. The origin of the inversion is unclear, but we propose that the original assignment, based only on nuclear Overhauser effect experiments, may well have been incorrect. We thank Thomas Munro for bringing this error to our attention. The Protein Data Bank (PDB) entry of the active μ-opoid receptor bound to the BU72 agonist has been updated as 5C1M. The original Article has not been corrected online.

1. Husbands, S. M. & Lewis, J. W. Morphinan cyclic imines and pyrrolidines containing a constrained phenyl group: high affinity opioid agonists. *Bioorg. Med. Chem. Lett*. **5**, 2969–2974 (1995).

Author Correction: Reversing a model of Parkinson's disease with in situ converted nigral neurons

https://doi.org/10.1038/s41586-020-2583-3

Correction to: *Nature* https://doi.org/10.1038/s41586-020-2388-4

Hao Qian, Xinjiang Kang, Jing Hu, Dongyang Zhang, Zhengyu Liang, Fan Meng, Xuan Zhang, Yuanchao Xue, Roy Maimon, Steven F. Dowdy, Neal K. Devaraj, Zhuan Zhou, William C. Mobley, Don W. Cleveland & Xiang-Dong Fu

In Fig. 5e of this Article, the labels 'Empty' and 'shPTB' were inadvertently swapped. In addition, 'Peking-Tsinghua Center for Life Sciences' should be added to affiliation 2 (associated with authors Xinjiang Kang & Zhuan Zhou) such that the full affiliation reads: 'State Key Laboratory of Membrane Biology and Peking-Tsinghua Center for Life Sciences, Institute of Molecular Medicine, Peking University, Beijing, China.'. The original Article has been corrected online.

Author Correction: The evolutionary history of lethal metastatic prostate cancer

https://doi.org/10.1038/s41586-020-2581-5

Correction to: *Nature* https://doi.org/10.1038/nature14347

Gunes Gundem, Peter Van Loo, Barbara Kremeyer, Ludmil B. Alexandrov, Jose M. C. Tubio, Elli Papaemmanuil, Daniel S. Brewer, Heini M. L. Kallio, Gunilla Hägnäs, Matti Annala, Kati Kivinummi, Victoria Goody, Calli Latimer, Sarah O'Meara, Kevin J. Dawson, William Isaacs, Michael R. Emmert-Buck, Matti Nykter, Christopher Foster, Zsofia Kote-Jarai, Douglas Easton, Hayley C. Whitaker, ICGC Prostate UK Group*, David E. Neal, Colin S. Cooper, Rosalind A. Eeles, Tapio Visakorpi, Peter J. Campbell, Ultan McDermott, David C. Wedge & G. Steven Bova

In the Supplementary Information of this Article, some errors were made in compiling the Supplementary Data file called 'Supplementary Variant Lists'. In the first worksheet (entitled 'subs') the clusters to which some single nucleotide variants (SNVs) were assigned were not reported and were replaced with 'NA' for 'not available'. The correct cluster numbers have now been inserted. Three mutations occurring in tumour A32 were incorrectly assigned to cluster 3 and have now been correctly assigned to cluster 2. Duplicate entries were present for some mutations in A32. These duplicate entries have now been removed. In the fourth worksheet (entitled 'copy_number') incorrect copy number information was reported for sample A31-c. The previous information, implying that A31-c was primarily diploid, has now been replaced with the copy number call used within the Article, which indicates that A31-c is primarily tetraploid. The Supplementary Information to this Amendment contains the corrected Excel file 'Supplementary Variant Lists'. These corrections do not change the authors' interpretation of the findings. The original Article has not been corrected.

Supplementary information is available in the online version of this Amendment.

Correspondence should be addressed to D.C.W.

---

*A list of participants of the ICGC Prostate UK Group and their affiliations appears in section 5 of the Supplementary Information of the original Article.

Author Correction: The dental proteome of *Homo antecessor*

https://doi.org/10.1038/s41586-020-2580-6

Correction to: *Nature* https://doi.org/10.1038/s41586-020-2153-8

Frido Welker, Jazmín Ramos-Madrigal, Petra Gutenbrunner, Meaghan Mackie, Shivani Tiwary, Rosa Rakownikow Jersie-Christensen, Cristina Chiva, Marc R. Dickinson, Martin Kuhlwilm, Marc de Manuel, Pere Gelabert, María Martinón-Torres, Ann Margvelashvili, Juan Luis Arsuaga, Eudald Carbonell, Tomas Marques-Bonet, Kirsty Penkman, Eduard Sabidó, Jürgen Cox, Jesper V. Olsen, David Lordkipanidze, Fernando Racimo, Carles Lalueza-Fox, José María Bermúdez de Castro, Eske Willerslev & Enrico Cappellini

In this Article, the sentence beginning 'However, pairwise divergence…' erroneously cited Fig. 3b instead of Fig. 2b. The full sentence should therefore read: 'However, pairwise divergence of the amino acid sequences between *H. antecessor* and the clade containing *H. sapiens*, Neanderthals and the Denisovan is larger than the divergence between the members of this clade (**Fig. 2b**, Supplementary Fig. 12, Supplementary Information).'. The Article has been corrected online.

Work

Your story Send your careers story to: naturecareerseditor@nature.com


GETTY

Success in a job application depends on intangible factors as well as publication metrics.

LOOK BEYOND METRICS

Survey explores how and why certain people get job offers. **By Nina Notman and Chris Woolston**

It takes at least 15 job applications to land a single offer, finds a survey of 317 early-career researchers who applied for faculty positions in a range of nations (J. D. Fernandes *et al. eLife* **9**, e54097; 2020). The results have shed light on a hiring process that is often opaque, frustrating and hard to predict. Contrary to common belief, the authors found that a publication in a high-profile journal isn't an absolute prerequisite for a successful application.

The survey was conducted by members of the Future PI Slack community, a postdoctoral support group. They collected responses from researchers who had applied for faculty positions between May 2018 and May 2019. Respondents hailed from 13 countries, although 72% were from the United States; 85% were in the life sciences. Overall, 58% received job offers, significantly above the average from other studies, suggesting that successful applicants were especially willing to take the survey. Only 26% had an authorship credit in *Cell, Nature* or *Science*.

The survey tracked conventional metrics of success such as fellowships, citations and publications, and found that these measures were only modestly effective at predicting which applicants would get job offers. The authors tried to construct a flow chart to predict the applicants' fate, but it was less than 60% accurate.

More is more

One clear lesson was that jobseekers shouldn't skimp on applications. Those who submitted more than 15 applications landed substantially more on-site interviews than those who didn't. They also received more job offers, but the correlation wasn't so strong, suggesting that the shotgun approach to applications can go only so far. Jobseekers do better when they send applications that are precisely tailored to the position sought, says survey co-author Chris Smith, manager of the postdoc programme at North Carolina State University in Raleigh.

Publication in a high-profile journal helped applicants, but it was no guarantee of success, the study found. Jobseekers who were first authors of a paper in *Cell*, *Nature* or *Science* received offers on 11% of their applications. For people who had no papers in those journals, the success rate per application was 2%.

The authors also polled 15 faculty members who had served on hiring committees to find out what makes an application successful. The results suggest that committees seek candidates who will be good colleagues and scientists, says the study's lead author, Amanda Haage, a biomedical scientist at the University of North Dakota in Grand Forks. The committees looked at affability as well as at track records, she says.

Intangible assets

Recruitment of academics is more holistic than many think, explains Robert Bowles, a careers adviser at the Royal Society of Chemistry in Cambridge, UK. Applicants "tend to forget about the intangibles", he says. "Publications and grants buy you a ticket into the lottery, but they are not going to win it for you."

When asked for their general thoughts on the application process, jobseekers had a nearly universal negative outlook. Most were frustrated that they did not receive feedback on their applications.

But faculty members on hiring committees find it impossible to provide detailed feedback on all applications. All 15 surveyed said that they typically receive more than 100 applications per job offer; 10 said they usually get more than 200.

It's just one more sign of a stark imbalance in academia. Jobseekers outnumber positions, and that disparity is expected to get worse in the wake of the current coronavirus pandemic.

In this environment, postdocs should keep in mind that unsuccessful applications do not mean failure, says biochemist Rosemary Bass, a careers adviser at the University of East Anglia in Norwich, UK. "We see people who think that making five applications and not getting an interview means that they are a reject," Bass says. "The current situation is bringing home the difficulties of the academic job market to PhD students and postdocs in a way that we as careers advisers have not managed to previously."

Nina Notman is a freelance writer in Salisbury, UK. **Chris Woolston** is a freelance writer in Billings, Montana.

The COVID-19 pandemic put paid to a planned gathering in County Tipperary, Ireland.

GETTY

TEAM BONDING IN A VIRTUAL STYLE

One laboratory made the most of lockdown by moving a retreat online. **By Rob Salguero-Gómez**

On 5 April, two weeks into the UK lockdown, my laboratory group and I were meant to have flown to Ireland. It would have been our first research retreat since I became a Department of Zoology faculty member at the University of Oxford, UK. The goal of the retreat, which was to have been held in a manor house in County Tipperary, was to enhance team dynamics and advance research projects.

I wanted the retreat to go ahead, so I organized a virtual version. Here are some steps our team took to make it a success.

Pitch the idea. Once it became clear that the retreat wouldn't be possible as we had planned, I organized an hour-long video conference with my group to discuss our options: cancel, postpone or do something different. The democratic vote was for a virtual version of the retreat, with the *in situ* one to be postponed until it was safe to hold it.

Plan together. At that online meeting, I asked my team what format it would prefer for the virtual retreat. We agreed to start each day at 9 a.m. with a statement of everybody's goals for the day, and to continue until 5 p.m., with two 30-minute breaks for morning and afternoon coffee, and a one-hour break for lunch. These breaks gave members the opportunity to chat informally through a video call.

We also organized a series of 30-minute skills workshops after lunch, run by volunteers from the lab, on academic writing, research presentations and developing grant proposals. It soon became clear to me that the schedule needed to be flexible because one of my postdocs much prefers working in the evening, and two PhD students are currently based in Brazil and California. We agreed that they could join in when they woke up, and then carry on with writing activities during their normal working hours.

Set one daily task. To help lab members be more productive during the retreat, I asked them in advance to choose a single project to focus on each day. Projects ranged from doing analyses to writing manuscripts, essays or grant proposals.

Screen out e-mails and other online distractions. A week before the virtual retreat, I encouraged my students and postdocs to identify 'urgent' e-mails to be dealt with in advance; all else would have to wait until after the retreat. As a lab, we turned on our 'out of office' automatic reply and agreed to not check e-mails during the retreat's writing slots.

Build in relaxation. In the absence of the Irish manor house and its surroundings, we organized social activities from 5 p.m. onwards, including virtual drinks and a pub quiz. We also found that having a time for a walk in each person's back garden, to disconnect from the screen, was invaluable.

Delegate tasks. Once I had taken care of the basic structure of the retreat and run the first session, I asked volunteers to help keep time and moderate subsequent events. This gave team members a chance to exercise these key skills. However, it was also especially important for me: a couple of weeks before the retreat, my wife and I started displaying the symptoms of coronavirus. We were not deemed ill enough by our doctor to seek hospital treatment. Instead, we managed our symptoms from home with medication and rest.

Provide feedback individually. I contacted each team member one by one, to ask how they were doing and to provide feedback on their projects. This ensured that they did not get stuck while I was focused on recuperation.

Organize a final wrap-up. We used the last hour of the whole retreat to discuss each lab member's progress and trials and tribulations, including my own. Creating a space for everybody to share their struggles regarding lack of motivation to write, as well as tips to do so efficiently, was greatly appreciated across the team. Each of us also explained our future steps, as well as setting out a rough timeline.

Keep track of post-retreat progress. I still hold a virtual weekly meeting with my lab members individually, for us to discuss how retreat-related projects are going.

In the past, I have attended writing retreats at which members were assigned a partner to check on their progress every two weeks. Sadly, this strategy didn't occur to me in time to implement it during our retreat. I also organized a poll to seek feedback on the event.

Staging the retreat virtually helped me navigate a fresh challenge while, I hope, providing my team with the support it needs in the middle of a pandemic. Now, most weeks, during our for-now-virtual lab meeting, I try to encourage the team with the promise that our retreat in Ireland will go ahead one day. We're looking forward to it.

Rob Salguero-Gómez is an associate professor in ecology at the Department of Zoology, University of Oxford, UK.

Where I work
Greg Rouse

Photographed by the Schmidt Ocean Institute.

I had sea worms on my mind during a March expedition through the Ningaloo Canyons off the northwest coast of Australia. Cruising aboard the RV *Falkor*, a research ship operated by the Schmidt Ocean Institute in Palo Alto, California, I was hoping to collect and sequence new deep-sea worm species. Everyone on board knew they were in for surprises, but nobody could have imagined the creature that suddenly appeared on our screen one day.

Here, in a moment of pure excitement, I'm standing with Nerida Wilson, a marine biologist at the Western Australian Museum in Perth and the expedition's chief scientist. Kaycee Handley, a master's student in Macquarie University in Sydney, is sitting in rapt attention. The *Falkor*'s remote submersible had just spotted a massive siphonophore, a colonial organism related to corals, sea anemones and jellyfish. We're still working on modelling the creature, but it's clearly well over 100 metres long, much longer than any animal previously recorded.

The screen shows the submersible's robot arm using a suction tube to collect a sample from the siphonophore. We're still sequencing the DNA to confirm the species. The description of the organism will be the first paper to come out of this cruise.

I also found my worms, including a new species of 'green bomber' that sheds glowing spheres to distract predators, and a new species of squid worm (genus *Teuthidodrilus*), so named because it has ten 'tentacles', including two for feeding.

As an Australian working in California, it was gratifying to be doing fieldwork in my home country. The oceans off Australia are an undiscovered world, and I'd hoped to be on the entire month-long cruise. But I had to go back to my laboratory halfway through, when the coronavirus began interrupting travel.

The *Falkor* is an amazing ship with an amazing crew. It offers a wonderful combination of science and outreach. I felt privileged to be on board.

Greg Rouse is a marine biologist at the Scripps Institution of Oceanography at the University of California, San Diego. **Interview by Chris Woolston.**

Matters arising

Heat detection by the TRPM2 ion channel

https://doi.org/10.1038/s41586-020-2510-7

Received: 11 September 2019

Accepted: 18 March 2020

Bruno Vilar[1], **Chun-Hsiang Tan**[1,2,3] & **Peter A. McNaughton**[1]✉

ARISING FROM I. Vandewauw et al. *Nature* https://doi.org/10.1038/nature26137 (2018)

The molecular mechanisms that underlie the distinct sensations of warmth and heat have remained unclear until recently. In 2016 we showed that the transient receptor potential (TRP) ion channel TRPM2 mediates the sensation of warmth in vivo in mice[1], whereas in 2018 Vandewauw et al.[2] found that three channels—TRPV1, TRPM3 and TRPA1—jointly mediate the sensation of painful heat. However, there was a discrepancy between the studies: we found that TRPM2 contributed to the thermal response of isolated somatosensory neurons[1,3], whereas Vandewauw et al.[2] proposed that TRPA1—and not TRPM2—was the only thermally activated ion channel in somatosensory neurons apart from TRPV1 and TRPM3[2]. Here we show that both TRPM2 and TRPA1, in addition to the established thermosensory ion channels TRPV1 and TRPM3, drive responses of sensory neurons to increases of temperature.

In our original paper[1] we used calcium imaging to show that around 10% of somatosensory neurons from the dorsal root ganglia (DRG) were activated by heat but did not express either functional TRPV1 or TRPM3, and we proposed that the thermal response in these neurons was driven by TRPM2. Here we use a similar method to test whether expression of TRPA1 could instead be the cause of thermal responses in these neurons (Fig. 1a; for the protocol of solution application see Fig. 2a), as proposed by Vandewauw et al.[2]. Figure 1a shows that responses to the selective TRPA1 agonist allyl isothiocyanate (AITC) are observed in around 25% of all DRG neurons, almost all of which (24%) also express TRPV1 and/or TRPM3, in agreement with previous studies[4,5]. A similar result was obtained in neurons from the trigeminal ganglia (TG)—which innervate the face and head—in which 41.5% in total express TRPA1, of which only 2.5% express TRPA1 in the absence of both TRPV1 and TRPM3 (Extended Data Fig. 1a). Notably, around 10% of DRG neurons, and 8% of TG neurons, were activated by heat but did not express functional TRPA1, TRPV1 nor TRPM3—similar to the proportion of TRPM2-expressing neurons identified in our original study[1].

Figure 1b shows that genetic deletion of *Trpm2* reduced the proportion of neurons in which thermal responses are not attributable to any of TRPV1, TRPM3 or TRPA1 from 10% to 3%, without significantly changing the proportions of neurons in other classes; this is consistent with TRPM2 driving the majority of thermal responses that are independent of TRPV1, TRPM3 and TRPA1. Apart from neurons expressing TRPM2 in isolation, thermal responses attributable to TRPM2 are also co-expressed with TRPV1 and TRPM3[1]. Figure 1c confirms this by showing that 38% of neurons remain thermally activated when responses mediated by TRPV1, TRPM3 and TRPA1 are blocked by selective antagonists. Genetic deletion of *Trpm2* reduces the proportion of neurons responding to heat when TRPV1, TRPM3 and TRPA1 are blocked from around 38% to around 7% (Fig. 1d). The small remaining proportion of unidentified heat-responsive neurons generate responses that are not attributable to any of TRPV1, TRPM3, TRPA1 or TRPM2. The mean response amplitude in wild-type neurons in the presence of inhibitors of TRPV1, TRPM3 and TRPA1 (Fig. 1c) was $\Delta F_{340}/F_{380} = 1.90 \pm 0.06$ (where F_{340}/F_{380} is the ratio of fluorescence intensities excited at 340 nm and 380 nm), whereas for unidentified heat responses (Fig. 1d) the response amplitude was $\Delta F_{340}/F_{380} = 1.59 \pm 0.16$ (Fig. 1e). The unidentified heat response may be due to the expression of an additional heat-sensitive mechanism—perhaps involving the anion channel Anoctamin 1[6]—although the possibility that it may be due to a non-specific response to heat cannot be excluded.

An alternative approach to determining the role of TRPM2 is to use a selective pharmacological blocker. We chose 2-aminoethoxydiphenyl borate (2-APB), which largely blocks TRPM2 at a concentration[7] of 25 µM, although higher concentrations activate members of the TRPV family[8–10]. Figure 2a, b shows that the response amplitude in thermally activated neurons with responses that are not attributable to TRPV1, TRPM3 or TRPA1 is strongly inhibited by 2-APB. When neurons from *Trpm2*$^{-/-}$ mice were tested in the same way (Fig. 2c), there was no significant effect of 2-APB on the amplitude of the small number of 'unidentified' thermal responses.

In neurons responding to only one of the agonists for TRPV1, TRPM3 or TRPA1 (Extended Data Fig. 2a), 2-APB caused a small reduction in thermal response amplitude (not significant in the case of the very small number of neurons expressing only TRPA1 in isolation). Because many neurons co-express TRPM2 with other TRP channels (Fig. 1c, d) it is likely that this reduction in response is due to an inhibitory effect of 2-APB on co-expressed TRPM2. Extended Data Fig. 2b supports this possibility, because in neurons from *Trpm2*$^{-/-}$ mice there was either no change in response amplitude upon application of 2-APB, or an increase in response amplitude in the case of TRPV1, which is known to be activated by 2-APB[8–10].

These experiments show that the responses of the TRPM2-expressing neurons identified in our original study[1] are not due to the expression of TRPA1, as was proposed by Vandewauw et al.[2]. Thermal responses that are not attributable to TRPV1, TRPM3 or TRPA1 are almost completely eliminated by either genetic deletion of *Trpm2* or pharmacological block of TRPM2, confirming our original proposal that these neurons express TRPM2[1].

We sought to identify the cause of the discrepancy between the above results and the work of Vandewauw et al.[2]. Changing the source of neurons (DRG or TG), the order of application of agonists and the heat stimulus, the culture conditions, the rise time of heat application and the starting temperature did not explain the discrepancy (Extended Data Fig. 1). However, terminating the temperature ramp at a lower level of 45 °C—as used by Vandewauw et al.[2]—rather than at the temperature of 48 °C used in our experiments, sharply reduced the proportion of heat-sensitive neurons with responses that are not attributable to TRPV1, TRPM3 or TRPA1 (Fig. 2a, d, e). This suggests that the reason why Vandewauw et al.[2] did not identify thermally activated neurons expressing TRPM2 was that their heat stimulus did not reach a sufficiently high temperature to activate TRPM2 in these isolated neurons.

---

[1]Wolfson Centre for Age-Related Diseases, King's College London, London, UK. [2]Department of Neurology, Kaohsiung Medical University Hospital, Kaohsiung Medical University, Kaohsiung, Taiwan. [3]Graduate Institute of Clinical Medicine, College of Medicine, Kaohsiung Medical University, Kaohsiung, Taiwan. ✉e-mail: peter.mcnaughton@kcl.ac.uk

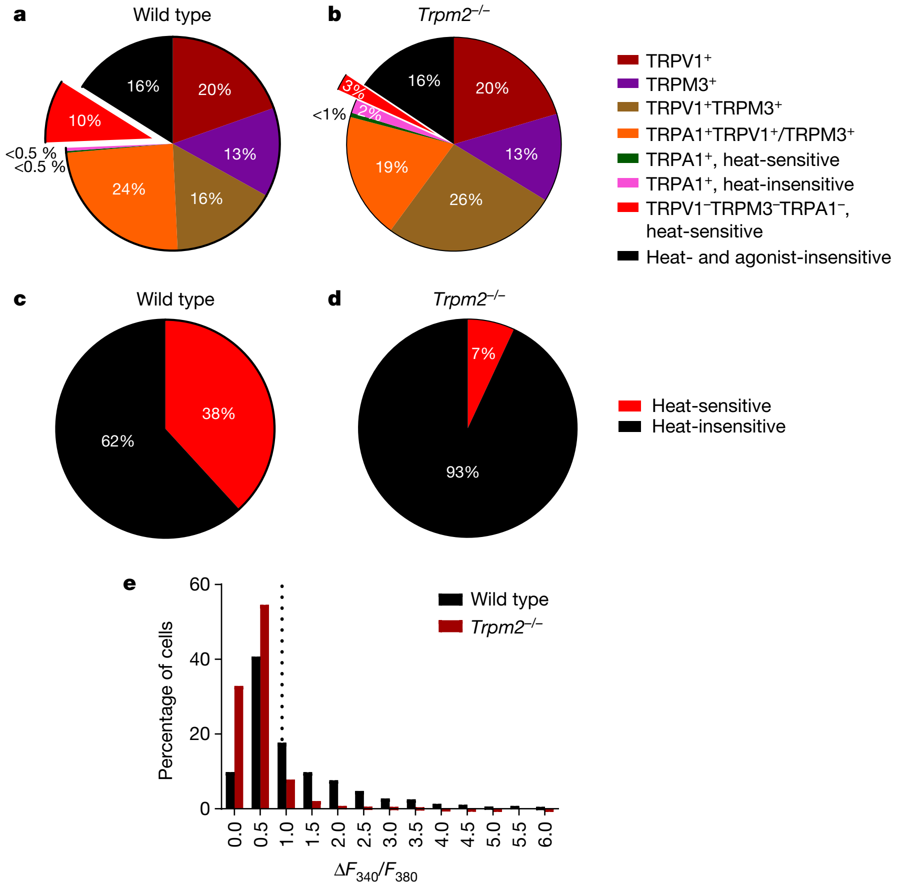

Fig. 1 | A fraction of thermally activated somatosensory neurons does not express TRPV1, TRPM3 or TRPA1. a, Proportions of DRG neurons expressing TRPV1, TRPM3 and TRPA1, and of heat-sensitive neurons expressing none of these TRP channels, obtained from increases in F_{340}/F_{380} in response to the application of selective agonists (see Methods for details). The experimental protocol is shown in Fig. 2a (except that TRPM2 blocker 2-APB was not applied). The pie chart shows mean data from 3 experiments as follows: neurons expressing only TRPV1 (19.6 ± 2.0%, mean ± s.e.m.); only TRPM3 (13.5 ± 0.2%); both TRPV1 and TRPM3 but not TRPA1 (16.2 ± 3.5%); TRPA1 together with either TRPV1 or TRPM3 (24.4 ± 1.6%); TRPA1 alone and responding to heat (0.2 ± 0.1%); TRPA1 alone and not responding to heat (0.5 ± 0.2%); heat-sensitive neurons not responding to agonists for any of TRPV1, TRPM3 or TRPA1 (9.5 ± 0.2%); and neurons not responding to heat nor to any of the TRP agonists but identified as viable from their response to a final pulse of KCl (16.1 ± 2.6%). See criteria in Methods for the identification of positive heat and agonist responses. Data from $n = 1{,}563$ neurons, 13 coverslips from 3 wild-type mice. **b**, Similar experiment performed on DRG neurons from *Trpm2*$^{-/-}$ mice. There is no significant difference in the proportions of any of the agonist-sensitive neurons compared with the wild type ($P > 0.05$, multiple *t*-test with Bonferroni correction). However, the proportion of heat-sensitive neurons with responses that are not attributable to TRPV1, TRPM3 or TRPA1 is significantly reduced by deletion of *Trpm2*, from 9.5 ± 0.2% in the wild type to 2.5 ± 0.8% in *Trpm2*$^{-/-}$ mice ($P = 0.009$, multiple *t*-test with Bonferroni correction). Data from $n = 660$ neurons, 14 coverslips from 3 *Trpm2*$^{-/-}$ mice. **c**, Proportion of DRG neurons responding to heat in the presence of an inhibitor cocktail blocking TRPV1, TRPM3 and TRPA1. See Extended Data Fig. 1c, top trace, for protocol. The mean percentage of heat-responsive neurons is 38.2 ± 4.4% and $\Delta F_{340}/F_{380} = 1.90 \pm 0.06$ (mean ± s.e.m.). Data from $n = 1{,}315$ neurons, 4 wild-type mice. **d**, Similar experiment to that shown in **c**, but on DRG neurons from *Trpm2*$^{-/-}$ mice. The mean percentage of 'unidentified' neurons with heat responses that are not attributable to TRPV1, TRPM3, TRPA1 nor TRPM2 was 6.9 ± 2.2% (mean ± s.e.m., significant difference from wild type, $P = 0.0007$, unpaired *t*-test) with $\Delta F_{340}/F_{380} = 1.59 \pm 0.16$ (mean ± s.e.m., significant difference from wild type, $P = 0.0237$, unpaired *t*-test). Data from $n = 1{,}794$ neurons, 4 *Trpm2*$^{-/-}$ mice. **e**, Amplitudes of $\Delta F_{340}/F_{380}$ in response to heat ramp from the experiments shown in **c** (wild-type neurons) and **d** (*Trpm2*$^{-/-}$ neurons). The threshold for accepting a significant heat response is shown by the vertical dotted line, which gives the intrinsic heat-sensitivity of the fura2 dye obtained from a heat ramp applied in a Ca-free solution (see details in Methods). Mean values of $\Delta F_{340}/F_{380}$ for neurons exceeding the threshold are given in **c** and **d**.

The deletion of *Trpm2* alters the behavioural sensation of warmth in vivo[1], but does not affect thermal sensation in the range of noxious heat, at temperatures of 42 °C and greater[1,3,11]. In addition, noxious heat sensation is abolished when *Trpv1*, *Trpm3* and *Trpa1*—but not *Trpm2*—are deleted[2]. These observations suggest that TRPM2 is activated in the range of 30 °C to 40 °C in vivo. However, the experiments described here show that, following neuronal isolation, the temperature threshold increases into the noxious temperature range, as is also found in expression systems[12]. A possible explanation is that a factor regulating the thermal sensitivity of TRPM2 may be lost following neuronal isolation.

Finally, we tested whether somatosensory neurons expressing TRPA1 can respond to thermal stimuli, as proposed by Vandewauw et al.[2]. We tested the heat sensitivity of identified TRPA1-expressing neurons from *Trpm2*$^{-/-}$ mice, in which TRPV1 and TRPM3 were pharmacologically blocked (Extended Data Fig. 3). We found that around 30% of all neurons were activated by a TRPA1 agonist—similar to the proportion of TRPA1-expressing neurons in the experiments shown in Fig. 1. In 34.7% of these TRPA1^{+} neurons we observed a response to heat that was inhibited by blocking TRPA1. In a further 5.5% of the total number of neurons, the response to heat was not due to any of TRPM2, TRPV1, TRPM3 nor TRPA1 (unidentified heat-responders, see also Fig. 1d). We conclude that TRPA1—often assumed to be activated only by cold[13]—does contribute to heat responses in somatosensory neurons, as reported by Vandewauw et al.[2]. In summary, there is clear evidence that TRPV1, TRPM3, TRPM2 and TRPA1 contribute to the thermal responses of somatosensory neurons,

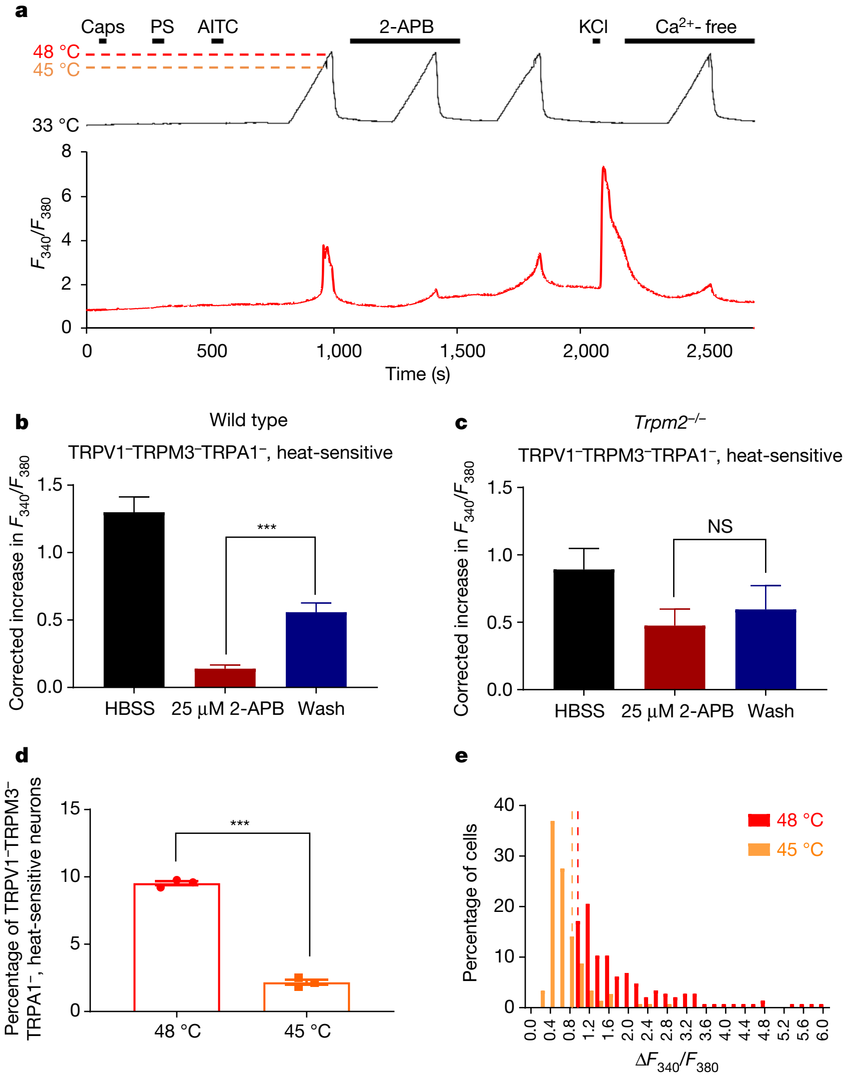

Fig. 2 | Pharmacological block of TRPM2 inhibits the heat response of heat-sensitive neurons not expressing TRPV1, TRPM3 or TRPA1. a, Effect of pharmacological block of TRPM2 on identified somatosensory neurons. Neurons expressing TRPV1, TRPM3 and/or TRPA1 were identified by brief application of the specific agonists capsaicin (Caps, 1 µM), pregnenolone sulfate (PS, 100 µM) and AITC (50 µM), respectively, followed by a heat ramp to 48 °C to activate all heat-sensitive neurons. The effect of the TRPM2 blocker 2-APB (25 µM) on heat-activated neurons was tested, followed by a pulse of KCl (50 mM) to test the viability of all neurons. At the end, the heat pulse was repeated in Ca-free solution to identify changes in F_{340}/F_{380} ($\Delta F_{340}/F_{380}$) arising from sensitivity of the fura2 dye to temperature. The example trace shows that the response to heat in a neuron not expressing any of TRPV1, TRPM3 or TRPA1 is strongly suppressed by the TRPM2 blocker 2-APB (25 µM). **b**, The increase in calcium-dependent fluorescence ratio F_{340}/F_{380} in response to heat in heat-sensitive neurons with responses that are not attributable to TRPV1, TRPM3 or TRPA1 is strongly suppressed by 2-APB (25 µM) ($n = 149$ neurons from 3 wild-type mice). The increase in F_{340}/F_{380} is corrected for each neuron by subtracting the increase in F_{340}/F_{380} measured from the heat ramp applied in Ca-free solution (see Fig. 2a). HBSS, Hank's balanced salt solution. **c**, Similar experiment on *Trpm2*$^{-/-}$ neurons. The few heat-sensitive neurons with responses that are not attributable to TRPV1, TRPM3 or TRPA1 (Fig. 1b) show no significant effect of 2-APB on response amplitude ($n = 20$ neurons from 3 *Trpm2*$^{-/-}$ mice). **d**, The percentage of responding neurons activated at 48 °C (ref. [1]) or at an earlier time point when the temperature had reached 45 °C (ref. [2]), as shown in **a**. The lower temperature reduced the proportion of heat-sensitive neurons with responses that are not attributable to TRPV1, TRPM3 or TRPA1 from 9.5 ± 0.2% in response to heating to 48 °C to 2.2 ± 0.2% in response to heating to 45 °C ($P < 0.0001$, unpaired t-test). $n = 1{,}563$ neurons from 3 wild-type mice. **e**, Amplitudes of $\Delta F_{340}/F_{380}$ in response to heat ramp reaching 48 °C and 45 °C, from experiments shown in **a**. The threshold for designating a heat response is shown by vertical dotted lines, which show the intrinsic heat sensitivity of the fura2 dye obtained from heat ramp applied in a Ca-free solution (see details in Methods). The mean $\Delta F_{340}/F_{380}$ in response to 48 °C was 2.04 ± 0.11 and to 45 °C was 0.67 ± 0.03 ($n = 149$ neurons, $P < 0.0001$, unpaired t-test).

and that a further unidentified heat sensor is present in a small minority of neurons.

Methods

Mice

Male mice on a C57BL/6J background, 9–18 weeks old, were used for all experiments. *Trpm2*$^{-/-}$ mice were a gift from Y. Mori. Mice were maintained on a 12 h light/12 h dark cycle.

Primary neuron cultures

Mice were euthanized by cervical dislocation, after which DRG or TG ganglia were excised then incubated in papain (2 mg ml^{-1} in Ca^{2+}-free and Mg^{2+}-free HBSS) for 30 min at 37 °C, followed by incubation in collagenase (2.5 mg ml^{-1} in Ca^{2+}-free and Mg^{2+}-free HBSS) for 30 min at 37 °C. Ganglia were re-suspended and mechanically dissociated in Neurobasal-A/B27 growing medium, which was prepared with Neurobasal-A medium supplemented with 0.25% (v/v) L-glutamine

200 mM (Invitrogen), 2% (v/v) B-27 supplement (Invitrogen), 1% (v/v) penicillin/streptomycin (Invitrogen) and nerve growth factor (NGF) (Sigma-Aldrich) at $50\ \mathrm{ng\ ml^{-1}}$ unless otherwise specified in the figure legends. Dissociated neurons were centrifuged and plated onto coverslips pre-coated with poly-L-lysine ($10\ \mu\mathrm{g\ ml^{-1}}$) and laminin ($40\ \mu\mathrm{g\ ml^{-1}}$). Neurons were kept in a 37 °C incubator with a 95% air/5% CO_2 atmosphere for at least 12 h before use, and all neurons were used within 24 h.

Extracellular solutions and perfusion system

Unless otherwise specified, all experiments were carried out with an extracellular solution containing 140 mM NaCl, 4 mM KCl, 1.8 mM $CaCl_2$, 1 mM $MgCl_2$, 10 mM HEPES and 5 mM glucose; the pH was adjusted to 7.4 with NaOH and the osmolarity was between 295–310 mOsm. Calcium-free extracellular solution was prepared with the formulation above except for the omission of calcium chloride. An eight-line manifold gravity-driven system controlled by an automated solution changer with a common outlet was used to apply solution to the cells. The solution was heated with a Peltier device regulated by a proportional gain feedback controller designed by V. Vellani (CV Scientific). In separate control experiments, the temperature in each experimental protocol was recorded daily by a miniature thermocouple at the cell location. All compounds applied were prepared as stock solutions first and then diluted to the concentration needed before experiments. Drugs used were 1 μM capsaicin (5 mM stock in ethanol), 100 μM pregnenolone sulfate (500 mM stock in DMSO), 25 μM 2-APB (500 mM stock in DMSO), 50 μM AITC (200 mM stock in DMSO), 100 μM HC030031 (100 mM stock in DMSO), 10 μM naringenin (100 mM stock in DMSO) and 5 μM AMG9810 (50 mM stock in DMSO). The inhibitor cocktail in Fig. 1c–e and Extended Data Fig. 1c was composed of the TRPA1 antagonist HC030031, the TRPV1 antagonist AMG9810 and the TRPM3 antagonist naringenin. A similar inhibitor cocktail but with the TRPA1 antagonist omitted for part of the experiment was used in Extended Data Fig. 3.

Calcium imaging

Cells were loaded with 5 μM fura-2-AM (Invitrogen) with 0.02% (v/v) pluronic acid (Invitrogen) in Neurobasal-A medium for 30 min at 37 °C. After loading, coverslips were placed in an imaging chamber in extracellular solution as above and transferred to a Nikon Eclipse Ti-E inverted microscope. Cells were continuously perfused with extracellular solution and were illuminated with a monochromator alternating between 340 nm and 380 nm (OptoScan; Cairn Research), controlled by WinFluor 3.2 software (J. Dempster, University of Strathclyde, UK). Emission was collected at 510 nm and the resulting pairs of images were acquired every two seconds with a 100-ms exposure time using an iXon 897 EM-CCD camera (Andor Technology). Image time series were converted to TIFF files and processed with ImageJ software. Images of the background fluorescence intensity were obtained for both wavelengths and subtracted from the respective image stack before calculating the F_{340}/F_{380} images. A minority of neurons exhibited an unstable F_{340}/F_{380} baseline in the absence of any applied stimulus—usually caused by poor dye loading but in some cases apparently due to low-frequency repetitive firing even in the absence of any treatment—and were removed from analysis. A positive response to all agonists was defined from the rate of increase of F_{340}/F_{380} ratio after agonist application between two consecutive time points after the application of the agonist, which exceeds the mean + 3.09 s.d. (cumulative probability value of 99.9%) of all such differences in the absence of any agonist. A heat-sensitive neuron is defined as a neuron with a peak increase in F_{340}/F_{380} during a heat stimulus that is larger than the mean + 3.09 s.d. of the peak increase in F_{340}/F_{380} during a heat stimulus in Ca-free solution in the same experiment (see Fig. 2a).

Statistical analysis

All data are expressed as mean ± s.e.m. Statistical analyses were performed with GraphPad Prism version 7.04 and data were tested for approximation to normality. All statistical tests were two-sided. All measurements were taken from distinct samples. The statistical test used is stated in each figure legend.

Ethical approval

Ethical approval was given by the Animal Welfare Ethical Review Board, King's College London and by the Home Office, UK Government. In the case of the experiment shown in Extended Data Fig. 1a, approval was given by the Institutional Animal Care and Use Committee, Kaohsiung Medical University.

Reporting summary

Further information on research design is available in the Nature Research Reporting Summary linked to this paper.

Data availability

All data are available from the corresponding author upon reasonable request.

1. Tan, C. H. & McNaughton, P. A. The TRPM2 ion channel is required for sensitivity to warmth. *Nature* **536**, 460–463 (2016).
2. Vandewauw, I. et al. A TRP channel trio mediates acute noxious heat sensing. *Nature* **555**, 662–666 (2018).
3. Tan, C. H. & McNaughton, P. A. TRPM2 and warmth sensation. *Pflugers Arch*. **470**, 787–798 (2018).
4. Bautista, D. M. et al. Pungent products from garlic activate the sensory ion channel TRPA1. *Proc. Natl Acad. Sci. USA* **102**, 12248–12252 (2005).
5. Bautista, D. M. et al. TRPA1 mediates the inflammatory actions of environmental irritants and proalgesic agents. *Cell* **124**, 1269–1282 (2006).
6. Cho, H. et al. The calcium-activated chloride channel anoctamin 1 acts as a heat sensor in nociceptive neurons. *Nat. Neurosci*. **15**, 1015–1021 (2012).
7. Togashi, K., Inada, H. & Tominaga, M. Inhibition of the transient receptor potential cation channel TRPM2 by 2-aminoethoxydiphenyl borate (2-APB). *Br. J. Pharmacol*. **153**, 1324–1330 (2008).
8. Chung, M. K., Lee, H., Mizuno, A., Suzuki, M. & Caterina, M. J. 2-aminoethoxydiphenyl borate activates and sensitizes the heat-gated ion channel TRPV3. *J. Neurosci*. **24**, 5177–5182 (2004).
9. Hu, H., Grandl, J., Bandell, M., Petrus, M. & Patapoutian, A. Two amino acid residues determine 2-APB sensitivity of the ion channels TRPV3 and TRPV4. *Proc. Natl Acad. Sci. USA* **106**, 1626–1631 (2009).
10. Mamatova, K. N. & Kang, T. M. Activation of rat transient receptor potential cation channel subfamily V member 1 channels by 2-aminoethoxydiphenyl borate. *Integr. Med. Res*. **2**, 112–123 (2013).
11. Haraguchi, K. et al. TRPM2 contributes to inflammatory and neuropathic pain through the aggravation of pronociceptive inflammatory responses in mice. *J. Neurosci*. **32**, 3931–3941 (2012).
12. Kashio, M. et al. Redox signal-mediated sensitization of transient receptor potential melastatin 2 (TRPM2) to temperature affects macrophage functions. *Proc. Natl Acad. Sci. USA* **109**, 6745–6750 (2012).
13. Peier, A. M. et al. A TRP channel that senses cold stimuli and menthol. *Cell* **108**, 705–715 (2002).

Acknowledgements We thank T. Buijs for discussions. This work was supported by Wellcome Trust Investigator Award grant 205006/Z/16/Z to P.A.M. and by grants from the Ministry of Science and Technology, Taipei, Taiwan (MOST 106-2314-B-037-097-MY2 and MOST 108-2320-B-037-034-MY3) to C.-H.T.

Author contributions All authors planned the study and co-wrote the manuscript. B.V. carried out all experimental work except that presented in Extended Data Fig. 1a, which was carried out by C.-H.T.

Competing interests The authors declare no competing interests.

Additional information

Supplementary information is available for this paper at https://doi.org/10.1038/s41586-020-2510-7.

Correspondence and requests for materials should be addressed to P.A.M.

Reprints and permissions information is available at http://www.nature.com/reprints.

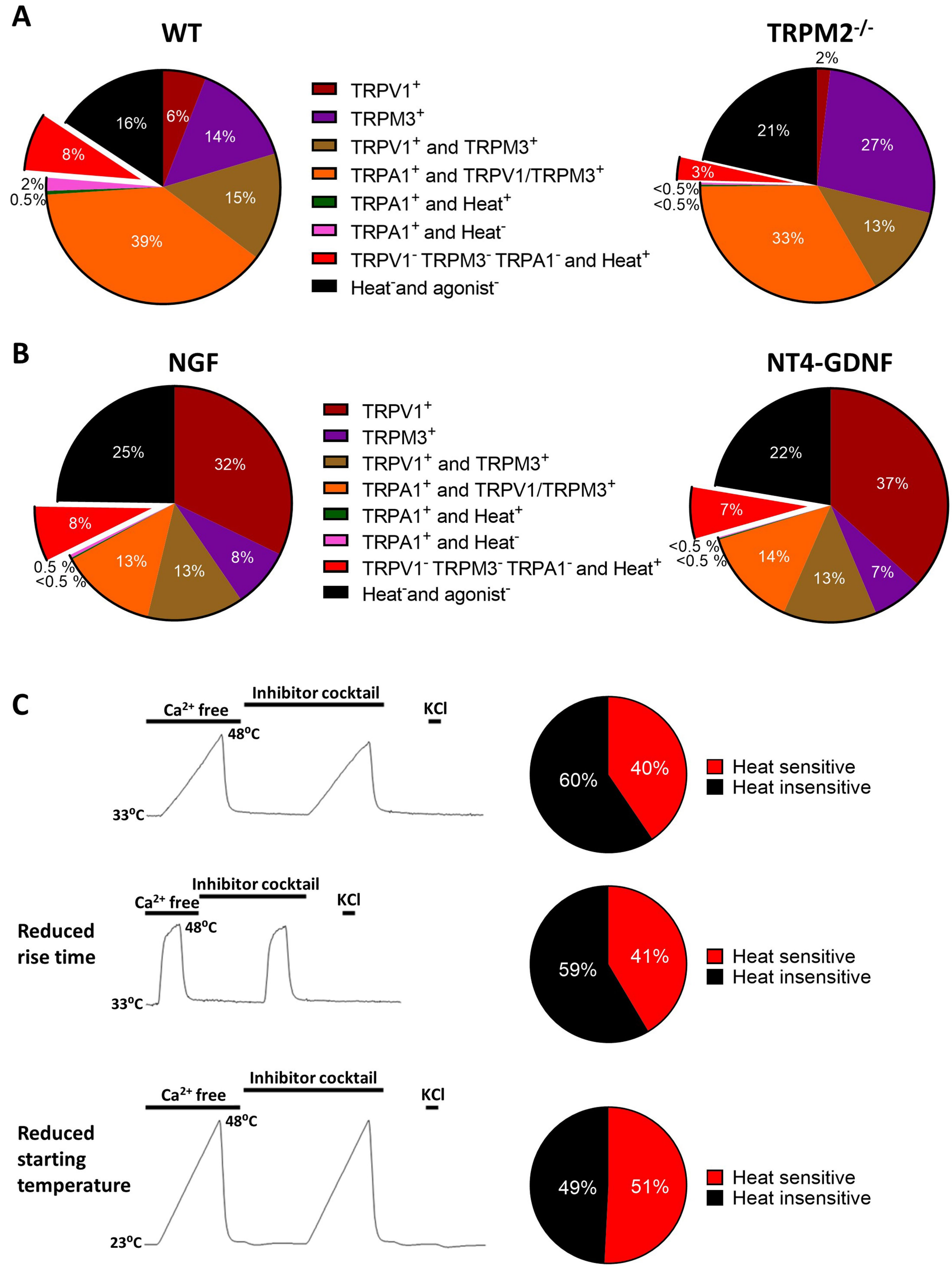

Extended Data Fig. 1 | See next page for caption.

Extended Data Fig. 1 | Changing the source of neurons, the order of application of agonists and the heat stimulus, the culture conditions, the rise time of heat application and the starting temperature do not significantly affect the proportions of heat-sensitive neurons with responses that are not attributable to TRPV1, TRPM3 or TRPA1 . a, Neurons from the TG were tested for heat and agonist sensitivity. Left, percentage distributions of heat-sensitive and agonist-sensitive neurons. TRPA1 is strongly co-expressed with TRPV1 or TRPM3 (39%), with few neurons expressing TRPA1 alone (2.5%). Heat-sensitive neurons that respond to heat but do not express any of TRPV1, TRPM3 or TRPA1 can be clearly identified (8%). $n = 388$ neurons from 1 wild-type mouse. Right, similar experiment on $n = 382$ TG neurons from 1 *Trpm2*$^{-/-}$ mouse. The proportion of heat-sensitive neurons with responses that are not attributable to TRPV1, TRPM3 or TRPA1 is significantly reduced compared with the wild type (from 8% to 3%, $P = 0.0077$, Fisher's exact test). The mean response amplitude of heat-sensitive neurons with responses that are not attributable to TRPV1, TRPM3 or TRPA1 was not significantly reduced by deletion of *Trpm2* ($\Delta F_{340}/F_{380} = 1.13 \pm 0.05$, $n = 31$ for wild type to 0.96 ± 0.08, $n = 13$ for *Trpm2*$^{-/-}$, difference not significant, $P = 0.0539$, unpaired *t*-test). **b**, Neurons from the DRG were tested for heat and agonist sensitivity using the protocol shown in Fig. 2a, but without the application of 2-APB and with agonists presented after heat rather than before. Left, neurons were cultured for 12 h in NGF[1]. See Methods for details. The pie chart shows data from 3 experiments on a total of 1,312 neurons from 3 wild-type mice on 12 coverslips as follows: neurons expressing only TRPV1 (32.2 ± 4.2%, mean ± s.e.m.); only TRPM3 (8.2 ± 1.2%); both TRPV1 and TRPM3 but not TRPA1 (13.3 ± 0.6%); TRPA1 together with either TRPV1 or TRPM3 (13.3 ± 0.9%); TRPA1 alone and responding to heat (0.2 ± 0.2%); TRPA1 alone and not responding to heat (0.4 ± 0.2%); heat-sensitive neurons responding to heat but not to agonists for any of TRPV1, TRPM3 or TRPA1 (7.6 ± 2.0%); and neurons not responding to heat nor to any of the TRP agonists but that were identified as viable from their response to a final pulse of KCl (24.8 ± 1.8%). The application of agonists before (Fig. 1a) or after the heat pulse (this Figure) does not significantly affect the proportion of heat-sensitive neurons with responses that are not attributable to TRPV1, TRPM3 or TRPA1 (9.5 ± 0.2% when agonists are applied before (Fig. 1a) and 7.6 ± 2.0% when applied after, $P = 0.3740$, unpaired *t*-test). The proportions of neurons in other categories are also not significantly affected, apart from a small reduction in the proportion of neurons expressing TRPA1 in combination with TRPV1 and/or TRPM3 (compare with Fig. 1a). Right, neurons cultured for 12 h in medium containing glial cell line-derived neurotrophic factor (GDNF) at 2 ng ml^{-1} and neurotrophin 4 (NT4) at 10 ng ml^{-1}, the same culture protocol used by Vandewauw et al.[2]. $n = 1{,}521$ neurons from 3 wild-type mice on 12 coverslips. The altered culture conditions had no significant effect on the proportions of heat-sensitive and agonist-sensitive neurons ($P > 0.05$, multiple *t*-test with Bonferroni correction). **c**, Left, protocols for determining the total proportion of DRG neurons in which heat responses are partly driven by a mechanism independent of TRPV1, TRPM3 or TRPA1. The heat ramp is first applied in a Ca-free solution, to identify changes in the F_{340}/F_{380} fluorescence ratio ($\Delta F_{340}/F_{380}$) arising from sensitivity of the fura2 dye to temperature, followed by an identical ramp in the presence of a cocktail of inhibitors of TRPV1 (AMG9810, 5 μM), TRPM3 (naringenin, 10 μM) and TRPA1 (HC-030031, 100 μM) (see details in Methods). A final pulse of KCl confirms viability of the neurons. Right, top: heat application in which the temperature was increased from 33 °C to 48 °C over 180 s (ref. [1]). $n = 710$ neurons from 2 wild-type mice on 3 coverslips. Middle, heat application in which the temperature was increased from 33 °C to 48 °C over 25 s (ref. [2]). $n = 99$ neurons from 1 wild-type mouse on 2 coverslips. Bottom, heat application in which the temperature was increased from 23 °C to 48 °C over 180 s (ref. [2]). $n = 657$ neurons from 1 wild-type mouse on 2 coverslips. Reducing the rise time of heat application or the starting temperature does not reduce the total proportion of heat-sensitive neurons with responses that are not attributable to TRPV1, TRPM3 or TRPA1. Differences not significant, $P = 0.9197$ (middle) and 0.3339 (bottom) respectively, unpaired *t*-test compared to top panel.

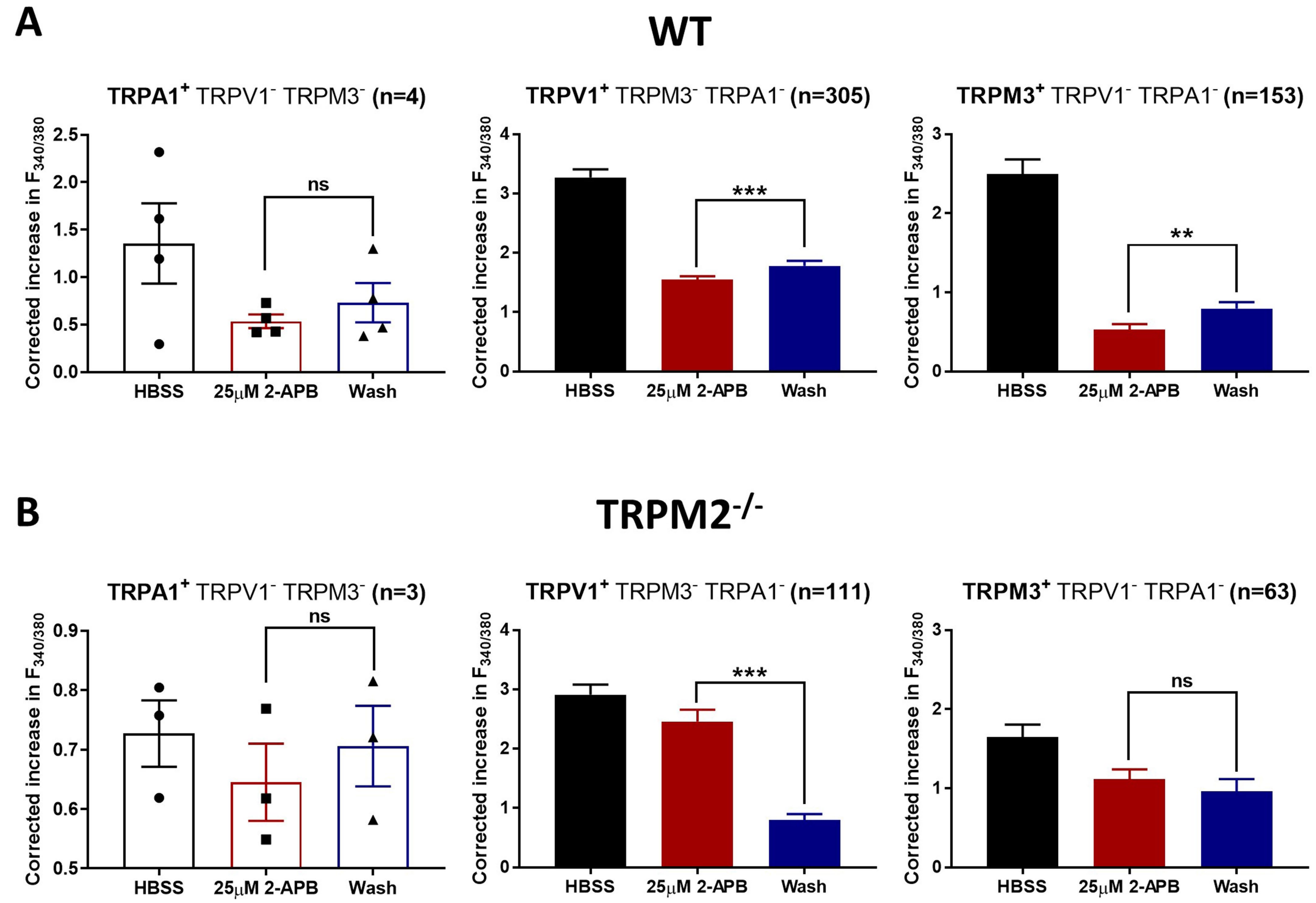

Extended Data Fig. 2 | Effect of TRPM2 blocker 2-APB on heat responses in neurons expressing only one of TRPA1, TRPV1 or TPRPM3. Neurons were identified as expressing only one of TRPA1 (left), TRPV1 (middle) or TRPM3 (right) and the effect of 2-APB (25 μM) was tested as shown in Fig. 2a. **a**, Wild-type neurons. Note that many of these neurons will co-express TRPM2, which is extensively expressed in somatosensory neurons (Fig. 1c). **b**, Similar experiments on *Trpm2*$^{-/-}$ neurons. Significance level during 2-APB application compared to that after wash is as follows: $^{*}P < 0.05$; $^{**}P < 0.01$; $^{***}P < 0.001$; NS, $P > 0.05$. One-way ANOVA followed by Bonferroni's post hoc correction.

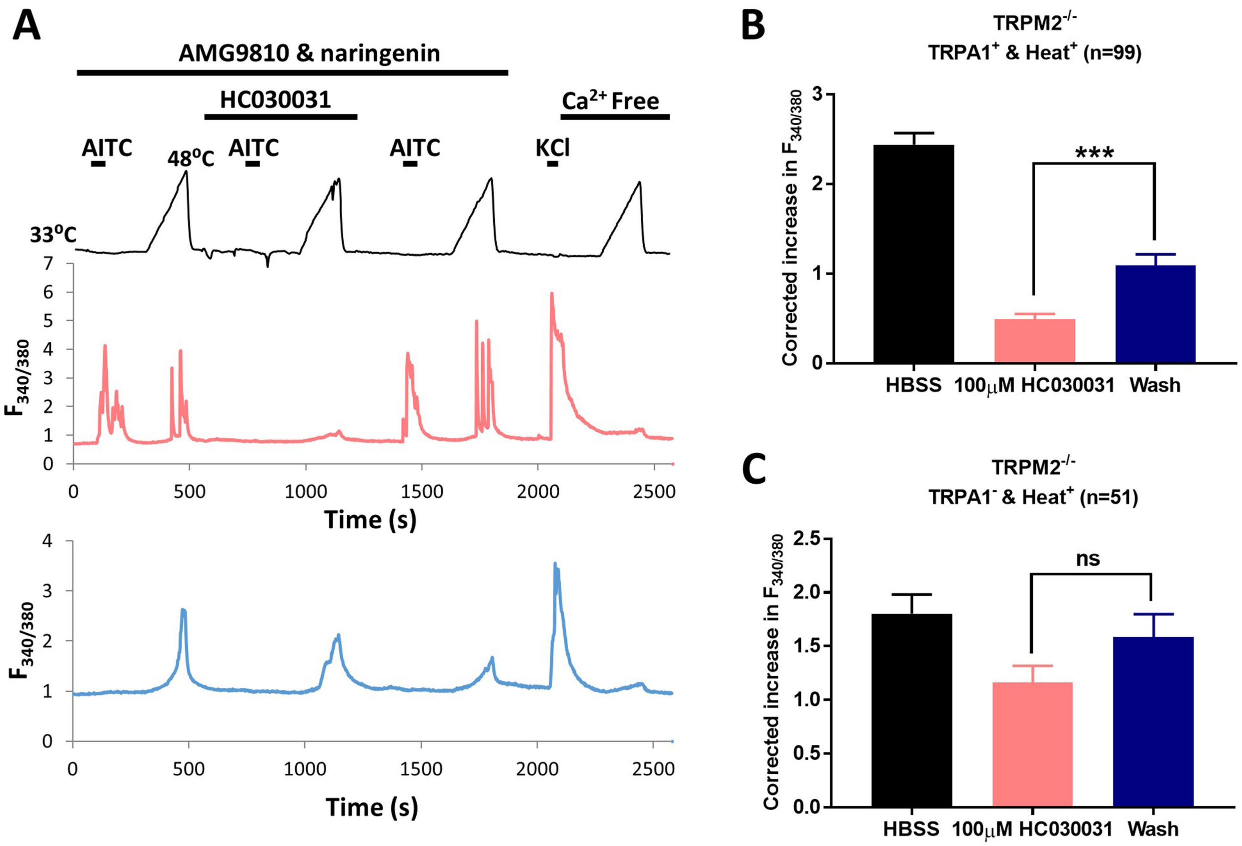

Extended Data Fig. 3 | A fraction of TRPA1$^+$ neurons from *Trpm2$^{-/-}$* mice responds to heat when TRPV1 and TRPM3 are blocked. a, Top trace shows protocol of solution changes used to identify neurons expressing TRPA1 and to test their activation by heat. TRPV1 and TRPM3 were blocked by AMG9810 (5 μM) and naringenin (10 μM) as shown. The calcium increase elicited by a heat ramp from 33 °C to 48 °C was tested in the absence (heat ramps 1 and 3) and the presence (ramp 2) of the TRPA1 blocker HC030031 (100 μM). Responses to the TRPA1-selective agonist AITC were tested as shown. The response to KCl (50 mM) and to the heat ramp in the absence of external Ca was tested at the end. Middle trace shows increases in $F_{340/380}$ in a neuron expressing TRPA1 in which the heat-activated Ca increase was suppressed by the TRPA1 blocker HC030031. TRPA1 was expressed in 31.2 ± 4.2% of the total population, but only a fraction of TRPA1$^+$ neurons (34.7% ± 9.81%) gave a significant Ca increase in response to 48 °C heat. Lower trace shows a different neuron in same preparation that is activated by heat but does not express TRPA1 (unidentified heat-responders). Representative data from 3 separate experiments on a total of 964 neurons. **b**, Heat response in TRPA1-expressing neurons is suppressed by the TRPA1 blocker HC030031 (see **a** for protocol (top) and example trace (middle)). ***$P < 0.001$, one-way ANOVA followed by Bonferroni's post hoc correction. **c**, Heat response in neurons not expressing TRPA1 (unidentified heat-responsive neurons, see **a** for example trace (bottom)) is not significantly reduced by the TRPA1 blocker HC030031 (100 μM). The proportion of unidentified heat-responders (5.5% ± 1.4%) is not significantly different from that in Fig. 1d.

nature research

Corresponding author(s): Peter A. McNaughton
Last updated by author(s): Mar 9, 2020

Reporting Summary

Nature Research wishes to improve the reproducibility of the work that we publish. This form provides structure for consistency and transparency in reporting. For further information on Nature Research policies, see Authors & Referees and the Editorial Policy Checklist.

Statistics

For all statistical analyses, confirm that the following items are present in the figure legend, table legend, main text, or Methods section.

n/a	Confirmed	
☐	☒	The exact sample size (*n*) for each experimental group/condition, given as a discrete number and unit of measurement
☐	☒	A statement on whether measurements were taken from distinct samples or whether the same sample was measured repeatedly
☐	☒	The statistical test(s) used AND whether they are one- or two-sided *Only common tests should be described solely by name; describe more complex techniques in the Methods section.*
☒	☐	A description of all covariates tested
☐	☒	A description of any assumptions or corrections, such as tests of normality and adjustment for multiple comparisons
☐	☒	A full description of the statistical parameters including central tendency (e.g. means) or other basic estimates (e.g. regression coefficient) AND variation (e.g. standard deviation) or associated estimates of uncertainty (e.g. confidence intervals)
☐	☒	For null hypothesis testing, the test statistic (e.g. *F*, *t*, *r*) with confidence intervals, effect sizes, degrees of freedom and *P* value noted *Give P values as exact values whenever suitable.*
☒	☐	For Bayesian analysis, information on the choice of priors and Markov chain Monte Carlo settings
☒	☐	For hierarchical and complex designs, identification of the appropriate level for tests and full reporting of outcomes
☒	☐	Estimates of effect sizes (e.g. Cohen's *d*, Pearson's *r*), indicating how they were calculated

Our web collection on statistics for biologists contains articles on many of the points above.

Software and code

Policy information about availability of computer code

Data collection	Calcium imaging data were collected using WinFluor 3.2 software (J. Dempster, University of Strathclyde, UK). Image time series were converted to TIFF files and processed with ImageJ software. This is stated in Methods
Data analysis	Statistical analyses were performed with GraphPad Prism version 7.04 and data were tested for approximation to normality. This is stated in Methods

For manuscripts utilizing custom algorithms or software that are central to the research but not yet described in published literature, software must be made available to editors/reviewers. We strongly encourage code deposition in a community repository (e.g. GitHub). See the Nature Research guidelines for submitting code & software for further information.

Data

Policy information about availability of data

All manuscripts must include a data availability statement. This statement should provide the following information, where applicable:

- Accession codes, unique identifiers, or web links for publicly available datasets
- A list of figures that have associated raw data
- A description of any restrictions on data availability

All data not provided within the paper are available on request from the authors. This is stated in Methods.

Field-specific reporting

Please select the one below that is the best fit for your research. If you are not sure, read the appropriate sections before making your selection.

☒ Life sciences ☐ Behavioural & social sciences ☐ Ecological, evolutionary & environmental sciences

For a reference copy of the document with all sections, see nature.com/documents/nr-reporting-summary-flat.pdf

Life sciences study design

All studies must disclose on these points even when the disclosure is negative.

Sample size	Sample sizes were determined from prior experience and were typically n>1000 neurons from n> or =3 animals. In Extended Data Fig. 1, smaller numbers of neurons and animals were used but numbers were always enough to give adequate statistical significance.
Data exclusions	Cells that did not respond to a depolarizing solution (see Fig. 2A) were excluded from analysis. A minority of neurons (c. 2%) exhibited an unstable F340/380 baseline in the absence of any applied stimulus, usually caused by poor dye loading but in some cases apparently due to low-frequency repetitive firing even in the absence of any treatment, and were also removed from analysis. This is stated in Methods.
Replication	Individual experiments were conducted on neurons in a single field of view on a single cover slip (typically c. 100 neurons in a single field of view), isolated from a single animal. Experiments were repeated on approx 4 cover slips from each single animal. To control for possible variability between animals this procedure was repeated on typically 3 animals (further details under "Sample Size" above).
Randomization	Not relevant as all animals were of the same strain (C57BL/6J, either WT or TRPM2-/-), were adult (9-18 weeks) and were raised under identical conditions. Stated in Methods.
Blinding	Data collection was automated so blinding was not necessary. The only exception was the exclusion of a small number of neurons exhibiting an unstable baseline, see above, which was judged manually. The proportions of these unstable neurons were similar in different treatment groups. Baseline instability was obvious and there is no possibility that results could have been skewed by biased omission of more neurons from certain treatment groups.

Reporting for specific materials, systems and methods

We require information from authors about some types of materials, experimental systems and methods used in many studies. Here, indicate whether each material, system or method listed is relevant to your study. If you are not sure if a list item applies to your research, read the appropriate section before selecting a response.

Materials & experimental systems

n/a	Involved in the study	
☒	☐	Antibodies
☒	☐	Eukaryotic cell lines
☒	☐	Palaeontology
☐	☒	Animals and other organisms
☒	☐	Human research participants
☒	☐	Clinical data

Methods

n/a	Involved in the study	
☒	☐	ChIP-seq
☒	☐	Flow cytometry
☒	☐	MRI-based neuroimaging

Animals and other organisms

Policy information about studies involving animals; ARRIVE guidelines recommended for reporting animal research

Laboratory animals	Male mice on a C57BL/6J background, 9 -18 weeks old, were used for all experiments. Stated in Methods.
Wild animals	The study did not involve wild animals.
Field-collected samples	The study did not involve samples collected from the field.
Ethics oversight	Ethical approval was given by the Animal Welfare Ethical Review Board, King's College London and by the Home Office, UK Government, or in the case of the experiment shown in Extended Data Fig. 1A, by the Institutional Animal Care and Use Committee, Kaohsiung Medical University. Stated in Methods.

Note that full information on the approval of the study protocol must also be provided in the manuscript.

Reply to: Heat detection by the TRPM2 ion channel

https://doi.org/10.1038/s41586-020-2511-6

Marie Mulier[1,2], Ine Vandewauw[1,2], Joris Vriens[3]✉ & Thomas Voets[1,2]✉

REPLYING TO B. Vilar et al. *Nature* https://doi.org/10.1038/s41586-020-2510-7 (2020)

In a recent study[1], we demonstrated that acute noxious heat sensing in mice depends on a trio of redundant heat-activated transient receptor potential (TRP) ion channels: TRPV1, TRPM3 and TRPA1. In the accompanying Comment[2], Vilar et al. do not challenge the findings of our original study but refer to the role of another heat-activated TRP channel, TRPM2, in mediating heat responses in isolated somatosensory neurons. In an earlier study[3], Tan and McNaughton had proposed that TRPM2 underlies TRPM3- and TRPV1-independent heat responses in isolated neurons and mediates warmth sensing, whereas findings reported in our study did not endorse this conclusion. Here we provide results that reconcile the apparent discordance between these earlier studies. Overall, our data and those of Vilar et al.[2] indicate that TRPM2 can mediate heat responses in isolated sensory neurons, but primarily at temperatures greater than 45 °C.

In 2016, Tan and McNaughton reported a new heat-sensitive mechanism in mouse sensory neurons, independent of the previously identified heat-sensitive TRP channels TRPV1 and TRPM3[3]. Neurons expressing this heat-sensing mechanism were activated by increasing temperatures over a range of temperatures between 34 °C and 48 °C (ref. [3]). These heat responses were potentiated by H_2O_2 and mediated by a calcium-permeable cation channel, leading the authors to propose the redox-sensitive channel TRPM2 as a molecular candidate[3]. In support thereof, Tan and McNaughton found a lower proportion of TRPM3- and TRPV1-independent heat-responsive neurons in TRPM2-deficient mice. Because these mice also exhibited a deficit in the avoidance of non-noxious warm temperatures, they concluded that TRPM2 acts as a warmth sensor in sensory neurons[3].

In our recent study, we demonstrated that acute noxious heat sensing in mice depends on a trio of TRP ion channels: TRPV1, TRPM3 and TRPA1[1]. Using isolated sensory neurons, we showed robust responses to a noxious heat stimulus of 45 °C provided that at least one of these three TRP channels is functional[1]. Notably, the combined elimination of all three TRP channels largely abolished sensory neuronal heat responses, and this was paralleled by loss of heat sensitivity in intact nerve terminals in the skin and a complete deficiency of acute heat-induced pain in vivo[1]. We further reported that residual heat-induced currents and calcium responses in sensory neurons from *Trpm3*$^{-/-}$*Trpv1*$^{-/-}$ double knockout (DKO$^{M3/V1}$) mice are potentiated by H_2O_2, but also that these responses are inhibited by the TRPA1 antagonist HC030031 and are largely abolished in *Trpv1*$^{-/-}$*Trpm3*$^{-/-}$*Trpa1*$^{-/-}$ triple knockout (TKO) mice[1]. We concluded that TRPM3- and TRPV1-independent, H_2O_2-stimulated heat responses are primarily mediated by TRPA1 rather than by TRPM2[1].

In the accompanying Comment, Vilar et al.[2] examine several possible reasons why both studies came to different conclusions regarding the contributions of TRPM2 and TRPA1 (refs. [1,3]). First, we note that their data endorse the contribution of TRPA1 to TRPM3- and TRPV1-independent heat responses. Second, Vilar et al.[2] pinpoint a potential explanation for the discrepancies between the studies concerning the role of TRPM2 in mediating heat responses—namely the stimulation temperature. In our original study[1], we used a 1-min heat pulse that reached a maximum temperature of 45 °C, whereas Tan and McNaughton used a slower temperature ramp with a maximum of 48 °C (ref. [3]) after about 3 min. Vilar et al.[2] now report that activation of the TRPM2-dependent heat responses occurs mostly at temperatures greater than 45 °C. This observation differs quantitatively from the results in their earlier study, in which the majority of TRPM3- and TRPV1-independent heat responses reported thresholds between 34 °C and 44 °C (ref. [3]), but is fully consistent with our earlier conclusion that TRPM2 in somatosensory neurons does not contribute significantly to responses to a 45 °C heat stimulus[1].

To corroborate our earlier conclusion that TRPM2 is not the main mediator of TRPM3- and TRPV1-independent heat responses at temperatures up to 45 °C[1], we performed intracellular calcium-imaging experiments in sensory neurons isolated from the dorsal root ganglia (DRG) and trigeminal ganglia (TG) of DKO$^{M3/V1}$ mice. Neurons were stimulated three times using our standard heat stimulus with a maximum at 45 °C, with the first and third heat stimuli performed in the presence of the TRPM2 antagonist 2-APB (250 µM), and the second application in the absence of this antagonist (Fig. 1a). A large subpopulation of both TG (47%) and DRG (34%) neurons showed robust heat responses to the first stimulation and gradually smaller responses to the second and third stimulus, most probably representing response rundown (Fig. 1a, b). The fact that these responses were not inhibited by 2-APB confirms that they are independent of TRPM2. Only a very small subset of neurons (less than 1% in TG and around 2.5% in DRG) exhibited a robust heat response in the absence, but not in the presence, of 2-APB (Fig. 1a, b).

Combined elimination of TRPV1, TRPM3 and TRPA1 in the TKO mice largely abolished neuronal responses to a 45 °C stimulus[1]. To assess the proposal of Vilar et al.[2] that TRPM2 acts as a heat sensor at higher temperatures, we performed experiments in which we stimulated TKO neurons with a heat ramp reaching a maximum temperature of 50 °C (Fig. 2a). Effectively, we observed robust heat responses in around 32% of the TKO neurons when using this stronger stimulation protocol, and around 90% of these responses were reversibly inhibited by 25 µM 2-APB (Fig. 2a, b). Overall, these data are consistent with the conclusion of Vilar et al.[2] that TRPM2 contributes to heat responses in isolated sensory neurons, but primarily at temperatures greater than 45 °C. To better quantify differences in thermal dependence, we estimated thermal thresholds for sensory neurons exhibiting heat responses attributed

---

[1] Laboratory of Ion Channel Research, VIB Center for Brain & Disease Research, Leuven, Belgium. [2] Department of Cellular and Molecular Medicine, University of Leuven, Leuven, Belgium. [3] Laboratory of Endometrium, Endometriosis & Reproductive Medicine, Department of Development and Regeneration, University of Leuven, Leuven, Belgium.
✉e-mail: Joris.Vriens@kuleuven.be; Thomas.Voets@kuleuven.vib.be

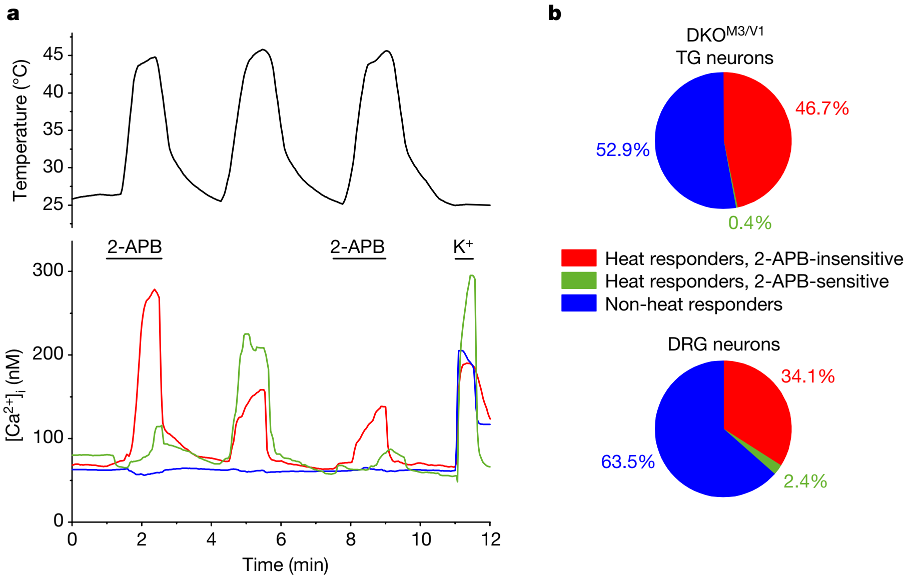

Fig. 1 | TRPV1- and TRPM3-independent responses to a 45 °C heat stimulus are not inhibited by the TRPM2 antagonist 2-APB. a, Representative examples of responses of DKO$^{M3/V1}$ DRG neurons to consecutive heat stimuli with a maximum temperature of 45 °C in the presence and absence of the TRPM2 antagonist 2-APB (250 µM, a supramaximal concentration to ensure full inhibition of TRPM2). $[Ca^{2+}]_i$, intracellular calcium concentration. **b**, Proportion of DKO$^{M3/V1}$ TG neurons ($n = 274$ from 2 mice) and DRG neurons ($n = 452$ from 2 mice) that exhibit 2-APB-sensitive and 2-APB-insensitive heat responses. Data in **a**, **b** are representative of six independent experiments.

either to TRPM2 or to TRPA1 (Fig. 2c). For the 2-APB-insensitive heat responses in DKO$^{M3/V1}$ neurons, which are primarily mediated by TRPA1[1], we obtained an average threshold of 41.3 ± 0.4 °C ($n = 37$). In comparison, 2-APB-sensitive heat responses in TKO neurons, which we attribute to TRPM2, exhibited a significantly higher threshold of 48.0 ± 0.2 °C ($n = 111$; $P < 10^{-5}$; Mann–Whitney test) (Fig. 2c).

Taken together, the results in the accompanying Comment[2] and the results we present here and in our previous study[1] converge on a model whereby four different TRP channels (TRPV1, TRPM3, TRPA1 and TRPM2) are able to generate heat responses in isolated sensory neurons. Moreover, the small subset of 2-APB-insensitive heat-responsive TKO neurons (Fig. 2a, b) implies the existence of at least one additional heat sensor that is yet to be identified. Most importantly, the collective findings demonstrate that the relative contribution of TRPM2 to the neuronal heat responses crucially depends on the stimulation temperature.

TRPV1, TRPM3 and TRPA1 are functional in intact sensory nerve terminals in the skin, where they initiate pain responses to locally applied chemical agonists or noxious heat[1,4–6]. Mice that lack all three of these channels lack a heat-withdraw reflex[1], indicating that TRPM2 does not incite heat pain signals in vivo. Notably, TRPM2-deficient mice reportedly have a deficit in warmth sensing, and largely lack the ability to discriminate between 33 °C and 38 °C (ref. [3]). There is a disconnect of at least 10 °C between the temperature range in this behavioural assay

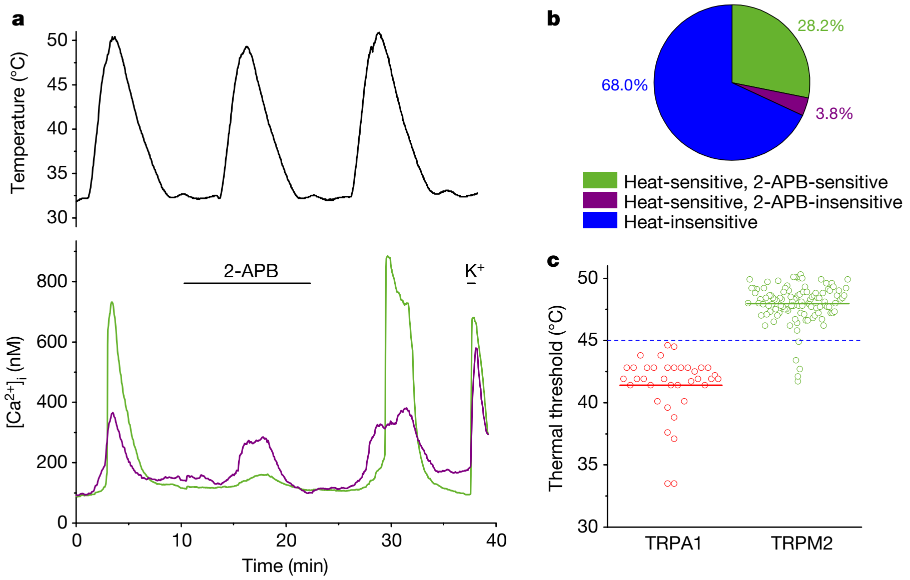

Fig. 2 | High-threshold 2-APB-sensitive heat responses in TKO sensory neurons. a, Responses of TKO DRG neurons to three consecutive heat ramps with a maximum temperature of 50 °C in the presence and absence of 2-APB (25 µM); shown are representative examples of a 2-APB-sensitive and a 2-APB-insensitive heat responder. **b**, Proportion of TKO DRG neurons ($n = 266$ from 2 mice) that exhibit 2-APB-sensitive and 2-APB-insensitive heat responses. **c**, Comparison of the thermal threshold of TRPA1-dependent heat responses (2-APB-insensitive heat responses in DKO$^{M3/V1}$ neurons) and 2-APB-sensitive heat responders in TKO neurons (attributed to TRPM2). The solid line indicates the mean.

and the thermal threshold of approximately 48 °C that is observed for TRPM2-dependent responses in isolated neurons. As pointed out by Vilar et al.[2], unidentified cellular factors that increase the sensitivity of TRPM2 to warmth may become lost during the process of collecting and culturing sensory neurons. The behavioural deficit in non-noxious warmth avoidance in TRPM2-knockout mice may also reflect the role of this channel in the preoptic area, a region of the hypothalamus that is involved in thermal homeostasis and behaviour[7].

Methods

We used 10–14 week-old male *Trpm3*$^{-/-}$*Trpv1*$^{-/-}$ (DKO$^{M3/V1}$) and *Trpa1*$^{-/-}$*Trpm3*$^{-/-}$*Trpv1*$^{-/-}$ (TKO) mice on a C57BL/6J background[1]. Mice were housed in a specific-pathogen-free facility at 21 °C on a 12 h light/12 h dark cycle with unrestricted access to food and water. All experiments using mice were approved by the KU Leuven Ethical Committee Laboratory Animals under project number P265/2015. The procedures for culturing primary sensory neurons and for fura-2-based calcium imaging were identical to those in our original study[1]. The thermal threshold was determined as the temperature at which the second time derivative of the intracellular calcium concentration reached a maximum during a heat ramp.

Reporting summary

Further information on research design is available in the Nature Research Reporting Summary linked to this paper.

Data availability

The data supporting the findings of this study are available within the paper or from the corresponding author upon reasonable request.

1. Vandewauw, I. et al. A TRP channel trio mediates acute noxious heat sensing. *Nature* **555**, 662–666 (2018).
2. Vilar, B., Tan, C.-H. & McNaughton, P. A. Heat detection by the TRPM2 ion channel. *Nature* https://doi.org/10.1038/s41586-020-2510-7 (2020).
3. Tan, C. H. & McNaughton, P. A. The TRPM2 ion channel is required for sensitivity to warmth. *Nature* **536**, 460–463 (2016).
4. Bautista, D. M. et al. TRPA1 mediates the inflammatory actions of environmental irritants and proalgesic agents. *Cell* **124**, 1269–1282 (2006).
5. Caterina, M. J. et al. Impaired nociception and pain sensation in mice lacking the capsaicin receptor. *Science* **288**, 306–313 (2000).
6. Vriens, J. et al. TRPM3 is a nociceptor channel involved in the detection of noxious heat. *Neuron* **70**, 482–494 (2011).
7. Song, K. et al. The TRPM2 channel is a hypothalamic heat sensor that limits fever and can drive hypothermia. *Science* **353**, 1393–1398 (2016).

Acknowledgements We thank all members of the Laboratories of Ion Channel Research and Experimental Gynecology and Obstetrics for comments and discussion. This work was supported by grants from KU Leuven Research Council (C1-TRPLe to T.V), the Research Foundation-Flanders (FWO G.084515N to J.V. and T.V.), the Queen Elisabeth Medical Foundation for Neurosciences (to T.V.), the Belgian Foundation Against Cancer (to J.V. and T.V.) and by the Planckaert-De Waele fund (to J.V.).

Author contributions M.M. and I.V. performed cellular calcium imaging experiments. M.M., I.V. and T.V. analysed the data. J.V. and T.V. supervised the project. T.V. wrote the manuscript with input from all authors. The other authors of the original paper[1] were not involved in the experiments described in this manuscript, but agree with the conclusions.

Competing interests The authors declare no competing interests.

Additional information

Supplementary information is available for this paper at https://doi.org/10.1038/s41586-020-2511-6.

Correspondence and requests for materials should be addressed to J.V. or T.V.

Reprints and permissions information is available at http://www.nature.com/reprints.

nature research

Corresponding author(s): Thomas Voets

Last updated by author(s): Mar 6, 2020

Reporting Summary

Nature Research wishes to improve the reproducibility of the work that we publish. This form provides structure for consistency and transparency in reporting. For further information on Nature Research policies, see Authors & Referees and the Editorial Policy Checklist.

Statistics

For all statistical analyses, confirm that the following items are present in the figure legend, table legend, main text, or Methods section.

n/a	Confirmed	
☐	☒	The exact sample size (*n*) for each experimental group/condition, given as a discrete number and unit of measurement
☐	☒	A statement on whether measurements were taken from distinct samples or whether the same sample was measured repeatedly
☒	☐	The statistical test(s) used AND whether they are one- or two-sided *Only common tests should be described solely by name; describe more complex techniques in the Methods section.*
☒	☐	A description of all covariates tested
☒	☐	A description of any assumptions or corrections, such as tests of normality and adjustment for multiple comparisons
☒	☐	A full description of the statistical parameters including central tendency (e.g. means) or other basic estimates (e.g. regression coefficient) AND variation (e.g. standard deviation) or associated estimates of uncertainty (e.g. confidence intervals)
☒	☐	For null hypothesis testing, the test statistic (e.g. *F*, *t*, *r*) with confidence intervals, effect sizes, degrees of freedom and *P* value noted *Give P values as exact values whenever suitable.*
☒	☐	For Bayesian analysis, information on the choice of priors and Markov chain Monte Carlo settings
☒	☐	For hierarchical and complex designs, identification of the appropriate level for tests and full reporting of outcomes
☒	☐	Estimates of effect sizes (e.g. Cohen's *d*, Pearson's *r*), indicating how they were calculated

Our web collection on statistics for biologists contains articles on many of the points above.

Software and code

Policy information about availability of computer code

Data collection	*Provide a description of all commercial, open source and custom code used to collect the data in this study, specifying the version used OR state that no software was used.*
Data analysis	OriginPro

For manuscripts utilizing custom algorithms or software that are central to the research but not yet described in published literature, software must be made available to editors/reviewers. We strongly encourage code deposition in a community repository (e.g. GitHub). See the Nature Research guidelines for submitting code & software for further information.

Data

Policy information about availability of data

All manuscripts must include a data availability statement. This statement should provide the following information, where applicable:

- Accession codes, unique identifiers, or web links for publicly available datasets
- A list of figures that have associated raw data
- A description of any restrictions on data availability

The data supporting the findings of this study are available within the paper or from the corresponding author upon reasonable request

Field-specific reporting

Please select the one below that is the best fit for your research. If you are not sure, read the appropriate sections before making your selection.

☒ Life sciences ☐ Behavioural & social sciences ☐ Ecological, evolutionary & environmental sciences

For a reference copy of the document with all sections, see nature.com/documents/nr-reporting-summary-flat.pdf

Life sciences study design

All studies must disclose on these points even when the disclosure is negative.

Sample size	Sample sizes are comparable to other previously reported calcium imaging data on neuronal DRGs
Data exclusions	No data were excluded from the analysis
Replication	Data from each figure originate from four individual experiments, performed on different days. All replicas were successful.
Randomization	Samples were not allocated to different groups. Samples used for each figure received the same experimental treatment
Blinding	Investigators were not blinded during the experiment nor the analysis.

Reporting for specific materials, systems and methods

We require information from authors about some types of materials, experimental systems and methods used in many studies. Here, indicate whether each material, system or method listed is relevant to your study. If you are not sure if a list item applies to your research, read the appropriate section before selecting a response.

Materials & experimental systems

n/a	Involved in the study
☒	☐ Antibodies
☒	☐ Eukaryotic cell lines
☒	☐ Palaeontology
☐	☒ Animals and other organisms
☒	☐ Human research participants
☒	☐ Clinical data

Methods

n/a	Involved in the study
☒	☐ ChIP-seq
☒	☐ Flow cytometry
☒	☐ MRI-based neuroimaging

Animals and other organisms

Policy information about studies involving animals; ARRIVE guidelines recommended for reporting animal research

Laboratory animals	10-14 weeks old male DKO mice animals (Trpm3-/- and Trpv1-/-) on a C57BL/6J background were used, and 10-14 weeks old male TKO mice animals (Trpa1-/-, Trpm3-/- and Trpv1-/-) on a C57BL/6J background were used
Wild animals	The study did not make use of wild animals
Field-collected samples	No field-collected samples were used in this study
Ethics oversight	The KULeuven Ethical Committee Laboratory Animals approved all animal experiments under project number P265/2015

Note that full information on the approval of the study protocol must also be provided in the manuscript.